

Society of Automotive Engineers
of China (SAE-China)
International Federation
of Automotive Engineering Societies (FISITA)
Editors

Proceedings of the FISITA 2012 World Automotive Congress

Volume 1: Advanced Internal
Combustion Engines (I)



Lecture Notes in Electrical Engineering

Volume 189

For further volumes:
<http://www.springer.com/series/7818>

Society of Automotive Engineers of China
(SAE-China) · International Federation of
Automotive Engineering Societies (FISITA)
Editors

Proceedings of the FISITA 2012 World Automotive Congress

Volume 1: Advanced Internal
Combustion Engines (I)



 Springer

The Springer logo, consisting of a stylized chess knight piece (horse) facing left, positioned to the left of the word 'Springer' in a serif font.

Editors
SAE-China
Beijing
People's Republic of China

FISITA
London
UK

ISSN 1876-1100
ISBN 978-3-642-33840-3
DOI 10.1007/978-3-642-33841-0
Springer Heidelberg New York Dordrecht London

ISSN 1876-1119 (electronic)
ISBN 978-3-642-33841-0 (eBook)

Library of Congress Control Number: 2012948289

© Springer-Verlag Berlin Heidelberg 2013

This work is subject to copyright. All rights are reserved by the Publisher, whether the whole or part of the material is concerned, specifically the rights of translation, reprinting, reuse of illustrations, recitation, broadcasting, reproduction on microfilms or in any other physical way, and transmission or information storage and retrieval, electronic adaptation, computer software, or by similar or dissimilar methodology now known or hereafter developed. Exempted from this legal reservation are brief excerpts in connection with reviews or scholarly analysis or material supplied specifically for the purpose of being entered and executed on a computer system, for exclusive use by the purchaser of the work. Duplication of this publication or parts thereof is permitted only under the provisions of the Copyright Law of the Publisher's location, in its current version, and permission for use must always be obtained from Springer. Permissions for use may be obtained through RightsLink at the Copyright Clearance Center. Violations are liable to prosecution under the respective Copyright Law.

The use of general descriptive names, registered names, trademarks, service marks, etc. in this publication does not imply, even in the absence of a specific statement, that such names are exempt from the relevant protective laws and regulations and therefore free for general use.

While the advice and information in this book are believed to be true and accurate at the date of publication, neither the authors nor the editors nor the publisher can accept any legal responsibility for any errors or omissions that may be made. The publisher makes no warranty, express or implied, with respect to the material contained herein.

Printed on acid-free paper

Springer is part of Springer Science+Business Media (www.springer.com)

Contents

Part I New Gasoline Direct Injection (GDI), Spark Ignition (SI) and Compression Ignition (CI) Engines and Components

A Novel Mechanism for Piston Deactivation Improving the Part Load Performances of Multi Cylinder Engines	3
F2012-A01-003 Alberto Boretti and Joseph Scalzo	
Novel Crankshaft Mechanism and Regenerative Braking System to Improve the Fuel Economy of Passenger Cars	19
F2012-A01-004 Alberto Boretti and Joseph Scalzo	
Experimental Investigation on Fuel Spray Optimization in Gasoline Direct Injection Engine	45
F2012-A01-006 Bo Jiang, Xiaoliang Pan, Fafa Liu, Chaojun Wang and Xiaochuan Feng	
Improvement of Fuel Economy and Vehicle Performance Through Pneumatic Regenerative Engine Braking Device (Reneged).	55
F2012-A01-012 Yan Zhang, Choyu Lee, Hua Zhao, Tom Ma, Jing Feng, Zhiqiang Lin and Jie Shen	
CAI Combustion of Gasoline and its Mixture with Ethanol in a 2-Stroke Poppet Valve DI Gasoline Engine	67
F2012-A01-013 Yan Zhang, Hua Zhao, Mohammed Ojapah and Alasdair Cairns	

Technologies for the Next Generation of Downsized Gasoline Engines	83
F2012-A01-016	
Paul Freeland, James Taylor, Dave OudeNijeweme, Marco Warth and Bernd Mahr	
Control System Development for Gasoline HCCI Engine Which Based on Heat Management	95
F2012-A01-019	
Jianyong Zhang, Zhen Huang, Qi Yin, Yitao Shen, Lin Chen and Shiliang Lv	
The Effect of Advanced Combustion Control Features on the Performance of a Highly Downsized Gasoline Engine	105
F2012-A01-021	
Karl Giles, Andrew Lewis, Sam Akehurst, Chris Brace and Nick Luard	
HCCI Cycle-by-Cycle Combustion Phase Control Based on Ion Current Technology in GDI Engine	119
F2012-A01-023	
Zhiyong Zhang, Liguang Li and Robert Dibble	
Efforts on Fuel Economy Improvement of 1.3 L TGDI Gasoline Engine	135
F2012-A01-024	
Chen Yang, Yuan Shen, Yi You and Fuquan Zhao	
Development of Two-Stage Turbocharger System with Electric Supercharger	147
F2012-A01-026	
Byeongil An, Hiroshi Suzuki, Motoki Ebisu and Hedeyuki Tanaka	
Effect of the Injection Method in DI CNG Engine on the Flame Propagation Process and Engine Performance	157
F2012-A01-027	
Xuedong Lin, Fang-en Yuan and Ya Huang	
Analysis of the Wear Behavior of Combustion Engine Components Using Radionuclide-Technique	171
F2012-A01-030	
Tamás Gergyé, Mathias Roman Dreyer, Bernhard Kehrwald and Wolfgang Optatzy	

A Super Clean Diesel Vehicle for US LEV-III SULEV Category: Second Report; Advanced A/F Control for NOx Reduction and for SCR Heat Up 183
 F2012-A01-031
 Jean Balland, Bart Schreurs, Michel Peters, Michael Parmentier, Julien Schmitt, Hans Hardam, Masatoshi Yamada, Hiroshi Uike, Toshiharu Takahashi, Yuji Yasui, Eiji Hashimoto, Hideki Matsunaga and Naohiro Sato

Research on Low Temperature Combustion of Homogeneous Charge Induced Ignition (HCII) in a Light-Duty Diesel Engine. 195
 F2012-A01-033
 Chao Yu, Jianxin Wang, Wenbin Yu, Jichun Liu and Dingwei Gao

The Impact of Modified Piston in Two Stroke Engine on Toxic Emissions and Fuel Consumption. 205
 F2012-A01-039
 Jerzy Merkisz, Maciej Bajerlein, Łukasz Rymaniak and Andrzej ZióŁkowski

Multi-Coil High Frequency Spark Ignition to Extend Diluted Combustion Limits 217
 F2012-A01-040
 Shui Yu, Xiaoye Han, Kelvin Xie, Meiping Wang, Liguang Li, Jimi Tjong and Ming Zheng

Multiple Injection and Boosting Benefits for Improved Fuel Consumption on a Spray Guided Direct Injection Gasoline Engine . . . 229
 F2012-A01-041
 Jason King and Oliver Böcker

Gray Cast Iron Cylinder Head Thermal Mechanical Fatigue Analysis 243
 F2012-A01-042
 Jun Li, Pengcheng Wang, Xiaojuan Cui, Kang Li and Rentao Yi

Development of FAW 2.0 L Turbocharged Gasoline Direct Injection Engine 259
 F2012-A01-043
 Jun Li, Jincheng Li, Yanfeng Gong, Haie Chen, MeiLan Qu, Jinyu Liu, Wei Li, Chunyu Xia, Huili Dou, Lei Fu, Xian Li and Tiejun Shen

Faw V6 High Performance Gasoline Engine for Executive Class Car	275
F2012-A01-044 Jun Li, Jincheng Li, Jianlong Song, Jinyu Liu, Weixing Hu, Yingjie Liu, Tao Yan, Linghai Han, Enwei Jiang, Zhengyong Liu and Tian Xia	
Air System Proposal and Testing for a Downsized Two-Stroke Diesel Engine	289
F2012-A01-045 Pavel Brynych, Jan Macek, Luděk Pohořelský, Jean-Charles Ricaud, Pierre-Yves Vallaude, Pascal Tribotté and Philippe Obernesser	
Part II Fuel Injection and Sprays	
Spray Characteristics of a Fuel Injector: A CFD Study	317
F2012-A02-003 J. Suresh Kumar, V. Ganesan, J. M. Mallikarjuna and S. Govindarajan	
Co-Simulation Modeling of High-Pressure Fuel System and Engine Performance System and Control System in Common Rail Diesel Engine	331
F2012-A02-008 Xinglan Xia, Kang Xu, Yin Liu, Min Liu, Shengli Wang and Chao Ma	
Applying a Diesel Spray Model With Different Size Distribution Functions to High Pressure Diesel Spray Cases	351
F2012-A02-011 Emekwuru G. Nwabueze	
Influence of Diesel Surrogates on the Behavior of Simplified Spray Models	361
F2012-A02-012 Jonas Galle and Verhelst Sebastian	
Coupled 1D/2D/3D Modeling of Common Rail Injector Flow and Nozzle Cavitation	375
F2012-A02-013 Valdas Čaika, Peter Sampl and David Greif	
Predicting the Effect of Fuel Path Controllable Parameters on the Performance of Combustion Controlled Diesel Engine	387
F2012-A02-014 Zhijia Yang and Richard Stobart	

Influence of Biocellulose Derived Fuel Blends on Injection Properties	401
F2012-A02-015	
Sorin Sacareanu, Anghel Chiru, Alexandru Bogdan Muntean and Cornel Stan	
Research on the Effect of the Parameters of Common-Rail System on the Injection Rate	411
F2012-A02-016	
Guanjun Yu, Liguang Li, Jun Deng, Zhiqiang Zhang and Lin Yu	
The Influence of Diesel Nozzle Structure on Internal Flow Characteristics	421
F2012-A02-017	
Weidi Huang, Zhijun Wu, Ya Gao, Huifeng Gong, Zongjie Hu, Liguang Li and Furu Zhuang	
Analysis of Internal Flow Characteristics for GDI Injector.	433
F2012-A02-018	
Bowen Zou, Shichun Yang, Kaiguo Li, Jingbo Li and Jungang Liu	
Characteristics of Flash Boiling Fuel Sprays from Three Types of Injector for Spark Ignition Direct Injection (SIDI) Engines	443
F2012-A02-019	
Gaoming Zhang, Min Xu, Yuyin Zhang and David L. S. Hung	
Part III Fuel and Lubricants	
World's First 100 % LPG Long Haul Truck Conversion	457
F2012-A03-008	
Alberto Boretti and Charles Grummisch	
Analysis of Engine Oil Containing MoDTC on the Thermo-Oxidation Engine Oil Simulation Test (TEOST 33C)	475
F2012-A03-009	
Linchun Wang, Liping Wang and Guiyun Li	
Effect of Ash-Less Antioxidants on Fuel Efficiency Retention of PCMO Containing MoDTC	483
F2012-A03-010	
Liping Wang, Linchun Wang, Guiyun Li and Xiaohong Xu	

Semi-Empirical Correlations of Physical and Chemical Delay Period of Diesel-Gasoline Combustion	493
F2012-A03-011	
Wei Jet Thoo, Arman Kevric, Hoon Kiat Ng, Suyin Gan and Paul Shayler	
The Energetic Potential of Engines Fueled with Biomass Derived Products.	503
F2012-A03-016	
Anghel Chiru, Sorin Sacareanu, Ruxandra-Cristina Stanescu, Cornel Stan and Peter Zima	
Fuel Formulation for Future Drive Train Developments.	515
F2012-A03-017	
Máté Zöldy, András Holló, Zoltán Szerencsés, Ferenc Kovács and Róbert Auer	
MoS₂ Production Mechanism of MoDTC	525
F2012-A03-018	
Kazuhiro Umehara, Yukio Tatsumi and Noriyoshi Tanaka	
Research on Cam & Tappet Friction Test Method for Anti-Wear Performance Evaluation of Engine Oil	533
F2012-A03-020	
Chensheng Zou, Shengjun Huang and Jun Yu	
An Experimental Study on Biodiesel Characteristics in a Common Rail Direct Injection Diesel Engine	545
F2012-A03-021	
Jae-Woong Kim, Hyung-Ik Kim, Yung-Jin Kim and Ki-Hyung Lee	
Engine Oil Antioxidant Selection for Delivering Superior Oxidation and Deposit Control Protection	559
F2012-A03-023	
Bo Liu and Vince Gatto	
Experimental Study of Influence of Gasoline Fuel with MMT on Aging Performance of Three-Way Catalyst	571
F2012-A03-024	
Shijin Shuai, Yinhui Wang, Junfeng Chen and Jianhua Xiao	

Part IV After Treatment and Emission Control

Study on Engine Performance Influenced by External Cooled EGR 587
 F2012-A04-004
 Nan Jiang, Jifeng Liu, Xueen Zhang, Xiaojun Cheng, Yang Yang, Jianxian Chen, Gan Chen, Jianguang Zhou, Yongsheng Long and Jie Bai

The Study on the Capacity of NOx Storage-Reduction Catalyst for Lean-Burn Engine 599
 F2012-A04-005
 Jianqiang Wang, Yuan Wang, Shuangxi Liu, Jidong Gao, Jie Ma and Meiqing Shen

New Techniques for Damage Assessment of Diesel Particulate Filters 609
 F2012-A04-006
 Tim Hands and Qiang Li

Dilution Air Refine System Used in Formaldehyde Measurement 625
 F2012-A04-007
 Peipei Dai and Yunshan Ge

A Study of SIC-Nanoparticles Porous Layer Formed on SIC-DPF Wall for Soot Oxidation 633
 F2012-A04-008
 Keita Ishizaki, Shinichi Tanaka, Atsushi Kishimoto, Masamichi Tanaka, Naoki Ohya and Nobuhiro Hidaka

Enhancement of Regeneration Performance by a New Catalyzed DPF 645
 F2012-A04-011
 Takeshi Matsumoto, Takeshi Mori, Satoshi Hirose and Hiroto Takeuchi

Three Way Catalyst Modeling for HEV After Treatment System Design 661
 F2012-A04-012
 Masayuki Tani, Masaaki Kubo and Shigemasa Shimojo

Investigations of Ammonia Emissions from Euro 5 Passenger Cars Over a Legislative Driving Cycle 671
F2012-A04-014
Piotr Bielaczyc, Andrzej Szczotka, Antoni Swiatek and Joseph Woodburn

A Study on Regulated and Unregulated Emissions from a Set of Five Gasoline and Ethanol Fueled Motorcycles. 687
F2012-A04-016
Renato Penteado, Luiz Carlos Daemme, Jürgen Krahl and Fátima Zotin

Strategies to Control Particulate Emissions of Gasoline Direct Injection Engines. 699
F2012-A04-018
Oliver Berkemeier, Klemens Grieser, Kay Hohenboeken, Evangelos Karvounis and K. Moritz Springer

A New Environmental Friendly Zirconium–Titanic–Ceria–Tungsten Mixed Oxides for Durable NH₃-SCR deNO_x Catalysts 715
F2012-A04-022
Jianqiang Wang, Jidong Gao, Jie Ma and Meiqing Shen

Under Actuated Air Path Control of Diesel Engines for Low Emissions and High Efficiency 725
F2012-A04-024
Chris Criens, Frank Willems and Maarten Steinbuch

A Novel Alkali-Catalyzed Alpha-Alumina DPF with High Catalytic Activity and Durability 739
F2012-A04-028
Keisuke Mizutani, Kensuke Takizawa, Hironobu Shimokawa, Shuhei Oe and Naohisa Ohyama

A Super Clean Diesel Vehicle for us LEV III SULEV Category 753
F2012-A04-030
Yuji Yasui, Hideki Matsunaga, Eiji Hashimoto, Naohiro Satoh, Bart Schreurs, Hans Hardam, Masatoshi Yamada and Toshiharu Takahashi

The Application of Nanometric Composite Materials in a Diesel Engine in the Aspect of Improvement of Deep Bed Filtration in a Diesel Particulate Filter 767
F2012-A04-031
Jerzy Merkisz, Pawel Fuc, Piotr Lijewski and Andrzej Ziolkowski

Study on the PM_{2.5} and Ultra Fine PM Characteristics of Diesel Vehicle with DPF Under the Different Driving Conditions 779
 F2012-A04-034
 Mengliang Li, Xiong Chen, Jiguang Wang and Yueyun Xu

The Model Based Control Strategy for an Advanced UREA-SCR System 789
 F2012-A04-036
 Zhi Liu, Hongrong Wang and Yongfu Wang

The NO_x Conversion Efficiency Depending on the Deviation of SCR System Components and Amount of Soot Loading in c-DPF 799
 F2012-A04-041
 Hyoung Sik Kim, Jong Ik Jeon, Chang Eun Choi and Won Kun Kim

Detailed Investigation of Filtration and Regeneration Processes in a Diesel Particulate Filter System 811
 F2012-A04-045
 Seungmok Choi and Kyeong Lee

Part V Flow and Combustion Diagnosis

Simulation of EGR Stratification on Timing-Sequential Regionalized Diesel Combustion. 827
 F2012-A05-004
 Zhaojie Shen, Zhongchang Liu, Jing Tian, Kang Li and Jiangwei Liu

Investigation on the Validity Region of Online Combustion and Torque Models of Gasoline Engines With Retarded Ignition 839
 F2012-A05-007
 Fangwu Ma and Zheng Qu

Development of Real Time Inlet Air Model of Diesel Engine Based on ‘V’ Cycle Mode 853
 F2012-A05-010
 Chao Ma, Yong Hang, Xiaowu Gong and Fu Wang

CFD Simulation and Optical Engine Diagnostics of Mixture Formation Processes in DI Gasoline Engine with Flexible Valvetrain 865
 F2012-A05-011
 Yi Zheng, Po-I Lee, Atsushi Matsumoto, Xingbin Xie and Ming-Chia Lai

Multidimensional CFD Simulation of a Diesel Engine Combustion: A Comparison of Combustion Models	879
F2012-A05-012 Arif Budiyanto, Bambang Sugiarto and Bagus Anang	
 Part VI Engine Design and Simulation	
Dual Fuel CNG-Diesel Heavy Duty Truck Engines with Optimum Speed Power Turbine	897
F2012-A06-003 Alberto Boretti	
The Effect of Intake Port Shape on Gasoline Engine Combustion in Cylinder	921
F2012-A06-006 Xiaodong Chen and Zhangsong Zhan	
Cycle-Resolved Computations of Stratified-Charge Turbulent Combustion in Direct Injection Engines	931
F2012-A06-007 Tomoaki Kubota, Nobuhiro Shinmura and Ken Naitoh	
Research on Torque-Angle Tightening of High Strength Bolt in Internal Combustion Engine	941
F2012-A06-016 Wenfeng Zhan, Jian Wu, Fake Shao and Chuhua Huang	
Computational Study of Soot Entrainment via Thermophoretic Deposition and Crevice Flow in a Diesel Engine	951
F2012-A06-017 Shin Mei Tan, Hoon Kiat Ng and Suyin Gan	
Experiment and Numerical Analysis of Temperature Field of Cylinder Head Based on a GW4D20 Diesel Engine	965
F2012-A06-018 Baixin Zhao, Dingwei Gao, Jingqian Shen, Zheng Zhao, Hao Guan, Gang Liu and Ying Guan	
Development and Validation of a Quasi-Dimensional Model for (M)Ethanol-Fuelled SI Engines	977
F2012-A06-019 Jeroen Vancoillie, Louis Sileghem, Joachim Demuyneck and Sebastian Verhelst	

A Development of Simplified Turbocharger Transient Heat Transfer Simulation Method (First Report) 995
 F2012-A06-020
 Kyung Sub Sung, Kil Min Moon, Dong Ho Chu and Sang Joon Park

A Detailed Analysis of the Initiation of Abnormal Combustion with Reaction Kinetics and Multi-cycle Simulation 1007
 F2012-A06-021
 Michael Heiss, Nikola Bobicic, Thomas Lauer, Bernhard Geringer and Simon Schmuck-Soldan

Modeling of Six Cylinder Diesel Engine Crankshafts to Verify Belt Load Limits 1019
 F2012-A06-022
 Kumar B. Dinesh, M. Nagarajan, Patil Shankar, P. Mahesh and N. Muralitharan

Model-Based Control and Calibration for Air-Intake Systems in Turbocharged Spark-Ignition Engines 1029
 F2012-A06-026
 Kunihiro Suzuki and Seiji Asano

Study on Dynamics Modeling and Analysis of Valvetrains 1043
 F2012-A06-028
 Caiyun Guan, Wenjie Qin and Xiaobo Wang

Mechanistic Modeling in System Engineering: Real-Time Capable Simulation of a TGDI Engine Powered Vehicle. 1055
 F2012-A06-032
 Johann C. Wurzenberger, Titina Banjac, Roman Heinzle and Tomaz Katrasnik

A Multi Zone Spray and Combustion Model for Formation of Polycyclic Aromatic Hydrocarbons and Soot in Diesel Engines. 1069
 F2012-A06-037
 Ali Salavati-Zadeh, Vahid Esfahanian, Asghar Afshari and Mahdi Ramezani

Evaluation of Crank Mounted Fan for TV and Crankshaft First Journal Bearing MOFT Analysis for 3.8 L 4 cyl. Diesel Water Cooled Engine 1079
 F2012-A06-038
 V. Sandeep, Singh Harsumel, D. Patil Shankar, P. Mahesh and N. Muralitharan

1-D Simulation of a Four Cylinder Direct Injection Supercharged Diesel Engine Equipped with VVT Mechanism	1089
F2012-A06-039	
Cristian Soimaru, Anghel Chiru and Daniel Buzea	
In-Cylinder Flow Oriented Intake Port Development of Diesel Engine	1099
F2012-A06-044	
Kang Li, Haie Chen, Wei Li, Huayu Jin and Jiaquan Duan	
The Development of FAW New 3L Diesel Engine	1111
F2012-A06-045	
Fanchen Meng, Jun Li, Fujian Hou, Wenlie Pi and Qun Chen	
Transient Behavior Study of HD Diesel Engine and the Effects of Turbochargers	1123
F2012-A06-047	
Yanbin Shi, Guangyong Zheng, Haie Chen and Lei Wang	
Combustion System Development of Direct-Injection Diesel Engine Based on Spatial and Temporal Distribution of Mixture and Temperature	1133
F2012-A06-048	
Jun Li, Kang Li, Haie Chen, Huayu Jin and Fang Hu	
Part VII Heat Transfer and Waste Heat Reutilization	
Numerical Investigation into the Cooling Process of Conventional Engine Oil and Nano-Oil Inside the Piston Gallery	1151
F2012-A07-002	
Peng Wang, Jizu Lv, Minli Bai, Chengzhi Hu, Liang Zhang and Hao Liu	
Applying Design of Experiments to Develop a Fuel Independent Heat Transfer Model for Spark Ignition Engines	1165
F2012-A07-004	
Joachim Demuyneck, Kam Chana, Michel De Paepe, Louis Sileghem, Jeroen Vancoillie and Sebastian Verhelst	

Performance Analysis of a Thermoelectric Generator Through Component in the Loop Simulation 1179
 F2012-A07-006
 Guangyu Dong, Richard Stobart, Anusha Wijewardane and Jing Li

Analysis and Simulation of Hybrid Electric Turbocharger and Application on ICE and HEV 1193
 F2012-A07-008
 Feng Tian, Guofeng Ren, Shumei Zhang and Lin Yang

New Compact and Fuel Economy Cooling System “SLIM” 1201
 F2012-A07-013
 Junichiro Hara, Mitsuru Iwasaki and Yuichi Meguriya

Influence of Operating Parameters on the Thermal Behavior and Energy Balance of an Automotive Diesel Engine 1213
 F2012-A07-014
 Christian Donn, Daniel Ghebru, Wolfgang Zulehner, Uwe Wagner, Ulrich Spicher and Matthias Honzen

Development of Electric Engine Cooling Water Pump 1229
 F2012-A07-016
 Atsushi Saito and Motohisa Ishiguro

Structure and Parameters Optimization of Organic Rankine Cycle System for Natural Gas Compressor Exhaust Gas Energy Recovery 1235
 F2012-A07-023
 Yongqiang Han, Zhongchang Liu, Yun Xu and Jing Tian

Study on Exhaust Heat Recovery Utilizing Organic Rankine Cycle for Diesel Engine at Full-load Conditions 1243
 F2012-A07-024
 Yan Chen, Yanqin Zhang, Hongguang Zhang, Bin Liu, Kai Yang and Jian Zhang

The Impact of Vehicle Heating Systems on the Energy Consumption Determined Based on the Vehicle Exhaust Emission Tests Under Actual Operating Conditions 1255
 F2012-A07-027
 Jerzy Merkisz, Maciej Bajerlein, Łukasz Rymaniak, Andrzej ZióŁkowski and Dariusz Michalak

Part VIII Emission Standard and International Regulations

Study on a Test Procedure for the NO_x Emission of Heavy Duty Vehicle 1269
 F2012-A08-004
 Mengliang Li, Yueyun Xu, Hui Guo, Maodong Fang and Long Sun

Application Research on SCR Post-Processing System in Non-Electronic Diesel Engine of Vehicles 1281
 F2012-A08-005
 Chenglin Deng, Yingfeng Zhang, Zhengfei Xu and Yan Yu

11L Diesel Engine to Meet China V with Doc 1291
 F2012-A08-007
 Pengcheng Wang, Jiangwei Liu, Fang Hu, Zhenbo Xu, Zhong Wang, Huayu Jin, Liu Yu, Xinchun Niu and Fanchen Meng

Part IX Other

Study the Failure About Spring Which Used on VVA Engine in System 1301
 F2012-A09-004
 Ling Lin, Haizhu He, Jun Mao, Liyun Kang, Maohui Wang, Yang Qiu and Yong He

The Impact of Oil-Based Diamond Nanofluids on Diesel Engine Performance 1313
 F2012-A09-006
 Hao Liu, Minli Bai and Yuan Qu

Citybus Microtrips Classification Using the Data Envelopment Analysis (DEA) Method Applied on Portable Emissions Measurement System (PEMS) Experimental Data 1321
 F2012-A09-007
 Jerzy Merkisz, Arkadiusz Barczak and Jacek Pielecha

Extended Charge Motion Design: CAE Based Prediction of Gasoline Engine Pre-ignition Risk 1333
 F2012-A09-009
 Jens Ewald, Matthias Budde, Bastian Morcinkowski, Rüdiger Beykirch, Adrien Brassat and Philipp Adomeit

Electric Water-Pump Development for Cooling Gasoline Engine 1345
F2012-A09-011
Wenxin Cai, Shenglin Xiong, Lizhi Fang and Shaoping Zha

Two Types of Variable Displacement Oil Pump Development 1357
F2012-A09-014
Dan OuYang, Wenxin Cai, Lei He and Yaojun Li

Considerations on Influencing Factors of Carbon Deposit in Gasoline Direct Injection Engine 1369
F2012-A09-015
Changhoon Oh

Air Intake Modules with Integrated Indirect Charge Air Coolers 1379
F2012-A09-022
Juergen Stehlig, Rene Dingelstadt, Johann Ehrmantraut, Rolf Mueller and James Taylor

Part I
**New Gasoline Direct Injection (GDI),
Spark Ignition (SI) and Compression
Ignition (CI) Engines and Components**

A Novel Mechanism for Piston Deactivation Improving the Part Load Performances of Multi Cylinder Engines

Alberto Boretti and Joseph Scalzo

Abstract Cylinder deactivation has been proposed so far for improved part load operation of large gasoline engines. In all this application, the cylinder deactivation has been achieved keeping the intake and exhaust valves closed for a particular cylinder, with pistons still following their strokes. The paper presents a new mechanism between the piston and the crankshaft to enable selective deactivation of pistons, therefore decoupling the motion of the piston from the rotation of the crankshaft. The reduced friction mean effective pressure of the new technology enables the use of piston deactivation in large engines not necessarily throttle controlled but also controlled by quantity of fuel injected. Results of performance simulations are proposed for V8 gasoline and Diesel engines producing significant savings during light operation, larger for the gasoline but still substantial for the Diesel.

Keywords Internal combustion engines · Fuel economy · Cylinder deactivation · Part load

List of Symbols and Acronyms

A_{cf} Constant term in Eq. (1)
 B Bore
 B_{cf} Peak cylinder pressure term in Eq. (1)

F2012-A01-003

A. Boretti (✉)
Missouri University of Science and Technology, Rolla, MO, USA

A. Boretti
University of Ballarat, Ballarat, VIC, Australia

J. Scalzo
Scalzo Automotive Research Pty Ltd, Melbourne, VIC, Australia

BDC	Bottom dead centre
BMEP	Brake mean effective pressure
BSFC	Brake specific fuel consumption
C_{cf}	Piston speed term in Eq. (1)
CR	Compression ratio
EVC	Exhaust valve closure
EVO	Exhaust valve opening
FMEP	Friction mean effective pressure
IMEP	Indicated mean effective pressure
IVC	Intake valve closure
IVO	Intake valve opening
NEDC	New European driving cycle
P_{max}	Maximum cylinder pressure
Q_{cf}	Quadratic piston speed term in Eq. (1)
RPM	Cycle-averaged engine speed
S	Stroke
S_{fact}	Speed factor in Eq. (1)
TDC	Top dead centre
WOT	Wide open throttle
η_b	Brake thermal engine efficiency
λ	Air-to-fuel equivalence ratio

1 Introduction

Cylinder deactivation is one of the major technologies developed to reduce the fuel consumption of large engines running low loads [1–25]. Cylinder deactivation is usually adopted in large spark ignition engines to run on part (usually half) of its cylinders during light load operation. This technology is aimed to large capacity engines (V6, V8 and V12 engines). For example, a V6 engine will run with all the six cylinders under high load for acceleration, switching to three cylinders under light load for cruising or low-speed drive. Pumping losses are significantly reduced when the engine is operated in the “part-cylinder” mode [1–25].

Cylinder deactivation effectively creates a variable displacement engine, which means you can enjoy the on-demand power of a large capacity engine together with the fuel economy of a smaller engine. Cylinder deactivation is used to reduce the fuel consumption and emissions of an engine during light load operation. In typical light load driving, the throttle valve is nearly closed and the engine needs to work to draw air and pumping losses are high. The use of cylinder deactivation at light load means the throttle valve can be opened further to provide the same power output. This reduces pumping losses and increases pressure in each cylinder. Cylinder deactivation is typically achieved keeping the intake and exhaust

valves closed for a particular cylinder. By keeping the intake and exhaust valves closed, it creates an 'air spring' in the combustion chamber, with the compression and decompression of the trapped exhaust gases having same effect overall. Fuel delivery to the disabled cylinders is also cut-off. The transition between normal engine operation and cylinder deactivation is also smoothed using changes in ignition timing, cam timing and throttle position.

Cylinder deactivation applied to relatively large displacement spark ignition engines improves light load efficiency. The engine displacement is optimally adjusted for load requirements. Power and torque are maximized for high load operation, and fuel economy is maximized for light load conditions.

The first mass-produced vehicle to employ cylinder deactivation was the 1981 Cadillac L62 V8-6-4 engine fitted to the 1981 Cadillac DeVille, Brougham, Eldorado and as an option in the Seville [19–21]. A new valve control system allowed the sequential deactivation of two pairs of cylinders. A series of solenoids were used to release the fulcrum on the intake and exhaust valves rocker arms. The lifters and pushrods continued to operate as normal but the rocker arms sat motionless and the valves remained closed due to valve spring tension. Opposing pairs of cylinders were deactivated rather than a bank of cylinders as done today. When increased engine power was required, the solenoids returned the rocker fulcrums to their normal operating position and full valve operation resumed. Highway fuel consumption was claimed to improve by around 30 percent with cylinder deactivation.

DaimlerChrysler was the first company following Cadillac to apply cylinder deactivation to mass produced cars [19, 20]. The first Mercedes models to appear with cylinder deactivation were the European-spec 1999 CL600, S600 and CL500. These vehicles were powered by either a DOHC 6.0 litre V12 or DOHC 5.0 liter V8. This cylinder deactivation system involved deactivating half of the engine's cylinders and follows the common principle of keeping the intake and exhaust valves closed preventing a fresh air-fuel charge entering the combustion chamber. The valves of each cylinder are kept closed using a pair of arms that replace the conventional engine's roller-type rocker arm. One of these arms follows the cam profile while the second arm connects to the valves. During normal engine operation the two arms are joined by a locking pin. When cylinder deactivation is required, solenoid-controlled oil pressure is used to move the locking pin. This disengages the two arms and the valves remain in their closed position. The system was claimed to improve fuel economy in city driving by 7 % and at steady cruise by 20 %.

Also released by DaimlerChrysler is the 5.7 liter HEMI V8 featuring cylinder deactivation [19, 20, 22]. The system was introduced in the 2004 Chrysler 300C, Dodge Magnum, Dodge Charger, Jeep Grand Cherokee, Dodge Durango, Dodge Ram and Jeep Commander. This cylinder deactivation system is known as MDS (Multi-Displacement System). MDS involves disabling 4 of the HEMI's 8 cylinders. It uses a special set of lifters which are referred to as lost motion devices. To enable 4 cylinder operations, the lifters are fed oil at high pressure. This oil pressure pushes on an internal locking pin that causes the lifter to collapse. Once the lifter collapses,

the camshaft is disengaged from the pushrod and valve and the cylinder is deactivated. The system was claimed to improve fuel economy by 10–20 %.

After its association with the 1981 Cadillac, GM waited until 2004 to re-release cylinder deactivation. The Displacement on Demand (DoD) system [19, 20, 23] was initially released in the GMC Envoy and TrailBlazer SUVs. The Vortec 5.3 liter V8 runs on all 8 cylinders during start-up, idle and heavy acceleration but switches to 4 cylinder mode on light loads. Like the HEMI, the GM system employs specially developed hydraulic lifters for the intake and exhaust valves. The lifters can be collapsed by disengaging an internal locking pin. The locking pin is disengaged using solenoids to alter oil pressure fed into the lifter. When the locking pin is disengaged and the lifter collapses, the camshaft is isolated and the valves remain closed. The system was claimed to improve fuel economy by 5–25 %.

For the 2005 model year, Honda introduced its Variable Cylinder Management (VCM) [19, 20, 24] system to the 3.5 liter Odyssey and 3.0 liter Accord Hybrid V6. Honda's VCM system deactivates an entire bank of cylinders at light load. Deactivation of cylinders is achieved by releasing a synchronizer pin that normally interlocks the cam follower and rocker arms. The synchronizer pin is released using hydraulic pressure which is controlled by a dedicated solenoid. Once the synchronizer pin is released, the cam follower continues to move against the camshaft but the rocker arms and valves remain in a closed position. The Odyssey's J35 3.5 liter VCM engine is claimed to return fuel consumption 10 % percent better than the non-VCM version.

Several other manufacturers have recently incorporated cylinder deactivation in their models. EPA (2008) suggests that CO₂ reductions associated to these systems range from 6 to 8 % [25].

Apart from [4], where a more difficult electro-mechanical system was proposed to deactivate both cylinders and pistons, all the previous solutions of cylinder deactivation actually deactivate just the intake and exhaust valve controlling the flow to and from an engine cylinder but not certainly the pistons. In this work, a novel purely mechanical system is proposed to stop not only intake and exhaust valves of deactivated cylinders, but also their pistons, thus savings significant frictional losses and therefore further increasing the fuel conversion benefits at low loads. In an internal combustion engine, typically the valve train assembly accounts for a 7–15 % of total frictional losses while the piston assembly is responsible for a 45–50 % of the total frictional losses [26–28]. This means that while stopping the motion of the valves of half the cylinders of a V8 may reduce total frictional losses by a few percent, stopping the piston motion in same cylinders may reduce the total frictional losses by 25 %.

In the following sections, the piston motion deactivation mechanism is presented in details. Then engine performance simulations are proposed for a V8 gasoline and a V8 Diesel engine, the first stoichiometric with throttle load control and the second lean burn with load control by quantity of fuel injected to assess the benefits in term of fuel economy of the solution. The major area of concerns of the mechanical design i.e. costs to benefits ratio, complexity, reliability, effectiveness steady state and transient, packaging are considered.

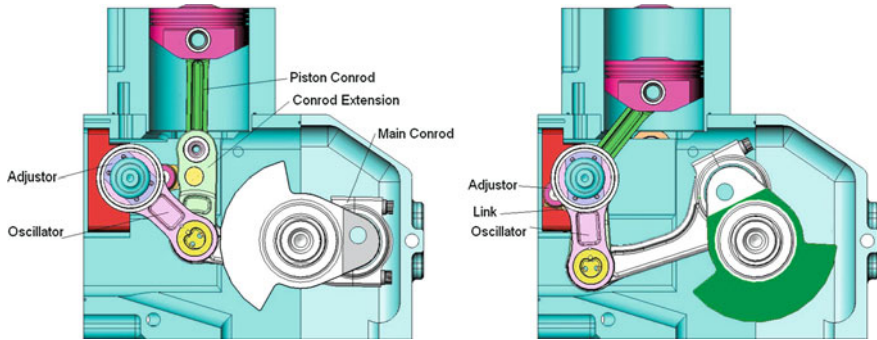


Fig. 1 a Piston deactivation mechanism with piston in the active position. b Piston deactivation mechanism with piston in the deactivated position

2 The Piston Deactivation Mechanism

Figures 1 and 2 presents the principles of operation of the piston deactivation mechanism. Figure 1a shows the piston in the active position, while Fig. 1b shows the piston in the deactivated position. The mechanism is essentially an adjustable four bar mechanism that comprises of an oscillating member positioned on the opposite side of the cylinder relative to the crankshaft, and connects to the crankshaft via the main con-rod. The piston connects to the oscillating mechanism via a small con-rod, a pair of con-rod extensions and a link, keeping the ‘triangular’ shaped mechanism in a fixed position. With this type of mechanism there is always an offset between the cylinder centre line and the crankshaft. This offset is of little consequence in V-type engines. For in-line engines this offset can be relatively small and can be used to advantage for front drive vehicle applications. The piston con-rod angular motion is very small throughout the piston cycle reducing piston side load further contributing to lower piston friction. By rotating the adjusting mechanism relative to the oscillators, the lower pins of the piston con-rod are positioned to be concentric with the rotational axis of the oscillators. In this position the piston motion is reduced to zero while the closed oscillating mechanism remains in synch with the crankshaft at all times.

This relative motion is achieved via the use of a helical spline actuating system (not shown) that allows activation and deactivation of the piston by a small axial movement of an actuator. This can be either hydraulic, a solenoid or other mechanical means. The relative angular motion can also be achieved by an internal hydraulic system that allows deactivation of the internal pistons of multi cylinder in-line engine as well as Vee engines. It is to be noted that all connections are pin jointed and use known conventional technologies and production techniques. Other techniques have been developed to avoid the need for an “offset” con-rod.

Figure 2a–c shows the internals of the typical V-6 engine in the two and four pistons running configurations with an included angle of 25°. The engine length and cylinder off set is not affected allowing standard heads to be maintained.

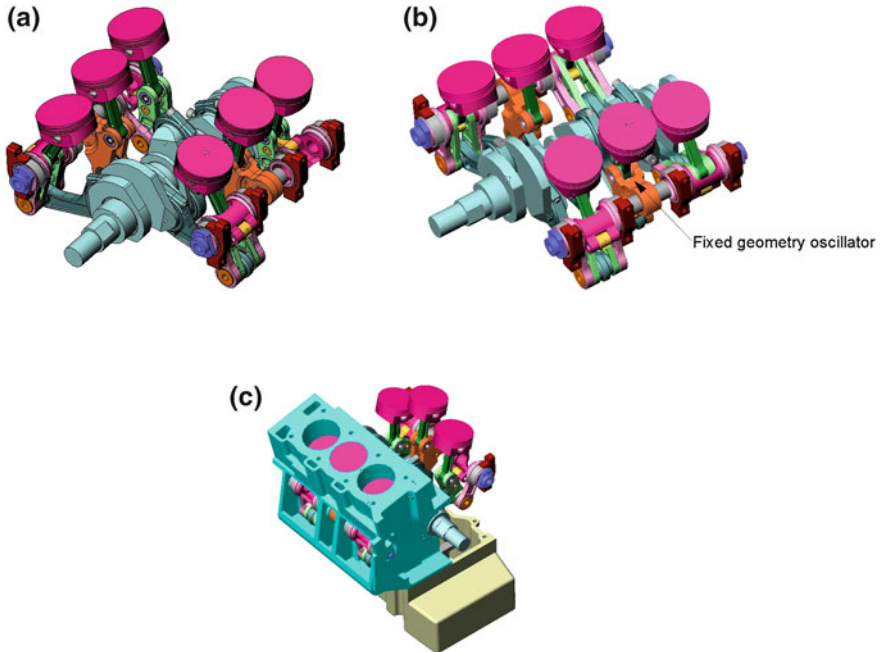


Fig. 2 **a** V6 engine with front two pistons deactivated, **b** V6 engine with front two and back two pistons deactivated, **c** complete V6 assembly

The overall height is much the same however it is wider at the bottom and narrower at the top due to the narrow V-angle. The V6 configuration requires a 1st order moment balance shaft that can be accommodated within the sump area driven at engine speed.

The same principle can be applied to V8 configurations allowing the external four pistons to be deactivated. However it is now possible to deactivate internal pistons in multi cylinder Vee engines. For the first time, the mechanism allows for the separation of the main con-rod from the piston and allows numerous engine configurations from V-types; in-line; boxer type; squat parallel; compact V-3s and many others.

Initial dynamic simulation studies indicate that the inertia and combustion loads on the various connections are within the bearing pressure limits of conventional bearing materials. At the 5000 rpm limit, peak bearing loads at the various pin connections are within the range of 10–25 MPa. However the big end bearing may see peak load of 40 MPa. These loads are highly dependent on the configuration of the mechanism and further refinements will substantially reduce these peak loads. It has also shown that the engine can be balanced to acceptable levels at all piston deactivation modes.

Computational results obtained for a three cylinder engine that has been constructed are presented in Fig. 3a–d. Figure 3a presents the modelled engine, while

Fig. 3b–e respectively shows the balancing characteristics of the engine running at different engine speeds on all pistons, with front or rear piston deactivated or with front and rear piston deactivated. It is to be pointed out that the cylinder deactivation is not intended to be used for heavy loads and high revolutions, but for low loads and low revolutions.

For a V6 engine the peak values are similar but this engine would require a balance shaft to improve the moments balance, running at engine speed in the opposite direction. It is interesting to note that the vertical and horizontal forces are of the 3rd order and within acceptable limits without a balance shaft. Another feature of the mechanism is that on Vee engines the angle between banks of cylinders can be from Zero (Parallel) to 60° without affecting balancing and firing order.

For what concerns friction, as a first approximation friction losses are modelled by using a modified form of the Chen–Flynn correlation [29, 30]. The correlation has a constant term (for accessory friction), a term which varies with peak cylinder pressure, a third term linearly dependent on mean piston velocity (for hydrodynamic friction) and a fourth term quadratic with mean piston velocity (for windage losses). The equation used to calculate the Friction Mean Effective Pressure (FMEP) is given below:

$$FMEP = A_{cf} + \frac{1}{ncyl} \sum_{i=1}^{ncyl} \left[B_{cf} \cdot (P_{cyl})_i + C_{cf} \cdot (S_{fact})_i + Q_{cf} \cdot (S_{fact})_i^2 \right] \quad (1)$$

with: $S_{fact} = \frac{1}{2} \cdot \text{RPM} \cdot S$, A_{cf} , B_{cf} , C_{cf} and Q_{cf} user inputs, P_{max} the maximum cylinder pressure, RPM the cycle-average engine speed and S the cylinder stroke. Each cylinder has its own contribution to the total engine friction based upon its own maximum cylinder pressure and stroke (folded into the speed factor, S_{fact}). A_{cf} is the constant portion of the Chen–Flynn friction correlation, B_{cf} the term which varies linearly with peak cylinder pressure, C_{cf} the term accounting for hydrodynamic friction in the power cylinder which varies linearly with the piston speed and Q_{cf} the term which varies quadratically with the piston speed and accounts for windage losses in the power cylinder. In case of cylinder deactivation, for sake of simplicity we assume the friction losses due to the alternative motions of pistons and valves are proportional to the number of active cylinders. For example, running half cylinder, we assume a reduction of 50 % of the friction losses due to the alternative motions of pistons and valves.

3 V8 Gasoline Engine Results and Discussion

Engine performance simulations have been performed with the WAVE code [29] for a V8 naturally aspirated gasoline engine. This engine, designed in the first half of the nineties, has a displacement of 4.4 L (4,398 cm³), rated power of 210 kW (286 HP) @ 5400 rpm and rated torque of 440 N·m @ 3600 rpm (redline at 6100 rpm). The fuel system is multipoint injection, the engine type is DOHC and

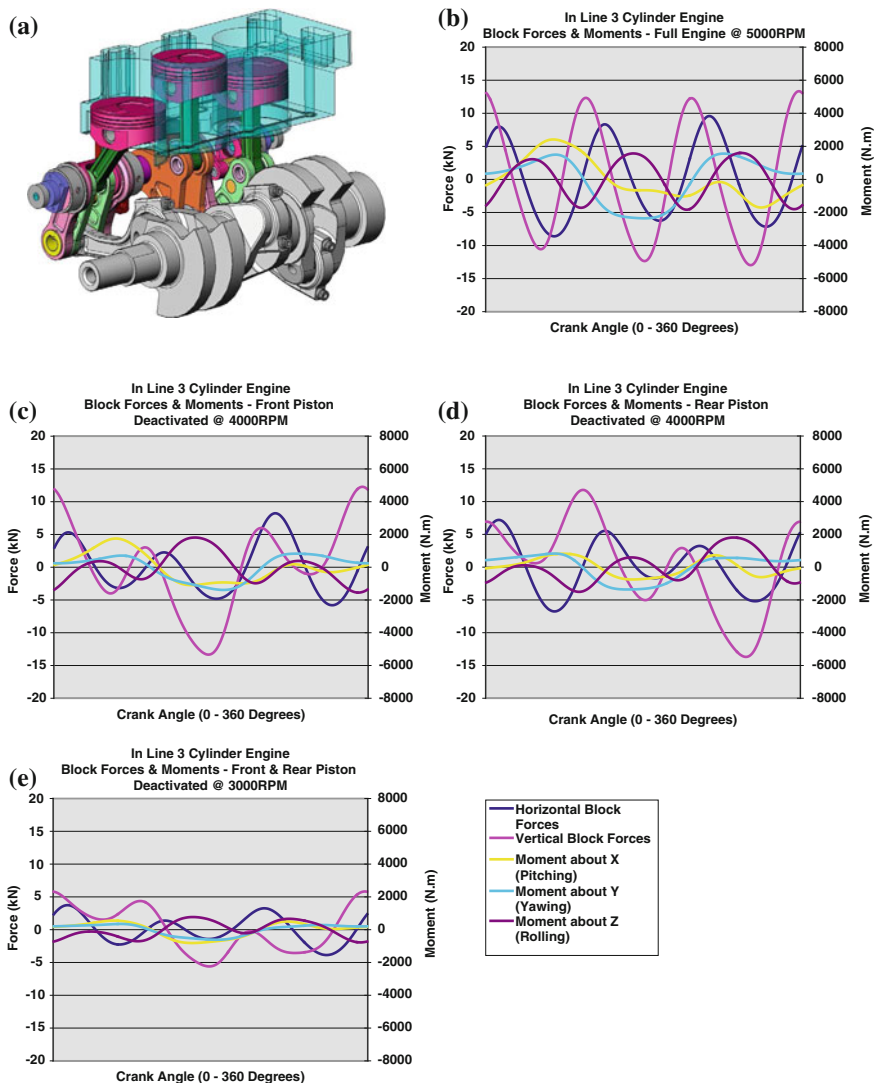


Fig. 3 **a** In-line 3 cylinder engine model, **b** block forces and moments for an in-line 3 cylinder engine, all the cylinder operational, **c** block forces and moments for an in-line 3 cylinder engine, front piston deactivated, **d** block forces and moments for an in—line 3 cylinder engine, back piston deactivated, **e** block forces and moments for an in-line 3 cylinder engine, back and front pistons deactivated

the catalyst is regular. The engine is naturally aspirated. Further details of the engine geometry relevant to the modeling activities are presented in Table 1. The engine is supposed to operate with all the 8 cylinders or with just 4. In this case, both pistons and valves of the inactive cylinders are motionless. The Chen–Flynn

Table 1 4.4 Litre V8 gasoline engine geometry

Displacement per cylinder [litres]	0.5498	No. of intake valve per cylinder	2
Number of cylinders	8	Intake valve dia. [mm]	30
Engine layout	V-8	Intake valve maximum lift [mm]	9
Compression ratio CR	10	IVO [deg]	360 (0)
Bore B [mm]	92	IVC [deg]	622 (+82)
Stroke S [mm]	82.7	No. of exhaust valve per cylinder	2
Connecting rod length [mm]	143	Exhaust valve diameter [mm]	27
Wrist pin offset [mm]	0	Exhaust valve maximum lift [mm]	9
Clearance volume [m ³]	0.6108×10^{-4}	EVO [deg]	140 (-40)
Engine type	S.I.	EVC [deg]	392 (+32)

Table 2 4.4 Litre V8 gasoline engine friction correlation parameters

Engine operation	V8	V8-4
A_{cf} [bar]	0.25	0.375
B_{cf}	0.004	0.006
C_{cf} [Pa-min/m]	500	750
Q_{cf} [Pa-min ² /m ²]	1.5	2.25

correlation parameters are presented in Table 2. The values proposed in the table follow the assumption of 50 % friction losses due to the alternative motions of pistons and valves. Values of baseline constant refer to a standard configuration. It is expected that the proposed mechanism could improve friction losses also when running with all the cylinders.

Figure 4a–c presents the computed brake engine thermal efficiency, brake torque and brake power for operation full load at wide open throttle, while Fig. 5a–c presents the computed friction torque and brake engine thermal efficiency for operation at 1 bar BMEP and brake engine thermal efficiency for operation at 2 bar BMEP with all the cylinders active and just half of them operational. Experimental results for torque and power are also presented in Fig. 4b, c. The values proposed in Table 2 for the engine friction correlation parameters for the V8 operation are obtained by fitting the difference in between the computed Indicated Mean Effective Pressure IMEP and the measured Brake Mean Effective Pressure BMEP.

The engine has WOT top efficiencies around 36 % and top BMEP values exceeding 12 bar. Operation with half the cylinders active reduces the friction losses of about 25 %. This brings a first advantage in the low load operation. Then operation of individual cylinders with double BMEP bring a second advantage in the low load operation. Figure 5b, c show the brake engine thermal efficiency can be increased by values 10–17 % to values 15–22 % for operation at 1 bar BMEP moving from low to high speeds, while improvements are less important but still

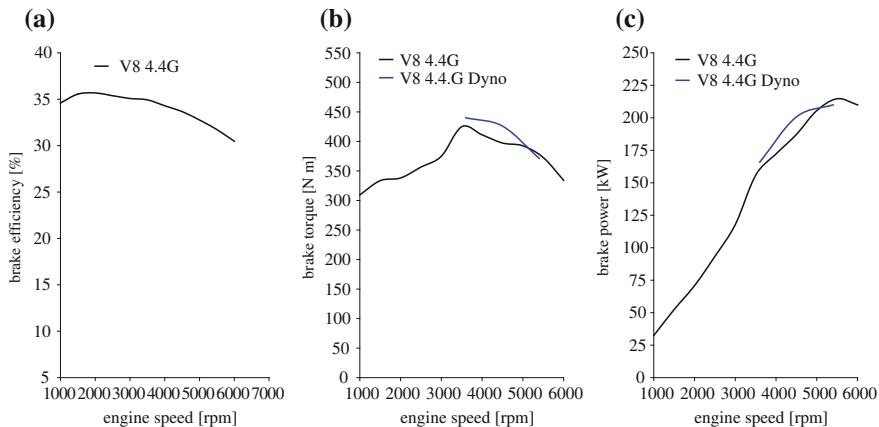


Fig. 4 **a** Brake engine thermal efficiency for operation full load, **b** brake torque for operation full load, **c** brake power for operation full load

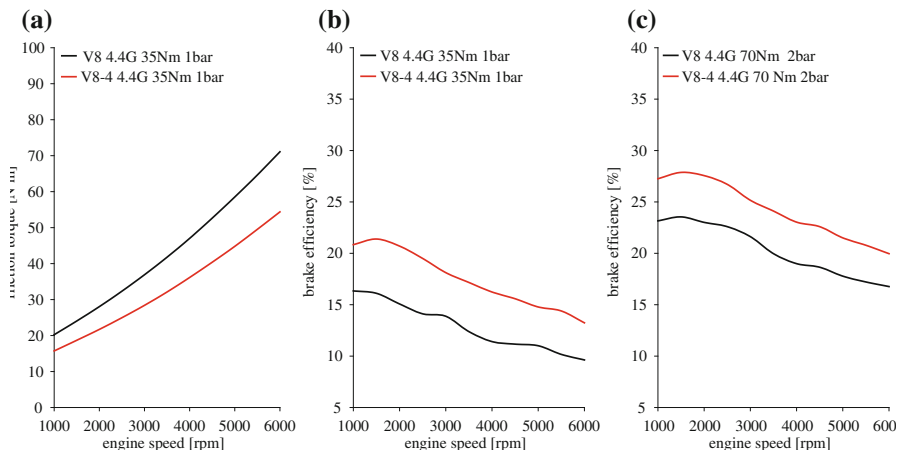


Fig. 5 **a** Friction torque for operation at 1 bar BMEP with all the cylinders or half cylinders active, **b** brake engine thermal efficiency for operation at 1 bar BMEP with all the cylinders or half cylinders active, **c** brake engine thermal efficiency for operation at 2 bar BMEP with all the cylinders or half cylinders active

significant for operation at 2 bar BMEP where brake efficiencies can be increased by values 17–24 % to values 21–27 % moving from low to high speeds. Considering these large naturally aspirated engines are typically working when installed in large sedans covering driving cycles like the city drive portion of the New European Driving Cycle (NEDC) the most of the time around 1 bar BMEP and 1,500 rpm, the fuel economy in these points of operation may be improved by more than 30 % (brake engine thermal efficiency 21.4 vs. 16.1 %, improvement in fuel economy over these operating points 33 %).

Table 3 4 Litre V8 turbo diesel engine geometry

Displacement per cylinder (litres)	0.4877	Number of intake valve per cylinder	2
Number of cylinders	8	Intake valve diameter [mm]	27
Engine layout	V-8	Intake valve maximum lift [mm]	8.5
Compression ratio CR	19.5	IVO [deg]	350 (-10)
Bore B [mm]	84	IVC [deg]	580 (+40)
Stroke S [mm]	88	No. of exhaust valve per cylinder	2
Connecting rod length [mm]	150	Exhaust valve dia. [mm]	24
Wrist pin offset [mm]	0	Exhaust valve max. lift [mm]	8.5
Clearance volume [m ³]	0.2636×10^{-4}	EVO [deg]	140 (-40)
Engine type	C.I.	EVC [deg]	370 (+10)

Table 4 4 Litre V8 turbo diesel engine friction correlation parameters

A_{cf} [bar]	V8	V8-4
B_{cf}	0.35	0.525
C_{cf} [Pa·min/m]	0.004	0.006
Q_{cf} [Pa·min ² /m ²]	400	600
A_{cf} [bar]	1	1.5

4 V8 Diesel Engine Results and Discussion

Engine performance simulations have been performed with the WAVE code [29] for a V8 turbo Diesel engine. This engine, designed in the second half of the nineties, has a displacement of 4.0 L (3,901 cm³), rated power of 175 kW (238 HP) @ 4000 rpm and rated torque of 560 N m @ 1750 rpm. The fuel system is direct injection, the engine type is DOHC and there is no catalyst. The engine is turbocharged with intercooler. Further details of the engine geometry relevant to the modelling activities are presented in Table 3. As in the previous application, the engine is supposed to operate with all the 8 cylinders or with just 4. In this case, both pistons and valves of the inactive cylinders are motionless.

The values of friction loss parameters proposed in the table below follow the assumption of 50 % friction losses due to the alternative motions of pistons and valves as in the previous application. Values of baseline constant refer to a standard configuration. It is expected than the proposed mechanism could improve friction losses also when running with all the cylinders. The values proposed in Table 4 for the engine friction correlation parameters for the V8 operation are obtained by fitting the difference in between the computed Indicated Mean Effective Pressure IMEP and the measured Brake Mean Effective Pressure BMEP.

Figure 6a–c presents the computed brake engine thermal efficiency, brake torque and brake power for operation full load (maximum amount of Diesel fuel injected) while Fig. 7a–c presents the computed friction torque and brake engine thermal efficiency for operation at 1 bar BMEP and brake engine thermal

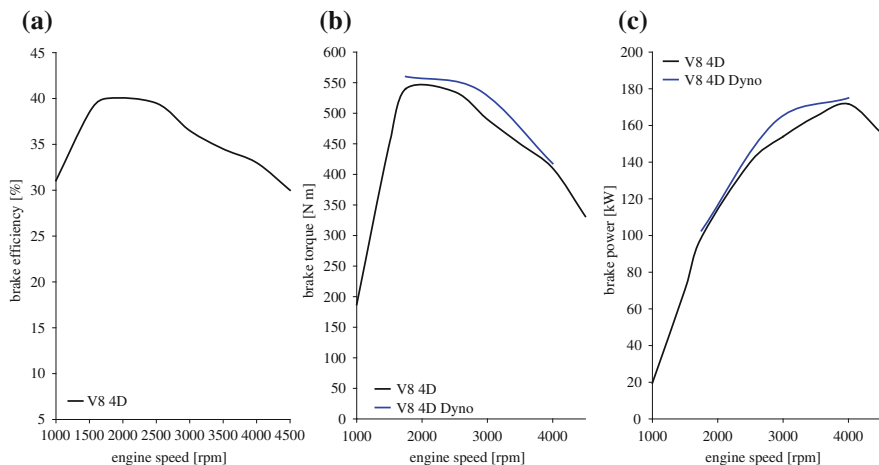


Fig. 6 **a** Brake engine thermal efficiency for operation full load, **b** brake torque for operation full load, **c** brake power for operation full load

efficiency for operation at 2 bar BMEP with all the cylinders active and just half of them operational. Experimental results for torque and power are also presented in Fig. 6b, c.

The engine has full load λ around 1.55, top efficiencies around 40 % and top BMEP values around 18 bar. Operation with half the cylinders active reduces the friction losses of about 25 %. This brings a first advantage in the low load operation. Then operation of individual cylinders with double BMEP bring a second advantage in the low load operation. Figure 7b, c shows the brake engine thermal efficiency can be increased by values 7.5–20 % to values 15–24 % for operation at 1 bar BMEP moving from low to high speeds, while improvements are less important but still significant for operation at 2 bar BMEP where brake efficiencies can be increased by values 14–26 % to values 21–30 % moving from low to high speeds.

Considering these large turbo charged lean burn engines are typically working when installed in large sedans covering driving cycles like the city drive portion of the New European Driving Cycle (NEDC) the most of the time around 1 bar BMEP and 1,500 rpm, the fuel economy in these points of operation may be improved by more than 20 % (brake engine thermal efficiency 23.5 vs. 19.5 %, improvement in fuel economy 21 %).

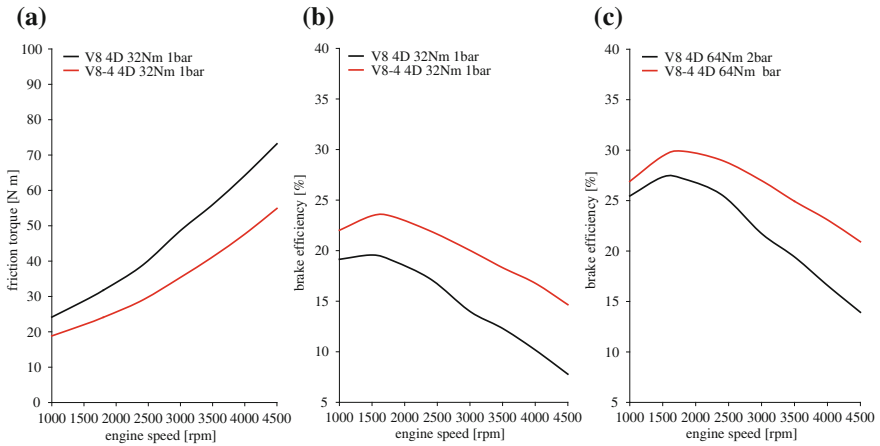


Fig. 7 **a** Friction torque for operation at 1 bar BMEP with all the cylinders or half cylinders active, **b** brake engine thermal efficiency for operation at 1 bar BMEP with all the cylinders or half cylinders active, **c** brake engine thermal efficiency for operation at 2 bar BMEP with all the cylinders or half cylinders active

5 Conclusions

The paper has presented a new mechanism able to deactivate not only valve motion as in standard cylinder deactivation mechanisms, but also piston motion. This brings significant advantages in the low load operation thanks to the additional benefit of reducing friction torque in addition to the operation at higher BMEP of the active cylinders.

Simulations performed for a V8 4.6 litres naturally aspirated gasoline engine show deactivation of half cylinders may improve the fuel economy of operating points typical of driving cycles of more than 30 %. Simulations performed for V8 4 litres turbo charged Diesel engine show deactivation of half cylinders may improve the fuel economy of operating points typical of driving cycles of more than 20 %.

If the benefits in terms of performance appear to be clear, the major area of concerns of the mechanism are costs, complexity, reliability, effectiveness steady state and transient, packaging.

It is obvious that the mechanism is more complex than the conventional piston–conrod–crank arrangement, however all of the connections are pin jointed and are easily pressure lubricated. The reliability should not be any different than a conventional engine given that the bearing pressures can be designed to be within the limits of conventional bearing materials, taking into consideration, the higher inertia loads produced by the mechanism. This will also have a limitation on the maximum engine speed, however engines adopting this approach, are designed for economy rather than very high speed. For the larger engines and in particular

diesel engines, the speed factor is generally not an issue as the mechanism can be designed to operate effectively up to 5000 rpm.

The additional components will also add costs and weight. The components are simple to manufacture in mass production and should not add more than 5–8 % to the cost of the overall engine, and similarly to the overall weight. This additional cost is miniscule compared to the fuel savings and can be recouped in a very short time.

For in-line engines, the packaging is similar to a conventional engine except for a small crankshaft offset that can be a benefit to front drive vehicles. For V type engines the packaging is very similar to a conventional engine and should not create any difficulties.

A prototype three cylinder 1.7 L piston deactivation engine has been completed and will be tested to confirm the effectiveness of the mechanism. This engine is based on one half of a GM Alloytec engine and utilizes the head, pistons and part of the cylinder block. The engine can operate on one, two or three piston.

It is to be noted that all of the nominated mechanisms are covered by granted or applied patents in the major vehicle producing countries.

While the cylinder deactivation is absolutely not a novelty, the way to achieve this deactivation, extended from no motion of valves to no motion of valves and pistons for the selected deactivated cylinders, is certainly an interesting new option offered by this paper.

In addition to the elimination of the piston-ring frictional losses for the deactivated pistons, the piston side force is substantially reduced due to the small conrod-cylinder angle, thus reducing the side load portion of the frictional losses. This reduction of side load friction may well compensate for the mechanism's extra pin joints frictional losses.

References

1. Watanabe E, Fukutani I (1982) Cylinder cutoff of 4-stroke cycle engines at part-load and idle. SAE paper 820156
2. Lucas GG, Hughes J, Manias A (1984) The application of a microprocessor to engine cylinder disablement. SAE paper 845066
3. Zheng Q (2001) Characterization of the dynamic response of a cylinder deactivation valvetrain system. SAE paper 2001-01-0669
4. Kreuter P et al (2001) Meta-CVD system an electro-mechanical cylinder and valve deactivation system. SAE paper 2001-01-0240
5. Leone TG, Pozar M (2001) Fuel economy benefit of cylinder deactivation—sensitivity to vehicle application and operating constraints. SAE paper 2001-01-3591
6. Fiorenza R et al (2003) VVT+Port deactivation application on a small displacement SI 4 cylinder 16 V engine: an effective way to reduce vehicle fuel consumption". SAE paper 2003-01-0020
7. Falkowski A et al (2004) Design and development of the DaimlerChrysler 5.7L HEMI® engine multi-displacement cylinder deactivation system. SAE paper 2004-01-2106

8. Bemman Y-J et al (2005) Passive exhaust system with cylinder deactivation. SAE paper 2005-01-2351
9. Douglas KJ et al (2005) Fuel economy improvement using combined CAI and cylinder deactivation (CDA)—an initial study. SAE paper 2005-01-0110
10. Vinodh B (2005) Technology for cylinder deactivation. SAE paper 2005-01-0077
11. Thompson S, Brechko A (2007) Front end accessory drive vibration control solutions for engines with cylinder deactivation. SAE paper 2007-01-0789
12. Fujiwara M et al (2008) Development of a 6-cylinder gasoline engine with new variable cylinder management technology. SAE paper 2008-01-0610
13. Rebbert M (2008) A new cylinder deactivation by FEV and Mahle. SAE paper 2008-01-1354
14. Maehara H et al (2009) Development of variable cylinder management system for large motorcycles. SAE paper 2009-01-1044
15. Ma Z (2010) Oil transport analysis of a cylinder deactivation engine. SAE paper 2010-01-1098
16. Maehara H et al (2010) Development of variable cylinder management system for large motorcycles—an effective way of reducing output change at switching of the number of working cylinders. SAE paper 2010-32-0117
17. <http://delphi.com/manufacturers/auto/powertrain/gas/valvetrain/cydeac/>. Retrieved 23 July 2010
18. http://www.etsap.org/E-techDS/PDF/T01-Adv_gasol_eng-GS-AD-gct.pdf. Retrieved 23 July 2010
19. http://autospeed.com.au/cms/title_Cylinder-Deactivation-Reborn-Part-1/A_2618/article.html. Retrieved 23 July 2010
20. http://autospeed.com.au/cms/title_Cylinder-Deactivation-Reborn-Part-2/A_2623/article.html. Retrieved 23 July 2010
21. http://en.wikipedia.org/wiki/Cadillac_V8_engine. Retrieved 23 July 2010
22. http://en.wikipedia.org/wiki/Chrysler_Hemi_engine. Retrieved 23 July 2010
23. <http://www.eaton.com/EatonCom/OurCompany/SuccessStories/DisplacementonDemand/>. Retrieved 23 July 2010
24. http://en.wikipedia.org/wiki/Variable_Cylinder_Management. Retrieved 23 July 2010
25. A study of potential effectiveness of carbon dioxide reducing vehicle technologies”, EPA420-R-08-004a, June 2008. <http://www.epa.gov/oms/technology/420r08004a.pdf> Retrieved 23 July 2010
26. Wong VW et al (2010) Low engine friction technology for advanced natural gas reciprocating engines. <http://www.netl.doe.gov/publications/proceedings/03/reciprocating/09-45wong.pdf>. Retrieved July 23, 2010
27. Comfort A (2003) An introduction to heavy-duty diesel engine frictional losses and lubricant properties affecting fuel economy—part I. SAE paper 2003-01-3225. <http://www.dtic.mil/cgi-bin/GetTRDoc?Location=U2&doc=GetTRDoc.pdf&AD=ADA460134>. Retrieved 23 July 2010
28. Fenske G (2009) Impact of friction reduction technologies on fuel economy. In: Chicago chapter meeting of the ‘Society of Tribologists and Lubricated Engineers’, March 2009. <http://www.chicagostle.org/program/2008-2009/Impact%20of%20Friction%20Reduction%20Technologies%20on%20Fuel%20Economy%20-%20with%20VGs%20removed.pdf>. Retrieved 23 July 2010
29. <http://www.ricardo.com/en-gb/Software/Productoffering-description/WAVE1/>. Retrieved 8 January 2010
30. Chen SK, Flynn PF (1965) Development of single cylinder compression ignition research engine. SAE paper 650733

Novel Crankshaft Mechanism and Regenerative Braking System to Improve the Fuel Economy of Passenger Cars

Alberto Boretti and Joseph Scalzo

Abstract Improvements of vehicle fuel economy may be achieved by the introduction of advanced internal combustion engines (ICE) improving the fuel conversion efficiency of the engine and of advanced power trains (PWT) reducing the amount of fuel energy needed to power the vehicle. The paper presents a novel design of a variable compression ratio advanced spark ignition engine that also permits an expansion ratio that may differ from the compression ratio hence generating an Atkinson cycle effect. The stroke ratio and the ratio of maximum to minimum in-cylinder volumes may change with load and speed to provide the best fuel conversion efficiency. The variable ratio of maximum to minimum in-cylinder volumes also improves the full load torque output of the engine. The paper also presents an evolved mechanical kinetic energy recovery system delivering better round trip efficiencies with a design tailored to store a smaller quantity of energy over a reduced time frame with a non-driveline configuration. Simulations show an improvement of full load torque output and fuel conversion efficiency. Brake specific fuel consumption maps are computed for a gasoline engine 2 litres, in-line four, turbocharged and directly fuel injected showings significant fuel savings during light and medium loads operation. Results of vehicle driving cycle simulations are presented for a full size car equipped with the 2 L turbo GDI engine and a compact car with a downsized 1 L turbo GDI engine. These results show dramatic improvements of fuel economies for

F2012-A01-004

A. Boretti (✉)

Missouri University of Science and Technology, Rolla, MO, USA
e-mail: a_boretti@yahoo.com

A. Boretti

University of Ballarat, Ballarat, VIC, Australia

J. Scalzo

Scalzo Automotive Research Pty Ltd, Melbourne, VIC, Australia

similar to Diesel fuel energy usage and CO₂ production. The turbo GDI engines with the alternative crank trains offer better than hybrids fuel economies if the vehicles are also equipped with the novel mechanical kinetic energy recovery system (KERS) recovering the braking energy to reduce the thermal energy supply in the following acceleration of a driving cycle.

Keywords Fuel economy · Carbon dioxide emissions · Environmentally friendly transport · Alternative crank train mechanisms · Variable compression ratio · Atkinson cycle · Mechanical kinetic energy recovery systems

1 Introduction

Direct fuel injection (DI), turbo charging (TC) and downsizing are the major features in stoichiometric gasoline engines currently being adopted to dramatically improve the fuel economy during driving cycles and therefore largely reduce the emissions of carbon dioxide. With these features, stoichiometric gasoline engines still have lower top and part load fuel efficiencies versus higher compression ratio, lean burning Diesel engines being controlled throttle-less by quantity of fuel injected, but have the advantage of much higher power densities for a better downsizing. Furthermore, stoichiometric gasoline engines have very low air pollutant emissions thanks to the well established three-way catalyst technology to meet future emission regulations much easier than Diesel [1, 2]. Major areas of development are variable valve actuation (VVA), exhaust gas recirculation (EGR), variable compression ratio (VCR), and alternative power cycles as well as crank train mechanisms all to boost the fuel conversion efficiency. Aim of this paper is to present a new crank train mechanism enabling variable compression ratio and variable Atkinson effect applied to one of the latest turbo GDI engine.

The Atkinson cycle engine is basically an engine permitting the strokes to be of different lengths. In the Atkinson cycle, the power and exhaust strokes are longer than the intake and compression strokes and should result in better fuel efficiency. Atkinson designed more than one engine to capitalize on this important property. The original Atkinson cycle engine allowed the intake, compression, power, and exhaust strokes of the four-stroke cycle to occur in a single turn of the crankshaft and was designed to avoid infringing patents covering Otto cycle engines. Because of the unique crankshaft design of the Atkinson engine, its expansion stroke can differ from its compression stroke and, with a power stroke longer than its compression stroke the engine can achieve larger thermal efficiency than a traditional engine. The disadvantage of the four-stroke Atkinson cycle engine versus the more common Otto cycle engine is reduced power density. Because a smaller portion of the compression stroke is devoted to compressing the intake charge, an Atkinson cycle engine does not take in as much charge as a similar Otto cycle engine would do. Although the Atkinson's original design is merely a historical curiosity, many

modern engines use unconventional valve timing to produce the effect of a shorter compression stroke/longer power stroke, but a few solutions have also been proposed with a different means of linking the piston to the crankshaft [3–10].

Variable compression ratio is the technology to adjust internal combustion engine cylinder compression ratios to increase fuel efficiency under varying loads [11–25]. Higher loads require lower ratios to be more efficient and vice versa. Variable compression engines allow for the volume above the piston at top dead centre to be changed. For automotive use this needs to be done dynamically in response to the load and driving demands. Output of spark ignition engines is controlled by the quantity of mixture introduced within the cylinder. Occurrence of knock limits the values of compression ratio and boost pressures that can be adopted in turbocharged spark ignition engines or the compression ratio that may be used in naturally aspirated spark ignition engines. If the compression ratio is set to avoid knock in the most unsafe wide open throttle operating points, then especially under light loading, the engine can lack torque. The solution is to be able to vary the compression ratio to suit the reduced amount of charge introduced within the cylinder. In all the variable compression ratio systems, the basic advantage is the one that may follow the increased indicated efficiency of the cycle actually not that much in absolute values (increasing the compression ratio the efficiency increase but the theoretical curve has an asymptotic limit). But obviously small changes in absolute values of efficiency may produce large percentage increases in fuel economy especially at very low loads. Coupling of variable compression ratio to turbo charging may increase the options to achieve better fuel economies through synergies with downsizing and pressure boost.

In the present approach, a new mechanism is defined to change not only the compression ratio but also the length of intake, compression, expansion and exhaust strokes as in Atkinson cycles. This system is employed to improve the light load efficiency as well as to boost the full load output and efficiency seeking operation in every point with same margins to knock and switching to expansion strokes longer than compression strokes when more efficient at light loads. The system is fitted on an in-line four cylinder turbocharged gasoline engine with direct fuel injection.

The idea of using a link of the piston to the crankshaft enabling both variable compression ratio and variable ratio of the expansion to the compression stroke is a novelty, as well as a novelty is the opportunity to use the technique to improve the fuel economy over the full range of loads and speed and boost the power output. Because the efficiency increase are limited (or the efficiency actually starts to reduce) increasing the compression ratio over a certain value, we consider here a maximum CR of 15.5:1 and a minimum CR of 9.5:1. The combustion chamber shape is optimized for the 15.5:1 CR, and the lower CR of 9.5:1 is obtained by increasing the piston to head clearances. The lowest CR operating conditions therefore may suffer from poor combustion chamber shape in addition to the penalty due to the reduced combustion pressure and temperature on the evolution of combustion. With regards to the Atkinson cycle effect, the lengths of the expansion, exhaust, intake and compression strokes differ. The TDC piston positions at the start of the expansion and the intake strokes, as well as the BDC

positions at the start of the exhaust and compression strokes also differ. The in-cylinder volumes in the two TDC and in the two BDC are therefore also different. The CR ratio when the Atkinson cycle is enabled refers to the ratio in between the maximum in-cylinder volume at the end of the expansion stroke and the minimum in-cylinder volume at the beginning of the expansion stroke. We consider here an exhaust to intake stroke ratio 1 (no Atkinson) to 1.05. Because of the variability of the stroke, the two TDC and the two BDC volumes differ. Therefore, CR with Atkinson is conventionally defined as the ratio of maximum to minimum in-cylinder volume over the two strokes.

Regenerative braking is finally considered to reduce the thermal engine energy supply when covering driving cycles characterized by accelerations following decelerations, where part of the propulsive power needed to accelerate the car may be the braking energy recovered with a regenerative device. Mechanical regenerative systems are much more efficient than electric regenerative systems permitting almost double the round trip efficiency wheels to wheels [26–32]. While first generation mechanical kinetic energy recovery systems (KERS) were delivering round trip efficiencies of 70 %, today's second generation mechanical KERS are designed to derive round trip efficiencies of almost 80 % thanks to the better attention to the power and energy storage capacity and times of passenger car applications and the focus on improving the efficiency of the constant variable transmission that was the weak part of the first generation KERS design as well as on the off driveline configuration.

2 Mechanism for Variable Compression and Stroke Ratios

The mechanism is comprised of a four bar mechanism that connects the piston to the crankshaft via an oscillating member, positioned on the opposite side of the cylinder relative to the crankshaft. The oscillating member is supported on an eccentric shaft that rotates at half shaft speed preferably in the same direction as the crankshaft, and driven by the crankshaft. A phasing mechanism between the crankshaft and the eccentric shaft allows relative angular motion between the two shafts. This relative motion allows the compression ratio to be altered continuously between two set limits. The size of the eccentric and angular movement of the control shaft determines the extent of the CR adjustment. The maximum angular phasing is approximately 50° and is determined by the control shaft eccentric offset generally not more than 5 mm.

Another feature of the mechanism is that it has an inherent Atkinson cycle phase as well as an exhaust gas retention phase, at various settings of the CR adjustment. Figure 1 shows the piston in the low and high CR positions at TDC and BDC positions. For a typical small engine in this position, when the engine is at a wider throttle open condition and under heavier loads, the induction stroke may be a little shorter than the compression stroke (by about 2 %) and this may produce a small supercharging effect. In addition, the induction stroke is shorter

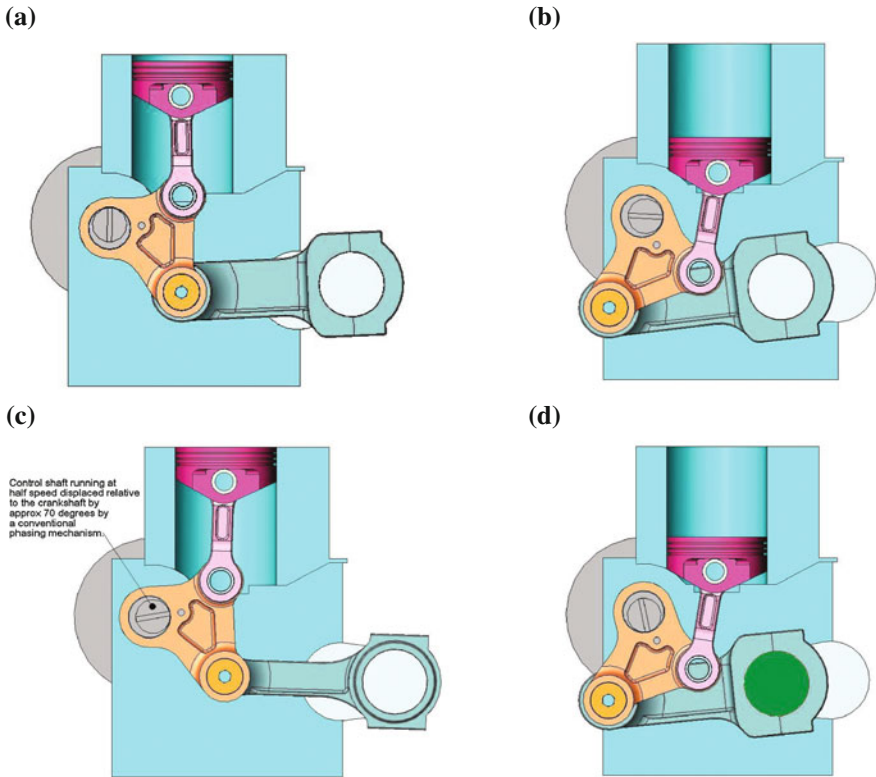


Fig. 1 Low and high CR mechanism at TDC (a, c) and BDC (b, d)

than the power stroke and this may produce an Atkinson effect (by about 11 %). Also there is no exhaust gas retention. In the high CR position, when the engine is at lower throttle settings and under lower loads, the induction stroke may be shorter than the compression stroke (by about 6 %) and this may produce a reasonable supercharging effect as well as the Atkinson effect (by about 11 %). Also there is a small gas retention feature. The mechanism can be configured in all in-line engines and all V type engines by having a control shaft for each bank of cylinders in a back to back arrangement with a common crankshaft. By varying the extent of the eccentricities and the geometric position of the eccentric shaft, a number of different characteristics can be achieved. For example, an Atkinson effect can be achieved in both low and high CR of up to 20 and 10 % respectively.

It is to be noted that all connections are pin jointed and use known conventional technologies and production techniques. The use of a forked piston con-rod allows the main con-rod to be received in the cavity. Initial dynamic simulation studies indicate that the inertia and combustion loads on the various connections are within the bearing pressure limits of conventional bearing materials. It has also

shown that the engine can be balanced to acceptable levels without the need of balance shafts.

The baseline engine the VCR and Atkinson engine is derived from has a compression ratio CR of 9.5:1. This is the value considered as the lower limit in the Variable Compression Ratio mechanism. For the upper limit, the CR of 15.5:1 is selected to provide the best trade-off for performance and complexity of the mechanism. Increasing the compression ratio, the engine brake thermal efficiency increases. However, after a certain value of the compression ratio, these increments became smaller and smaller, and any further increases of the compression ratio does not warrant the increased structural implications.

The occurrence of knock also limits the maximum compression ratio the engine can use. When using higher compression ratios the turbocharger boosting should be reduced to avoid knock by-passing the turbocharger through the waste gate open. Finally, the complexity of the mechanism increases requiring larger variations, and this may bring additional frictional losses. This value $CR = 15.5$ follows a preliminary consideration of all these factors. A better analysis may very likely suggest different upper as well as lower boundaries. The use of a variable compression ratio permits to operate the engine close to a preselected margin to the occurrence of knock. The compression ratio became another parameter to be optimized over the speed and load range as it is for the waste gate opening and the spark timing to deliver knock-free the best engine brake thermal efficiency or maximize the torque and power output.

Combustion chambers designed for a CR of 9.5:1 usually do not need too much of squish areas or crowned pistons. Therefore, if the combustion chamber is designed in the variable compression ratio engine for a CR of 15.5:1, when the reduced compression ratio is obtained by increasing the Top Dead Centre (TDC) piston-to-head clearance, we can expect to move from a combustion chamber better than the 9.5:1 fixed compression ratio one to another similar to the 9.5:1 fixed compression ratio one. We do not expect therefore higher engine out emissions especially higher unburned hydrocarbon emissions when lower compression ratio are used in the variable compression ratio mechanism. The combustion chamber shape may be optimized for the higher CR of 15.5:1, with the lower CR of 9.5:1 being obtained by increasing the piston to head clearances. The lowest CR operating conditions therefore may suffer from the only relatively poorer combustion chamber shape in addition to the penalty due to the reduced combustion pressure and temperature on the evolution of combustion. The mechanism permits to change freely the compression ratio in between the minimum and maximum values. The response to changes in compression ratio is similar to the response to the variable valve timing mechanism in modern engines, however this is a subject that needs to be further investigated. The virtual elimination of piston side thrust due to the small piston conrod angular movement will reduce piston friction and may well compensate for any friction caused by the additional pin connections. This will also need to be further investigated.

With reference to the Atkinson cycle effect, the lengths of the expansion, exhaust, intake and compression strokes differ. The TDC piston positions at the

start of the expansion and the intake strokes, as well as the BDC positions at the start of the exhaust and compression strokes also differ. The in-cylinder volumes in the two TDC and in the two BDC are therefore also different. The CR ratio when the Atkinson cycle is enabled refers to the ratio in between the maximum in-cylinder volume at the end of the expansion stroke and the minimum in-cylinder volume at the beginning of the expansion stroke. We consider here an exhaust to intake stroke ratio 1 (no Atkinson) to 1.05. Because of the variability of the stroke, the two TDC and the two BDC volumes differ. Therefore, CR with Atkinson is conventionally defined as the ratio of maximum to minimum in-cylinder volume over the two strokes.

The major areas of concern of the mechanism are costs, complexity, reliability, effectiveness steady state and transient, packaging. It is obvious that the mechanism is more complex than the conventional piston-conrod-crank arrangement, however all of the connections use pressure lubricated conventional pin joints and the eccentric shaft is hydro-dynamically lubricated. The reliability should not be any different than a conventional engine given that the bearing pressures can be designed to be within the limits of conventional bearing materials, taking into consideration, the higher inertia loads produced by the mechanism. This will also have a limitation on the maximum engine speed, however engines adopting this approach, are designed for economy rather than very high speed. For the larger engines the speed factor is generally not an issue as the mechanism can be designed to operate effectively up to 5000 rpm. In comparison with other known mechanisms used for VCR, this mechanism offers simplicity and compactness. The additional components will also add costs and weight. The components are simple to manufacture in mass production and should not add more than 5 % to the cost of the overall engine, and similarly to the overall weight. This additional cost is small compared to the fuel savings and can be recouped in a very short time by the customer. For in-line engines, the packaging is similar to a conventional engine except for a small crankshaft offset that can be a benefit to front drive vehicles. For V type engines the packaging is very similar to a conventional engine and should not create any difficulties. It is to be noted that patent protection has been applied for the nominated mechanism in all the major vehicle producing countries.

While the variable compression ratio is absolutely not a novelty, the way to achieve this variability and the control of this feature linked to a knock sensor to operate all over the range of engine speeds and loads as close as possible to about same margin to knock is certainly an interesting new option offered by this paper.

3 Engine Results for a 2 Litres Turbo GDI

Engine performance simulations have been performed with the GT-SUITE code [33] for a 2 Litres in-line four cylinder turbo charged gasoline engine. The engine geometry (baseline) is presented in Table 1. For the evaluation of benefits of the alternative crank train mechanisms proposed here, there is no reason to modify the

Table 1 2 L in-line four gasoline engine geometry

Displacement per cylinder (L)	0.4995	Number of intake valve per cylinder	2
Number of cylinders	4	Intake valve diameter (mm)	34.5
Engine layout	L-4	Intake valve maximum lift (mm)	10.05
Compression ratio	10	IVO (deg)	358 (-2)
Bore (mm)	86	IVC (deg)	619 (+79)
Stroke (mm)	86	No. of exhaust valve per cylinder	2
Connecting rod length (mm)	143	Exhaust valve dia. (mm)	31
Wrist pin offset (mm)	0	Exhaust valve maximum lift (mm)	10
Clearance volume (L)	0.0550	EVO (deg)	131 (-49)
Engine type	S.I.	EVC (deg)	384 (+24)

design of the intake to follow the variable compression ratio or the variable compression ratio and stroke ratio. Further refinements of the design of the engine with alternative crank train mechanisms are certainly possible in both the intake and the exhaust systems including pipe lengths and diameters as well as valve lift profiles. These refinements may certainly further improve the brake fuel conversion efficiency as well as the torque output.

A modified form of the Chen–Flynn correlation is used to model friction [33, 34]. The correlation has a constant term (for accessory friction), a term which varies with peak cylinder pressure, a third term linearly dependent on mean piston velocity (for hydrodynamic friction) and a fourth term quadratic with mean piston velocity (for windage losses). Values used for the operation with all the cylinders are presented in Table 2. A_{cf} is the constant portion of the Chen–Flynn friction correlation, B_{cf} the term which varies linearly with peak cylinder pressure, C_{cf} the term accounting for hydrodynamic friction in the power cylinder which varies linearly with the piston speed and Q_{cf} the term which varies quadratically with the piston speed and accounts for windage losses in the power cylinder. The equation used to calculate friction is given below:

$$FMEP = A_{cf} + \frac{1}{ncyl} \sum_{i=1}^{ncyl} \left[B_{cf} \cdot (P_{cyl})_i + C_{cf} \cdot (S_{fact})_i + Q_{cf} \cdot (S_{fact})_i^2 \right] \quad (1)$$

with: $S_{fact} = \frac{1}{2} \cdot RPM \cdot S$, A_{cf} , B_{cf} , C_{cf} and Q_{cf} user inputs, P_{max} the maximum cylinder pressure, RPM the cycle-average engine speed and S the cylinder stroke. Each cylinder has its own contribution to the total engine friction based upon its own maximum cylinder pressure and stroke (folded into the speed factor, S_{fact}).

The proposed parameters for the FMEP correlations are those following fit of experimental data from measured BMEP and IMEP (output of torque meter and pressure cycles recorded through an in-cylinder pressure sensor) of the GDI turbo engine with a traditional crank train. Despite the new crank train it is not expected to have FMEP values differing too much from those defined above, the subject obviously need further investigation, with assembly of an engine now planned for future tests. Only these experiments may provide a better estimation of the FMEP

Table 2 2 L in-line four gasoline engine friction correlation parameters

Engine operation	L-4
A_{cf} (bar)	0.3
B_{cf}	0.006
C_{cf} (bar s/m)	0.09
Q_{cf} (bar s ² /m ²)	0

versus speed and load of the new engine with a novel crank train mechanism never tested before.

Combustion is modeled using a non-predictive Wiebe combustion model [33] with the look up table from the baseline configuration modified by using the predictive Spark Ignition turbulent combustion model [33] simulations. Simulations were performed with either (1) a non-predictive Wiebe function combustion model [33] with angles for 50 % mass fuel burned and angles for 10–90 % combustion tabled versus engine speed and BMEP from data measured for a GDI turbo engine and a traditional crank train, and (2) a predictive Spark Ignition turbulent combustion model [33] calibrated to reproduce these same experimental data. These two models are very well known models adopted in engine performance simulations over several decades with details eventually available in [33]. This latter predictive model properly calibrated was then used to evaluate the combustion performances with variable spark timing for all the engine solutions considered with the novel crank trains. Knock limited maximum brake torque spark timings were obtained performing simulations for different values of the spark advance and monitoring torque and knock index to select the best spark advance within the constraints. It is worth mentioning that in consideration of the fact the predictive spark ignition turbulent combustion model may fail in some points of a full engine map, we decided to run the final simulations with a non-predictive Wiebe function combustion model [33] having angles for 50 % mass fuel burned and angles for 10–90 % combustion tabled versus engine speed and BMEP from data measured for the GDI turbo engine and a traditional crank train corrected for the results of the predictive spark ignition turbulent combustion model for the actual engine crank trains simulated.

The simple knock model is based on the Douaud and Eyzat induction time correlation [33, 35]. The induction time (ignition delay) in seconds is calculated at every time step using the equation:

$$\tau = \frac{0.01869}{A_p} \cdot \left(\frac{ON}{100}\right)^{3.4107} \cdot P^{-1.7} \cdot \exp\left(\frac{3800}{A_T \cdot T}\right) \quad (2)$$

where A_p is a user-entered pre-exponential multiplier, ON the user-entered fuel octane number (RON 95 in the particular application to gasoline), P the cylinder pressure (kg_f/cm²), A_T the user-entered activation temperature multiplier and T the unburned gas temperature (K). In general, this induction time continually decreases as combustion progresses and the unburned zone temperature rises. The

end-gas auto-ignites (knocks) if the induction time is less than the flame arrival time. The model assumes that auto-ignition occurs when:

$$\int_{t_0}^{t_i} \frac{d\tau}{\tau} = 1 \quad (3)$$

where t_0 is the start of end-gas compression, t_i the time of auto-ignition and t the induction time, defined above. This model is used just for a first computational assessment of the advantages of the knock controlled variable compression ratio operation. The model represents major factor affecting knock. At high compression ratios, even before spark ignition, the fuel–air mixture may be compressed to a high pressure and temperature which promotes auto ignition. At low engine speeds the flame velocity is slow and thus the burn time is long, and this results in more time for auto ignition. At high engine speeds, there is less heat loss so the unburned gas temperature is higher which again promotes auto ignition. All these competing effects are included in the Douaud and Eyzat induction time correlation [35] despite their description is quite simplified.

Modeling of turbo charged engines is not a novelty [33] and the baseline turbo charged GDI engine was modeled as usual introducing the measured maps of turbine and compressor, the one of turbine given as reduced speed, reduced mass flow rate, pressure ratio and efficiency, and the one of the compressor given as actual speed and mass flow rate, pressure ratio and efficiency. The waste gate opening was adjusted to achieve stable operation within the mapped area and the measured pressure out of the compressor of the baseline turbo charged GDI engine. With alternative crank trains, the same turbocharger was used and the waste gate opening was adjusted to get the maximum boost pressure compatible with stable operation within the mapped area. The optimization of boost pressure and compression ratio for maximizing the brake fuel conversion efficiency and the brake torque output within the knock limits has not been performed at this stage because the model of the FMEP with the alternative crank train mechanisms need first to be improved to make this latter optimization meaningful. The scope of the paper is to perform a first assessment of the performance increases of the novel crank train mechanisms and not to compute the optimum compression ratio, direct injector injection profile, spark advance and waste gate opening of the turbo-charger coupled to the modified crank trains.

The compression ratio was selected to be the largest possible within the limits of about the same knock resistance of the baseline GDI turbocharged engine in the worst (for knock) operating point. The $CR = 15.5$ value of the maximum compression ratio has been selected conservatively, and the largest values may possibly follow further refinements of the model. However, the relative benefits in terms of efficiency and torque output reduce further increasing the compression ratio, and it may not be reasonable for structural reasons to further boost the compression ratio. For what concerns the Atkinson effect, the selection of the stroke ratio is even more arbitrary than the selection of the maximum compression

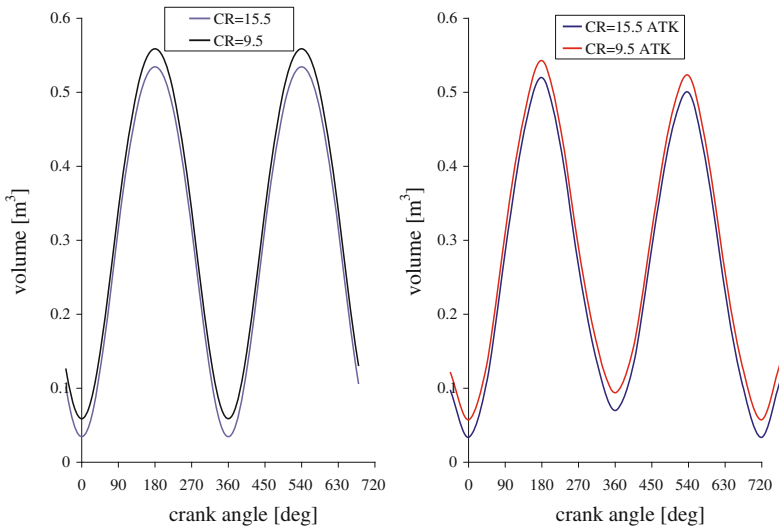


Fig. 2 Volume versus crank angle with different compression ratios without (*left*) and with (*right*) Atkinson effect

ratio described above, and a further optimized stroke ratio may follow a better consideration of the compelling efficiency benefits and structural downfalls making the mechanism more complicated.

Every user of GT-POWER knows that comparing engine concepts differing in the crank train mechanism only may start the activity from a validated engine model and then change only the minimum necessary in the model to avoid biasing the results. The proposed approach has no downfall, with the only exception of the prediction of FMEP. In the knowledge of the Authors, there is no tool able to accurately predict the FMEP of a novel innovative crank train mechanism as the one proposed. Unfortunately the use of the Chen–Flynn correlation [33] with the same parameters of the baseline engine with a standard crank train is the only option to produce an estimation of the FMEP the new mechanisms could have before testing on an engine dynamometer a prototype of an engine with the novel mechanism.

Figure 2 presents the in-cylinder volume over the 4 strokes of the engine for a power stroke. The combustion Top Dead Centre (TDC) is located at 0° crank angle. Figure 2 on left refers to the operation with variable ratio of minimum to maximum volumes but no Atkinson cycle effect, while Fig. 2 on right refers to the operation with the Atkinson cycle effect enabled.

Figure 3 presents the brake mean effective pressure (BMEP), brake efficiency and power for operation full load with the 9.5 compression ratio determined by the necessity to avoid knock around 3,000 Rpm, and for operation with a variable compression ratio higher than that for a similar margin to knock over the full range of engine speeds. The adoption of compression ratios larger than 9.5 improves the

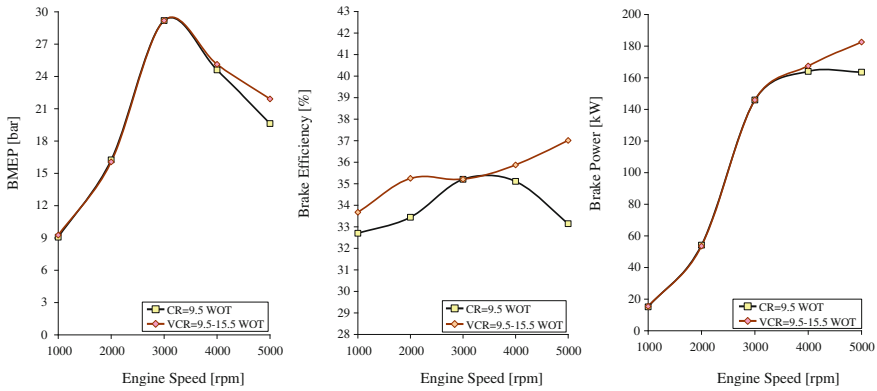


Fig. 3 BMEP, brake thermal efficiency and power with fixed and variable (maximum efficiency limited by knock) compression ratio

fuel conversion efficiency as well as the power and torque outputs especially at the higher speeds. Operating at full load with variable CR, a CR = 9.5 is used at 3,000 rpm, while higher CR are then used above and below this engine speed. At 5,000 rpm, the maximum CR = 15.5 is used, while lower values are adopted at low engine speeds. The 1,000 rpm is more critical for knock than the 2,000 rpm and the knock likeliness for the 4,000 rpm is in between the 3,000 and the 5,000 rpm points.

Figure 4 presents the part load efficiencies operating respectively at 20, 15, 10, 5, 2.5 and 1 bar BMEP with the fixed compression ratio 9.5 and no Atkinson, with a variable compression ratio 9.5–15.5 to maximize efficiency while keeping same safety to knock and no Atkinson, and finally with the variable compression ratio 9.5–15.5 and the Atkinson effect. Operating at part load with variable CR, as a general trend the operating CR is increased when reducing the load, even if some exception occurs especially at higher loads, where a lower CR may occasionally be required to provide same propensity to knock than in a point at higher load and same speed. At 1 bar and 2 bar BMEP load, obviously CR = 15.5 at all the speeds. At full load, the Atkinson effect produces a significant reduction in torque and power outputs. However, starting from high loads there are some points of operation where the engine benefits in terms of fuel conversion efficiency from adoption of the Atkinson effect. The benefits of the variable compression ratio are already evident at high loads. Reducing the loads, the benefits of the variable compression ratio are still significant and the Atkinson effect further improves the fuel conversion efficiency. At 7.5 bar BMEP, the fuel conversion efficiency improves by up to 30 % thanks to the coupled effect of variable compression ratio and Atkinson. At 5 and 2.5 bar BMEP the coupled effect of variable compression ratio and Atkinson almost double the fuel conversion efficiency. At 1 bar BMEP, the fuel conversion efficiency improvements reduce but are still around 30–50 % better.

Due to the use of a same coefficient Chen–Flynn correlation, differences in FMEP are minimal (only the different maximum pressure may introduce

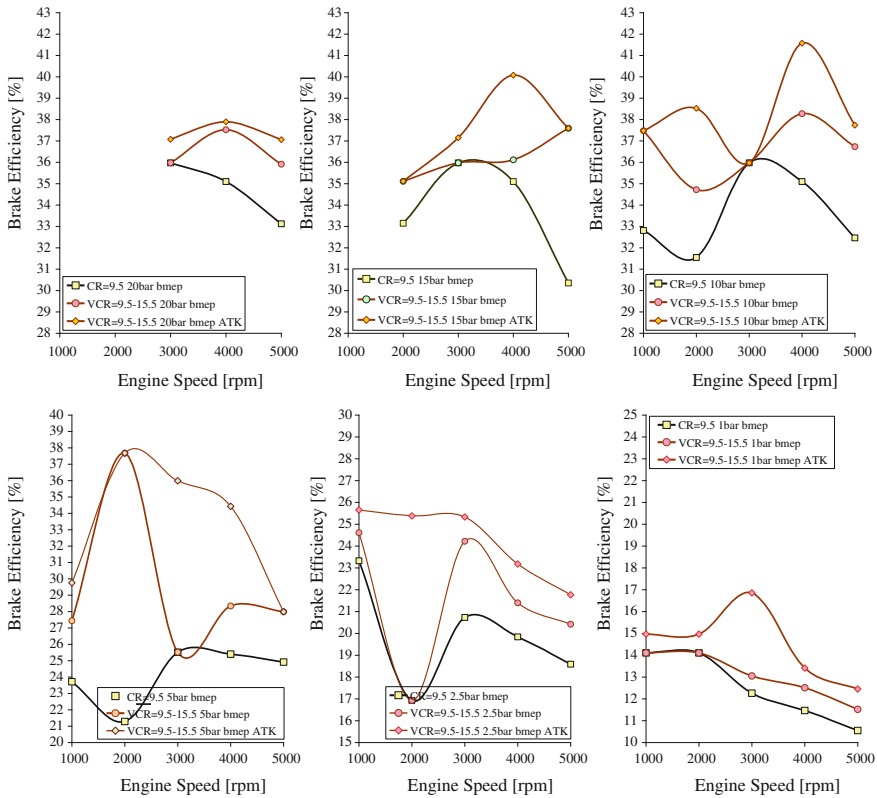


Fig. 4 Brake thermal engine efficiency with fixed compression ratio, variable compression ratio (maximum efficiency limited by knock) and variable compression ratio and Atkinson effect for operation at various BMEP

differences). Changes of pumping mean effective pressure PMEP are certainly much larger but still not the driving force for brake fuel conversion efficiencies and torque outputs. The use of the proposed novel crank train mechanism is not expected to impact too much on the vehicle fuel economy through downsizing, because the increases in FMEP currently neglected what may be significant especially at higher speeds it may offset the increase in IMEP producing the increase in top power output.

4 Kinetic Energy Recovery System

Fuel economy is measured over test cycles. The ECE + EUDC cycle is a test cycle performed on a chassis dynamometer used for emission certification of light duty vehicles in Europe [EEC Directive 90/C81/01]. The entire cycle includes four

Table 3 Main characteristics of ECE and EUDC cycles

Characteristics	ECE 15	EUDC
Distance (km)	$4 \times 1.013 = 4.052$	6.955
Duration (s)	$4 \times 195 = 780$	400
Average speed (km/h)	18.7 (with idling)	62.6
Maximum speed (km/h)	50	120

ECE segments, repeated without interruption, followed by one EUDC segment. Before the test, the vehicle is allowed to soak for at least 6 h at a test temperature of 20–30 °C. It is then started and the emission sampling begins at the same time. This cold-start procedure is also referred to as the New European Driving Cycle (NEDC). The ECE cycle is an urban driving cycle, also known as UDC. It was devised to represent city driving conditions, e.g. in Paris or Rome. It is characterized by low vehicle speed, low engine load, and low exhaust gas temperature. The EUDC (Extra Urban Driving Cycle) segment has been added after the fourth ECE cycle to account for more aggressive, high speed driving modes. The maximum speed of the EUDC cycle is 120 km/h. Table 3 summarizes the parameters for both the ECE and EUDC cycles.

Being cycles characterized by accelerations following decelerations, the energy needed to re-accelerate a car following a deceleration may be reduced recovering the braking energy. This is done more efficiently with mechanical rather than electric systems. It is a fundamental of physics that transforming energy from one form to another inevitably introduces significant losses. This explains why the efficiency of battery-based hybrids is so low for a regenerative braking cycle. When a battery is involved, there are four efficiency reducing transformations in each regenerative braking cycle. (1) Kinetic energy is transformed into electrical energy in a motor/generator, (2) the electrical energy is transformed into chemical energy as the battery charges up, (3) the battery discharges transforming chemical into electrical energy, (4) the electrical energy passes into the motor/generator acting as a motor and is transformed once more into kinetic energy. The four energy transformations reduce the overall level of efficiency. If the motor/generator operates at 80 % efficiency under peak load, in and out, and the battery charges and discharges at 75 % efficiency at high power, the overall efficiency over a full regenerative cycle is only 36 %. The ideal solution is thus to avoid all four of the efficiency reducing transformations from one form of energy to another by keeping the vehicle's energy in the same form as when the vehicle starts braking when the vehicle is back up to speed. This can be done using high-speed flywheels [26–32]. A mechanically driven flywheel system has losses, due to friction in bearings and windage effects, which make it less efficient than a battery-based system in storing energy for long times. Over the much shorter periods required in cut-and-thrust traffic, a mechanically driven flywheel is much more effective, providing an overall efficiency over a full regenerative cycle of more than 70 %, almost twice the value of battery-based hybrids [26–32] (Fig. 5).

Figure 6 presents the prescribed velocity, acceleration, product of velocity by acceleration and kinetic energy of a passenger car covering the NEDC. The

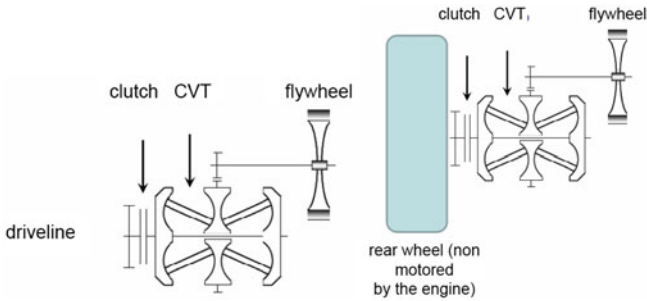


Fig. 5 Schematic flywheel of the driveline (*left*) and a non driveline (*right*) mechanical hybrid systems

acceleration is roughly the propulsive or the braking force per unit mass of the car, while the product of velocity by acceleration is roughly the propulsive or the braking power per unit mass of the car and the kinetic energy difference over a braking event is roughly the theoretically available braking energy. Neglecting the unrealistic final deceleration where the car comes to rest from 120 km/h in few seconds that no European driver has possibly never covered and all the braking energy with a mechanical KERS is lost, a passenger car KERS can be designed to store less energy and with a smaller charging or discharging rate and over a reduced time than a 60 kW–0.4 MJ 2009 F1 strategic KERS or a 120 kW–2 MJ 2014 F1 strategic and fuel economy KERS. The braking power is less than 7.5 W per kg of mass of the car over the city driving sections. This translates in braking powers of only 9 kW for a 1,200 kg car. The braking energy is less than 100 J per kg of mass of the car over the city driving sections. This translates in braking energy to be stored of only 120 kJ for a 1,200 kg car. These and not the F1 figures are the numbers that passenger car KERS must be designed for.

While the first generation KERS for passenger car applications was derived from the 2009 F1 KERS design [36, 37], the second generation KERS is being developed for much smaller braking powers and braking energy than those of 2009/2011 and 2014 F1 KERS. Furthermore, the braking energy is used immediately after stored, and this further facilitates the design. Also focusing on the CVT that is the most inefficient part of the KERS and the off driveline configuration working on the non motored wheels, the latest designs have shown the opportunity to increase the round trip efficiency wheels-flywheels-wheels of a regenerative braking event from the 70 % of the first generation to the 80 % of this second generation while achieving a cost for mass production estimated in the order of 600 \$.

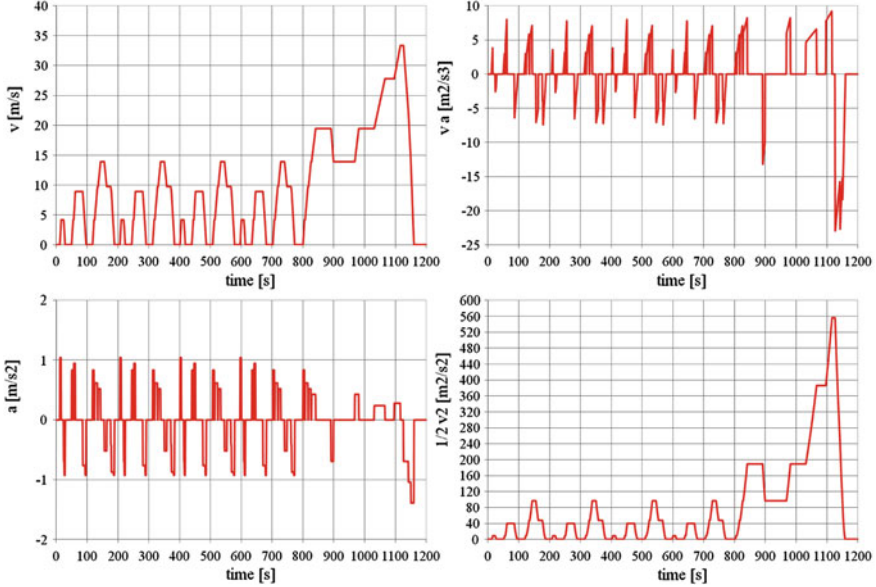
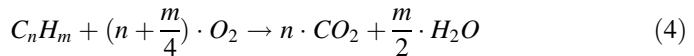


Fig. 6 Prescribed velocity, acceleration, product of velocity by acceleration and kinetic energy of a passenger car covering the NEDC

5 Vehicle Fuel Economy Results

New European Driving Cycle (NEDC) simulations have then been performed with the Lotus Vehicle Simulation software [38]. In order to calculate the vehicle environmental friendliness, we use here the fuel energy in addition to the CO₂ emission as a parameter, and we use two conventional hydrocarbon fuels to replace pump Diesel and Gasoline/Petrol. We use here the GT-SUITE reference fuels “*Diesel no. 2*” for Diesel, and “*Indolene*” for Gasoline/Petrol [33]. For this conventional Diesel fuel, C = 13.5, H = 23.6 and LHV = 43,250 kJ/Kg, while for the conventional Gasoline/Petrol fuel C = 7.93, H = 14.8 and LHV = 43,950 kJ/Kg. Generally, the chemical equation for stoichiometric burning of hydrocarbon in oxygen is:



and CO₂ emissions can be computed accordingly. Average CO₂ emissions from these hydrocarbon fuels are computed considering an oxidation factor to be applied to the carbon content to account for a small portion of the fuel that is not oxidized into CO₂. The IPCC [39] guidelines for calculating emissions inventories require that for all oil and oil products, the oxidation factor is 0.99 (99 % of the carbon in the fuel is eventually oxidized, while 1 % remains un-oxidized). Therefore we assume a production of CO₂ of 2621 and 2332 g/L for Diesel and Gasoline/Petrol fuels respectively.

Table 4 Full size passenger car vehicle parameters

Mass m (kg)	1810
Frontal area A (m ²)	2.250
Drag coefficient C_D	0.298
Rolling tire radius R (m)	0.3160
Transmission	5-speed automatic
Transmission ratios	3.22/2.29/1.55/1.00/0.75
Final drive ratio	2.730

The novel crank train mechanism is obviously expected to produce much larger benefits during the city driving rather than the highway driving, but this obviously depends on the actual engine BMEP and speed operating points covered during the cycle and where they fall in the BSFC versus BMEP and speed map of the engine, ultimately a function of vehicle mass and aerodynamic as well as of gear and final drive ratios just to name the most influencing parameters.

5.1 Full Size Passenger Car

NEDC simulations have been performed first for a large full size passenger car equipped with a 4 litres naturally aspirated gasoline engine and with the new 2 L turbo GDI engine described above. The main vehicle parameters are summarized in Table 4. The model has been validated for the car equipped with the 4 litres naturally aspirated, port fuel injection gasoline engine, with computed fuel economies within a 5 % of measured values. The cold start behaviour is simulated. The vehicle model is then modified to use the brake specific fuel consumption maps of the 2 litres high power density, turbo charged, direct injection, gasoline engines with fixed compression ratio 9.5, variable compression ratio 9.5–15.5, and finally variable compression ratio 9.5–15.5 and Atkinson cycle effects. These changes that could be extremely costly on a real vehicle just require a few modification of the model to obtain fuel economies that are expected not to be that far from actual values. Figure 7 presents the brake specific fuel consumption maps for the 4 litres naturally aspirated gasoline engine and the 2 L GDI turbo charged engines with fixed compression ratio, variable compression ratio and variable compression ratio plus variable stroke ratio.

The 4 L, in-line six cylinders, throttle body controlled, naturally aspirated gasoline engine with maximum power 190 kW and maximum torque 380 N m is replaced by the high tech, 2L, in-line four, turbo charged gasoline engines described above, having 164.0 kW maximum power and 464.5 N m maximum torque with compression ratio 9.5 and 182.6 kW maximum power and 464.5 N m maximum torque with variable compression ratio 9.5–15.5 (the Atkinson effect is active at low loads only). Downsizing permits reduced top speeds but sharpest accelerations with reference to the baseline large gasoline engine. Vehicle, tyre,

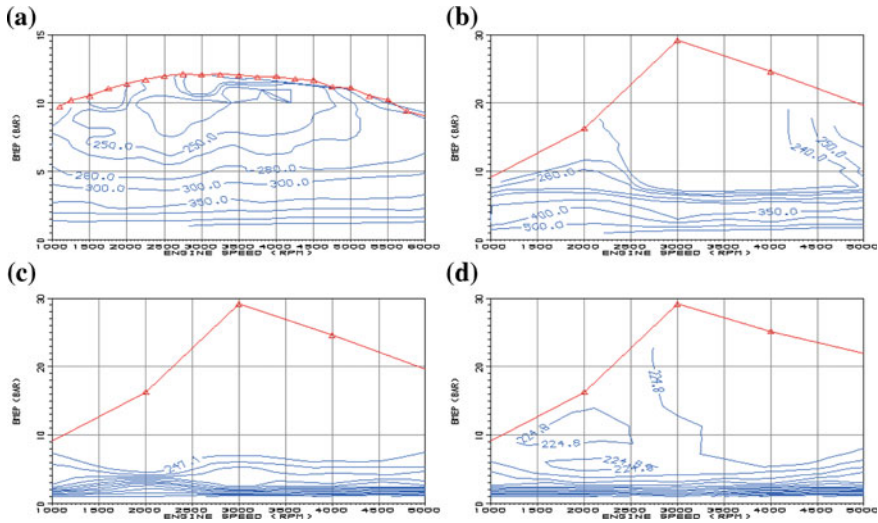


Fig. 7 Brake specific fuel consumption maps for the **a** 4 L naturally aspirated gasoline engine, **b** 2 L GDI turbo charged engines with fixed compression ratio (FCR), **c** 2 L GDI turbo charged variable compression ratio (VCR), **d** 2 L GDI turbo charged VCR and variable stroke ratio (ATK)

driveline and gearbox data are kept constant, as well as the shift strategy, that is the one defined for optimum use of the 4L gasoline engine. During braking the fuel flow rate is the zero BMEP value for the selected speed. The displacement effect shifts up by a factor of $4/2 = 2$ the operating BMEP versus engine speed of the small engines. The naturally aspirated 4L gasoline engine works the most of the time at 1.5 bar BMEP and 1500 rpm, while the turbocharged 2L gasoline engines work the most of the time at 3 bar BMEP and 1500 rpm. Table 5 summarizes the fuel economy results of the different engines.

Despite the shift strategy and that the gear ratios are not optimized for the 2 L engine, all the three high power density TC GDI engines produce dramatic improvements in the fuel usage over the cycle. While the 4 L gasoline engine uses 937 g of fuel to cover over the 1180 s total cycle time the 11.028 km distance travelled of the NEDC for a fuel consumption of 11.3 L per 100 km, the downsized 2 L TC GDI CR = 9.5 engine already provides a 29 % better fuel economy, with 738 g of fuel used in the test or a fuel consumption of 8.9 L per 100 km. The adoption of the variable compression ratio VCR = 9.5–15.5 in the 2 L TC GDI engine boost the fuel economy of an additional 12.7 %, while the further adoption of the Atkinson effect expands of another 5.7 % the fuel economy benefits.

In terms of fuel energy, the small high tech engine 2 L TC GDI VCR = 9.5–15.5 with Atkinson effect therefore uses 53 % less fuel energy than the large naturally aspirated low tech gasoline engine. This is due to the higher BMEP permitted by downsizing (two times larger operating BMEP following the displacement ratio), the larger top brake efficiency permitted by the high compression ratio, the cooling due to

Table 5 Fuel consumption results for the full size passenger car equipped with the 4 L naturally aspirated gasoline and the 2 L Turbo GDI engines with various crank trains

Engine	4 L NA Gasoline	2 L TC GDI CR = 9.5	2 L TC GDI VCR = 9.5-15.5	2 L TC GDI VCR = 9.5-15.5 Atkinson effect
Power train	std	std	std	std
Litres per 100 km	11.33	8.79	7.80	7.38
km per litre	8.83	11.38	12.82	13.55
Grams per km	84.94	65.91	58.50	55.34
MJ of fuel energy per km	3.73	2.90	2.57	2.43
Fuel efficiency improvement (%)	0.00	22.40	31.12	34.85
		0.00	11.24	16.05
			0.00	5.41
Grams of CO ₂ per km	264.2	205.0	181.9	172.1
CO ₂ emission improvement (%)	0.00	22.40	31.12	34.85
		0.00	11.24	16.05
			0.00	5.41

Table 6 Compact size passenger car vehicle parameters

Mass m (kg)	1336
Frontal area A (m ²)	2.2
Drag coefficient C_D	0.298
Rolling tire radius R (m)	0.3080
Transmission	5-speed manual
Transmission ratios	3.778/1.944/1.185/0.816/0.625
Final drive ratio	3.389

direct injection, the high boost from turbo charging partially recovering the exhaust waste heat, the spark advances closer to maximum brake torque, and the larger part load efficiencies due to the factors above plus the variable compression ratio and the Atkinson effect.

5.2 Compact Size Passenger Car

NEDC simulations have then been performed for a small compact size passenger car equipped with a 1.6 L Diesel TDI engine and with a version downsized to 1 L of the new 2 L turbo GDI engine described above. For sake of simplicity, the 1 L turbo GDI engine is supposed to be obtained by scaling all the geometrical parameters to produce (about) the same indicated specific fuel consumption (ISFC) curves versus IMEP and speed but a curve of friction mean effective pressure (FMEP) versus speed improved for the lower mean piston speed (stroke of 68 mm vs. the 86 mm of the 2 L engine). Consequently, if $\Delta FMEP$ is the difference in FMEP computed with the longer and shorter stroke, a very first approximation of the BSFC curves versus BMEP and speed is obtained multiplying by the ratio $IMEP/(IMEP + \Delta FMEP)$, while a very first approximation of the curve of WOT BMEP versus speed is obtained dividing by the ratio $IMEP/(IMEP + \Delta FMEP)$. These results are obviously only preliminary.

The main vehicle parameters are summarized in Table 6. The model has been validated for the car equipped with the 1.6 L TDI Diesel engine, with computed fuel economies within a 5 % of measured values. The cold start behaviour is simulated. The vehicle model is then modified to use the brake specific fuel consumption maps of the 1 L high power density, turbo charged, direct injection, gasoline engines with fixed compression ratio 9.5, variable compression ratio 9.5–15.5, and finally variable compression ratio 9.5–15.5 and Atkinson cycle effects. These changes that could be extremely costly on a real vehicle just require a few modification of the model to obtain fuel economies that are expected not to be that far from actual values.

The 1.6 L TDI Diesel engine with maximum power 81 kW and maximum torque 250 N m is replaced by the high tech, 1 L, in-line four, turbo charged gasoline engines described above, having 82 kW maximum power and 233 N m maximum torque with compression ratio 9.5 and 91.3 kW maximum power and

Table 7 Fuel consumption results for the compact size passenger car equipped with the 1.6 TDI diesel and 0.9 L TGDl gasoline engines with first and second generation mechanical KERS

Engine	1.6 L TDI diesel	1 L TC GDI CR = 9.5 engine	1 L TC GDI VCR = 9.5-15.5	1 L TC GDI VCR = 9.5-15.5	1 L TC GDI VCR = 9.5-15.5	1 L TC GDI VCR = 9.5-15.5
Power train	std	std	std	Atkinson effect std	Atkinson effect KERS 1st generation	Atkinson effect KERS 2nd generation
Round trip regenerative braking efficiency (%)	0	0	0	0	70	80
Fuel lower calorific value (kJ/kg)	43,250	43,950	43,950	43,950	43,950	43,950
Hydrocarbon fuel composition	C = 13.5 H = 23.6	C = 7.93 H = 14.8	C = 7.93 H = 14.8	C = 7.93 H = 14.8	C = 7.93 H = 14.8	C = 7.93 H = 14.8
Fuel density (kg/L)	0.835	0.75	0.75	0.75	0.75	0.75
CO ₂ production (g/L)	2621	2332	2332	2332	2332	2332
Litres per 100 km	3.85	5	4.5	4.22	3.42	3.31
km per Litre	25.98	20.01	22.22	23.68	29.24	30.27
Grams per km	32.14	37.49	33.75	31.67	25.65	24.79
MJ of fuel energy per km	1.39	1.65	1.48	1.39	1.13	1.09
Fuel efficiency improvement (%)	0.00	-18.55	-6.72	-0.14	18.88	21.42
		0.00	9.98	15.52	31.57	33.80
			0.00	6.16	23.99	26.20
			0.00	0.00	19.00	21.42
g of CO ₂ per km	100.9	116.6	105	98.5	79.80	77.13
CO ₂ emission improvement (%)	0.00	-15.60	-4.07	2.35	20.90	23.55
		0.00	9.98	15.52	31.57	33.85
			0.00	6.16	23.99	26.54

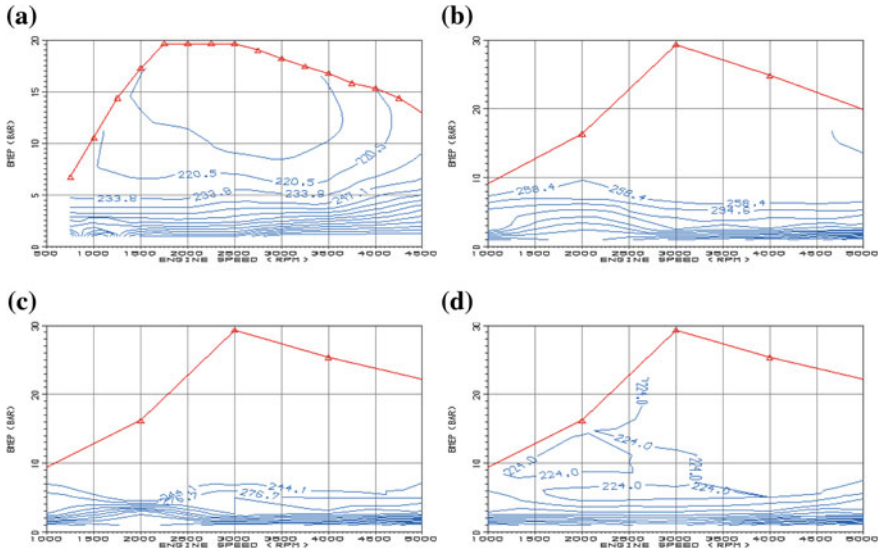


Fig. 8 Brake specific fuel consumption maps for the **a** 1.6 L TDI Diesel, **b** 1 L GDI turbo charged engines with FCR, **c** 1 L GDI turbo charged engines with VCR and **d** 1 L GDI turbo charged engines with VCR and ATK

233 N m maximum torque with variable compression ratio 9.5–15.5 (the Atkinson effect is active at low loads only). Downsizing permits same top speeds and sharpest accelerations with reference to the baseline Diesel engine because of the low power density of lean burn Diesel. Vehicle, tyre, driveline and gearbox data are kept constant, as well as the shift strategy, that is the one defined for optimum use of the 1.6 TDI Diesel engine. During braking the fuel flow rate is the zero BMEP value for the selected speed. The displacement effect shifts up by a factor 1.6 the operating BMEP versus engine speed of the small engines. Table 7 summarizes the fuel economy results of the different engines.

Despite the shift strategy and the gear ratios are not optimized for the 1L engine, the high power density TC GDI engines with VCR and with and without Atkinson effect produce fuel usages over the cycle comparable to Diesel. The adoption of the variable compression ratio $VCR = 9.5\text{--}15.5$ and Atkinson effect in the 1 L TC GDI engine boost the fuel economy to values similar to those of best available Diesel engines. Despite the Diesel has much better top as well as part load fuel efficiencies for the lean combustion and the throttle-less load control by quantity of fuel injected, the downsizing of the higher power density gasoline engine and the part load benefits of VCR and Atkinson effect even in an engine controlled by throttle and stoichiometric produce about same fuel energy economy over the NEDC and about same CO_2 production. Figure 8 presents the brake specific fuel consumption maps for the 1.6 L TDI Diesel engine and the 1 L GDI turbo charged engines with fixed compression ratio, variable compression ratio and variable compression ratio plus variable stroke ratio.

Engine performance and vehicle fuel economy simulations are very well established approaches; with very well known abilities to well predict engine and chassis dynamometer results for engines and power train not differing too much from those used for the preliminary validation of the model. The baseline model for the engine, with turbo charging and GDI and a traditional crank train, and the baseline model for the vehicle, with the measured BSFC versus BMEP and speed of the engine above as an input and the traditional power train, are validated models. Changes in the crank train mechanism that concerns the engine and in the kinetic energy recovery system that concern the vehicle power train are not expected to reduce too much the reliability of the results, even if their modeling certainly introduces the uncertainties only of the final engine dynamometer and chassis vehicle dynamometer tests of the prototypes engine and vehicle may dissipate.

6 Conclusions

The paper has presented a new mechanism able to change the compression ratio of the engine as well as the ratio between the compression and the expansion strokes. This brings advantages over the full range of loads and speeds. Operation with the maximum compression ratio permitted by knock improves the fuel efficiency over the full range of loads and also increases the maximum power output. Addition of the Atkinson effect helps to further boost the medium to low load efficiency.

Simulations performed for a 2 L turbocharged GDI engine show that adjusting the compression ratio from the low speed knock limited value of $CR = 9.5:1$ to achieve about same margin to knock all over the range of engine speeds and loads up to a CR of $15:1$, the maximum power is increased by 11 % and the maximum brake efficiency by 3.3 %, while operating at 1 bar BMEP and 2 bar BMEP fuel conversion efficiencies are up to 10 % better. The benefits of the variable compression ratio increase reducing the loads. The Atkinson effect further improves the fuel conversion efficiency especially at very low loads.

At 7.5 bar BMEP, the fuel conversion efficiency improves of up to 30 % thanks to the coupled effect of variable compression ratio and Atkinson. At 5 and 2.5 bar BMEP the coupled effect of variable compression ratio and Atkinson almost double the fuel conversion efficiency. At 1 bar BMEP, the fuel conversion efficiency improvements reduce but are still around 30–50 % better.

Replacing a 4 L naturally aspirated gasoline engine of a full size car with the 2 L TC GDI engines produce dramatic improvements in the fuel usage over the NEDC cycle. While the 4 L gasoline engine has a fuel consumption of 11.3 Litres per 100 km, the downsized 2 L TC GDI $CR = 9.5$ engine provides a 29 % better fuel economy, with a fuel consumption of 8.9 L per 100 km. The adoption of the variable compression ratio $VCR = 9.5–15.5$ in the 2 L TC GDI engine boost the fuel economy of an additional 12.7 %, while the further adoption of the Atkinson effect provides another 5.7 % to the fuel economy benefits.

Replacing a 1.6L TDI Diesel engine of a compact size car with the 1L TC GDI engines produce about same fuel energy usage and CO₂ production with variable compression ratio VCR = 9.5–15.5 and the Atkinson effect, with a fuel economy of 4.2 L of gasoline fuel and less than 100 g of CO₂ per km.

Further improvements of the engine fuel conversion efficiency is achieved by the adoption of fully variable valve actuation (VVA) and exhaust gas recirculation (EGR) to control the load throttle less thus reducing the pumping losses as well as to improve the efficiency of the combustion process changing speed and load [40, 41].

Significant improvements of the vehicle fuel economy may be further enhanced by the adoption of a purely mechanical flywheel based Kinetic Energy Recovery System (KERS) [36, 37] dramatically reducing the amount of energy to be delivered by the thermal engine. The 1 L TC GDI engine with variable compression ratio and Atkinson effect installed on a compact car may permits when coupled to a first generation kinetic energy recovery system a fuel economy of 1.13 MJ of fuel energy per km and tailpipe CO₂ emissions of 79.8 g of CO₂ per km.

The fuel economy and the tailpipe CO₂ emissions may be further reduced to 1.09 MJ of fuel energy per km and 77.1 g of CO₂ per km by moving to second generation KERS specifically developed for the low power and low energy storage and short times of the passenger car applications, where also focusing on the CVT and using non driveline configurations the round trip efficiencies of the regenerative braking process are currently projected to the 80 % mark from the previous 70 %.

In terms of CO₂ reduction, an evolutionary breakthrough may be the eventual replacement of fossil fuels like gasoline with bio fuels like ethanol being almost carbon neutral in the short term rather than over geological ages. The bio ethanol also has the advantage of the increased resistance to knock especially in a direct injection engine, thanks to the better octane number as well as the larger heat of vaporization, translating in higher compression ratios, spark timings closer to maximum brake torque and higher boost pressures than gasoline, for better fuel conversion efficiencies and power density the latter permitting further downsizing [40, 41].

References

1. EPA report (2010) A study of potential effectiveness of carbon dioxide reducing vehicle technologies. <http://www.epa.gov/oms/technology/420r08004a.pdf>. Retrieved 1 Sept 2010
2. EERE report (2010) 2009 Advanced combustion engine R&D annual report. http://www1.eere.energy.gov/vehiclesandfuels/pdfs/program/2009_adv_combustion_engine.pdf. Retrieved 1 Sept 2010
3. Saunders RJ et al (1989) Variable valve closure timing for load control and the Otto Atkinson cycle engine. SAE paper 890677
4. Blakey SC et al (1991) A design and experimental study of an Otto Atkinson cycle engine using late intake valve closing. SAE paper 910451
5. Boggs DL et al (1995) The Otto–Atkinson cycle engine–fuel economy and emissions results and hardware design. SAE paper 950089

6. Cao Y (2007) Thermodynamic cycles of internal combustion engines for increased thermal efficiency, constant-volume combustion, variable compression ratio, and cold start. SAE paper 2007-01-4115
7. Gheorghiu V (2009) CO₂-emission reduction by means of enhanced thermal conversion efficiency of ice cycles. SAE paper 2009-24-0081
8. Gheorghiu V (2010) CO₂-emission reduction by means of enhancing the thermal conversion efficiency of ice cycles. SAE paper 2010-01-1511
9. Shkolnik N et al (2010) High efficiency hybrid cycle engine. SAE paper 2010-01-1110
10. Akihisa D et al (2010) Research on improving thermal efficiency through variable super-high expansion ratio cycle. SAE paper 2010-01-0174
11. Wallace WA, Lux FB (1964) A variable compression ratio engine development. SAE paper 640060
12. Basiletti JC, Blackburne EF (1966) Recent developments in variable compression ratio engines. SAE paper 660344
13. Sobotowski R et al (1991) The development of a novel variable compression ratio, direct injection diesel engine. SAE paper 910484
14. Pischinger S et al (2001) Variable compression in SI engines. SAE paper 2001-24-0050
15. Mender C, Gravel R (2002) Variable compression ratio engine. SAE paper 2002-01-1940
16. Schwaderlapp M et al (2002) Variable compression ratio—a design solution for fuel economy concepts. SAE paper 2002-01-1103
17. Moteki K et al (2003) A study of a variable compression ratio system with a multi-link mechanism. SAE paper 2003-01-0921
18. Roberts M (2003) Benefits and challenges of variable compression ratio (VCR). SAE paper 2003-01-0398. <http://www.prodrive.com/up/vcr.pdf>. Retrieved 2 Aug 2010
19. Rabhi V, Beroff J (2004) Study of a gear-based variable compression ratio engine. SAE paper 2004-01-2931
20. Rabhi D et al (2005) Gear design and dimensioning study for a variable compression ratio engine. SAE paper 2005-01-3131
21. Rosso P et al (2006) A variable displacement engine with independently controllable stroke length and compression ratio. SAE paper 2006-01-0741
22. Tanaka Y et al (2007) A study of a compression ratio control mechanism for a multiple-link variable compression ratio engine. SAE paper 2007-01-3547
23. Ishikawa S et al (2009) Advanced design of variable compression ratio engine with dual piston mechanism. SAE paper 2009-01-1046
24. Kadota M et al (2009) advanced control system of variable compression ratio (VCR) engine with dual piston mechanism. SAE paper 2009-01-1063
25. Heywood JB (2005) Improving the spark-ignition engine. In: 2005 ERC symposium, Madison, WI (US), June 2005. <http://www.erc.wisc.edu/documents/symp05-Heywood.pdf>. Retrieved 2 Aug 2010
26. Stone R (2009) Full-toroidal variable drive transmission systems in mechanical hybrid systems—from Formula 1 to road cars. In: CTI symposium and exhibition: automotive transmissions, Berlin, Germany, December 2009. http://www.torotrak.com/Resources/Torotrak/Documents/Mech%20hybrid%20paper_CTI%20Berlin09.pdf. Retrieved 11 November 2011)
27. Body W, Brockbank C (2009) Simulation of the fuel consumption benefits of various transmission arrangements and control strategies within a flywheel based mechanical hybrid system. In: VDI transmissions in vehicles conference and exhibition, Friedrichshafen, June 2009. <http://www.torotrak.com/Resources/Torotrak/Documents/VDI%20Friedrichshafen%202009.pdf>. Retrieved 11 November 2011)
28. Brockbank C, Greenwood C (2009) Full-toroidal variable drive transmission systems in mechanical hybrid systems—from Formula 1 to road vehicles. In: CTI symposium and exhibition: automotive transmissions, Detroit, May 2009. <http://www.torotrak.com/Resources/Torotrak/Documents/CTI%20Detroit%20Paper%202009.pdf>. Retrieved 11 November 2011)

29. Brockbank C (2009) Application of a variable drive to supercharger and turbo compunder applications. SAE paper. 09PFL-0925. http://www.torotrak.com/Resources/Torotrak/Documents/SAE_WC_2009_09PFL-0925_Variable_Drive_Boost_System.pdf. Retrieved 11 November 2011)
30. Brockbank C, Cross D (2009) Mechanical hybrid system comprising a flywheel and CVT for motorsport and mainstream automotive applications. SAE paper 09PFL-0922. http://www.torotrak.com/Resources/Torotrak/Documents/SAE_WC_2009_09PFL-0922_KERS.pdf. Retrieved 11 Nov 2011)
31. Brockbank C, Greenwood C (2008) Full-toroidal variable drive transmission systems in mechanical hybrids—from Formula 1 to road vehicles. In: CTI innovative automotive transmissions conference and exhibition, Berlin, December 2008. http://www.torotrak.com/Resources/Torotrak/CTI_Berlin_2008.pdf. Retrieved 11 Nov, 2011
32. Brockbank C, Greenwood C (2008) Formula 1 mechanical hybrid applied to mainstream automotive. In: VDI Getriebe in Fahrzeuge Conference, June 2008. http://www.torotrak.com/Resources/Torotrak/VDI_2008.pdf. Retrieved 11 Nov 2011
33. http://www.gtisoft.com/products/p_GT_SUITE.php. Retrieved 1 Sept 2010
34. Chen SK, Flynn PF (1965) Development of single cylinder compression ignition research engine. SAE paper 650733
35. Douaud AM, Eyzat P (1978) Four-octane-number method for predicting the anti-knock behavior of fuels and engines. SAE paper 780080
36. Boretti A (2010) Comparison of fuel economies of high efficiency diesel and hydrogen engines powering a compact car with a flywheel based kinetic energy recovery systems. Int J Hydrogen Energy. doi:/10.1016/j.ijhydene.2010.05.031
37. Boretti A (2010) Improvements of vehicle fuel economy using mechanical regenerative braking. In: SAE paper 2010-01-1683 at SAE 2010 annual brake colloquium and engineering display, Phoenix, AZ, USA, October 2010
38. <http://www.lesoft.co.uk/index1.html>. Retrieved 20 Jan 2010
39. <http://www.ipcc.ch/>. Retrieved 13 Sept 2010
40. Boretti A (2010) Performances of a turbocharged E100 engine with direct injection and variable valve actuation. In: SAE paper 2010-01-2154 at SAE 2010 power trains, fuels and lubricants meeting, San Diego, CA, USA, October 2010
41. Boretti A (2010) Use of variable valve actuation to control the load in a direct injection, turbocharged, spark-ignition engine. In: SAE paper 2010-01-2225 at SAE 2010 power trains, fuels and lubricants meeting, San Diego, CA, USA, October 2010
42. http://www.direct.gov.uk/en/Motoring/OwningAVehicle/HowToTaxYourVehicle/DG_4022118. Retrieved 13 Sept 2010
43. <http://www.vcacarfueldata.org.uk/>. Retrieved 13 Sept 2010
44. <http://carboncalculator.direct.gov.uk/index.html>. Retrieved 13 Sept 2010

Experimental Investigation on Fuel Spray Optimization in Gasoline Direct Injection Engine

Bo Jiang, Xiaoliang Pan, Fafa Liu, Chaojun Wang
and Xiaochuan Feng

Abstract Optical Visualization system was applied to record images of the processes of spray, mixed gas formation and combustion in a homogenous GDI engine. Fuel spray was optimized by visual analysis of the images, thus improved the quality of mixed gas and combustion in the cylinder, it can provide the reference for injector selection and EMS calibration.

Keywords Endoscope · Spray · GDI · Heat release rate · Wetting

Definitions/abbreviations

Λ	Relative air-to-fuel ratio
WOT	Wide open throttle
SOI	Start of injection
MFB	Mass fraction burned
CA	Crank angle
BSFC	Brake specific fuel consumption
IMEP	Indicative mean effective pressure

F2012-A01-006

B. Jiang (✉) · X. Pan · F. Liu · C. Wang · X. Feng
Changan Auto Global R&D Center of Changan Automobile Co LTD, Beijing, China
e-mail: sunqiemail@163.com

1 Introduction

In the recent years, as fuel consumption and emissions control regulations become more severe, improvement in fuel efficiency and reduction in exhaust emissions are the main goals. The concept of turbocharged downsized engine has the potential to achieve such goals. Compared with PFI engine, fuel–air mixture preparation is in the cylinder in GDI engine, fuel vaporizes to drop the gas temperature, and that the mixed gas stays less time in the cylinder therefore knock tendency is down, this is the advantage of GDI engine to apply turbocharged technology. Furthermore, compared with homogenous charge mode, layered lean charge mode has disadvantages in emission control and combustion stability, and that the quality of domestic gasoline restricts extend of layered lean mode GDI. Overall, homogenous GDI engine becomes the trend of domestic gasoline now.

Intake port of the conventional PFI engine is like a preparative volatilization chamber, it increases the time of fuel evaporation. For fuel directly inject in the combustion chamber in GDI engine, the time of fuel vaporization is so short that it is difficult to form homogenous mixed gas, and that fuel direct injection may engender wall wetting. It makes the rich gas around burn incompletely, thereby solid particle and HC emissions increase. If wetting is excessive, it would also affect fuel consumption and oil dilution badly.

2 Experimental Study

The engine used in the present work is shown as Table 1. Figures 1 and 2 show the spray images of selected Delphi 6 holes injector, it shows with 50 and 100 bar rail pressure slightly separated streams. Spray penetration with 150 bar compared to 100 bar results in more droplets with smaller sizes.

AVL Visioscope system was applied in the experimental study. At first, endoscope and light guide was installed for optical access to the combustion chamber, and record of engine synchronized images of spray, mixed gas formation and combustion on crank angle base by a camera, then post-process and analyze these images compared with reference records. As the max recording rate of the system is limited, it is unable to record image by every degree of crank angle, it records an image at the preset angle position every one or two cycle, merge the images recorded at different angles together as one cycle. For combustion stability in homogenous GDI engine is not bad generally, this new method of visual analysis is resultful to contrast macroscopically images of spray, mixed gas formation and combustion under different injection strategies.

According the cylinder size parameters, design how to install endoscope and light guide, and find out the best view to observe injection and combustion phenomena, as shown in Fig. 2. At the same time make sure there is no interference between the adapter and the peripheral engine parts, as shown in Fig. 3. Straight

Table 1 Basic engine characteristics

Concept	4cyl. in-line, air guide GDI, turbocharged
Combustion mode	Homogenous, $\lambda = 1$
Valve train	DVVT
Displacement	1.499L
Compression ratio	9.7:1

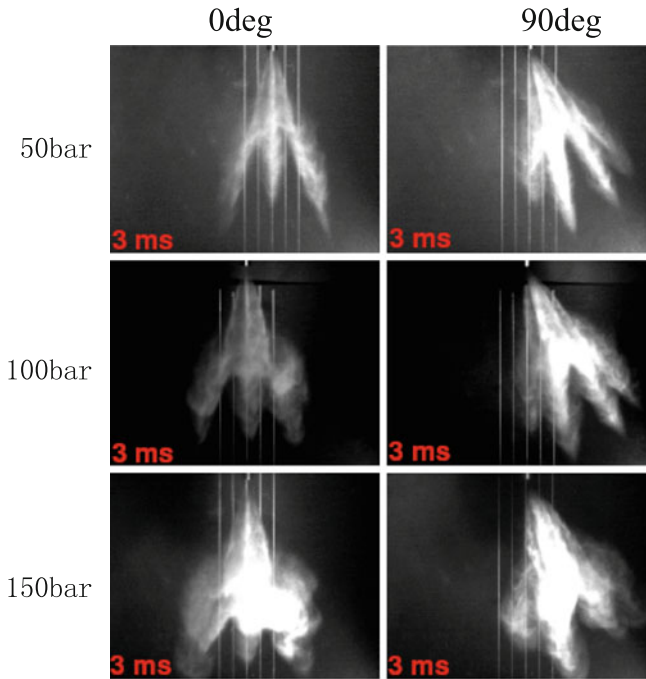
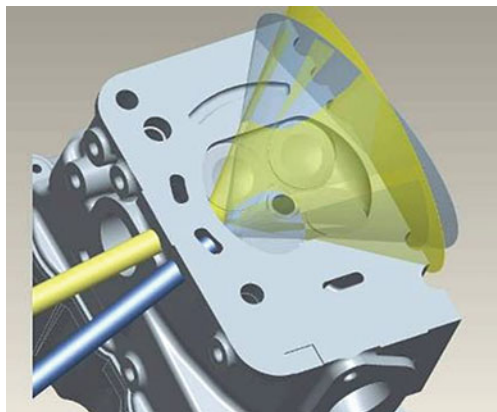


Fig. 1 Injector spray image

Fig. 2 View cone of endoscope and light guide



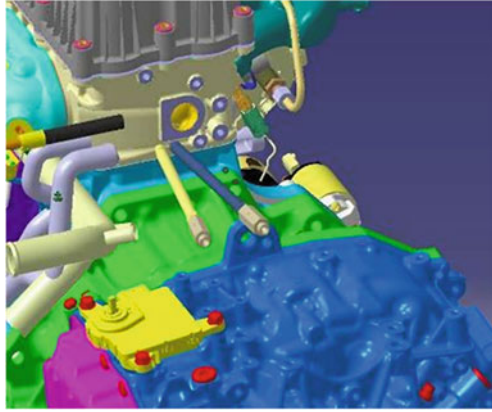


Fig. 3 Layout of optic access

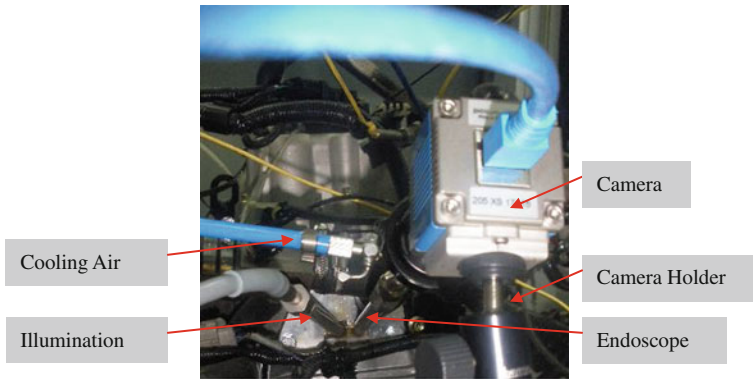


Fig. 4 Installation of experimental rig

forward view endoscope and light head are adaptive to view the sight through the optical access to the combustion chamber with almost no combustion interference. Figure 4 shows the experimental rig for injection and combustion visualization.

3 Results and Discussion

3.1 Visual Analysis of Spray and Combustion

Spray of homogenous GDI engine is during the intake stroke generally, thus get more time to form homogenous mixed gas. If injection timing is too early, spray tip penetration over the top of piston will cause wall wetting, and that cylinder

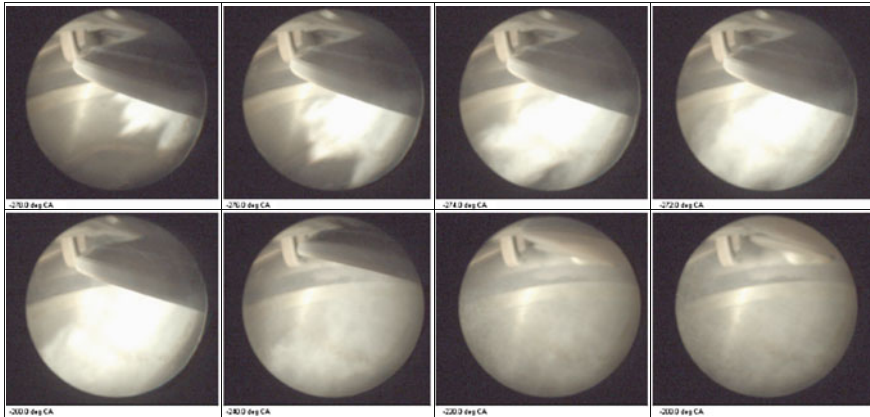


Fig. 5 Spray images during the intake stroke

pressure and airflow rate is low, spray resistance will be less, it go against spray break up into more droplets, and increase the risk of touching cylinder wall. In the other way if injection timing is too late, there will be no enough time to form homogenous mixed gas. So injecting at the optimal time and making the airflow tumble strongly is good for spray vaporization and fuel–air mixture.

Figure 5 shows the process of spray vaporization in the intake stroke. The white brume injected is made of a great many fuel droplets, and we can observe that whether spray tip touch the cylinder wall with different angles of view. Along with fuel vaporizing, the picture becomes clearer. It can provide the reference for spray development by contrasting the pictures of wall wetting and vaporization rate.

When engine load is high, split injection sometimes is necessary, usually the first injection is during intake stroke, and the second injection is during compression stroke. As shown in Fig. 6, when the second injection starts, there are a lot of droplets not vaporized completely.

The shape of spray in compression stroke is like as single injector spray image, fuel bunch of each hole diffuses and vaporizes rapidly.

If the quality of mixed gas is bad, liquid fuel will stay on the surface of piston and cylinder wall, it burnings with visual flame, as shown in Fig. 7. Actually they are the soot resulted of incomplete combustion, because liquid fuel gasify into rich gas above the surface. As the light of Visoscope system cannot penetrate through the thick soot, it reflects visible light that we saw. Normally, complete combustion of homogenous gas is sightless.

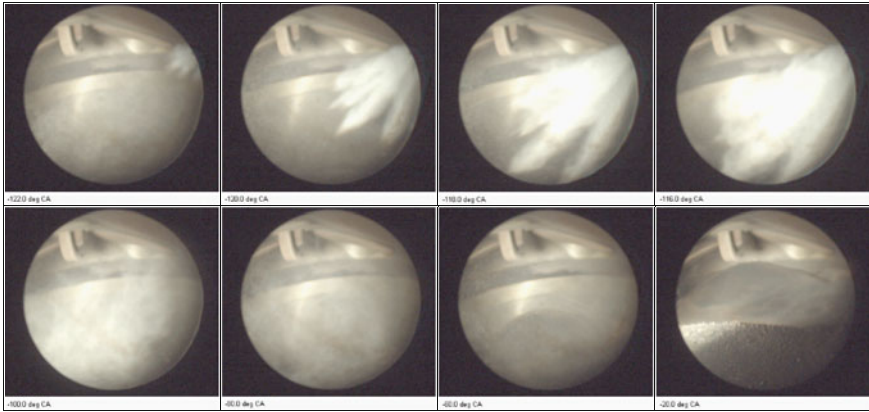
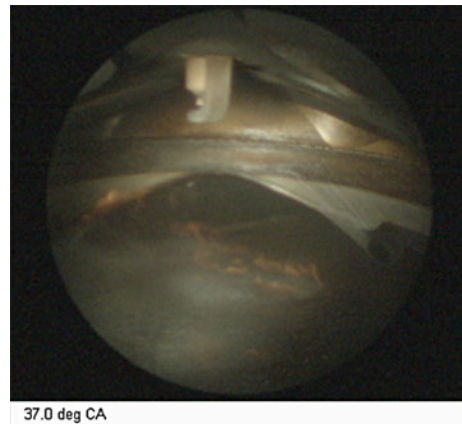


Fig. 6 Spray images during the compression stroke

Fig. 7 Flame image of incomplete combustion



3.2 Effect of Optimizing Spray on Combustion

As shown in Fig. 8, at 1500 r/min WOT original SOI was -285°CA , there is a bit visible piston wetting, result in the soot flame in the evening of combustion. As SOI advanced, more wetting and soot flame is created. Whereas SOI delayed, the flame of abnormal combustion reduces visibly. As the quality of mixed gas improves, the rate of heat release grows and combustion stability is better, furthermore it is helpful to BSFC, as shown in Figs. 9 and 10. When the SOI is close to the optimal point, the rate of heat release is hardly any affected.

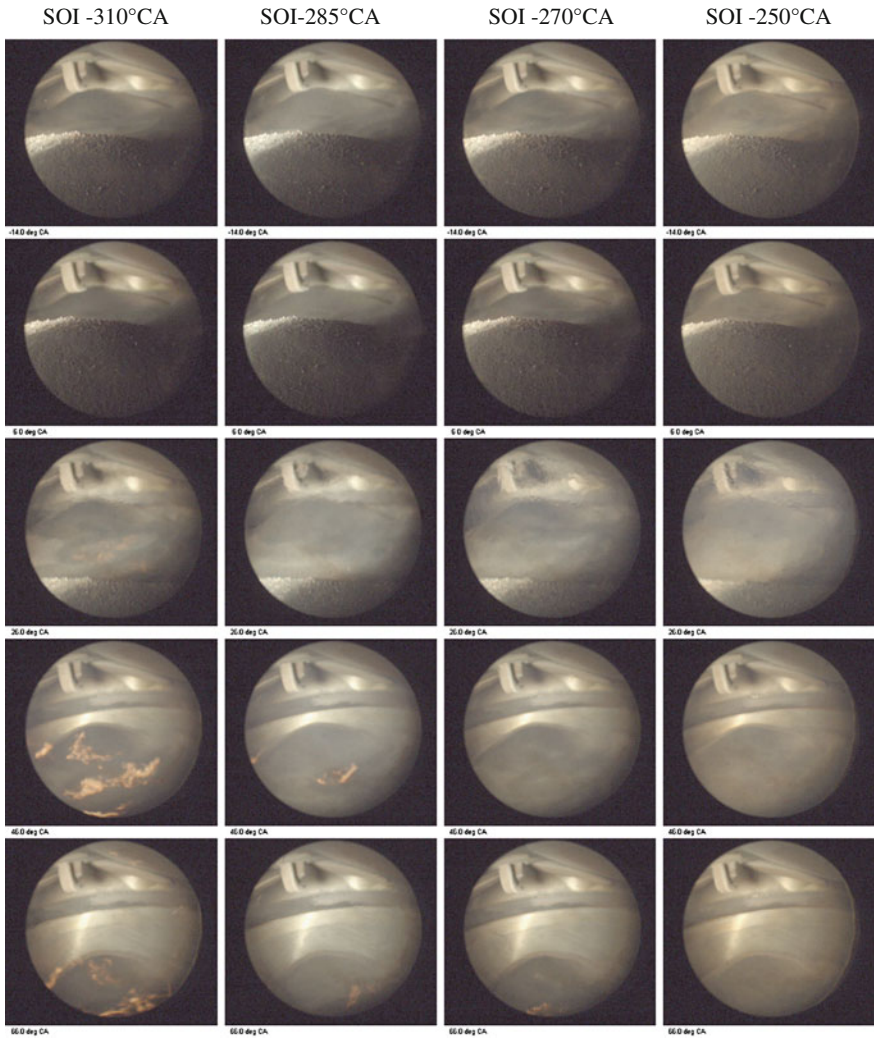


Fig. 8 Combustion images with different SOI

4 Conclusions

An experimental study was performed to investigate on fuel spray development and combustion visualization by using AVL Visioscope system in a GDI engine. By images contrast and cylinder pressure analysis, injection pressure, proportion and timing were all optimized, it can be concluded that it's an effective way to enhance the fuel-air mixing and hence to improve the engine performance.

Fig. 9 Rate of heat release with different SOI

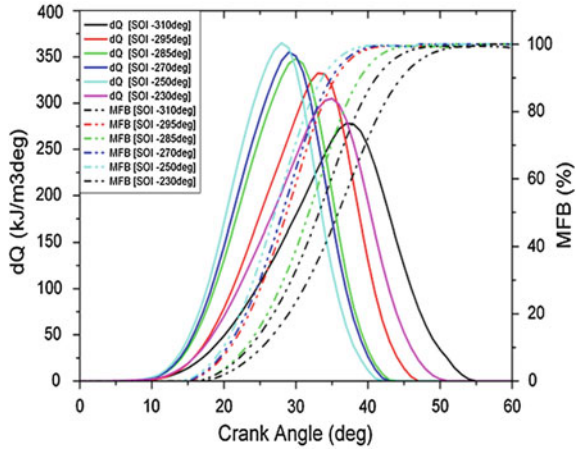
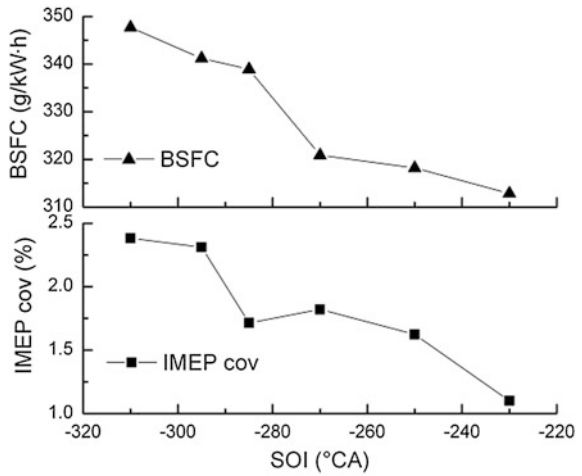


Fig. 10 BSFC and IMEPcov with different SOI



- Spray development can reduce wetting and hence to reduce HC and particle emission as well as oil dilution.
- When wetting was excessive, rich gas would be formed in part area above the surface, burning with visual flame which are the soot resulted of incomplete combustion.
- The result shows that, injection timing optimization is very important for improving the quality of mixed gas and combustion. If injection timing is too early, the mixture will be not homogenous and wetting becomes grave as well as unusual flame is more. Those make the heat release slowly and affect the combustion stability and fuel consumption. When start of injection is close to the optimal point, the effect will be less and the fuel consumption is lower.

References

1. Mittal M (2011) High-speed flow and combustion visualization to study the effects of charge motion control on fuel spray development and combustion inside a direct-injection spark-ignition engine. SAE technical paper, 2011-01-1213, MSU College of Engineering
2. Yang S, Li J, Li D (2007) Development trend of GDI engine, automobile engineering, issues 5, 2007-10
3. Yu P, X, Zhang, J Zeng (2010) Numerical method analysis of the processes of mixed gas formation in GDI Engine, Design compute research, issues 11

Improvement of Fuel Economy and Vehicle Performance Through Pneumatic Regenerative Engine Braking Device (Reneged)

Yan Zhang, Choyu Lee, Hua Zhao, Tom Ma, Jing Feng, Zhiqiang Lin and Jie Shen

Abstract Over the last few years, a new and cost-effective pneumatic regenerative engine braking (RegenEBD) concept has been researched and developed in order to improve the fuel economy of inner city buses. The RegenEBD concept is realised by swapping a standard engine braking device from the exhaust side to the intake side and implementing a proprietary one-way intake design. The engine is operated as a compressor during the vehicle deceleration through the action of RegenEBD so that the vehicle's kinetic energy can be converted into pneumatic energy in the form of compressed air. Regenerative stop-start can then be realised through the use of a standard air starter motor. In this paper, the prototype RegenEBD engine and bus are first presented. This is followed by a discussion on the engine testing results and preliminary bus driving tests. Experimental results show that the fuel economy can be improved by 5–10 % for inner city buses, and there is potential for improved vehicle performance through instant boost by the regeneratively produced compressed air.

Keywords Pneumatic · Regenerative · Engine braking · Air hybrid · Stop-start

F2012-A01-012

Y. Zhang (✉) · C. Lee · H. Zhao · T. Ma
School of Engineering and Design, Brunel University, London, UK
e-mail: yan.zhang@brunel.ac.uk

J. Feng · Z. Lin · J. Shen
Yuchai Machinery Company, Yulin, Guangxi, China

1 Introduction

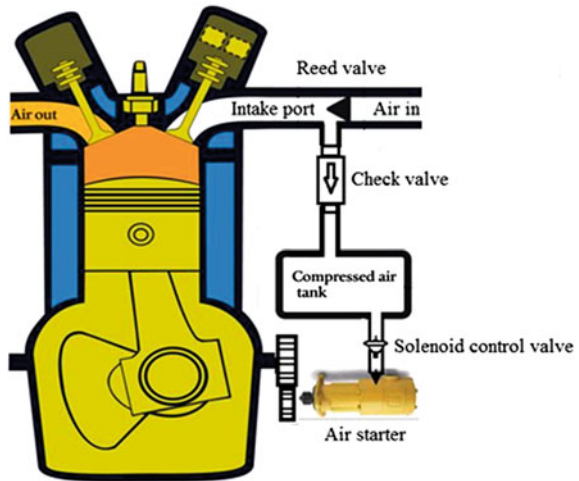
It is recognised that the hybrid powertrain with regenerative energy recovery is one of the most effective means to low carbon vehicles in the short to medium term. In the city and urban areas where a lot of stop–start operations are involved, the most beneficial way for the buses and delivery vehicles to save fuel is to recover the regenerative energy and switch off the engine when stationary. Over the last few years, a number of electric hybrid buses were developed and introduced to the public transport in big cities in the world, such as London and New York. Compared to the conventional diesel buses, the electric hybrid buses in London achieved on average around 15 % fuel saving [1]. It is also found that a double decker bus can cost 50 % extra when it is modified from the convention diesel bus to an electric hybrid bus [2]. According to the gain in fuel consumption on the electric hybrid bus, the payback period will be estimated to be about 20 years.

Another way to realise the hybrid powertrain concept is to store the regenerative energy in the form of compressed hydraulic fluid. Vehicles equipped with this system are called Hydraulic Hybrid Vehicles (HHV), which have high braking power density and are very suitable to the stop–start operation [3]. Similar to the electric hybrid, the hydraulic hybrid powertrain involves a completely separate and additional hydraulic motor to the existing vehicle and a new vehicle transmission system, the cost and weight would be expected to be high though perhaps less than the equivalent electric hybrid.

Unlike the electric and hydraulic hybrids, air hybrids can be implemented without adding an additional power unit to the vehicle and installing a new transmission system when it is applied to a reciprocating internal combustion engine. In this case, the engine itself works as a compressor during braking/ deceleration or an expander for starting/acceleration, transmitting power through the pistons and the crankshaft of the engine thus braking or propelling the vehicle using the existing drivetrain of the vehicle. For buses and parcel delivery vehicles, pneumatic energy can be stored at moderate pressure (<10 bar) in an existing air storage tank, which is initially designed for storing the service air on the bus [4]. This system recovers the vehicle's kinetic energy through engine braking and reuses the stored compressed air for stop–start operation. A low cost and practical solution has been proposed to implement the regenerative engine braking system on the inner city buses [5–7].

In the previous work [5, 6], authors had presented the modelling results of the RegenEBD system. The vehicle driving simulation shows good fuel consumption improvement in both Millbrook London Transport buses and Braunschweig driving cycles. In this paper, the functionality of the most popular bus engine equipped with a new RegenEBD system is investigated and discussed. This is followed by the results of a prototype RegenEBD bus driven in two China city bus driving cycles.

Fig. 1 Schematic diagram of the RegenEBD system



2 Principle of Operation

The schematic diagram of the engine with a RegenEBD system is shown in Fig. 1. The RegenEBD system allows the pneumatic regenerative engine braking to be realised by swapping a standard engine braking device from the exhaust side to the intake side and implementing a proprietary one-way intake design,. The function of the introduced components in the system enables the engine to be operated in the normal firing mode, compressor mode and stop–start mode. Firstly, a reed valve is installed close to the intake port and allows the air to be introduced into the cylinder in both normal firing mode and compressor mode. The variable valve exhaust braking (VVEB) device, shown in Fig. 2 is installed on one intake valve and is actuated in the compressor mode during the vehicle deceleration operation.

Figure 3 shows the valve timing diagrams for the normal firing mode and the compressor mode. During the normal firing mode, both intake and exhaust valves operate with their default lift profiles. During the vehicle braking operation, the fuel injection is switched off and the VVEB is actuated so that one intake valve remains open with a 1.25 mm lift after the intake stroke. As shown in Fig. 4, the induced air is compressed into the air tank through one intake valve and the check valve during the compression process, working as a 4-stroke compressor driven by the kinetic energy of the decelerating vehicle. The compressed air stored in the air tank can then be used to crank start the engine through the air starter motor mounted on the engine’s flywheel. Thus, the regenerative stop–start operation can be achieved with fairly simple control measures.

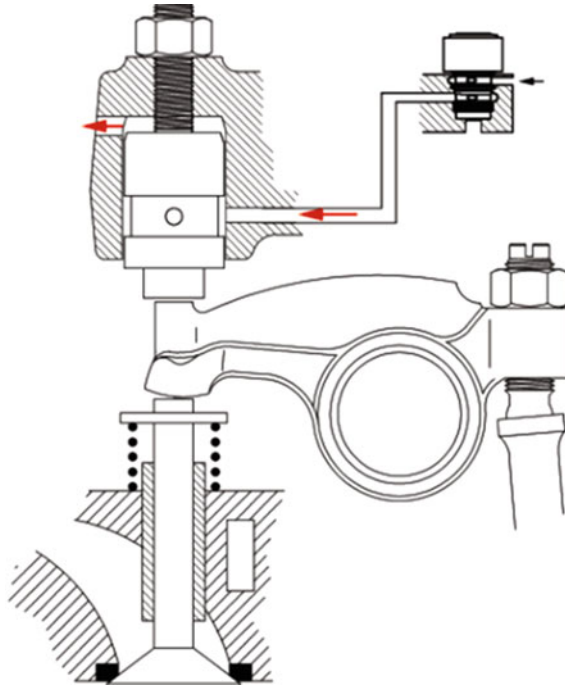


Fig. 2 Schematic of the VVEB device

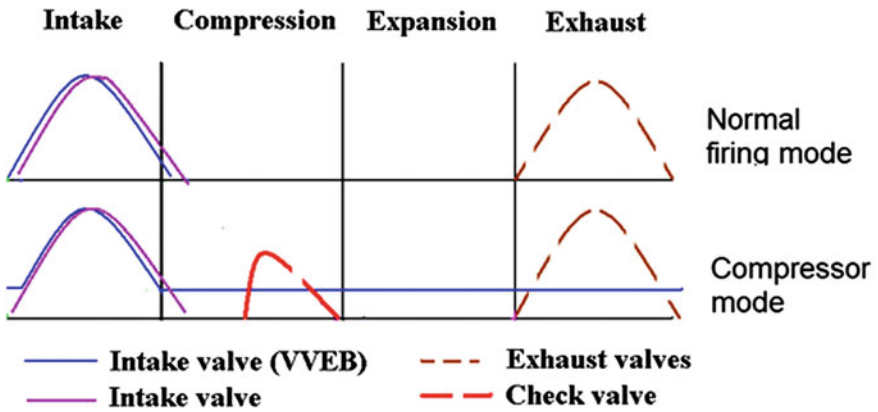


Fig. 3 Engine valves and check valve timing for the normal firing mode and compressor mode

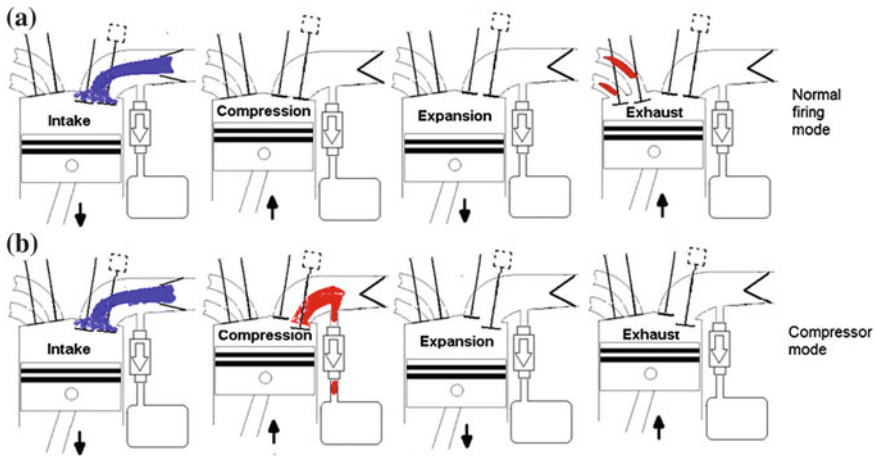


Fig. 4 Four-stroke engine cycle for the normal firing mode (a) and compressor mode (b)

3 Experimental Setup

3.1 RegenEBD Engine Test Bed

Figure 5 shows the RegenEBD engine on a test bed. The YC6A 6-cylinder diesel engine is widely used in the inner city buses in China. Details of the engine and characteristics of various valves are given in Tables 1 and 2 respectively. A sandwich plate, which accommodates six reed valves, is installed between the engine intake port and manifold. On the bottom of the sandwich plate, 6 one-way check valves are screwed in and the other end was connected to a joint volume, which is connected to an air tank via a flexible hose for collecting the compressed air during the air charging process. In order to store sufficient amount of compressed air for the usage of the air starter, the size of the air tank is 160 L according to the recommendation of the air starter manufacturer [8]. The engine is coupled with a 230 kW AC motor dynamometer so that the engine can be operated in both the normal firing mode and compression mode by applying braking and motoring torque respectively. The VVEB valve is installed on the intake side in the cylinder head under the cylinder head cover and it is controlled by an addition control unit.

3.2 Prototype Bus Specification

As shown in Fig. 6, the prototype bus is modified from a widely used city bus in China, of which the specifications are shown in Table 3. The modification is on the diesel engine only. Therefore, the bus can operate as usual when the RegenEBD system is disabled.

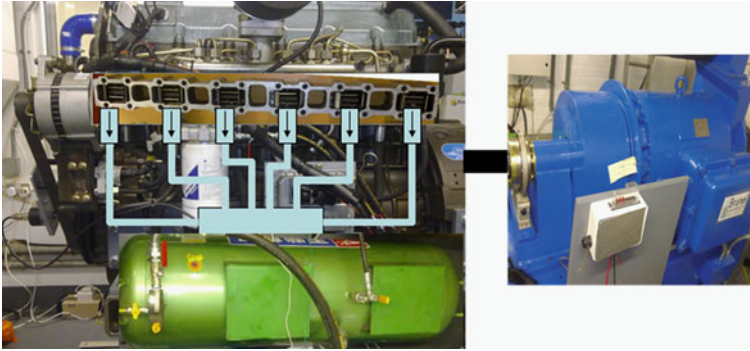


Fig. 5 RegenEBD engine test bed

Table 1 Engine dimensions and characteristics

Number of cylinders	6
Cylinder bore	105 mm
Piston stroke	132 mm
Displacement volume	7.25 L
Compression ratio	17.5:1
Rc in air hybrid mode	4.23:1

Table 2 Valves dimensions and characteristics for each cylinder

Intake valve	2
Diameter	32.5 mm
Opening point (normal)	61° before TDC
Closing point (normal)	91° after bottom dead centre (BDC)
Maximum lift	9.6 mm
Exhaust valve	2
Diameter	29.5 mm
Opening point	105° before BDC
Closing point	67° after TDC
Maximum lift	9.7 mm
Throttle valve	1
Diameter	32.4 mm
Check valve	1
Diameter	25.4 mm

4 Results and Discussion

4.1 Air Charging Tests

During the compressor mode operation, compression will take place with an enlarged volume at the top dead centre because of the additional auxiliary volume

Fig. 6 City bus with RegenEBD installed on board



Table 3 City bus specifications [9]

Kerb weight	16500 kg
Aerodynamic drag coefficient	0.5
Frontal area	5.69 m ²
Air density	1.225 kg/m ³
Wheel radius	0.508 m
Rolling resistance coefficient	0.013
Air tank volume	151 L
Starting tank pressure	6 bar
1st gear ratio	6.9:1
2nd gear ratio	4.13:1
3rd gear ratio	2.45:1
4th gear ratio	1.49:1
5th gear ratio	1:1
Final drive ratio	5.125:1
Additional mass of air starter	15 kg
Additional mass of air tank	100 kg

formed between the intake valves, the Reed valve, and the check valve for each cylinder. The effective compression ratio will be less than the engine’s geometric compression ratio. It will determine the maximum pressure the air tank can be topped up and the air charging efficiency of the system in the compressor mode. The effective compression ratio of the RegenEBD system was calculated from the pressure trace measured in the intake port when the engine was running in the compressor mode. Figure 7 shows the intake port pressure trace in the compressor mode at 1500 rpm obtained from a piezo-resistive pressure transducer. It can be seen that there was a lag between the intake port pressure and in-cylinder pressure calculated from the adiabatic compression equation, because of the low intake valve lift activated by the VVEB device in the compression and expansion strokes. Although the peak pressure in the intake port is 6.2 bar, the pressure drop across the check valve and flow losses in the pipe, the maximum pressure the air tank could reach was about 5.3 bar.

The air tank charging rate was also investigated at engine speeds between 800 and 2000 rpm. The tests were carried out by running the engine in the normal firing operation conditions. As soon as the ECU received the braking signal from

Fig. 7 Intake port pressure during air charging process at 1500 rpm

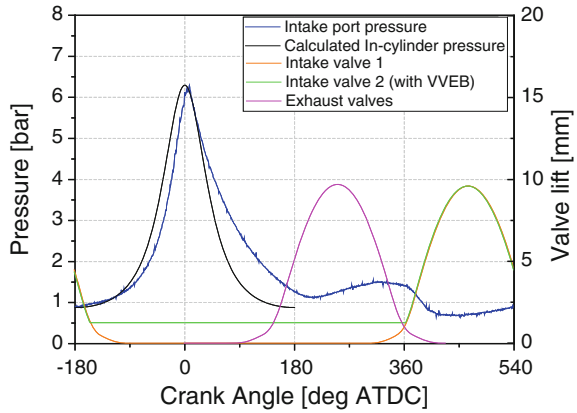
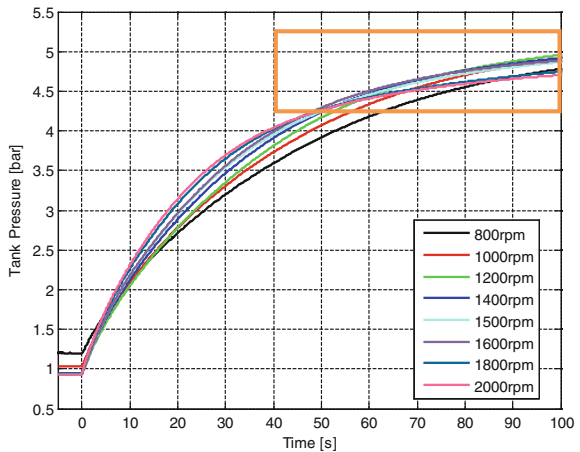


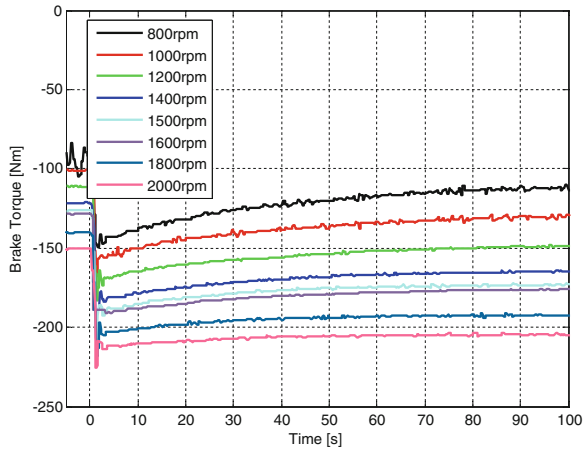
Fig. 8 Air tank pressure during air charging process



the brake pedal, fuelling was cutting off and the VVEB valve was switched on. Then the RegenEBD was enabled and the engine was running as a compressor. Figure 8 shows the tank pressure values against the engine cycles at different engine speed. When the engine topped up the air tank from the ambient, it took more cycles for the tank pressure to get to the maximum. During the real bus driving operation, the tank pressure will be always over 4.2 bar, as the minimum tank pressure to successfully drive the air start is 4.7 bar and the pressure drop of a single start by air starter is 0.5 bar. Therefore, only the data over 4.2 bar in the curve (in the orange box) will be of use when the bus is running in the real driving cycles.

Figure 9 shows the engine braking torque generated by the engine running in the compressor mode in the speed range from 800 to 2000 rpm. It can be seen that in the first cycle when the engine was switched into the compressor mode from the normal firing mode there was a sudden dip on each curve, i.e. a surge in braking torque. This is because the charging rate was the highest in the first brake cycle. As

Fig. 9 Engine braking torque



the tank pressure increased, the braking torque started to decrease. Since the braking torque generated by the engine in the compressor mode is much less than the total braking torque required by the vehicle, the existing brake system on the bus is used during braking without implementing additional control over the RegenEBD or altering the existing brake system.

4.2 Starting Test Using Air Starter

Figure 10 shows the warm start-up process of the engine cranked by the air starter when the coolant temperature is 80°C and the air tank pressure is 4.7 bar. It can be seen that it took about 1.5 s for the engine to start from 0 to 800 rpm where engine was ready to drive the vehicle. During the cranking process, the tank pressure dropped from 4.7 bar down to 4.2 bar when the engine was motored to the crank speed of 200 rpm, when the fuel injection started. Any pressure lower than 4.7 bar will cause unreliable starting processes.

4.3 Prototype RegenEBD Bus Running in City Bus Driving Cycles

The prototype bus test was done with the same bus running in the bus driving cycles of two typical cities in China. The fuel consumption was measured by weighing the fuel tank on the bus before and after running the driving cycle, and then converted into specific fuel consumption from the mileage shown on the dash board. Figure 11 shows the measured specific fuel consumption in two city bus driving cycles. City A is a typical big city in China, and City B. relatively small

Fig. 10 Warm starting process (tank pressure: 4.7 bar, coolant temperature: 80°C)

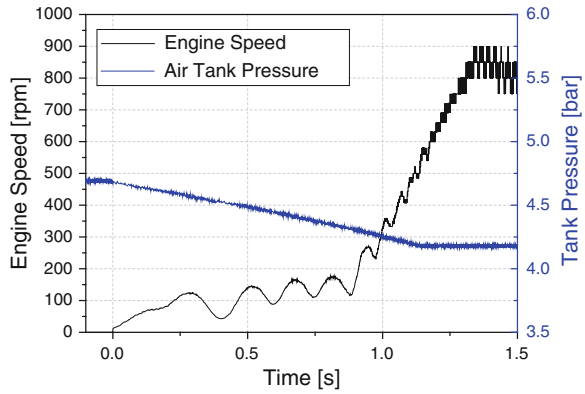
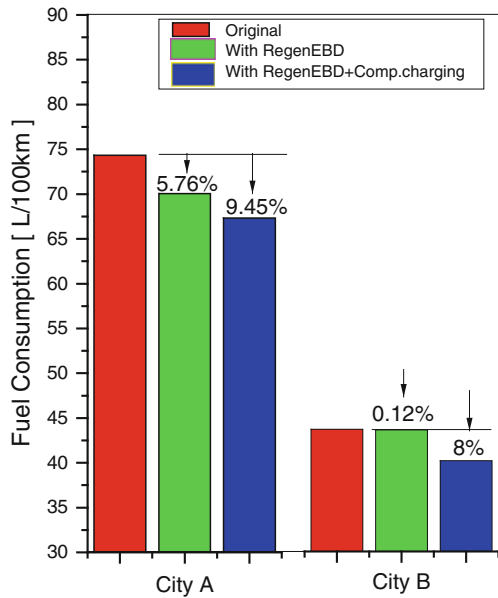


Fig. 11 Fuel consumption of the RegenEBD bus



city. 5.76 % fuel saving was achieved on the RegenEBD bus in City A. However, in City B there was no significant fuel saving as in the big city the road condition is much better so the bus can run at relatively high speed. As a result, more air can be charged during each brake/deceleration process, so the engine can be switched off during idle. In City B, the bus was running at lower speeds because of the road and traffic conditions. In this case, less air can be stored through RegenEBD. When the air tank pressure was lower than 4.7 bar, the engine was not switched off to avoid the risk of failure to restart the engine. To overcome this problem, the engine belt driven compressor was connected to the tank for further topping up the air tank. With the compressor charging, the RegenEBD system has enough air in the tank for restarting the engine. Then more switch-offs during idle occurred, which

reduced the fuel consumption by 8 % in City B driving cycles. The same method was also applied on the engine to restore more air in the tank for more stop–start operations in City A driving cycle. Results show that the fuel consumption was further reduced so that a reduction of 9.45 % was achieved compared with that of the original bus.

5 Conclusions

A cost-effective pneumatic regenerative stop–start hybrid system (RegenEBD) for buses and parcel delivery vehicles has been proposed and investigated on a bus diesel engine on an engine test bed. A city bus equipped with the RegenEBD engine was commissioned to demonstrate the potential of the RegenEBD.

The engine testing results show that the compressed air could be generated using simple production components and the air starter was a simple and effective ways to achieve regenerative stop–start operations.

The demonstrate bus results show that the fuel economy can be improved by 5–10 % for inner city buses. The improvement of fuel economy may vary depending on different inner city driving cycles. In some small cities, where the road conditions are not as good as that in big cities and the bus speed is relatively low, the air storing efficiency is lower, resulting in less stop–start operation can be adopted.

In order to improve the air charging efficiency and hence fuel economy, alternative intake designs without permanent Reed valves are being developed and their performance and effect on RegenEBD system will be reported after the engine and vehicle tests have been completed.

Acknowledgments We would like to acknowledge the financial support of EPSRC (Engineering and Physical Science Research Council) of UK for the RegenEBD research carried out at Brunel University.

References

1. London's hybrid bus trials—the results (2010). <http://www.cvenengineering.com/>. Last accessed December 2010
2. Hybrid buses (2010) Transport for London surface transport panel, 30 June 2010
3. Batavia B (2009) Hydraulic hybrid vehicle energy management system. SAE paper 2009-01-1772
4. Trajkovic S, Tunestal P, Johansson B (2010) Vehicle driving cycle simulation of a pneumatic hybrid bus based on experimental engine measurements. SAE paper 2010-01-0825
5. Lee C, Zhao H, Ma T (2010) A low cost air hybrid, oil & gas science and technology. Rev IFP 65(1):19–26
6. Lee C, Zhao H, Ma T (2010) The performance characteristics of a production oriented air hybrid powertrain. SAE Int J Engines 3(1):609–619

7. Lee C, Zhao, H, Ma T (2011) Pneumatic regenerative engine braking technology for buses and commercial vehicles. SAE paper 2011-01-2176
8. Vane Starters (Ingersoll Rand) (2010). <http://www.ingersollrandproducts.com/airstarters/pdfs/f-237KB.pdf>. Last accessed March 2010
9. Private communication with China Yuchai International Limited, 2012

CAI Combustion of Gasoline and its Mixture with Ethanol in a 2-Stroke Poppet Valve DI Gasoline Engine

Yan Zhang, Hua Zhao, Mohammed Ojapah and Alasdair Cairns

Abstract Controlled Auto Ignition (CAI), also known as Homogeneous Charge Compression Ignition (HCCI), is one of the most promising combustion technologies to reduce the fuel consumption and NO_x emissions. Currently, CAI combustion is constrained at part load operation conditions because of misfire at low load and knocking combustion at high load, and the lack of effective means to control the combustion process. Extending its operating range including high load boundary towards full load and low load boundary towards idle in order to allow the CAI engine to meet the demand of whole vehicle driving cycles, has become one of the key issues facing the industrialisation of CAI/HCCI technology. Furthermore, this combustion mode should be compatible to different fuels, and can switch back to conventional spark ignition operation when necessary. In this paper, the CAI operation is demonstrated on a 2-stroke gasoline direct injection (GDI) engine equipped with a poppet valve train. The results shown that the CAI combustion can be readily achieved in the 2-stroke cycle of a poppet valve engine and the range of CAI combustion can be significantly extended compared to the 4-stroke cycle operation. In addition, the effects of ethanol concentration on 2-stroke CAI operational range, combustion process, emissions and efficiencies are studied and presented.

Keywords 2-stroke · Poppet valve · CAI · Ethanol · E15 · E85

F2012-A01-013

Y. Zhang (✉) · H. Zhao · M. Ojapah · A. Cairns
School of Engineering and Design, Brunel University, London, UK
e-mail: yan.zhang@brunel.ac.uk

1 Introduction

Controlled Auto-ignition (CAI) or HCCI combustion has been the subject of extensive research over the last decade in the four-stroke spark ignition engines for improved part-load fuel consumption and low exhaust emissions [1]. Many approaches have been attempted to achieve CAI operation on the four-stroke spark ignition engines, such as intake air heating, high compression ratio, dual fuel, recycling the exhaust gas, and so on [2]. Amongst these approaches, internally recycling the exhaust gas, such as residual gas trapping [3–6] and exhaust gas rebreathing [7], have been proved most effective in achieving CAI combustion and demonstrated their potential to be incorporated in the production gasoline engine.

One of the challenges facing the CAI combustion operation is its narrow operating load range, limited at high load by the violent combustion and at very low load by the misfire. In order to extend the load range of CAI combustion for automotive applications, a systematic research [8, 9] has been carried out by the authors on such combustion process in a single cylinder engine that is capable of both 4-stroke and 2-stroke operations through flexible variable valve actuation. As part of a consortium over the last several years, the authors worked with industrial partners in developing 2/4-stroke switchable engine technologies through engine downsizing [10], from which the current research on 2-stroke CAI via poppet valve operation have been initiated and performed. In order to overcome the high HC and CO emissions and durability issues associated with the conventional crankcase scavenged 2-stroke engines, the 2-stroke poppet valve engine has been developed using the same engine architecture as the current 4-stroke engine. In addition, direct fuel injection is applied to avoid short-circuiting fuel during the scavenging process. Controlled Auto Ignition is initialized by residual gases trapped in the cylinder through incomplete scavenging, which is inherent to the 2-stroke operation. A fully variable valve train is mounted on the cylinder head so that varied amount of residual gas fraction can be obtained through controlling scavenging process to achieve CAI combustion process at different engine operating conditions.

In this work, CAI combustion is demonstrated over different engine speed and load conditions on the 2-stroke poppet valve DI engine. Spark assisted CAI combustion and ethanol blended fuels are used to extend 2-stroke CAI operational range on the engine. Detailed analysis of combustion process, emissions and efficiencies are performed and presented in the paper.

2 Experimental Setup

The work was performed on a single cylinder direct injection camless engine as shown in Fig. 1. The specifications of the engine are given in Table 1. An electro hydraulic valvetrain system was used to enable independent control of valve

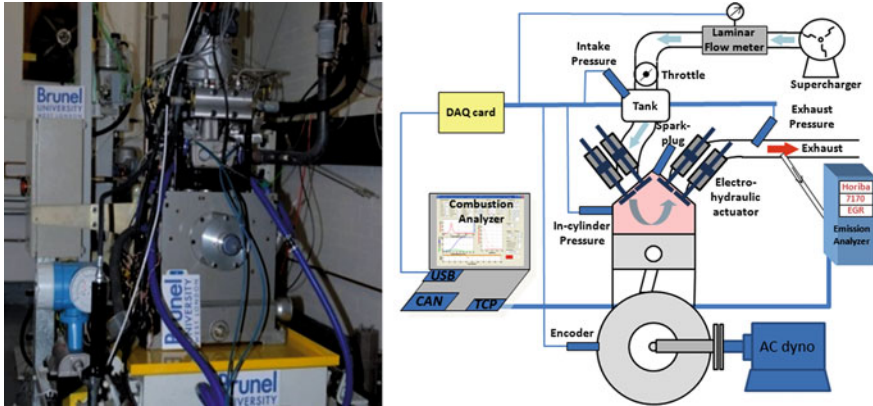


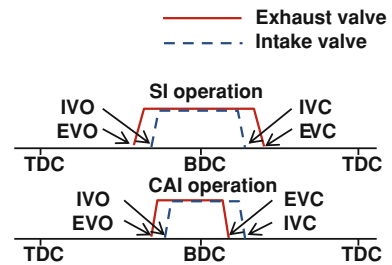
Fig. 1 Camless DI gasoline engine and the schematic of test setup

timings and lifts. The fuel was injected by a Denso double-slit GDI injector [11], mounted under the intake port. The fuel injection pressure was set to 100 bar. The instantaneous fuel flow rate was measured by a fuel flow meter installed between the high pressure fuel pump and injector. Compressed air was supplied by an AVL supercharger system at a pre-set boost pressure and temperature through the closed loop control of heaters and heat exchangers. The intake mass flow rate was measured by a laminar air flow meter. Both the instantaneous intake and exhaust pressures were measured by two piezo resistive pressure transducers. The exhaust emissions were analysed by a Horiba 7170DEGR gas analyser system. The instantaneous in-cylinder pressure was measured by a piezo-electric pressure transducer from which the heat release and combustion characteristics were calculated and displayed on-line using an in-house Labview data acquisition and combustion analysis programme. The engine TDC was determined dynamically according to the reference [12]. The engine is mounted on a dynamic engine testbed with fully automated coolant and oil conditioning circuits and driven by an AC motor so that both motored and fired operations could be performed.

The intake and exhaust valve timings used for the 2-stroke CAI operation in this work are illustrated in Fig. 2, in which the conventional 2-stroke spark ignition (SI) valve timings are also plotted as a reference [13, 14]. In the 2-stroke SI operation, in order to make use of the momentum of the fresh charge and achieve the post-scavenging, the exhaust valves are closed after the intake valves. In the 2-stroke CAI operation, in order to trap more burnt gas in the cylinder, both the intake and exhaust valve durations are shortened. The amount of the residual gas is controlled principally by the exhaust valve closing time which is varied depending on the requirement of the operation conditions. In the 2-stroke engine, fuel injection is timed to take place immediately after all the valves are closed in order to prevent fuel from being short-circuited to the exhaust, which is a major drawback of conventional 2-stroke engines. A lambda sensor was used to achieve the closed loop control of the air to fuel ratio so that the measured air to fuel ratio

Table 1 Engine specifications

Bore × stroke	81.6 × 66.94 mm ²
Swept volume	0.35L
Compression ratio	11.78:1(Geometric)
Combustion chamber	Pent roof/4 valves
Valve train	Electro-hydraulic actuation
Fuel injection	Direct injection
Fuel	Standard gasoline (RON 95), E15 and E85
Injection pressure	100 bar
Air/fuel ratio	Stoichiometric in exhaust
Intake temperature	25 °C

Fig. 2 Intake and exhaust valve timings for 2-stroke SI and CAI operation

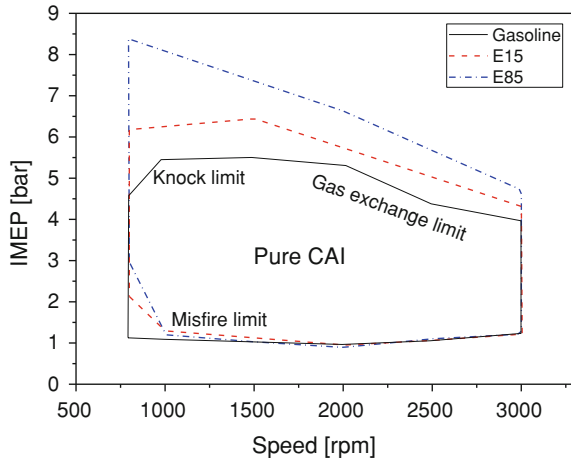
in the exhaust was maintained at stoichiometric. However, as to be discussed later, the in-cylinder air to fuel ratio was lower than the one measured by the exhaust lambda sensor because of the short-circuiting of air.

3 Results and Discussion

3.1 Operating Range

Firstly, the load-speed operating range of 2-stroke pure CAI of gasoline, E15 and E85 was investigated. The operating ranges of CAI combustion with exhaust lambda 1 are shown in Fig. 3. The engine speed was varied from 800 to 3000 rpm, and the load was varied from the minimum to the maximum by adjusting the boost pressure [3]. In the case of the 2-stroke poppet valve CAI operation, the engine output is determined by the scavenging ratio of the fresh air to the total in-cylinder charge. With the same valve timings, by increasing boost pressure, more fresh air is inducted and more exhaust gases are displaced, resulting higher power output. The pure CAI operation is defined as operational conditions where spark ignition does not have significant effect on the combustion phase. At low load operation, the boost pressure was lower, less exhaust gas was scavenged. The very high residual gas fraction led to unstable combustion and misfire, which limited the

Fig. 3 Operating range of 2-stroke CAI fuelled with gasoline, E15 and E85



operation range at low load boundary. It is noted that at low speed, the more ethanol was blended in the gasoline, the more difficult the mixture could get auto ignited due to the low mixture temperature caused by the charge cooling effect of ethanol injection. Therefore, the low load boundary of E85 occurred at higher IMEP values than that of gasoline and E15 at 800 rpm. When the engine speed increased, the difference in the low load CAI limits between gasoline and its mixture with ethanol disappeared because of the reduced heat loss and higher thermal loading at higher engine speeds.

At 1000 rpm, when IMEP was over 5.5 bar, combustion became very rapid and the rate of pressure rise exceeded the pre-defined knock limit of 5 bar/CA. This is because the combustion process was accelerated due to the higher in-cylinder temperature and less dilution of the residual gases at higher load conditions. It can be seen that the knock limit was extended by 0.7–6.2 bar IMEP when blending 15 % ethanol in gasoline. E85 further extended the load range by 3–8.5 bar IMEP. This is a result of slower heat release rate of ethanol than gasoline. In the case of gasoline, the upper load boundary moved up slightly as the engine speed was changed from 800–1000 rpm, as to be explained later.

For all three fuels, it is noted that the upper load limits would fall with the engine speed. For gasoline and E15, this occurred at 2000 and 1500 rpm respectively, whilst E85 fuel exhibited continued decrease in the upper load limit of CAI operation with the engine speed. This can be explained by the flow characteristics of the camless valve actuation system. Because the valves were operated independently from the engine's own rotation by the electro-hydraulic actuation, for a given intake and exhaust valve profile, the valve opening durations remained constant in mille-seconds but they became less in terms of crank angles as the engine speed increased. In addition, due to the finite opening and closing speeds of the electro-hydraulic valves, the valves could not reach their maximum lift at 1500 rpm and above in the two-stroke mode. Although the valve durations were increased at higher engine speed operations to compensate for the reduction in the

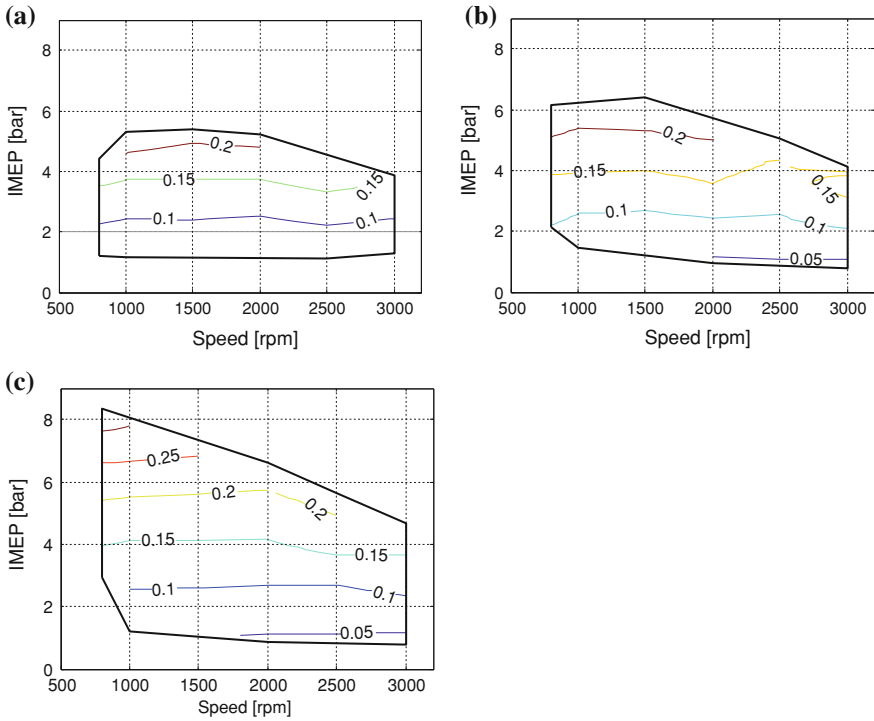
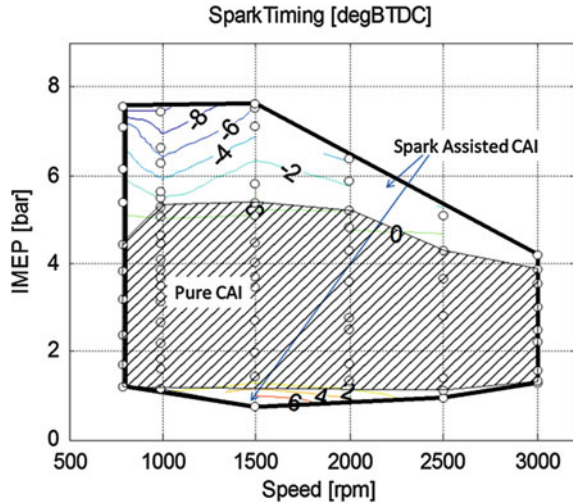


Fig. 4 Air flow rate [g/cycle] over 2-stroke CAI operating range. **a** Gasoline. **b** E15. **c** E85

air flow rate caused by the reduced valve lift, it's still not sufficient for the high load operation. This resulted in the gas exchange limit at higher speeds on the CAI operating range. Because ethanol has a lower stoichiometric air fuel ratio than gasoline, the addition of ethanol reduced the amount of air required for combustion and hence could produce more output for the same amount of air trapped in the cylinder than gasoline. This is illustrated by the air flow rate values for gasoline (Fig. 4a), E15 (Fig. 4b), and E85 (Fig. 4c). Therefore, at 3000 rpm, E15 extended the gas exchange limit by half bar IMEP and E85 1.5 bar IMEP, compared with gasoline CAI operating range.

In addition to the pure CAI operating range, spark assisted CAI combustion was used to extend the operational range of low temperature combustion with high dilution [15]. Figure 5 shows the extended 2-stroke CAI operating range with the spark assisted CAI operation. Although there was no noticeable effect of spark ignition seen on the combustion process within the pure CAI operating range, the spark was kept on but the spark timing was set at TDC. The pure CAI operating zone was sandwiched by two regions of the spark assisted CAI operation, where the combustion could not be started or completed without spark. However, the effects of the spark on the spark assisted CAI operation zone at higher load and idle conditions are different, which can be seen from the spark timing values shown in Fig. 5. In the

Fig. 5 Spark timing in 2-stroke spark assisted CAI operational range

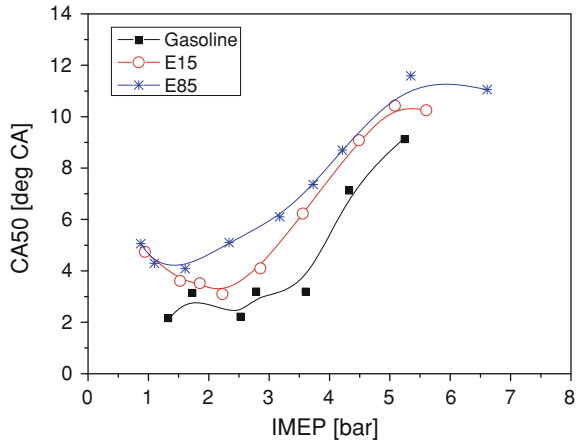


high load spark assisted CAI operation, the combustible charge of air/fuel mixture became higher and less burned gases were trapped. This led to lower compressed charge temperature than the autoignition temperature and required spark ignition to ignite the mixture. The spark timing, however, was retarded to prevent knocking combustion. In the spark assisted CAI operation at idle, the spark timing was advanced before TDC to help to stabilize the combustion process, which would suffer from slow combustion due to high dilution rate.

3.2 *Effects of Ethanol Concentration on 2-Stroke CAI Combustion Process*

Figure 6 shows 50 % mass fraction burnt crank angle (CA50) as a function of the engine load, IMEP, at 2000 rpm with gasoline, E15 and E85. It can be seen that the combustion phase was retarded with increasing engine load in most cases. As explained above, load in the 2-stroke CAI operation was determined by the scavenging rate. As the load increased, there were more fresh charge but less residual gas trapped, resulting in the lower in-cylinder temperature. Therefore, the start of autoignition combustion was delayed until the charge temperature was compressed to the autoignition temperature. At the highest load conditions, autoignition could not start and spark ignition was introduced after TDC to initiate the combustion process. At the low load conditions, the start of combustion for E15 and E85 advanced slightly as the load was changed from 1 to 2 bar IMEP. At such low load, the largest amount of burned gas was trapped and the burned gas temperature was at their lowest value. In addition, there was a relative large percentage of unburned or partially burned fuels in the trapped charge which

Fig. 6 CA50 in 2-stroke CAI operation at 2000 rpm



would contribute to the autoignition chemistry leading to the start of the high temperature combustion reactions. Since the autoignition process is affected by the charge dilution, temperature, and chemical species in the cylinder charge, the small changes observed could have been caused by any of these factors. Further studies would be needed to understand the relative importance of each effect.

As shown in Fig. 7, the combustion duration of all three fuels initially decreased with load due to lower dilution effect by the reduced amount of burned gas trapped in the cylinder at higher load. Beyond 4.2 bar IMEP, E15 and E85 showed increased combustion duration. As shown in Fig. 3, at such high load conditions, spark ignition was critical to initiate the combustion process in the form of flame propagation. Because of the relatively high temperature of the end gas region, multiple autoignition combustion would take place in conjunction with the flame propagation. This can be illustrated by the mass fraction burned curves at 4.2 and 6.6 bar IMEP values for E85 plotted in Fig. 8. It can be seen that the heat release process is characterised by a relatively slow first part and then followed by a faster second part. As previous studies have shown [16, 17], the two stage heat release process was a result of the hybrid combustion of flame propagation and multiple autoignition burning in the spark assisted CAI region. As the load increased beyond 4.2 bar IMEP, flame propagation became dominant over the multiple autoignition combustion and accounts for a greater part of the combustion and heat release process, resulting in an increase in the overall combustion duration.

3.3 Emissions

Figure 9 shows the unburned hydrocarbon (uHC) emissions as a function of engine output at 2000 rpm. The presence of ethanol reduced the uHC emissions

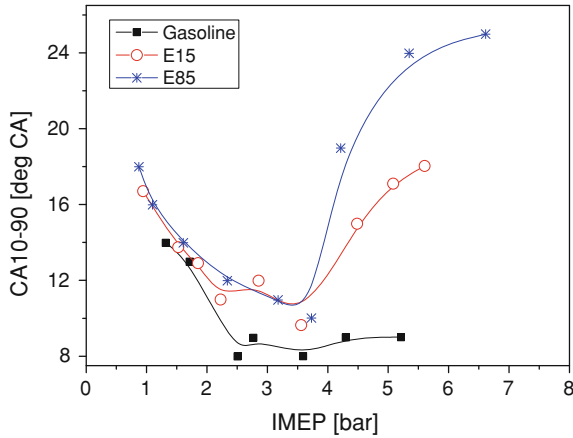


Fig. 7 CA10-90 in 2-stroke CAI operation at 2000 rpm

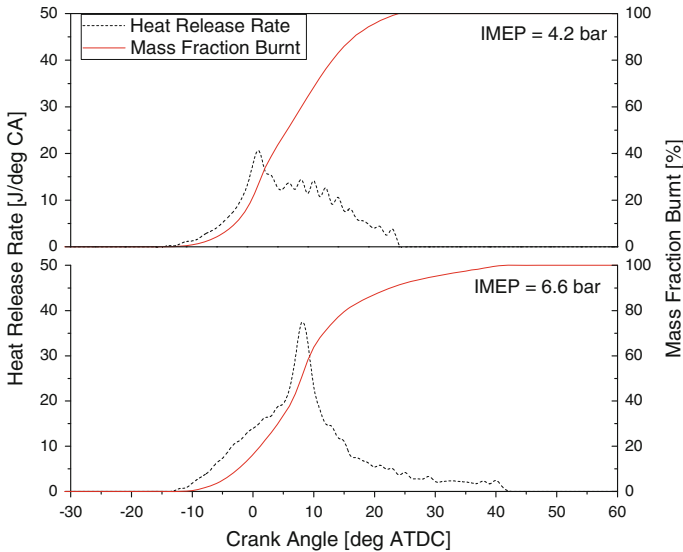
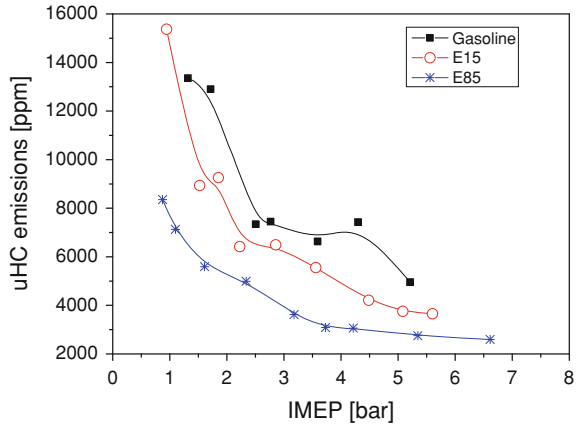


Fig. 8 Heat release rate and mass fraction burnt of E85 at 2000 rpm

throughout the load range. E85 produced about 50 % less uHCs than gasoline. As the combustion temperature became higher with load, more complete combustion could take place and hence less uHC emissions. As reported by the authors [18], the uHC emissions from the 2-stroke CAI combustion was not much different from the 4-stroke SI operations in the same engine. One major source of uHCs from this engine is due to the inadequate optimisation of fuel spray and combustion chamber design, which resulted in fuel impingement on the piston and cylinder

Fig. 9 uHC emissions in 2-stroke CAI operation at 2000 rpm



wall. It is expected that multiple fuel injection from a fast acting injector at higher injection pressure together with an appropriate designed piston top would lead to significant reduction in the uHC emissions.

The CO emission results in Fig. 8 show that E15 and E85 fuels produce less CO emissions, particularly at high load conditions, because of the more effective oxidation reactions of oxygenated ethanol. It is noted that gasoline produced significantly more CO at higher load whilst the CO emissions from E15 and E85 fuels remained relatively insensitive to the load. In order to explain the results, it is necessary to understand the air short-circuiting and its effect on in-cylinder air/fuel ratio.

As Fig. 2 shows, there was an overlap period between the intake process and exhaust process in the 2-stroke CAI mode operation. During this overlap period, it is likely that a fraction of air could flow directly out of the exhaust valves, a phenomenon known as air short-circuiting. In order to quantify the air short-circuiting rate, a fast response CO₂ analyser was adopted to measure the cycle-resolved air short-circuiting rate [18]. The in-cylinder air/fuel ratio was then deducted from the exhaust lambda value. As shown in Fig. 10, the short-circuiting rate increased with the engine load or boost pressure, combustion took place with richer fuel and air mixture at higher load, resulting in higher CO emissions with gasoline as shown in Fig. 11. When ethanol was introduced, the stoichiometric air to fuel ratio decreased. Hence less air at lower boost pressure was needed, reducing the short-circuiting rate. At low loads, the effect of ethanol on improving CO emissions becomes less significant because of the lower short-circuiting rate and lower combustion temperature of ethanol.

Figure 12 shows the NO_x emissions in the 2-stroke CAI operation fuelled with gasoline, E15 and E85 at an engine speed of 2000 rpm. E85 had significant effect on reducing NO_x emissions at high loads mainly due to the cooling effect of

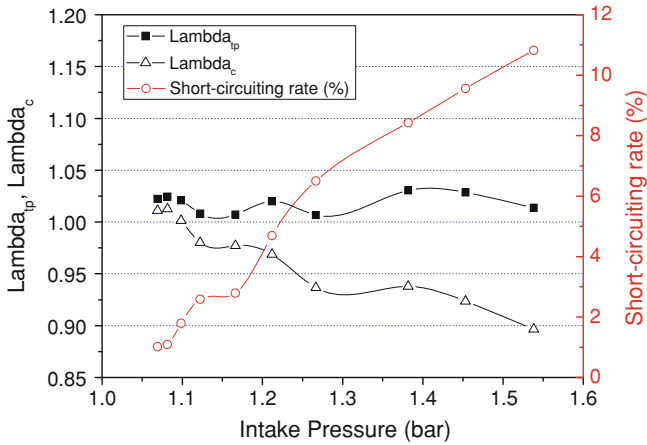
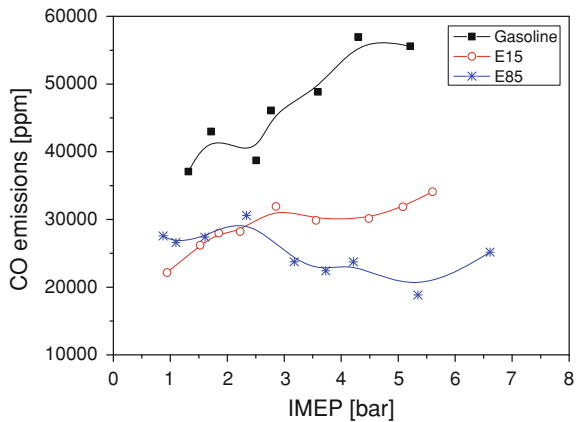


Fig. 10 The effect of short-circuiting on in-cylinder lambda (λ_c) and exhaust lambda (λ_{tp})

Fig. 11 CO emissions in 2-stroke CAI operation at 2000 rpm

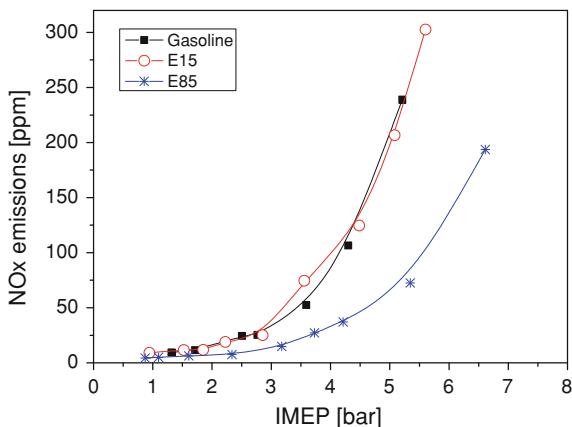


ethanol. However, this effect became less significant at low loads as the combustion temperature and NOx emission were very low (<100 ppm).

3.4 Efficiencies

In order to compare the fuel economy and take into account of the different calorific values of gasoline and ethanol, combustion efficiency, thermodynamic efficiency and indicated fuel conversion efficiency are calculated and analysed for gasoline and its blends with ethanol.

Fig. 12 NOx emissions in 2-stroke CAI operation at 2000 rpm



Combustion efficiency is defined as the ratio of the heat leased from the fuel to the chemical energy of the fuel, and its formula is:

$$\eta_{Combustion} = \frac{Q_1}{E_{fuel}} = 1 - \frac{G_{CO} \times 10.1 + G_{HC} \times 43}{Fuel\ flow\ rate \times LHV}$$

where, Q_1 is the heat leased by fuel E_{fuel} is the chemical energy of fuel G_{CO} is CO emission mass flow rate G_{HC} is HC emission mass flow rate LHV is Low heat value of fuel.

Thermodynamic efficiency is defined as the ratio of the gross work of the cycle to the heat leased by fuel, and its formula is:

$$\eta_{Thermodynamic} = \frac{W_{Gross}}{Q_1} = \frac{IMEP_{Gross} \times V_s}{Fuel\ flow\ rate \times LHV \times \eta_{Combustion}}$$

where, W_{Gross} is the gross work of the cycle $IMEP_{Gross}$ is the gross indicated mean effective pressure V_s is the displacement volume

Indicated efficiency is defined as the ratio of the gross work of the cycle to the chemical energy of fuel, and its formula is:

$$\eta_{Indicated} = \frac{W_{Gross}}{E_{fuel}} = \eta_{Thermodynamic} \times \eta_{Combustion}$$

Figure 13 shows their combustion efficiency values in the 2-stroke CAI operation at 2000 rpm. It can be seen that the combustion efficiency is relatively low on this engine due to the rich mixture in the combustion chamber caused by the short-circuiting of the air and non-optimized injection system, as mentioned above. However, compared with gasoline, the combustion efficiency was improved by 3–5 % by blending 15 % ethanol in the gasoline. Further increasing ethanol concentration to 85 % in the fuel could further improve the combustion efficiency at high load operation, but at low load operation the low temperature of the mixture caused by the higher latent heat value of ethanol led to lower combustion efficiency.

Fig. 13 Combustion efficiency in 2-stroke CAI operation at 2000 rpm

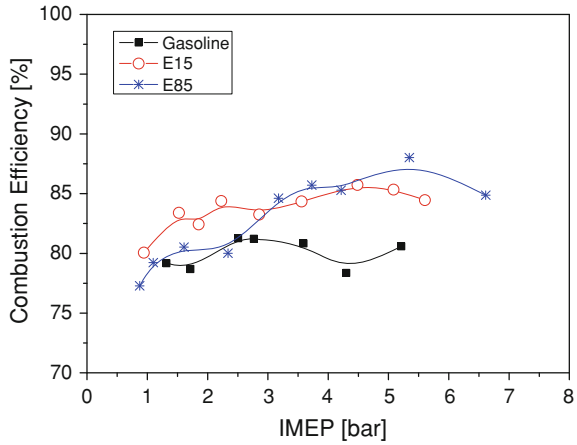
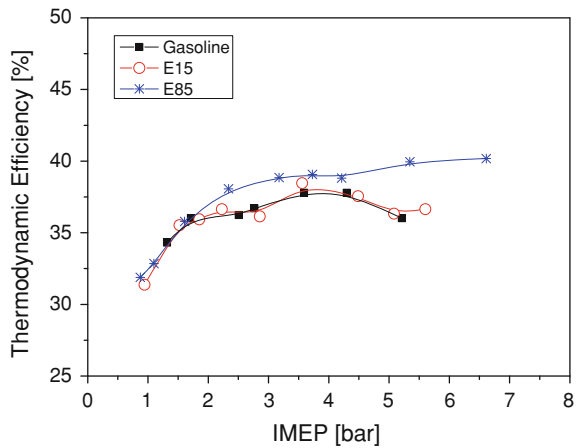


Fig. 14 Thermodynamic efficiency in 2-stroke CAI operation at 2000 rpm

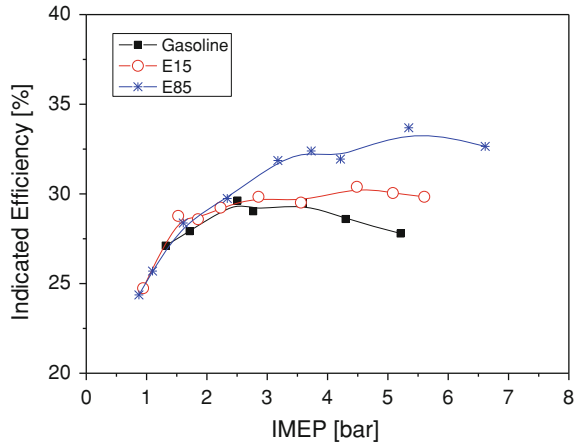


This is also reflected by the higher CO emissions of E85 at low load shown in Fig. 11.

The best thermodynamic efficiency was obtained with E85 at high load operation, shown in Fig. 14. This was the result of optimised combustion phasing as shown in Fig. 6 and reduced heat loss during the combustion process because of the lower charge and combustion temperature of ethanol. The presence of ethanol had little effect at low load operations.

Figure 15 shows the combined effect of combustion efficiency and thermal efficiency, as measured by the indicated fuel conversion efficiency. At 5 bar IMEP and 2000 rpm, the indicated efficiency can be improved by 5 % with E85 and 2 % with E15.

Fig. 15 Indicated fuel conversion efficiency in the 2-stroke CAI operation at 2000 rpm



4 Conclusions

In this paper, CAI combustion has been demonstrated on a poppet valve DI gasoline engine operating in the 2-stroke cycle. Gasoline and its mixture with ethanol, E15 and E85, were used and their ranges of CAI operations were determined as a function of the engine speed and load. Their combustion and heat release characteristics, emissions, and their combustion and thermodynamic efficiencies were determined and analysed. The results show that

1. 2-stroke CAI combustion operation can be achieved over a wide range of engine speed and load conditions, including idle operations that could not be achieved with 4-stroke operations.
2. The presence of ethanol allowed CAI combustion to be extended to higher load conditions. In the case of E85 the maximum IMEP of 8.4 bar was obtained at 800 rpm, significantly higher than the 4-stroke equivalent. Further improvement in the high load range at higher engine speeds can be achieved with a faster camless system or mechanical camshafts.
3. CO, uHC and NO_x emissions are significantly reduced by injecting ethanol blended fuels. E85 has greater effect on the emission reduction than E15.
4. Both combustion efficiency and thermodynamic efficiency are improved by the presence of ethanol because of the optimum combustion phasing and lower heat loss. E85 improved indicated fuel conversion efficiency by over 5 % at 2000 rpm.

The above results were obtained by keeping the relative air to fuel ratio to stoichiometric in the engine exhaust. Because of the air short-circuiting effect, the in-cylinder air to fuel ratio was lower and fuel rich combustion took place. Further works are currently being carried out to minimize the fuel consumption by increasing the air to fuel ratio at each operating condition. In addition, future improvement in the fuel injector and combustion chamber design are expected to

further reduce the uHC and CO emissions and improve the thermal efficiency and indicated fuel conversion efficiency, making the 2-stroke poppet valve engine a viable low emission and high efficiency IC engine for automotive applications.

References

1. Zhao H (ed) (2007) HCCI and CAI engines for the automotive industry. Woodhead Publishing, Cambridge
2. Zhao F, Asmus TW, Assanis DN, Dec JE, Eng JA, Najt PM (2003) Homogeneous charge compression ignition (HCCI) engines, key research and development issues, SAE Publication PT-94, Society of Automotive Engineers
3. Lavy J et al (2000) Innovative ultra-low NO_x controlled auto-ignition combustion process for gasoline engines: the 4-SPACE project. SAE paper 2000-01-1837
4. Koopmans L et al (2001) A four stroke camless engine, operated in homogeneous charge compression ignition mode with commercial gasoline. SAE paper 2001-01-3610
5. Law D et al (2001) Controlled combustion in an IC-engine with a fully variable valve train. SAE paper 2001-01-0251
6. Zhao H et al (2002) Performance and analysis of a 4-stroke multi-cylinder gasoline engine with CAI combustion. SAE paper 2002-01-0420
7. Fuehrhapter A et al (2003) CSI—Controlled auto ignition—the best solution for the fuel consumption—versus emission trade-off? SAE paper 2003-01-0754
8. Zhang Y, Zhao H et al (2011) Effects of injection timing on CAI operation in a 2/4-stroke switchable GDI engine. SAE paper 2011-01-1773
9. Zhang Y, Zhao H et al (2011) Experiment and analysis of a direct injection gasoline engine operating with 2-stroke and 4-stroke cycles of spark ignition and controlled auto-ignition combustion. SAE paper 2011-01-1774
10. Osborne RJ, Stokes J, Lake TH et al (2005) Development of a two-stroke/four-stroke switching gasoline engine—the 2/4SIGHT concept, SAE paper 2005-01-1137
11. Sadakane S et al (2005) Development of a new V-6 high performance stoichiometric gasoline direct injection engine. SAE paper 2005-01-1152
12. Zhao H, Ladommatos N (2001) Engine combustion instrumentation and diagnostics, P29, SAE
13. Heywood JB, Sher E (1999) The two-stroke cycle engine, P3, SAE
14. Heywood JB (1988) Internal combustion engines fundamentals, P29. McGraw-Hill Inc, New York
15. Zhang Y, Zhao H, Ojapah M, Cairns A (2011) Analysis of CAI/HCCI combustion in a 2-stroke poppet valve engine. In: ImechE conference on internal combustion engines: improving performance, fuel economy and emissions, London
16. Yang C, Zhao H, Megaritis T (2009) In-cylinder studies of CAI combustion with negative valve overlap and simultaneous chemiluminescence analysis. SAE technical paper 2009-01-1103. doi:[10.4271/2009-01-1103](https://doi.org/10.4271/2009-01-1103)
17. Zhang Y, Zhao H, Xie H, Hou S, Yang C (2010) Characterization and heat release model development of SI-CAI hybrid combustion and its application to a 4-stroke gasoline engine operating with highly diluted mixtures. In: 33rd international symposium of combustion, 3E07. Tsinghua University, Beijing, China
18. Zhang Y, Zhao H (2012) Measurement of short-circuiting and its effect on CAI or HCCI combustion in a two-stroke poppet valve engine. In: Proceedings of the institution of mechanical engineers. Part D J Automob Eng doi:[10.1177/0954407011434252](https://doi.org/10.1177/0954407011434252)

Technologies for the Next Generation of Downsized Gasoline Engines

Paul Freeland, James Taylor, Dave OudeNijeweme, Marco Warth and Bernd Mahr

Abstract Gasoline engine downsizing has been demonstrated to give significant reductions in vehicle fuel consumption and CO₂ emission levels by effectively moving the engine operating points for any given drive cycle to a more efficient region of the BSFC map. The limit to which downsizing can offer advantages to fuel efficiency therefore comes when the average engine operating points are centred around the minimum BSFC region. To take downsizing further, a number of complementary technologies are being explored with the aim of increasing overall efficiency and extending the operating region of optimum efficiency. Additional benefits can be derived from secondary effects when technologies are combined. This paper summarises such complementary technologies and discusses how they can be used in practice to further optimise gasoline engine efficiency.

Keywords Downsizing · Gasoline · CO₂ emission · Atkinson cycle · Alternative fuels

Abbreviations

AFR	Air/fuel ratio (mass)
BMEP	Brake mean effective pressure
BSFC	Brake specific fuel consumption
CO ₂	Carbon dioxide
FBP	Final boiling point (ref: fuel distillation curve)
FMEP	Friction mean effective pressure
IBP	Initial boiling point (ref: fuel distillation curve)

F2012-A01-016

P. Freeland · J. Taylor · D. OudeNijeweme · M. Warth · B. Mahr (✉)
MAHLE Powertrain Ltd, Northampton, UK
e-mail: marco.warth@mahle.com

LHV	Lower heating value (or lower calorific value of fuel)
RON	Research octane number
RVP	Reid vapour pressure (ref: fuel volatility)
ULG	Unleaded gasoline
WCEM	Water cooled exhaust manifold

1 Introduction

The reduction of CO₂ emissions, combined with increasingly stringent regulations for other tailpipe pollutants remains the dominant challenge for the development of future internal combustion engines. To realise these goals, significant measures need to be employed to improve vehicle fuel efficiency.

Gasoline engine downsizing provides a very cost-effective approach to improving fuel consumption by moving engine operating points to more efficient regions of the operating map, see Fig. 1. It is envisaged that an increasing number of downsizing engines will be developed over the coming years, and that the degree of downsizing (and thereby the specific power output) of engines will also increase in order to help meet this requirement. This will make technologies that help to maintain efficient engine operation at high loads more and more important.

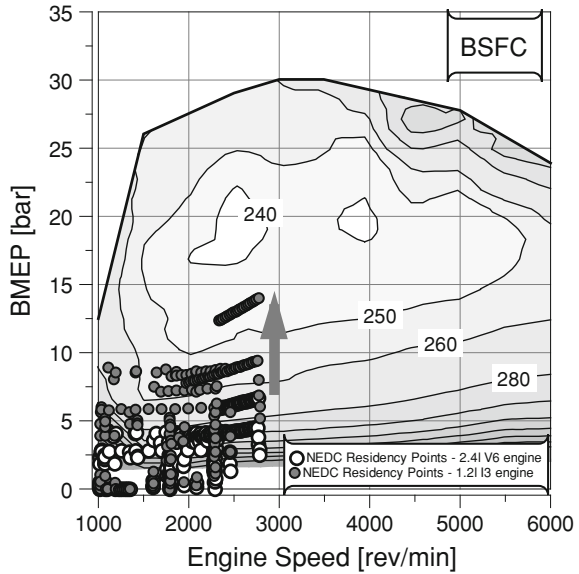
The biggest improvement in efficiency from the downsizing concept comes from de-throttling, which offers significant benefits when operating at light load conditions such as during the NEDC drive cycle. However, in order to maintain vehicle performance requirements engine specific power has to be increased through pressure charging, which can lead to poorer efficiencies at higher loads due to the need for reduced compression ratio, retarded combustion, and over-fuelling for component protection.

This reduction in high load efficiency can offset or potentially even negate the fuel consumption benefits of downsize engines when a vehicle is driven with wider throttle openings [1]. In this respect, with highly downsized engines vehicle fuel efficiency becomes much more sensitive to driving style, and vehicle CO₂ emissions levels will depend more strongly on the drive cycle being followed than is the case with larger naturally aspirated engines which inherently present a flatter BSFC map at high load.

1.1 Synergistic Technologies Beneficial to Downsizing

The following technologies all offer the potential to improve efficiency, especially at high load conditions:

Fig. 1 Illustration of the effect of downsizing on the operating points of an engine during the NEDC



- Increased temperature exhaust components.
- Increased Octane fuels (alcohol blends).
- Water Cooled Exhaust Manifold (WCEM).

The effects of these technologies are evaluated further in this paper.

2 High Temperature Exhaust Components

The simplest way of reducing the amount of overfuelling required at high loads for exhaust component protection is to use materials capable of withstanding higher temperatures. Typically, the limiting component on turbocharged engines is the turbine itself, and the material specification is dictated by component price. For high-volume, low specific output engines, typical limits for pre-turbine gas temperature range between 900 and 950 °C. For higher specific output engines, and where component piece price is less important, it is quite common to use a higher nickel content alloy that can withstand operation with pre-turbine gas temperatures of up to 980 °C. Several suppliers are now offering turbocharger assemblies that can withstand up to 1050 °C pre-turbine gas temperatures.

Results from testing conducted with the MAHLE downsize demonstrator engine, comparing the overfuelling requirement for a 980 °C pre-turbine temperature limit, versus that required for a 1050 °C specification turbocharger are shown in Fig. 2.

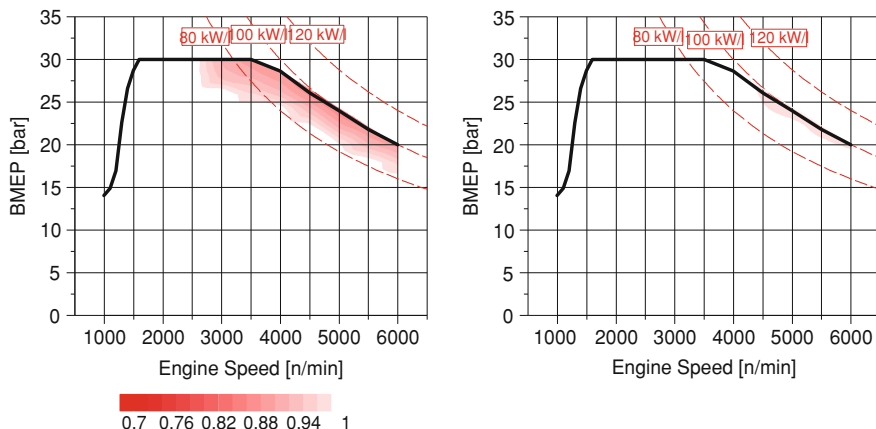


Fig. 2 Overfuelling map for the 980 °C turbocharger (*left*) and the 1050 °C turbocharger map (*right*)

This increased temperature limit significantly reduced the amount of enrichment needed to the extent that with this turbocharger, lambda 1 fuelling could be maintained up approximately 95 kW/L. The richest overfuelling required was $\lambda = 0.96$, for 100 kW/L at 5500 rev/min.

3 Increased Octane Fuels

An alternative to simply increasing the thermal resilience of the exhaust components is to use fuels that have a higher resistance to knock. At high load, these enable the spark timing, and hence the combustion phasing, to be advanced to more favourable settings. This both reduces exhaust gas temperatures directly, and increases the thermal efficiency of the engine which in turn reduces the engine boost requirement. This then gives further benefits in that compressor work is reduced, leading to lower charge air temperatures, and turbine work is reduced which leads to lower pre-turbine exhaust pressures and reduced pumping work and residual gas fractions.

Due largely to increased evaporative cooling properties and, to a lesser extent, increased auto ignition temperatures, blending alcohols into gasoline has proven very successful in increasing the RON rating of the blend [2]. Direct injection of these fuel blends into the engine cylinder enables the maximum advantage of the high latent heat of vaporisation to be realised, further reducing in-cylinder gas temperatures and thereby enabling optimum combustion phasing or higher compression ratios for a given charge air temperature to be achieved. The combination of alcohol fuel blends, downsizing and direct injection are therefore all mutually beneficial.

Table 1 Fuel properties for the gasoline and alcohol blends evaluated

Fuel	RON	Density (kg/m ³)	RVP (kPa)	IBP (°C)	FBP (°C)	C (%) m/m)	H (%) m/m)	O (%) m/m)	LHV (%) m/m)
95 RON ULG	95	0.74	48	37	167	86.6	13.3	0.1	43.2
Bu16	98	0.75	43	41	163	82.9	13.4	3.7	41.5
E10	99	0.75	55	40	166	82.7	13.3	4	41.4
E22	102	0.73	53	41	164	78.5	13.4	8.1	39.4
102 RON ULG	102	0.75	102	37	122	84.7	12.8	2.5	41.8
E85	106	0.78	40	52	83	56.9	13	30.1	29.6

However, it needs to be considered that blending alcohols with gasoline also reduces the calorific value of the blend, requiring a higher fuel flow rate for a given power output.

During development of the downsize demonstrator engine, a study was made of the effects of different alcohol blends on engine operation. The pertinent properties of the fuels used during this study are given in Table 1.

3.1 Full Load Effects

Figure 3 shows a comparison of some of the key full load performance parameters between operation on 95 RON gasoline and the same fuel blended with 85 % ethanol (E85). For a set torque value, the boost requirement with the E85 fuel was lower than with 95 RON gasoline, yet the mass based BSFC values were greater. This is due to the reduced calorific value of the E85 fuel. On the positive though, the E85 fuel did allow nearer to optimum combustion phasing and air fuel ratio's closer to lambda 1 to be maintained as the engine approached peak power at 5000 rev/min. Indeed, the reason why combustion phasing remained slightly retarded from optimum was not the knock limit, but rather the peak combustion pressures design guide limits at this stage, as the engine's robustness had not been fully validated.

Because of the increasing difference in lambda values as engine speed increased, the BSFC values between the two fuels began to converge. As the engine approached maximum speed at 6000 rev/min, the advanced spark timing and reduction in overfuelling on E85 meant the mass based BSFC was approaching that of 95 RON gasoline.

Figure 4 shows a comparison of the lambda values required to maintain safe exhaust temperature limits which was conducted later during the engine's development program on a wider range of gasoline and alcohol fuel blends than were performed previously and over a wider range of engine loads. It can be seen that a significant degree of over fuelling was required on the 95 RON and 98 RON fuels.

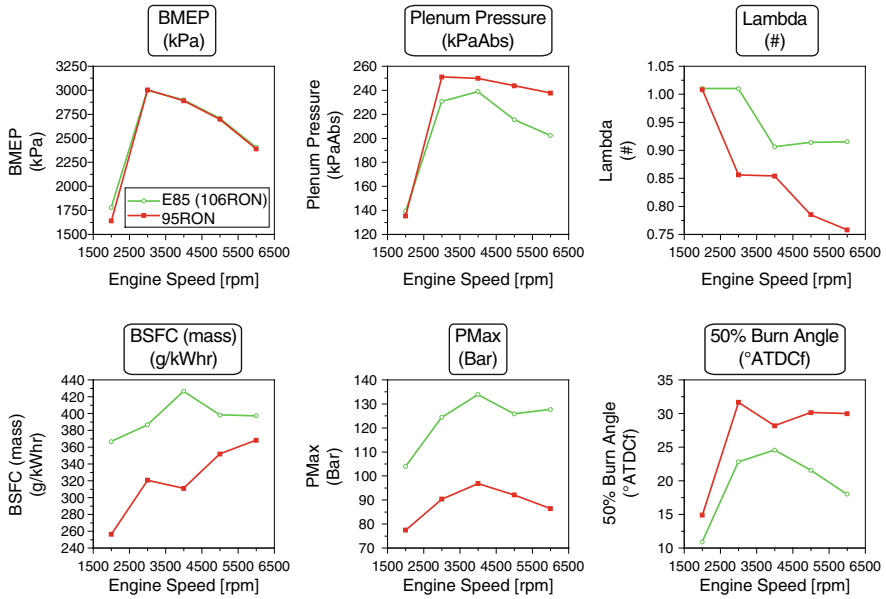


Fig. 3 Comparison of full load performance factors with 98 RON gasoline and E85 fuels

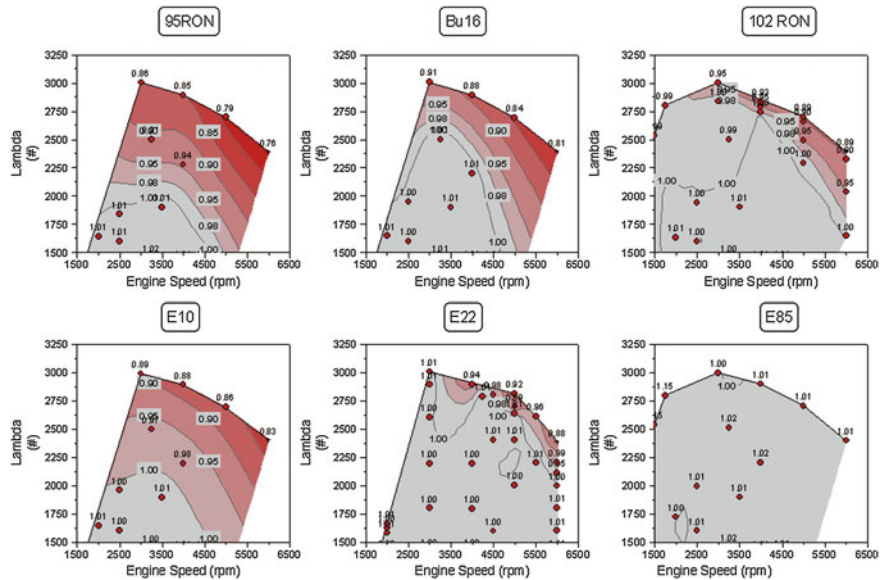


Fig. 4 Lambda values for exhaust component protection for different blends of fuel

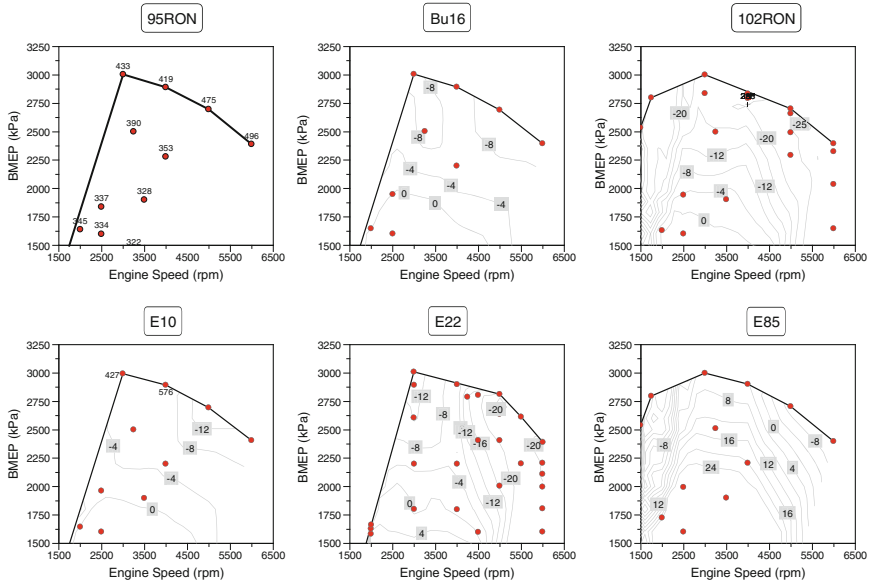


Fig. 5 Volumetric BSFC values (cm^3/kWh) for 95 RON gasoline and relative difference for the other blends

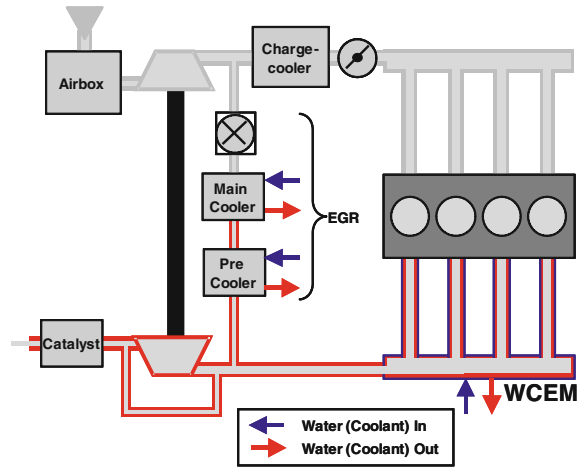
However, when fuels with 102 RON were used (the E22 blend and the 102 RON gasoline), engine over fuelling was almost eliminated, and for the high RON fuel (E85), the engine could now run stoichiometric across the engine map.

Figure 5 shows the relative difference in volumetric BSFC, which accounts for the difference in fuel density, on each fuel compared to operating the engine on 95 RON gasoline. Increasing the octane rating of the gasoline fuel by three octane numbers from 95 RON to 98 RON resulted in between a 0 and 12 % reduction in BSFC over the full load region of the map. The largest benefits came where the over fuelling requirements were greatest. The level of improvement given by the E22 blend was even greater than this, with volumetric BSFC benefits improved by up to 20 % compared to 95 RON. The higher calorific value of the 102 RON gasoline, showed an even greater benefit of up to 25 % over the 95 RON gasoline. E85 generally gave worse BSFC values up to the peak power region, but around peak power it achieved a 5 % improvement in volumetric BSFC over 95 RON despite its far inferior calorific value.

4 Water Cooled Exhaust Manifold

A WCEM is a direct approach to reduce overfuelling by cooling the exhaust gas before it enters the turbine housing of the turbocharger assembly. However, it should be noted that although a WCEM can reduce turbine entry temperatures

Fig. 6 MAHLE designed WCEM and EGR circuit (schematic)



significantly by extracting heat after the exhaust port, it has negligible impact on exhaust port temperatures themselves. Therefore, beyond a certain level of heat extraction the port temperatures then become the limiting factor regarding the overfuelling requirement. In this situation, additional benefits can be derived from using a combination of WCEM and full load EGR.

4.1 Engine/Manifold Installation

A 1.4 L production turbocharged engine was used for these investigations. This engine was also fitted with a high pressure EGR circuit. This took exhaust gas from the WCEM (pre-turbine) via the integrated wastegate; the EGR was then cooled through an EGR pre- and main cooler. The EGR rate was metered by an EGR valve and drawn into the intake pre-charge cooler. An independent cooling rig was used to cool the EGR to less than 100°C. A schematic of the WCEM and EGR circuits is shown in Fig 6.

4.2 Results

Initial testing with the WCEM demonstrated that the cooling capacity of the WCEM could reduce pre-turbine gas temperatures by approximately 130 °C. However, it was also observed during the run-up line that the addition of the WCEM led to a further degradation of available torque due to the reduction in exhaust gas enthalpy. The effect was to delay the speed at which target torque could be achieved by approximately 500 rev/min.

Fig. 7 Effect of the MAHLE WCEM on overfuelling and BSFC on a highly boosted four cylinder engine

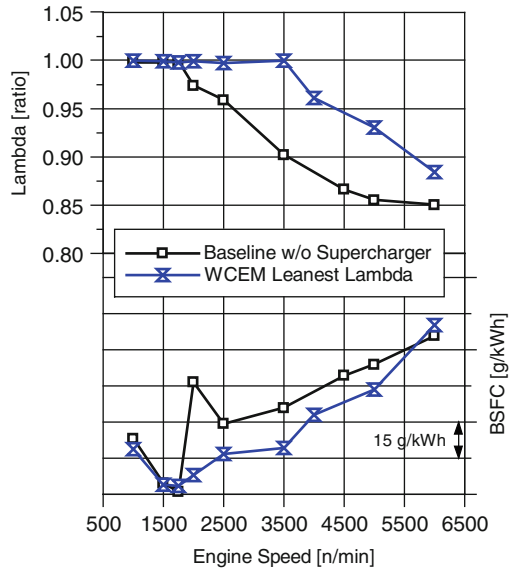


Figure 7 shows the exhaust lambda and fuel consumption effect of the WCEM alone. It should be pointed out that although the maximum pre-turbine temperatures encountered were only 915 °C, there was still a requirement to enrich fuelling above 3500 rev/min in order to keep exhaust port temperatures below their limit of 950 °C.

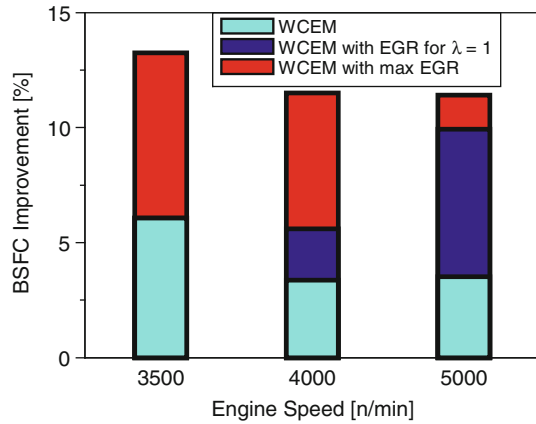
This demonstrates that the benefit of removing heat after the exhaust ports is limited, and that to optimise the benefits of a WCEM, either of two approaches can be taken:

1. The WCEM design could be re-optimised to ensure that the exhaust port temperature limit is reached at the same point as the current pre-turbine temperature limit. This could be achieved by reducing the “gas-wetted” area of the manifold, thereby enhancing catalyst light-off times and potentially low-speed BMEP performance.
2. A lower cost turbine material could be selected, to take financial advantage of the lower gas temperatures fed to the turbine.

During this testing it was noticed that the gains in fuel consumption were not as great as the change in lambda should offer. This was due to the fact that increased boost pressure was required to maintain target torque, which was considered to be due to a combination of the leaner lambda values at low speeds, and the removal of the exhaust flow splitter from the manifold.

Figure 8 shows a comparison between the fuel consumption benefits achieved through application of WCEM technology alone, the WCEM in conjunction with the minimum EGR for $\lambda = 1$, and the WCEM with maximum EGR.

Fig. 8 The BSFC improvements obtained with the WCEM and with the further addition of cooled EGR



At 3500 rev/min, the addition of the WCEM alone allowed a reduction in overfuelling sufficient to give approximately 6 % improvement in BSFC. Adding cooled EGR at this speed enabled lambda 1 fuelling and increased the BSFC benefit to 16 %.

At 4000 rev/min, the addition of the WCEM gave an initial benefit of approximately 3 % in BSFC. Adding sufficient EGR to enable lambda 1 fuelling brought an additional 2 % benefit to BSFC, whilst adding further EGR to suppress knock increased the BSFC benefit to approximately 12 %.

At 5000 rev/min, the initial benefit achieved with just the WCEM was very similar to that given at 4000 rev/min. However, as fuel enrichment was greater, then the extra benefit achievable by adding sufficient EGR to give lambda 1 fuelling was greater, taking the improvement in BSFC up to approximately 11 %. Thereafter some further benefit was achieved by increasing EGR rates, although the amount was limited to around 2 % because further EGR rates prevented target power from being achievable.

5 Conclusions

The greatest reductions in high load fuel consumption with highly boosted downsize engines comes from the need to keep exhaust gas temperatures within safe limits for component durability, and the need to retard spark timing from optimum, due to knock. The technologies demonstrated here have all shown significant benefits in alleviating these problems:

- The use of a turbocharger assembly rated for 1050 °C on the Downsize demonstrator engine has demonstrated the feasibility of a 100 % lambda 1 concept giving 100 kW/litre specific power output. Such a concept would also enable high catalyst conversion efficiencies to be maintained throughout the entire

operating range of the engine. This level of technology is readily available now, and the only constraint is that of component price. Therefore it offers one of the easiest solutions to implement where the efficiency improvements justify increased costs.

- The use of alcohol blended fuels have demonstrated reductions in full load BSFC of between 5 and 25 % despite reductions in calorific value, due to a reduced tendency for knock brought about by the increased latent heat of evaporation of the fuels when used in direct injection engines. However, BSFC at part load conditions increased, approximately proportionally to the calorific value of the fuel. Therefore, the advantages of these fuels become more relevant with extreme downsizing concepts, and even then, the total alcohol content needs to be kept below about 20 % to avoid significant reductions in the heating value. Currently, in many markets the availability of alcohol blended fuels is limited, and most manufacturers regard the available fuel grades as a design constraint rather than an engine efficiency variable. To overcome this is likely to require a significant increase in customer demand, which may require further legislative incentives as well as significant marketing efforts.

The use of a water cooled exhaust manifold has shown the capability to reduce pre-turbine gas temperatures by up to 130 °C, thereby allowing reductions in the amount of overfuelling required, and giving benefits of up to 5 % reductions in fuel consumption. However, the overall benefits in reduced overfuelling are limited as exhaust port temperatures then become the limiting factors. It does appear that WCEM technologies can give very worthwhile commercial benefits in allowing cheaper components and reduced parts count, and in conjunction with cooled EGR, total fuel consumption benefits of around 14 % at high load are achievable. The additional benefits of faster warm-up times, and reduced parts count make this technology very attractive for engine manufactures.

References

1. Lenaers G (2009) Real life CO₂ emission and consumption of four car powertrain technologies related to driving behaviour and road type. SAE technical papers 2009-24-0127
2. Oudenijeweme D et al (2011) Downsizing and biofuels: synergies for significant CO₂ reductions” 20. Aachener Kolloquium Fahrzeug- und Motorentechnik

Control System Development for Gasoline HCCI Engine Which Based on Heat Management

Jianyong Zhang, Zhen Huang, Qi Yin, Yitao Shen, Lin Chen
and Shiliang Lv

Abstract Homogenous Charge Compression Ignition (HCCI) technology shows a great fuel economy potential for gasoline engine. In the project, a 4-cylinder 1.5 L PFI gasoline engine with HCCI and SI combustion mode was developed based on optimized heat management. The exhaust gas energy and coolant energy are used for heating intake air to suitable temperature as soon as possible. The exhaust turbocharger and EGR are used to expand HCCI operating range. Also cylinder pressure sensors are used for combustion feedback control and cylinder balance control. For this HCCI prototype engine, an innovative control system was developed for this complicated system. Control System has two ECUs, one ECU is for cylinder pressure sensor processing, which calculate combustion character values in real time and send to main ECU by CAN bus; another ECU is main ECU, which control injection system, ignition system, heat management system, etc. The control algorithm for mode transition between HCCI and SI was developed. Cylinder balanced algorithm base on CA50 was also developed to optimize emission and engine performance. By the optimized heat management system and control system algorithm, the HCCI engine can get 20 % fuel economy benefit in HCCI mode in part load, and also reach a wider operating range by the combination of turbocharger and EGR technology.

Keywords HCCI engine · Engine heat management · HCCI control algorithm · Mode transition · Cylinder balance

F2012-A01-019

J. Zhang (✉) · Z. Huang
Shanghai Jiaotong University, Shanghai, China
e-mail: zhangjianyongzjy@163.com

Q. Yin · Y. Shen · L. Chen · S. Lv
SAIC Motor Technical Center, Shanghai, China

1 Introduction

Homogenous Charge Compression Ignition (HCCI) technology shows very high potential for better fuel consumption and lower emissions. The principle of HCCI combustion is auto ignition of a very lean and homogenous air/fuel mixture. The key point to realize HCCI combustion is that mixture temperature should reach the auto ignition temperature at certain time in cylinder. Many techniques have been used to realize HCCI mode, such as negative valve overlap [1], variable compression ratio [2], intake air heating [3], dual fuel combustion [4], etc.

Besides engine system change, the control system of HCCI engine also meets a great challenge. Cylinder pressure sensor should be used for combustion state feedback and auto ignition control. The control system should also realize smooth mode transition between SI and HCCI mode.

The research work relates to use heat management to achieve auto ignition temperature for HCCI combustion. The control system realized cylinder pressure based feedback control for multiple cylinder balance and engine torque control. Two ECU prototypes are used for HCCI engine, the main ECU does engine control mainly, and another ECU only do cylinder pressure sensor processing and send combustion information to main ECU by CAN.

2 Experimental Setup

The test engine is 1.5 L port fuel injection (PFI) engine. The specifications of the engine are shown in Table 1.

The piston geometry was changed increase compression ratio from 10.5:1 to 13:1. So the mixture temperature could be higher after compression. In the research, heat management and higher compression ratio are used for increasing mixture temperature.

A new heat management was realized to reach the mixture temperature for HCCI and SI. The structure of heating system was shown in Fig. 1. The heat management system has two stage heat exchangers. The intake air was heated by coolant heat exchanger and then heated by exhaust heat exchanger. The intake system has three throttles at main pipe, cold pipe and hot pipe to realize fast air temperature control. Also the system was designed together with EGR system and charger system. The heat exchangers are controlled by four valves. The throttles and valve are controlled for realizing different intake air temperature according to system requirement, as shown in Table 2.

Table 1 Engine specification

Engine type	PFI, 4 valve DOHC gasoline
Bore	75 mm
Stroke	84.8 mm
Displacement	1.498 L
Compression ratio	13:1

The HCCI engine was tested in dynamometer, as shown in Fig. 2. The intake manifold was built with metal material and thermal insulation coating on surface. The intake air temperature sensor in intake manifold is fast thermocouple sensor. The Kistler sensors were integrated in spark plugs in four cylinders.

The control system for research engine was based on prototype ECU. Control System structure was shown in Fig. 3. One 128 pin Mototron ECU was used for main control ECU, another 112 pin Mototron ECU was used as cylinder pressure processing ECU.

3 Control Algorithm

The engine control software structure is shown in Fig. 4. It has normal engine control functions, integrated with HCCI control functions. Driver command is interpreted to torque demand, and then the system decides which combustion mode according torque demand and engine state. When target combustion mode is determined, the charge system calculates the desired throttle angle. The injection time will be calculated according to target air/fuel ratio. The ignition angle is restrained by knocking limit and torque demand. The heat exchanger valves are controlled by intake air desired temperature.

The 112 pin Mototron ECU samples four cylinder pressure signals and crank sensor signal, and then calculated all combustion state information in each cycle. All combustion state information is sent to main ECU by CAN. The maximum pressure p_{Max} and maximum pressure increasing rate $(dp_{Max}/d\phi)_{Max}$ are mainly used for engine protection and knock detection.

According to thermodynamic law, without considering heat transfer to wall, rate of heat release ROHR is calculated as

$$ROHR(i) = \frac{\kappa}{\kappa - 1} \cdot p(i) \cdot [V_{cyl}(i) - V_{cyl}(i - 1)] \\ + \frac{1}{\kappa - 1} \cdot V_{cyl}(i) \cdot [p(i) - p(i - 1)]$$

where κ is isentropic exponent.

Accumulated heat release is calculated as

$$AHR(i) = AHR(i - 1) + ROHR(i) \cdot [\phi(i) - \phi(i - 1)]$$

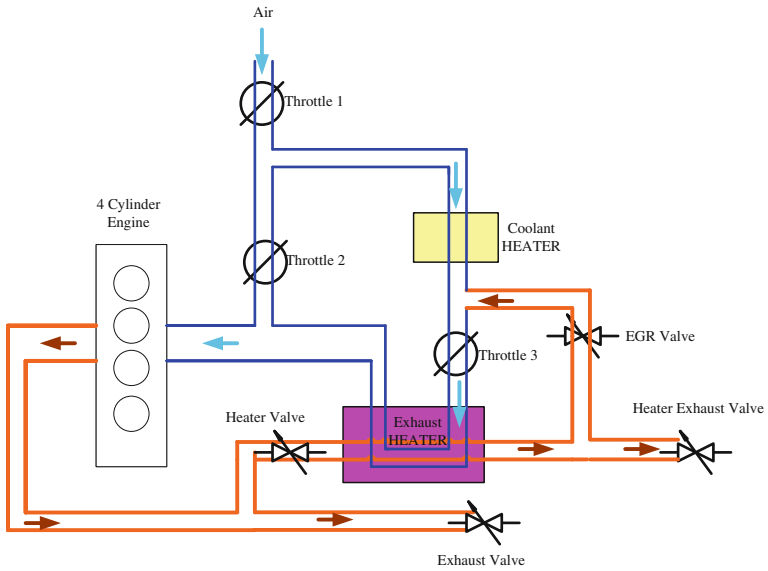
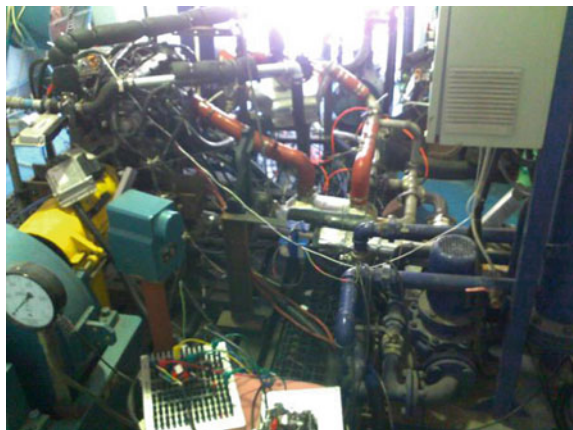


Fig. 1 Heat management system structure

Table 2 Heat management system control

Mode	SI	HCCI
Throttle 1	Open	Open
Throttle 2	Open	Closed
Throttle 3	Closed	Open
Heater valve	Closed	Open
Exhaust valve	Open	Closed
Heater exhaust valve	Open	Open
EGR valve	Closed	Open

Fig. 2 4-cylinder HCCI engine with heat management



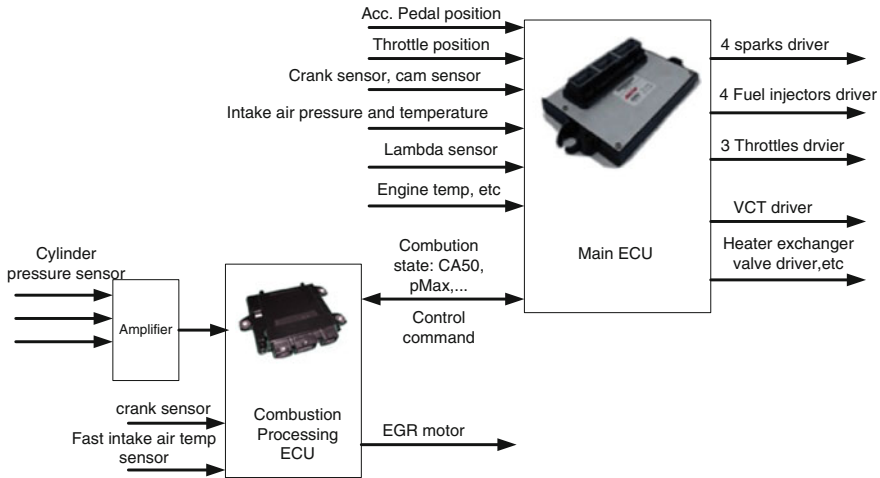


Fig. 3 Control system structure

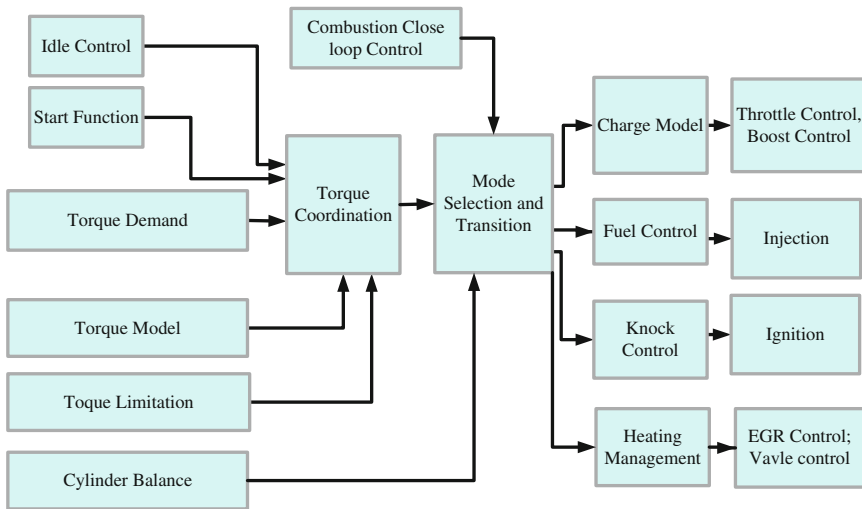


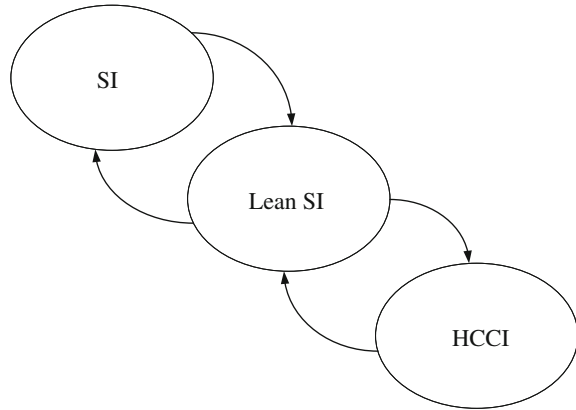
Fig. 4 HCCI engine control software structure

CA10 is the crank angle when AHR reaches 10 % of maximum, and CA50 is the crank angle when AHR reaches 50 % of maximum. CA10 and CA50 are used as combustion state and misfire monitoring for HCCI control.

The indicated mean effective pressure for each cylinder is calculated as $IMEP = \frac{1}{2 \cdot V_h} \sum ([p(i) + p(i - 1)] \cdot [V_{cyl}(i) - V_{cyl}(i - 1)])$ where V_h is the one cylinder displacement for each cylinder.

With IMEP information the ECU can get the torque value in each cycle, so the torque model could be more simple and accurate.

Fig. 5 HCCI mode transition



The main combustion modes are SI and HCCI. HCCI can be realized in part load. In high load, engine should return to SI load due to knocking and stabilization limitation. Because of heat inertia, the heat management system cannot change intake air temperature to target temperature in few cycles. So there is Lean SI mode between SI and HCCI mode. In Lean SI mode, the mixture is ignited by spark in lean combustion. The target lambda value is in the range from 1 to 1.5, which is depends on current intake temperature. External EGR is integrated in Lean SI to decrease NO_x emissions.

When the engine combustion needs to change from SI to HCCI mode, the heat management system changes the valve opening state to increase intake air temperature. Before temperature reaching HCCI combustion threshold temperature, the engine state is Lean SI mode, in which torque is still determined by fuel injection quantity and ignition angle. When the HCC combustion threshold is reached, the throttle will be fully opened, and ignition can be disabled, mixture can ignite automatically. When the engine combustion needs to change HCCI to SI mode, the heat management system changes the valve opening state to decrease intake air temperature. Before the temperature reaching the SI combustion threshold, the engine state should go to Lean SI mode first (Fig. 5).

Cylinder balanced algorithm will trigger when the variance of peak cylinder pressure in four cylinders exceeds high limit parameter. The calculation is based on cylinder pressure signal sampling and processing. In SI mode, the throttle open angle and ignition angle will be tuned to realize cylinder balance. In Lean SI mode, the injection fuel quantity and ignition angle will be tuned to realize cylinder balance. In HCCI mode, the injection fuel quantity will be tuned to realize cylinder balance.

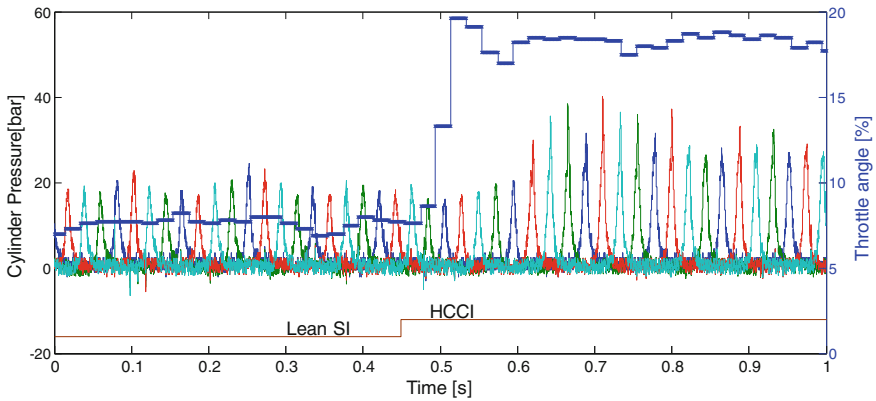


Fig. 6 Transition from lean SI to HCCI mode

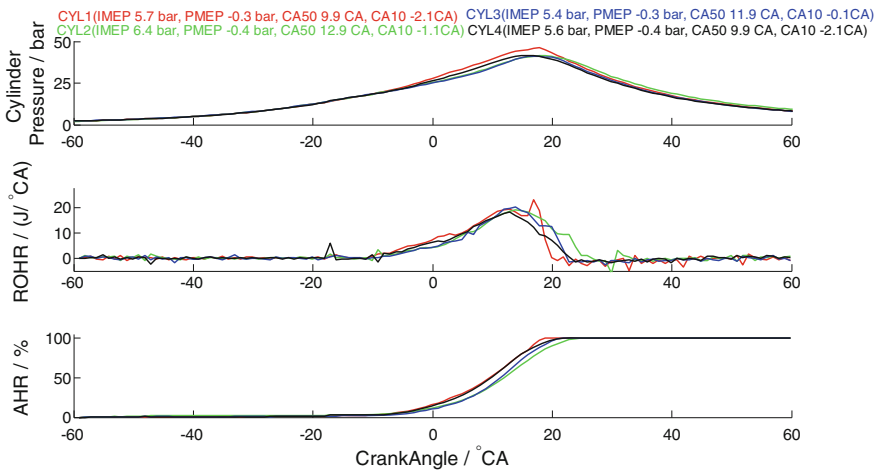


Fig. 7 Heat release in HCCI mode

4 Experiment Results

The HCCI engine heat management system starts to heat intake air when torque command needs system to go to HCCI mode. The heat valve is opened and exhaust pipe valve is closed, so the intake air will be heated by coolant and exhaust gas in hot pipe intake flow. The throttle in cold pipe will be closed. The intake air temperature begins to increase. The throttle angle will increase slowly to reach the target air/fuel ratio. After about 15 min, when the temperature reaches the auto ignition temperature (about 200 °C), the throttle will open to reach a high air/fuel ratio, target lambda would be about 2–2.5, and the ignition angle will be disabled or delayed to a late angle after TDC. The mixture could be auto ignited in this

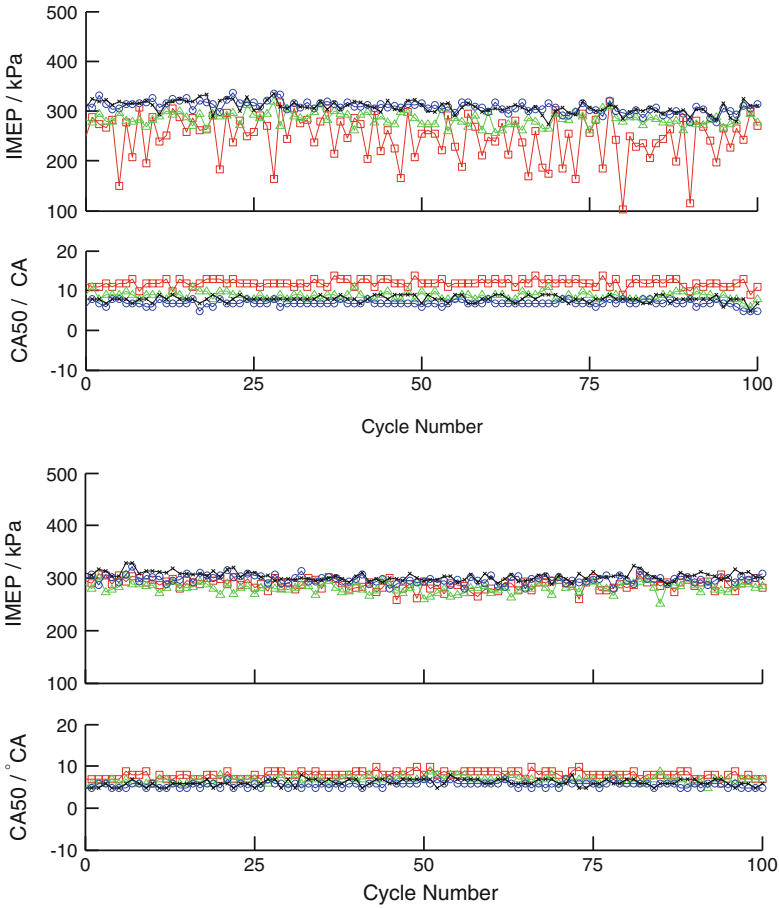


Fig. 8 Comparison of cylinder balance method. **a** Without cylinder balance. **b** With cylinder balance

temperature, as shown in Fig. 6. In HCCI mode, the heat release characteristic has been refined, as shown in Fig. 7.

When engine needs to change mode from HCCI to SI, the heat management system first opens cold pipe throttle and closes hot pipe throttle. The heat valve will be closed and exhaust valve will be open. Engine firstly changes to Lean SI mode to prevent knocking when intake air temperature does not reach the low threshold. After the intake air temperature reaches the low threshold (about 70 °C), the engine changes to SI combustion mode. The throttle will be controlled by target air charge from torque demand and the fuel injection quantity will be calculated by stoichiometric air/fuel ratio.

In HCCI mode, the engine torque is mainly determined by injected fuel quantity. For multiple cylinders engine, there is temperature deviation for different

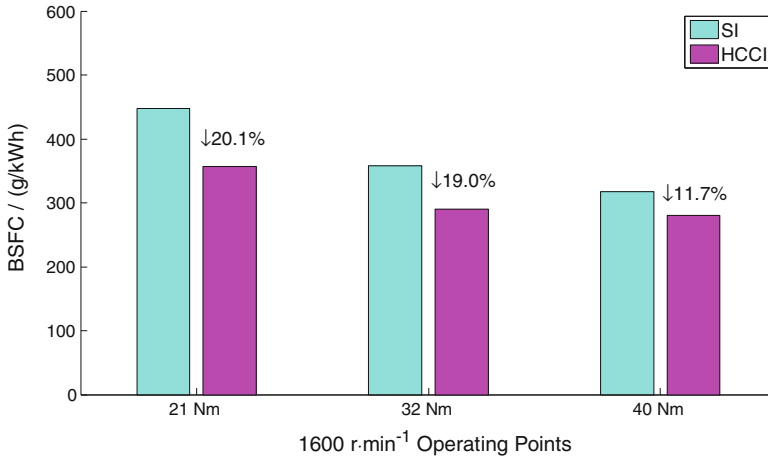


Fig. 9 Fuel consumption in HCCI mode (1600 r/min)

cylinder due to intake system, so the cylinder pressures are different for the four cylinders. The cylinder balance algorithm detects the variation of four cylinder pressures, and starts when the variation exceeds the high threshold. The algorithm mainly tunes the injected fuel quantity for each cylinder according to torque demand. The effect is shown in Fig. 8.

In part load, HCCI mode can get a great fuel consumption benefit because of lean homogenous combustion and low pump loss. Figure 9 shows in 1600 r/min, the BSFC in HCCI could be 20.1 to 11.7 % lower than in SI mode. The fuel consumption benefit is mainly come from lean burning, lower pump loss and exhaust heat reuse.

5 Conclusion

A 4 cylinder HCCI engine prototype has been built. The control system can realize HCCI control base on cylinder pressure feedback. This research engine shows a great potential of fuel consumption improvement in part load.

With the cylinder pressure feedback, an additional combustion processing ECU is used, which calculated all current combustion information. If the calculation capability of ECU becomes more powerful, all function could be integrated in one main ECU.

For multiple cylinders engine, the variation of cylinders and cycles is inevitable, cylinder balance algorithm could make cylinder pressure and CA50 of each cylinder become more close to mean value. With this, the engine could run smoothly.

With the heat management system, the coolant water and exhaust gas could be used to heat intake air to auto ignition temperature. Due to heat inertia, the intake air temperature need about 15 min from 50–200 °C and about 3 min from 200 to 60 °C. So the Lean SI mode is necessary between SI and HCCI mode transition. In future, the heat management should be improved to short the temperature change time. Also the heat management system will be redesigned in more compactable package for vehicle application.

Now the HCCI combustion mode is mainly used in part load, the operating range should be extended by turbocharger and external EGR.

References

1. Lavy J et al (2000) Innovative ultra-low NO_x controlled auto-ignition combustion process for gasoline engines: the 4-SPACE project. SAE paper 2000-01-1837
2. Christensen M, Hultqvist A, Johansson B (1999) Demonstrating the multi fuel capability of a homogeneous charge compression ignition engine with variable compression ratio. SAE paper 1999-01-3679
3. Yang J, Culp T, Kenney T (2002) Development of a gasoline engine system using HCCI technology—the concept and the test results. SAE paper 2002-01-2832
4. Chen Z, Konno M, Oguma M, Yanai T (2000) Experimental study of CI natural-gas/DME homogeneous charge engine. SAE paper 2000-01-0329

The Effect of Advanced Combustion Control Features on the Performance of a Highly Downsized Gasoline Engine

Karl Giles, Andrew Lewis, Sam Akehurst, Chris Brace
and Nick Luard

Abstract This paper concludes the preliminary findings of a study on the effects of valve timing and manifold air temperature on the combustion performance of a 60 % downsized, turbocharged and supercharged SI engine. Experimental data was gathered on a four cylinder, 2.0 litre prototype engine running at 1,000 rpm, $\lambda = 1$ with a constant intake manifold pressure of 2,200 mbar(A) and a targeted exhaust manifold pressure of 1250 mbar. A hybrid experimental approach using Design of Experiments theory guided by 1D simulation predictions was used to derive an efficient experimental procedure using Matlab's Model Based Calibration (MBC) toolbox in order to minimise the volume of testing required to characterise the engine behaviour at this condition. Experimental data was used to produce empirical models for engine responses such as torque, BSFC and NOx emissions and IMEP coefficient of variance (CoV). The model inputs were intake and exhaust cam phasing, manifold air temperature and spark advance. It was found that quadratic approximations for all of the responses modelled provided acceptable model fit in terms of statistical metrics such as R^2 , RMSE and PRESS equivalents. Optimisation studies based on the empirical models to determine the locations of best engine performance in terms of the responses modelled were completed. A maximum torque of 416Nm was predicted at the condition of maximum intake cam advance and exhaust cam retard (maximum valve overlap). This was attributable to an observed peak in engine airflow, a result of favourable manifold pressure pulsation interactions between cylinders. BSFC and at this point was found to be 365 g/kWh. As expected, manifold

F2012-A01-021

K. Giles (✉) · A. Lewis · S. Akehurst · C. Brace
University of Bath, Bath, UK
e-mail: agjl20@bath.ac.uk

N. Luard
Lotus Cars, Cheshire, UK

air temperatures of 28 °C (coldest tested) were predicted to give the best torque performance due to the improved volumetric efficiency and combustion phasing achievable with colder charge temperatures. A minimum BSFC of 219 g/kWh was predicted to occur in the region of 0° intake cam advance and 28° exhaust cam retard (from maximum opening points of 150 °aTDC and 126°bTDC respectively). This gain in BSFC however comes at the cost of a 150 Nm drop in brake torque. The reduction in torque output was due to a reduction in engine airflow (a response largely dictated by intake cam phasing). However improved scavenging of exhaust gas residuals and an in-cylinder mixture closer to $\lambda = 1$ are likely to have improved combustion efficiency at this point, resulting in a proportionally better BSFC. Small changes in the available combustion parameters have been shown to have significant impact on the combustion behaviour leading to trade-offs in performance and efficiency. Optimisation studies for NO_x emissions were also performed, the results of which shall be discussed herein.

Keywords Downsized • Gasoline • Design of experiments • 1D engine simulation • High BMEP

1 Introduction

Future emissions legislation is the main driving force behind engine research and development. Previously the focus of development has been on the reduction of PM and CO emissions, however there has been a shift towards reducing fuel consumption and hence CO₂ emissions in particular. EU legislation stipulates an OEM fleet average of carbon dioxide emissions of 130 g/km by 2015. This legislation will be phased in from 2012 and will incur a sliding penalty system for vehicles which exceed this figure. The result of this legislation is the rapid development of new and more efficient technologies. An increasingly common method of improving fuel economy is by using a boost system coupled with a downsized engine. Turbocharged engines are becoming a common replacement of larger naturally aspirated engines, however pushing the boundaries of the boost levels and the extent of the engine downsizing may still provide increased savings.

Researchers seeking to increase the levels of boost in an internal combustion engine will inevitably be faced with a large number of difficulties. These technical challenges are well known and include increasing an engine's tolerance to higher mean peak cylinder pressures without incurring the need for significant compression ratio reduction. Increased inlet manifold temperatures and pressures has a knock on effect on all ensuing processes, increasing the likelihood of pre-ignition (PI) or self-ignition (knock). In order to prevent these phenomena, more careful control of the combustion process is necessary. The most common method of PI and knock prevention is spark retard. Unfortunately this has a significant trade-off with power and economy, in addition to raising the exhaust gas temperature and causing problems with high rates of heat transfer in the engine and turbo-machinery.

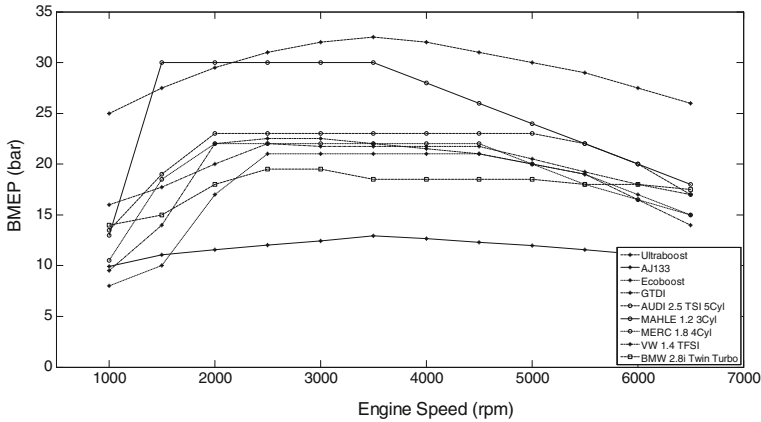


Fig. 1 Engine competitors

A collaborative investigation into engine downsizing named Ultraboost aims to produce an engine which pushes the boundaries of engine downsizing and charging. It draws on the expertise from a consortium of technical partners including Jaguar Land Rover (JLR), Lotus Engineering, Shell Fuels, GE Precision Engineering, CD-adapco, Imperial College London, University of Leeds and University of Bath, with funding support from the UK government-backed Technology Strategy Board (TSB). The primary objective of the project is to achieve a 35 % reduction in tailpipe CO₂ emissions relative to JLR’s 5.0 litre naturally aspirated V8 engine, whilst maintaining the original engine’s torque and power delivery characteristics. The peak BMEP target was set at 35 bar but the transient performance was also critical, leading to a requirement for a flat torque curve and thus a target of 25 bar BMEP to be available at both 1,000 and 6,000 rpm. Performance targets of this magnitude result in challenging combustion conditions with high probabilities of detrimental abnormal combustion effects such as pre-ignition and knock taking place. Figure 1 shows the current engines on the market and in development that are aiming to achieve high BMEP targets. The baseline AJ133 engine is also shown for comparison to the targets set out for Ultraboost.

The prototype engine was designed primarily by JLR and GE Precision Engineering with input from other consortium members and is based on an existing Jaguar Land Rover direct injection naturally aspirated gasoline V8 with extensive modifications having been made to incorporate features required for high output, four cylinder operation [1]. The downsized engine is equipped with a highly versatile combustion system, comprising of both port fuel injection (PFI) and 200 bar spray guided direct injection (SGDI) for improved mixture preparation, volumetric efficiency, knock resistance and transient response. Additional features include variable valve timing and cam profile switching on both the inlet and exhaust cam shafts to reduce the throttling requirement and to improve fuel economy and scavenging.

2 Methodology

Due to the increasing complexity of modern day engines, the amount of time spent testing and calibrating has risen dramatically in recent years. One way to reverse this trend is to employ Design of Experiments (DoE) theory and Model-Based Calibration (MBC) processes when developing testing procedures for new engines [2]. Empirically derived statistical representations of engine responses produced using the aforementioned practices enable large quantities of analysis to be performed whilst minimising the time spent gathering the necessary data to build the models, thus enabling faster feedback to the overall engine development process. This is an excellent approach but it does have its weaknesses. Where large numbers of independent variables are considered the test campaigns become very long and are difficult to manage. In addition the process gives very limited opportunity to re-use prior knowledge, which it would appear would be a desirable capability. Bayesian approaches have been described by Brace [3] which offer an approach to address this issue but are not widely adopted. Here a hybrid approach has been developed which uses a 1D simulation environment to inform the experimental design phase and so to replace several of the degrees of freedom that would traditionally have been included in the experimental investigation.

The prototype engine's boosting system was selected through a detailed investigation into a wide variety of systems available. The assessment criteria were based on both the technical requirements and the customer needs. Two stage, three stage, parallel and serial systems were all considered. A series two stage system utilising a high pressure supercharger and a low pressure turbocharger was selected as the most suitable system. This configuration was found to deliver the required high boost pressure at high speeds whilst maintaining a good transient response at low engine speed. A significant programme of supporting investigation was performed through 1D simulation. Crucially, the development process required the combustion system characterisation to be performed in advance of the boost hardware being available.

The performance envelope of the prototype engine was investigated at the Powertrain and Vehicle Research Centre (PVRC) engine test facility based at the University of Bath. The expected high peak power output required the installation of a tandem dynamometer system comprising of an AC and an eddy current machine. To characterise the combustion system a combustion air handling unit (CAHU) was used to simulate the intake air conditions expected from the specified boosting hardware. The system actively controls the boost pressure, exhaust back pressure and air charge temperature. The exhaust back pressure is controlled by a butterfly valve located on the exit of the exhaust manifold and is then used to replicate the pressure that would be expected due to the presence of a turbine. The facility also includes emissions measurement, combustion analysis equipment and dynamic fuel consumption measurement.

The flexibility offered by the CAHU introduces a dilemma; the freedom of inlet and exhaust manifold conditions presents a very large space in which the

experimental programme can be designed. There was a significant risk that an exhaustive experimental programme would delay the development programme. The large number of degrees of freedom motivated a hybrid approach to the experimental programme, combining the 1D simulation with traditional DoE tools on test rig. Specifically, the simulation work provided target inlet manifold pressures and temperatures and associated exhaust back pressures for both a low pressure biased operating condition and a high pressure biased condition, i.e., when the boost pressure was delivered primarily from the turbocharger or the supercharger, respectively. These target conditions could then be fed into the testing programme as control limits for the CAHU. Otherwise a wide range of inlet and exhaust manifold conditions would need to be included in the experimental design, making the campaign duration excessive.

The aim of this paper is to describe the downstream experimental procedure undertaken and the results obtained at a single engine speed and boost condition to investigate the effects of the combustion control actuators installed on this engine. The 1D simulation exercise is documented elsewhere. Initial testing was focussed on achieving the target limiting torque curve. It was found that in order to provide sufficient air flow the high lift cam profiles were required. The work described in this paper detail the effects of the variable valve timing on both the inlet and exhaust cams, in addition to effects of the air charge temperature. The air charge temperature is an important factor to investigate as it will determine the specification of the intercooler.

3 Empirical Model Building

The tool used throughout this work was the MBC Toolbox from Mathworks. DoE and MBC techniques were used in the early stages of testing to produce optimised calibration tables for spark advance (SA°) and air charge temperature (ACT). The two inputs to the relevant engine control feature are intake and exhaust cam phasing (ICP and ECP respectively). Optimisation studies have been carried out on the basis of either maximising torque output or minimising BSFC and gaseous emissions. Since calibration effort at this early stage has been focussed around limiting torque conditions, for a given engine speed, intake and exhaust manifold pressures have been held constant at target conditions predicted by 1D simulations of the engine. Clearly, if physical turbomachinery were used to achieve these target conditions instead of the CAHU, the exhaust conditions would interact with the turbine and compressor operating point, resulting in small changes in manifold pressures. This effect is overlooked at this stage for the sake of simplicity. Table 1 below summarises the test conditions and variable ranges covered by this piece of work. At each test point, a simple spark sweep was performed. Spark advance (SA°) was varied between a retard limit resulting in an IMEP CoV greater than 3 % for all four cylinders and an advanced limit ($KLSA^\circ$) dictated by knock thresholds calculated within the indicating system, an AVL Indimaster system.

Table 1 Boundary conditions within which the cam phasing and ACT investigation was carried out

Variable	Range tested
Engine speed	1000 rpm
Intake manifold pressure	2200 mbar
Exhaust manifold pressure	1250 mbar
Intake cam phasing (ICP)	0° → 62°
Exhaust cam phasing (ECP)	-48° → 0°
Air charge temperature (ACT)	28 → 78 °C
Spark advance (SA°)	3 % IMEP CoV → KLSA°

4 Design of Experiment

The following criteria were devised in order to select the most appropriate experimental design from the options available within the MBC Toolbox;

- All test points must lie within the testable range of the engine parameters being varied.
- Test points have to be present in the corners of the experimental region, so that behaviour at the extremes of cam travel and ACT are accurately characterised.
- No more than 20 test points should be required.

Of the available designs to choose from, only the Composite Face-Centred (CCF) design satisfied all of the selection criteria highlighted above. A 19 test CCF design with five repeated centre points was therefore created. At each of the 19 test locations, data were collected for the four engine responses of interest (brake torque, BSFC, NO_x mass flow rate and IMEP CoV), and were later used to build statistical response models. Since spark advance represents one of the most influential engine control parameters, yet is relatively easy to vary and measure the effect of, spark sweeps were performed at each test point between the previously mentioned 3 % CoV limit and KLSA°. This allowed spark advance to be incorporated as an input variable to the models generated, and facilitated the identification of erroneous data since the characteristic profiles of engine responses to varying spark advance are well known.

5 Response Modelling

A single stage modelling approach was chosen due to ease with which models can be created and analysed. Due to the large number of degrees of freedom incorporated into the design of this engine, it was assumed that simple polynomial models may not be sufficient to accurately represent the non-linear behaviour of some engine responses. A selection of quadratic radial basis function (RBF) models, differing only in the number of RBF centre points permitted, was therefore generated in addition to simple linear and quadratic models. RBF models are a

Table 2 Summary statistics for different torque response models

Model type	No. observations	No. model parameters	RMSE (Nm)	Press RMSE (Nm)	R2	Press R2	Validation RMSE (Nm)
Quadratic	63	12	3.82	4.38	0.995	0.992	12.42
Cubic	63	25	1.93	2.27	0.999	0.998	135.02
Quadratic-RBF-10	63	21	1.65	1.84	0.999	0.999	13.94
Quadratic-RBF-20	63	24	1.67	1.71	0.999	0.999	10.73
Quadratic-RBF-30	63	24	1.67	1.71	0.999	0.999	10.73

flexible type of model that is potentially better suited to characterising complex behaviour from advanced engine types [2].

A stepwise regression model which minimises the predicted error sum of squares (PRESS) was used to eliminate any redundant model terms which resulted in over fitting of the models. The best model for a given engine response was chosen based on statistical metrics such as R^2 , RMSE and PRESS equivalents. PRESS R^2 and PRESS RMSE differ from their original forms in that they are the average values of the original statistic derived when one data point is omitted from the calculation. They provide a good indication of the predictive quality of a model and if significantly different to their original forms, represent a strong indication of model over fitting [4, 5]. A summary of the statistical metrics used to evaluate a typical selection of models for an engine response (torque in this case) is presented in Table 2.

Based on the statistics presented in Table 2, it is clear to see that a quadratic RBF model with 20 permitted centre points results in the best overall fit. This is confirmed by comparison with five independently acquired validation test points and the corresponding validation root mean square error (RMSE). For this particular response, the Quadratic-RBF-20 model was therefore selected for subsequent optimisation studies.

Table 3 below identifies the models chosen to represent each of the five engine responses and summarises their fit and validation statistics. In some cases, a quadratic RBF model was the obvious choice, however for certain engine responses the RBF models were highly susceptible to variation in the data collected at the five repeated centre points. This susceptibility resulted in unrealistic features in the response surfaces. An example of this phenomenon can be seen below in Fig. 2, which compares the response surfaces for both simple quadratic and quadratic RBF NOx response models. In cases where this phenomenon was spotted, the validation RMSE of the RBF models was poor in comparison to that of the simple quadratic models.

It can be seen from Table 3 that all of the chosen models have excellent R^2 results and good RMSE results considering the relative ranges of the data collected for each response. PRESS statistics are very similar to their non-PRESS equivalents, indicating that the chosen models are not over-fitted. Although validation

Table 3 Summary statistics for models selected for optimisation studies

Engine response	Best model	No. model parameters	RMSE	Press RMSE	R2	Press R2	Validation RMSE
Torque (Nm)	Quadratic-RBF-20	24	1.67	1.71	0.999	0.999	10.73
BSFC (g/kWh)	Quadratic (linear in ACT)	10	12.29	13.59	0.933	0.903	23.48
NOx (g/h)	Quadratic	10	61.18	66.36	0.931	0.904	79.76
IMEP CoV (%)	Quadratic-RBF-10	18	0.45	0.47	0.899	0.856	0.90

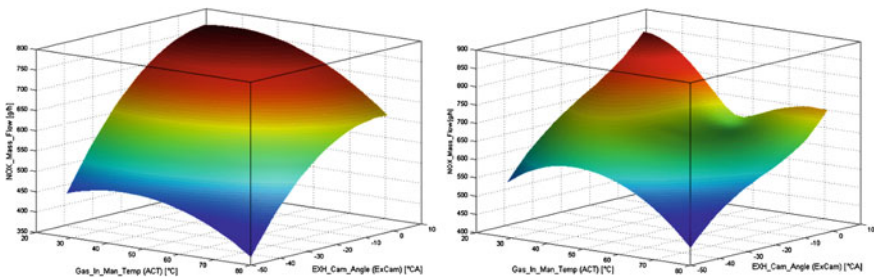


Fig. 2 Comparison of simple quadratic (*left*) and quadratic-RBF (*right*) NOx response models as a function of inlet manifold temperature and exhaust camshaft phasing, showing the RBF model over fitting whereas the quadratic predicts a much smoother response

RMSE results in Table 3 are typically a factor of two greater than the model RMSE results, it should be noted that the test points used for validation were located in regions where no experimental data existed to aid in model fitting. The validation RMSE results therefore indicate that a good level of model accuracy is maintained in these regions.

6 Optimised Calibration Results

Following on from the selection process, models for the five engine responses were exported to the CAGE Browser of Matlab's MBC Toolbox. CAGE provides tools for the automated calibration of lookup tables in accordance with objectives set by the user. This feature was used to generate calibration tables for SA° and ACT, optimised on the basis of either maximising torque output or minimising BSFC and gaseous emissions. Of course the final calibration must take account of both objectives and here a subjective judgment is still necessary. The two inputs to the calibration tables were intake and exhaust cam phasing.

The optimisation algorithms were constrained to only produce solutions within the operating envelope of the engine by implementation of a convex hull boundary

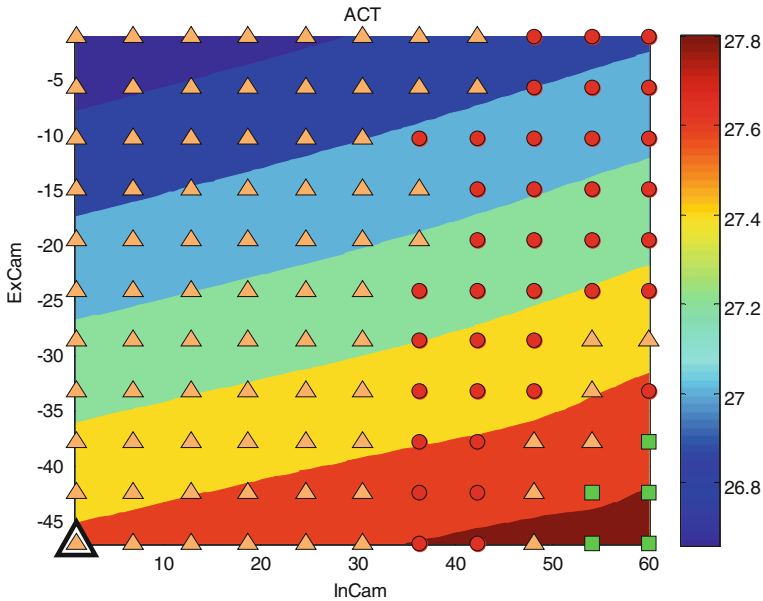


Fig. 3 Contour plot from torque constrained BSFC CAGE optimisation. *Contours* indicate the air charge temperature. The *triangular* points indicate regions where solutions could not be met within the computational limits imposed on the algorithm. *Circular* points indicate that the search algorithm was unable to meet one or more of the model constraints. Valid solutions (indicated by *square* shaped markers) are only predicted around the maximum valve overlap condition of $ICP = 62^\circ$ and $ECP = -48^\circ$

model constraint applied to the experimental data points. A further constraint prevented solutions arising in which IMEP CoV exceeded 3 %, a commonly set threshold to ensure acceptable driveability is maintained [6]. Of the two types of optimisation study performed, one type was additionally subject to a torque constraint demanding a minimum brake torque of 410 Nm. This constraint, corresponding to a BMEP of 25 bar, is defined by the targets specified in the original project brief. The optimisations that were not subject to the torque constraint shall hereafter be referred to as unconstrained optimisations. They were carried out in order to gain a better understanding of the interactions between the engine control parameters and their influence on engine responses.

Torque constrained optimisation studies revealed that the envelope of cam phasing solutions capable of achieving the torque target was very small, limited only to very high valve overlap conditions. This is illustrated in Fig. 3, showing the region of valid cam phasing solutions capable of achieving this target torque. Table 4 summarises the best torque constrained solutions for the various optimisation studies performed. In order to satisfy the torque requirement in addition to the objectives of the respective optimisations, it can be seen that only the coldest ACT would suffice. This confirms initial judgements that the charge cooling requirement of the engine will be pivotal in meeting the project’s torque

Table 4 Best torque constrained optimisation solutions for BSFC and NOx

Optimisation Objective	Best solution	ICP (°)	ECP (°)	ACT (°C)
Min. BSFC	327 g/kWh	55	-40	28.0
Min. NOx	132 g/h	62	-48	28.0

Table 5 Best unconstrained optimisation solutions for BSFC and NOx with corresponding torque values

Optimisation objective	Best solution	ICP (°)	ECP (°)	ACT (°C)	Torque (Nm)
Min. BSFC	219 g/kWh	0	-29	28	273
Min. NOx	50 g/h	62	-48	78	321

objectives. It is also worth noting that although the values of minimum BSFC do not vary greatly within this small performance envelope (variation less than 11 % and 9 % respectively), NOx emissions vary considerably. At the point of best BSFC, NOx emissions are predicted to be 364 g/h, equating to an almost three-fold increase over the minimum values predicted at the nearby maximum valve overlap cam combination. NOx production was found to be highly sensitive to valve overlap, with experimental observations ranging from 760 g/h at low overlap conditions down to 14 g/h at maximum valve overlap conditions.

From the unconstrained optimisation studies, it was found that significant benefits in the modelled engine responses could be achieved but at the cost of much reduced torque. Table 5 summarises the best unconstrained optimisation results that were predicted and the corresponding torque model values.

7 Discussion

As previously stated, maximum torque was observed to occur in the region of maximum valve overlap. 1D simulation has predicted that trapped exhaust gas residuals are minimised at this condition due to improved scavenging, thus implying that for a given spark advance, losses due to cyclic variability are reduced and the gas properties of the working fluid improved. Specific airflow at this condition was on average 45 % higher than that observed at low valve overlap, also suggesting that considerably better scavenging takes place under high overlap conditions. 1D simulation predicts maximum trapped residuals of 3.8 % at minimum valve overlap conditions.

The lowest unconstrained BSFC was predicted to occur in the region of ICP = 0° ECP = -29° and ACT = 28 °C. Low ACTs increase the knock margin permitted for a given set of manifold conditions, allowing for improved spark timing and combustion phasing. This in turn improves torque output and

reduces BSFC. Across the board of cam phasing combinations, ACTs of 28 °C were required in order to minimise BSFC. At the best unconstrained BSFC cam phasing combination, an increase in ACT of 50 °C from 28 °C resulted in a 4.6 % increase in BSFC, whilst the same increase in ACT at the maximum overlap condition gave a 2.8 % increase. This data demonstrates the importance of specifying the right charge cooling system for the following phase of the project when physical turbomachinery will be used to provide the target boost pressures.

The combination of intake and exhaust cam phasing at the point of best unconstrained BSFC are favourable because although airflow is low at this condition due to the late opening and closing of the intake valves, there is good scavenging and little bypass of fresh charge through the combustion chamber. This results in close to stoichiometric in-cylinder conditions with low trapped residuals, therefore maximising combustion efficiency. High levels of exhaust gas residuals are known to decrease efficiency at full load [6].

High valve overlap penalises fuel economy due to a percentage of the fresh air charge passing straight through the combustion chamber and into the exhaust manifold. This results in rich in-cylinder conditions and reduced combustion efficiency, and explains the high BSFC seen at this condition. The highest observed carbon monoxide production rates ($\sim 3.8\%$) were measured at maximum valve overlap conditions, also implying rich in-cylinder conditions.

Minimum unconstrained NO_x emissions of 50 g/h were predicted to occur at maximum valve overlap conditions and ACT = 78 °C. Since NO_x production is highly temperature sensitive [6], one must assume that combustion temperatures at this condition are substantially cooler than conditions with reduced valve overlap. Exhaust port temperature data shows this to be true, with an observed drop in average gas temperatures of approximately 120 °C compared to those recorded at low valve overlap conditions (for nominally the same ACT and SA°). Combined with the increased CO production measured at high overlap conditions, these observations reinforce the theory of decreasing in-cylinder AFR with increasing valve overlap due to scavenging of fresh air straight into exhaust manifold. Given the temperature sensitivity of the rate of NO_x production, it is curious that the response models predict high ACTs as beneficial for NO_x reduction. However, the difference in the observed values recorded at the extremes of the ACT range for the maximum valve overlap condition is almost negligible (approximately 1 g/h). Due to the non-linear nature of the NO_x response around the maximum overlap condition, residual errors in this region are comparatively high. Although the general trend is correctly predicted, the accuracy of the NO_x response model in this region is therefore questionable.

8 Conclusions

In this study, a new design of downsized engine combustion system was characterised using an external air handling unit to emulate the effect of turbomachinery. A hybrid approach was developed; combining the use of DoE and MBC principles guided by predictive work conducted using a 1D engine simulation. The resulting statistical representations of engine responses were used to determine cam phasing, ACT and SA° combinations capable of satisfying a range of user defined constraints. The adoption of DoE principles helped to minimise the amount of time spent acquiring the necessary data to characterise the engine responses. Simple quadratic and quadratic RBF model fits were found to represent the engine responses with acceptable accuracy, although great care should be taken in selecting the most appropriate model. Statistical metrics should not be relied on alone and a subjective assessment of the quality of fit must be included.

A maximum predicted brake torque of 416 Nm was found to occur at the point of maximum valve overlap and minimum ACT, a combination of engine inputs which corresponded with maximum observed engine airflow and minimum predicted trapped exhaust gas residuals (from 1D simulation). This result exceeds the target specified by the project brief by 6 Nm. Minimum NO_x emissions were observed to occur at this cam phasing combination too as a result of much reduced combustion temperatures arising from rich in-cylinder conditions. Predicted BSFC at this point was 365.6 g/kWh. The lowest predicted BSFC satisfying the target torque of 410 Nm was 327 g/kWh, whilst the lowest unconstrained predicted value of BSFC was 219 g/kWh occurring at $ICP = 0^\circ$ $ECP = -29^\circ$ and $ACT = 28^\circ C$. This combination provided a good compromise between trapped exhaust gas residuals and scavenging of fresh charge, proving favourable in-cylinder conditions and good combustion efficiency. The torque output at this condition was 273 Nm.

9 Future Work

The authors are confident that the use of hybrid experimental design processes employing DoE and MBC principles guided by 1D simulation has the potential to yield sufficiently accurate results in a much reduced time scale compared to traditional calibration methods. Having gained confidence in the approach adopted in the course of this preliminary piece of work, the next stage would be to apply the same philosophy across the entire engine speed range.

Much scope exists for improvement of the empirical models created in the course of this study. It would be valuable to compare model predictions after adding a number of points to the experimental design between the boundary and the core of the design region. This would likely improve the accuracy of the quadratic models and would permit the authors to experiment with higher order

models. Implementation of a two stage modelling approach to investigate whether any improvements can be made to the accuracy of the response models [2, 7] would also be highly beneficial.

Other calibration tasks could be treated in the same hybrid manner, replacing experimental assessment of some degrees of freedom and reserving the experimental approach for areas in which the 1D simulation is incapable of producing good quality predictions. These include the detailed combustion response within the engine, prediction of cyclic variability and the response of turbomachinery in operating areas not mapped on gas stands.

Of particular interest would be the adoption of Bayesian methods as discussed by Brace [3]. Here there is a rich source of prior knowledge from the 1D simulation and this could be used to accelerate the experimental phase of the work and to better integrate the development process.

References

1. Carey et al C (2011) Extreme engine downsizing. Presented at the Innovations in fuel economy and sustainable road transport, Pune, India
2. Morton TM et al (2003) Model-based optimal calibration of a dual independent variable valve-timing engine. In: Röpke K (ed) Design of experiments (DOE) in der Motorenentwicklung, vol 1. Expert-Verlag, Berlin, pp 77–85
3. Brace CJ et al (2011) The use of a Bayesian weighted least-squares approach to accelerate empirical engine model generation. Proceedings of the institution of mechanical engineers. Part D J Automob Eng 225:366–394
4. Burke RD et al (2012) Systems optimisation of an active thermal management system during engine warm-up. Proceedings of the Institution of mechanical engineers. Part D J Automob Eng
5. The MathWorks (2011) Model-based calibration toolbox user's guide
6. Stone R (1999) Introduction to internal combustion engines, 3rd edn. Macmillan, Basingstoke
7. Holliday T et al (1998) Engine-mapping experiments: a two-stage regression approach. Technometrics 40:120–126, 1998/05/01 1998

HCCI Cycle-by-Cycle Combustion Phase Control Based on Ion Current Technology in GDI Engine

Zhiyong Zhang, Liguang Li and Robert Dibble

Abstract Homogenous charge compression ignition gains attention increasingly because of its high efficiency and low emissions. The combustion phase control has been one of the key technological issues which affect its industrialization of HCCI combustion technology. In recent years, ion current detection technology gains more and more attention due to its simple structure, low cost and its containing of large information of combustion. The signal can be used to detect combustion state and to realize closed-loop control of combustion process according to certain strategies. In this paper, the cycle-by-cycle control strategy of combustion phase was established, employed ion current signals and flexible injection strategy of GDI engine. According to ion current signal phase features in two preceding cycles, fuel amount injected in the next cycle will be adjusted to stabilize combustion. The experiments were done based on a GDI-HCCI test bench. The results show the first injection has obvious effect on both combustion and ion current signal phases. The fuel amount injected in the next cycle can be regulated by first injection. CA50 can be predicted by ion current signal difference dI_{min} . The combustion phase can be controlled within 2°CA . The maximum concentration of HC decreased from 18,000 to 4,000 ppm after combustion phase control was applied. The issue of this study is that fuel amount injected need to be calibrated in different work conditions. The detection circuit needs to be optimized because the signal is a little weak under direct injection method.

F2012-A01-023

Z. Zhang (✉) · L. Li
Tongji University, Shanghai, China
e-mail: zhang0zhiyong@sina.com

R. Dibble
University of California, Berkeley, CA, USA

Keywords Homogenous charge compression ignition · Combustion phase · Closed-loop control · Gasoline direct injection · Cycle by cycle

1 Introduction

In recent years, HCCI engines offer promise due to low emissions and high efficiency. Comparing with the SI engine or diesel engine, it is hard to control combustion phase on a HCCI engine directly. Hence, it is very necessary to obtain a method to sense HCCI combustion phase and combustion state. Unlike the traditional SI or diesel engines, the phase of HCCI combustion is very sensitive to critical conditions. For HCCI combustion, the control method based on work condition can't meet the demand. It should adopt the cycle-by-cycle control strategy.

The ion current detection technology supplies a new control strategy based on cycle-by cycle for phase control of HCCI combustion. Some research showed that the signal characteristics of ion current have intense correlation with HCCI combustion phase, which can be used to estimate combustion phase [1–3]. Fuehrhapter. A [4] realized the HCCI combustion utilizing CSI system of AVL Company and estimate the 50 % burned mass fraction in virtue of ion current. Petter Strandh et al. [5] have done excellent research about closed-loop control of HCCI combustion using cylinder pressure sensor and ion current sensor. Their pioneering study found that CA50 ion has the similar control result. Xie Hui [6] studied the correlation between ion current signal characteristics and HCCI combustion phase. The results show that the inflexion phase and peak phase have the better liner correlation with HCCI combustion phase and the correlation coefficient reaches 0.95. Guangyu Dong [7] proved the feasibility of combustion feedback employing ion detection technology and did some arithmetic disposal.

Gasoline direct injection is a good way to achieve HCCI combustion, as it has flexible injection strategy and control ability to realize cycle-by-cycle combustion. Therefore, in this paper, some experiments about feedback control of combustion phase were done on a GDI-HCCI test bench. It brought forward a novel control strategy based on cycle-by-cycle.

2 Test Bench

Schematic layout of the experiment is shown in the Fig. 1. The engine tested is rebuilt basing on a two-cylinder diesel engine, including the restructure of fuel supplying system, combustion system, electric control system, cooling system etc. One cylinder is PFI spark-ignition combustion, the other is GDI-HCCI combustion. An intake charge pre-heater is installed before intake fold of GDI-HCCI cylinder, with intake temperature regulated by a temperature controller. Specifications of test

Fig. 1 The schematic diagram of the test bench

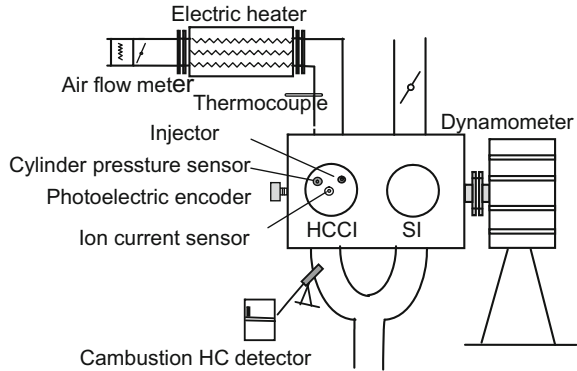


Table 1 Specifications of the test engine

Bore (mm)	95
Stroke (mm)	114
Compression ratio	11.5
Fuel injection type	Direct injection
Fuel type(Gasoline)	No.93
Injection pressure (MPa)	8

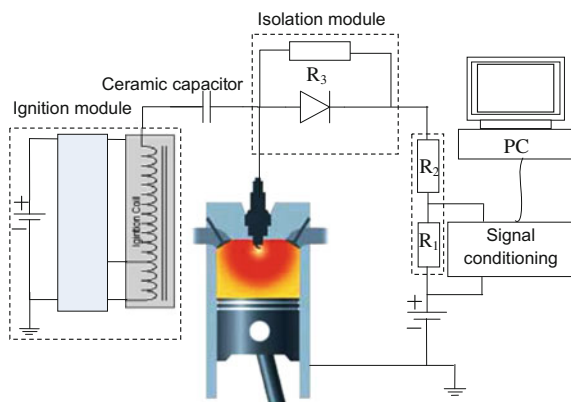
engine are listed in Table 1. Electric control system is developed to realize multi-injection in one cycle. High-pressure common-rail system is adopted to realize GDI, with its maximum pressure of 8 MPa. Inductance coil is used as ignition module. Cylinder pressure is measured by Kistler 6125B piezoelectric pressure transducer, and the output of charge signal is converted into voltage signals by Kistler5011 charge amplifier. HC emissions are measured by Combustion HFR500 Fast Response Emission Detector, its response time is less than 0.9 ms, and transporting time is less than 5 ms.

No.93 gasoline (octane number) is used in experiments. The experimental process is as follow: HCCI cylinder starts in GDI mode firstly, with spark ignition, and then operates in idle condition, and intake charge pre-heater is switched on simultaneously. When temperatures of cooling water and intake charge reach desired temperatures, spark ignition is cut off and the engine runs in HCCI mode.

3 Ion Current Signal Measurement Systems

Ion current detecting system is the premise of this research. Figure 2 shows the measurement system of ion current signal. When an electric field is imposed across the reaction zone in a flame, due to the presence of ions and electrons, current flows through the circuit and the voltage over resistance R_1 reflects the strength of ion current. A high voltage insulation mode is connected to the circuit to diminish the effect of ignition coil discharge when spark plug re-sparks after misfire.

Fig. 2 An ion current signal measurement system



Regarding the convenience of data collection and feedback control, a signal conditioning module is applied; including signal power amplifying, wave filtering, voltage limiting, signal reversing and integration.

4 Effects of Injection Strategy on Ion Current Signal

In GDI engine, two-stage gasoline direct injection strategy is often adopted to control combustion. The first stage is in intake stroke and the second stage is in compression stroke. Some studies have shown that the two-stage injection strategy is helpful to HCCI combustion, which can avoid knocking and lower the emission of HC and CO. In order to study the combustion phase control strategy based on ion current feedback, some experiments were done and the ion signal characteristics were studied in the two-stage injection strategy. The experiments were done with intake temperature at 200 °C(573 K) and water temperature at 90 °C(363 K).

4.1 Effect of Injected Fuel Quantity in Two-Stage Injection Strategy

Figure 3 shows the influence of the first injected fuel amount on cylinder pressure, rate of heat release and ion signal. It can be seen that the phases of cylinder pressure, rate of heat release and ion signal advance increasingly as the first injected fuel amount increase from 9.5 to 12.6 mg. The peak phase of heat release rate advanced from 21.9 to 14.2° CA. The peak phase of ion current advanced from 30.3 to 20° CA. The peak of rate of heat release increase increasingly and the peak of ion current strengthen increasingly. The analysis is follows: as the increase

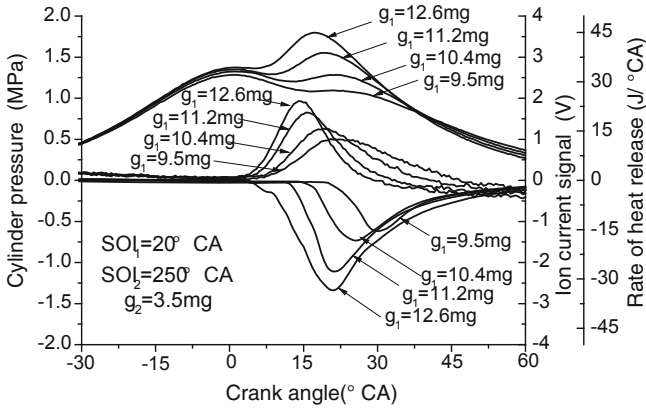


Fig. 3 The contrast of cylinder pressure, ROHR and ion current signal under the different first fuel injection quantity

of first injected fuel amount, the rate of chemical reaction speed up, which advances the ignition timing of HCCI combustion. The increase of total injected fuel amount increase the accumulation of heat release, which increase the quantity of flame ions to produce stronger ion current. On the other hand, the atomization and heat absorption of fuel increase, which lowers the temperature of mixture and increase the intake amount. The compression pressure also increases with it.

Jianxin Wang [8] studies found that a small amount of injected fuel in compression stroke can form stratified mixture, which is helpful to control ignition timing and combustion rate. But because the atomization and evaporation time is limited, the second injected fuel amount should not be too late. If second injection is too late, the emission of HC and CO would increase.

Figure 4 is the changes of cylinder pressure, rate of heat release and ion current signal employing two-stage injection in the same condition, with the second fuel injection quantity change. It shows, with the increase in the amount of secondary fuel injection and the circulating amount of fuel, the peak of the ion current signal is gradually increased. Secondary fuel injection quantity from 3.2 mg gradually increased to 4.0 mg. Then, the peak phase of rate of heat release is 3° CA advance slightly, but the peak phase change of the ion current is not regular. Analysis suggests that as the second fuel injection quantity is increased, the size zone of higher fuel concentration increases. This zone is compression-ignited firstly and ignition time advances. The zone ignition triggers the compression ignition of the rest of the mixture to advance the combustion phase. Because ion current signal is a local signal, the effect of the local concentration caused by the second fuel injection quantity and spark plug location has a great impact on the ion current.

As the concentration distribution caused the different secondary fuel injection quantity is affected by the flow field in cylinder, the changes in the phase of ion current signal is not regular. Compared with the change for the first fuel injection quantity, it is more difficult to estimate the combustion phase by the ion current

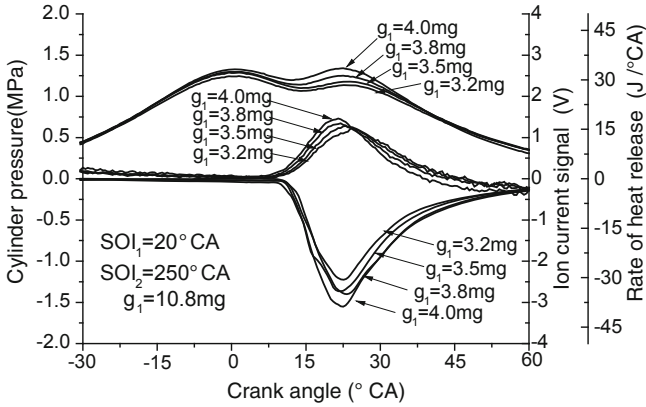


Fig. 4 The contrast of cylinder pressure and ion current signal under the different second fuel injection quantity

signal characteristics, and to control the combustion phase by controlling the secondary fuel injection quantity.

From the combustion phase and ion current point of view, the change of its first fuel injection quantity has a greater effect than the second fuel injection quantity. Changes of the first fuel injection quantity can cause large changes in the combustion phase. Therefore, comparing the two, by adjusting the first fuel injection quantity, to control combustion phase should be more effective in theory.

4.2 Effects of Two-Stage Injection Timing

Figure 5 is the comparison of cylinder pressure, rate of heat release and ion current signal for the different first injection timing. It shows that, with the first injection timing gradually delayed from 20° to 80° CA ATDC (on the intake stroke) the combustion phase and the peak phase of ion current is gradually delayed. But in the process of the first injection timing changes from 20° to 60° CA ATDC, the peak phase of rate of heat release postpones from 14° to 15.5° CA, delayed only 1.5° CA, with no change significantly. Analysis suggests that the first injection forms a homogeneous mixture. With the changes of first fuel injection timing in the earlier CA range, there is plenty of time for fuel atomization and evaporation. Therefore, the injection location is not significant for the formation of homogeneous mixture in the compression stroke, resulting in insignificant changes in the combustion phase. When the first injection timing is delayed to the 80° CA (intake stroke) and above, the change in the combustion phase becomes obvious, but the strength of ion current signal is significantly weakened. Analysis suggest that the fuel is not completely atomized and evaporated, which causes a delay in the combustion phase and also leads to burning deterioration that reduces the number

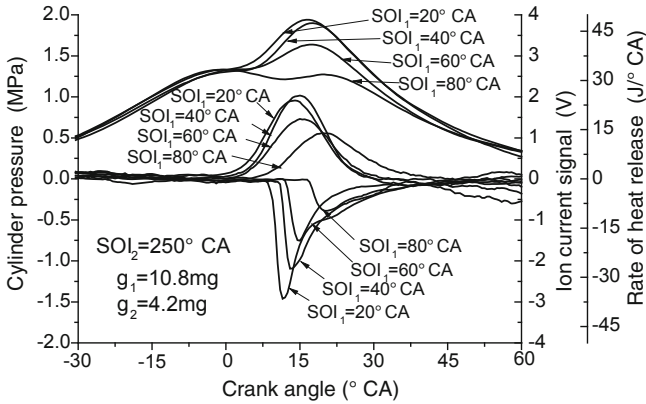


Fig. 5 The comparison of cylinder pressure and ion current signal under different first injection timing

of flame ions. From the control point of view, the first fuel injection timing need to change in tens of degrees after top dead centre in order to bring changes in the combustion phase of 1–2° CA, while for the first fuel injection timing cannot be too late, resulting in a limited range of adjustment. Therefore, it is not desirable to control the combustion phase by adjusting the first fuel injection timing.

Figure 6 is the comparison of cylinder pressure, rate of heat release and ion current signal under the different second injection timing. It shows that in advance with the second injection timing, the position of heat release advances slightly, indicating that the secondary fuel injection can trigger combustion effectively. However, the magnitude and phase of the ion current signal is not significantly affected by the position change of the secondary fuel injection. Analysts believe that due to changes in the secondary fuel injection location, the distribution of dense or dilute district caused by the secondary injection changes, which affects the ion generation of the local area of the spark plug, resulting that the peak position change of ion current signal is not obvious.

The Study found that, compared to the amount of injection fuel, the influence of injection timing on the phase of ion current or combustion is smaller. Larger change of injection timing can only lead to smaller change of combustion phase. Therefore, to control combustion phase by changing the injection timing is not optimistic for control sensitivity.

In summary, it is more reliable to adjust the combustion phase by adjusting the first fuel injection amount. This method will be adopted and discussed in the following content. The ion current signal will be used to detect the combustion phase real-time in-cycle. According to the changes of combustion phase for several consecutive cycles, the combustion phase of the next (subsequent) cycle will be adjusted by adjusting the first injection quantity.

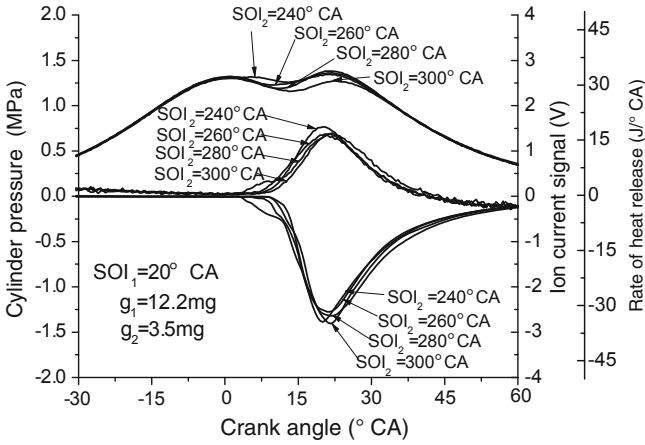


Fig. 6 The comparison of cylinder pressure and ion current signal under different second injection timing

5 Relations of Phase Characteristics Between Combustion and Ion Signal

For feedback control needs, it is necessary to quantitatively study the corresponding relations between the phases of ion current characteristics and the combustion phase. Figure 7 is the cloud images of the peak of ion current differential signal, dI_{min} and combustion phase CA_{50} under the different first injection quantity in consecutive 50 cycles. Table 2 lists the correlation coefficients between dI_{min} and CA_{50} under four different first injection quantities.

6 Feedback Control Strategy of Combustion Phase Based on Ion Current Signal

6.1 Forecast of Combustion Phase Based on Ion Current Signal

As described above, there is linear correlation between dI_{min} and CA_{50} . The relationship between the two can be expressed as the following formula:

$$CA_{50} = ION_{50} + f(\Phi, T_{in}, T_{water}, \dots)$$

The function is affected by many factors. It is not possible to accurately present the mathematical model of the function. This paper attempts to get the fitting of the function by means of mathematical multiple regression statistics. The key is to find the most important factors that affect the difference value of CA_{50} and dI_{min} , but also considering the operation is simple.

Fig. 7 The correlation of dI_{min} and CA_{50} under the different first injection quantity

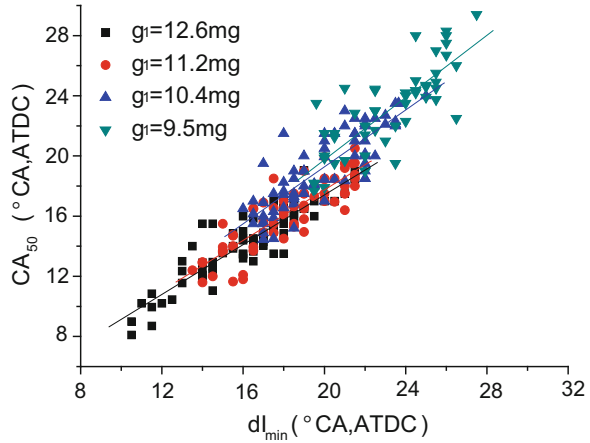


Table 2 The correlation coefficient between dI_{min} and CA_{50} for the different first injection quantity

First injection quantity g_1 (mg)	9.5	10.4	11.2	12.6
Correlation coefficient	0.80	0.85	0.89	0.91

The main factors that affect ion current are the three main factors, which are air/fuel ratio, temperature, water temperature. In order to verify the feasibility of the proposed control strategy, a stable test conditions is selected below. The intake temperature and water temperature remain constant, only changing the fuel injection strategy. In this case, the formula can be simplified to $CA_{50} = ION_{50} + f(\Phi)$.

The following fitting function shown in Fig. 8 is obtained by the Method of Least Squares to fit experimental data of different air–fuel ratio (different first injection quantity):

$$CA_{50} = dI_{min} - (269.8 - 65.1 \times g_1 + 5.31 \times g_1^2 - 0.14 \times g_1^3)$$

CA_{50} values calculated using the fitting formula is shown in Fig. 9. From the figure, there is no difference nearly between the calculated value and the actual value, which can meet the needs of actual control.

6.2 Combustion Phase Control Algorithm Among Cycles

From the analysis above, we can know, the combustion phase extracted from ion current signal is from the current cycle. Ion current was only used as a method to detect combustion. How to control combustion by the signal, there is no arithmetic. The ion current only is as a means of combustion detecting. How to

Fig. 8 The change of the difference of dI_{min} and CA₅₀ with the first injection quantity

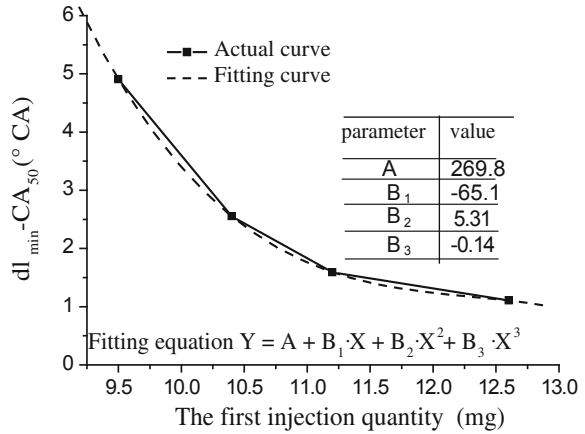
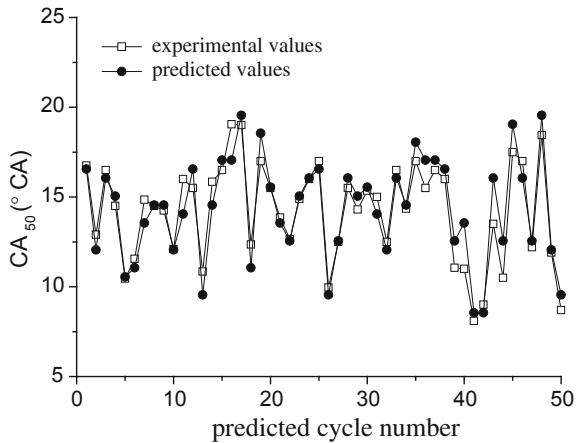


Fig. 9 The actual experimental values and predicted values of CA₅₀



estimate the combustion phase CA₅₀ in the next cycle by the front cycles, and achieve the combustion control among cycles, there is no ready-made control algorithm. Therefore, it is necessary to design a certain control algorithm, by which to judge fluctuations among cycles, thereby to provide the basis for adjustment of injection quantity.

A method of discriminated analysis is adopted, which is an assorted method based on multivariate statistical. Some test samples can be classified automatically by this method according to their characteristics, in the case of no a priori knowledge. In this paper, the results of continuous three cycles are analyzed, which come from a large number of experimental data. The combustion phase come from the two cycles before, which is forecast from ion current, are defined as Cycle1_CA₅₀ and Cycle2_CA₅₀. The phase difference of the two cycles between is defined as e, and $e = \text{Cycle2_CA}_{50} - \text{Cycle1_CA}_{50}$. The target phase is defined as Object_CA₅₀. The test results can be roughly divided into the following six cases.

- (1) Cycle1_CA50 < Object_CA50, Cycle2_CA50 < Object_CA50 $\Delta e < 0$;
- (2) Cycle1_CA50 < Object_CA50, Cycle2_CA50 < Object_CA50 $\Delta e > 0$;
- (3) Cycle1_CA50 > Object_CA50, Cycle2_CA50 > Object_CA50 $\Delta e > 0$;
- (4) Cycle1_CA50 > Object_CA50, Cycle2_CA50 > Object_CA50 $\Delta e < 0$;
- (5) Cycle1_CA50 > Object_CA50, Cycle2_CA50 < Object_CA50;
- (6) Cycle1_CA50 < Object_CA50, Cycle2_CA50 > Object_CA50.

Control methods developed under different circumstances as follows: [1] for the two consecutive cycles, the phases are in advance of the target phases, and the advance angle of the second cycle has distensible trend. According to the control strategy, when reducing the first fuel injection quantity, combustion phase can postpone. So it should be to reduce the first injection quantity, [4] for the two consecutive cycles, the phases are lagged behind the target phases, and the lagged angle of the second cycle has distensible trend. According to the control strategy, when adding the first fuel injection quantity, combustion phase can advance. So it should be to add the first injection quantity. In the other four cases, Cycle1_CA50 and Cycle2_CA50 fluctuations in the vicinity of the target phase. There is no trend of phase deviation. The ECU doesn't correct the first injection quantity for these cases. At the same time, the test is observed within a certain window of the ion current signal. For the light load misfire conditions, some cycles have no ion current signal. Then, the phase of right border of the window is as CA50 of this cycle. If it is determined that the misfire occurs in two consecutive cycles, so process it according to the case [4]. From the follow-up results after a number of cycle control, combustion phase is basically maintained in the vicinity of the target phase $\pm 2^\circ$ CA, initially achieved the desired control purposes.

6.3 Phase Control Strategy of HCCI Combustion Among Cycles

Because there are good correlation between peak phase of ion current and combustion phase, the combustion phase can be feedback control by ion current signal. And by adjusting injection mass sensitively, the combustion phase can be controlled. Meantime, because GDI can be flexible to adjust the fuel injection quantity in compression stroke, after making a judgment to adjust the fuel injection quantity of the next cycle, it is promising to achieve closed-loop control of HCCI combustion phase.

The basic control law is that, when the ion current signal of current cycle is detected, the combustion phase CA50 was estimated by the peak phase of it. The difference value between experimental value and target value is observed. The injection mass of the second stage was modified in the next cycle. When the engine run in the next cycle, modified injection strategy was adopted to stabilize combustion. The control strategy is shown in Fig. 10.

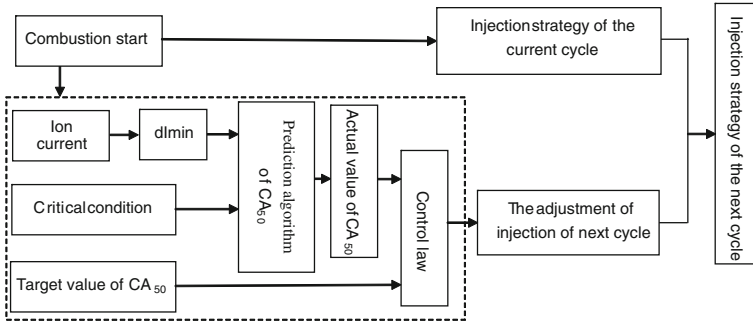


Fig. 10 The control strategy of HCCI combustion phase based on feedback by ion current signal

To initially verify the feasibility of the proposed control strategy, a relatively simple ratio algorithm is selected. Ratio parameter K is adjusted by the experiments, which has the satisfactory and successful results. The control law is as follows: $\Delta g = K \times e$

7 Experimental Results

The control experiment was done with engine speed at 1,200 r/min. Intake temperature is 200 °C(573 K) and cooler temperature is 50 °C(323 K). 12 °CA was selected as the target phase.

Figure 11 is the experimental result in consecutive 20 cycles. The peaks of cylinder pressure and ion current varied acutely. The combustion is unstable. Misfire is found in the cycles of 3, 8, 13, 6 and 17. In these cycles, there is no ion current signal and the concentration of HC reaches about 18,000 ppm. After the control, the combustion phase becomes stable, which is because the injected fuel amount is adjusted in time in the cycles that combustion phase is too early or too late.

As combustion is better, the peak fluctuate of ion current signal is lowered. The concentration of HC fall to $4,000 \times 10^{-6}$.

Figures 12 and 13 show the fluctuation of CA50 and IMEP in consecutive 20 cycles. It can be seen, the fluctuation of CA50 is very obvious. In the misfire cycle, the ion current signal can't be used to estimate CA50. In this case, 20° CA is used as the estimated value of combustion phase of this cycle in the ECU. The fluctuation is also very obvious. The maximum reaches 0.34 MPa. After close-loop control, the fluctuation range decreased greatly to about $\pm 2^\circ$ CA. The IMEP becomes relatively stable, which is about 0.28 MPa.

The test results show that combustion stability and HC emissions greatly improved through the use of closed-loop feedback among cycles. The experiment also found that the magnitude of the adjustment value of the first fuel injection

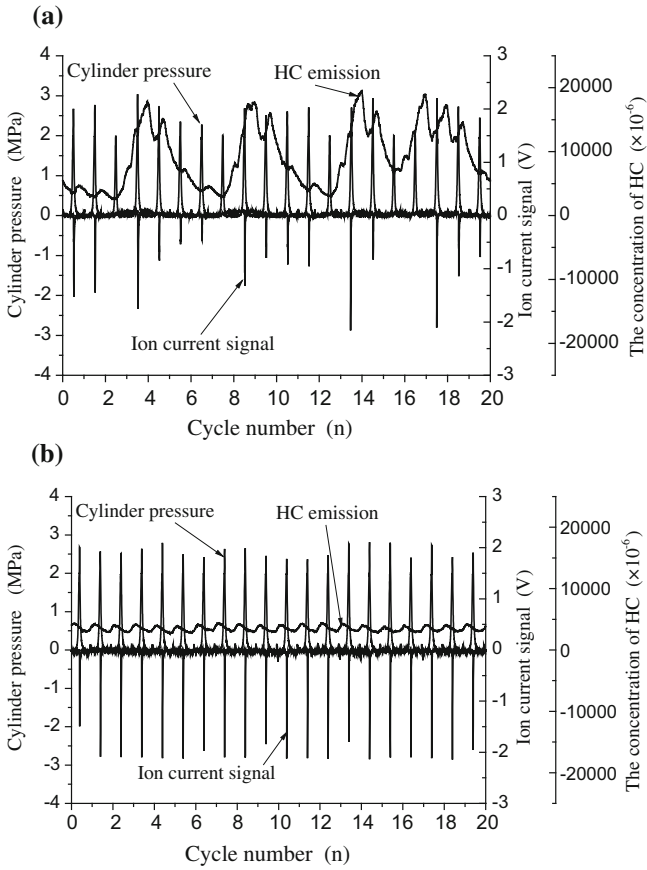


Fig. 11 The comparison of cylinder pressure, ion current and HC emissions before and after control. **a** before control **b** after control

Fig. 12 The comparison of CA₅₀ before and after control

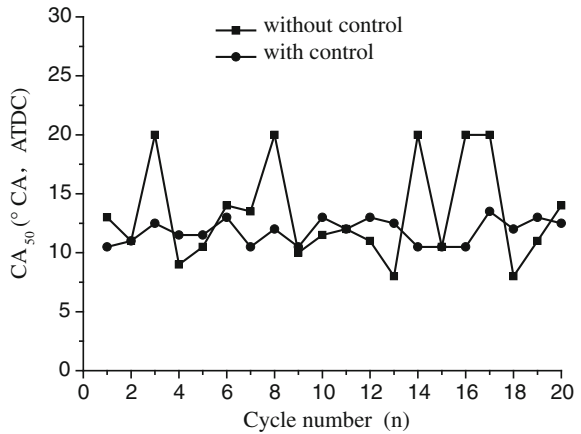
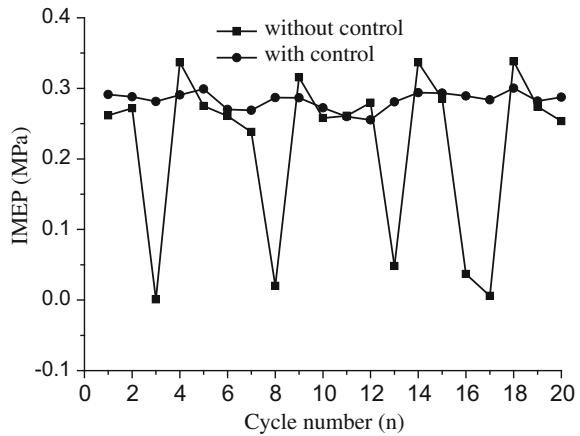


Fig. 13 The comparison of IMEP before and after control



quantity has a great influence on HC emissions and the system response. When the adjustment is excessive, the system response is too slow. In the transition process, knocking and misfire will occur. Further calibration is needed for the product engine for getting the right adjustment value of the first fuel injection amount.

8 Conclusions

- (1) The effect of injected fuel amount and injection timing under double-injection mode on HCCI combustion characteristics, as well as ion current signal characteristics, is studied. The results show that fuel amount in first injection has an obvious effect on both combustion and ion current signal phases.
- (2) In HCCI combustion, combustion phase feedback control strategy between cycles based on ion current signal is put forward. CA50 is estimated by the phase feature dI_{min} of ion current differential signal. According to ion current signal phase features in two cycles before, fuel amount injected in the next cycle will be regulated to stabilize combustion.
- (3) The control experiment was done. The results show that the control strategy lower variations of cylinder pressure and IMEP effectively, HC emissions are also controlled in a low level.

Acknowledgments This work was supported by the National Basic Research Priorities Program (973) of China (No.2007CB210005) and the 111 Project (No. B08019)

References

1. Henein NA (2010) Characteristics of ion current signals in compression ignition and spark ignition engines[C]. SAE 2010-01-0567
2. Zhu GG, Hung DLS, Winkelman J (2006) Combustion characteristics detection for low pressure direct injection engines using ionization signal[C]. SAE 2006-01-3317
3. Yoshiyama S, Tomita E, Mori M et al (2007) Ion current in a homogeneous charge compression ignition engine. SAE 2007-01-4052
4. Fuerhapter A, Unger E, Piock WF (2006) New AVL CSI engine—HCCI way to work in multi-cylinder gasoline engine [J]. Foreign Intern Combust Engine 38(5):6–11
5. Strandh P, Christensen M, Bengtsson J et al (2003) Ion current sensing for HCCI combustion feedback[C]. SAE 2003-01-3216
6. Xie Hui, Sun Yanhui, Zhaoming Wu (2007) Ion current-based method for gasoline HCCI combustion phase detecting. J Tianjin Univ 40(9):1089–1093
7. Dong G, Wu Z, Li L et al (2009) Method of ion current detection for HCCI combustion on SI/HCCI dual mode engine[C]. In: 2009 IEEE intelligent vehicles symposium
8. Wang Z, Wang J, Shuai S et al (2005) Effects of spark ignition and stratified charge on gasoline HCCI combustion with direct injection. SAE 2005-01-0137

Efforts on Fuel Economy Improvement of 1.3 L TGDI Gasoline Engine

Chen Yang, Yuan Shen, Yi You and Fuquan Zhao

Keywords Turbocharged · Gasoline direct injection · Dual variable valve timing · Thermal efficiency · Friction optimization

1 Introduction

The Geely GETEC engine family is a key element of Geely's global blueprint for sustainable development. The members with higher performance and efficiency in the family will replace preceding larger displacement naturally aspirated (NA) petrol engines in a very wide range of vehicle applications, to meet increasingly stringent legislations around the world. It will give the customers significantly improved fuel economy and emissions without compromising driving performance feel, comfort and unaffordable cost.

The combination of turbo charging, gasoline direct injection and dual variable valve timing (VVT) represents the state-of-the-art of modern gasoline engine [1]. It is widely accepted that engine downsizing in combination with pressure charging (primarily turbocharging) and direct fuel injection is the most appropriate and synergistic technology to simultaneously meet future requirements and achieve customer satisfaction. Recently in the market it is apparent that a continuously growing number of applications are using downsizing as a crucial step in the CO₂ emission reduction strategy [2].

During development and now in real world applications with the customers, CO₂ reduction and fuel economy can be further improved by introducing downsizing strategy. However, the challenges to realize a high downsizing, together with the best possible efficiency for NEDC and real world fuel consumption are [3]:

F2012-A01-024

C. Yang (✉) · Y. Shen · Y. You · F. Zhao
Geely Automobile Research Institute, Hangzhou, China
e-mail: 3000821025@163.com

- high low end torque and good transient response at low speeds to ensure excellent drivability.
- optimization of knocking combustion at high loads to realise a high compression ratio and a good combustion, as a prerequisite for high efficiency and high low end torque.
- further reduction of pumping losses at part load.
- as small as possible over fuelling area at high loads and speeds (for thermal protection of the exhaust side).

As a global automaker, Geely is continuously striving for making products more competitive by significantly reducing environment impact, enhancing value to society and keeping focus on efficiency and affordability. In the context of downsizing through turbo-charging, gasoline direct injection and other latest technologies, Geely put extreme effort on developing 1.3 L TGDI with better efficiency based on current 1.3 L TC engine from B-platform. This new engine, first application of gasoline direct injection, will be installed on B-class vehicle, instead of current 1.8 L NA gasoline engine from C-platform. The article covers the design of key systems and components which significantly influenced on the engine fuel consumption. Additionally engine performance and fuel economy assessments are also discussed and compared to the larger displacement predecessor.

2 Targets and Key Concept Decisions

The 1.3 L TGDI engine was upgraded from base 1.3 L TC engine of B-platform through introducing advanced gasoline direction injection combustion mode. Simultaneously maximum commonality was required to decrease the product cost so as to elevate competitiveness and affordability. In addition, it will be installed on B segment vehicle with 6-speed manual transmission (MT) to replace current 1.8 L NA engine, and 13 % reduction of fuel consumption is expected without employment of other measures. Extremely excellent fuel economy will be considered constantly prior to other requirements. Furthermore significantly better torque over the whole engine speed range, quick time-to-torque response, good NVH performance are prerequisite to achieve rigorous requirements of customers in the real world driving applications.

As noted previously, the new derivative was derived from the 1.3 L TC engine, and top-level base architectures were carried over. Shown in Table 1, higher power and torque at wider engine speed as well as better fuel consumption were requested as preliminary program objectives.

In the light of development targets, the right combination of elements were extracted from the landscape of realistically applicable technologies to fulfill expected requirements. Although challenging, realization of the above objectives was essential in order to ensure widespread applications supporting current and future market. A comprehensive set of actions as follows was selected to improve thermal efficiency and decrease friction and pumping losses:

Table 1 Engine technical data and targets

Attribute	B-1.3 L TC	B-1.3 L TGDI	C-1.8 L NA
Bore × stroke (mm × mm)	75 × 73.5		79.3 × 91.5
Bore spacing (mm)	82		87
Max. power (kW at RPM)	98 at 5,500	110 at 4,900–5,500	98 at 6,000
Max. torque (Nm at RPM)	185 at 2,000–4,500	215 at 1,500–4,900	170 at 4,000
Compression ratio	9.5:1	9.9:1	10.0:1
Peak firing pressure (bar)	90	95	75
Emission	EURO V		
Fuel	RON 93		

- The synergy between boosting and direct injection had been repeatedly demonstrated to be effective solution for downsizing [2–5].
- Compared to base engine, extra exhaust VVT was deployed to enable excellent low end torque characteristics combined with good part load fuel economy and emission.
- Fast combustion system was developed to adapt to gasoline direct injection.
- Special attention was paid to reduce friction of piston rings, valvetrain and FEAD system.

In summary, the 1.3 L TGDI engine combines excellent power, torque and drivability with fuel economy targeted to be class-leading.

3 Efficient Combustion System Design

3.1 Fast Combustion Chamber

It was the second application of Geely's engines to be featured with the DI combustion system based on side injection. The combustion system is completely new compared to the base MPI TC engine, and consists of the intake and exhaust ports, dome-roof combustion chamber, piston bowl crown, and side-mounted injector, shown in Fig. 1. Lateral injector layout was adopted due to minimum modifications on current cylinder head and less coking tendency at injector tip. Nevertheless several challenges had to be avoided during the development course, for instance valves impingement, wall wetting and oil dilution.

In the design phase, intake port was redesigned in order to satisfy the requirements of new combustion mode and reduce the knock risk in highly boosted engine. The tumble ratio was improved from 2 to 2.2, which helped to fasten mixture preparation and flame propagation. The multi-hole solenoid injectors were selected as an overall affordable solution, and were captured beneath the intake ports. The peak injection pressure was targeted to 150 bar with the potential to be increased up to 200 bar for future update.

Fig. 1 Graphical display of combustion system



The interaction of the fuel spray with the high tumble charge motion leads to deflection of the spray in the cylinder. This deflection depends on the level of the injector spray pattern, tumble motion and hence the engine speed [2]. Optimal combination of motion charge, injector location and spray pattern, and piston top shape is advantageous for reliable and fast combustion, and minimal wall wetting and oil dilution. This aspect was optimized repeatedly by means of CFD simulations in terms of in-cylinder air motion, fuel spray, mixture formation and distribution, seen in Fig. 2.

In the development phase, a prototype engine was used to determine the optimal combination of variants in the light of performance, economy and emission. Afterwards investigations on transparent engine were carried out. As a result of using laser induced fluorescence (LIF), the interaction of the jets with the combustion chamber walls, induction valve and piston was directly visible [6]. Any impingement of liquid fuel on the liner or excessive impingement of liquid fuel on e.g., the piston crown could be observed and countermeasures on the hardware and the parameter setting side could be defined [7]. Thanks to this tri-element methodology, early, rapid and cost-effective combustion system design and development was allowed. Based on the investigations mentioned above the 6-holes injector was selected and positioned with 25 degree to cylinder head bottom flange.

Thanks to the efforts in the design and development of combustion system, the optimum option displayed best results in terms of consumption, smooth running and emissions both in the simulation and on the engine test rig. Figure 3 plots the comparison of combustion duration between new engine and predecessor, and it indicates that faster combustion of new engine was achieved in the most WOT

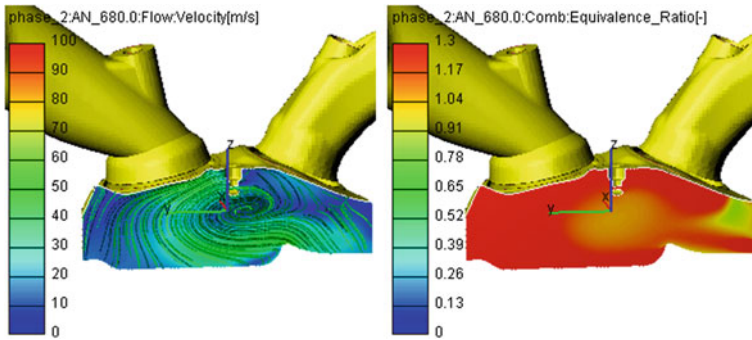


Fig. 2 CFD assessment of in-cylinder flow and homogenization (4900 rpm WOT at 680 CAD)

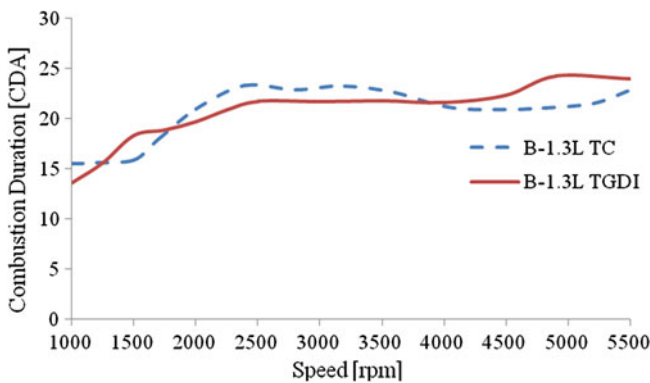


Fig. 3 Comparison of combustion duration at WOT operation

operation, and entirely at very good level. Therefore enrichment can be kept low for component protection due to the short ignition delay, fast combustion and the high knock resistance.

3.2 Dual Independent Variable Valve Timing Units

Downsizing concepts normally use intake or dual VVT to provide further improvements when combined with pressure charging and GDI [3]. In the new engine dual independent VVT system was implemented, and compared to base engine, exhaust VVT was added due to economy and emission considerations. Continuously variable hydraulic actuators of both intake and exhaust camshafts operated in an adjustment range of 51.5 degrees with respect to crankshaft.

The variable valve timing system comprises of a hydraulic actuator, oil control valve (OCV) and cam position sensors for intake and exhaust systems. The vane

type VVT actuators are positioned at the front end of camshafts, and both OCVs and cam position sensors are mounted on the cylinder head cover. In order to achieve rapid adjustment response with good regulation characteristics at both the highest and lowest oil temperatures and over the entire running operations, special attention was paid to design the path the oil must travel from the OCV to the phase adjuster. In the end the extremely short route was realised.

Combined with turbo charging and GDI, smart strategies could be employed for the operation of dual cam phasers. They are as follows:

- At part load the exhaust cam is shifted to late close to re-draw exhaust gas into the cylinder, fulfilling internal EGR for de-throttling. Meanwhile the intake valve is also closed late. As a result pumping loss is reduced.
- At high load it is allowed to be run in large valve overlap, fulfilling scavenging of fresh air from the intake to the exhaust, further improving the knock threshold of the engine and enabling higher torque. This is not possible on port fuel injection engines as it results in unburnt mixture being drawn into the exhaust manifold, increasing fuel consumption, HC emissions and potentially damaging the catalysts [3].

3.3 High Pressure Fuel Injection System

The complete fuel injection system is shown in Fig. 4, consisting of high pressure pump, high and low pressure fuel lines, high pressure fuel rail and solenoid injectors. The entire system is assembled as a preassembled unit with 4 bolts to the cylinder head.

The fuel pump, mounted on the cam cover, is a single plunger, demand delivery design, which is driven by intake camshaft via a 3 mm lift/4 lobe cam and associated barrel follower. As displayed in Fig. 4, a nozzle with diameter of 0.8 mm is designed to draw the oil from the oil gallery in the cylinder head, and to cool the tappet roller and cam profile. This pump can deliver 0.75 cm³ fuel per cam revolution, which is sufficient to meet the maximum demand at rated power running, therefore it is functionally acceptable. Although a 4 mm lift/3 lobe cam was considered as an alternative to replace the 3 mm lift/4 lobe cam, the latter was advantageous for lower mean driving torque and less pressure fluctuation in the high pressure fuel rail. As a consequence, better fuel economy was realized.

The fuel injectors are captured by the respective fuel rails, and mechanically oriented to ensure consistent spray pattern. Then the injectors are pressed to the cylinder head and the rail is fixed to the cylinder head through four bolts. In order to allow for tolerance alignment and flexible assembly, the injector electrical socket has 20 degree rotation.

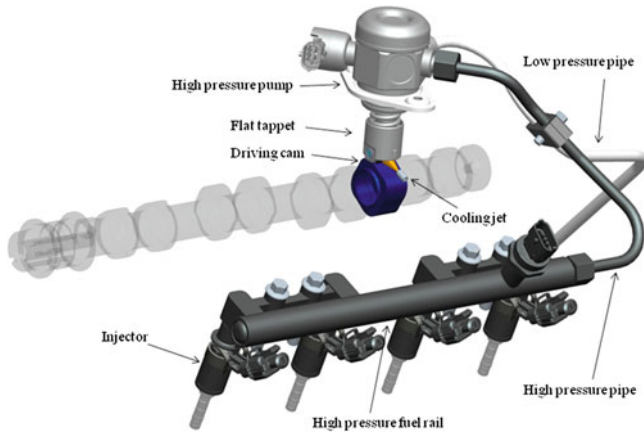


Fig. 4 High pressure fuel injection system

3.4 Ignition System

The ignition system was revised from base engine to be capable of firing with greater ignition pressures due to the higher boost requirement and in-cylinder turbulence. In addition, the ignition system also is required to be totally reliable since any misfire or retarded combustion can disrupt the charge motion and lead to abnormal combustion.

The ignition system consists of the ignition coils and spark plugs. The ignition coils are high energy design, and each cylinder has its own coil directly mounted on top of the cam cover. The coil can provide ignition energy up to 65 mJ with a breakdown voltage of greater than 30 kV.

The spark plug is a J-type fine wire and M12 thread design with platinum-iridium center electrode and a copper core/platinum-iridium ground electrode. The application of double platinum-iridium tips was for increased durability and spark plug gap was also optimized for reliability.

3.5 Turbocharging System

The development challenge with downsizing engines is that high specific power output has to be achieved in combination with excellent fuel consumption [7]. The boosting system of this engine was optimized for excellent low end torque and quick response as well as better fuel economy. Efforts were put on the choice of the most suitable solution for targeted performance and fast transient response. Two mono-scroll turbochargers were investigated in detail for thermodynamic simulation and development. The small turbine was finalized due to its low rotor inertia and therefore excellent transient response.

The turbine is with 37 mm diameter, 76 trim wheel and A/R 0.337 housing, while the compressor is with 41 mm diameter, 62 trim wheel and A/R 0.54 housing. The peak temperature before turbine inlet is less than 950 °C, and the maximum speed of the rotating assembly is 250,000 rpm. The wastegate is controlled by vacuum actuator, which is integrated on the compressor house as well as electric dump valve.

4 Consistent Optimization of Parasitic Friction

4.1 Piston and Ring Package

Pistons and rings contribute substantial share to entire engine friction losses. As reported in [8], it is said that pistons and rings share in total engine friction are around 17 % and 23 % respectively, and in detail the contributions of first compression ring, second compression ring and oil ring are 40, 20 and 40 % separately, therefore it has a significant potential for bring down friction of piston groups.

In order to decrease the inertial force, the piston was optimized by minimizing the piston compression height (29.55 mm), pin-bosses distance and skirt length. Graphite coating treatment was given to piston skirt to reduce friction loss.

Further potential for reducing friction was gained by optimizing the piston rings with advanced coating technology and low tangential tensions. DLC coating was applied on the first compression ring to lower friction coefficient. The axial height of second compression ring was reduced by 0.3 mm, and subsequently tangential force was decreased. New type oil ring was designed, and tension force was reduced significantly by 25.4 %.

4.2 Valve Train

Valve train layout (DOHC, RFF, HLA etc.) and timing drive were mainly carried over from base engine. Preceding linear valve spring was replaced by nonlinear spring to further decrease driving torque. For this GDI engine, high pressure fuel pump was driven by 4-lobe cam on the intake camshaft among the third and the fourth cylinder. Since the absolute orientation of this 4-lobe cam relative to the intake cam of fourth cylinder can effectively influence the driving torque, special focus was paid to this issue, and detailed investigations were performed using simulation method.

Valve train dynamics simulation was performed to determine the optimal orientation of fuel pump driving cam in the form to intake camshaft driving torque and timing chain dynamic tensile force. Figure 5 plotted the variation of intake camshaft driving torque against relative crank angle between cylinder-4 maximum

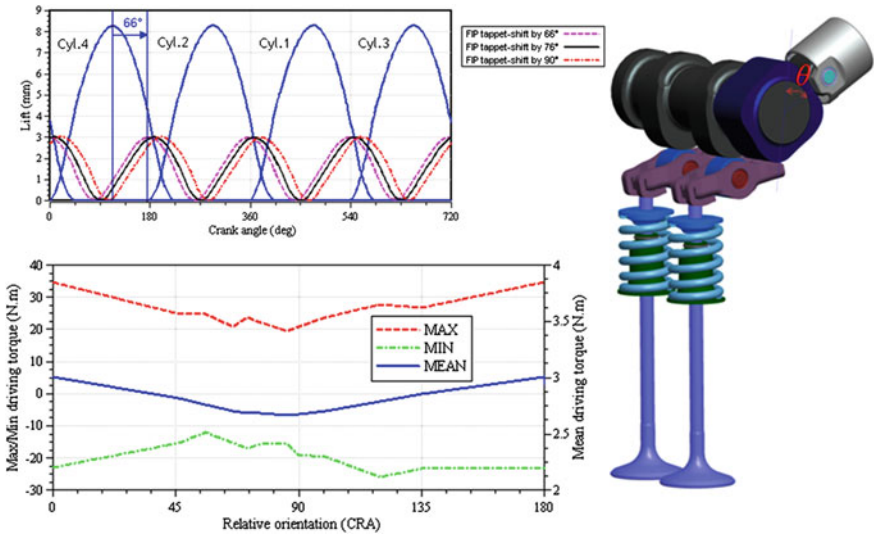


Fig. 5 Influence of 4-lobe cam orientation on driving torque

lift and following fuel pump maximum lift. Also assembling complexity was considered. In the end, 66 CRA was defined as the best solution.

4.3 Front End Belt-Driving System

Low tension, low friction loss belt drive is constantly expected to fulfill highly efficient engine. The optimization of front end auxiliary drive (FEAD) system can be significant contributor to the bottom line reduction of consumption for every engine. For this GDI engine, FEAD system was mainly carried over from base engine. In order to improve fuel economy and belt vibration level as well as components durability, extra overrunning alternator pulley was deployed. Compared to the system without OAP, the belt preload force was remarkably diminished from 450 to 320 N as well as dynamic tensile force. In that case, the benefits such as low hub loads, low friction, longer component durability, better NVH behavior were derived.

5 Performance and Fuel Economy

Thanks to the various optimization measures with regard to charge motion, combustion process and low-friction design, the outcome is reflected in stationary and dynamic full load behavior. As shown in Fig. 6, 1.3 L TGDI engine already

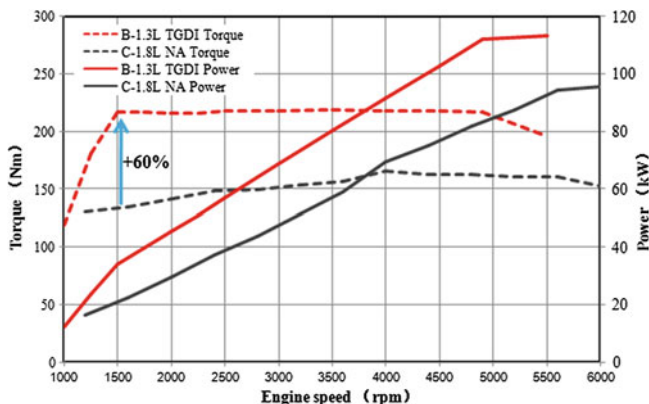


Fig. 6 Comparison of torque and power output

achieves its knee point at 1,500 rpm with 215 Nm torque, and keeps constant until 4,900 rpm. Meanwhile it has a wide power output band of 110 kW between 4,900 and 5,500 rpm. Compared to the 1.8 L NA engine, the low end torque at 1,500 rpm is considerably elevated by 60 %, which guarantees excellent responsiveness, drivability and superb performance. Due to this high low end torque characteristics downspeeding strategy could be combined together, which leads to lower engine speed and helps to offer additional noticeable fuel economy.

In part load based on DVVT de-throttling effect, the engine is running with high amounts of internal EGR, and it is achievable to realise outstanding part load fuel economy. The BSFC at 2,000 rpm/2 bar BMEP exhibits class-leading position for TGDI engines in the benchmark.

Moreover fuel consumption in NEDC and realistic driving were assessed in a 6-speed MT vehicle with the weight of 1,280 kg, and compared to larger displacement 1.8 L NA engine. The simulation results indicated that the fuel consumption was decreased from 7.54 to 6.47 L/100 km, with reduction of 14.2 %. Figure 7 demonstrated the fuel consumption of two engine respectively at different constant vehicle speed. It was shown that in the conditions of the same gear and vehicle, the vehicle with 1.3 L TGDI engine was more frugal than the one equipped with 1.8 L NA engine. The root cause of this improvement was that thanks to downsizing strategy, friction optimization and other fuel-saving measures, the new engine was constantly running in more efficient zone in the BSFC map.

6 Summary and Outlook

As the first TGDI engine of Geely, this new engine was developed based on the architecture of preceding 1.3 L TC MPI, and outstanding fuel economy, robust output and excellent responsiveness were targeted attributes. For these purposes,

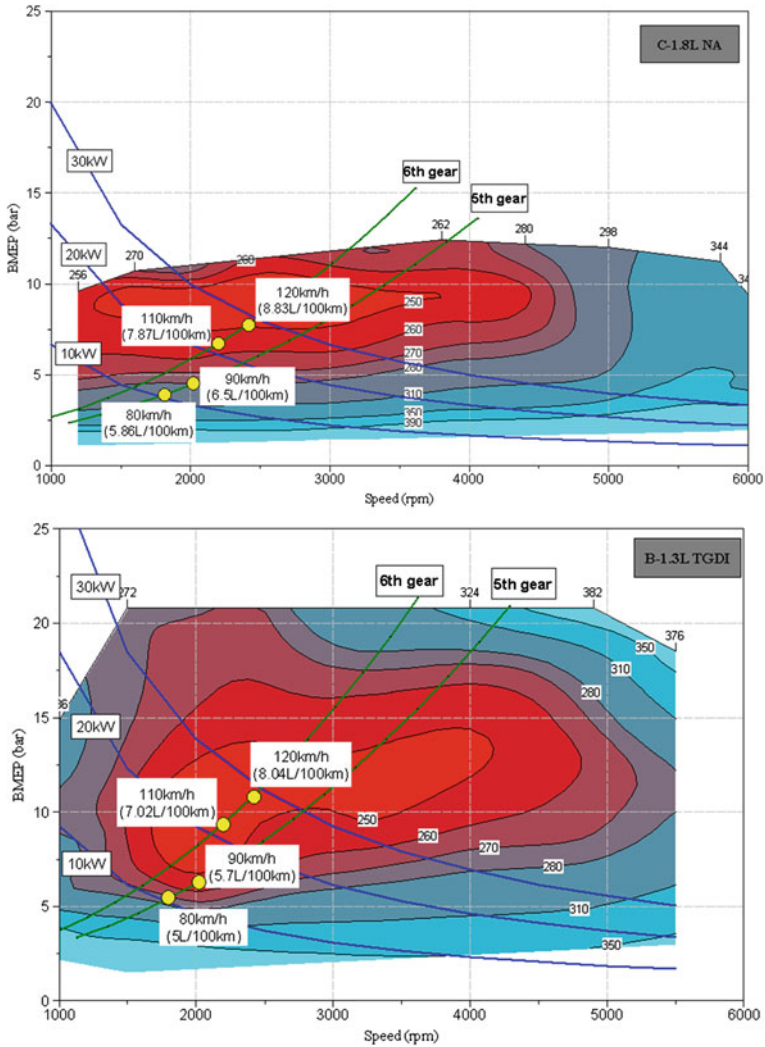


Fig. 7 Comparison of fuel consumption at constant vehicle speed

extraordinary focuses were emphasized on the efficient combustion system development and low friction optimization. Thanks to the suitable combination of advanced technologies, the resultant BSFC of 2,000 rpm/2 bar represents the lowest level in the low displacement segment. At the same time torque and power are considerably exceeding the performance of a 1.8 L NA engine, especially at low end. In the real application substantial fuel consumption reduction was fulfilled, since the downsizing TGDI engine is often running in the more efficient range.

The new TGDI engine is thus ideally equipped to meet the stringent requirements for worldwide use in all markets. For further upgrade intelligent thermal

management, lightweight design and start-stop system will be deployed as optional solutions, which can contribute to additional fuel economy improvement.

Acknowledgments The authors would like to profoundly acknowledge the following colleagues for their support: Mr. Chao Wang, Dr. Yunqing Liu, Ms. Na He, Mr. Lianjun Shen, Mr. Pingtao Yan and Mr. Dongrong Wang. Their contributions were essential for writing this paper successfully.

References

1. Königstein A, Grebe UD, Wu K-J, Larsson P-I (2008) Differentiated analysis of downsizing concepts [J]. *MTZ* 69(06):5–11
2. Weber , Brumley A, Filipe D, Whiston P (2010) 1.6 SCTI: the new EcoBoost DI-turbo engine with central direct injection for ford's volume carlines [C]. In: 19th Aachen Colloquium vehicle and engine technology
3. Korte V, Fraser N, Taylor J, Dingelstadt R (2011) Efficient downsizing for future gasoline engines [J]. *MTZ* 72(05):42–48
4. Borrmann D, Brinkmann F, Walder K, Pingen B (2002) Gasoline direct injection and turbo charging—a new opportunity for downsizing [C]. In: 11th Aachen Colloquium vehicle and engine technology
5. Fraidl GK, Kapus PE, Piock WF (2005) The turbocharged GDI—the competitor to the diesel engine? [C]. In: 26th international Vienna engine symposium
6. Hadler J, Szengel R, Middendorf H (2009) Minimum consumption—maximum force TSI technology in the new 1.2L engine from volkswagen [C]. In: 30th international Vienna engine symposium
7. Kunde O, Hansen J, Zenner T, Kapus P (2010) The new 2.0 SCTI EcoBoost gasoline engine from ford [C]. In: 19th Aachen Colloquium vehicle and engine technology
8. Königstein A, Grebe UD, Wu K-J, Larsson P-I (2012) Piston ring coating reduces gasoline engine friction [J]. *MTZ* 73(05):40–43

Development of Two-Stage Turbocharger System with Electric Supercharger

Byeongil An, Hiroshi Suzuki, Motoki Ebisu and Hedeyuki Tanaka

Abstract To satisfy both environmental regulations and better drivability requirements, high-level control of automobile engines is currently in demand, and electrification is in progress. An electric supercharger, in which a supercharging compressor is driven by a high-speed motor instead of an exhaust turbine, improves the transient response of the turbocharger by due to the motor high-speed response. An engine with an electric supercharger offers comparable fuel consumption to a naturally aspirated engine, and is expected to facilitate the downsizing of engines. The electric supercharger prototype consists of a centrifugal compressor impeller and a high-speed motor rotor, supported by grease lubricated ball bearings. In this paper, we explained development of grease-lubricated electric supercharger and electric two-stage supercharger system combined with another turbocharger at 12 V power supply specifications. Specially, this paper introduces the result of the engine bench test and simulation using engine simulation tool (GT-Power). Moreover, we report the performance test results exhibiting a high-speed response of 0.7 s acceleration time to attain a compressor operating point rated at 2.4 kW, 90,000 rpm. As a result of engine test using a 1.5 L gasoline engine, the electric two-stage turbocharger demonstrated the 43 % improvement in a response time at 1,500 rpm as compared with normal two-stage turbocharger. Also, the electric two-stage supercharger was found to be effective in the catalytic activity of the cold start when the turbine outlet temperature over 100 °C higher than the two-stage

F2012-A01-026

B. An (✉) · H. Suzuki · M. Ebisu
Mitsubishi Heavy Industries, LTD, Tokyo, Japan
e-mail: byeongil_an@mhi.co.jp

H. Tanaka
Mitsubishi Electric Corporation, Tokyo, Japan

turbocharger. We aim to accelerate technical development towards production, and to contribute ever tightening CO₂ reduction with automobile engines from now on.

Keywords Electric supercharger · Engine downsizing · Transient response · Motor and inverter · Engine simulation

1 Introduction

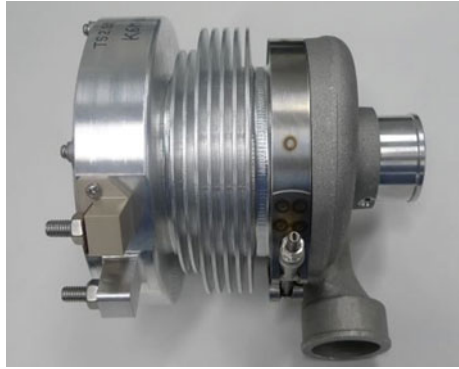
With the ongoing movement toward global environmental protection, regulations of controlling the exhaust emissions and fuel consumption of automobiles are being enforced. Turbochargers have improved the performance of diesel engines; currently, almost all diesel vehicles are equipped with turbochargers. More and more gasoline engines are also being fitted with turbochargers to decrease weight and increase efficiency. In recent years, engine controls have become widely diversified for the sake of both the environment and operating performance. Also, electrification has produced the present generation of hybrid and electric vehicles, and progress continues. Batteries are also expected to improve in response to this trend. Current electrification projects impacting turbochargers include the application of electronic control actuators. Moreover, advances in power electronics have led to the development of ultra high speed motors and generators with higher capacity, which are now available for use in turbochargers. The centrifugal compressor is directly connected to a high speed motor, and the compressor boost pressure is controlled by the motor speed, independent of the exhaust gas condition. This electric supercharger and electric two-stage supercharger system are expected to contribute to lower fuel consumption, the reduction of exhaust loss, and the downsizing of engines. This paper was introduced on the development of electric supercharger and electric two-stage supercharger system combined with another turbocharger. In addition, the effect of improving low-end torque and transient response was investigated by means of the simulation and engine bench test.

2 Development of Electric Supercharger

2.1 Development Concepts

The concepts of electric supercharger are:

- The power source should be a conventional 12 V lead-acid battery for automotives.
- The “all-in-one” electric supercharger (Impeller, motor and inverter in one single unit).
- Grease lubrication eliminates the need for lubrication oil piping.
- Development of high efficiency compressor wheel.
- Development of high-speed motor driving over 90,000 rpm.

Fig. 1 Electric supercharger

The goals of the electric supercharger are to deliver instant boost (none-turbo-rag) at low engine speeds, as well as to achieve extreme downsizing of the engine.

2.2 Construction and Features

Figure 1 shows the developed electric supercharger, in which two ball bearings support the impeller of centrifugal compressor and the rotor of high-speed motor. These bearings with grease contribute to response improvement (Fig. 2) through reduced mechanical losses, and eliminate oil plumbing for lubrication. The intake air of the engine is utilized to continuously cool down the motor and inverter generating heat due to large current flowing through these devices.

2.3 Power Electronics Technology

2.3.1 High Speed Motor

For this electric supercharger, a field magnet type synchronized motor is chosen. This motor can be characterized as follows:

- Robustness due to iron core with no magnet.
- High torque using field magnet on stator.
- No conductors (brushes).

Figure 3 shows the structure of the motor. Taking the voltage into consideration, the stator winding has only 1 turn. The motor output with 12 V supply reaches 2.4 kW and gains boost pressure ratio of 1.6 in 0.7 s. The total motor efficiency, including mechanical losses, realizes 83 %.

Fig. 2 Response time of electric supercharger

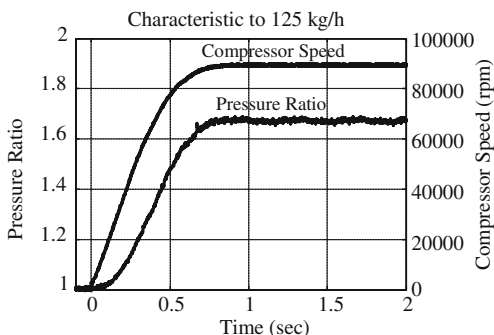
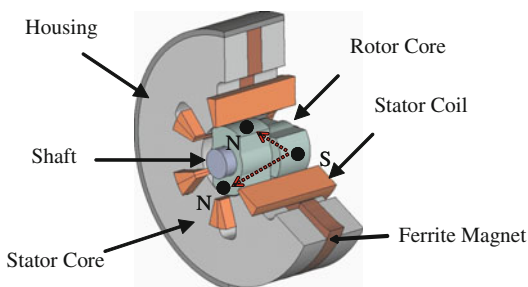


Fig. 3 Schematics of motor structure



2.3.2 Inverter

The inverter is a general pulse-width-modulation (PWM) voltage source type. A field-effect transistor (FET), which allows high-speed switching, is used as a semiconductor switching device. A general-purpose microcomputer is employed for the motor control. The inverter handling large current is built-into the motor in order to minimize electrical losses. This compact design results in elimination of wires between the two, and requires only a DC harness from the power supply. Detection of rotor position enables this compressor to produce the largest torque from zero rpm. An implementation of this method helps not only to realize a good response at the time of initial drive, but also to minimize electricity consumed when this electric supercharger is at standstill. Figure 4 shows the electric load of electric supercharger charger. Initial current is controllable, to prevent blackout.

3 Electric Two-Stage Supercharger System

Figure 5 shows schematics of electric two-stage supercharger system combined with another turbocharger. This electric two-stage supercharger system is composed of electric supercharger and normal turbocharger with west-gate valve, two air bypass valves. Compressor intake air is utilized to cool the motor and the

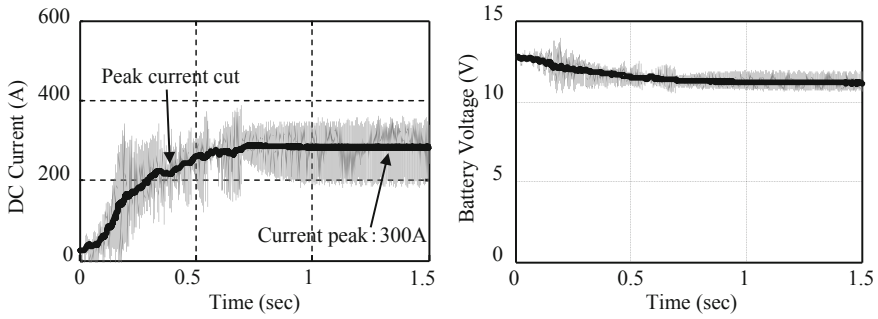


Fig. 4 Electric load of electric supercharger charger

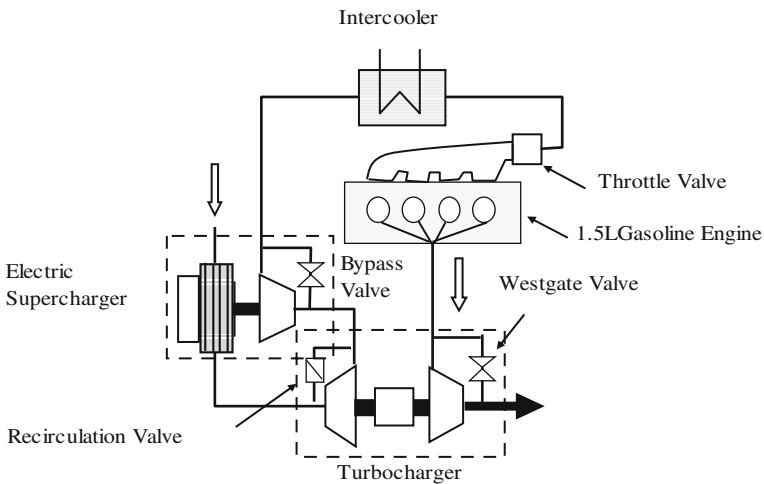


Fig. 5 Schematics of electric two-stage supercharger system

inverter. Because the motor and inverter are upstream of the compressor intake, they are cooled whenever the electric supercharger rotates. The cooling airflow varies with the compressor working point and is favorable to high heat reduction in the motor and inverter when the flow volume is large.

4 Engine Simulation Results

Figure 6 shows a comparison of transient response in the 1.5 L gasoline engine. It shows that turbo-lag is dramatically reduced and low-end torque are achieved in around 1.0 s at engine speeds 1,500, 1,750 rpm. Furthermore, a rapid increase of engine torque must be converted into a wheels torque for deliver good vehicle response. The results of engine simulation, electric two-stage turbocharger have

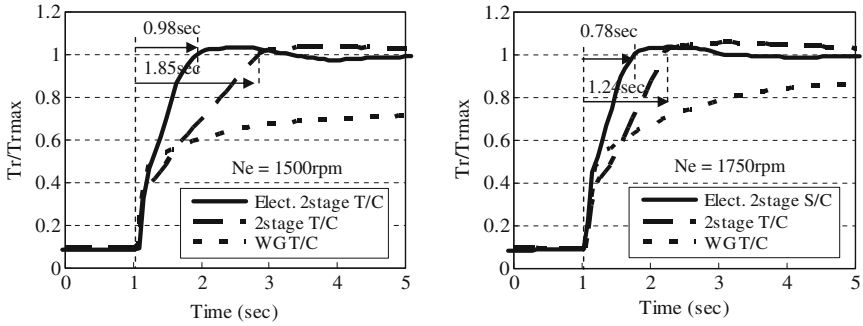


Fig. 6 Comparison of transient response at engine speed 1500, 1750 rpm

Fig. 7 Engine speed versus steady torque

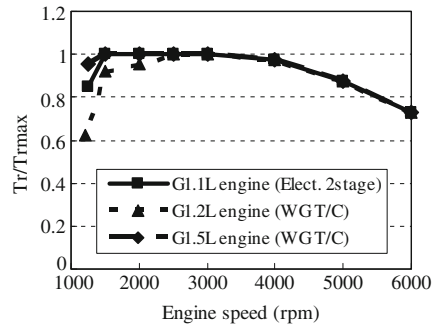
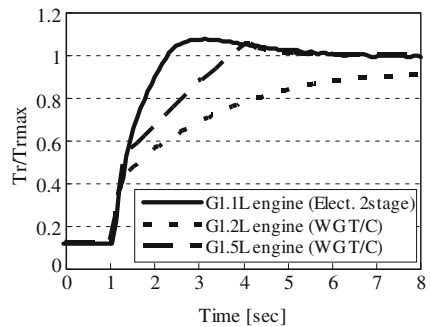


Fig. 8 Response time versus steady torque



been improved transient response as compared with normal two-stage turbo-charger at 1,500 rpm about 47 % and 1,750 rpm about 37 %. We investigated to the extreme engine downsizing, without vehicle drivability drop using engine simulation. Figure 6 shows a relationship between steady-state torque and engine speed. Figure 7 shows a relationship between steady-state torque and transient response time. It can be downsized to 1.1 L gasoline engine keeping same low end torque and transient performance as 1.5 L gasoline engine with west-gate turbo-charger (WG T/C) (Fig. 8).

Fig. 9 Engine torque versus response time

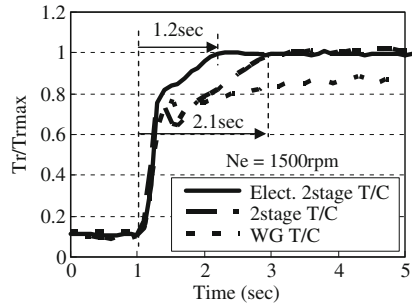


Fig. 10 Back pressure versus response time

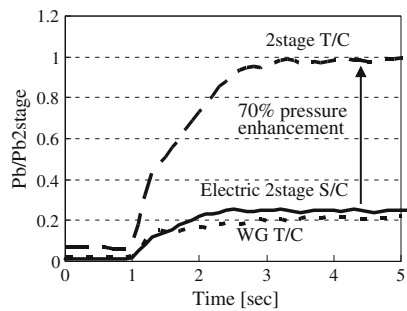
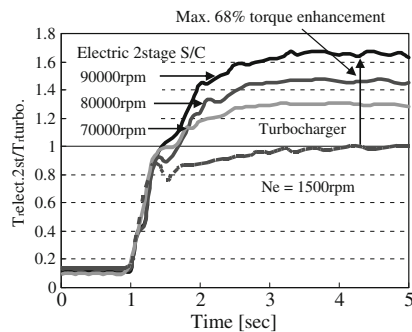


Fig. 11 Effect of electric motor speed on transient response



5 Engine Test Results

The engine used in this experiment is four strokes, turbo charging multi-port injection (MPI) gasoline engine. The evaluation of response test was used engine specification with 110 kW maximum power output and 1.5 L displacement. Figure 9 shows comparison of transient response at engine speed 1,500 rpm. As a result of engine test using 1.5 L gasoline engine, the electric two-stage turbocharger shows the 43 % improvement in a response time at 1,500 rpm as

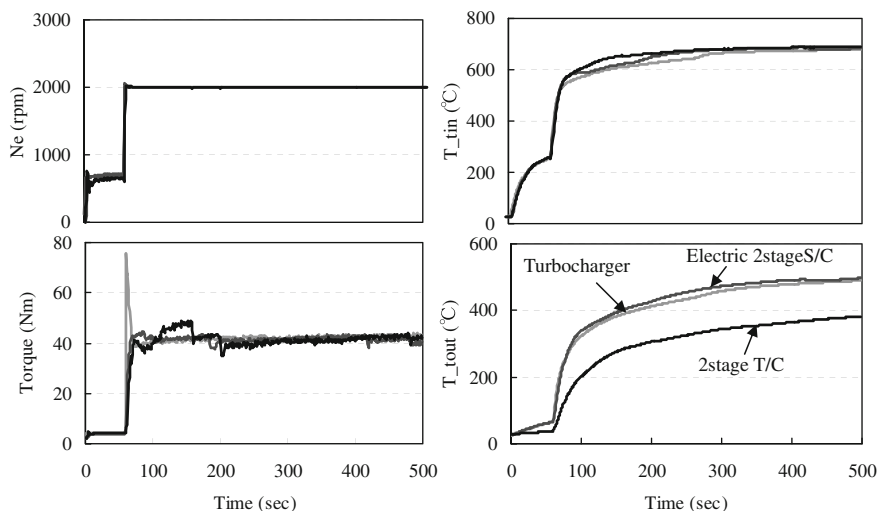


Fig. 12 Turbine outlet temperature comparison during engine cold start

compared with normal two-stage turbocharger. In this case, the assist of electric supercharger is 70,000 rpm; it is possible to further improve response by increasing the maximum up to 90,000 rpm. We measured the transient response while changing from 70,000 to 90,000 rpm at constant engine speed 1,500 rpm in order to verify the performance of the electric supercharger. Figure 10 shows a comparison of engine back pressure on response time. The two-turbocharger was confirmed about 70 % enhancement of engine back pressure compared with electric two-stage turbocharger.

Figure 11 shows an effect of electric motor speed on transient response. From the result, electric two-stage turbocharger is confirmed max. 68 % torque enhancement compared with west-gate turbocharger. When compared to an exhaust-driven turbocharger, electric two-stage turbocharger is able to deliver instant torque at low engine speed, without any corresponding increase in exhaust back pressure (Fig. 10). As a result, the improved low-end torque is effective to reduce pumping losses and combustion instability. Figure 11 shows the changes in the exhaust temperature rise during engine cold start. The test conditions in the idling after 50, 500 s combined adjustment 2,000 rpm with 40 N.m engine torque. As the test conditions, we were set to give the step command with the same torque from idle to 2,000 rpm assumes a engine cold start. The electric two-stage supercharger was found to be effective in the catalytic activity of the cold start when the turbine outlet temperature over 100 °C higher than the two-stage turbocharger (Fig. 12).

6 Conclusion

In order to reduce harmful exhaust emission and vehicle fuel consumption, demands on development of new supercharger system with high performance are increasing. In this paper, we explained development of grease-lubricated electric supercharger and electric two-stage supercharger system at 12 V power supply specifications.

Also, the effect of improving low-end torque and transient response was confirmed by means of the engine simulation and engine bench test. Furthermore, the electric two-stage supercharger is found to be effective in the catalytic activity of the cold start compare with two-stage turbocharger.

Effect of the Injection Method in DI CNG Engine on the Flame Propagation Process and Engine Performance

Xuedong Lin, Fang-en Yuan and Ya Huang

Abstract Test with optical single cylinder engine, in-cylinder with twin jet layout, dual spark plug ignition conditions, with the combination of calculation of 3D simulation software and experiment, analyzed the effect of different mixture concentration distribution characteristics of different jet and different ignition on the flame propagation, the temperature field, the lean combustion process and NO_x emission characteristics. The result showed that the mixture concentration gradient near the spark plug in the organized lean combustion process had a great effect on the flame propagation and combustion stability. The greater the concentration gradient was, the circulation changes would be smaller, the combustion would be more stable, but the NO_x emissions would increase; With the use of dual-point ignition, the air flow movement in the cylinder had a “traction” of the incipient flame, the difference moment of formation and of two flame and the interaction of the two flame affected the whole flame propagation; The NO was generated first when the temperature of cylinder was greater than 2,000 K and equivalence ratio was at the range of 0.8–1, within the range of the concentration of the mixture, the increasing of the temperature led to the significantly improving of the NO formation rate, and the maximum NO production rate appeared after the peak of the heat release rate. The thin out mixture led to the decreasing of the peak of heat release rate and the lag of the crank angle corresponding to the position led to the decreasing of NO formation rate.

F2012-A01-027

X. Lin (✉) · F. Yuan · Y. Huang
State Key Laboratory of Automotive Simulation and Control, Changchun, China
e-mail: yuanfangen@hotmail.com

Keywords DI CNG engine • Lean combustion • Flame propagation • Visualization • NO_x emissions • Influencing factor

1 Foreword

With the development of low-carbon economy era of increasingly stringent demand of energy saving and emission reduction of vehicle engine, as one of the main alternative fuels, natural gas is widely used due to its relatively high H/C, its CO₂ emissions that would reduce about 25 % relative to gasoline engine after combustion and its relatively low CO, HC and particulate matter emissions [1, 2]. But the gas inlet jet CNG mixture calorific value is low, and the mixture into the cylinder showed a gaseous state, which reduced the volumetric efficiency of the engine and CNG engine power was reduced by 10 % or more, the direct injection technology that can effectively solve this problem has become the development trend [3].

In the organization of lean combustion of ignition CNG engine, whether the mixture concentration is rational or not had a direct effect on the flame propagation process, and even the whole combustion process and emission characteristic [4, 5]. The irrational organization of mixture can easily lead to combustion instability and the flameout. It was clear that whether the matching of organizations of mixture rationally and ignition was reasonable or not had a large impact on the combustion process. But few studies on how to control the lean combustion process domestic and overseas. Therefore, in this paper, by the use of a combination of direct injection CNG model engine of optical test and the calculation of 3D simulation software, we studied the effect on flame propagation, combustion process and emissions performance of distribution of in-cylinder concentration field and temperature field of different jet and ignition in macro and micro perspective. Thus to provide the basis for the study of achieving high efficiency and low emissions performance of spark ignition direct injection engine.

2 Experiment Device

The main technical parameters of the experimental prototype and the main component of natural gas fuel is shown in Tables 1 and 2.

Figure 1 is a schematic diagram of the optical test system. The system consists of intake system, CNG injection system, frequency conversion motoring system, the ignition control system, the optical collection system and the optical single-cylinder testing machine. The cross-sectional diagram of the single-cylinder machine is shown in Fig. 2. Two vertical injectors lay in the cylinder head and the injection pressure was about 5 Mpa to achieve the different jet. The observation window was

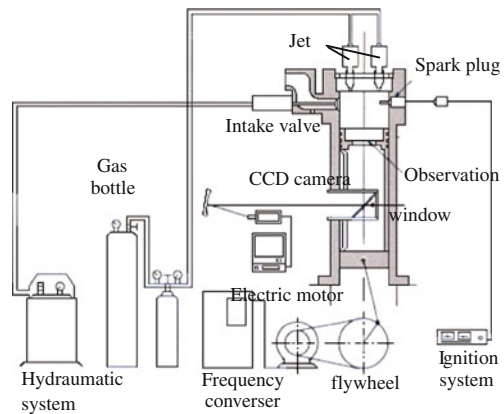
Table 1 The main technical parameters of the experimental prototype

Type	Single-cylinder four-stroke spark ignition
Cylinder parameter (mm)	135
Stroke (mm)	280
Output volume (L)	4.0
Compression ratio	6.13

Table 2 The main component of natural gas fuel

	CH ₄	C ₂ H ₆	C ₃ H ₈	C ₄ H ₁₀	N ₂
Vol%	85.45	4.51	3.39	3.71	2.94

Fig. 1 Schematic diagram of experimental device



set up at the top of piston to observe the process of flame propagation of combustion chamber, the flame propagation characteristic was observed in different injection conditions with the 563/sec continuous shooting by high-speed CCD camera, the visualization rate of the combustion chamber was about 67 % of cylinder diameter; The indicator diagram was made up at the same time to analyze the combustion process. The average processing of ten cycles that was measured each conditions made up the experimental data. The NOx emissions was measured with the manufacture of Japan’s Shimadzu NDA-7,000 type NOx measurement instrument.

According to the specific characteristics of the single-cylinder experimental prototype, the test speed is set to 200 or 400 r/min. At that speed, through the adjustment of the inlet entrance, the intake swirl ration is set to $sw = 6.0$ to improve the cylinder air flow motion intensity. The installation location of injector and spark plug and their serial number is shown in Fig. 2.

Table 3 shows that the dual-pint ignition was used, the ignition timing is fixed at $(\theta_{i1}, \theta_{i2}) = (-4, -3) \text{ }^\circ\text{CA}$. Δt was experienced from the end of injection and the moment of ignition under different experiment conditions. The length of time of the formation of mixture after the direct injection is directly indicated by the size of Δt (Fig 3).

Table 3 Injection timing in different experiment conditions

n (r/min)	ϕ	Moment of injection °CA BTDC	Δt (ms)
200	0.93	120	-3.3
	0.84	120	16.7
	0.70	120	31.7
		180	81.7
		90	6.7

Fig. 2 Schematic diagram of position of spark and jet

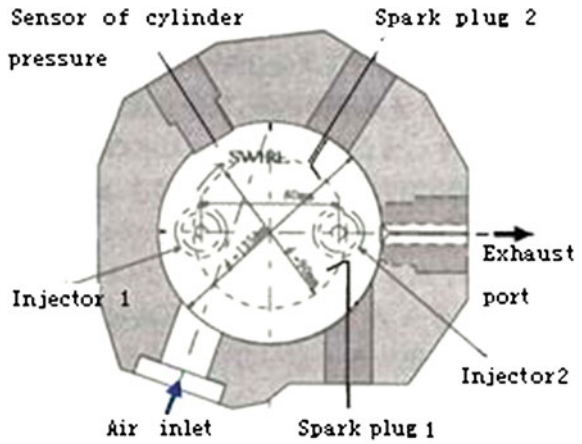
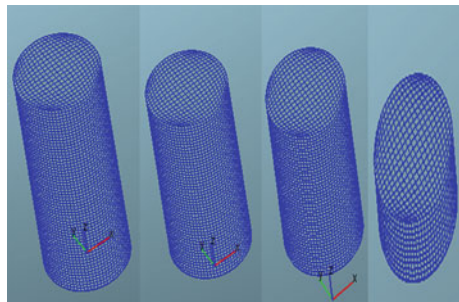


Fig. 3 Calculation mesh



3 The Establishment of Simulation Model and Verification

3.1 Establish Model

Created the cylinder model using Cylinder method in Topology in the FIRE, and the mesh was created automatically.

Fig. 4 Comparison of the law of heat release

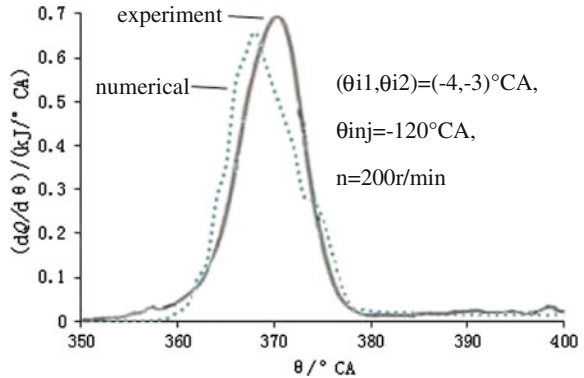
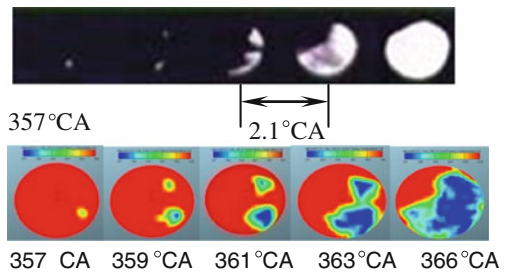


Fig. 5 Comparison of flame propagation



3.2 Boundary Condition and the Verification

Setting the pressure at inlet of cylinder as 0.9 bar, temperature as 350 K, the engine speed as 200 rpm, inlet swirl ratio as 6.0. The top face of piston was moving boundary, and its temperature was setting as 593 K. The wall of cylinder and bottom of cylinder was fixed boundary, and their temperature was setting as 403 and 593 K.

Criteria $k-\epsilon$ model, the EBU turbulent diffusion model and PDF combustion model was selected as Computational model.

The comparison of results of simulation and the actual measurement of the law of heat release and flame propagation can be seen on Figs. 4 and 5 respectively, it was shown that they were in a good coincide with each other [6].

4 The Results of Experiment and Analysis

4.1 The Effect on Combustion Process of the Quality of Jet

It can be seen from the data in Table 3, when the timing of injection was $120^\circ CA$ before the top dead center of compression, the timing of injection was $(-4, -3)^\circ CA$,

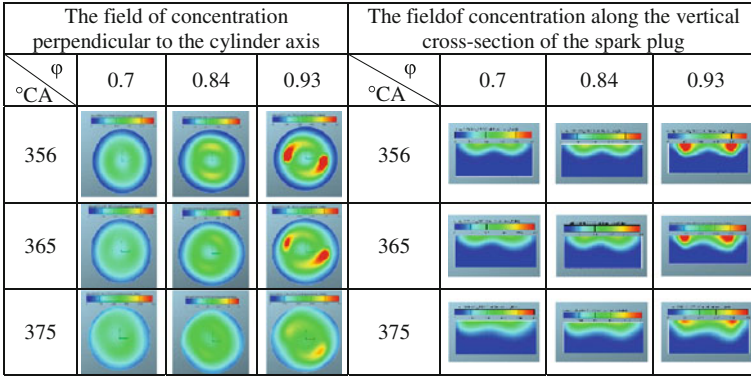
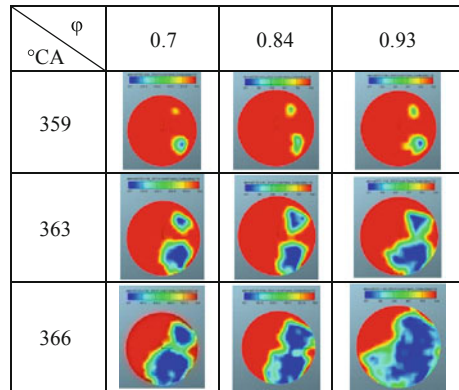


Fig. 6 The effect of equivalent ration on concentration field

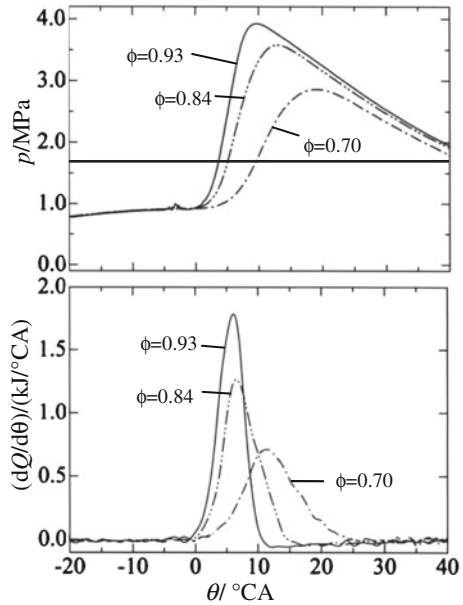
Fig. 7 The effect of different equivalent ratio on the speed of flame propagation



when the quality of jet (the average equivalence ratio was increased) was increased, due to the fixed pressure of jet, the duration of jet was extended, Δt was decreased. Especially when $\phi = 0.93$, $\Delta t = -3.3$ ms, it was shown that the jet process was still continuing during the ignition. It can be seen from concentration distribution in Fig. 6, with the increasing of the quality of jet (ϕ), the inhomogeneity of distribution of concentration increased at the center of jet along the air flow in cylinder especially near the spark plug.

It was shown in Fig. 7 that the time of formation of flame center after the spark plug arcing, with the increasing of the quality of jet (ϕ), the concentration gradient increased with the increasing near the spark plug, the area of flame expanded rapidly, indicating the increasing of the speed of flame propagation. As with Dual-point ignition, the first flame formed by arcing of the first spark plug located in the gas flow downstream, which was drag by the “pulling” effect of air flow in the cylinder, expanded rapidly along the direction of air flow, increasing its turbulent flame propagation speed; After the arcing of the second spark plug located in the air flow upstream, the second flame squeezed by “squeezing” effect of the first

Fig. 8 The effect of equivalent ration on the combustion



flame, the pace of expansion of which was slow down, made the traction of the air flow of cylinder of the flame weaken, thus, the speed of the flame slowed down. And as the former flame was pushed by the second flame, the “traction” effect of intensity of air flow in cylinder on the flame would be more obvious with the mixture became more thin and uniform.

Figure 8 shows the effect of quality of jet (indicated with different average equivalent ratio) on the indicator diagram. With the increasing of ϕ , the inhomogeneity of the mixture increased as is shown in Fig. 6, the duration of combustion was shortened, the heat release center was closer to the top dead center, so that the peak of the pressure in the cylinder and the rate of pressure rise increased accordingly. It was shown in Fig. 9 that the effect of the quality of jet (ϕ) on the indicated mean pressure P_{mi} , the fluctuations of cycle and NOx emissions. When the lean combustion was organized in the direct injection CNG engine, with the certain injection method and timing respectively, the smaller quality of jet and the shorter pulse width of jet duration led to sufficient time of the formation of mixture, the formation of mixture would be more uniform and thin. Therefore, the rate of heat release was slow, the indicated mean pressure P_{mi} decreased, so the value σ of the standard deviation of the value of the P_{mi} increased due to the large changes of the state of the mixture near the spark plug. NOx emissions remained unchanged when $\phi < 0.84$, suggesting that the impact of the changes of the concentration of oxygen and the temperature of combustion on the formation of NOx canceled out with each other.

It can be seen from the effect of different equivalent ratio on the temperature field of cylinder in Fig. 10 that the distribution of temperature field was essentially

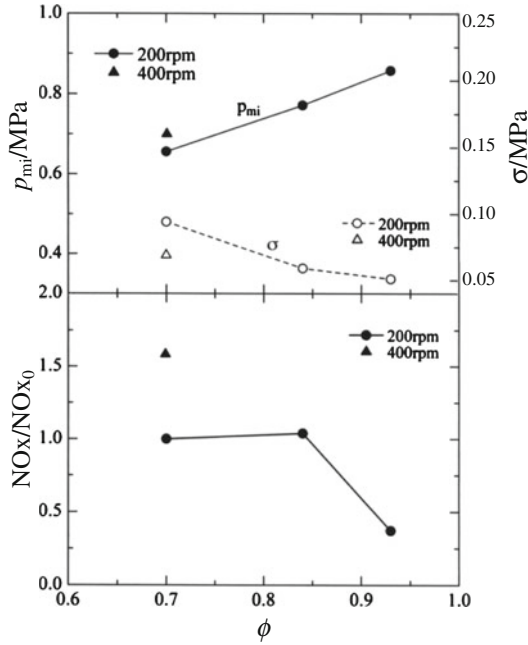


Fig. 9 The effect of equivalent ratio on the engine pressure and exothermic rate performance

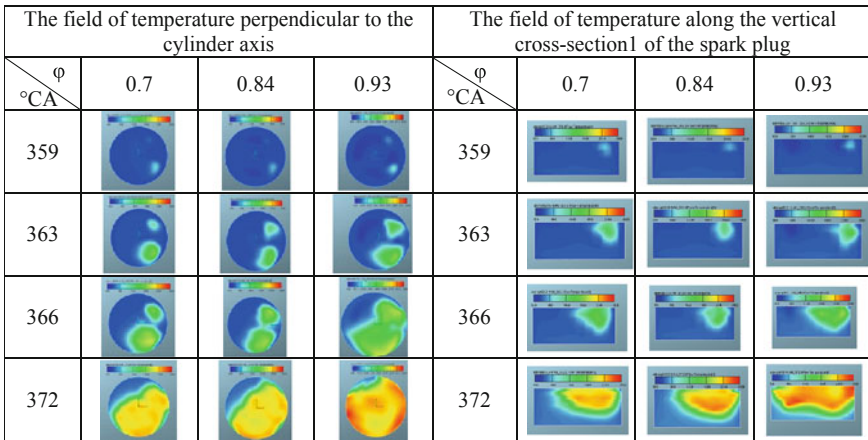


Fig. 10 The effect of equivalent ratio on the field of temperature

similar to the flame propagation characteristic, the greater concentration gradient of mixture led to the faster rate of combustion, the distribution characteristic of vertical gradient of temperature was related to the distribution of the concentration of mixture, but the highest temperature appeared in the zone of appropriate

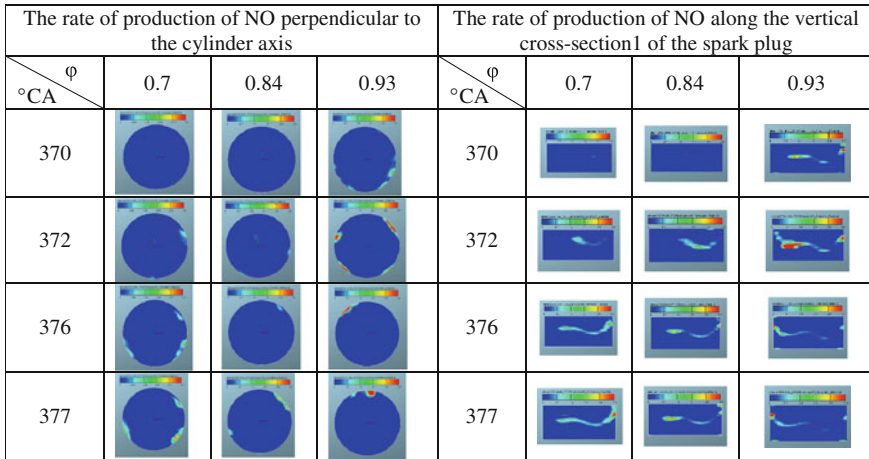


Fig. 11 The effect of different equivalent to on the rate of production of NO

concentration of mixture. It was shown that the effect of different equivalent ratio on the rate of NO production in Fig. 11. The dependence of the field of concentration and the field of temperature can be seen with the combination of the characteristic of the distribution of mixture. The highest rate of NO production was not appeared in the zone of high temperature, but in the zone of right temperature and concentration. When there were more quality of jet, $\phi = 0.93$, the concentration gradient of mixture was larger in cylinder, the rate of combustion was faster, the rate of initial heat release was higher, therefore the moment of the generation of NO would be early, the generation of NO would be relatively delayed with mixture becoming thin and uniform, and the rate of generation of NO would reduce. It was indicated that the rate of production of NO was closely related to the distribution of the field of temperature and the field of concentration.

4.2 The Effect of Injection Timing on Combustion Process

In order to analyze the influence of different injection times to combustion process, chose the average equivalent ratio with $\phi = 0.7$, two injector spraying at the same time, ignition timing with $(-4,-3)^\circ$ CA. The Figs. 12 and 13 show that, when injection timing was chosen before TDC 90° CA, the duration from injection end to ignition timing (Δt) is much shorter, the formation time of mixture is much shorter, So the concentration gradient of mixture is larger in the cylinder, the of flame propagation is accelerated. Therefore, as the Figs. 14 and 15 show that, not only improves the early heat release rate and its peak, shorten the duration of combustion, but also improves the highest cylinder pressure and the increase rate of pressure obviously, meanwhile the cyclic variation σ has been obviously

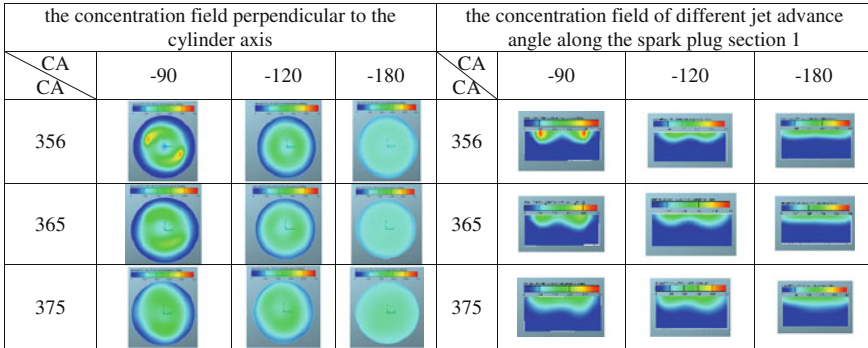
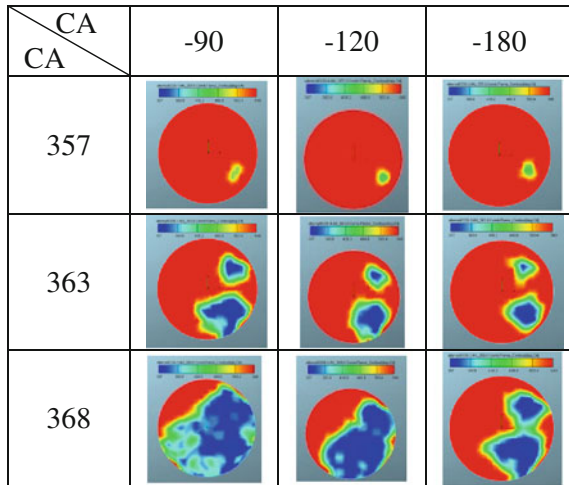


Fig. 12 The effect of different injection timing on the concentration field

Fig. 13 the case of flame propagation perpendicular on the plane of the Z axis for different jet timing



decreased. It improves the stability of lean combustion, however, the emission of NO_x increases.

Figures 16 and 17 showed the effect of different injection timing on temperature field and the production rate of NO_x. Combined with the concentration distribution showed in Fig. 12, shows that, the injection timing comes later, the concentration gradient of the mixture will be larger, it also displays in the flame propagation and the distribution of temperature field. It also suggests that, the production zone of NO_x exists not only at high temperature zone, also at appropriate concentration gradients and low temperature zone. It follows that, for the process of lean burn bases on the stratification of the concentration, the concentration of mixture in the cylinder effects on formation of NO_x directly, especially prompt NO.

Fig. 14 The effect of injection timing on combustion pressure and the law of heat release

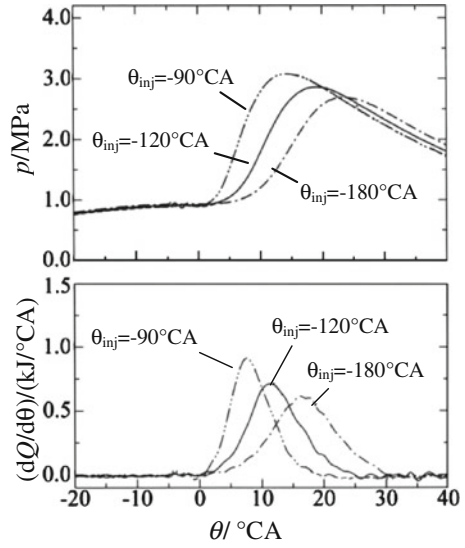
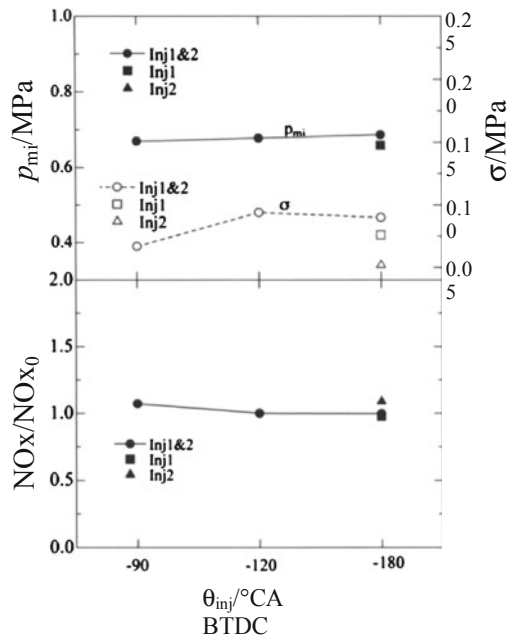


Fig. 15 The effect of injection method on performance



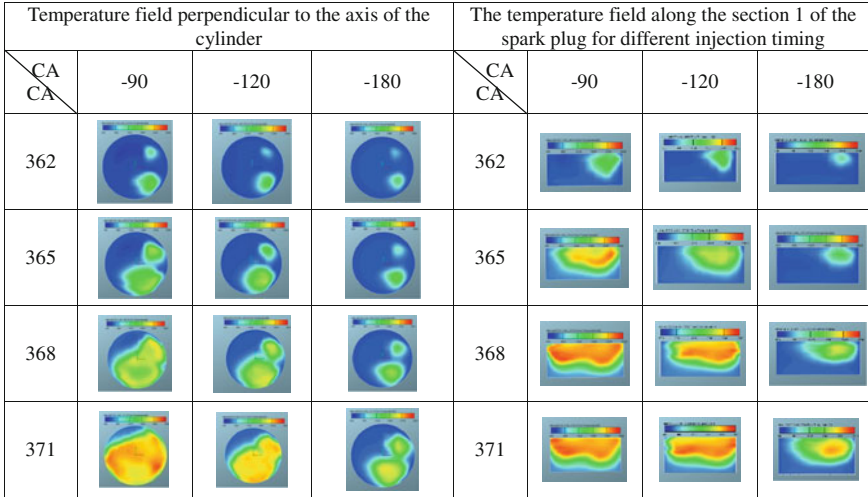


Fig. 16 The effect of different injection timing on temperature field

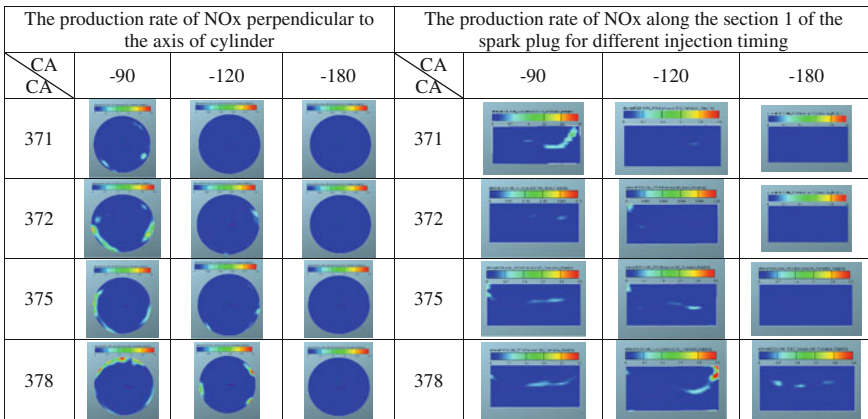


Fig. 17 The effect of different inject timing on the production rate of NOx

5 Conclusion

- (1) In the two-point ignition mode, there were obvious interactions between the two flame, due to the inner flow motion, and if the concentration distribution near the flame was more inhomogeneous, the interaction was more evidently, which could accelerate the flame propagation speed and make the combustion process more stable.
- (2) Based on the mixture concentration inhomogeneous distribution of the DI lean burn CNG engine, the NOx formation mechanism not only depend on

Zeldovich high temperature oxygen-rich conditions, but also have a direct relationship with the mixture concentration distribution characteristics.

- (3) In the lean combustion process, under certain range of thin mixture, the larger gradient of the mixture concentration would make Cyclic variations smaller, combustion more stable, but increase in NO_x emissions. The result showed that the formation of NO_x also have a direct relationship with the mixture concentration gradient distribution.

References

1. 木戸口善行等、噴射制御による直接噴射式天然ガス内燃機関の希薄燃焼に関する研究。自動車技術会論文集。July 2010 41(4):859-864
2. Hu C-M, Hou S-z (2010) Influence factors of combustion characteristics of a low pressure direct injection CNG engine. JCombust Sci Technol[C] 16(5):446-451
3. Iyer RC (2008) Investigations on the influence of ignition voltage, higher compression ratio and piston crown geometry on the performance of compressed natural gas engines[C]. SAE Paper 2008-01-1762
4. Zhang H, Shen G (2007) CFD simulative calculation of the combustion process for a CNG engine. Small Intern Combust Engine Motorcycle[C] 36 (5):9-11
5. 林学東等. 天然ガス筒内噴射時の燃焼過程の可視化観察と性能評価. 日本自動車技術会 (1999) 年秋季大会学術講演会前刷集. 72-99(9939794):9-12
6. Lin X, Huang Y, Yuan F (2011) Effect of the injection method in GDI CNG engine on the flame propagation process and engine performance[C]. Automot Eng

Analysis of the Wear Behavior of Combustion Engine Components Using Radionuclide-Technique

Tamás Gergye, Mathias Roman Dreyer, Bernhard Kehrwald
and Wolfgang Optatzy

Abstract The aim of this study is the analysis of wear behaviour of a timing chain in real engine operation in terms of the influence of variable operating parameters. Further experiments were carried out with used motor oil. During the wear measurements could be seen, that the variation of the oil temperature showed a minor effect on the wear behaviour. However the use of aged oil showed a significant change of the wear behaviour. This means, that in the design of chain drive systems and oil change intervals this correlation has to be considered for maintaining the targeted engine life. Fundamental experiments on a tribometer using different types of carbon black oil will help to describe this phenomena more accurately.

Keywords Radionuclide-technique (RNT) · Friction · Wear · Timing chain · Break-in

1 Introduction

The ever increasing demands on internal combustion engines are characterized by decisive environmental protection, sustainability and emissions requirements call for a permanent development in the area of powertrains. The reduction of power

F2012-A01-030

T. Gergye (✉) · M. R. Dreyer
Széchenyi István University, Gyor, Hungary
e-mail: extern.tamas.gergye@audi.hu

B. Kehrwald · W. Optatzy
IAVF Antriebstechnik GmbH, Karlsruhe, Germany

dissipation in the powertrain against the background of continued scarcity of resources and the increase of anthropogenic CO₂ emission is just in the foreground as the wear behavior of tribological stressed systems that ultimately determine the lifespan of a product.

In a combustion engine, there is a plurality of tribologically stressed systems. The timing chain which represents the connection of the crankshaft to the valve drive is one of them. It consists of a plurality of pins and plates during the operation of a tribological stress, and thus also subject to wear. In this paper, the wear behavior of the tribological system latch and pin in a timing chain by means of an internal combustion engine, using the RNT method, was examined and evaluated. In particular, the online wear behavior in different operating points and the influence of varying parameters and their effect has been studied in detail as far as possible.

2 Analysis of the Tribological Systems

The energy, which is introduced during friction processes in the surface can be divided into three parts.

For the extraction of the wear particles from the surface, which are loaded by friction, a part (E_W) of the complete friction energy (E_R) is required. This energy corresponds to the bonding energy of the wear particles [1].

The second part is used for the tribomutation of the material. [1] The tribomutation is the change of the near surface layers by friction energy. This change can create a new element composition, changes in chemical bonding or structural changes. During the final machining of the surface of the component can be prepared for the operation by the variation of the final machining parameters.

The third part goes into heat. [1]

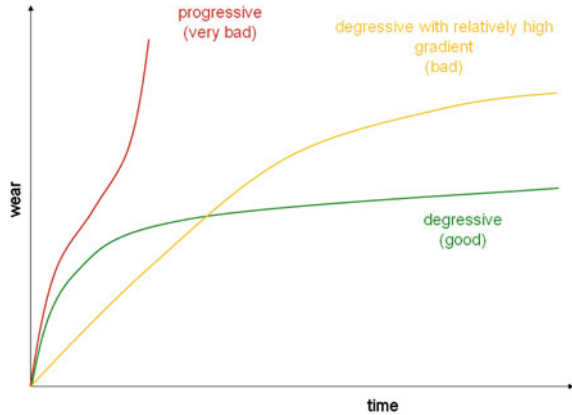
$$E_R = E_Q + E_{TM} + E_W \quad (1)$$

E_R	friction energy
E_Q	thermal energy
E_{Tm}	energy for the tribomutation
E_W	bonding energy of the wear particles

In an optimized tribosystem the wear rate of the wear processes appear in the range of nm/h scale. The wear is a property of a system, which cannot be described with a single parameter. The relationship of the individual parameters can be shown by: [2]

$$P = P(b, p, u, \tau) \quad (2)$$

Fig. 1 Characteristics of the different wear curve [4]



- P properties of the tribological systems: friction, wear, stability, sensitivity
- b operating parameters: speed, load, temperature
- p parameter: macro- and microgeometry, material, heat treatment, final machining, lubrication, lubricant
- u environment: dust, humidity, salt content in the air
- τ lifetime, the age of the wear incl. engine shutdown

Due to these large numbers of parameters, which also can influence each other, it is not possible to predict the wear behavior of tribological systems. If something changes in the system, the wear behavior of the tribological system will be changed too. Changing only the material combinations is today no more sufficient to represent a sufficiently robust tribological system.

In order to the investigations can be compared with each other under uniform boundary conditions, it is necessary to make base investigations on tribometer with the combination of the continuous wear measurement. The continuous wear measurement will be showed in more details in the next chapters.

Beside the variation of material, lubricant and temperature in the engine life is a very important period the running-in. The first few minutes to hours of the engine operation have a significant influence on the subsequent friction and wear behavior of the tribological system. The influence of different running-in procedures on the subsequent wear behavior of the components was investigated by Kehrwald [3]. He noted, that a rough running-in associated with a high application of energy has a favourable influence on the friction and wear behavior [3].

That means in details: the running-in shows, that the load for the tribomutation is enough and the surface of the components are conditioned during the running-in by tribomutation. If this energy is not enough, the wear can run with a non-degressive or at least with a slightly progressive (with relatively high gradient) curve (see Fig. 1).

A good running-in can be characterized with an initial high wear rate, which rapidly decreases after the start and afterward the wear rate runs nearly constant forward. The wear curve can be described with the following function [5].

$$w = c + \underbrace{\frac{\delta w_e}{\delta t} t}_{\text{wear rate}} + \underbrace{a_1 \left(1 - e^{-\frac{t}{b_1}}\right)}_{\text{rough running-in}} + \underbrace{a_2 \left(1 - e^{-\frac{t}{b_2}}\right)}_{\text{fine running-in}} \quad (3)$$

a1; a2; b1; b2 parameters
 w_e running-in wear
 c constant
 w wear

In a high application of energy the wear curve can change over to the direction of progressive behavior, which may result the damage of the components.

Because the wear mechanisms happen in the nanometer scale and in a relatively short time, it is necessary to analyse these phenomena with a suitable measuring method. The online wear measurement using the radionuclide-technique is a measurement method, which accomplishes the here described requirements.

3 Wear Analyse Using the Radionuclide-Technique

The online wear measurement using the radionuclide-technique has the advantage, that the wear can be determined immediately, also online in contrast to the discontinuous measurement methods like profilometry or optical measurement. The wear behavior of the tribological system can be assigned to the influence of engine operating points, parameter variations, environmental influence and the effects of the previous operating points. That means, the engine must not be disassembled with expensive time-consumption. There are two different measuring methods, the so called thin-layer difference method and the filter concentration method (see Fig. 2). In details only the filter concentration method will be shown.

For this measurement the corresponding components were labeled weak radioactivity and these were mounted in the engine. The changes of mechanical and chemical properties of the material due to the activation are negligible. During the operation of the engine the wear particles are produced, which get in the engine oil. From the oil sump a small flow volume is removed and pumped through the flow sensor measuring head. In this measuring head the radioactivity of the wear particles is measured with a NaJ scintillator. The original filter of the engine is replaced with an adapter. Due to this adapter the radioactivity of the wear particles can be measured in the filter with a NaJ scintillator. The wear is proportional to the increase of the emitted radiation and corresponds to the increase of the wear particles in the engine oil and in the filter. The time derivate of the wear (wear rate) is a very important quantity for engine developers.

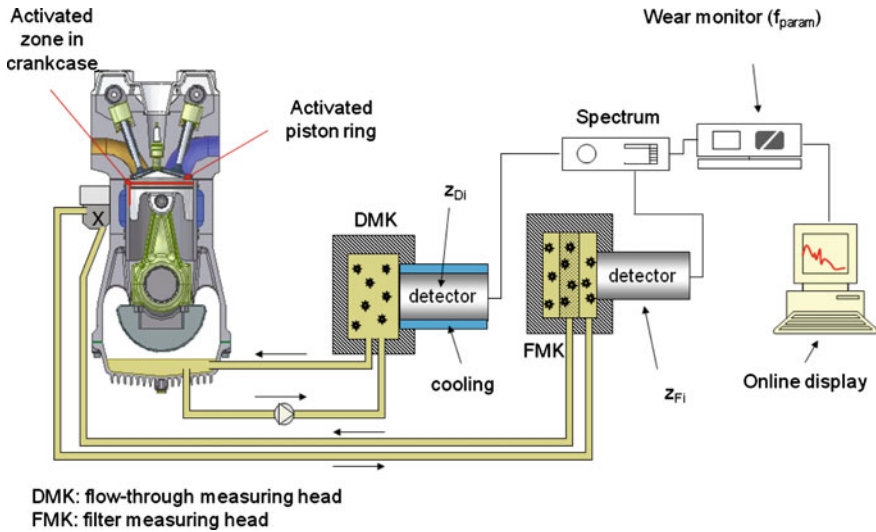


Fig. 2 Filter concentration method [4]

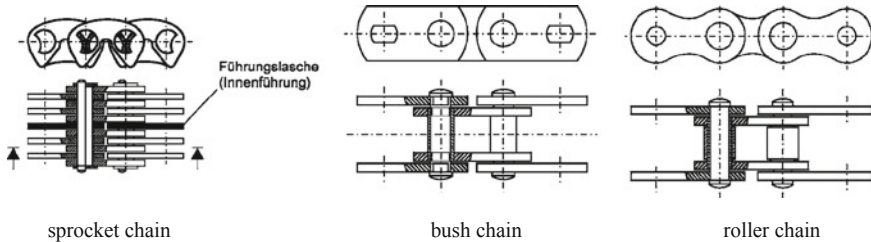


Fig. 3 Different chain types [6]

4 Setting Up the Investigation to Determine the Wear of the Timing Chain Using Radionuclide-Technique

In a timing chain the significant proportion of friction and wear produce in the tribological contact between chain pins and chain plates. Further portions are caused by the penetrate of the chain into gear teeth of the sprocket and between the chain and guide elements. Various chain types are shown in Fig. 3.

In order to measure wear in the components of a timing chain (lash and pin) with radionuclide technique the contact surfaces of the chain lash and chain pin must be activated with radiation.

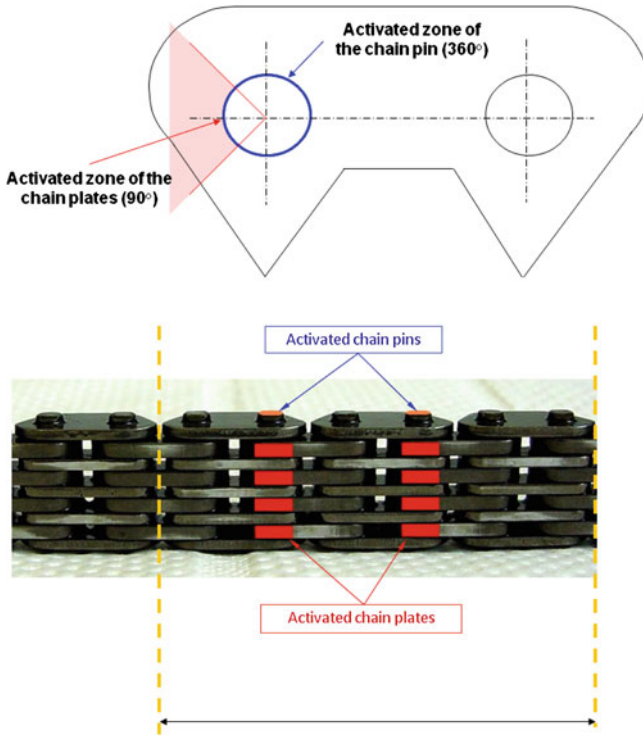


Fig. 4 Activation of the timing chain *top*: activated zone of chain pins and chain plates; *down*: place of the activated components [4]

The timing chain of an internal combustion engine works in the oil chamber of an engine and runs in oil, therefore the filter concentration measuring method was used in these tests.

The experiments examined the wear in the tribological system of chain lash and pin. The summed wear, that each chain component experiences results in the elongation of the chain.

For the actual tests two pins and eight lashes were radio-activated. The cylindrical surface of the pins was 360° around activated while the surface of the lashes had only 90° of activation where the pin would exert pressure on the lash. The surface of the pins had an about 10 μm thick wear resistant vanadium layer. This vanadium in the surface layer was transformed to Cr-51 nuclide. The chain lashes were made of steel that was transformed on the surface to Co-56 nuclide. Figure 4 shows the activated areas of the chain components.

Fig. 5 Wear map of the chain pins—75 h with 90 °C oil temperature [4]

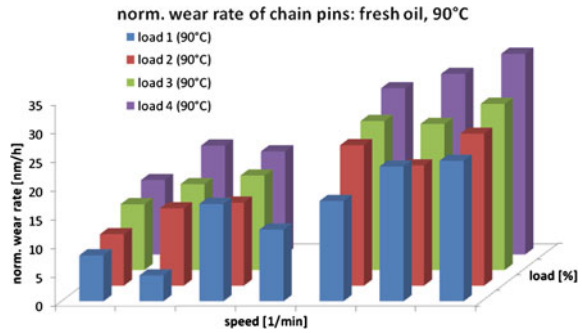
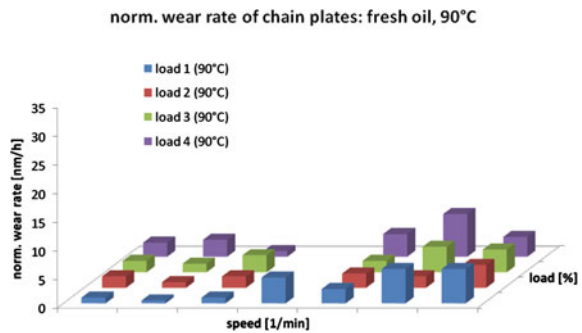


Fig. 6 Wear map of the chain plates—75 h with 90 °C oil temperature [4]



5 Interpretation of the Results

5.1 Wear Maps

After the components were activated the engine was assembled with the activated chain. Then the engine was exercised on the engine dynamometer of the Department of Internal Combustion Engines at the Széchenyi István University where the test cell is equipped with a radionuclide measuring technique equipment. After a running-in process, the engine was exercised through the whole engine speed-torque map with varying oil quality.

The first experiments used fresh (unused) oil that was conditioned to 90 °C. The results showed an obvious tendency: the wear rate increased with increasing the engine speeds as Fig. 5 indicates. The wear rate was almost doubled at the higher engine speed regions and the effect of load was also similar.

The results showed a clear tendency of wear rate that seemed to be proportional to engine speed and load as Fig. 6 shows.

After the complete test at 90 °C, five operating points of the engine were selected and wear rates were measured at these operating points with the oil temperature conditioned to 120 °C. Figures 7 and 8 show the results. The higher

Fig. 7 Wear map of the chain pins—15 h with 120 °C oil temperature [7]

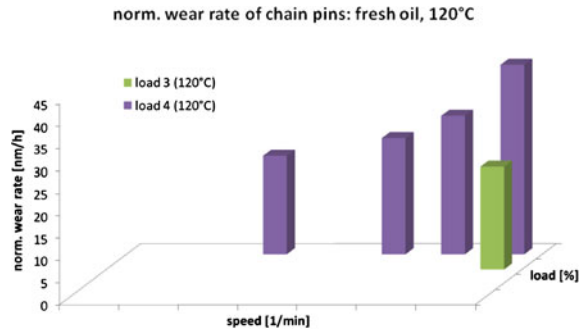


Fig. 8 Wear map of the chain plates—75 h with 120 °C oil temperature [7]

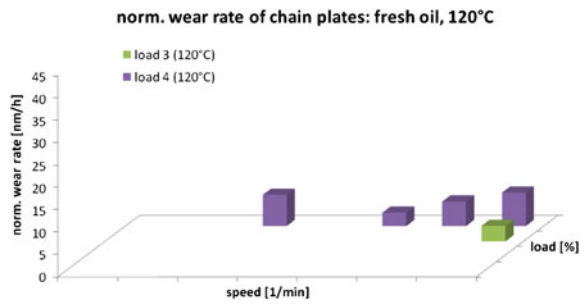
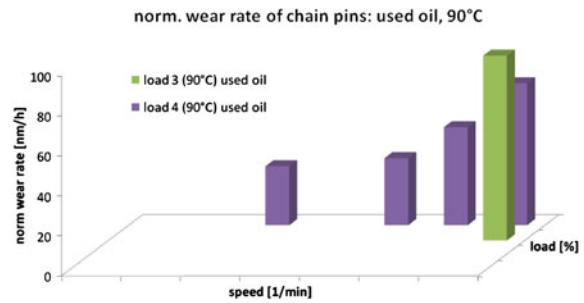


Fig. 9 Wear map of the chain pins—15 h with 120 °C oil temperature and used oil [7]



temperatures had no obvious effect on the wear of pins or lashes as it can be seen in Figs. 7 and 8.

At this point the oil was changed to used oil (15,000 km) and the wear rate was measured in the selected five operating points while engine was exercised again on the dynamometer. The used oil on the other hand had a remarkable increasing effect on wear rate. The wear rate of the pins at 90 °C of used oil is about two times of that of fresh oil while the wear rate of the lashes at the same test was ten times higher with used oil as it was with fresh oil (Figs. 9 and 10).

Fig. 10 Wear map of the chain plates—15 h with 120 °C oil temperature and used oil [7]

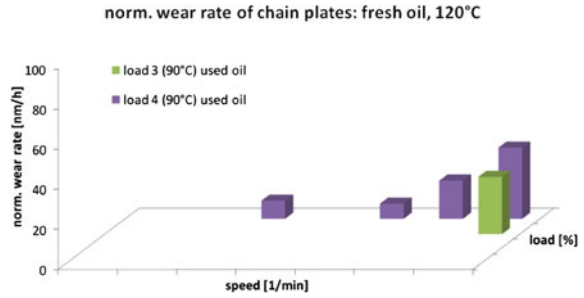
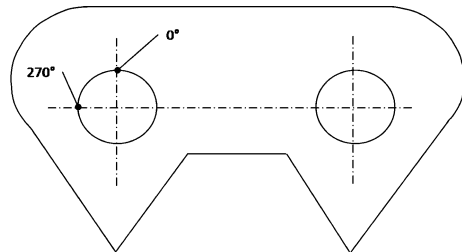


Fig. 11 Measuring point on chain pins and chain plates [7]



5.2 Consideration of the Local Distribution of the Wear

Note must be taken that RNT experiments measure the total wear of all the components. In order to analyze wear in the local point of the components, the components must go through a measuring process before and after the test where the critical areas of the components would be measured than measured values before and after the experiments would be compared. This before and after measurements of the activated components were performed on a profile measuring machine. The profiles of the pins and lashes were measured at 0° and 270° as shown in Fig. 11.

Evaluation of the pin surfaces was not possible because the orientation could not be identified after the tests since the pins have rotated.

However, an after measurement was performed on the chain pins and chain plates and Fig. 12 shows the results. As Fig. 12 indicates that the main shape of the surface profile did not change only the surfaces were polished.

6 Conclusions

The present article gives an overview of the radionuclide measuring technique (RNT) used at the Széchenyi István University. RNT makes online wear measurement in an engine possible; it was applied to measure wear in the timing

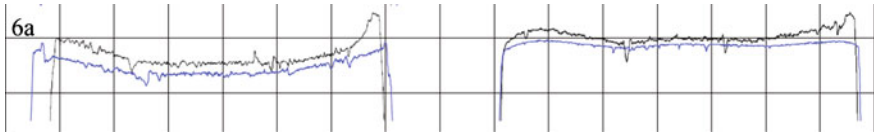


Fig. 12 Comparison of the surfaces of chain pins before and after the measuring [7]

Fig. 13 Comparison of the results of chain pins [4]

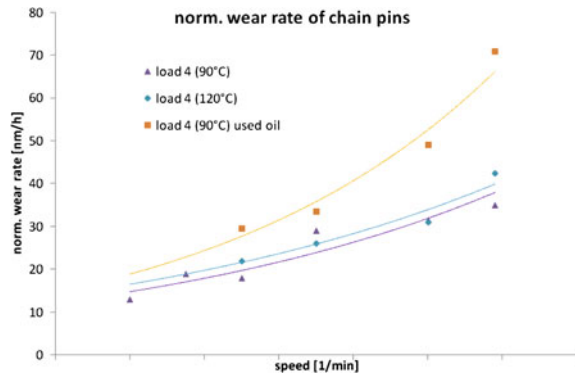
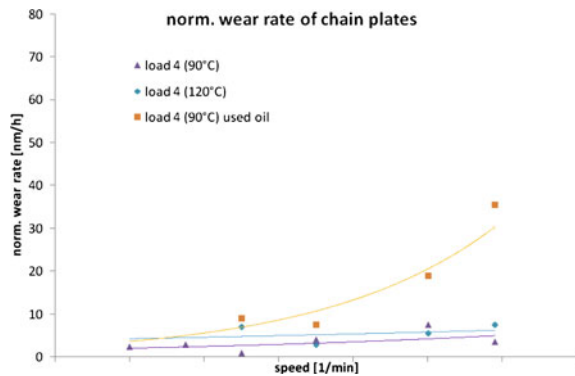


Fig. 14 Comparison of the results of chain plates [4]



chain of a 4-cylinder engine. In this experiment the components (chain pins and chain plates) were activated with thin layer activation and the radioactivity of the removed particles in the oil was measured. The paper presents the wear results of the components after the running-in process. The results have shown that oil temperature has a minor effect on chain wear. A test was also performed with used oil and the test with used oil has shown a significant wear rate increase (Figs. 13 and 14).

References

1. Kehrwald B, Gervé A (1995) Verschleißanalyse von Gleitlagern in Verbrennungsmotoren, GfT-Fachtagung, Göttingen, 27–28. November 1995. Moers, Germany
2. Gervé A (1992) Improved tribological properties by ion implantation, third international conference on plasma surface engineering, Garmisch-Partenkirchen
3. Kehrwald B (1998) Untersuchung der Vorgänge in tribologischen Systemen während des Einlaufs, Dissertation an der Fakultät für Maschinenbau der Universität Karlsruhe
4. Dreyer MR, Gergye T (2012) Tribologische Untersuchung einer Steuerkette.,2. Győrer Tribologie Tagung, Győr, 4–5. Juni 2012. Universitas-Győr Nonprofit Kft, pp 173–186. ISBN 978-963-9819-89-4
5. Scherge M, Gervé A, Berlet P, Kopnarski M, Oechsner H, Scheib M (2001) Tribomutation von Werkstoffoberflächen im Motorenbau am Beispiel des Zylinderzwickels II, Vorhaben Nr. 716, 31.10.2001
6. Steinhilper W, Sauer B (2008) Konstruktionselemente des Maschinenbaus 2 (Grundlagen von Maschinenelementen für Antriebsaufgaben), 6. Auflage. Springer Verlag, p 718
7. Dreyer MR, Gergye T (2012) Tribológiai vizsgálatok belső égésű motorokon—online kopásmérés radionukleációs technika segítségével egy vezérműlánc példáján, A Jövő Járműve, Győr, 2012 In Proceeding

A Super Clean Diesel Vehicle for US LEV-III SULEV Category: Second Report; Advanced A/F Control for NO_x Reduction and for SCR Heat Up

Jean Balland, Bart Schreurs, Michel Peters, Michael Parmentier, Julien Schmitt, Hans Hardam, Masatoshi Yamada, Hiroshi Uike, Toshiharu Takahashi, Yuji Yasui, Eiji Hashimoto, Hideki Matsunaga and Naohiro Sato

Abstract The objective for this research is to develop LEV_{III} SULEV technology for midsize passenger cars with SCR equipped diesel engines. The key for SULEV is to lower NO_x over the whole emission cycle. From the engine control standpoint, this paper describes a unique NO_x reduction technology with three-way conversion reaction until the SCR is heated up. Operating the engine at stoichiometric A/F allows a high conversion efficiency of both NO_x and HC using a DOC. Furthermore, it allows rapid heat up of the SCR due to exothermal effect and reduced mass flow. The control system regulates the airflow in order to achieve stoichiometric A/F by controlling EGR flow as first priority. The amount of fuel is determined by the advanced torque control modelled by combustion efficiency so that the A/F can be controlled to stoichiometry maintaining driver requested torque. In combination with the unique SCR system, the FTP75 and US06 emissions test results for NO_x + NMHC are below the proposed LEV_{III} SULEV regulation by a reasonable margin [1]. Stoichiometric mode is activated to control the NO_x before the SCR is activated and when SCR efficiency is dropping at high exhaust flow; Stoichiometric mode supplement for lack of efficiency of SCR to achieve the LEV_{III} targets. Fuel consumption penalty is minimized by a unique stoichiometric A/F control concept where AF target is achieved mostly with EGR control. The base structured engine control has advanced model-based functions

F2012-A01-031

J. Balland (✉) · B. Schreurs · M. Peters · M. Parmentier · J. Schmitt
Delphi Automotive PLC, Troy, MI, US
e-mail: masatoshi.yamada@delphi.com

H. Hardam · M. Yamada · H. Uike · T. Takahashi
Delphi Automotive Systems Japan, Ltd, Tokyo, Japan

Y. Yasui · E. Hashimoto · H. Matsunaga · N. Sato
Honda R&D Co., Ltd Automobile R&D Center, Tokyo, Japan

such as air management with simultaneous control of VGT/EGR/throttle, torque structure, temperature and pressure estimator and precise A/F control, which are the main enablers to realize stoichiometric control.

Keywords Diesel • Emission • SCR • Air–fuel ratio • EGR

1 Introduction

The increasing number of vehicles has resulted in increasing air pollution. Therefore, a series of stricter emissions standards have been implemented to solve these pollution problems. In parallel, diesel engine system content and complexity has drastically increased in order to achieve both enhanced performance and compliance with strict emissions legislation.

The main challenge for the diesel engine is to maintain its relative advantage of low CO₂ emission in a cost effective and robust manner whilst continuing to meet the emissions requirements.

The current most stringent emissions regulation is US LEV_{III} SULEV. This has been proven to be difficult to achieve with a conventional diesel engine system control. A technology breakthrough for diesel engine system control has been required over additional engine and after-treatment hardware from a cost and reliability standpoint. In order to realize this, new concepts for engine and SCR control have been developed with an innovative approach. A stoichiometric A/F control has been developed as a key emission control before SCR is activated. The SULEV emissions were achieved through the combined use of newly developed engine and SCR control. This paper describes the emission control strategy from the engine control side before SCR is activated and what benefits can be obtained from them.

2 LEV_{III} SULEV Emission Strategy

The overall emission strategy is to introduce higher rate of EGR flow to reduce engine-out NO_x and enable stoichiometric A/F control to reduce NO_x and HC with a three-way conversion reaction in the DOC until SCR is activated. A unique SCR heat up and mode management control contributed to rapid SCR activation. After it is activated, a newly developed SCR control reduces NO_x emission with superior conversion efficiency.

2.1 *Early and High EGR Usage*

Figure 1 shows the first 500 s of FTP 75 with a plot of inert EGR rate which is used as an essential parameter to represent NO_x reduction. Conventional EGR rate is not a suitable parameter in lean combustion since the excess air recirculated with

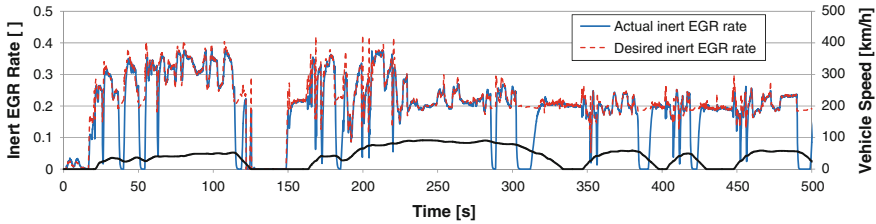


Fig. 1 Inert EGR trace on FTP75 test cycle

the EGR has no impact on NO_x generation process that is strongly related to combustion temperature.

EGR must be ramped up quickly and kept at 30–35 % of the inert EGR rate to reduce NO_x effectively until SCR is activated. This strategy can be realized from dynamic EGR control. When running this level of EGR rate there is no air reserve and the EGR tends to strangle the engine. It is essential to have dynamic EGR control in order to reduce EGR when fresh air is required to produce driver torque demand. Thus, the EGR trace is more dynamic as a result of meeting the torque demand in transient conditions. After SCR is activated at around 230 s and higher engine-out NO_x can be tolerated, the EGR is set to 20 % for better fuel economy.

The dynamic EGR model calculates the inert gas concentration of the EGR flow and the delay time to transfer from the exhaust manifold to the intake port. This model allows tracking of the demanded inert EGR and accurate estimation of the actual in-cylinder inert gas concentration. The EGR rate control benefits from the precision of the modelled signals in dynamic operation. It provides an automatic compensation of the combustion phase shift by the main-injection timing adjustment based on the modelled inert EGR rate (Fig. 2).

2.2 *Smoke Limit Control*

Arbitration between NO_x and smoke is required mostly in acceleration when the turbo is lagging and boost is insufficient. This is done by the smoke limit control with EGR flow limitation.

The software is constantly calculating the maximum EGR rate if the engine were to run at the smoke-limit A/F with the current boost pressure. Based on the amount of fuel entering the engine to deliver the torque, the minimum amount of fresh air necessary to run the engine at the smoke-limit A/F can be calculated. The difference between the actual airflow and this minimum airflow corresponds to the possible extra EGR flow to run at smoke-limit A/F.

During transient conditions like accelerations or shift maneuvers, where the actual boost pressure is different from the steady state boost pressure (and thus the amount of available fresh air), the EGR rate will be automatically limited such that the A/F will not go below the smoke-limit A/F while delivering the driver torque demand.

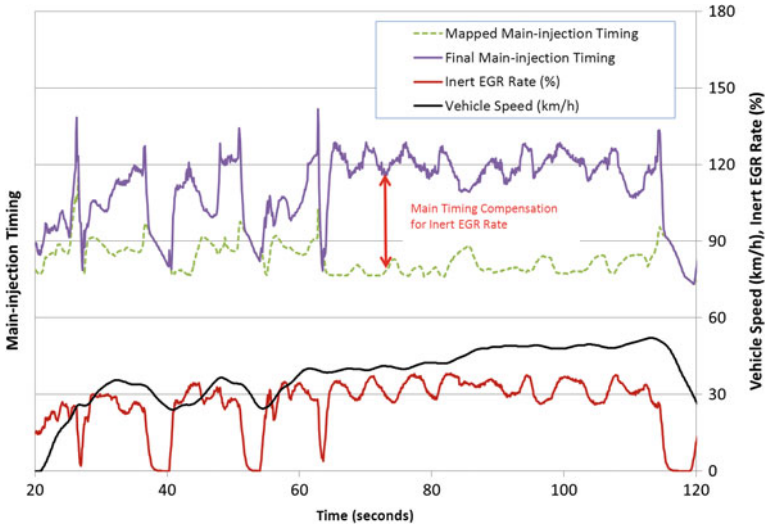


Fig. 2 Main-injection timing compensation based on inert EGR

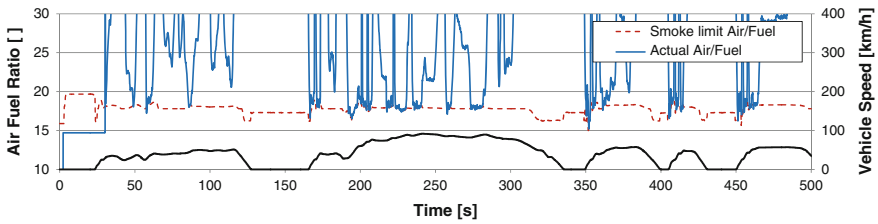


Fig. 3 A/F trace on FTP75 (lean operation)

The A/F trace in Fig. 3 shows that A/F is very closely controlled around the smoke limit target when reaching the limit in acceleration.

2.3 Stoichiometric Combustion Mode

Figure 4 shows the concept for the stoichiometric control, i.e. decreasing the smoke limit A/F to stoichiometry when it is required. The stoichiometric control is detailed in the next section.

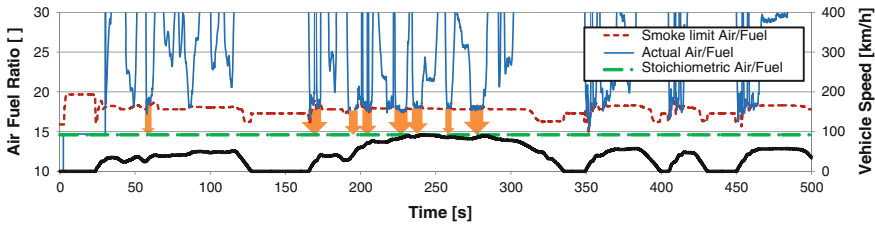


Fig. 4 Stoichiometric mode concept based on smoke limit control

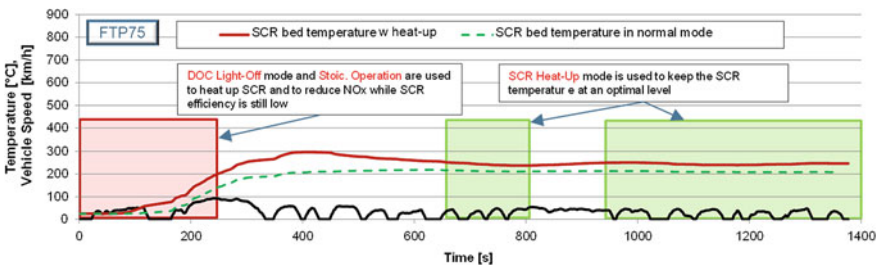


Fig. 5 SCR bed temperature trace on FTP75

2.4 SCR Heat-Up and Temperature Management

SCR has a target temperature of around 250°C for highest NO_x conversion. The algorithm described below allows achieving the target temperature earlier and to maintain the temperature throughout the cycle, as can be seen from Fig. 5.

Thermal management can be achieved by switching discrete operating modes from normal mode to heating mode in an optimum manner. The SCR is located behind the DOC and DPF which have high thermal inertia and are acting as thermal buffer for the heat going to the SCR. Thus it has been difficult to realize appropriate mode switching based on measured temperature due to the slow reaction caused by these large thermal inertias. In order to optimize temperature management, a temperature prediction model taking into account such thermal inertias has been developed.

Depending on the thermal state of each component in the line, the future SCR temperature may increase too much (overshoot, excessive fuel consumption and/or NH₃ slip) or be insufficient (undershoot, insufficient NO_x conversion).

By using the measured temperature and an estimation of the long term temperature of each component, the algorithm gives, in real time, a prediction of the future minimum and maximum temperature of each component. It has embedded a thermal model of the components consisting of both first order lag filter modelling the inertia of each catalyst and temperature loss models for pipes.

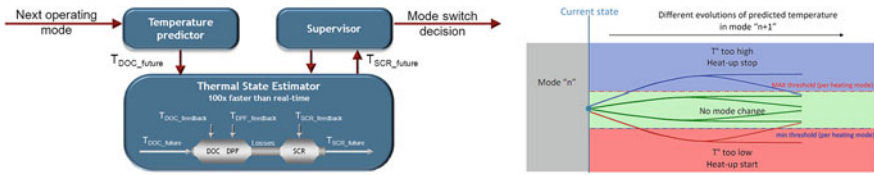


Fig. 6 Thermal state estimator diagram

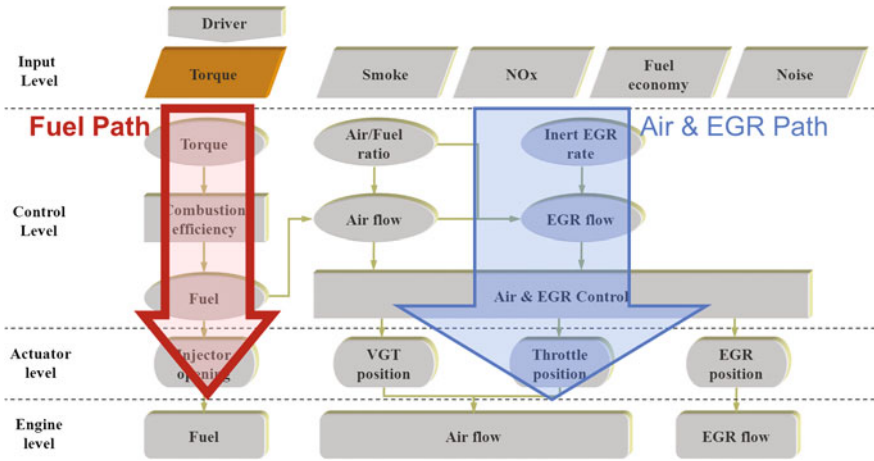


Fig. 7 Conventional fuel and air/EGR structure (fuel-lead mode)

The models run typically 100 times faster than real time, e.g., every 2 s, a simulated temperature prediction of 200 s into the future is performed.

The decision to switch mode is based on the predicted temperature of the next mode. Figure 6 shows the diagram how to decide the mode switching.

3 Engine Control Features for Stoichiometric Operation

3.1 Fuel-Lead Structure

Conventional diesel control is structured around two parallel and quite independent control paths shown in Fig. 7. The driver torque demand has the highest priority and is attained through the fuel path. The air and EGR path is controlled independently with its own dynamics in lower priority [2].

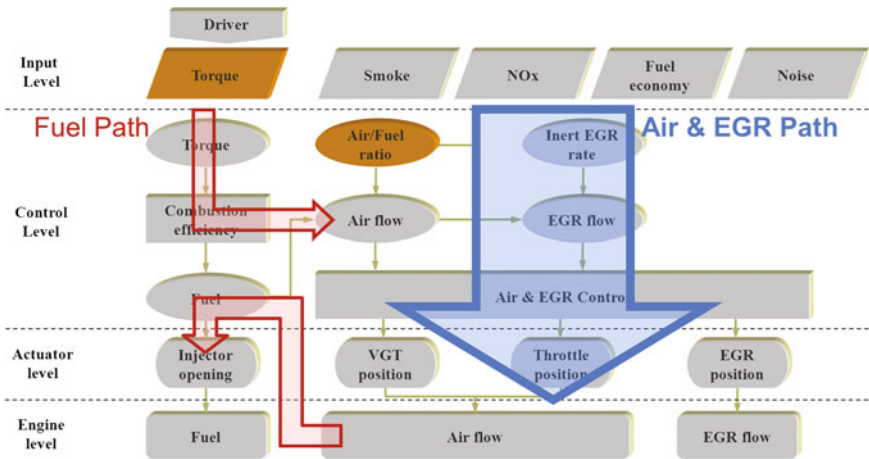


Fig. 8 Fuel and air/EGR structure for stoichiometric mode (air lead mode)

3.2 Air-Lead Structure

In stoichiometric mode, the control structure has to be changed as shown in Fig. 8.

As the target A/F is fixed to stoichiometry, the fuel control has to be synchronized to the air control and can only be as fast as the air dynamics. The fuel path has been changed where the fuel calculation is now linked to the air path and the actual air flow. Accordingly the highest priority has been moved to air and EGR path. So the control structure in stoichiometric operation switches from a fuel-lead mode to an air-lead mode.

3.3 Air-Lead Heat-Up Mode

The purpose of this mode is to operate at stoichiometry in a very wide engine operation range to heat up the SCR by utilizing exothermal reaction and reducing NO_x, HC and CO emissions in the DOC. This mode is started at the beginning of the cycle as soon as the DOC is active (Fig. 9).

3.4 Air-Lead Transient Mode

The purpose of this mode is to operate the stoichiometric mode only at higher engine loads where higher engine-out NO_x is produced. Figure 10 shows stoichiometric mode being used during US06 when SCR conversion efficiency is dropping due to high exhaust gas flow when the vehicle is accelerating.

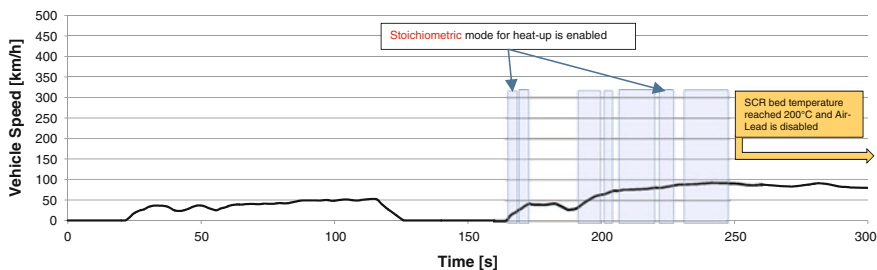


Fig. 9 Air lead heat up mode

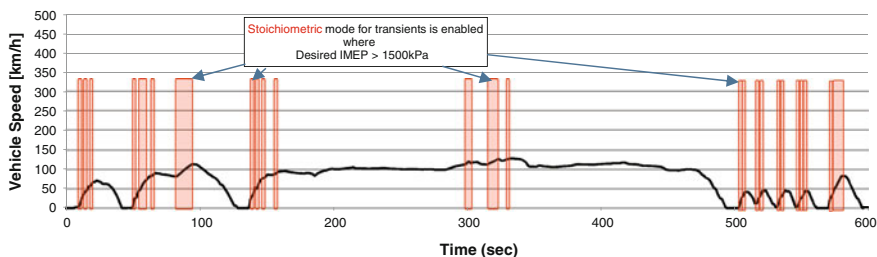


Fig. 10 Air lead transient mode

3.5 Air-Lead Stoichiometric A/F Control

The air-lead mode enables much tighter control of the A/F by regulating the intake air flow by means of EGR rate control (Fig. 11). The EGR rate is calculated so that enough fresh air remains for the engine to produce the driver torque demand at stoichiometry. The fuel injection quantity can then be controlled to achieve target A/F with after-injection quantity trimming as fine adjustment based on the actual intake air flow. The fuel injection can be controlled purely to maintain the target A/F rather than to meet the torque demand.

This tight A/F control is required to obtain high converter efficiencies for NO_x, HC and CO emissions with the use of the three-way conversion effect where the A/F remains as close as possible to stoichiometry.

3.6 Fast Closed Loop A/F Control

In addition to the air-lead A/F control, a fast closed-loop A/F control enables the A/F in a narrow band around stoichiometry (Fig. 12). The A/F control system observer predicts the A/F at lambda sensor location based on the commanded A/F in the cylinders using an A/F transient model. The model accounts for the physical effects of transport delay and dynamics from cylinder to sensor. The estimated A/F

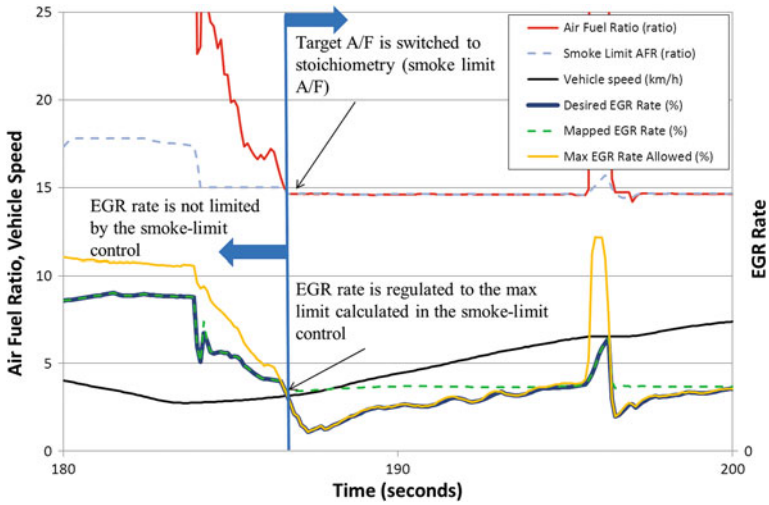


Fig. 11 Control parameters behavior when switched to stoichiometric mode

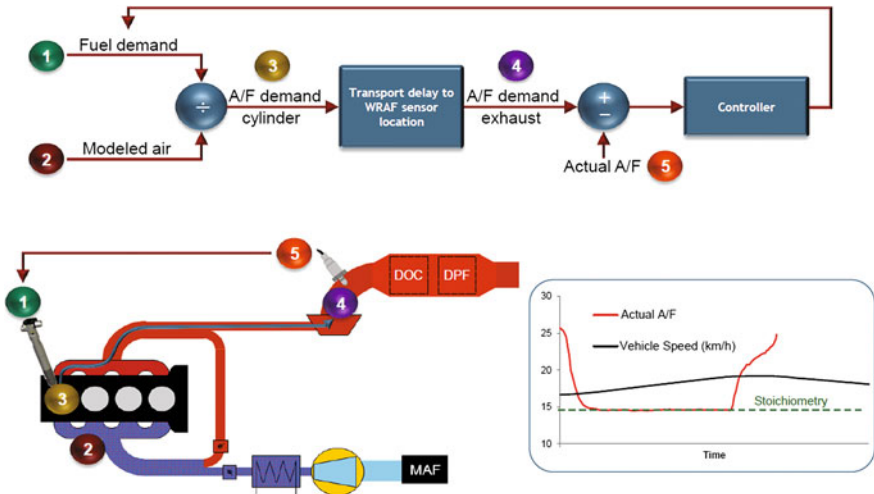


Fig. 12 Closed-loop air fuel control structure

is then compared to the measured A/F from the lambda sensor to produce an estimate of the A/F control error. The A/F controller closes the loop on fuel demand and compensates for fueling errors identified by the observer.

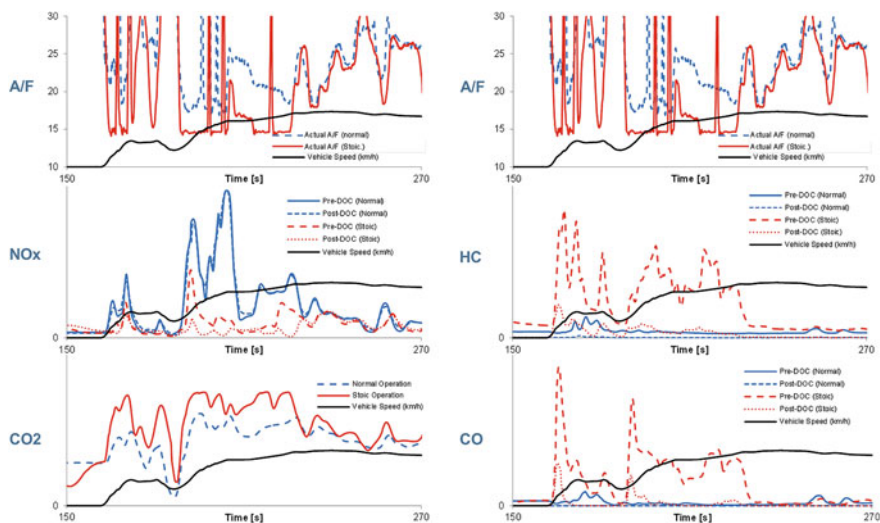


Fig. 13 Emissions and A/F traces on FTP75 2nd hill

4 Stoichiometric Mode Results

Vehicle test results show the effect of stoichiometric control on both FTP75 (Fig. 13) and US06 (Fig. 14) modes. The graphs superimpose two tests, dotted line in normal mode with lean conditions and solid line in stoichiometric mode. For each mode, both engine out and tailpipe emissions are plotted for HC, CO, NOx and CO₂. NOx peaks at typical accelerations can be observed in normal mode. In stoichiometric mode, engine-out NOx is reduced with higher EGR then further reduced by the DOC. Engine-out HC and CO are much higher in stoichiometric mode nevertheless they are efficiently oxidized in the DOC. Stoichiometric combustion causes high CO₂ but it can be minimized by limiting the stoichiometric mode opportunities in the whole emission cycle.

Figure 14 shows the example on the US06 2nd hill. It shows similar behavior as FTP75 mode but the load is higher in acceleration. A/F in normal mode is lower than the previous example so that the high conversion efficiency in the DOC is very clearly observed.

5 Summary

The concept of running a diesel engine in stoichiometric mode has been implemented on a midsize diesel vehicle. Stoichiometric mode can achieve three-way conversion reaction with high conversion efficiencies. The mode is not used continuously as with gasoline engines but rather in acceleration when NOx is high

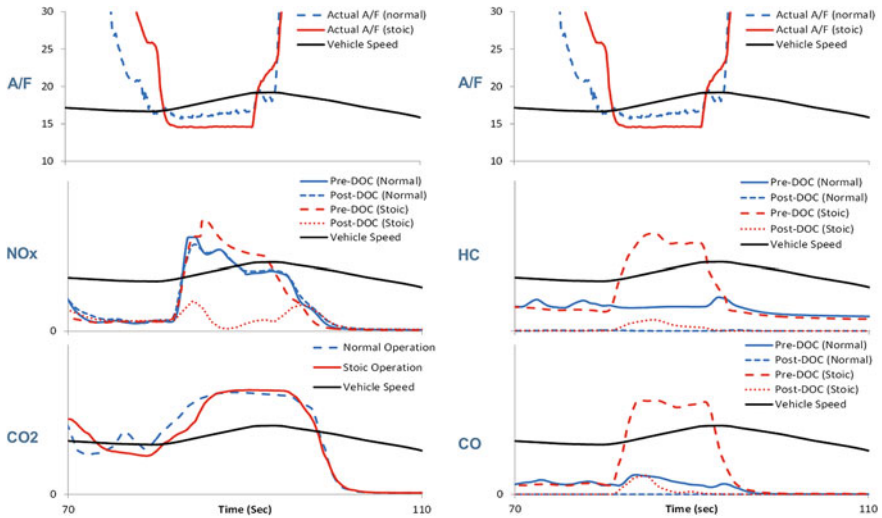


Fig. 14 Emissions and A/F traces on US06 2nd hill

and it is already close to stoichiometry. The NO_x reduction benefits are high and CO₂ penalties can be minimized due to both short activation time and a unique air-lead A/F control. Challenges of controlling stoichiometric operation on a vehicle under real driving conditions have been achieved along with excellent drivability. In the SULEV project, the stoichiometric A/F control contributes to achieving US LEV_{III} SULEV emissions legislation in combination with the unique SCR control.

References

1. Matsunaga H (2012) A super clean diesel technology for US LEV-III SULEV. JSAE, Yokohama 244-20125267
2. Schöppe D, Geurts D, Balland J, Schreurs B, Peters Michel (2009) Delphi diesel structured engine control to achieve most stringent emission legislation. In: 7th symposium powertrain control systems for motor vehicles, Berlin, 18–19 June 2009

Research on Low Temperature Combustion of Homogeneous Charge Induced Ignition (HCII) in a Light-Duty Diesel Engine

Chao Yu, Jianxin Wang, Wenbin Yu, Jichun Liu and Dingwei Gao

Abstract Homogeneous Charge Induced Ignition (HCII) is an innovative combustion mode that has the potential to achieve high-efficiency and low-emission combustion. The effects of cooled Exhaust Gas Recirculation (EGR) and hot EGR on the combustion characteristics, emissions characteristics and thermal efficiency are studied contrastively in a light-duty diesel engine. The results show that as EGR rate increased, NO_x emissions reduced significantly. Cooled EGR resulted in lower NO_x emissions than hot EGR. At low load, Hot EGR can decrease the THC emissions in HCII mode and improve the combustion, with a biggest indicated thermal efficiency increase of 2 %. As EGR rate increased, the NO_x emissions decreased and smoke emissions increased in diesel Compression Ignition (CI) combustion at high load, exhibiting the classical NO-soot trade-off. However, in HCII mode, the NO_x emissions decreased and smoke emissions were maintained at a low level, which demonstrated that low temperature was achieved apparently. EGR is an effective technology to reduce the combustion noise in HCII mode at high load. As EGR ratio increased, the ignition delay increased in general. Comparing to diesel CI combustion, the ignition delay in HCII mode increased more significantly, which was beneficial to the fuel-air mixing. At high load, the combustion duration in HCII mode was shorter than diesel CI combustion, and the combustion was closer to constant volume combustion, which was conducive to improving thermal efficiency.

F2012-A01-033

C. Yu (✉) · J. Wang

State Key Laboratory of Automotive Safety and Energy, Department of Automotive Engineering, Tsinghua University, Beijing, China
e-mail: appleofyt@gmail.com

W. Yu · J. Liu · D. Gao

Great Wall Motor Co., Ltd. Engine R&D Center, Beijing, China

Keywords Homogeneous charge induced ignition (HCII) · Exhaust gas recirculation (EGR) · Combustion · Emissions · Thermal efficiency

1 Introduction

Energy saving and environmental protection have been the focus of technological progress in internal combustion engine. The thermal efficiency of Spark Ignition (SI) engines is lower than that of CI engines due to low compress ratio, high pumping loss, difficult to achieve lean-burn and large cycle variation. The emission problems of CI engines are more difficult to solve due to the trade-off between NO and soot emissions caused by diffusion combustion.

Comparing to the combustion in conventional SI engines, the HCII is capable of lean combustion at higher compression ratios. The auto-ignition of the direct-injected diesel establishes ignition events in the combustion chamber at multiple sites, and thus initiates rapid heat release close to constant volume combustion. In this way, HCII avoids several drawbacks that lower the thermal efficiency of SI engines, and may achieve the high thermal efficiency comparable to diesel engines. Researches by Wang et al. [1, 2] show that the thermal efficiency of HCII is significantly higher than SI combustion and equal or even higher than diesel CI combustion. Alger et al. [3] used HCII as a means of high-energy ignition systems with large amounts of EGR to increase the thermal efficiency.

Meanwhile, soot emissions can be reduced dramatically because the homogeneity of the cylinder charge is significantly enhanced by the port injection of gasoline fuels. Studies by Wang et al. [4] show that the soot emissions of CI engines significantly reduced with the increase of gasoline ratio. The HCII combustion needs to be controlled in low temperature combustion region in order to mitigate NO_x emissions. In fact, the enhanced fuel–air mixing of HCII is a substantial advantage to achieve low temperature combustion. The research by Yu et al. [5] shows that, in HCII mode, there is no apparent trade-off between NO_x and soot emissions when EGR is applied; the low temperature combustion is achieved with a moderate level of EGR application (lower than 40 %). The potential of HCII to achieve low temperature combustion with low NO_x and soot emissions has been reported by Ma et al. [6], by Inagaki et al. [7] and by Reitz et al. [8–10].

However, so far, HCII combustion mode still has problems of high THC emissions and low combustion efficiency at low load [11]. Meanwhile, HCII combustion mode also suffered high pressure rise rate and large combustion noise at high load [12, 13].

Considering more researches are conducted in heavy-duty diesel engines, a light-duty diesel engine is used in this study. The application of HCII technology on light-duty diesel engine is studied in detail. Aiming at the problem of high THC emissions in HCII mode at low load, hot EGR is applied to increase the intake

Table 1 Major parameters of the test engine

Engine type	GW4D20
Displacement	0.5 L
Compression ratio	16.7
Bore	83.1 mm
Stroke	92 mm
Connecting rod length	145.8 mm
Diesel injection system	High-pressure common rail
Diesel injection pressure	40–180 MPa
Gasoline injection system	Low-pressure common rail
Gasoline injection pressure	0.2–0.3 MPa

temperature and improve the combustion. Aiming at the problem of high pressure rise rate at high load, cooled EGR is used to reduce the combustion noise. The effects of cooled EGR and hot EGR on the combustion characteristics, emissions characteristics and thermal efficiency are studied contrastively in a light-duty diesel engine.

2 Equipment and Method

A four-cylinder common rail diesel engine was modified into a single-cylinder research platform to conduct the experiments. The major engine parameters are listed in the Table 1. The intake and exhaust systems, and the diesel and gasoline fuel supply systems were specially designed for the targeted single cylinder. There was no fuel supplied for the other three cylinders of this engine.

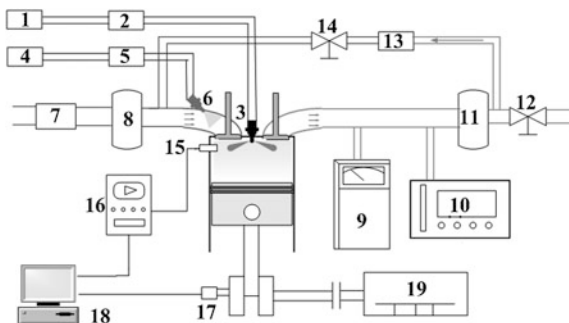
Gasoline is port-injected and controlled electronically, and its injection duration and injection timing can be adjusted flexibly. Diesel used as a pilot fuel is directly injected into the cylinder, and its injection pressure, injection duration, injection timing and number of injection events can also be adjusted flexibly.

Figure 1 illustrates the schematic of the engine test bench. Combustion characteristics were analyzed using an AVL Indicom 621 Combustion Analyzer. Exhaust gas emissions, such as CO, HC and NO_x were analyzed by AVL's CEB-II. Smoke emissions were measured by AVL's 439 opacimeter.

The gasoline ratio is defined as the energy ratio of the gasoline to the total fuel in each cycle. The EGR rate is determined by the ratio of intake CO₂ concentration to the exhaust CO₂ concentration. An exhaust pressure valve and an EGR flow regulating valve are installed to adjust EGR rate. A water-cooled EGR cooler is used to condition the EGR stream when cooled EGR is used. The exhaust gas is not cooled when hot EGR is used. The combustion efficiency is calculated based on the energy in the exhaust emissions [14].

Engine operating condition is listed in Table 2. The engine speed was controlled at 1,600 r/min. The common rail pressure was controlled at 80 MPa. The fuelling rate was controlled at 12.7 mg per cycle at low load and 22.9 mg per cycle

Fig. 1 The schematic layout of the engine test bench



- 1-Diesel tank 2-Diesel consumption meter 3-Diesel injector
- 4-Gasoline tank 5-Gasoline consumption meter 6-Gasoline injector
- 7-intake air flow meter 8-Intake surge tank 9-exhaust smoke meter
- 10-Exhaust analyzer 11-Exhaust surge tank 12-Exhaust pressure valve
- 13-Exhaust cooler 14-EGR flow regulating valve 15-Pressure sensor
- 16-Charge amplifier 17-encoder 18-Combustion analyzer
- 19-Dynamometer

Table 2 Engine operating condition

Engine speed	1,600 r/min			
Common rail pressure	80 MPa			
CA50	10°CA ATDC			
Cycle fueling rate	12.7 mg		22.9 mg	
Gasoline ratio	0	40 %	0	67 %

at high load separately. The gasoline fuelling rate was converted to corresponding diesel mass rate based on their lower heating values. EGR has a big influence on the combustion phasing which is important for the combustion and emissions characteristics. CA50 is defined as the crank angle at which 50 % fuel mass fraction has combusted. To counteract the effects of combustion phasing, CA50 was controlled at 10°CA ATDC by adjusting the diesel injection timing.

3 Results and Discussion

3.1 Effects of EGR on Engine Performance

The intake air temperature has a big influence on the combustion and emissions. The intake air temperature is apparently different when cooled EGR and hot EGR were introduced separately. Figure 2 shows the effects of EGR on intake air temperature. As EGR rate increased, cooled EGR nearly had no effects on intake air temperature. However, hot EGR increased the intake air temperature

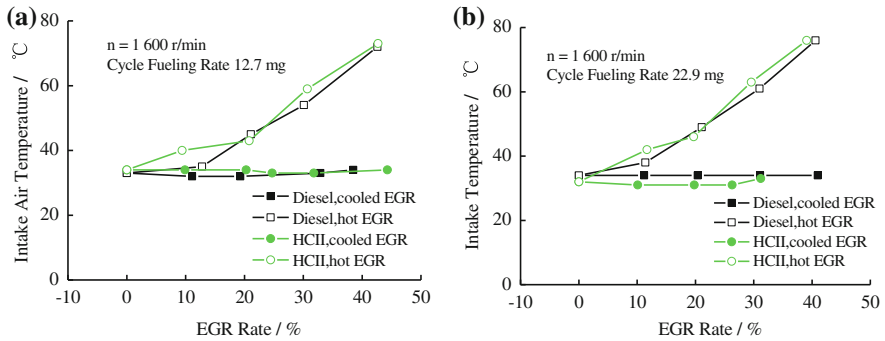


Fig. 2 Effects of EGR on intake air temperature. **a** Low load, **b** High load

significantly. The more EGR rate increased, the more intake air temperature increased. The intake air temperature increased to about 75 °C when EGR rate was 40 %.

Figure 3 shows the effects of EGR on indicated thermal efficiency. As EGR rate increased, the indicated thermal efficiency increased at low load, but decreased at high load. The indicated thermal efficiency was nearly equal to diesel CI combustion. Both cooled EGR and hot EGR can improve the indicated thermal efficiency of HCII mode at low load, with an increase of 2 %. Because intake air boost was not applied in this experiment, the intake air flow was apparently insufficient when large amounts of EGR were applied, which led to the reduction of indicated thermal efficiency at high load.

3.2 Effects of EGR on Emissions Characteristics

Figure 4 shows the effects of EGR on NOx emissions. As EGR rate increased, NOx emissions reduced significantly. Cooled EGR resulted in lower NOx emissions than hot EGR. When EGR rate increased to 40 %, NOx emissions reduced to near zero. The reduction of NOx emissions was due to the reduced combustion temperature when cooled exhaust gas was recycled to cylinder.

Figure 5 shows the effects of EGR on smoke emissions. As EGR rate increased, the smoke emissions in HCII mode maintained at a low level. However, the smoke emissions in diesel CI combustion were kept almost constant at low load, but increased significantly at high load. As EGR rate increased, the NOx emissions decreased and smoke emissions increased in diesel CI combustion, exhibiting the classical NO-soot trade-off. However, as EGR rate increased, the NOx emissions decreased and smoke emissions maintained at a low level, which demonstrated that low temperature was achieved apparently. HCII can achieve low temperature when combined with EGR, with extremely low NOx and smoke emissions.

Figure 6 shows effects of EGR on THC emissions. As EGR rate increased, the THC emissions in HCII mode reduced at low load. Hot EGR resulted in lower

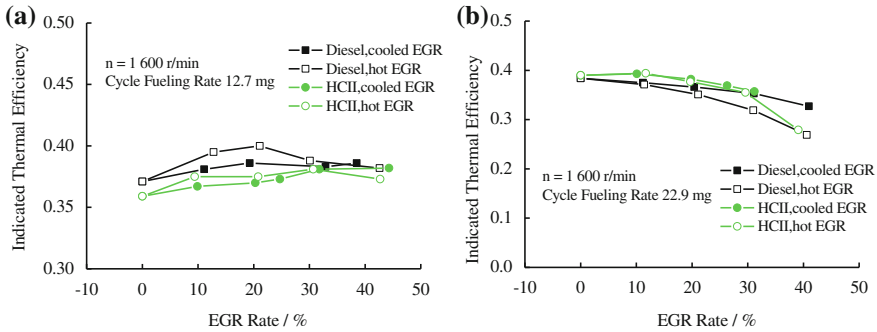


Fig. 3 Effects of EGR on indicated thermal efficiency. **a** Low load, **b** High load

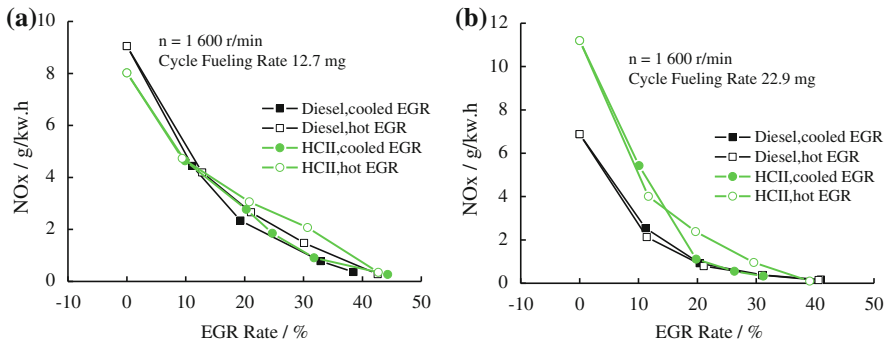


Fig. 4 Effects of EGR on NOx emissions. **a** Low load **b** High load

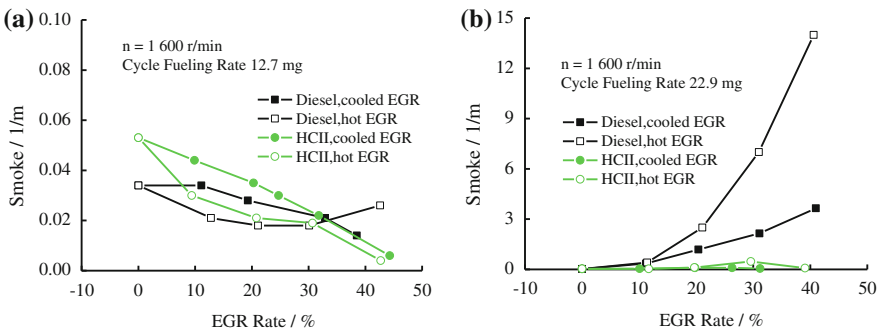


Fig. 5 Effects of EGR on smoke emissions. **a** Low load, **b** High load

THC emissions than cooled EGR, with a biggest reduction of about 54%. The intake air temperature increased, and thus, the in-cylinder temperature increased when hot EGR was applied, which improved the oxidation of unburned THC. As EGR rate increased, the THC emissions in diesel CI combustion increased as a

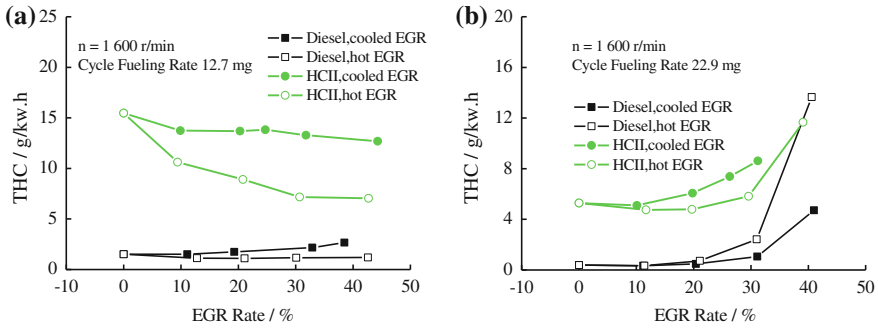


Fig. 6 Effects of EGR on THC emissions. **a** Low load, **b** High load

whole. It is because as EGR rate increased, the intake air reduced, and more local rich fuel–air mixtures appeared.

3.3 Effects of EGR on Combustion Characteristics

Figure 7 shows effects of EGR rate on cylinder pressure and heat release. Both the maximum cylinder pressure and the heat release rate reduced when large amounts of EGR were applied. The reduction in HCII mode was greater than diesel CI combustion.

Figure 8 shows the effects of EGR on ignition delay. As EGR ratio increased, the ignition delay increased in general. It was because exhaust gas decreased the in-cylinder temperature. Comparing to diesel CI combustion, the ignition delay in HCII mode increased more significantly, which was beneficial to the fuel–air mixing.

Figure 9 shows the effects of EGR on combustion duration. As EGR rate increased, the combustion duration increased at low load. The increase of combustion duration in diesel CI combustion is more significant than HCII mode. As EGR rate increased, the combustion duration initially increase and then decrease at high load. At high load, the combustion duration in HCII mode was shorter than diesel CI combustion, and the combustion was closer to constant volume combustion, which was conducive to improving thermal efficiency.

Figure 10 shows the effects of EGR on the maximum pressure rise rate. As EGR rate increased, the maximum pressure rise rate decreased at low load. However, as EGR rate increased, the maximum pressure rise rate in diesel CI combustion initially increased and then decreased at high load. The maximum pressure rise rate in HCII mode decreased significantly at high load with the increase of EGR. The reduction of the maximum pressure rise rate in HCII mode was more significant than diesel CI combustion. It is demonstrated that EGR is an effective technology to reduce the combustion noise in HCII mode at high load.

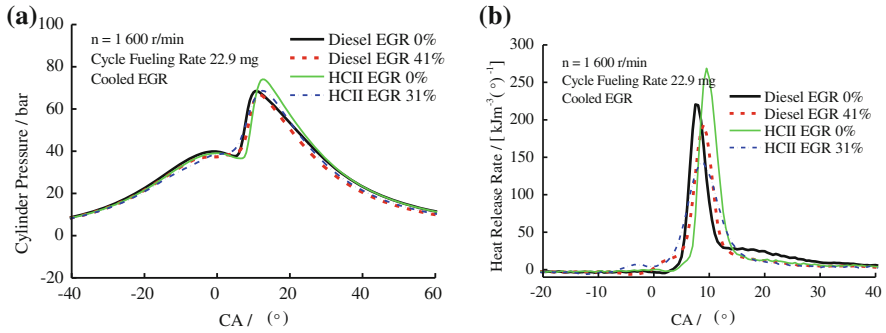


Fig. 7 Effects of EGR rate on cylinder pressure and heat release. **a** Cylinder pressure, **b** heat release rate

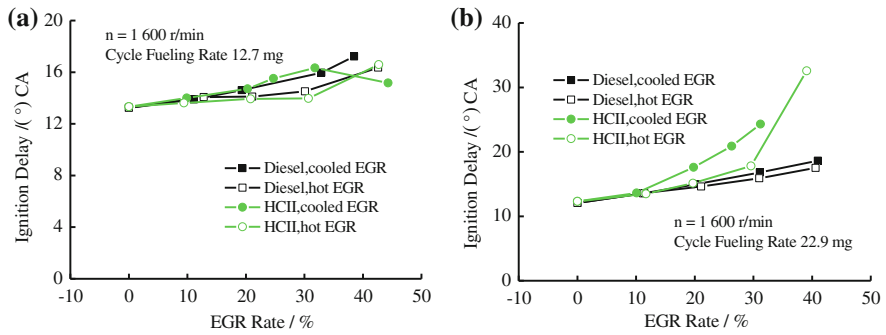


Fig. 8 Effects of EGR on ignition delay. **a** Low load, **b** High load

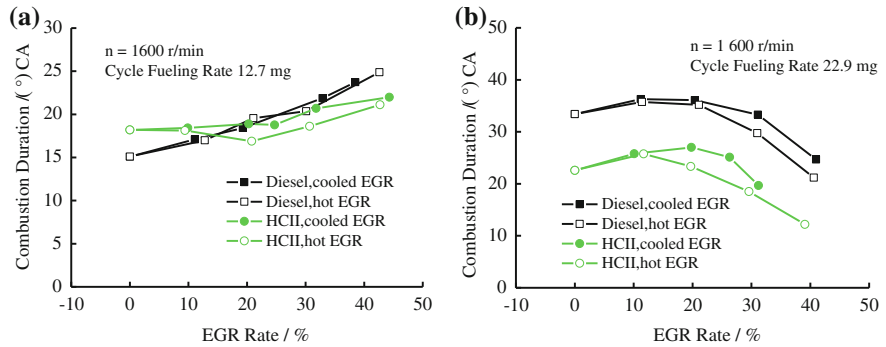


Fig. 9 Effects of EGR on combustion duration. **a** Low load, **b** High load

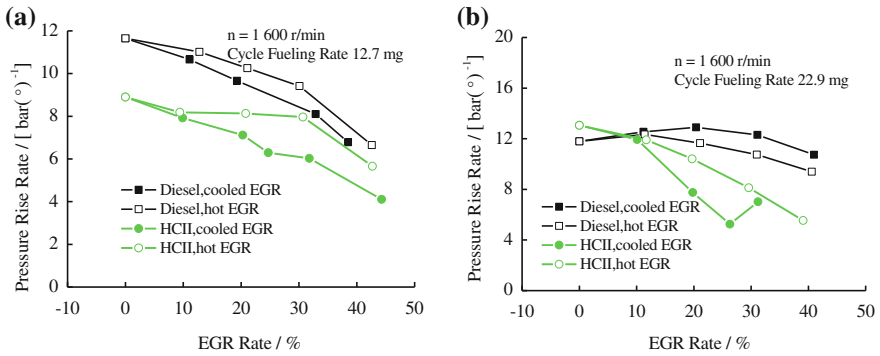


Fig. 10 Effects of EGR on the maximum pressure rise rate. **a** Low load, **b** High load

4 Conclusion

- (1) As EGR rate increased, NO_x emissions reduced significantly. Cooled EGR resulted in lower NO_x emissions than hot EGR
- (2) At low load, Hot EGR can decrease the THC emissions in HCII mode and improve the combustion, with a biggest indicated thermal efficiency increase of 2 %.
- (3) As EGR rate increased, the NO_x emissions decreased and smoke emissions increased in diesel CI combustion at high load, exhibiting the classical NO-soot trade-off. However, in HCII mode, the NO_x emissions decreased and smoke emissions maintained at a low level, which demonstrated that low temperature was achieved apparently.
- (4) As EGR rate increased, the maximum pressure rise rate decreased in general. The reduction of the maximum pressure rise rate in HCII mode was more significant than diesel CI combustion. It is demonstrated that EGR is an effective technology to reduce the combustion noise in HCII mode at high load.
- (5) As EGR ratio increased, the ignition delay increased in general. Comparing to diesel CI combustion, the ignition delay in HCII mode increased more significantly, which was beneficial to the fuel–air mixing.
- (6) At high load, the combustion duration in HCII mode was shorter than diesel CI combustion, and the combustion was closer to constant volume combustion, which was conducive to improving thermal efficiency.

References

1. Jiang HF, Wang JX, Shuai SJ, Visualization and performance analysis of gasoline homogeneous charge induced ignition by diesel. SAE paper 2005-01-0136
2. Wang JX, Jiang HF, Wang YJ et al (2004) Study on the combustion characteristics of homogeneous charge induced ignition (HCII) for gasoline engine. Trans CSICE 22:391–396

3. Alger T, Hanhe S, Roberts CE et al, The heavy duty gasoline engine—a multi-cylinder study of a high efficiency, low emission technology. SAE paper 2005-01-1135
4. Wang Y, Su WH, Xie H et al (2002) A study on emission characteristics of a diesel/gasoline dual fuel engine. *Autom Eng* 24:221–223
5. Yu C, Wang JX, Wang Z et al (2011) *Autom Saf Energy* 2(3):263–270
6. Ma SY, YaoMF, Tong LH et al (2012) An experimental study on combustion and emissions of gasoline/diesel dual fuel HPC. *Trans CSICE* 30(1):1–8
7. Inagaki K, Fuyuto T, Nishikawa K, et al, Dual-fuel PCI combustion controlled by in-cylinder stratification of ignitability. SAE paper 2006-01-0028
8. Tamagna D, Gentili R, Ra Y, et al, Multidimensional simulation of the influence of fuel mixture composition and injection timing in gasoline-diesel dual-fuel applications. SAE paper 2008-01-0031
9. Kokjohn SL, Hanson RM, Splitter DA, et al, Experiments and modeling of dual-fuel HCCI and PCCI combustion using in-cylinder fuel blending. SAE paper 2009-01-2647
10. Hanson RM, Kokjohn SL, Splitter DA, et al, An experimental investigation of fuel reactivity controlled PCCI combustion in a heavy-duty engine. SAE paper 2010-01-0864
11. Dishy A, Takahashi Y, Iwashiro Y, et al, Controlling combustion and exhaust emissions in a direct-injection diesel engine dual-fueled with natural gas. SAE paper 952436
12. Ishiyama T, Shioji M, Mitani S, et al, Improvement of performance and exhaust emissions in a converted dual-fuel natural gas engine. SAE paper 2000-01-1866
13. Lin ZQ, Su WH, A study on the determination of the amount of pilot injection and rich and lean boundaries of the pre-mixed CNG/air mixture for a CNG/diesel dual-fuel engine. SAE paper 2003-01-0765
14. Marriott C, Kong S, Reitz R, Investigation of hydrocarbon emission from a direct injection-gasoline premixed charge compression ignited engine. SAE paper 2002-01-0419

The Impact of Modified Piston in Two Stroke Engine on Toxic Emissions and Fuel Consumption

Jerzy Merkisz, Maciej Bajerlein, Łukasz Rymaniak
and Andrzej ZióŁkowski

Abstract The Institute of Combustion Engines and Transport conducted tests on exhaust emissions for two motorized scooters fitted with two-stroke engines differing from each other with the type of the applied pistons. The research was conducted on a chassis dynamometer according to a specially prepared test that aimed at reflecting the conditions of the actual use of the vehicle. The presented tests were performed in order to determine the influence of the lubricant on the exhaust emission components. The authors also tested the in the emission of NO_x, CO, HC and CO₂. In the first stage of the testing, measurements were made with respect to a standard mixture of gasoline and oil. Subsequent measuring cycles were conducted for leaner mixtures. The tests on the concentrations of individual components were realized with the use of a portable analyzer SEMTECH DS manufactured by Sensors Inc. The portable analyzer was also designed to measure the mass flow of the exhaust and the concentration of the exhaust components such as CO, HC, NO_x, CO₂ and O₂. A consumption of fuel with a second by second resolution was measured gravimetrically. The fuel consumption in the test drive was measured with the use of a carbon balance method.

Keywords Exhaust emissions · Fuel consumption · Piston · Scooter · Two-stroke engine

F2012-A01-039

J. Merkisz (✉) · M. Bajerlein · Ł. Rymaniak · A. ZióŁkowski
Poznan University of Technology, Poznan, Poland
e-mail: maciej.bajerlein@put.poznan.pl

Fig. 1 A scooter when tested on the chassis dynamometer



1 Introduction

Presently, transportation is one of the fundamental factors of economic development worldwide. Today vehicle manufacturers offer more hybrid, electric and alternative fuel-powered vehicles than ever [4]. As regards road transportation, there are many categories of vehicles with respect to design, type of use, operating conditions etc. Motorcycles and motorized scooters belong to a unique category of the discussed sector. They play a very important role both in urban agglomerations and non-urbanized areas. Single-track vehicles ensure prompt transportation even in situations of high traffic intensity or bad conditions of the roads. As far as motorized scooters are concerned, an additional benefit is the eligibility to drive it without a special license. The only requirement is appropriate age as forced by the legislation. An increased interest in vehicles fitted with two-stroke engines has been recorded in the automotive sector. The growth of the number of such vehicles on roads and, in particular, in cities, has a very negative influence on the environment protection. Due to the nature of operation of a two-stroke engine and the need to supply the lubricating oil in the fuel, such vehicles are characterized by high exhaust emissions and, heavy hydrocarbons in particular.

2 Research Methodology

2.1 Research Object

The objects of the research were two motorized scooters. The difference between them was the design of the piston. A scooter fitted with a standard piston was tested first (manufacturer specifications). The second measurement series was realized with a modification of the engine (scooter with a piston of special design

Table 1 Technical specifications of the tested scooters

Type	Two-stroke, spark ignition
Displacement	0.49 ccm
Maximum speed with the speed limiter	45 km/h
Maximum speed without the speed limiter	75 km/h
Maximum engine speed	9,000 rpm
Engine power output	3.3 kW (4.5 Km)
Engine start-up	Electrical and kick-start-startelektryczny i nożny
Brake front/rear	Disc/hydraulic
Tire size front/rear	130/60-13
Dimensions: length/width/height	1880/740/200 mm
Weight	92 kg
Maximum payload	150 kg
Seating capacity	2

was fitted Fig. 1). This piston enables the engine operation on mixtures of lower oil content than the manufacturer specifies. Table 1 presents the basic technical specifications of the vehicles.

From the patents description no. 10 2005 030 556 “Multipart Piston and Method of Multipart Piston Manufacturing” (patent application PCT/EP2006/005986) it results that the applied piston is a multipart one with at least one upper part and one lower part with the piston wall (sliding part) and at least a part of the piston crown forms the upper Page 3 of 8 part [7]. The other assumption of the discussed design is that the upper part of the piston is made from material other than the one in the lower part. The lower part of the piston is made of aluminum or an aluminum alloy and is used as a casing for a titanium, austenitic iron, steel or other, material having similar thermal properties as the material that the lower part of the piston is made of.

Connecting the individual parts of the piston may be realized in different ways. The first one is filling the upper part with alloy during the process of manufacturing of the lower part. Another way is pressing the upper part into the lower part in the sintering process. Yet another way to produce a multipart piston is to make the lower part so that empty space is left for the upper part (This same space can be decremented from the lower part). Into the empty space liquid material is poured that forms the upper part upon bonding (the empty space in this method is a mold to make the cast of the upper part). In the case of a large piston a particularly advantageous solution is the threaded connection that joins the lower and the upper part of the piston. To that end we need to make an empty space in the lower part of the piston (the internal space of the piston limited by the piston walls). Subsequent steps are: forming of an internal thread in the bore, screwing in the counter-element to secure against possible unscrewing of this part of the piston [7].

The described technology is designed for the implementation of new pistons into production but it may also be used for the already existing pistons—particularly advantageous is the last of the described methods. As for the scope of application in

Fig. 2 The view of the SEMTECH DS device during tests



the patent description, all combustion engines have been listed (two and four stroke, low and high capacity gasoline and diesel engines). Since, the lower and the upper parts cannot be soldered nor can they be welded the joint of these two elements limits the thermal conductivity between these parts. This results in that the lower part of the piston can have a lower temperature than the upper part of the piston. The connection of the two parts shows a 5–60 % lower thermal conductivity than the material that the lower part is made of. A lower thermal conductivity of the joint between the lower and the upper part of the piston positively limits the heating up of the lower part of the piston during engine operation. Hence, we can significantly reduce the amount of oil added to the fuel in the case of two stroke engines as compared to a conventional monolithic piston solution [7].

2.2 Exhaust Emission Equipment

The exhaust emissions (including the toxic ones) were measured with a portable exhaust emission analyzer SEMTECH DS manufactured by SENSORS Inc. (Fig. 2). The device is one of the most modern measurement systems in the category of Portable Emissions Measurement Systems (PEMS). It measures the exhaust emissions in both gasoline and diesel engines in a wide range of their displacements. Its application enables the measurement of the fuel consumption, mass exhaust gas flow, oxygen content and the content of other exhaust components in the exhaust gases such as: CO, CO₂, NO, NO₂, THC etc.

The portable analyzer is coupled with a mass flow meter where a probe is fitted that samples the exhaust gases. The tested gas volume is transported through a special heated line where the temperature of 191 °C is maintained. This solution prevents hydrocarbons from condensing before their concentration is measured. Subsequently the sample goes through a filter where particulate matter is eliminated. Now the prepared exhaust gases are accurately measured in individual

Table 2 Technical specifications of the portable exhaust emission analyzer SEMTECH DS [6]

Parameter	Measurement method	Accuracy (%)
Exhaust component concentration:	NDIR—analyzer, measurement range 0–10 %	±3 ±2.5
CO	FID—analyzer, measurement range 0–10,000 ppm	±3 ±3
HC	NDUV—analyzer, measurement range 0–3,000 ppm	±1
NO _x = (NO + NO ₂)	NDUV—analyzer, measurement range 0–20 %	±1
CO ₂	Electrochemical analyzer, measurement range 0–20 %	
O ₂	Mass flow rate T _{max} to 700 °C	±2.5 of the range ±1 of the range range
Warm up time	900 s	
Response time	T ₉₀ < 1 s	
Supported diagnostic systems	SAE J1850/SAE J1979 SAE J1708/SAE J1587 CAN SAE J1939/J2284	

analyzers. In the first place the emission of hydrocarbons is measured in the Flame Ionization Detector analyzer (FID). Another stage is chilling of the sample to 4 °C and sending it to the Non-dispersive Ultra Violet Detector analyzer (NDUV) responsible for the measurement of nitric monoxide and nitric dioxide. The next stage is the measurement of the carbon monoxide and carbon dioxide through an Non-dispersive Infra Red Detector analyzer (NDIR). The last stage is the measurement of oxygen through an electrochemical sensor. All the analyzers are calibrated and reset prior to the measurement to ensure that the ambient air pollution is taken into account. This takes a few minutes to complete. The sampling frequency range for each analyzer is different. For this reason for the measurement of all the components must assume the highest frequency that can be obtained by each of the analyzers. The basic technical specifications have been given in Table 2.

2.3 The Applied Fuel

The theory of operation of a two-stroke engine is to realize the intake, compression, power and exhaust strokes in a single engine crankshaft revolution. Hence, a full work cycle takes place within two strokes: from bottom dead center (BDC) to top dead center (TDC) and vice versa. The design of the solution requires a use of a mixture of gasoline and oil that will ensure proper operation of the piston assembly.

Table 3 Technical data of the SOFT-ENGINE s.r.l. INERTIAL 70 [9]

Dynamometer	Inertia
Maximum power output taken off by the dyno	59 kW (80 Km)
Maximum speed taken off by the dyno	180 km/h
Dimensions: length/width/height	1900/800/4200 mm
Weight	450 kg
Software	INERTIAL 3.0

For the tests the authors used BP 95 gasoline type. It is an unleaded gasoline of the octane number of 95 purchased at one of the BP gas stations. The lubricant used was 2 TAKT TEILSYNTHETISCHES 1052 by LIQUI MOLY GmbH. It is universal semi synthetic oil for two-stroke air-cooled and liquid cooled engines. It can be added to the fuel directly in the tank or through a dispenser fitted in the fuel system. Thanks to its good physical properties the manufacturer recommends its application in a wide range of vehicles and machines such as the likes of motorcycles, gardening tools, rotary snowplows [8].

2.4 Chassis Dynamometer

The tests on the scooters were performed on a scooter chassis dynamometer INERTIAL 70 manufactured by SOFT-ENGINE s.r.l. The stand enables the measurement of the instantaneous power output and torque on the wheels of the vehicle, the covered distance, acceleration and speed. During the preparation of the stand the values of ambient temperature, pressure and humidity are entered into the system including the adjustment values. The last parameter is vehicle specific. Large amount of information positively influences the accuracy of the measurement. The technical specifications of the chassis dynamometer have been shown in Table 3.

3 Test Results

In order to conduct an analysis of ecological indexes for scooters, measurements of emissions of toxic components were made. A vehicle equipped with a standard piston (marked as st) was tested for a 1:30 mixture of petrol and oil. The other scooter equipped with a modified piston (marked as md) was fuelled with a mixture in the following proportions: 1:30, 1:100 and 1:200. Before commencement of each measuring series and testing of a given oil to fuel ratio, the vehicles operated on full throttle characteristics for 180 s. This was aimed at combustion of fuel in the fuel feed system that was left after the previous measuring series as well as forcing a high intensity flow through the measuring devices in which the fuel from previous series of tests was left. Additionally, before the commencement of

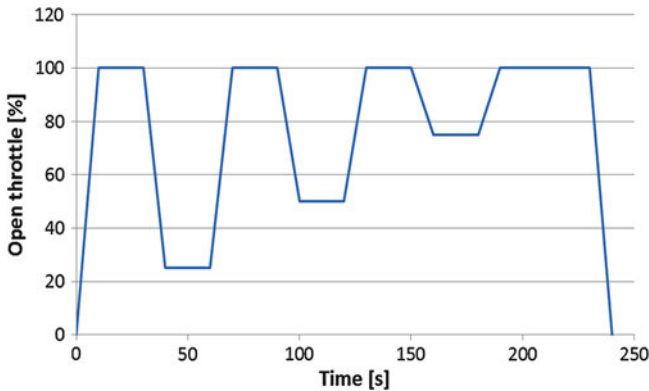


Fig. 3 The assumed course of testing for a motorized scooter

the first measurements, the scooter engines were warmed up operating under small load for several minutes. Under each measuring series, they performed three trials lasting 240 s each, when scooters operated according to a specially prepared test reflecting the real operation of a vehicle (Fig. 3). In the testing, the largest share of operation of the fuel unit is for the full throttle characteristics due to the nature of operation of the tested motorized scooter and its low maximum speed. The engine speed was adjusted by the throttle control on the handlebar. During the measurements, emissions of CO_2 , CO , NO_x , THC were recorded as well as fuel consumption (gravimetric method).

Averaged measurement results for all tests in each measuring series have been presented in Fig. 4. Table 4 presents percentage changes in the emissions of the tested vehicles for each measuring series. Results for the cycle, in which a vehicle with a standard piston was fuelled with the 1:30 mixture as recommended by the manufacturer, constituted a reference for other measurements. The exhaust emissions for both tested vehicles fuelled with the same mixture of fuel and oil were on a similar level.

The obtained values indicate that the largest emission of carbon dioxide occurred for fuelling with the 1:30 mixture of fuel and oil for the vehicle fitted with a standard piston. For 1:100 and 1:200 mixtures similar results were obtained and were lower by 7 % (1:100) and 9.4 % (1:200) than for the richest mixture. The emission of the discussed component is proportional to the fuel consumption and, therefore, it may be stated that largest fuel consumption occurred in the case of use of the rich 1:30 mixture. The results of the averaged emission of carbon dioxide and hydrocarbons also indicate that the highest values are obtained for fuelling of the engine with the 1:30 mixture. The larger the oil to petrol ratio, the lower the emission of the exhaust components. This results from the fact that there are lighter hydrocarbons in leaner mixtures that are less prone to combustion and may lead to incomplete combustion. The lower contents of hydrocarbons may also prove that the scavenging process has improved.

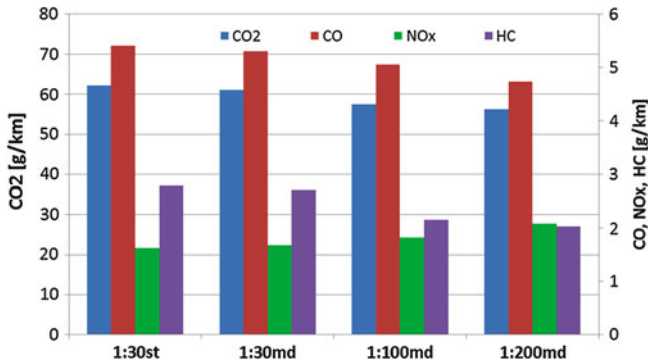


Fig. 4 A comparison of the results of the road emission of CO₂, CO, NO_x, and HC

Table 4 Changes in the emissions of CO₂, CO, NO_x and HC for a scooter fitted with a modified piston as compared to a standard structure

Exhaust component	1:30st (%)	1:30md	1:100md (%)	1:200md (%)
CO ₂	100	98.3	92.5	90.6
CO	100	98.2	93.5	87.6
NO _x	100	103.1	111.7	127.6
HC	100	97.1	77.1	72.8

The measuring cycle, in which a vehicle was fuelled with the 1:200 mixture was characterized by the lowest emission of nitric oxides. This proves that the greatest thermal efficiency was obtained, which is very favorable in the context of a decrease of both the fuel consumption during driving and the emission of CO₂. This also means high efficiency of the combustion process in the cylinder. The remaining drives are similar, however, they decrease with an increase of the oil content in the fuel. The properties of the lubricating oil are responsible for the obtainment of similar results. The lubricating oil has longer hydrocarbon chains that are characterized by greater calorific value and a negative impact of the structure of these chains on the course of the combustion process.

During the exhaust emission tests, fuel consumption was also measured. A gravimetric method was used here that determined the time of decrease of the determined mass of fuel collected in the measuring device. Averaged results for all tests in each measuring series were compared in Table 5.

In order to verify the correctness of the results of the exhaust emission tests and the fuel consumption (second by second measurement resolution), fuel consumption was calculated with the use of the carbon balance method [1]. The method involves determination of the amount of fuel consumed based on the measured emissions of CO₂, CO and HC. The results of the calculations were compared in Table 6. For spark ignition engines the following formula is used:

Table 5 Recorded results for fuel consumption (second by second measurement resolution)

Cycle	Ge [g/s]
1:30st	0.619
1:30md	0.604
1:100md	0.548
1:200md	0.532

Table 6 The consumption of fuel as calculated with the use of the Carbon Balance Method

Cycle	Fuel consumption [dm ³ /100 km]
1:30st	3.80
1:30md	3.72
1:100md	3.59
1:200md	3.42

$$FC_W = \frac{1154}{\rho_{fuel}} \cdot [(0.866 \cdot HC) + (0.426 \cdot CO) + (0.273 \cdot CO_2)] \quad (1)$$

where

FC fuel consumption in [dm³/100 km] or [m³/100 km] depending on the fuel type

HC, CO, CO₂ measured emissions of toxic components [g/km];

ρ_{fuel} density of the tested fuel at 15 °C [g/cm³]

When determining the fuel density, the influence of the lubricating oil on this parameter was considered. Differences in the values of the fuel consumption calculated based on the measurement of fuel consumption with a second by second resolution and the Carbon Balance method amount to 8 % in the worst scenario, which proves that the measurements of the emissions and the consumption of fuel were carried out correctly.

Along the measurements of the exhaust emissions and fuel consumption the power generated by the vehicle was also tested. Table 7 presents the instantaneous values of the maximum power reached by the scooter during each series.

4 Summary

Two-stroke engines are characterized by high exhaust emissions, particularly hydrocarbons. This results from the need to mix the lubricating oil with the fuel so as to prevent engine lockup. Motorized scooters powered with this type of engines are not usually fitted with aftertreatment systems due to limited production costs. Yet, all newly registered motorcycles and motorized scooters in the European Union must meet the appropriate requirements related to their homologation [2, 3, 5].

Table 7 Recorded results of the instantaneous maximum power

Cycle	Maximum power (kW)
1:30st	1.91
1:30md	1.82
1:100md	1.98
1:200md	1.75

In terms of environment protection we need to take every effort to make two-stroke vehicle engines as ecological as can be. This can be obtained through the application of special design solutions in the engines that will allow the use of fuel/oil mixtures of lower oil content.

The analysis of the obtained results indicates that the vehicle fuelled with fuel containing less lubricating oil consumes less fuel. Based on the obtained data, we may conclude that a decrease in the oil content leads to an improvement of the efficiency of the combustion engine. In the event that the 1:100 mixture of fuel was used and considering the generated instantaneous maximum power, the fuel consumption was at a low level equaling 3.59 dm³/100 km. Therefore, the generated mechanical power required a supply of the smallest quantities of chemical energy. The use of fuel in this proportion ensured sufficient lubrication, as there was no growth of friction losses. For the mixture of 1:200 the lowest gas mileage equaling 3.38 dm³/100 km was obtained, however, in this case no high power was generated, which is connected with an increase of the friction losses.

The ecological indexes improved significantly for the vehicle powered with fuel containing less lubricating oil than recommended by the manufacturer. We may state that in the case of fuel consumption, a lower content of oil means lower exhaust emissions of the vehicle. An increase in the emission was recorded exclusively for NO_x, which proves that a higher temperature in the combustion chamber. It may cause improve thermal efficiency was obtained favorable in the context of a decrease of gas mileage and a decrease of the emission of CO₂.

Presently, the Institute of Combustion Engines and Transport of Poznan University of Technology is conducting tests on vehicles powered by small displacement two-stroke engines. The research presented in the paper constitutes a fragment of the entire series of tests conducted on this type of vehicles. Additionally, the Institute prepares a unique test that will reflect the actual driving conditions for motorized scooters to the greatest possible extent.

References

1. Gao Y, Checkel MD (2007) Experimental measurement of on-road CO₂ emission and fuel consumption functions. SAE Technical Paper Series 2007-01-1610
2. Commission Regulation (EC) No. 692/2008 of 18 July 2008 implementing and amending Regulation (EC) No 715/2007 of the European Parliament and of the Council of 20 June 2007

- on type approval of motor vehicles with respect to emissions from light passenger and commercial vehicles (Euro 5 and Euro 6) and on access to vehicle repair and maintenance information. OJ L 1991/1, 29.7.2008
3. Directive 2002/24/EC OF the European Parliament and of the Council of 18 March 2002 relating to the type-approval of two or three-wheel motor vehicles and repealing Council Directive 92/61/EEC. OJ 124/1, 9.5.2002
 4. Merkisz J (2009) The automotive market in the time of global economic crisis. *Combust Engines* 3–13
 5. Regulations of the Polish Minister Infrastructure of 28 July 2005 on type approval of motor vehicles with two or three wheels, some vehicles with four wheels and motorcycles (OJ No 162, pos. In 1360, as amended)
 6. Sensors Inc (2010) Emissions measurement solutions. SEMTECH[®] DS on board in –use emissions analyzer, Erkrath
 7. Patents no. WO 2007/025581 and 10 2005 030 556 „MULTIPART PISTON AND METHOD OF MULTIPART PISTON MANUFACTURING” (patent application PCT/EP2006/005986)
 8. http://www.liquimoly.pl/features/katalog?page=shop.product_details&flypage=flypage.tpl&product_id=245&category_id=51
 9. <http://www.soft-engine.org/pagine.web/inglese/lowcost01.html>

Multi-Coil High Frequency Spark Ignition to Extend Diluted Combustion Limits

Shui Yu, Xiaoye Han, Kelvin Xie, Meiping Wang, Liguang Li, Jimi Tjong and Ming Zheng

Abstract A reliable ignition process is desirable for the ignition of a lean and/or EGR diluted cylinder charge commonly adopted to achieve clean and efficient engine combustion. In this work, ignition of a diluted propane-air mixture is investigated using a high energy spark ignition system. Efforts are dedicated towards development of a novel ignition system that improves the ignition quality whilst keeping within the bounds of current spark ignition hardware to facilitate potential application in future clean combustion engines. A multi-coil ignition system was developed to adjust the spark energy and the discharge pattern. With enhanced primary voltage up to 120 V, a multi-spark strategy with frequency up to 20 kHz can be implemented. The combustion visualization results show that the application of both multi-coil and multi-spark strategy can promote the flame propagation. The high frequency multi-spark strategy shows better ignition quality compared to a single-spark strategy. With discharge energy enhancement by coupling more coils, the ignition success rate is increased under diluted mixture conditions. The diluted combustion limits are therefore extended with the help of these spark strategies.

Keywords High frequency ignition · Multi-coil · Spark ignition · Combustion limit · Discharge characteristics

F2012-A01-040

S. Yu · X. Han · K. Xie · M. Wang · M. Zheng (✉)
Department of Mechanical Automotive & Materials Engineering,
University of Windsor, Ontario, Canada
e-mail: yushui@uwindsor.ca

L. Li
Tongji University, Shanghai, China

J. Tjong
Ford Motor Company Canada, Oakville, Canada

1 Introduction

A lean and/or EGR diluted cylinder charge is typically applied to achieve clean and efficient engine combustion, provided a reliable ignition process prevails. Such combustion systems as the spark assisted compression ignition (SACI) and gasoline direct injection (GDI) require a robust ignition source to ensure successful and stable combustion. The optimization of the sparking strategy is necessary to overcome the inherent difficulties of ignition in the lean, EGR diluted, and turbulent mixture inside the engine. Deep understanding of the ignition initiation and the flame kernel formation is crucial, as it directs the improvement of ignition systems. The evolution of a spark discharge plasma channel to a self-sustained flame propagation is one of the key stages to ensure the successful combustion in the spark ignition engines [1]. Once the self-sustained flame propagation is started, the mixture composition and the flow structure control the flame propagation. Therefore, the sparking pattern will play a crucial role particularly during the early flame kernel development process.

In the past decades, diverse spark ignition approaches were applied to improve the ignition quality. Furthermore, the spark discharge pattern control strategies are increasingly more complex. The pulsed direct current ignition (PDCI) systems, such as plasma jet ignition [2] and rail-plug ignition [3], parallel a capacitor to the spark gap as an energy storage device. The breakdown process of the spark discharge triggers the release of the stored energy from the capacitor. As a result, the transient power and the overall energy of spark discharge are enhanced dramatically. The other effective way to enhance the transient power is through managing the discharge process to enhance the energy during breakdown phase. By simply replacing the internal resistor of a conventional spark plug with a high-voltage capacitor, the energy discharged during the breakdown phase can be increased significantly [4]. It is reported that the breakdown phase has a significantly higher impact on ignition than the subsequent arc and glow discharge phases [5]. The ignition test results of the peaking capacitor method (also called breakdown ignition method) showed significant extension of the ignition limits [6]. The basic principle, by which the PDCI and the breakdown ignition can extend the ignition limit, is the large increase of the peak discharge current. Higher discharge current generates a hotter plasma kernel. It extends the ignition limit at the cost of accelerated spark electrode erosion. Pulsed corona discharge ignition has also been applied to improve diluted combustion [7]. Instead of generating a high-current, hot plasma channel, the pulsed corona ignition generates low temperature equilibrium plasma which extends the lifetime of the electrode. Moreover, the corona discharge ignition offers the opportunity for bulk ignition. The ability to extend lean limit by corona discharge has been demonstrated in HCCI type of combustion [8].

The above discussed ignition methods exhibit the ability to improve the ignition of lean/diluted mixture. However, the system complexity, the cost, and the durability become the main barrier for extensive application of those systems. It is still worthwhile explore the improvement of the conventional ignition system. Through

the management of the spark discharge process and optimization of the spark discharge pattern, the ignition ability under critical mixture conditions could be improved substantially. For different mixture conditions, the requirements of the ignition parameters such as the discharge current and the duration are different. For instance, for mixtures with strong gas motion, a long duration spark was preferred to increase the possibility to catch the optimum mixture pocket near the spark gap. The lower peak current, longer duration spark performed better than the higher peak current, shorter duration spark [9]. It was also reported that the multi-spark strategy enhanced the ignition ability considerably under strong air motion condition [10]. However, with respect to extending the ignitable limit, the enhancement of the discharge peak current and the transient power may be more important. Through proper management, the spark discharge process could be combined with long duration and temporal high transient power. In this work, a multi-coil high frequency ignition system was developed to adjust the discharge pattern. The effect of spark discharge pattern on the early flame kernel development process and the ability to extend the diluted combustion limit in quiescent pre-mixed propane-air mixtures were investigated.

2 Experimental Setup

A multi-coil ignition system was built to control the spark ignition process. The ignition energy could be raised significantly with the multi-coil system. In addition, the discharge mode was controlled to generate different discharge profiles such as high current discharge, long duration discharge, and multi-spark discharge. A National Instruments cRIO FPGA controller was programmed to promptly command the multi-coil ignition system.

A standard J-gap spark plug with a 5 k Ω internal resistor and an iridium central electrode tip was used as in this study, with a nominal gap size of 1.0 mm. The spark discharge process was characterized by measurement of the discharge voltage and current profiles. As the discharge process showed high repeatability under the tested conditions, measurements of the current and discharge voltage were conducted separately from the visualization and ignition success rate tests. The discharge voltage was measured by a P6015 high-voltage probe connected to the high voltage side of the spark plug. The method used to measure the discharge current was to mount a second electrode opposed to the high-voltage electrode in lieu of the ground electrode. The opposed electrode incorporated a sensing resistor, from which the current was indirectly obtained by measuring the voltage drop. The discharge energy was estimated by integrating the measured discharge voltage and current.

An optically accessible combustion chamber, with a cylindrical inner volume of 25 mm diameter and 25 mm length, was designed and used to quantify the flame propagation visually and through measurement of the combustion pressure. The chamber was operated under constant volume combustion conditions, using two recessed 1/4 inch ports for filling and exhausting the chamber. The flame

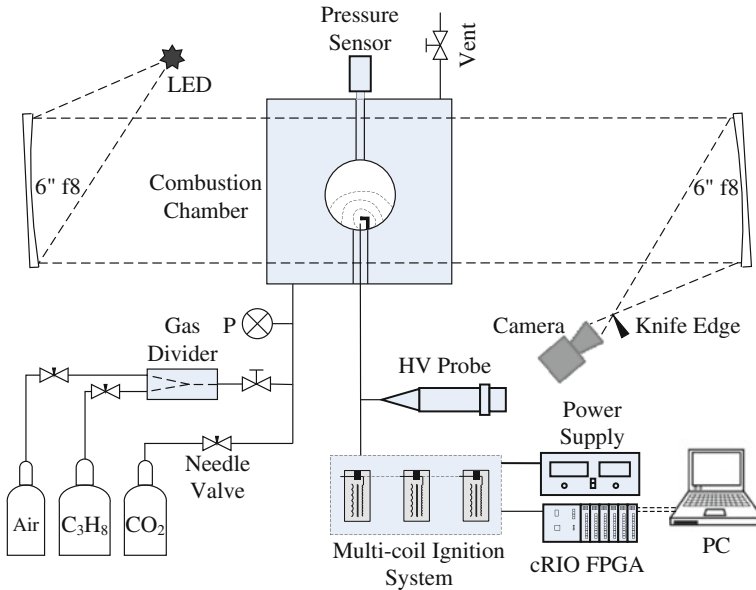


Fig. 1 Experimental setup

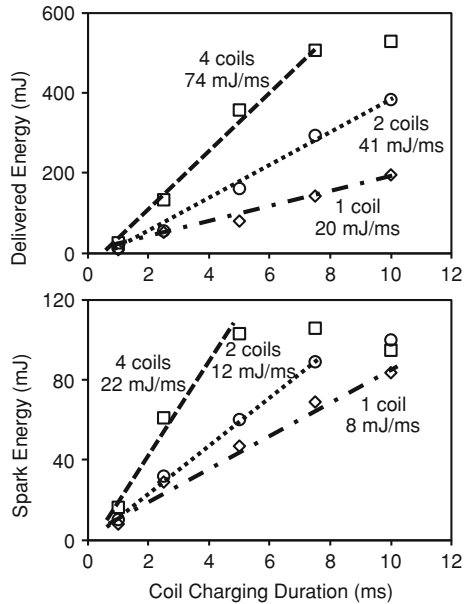
development was recorded using a shadowgraph imaging system, which consisted of two 6-inch parabolic mirrors, a white LED light source, and a pinhole of 0.4 mm diameter. A high-speed video camera was used to record the shadowgraph images at 15,000 frames per second at a nominal resolution of 64 $\mu\text{m}/\text{pixel}$. An EnviroNics 4040 gas divider was employed to feed the chamber with propane-air mixture at designated ratios. Additionally, carbon dioxide was supplied to simulate EGR dilution effect. The concentration of the gas mixture was measured by an FTIR analyzer to validate the concentration of constituent gases. In these tests, the experiments were conducted under ambient pressure and temperature. The chamber pressure was measured to analyze the combustion. Two types of the tests were carried out with the chamber: visualization of the flame kernel development, and ignitability tests to evaluate the combustion limits. For these tests, the spark plug was used without any modifications. The test setup is shown in Fig. 1.

3 Results and Discussions

3.1 Spark Discharge Current and Energy Evaluation

The spark discharge voltage and current profiles of the tested spark plug have been reported in the authors' previous investigation [11]. The total spark energy was estimated by integrating the discharge voltage and current. The discharge voltage measurement was located at the high-potential terminal of the spark plug.

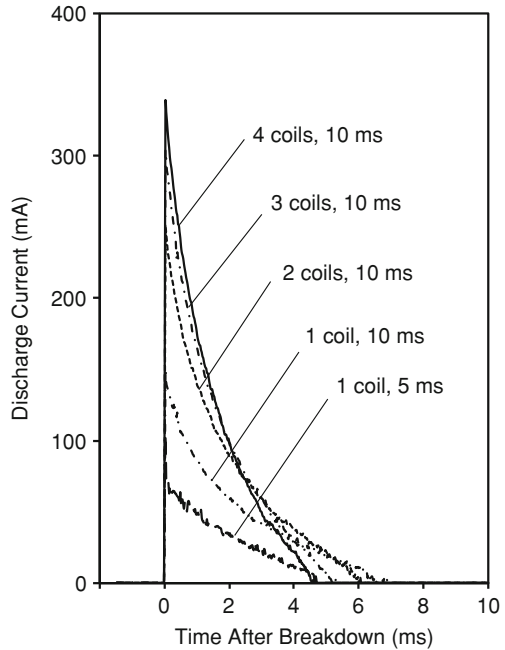
Fig. 2 Spark energy as functions of charging duration at 12 V primary voltage using multiple coils



The voltage at the electrode gap was obtained by subtracting the voltage drop across the internal resistor from the measured voltage at the spark plug high-voltage terminal. The current in the secondary-coil loop was assumed to be identical, i.e. same transient current goes through the internal resistor and the spark gap. The total discharge energy calculated directly from the measured voltage and current is defined as the *delivered energy* which includes the energy dissipated on the internal resistor. The energy calculated from the voltage over the spark gap and current is defined as the *spark energy* which excludes the energy dissipated on the internal resistor. Figure 2 shows comparisons of the discharge energy under different conditions. When a single coil is used, the delivered energy and the spark energy increased with the coil charging duration at a rate of approximately 22 mJ/ms and 8 mJ/ms, respectively. Increasing the number of coils used to two coils and four coil increased the delivered energy nearly linearly with the number of coils. In the case of four coils and charging times in excess of 8 ms, the delivered energy began to plateau at approximately 550 mJ. The effective spark energy charging rate is in general notably lower than the delivered energy and further lose effectiveness when the number of coils is increased. Similar to the delivered energy, the spark energy also reached a plateau at approximately 100 mJ. The implication is that proportionally more energy dissipated on the internal resistor at higher discharge energy levels. Besides the discharge energy, the discharge current is also an indicator of the spark intensity, with perhaps an even more direct relationship.

Figure 3 shows the discharge current comparisons for different number of coils used in parallel. For a single coil, a longer charging duration produced higher current and longer discharge duration. When more coils were coupled together

Fig. 3 Comparison of discharge current at 12 V primary voltage using multiple coils



with the same charging duration, the peak discharge current was enhanced, but the discharge duration was reduced slightly. For arc discharge, the voltage and current do not comply with the traditional Ohm's law. The discharge voltage will decrease with the increase of current. A higher discharge current produces a hotter plasma channel and more excited ions in the plasma, resulting in a decrease of the voltage needed to maintain the plasma. Due to the anti-Ohm law characteristic of the arc discharge, the energy calculated from the integration of the voltage and the current could decrease even with an increased discharge current. For comparisons in the subsequent sections, the plots are marked with parameters such as the charging duration, primary voltage and the number of coil, but omit the discharge energy values.

A high frequency multi-spark strategy using the test system is demonstrated in Fig. 4. The primary voltage was enhanced to 120 V so that the coil can be charged quickly to generate multiple spark discharges with the frequency up to 20 kHz. The overall spark duration is about 1.5 ms, with the total delivered energy less than 20 mJ, as shown in Fig. 4a and c. Details of the period preceding and immediately after the gap breakdown are shown in Fig. 4b and d. The five short-duration high frequency discharges last about 0.1 ms with the cumulative energy about 1.2 mJ. For each individual short-duration spark, the voltage and current oscillate during breakdown stage. For a typical single-spark discharge, the breakdown process usually lasts a few tens of nanoseconds with the peak current up to hundreds of amperes [12]. The extremely high peak current will initiate the spark plasma and ignition. Previous research has already shown that the

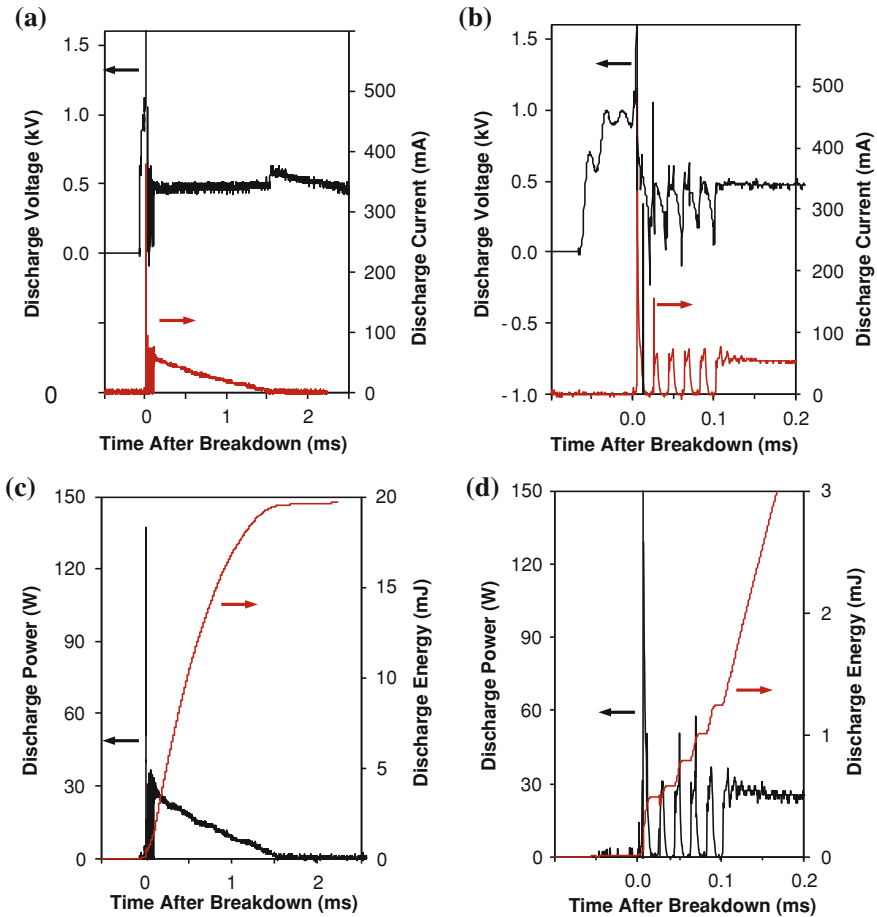


Fig. 4 High-frequency multi-spark charging and discharging characteristics at 120 V primary voltage. **a** Discharge voltage and current. **b** Expanded view of discharge voltage and current. **c** Discharge power and energy. **d** Expanded view of discharge power and energy

breakdown phase impacts the ignition more than the following arc or glow phase. For the high frequency multi-spark strategy, the breakdown of an individual spark will be affected by the previous discharge. The first spark has the highest breakdown voltage, while the following ones have lower breakdown voltage as the gas between the gap has already been excited and the temperature remains high. The result is that a reduced breakdown voltage is required. It should be noted that the peak current of each short spark may be significantly higher than that presented in Fig. 4b, as the resolution of the measurement is not fine enough to reveal the details at tens of nanosecond scale.

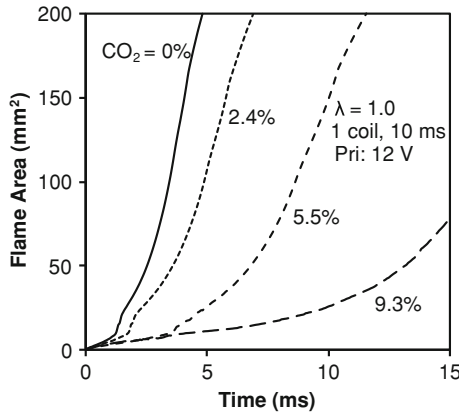


Fig. 5 Effect of CO₂ dilution on flame propagation

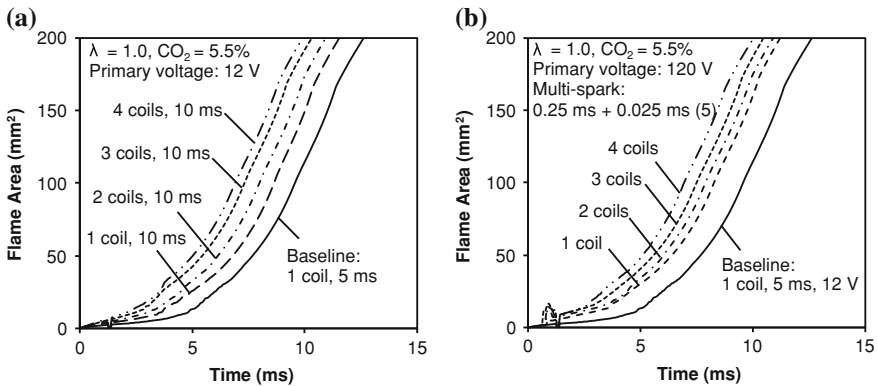


Fig. 6 Comparison of flame propagation under various sparking strategies at low CO₂ dilution. **a** Low-voltage, single-spark strategies. **b** High-voltage, multi-spark strategies

3.2 Effect of Sparking Strategies on the Flame Propagation

The mixture strength is the primary factor that determines the inflammability and the flame propagation velocity. The flame propagation was analyzed by computing the flame cross-sectional area as captured in shadowgraph images of the spark and combustion process. Figure 5 shows the growth of the flame cross-sectional area under different CO₂ dilution conditions. The flame propagation is slowed significantly by the effects of dilution. At the optimum mixture strength, the ignition source may not impact the combustion and the flame propagation very significantly. However at less optimal mixture conditions, the ignition energy and the discharge pattern can impact the initiation stage significantly and the cumulative effect can result in significant differences in the overall combustion characteristics.

Fig. 7 Ignition success rate as a function of coil charging duration at low CO₂ dilution

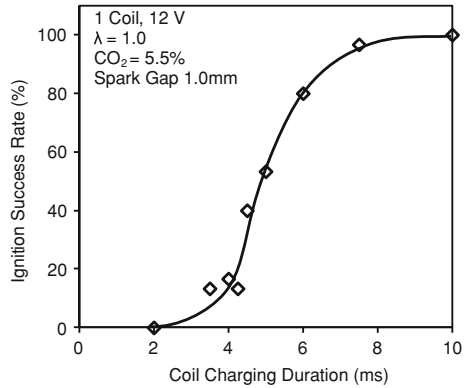


Fig. 8 Enhanced spark energy to extend CO₂ dilution limits

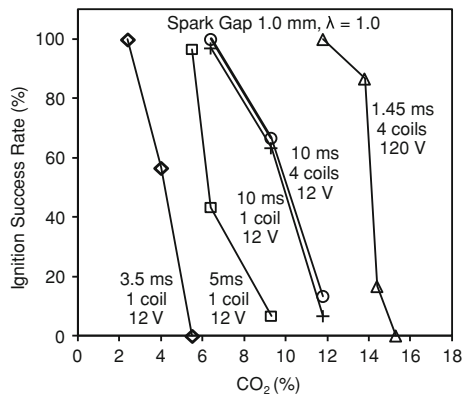


Figure 6a shows the flame propagation characteristics for a set of tests conducted by varying the number of coils for a high energy single-spark ignition. A relative low energy single-spark ignition event with 5 ms of charging time has also been plotted to provide a baseline for the high energy spark ignition tests. Between a low energy and a high energy spark ignition event, substantial improvement in flame speed was observed. When the number of coils was increased from one through four, a monotonous improvement in flame propagation was observed.

The effects of different multi-spark strategies on the flame propagation are demonstrated in the Fig. 6b. A representative result from a single spark strategy has also been plotted for comparison with the multi-spark strategy. A noticeable improvement in the flame propagation speed was evident from the results. Furthermore, with the same spark strategy, higher number of coils resulted in accelerated flame propagation. A consistent reduction in the flame travel time was observed when the number of coils was increased from 1 to 4. The overall discharge energy of the multi-spark strategy with a single-coil set was less than 20 mJ which was much lower than the lowest energy employed in the single-spark

discharge strategies. The improvement of the flame propagation may possibly be due to the high current spikes during the breakdown phase of each short spark.

3.3 Effect of Sparking Strategies on the Diluted Combustion Limits

In addition to the flame propagation speed, the ignition quality was evaluated by the ability to ignite propane-air mixtures of different strengths in a test chamber. In this study 30 repeated ignition tests were conducted for each condition reported. The percentage of successful ignitions is reported as the *ignition success rate*. Figure 7 demonstrates the effect of the changing the coil charging duration on the ignition success rate. CO₂ dilution was implemented in this set of tests to create marginally ignitable conditions. The results indicated that as the coil charging time was increased, the ignition likelihood improved. The energy level required to achieve 100 % ignition at this condition was approximately 80 mJ of spark energy.

Further testing was conducted to study the likelihood of ignition in a propane-air mixture with strong CO₂ dilution (up to 15.3 % CO₂). The test points for the different spark ignition strategies reported in the Fig. 8 were selected from a pool of test results to demonstrate the CO₂ dilution limit for each spark strategy. It was observed that with a longer coil-charging duration, higher CO₂ dilution could be tolerated. This was seen as the charging time was increased from 3.5 to 5 ms, and then to 10 ms using a single coil with a primary voltage of 12 V. The level of CO₂ dilution at which reliable ignition was still obtained increased from 2.4 to 5.5 %, and to 6.4 %, respectively. Only a slight improvement was attained in the ignition success rate when the number of coils utilized was increased from one to four. However, a significant improvement was further realized when the primary coil voltage was increased to 120 V.

4 Conclusions

Extensive tests have been conducted with an ignition system featuring enhanced spark energy and managed discharge. Conclusions can be remarked as follows:

- (1) A multi-coil ignition system has been developed and implemented to successfully adjust the spark energy and the discharge pattern. With enhanced primary voltage up to 120 V, the ignition system can produce up to 20 kHz high frequency multi-spark discharge.
- (2) With multiple coils coupled together, enhanced peak discharge current and reduced discharge duration were observed. At high discharge currents, the discharge energy reached apparent saturation. For the setup employed in this

study, the highest delivered energy utilizing 12 V primary charging voltage was 550 mJ while the energy discharged across the gap was 100 mJ.

- (3) For both the low primary voltage single-spark strategy and the high primary voltage high-frequency multi-spark strategy, the flame propagation was promoted substantially when multiple coils were coupled together.
- (4) At relatively low energy levels, the combustion with high frequency multi-spark strategy showed faster flame propagation than a single-spark strategy.
- (5) The ignition success rate tests showed that the discharge energy enhancement significantly increased the likelihood of ignition in mixtures under carbon dioxide dilution.

Acknowledgments The research at the Clean Diesel Engine Laboratory is sponsored by the Canada Research Chair program, NSERC, CFI, OIT, AUTO21, and the University of Windsor.

References

1. Ko Y, Anderson RW, Arpaci VS (1991) Spark ignition of propane-air mixtures near the minimum ignition energy: part I, an experimental study. *Combust Flame* 83:75–87
2. Yoshida K, Shoji H, Tanaka H (1999) Performance of newly developed plasma jet igniter. SAE Paper, 1999-09-28
3. Hall MJ, Matthews RD, Ezekoye OO (2007) Railplug ignition operating characteristics and performance: a review. SAE Paper, 2007-01-1832
4. Rohwein GJ (1997) An efficient power-enhanced ignition system. *IEEE Trans Plasma Sci* 25(2):306–310
5. Maly R, Vogel M (1978) Initiation and propagation of flame fronts in lean CH₄-air mixtures by the three modes of the ignition spark. In: *Proceedings of the 17th symposium (international) on combustion*, The Combustion Institute, Pittsburgh, pp 821–831
6. Dale JD, Checkel MD, Smy PR (1997) Application of high energy ignition systems to engines. *Prog Energy Combust Sci* 23:379–398
7. Shiraishi T, Urushihara T, Gundersen M (2009) A trial of ignition innovation of gasoline engine by nanosecond pulsed low temperature plasma ignition. *J Phys D Appl Phys* 42:1–12
8. Suess M, Guenther M, Schenk M, Rottengruber H-S (2012) Investigation of the potential of corona ignition to control gasoline homogeneous charge compression ignition combustion. *Proc Inst Mech Eng [D]: J Automob Eng*, 226:275–286
9. Matsumoto O, Kuboyama T, Moriyoshi Y, Shiraishi T (2011) Effect of spark discharge characteristics on initial flame kernel growth under highly diluted with strong gas motion fields
10. Kono M, Hatori K, Linuma K (1984) Investigation on ignition ability of composite sparks in flowing mixtures. In: *Proceedings of the 20th symposium (international) on combustion*, The Combustion Institute, Pittsburgh, pp 133–140
11. Yu S, Xie K, Han X, Jetric M, Gao T, Zheng M (2011) A preliminary spark characteristics study for unconventional cylinder charge with strong air movement. In: *Proceedings of the 2011 ASME ICE Division*, ICEF2011-60132, pp 461–470
12. Heywood JB (1988) *Internal combustion engine fundamentals*. McGraw-Hill, Singapore

Multiple Injection and Boosting Benefits for Improved Fuel Consumption on a Spray Guided Direct Injection Gasoline Engine

Jason King and Oliver Böcker

Abstract The combination of turbocharging and direct injection offers a significant potential for SI engines to improve fuel consumption, specific power output, raw emissions and transient behavior. To realize the full benefit of this combination Ricardo uses spray guided lean stratified operation with multiple injections. The Ricardo T-SGDI concept has already been presented at various international conferences and is constantly being developed using modern optimization techniques. This paper shows the latest results of the T-SGDI engine with a maximum brake thermal efficiency about 41 % and a BSFC of about 278 g/kWh at 2000 rpm and 2 bar BMEP. Additionally, the stabilization of combustion through the multiple injections allows EGR rates of up to 35 % in order to reduce NO_x raw emissions. Further, this engine achieves 30 bar BMEP and 100 kW/l. These outstanding values are possible by combining different mechanisms such as charging, multiple injection, high Exhaust Gas Recirculation (EGR) rates plus the appropriate charge motion and combustion chamber design. At low loads, the multiple injections ensure stable combustion, even with residual gas fractions of up to 35 %. At medium loads the Ricardo Multiple Injection Variable Injection Separation (MIVIS) Strategy, through the distribution of the injection processes during the intake and compression strokes, in combination with boosting means that the lean operating range can be up extended to BMEP of 15 bar. At WOT, injection during both the induction and compression strokes leads to higher knock mitigation and, above 30 bar BMEP, to 50 % MFB at the thermodynamic optimum. The

F2012-A01-041

J. King (✉)

Ricardo, Leamington Spa, UK
e-mail: jason.king@ricardo.com

O. Böcker

Ricardo Deutschland GmbH, Schwäbisch Gmünd, Germany

Ricardo T-SGDI concept thus achieves the efficiency of modern direct injection diesel engines whilst retaining the positive characteristics of a gasoline engine, such as a wide engine speed range and spontaneous power response.

Keywords SGDI · Gasoline · Boosted · Stratified · Injection

Abbreviations

°CA	Degree Crank Angle
AFR	Air to Fuel Ratio
aIgn	Angle of Ignition
ATDC	After Top Dead Centre
BTDC	Before Top Dead Centre
BMEP	Brake Mean Effective Pressure
BTE	Brake Thermal Efficiency
CAFE	Corporate Average Fuel Economy
CoV	Coefficient of Variation
DoE	Design of Experiments
EGR	Exhaust Gas Recirculation
HC	Hydro Carbon
IMEP	Indicated Mean Effective Pressure
MBT	Minimum Spark Advance for Best Torque
MFB	Mass Fraction Burned
NO _x	Nitric Oxides
OEM	Original Equipment Manufacturer
PFI	Port Fuel Injection
SGDI	Spray Guided Gasoline Direct Injection
SPM	Stochastic Process Model
VVT	Variable Valve Timing

1 Introduction

Future emission legislation puts further pressure on the development of new, highly efficient gasoline combustion engines. In the past, the development focus was on the reduction of the toxic emissions but now the reduction of fuel consumption, hence carbon dioxide emissions, is especially important. The second generation gasoline direct injection combustion system, commonly referred to as the spray guided (SGDI) combustion system, has been proven to simultaneously reduce fuel consumption, and meet the most stringent exhaust gas emissions legislation. Whilst SGDI engines can be operated in a homogenous charge mode, the greatest fuel consumption benefit is achieved with unthrottled lean stratified operation. In this mode, fuel is injected late in the compression stroke [1, 2], and

[3]. Stable combustion of ultra lean mixtures with air-to-fuel ratios (AFR) of up to 146:1 have been reported [4].

On the other hand, SGDI engines can suffer from high cycle-to-cycle variability due to the limited amount of time available for proper mixture preparation under stratified conditions [5]. Furthermore, due to the excess oxygen in the combustion chamber at lean operating conditions and a higher mass flow through the engine at part-load, the engine out specific Nitric Oxides (NO_x) emission levels are often higher than in a comparable homogeneous charge direct injection or Port Fuel Injection (PFI) engine. A common measure to reduce the levels of NO_x emissions is the use of re-circulated exhaust gas (EGR). Whether by internal or external re-circulation, EGR reduces the oxygen concentration and increases the specific heat capacity of the charge, thereby leading to a decrease in the peak cylinder pressure and temperature hence a reduction in NO_x emissions. However, increasing the EGR level above 30 % can lead to an increase of particulate emissions, due to an overly rich mixture, and an increase of Hydro Carbon (HC) emissions, due to flame quenching as a result of insufficient local oxygen concentration [6].

Finally, SGDI engines tend towards over-advanced combustion phasing [7] as a result of the close relationship between start of injection and time of ignition plus the inability to retard the start of injection sufficiently (due to subsequent fuel impingement on the piston crown and insufficient mixture preparation). The angle of 50 % mass fraction burned (MFB) lies close to (or even before) top dead centre (TDC). This results in a reduction in thermal efficiency that promotes an increase in the formation of NO_x emissions due to the higher in-cylinder gas temperature and pressure.

One potential solution to mitigate these effects is the use of multiple fuel injections. Advanced injection strategies have the potential to improve the mixture preparation process and, therefore, enhance the combustion stability. In this paper, it will be shown that multiple injection strategies can be utilised to retard the angle of 50 % MFB closer to the thermodynamic optimum. The resulting lower peak combustion temperatures lead to reduced NO_x emissions. The heat release analysis has indicated a greater proportion of pre-mixed combustion with the multiple injection strategy.

2 Concept Description

The Ricardo T-SGDI is a turbocharged gasoline direct injection engine with stratified combustion, multiple injections (via a piezo injector) and high EGR. Figure 1 shows the configuration and the layout of the combustion chamber.

Figure 2 shows the speed-load range potential of using the SGDI combustion system in a highly boosted engine. The effective stratified NA operating range remains unchanged at up to 7 bar BMEP, as this limit is simply defined by the load where the engine approaches a lambda 1 operating region at WOT. The fuel

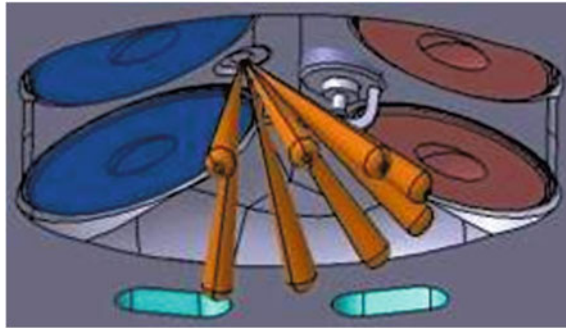


Fig. 1 Central injector position

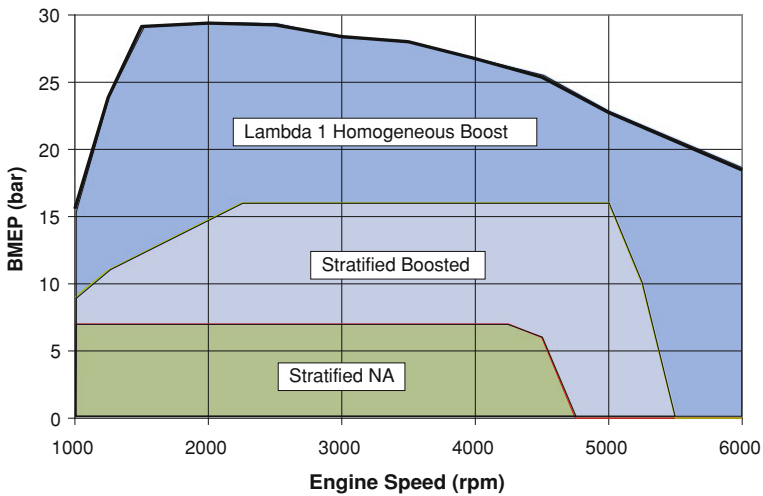


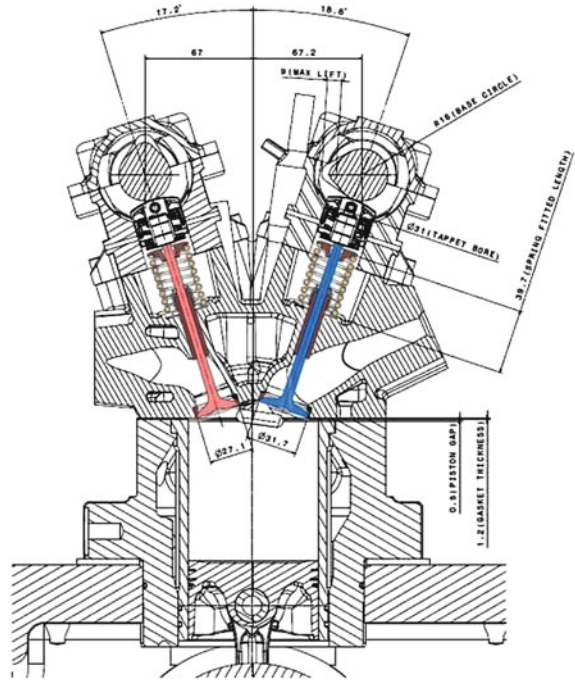
Fig. 2 SGDI boosted engine speed-load range versus operating mode

consumption benefit through stratified operation in this area of the map is considerable.

However, when combined with a boosting system, the late injection stratified operating region can be extended to more than 15 bar BMEP since the airflow through the engine is increased above the levels for an NA engine thus a higher load is achieved before approaching lambda 1. Furthermore, the Multiple Injection Variable Injection Separation (MIVIS) strategy with injections during both intake and compression stroke (to realize a mixture of very lean homogeneous and stratified operation) leads to an extended lean burn part of the engine map. The result is the ability to remain unthrottled throughout most of the engine map.

Above the stratified boosted operating region the injection timing reverted to an early injection to ensure the air utilization was maximized whilst also enabling the best possible in-cylinder charge cooling. Using multiple injection strategies the

Fig. 3 Cross-sectional view of SGDI cylinder head



fuel can be injected late enough so that the majority of it evaporates after IVC whilst still maintaining a fully homogenous mixture at SOC. This leads to a significantly lower end of compression temperature and subsequently lower exhaust gas temperature. Thus, there is no requirement for over-fuelling to cool the charge even at high boost levels. Testing showed the engine can be operated at up to 30 bar BMEP without any kind of additional knock mitigation technology and with comparatively advanced 50 % MFB timing.

3 Experimental Set-Up

The research engine utilizes a spray-guided direct injection combustion system. The cylinder heads featured a transverse orientation spark plug and injector layout, i.e. the axis of the spark plug and injector was perpendicular to the crankshaft axis. A piezoelectric actuated, outwardly opening injector was located between the intake valves, whilst the spark plug was located between the exhaust valves. Both injector and spark plug were slightly tilted towards the cylinder axis (Fig. 3). Table 1.

Table 1 Test engine specifications

Type	4 stroke
Combustion System	Spray guided gasoline direct injection
Bore × Stroke (mm)	86 × 86
Compression ratio (-)	11.5:1 for NA SCRE, 10.7:1 boosted SCRE & multi
Injector	Piezoelectric actuation, outwardly opening pintle
Max. fuel pressure (bar)	230

4 Design of Experiments

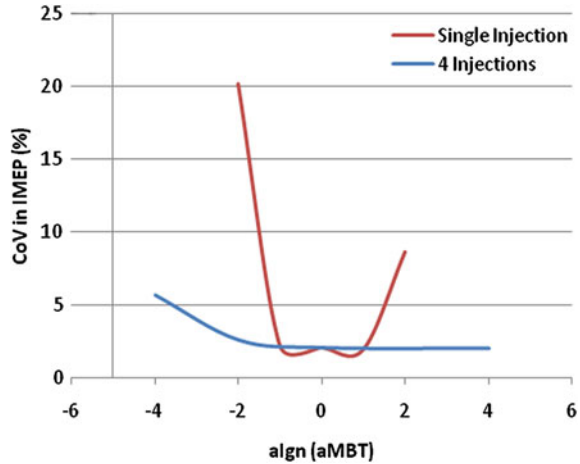
The multi-cylinder engine was designed with the capability to investigate a wide range of variables. A summary of the key Design of Experiments (DoE) variables used is given here:

- Engine speed (600–6700 rev/min)
- Start of Injection Timing (15–330° BTDCF)
- Fuel Quantity/Load (0.1–1.5 ms)
- Fuel pressure (10–220 bar)
- Inlet Valve Timing (MOP 90–130° ATDC NF)
- Exhaust Valve Timing (MOP 90–130° BTDC NF)
- Throttle (5–100 %)
- Inlet Valve Lift (3 mm & 9 mm)
- Exhaust Valve Lift (3 mm & 9 mm)
- External EGR rate (0–35 %)
- Spark Energy (35–85 mJ)
- Multiple Strike Spark (1–20 with independent control)
- Multiple injections (5 independent injection quantities [min. 0.1 ms] and timing on SCRE; up to 15 pre-spark and 5 post spark injections for multi-cylinder)
- Boost (up to 3 bar (abs))

Using the DoE method, a series of screening experiments were undertaken on the SCRE to understand the sensitivities of all the variables on key responses such as fuel consumption, emissions and combustion stability. Subsequently, a global engine model was created that was used to reduce the number of variables and their ranges for further experiments. The variables for the multiple injection DoE presented here were:

- Engine speed
- Engine load (by means of total injection duration)
- EGR level
- Start of the first injection (SOI)
- Number of injections
- Injection profile shape factor

Fig. 4 Comparison of combustion stability for single and multiple injection strategies at 1500 rev/min and 4.1 bar IMEP



Throughout the testing, the EGR rate was varied between 0 and 35 % and the throttle position was maintained at wide open position. Where high levels of EGR could not be achieved, some throttling was applied to promote EGR flow. The maximum EGR rate was also limited by the threshold for combustion stability evaluated during the testing. The threshold was set well above the target of 5 % Coefficient of Variation (CoV) in Indicated Mean Effective Pressure (IMEP) to ensure that trends were captured that could be examined with the DoE model. Finally, the start of the first injection timing was varied between 20 and 50°C A BTDCF. For all speeds and loads within the model space, the calibration was optimized to minimize fuel consumption subject to a constraint for combustion stability (using the CoV in IMEP model) and a target NO_x level. The results are discussed below.

5 Test Results

The combustion performance of the engine was evaluated for single and multiple fuel injection strategies. The variation in CoV in IMEP, used as a measure of operating stability, was compared to an angle of ignition relative to the angle of ignition for minimum advance for best torque timing (MBT at 0°). The results are shown in Fig. 4 for both a single and multiple injection case at an engine speed of 1500 rpm with wide open throttle conditions. The engine load was 4.1 bar IMEP and a shape factor of 1.9 was applied to the multiple injection profile; the mid injection quantity was 1.9 times the quantity of the first and last injections. Under these operating conditions, the engine operation is more sensitive to ignition angle (after MBT) for a single injection event than for an injection strategy with four injections. For a multiple injection strategy, stable operation (defined here as a

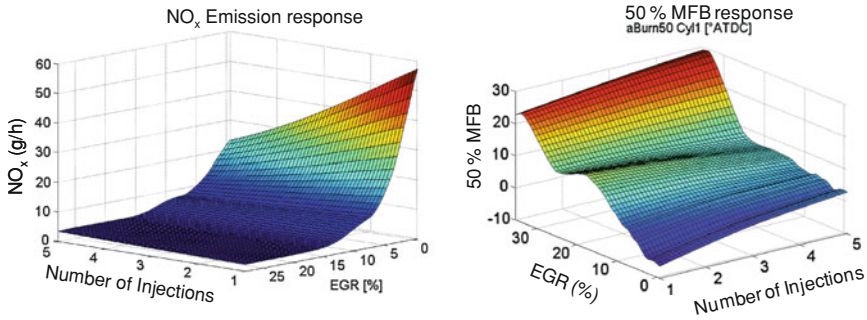


Fig. 5 Comparison of NO_x, angle of 50 % MFB and % EGR with number of injections at 2000 rev/min, 1.5 bar BMEP

CoV in IMEP below 5 %) could be achieved for a wider ignition angle range compared to single injection.

In the presented case, the range of ignition angle for stable operation could be increased from 2°CA for a single injection to 7°CA when applying four injections. The analysis of the combustion data showed that multiple fuel injections can be used to phase the combustion. The improvement in thermal efficiency is associated with a lower peak cylinder gas pressure (42 bar compared to 53 bar) and, therefore, a lower peak cylinder gas temperature. As a result, the NO_x emissions at this point were reduced by 70 %. A further improvement in NO_x emissions and thermal efficiency was achieved by using external EGR, with a more retarded angle of 50 % MFB.

Figure 5 shows that the NO_x emissions were reduced by increasing the number of injections, resulting in a later 50 % MFB and increasing the combustion duration. The reduction in the maximum in-cylinder pressure (P_{Max}) and the resulting changes in the combustion parameters increased confidence in the accuracy of the interpolated DoE models. The fuel consumption was observed initially to show a small improvement with the increased number of injections, due to more favourable angle for 50 % MFB. However, this was compromised due to an increase in the B10-90 burn duration.

Figure 6 shows an early set of fuel consumption results taken from the multi-cylinder SGDI engine versus Brake Mean Effective Pressure (BMEP) at 2000 rev/min engine speed. It can be clearly seen that the lean NA operating window achievable was up to 7 bar BMEP; in fact it was possible to operate up to $\lambda = 1$ with a late injection window. Using typically two and then five close-spaced late injections to maintain engine stability, a further improvement in BSFC was measured versus NA stratified operation. A best BSFC of 221.8 g/kWh was achieved at 6.9 bar BMEP. Finally, a new MIVIS strategy has been under development to enhance the BSFC in the region approximately 8–15 bar BMEP. From Fig. 6 it can be seen that choosing the optimum stratified operating strategy as the load increases, i.e. NA stratified, to boosted stratified, to MIVIS, can result

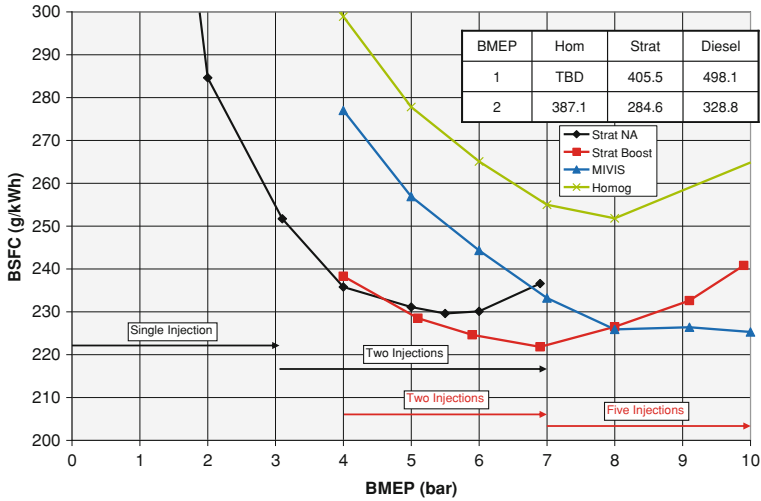


Fig. 6 SGDI multi cylinder fuel consumption versus load at 2000 rev/min

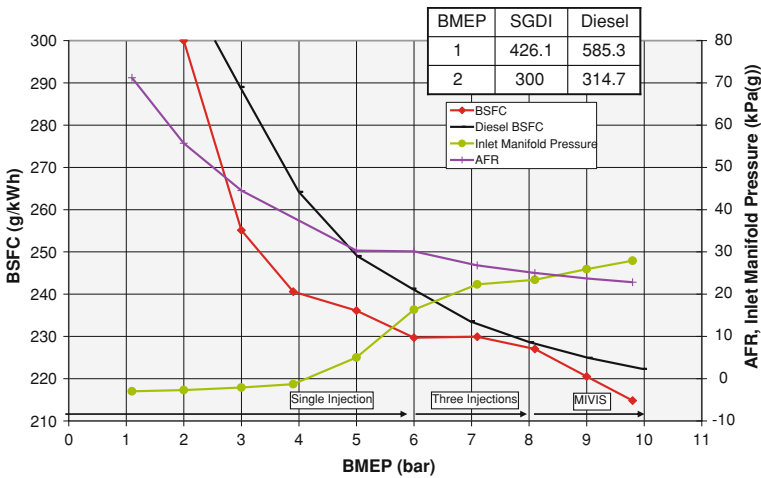


Fig. 7 SGDI multi-cylinder fuel consumption at 2500 rev/min

in a considerable improvement in engine BSFC throughout the load range versus conventional gasoline engine operation.

Figure 7 shows fuel consumption results taken from the multi-cylinder SGDI engine versus BMEP at 2500 rev/min engine speed. As with the 2000 rev/min stratified engine operation BSFC shown in Fig. 6, at 2500 rev/min for best results there is a transition from stratified NA via stratified boosted to MIVIS operation as the load increases.

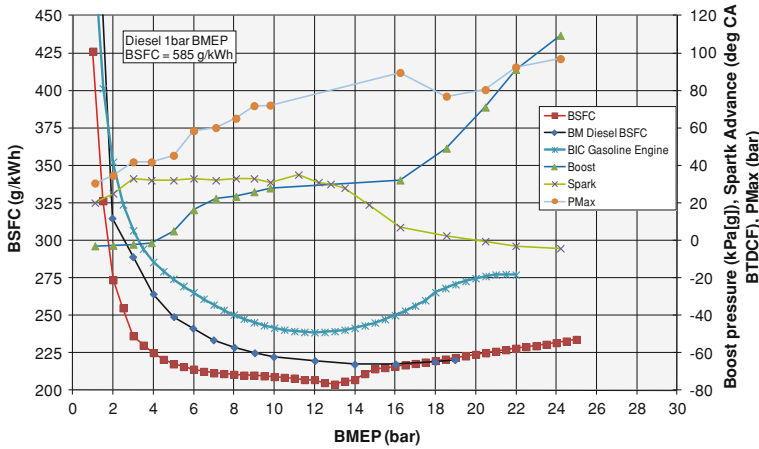


Fig. 8 SGDI multi-cylinder fuel consumption at 2500 rev/min

The best BSFC achieved was 215 g/kWh at about 10 bar BMEP, giving a calculated brake thermal efficiency of 39 %. For comparison purposes, the BSFC of a benchmark 1.6 l EU4 diesel engine is shown in the figure, and as at 2000 rev/min, the SGDI engine was superior up to the BMEP levels shown in the graphs.

Figure 8 shows a wider load range of data taken from the SGDI engines at 2500 rev/min engine speed. The best point in BSFC is at 13 bar BMEP with 203 g/kWh, this means a brake thermal efficiency about 41 %. The BSFC from 16 bar BMEP upwards was achieved with conventional homogenous lambda 1 operation. Comparing the higher load BSFC with other benchmark gasoline engine data showed that it was still excellent, and was enabled through the SGDI’s ability to operate without fuel cooling throughout the load range, with good knock mitigation and relatively advanced spark timing.

Using the advanced multiple injection strategies up to 10 bar BMEP it was possible to set the spark to Minimum Spark Advance for Best Torque (MBT) and thus achieve high efficiency with very low BSFC. Figure 8 also shows the mean peak cylinder pressure versus BMEP, with levels starting at 30 bar at 1 bar BMEP, rising to 72 bar at 10 bar BMEP, and the highest figure of 97 bar at 24 bar BMEP. Despite the WOT operation across the entire load range, and the reasonable levels of boosting above 16 bar BMEP, it can be seen that PMax remained more than acceptable: well below the design limit of 110 bar and considerably below what was measured from the benchmark diesel engine.

Figure 9 shows the energy balance of the homogeneous naturally aspirated mode compared with the boosted stratified mode at 2500 rev/min, 8 bar BMEP. The heat losses of the stratified mode are significantly reduced due to the insulation of the surrounding air and the exhaust energy losses are reduced by turbocharging.

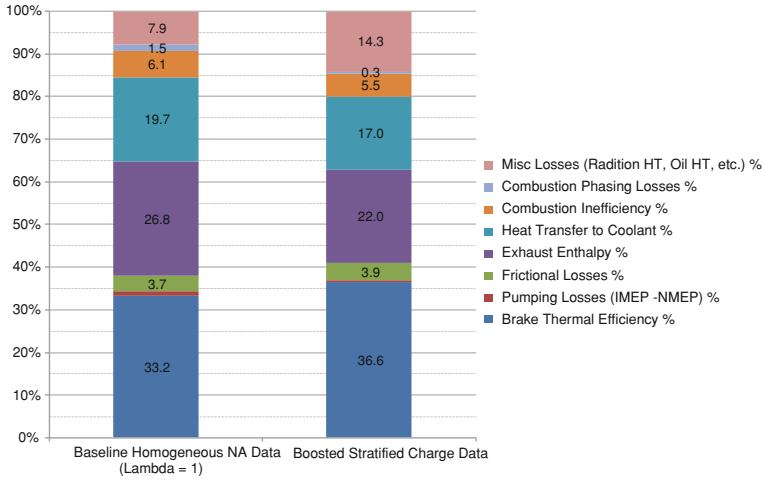


Fig. 9 Energy balance at 2500 rev/min, 8 bar BMEP

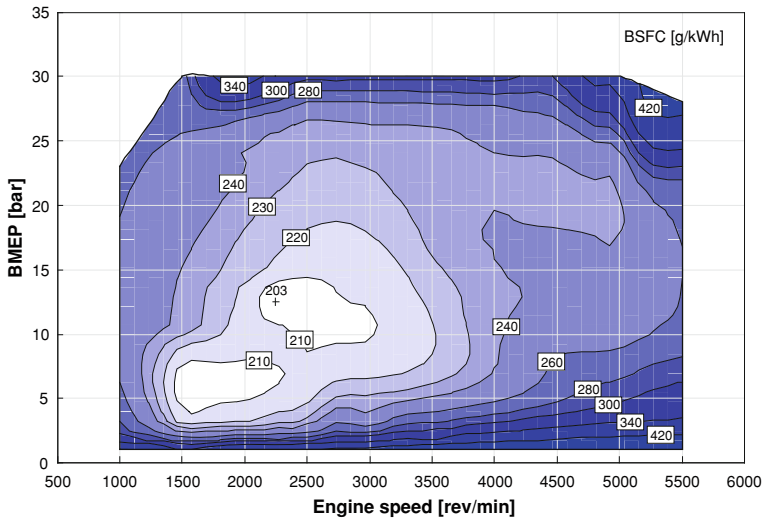


Fig. 10 BSFC map Ricardo T-SGDI engine

The BSFC map in Fig. 10 shows best in class fuel consumption values along the road load: even better than seen in modern diesel engines. The maximum brake thermal efficiency was achieved at 2200 rev/min and about 12 bar BMEP with BSFC being recorded at 203 g/kWh.

6 Summary and Conclusions

In the last four years Ricardo has developed a multi-cylinder gasoline DI engine with stratified combustion and multiple injections. Ricardo started in 2008 with literature studies, engine benchmarking, design studies, fuel spray characterization and CFD spray and combustion modelling. The next step was the combustion system development by means of an optical single cylinder engine in order to design the combustion system in detail, a definition of the control system and a validation of the CFD models.

With the results of the single cylinder research engine a 4 cylinder engine was built to demonstrate the real potential of the T-SGDI concept. An in-house design of experiments process was utilized to determine the optimal operating parameters for part load lean stratified operation in a spray guided gasoline direct injection engine with respect to fuel consumption, engine operation stability and engine out emissions. The variables for the DoE were engine speed, engine load by means of total fuel quantity, number of injections, injection shape factor and EGR rate.

It could be shown that the application of multiple injections can be used to retard the 50 % MFB angle to a thermodynamic optimized position when compared to a single injection event. As a result, the peak in-cylinder gas pressures and temperatures were lower, leading to reduced engine out NO_x emissions. Furthermore, the range of ignition angle for stable combustion could be increased, when using multiple injections compared to a single injection event. The combustion system has been proven to be comparable to market leading systems, with robust stratified NA engine operation to loads of up to 7 bar BMEP and engine speeds of up to 4500 rev/min.

Combining advanced multiple injection strategies with boosting enabled the stratified operating range to be extended to over 15 bar BMEP, with a further significant improvement in fuel consumption to class leading levels. As the load exceeded 8 bar BMEP the MIVIS injection strategy was superior, in fuel consumption terms, to the multiple injection strategy used at the lower loads and on the single cylinder engine in order to minimize NO_x emissions. The extended WOT part load operating region also increased the mass flow through the engine when compared to a conventional throttle boosted gasoline engine: this resulted in an improved turbocharger transient response, which is a key issue particularly for downsized gasoline engines where the downsizing could be as high as 50 %. Finally, the robustness of the SGDI combustion system to the highest loads, in combination with the latest boosting and future knock mitigation technologies, has been clearly demonstrated.

With these measures the T-SGDI engine achieves a maximum brake thermal efficiency about 41 % at 2500 rev/min and 13 bar BMEP. The best fuel consumption at 2000 rev/min, 2 bar BMEP is about 278 g/kWh.

Acknowledgments The authors would like to thank all the team members who have contributed to the work reported here and the directors of Ricardo for permission to publish this paper.

References

1. Lückert P, Waltner A, Rau E, Vent G, Schaupp U (2006) Der neue V6-Ottomotor mit Direkteinspritzung von Mercedes-Benz, MTZ, pp 830–840
2. Schwarz Ch, Schünemann E, Durst B, Fischer J, Witt A (2006) Potentials of the spray-guided BMW DI combustion system. SAE Paper 2006-01-1265
3. Spicher U, Kubach H, Häntsche JP (2006) Die strahlgeführte Direkteinspritzung als Zukunftskonzept für Ottomotoren. MTZ-Konferenz Motor, Stuttgart
4. Reissing J (1999) Spektroskopische Untersuchungen an einem Ottomotor mit Benzin-Direkteinspritzung. Dissertation, Universität Karlsruhe (TH)
5. Kneifel A, Heidenreich Th, Velji A, Spicher U (2007) Experimentelle und numerische Untersuchungen an einem Ottomotor mit strahlgeführter Direkteinspritzung zur Erweiterung des Schichtladekennfeldes durch Aufladung, Berichte zur Energie- und Verfahrenstechnik, Schriftenreihe Heft 7.1, Haus der Technik
6. Sarikoc F, Kettner M, Velji A, Spicher U, Krause A, Elsässer A (2006) Potential of reducing the NOx emissions in a spray guided DI gasoline engine by stratified exhaust gas recirculation (EGR). SAE Paper 2006-01-1261
7. Basshuysen R (2008) Ottomotor mit Direkteinspritzung, Chapter 3, 2. Auflage. Vieweg + Teubner, Wiesbaden
8. Bäcker H, Tichy M, Lohfink C (2006) Einspritzstrategien für direkteinspritzende Benzinmotoren, Direkteinspritzung im Ottomotor

Gray Cast Iron Cylinder Head Thermal Mechanical Fatigue Analysis

Jun Li, Pengcheng Wang, Xiaojuan Cui, Kang Li and Rentao Yi

Abstract Heavy duty diesel engine cylinder head crack is one of the main problems which affects engine durability. With the increasing requirements for better engine performance, less exhaust emission and lower fuel consumption, increased combustion pressure and elevated temperature make the engine cylinder head to be the most complicated and critical part for the engine design. The objective of this study was to apply cylinder head TMF simulation method to improving cylinder head structure and increasing its TMF life. Machined samples of gray cast iron (GJL 250) taken from cylinder head were used in material tests and material properties under different temperature were obtained from the tests. The finite element model of the whole assembled engine cylinder head/block was built and stress-strain curve were gained by cylinder head cold-hot cycle simulation. Then, cylinder head TMF life was calculated and different life prediction approaches were compared with each other and also with test results. Simulation and test results were generally in good agreement. The position of minimum TMF life from Ostergren approach, which considers mean stress effect, agree quite well with the early crack position of the cylinder head. By optimizing the cylinder head structure, TMF life of the cylinder head was greatly increased. Design standards, the best ratio between valve diameter and the distance of valve centers, maximum valve angle and optimized cylinder head wall, were set for the design of cylinder head of gray cast iron. Based on the creation of the whole assembled FE model of engine cylinder head/block and the application of the cold and hot cycle analysis and life prediction, TMF life of gray cast iron cylinder head were guaranteed at engine early development stage, and time and cost were saved.

F2012-A01-042

J. Li (✉) · P. Wang · X. Cui · K. Li · R. Yi
China FAW Group Corporation, R&D Center,
No.1063, Chuangye Street, Changchun, China
e-mail: lj_qy@faw.com.cn

Keywords Gray cast iron · Cylinder head · Finite element (FE) · Thermal mechanical fatigue (TMF) · Plastic strain

1 Introduction

One of the main durability problems of heavy duty diesel engine is cylinder head crack at the valve bridge area. With the rising demand for engine efficiency and exhaust emissions standard, increased combustion pressure and elevated temperature make cylinder head to be the most critical and complicated part for engine design. Up to now the material used for heavy duty diesel engine cylinder head include gray cast iron (GJL 250), compacted graphite iron (CGI) and molybdenum cast iron. Compared with CGI and molybdenum cast iron, gray cast iron has the advantages of simpler casting process and easier to machine and is still the main material of choice for the cylinder head of heavy duty diesel engine. This research studied TMF life of 4-valve, single part cylinder head and described how to make cylinder head TMF life satisfactory at the early design stage. Through the development of heavy duty diesel engine, advanced cylinder head for heavy duty diesel engine were designed and manufactured in FAW China.

2 Gray Cast Iron (GJL 250) Material Properties

The chemical composition of gray cast iron is listed in Table 1. Machined samples from cylinder head were used in material tests and material properties under different temperature were obtained from the tests. Figures 1, 2 and 3 are material stress–strain curves in tension and compression, heat conduction and expansion coefficient.

Gray cast iron is brittle in tension. This is because the microstructure of the material, which consists of a distribution of graphite flakes in a steel matrix. The graphite flakes are as stress concentrators and decrease mechanical properties in tension. On the other hand, the graphite flakes transmit stresses in compression and material response in compression is governed by its steel matrix alone. So yield stress in compression is a factor of three or more higher than the yield stress in tension [1].

The effects of temperature can be seen from Figs. 1, 2 and 3. Visibly change of stress–strain curve from 300 to 400 °C is in Fig. 1. Thermal conductivity goes down and thermal expansion coefficient goes up as temperature rises in Figs. 2 and 3. This tells how important to control the temperature of cylinder head during engine working. All the material properties will be used as input data in cylinder head TMF life simulation.

Elastoplastic constitutive model of gray cast iron is one of the most important issues that should be thinking for the TMF life simulation. Elastic behavior was

Table 1 Chemical compositions of gray cast iron

C (%)	Si (%)	Mn (%)	P (%)	S (%)	Cu (%)	Cr (%)
3.4	2.05	0.6	<0.05	<0.05	0.5	<0.2

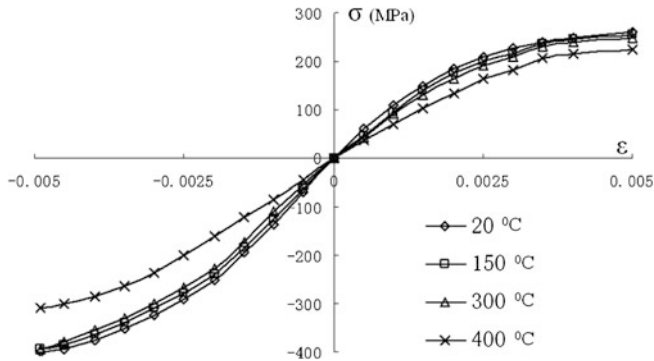


Fig. 1 Stress-strain curve of gray cast iron at different temperatures

Fig. 2 Thermal conductivity of gray cast iron at different temperatures

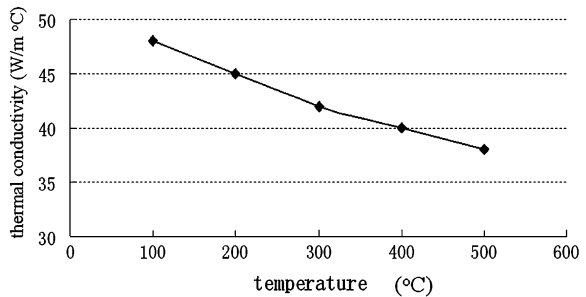
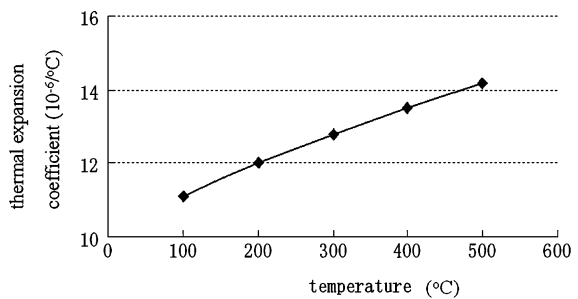


Fig. 3 Thermal expansion coefficient of gray cast iron at different temperatures



assumed linear isotropic with the same stiffness in tension and compression. Plastic behavior was assumed to satisfy rate-independent model. The yield condition is used to decide stress state for plastic deformation. A composite yield surface describes the different yield condition in tension and compression. The

maximum principal stresses govern the tension yielding and the deviator stresses govern the compression yielding. It is expressed as follows [1–4].

Stress tensor at a coordinate system can be represented as:

$$\sigma_{ij} = \begin{bmatrix} \sigma_x & \tau_{xy} & \tau_{xz} \\ \tau_{xy} & \sigma_y & \tau_{yz} \\ \tau_{xz} & \tau_{yz} & \sigma_z \end{bmatrix} \quad (1)$$

Decompose stress tensor (1) into a sum of two parts, equivalent pressure stress (2) and deviator stress (3),

$$\begin{bmatrix} \sigma_m & 0 & 0 \\ 0 & \sigma_m & 0 \\ 0 & 0 & \sigma_m \end{bmatrix} \quad (2)$$

in which:

$$\sigma_m = \frac{1}{3}(\sigma_x + \sigma_y + \sigma_z)$$

$$s_{ij} = \begin{bmatrix} \sigma_x - \sigma_m & \tau_{xy} & \tau_{xz} \\ \tau_{xy} & \sigma_y - \sigma_m & \tau_{yz} \\ \tau_{xz} & \tau_{yz} & \sigma_z - \sigma_m \end{bmatrix} \quad (3)$$

$\sigma_1, \sigma_2, \sigma_3$ represent σ_{ij} three principal stresses, so the first invariant of stress tensor or equivalent pressure stress,

$$p = -\sigma_m = -\frac{1}{3}(\sigma_x + \sigma_y + \sigma_z) = -\frac{1}{3}(\sigma_1 + \sigma_2 + \sigma_3) \quad (4)$$

The second invariant of the deviator stress tensor,

$$J_2 = \frac{1}{6} [(\sigma_1 - \sigma_2)^2 + (\sigma_2 - \sigma_3)^2 + (\sigma_3 - \sigma_1)^2]$$

and the third invariant of the deviator stress tensor,

$$J_3 = (\sigma_1 - \sigma_m)(\sigma_2 - \sigma_m)(\sigma_3 - \sigma_m)$$

For studying plastic deformation, different stress invariant was used in defining plastic model. The three stress invariants p, q, θ were chosen to define gray cast iron plastic model, in which,

$$q = \sqrt{3J_2} \quad (5)$$

$$\cos(3\theta) = \frac{3\sqrt{3} J_3}{2 J_2^{3/2}} \quad (6)$$

In formula (4), (5) and (6) p, q, θ are used for studying yield locus of gray cast iron. Yield function can be expressed,

$$f(p, q, \theta, \chi) = 0$$

where χ is the hardening parameter. Yield surface on $p - q$ plane has intersection of two loci, given by

$$f_t = \frac{2}{3} \cos \theta \cdot q - p - \sigma_t(\chi) = 0$$

and

$$f_c = q - \sigma_c(\chi) = 0$$

In which f_t and f_c are respectively the yield condition in tension and compression on $p - q$ plane, $\sigma_t(\chi)$ and $\sigma_c(\chi)$ are current yield stress in tension and compression and can be obtained from uniaxial tension and compression tests.

Nonassociated flow rule [2, 3, 1] is considered for the plastic model and plastic potential defines the relation of the increase of plastic strain with the stress. If $G(p, q, \chi)$ is plastic potential and it has,

$$d\varepsilon_{ij}^{pl} = d\lambda \frac{\partial G}{\partial \sigma_{ij}}$$

$d\lambda$ is nonnegative plastic multiplier. ε_{ij}^{pl} is plastic strain. On the $p - q$ plane, plastic potential $G(p, q, \chi)$ will take one of the two values, which is potential G_t in tension region and potential G_c in the compression region. The relations are,

$$\begin{aligned} \frac{(p - G_t)^2}{a^2} + q^2 &= 9G_t^2 & p < \frac{\sigma_c}{3} \\ q &= 3G_c & p \geq \frac{\sigma_c}{3} \end{aligned}$$

where a relates to $\sigma_t(\chi)$ and $\sigma_c(\chi)$.

Gray cast iron hardening rule is different from ordinary steels. Graphite flakes have unlike effect on hardening behavior in tension and compression. User supplied material subroutine for gray cast iron kinematic hardening model should apply to the analysis under reversed cyclic loading [3, 5].

3 The Load Case and Boundary Conditions of Cylinder Head FE Analysis

The load cases in FE analysis include cold and hot cycle to simulate the different circumstance of cylinder head. The cold load case is applying assembly forces at room temperature. The assembly forces include bolt pre-tension and valve seat and guide overlap. Maximum value of bolt force and overlap were used in the load case. Hot load case contains assembly force, high temperature field and maximum

fire pressure. Fire pressure in reality is high frequency force applied on the fire deck of cylinder head. Here assumes that fire pressure acts as a continuous force on cylinder head.

Heat boundary conditions are from CFD simulation. The coolant and gas temperature and the heat convection coefficients on the wall surface were gained at maximum rated power of the engine.

In the heat transfer of coolant side not only heat convection was taken into account, but also sub-cooling of nucleate boiling effect at the areas of low velocities of coolant flow and high heat flux. Total coolant heat flux at an area were composed of convection component and nucleate boiling component, written as [5–8],

$$q_w = q_{fc} + q_{nb} = h_{fc}(T_w - T_b) + h_{nb}(T_w - T_s)$$

T_w, T_b, T_s are wall surface temperature, coolant temperature and coolant saturation temperature. h_{fc} and h_{nb} are forced convection heat transfer coefficient and nucleate boiling heat transfer coefficient.

Combustion and gas exchange process is very complicated in combustion chamber. Recent developed combustion and gas exchange CFD simulation make it possible to get distributed heat flux, gas temperature and convection heat transfer coefficient in combustion chamber. Because gas temperature and heat transfer coefficient changed continuously in combustion chamber, averaged gas temperature and heat transfer coefficient were used to FE mesh. The averaging of heat flux is written as,

$$\bar{q} = \frac{1}{720} \int_0^{720} q(\phi) d\phi = \frac{1}{720} \int_0^{720} h(\phi)(T_g(\phi) - T_w) d\phi = \bar{h}(\bar{T}_g - T_w)$$

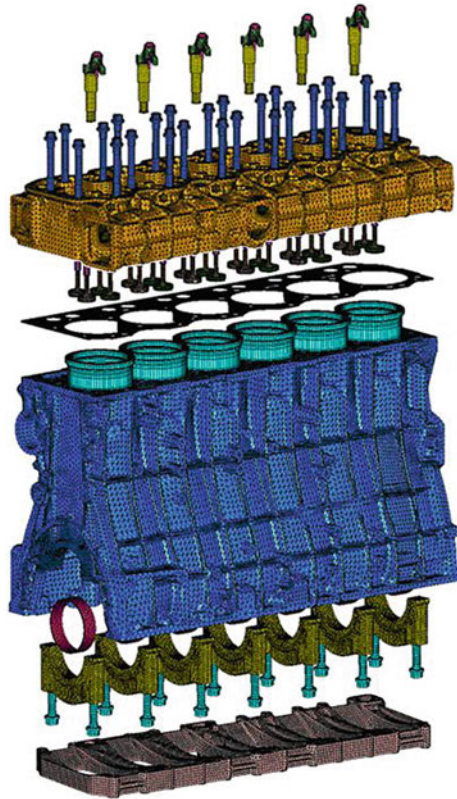
where $h(\phi)$ and $T_g(\phi)$ are, instantaneous crankshaft angle dependent, heat convection coefficient and gas temperature on an element surface. T_w is the wall surface temperature. \bar{h} and \bar{T}_g are average heat transfer coefficient and gas temperature at one engine cycle and,

$$\bar{h} = \frac{1}{720} \int_0^{720} h(\phi) d\phi$$

$$\bar{T}_g = \frac{1}{\bar{h} \cdot 720} \int_0^{720} h(\phi) T_g(\phi) d\phi$$

Self-made software for coupling between ABAQUS and CFD code was used to map the boundary conditions.

Fig. 4 Whole assembled engine cylinder head/block FE model



4 Cylinder Head FE Analysis and Results

Whole assembled engine cylinder head/block FE model is shown in Fig. 4. Cylinder head and block use quadratic tetrahedron element. Other parts, such as bolt, valve seat, valve guide, gasket and fuel injector, use linear brick and triangular prism element. Nodes number are about 3 million and elements number are about 1.6 million. Finer mesh should be built on fire deck of the cylinder head. Contact surface were created at contact areas, like bolt, valve seat, valve guide, injector and gasket with cylinder head. Master surface should cover slave surface and may have less nodes than slave surface, which can make convergence easier. Different friction coefficient should be given at different contact area. The contour of results will be smoother if the surface of brick element is used as master surface. FE model and contact surface of cylinder block should be simplified. Cylinder head material properties are temperature dependent, including elastic modulus, heat conduction and expansion coefficient. Because gray cast iron has different yield stress in tension and compression, stress and plastic strain curve from uniaxial tests in tension and compression are taken as gray cast iron hardening input data for the plastic model. Gasket of the cylinder head and other parts may use linear material

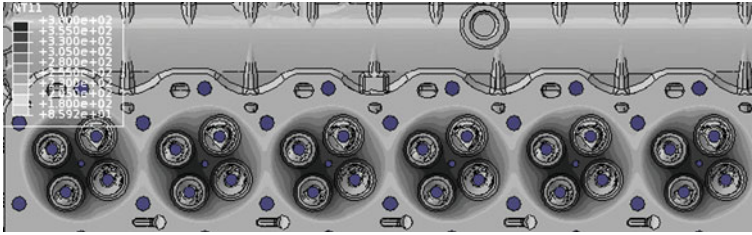


Fig. 5 Cylinder head temperature field

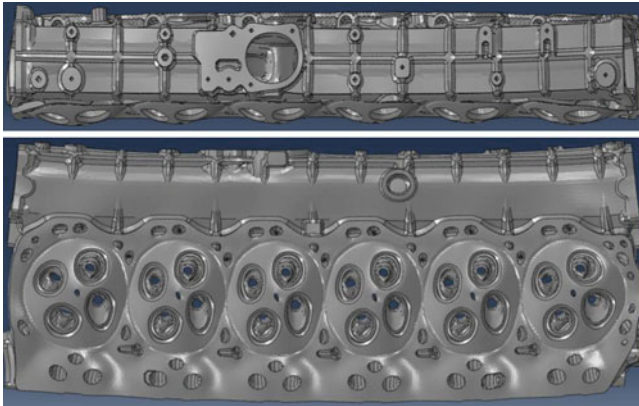


Fig. 6 Cylinder head deformation in assembly plus thermal load case *Upper* side view, *Lower* bottom view. Scale factor: 200)

properties. Gasket linear properties should be got from gasket loading and unloading curves. Thickness and gaps of the gasket should be given at different gasket areas, which include bead, stopper and body areas.

Figure 5 shows temperature field of whole cylinder head. Figure 6 displays whole cylinder head deformation in assembly plus thermal load case, the upper one is side view and the lower one is bottom view. Figure 7 exhibits the maximum tensile stress in assembly load case (A) and plastic strain in assembly plus thermal and firing load case (B) on the fire deck of inner cylinder head.

5 TMF Life Prediction Approaches

Cylinder head endures out of phase TMF, Which means that maximum stress occurs at the low temperature and minimum stress at high temperature. Figure 8 (left) shows the stress–strain curve of a node at the valve bridge of the cylinder head in the first cold and hot cycle. Three approaches, as follows, were used for life prediction.

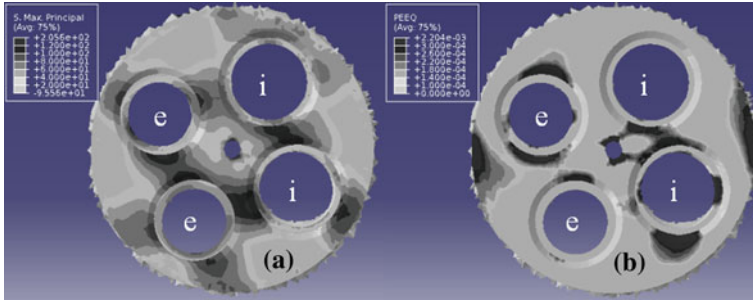


Fig. 7 Maximum principal stress in assembly load case (a) and Plastic strain in assembly plus thermal and firing load case (b) on the fire deck of inner cylinder head

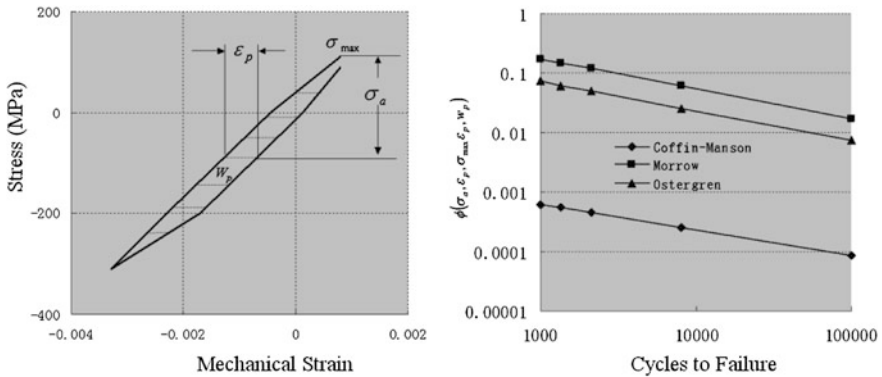


Fig. 8 Local stress versus strain curve (left) and $\epsilon_p, \sigma_{Max}\epsilon_p, w_p$ versus life curves (right)

Coffin-Manson equation [9, 10], relating plastic strain with life,

$$\epsilon_p = A_1(N_f)^{C_1} \tag{7}$$

Ostergren equation [11], which is based on Coffin-Manson equation and include average stress effect on life,

$$\sigma_{Max}\epsilon_p = A_2(N_f)^{C_2} \tag{8}$$

Morrow equation [12], correlating plastic strain energy in a cycle with life,

$$W_p = A_3(N_f)^{C_3} \tag{9}$$

where N_f is the number of cycles to failure. A_i and C_i are material coefficient. σ_{Max} is the maximum stress. ϵ_p is plastic strain. w_p is plastic strain energy in a cycle, which is the inside area of the stress–strain curve.

Through tests and simulations, Fig. 8 (right) demonstrates $\epsilon_p, \sigma_{Max}\epsilon_p$ and w_p versus life curves of gray cast iron cylinder head in logarithmic scales.

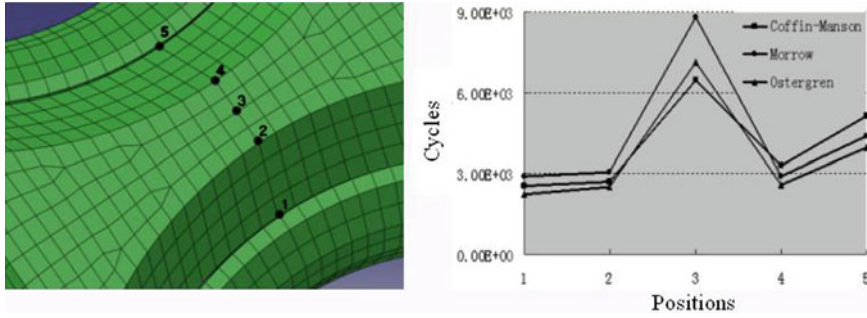


Fig. 9 Comparison of number of cycles from three TMF life prediction approaches

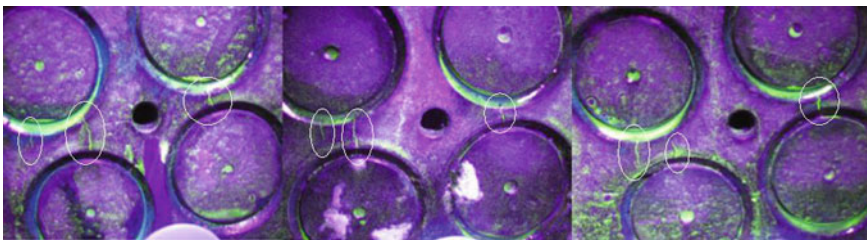


Fig. 10 The position of cracks at cylinder head

6 Comparison of TMF Life Prediction Approaches for Gray Cast Iron Cylinder Head

Figure 9 shows the life of 5 nodes at middle section of intake valve bridges from above three TMF life prediction approaches. The three approaches give close results at nodes 1, 2 and 4 from simulations. In prototype engine tests, the average number of cycles to failure is about 3,800, which is higher than simulation results. Figure 10 gives the crack position of cylinder head in engine tests.

Figure 11 displays the contour of life from the calculation of the three TMF life prediction approaches, in which Coffin-Manson and Morrow approaches showed the lowest number of cycles at the bottom of the intake valve where, however, has no crack. The contour in the middle of Fig. 11 from Ostergren approach showed the lowest number of cycles more corresponding to engine test results in Fig. 10. The reasons can be found from Fig. 7, which showed the tensile stress in cold load case and plastic strain in hot load case, and in fact the crack occurred at where both tensile stress and plastic strain were high. Because gray cast iron has lower tension strength, $\sigma_{Max}\epsilon_p$ represent the coactions of maximum tensile stress and plastic strain on cylinder head in cold and hot load cycle. Figure 12 shows the life distribution on fire deck of the whole cylinder head from Ostergren approach. Because inner cylinder (2, 3, 4 and 5) are more constrained than outer cylinder

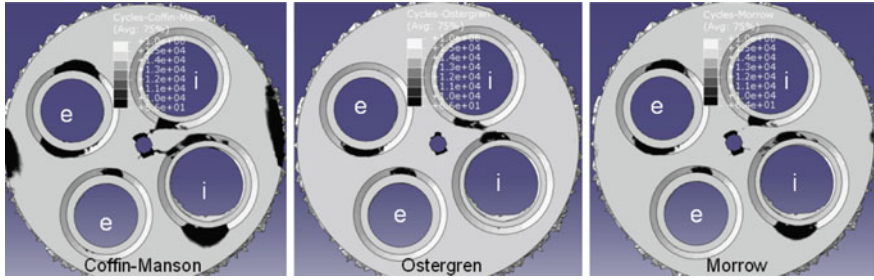


Fig. 11 Contour of number of cycles of inter cylinder head from the three TMF life prediction approaches

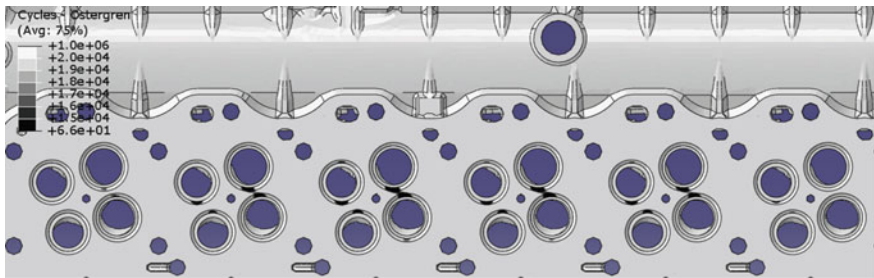


Fig. 12 Contour of number of cycles from Ostergren approach on the fire deck of the whole cylinder head

(1, 6) in thermal load. The different life between inner and outer cylinder can be recognized in the whole cylinder head TMF life simulation and engine tests indicated all cracks were in inner cylinders.

7 The Improvement of Cylinder Head Structure

Three main aspects to improve cylinder head TMF life were summarized below.

7.1 The Optimum Ratio

Because valve bridges of cylinder head endure tensile stress in cold load case and compression stress in hot load case, apparently the width of the valve bridge influences the magnitude of stress here. From Fig. 6 the bottom intake port became ellipse under thermal load and the ellipse’s major axis was approximately vertical to the valve bridge. This kind deformation increased compression stress at valve bridges. So both the width of the valve bridge and the diameter of valve port are

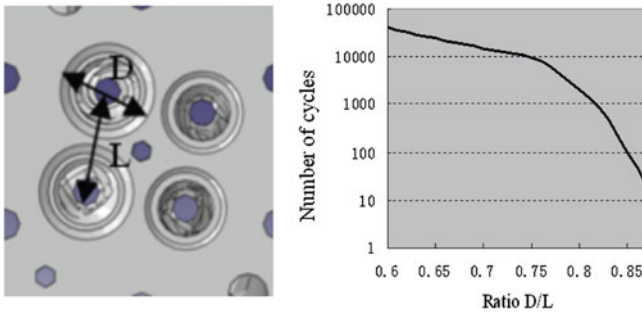
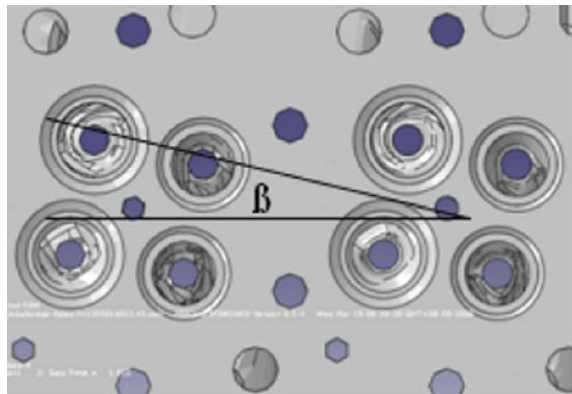


Fig. 13 The optimum ratio of valve port diameter to the distance between the valve centers

Fig. 14 Valve port angle



the most important design parameters affecting the TMF life of cylinder head. The ratio of D to L was used for studying TMF life of cylinder head. D is the diameter of valve port and L is the distance between the center points of the valves (Fig. 13 left). Our research, through simulations, studied how the different ratios affect on TMF life of cylinder head and indicate that life drop quickly at certain value of the ratio (Fig. 13 right). The optimum ratio is 0.75 for gray cast iron cylinder head. For other material, which has a better TMF strength than gray cast iron, the ratio may be a little higher.

7.2 The Maximum Angle

For heavy duty diesel engine, usually diamond shaped valve seat are used in cylinder head (Fig. 14). The layout of the four valves in each cylinder head portion has effect on the cylinder head TMF life. Increasing the angle β can reduce the compression stress at exhaust–exhaust and intake–intake valve bridge under the

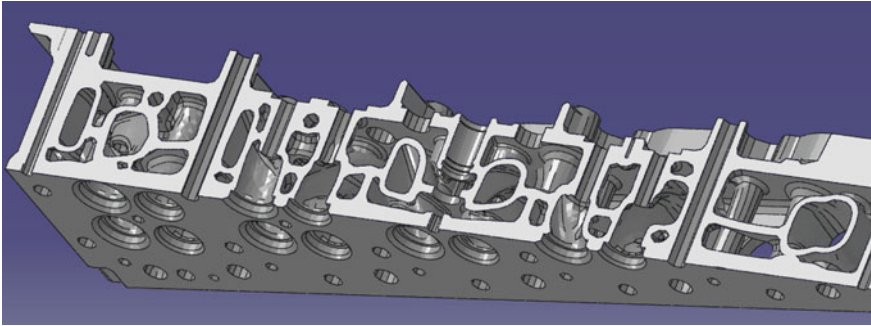


Fig. 15 Section of cylinder head with optimum wall thickness and geometry

thermal load. So increasing the angle β ($0 \leq \beta \leq 45$) as much as possible from the view of all cylinder head parts distribution, the TMF life of cylinder head will have a certain increase.

7.3 The Optimum Geometry for Fire, Middle and Upper deck and Air Passage Wall

Cylinder head section, which showed double cooling jacket and fire, middle and upper deck, is in Fig. 15. Structure optimization was done for the head, which include optimizing the distance between the fire and the middle deck and optimizing the shape and thickness of the three decks and air passage wall. The best distance between the fire and the middle deck is as close as possible on the premise of ensuring good cooling flow. In this way, arc shaped middle deck gave the strongest support to the fire deck. Thickness changed at different sections of the fire deck, which have the thickness of exhaust-exhaust bridge about 5 mm thinner than the other area of the deck, can bring good cooling conditions for the fire deck and keep the maximum temperature of the cylinder head under 350 °C. Upper deck need to have good stiffness to support cylinder head bolt force. Air inlet and outlet passage wall need to have moderate stiffness as assistant to sustain both assembly force and fire pressure. Inlet passage wall need to be thicker than outlet passage wall, especially the section under the middle deck, for the intake-intake bridge was usually narrower and its temperature was lower than exhaust-exhaust bridge.

The contribution, on life prolonging, of each structure optimization with Osgren approach is shown in Fig. 16. The optimum ratio showed the most benefit. The valve seat angle didn't give much improvement because they could only turn a small angle. The optimum wall displayed an adequate rising of life.

The improved cylinder head has passed all TMF tests and, up to now, no any cracks occurred in customer application.

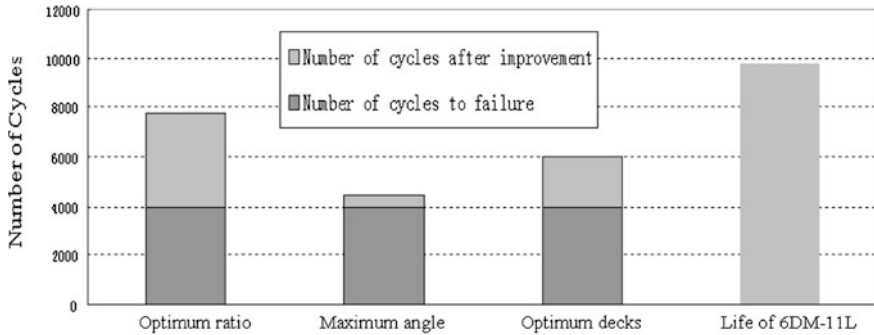


Fig. 16 Contribution on TMF life of each structure improvement

8 Conclusion

Based on the creation of the whole assembled FE model of engine cylinder head/block and the application of the cold and hot cycle analysis and life prediction, cylinder head TMF life simulation gave an adequate results compared with the tests. Ostergren approach gave a right crack position for minimum life. Design standards, the best ratio between valve diameter and the distance of valve centers, maximum valve angle and optimized cylinder head wall, were set for the design of cylinder head of gray cast iron. Through cylinder head structure improvement and optimization, cylinder head TMF life increased twice as much as the life before. Whole cylinder head TMF life simulation have improved the quality of cylinder head design, reduced engine development time and saved cost.

References

1. ABAQUS Finite element software theory manual. Abaqus 6.11, 4.3.7
2. Hjelm HE (1994) Yield surface for grey cast iron under biaxial stress. *Trans ASME J Eng Mater Technol* 116(2):148–154
3. Josefson BL, Stigh U, Hjelm HE (1995) A nonlinear kinematic hardening model for elastoplastic. *Trans ASME J Eng Mater Technol* 146/117
4. Altenbach H, Stoychev GB, Tushtev KN (2001) On elastoplastic deformation of grey cast Iron. *Int J Plast* 17:719–736
5. Zieher F, Langmayr F, Jelatancev A, Wieser K (2005) Thermal mechanical fatigue simulation of cast iron cylinder heads. SAE 2005-01-0769
6. Chen JC (1963) A correlation for boiling heat transfer to saturated fluids in convective flow. ASME Paper No. 63-HT-34
7. Steiner H, Kobor A, Gebhard L (2005) A wall heat transfer model for subcooled boiling flow. *Int J Heat Mass Transf* 48:4161–4173
8. Torregrosa A, Olmeda P, Degraeuwe B, Reyes M (2006) A concise wall temperature model for DI diesel engine. *Appl Therm Eng* 26:1320–1327
9. Manson SS (1952) Behavior of materials under conditions of thermal stress. National Advisory Committee on Aeronautics, Report 1170

10. Coffin LF (1954) A study of the effects of cyclic thermal stresses on a ductile metal. *Trans Am Soc Mech Eng* 76:931–950
11. Ostergren WJ, Whitehead JR (eds) (1979) *Methods for predicting material life in fatigue*. American Society of Mechanical Engineers, New York
12. Feltner CE, Morrow JD (1961) Microplastic strain hysteresis energy as a criterion for fatigue fracture. *J Basic Eng ASSME* 83:15–22

Development of FAW 2.0 L Turbocharged Gasoline Direct Injection Engine

Jun Li, Jincheng Li, Yanfeng Gong, Haie Chen, MeiLan Qu, Jinyu Liu, Wei Li, Chunyu Xia, HuiLi Dou, Lei Fu, Xian Li and Tiejun Shen

Abstract Chinese passenger cars market is facing the transition from PFI to GDIT. In a predictable future, PFI engine will still dominate the market. The authors developed a direct injection turbocharged (GDIT) 2.0 L gasoline engine based on a port fuel injection turbocharged (PFIT) engine. The combustion system hardware was optimized by CFD simulations. Thermodynamic calculations were carried out to confirm the performance of turbocharger and the air exchange management system design. The reduced wall thickness design method of block was used and the low friction loss technologies such as Physical Vapor Deposition (PVD) and Diamond-Like Carbon (DLC) were also adopted for engine design. The optimized construction design reduced the engine's gross weight about 2 kg. The friction loss reduced 10 %. The GDIT engine's lowest BSFC reaches 238 g/kWh. The GDIT engine's BSFC at 2,000 rpm 2 bar BMEP reaches 373 g/kWh. The rated power of the engine reaches 145 kW. The maximum torque reaches 280 Nm at the speed of 1,500 r/min.

Keywords Gasoline direct injection · Development · Combustion system · Performance · Emission

F2012-A01-043

J. Li (✉) · J. Li · Y. Gong · H. Chen · M. Qu · JinYuLiu · W. Li · C. Xia · H. Dou · L. Fu · X. Li · T. Shen
China FAW Co., Ltd R&D Center, Changchun, China
e-mail: lj_qy@faw.com.cn

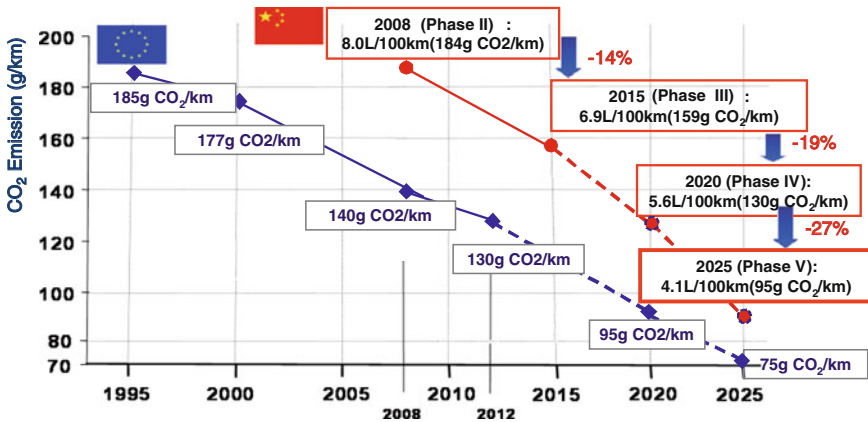


Fig. 1 Comparison of China and EU CO₂ emission trends

Fig. 2 FAW H7 profile



1 Introduction

On December 30 2011, Chinese government announced the new fuel consumption evaluation methods and targets for passenger cars (GB 27999—2011) which also called phase III fuel consumption regulation. The new regulation requires Chinese passenger cars company average fuel consumption reduces about 15 % to 6.9 L/100 km. The advanced low carbon technologies have to be adapted to new generation internal combustion engines in order to meet the regulation limits (Fig. 1).

FAW developed Hong Qi saloon car for military review of china 60th anniversary in 2009. The historic event indicated the beginning of FAW strategy to enter high quality passenger car market.

The new Hong Qi H7 installed PFI V6 engine started to SOP in middle of 2012. In order to enhance H7 car's quality and meet the phase III fuel consumption limits, FAW developed 1.8 L/2.0 L GDIT engine platform. The 2.0 L GDIT is the



Fig. 3 FAW GDIT engine family

Table 1 Parameters of engines based on 0.5L combustion system

Engine type	1.8PFIT	2.0PFIT	1.8GDIT	2.0GDIT	V6 2.5	V6 3.0
B*S (mm)	84*81	84*90	84*81	84*90	84*75	84*90
Displacement (L)	1.796	1.995	1.796	1.995	2.494	2.993
CR (-)	9.3:1	9.3:1	10.3:1	10.3:1		
Valves number (-)	16	16	16	16	24	24
Rated power (kW)	125	145	132	145	150	170
Speed for rated power (r/min)	5,500				6,300	6,000
Max. torque (N.m)	235	260	250	280	242	300
Speed for Max. torque (r/min)	2,000–4,000		1,500–4,000		3,000	
Min. BSFC at full load (g/kW.h)	276	263	263	253	276	263
BSFC 2,000 r/min 2 bar BMEP (g/kW.h)	395	385	392	371	410	377
Fuel supply (-)	PFI	PFI	GDI	GDI	PFI	PFI
Peak injection pressure (bar)	4	4	150	150	4	4
Peak combustion pressure (bar)	90	90	110	110	70	80
Emission (-)	CN IV/V	CN IV/V	CN V	CN V	CN V	CN V

first engine type and the development process has been finished. The SOP time is February 2013 [1] (Fig. 2).

2 Engine Concept Design

For improving passenger cars fuel economy and increasing the vehicles competitiveness, FAW set up “Blue Way” strategy in 2011. By 2015, the engine platform will be upgraded from PFI to GDI. GDI engines listed in Fig. 3 will cover almost

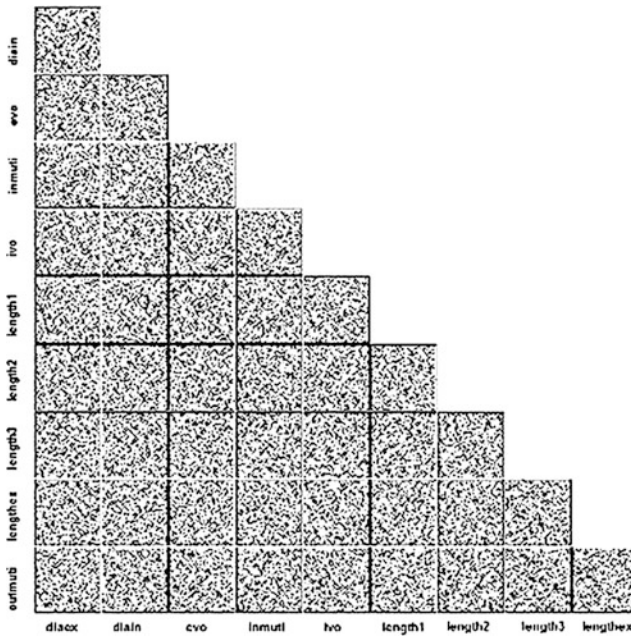


Fig. 4 Parameter selection of DoE

all FAW passenger cars and fuel consumption values of the vehicles that installed GDIT engines will be 8–15 % less than phase III limits. 2.0 L GDIT is the first GDI engine for production.

To meet the requires of common application and low cost production, a 0.5 L gasoline combustion system was developed and all the V type engines and 1.8/2.0 L engines are derived from this combustion system. Table 1 lists the engines parameters. The common combustion system design also realise the issue that GDI and PFI engines product in one line.

According to acceleration requirement for the vehicle, the rated power and maximum torque are set as 145 kW and 280 Nm for GDIT engine. Combustion system optimization and low friction technologies were used.

3 Combustion System Development

3.1 Thermodynamic Calculation

The variable parameters of the engine’s gas exchange system include camshaft phases, valve lifts, length and diameter of inlet and exhaust pipes, inlet pipe plenum volume, et al. The calculation points by GT-Power will exceed thousand

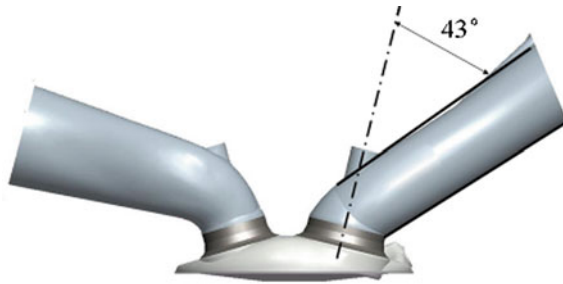


Fig. 5 Inlet and exhaust port design

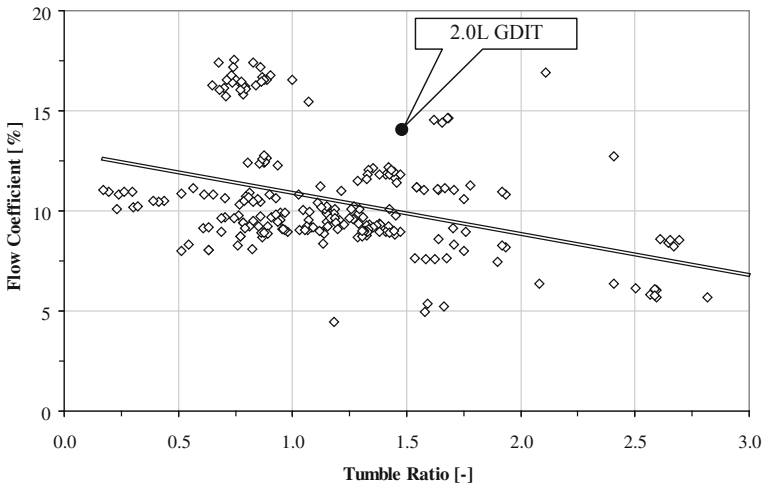


Fig. 6 Inlet port flow characteristics

when optimizing these parameters as the traditional optimized method even if two or three levels are selected for each parameter. For the first time, the DoE method was used for engine thermodynamic calculation. Figure 4 list the parameters selected for analysis. DoE method reduces the simulation process duration and reduces the time of engine development.

3.2 Inlet/Exhaust Port Development

High tumble ratio is helpful for excellent mixing of air and fuel so that achieving fast combustion spread in combustion chamber. But the inlet port flow efficiency can not be reduced too much, which will result in the engine power loss. The port was defined as shown in Fig. 5 according to several times optimization calculation

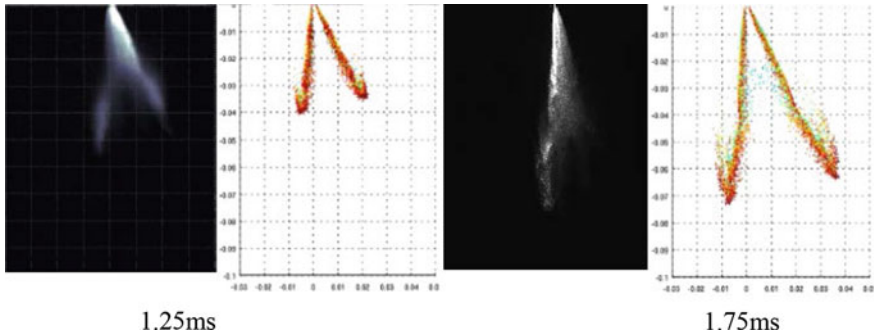


Fig. 7 Spray cone angle and penetration distance comparison between CFD and spray picture

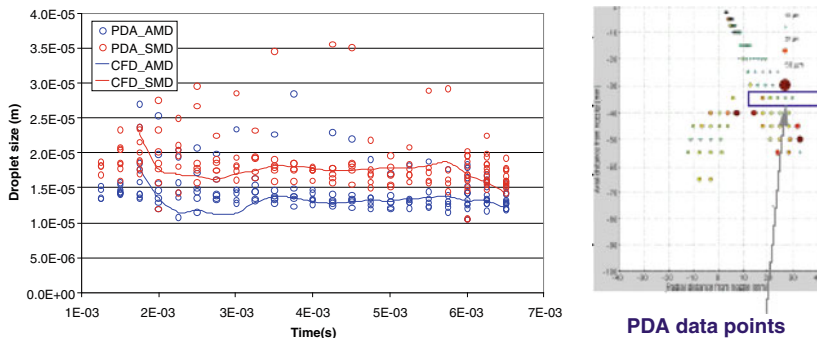


Fig. 8 SAMD and AMD comparison between CFD and PDA measure results

and rig tests. The bottom of the inlet ports keep straight and the angle between inlet port and inlet valve is defined as 43 deg. The upgraded inlet ports design realise the balance between high tumble ratio and high flow efficiency shown as Fig. 6. The inlet air flow speed is distributed between 95 and 100 m/s, and the outlet air flow speed between 90 and 95 m/s.

3.3 CFD Simulation

For side injector layout combustion system, soot emissions will be caused by fuel impacting on intake valves, piston top, and cylinder liner. The oil dilution will also happen when cylinder liner wetting. In cylinder CFD can simulate the process of fuel to air mix and support the optimization of combustion system parameters [2, 3].

In order to improve the accuracy of CFD simulation for GDIT in cylinder process, the spray model of Star-CD was calibrated by spray test in constant volume vessel. The simulation results shown in Figs. 7 and 8 indicate that the



Fig. 9 Piston and fuel spray layout

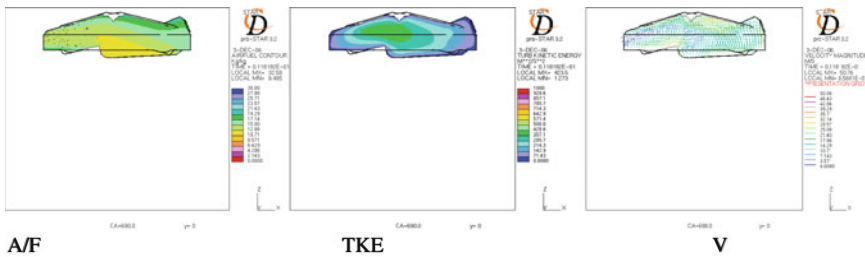


Fig. 10 CFD results for A/F ratio, TKE and gas velocity

calibrated spray model can calculate the spray characteristics such as spray angle, spray penetration distance, fuel droplets size accurately.

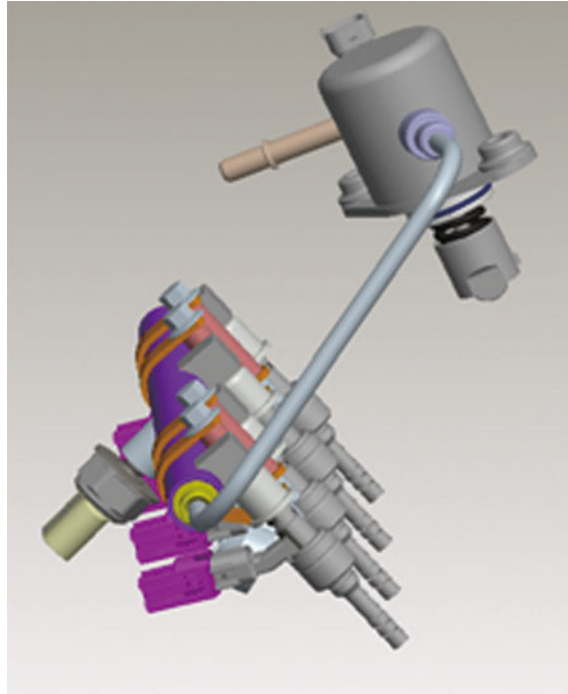
The effects of piston surface geometry and fuel spray layout on in cylinder mixture distribution, turbulent kinetic energy and gas velocity were calculated by the calibrated CFD model. The piston surface shape and spray angles as shown in Fig. 9 were determined through analysing the mixture concentration and gas flow velocity around spark plug at ignition timing.

The lambda value is about 0.8 which is suitable for the flame kernel built up at the ignition time as shown in Fig. 10. The gas velocity and turbulent kinetic energy near spark plug are distributed between 5–25 m/s and 10–200 m²/s² when engine speed are increasing from 1,000 to 5,500 r/min. The parameters described above are suitable for flame kernel formation and combustion flame rapid spread.

3.4 High Pressure Fuel Supply System

The injectors and fuel pump as shown in Fig. 11 with the injection pressure of 150 bar were selected ensuring the fuel supply and atomization quality. The high pressure pump is installed at the rear of the engine and driven by intake camshaft. Three drive lobes and the volume of high pressure chamber keep the fuel pressure fluctuations at a low level, so that different cylinder fuel supply can be ensured

Fig. 11 High pressure fuel supply system



consistently. The six injector holes distribution and fuel injection characteristics reduce the possibility of fuel collision on cylinder chamber surface.

3.5 Turbocharger Matching

The turbocharger should guarantee the vehicle has excellent dynamic performance within a large range of altitude in China. The test results of turbocharger selected by GT—Power shown in Fig. 12 indicates that, the turbocharger will not exceed the surge boundary or speed limits when the engine is operated between sea level and 3,000 m altitude. The operation lines of the turbocharger will also be distributed in the high efficiency region.

The defined turbocharger ensures the engine could reach the maximum torque output of 280 Nm when engine operated between 1,500 and 3,000 r/min even at 3,000 m altitude level. However, the increased altitude will cause the torque loss when engine is operated at low and high speeds as shown in Fig. 13.

The exhaust pulse energy is adopted excellently and the expected engine's transient performance is gained by optimizing the combustion system and turbocharger design. The acceleration time from 0 to 90 % of engine in full load is 1.41 s. at the engine speed of 2,000 r/min shown as Fig. 14.

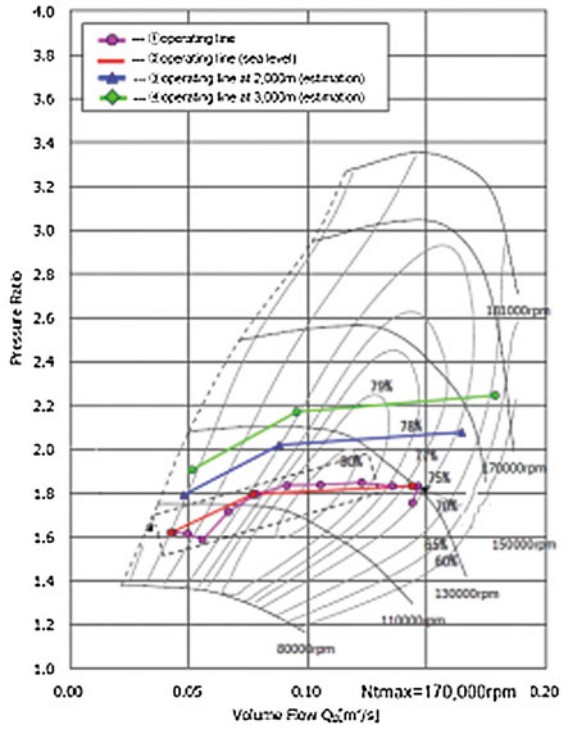


Fig. 12 Efficiency distribution of turbocharger

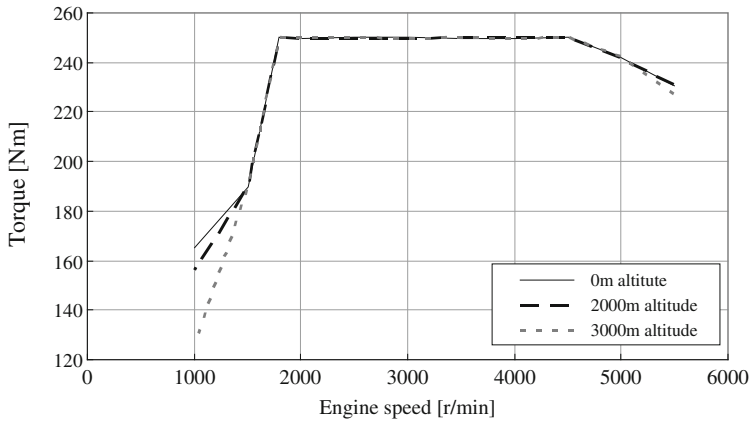


Fig. 13 Effects of altitude on engine performance

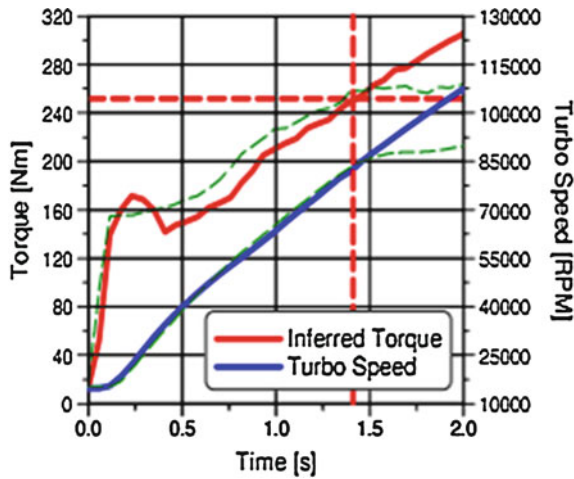


Fig. 14 Engines' transient response characteristics

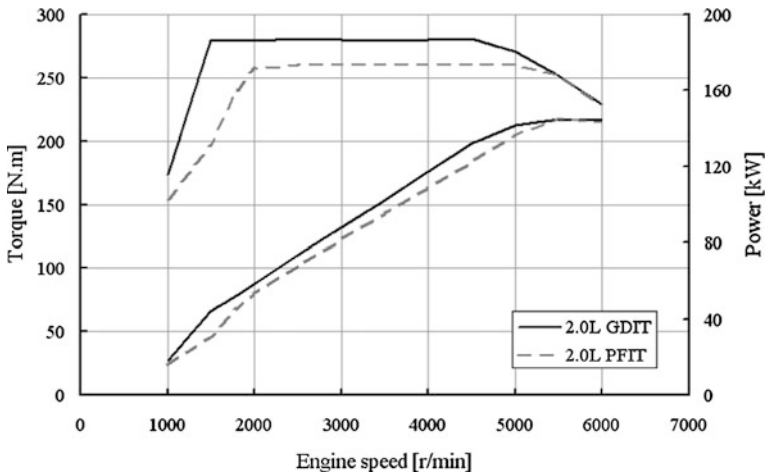


Fig. 15 Engine torque and power figure

3.6 Engine Power and Economy

2.0 L GDIT engine reaches higher torque and power output than that of PFIT engine as shown in Fig. 15 for better knock suppression compared to PFIT engine. The maximum torque of GDIT engine is 8 % bigger than that of PFIT engine. The BSFC at 2,000 r/min, 2 bar BMEP is 4.4 % lower than that of PFIT engine as shown in Fig. 16.

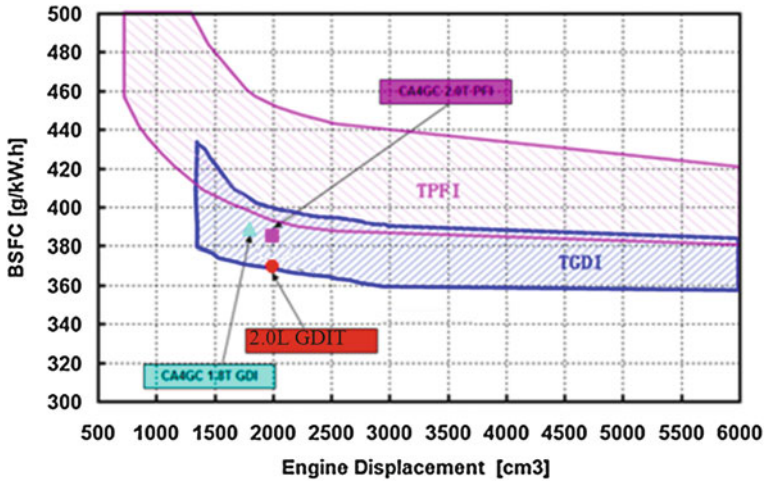


Fig. 16 BSFC at 2000 r/min, 2 bar BMEP

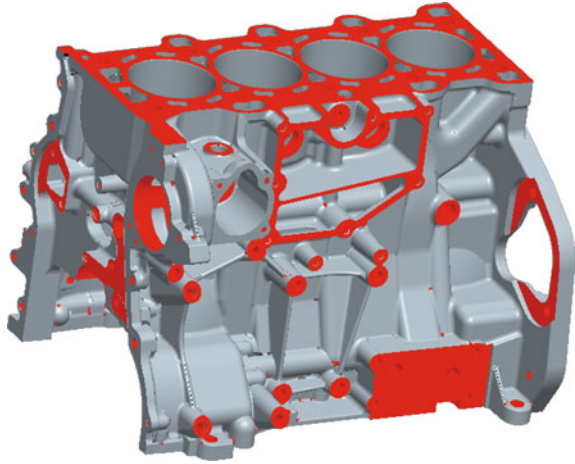
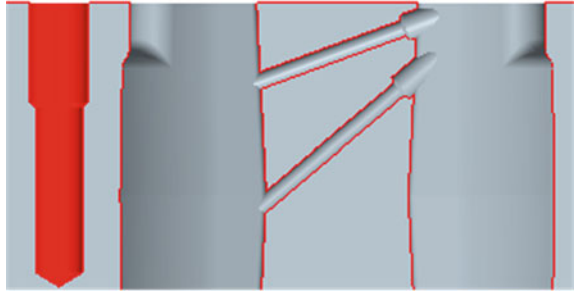
4 Engine Design

The maximum torque and peak pressure of 2.0 L GDIT engine are increased 20 Nm and 20 bar compared with those of PFIT engine. Therefore, the higher mechanical and thermal intensity are expected. Moreover, the lightweight, low friction and low NVH technologies should be considered to meet customers' expectation for low fuel consumption and good drive comfort.

4.1 Cylinder Block

The 3.5 mm wall thickness of the cast iron cylinder block shown as Fig. 17 makes the 2.0 L GDIT engine's mass reduced about 2 kg than that of PFIT engine. The "gantry" structure enables the block can sustain 110 bar cylinder peak pressure and 280 Nm torque output.

Two cooling holes as shown in Fig. 18 were added between the GDIT engine's adjacent cylinders to enhance the cooling effect. The holes slope down from inlet side to the exhaust side and improving the uniformity of the cylinder walls temperature distribution. The maximum temperature of the cylinder wall is less than 200 degrees centigrade and the maximum temperature at the holes is about 127 degrees centigrade shown in Fig. 19 which can both meet the cooling requirement.

Fig. 17 Cylinder block**Fig. 18** Structure of double lean cooling holes

4.2 *Cylinder Head*

In order to realize lightweight design, machine area of the aluminium alloy cylinder head as shown in Fig. 20 was reduced as small as possible. The differentiation of the wall thickness increases the cylinder head nature frequency and stiffness so that reduce the resonance possibility and reduce engine's NVH.

4.3 *Crankshaft and Piston*

PVD coating is used on the piston ring. The material of the first ring was changed from ductile iron to spring steel. The oil ring material was changed to steel so that reduce the mass. The friction loss of the piston group was reduced about 10 % compared with that of PFIT engine.

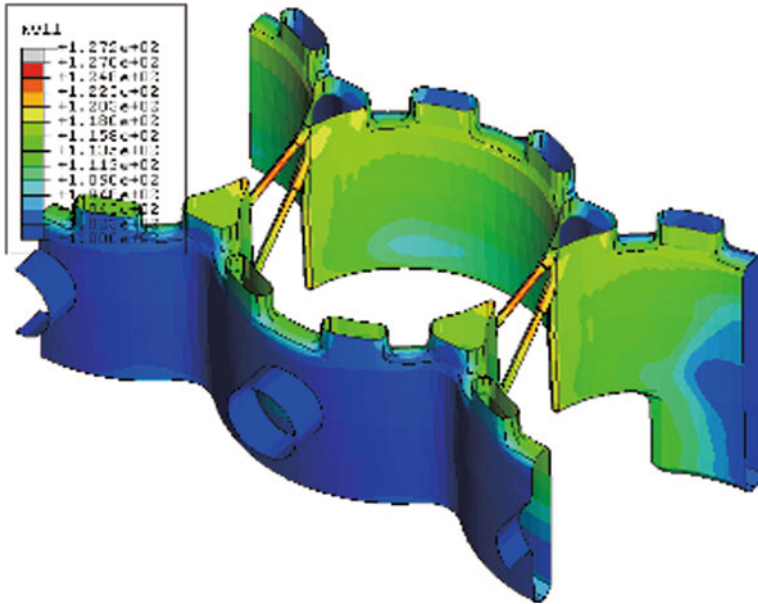
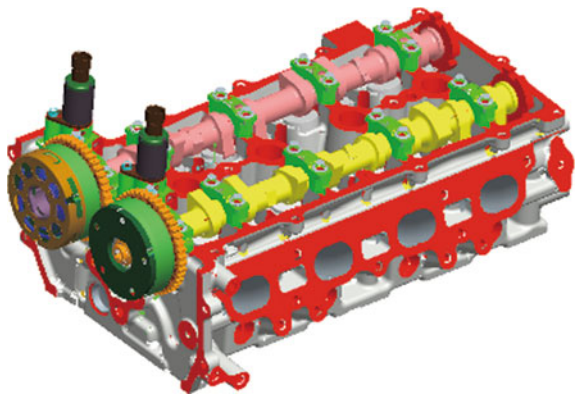


Fig. 19 Cylinder wall temperature distribution

Fig. 20 Cylinder head profile



The mass of the crankshaft group was reduced about 0.5 kg compared with that of PFIT engine for lightweight design of crankshaft arm and balance block in the case of same inertial force balance results (Fig. 21).



Fig. 21 Crankshaft and piston picture

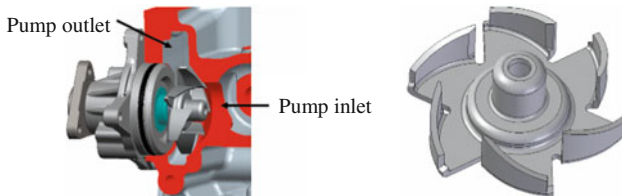


Fig. 22 Coolant pump and impeller profile

4.4 Cooling System

In order to enhance the cooling capacity, a new designed pump impeller was selected as shown in Fig. 22 for the GDIT engine. The impeller height was increased 3 mm compared with that of PFIT engine and the profile of the impeller was optimized by CFD simulation shown as Fig. 23. The flow rate of the new coolant pump increases about 10 % while the efficiency of the pump keeps unchanged.

4.5 Lubrication System

A lubrication oil gallery was added for the high pressure fuel pump based on the PFIT engine's lubrication system as shown in Fig. 24. The gallery on the cylinder head cover connects the oil gallery on cylinder head with the tappet of the high pressure fuel pump. The friction loss of the tappet is reduced more than 20 % and the tappet's durability is also increased by the lubrication.

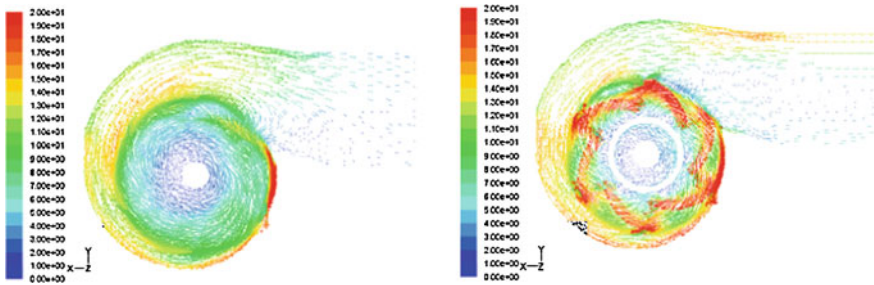


Fig. 23 Comparison of engine coolant pump flow velocity case 1 coolant flow velocity of FPIT pump case 2 coolant flow velocity of GDIT pump

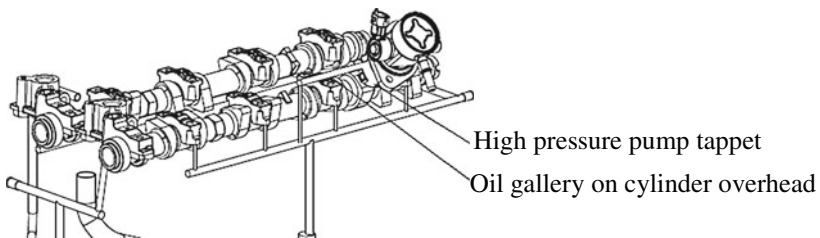


Fig. 24 Lubrication gallery for high pressure pump tappet

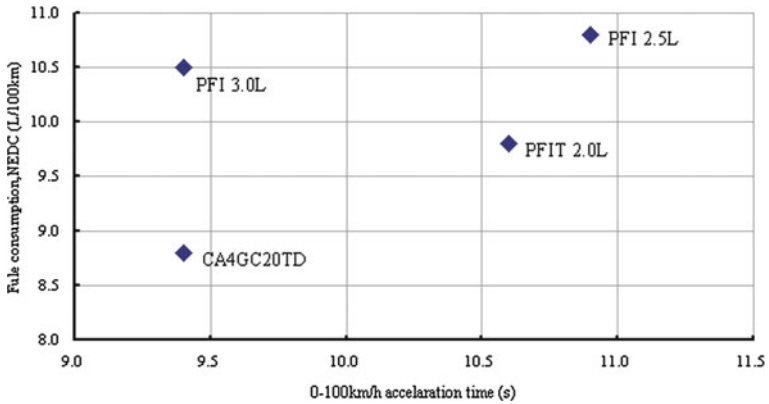


Fig. 25 Vehicle fuel and dynamic performance

5 Vehicle Performance

As a high end passenger car, several engine types are supplied for Hong Qi H7. The mass of H7 is 1815 kg. The fuel consumptions reach 10, 10.5 and 9.8 L/100 km when installed 3.0 L V6 engine, 2.5 L V6 engine and 2.0 L PFIT engine.

All of these three fuel consumption are exceed 9.2 L/100 km, which is the fuel consumption limit of phase III fuel consumption regulation.

The vehicle fuel consumption was reduced to 8.8 L/100 km which is 4 % more lower than the phase III fuel consumption limit when installed the 2.0 L GDIT engine. The vehicle dynamic performance with 2.0 L GDIT engine is also better than that of installing other engines (Fig. 25).

6 Summary

As the next generation of PFIT engine, GDIT engine shows a lot of advantages. GDIT engine can enhance torque output and supply more fun to drive for customers, at the same time, GDIT engine also supply better fuel economy compare with PFIT engine.

2.0 L GDIT engine is the first engine type for FAW “Blue Way” strategy. Double VVT, turbocharger and some advanced technologies are adopted for this engine. The engine will realize SOP in early 2013 and series of GDIT engines will be launched after that.

References

1. Li J, Gong Y, Li K, Dou H (2010) FAW’s low carbon strategies for car powertrain [J]. *Automot Eng* 07:5–8
2. Chen H, Gong Y, Li W, Li K, Li J (2010) Spray simulation of gasoline direct injection engine [J]. *Automot Eng* 01:13–17
3. Li J, Gong Y, Li W, Chen H, Liu J, Li J, Li K, Dou H (2010) Study on combustion characteristics of gasoline direct injection engine [J]. *J Xi’an Jiaotong Univ* 07:15–19

Faw V6 High Performance Gasoline Engine for Executive Class Car

Jun Li, Jincheng Li, Jianlong Song, Jinyu Liu, Weixing Hu,
Yingjie Liu, Tao Yan, Linghai Han, Enwei Jiang,
Zhengyong Liu and Tian Xia

Abstract The first Chinese V6 high performance gasoline engine, named CA6GV, was designed and developed by FAW for its executive class car—“Hongqi”, which is the first executive class car of Chinese brand. Achieving the performance of an executive class car was only the starting point, the development target of the engine is to reach the performance of the state of the art of similar V6 engines world wide. The engine distinguishes itself by dual VCT, variable plenum volume plastic intake manifold, 2 stage double side drive silent chain timing system and all aluminium light weight design, low friction technology and dedicated EMS system calibration, the specific torque and power of the engine reached 100 Nm/l and 57 kW/l separately. The engine also have a very good full load torque curve, it can keep above 90 % maximum torque from 2,000 to 5,500 rpm which can provide the car excellent drivability. At the same time, the engine achieves very good part load fuel consumption and excellent NVH behavior. It can also meets the latest emission standard Euro V.

Keywords V6 · High performance · Gasoline engine · Executive class car

F2012-A01-044

J. Li (✉) · J. Li · J. Song · J. Liu · W. Hu · Yingjie Liu · T. Yan ·
L. Han · E. Jiang · Z. Liu · T. Xia
China FAW Co., Ltd R&D Center, Changchun, China
e-mail: lj_qy@faw.com.cn

1 Introduction

Chinese automotive market developed very quickly in recent years. In the year of 2010, the overall production volume reached 17 million, and 13.5 million are passenger cars. Chinese local manufactures produced 5 million passenger cars last in 2010, but most of them are economic cars. Lack of high performance engine is one of the main reasons for Chinese manufacturer can not produce high level executive cars.

In order to produce its own executive C class cars, FAW decided to develop a V6 engine named CA6GV in the year of 2009, and this engine series includes 2.5 and 3 l version. Most of the up to date gasoline engine technologies such as all aluminum light weight design, inlet and exhaust VCT, variable plenum volume intake manifold, double side silent chain timing system and cylinder deactivation control were introduced in this engine, all these technologies together with dedicated EMS calibration and NVH development enable this engine to be a high performance V6 engine for high level C class car. The CA6GV engine is a key factor for FAW to enter high level end passenger car market in the future [1].

Figure 1 shows the main structure of CA6GV engine.

2 Developing Objectives

The goal of CA6GV engine is aimed to achieve competitive performance of similar world class engines and enable FAW C class car have powerful drivability, good NVH behavior, low fuel consumption and can meet latest EURO5 or even Euro6 emission legislation. The engine developing objectives were set as following:

- (1) Achieving top-level competitive performance of similar world class engines, especially excellent low and medium engine speed torque in order to suit Chinese local drive habit.
- (2) Excellent NVH behavior for “C” class car, especially noise level.
- (3) Low fuel consumption in order to reduce FAW fleet CO2 emission level.
- (4) Achieving more than 10,000 km service interval.
- (5) Low engine weight with high engine robustness.
- (6) Compact engine size especially engine height which can enable the engine to be used in four wheel drive car.
- (7) Meet Euro5 emission legislation and has the potential to meet Euro6 legislation.

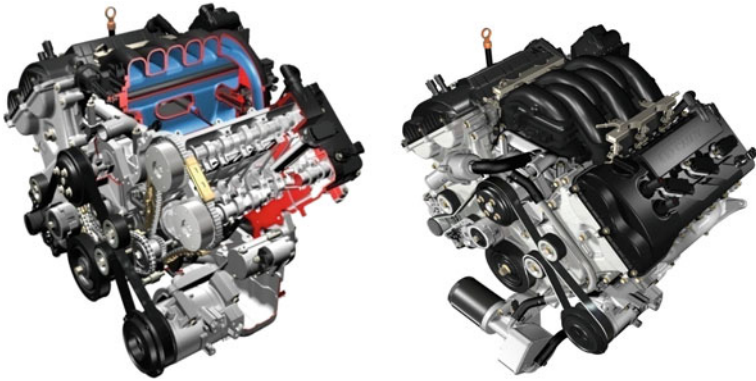


Fig. 1 Over all view of CA6GV engine

3 Engine Concept and Main Technical Features

In order to meet engineering targets, the following concept and technology were introduced into the engine design:

- (1) 90 degree bank angle in order to get smaller engine height, this also enable to develop a 4 wheel driven car much easier.
- (2) Offset Crankpin and small bank offset (19 mm) were adopted in order to obtain compact engine length.
- (3) All aluminum light weight design with 165 kg engine weight.
- (4) In order to obtain outstanding torque characteristic, dual VCT and variable plenum volume intake manifold were adopted, which provided the engine a very good engine torque curve and good fuel consumption. The maximum engine torque of 300 Nm can be reached at 3,000 rpm, and 90 % maximum torque can be kept from 2,000 to 5,500 rpm which can provide the car excellent drivability behavior.
- (5) 2 stage silent chain timing system and balancing shaft were adopted, the first stage is double side driving silent chain and plays an important role for the engine's very good NVH behavior.
- (6) Cylinder deactivation and variable valve lift system were developed and can used as a selective system.
- (7) Combined PFI and GDI combustion system, the engine can be up graded to GDI engine easily or work at PFI + GDI mode.

Engine	2.0 TPFI	2.0 TGDI	2.5 PFI	3.0 PFI	3.0 TGDI	4.0 TPFI	6.0 PFI
Type	I 4	I 4	V6	V6	V6	V8	V12
Bore [mm]	84	84	84	84	84	84	84
Stroke [mm]	90	90	75	90	90	90	90
Disp. [cc]	1995	1995	2494	2993	2993	3990	5986
CR (-)	9.3	10.3	10.3	10.3	10.3	9.3	10.3
Valve No. [-]	16	16	24	24	24	32	48
Rated Power [kW]	145	150	145	170	248	300	300
Rated speed [rpm]	5500	5500	6300	6000	5500	5500	5600
Max. torque [Nm]	260	280	242	300	445	550	530
Speed [rpm]	2000-5000	1800-5000	3000	3000	2500-5000	1700-5000	4000
BSFC@2000rpm 2bar BMEP [g/kW.h]	385	371	390	377	370	380	360
Emission level	CN 5	CN 5	CN 5	CN 5	CN 5	CN 5	CN 5

Fig. 2 Main parameters of FAW gasoline engine family for executive class cars

4 Basic Engine Design and CAE Analysis

The main engine dimensions and performance of CA6GV is as following, as a matter of fact, CA6GV is the third member of FAW engine family for it's "Hongqi" car, including inline four cylinder, V6, V8 and V12 versions, all the members in this family were developed based on same combustion system. In this way, FAW can set up and update the whole engine family very quickly. FAW gasoline engine family for executive class cars are as following (Fig. 2).

4.1 Cylinder Block and Bottom End Design

4.1.1 Cylinder Block

The cylinder block is designed with 90 degree bank angle in order to reduce the engine height, it uses deep skirt concept and cast in iron liner. The block are manufactured by low pressure precision sand casting process which will provide a very flexible design freedom of the block compared with the high pressure casting process. The T7 heat treatment process will provide the block a proper strength and minimum bore distortion and friction. Further more, the casting process was developed dedicatedly in order to get more than 95 % contact area between the liner and the block, this is very important for controlling the bore distortion, abnormal wear of the bore, and oil consumption, but it is very difficult to meet the contact target without high pressure die casting process, so careful casting analysis was done (Fig. 4). In order to get good NVH behavior without increase the weight, the block was reinforced by usable structure such as the oil drain at the two sides of the block and the breather system in the valley, eight side bolts are used to

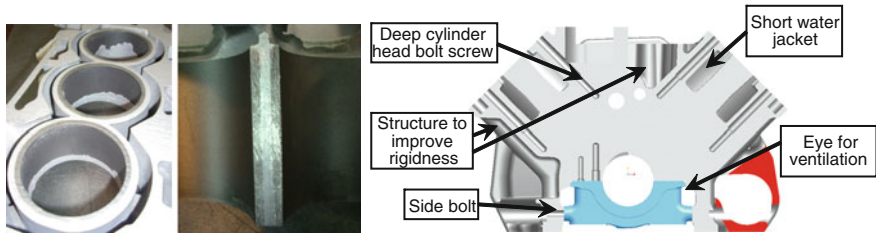


Fig. 3 Structure of CA6GV aluminum block

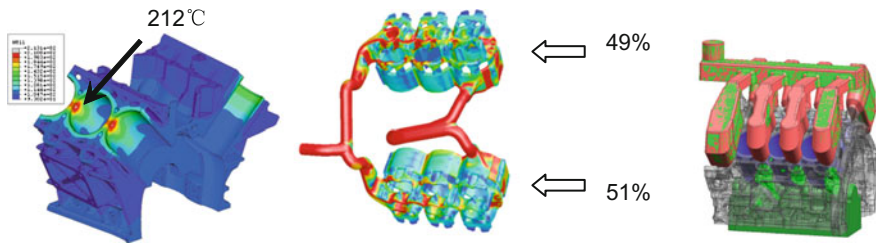


Fig. 4 Analysis of cooling, flow and casting process of the cylinder block

fasten the skirt to the main bearing caps thus the vibration of the skirt was controlled (see Fig. 3). With above measures, the weight of the block is only 30 kg which comparable with the high pressure die casting block but with much better NVH behavior.

In order to have good cooling of the block, short water jacket concept was used, the height of the water jacket is only 70 % of the stroke which increased the flow rate and reduced the temperature of the block especially the top ring position between neighbor cylinders. With fine tuning of the water jacket design by supporting of CFD analysis, the highest temperature of the cylinder bore was controlled under 212 °C in spite of that there is no inter cooling between cylinders, and the flow rate difference between two banks is within 2 % (see Fig. 4).

4.1.2 Crankshaft

Because of the 90 degree bank angle design, the crank pins of opposite cylinders are offset by 30 degree, this will give a possibility of not use shared collar between the offset crank pins like the crankshaft used for V6 engine with 60 degree bank offset angle. In such a way the engine length can be reduced by about 30 mm, the weight of the engine was reduced accordingly, this makes CA6GV to be a compact engine (see Fig. 5).

Further more, because the three pairs of crankpins are distributed in 120 degree spacing, normally this will need very complicated forging process and cause expensive cost. Then a forging process was developed with special design web

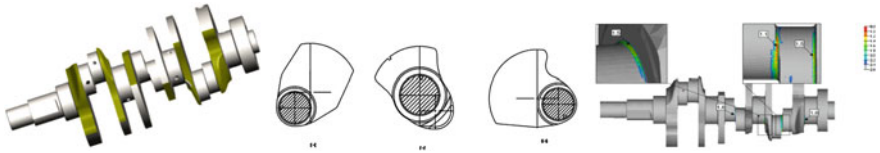
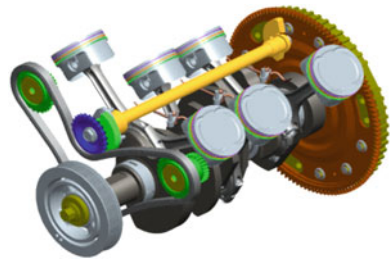


Fig. 5 Offset crankpin, special designed web and FE analysis of the crankshaft

Fig. 6 Balancing shaft



shape, this makes one direction forging die split possible while the crankshaft also be well balanced. FEA analysis and later fatigue test showing that the crankshaft has reasonable safety factor.

4.1.3 Balancing Shaft

In order to get excellent NVH behavior, a chain driven balancing shaft was used and 100 % 1st order reciprocating inertia momentum can be eliminated. The balancing shaft is driven by back side of the first stage chain which is a double side silent chain (see Fig. 6).

4.2 Cylinder Head and Valve Train

High performance and low fuel consumption is very important for V6 engine, thus the cylinder head was designed based on the combustion system which was developed for the overall engine family for FAW executive class car (see Fig. 7).

The combustion system can be adapted to both PFI and GDI with only a reasonable difference on the intake port tumble level, this makes both type of engines can share one production line, and because the inline four cylinder GDI engine has already been developed, so the V6 GDI engine can be developed very quickly.

The valve train is four valve with Roller Finger Followers (RFF) type design, both intake and exhaust VCT are used. In order to get better fuel consumption, cylinder deactivation system is also protected for the engine. Valve springs are

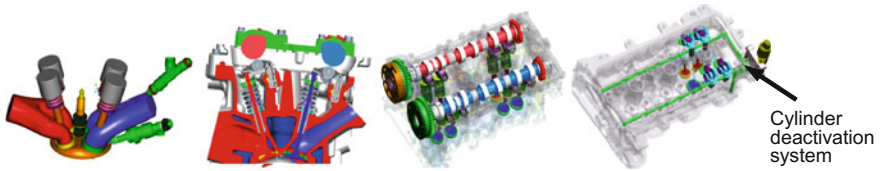


Fig. 7 Combustion system, cylinder head and valve train of CA6GV

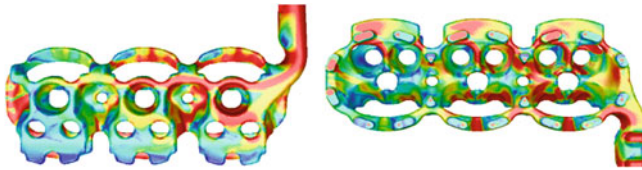


Fig. 8 CFD analysis of water flow in the cylinder head

dual rate design which is realized by non-constant coil pitch at both ends of the spring, this will enable the valve train a very good dynamic performance while reducing the overall spring force and thus valve train friction. All above features enable the engine has both good power and part load fuel consumption.

The cylinder head cooling is critical because of the high specific power and torque of the engine which will cause high temperature and knocking, so dedicated water jacket design and CFD analysis of the cylinder head was done together with the block (see Fig. 8).

The water jacket of the cylinder head was designed as compact as possible in order to increase the flow speed at critical area such as exhaust to exhaust valve seat bridge and exhaust to spark plug bridge, the volume of water jacket of each cylinder head is below 668 cc. After several careful optimization of the water flow by CFD, the water flow speed at above mentioned area were all controlled at about 2 m/s, which is much better for the cooling of the cylinder head.

4.3 Variable Plenum Volume Intake Manifold

Variable plenum volume intake manifold (Fig. 9) have been adopted to obtain excellent torque curve of the engine which is very important for executive class car. Variable manifold runner length concept was also researched during engine performance development stage, but it can not meet required torque curve.

The valve to control the plenum volume was designed to be a long narrow plate with rubber edge, thus the valve can be closed tightly, there will be absolutely no flow between the plenums, compared those design with leakage, the torque can be improved by about 3 %. The shape of the runner was designed tapered shape which also improved the charging efficiency.

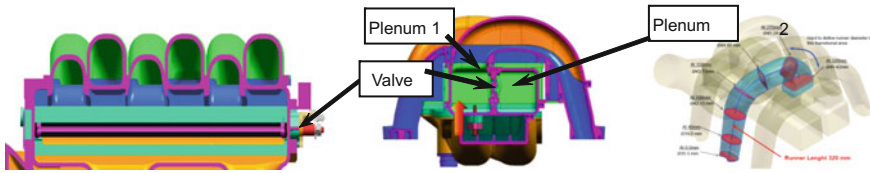


Fig. 9 Variable plenum volume intake manifold

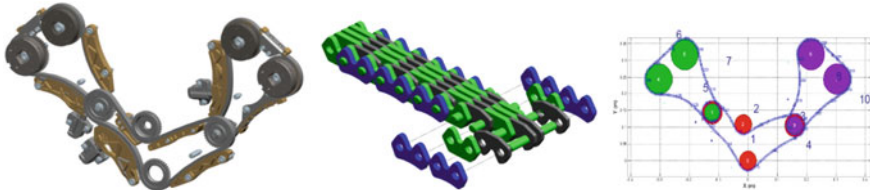


Fig. 10 Chain driving system

4.4 Chain Driving System

The chain driving system is two stage three layer silent chain design (Fig. 10), compared with one stage design, the advantage of 2 stage design is as following:

- Avoiding cam phase change and thus engine performance deterioration by elongation of the long one stage chain;
- Avoiding resonance caused by low stiffness of one stage system;
- Avoiding system vibration caused by crank sprocket with few teeth.

The first stage was originally roller chain design, but it caused unacceptable noise, then it was replaced by double side silent chain, and the near field noise (front end of the engine) is reduced by 6 dB(A) together with the reduction of the chain tension force which was optimized by simulation.

5 Performance and Emission Development

The performance develop was based on the requirement from the vehicle. The full load, part load, cold start, idle stability were all optimized.

The full load was optimized in order to obtain maximum charge efficiency, the point of 50 % mass fraction burn was controlled to 8–10° CA ATDC and the COV was controlled within 3 %. Above targets are met by fine tuning of intake and exhaust VCT, parameters of variable plenum volume intake manifold by DoE. Figure 11 shows the final performance of CA6GV 3 l engine.

The torque at 1,000 rpm reached 226 Nm, maximum torque reached 300 Nm at 3,000 rpm and the rated power reached 170 kW at 6,000 rpm, 90 % of maximum

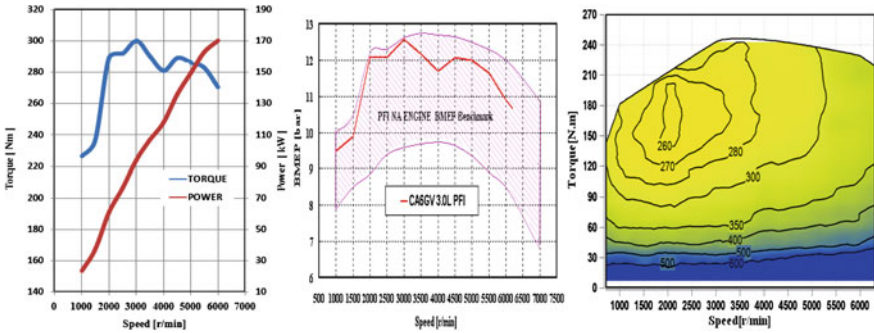


Fig. 11 Full load performance and BSFC MAP of CA6GV engine

torque is achieved within 1,900–6,000 rpm, this provide the car a very good drivability. The excellent power curve is achieved by combination of following factors:

- Good combustion system with fine tuned intake port design which have high tumble level while keeping high flow rate.
- Dedicated variable plenum volume intake manifold design which ensured the low end torque and maximum torque while providing the required rated power.
- Fine tuned cam timing combined with intake and exhaust VCT provide high charge efficiency in a wide engine speed range.
- Increased valve lift thanks to the RFF valve train design.

The engine also have very good fuel consumption, the fuel consumption at 2,000 rpm 2 bar BMEP is 376 g/kWh, the speed range of 280 g/kwh is from 1,000 to 4,700 rpm, all them can enable the car has a very good NEDC fuel consumption.

The emission target of FAW executive car is to meet Chinese stage 5 regulation (identical to EU5), and the curb weight of the car is about 1,780 kg which is a big challenge for the engine with PFI and without secondary air injection, especially HC emission. In order to meet the emission target, following measures are taken:

- Optimization of engine cold start raw HC emission by activate the intake VCT and increase the overlap the exhaust and inlet stroke, by this way some internal EGR is introduced and the in cylinder temperature is increased. Further more, internal EGR will also decrease the combustion rate and provide more time for burning of the HC. By this method, the raw HC emission at cold start stage was reduced by more that 30 % (see Fig. 12).
- Cast iron exhaust manifold was replaced by fabricated steel manifold which can reduce the heat losses and help the fast catalyst light off.
- Dedicated cold start calibration including air/fuel ratio, injection timing and quantity and ignition timing.

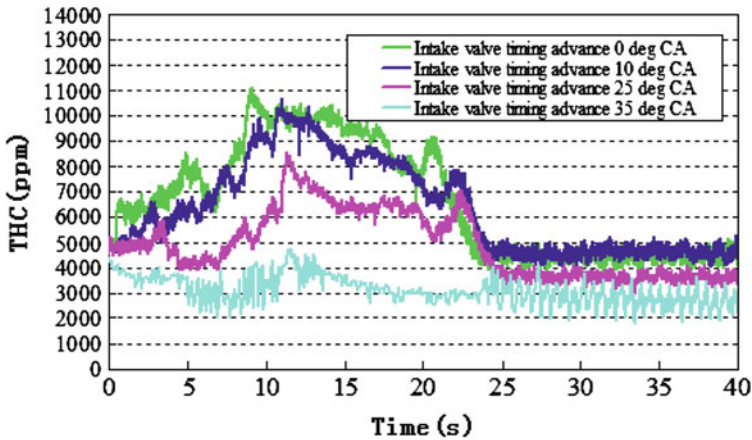


Fig. 12 Affect of intake VCT on HC emission during cold start

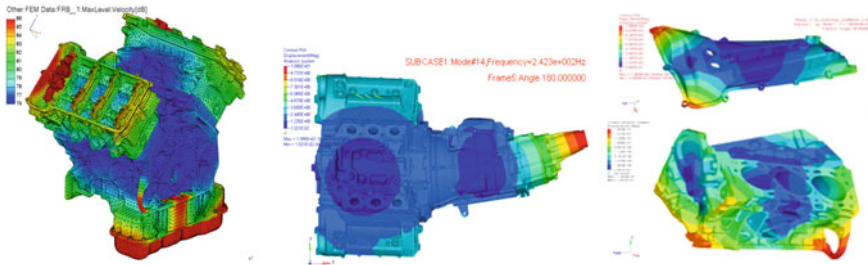


Fig. 13 Mode analysis of main engine structural components

6 NVH Development

Excellent NVH behavior is one of the most important requirement for executive class car, in order to meet the tough NVH target, the following tasks were completed:

- Detailed 3D design supported by mode analysis (see Fig. 13) of main structural parts such as cylinder head, block, timing chain cover, all brackets for accessories and the connection between engine and gear box, this provides a good foundation of NVH.
- Compared with roller chain system, silent chain driving system—especially the double side silent chain of the first stage reduced the engine frond side noise by 6 dB(A), and the over all engine noise was reduced by 3.5 dB(A).
- A sound energy based noise source high efficiency investigation method was used, compared with traditional method, the time to locate the noise source was reduced by 5/6.

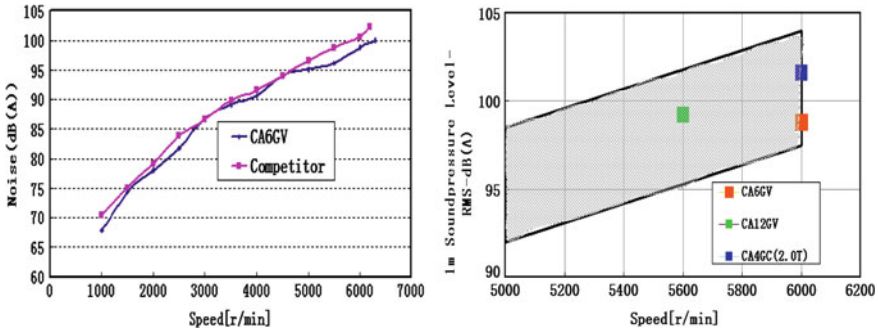


Fig. 14 Noise level of CA6GV engine

Finally, CA6GV obtained a excellent NVH behavior especially noise level, the 1 m noise at rated power is only 98.7 dB(A). Figure 14 shows the noise of CA6GV together with a very good competitor V6 engine for C class car, CA6GV's noise is lower at almost full engine speed. The noise of CA6GV is also at lower position in the benchmarking scatter band.

7 Mechanical Development

High quality is the number one requirement for the engine of executive class car, so a dedicated designed 3 stage mechanical development was completed, including durability test of structural parts, system functional development, engine durability test and vehicle durability test as well as climate test. The overall engine test time was more than 10,000 h and the accumulated vehicle test millage was more than 2 million kilometers. All the engine durability test procedures were designed based on Chinese driving habit and driving cycle developed by FAW for this kind of car, so the engine will be suitable for Chinese market very well.

The key results of mechanical development are as following:

- Very low bore deformation in each order, the 2nd order deformation is below 8μ , the higher order deformation is further lower, they are $0.5-2 \mu$ lower than similar engines. Together with fine tuned platform type honing the engine have a very low friction loss, low blow by and low oil consumption. The blow by is less than 36 l/min at any engine condition; oil consumption is less than 0.08 % of fuel consumption; air in oil is controlled within 15 % at most serious engine condition; oil in the blow by is controlled below 0.93 g/l blow by gas. All these provide a very good basis of the engine function and quality.
- All parts bear high heat load such as head, block, piston, exhaust valves were well developed. The maximum temperature between twp cylinders is controlled below $219 \text{ }^\circ\text{C}$ in spite of that there is no inter bore cooling. Thanks to the oil cooling jet and the specially designed piston bottom shape, the maximum piston

temperature was controlled below 260 °C which is at the first piston ring groove. The maximum cylinder head temperature is controlled below 205 °C which is at the bridge of two exhaust valve seats. All of them can pass the severe 3,000 cycle thermal shock test.

- Based on above results, the engine can reach a service interval of more than 10,000, 250,000 km B10 life can also be ensured.

8 Summary and Outlook

The launch of the new CA6GV V6 engine marks the executive car of FAW successful, which is also the first Chinese brand executive car in China. The engine achieves the performance of state of the art of similar engines of the world, this announced that FAW has entered the club of executive class car in Chinese market, and this provide a good basis for FAW to develop further variants of engines and cars of this class.

Together with the new executive class car—Hongqi H7, the new CA6GV V6 engine thus represents a milestone in FAW's strategy to develop high level class cars strategy.

The application of

- all aluminum light weight design, especially precision sand casting aluminum block with cast in liner;
- intake and exhaust VCT with protected cylinder deactivation design;
- dedicated variable plenum volume intake manifold design;
- two stage three layer silent chain timing drive system especially double side silent chain for the first stage;
- strategy to reduce cold start HC emission by activate the inlet VCT and introduce internal EGR;
- extensive CAE analysis including fatigue and NVH analysis;
- extensive mechanical development based on dedicated test process derived from Chinese driving habit and driving process; has enabled the engine reached the performance of state of the art of similar engine of the world and significantly improved the characteristics of the “Hongqi” engine family.

Accompanying the coming of Chinese stage 3 fuel consumption regulation from 2015 and the predicted stage 4 regulation in the year of 2020, FAW will continuously develop the “Hongqi” engine family including CA6GV. Turbo GDI, downsizing and down speeding concept will be introduced, we expect that CA6GV engine will play a more important role in order to support FAW's strategy to develop its high level end cars in the future, this will also help to improve the technical capability of FAW in other engine families.

Reference

1. Wolfgang Samenfink, Hartmut Albrodt, Michael Frank, Markus Gesk, Anja Melsheimer and Jens Thurso. Strategies to Reduce HC-Emissions During the Cold Starting of a Port Fuel Injected Gasoline Engine. SAE TECHNICAL PAPER SERIES, 2003-01-0627

Air System Proposal and Testing for a Downsized Two-Stroke Diesel Engine

**Pavel Brynych, Jan Macek, Luděk Pohořelský, Jean-Charles Ricaud,
Pierre-Yves Vallaude, Pascal Tribotté and Philippe Obernesser**

Abstract This paper introduces a research work on the air loop system for a downsized two-stroke two cylinder diesel engine conducted in framework of the European project dealing with the powertrain for Future Light-duty vehicles—POWERFUL. The main objective of the work presented in this paper was to test engine air loop system devices selected based on 1D-simulations and to verify their characteristics used for 1D-simulations. With respect to the power target of 45 kW and scavenging demands of the two cylinder two-stroke engine with a displacement of 0.73 l, a two stage boosting architecture was required. Further, to allow engine scavenging at any operation, supercharger had to be integrated in the air loop. Various air loop system layouts and concepts were assessed based on the 1-D steady state simulation at full and part load with respect to the fuel consumption. Among the investigated boosting devices were the positive displacement and centrifugal superchargers driven from the crankshaft and placed upstream or downstream of the turbocharger with either the waste gate or variable turbine. Due to the high boost pressure ratios above five and low mass flows, all boosting devices got at their limits or out of their working range even in the two stage configuration. The simulation part of the work has been presented on SAE World Congress 2012 held in Detroit (USA) (SAE paper no: 2012-01-0831), but the main results will be also presented in this paper to highlight the main issues met during the whole research work. The best

F2012-A01-045

P. Brynych (✉) · J. Macek · L. Pohořelský
Czech Technical University, Prague, Czech Republic
e-mail: pavel.brynych@fs.cvut.cz

J.-C. Ricaud · P.-Y. Vallaude
Le Moteur Moderne, Palaiseau, France

P. Tribotté · P. Obernesser
Renault, Boulogne, France

compromise regarding the feasibility, power target and fuel consumption was the configuration with the positive displacement supercharger placed downstream of the waste gate turbocharger. However, the biggest drawback of this solution was the necessity of sufficient air cooling between the stages due to the limitation of the maximum temperature at the outlet of the supercharger at 150 °C. On the other hand, the boosting system with the supercharger upstream of the turbocharger required small compressor wheel to avoid surge and was ruled out due to the turbocharger procurement feasibility. After the selection of suitable boosting devices, its testing followed. There had been two types of supercharger tested, Roots type and mechanically driven centrifugal compressor with Continuously Variable Transmission (CVT). Concerning turbocharger, there has been tested device with waste-gate turbine at open loop test rig at different temperatures at turbine inlet. The measured data has been then compared with “paper characteristics” delivered by producers of tested boosting devices for simulation use. The greatest differences in measured and “paper data” had been detected at T/C turbine efficiency.

1 Introduction

The project described in this paper follows the European Union’s agreed strategy to fight the climate change and to improve the fuel economy of cars and focuses research, development, validation and demonstration of compression ignition (CI) engine for a (1) small passenger car and (2) light duty vehicle intended for the vehicle fleet in 2020 which can achieve CO₂ emission objective of 95 g/km. Further the project aims to meet near zero emission level, i.e. CO, HC, NO_x and PM figures at least 10 % less than the Euro 6 emission limits during the real world driving conditions and within the useful life of the engine.

To demonstrate that ambitious CO₂ target by the engine itself only (also not by the vehicle weight or drag coefficient optimizations, start and stop system, etc.), Renault proposes to develop a new engine concept based on (a) downsizing by reducing the number of cylinders (b) new boosting architecture combining the positive displacement or centrifugal compressor with turbocharger and (c) two-stroke engine cycle. Moreover, to meet near zero NO_x and soot emission, Renault proposes to combine HCCI combustion with the low temperature combustion, i.e. meeting near zero emissions while avoiding expensive after-treatment system. The combination of the homogeneous combustion to limit the soot and the low temperature combustion by adding exhaust gas recirculation to limit the NO_x seems to be a promising concept towards the main emission objectives. However, using HCCI combustion is strongly limited due to the noise level in high load conditions and combustion stability in low load conditions. Therefore, the main innovative step is to move from the four-stroke engine to the two-stroke engine to achieve higher torque and power output than the four-stroke engine (theoretically twice as high in the two-

stroke operation as in the four-stroke operation) in the limited area of HCCI combustion.

The two-stroke diesel engines are nowadays used for their high efficiency and high specific power as a powertrain for freight ships and stationary applications such as the electric power generators—[1]. The mass produced carbureted two-stroke engines for passenger vehicles [2] suffered from (a) high fuel consumption due to the short-circuit of the fuel to the exhaust during the scavenging and (b) high unburned hydrocarbon emissions. In [3], there is a nice overview of the two-stroke diesel engine prototypes developed by Toyota (2.5 l, 4-cylinder, supercharged, 100 kW), AVL (0.98 l, 3-cylinder, combined boosting architecture with turbo and supercharger, 50 kW), Yamaha (1.0 l, 2-cylinder, crankcase scavenging, 33 kW) and Daihatsu (1.2 l, 2-cylinder, combined boosting architecture with turbo and supercharger, 65 kW) for the passenger cars since 1990s showed together with the progress the two-stroke engine technology made. Nonetheless, none of the prototypes has been represented in the mass automotive production. Considering the nowadays available CFD tools and power electronics for control and fuel injection, the application of the two-stroke engine for passenger car is getting popular again. Moreover, as a consequence of its principle advantage, the two-stroke engine offers a unique opportunity of engine downsizing by reduction of the engine cylinders with NVH (noise-vibration-harshness) significantly better than at the four-stroke engine [4]. Additionally, the internal exhaust gas recirculation can be used to support the realization of the lean mixture combustion at low temperature [3].

The turbocharged passenger vehicle diesel engine is the state of the art and the development of the fuel efficient turbo/supercharged SI engines is getting into foreground of many OEMs as well. Air systems of those four-stroke engines comprise various boosting architectures (one stage, serial sequential two stage, combined with turbo- and supercharger, parallel, etc.) to enable required low and high end performance at satisfactory transient response. In contrary to the four-stroke engine, there is a vital need to reach the positive pressure drop across the engine (i.e. the boost pressure higher than the backpressure) to allow for the scavenging of the two-stroke engine. Therefore, the air system of the two-stroke engine is responsible both for the boosting and scavenging of the engine cylinders and the sizing of the turbo-and supercharger devices influences not only the power curve and fuel consumption but also the combustion. Thus, because of a strong interaction among boosting, scavenging and combustion, the two-stroke engine is very sensitive to the variation of the engine parameters.

One may sum up the project objectives as following:

- CO₂ objective of 95 g/km both for passenger cars and light duty vehicles
- Near zero NO_x emission without NO_x aftertreatment
- Negligible soot emissions with a reduced volume particulate filter
- Unburnt Hydrocarbon and CO emission meeting Euro 6 standards

Table 1 Engine geometrical data

Bore	76	mm
Stroke	80.5	mm
No of cylinders	2	
Displacement	0.73	l
Connecting rod length	133.8	mm
Compression ratio	17.2	
No of valves per cyl	4	

The engine concept focusing on the project targets can be summarized as following:

- Downsized engine to limit the fuel consumption
- HCCI with low thermal combustion to reduce the soot and NO_x emissions
- Two-stroke engine to enlarge the HCCI operation to the whole engine range
- VVT air management system to balance air and internal exhaust gas recirculation
- Advanced air boosting architecture with turbocharger and supercharger (positive displacement or centrifugal, either mechanically or electrically driven)

This paper deals with the test work on the air system boosting devices for the engine concept introduced above done under the Josef Bozek Research Centre (JBRC) leadership together with ČZ Strakonice a.s., TURBO Division, Le Moteur Moderne (LMM) and Renault as the main partners. Using test bed of ČZ Strakonice all the above mentioned boosting devices characteristics have been measured.

2 Engine Specification, Power Targets and Studied Configurations

The geometry of the concept engine presented in Table 1 is based on the Renault K9K 1.5 dCi power unit. Required power output is set to 45 kW at 3,000 rpm while keeping constant torque from 1,000 to 3,000 rpm (Fig. 1). All investigated concepts of the air system (presented in Table 3) were assessed at the full and part load. The part load points (Table 2) were selected based on the New European Driving Cycle (NEDC) pattern by Renault according to the previous experience. The maximum acceptable internal exhaust gas recirculation (IGR) is 40 %. Therefore, for higher IGR the external EGR (which is applied only in part load) should be reduced. All air loop concepts have a two stage boosting layout with a turbocharger either in the low pressure (LP) or high pressure (HP) stage arranged serially with (a) mechanically driven positive displacement or centrifugal supercharger (b) e-booster or (c) turbocharger with electrical assisted turbine. A concept solely equipped with turbochargers was abandoned with respect to the engine starting and scavenging sensitivity on the power of the two-stroke engine.

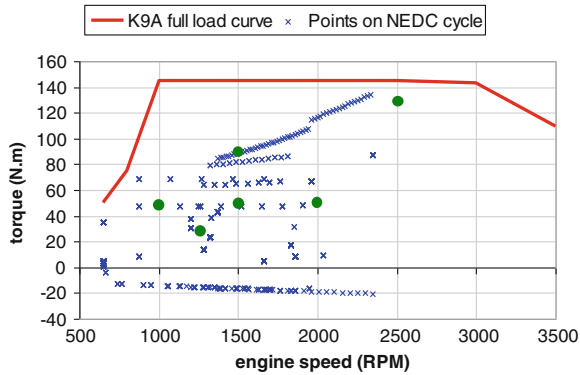


Fig. 1 Full load requirements and investigated part load (green) points

Table 2 Part load points definition

		Point 1	Point 2	Point 3	Point 4	Point 5	Point 6
Engine speed	RPM	1,250	1,000	1,500	2,000	1,500	2,500
Torque	N.m	25	50	50	50	90	130
BMEP	bar	2.15	4.3	4.3	4.3	7.7	11.2
EGR rate	%	20	20	20	20	15	15

Table 3 Assessed air system configurations

Type	LP stage	HP stage	Cooled EGR loop
C1	Mechanical positive displacement charger	Turbocharger	LP
C2	Mechanical positive displacement charger	Turbocharger	MP
C3	Turbocharger	Mechanical positive displacement charger	LP and MP
C4	Mechanical centrifugal charger	Turbocharger	LP and MP
C4b is	Turbocharger	Mechanical centrifugal charger	LP and MP
C6	Turbocharger	e-boost	LP and MP
C6b is	e-boost	Turbocharger	LP and MP
C7	Turbocharger	Turbine assisted electrically	LP and MP
C8	Turbin assisted electrically	Turbocharger	LP and MP

Additionally, configurations with (a) variable (b) single or with (c) dual super-charger drive were simulated. Moreover, in the part load, the low pressure (LP) and middle pressure (MP) cooled EGR loops were evaluated (Fig. 2).

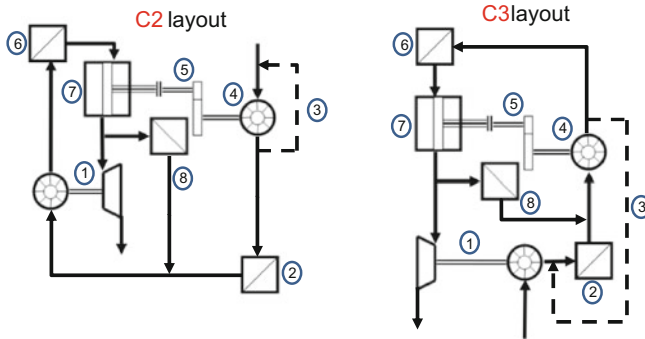


Fig. 2 Scheme of the boosting configurations with supercharger in HP stage—C3 (*right*) and LP stage—C2 (*left*) with middle pressure (MP) EGR loop where 1-turbocharger, 2-LP intercooler, 3-supercharger by-pass, 4-supercharger, 5- supercharger transmission, 6-HP intercooler, 7-engine, 8-EGR loop with EGR valve and intercooler and 9-turbocharger bypass

3 Air System Conception

The air systems of the two-stroke diesel engine prototypes from AVL (1.0 l, 3-cylinder) and Daihatsu (1.2 l, 2-cylinder) which are the most similar to the engine concept being developed in framework of this work comprise a serial architecture with a mechanical supercharger and turbocharger. Whereas the AVL engine had the mechanical supercharger arranged downstream of the turbocharger the Daihatsu placed the mechanical supercharger upstream of the turbocharger [5]. Placing of the mechanical supercharger in the high pressure (HP) stage enables (1) sizing the supercharger smaller than in the low pressure (LP) stage and (2) lower supercharger speed. On the other hand, even with the intercooler upstream, the supercharger inlet temperature is higher in the HP stage than in the LP stage increasing the required supercharger power input. Therefore, authors tried to systematically proceed towards the most suitable and in the same time procurable configuration. One of the main project challenges was (a) to comply with high boost to compensate the downsizing effect and (b) to accommodate the scavenging needs of the two-stroke engine. In the following Table 4 there is overview of all the investigated boosting concepts.

4 Global Configuration Comparison

For better and illustrative representation of the particular configuration tested, the fuel consumption in the New European Driving Cycle (NEDC) was preliminary estimated based on the results at the part load while applying a weighting coefficient to the BSFC computed for each operating point. As illustrated in Fig. 1, the engine runs through several operating points during the NEDC cycle. The weighting

Table 4 Overview of the investigated air system concepts

	Low Pressure Stage	High Pressure Stage	EGR loop	TC	Drive system
Mechanical Supercharger	Positive displacement charger -	Turbocharger	X Cooled LP or MP	X Variable geometry turbine - Fixed geometry turbine	X Variable gear ratio - Single gear ratio Dual gear ratio
	Centrifugal charger				
Electrical Boost devices	Turbocharger	e-Boost			External e-Power
	e-Boost	Turbocharger			
	Turbocharger + TAE (turbine assisted electrically)				

Table 5 Part load weighting coefficients

Engine speed (rpm)	1,250	1,000	1,500	2,000	1,500	2,500
Torque (N.m)	25	50	50	50	90	130
Weightening coef. (%)	36.4	17.1	23.2	13.0	7.4	2.9
Equivalent time (s)	385	181	246	138	7.4	31

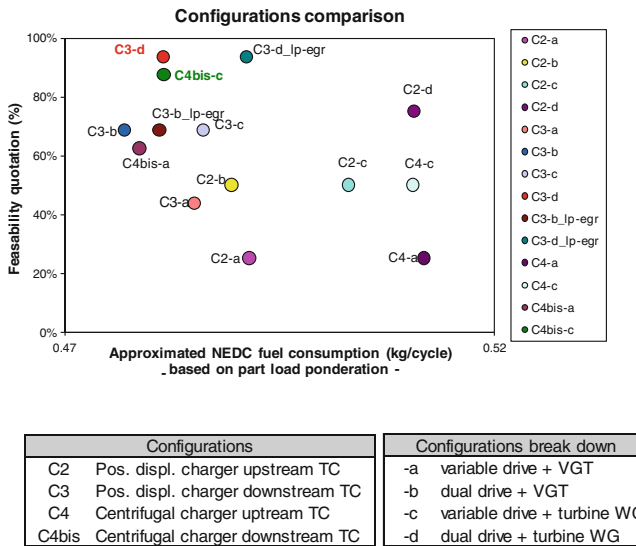


Fig. 3 Global comparison of the simulated configurations

coefficients correspond to the equivalent time in seconds that the engine dwells in the studied part load point (see defined part load points in Table 3) or in its close proximity during the driving cycle. The equivalent time (Table 5) was estimated for Renault Twingo with a mass of 925 kg on R14 tires and a drag coefficient of 0.68.

Figure 3 represents the NEDC fuel consumption of each configuration in relation to their technology feasibility. With respect to the computation assumption

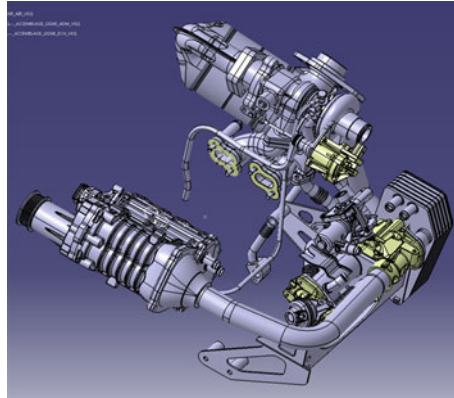


Fig. 4 Design of the most preferred air loop system with the supercharger downstream of the waste gate turbocharger—C3-d

(steady state simulation only), the computed value of the NEDC fuel consumption serves as a classification tool to show the qualitative comparison. Further, the configurations with the electric boosting device are not displayed.

The global comparison reveals that the configuration C3-d with the mechanical positive displacement charger downstream of the waste gate turbocharger appears to be the best compromise regarding the air system feasibility, power achievement and fuel consumption. Also, the solution C4bis-c with the centrifugal charger set downstream of the waste gate turbocharger and the variable supercharger drive arises as the backup architecture. However, as the variable drive of the centrifugal compressor is in the early stage of the development the configuration C3-d should be the principal solution. Figure 4 presents the design of the preferred air system.

The configurations with the supercharger placed downstream of the turbocharger benefits from the lower fuel consumption than the configuration with the supercharger upstream of the turbocharger. The supercharger in the LP stage has to spin faster partially because of the low pressure EGR loop necessity. At the part load, the variable drive of the positive displacement supercharger does not show any significant fuel benefit mainly due to the higher mechanical losses.

5 Boosting Devices Tests

5.1 Roots Type Supercharger

The testing work started with Roots type supercharger testing. Roots compressor is a positive displacement supercharger with compression ratio depending on pressure in outlet piping. It uses a shock compression to compress the delivered gas. Scheme of the used test bed is shown in Figs. 5 and 6

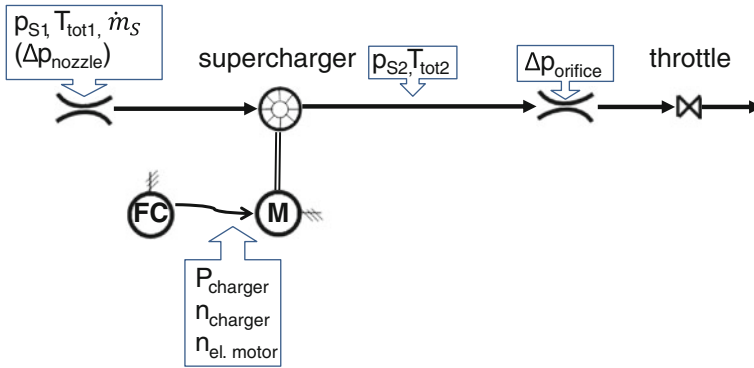


Fig. 5 Roots type supercharger test bed scheme

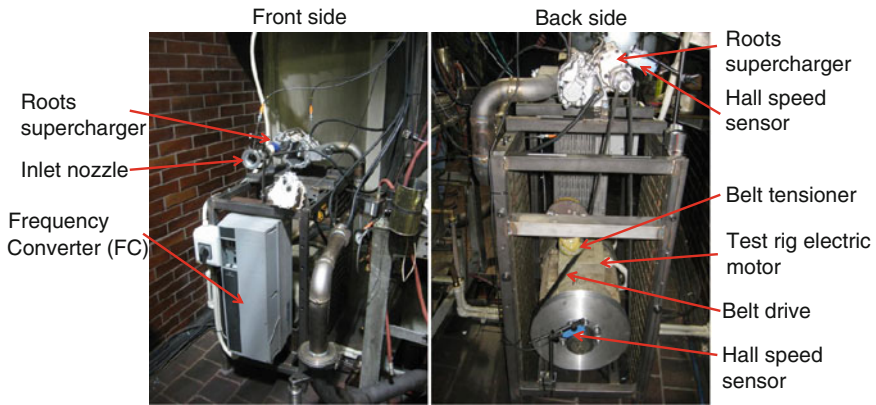


Fig. 6 Roots type supercharger test rig

Following figures presents the supercharger test rig at ČZ Strakonice, TURBO Division used for supercharger characterization.

The supercharger testing consisted of measuring static pressures p_{S1} , p_{S2} and total temperatures T_{tot1} , T_{tot2} together with inlet mass flow rate evaluation at inlet nozzle \dot{m}_S . The air mass flow rate has been evaluated via standard nozzle according to DIN 1952 [6] or EN-ČSN 22 7710, which defines mass flow rate through a nozzle as following:

$$\begin{aligned} \dot{m} &= M\alpha\varepsilon A \sqrt{2 \frac{p \left(1 + \frac{r(M\alpha\varepsilon)^2 \Delta p}{c_p p} \right)}{r T_{tot}}} \Delta p \\ &= (M\alpha\varepsilon)^2 A \Delta p \sqrt{\frac{2}{c_p T_{tot}} \left(1 + \frac{c_p p}{r(M\alpha\varepsilon)^2 \Delta p} \right)} \dots [\text{kg} \cdot \text{s}^{-1}] \end{aligned}$$

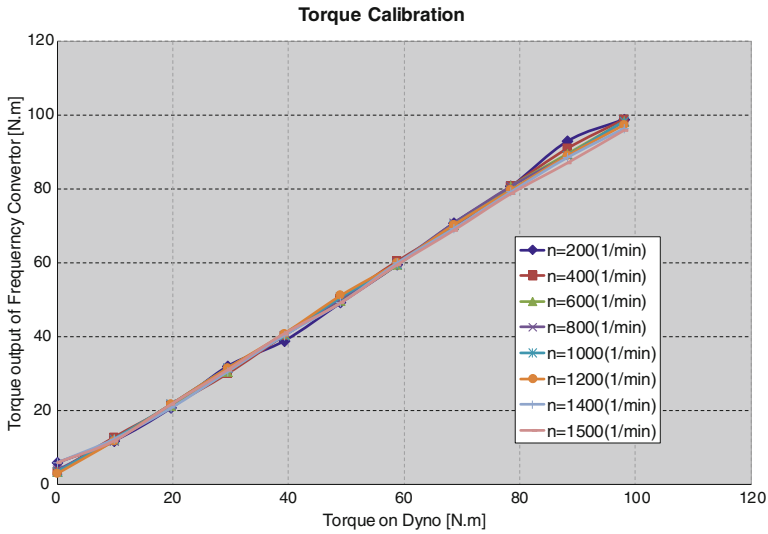


Fig. 7 FC torque calibration results

where $M = (D_{ori}/D)^2$ is a cross section ratio, D_{ori} is an internal orifice diameter, D pipe diameter, α is a discharge coefficient dependent on M , ε expansion coefficient, A is the pipe cross section, T_{tot} is a total temperature of the flow, c_p is isobaric specific heat capacity, p is barometric pressure, r is specific gas constant, Δp pressure difference at an orifice.

Next to pressures, temperatures and air mass flow the standard isentropic efficiency has been found according to

$$\eta_{K,S} = \frac{P_i}{P_e} = \frac{\dot{m} \cdot c_p \cdot (T_{tot2,s} - T_{tot1})}{\dot{m} \cdot c_p \cdot (T_{tot2} - T_{tot1})} = \frac{T_{tot1} \cdot \left(\frac{T_{tot2,s}}{T_{tot1}} - 1 \right)}{(T_{tot2} - T_{tot1})} = \frac{T_{tot1} \cdot \left(\left(\frac{p_{tot2}}{p_{tot1}} \right)^{\frac{\kappa-1}{\kappa}} - 1 \right)}{(T_{tot2} - T_{tot1})}$$

$$= \frac{T_{tot1} \cdot \left(\pi^{\frac{\kappa-1}{\kappa}} - 1 \right)}{(T_{tot2} - T_{tot1})}$$

where P_i is the isentropic input power of the supercharger, P_e is the shaft supercharger input power, \dot{m} is supercharger mass flow rate, $T_{tot2,s}$ is output temperature by isentropic compression, π is a compression ratio and κ is Poisson constant. The supercharger input power was computed from supercharger shaft torque and supercharger shaft speed determined by Hall type sensor. The supercharger shaft torque was determined by Frequency Converter (FC) output current. Before start of the supercharger testing, FC output torque had been calibrated on dynamometer test bed with following results presented in Fig. 7.

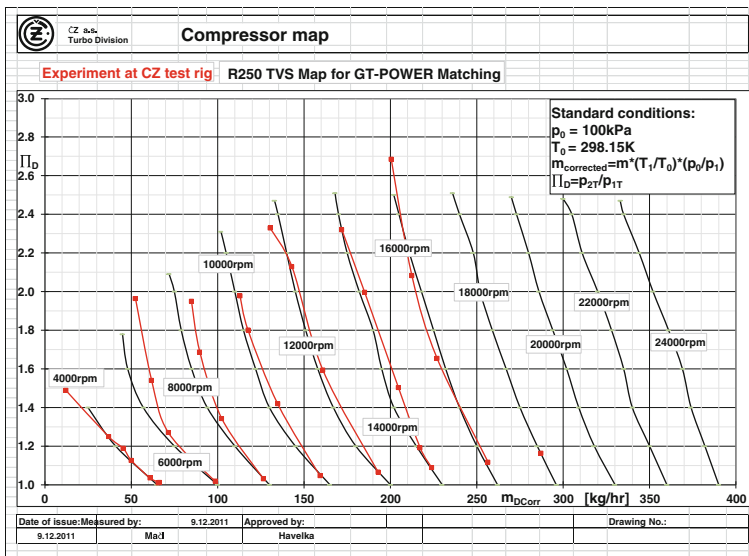


Fig. 8 Pressure ratio versus mass flow rate characteristic of Roots type supercharger

Moreover, by this calibration there has been realized, that 2 V of FC output current mean about 98.4 Nm electric motor shaft torque. Supercharger shaft power is then

$$P_e = \frac{2\pi n_M}{60} \cdot M_M$$

where n_M is electric motor shaft speed and M_M is electric motor shaft torque. Supercharger shaft power is lower than test rig electric motor shaft power due to efficiency of belt drive connecting these two devices. However, the “paper characteristic” proposed by superchargers producer has included this efficiency. That is why electric motor shaft power and supercharger shaft power could be taken as one value. But practically there is a well-known difference between these two values.

Regarding results of these tests the measured data seems to be quite similar to superchargers “paper characteristic” used for simulations as shown on Figs. 8 and 9. The measured efficiency is even a little bit higher than promised by producer. During Roots type supercharger testing a few issues has been met. Firstly, all the speed lines could not be measured up to the highest pressure ratios due to the outlet temperature limitation (170 °C; 150 °C for simulations). The higher speed lines were not verified because of need to modify the step up gear ratio between the test rig electric motor and the supercharger. Secondly, even if the temperature limitation has been followed, the supercharger got seized during the test. Due to probably fast change of pressure ratio and supercharger speed the rotor face has got in touch with casing and has been milled (see Fig. 10).

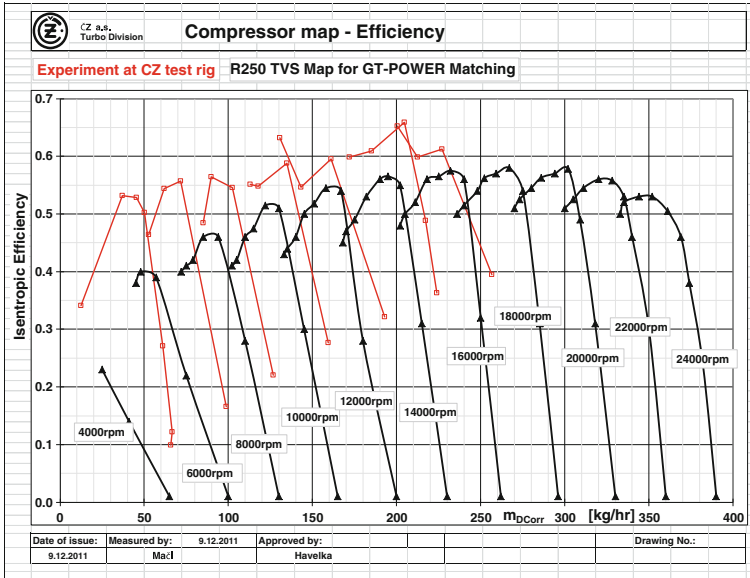


Fig. 9 Isentropic efficiency versus mass flow rate characteristic of Roots type supercharger

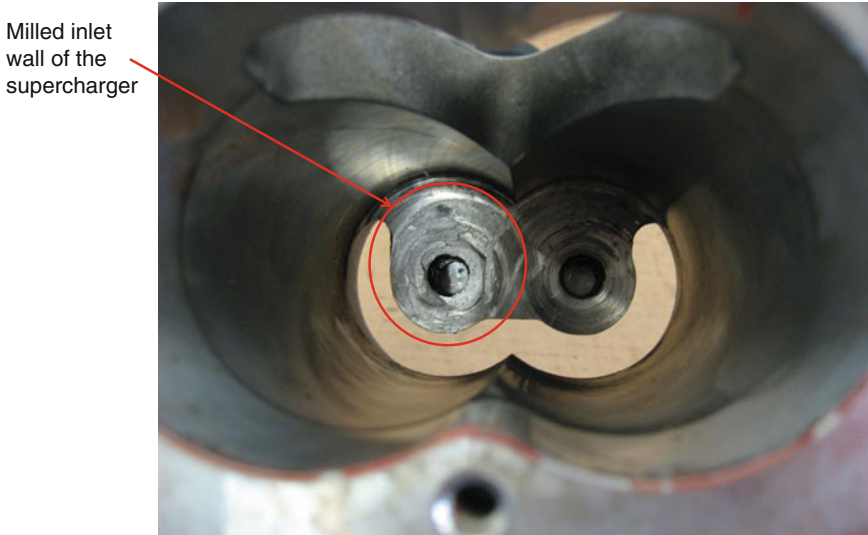


Fig. 10 Supercharger casing face after the rotor seizure

Table 6 Key operating data and limits of the centrifugal supercharger

Key operating data and limits		
Maximum variator input speed	(rpm)	21,000
Maximum variator output speed	(rpm)	17,500
Maximum variator ratio	(-)	2.4
Minimum variator ratio	(-)	0.5
Planetary gearbox set up ratio	(-)	12.51
Maximum compressor speed	(rpm)	219,000
Maximum variator control pressure	(bar)	25
Minimum variator control pressure	(bar)	1
Maximum supercharger oil temperature	(°C)	100
Maximum CVT bearing temperature	(°C)	130

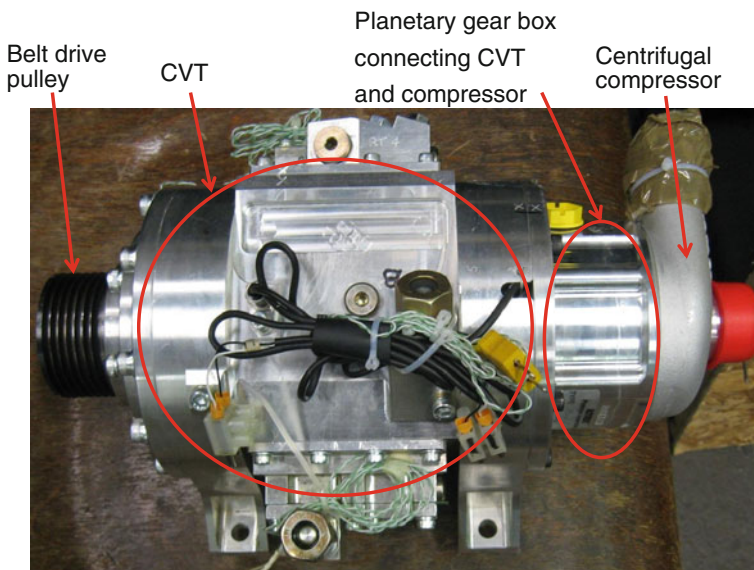


Fig. 11 Mechanically driven centrifugal supercharger layout

5.2 Mechanically Driven Centrifugal Supercharger

The test of mechanically driven centrifugal supercharger has been done on the same test rig and with the same methodology like Roots type supercharger one (Fig. 5). However, the centrifugal supercharger had opposite to the Roots supercharger hydraulically controlled transmission ratio of the Continuously Variable Transmission (CVT). The control strategy involved one grade of freedom more and additional hydraulic equipment was needed. The supercharger’s CVT has been solved like roller one. Following Table 6 summarizes centrifugal supercharger data: (Figs. 11, 12).

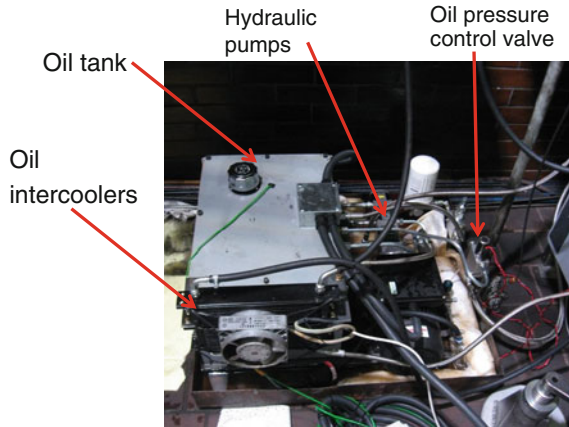


Fig. 12 Additional hydraulic equipment

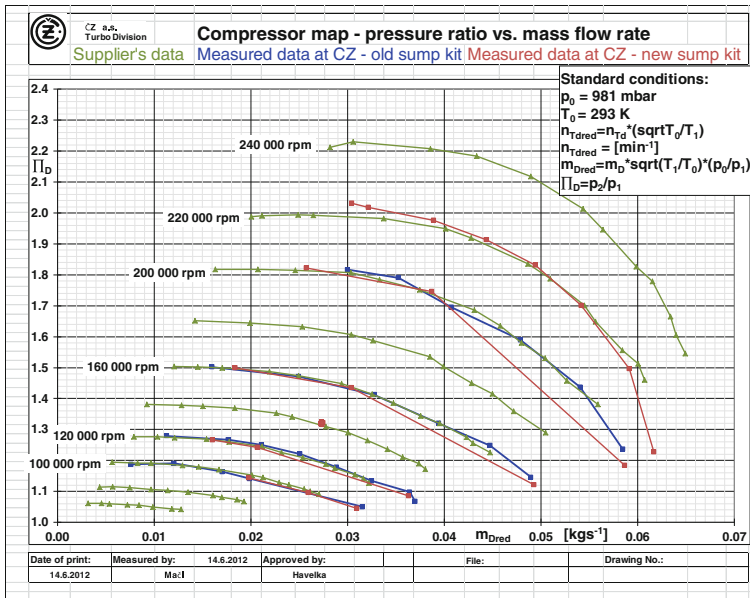


Fig. 13 Centrifugal supercharger standard characteristics comparison (measured vs. provided for 1-D simulations)

And following figures show the device layout and additional hydraulic equipment.

Regarding tests results of pressure ratio versus mass flow rate characteristic there has been realized a good agreement between measured data at ČZ Strakonice test bed and data used for 1-D simulations mentioned above (Fig. 13). Nevertheless, surge limit of the compressor is shifted to higher mass flow rates by measured

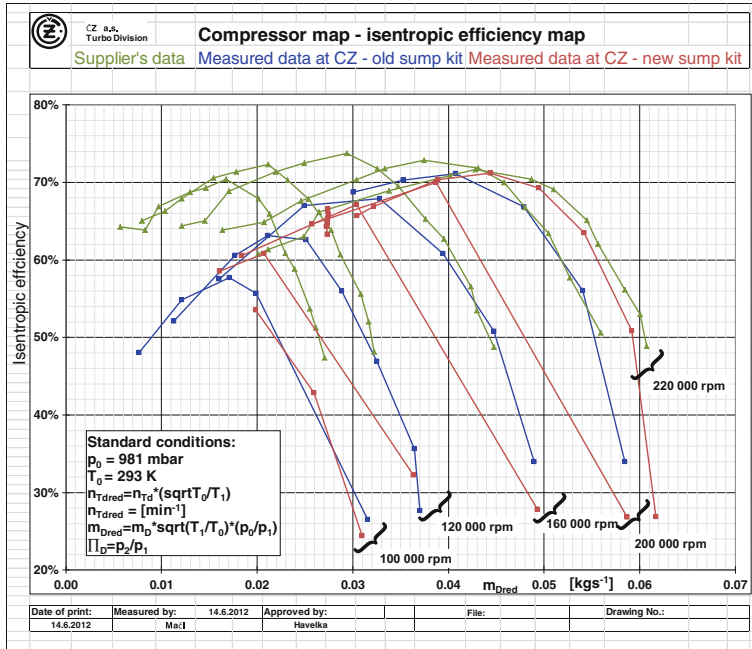


Fig. 14 Centrifugal supercharger isentropic efficiency characteristic

characteristic than by original data. During testing a new oil sump kit has been provided by device supplier to improve mechanical efficiency of the CVT. Concerning isentropic efficiency there is large difference at low compressor speeds (up to 20 %) and small difference (about 2 %) at high compressor speed (Fig. 14).

Next to pressure ratio versus mass flow rate characteristic and isentropic efficiency total mechanical efficiency of the whole device has been evaluated. Theoretically, total mechanical efficiency of the whole power train of the centrifugal supercharger is summarized in the following equation:

$$\eta_{mech_total} = \eta_{mech_belt_drive} \cdot \eta_{mech_CVT} \cdot \eta_{mech_planet_gearbox} \cdot \eta_{mech_compressor}$$

which includes mechanical efficiency of a belt drive connecting test bed electric motor (or combustion engine in a car) and CVT input; mechanical efficiency of the CVT; mechanical efficiency of planetary gear box connecting CVT and compressor and finally mechanical efficiency of centrifugal compressor. Because this methodology of measuring and computing of mechanical efficiency would be too complicated regarding integration of CVT, planetary gear box and compressor into one device without any possibility to separate them from each other, the total mechanical efficiency of the whole device has been computed from test rig electric motor power output and centrifugal compressor power input like mentioned in the following equation:

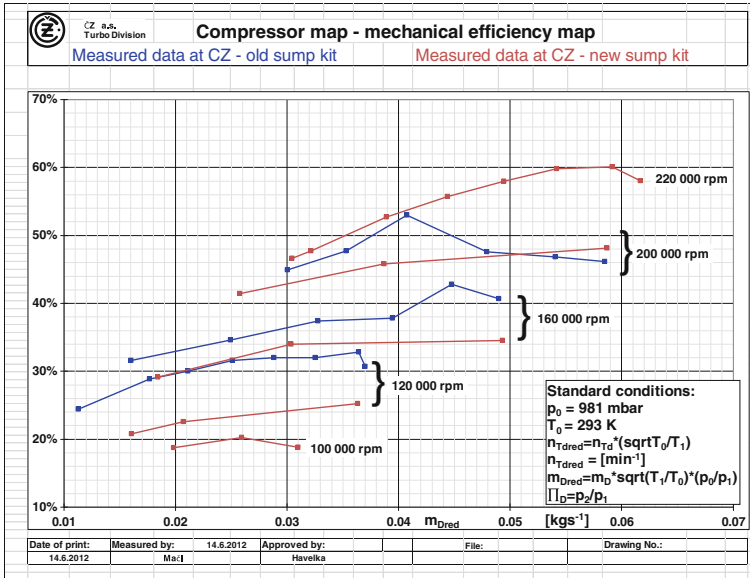


Fig. 15 Centrifugal supercharger total mechanical efficiency versus mass flow rate

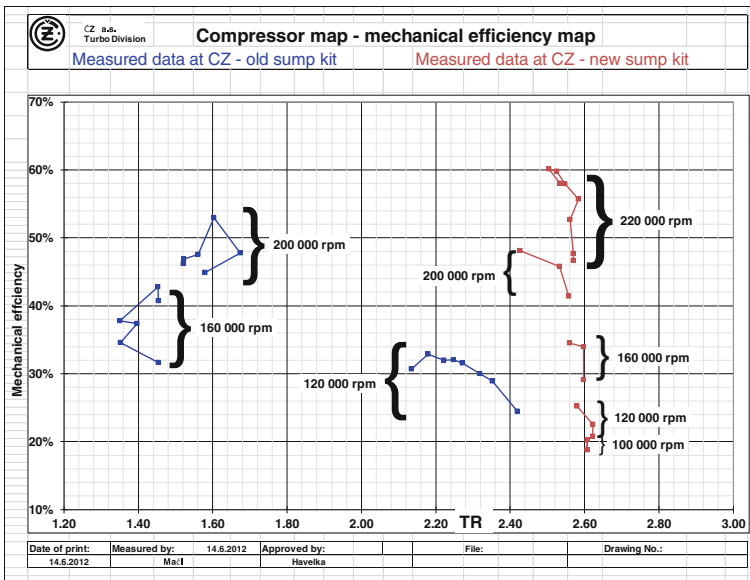


Fig. 16 Centrifugal supercharger total mechanical efficiency versus transmission ratio

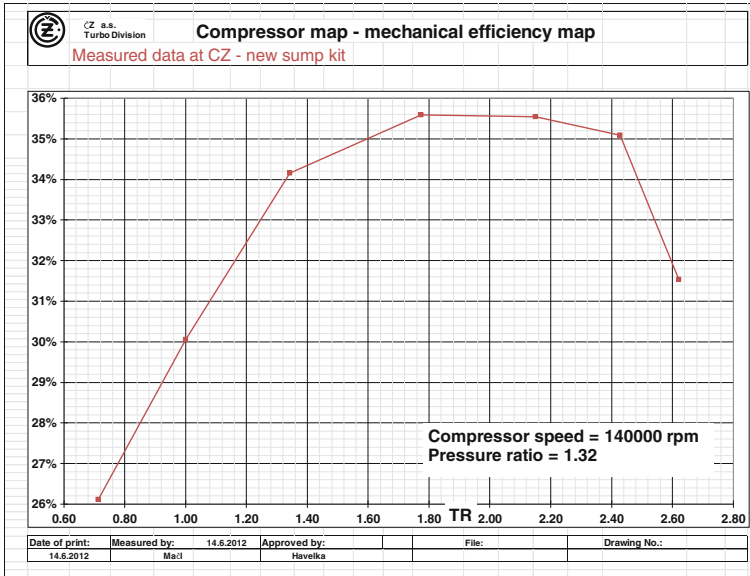


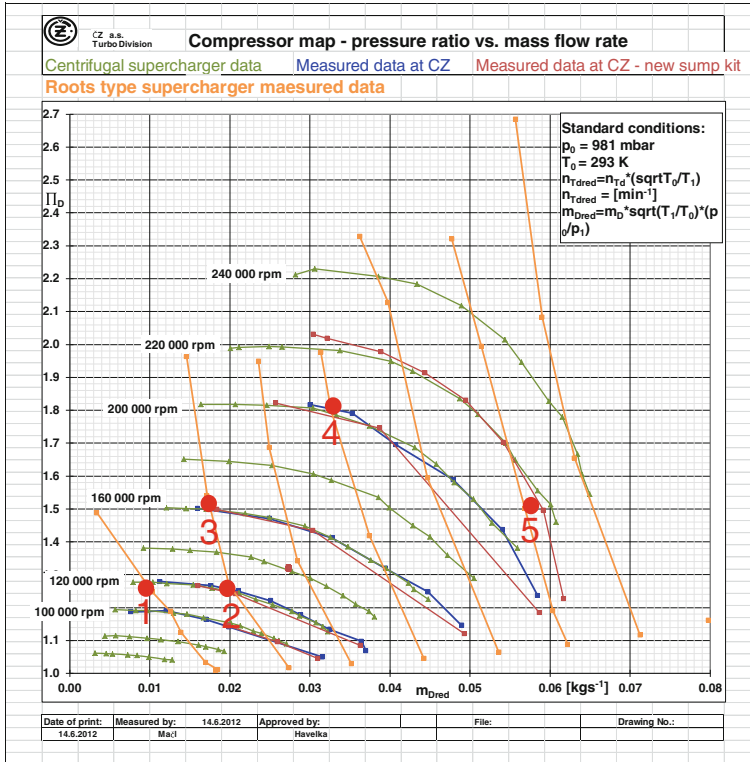
Fig. 17 Total mechanical efficiency at constant compressor load and speed

$$\eta_{mech_total} = \frac{\dot{m} \cdot c_p \cdot (T_2 - T_1)}{M_{el_mot} \cdot \frac{2 \cdot \pi \cdot n_{el_mot}}{60}}$$

where \dot{m} is a compressor mass flow rate, c_p is isobaric specific heat capacity, T_1 temperature at compressor inlet, T temperature at compressor outlet, M_m is electric motor shaft torque and N_m is electric motor shaft speed. The power input of the additional hydraulic equipment has not been taken into account. The results of total mechanical efficiency evaluation are plotted in following figures depending on compressor mass flow rate (Fig. 15) and depending on transmission ratio (Fig. 16). Unfortunately, the supplier of the device has not provided us total mechanical efficiency data. That is why our measured data couldn't be compared with them.

As it is obvious from Fig. 15 total mechanical efficiency of the centrifugal supercharger is higher the higher the CVT output speed thus the CVT transmission ratio. As the tests with new and old sump kit has been done with different CVT transmission ratio and the mechanical efficiency is obviously dependent on CVT transmission ratio there is no possibility to evaluate the contribution of the new sump kit to total mechanical efficiency of the whole device. The transmission ratios used by tests are plotted in the Fig. 16.

As the last point of the testing this supercharger mechanical efficiency at constant load and different CVT transmission ratio has been investigated. The constant compressor load has been defined by constant pressure ratio of 1.32



Selected points					
Point Nr.	Mass flow	Pressure ratio	Test rig electric motor shaft power		
			Roots	Centrifugal	
	[kg/s]	[-]	[kW]	[kW]	
1	0.010	1.25	0.55	1.97	
2	0.020	1.27	0.91	2.90	
3	0.017	1.54	1.56	3.34	
4	0.033	1.80	3.74	5.63	
5	0.057	1.50	3.66	7.23	

Fig. 18 Points selected for the test rig electric motor power output comparison

and constant speed has been set at value of 140,000 rpm. To reach the constant compressor speed the CVT transmission ratio and the test rig electric motor speed have varied. At this point total mechanical efficiency differs in range of 10 % with the highest value about 35 % in the transmission ratio range of 1.8–2.4 (Fig. 17). The result is influenced by the test rig electric motor mechanical efficiency change while its speed is changing, but influence of this circumstance is negligible in compare to the whole system mechanical efficiency change.

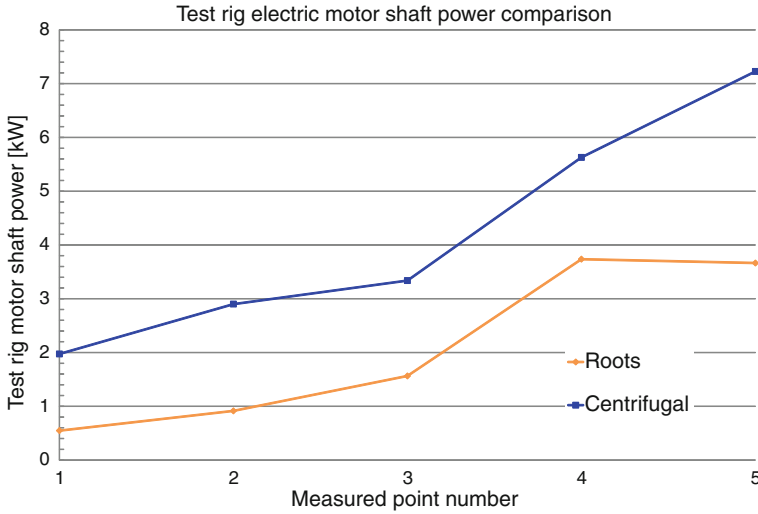
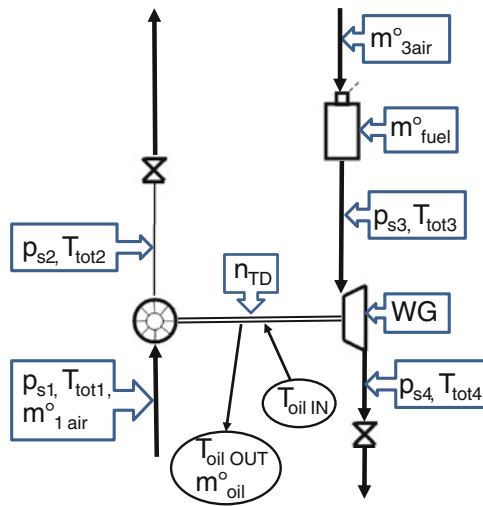


Fig. 19 Test rig electric motor power output comparison

Fig. 20 Turbocharger test rig scheme



The comparison of the test rig electric motor power output during Roots type supercharger and mechanical driven centrifugal supercharger testing follows. The power output has been compared in the same points of the pressure ratio versus mass flow rate characteristic (Fig. 18) because this point of view is decisive for use of the supercharger in conjunction with a combustion engine.

As it is obvious from Fig. 19 the power consumption of the centrifugal supercharger is in most of the selected points twice higher than by Roots type

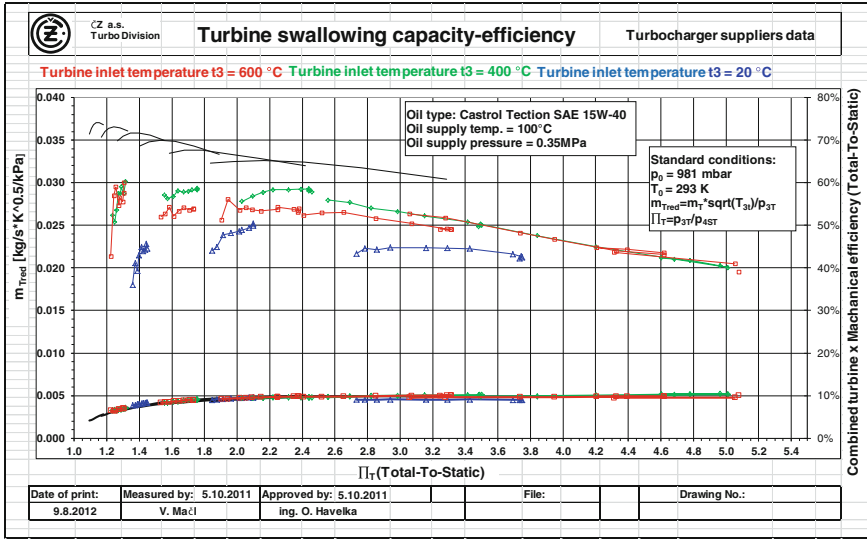


Fig. 21 Turbocharger testing results—Turbine swallowing capacity and efficiency

supercharger. Moreover, the power input of the additional hydraulic equipment of the centrifugal supercharger has not been involved in this comparison.

5.3 Turbocharger Testing

The turbocharger testing has been done in open loop test rig configuration (Fig. 20) which is more useful for measuring the standard turbine map $\dot{m}_{Tred} = f(\pi_T, n_{Tred})$ and standard compressor map $\pi_C = f(\dot{m}_{C,corr}, n_{C,corr})$ than auto-run (closed loop), where turbine is fitted by air from turbocharger compressor. During tests waste-gate of the turbocharger has been closed.

Static pressures and total temperatures have been measured upstream and downstream compressor and turbine together with turbocharger speed. Air mass flows have been measured upstream both machines using orifices and evaluated by the same equation like the superchargers mass flow rate mentioned above. Additionally, oil temperature at inlet and outlet and oil mass flow rate has been measured.

The results are presented in the next figures. Firstly for turbine with reduced mass flow rate to respect reduced Reynolds number (Re) on turbine side due to higher kinematic viscosity of hot gas than on compressor side. Because the similarity of compressor and turbine aerodynamics calls for the same Mach number inside blade ports, the same incidence angles and the same Reynolds numbers [7]. The reduced mass flow rate is then

$$n_{red} = \frac{n}{\sqrt{T_{tot,in}}} \dot{m}_{red} = \frac{\dot{m} \sqrt{T_{tot,in}}}{P_{tot,in}} n_{corr} = n \sqrt{\frac{T_{ref}}{T_{tot,in}}} \sqrt{\frac{\kappa_{ref} T_{ref}}{\kappa r}}$$

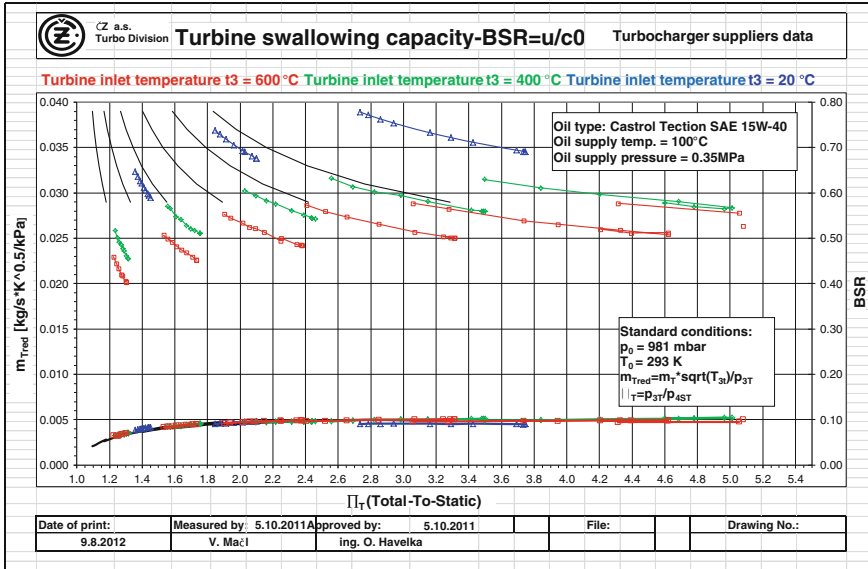


Fig. 22 Turbine swallowing capacity and blade speed ratio testing results

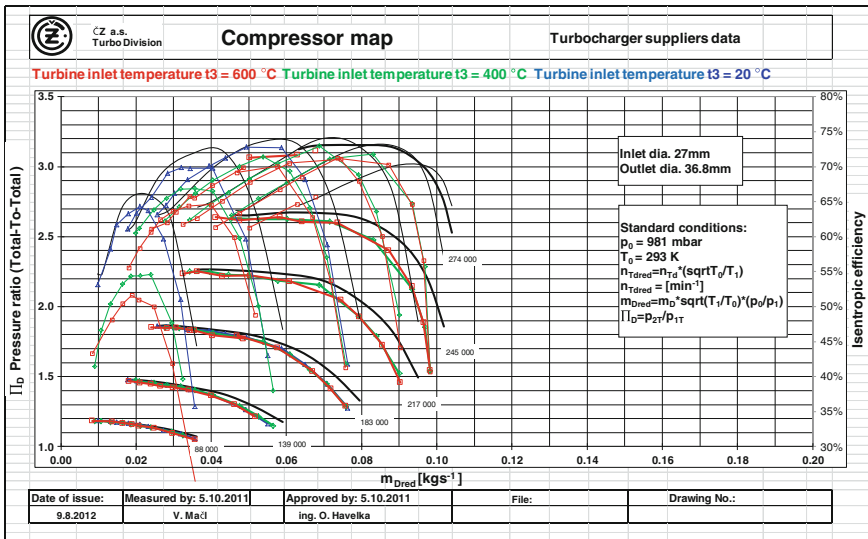


Fig. 23 Compressor pressure ratio and isentropic efficiency testing results

reduced speed is. If the inlet conditions are often almost unchanged at compressor inlet, the correction of mass flow rate and speed is used instead of reduction to respect the dependence of mass flow rate on specific gas constant r and $\kappa = c_p / c_v$ in some

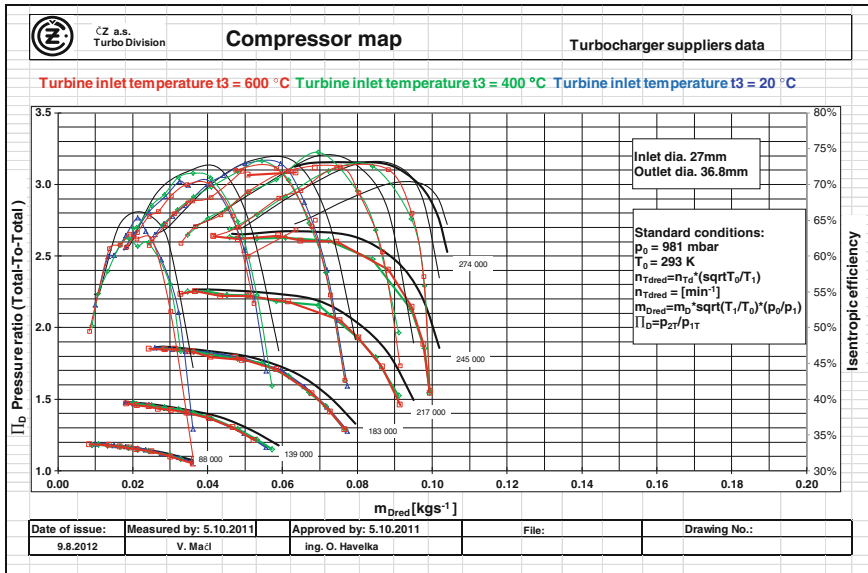


Fig. 24 Compressor isentropic efficiency testing results evaluated using regression interpolation

cases like using EGR upstream of compressor or using specific fuels, which yields burned gas very different from hydrocarbon fuels (hydrogen for example). The

corrected mass flow is $\dot{m}_{corr} = \frac{\dot{m} \sqrt{T_{tot,in}}}{p_{tot,in}} \frac{p_{ref}}{\sqrt{T_{ref}}} \sqrt{\frac{\gamma K_{ref}}{\gamma K}}$ and finally K corrected speed is

$n_{corr} = n \sqrt{\frac{T_{ref}}{T_{tot,in}}} \sqrt{\frac{\gamma K_{ref}}{\gamma K}}$. Another dimensionless parameter, which takes the gas

properties into account, is blade-speed ratio (BSR), which is defined from ideal velocity after isentropic expansion c_s and from blade tip speed u_T :

$$BSR = x = \frac{u_T}{c_s} = \frac{\pi D_T}{60} \frac{n_{Tred}}{\sqrt{c_p T \left[1 - \left(\frac{p_4}{p_{3tot}} \right)^{\frac{\gamma_T - 1}{\gamma_T}} \right]}}$$

In Fig. 21 there is comparison of measured data at three different turbine inlet temperatures, e.g., $t_3 = 600; 400$ and 20 °C with turbocharger suppliers data measured at 600 °C (black curves). As it is obvious from the diagram there is good agreement concerning the turbine swallowing capacity, but there are large differences in turbine efficiency (about 10 %). Figure 22 compares then the blade speed ratio computed from measured data and from data given by the turbocharger supplier (black curves). The measured BSR is the highest for the value of turbine inlet temperature of 20 °C , which is in compliance with the BSR definition. But if comparing the measured data at 600 °C and the suppliers data, which were measured also at 600 °C , there are another great differences in BSR.

Concerning compressor side, the rough testing results are shown in Fig. 23. From pressure ratio versus mass flow rate point of view the measured data quite agree with

the “paper characteristic” even if the measured pressure ratio is significantly lower at higher turbocharger speed (over 200,000) than the “paper” one. On the other hand, measured surge line seems to be shifted to lower mass flow rate, which seems promising for the project use. From the compressor isentropic efficiency point of view, there are great differences between each measurement with different turbine inlet temperatures. This is caused by heat transfer between turbine and compressor casing, which significantly affects the turbine and compressor efficiency. As a result of that, the turbine power determined from total enthalpy difference is higher than really it is, because the turbine outlet temperature is lower due to the thermal flux from turbine to compressor casing. On the other hand, the air temperature at compressor outlet is higher than it would be after adiabatic compression, which deteriorates the compressor efficiency. To avoid this phenomena turbine driven by cold air has been tested, where no thermal flux between turbine and compressor casing has been present (Fig. 24). Simultaneously the mechanical loss power can be found from oil temperature difference at inlet and outlet without being influenced by turbine impeller heat flux. The most accurate method is based on regression interpolation for the same average temperatures of oil and turbine air for finding mechanical losses or the same average temperatures of air at compressor and turbine sides for finding compressor isentropic efficiency [7].

5.4 Summary/Conclusions

This paper deals with the European research project POWERFUL coordinated by Renault, focused on the development of a downsized two-stroke two cylinder compression ignition 0.73l engine with the HCCI combustion. The air management of such innovative engine requires an advanced boosting architecture design. Therefore, to find technical solutions for the air loop system, large amount of 1-D steady state simulations has been carried out. The simulation task has been split up among (1) Le Moteur Moderne (2) Josef Božek Research Centre at the Czech Technical University in Prague and (3) Renault. The second part of this paper deals with testing of selected boosting devices during 1-D steady state simulations. These tests has been made using ČZ Strakonice a.s., Turbo Division test rig.

The basis GT-POWER model was calibrated by Renault based on the preliminary test rig results and included several assumptions related to the scavenging, combustion and thermal characteristics.

To achieve the engine power target of 45 kW, two boosting stages are required. With regard to the scavenging needs of the two-stroke engine, a supercharger is compounded with the turbocharger. Several configurations were investigated and compared with respect to the fuel consumption: (a) positive displacement or centrifugal supercharger set upstream or downstream of the turbocharger (b) supercharger driven mechanically or electrically (c) variable or fixed mechanical transmission (d) waste gate or variable geometry turbine and (e) low or middle pressure EGR loop.

The overall air management system needs to provide around 5.4 bar_{Absolute} of boost pressure at the fresh air mass flow rate of 80 g/s to achieve the 45 kW engine power target. These requirements lead to unusual high pressure ratios at low mass flow rates even with the two stage architecture. Therefore, at least one of the boosting components is getting out of the range of the common provider availabilities.

The best compromise regarding the air loop feasibility, power achievement and fuel consumption is a configuration combining the mechanical positive displacement charger set downstream of the waste gate turbocharger. The charger is driven by a mechanical dual drive system supplied by its supplier which is equivalent to a gear box with two gear ratios. Additionally, the engine air flow needs to be controlled by a charger by-pass. The main drawback of this solution is a necessity of efficient charge air cooling between the boosting stages to limit the Roots type supercharger outlet temperature to 150 °C. Moreover, the procurable charger is larger than required (250 cm³ instead of idealistic charger with 150 cm³) which would lead to operations in non-optimal efficiency areas.

The drawback of the configuration with the supercharger in the high pressure stage would be reduced in the configuration setting the supercharger upstream of the turbocharger [8]. Nevertheless, the feasibility of that configuration is limited by the procurement of a small turbocharger compressor wheel. Additionally, such configuration leads to higher fuel penalties particularly because the EGR loop needs to be set on the low pressure exhaust branch which heightens the charger power demand.

As a backup solution, a configuration setting the centrifugal charger downstream of the waste gate turbocharger is selected. Moreover, the charger is driven using a variable gear ratio system which brings more engine control possibilities than the dual drive system. As the variable drive system is still in the early prototyping stage, the configuration with positive displacement charger stays the principal solution.

In the further work selected boosting devices characteristics have been verified on the test rig. Concerning Roots type supercharger the measured characteristic correspond to that used for 1-D simulations [9]. The main issue met during testing this device was the outlet temperature limitation. Even if this limitation has been shifted from 150 °C used for simulations to 170 °C all the speed lines couldn't be verified up to the highest pressure ratios. Moreover, even if the temperature limitation has been followed, the supercharger got seized during its testing.

Regarding mechanically driven centrifugal supercharger with continuously variable transmission pressure ratio versus mass flow rate characteristic there was realized a good agreement between measured data at ČZ Strakonice test bed and data used for 1-D simulations. Nevertheless, surge limit of the compressor is shifted to higher mass flow rates by measured characteristic than by original data, which can cause problems at low engine speeds. Concerning isentropic efficiency there is large difference at low compressor speeds (up to 20 %) and small difference (about 2 %) at high compressor speed. Next to the pressure ratio versus mass flow rate characteristic and isentropic efficiency total mechanical efficiency of the whole device has

been evaluated and has reached up to 60 % at the highest compressor speed and CVT transmission ratio. As the last point of the testing this supercharger mechanical efficiency at constant load and different CVT transmission ratio has been investigated. At constant compressor load defined by constant pressure ratio of 1.32 and constant speed of 140,000 rpm total mechanical efficiency differs in range of 10 % with the highest value about 35 % in the transmission ratio range of 1.8–2.4. Nevertheless, power consumption of the centrifugal supercharger without power input of the additional hydraulic equipment is in most of the selected points twice higher than by Roots type supercharger.

At waste-gate turbocharger here is good agreement concerning the turbine swallowing capacity, but there are large differences in turbine isentropic efficiency (about 10 %), which is decisive for possibility to reach the engine peak power. There are too great differences in BSR comparing measured data at turbine inlet temperature of 600 °C. At compressor side from pressure ratio versus mass flow rate point of view the measured data quite agree with the “paper characteristic” even if the measured pressure ratio is significantly lower at higher turbocharger speed (over 200,000) than the “paper” one. On the other hand, measured surge line seems to be shifted to lower mass flow rate, which seems promising for the project use. Avoiding heat transfer from turbine to compressor casing with help of regression interpolation fitted by data measured at turbine driven by cold air, the compressor isentropic efficiency seems to be comparable with “suppliers data” and with data measured at different temperatures at turbine inlet.

Acknowledgments This research has been sponsored by the European Union in framework of the POWERFUL project, seventh framework program FP7/2007-2013, theme 7, sustainable surface transport, grant agreement No. SCP8-GA-2009-234032. Further, the project was also financially supported by the Ministry of Education, Czech Republic, as a project 7E10051. The authors gratefully appreciate this support.

This research has been realized using the support of EU Regional Development Fund in OP R&D for Innovations (OP VaVpI) and Ministry for Education, Czech Republic, project # CZ.1.05/2.1.00/03.0125 Acquisition of Technology for Vehicle Center of Sustainable Mobility. This support is gratefully acknowledged.

References

1. Heywood JB, Sher E (1999) The two—stroke cycle engine: its development, operation and design. Taylor and Francis, Philadelphia. ISBN 1-56032-831-2
2. Wyczalek FA (1991) Two-stroke engine technology in the 1990s. SAE Paper 910663
3. De Marco CA, Mattarelli E, Paltrinieri F, Rinaldini CA (2007) A new combustion system for 2-stroke HSDI diesel engines. SAE Technical Paper, 2007-01-1255
4. Duret P (2011) The small gasoline DI 2-stroke engine: an adapted range extender for electric vehicles? Keynote paper presented at SIAT-2011
5. Knoll R (1998) AVL two-stroke diesel engine. SAE Paper 981038
6. DIN 1952 VDI-Durchfluß. Meßregeln, Ausgabe 1943
7. Macek J, Pohorelský L (2010) Supercharger and turbocharger tests at CZ a.s. Strakonice. ČVUT Praha 2010

8. Servant C, Quechon N, Obernesser P Two-stroke engine e.g. two-stroke diesel engine, has air deflector located downstream of part of seat in intake valve of intake duct, and directing air flow from intake duct towards lower part of combustion chamber. Patent Renault FR2931880
9. Gamma Technologies (2010) GT-POWER users' manual version 7.1. 2010

Part II
Fuel Injection and Sprays

Spray Characteristics of a Fuel Injector: A CFD Study

J. Suresh Kumar, V. Ganesan, J. M. Mallikarjuna
and S. Govindarajan

Abstract Main function of a fuel injector used in internal combustion (IC) engines is to properly atomize liquid fuel for vaporizing and mixing with air. In order to achieve good vaporization and mixing, location of the fuel injector inside the combustion chamber is very critical especially in gasoline direct injection engines. In automotive engines, vehicle layout possesses main constraint to mount the fuel injector at a particular location and orientation. In the present study, a conventional carburetor fitted engine was operated with port fuel injection to meet the future emission standards for a two-wheeler application. In general, for gasoline port injection engines, straight cone angle fuel injectors are mainly employed. The direction of fuel spray (cone angle) should be targeted to minimize the wall wetting, which in turn affects the performance and emission characteristics of the engine. Therefore, it is important to study the fuel spray characteristics in these engines. In this study, a CFD analysis has been carried out on a fuel injector to understand the effect of cone angle (8 and 18°) on fuel penetration, droplet size, and evaporation characteristics. In order to carry out CFD analysis, a fuel injector commonly used for Indian two-wheeler application is considered. The geometric model of the injector is generated using ProE software. The model is meshed with polyhedral cells and surface refinement is done at injector and intake pipe regions. The meshed model has a grid density of 0.2 million cells. Analysis has been carried out with inlet air velocity (at the outlet of throttle body) and

F2012-A02-003

J. Suresh Kumar · V. Ganesan · J. M. Mallikarjuna (✉)
Internal Combustion Engines Laboratory, Department of Mechanical Engineering, Indian
Institute of Technology Madras, Chennai 600036, India
e-mail: manikumariitm@yahoo.co.in

S. Govindarajan
UCAL Fuel Systems Ltd, Ambattur, 600058, India

pressure outlet boundary conditions (cylinder pressure at bottom dead center). Outer surfaces are considered as walls with no-slip boundary condition and intake temperature used was measured from an actual engine, which is used as the boundary conditions. In this study, wide-open throttle position is selected for detailed numerical analysis. Out of the two cone angles considered, 8° is found to be better in terms of lower sauter mean diameter (SMD), fuel evaporation and penetration. However, higher cone angle is found to be better, due to larger spread of fuel and higher probability of getting energy from incoming air so that the size of droplet can be smaller and mixing with the air will be faster, which will enhance the fuel evaporation. At wide-open throttle position, due to higher air velocities, air–fuel mixing is better due to higher evaporation rate with a lesser particle diameter. The CFD results have been compared with steady state measurements in a test bench and the predicted results found to match with experimental results reasonably well with a maximum deviation less than about 6 %.

Keywords Fuel injector · CFD · Spray characteristics · Velocity · Droplet size

1 Introduction

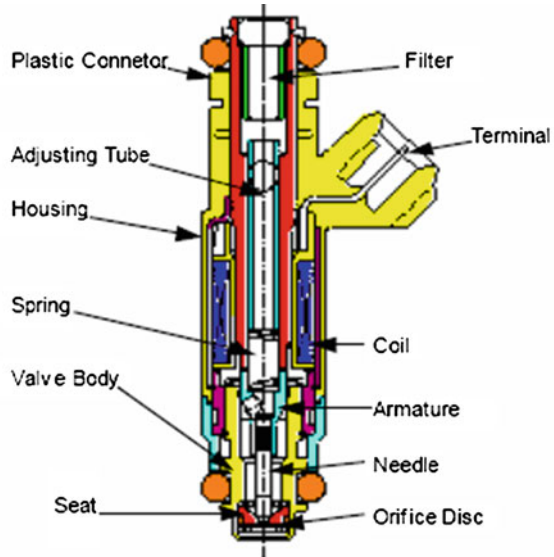
For gasoline fuel injection systems, spray atomization and proper distribution have greater impact on engine performance and emissions. Mixture formation process starts with the injection of liquid fuel. Normally the spray can be defined by mean droplet size, initial velocity, pattern and targeting. The fuel droplet interacts with air, creating fuel vapour and wall films. The process starts with evaporation of liquid fuel and the formation of combustible air–fuel mixture. Reduction in the SMD will improve the rate of evaporation due to overall increase in surface area.

Figure 1 shows the schematic diagram of a fuel injector under consideration. The injector has an orifice plate and the major components include valve body and valve seat. The spray distribution and atomization are mainly controlled by the orifice design and valve/seat geometry.

Possibility of wall impingement is more in IC engines, where the fuel injector is placed in the intake manifold. Spray impingement results in spray splashing and wall film formation. Therefore, appropriate mixing with proper spray development and distribution is must to meet the transient conditions. For a given injector design, since the diameter and number of holes are fixed, the SMD gets automatically fixed. Therefore, the main challenge is to place the injector at the appropriate position for the given engine layout. The injector position controls the droplet distribution, spray tip penetration and spray angle. This is mainly due to the transient conditions in which air enters the intake manifold and mixes with the fuel.

The main objectives of the present study are to investigate the effect of cone angle and predict the fuel droplet size, evaporation and penetration characteristics. Two different cone angles are selected for the study. Numerical study has been

Fig. 1 Schematic of fuel injector (Ren and Sayar [4])



carried at five different engine conditions covering the entire range of operation in order to understand the effect of air velocities and results of at wide-open throttle position is presented and discussed. In order to simulate the actual condition of the engine, velocity boundary condition is imposed at the inlet and cylinder pressure at bottom dead centre is considered as outlet conditions.

2 Literature Survey

Burger et al. [1] in their work predicted fuel injection and spray penetration within the intake port of a spark ignition engine. They have carried out parametric study on understanding the fuel penetration process. They have concluded that the penetration time for a core droplet is shorter than the droplet at the tip of the spray. They concluded that the fuel preparation process was influenced by secondary effects, including droplet breakup and wall interaction. David et al. [2] examined the drop size distribution and spray image of transient sprays. In their experiment, they have observed that the droplet size decreased as the spray progresses downstream. Manshik et al. [3] investigated the liquid fuel film on wall by integration continuity, momentum and energy equations and validated the film thickness with optical measurements. Ren and Sayar [4] predicted numerically flow inside the nozzle, its direction and shape of the liquid jet at the nozzle exit. They have concluded that atomization could be improved by modifying the length to diameter ratio of nozzle. Han and Xu [5] modeled the wall film dynamics of impinging sprays. They have observed that large liquid fuel deposition on the

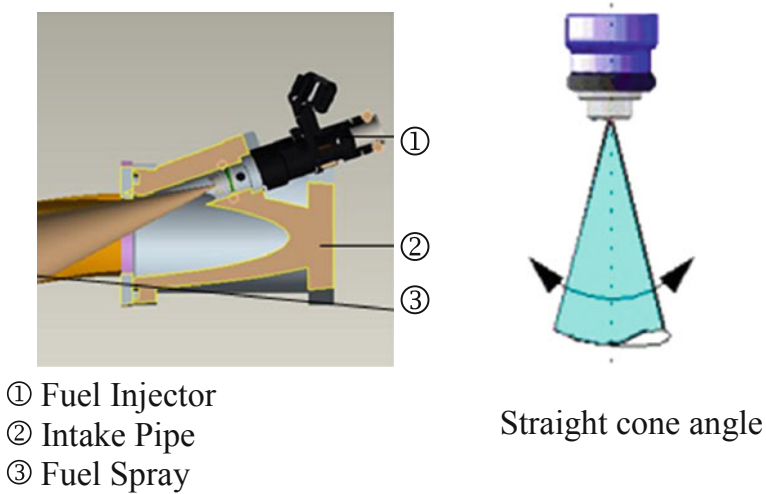


Fig. 2 Three dimensional model and spray structure

valve and port surfaces and concluded that this could be the source of deposition of fuel on valves, heads, liner and piston surfaces with open valve injection.

3 CFD Analysis

3.1 Fuel Injector Geometry and Spray Structure

The fuel injector geometry under consideration is as shown in Fig. 2. It consists of an intake pipe, in which the fuel injector is positioned. The fuel spray is also shown in Fig. 2a. The cone angle is shown in Fig. 2b. Cone angle is the included angle through which the spray spreads. For the present study, two cone-angles of 8 and 18° are considered. In case of straight spray, cone angle, will be zero.

3.2 Numerical Methodology

The present study takes into account the dispersed multi-phase flow (LaGrange model). In this, the flow is treated as continuous phase, and one or more dispersed phase in the form of liquid droplets or gas bubbles. The motion of the dispersed phase will be influenced by that of the continuous phase and vice versa via displacement and interface momentum, mass and heat transfer effects.

The governing equations for mass, momentum and energy for the dispersed phase are considered for each individual element. The governing equations for the carrier phase are expressed in Eulerian form and suitably modified to take account of the presence of the dispersed phase. Modeling of film formation and dynamics includes solving of mass, momentum and energy equations using thin film assumption using numerical methods.

3.3 Governing Equations

The instantaneous fluid velocity and droplet velocity are denoted by u and u_d . Where subscript d denotes droplet dispersed phase. The momentum equation for a droplet of mass m_d is [6].

$$m_d \frac{d\mathbf{u}_d}{dt} = \mathbf{F}_{dr} + \mathbf{F}_p + \mathbf{F}_{am} + \mathbf{F}_b \quad (1)$$

where, F_{dr} is drag force, F_p is pressure force, F_{am} is virtual mass force required to accelerate the carrier fluid entrained by the droplet, F_b is body force.

The mass equation for a droplet of mass m_d is,

$$\frac{dm_d}{dt} = -A_s F_m \quad (2)$$

where, F_m is the mass transfer rate per unit surface area, A_s is the droplet surface area.

The droplet energy balance equation is given by,

$$m_d c_{p,d} \frac{dT_d}{dt} = -A_s \dot{q}_d'' + h_{fg} \frac{dm_d}{dt} \quad (3)$$

where, $C_{p,d}$ is droplet specific heat, A_s is droplet surface area, h_{fg} is latent heat of phase change, q_d'' is the surface heat flux.

As explained earlier, droplets may become unstable under the action of the interfacial forces induced by their motion relative to the continuous phase. For the present analysis, for droplet, Reitz and Diwakar model is used [6]. According to this model, droplet break up is due to aerodynamic forces, which occurs due to, bag break-up, resulting from non-uniform pressure field around the droplet and stripping break-up, in which liquid is sheared from the droplet surface. The break-up rate is calculated from,

$$\frac{dD_d}{dt} = - \frac{(D_d - D_{d,stable})}{\tau_b} \quad (4)$$

where, D_d is the instantaneous droplet diameter, $D_{d,stable}$ is the theoretical criterion for onset of break-up, τ_b is the characteristic time scale.

For bag break-up, the instability is determined by a critical value called Weber number, which is given by

$$\text{We} \equiv \frac{\rho |\mathbf{u} - \mathbf{u}_d|^2 D d}{2\sigma_d} \quad (5)$$

where, σ_b surface tension coefficient, C_b is the empirical value.

For stripping break-up, the criteria for onset regime is

$$\frac{\text{We}}{\sqrt{\text{Re}_d}} \geq C_{s1} \quad (6)$$

where, Re_d is droplet Reynolds number and C_{s1} is constant (0.5).

3.4 Discretization

In the discretization of the computational domain, the Lagrangian conservation equation of dispersed particles in a continuous fluid phase is of first-order differential form. These equations are integrated along the trajectories of each of the computational parcels comprising the statistical sample of real population.

3.5 Boundary Conditions

The injection process includes the flow in the nozzle hole and atomization. The atomization gives rise to a fuel droplet spray represented by a set of computational parcels, each containing a number of droplets. The histories of computational parcels are obtained from Lagrangian conservation equations of mass, momentum, and energy. As mentioned earlier, air velocity at inlet is considered at the entry of the pipe and cylinder pressure at bottom dead center (BDC) as outlet condition.

3.6 Meshed View

Figure 3 shows the meshed view of the computation domain under study. The fuel injector location in the intake pipe is shown from which the fuel starts traveling before meeting with the incoming air. A section (A-A) is taken at a distance of 10 mm from the injector tip location is also shown, in which the grid independency was checked for different number of cells and the details are given in the following sections.

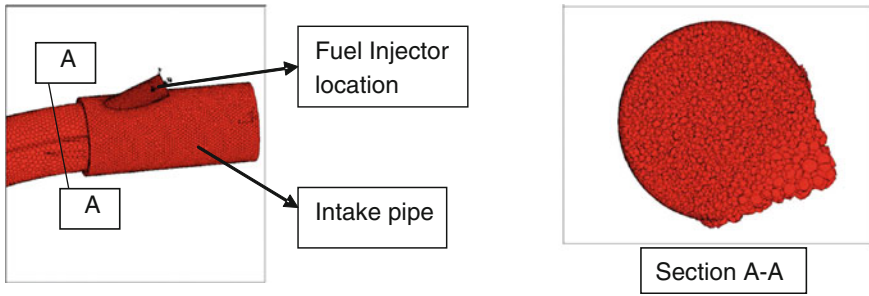


Fig. 3 Meshed view of computational domain

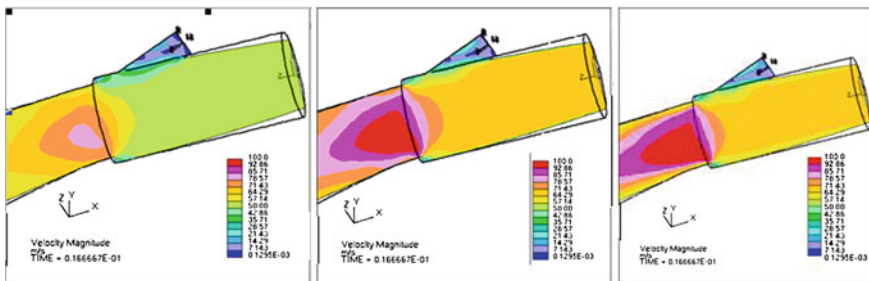


Fig. 4 Velocity plot for 0.1, 0.2 and 0.4 million cells respectively

3.7 Grid Independence Study

Grid independence study was conducted for the geometry under consideration. An initial model with a grid size of 0.2 million cells was made. Coarser grid size of 0.1 million cells and finer size of 0.4 million cells were considered. For all the cases, same initial and boundary conditions are employed. The analysis shows the contour plots of velocity (Fig. 4) that the variation of flow pattern and velocity values with 0.2 and 0.4 million cells are almost same. A section A-A at a distance of 10 mm was taken and a group of cells is identified to observe the change in velocity. The velocity at the downstream of the pipe varies between 70–100 m/s for 0.2 and 0.4 million cells, whereas the velocity varies between 50–70 m/s for 0.1 million cells. This is mainly due to the coarse nature of 0.1 million cells. Therefore, finally, 0.2 million cells are selected considering the computational expenses and time (Fig. 5).

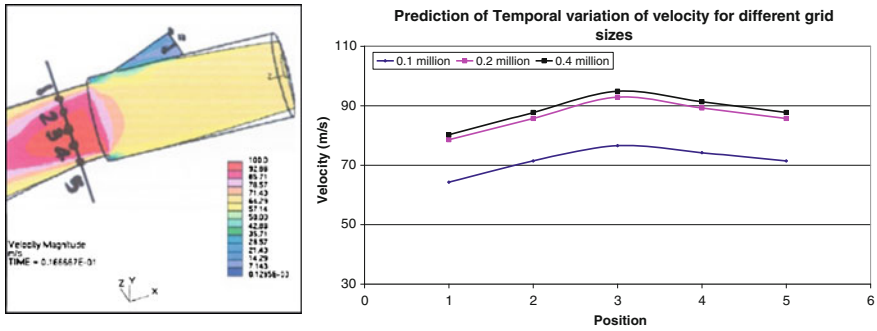


Fig. 5 Prediction of temporal variation of velocity for different grid sizes

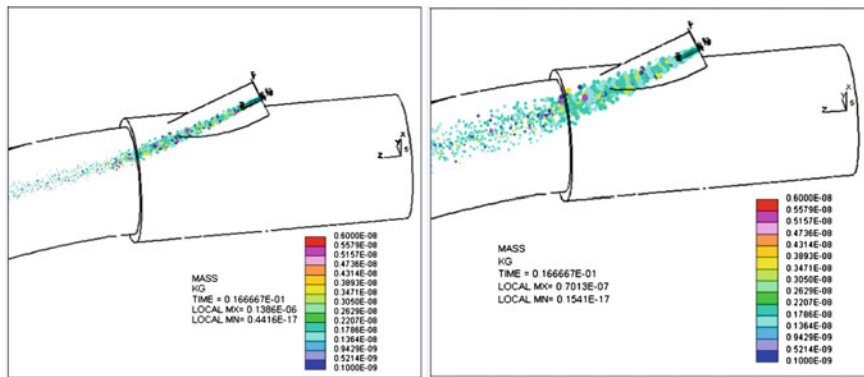


Fig. 6 Droplet mass distribution for straight cone angle injector

4 Results and Discussions

A detailed numerical analysis has been carried out to analyze the effect of straight and bent cone angle for different throttle openings and results of wide-open throttle conditions are presented and discussed in detail in the following sections. For all the analysis, inlet air velocity was specified as inlet condition at the entrance of the pipe and cylinder pressure was specified at the outlet of the pipe as outlet boundary condition.

In this section, the results obtained from numerical predictions for 8 and 18° cone angles are presented and discussed. From Fig. 6, it is seen that for 8°, the injected stream of fuel is narrow compared to 18° cone angle. For both the cases, it is observed that the droplet density is high closer to exit of the injector. Ren and Sayar suggests [4] that the fuel droplets could be treated as a very dense mixture in air. This is quite evident from the Fig. 6. Initially the spray is in pure liquid form and start entraining the air, thereby vapourizing the fuel as it moves the

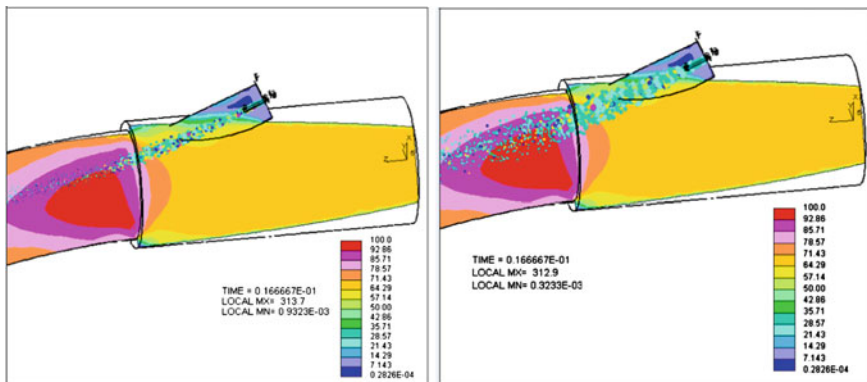


Fig. 7 Velocity plot of air and fuel for straight cone angle injector

downstream of the pipe. It mixes with the incoming air and the temperature of the molecule of fuel reduces. As the fuel stream moves downward, the liquid fuel droplets become a small fraction of jet volume. The velocity of small droplets relative to the vaporized fuel and entrained air is low, and spray acts as a gas jet. Since the mass of a droplet is proportional to its size, a large droplet has higher momentum than a smaller droplet and penetrates further. Larger droplets need more time to evaporate due to their smaller surface area to volume ratio. These larger droplets do have higher potential for wall wetting. It can be seen from Fig. 6 that the larger droplet penetrates and higher mass droplets are yet to be evaporated for 18° cone angle.

Figure 7 shows the velocity plot super imposed with droplet mass distribution. Ren and Sayar suggests [4] that the initial element of fuel, which leaves the orifice, has a relatively low velocity. A very significant observation from Fig. 7 is that the velocity of incoming air distributes the fuel about the spray axis. It is also observed that the distortion of fuel droplets due to turbulent air flow past the fuel, which carries the fuel particles rapidly to downstream. This also causes separation of the fuel droplets from the spray plume by entrainment of air into the highly turbulent incoming flow.

The velocity value varies between 70–100 m/s for both the cases. There is a centre core region with higher velocity values and it progressively reduces towards the wall of the intake pipe. With the super-imposed droplets, 8° cone angle is mostly exposed to higher velocity region 95–100 m/s, compared to 18° cone angle spray, which is exposed between 70–100 m/s. This may lead to comparatively lesser amount of fuel evaporation of droplet. With the higher spread with 18° cone angle, there are possibilities of few droplets moving towards the wall of the intake pipe. These will adhere to wall and forming a fuel film with additional droplets from the subsequent cycles. This addition of fuel may also cause momentary fuel enrichment causing instability to the air–fuel ratio.

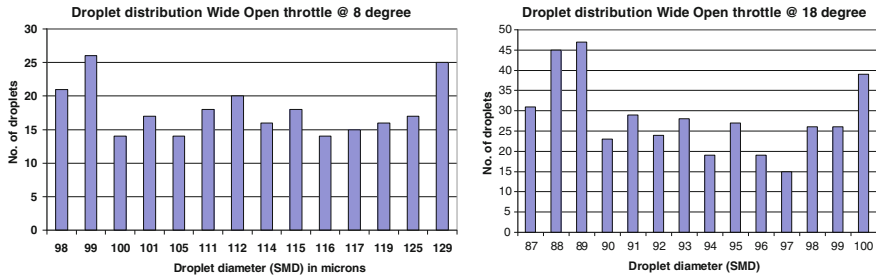
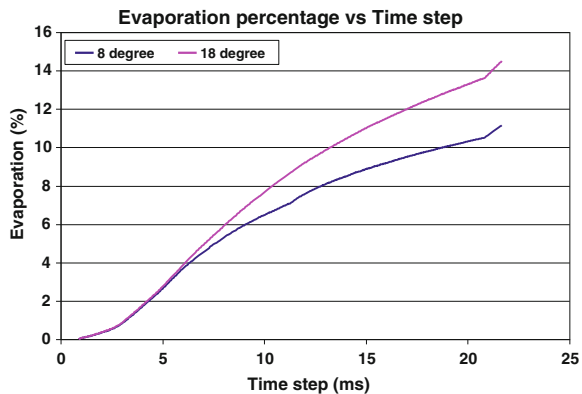


Fig. 8 Comparison of droplet size distribution at 8° cone angle with wide throttle

Fig. 9 Fuel evaporation characteristics at wide-open throttle



4.1 Comparison of Droplet Size Distribution

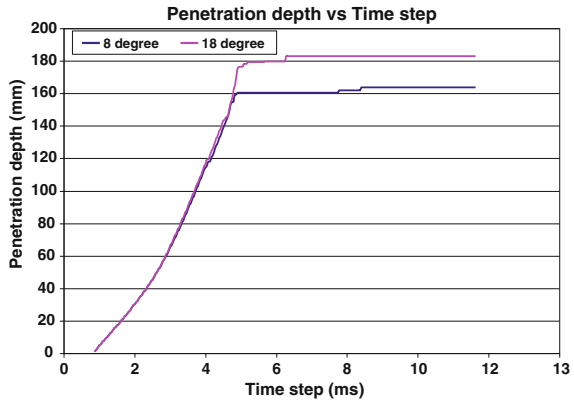
Figure 8 shows the comparison of the droplet diameter (SMD) for 8 and 18° cone angles at wide open throttle operation.

From Fig. 8, it is seen that the maximum number of droplets at wide-open throttle with cone angles of 18 and 8° have 89 and 99 microns respectively. Even though the overall pattern is similar, the range of droplet diameters differs for both the cases. The SMD range for 18° is 87–100 microns and it is 98–129 microns for 8° cone angle. This is attributed to the better air–fuel mixing at 18° cone angle with wide spread of fuel which gets more heat energy from ambient air.

4.2 Fuel Evaporation Characteristics

Further to this study, fuel evaporation characteristic is described below for wide-open throttle positions. From Fig. 9, it is observed that the evaporation percentage is high (15 %) for 18° cone angle when compared to 8° cone angle (11 %). This is

Fig. 10 Fuel penetration characteristics at wide-open throttle



due to better air–fuel mixing in 18° with wider spread of fuel, which is exposed to the high temperature air, thereby the outer surface of droplets evaporate. It can also be observed that, as time progresses, the evaporation percentage increases which means, it allows the fuel more time of exposure to the high temperature air. In addition, it is seen that that until 5 ms, the evaporation percentage is small beyond which it drastically increases.

4.3 Fuel Penetration Characteristics

Fuel penetration depth characteristic is described below for wide-open throttle positions. From Fig. 10, it is observed that the penetration depth is high (183 mm) for 18° cone angle when compared to 8° (163 mm). This is due to smaller SMD for 18° cone angle. It is also observed that the penetration depth increases rapidly up to 5 ms then stabilizes afterwards.

4.4 Validation of Numerical Results

The experimental set-up used for the measurement of fuel injector performance consists of a test fluid reservoir, which contains the fuel to be tested. Fuel is supplied through the re-circulating pump at higher pressure. A pressure relief-valve arrangement as shown in Fig. 11 is used to release the excess pressure and excess fuel is sent back to the tank. A fuel filter is placed in the fuel line. A fuel flow meter fitted in the system is used to measure the fuel flow rate through the fuel injector. Necessary fuel head is maintained in order to avoid any fuel starving when the injector is opened for longer time. Fuel pressure can be adjusted and set using the lever control valve as shown in Fig. 11.

The fuel injector is supplied with pulsed voltage using the driver card as shown in Fig. 11. The voltage supplied and the duration of injection opening were adjusted with the help of an in-built electronic circuit. The driver card was

Fig. 11 Experimental test setup for measuring flow through the fuel injector

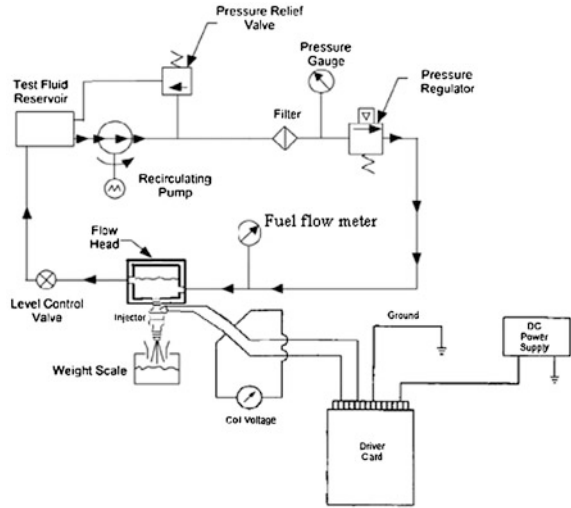
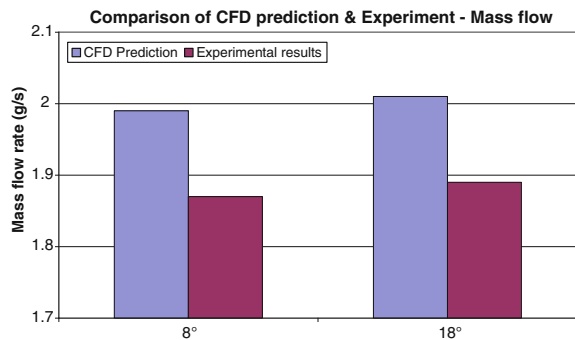


Fig. 12 Comparison of CFD predictions and experimental results



supplied with 24 V DC. A measuring scale was provided at the bottom of the injector, which was used to collect the injected fuel to calculate the static and dynamic flow through the injector.

Figure 12 shows the comparison of CFD predictions and experimental results for wide-open throttle performance for 8 and 18° cone angles. The CFD predicted results are matching reasonably well with the experimental results within an error of about 6 %.

5 Conclusions

The CFD analysis gave a good insight of flow physics in the port fuel injection system. For both the cone angles, the droplet density is high closer to exit of the injector. Initially, the spray is pure liquid form and start entraining the incoming

air, thereby, vapourizing the fuel as it moves downstream of the pipe. As the fuel stream moves downward, the liquid fuel droplets become a small fraction of jet volume. With the higher spread with 18° cone angle, there are possibilities of few droplets moving towards the wall of the intake pipe. This will adhere forming a fuel film with additional droplets from the subsequent cycles. This addition of fuel may also cause momentary fuel enrichment leading to instability in the air–fuel ratio. Out of 8° and 18° cone angles, smaller cone angle is preferable because the spray is narrow with smaller droplet size. In addition, there is less probability of liquid film and droplets attaching to the pipe wall with smaller cone angle. Hence, 8° cone angle is more preferable. The CFD results are matching reasonably well with the experimental results within an error of about 6 %.

References

1. Burger M, Schmehl R, Gorse P, Dullenkoph K, Schafer O, Koch R, Wittig S (2002) Predictions of transient fuel spray phenomena in the intake port of a SI-engine. SAE Paper No. 2002-01-2695
2. David LS, William A, Lee EM, David Mc, Carlos AO, Francis EB (2004) A novel transient drop sizing technique for investigation the role of gasoline injector sprays in fuel mixture preparation. SAE Paper No. 2004-01-1349
3. Manshik K, Hoon C, Youngman C, Kyoungdoug M (2011) Computational and optical investigation of liquid fuel film on the cylinder wall of an SI engine. SAE Paper No. 2003-01-1113. p 12
4. Ren W, Sayar H (2001) Influence of nozzle geometry on spray atomization and shape for port fuel injector. SAE Paper No. 2001-01-0608
5. Han Z., Xu Z (2004) Wall film dynamics modeling for impinging sprays in engines. SAE Paper No. 2004-01-0099
6. Star CD User Manual Version 4.10
7. James AS, David RL, John CS (1980) An experimental and analytical study of engine fuel spray trajectories. SAE Paper No. 800135
8. Ferizinger JH, Peric M (1996) Computational methods for fluid dynamics. Springer, Berlin
9. Heywood JB (1988) Internal combustion engine fundamentals. McGraw Hill International Edition, New York
10. Shaw CT (1992) Using computational dynamics, Prentice Hall, Englewood Cliffs
11. Versteeg HK, Malalasekara W (1995) An introduction to computational fluid dynamics—the finite volume method. Longman Group Limited, Harlow

Co-Simulation Modeling of High-Pressure Fuel System and Engine Performance System and Control System in Common Rail Diesel Engine

Xinglan Xia, Kang Xu, Yin Liu, Min Liu, Shengli Wang
and Chao Ma

Abstract The isolated sub-models may not yield adequate information to deal with system-level interactive issues in the diesel engine, especially when it comes to transient behavior. In this paper, at first the sub-models, which represent high-pressure fuel system and engine performance in common rail diesel engine, have been described with AMESim code, and fuel injection flow rate and cylinder pressure obtained by measurement are used to validate the sub-models. Then the validated sub-models, together with the sub-model of control system which is made with Matlab/Simulink, have been combined and a powerful complete co-simulation model is established. Intensive validation and application runs are underway. Several initial application runs indicate that the model is very effective in describing and analyzing the transient behavior connections among injectors, high-pressure pump, controller and engine parameters. An example of engine performance variability vs. the variability of injector control-valve-lift is simulated. It is found that the control-valve-lift variation has different impact for idle speed condition and maximum torque condition. Also, several initial runs indicate control strategy has great effect on the characteristic of fuel injection and engine performance, and the fluctuation of engine speed can be greatly reduced if control strategy is optimized.

Keywords Co-simulation · Fuel system · Engine performance · Control system

F2012-A02-008

X. Xia (✉) · K. Xu · Y. Liu · M. Liu · S. Wang · C. Ma
FAW Co., Ltd R&D Center Wuxi Fuel Injection Equipment Research Institute, Wuxi, China
e-mail: xxl@wfiери.com

1 Introduction

The characteristics of fuel injection play an important role in the performance and exhaust emission of diesel engine. In common rail fuel system, the characteristics of fuel injection is concerned both the structure parameters of injector and control strategy of control system (or electronic control unit—ECU). Meanwhile, the speed of the engine and the pressure in the rail pipe are feed to ECU, and the ECU issues commands to adjust fuel injection time and fuel injection duration according to the signal received and interior control strategy. Thus, fuel supply system and engine performance system and ECU constitute an interactive feedback system [1]. The isolated sub-models may not yield adequate information to deal with the system-level interactive issues, especially when it comes to transient behavior. In order to deal with this system-level interactive issues, with fuel supply system as a kernel system, the co-simulation model of fuel supply system and engine performance system and control system is established in common rail diesel engine.

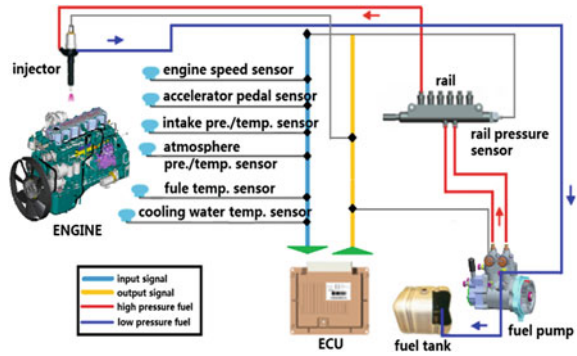
First, with AMESim code the sub-model of one dimensional mechanical-hydraulic fuel supply system, in which the influence of the structure parameters of fuel injector to its dynamic performance can be simulated, is established and validated. Second, a 6 cylinder in line turbocharge diesel engine model is established with IFP-Engine sub-model in AMESim code, which is validated with measurement date. Third, the sub-model of control system, in which the measurement of feedback signal and issue of control signal and the realization method of control strategy are consistent with ECU in real diesel engine, is established and tested with Matlab/simulink code. Finally, a powerful co-simulation model for supporting fuel system design optimization, engine performance variability reduction and field issue trouble-shooting has been developed.

With the co-simulation model, the engine performance variability and injection performance vs. the variability of control-valve-lift and pre-load of nozzle spring in injector is simulated, and the influence of control strategy on the performance of fuel injection system and engine performance is also simulated.

2 Simulation and Validation of Fuel Supply System

The scheme of common rail system in diesel engine is shown in Fig. 1. The fuel is supplied from fuel tank to rail pipe by fuel supply pump. The rail pressure sensor in the rail pipe measures pressure and feeds back to ECU, and ECU controls the open and close of solenoid valve in fuel supply pump and fuel injector according to receiving signal of rail pressure, speed of engine, intake pressure etc. The main components of fuel supply system are fuel injector, fuel supply pump and rail pipe.

Fig. 1 Scheme of common rail system in diesel engine



2.1 Fuel Injector Model

The structure sketch of fuel injector is shown in Figs. 2, 3 is its AMESim model scheme. In the AMESim model, the injector model is complex and begins at the common rail, which is modeled as a pressure boundary (rail pressure 18). After the high pressure fuel flows into fuel injector, it is splits into two branches: one going through connecting tube and inlet orifice 16 up to hydraulic control volume 15, and the other via connecting tube and nozzle volume 14 down to nozzle 12. The motion of the armature 2 and ball poppet valve 3 controls the opening and closing of the outlet orifice 17. When solenoid valve is electrified, the armature 2 and ball poppet valve 3 move up and open the outlet orifice 17, and the solenoid force is calculated by FLUX code. Then, the high pressure fuel in hydraulic control volume 15 goes through outlet orifice 17 and enters low pressure fuel tank (pressure boundary 19). Because effective area of outlet orifice 17 is greater than that of inlet orifice 16, the fuel quantity and fuel pressure in hydraulic control volume 15 become low, and the hydraulic pressure forced on the upper end of control piston 4 becomes low. When the hydraulic force in lower end of needle valve is greater than resultant force of pre-load of needle spring and the hydraulic pressure forced on the upper end of control piston, the needle valve 7 in nozzle 12 opens and the fuel flows through nozzle hole and is injected into cylinder. When the electric current in solenoid valve is cut off, the armature 2 and poppet ball valve 3 move down because of action of the spring force in solenoid valve spring. Thus, the outlet orifice 17 is closed, and the pressure in hydraulic control volume 15 increases. When resultant force of pre-load of needle spring and the hydraulic pressure forced on the upper end of control piston is greater than the hydraulic force in lower end of needle valve, the needle valve closes and fuel injection ends. In the model, the leakage is also considered. There are small clearance between the control piston and injector body, and between the upper part of needle valve and needle valve body. These clearance can result in leakage, and leakage fuel is introduced into fuel tank 19.

When the rail pressure is 60 and 120 MPa, the calculated and measured fuel injection quantity at different injection pulse duration are shown in Fig. 4, and the

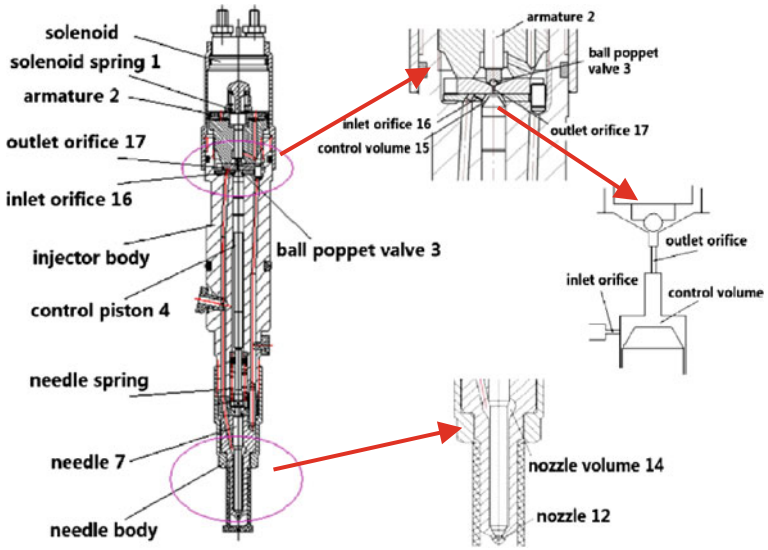


Fig. 2 Sketch of fuel injector

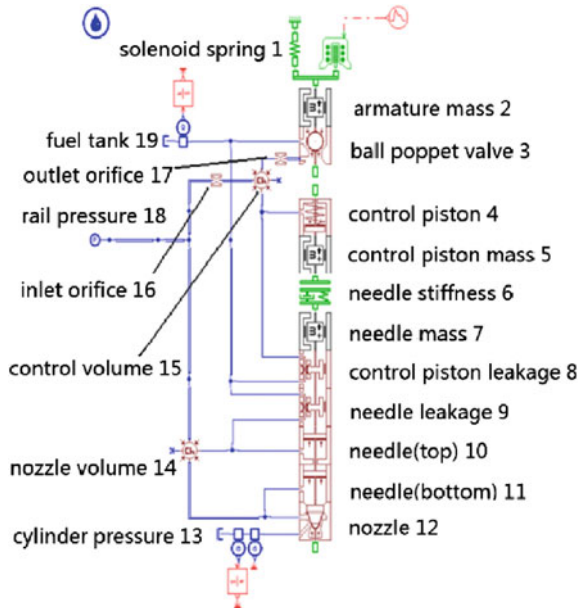


Fig. 3 AMESim model of fuel injector

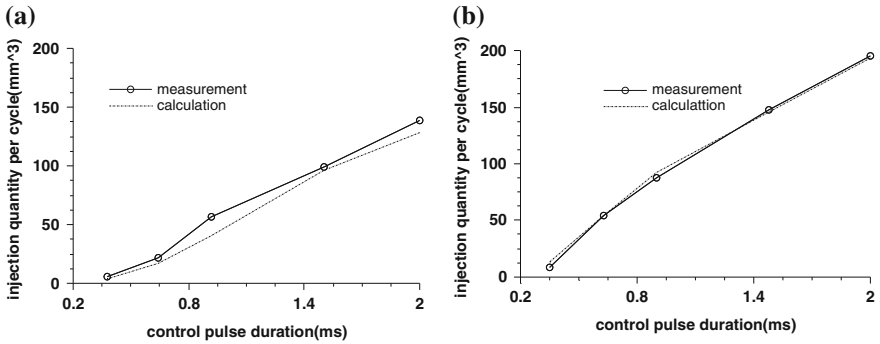


Fig. 4 The calculated and measured fuel injection quantity per cycle. **a** Rail pressure 60 MPa, **b** Rail pressure 120 MPa

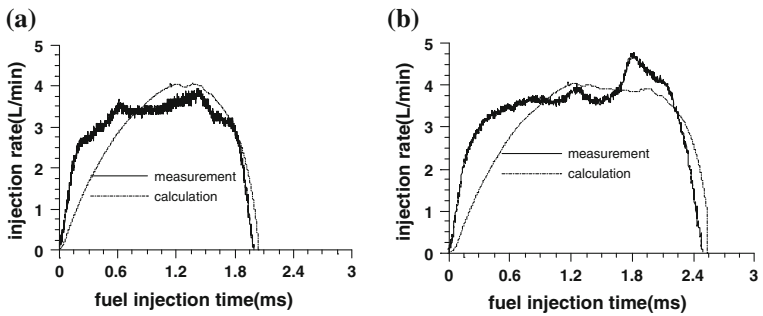


Fig. 5 The calculated and measured fuel injection flow rate. **a** Rail pressure 60 MPa and injection pulse duration 2 ms, **b** Rail pressure 120 Mpa and injection pulse duration 2 ms

calculated and measured injection flow rate is shown in Fig. 5. It is found that the calculated and measured results are in good agreement.

2.2 Fuel Supply Pump and Rail Pipe Model

The fuel is transported from fuel tank to the rail pipe by fuel supply pump. Figure 6 is the sketch of fuel supply pump structure and Fig. 7 is AMESim model for fuel supply pump and rail pipe system. In the model, two plunger pumps, rail pipe, six flow restrictor valve and one pressure restrict valve are included. In the plunger pump model, one pump delivers fuel to cylinder 1,2,3, and the other to cylinder 4,5,6.

In the fuel supply pump, when cam is in its ascending phase, the plunger moves up. Then, ECU issues command, and solenoid valve is electrified, and the armature moves right, and the fuel inlet valve is closed. Meantime the plunger volume is

Fig. 6 Fuel supply pump structure

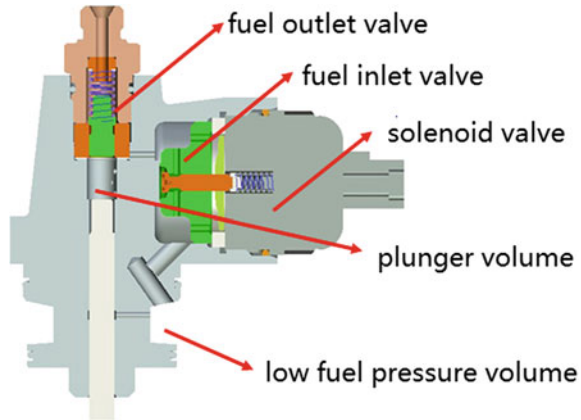
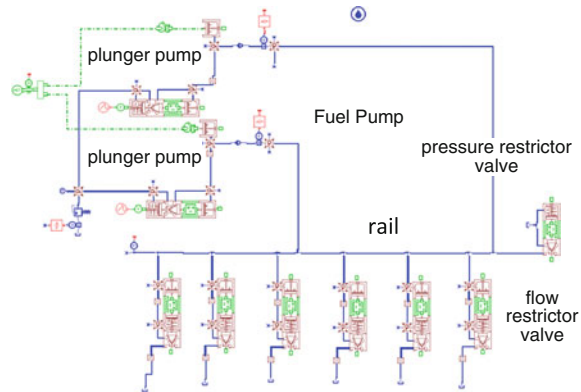


Fig. 7 Fuel supply pump and rail pipe model



separated with low pressure volume, and a closed volume is formed. When the plunger continues to move up, the pressure in plunger volume increases. After the pressure in the plunger volume is greater than the liminal value, the fuel outlet valve opens, and high pressure fuel flows into rail pipe. When cam is in its descending phase, the current in solenoid is cut off, and the plunger moves down in the spring force. Meantime, the plunger volume and the low pressure volume are connected, and low pressure fuel goes into the plunger volume.

3 Simulation and Validation of Engine Performance

The IFP-Engine module is sub-model of one-dimensional engine performance simulation in AMESim code, in which the sub-models of combustion model and heat transfer model are included. In order to simulate engine performance, the sub-models of intake and exhaust system, turbocharger and friction loss model are

added. In one-dimensional engine performance simulation, the most important sub-model is combustion model and turbocharger model.

3.1 Combustion Model

In combustion model, the combustion heat release is calculated using a model based by Barba [2]. After the beginning of the fuel injection, an auto-ignition delay is computed using a model based on an Arrhenius law. When the auto-ignition delay is reached, the combustion starts. The injected fuel in pre-mixed zone burns with a premixing model, whereas the remaining fuel burns with a diffusion model. The model could compute up to 3 different injections. For each injection an auto-ignition delay is defined and the injected fuel could burn either in a pre-mixed or a diffusion zone. The effects of the residual burned gases are taken into account in the calculations of the auto-ignition delay. The equation for the auto-ignition delay is presented below:

$$\theta = (1 + 10X_{res})A_t p^{-n} e^{\frac{T_a}{T}}$$

where T is the temperature in the combustion chamber in K, p is the pressure in the combustion chamber in Pa, X_{res} is the molar fraction of the burned gases in the combustion chamber before the combustion, A_t is the gain for auto-ignition delay, n is the power gain for auto-ignition delay, T_a is the activation temperature for auto-ignition delay. When $1000/\theta$ is equal to unit one, the pre-mixed combustion starts.

The pre-mixed combustion is divided into two mode. The first burning mode is defined as the propagation of a flame in a homogeneous zone. This zone is supposed to be spherical and the propagation of the flame is computed using a standard flame propagation model [3]. Using the hypothesis of a spherical shape for the flame, the combustion heat release rate $\frac{dQ_{prel}}{dt}$ produced by this burning mode is:

$$\frac{dQ_{prel}}{dt} = H_u \bar{\rho}_f^u U_T S_L$$

where H_u is the fuel low heating value in J/kg, $\bar{\rho}_f^u$ is the averaged density of the fuel in the unburned part of the pre-mixed zone. When the flame is initiated in the pre-mixed zone, it is automatically divided into 2 parts, a burned and an unburned zone. These zones are separated by the flame, which propagates from the burned zone to the unburned one. U_T is the turbulent flame speed, computing using the Metghalchi and Keck correlation [4]. The S_L is the laminar flame surface area computed with the hypothesis of a spherical flame [5], which is not affected by the turbulence in the chamber.

With the local evolution of the Fuel/Air equivalence ratio in the pre-mixed zone, the evolution of the mass of the gas in the burned and unburned zones has been computed. In addition to this phenomenon, Barba defines a second burning mode, which is representative of the multiplication of the ignition location in the pre-mixed zone. This multiplication induces a reduction of the total flame surface. The combustion heat release rate for this burning zone $\frac{dQ_{pre2}}{dt}$ is defined as:

$$\frac{dQ_{pre2}}{dt} = \frac{1}{3} H_u \frac{(m_f^{ug})^3}{m_{fg} + m_{rg}} \frac{U_L}{R_z}$$

where m_f^{ug} is the available mass of fuel in the unburned zone, m_{fg} is the mass of entrained fresh air in the zone, and m_{rg} is the mass of entrained residual burned gas in the zone and R_z is the radius of the pre-mixed zone (with the hypothesis of a spherical shape).

The total combustion heat release rate for the premixing combustion is the minimum of the combustion heat release rate for the burning mode 1 and 2, as:

$$\frac{dQ_{pre}}{dt} = \text{Min} \left(\frac{dQ_{pre1}}{dt}, \frac{dQ_{pre2}}{dt} \right)$$

The Barba turbulent combustion model [2] is connected to a mixing frequency defined with the averaged piston velocity and the spray turbulent kinetic energy. Using a frequency model to define the mixing controlled combustion, the combustion heat release rate $\frac{dQ_{diff}}{dt}$ becomes:

$$\frac{dQ_{diff}}{dt} = H_u f_m m_{diff}$$

where f_m is the mixing frequency (Hz) and m_{diff} is the available mass of fuel in the diffusion combustion zone (kg). The mixing frequency f_m controls the combustion.

A first approach is to consider the mixing frequency as the quotient of a characteristic mixing velocity and a characteristic mixing length. The characteristic mixing length L can be defined as:

$$L = \sqrt[3]{\frac{\Phi V_{cyl}}{n_N}}$$

where Φ is the averaged Fuel/Air equivalence ratio, V_{cyl} is the current cylinder volume (m^3) and n_N is the number of holes of the injector. L is proportional to the cubic root of the current cylinder volume. The actual Fuel/Air equivalence ratio takes into account that the characteristic mixing length is not only given by the actual cylinder volume but also by the concentration of oxygen. Finally, the number of nozzle holes influences also the mixing length.

The characteristic mixing velocity is proportional to the turbulent kinetic energy in the chamber and to the piston averaged speed. The turbulence is mainly

generated by the injected spray and defined with a creation and a dissipation term. The two components of the characteristic mixing velocity U_{mix} are summed up according to :

$$U_{\text{mix}} = \sqrt{C_G u_{\text{pis}}^2 + C_k k}$$

where u_{pis} is the averaged piston velocity (m/s) and k is the spray turbulent kinetic energy (m^2/s^2). The two parameters C_G and C_k are important parameters for this model.

Finally, the combustion heat release rate for the mixing controlled combustion is defined as:

$$\frac{dQ_{\text{diff}}}{dt} = H_u \frac{\sqrt{C_G u_{\text{pis}}^2 + C_k k}}{\sqrt[3]{(\Phi V_{\text{cyl}})/n_N}} m_{\text{diff}}$$

3.2 Turbocharger Model

The turbocharger model is composed of sub-models of turbo and compressor and an inertia element. The compressor sub-model is ICECOMP02 model in AMESIM, which is a compressor model for multi-gas applications. The main input data for this sub-model is a performance map (Fig. 8) which follows the standard SAE format. This map usually does not cover the whole operating range of the compressor, so pre-processing functions are integrated in the sub-model to extend the range of the map to the critical regions (low and high speeds, surge, choke).

The turbo sub-model is CETRBSS02 model, which is a single-scroll turbine model for multi-gas applications. The main input data for this sub-model is a performance map (Fig. 9) which also follows the standard SAE format. This map usually does not cover the whole operating range of the turbine, so pre-processing functions are also integrated in the sub-model to extend the range of the map to a wider operating range.

3.3 Validation of Diesel Engine Performance Model

The model of the diesel engine performance simulation is established with IFP-Engine module in AMESim. Figure 10 is the scheme of the model, in which the intake and exhaust system, and the compressor and turbo system are included. Table 1 is the basic specification of the engine. When combustion in the cylinder is simulated, the fuel injection flow rate, which is obtained from experiment in different control pulse duration (Fig. 11), is an important input data. In late

Fig. 8 Performance map of compressor

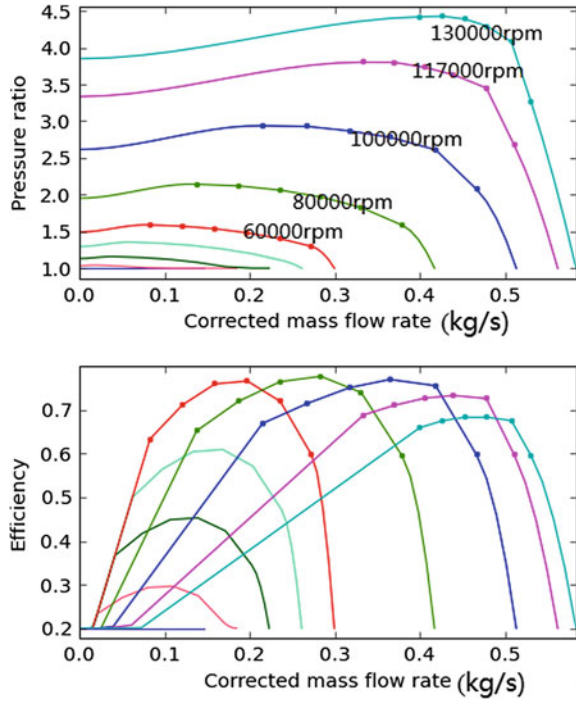
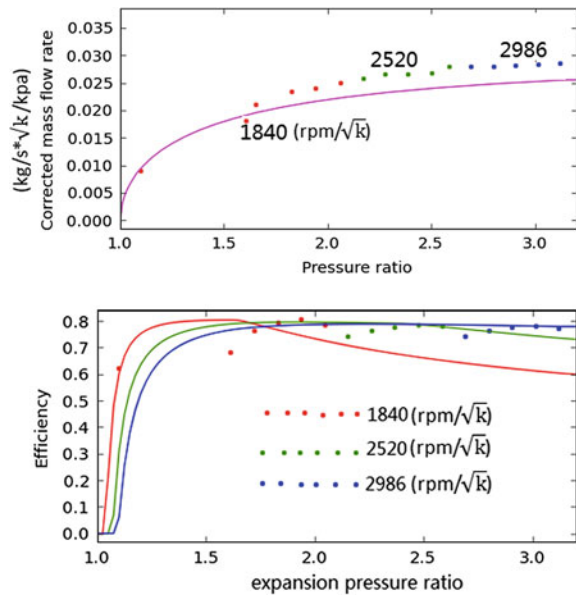


Fig. 9 Performance map of turbo



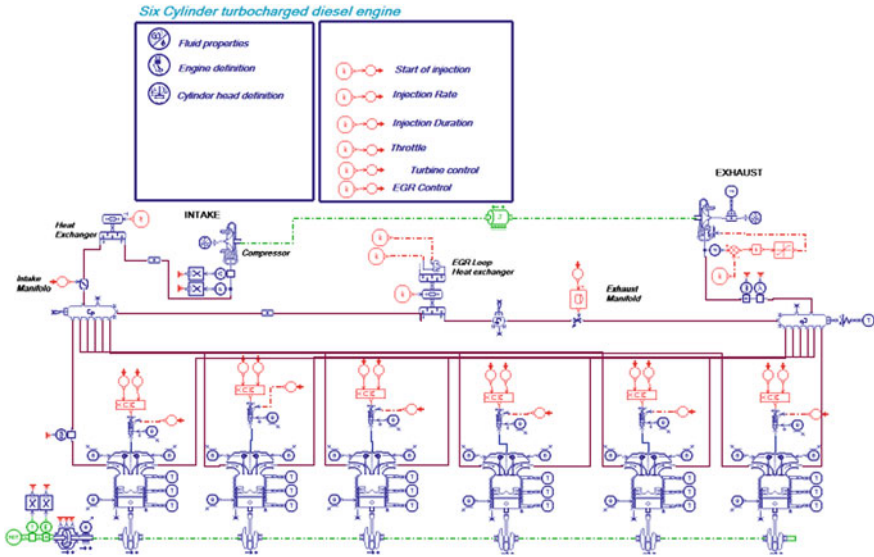
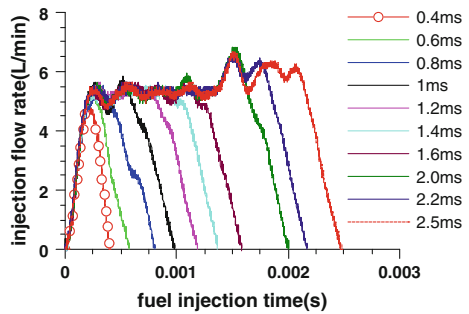


Fig. 10 Engine model scheme

Table 1 The engine specification

Engine type	6 cylinder diesel engine in line with turbo-charge and inter-cooling system
Bore × Stroke	110 × 135 mm
Displacement	7.69 L
Length of connect road	270 mm
Compression ratio	17.5
Fuel system	FAW WFIERI CR
Rated power	212 kW
Rated speed	2300 r/min
Nozzle number	8
Nozzle diameter	0.18 mm

Fig. 11 Fuel injection flow rate



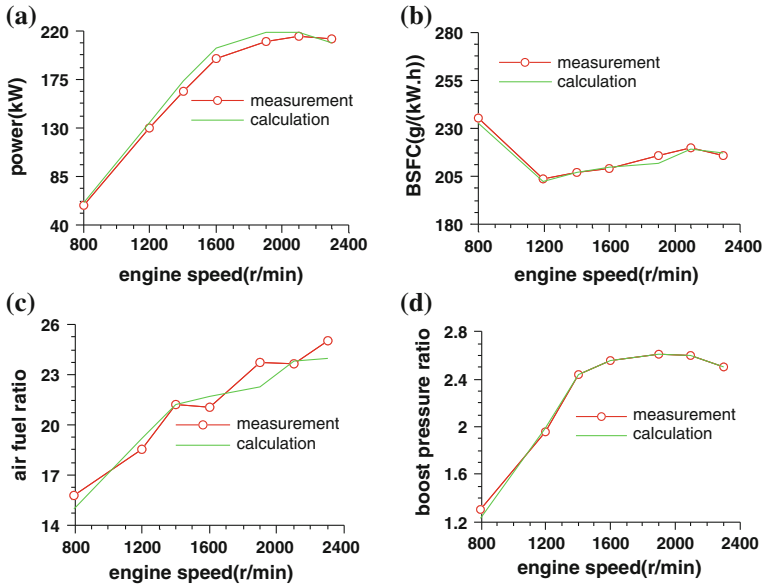


Fig. 12 Comparison of diesel engine performance

co-simulation model, the fuel injection flow rate is calculated from the fuel supply system sub-model.

The measured and simulated diesel engine performance is shown in Fig. 12, and the cylinder pressure is shown in Fig. 13. A good agreement is achieved between them, which indicates the sub-model of engine performance simulation has high accuracy.

4 Control System Model

The control system processes the engine operative conditions and, according to the speed and load values, it sets the optimal injection time, quantity and quality of the injection, aimed at controlling combustion noise, fuel consumption, operation roughness and exhaust pollutant emissions.

The control system model which is simulated with Matlab/simulink, shown in Fig. 14, consists of different sections: the fuel injection quantity, the objective rail pressure, fuel supply time, fuel injection time, fuel injection duration etc. In the control system model, the processing of engine speed signal and the rail pressure signal, and the time of sampling of the rail pressure and the fuel injection pulse duration are consistent with ECU in real engine. The signal of engine speed, opening degree of accelerator pedal, intake air pressure, intake air temperature, atmosphere pressure, atmosphere temperature, cooling water temperature and fuel

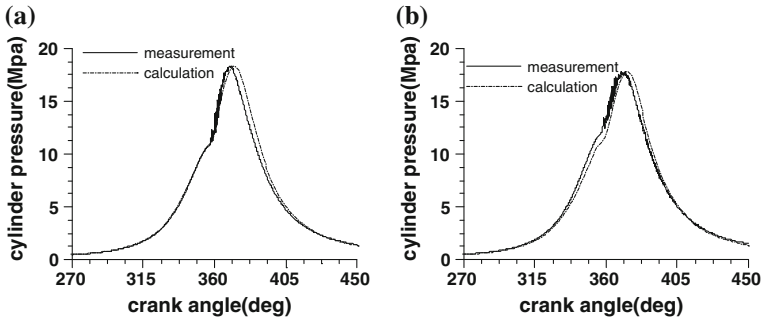


Fig. 13 The comparison of cylinder pressure (a) 1390 r/min and 100 % load (b) 2110 r/min and 100 % load

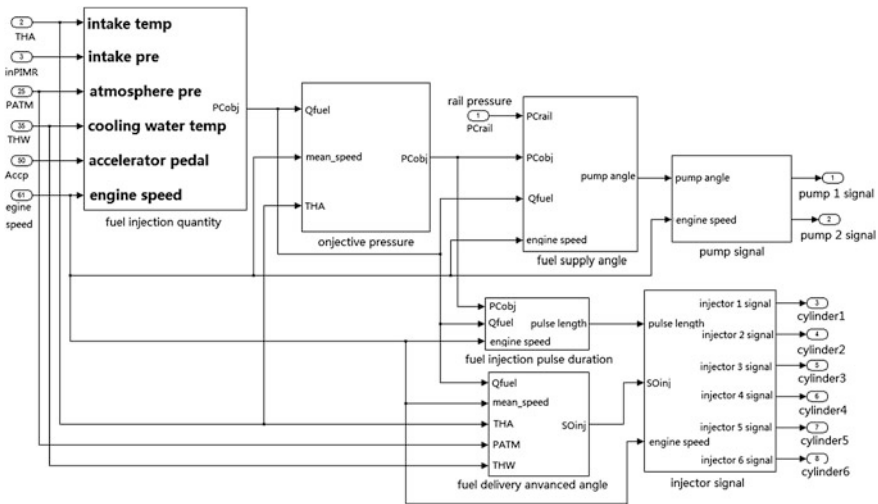


Fig. 14 Control system model scheme

temperature, is input into control system, and control signal of solenoid valve of fuel supply pump and solenoid valve of fuel injector is output from control system.

5 The Results of Co-Simulation

Figure 15 is co-simulation model of high-pressure fuel system and engine performance system and control system in common rail diesel engine, in which the sub-models of fuel supply pump, rail, fuel injector, engine, turbocharger and ECU are included. Figure 16 is the results calculated according to the model in Fig. 15, in which the history of engine speed and rail pressure varies with the opening

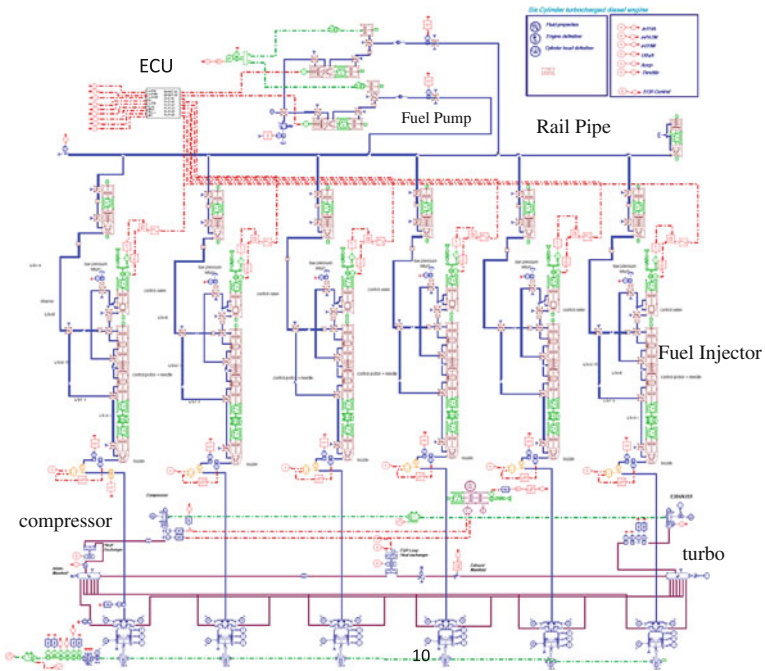


Fig. 15 Co-simulation model

degree of engine accelerator pedal is shown. In the Fig. 16, the initial opening degree of engine accelerator pedal is 50 % and the load is 600 N.m. Then, the opening degree of engine accelerator pedal is increased to 100 %. Again, the opening degree of engine accelerator pedal is decreased to 50 %. According to results in Fig. 16, the engine speed and the rail pressure can vary consistent with the opening degree of engine accelerator pedal, which indicates the co-simulation model can work properly.

5.1 The Influence of Control Valve Lift

The variability of injector control-valve-lift has great influence on engine performance variability. Normally the injector control-valve-lift is 0.07 mm. In the idle speed condition (650 r/min), shown in Fig. 17, when injector control valve lift increases, the needle lift, fuel injection flow rate and cylinder pressure have greater change in sequence four cycles, and the fluctuation amplitude of engine speed and rail pressure increases (Fig. 18), which will result in the increase of vibration in the engine performance. When the injector control valve lift is 0.07, 0.10, 0.12 mm respectively, the engine speed is 650 ± 15 r/min, 640 ± 20 r/min, 635 ± 27 r/min, which indicates that the engine speed decreases from 650 to 635 r/min and

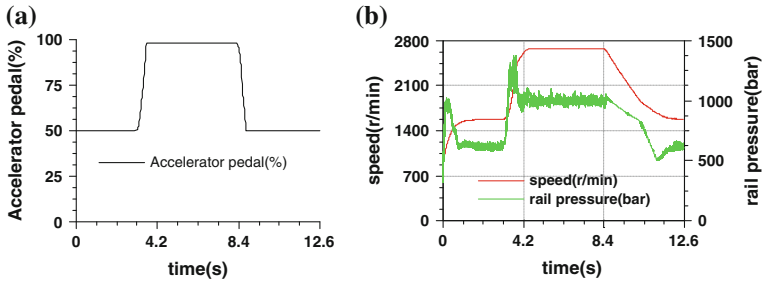


Fig. 16 Engine speed and rail pressure vs. opening degree of engine accelerator pedal. **a** opening degree of engine accelerator pedal, **b** engine speed and rail pressure

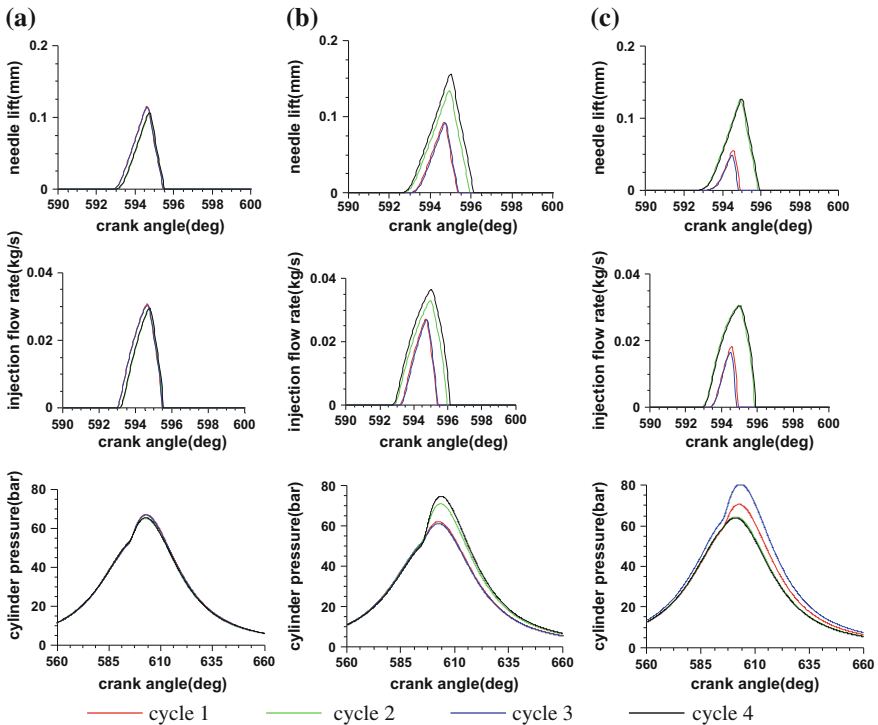


Fig. 17 The influence of control valve lift in idle speed condition

speed fluctuation amplitude increases from ± 15 r/min to ± 27 r/min. In the maximum torque condition (1150 N.m), when injector control valve lift increases, the needle lift, fuel injection flow rate and cylinder pressure have also some changes in different cycle, but their fluctuation amplitude is not as big as that in idle speed condition. when the injector control-valve-lift is 0.07, 0.10, 0.12 mm,

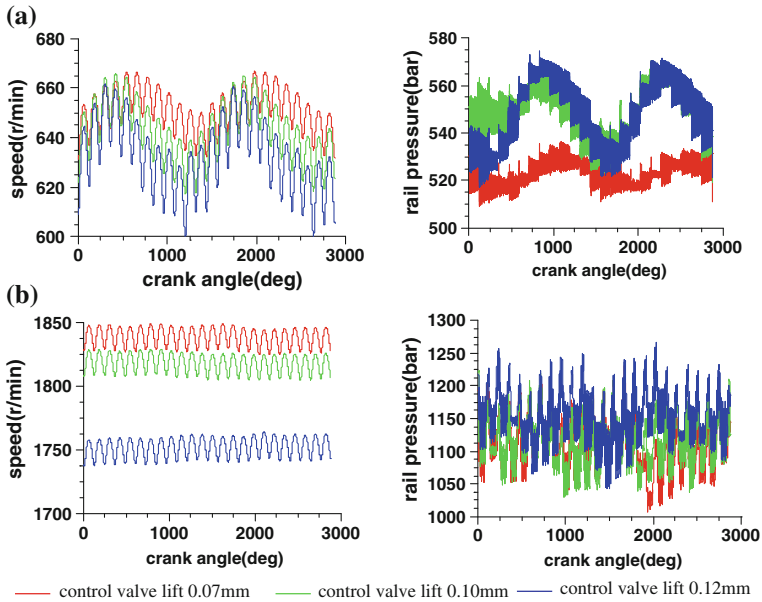


Fig. 18 The influence of control valve lift on engine speed and rail pressure. control valve lift 0.07 mm control valve lift 0.10 mm control valve lift 0.12 mm. (a) idle speed condition (b) maximum torque condition

the engine speed is 1838, 1820, 1748 r/min respectively (Fig. 18). The decrease of engine speed will result in decrease of the power output in the engine. Meantime the rail pressure decrease slightly, but the fluctuation amplitude of engine speed and rail pressure is not big.

5.2 The Influence of Pre-load in Needle Spring

The variability of preload in needle spring has also important influence on engine performance variability, especially in idle speed condition (650 r/min). When the preload in needle spring is 55 N, 43 N, 33 N respectively, the needle lift and fuel injection flow rate and the cylinder pressure for sequence four cycles are shown in Fig. 19. With the decreasing of preload of needle spring, the fluctuation amplitude of needle lift, fuel injection flow rate and cylinder pressure increases slightly, which results in the fluctuation amplitude of engine speed and rail pressure increases slightly (Fig. 20). In the maximum torque condition (1150 N.m), with the decreasing of preload in needle spring the engine speed increases, but the fluctuation amplitude of the engine speed has no distinct change, and the rail pressure and its fluctuation amplitude have also no distinct change. When the preload of needle spring is 55 N, 43 N and 33 N, the average engine speed is 1838, 1847 and 1856 r/min respectively.

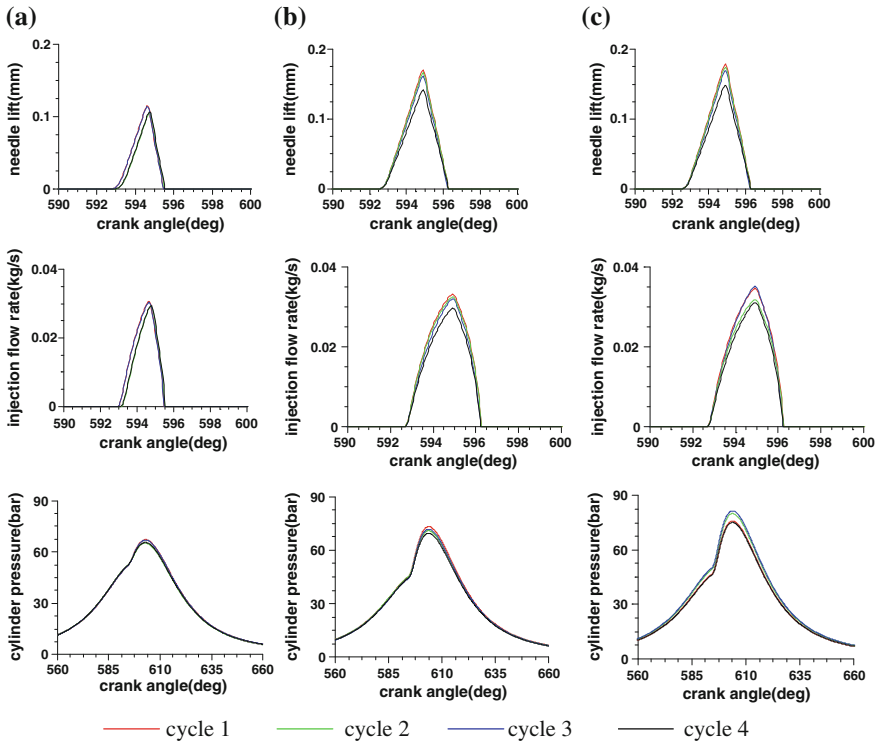


Fig. 19 The influence of preload of needle spring in idle speed condition. (a) preload of needle spring 55 N (b) preload of needle spring 43 N (c) preload of needle spring 33 N

5.3 The Effect of Control Strategy

The control strategy has great effect on engine performance, and Fig. 21 is the results calculated with/without fuel injection quantity balance method in control strategy in idle speed condition. When fuel injection quantity balance method in control strategy is not used, the fluctuation amplitude of engine speed, rail pressure, injected fuel quantity per cycle per cylinder, cylinder pressure is 620–666 r/min, 505–540 bar, 3.8–14.2 mg, 61–71 bar respectively. When fuel injection quantity balance method in control strategy is used, the fluctuation amplitude of engine speed, rail pressure, injected fuel quantity per cycle per cylinder, cylinder pressure is 640–662 r/min, 515–535 bar, 10.2–11.5 mg, 65.6–67.0 bar respectively. The percentage of fluctuation of engine speed, rail pressure, injected fuel quantity per cycle per cylinder, cylinder pressure decreases 56.5, 41.2, 87.5, 86 % respectively when fuel injection quantity balance method is used. The calculated results indicate control strategy has great effect on the characteristics of fuel injection and engine performance, and the fluctuation of engine speed can be greatly reduced if control strategy is optimized.

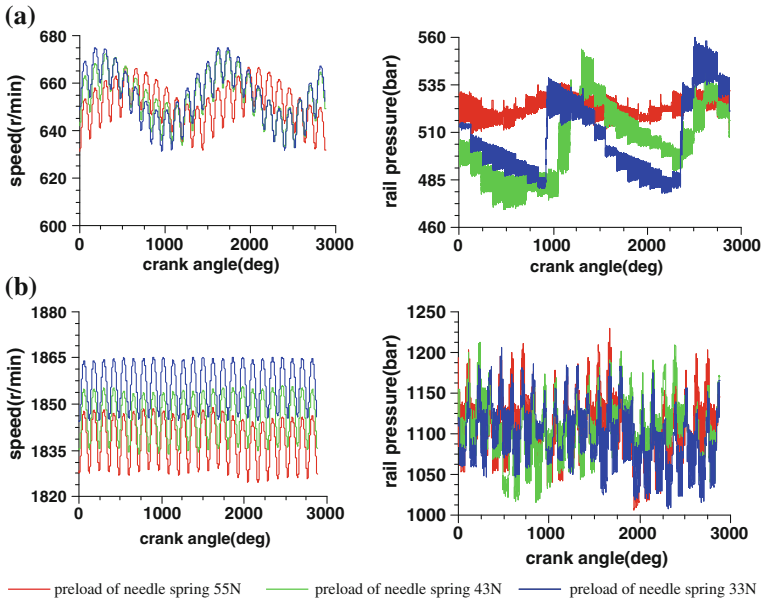


Fig. 20 The influence of preload of needle spring on engine speed and rail pressure. Preload of needle spring 55 N preload of needle spring 43 N preload of needle spring 33 N. (a) idle speed condition (b) maximum torque condition

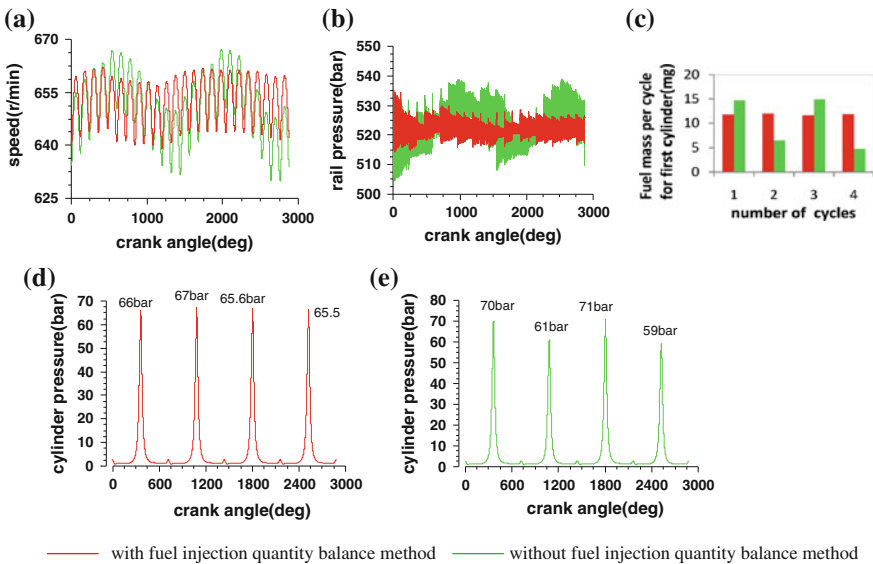


Fig. 21 The effect of control strategy. (a) engine speed (b) rail pressure (c) fuel injection quantity per cycle per cylinder (d) cylinder pressure with fuel injection quantity balance method (e) cylinder pressure without fuel injection quantity balance method

6 Conclusion

The co-simulation method of high-pressure fuel system and engine performance system and control system in common rail diesel engine is a powerful tool for supporting engine performance design optimization. Both engine performance in the steady state condition and fluctuation of engine speed in the transitional process can be simulated in this co-simulation model. The fast transient response of fuel injection rate on engine performance can be accurately simulated in the model. The influence of control strategy on fuel system and engine performance can be also well simulated. Several initial application runs are made and some conclusions are obtained.

- (a) The injector control valve lift has important influence on engine performance. In idle speed condition, the increasing of control valve lift will result in the increasing of fluctuation amplitude of engine speed. In the maximum torque condition, the increasing of control valve lift will result in the decreasing of engine speed and power output.
- (b) The variability of preload in needle spring has also great influence on engine performance variability. In the idle speed condition, with the decreasing of preload in needle spring, the fluctuation amplitude of engine speed and rail pressure increases. In the maximum torque condition, with the decreasing of preload in needle spring the engine speed increases.
- (c) Control strategy has great impact on the characteristics of fuel injection and engine performance, and the fluctuation amplitude of engine speed and rail pressure can be greatly reduced if fuel injection quantity balance method is used in control strategy.

References

1. Chiavola O, Giulianelli P (2001) Modeling and simulation of common rail systems. SAE 2001-01-3183
2. Barba C, Burkhardt C, Boulouchos K (2000) A phenomenological combustion model for heat release rate prediction in high speed DI diesel engines with common-rail injection. SAE 2000-01-2933
3. Lafossas FA, Colin O, Le Berr F, Menegazzi P (2005) Application of a new 1D combustion model to gasoline transient engine operation. SAE 2005-01-2107
4. Metghalchi M, Keck JC (1982) Burning velocities of mixtures of air with methanol, isooctane and indolene at high pressure and temperature. *Combust Flame* 48:191–210
5. Barba C, Burkhardt C, Boulouchos K (2000) A phenomenological combustion model for heat release rate prediction in high-speed DI diesel engines with common rail injection. SAE 2000-01-2933
6. Candel S, Poinso T (1990) Flame stretch and the balance equation for the flame area. *Combust Sci Tech* 70:1–15

Applying a Diesel Spray Model With Different Size Distribution Functions to High Pressure Diesel Spray Cases

Emekwuru G. Nwabueze

Abstract In diesel engine sprays, smaller sized droplets aid the combustion process, thus reducing emissions. Thus, it is important for diesel engine spray models to satisfactorily represent hydrodynamic mechanisms. A further development of a diesel spray model that uses different size distribution functions has been presented. In this model transport equations are constructed to calculate three moments of the droplet size distribution, a fourth moment is calculated from a gamma size distribution function, while the results of the droplet break up process are derived from an assumed size distribution function. Together these present the complete hydrodynamics characterisation of the diesel spray. The motivation for using different size distributions is to reduce the complexity of the spray modelling process and reduce the computational expense. The model has been applied to high-pressure diesel spray cases with the experimental data characterised by diesel spray penetration at different injection pressure values. The results from the model indicate that diesel spray penetration is over predicted at the start of injection but this improves as the fuel injection progresses.

Keywords Droplet size distribution function · Droplet size moments · Sprays · Modelling · Droplet break up

Nomenclature

$n(r)$	Number size distribution
Q	Droplet moment
Q_0	Total number

F2012-A02-011

E. G. Nwabueze (✉)
Midlands Simulation Group, School of Technology, University of Wolverhampton,
Wolverhampton, UK
e-mail: n.emekwuru@wlv.ac.uk

Q_1	Sum of radii, m
Q_2	Sum of squares of radii, m^2
Q_3	Sum of cubes of radii, m^3
r	Radius, m
t	Time, s
U	Velocity, ms^{-1}
x	Coordinate direction, m

Greek Symbols

ε	Dissipation Rate, m^2s^{-3}
α	Nondimensional size parameter

Subscripts

32	Sauter mean
i	Moment index
i, j	Velocity component
l	Liquid

Acronyms

DDM	Discrete droplet model
-----	------------------------

1 Introduction

With the increased concerns in the emission levels from automobiles, representing diesel engine sprays more accurately in spray models is essential to aiding the understanding of the structure of the sprays and also in optimising the injection design process.

Diesel spray models in use typically present the complete hydrodynamic nature of diesel sprays by tracking computational droplet classes, the so-called Discrete Droplet Model (DDM) method, with its pioneers including Dukowicz [1], and Gosman and John [2]. Each of these droplet classes represents a large number of droplets of the same size, temperature and velocity. Changes in these variables for each droplet class are computed by solving the ordinary differential equations governing the mass, energy, and momentum conservation for a representative droplet member of the class. The liquid and gas phases are linked using source terms in the equations. However, this method can be computationally intensive as it might be necessary to track a large number of classes of droplets to achieve stochastically significant solutions. A diesel spray model that uses droplet break up models based on different size distribution functions has been presented and applied to diesel spray cases [3]. In this model the complete hydrodynamics

characteristics of diesel sprays are represented by three moments of the droplet distribution function calculated from transport equations, with a further moment calculated from a gamma size distribution without the need for deriving a transport equation for the moment. Two different droplet break up models were presented for the model. The first was based on whether the results of the droplet break up processes were derived from approximations, using an assumed size distribution function, and the second was based on empirical data, using a gamma size distribution function. Experimental data from Hiroyasu and Kadota [4] were used to check the applicability of the diesel spray model. The computational results from both droplet break up models indicated that the model performed reasonably for the prediction of diesel spray tip penetration at different ambient pressure conditions, and for the prediction of diesel droplet sizes at several axial distances from the injector, at different ambient pressure conditions. It was also indicated that the droplet break up model based on the assumed droplet function was less computationally expensive. Thus this represented some progress with an earlier moments based diesel spray model that used one droplet size distribution [5]. The moments based diesel spray models do not track droplet classes as in the DDM method, therefore reducing the complexity and computational expense required [5].

This paper presents the results of a development of the diesel spray model presented in [3] with its application to high-pressure diesel spray cases. For the present case different distribution functions have been used for the fourth moment and for the droplet break up modelling. The next section of the paper describes the numerical implementation of the spray model, while *The Results and Discussions* section presents the results from the model applied to high-pressure diesel spray experimental data. The *Conclusions* section presents the highlights of the study.

2 The Numerical Methods

The novelty of the moments diesel spray model is that, instead of considering and tracking droplet classes, the moments of the droplet size distribution are used to describe the distribution of the droplet sizes. This approach used is presented next.

2.1 Moments of the Droplet Number Probability Distribution

If the integral over all droplets provides the total number of droplets per unit total volume, then this total number of droplets can be designated by Q_0 , so that

$$Q_0 = \int_0^{\infty} n(r)dr \quad (1)$$

where $n(r)$ is defined as a multiple of the probability density function of the droplet radius.

The i th moment of the droplet number probability distribution is thus defined as

$$Q_i = \int_0^{\infty} n(r)r^i dr \quad (2)$$

The second moment, Q_1 , is the total sum of radii of the droplets per unit total volume. The total surface area of the droplets per unit total volume is $4\pi Q_2$, and the total volume of the droplets per unit total volume is $\frac{4\pi Q_3}{3}$.

These first four moments, Q_0 to Q_3 , used in the model can be used to represent a lot of information about the spray, and they are used to build a fully poly-dispersed diesel spray model [5, 6].

2.2 The Moment Transport Equations

In the model presented here, only the last three moments, Q_1 to Q_3 , need to be calculated by solving the transport equations for the moments. A gamma number size distribution is used to calculate the first moment; this is highlighted in the *Droplet size distribution* sub-section. From [6], the set of the moment transport equations (for $i = 1, 2, 3$), can be written as:

$$\frac{\partial}{\partial t}(Q_i) + \frac{\partial}{\partial x_j}(Q_i U_{ij}) = -S_{Q_i} \quad (3)$$

The source term S_{Q_i} represents the effects of the droplet breakup, droplet collisions, and evaporation on the moments. The form of the distribution function used for the droplet breakup process is treated in this study, evaporation is neglected here and the other effects have been treated in [6].

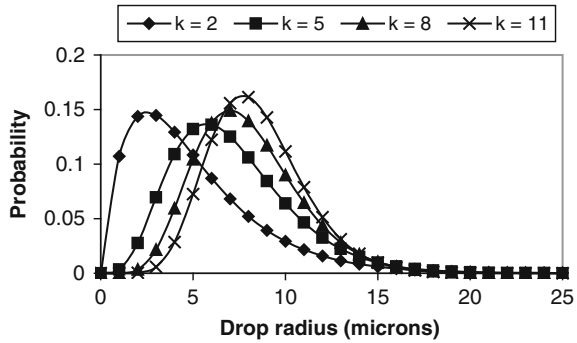
2.3 Droplet Size Distribution

Two different droplet size distributions have been used for the model presented in this paper. The first, a gamma distribution function, has been used for the first moment, Q_0 , while the second, an assumed size distribution function, has been used for the results of the droplet break-up process.

The Gamma distribution function

The first moment, Q_0 , is calculated from a gamma distribution function. The gamma function can be defined by the integral:

Fig. 1 Gamma distributions for values of k with r_{32} fixed at $10 \mu\text{m}$



$$\Gamma(k) = \int_0^{\infty} e^{-x} x^{k-1} dx \tag{4}$$

The moments of this distribution in Eq. (4) are given by:

$$Q_i = Q_0 \int_0^{\infty} \frac{\alpha^k}{\Gamma(k)r_{32}^k} r^{k+i-1} e^{-\alpha(\frac{r}{r_{32}})} dr \tag{5}$$

Two parameters in Eq. (5), r_{32} and k , define the functional form of the gamma distribution and Fig. 1 shows examples of gamma distributions as a function of k with r_{32} fixed at $10 \mu\text{m}$.

Then, the partial integration of Eq. (5) leads to

$$Q_0 = \frac{(k+2)}{kr_{32}} Q_1 \tag{6}$$

The advantages of this method have been highlighted in [6] and include the calculation of less transport equations in the model, as Q_0 is calculated directly from a gamma distribution which, in turn, is also used to describe the inlet conditions, the form of the drag model, and the break-up and collision models.

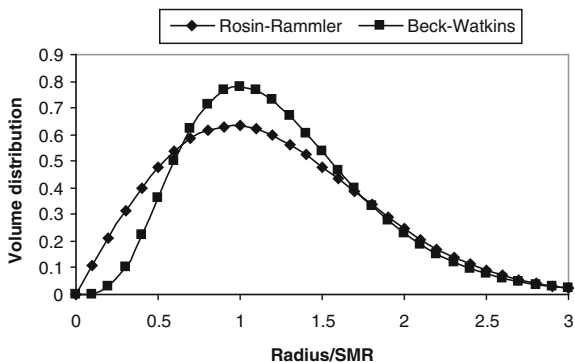
The Assumed size distribution function

The method for determining the results of the droplet breakup process assumes that:

- There is a critical radii above which the droplets become unstable,
- That stripping break-up occurs in preference to bag break-up,
- That the values of the number of droplets potentially undergoing each type of break-up can be determined from an assumed droplet size distribution.

An assumed distribution function (Fig. 2), chosen to match the Rosin–Rammler volume distribution with an exponent of 2, has been used to provide the number of droplets that may undergo bag break-up or stripping break-up. It has this form,

Fig. 2 The assumed distribution function from Beck and Watkins [7] compared with a Rosin–Rammler distribution function with exponent = 2



$$n(r) = \frac{16r}{r_{32}^2} \exp\left(-\frac{4r}{r_{32}}\right) \tag{7}$$

In this function Eq. (7), the SMR (r_{32}) is used because all the droplet moments are presented in terms of the droplet radii; it is not the same as the Rosin–Rammler mean radius [3, 7]. Details of this assumed function can be found elsewhere [3, 7]. The methodology used for determining the results of the droplet break-up process from this assumed distribution function has been detailed in Ref. [3]. The advantages of this method include less numerical complexity in the development of the spray model and less computational expense compared to a method based on empirical based correlations [3]. However, the methodology based on the assumed distribution function has hitherto not been applied to high-pressure diesel engine spray cases.

2.4 Model Solution and Discretization Methods

As discussed in the previous sections, the first four moments, Q_0 to Q_3 , are used in the spray model presented here. The first moment is calculated directly from the general gamma distribution function while transport equations are written for the last three moments. The spray model is closed by equations for the energy of the liquid phase and the gas-phase. An Euler implicit scheme is used for the temporal differencing while a hybrid central/upwind scheme is used for the spatial differencing. All the equations are solved using an Eulerian scheme, and discretized using the finite volume approach. The spray cases are considered axisymmetric. The carrier gas is considered turbulent, and the turbulence is modelled by the turbulent kinetic energy/dissipation rate ($k - \epsilon$) model of Launder and Spalding [8]. The moments spray model has been extensively treated in Ref. [6].

Table 1 Experimental conditions for the data of Hiroyasu and Arai [9]

	Case A	Case B	Case C
Ambient pressure (MPa)	3.0	3.0	3.0
Injection pressure (MPa)	10.0	20.0	30.0
Spray angle (deg)	16	20	20
Injection velocity (m/s)	90.4	140.8	177.5

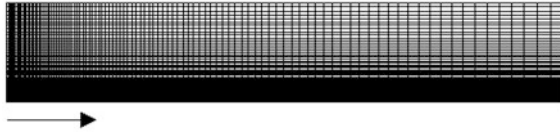


Fig. 3 The 2-dimensional computational chamber used for the numerical solutions. It consists of 109×73 cells. The domain is $0.2 \text{ m} \times 0.037 \text{ m}$. The injector is located on the *bottom left* hand side, and sprays across the centerline to the *right*

3 The Results and Discussions

The penetration data used for validating the model are from the work of Hiroyasu and Arai [9].

The injection pressure values from the data are up to 3 times higher than those presented in previous studies [3], and also allow the performance of the model to be compared at different injection pressure cases, as well as different ambient pressure cases. The qualitative as well as quantitative performances of the model at extended range of injection pressure values are also further assessed.

3.1 Experimental Data from Hiroyasu and Arai

The experimental data used for the study are from the work of Hiroyasu and Arai [9], collected by using high-speed Schlieren photographs to observe and analyse diesel spray behaviour at various injection pressure conditions of 10, 20, and 30 MPa (see Table 1). They derived empirical equations for spray tip penetration to aid the description of the spray structure, and, thus, proposed the division of the spray structures into incomplete and complete spray categories.

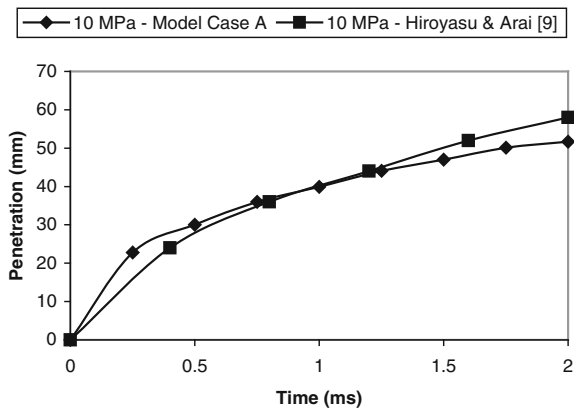
3.2 Numerical Considerations

The mesh size used was based on sensitivity studies previously carried out in [3, 5]. In those studies, the effect of the mesh density on the spray tip penetration

Table 2 Numerical, physical, and injection conditions used to simulate the experimental data of Hiroyasu and Arai [9]

	Model Case A	Model Case B	Model Case C
Ambient pressure (MPa)	3.0	3.0	3.0
Injection pressure (MPa)	10.0	20.0	30.0
Spray angle (deg)	16	20	20
Injection velocity (m/s)	90.4	140.8	177.5
Computational chamber radius (m)	0.200	0.200	0.200
Computational chamber axial length (m)	0.037	0.037	0.037
Computational time step (μm)	2.0	2.0	2.0
Total computational time (ms)	20	20	5

Fig. 4 Comparison of computed spray penetration with experimental data from Hiroyasu and Arai [9] for 10 MPa fuel injection pressure case



results was evaluated by varying the number of cells in the mesh from 54×36 , 81×59 , to 109×73 . The predicted spray tip penetration data are insensitive to the mesh size, and the 103×73 mesh size is chosen because dense cells are desired at the spray tip positions. The computational chamber is 2-dimensional and is 0.2×0.037 m in size (Fig. 3). Parametric tests indicate that with increases in ambient pressure values, the model predicts decreased spray tip penetration values [3], thus behaves as expected.

4 Discussion

The numerical and physical parameters used for simulating the experimental data of Hiroyasu and Arai [9] are presented in Table 2.

Results from the experimental data from Hiroyasu and Arai [9] show that the spray tip penetration increases with increasing fuel injection conditions. 1 ms after the fuel had been injected, the experimental data indicate that for the 10 MPa injection pressure case, the fuel tip penetration at this time is 40 mm, for the

Fig. 5 Comparison of computed spray penetration with experimental data from Hiroyasu and Arai [9] for 20 MPa fuel injection pressure case

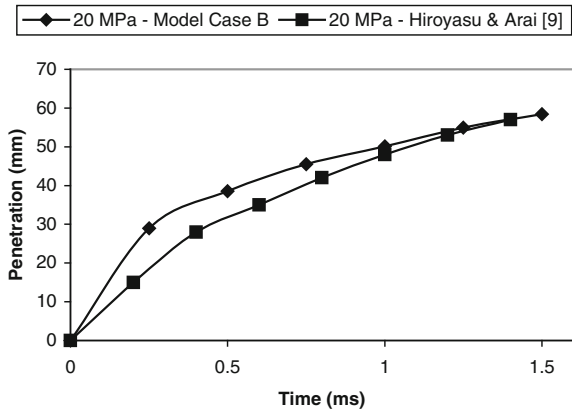
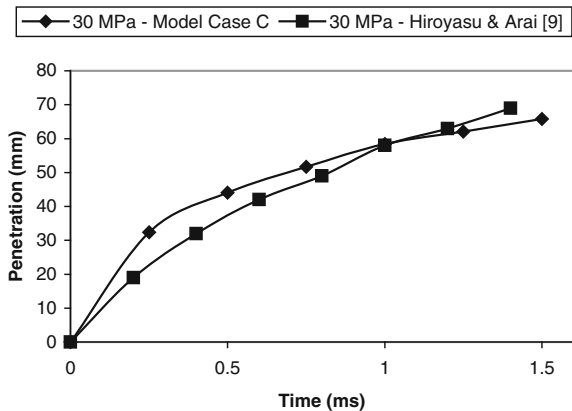


Fig. 6 Comparison of computed spray penetration with experimental data from Hiroyasu and Arai [9] for 30 MPa fuel injection pressure case



20 MPa injection case pressure, 50 mm, and for the 30 MPa injection case pressure, about 58 mm (Figs. 4, 5, 6).

The numerical results agree with the experimental trend. The model generally over predicts the fuel tip penetration at early injection times, and the prediction trend improves with the fuel spray injection time. For the 10 MPa fuel injection case, at later injection times the spray tip penetration is under predicted. This has been a feature of this model [3], and the form of the drop drag model is currently under investigation. However, for the 20 and 30 MPa fuel injection cases, the predictions improve at later spray injection times. Because the momentum transfer model is a key determinant of the predicted fuel spray tip penetration, and it depends on the values of the four moments used in the model, then the approach used to describe the moments of the droplet size distribution can be said to be applicable to such high pressure diesel spray cases.

5 Conclusions

The diesel spray model, which has been extended in this work, was developed and presented previously [3, 5, 6]. The application is based on [3], in which different size distribution functions are used for the calculation of the fourth moment, and the results of the droplet breakup process. Three other moments are calculated from transport equations, and the four moments are used to represent the complete hydrodynamics of the fuel spray. The motivations for using different size distribution functions include less modelling complexity and more computational efficiency [3].

In this work, the method has been applied to high-pressure diesel spray cases for the first time. The numerical results indicate that the fuel spray tip penetration is under predicted at early injection times, but the predictions improve at later injection times, especially for the high fuel injection pressure cases. This continues a trend noticed in the low fuel pressure test cases [3]. Thus, it is hoped that the further work currently being carried out, including the evaluation of new drop drag models, will aid the predictive capacities of the model at initial fuel spray injection times.

Acknowledgments Dr. N.G. Emekwuru holds the University of Wolverhampton ERAS 2011/12 Fellowship, which partly supported this work.

References

1. Dukowicz JK (1980) A particle-fluid numerical model for liquid sprays. *J Comput Phys* 35(2):229–233
2. Gosman AD, Johns RJR (1980) Computer analysis of fuel-air mixing in direct injection engines. SAE Paper 800091
3. Emekwuru NG (2012) A number size distribution moment based solid cone diesel spray: assessment of droplet breakup models based on different distribution functions. SAE Paper 2012-01-1260
4. Hiroyasu H, Kadota T (1974) Fuel droplet size distribution in diesel combustion chamber. SAE Paper 740714
5. Emekwuru NG, Watkins AP (2011) Application of a moments spray model to solid cone diesel sprays. SAE Paper 2011-01-1843, JSAE Paper 20119080
6. Emekwuru NG, Watkins AP (2010) Analysis of a two-fluid sprayer and its use to develop the number size distribution moments spray model. Part II: a computational analysis. *Atomization Sprays* 20(8):653–672
7. Beck JC, Watkins AP (2002) On the development of spray sub-models based on the droplet size moments. *J Comput Phys* 182(2):596–621
8. Launder BE, Spalding DB (1972) *Mathematical models of turbulence*. Academic Press, London
9. Hiroyasu H, Arai M (1990) Structures of fuel sprays in diesel engines. SAE Paper 900475

Influence of Diesel Surrogates on the Behavior of Simplified Spray Models

Jonas Galle and Verhelst Sebastian

Abstract Numerous experimental investigations make use of diesel surrogates to make the computational time reasonable. In the few studies where measured (surrogate and real diesel) and computed (surrogate only) results have been compared, the selection methodology for the surrogate constituent compounds and the measures taken to validate the chemical kinetic models are not discussed, and the range of operating conditions used is often small. Additionally, most simplified models use tuning variables to fit model results to measurements. This work makes the comparison between some frequently used diesel surrogates using a simple 1D vaporizing spray model, with the spray cone angle as the tuning parameter. Results show that liquid length and fuel fraction strongly depend on the physical properties of the used fuel for a fixed spray angle. These parameters are important for modeling auto-ignition and pollutant formation. The spray angle is varied till the spray length is the same for each surrogate. Results show important differences between other spray parameters such as local mixture fraction and axial velocity.

Keywords 1D spray model · Diesel · Surrogates

Abbreviations and Symbols

c_p	Heat capacity
D	Nozzle diameter
EGR	Exhaust gas recirculation
f	Fuel mass fraction

F2012-A02-012

J. Galle (✉) · V. Sebastian
Department of Flow, Heat & Combustion Mechanics,
Ghent University, Ghent, Belgium
e-mail: jonas.galle@ugent.be

h	Enthalpy
I	Momentum
k	Shape factor of a Gaussian profile
Le	Lewis number
M	Molar mass
\dot{M}	Mass flow rate
NO _x	Nitrogen oxides
P	Pressure
Pr	Prandtl number
r	Radial position step
R	Radius of the spray
R _{index}	Specific gas constant
Sc	Schmidt number
t	Time step
T	Temperature
u	Axial spray velocity
UHC	Unburned hydro-carbons
x	Axial position step
Y	Mass fraction
θ	Spray angle
ρ	Density
φ	Vapor fraction
Indices	
a	Ambient property
c	Critical property
cl	Property on spray axis
evap	Total evaporation condition
f	Fuel property
i	Position variable
j	Time variable
mix	Mixture property
sat	Saturation property
0	Initial condition

1 Introduction

One of the main motives for combustion research is the increasingly stringent exhaust emission regulations to reduce the environmental impact. A further understanding of the combustion process and the possibility to model is needed in order to deal with the emission trade-offs. For direct injected diesel engines it is widely known that common-rail injection can lower soot and unburned hydrocarbon (UHC) emissions significantly as well as NO_x, exhaust gas circulation

(EGR) reduces nitrogen oxides (NO_x) and slightly increases soot and UHC, supercharging decreases soot but slightly increases NO_x. These statements depend on more parameters such as injection timing, inlet temperatures, engine load & speed, combination of strategies, etc. The variety of parameters influencing the spray and combustion process makes the prediction of power output and emission formation very complex. For decades, researchers have been trying to understand and predict the in-cylinder processes by the use of experimental setups such as research engines and optical combustion chambers and modeling cases. One other issue is the fuel itself. The common fossil derived diesel fuel has a complex chemical composition and depends on the place of origin and production processes. This is the main reason to model with diesel surrogates. These diesel substitutes are chosen in such way that they approximate certain properties of fossil derived diesel fuel. Through this work, the term “diesel” will refer to fossil derived diesel. Usually only a few target properties are taken. The next paragraph gives an overview of commonly used surrogates and the motivation for choosing them. The second part describes the 1D spray model that will be used in this work to show (in the third section) that the choice of the surrogate fuel can significantly influence the results for a vaporizing spray.

2 Diesel Surrogates

Researchers have switched in the direction of using model fuels or surrogates in order to simplify the modeling efforts and to match application targets for conventional diesel combustion. Diesel has complex reaction kinetics and is a mixture of hydrocarbons of which composition depends on the place of origin, standards and production process. In general, the basic composition of diesel [1] consists of iso-parafins (25–50 %), cycloparafins (20–40 %) and aromatics (15–40 %).

Further, the wide range of hydrocarbon lengths makes it hard to predict the evaporation and combustion behavior; a boiling range (190–300 °C) is usually defined instead of a single boiling point for one component fuels.

Surrogates are selected based on one or a few chemical and physical properties which are comparable to diesel. Important parameters that are desired to meet those of diesel include chemical composition (determines strongly the combustion species and emissions), surface tension, viscosity, vapor/liquid equilibrium, distillation trajectory, molecular and thermal transport properties, ... Moreover, most parameters vary with temperature and pressure, suggesting that this dependency should fit as well. A surrogate that would cover all these chemical and physical properties of the fuel that need to be considered in the engine process, would likely require more components than can be handled in current computational codes. For this reason the surrogate composition needs to be limited.

Usually these surrogates are single component liquids or mixtures of a few simple molecules.

A common surrogate is n-heptane, preferred for its comparable cetane number (~ 55), according to European and Japanese standards [1]. Additionally, detailed chemical-kinetic mechanisms for low-, intermediate- and high-temperature n-heptane oxidation are available. Others are using n-hexadecane (or cetane, $C_{16}H_{34}$) or n-dodecane ($C_{12}H_{26}$) in order to obtain a high density ratio, similar to diesel engine sprays [2]. Stralin and Wahlin [3] use n-dodecane for its high boiling temperature characteristics, comparable to diesel.

However, some difficulties exist when selecting a suitable surrogate fuel. For surrogates with comparable cetane number, ignition behavior will not match for a wide range of relevant diesel engine operation conditions [1]. The ignition behavior may also differ since the first stage (low temperature) heat release will exhibit a different dependence on temperature and pressure. One key factor is the multi-component composition of diesel and different oxidation and pyrolysis kinetics. Short molecules are more likely to vaporize first [4] and aromatic hydrocarbons are more likely to delay ignition [5]. Moreover the difference in hydrogen/carbon (H/C) ratio, molecular structure and local mixture fraction will reflect in different predicted pollution formation. The H/C-ratio can be readily matched with a single-component surrogate, however the similarity of the combustion behavior cannot be guaranteed [1]. Improvements can be made by using a multi-component surrogate. Natelson et al. [6] modeled diesel by using a mixture of (1:1:1) n-decane, n-butylcyclohexane and butylbenzene to approach the average hydrocarbon composition, while Peters et al. [7] proposed a mixture of 70 vol % of n-decane and 30 vol % methyl-naphthalene for the same reason and additionally to improve combustion similarity. The latter mixture is also able to meet comparable cetane number and density. Furthermore, comparable ignition delay and heat release from experiments in an optical engine were found. From experimental investigation one usually concludes that the emission prediction is insufficient. The main reason is that oxidation and pyrolysis kinetics of the combustion are strongly influenced by aromatics, cycloparafins and iso-parafins. This was the main motivation for Gustavsson et al. [8] to add toluene to n-heptane. The local mixing phenomena and local pollutant formation cannot be predicted by single component surrogates as n-heptane but the general pollutant formation seemed to be in agreement with experiments.

As a conclusion, while engine experiments with surrogates are capable of providing much insight, they may not accurately reflect the combustion behavior of real diesel fuel; choices only based on physical properties might not be appropriate to predict the chemical processes.

An overview of diesel surrogate can be found in the overview papers of Farrell et al. [1] and Battin-Leclerc [9].

3 1D Vaporizing Spray Model

In direct injected internal combustion engines, such as turbines, piston engines and liquid fueled rocket engines, fuel (and oxidizer) is usually injected as a compressed liquid in a supercritical environment. This has a direct influence on the spray characteristics since in the supercritical state of a fluid, no distinction can be made between liquid and vapor. The concept surface tension, which is a key parameter for breakup, vanishes. The mixing of the spray with the surrounding air cannot be described anymore by breakup and dispersion of droplets; the number of droplets from the spray diminishes and the air entrainment becomes a pure diffusion mechanism, thus the gas jet theory is applicable. This is the main idea of the present 1D model for high pressure vaporizing sprays.

Modeling of sprays has already been confirmed to be very difficult. The breakup of the spray which is usually correlated with the spray cone angle is a struggle for the modeler since the process is influenced by the complex chamber turbulence, nozzle cavitation and turbulence, and temperature and pressure gradients. For 0D and 1D models, the breakup physics are usually avoided, and the cone angle is used as a model input or tuning parameter [2, 10]. Further, the supercritical state suggests that the breakup is not considered anymore as the main mixing process, rather the entrainment of hot ambient gases.

3.1 Methodology

The spray model used here is based on the model proposed by Payri et al. [2, 10]. Their model is briefly described in this section. More details can be found in Payri et al. [2, 10] and Desantes et al. [11]. The model considers an isothermal stationary spray as a symmetric cone (cfr. Fig. 1) with variable radial values for the axial velocity u_{c1} , fuel mass fraction f_{c1} and enthalpy h_{c1} . For modern automotive and heavy duty diesel engines (high pressure common-rail injection) the liquid length is found to be almost independent of the injection pressure. Experimental results suggest that the droplet sizes under realistic engine conditions are so small that atomization is no longer a limitation in the evaporation of the spray. The main contribution to evaporation is then the mixing with the hot surrounding air, resulting in the so called “mixing limited hypothesis”; the vapor and liquid fraction are each time in equilibrium (saturated situation). Further, droplets reach a dynamic equilibrium with the air very close to the nozzle and local transfer rates of momentum, mass and energy between liquid droplets and surrounding air are fast in comparison to the rate of development of the flow field as a whole. Both arguments above assume the spray behavior to be similar to the gas jet theory, even under non-vaporizing conditions in which the problem is undoubtedly a two-phase flow.

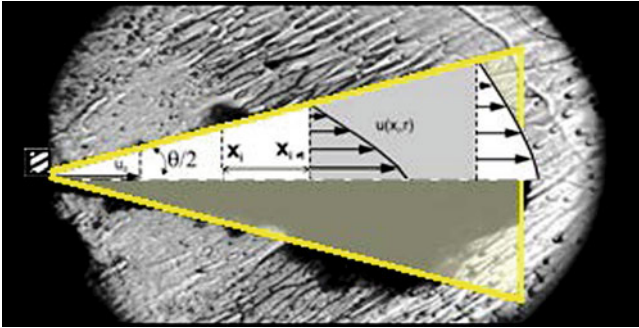


Fig. 1 Spray development assumed by the 1D model

3.2 Hypotheses

Hypotheses need to be made in order to arrive to a simplification of the complex process of a vaporizing spray. The most important assumptions are listed below and mentioned in Payri et al. [2]

- The pressure in the whole spray is equal to the surrounding chamber pressure
- Le, Pr and Sc are set to 1
- the whole spray is considered as a homogeneous mixture with a mixture density ρ_{mix} (no droplets are considered)
- ambient air is at rest (velocity = 0)
- the spray cone angle is constant and input for the model (tuned to experiments)
- Gaussian distributions are used for the conserved parameters axial velocity u_{cl} , fuel mass fraction f_{cl} and enthalpy h_{cl} . This assumption leads to the following relations:

$$\frac{u(x, r)}{u_{cl}(x)} = \left[\frac{f(x, r)}{f_{cl}(x)} \right]^{1/Sc} = \left[\frac{h(x, r) - h_{a,\infty}}{h_{cl}(x) - h_{a,\infty}} \right]^{1/Pr} = e^{-k\left(\frac{r}{x}\right)^2} \quad (1)$$

With k the shape factor of the Gaussian profile

3.3 Derivation and Implementation

The equations for conservation of fuel mass, momentum and energy are used to describe the vaporizing spray process. This set of equations can be reduced to two equations (Eqs. 2 and 3); the assumption that leads to Eq. 1 implies that the mass and energy equation do not give additional information.

Table 1 Initial conditions for the 1D spray model

θ	33.62°	$u_{c1}(0,0)$	150 m/s
D_0	200 μm	$T_{f,0}$	900 K
$x(0)$	$D_0/[2.\tan(\frac{\theta}{2})]$	$T_{a,0}$	400 K
$f_{c1}(0,0)$	1	P_a	8 MPa

$$I_0 = I(x) = \int_0^R 2\pi\rho_{mix}(x, r)r.u^2(x, r)dr \quad (2)$$

$$\dot{M}_{f,0} = \dot{M}_f(x) = \int_0^R 2\pi\rho_{mix}(x, r)r.f(x, r).u(x, r)dr \quad (3)$$

All physical properties are only temperature dependent and derived from the DIADEM DIPPR database and [12].

3.4 Initial Conditions

The same initial conditions are taken for this work as used in Payri et al. [10] for comparison, unless stated otherwise (cfr. Table 1). Cetane has been used as the diesel surrogate

4 Results and Discussion

This section compares 6 common diesel surrogate fuels: cetane, decane, n-heptane, n-dodecane, n-octane and n-heptadecane. The critical temperature and pressure for the investigated surrogates are shown in Table 2. These parameters are the only fuel constants (temperature and pressure independent) which can significantly influence the spray formation and combustion. When the spray exceeds the critical conditions, no liquid phase can exist anymore as suggested by the assumption of saturation. First a comparison of the fuel properties used in the 1D model has been done. Next the spray state parameters are considered, followed by the influence of the fuel choice on the modeled results for the liquid length. These results were obtained with the same spray angle input for the different surrogates. As mentioned earlier the spray cone angle was tuned with experiments for cetane [2]. In the last section, the spray angle was tuned for the other surrogates until a similar liquid length was found as for cetane. The results are only based on modeling work and were not confirmed with experiments.

Table 2 Critical properties of the investigated diesel surrogates

	Cetane	n-dodecane	n-heptane	Decane	Octane	Heptadecane
Formula	C ₁₆ H ₃₄	C ₁₂ H ₂₆	C ₇ H ₁₆	C ₁₀ H ₂₂	C ₈ H ₁₈	C ₁₇ H ₃₆
P _c [bar]	14.0	18.3	27.4	21.1	24.9	13.4
T _c [K]	723.0	658.0	540.2	617.7	568.7	736.0

4.1 Fuel Parameters

The model uses only a limited amount of fuel properties. Other fuel properties that might be important for the spray development include surface tension, viscosity and heat conductivity. Viscosity and surface tension will mostly influence the breakup and atomization, together with cavitation and turbulence. This process is avoided by having the spray angle an input for the model. Heat conductivity is considered to be infinitely high by the mixing limited hypothesis (no time is required to heat the fuel by conduction). The saturation pressure P_{sat} is considered and will determine the vapor fraction Y_{fv} . The heat capacity c_p will influence temperature by the heat that can be absorbed by the fuel. The mass flow rate and momentum will be strongly depending on the density of the spray ρ_{mix} , determining the axial spray velocity. The 6 different surrogates show significant differences for liquid density, saturation pressure and enthalpy as shown in Fig. 2 for a temperature range from 350 to 1350 K. For low temperatures the density difference is small, but becomes bigger when reaching the critical temperature. The main difference between the investigate alkanes is the chain length; the more the length approaches cetane, the more the results are in agreement with cetane. The liquid density has an important contribution to the total spray density since the value is about 10–40 times higher than the vapor density. The big difference compared to the reference surrogate cetane can be reduced if the spray density is considered: near the critical temperature T_c , the liquid fraction will be small (cfr. section State parameters). The saturation pressure for the different surrogates shows big differences. In the vaporizing spray the influence of the saturation pressure is found in the assumption that the spray is saturated on every time and position:

$$\varphi(x, t) = \frac{1 - f(x, t) M_f P_{\text{sat}} - 1}{f(x, t) M_a P_a} \quad (4)$$

4.2 State Parameters

State parameters are independent of the spray process in the model and determined by the fuel mass fraction f_{cl} , but might have an important influence on the spray modeling results. For the vaporizing spray these include the spray density,

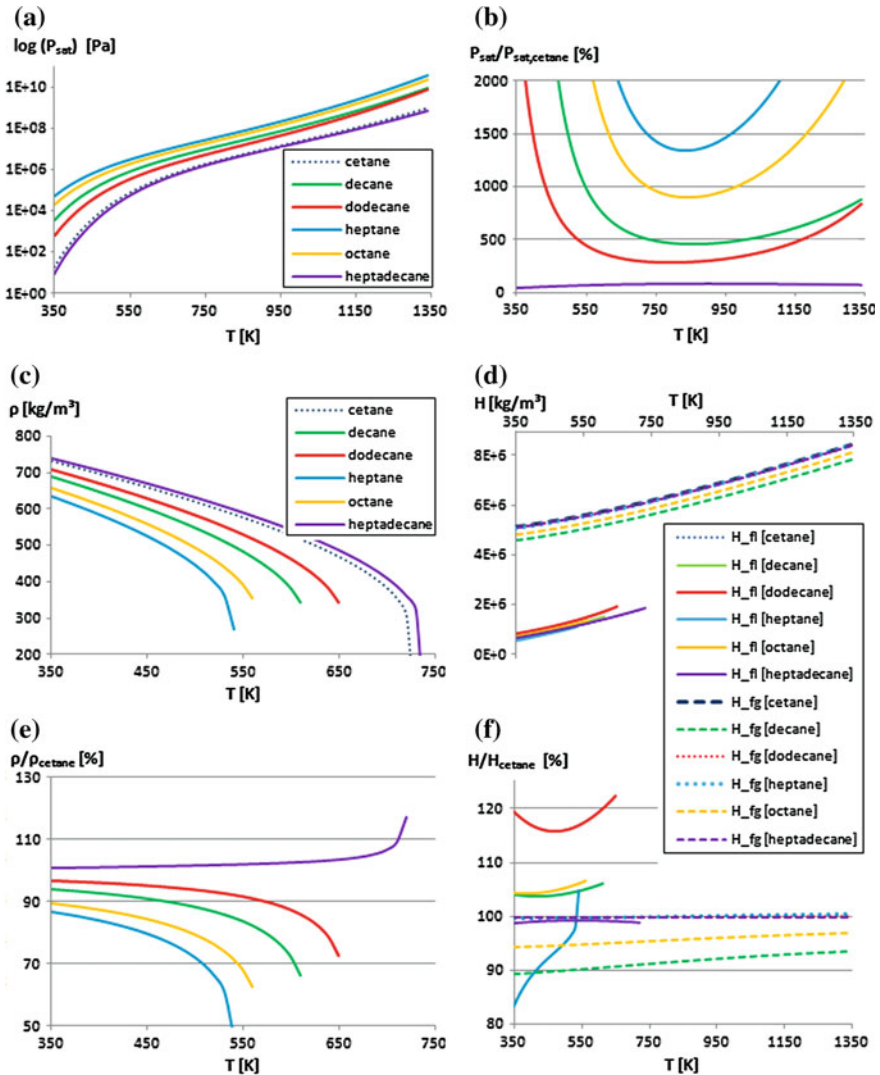


Fig. 2 (Top left) liquid density for 6 diesel surrogates (bottom left) liquid density relative to cetane (top right) saturation pressure for 6 diesel surrogates (bottom right) saturation pressure relative to cetane

temperature, vapor fraction and saturation pressure. A relative comparison with cetane is done for the liquid density and saturation pressure to better point out the difference (cfr Fig. 3). The vertical dotted lines represent the fuel fraction at which the liquid fraction becomes zero ($Y_v = f = f_{evap}$), also defined as the spray liquid length. The amount of fuel vapor under saturated conditions is completely determined by the saturation pressure as mentioned in the previous section. As a

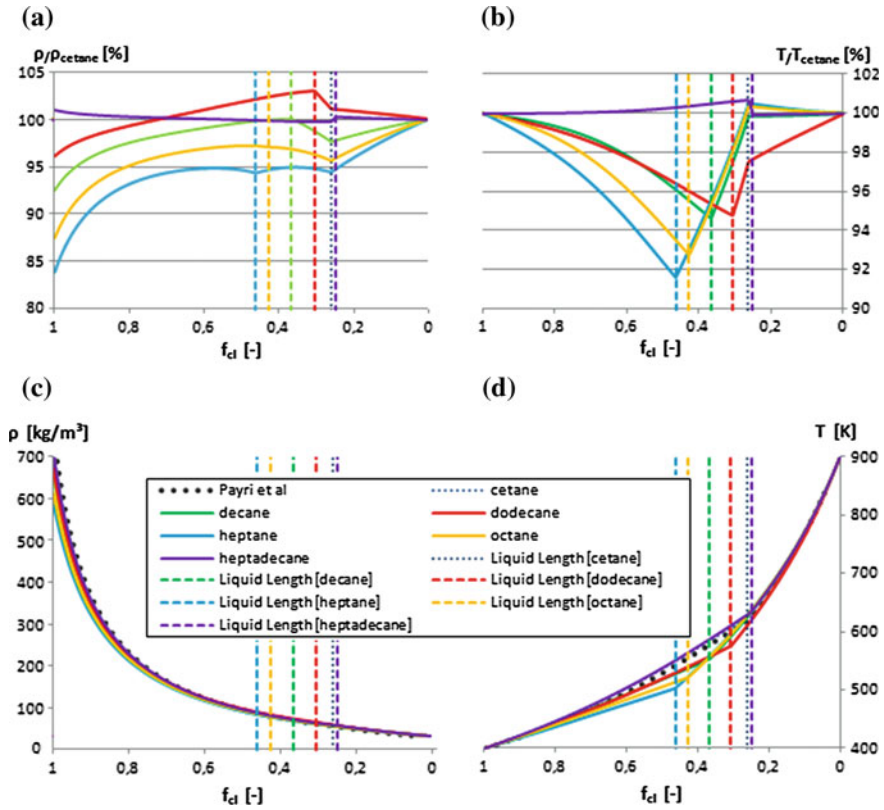


Fig. 3 Comparison of the relation state parameters among the fuels

consequence, the big differences in saturation pressure do influence the fuel vapor & liquid fraction. The fuel fraction f_{evap} differs from 0.25 up to 0.46 for the investigated surrogates. As could be expected, the highest f_{evap} corresponds with the most volatile surrogate (= surrogate with the highest saturation pressure). The differences among the investigated fuels for the temperature dependence of the density was rather small and has also little effect on the density-fuel fraction relation as was found on Fig. 4a,c. The differences are biggest for high fuel fractions since these conditions represent the biggest amount of (liquid) fuel.

4.3 1D Vaporizing Spray Model

The axial spray velocity u_{cl} along the spray axis is plotted in Fig. 4 for the different surrogate fuels. Again, the significant differences in the state parameters are reflected in the position of the liquid length. A summary for the different

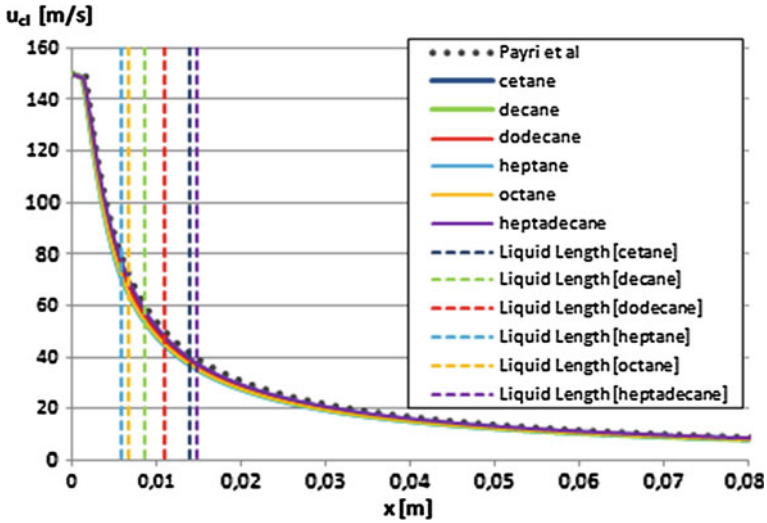


Fig. 4 Summary of the comparison of the liquid length (x_{evap}), temperature (T_{evap}) and fuel fraction ($fevap$) at total evaporation between the different surrogates for the same boundary conditions (the y-axis shows the percentage compared to cetane, the values on the boxes represent the absolute value)

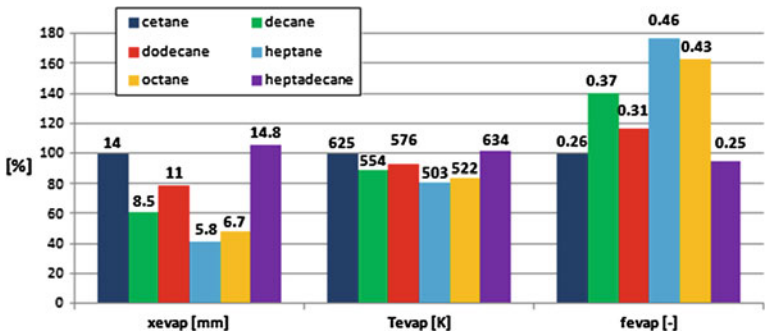


Fig. 5 Summary of the comparison of the liquid length (x_{evap}), temperature (T_{evap}) and fuel fraction ($fevap$) at total evaporation between the different surrogates for the same boundary conditions (the y-axis shows the percentage compared to cetane, the values on the boxes represent the absolute value)

surrogates of the liquid length (x_{evap}), temperature (T_{evap}) and fuel fraction ($fevap$) at total evaporation is given in Fig. 5. These spray properties are crucial for the model since start of combustion is determined by the combination of mixture energy (dominated by the temperature) and local mixture fraction, apart from the fuel composition. Further, if the liquid fuel reaches the wall of the

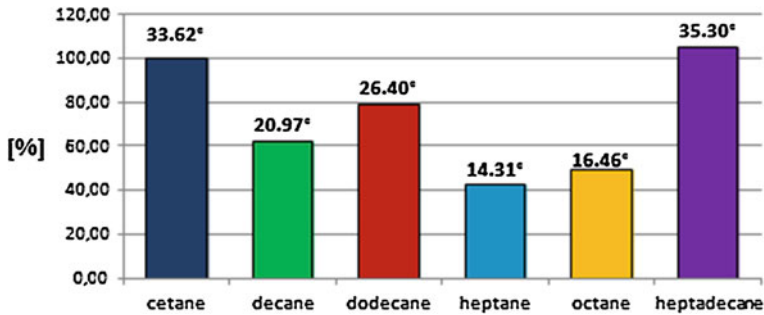


Fig. 6 Tuned spray angle for similar liquid length (the y-axis shows the percentage difference compared to cetane, the values on the boxes represent the absolute tuned spray angle)

cylinder, incomplete combustion may occur, resulting in soot and UHC emissions. From these results, the cylinder needs to be more than twice bigger before the cetane fuel is totally evaporated compared to heptane.

4.4 Spray Angle Tuning

The fuel properties were the only changes made to the spray model. All other parameters and initial conditions were kept the same, including the spray angle which was tuned for cetane by Payri et al. [2] and not for the other surrogates. In this section, the spray angle was tuned for each surrogate in such way that the obtained liquid length is the same as for the reference surrogate, cetane. From experimental efforts it is known that the determination of the spray angle is very difficult (standard deviations between 5 up to 10 %) and strongly depends on the used definition [13]. This is the main motivation to choose the spray parameter as a tuning parameter. Nevertheless, the difference in spray angle is up to more than 50 % compared to the reference surrogate (cfr Fig 6). Due to the hypotheses, this has significant consequences for the local mixture fraction and axial velocity, which deviates a lot from the cetane values and might affect the ignition, combustion progress and pollutant formation. This was not yet investigated in this work.

5 Conclusions

Surrogates are capable to provide insights in the atomization and combustion process under high temperature and pressure conditions, but care should be taken when using surrogates to predict the diesel engine outputs. Only vaporizing sprays were investigated by the use of a simplified spray model. The model is able to predict experiments with cetane as was demonstrated by Payri et al. [2]. The

quantitative results may not be directly useful for further calculations, since all calculations were based on experiments with cetane. Nevertheless some important remarks can be made concerning the use of surrogates in modeling work. The following conclusions can be derived from this work:

- A real single- or few-component surrogate that would cover all the chemical and physical properties of diesel relevant for in-cylinder processes is not possible, both because of the available information as for the required resolving time
- For simplified 1D models, the fuel parameters with the strongest influence on the hypotheses should be considered when choosing a surrogate. In the considered model, the mixing limited hypothesis states that vaporization is determined by the saturation pressure. Strong differences in this parameter among the surrogates will result in strong differences of the spray characteristics.
- Axial spray velocity and local mixture fraction are difficult to measure experimentally and are usually derived from modeling work. Parameters in the model are tuned in such way that the more readily measurable parameters fit to the experiments. For this model, the spray angle is tuned. Depending on the surrogate significant different local mixture fractions (f) and velocities are found. This will definitely influence the succeeding ignition, combustion and emission formation.

Acknowledgments The research is carried out in the framework of a Ph.D. which is funded by a grant (SB-81139) of the Institute for the Promotion of Innovation through Science and Technology in Flanders (IWT-Vlaanderen). This financial support is gratefully acknowledged.

References

1. Farrell JT, Cernansky NP, Dryer FL, Friend DG, Hergart CA, Law CK, McDavid RM, Mueller CJ, Patel AK, Pitsch H (2007) Development of an experimental database and kinetic models for surrogate diesel fuels. SAE 2007-01-0201
2. Pastor JV, Lopez JL, Garcia JM, Pastor JM (2008) A 1D model for the description of mixing-controlled inert diesel sprays. Fuel 87:2871–2885
3. Stralin P, Wahlin F, Angstrom H-E (2003) Effects of injection timing on the conditions at top dead center for direct injected HCCI. SAE 2003-01-3219
4. Struckmeier D, Tsuru D, Kawauchi S, Tajima H (2009) Multi-component modeling of evaporation, ignition and combustion processes of heavy residual fuel oil. SAE paper 2009-01-2677
5. Wanga H, Warner SJ, Oehlschlaeger MA, Bounaceur R, Biet J, Glaude P-A, Battin-Leclerc F (2010) An experimental and kinetic modeling study of the autoignition of a-methylnaphthalene/air and a-methylnaphthalene/n-decane/air mixtures at elevated pressures. Combust Flame 157:1976–1988
6. Natelson RH, Kurman MS, Cernansky NP, Miller DL (2008) Experimental investigation of surrogates for jet and diesel fuels. Fuel 87:2339–2342
7. Peters N, Pitsch H, Barths H (1999) 3D simulation of DI diesel combustion and pollutant formation using a two-component reference fuel. Oil Gas Sci Technol 54:233–244

8. Gustavsson J, Golovitchev VI (2003) Spray combustion simulation based on detailed chemistry approach for diesel fuel surrogate model. SAE 2003-01-1848
9. Battin-Leclerc F (2008) Detailed chemical kinetic models for the low-temperature combustion of hydrocarbons with application to gasoline and diesel fuel surrogates. *Prog Energy Combust Sci* 34:440–498
10. Payri R, Desantes JM, Garcia JM, Salvador FJ (2007) A contribution to the understanding of isothermal diesel spray dynamics. *Fuel* 86:1093–1101
11. Desantes JM, Salvador FJ, Lopez JJ, De la Morena J (2011) Study of mass and momentum transfer in diesel sprays based on X-ray mass distribution measurements and on a theoretical derivation. *Exp Fluids* 50:233–246
12. Perry R, Green DW, Perry's chemical engineers' handbook. ISBN-10: 0071422943
13. Galle J, Demuynck J, Vancoillie J, Verhelst S (2012) Spray parameter comparison between diesel and vegetable oils for non-evaporating conditions. SAE paper 2012-01-0461

Coupled 1D/2D/3D Modeling of Common Rail Injector Flow and Nozzle Cavitation

Valdas Čaika, Peter Sampl and David Greif

Abstract To facilitate advanced combustion strategies and meet stringent emission regulations of CI engines, the computational models have to accurately predict the injector flow and cavitation development in the nozzle. This paper describes a coupled 1D/2D/3D modeling technique for the simulation of the fuel flow and nozzle cavitation in diesel injection systems.

Keywords CI engine · Fuel injection · Numerical simulation · Fluid dynamics · Nozzle cavitation

The technique is based on the 1D modeling of the injector flow, combined with 1D/2D multi-body dynamics of the mechanical components and 3D modeling of the nozzle inner flow and cavitation using a multi-fluid method. The 1D/2D model of injection system is created with AVL software Boost-Hydsim. The computational meshes, including the sac volume and holes are generated with AVL meshing tool Fame. 3D calculations are performed with AVL software Fire. The co-simulation procedure is controlled by Boost-Hydsim. Initially Hydsim performs a standalone 1D simulation until the axial needle lift reaches a prescribed tolerance. From this instant Hydsim initiates the 1D/2D/3D co-simulation with the Fire multiphase solver. An alternative option is to perform co-simulation at the user-defined intervals (e.g. pilot and main injection). During the co-simulation process

F2012-A02-013

V. Čaika (✉) · P. Sampl
AVL LIST GmbH, Graz, Austria
e-mail: valdas.caika@avl.com

D. Greif
AVL Slovenia d.o.o, Maribor, Slovenia

Hydsim transmits to Fire the displacement vector of the needle tip and fuel pressure and temperature at the nozzle interface. Based on this data, Fire moves the computational mesh, adjusts boundary conditions, computes the time step and sends back to Hydsim the hydraulic force vector acting on the needle tip, sac pressure and mass flow rate through the needle seat and nozzle holes. Basic 1D/3D nozzle flow simulation technique is already described in the previous works of the authors [1, 2]. However, it was limited to 1D (longitudinal) needle motion both from 1D injector modeling in Hydsim and 3D nozzle flow calculation in Fire. Moreover, only simple segment meshes with a single hole were considered. Now both software codes are extended in such a way that 2D motion (translation in x, y and z directions) of the needle can be simulated in Hydsim and mesh movement represented in Fire respectively. Numerical modeling and experimental analysis of cavitation in diesel nozzles has been carried out by Alajbegovic et al. [3], Arcoumanis et al. [4], Chen and Heister [5], Schmidt and Corradini [6], Sou and Kinugasa [7], Yuan and Schnerr [8] and other authors. Most of the cavitation models are based on the Eulerian or Lagrangian formulation or their combination. A comprehensive survey of the cavitation models for diesel injection nozzles is provided by Giannadakis et al. [9]. Cavitating flow simulation in Fire standalone using the standard multi-fluid method has been performed by Wang and Greif [10]. One-dimensional modeling of the injector needle and its effect on the nozzle cavitation has been studied by Čaika and Sampl [1] and Payri et al. [11].

1 Theoretical Basis

1.1 Multi-Fluid Method

Within the framework of the multi-phase flow, each phase is considered a continuum media and the conservation laws apply. An ensemble averaging is used to remove the microscopic interfaces. This results in macroscopic conservation equations analogous to their single-phase counterparts. The difference from single phase is the new variable (volume fraction) and new interfacial exchange terms. The averaged continuity and momentum equations follow from the work of Drew and Passman [12]:

$$\frac{\partial \alpha_k \rho_k}{\partial t} + \nabla \cdot \alpha_k \rho_k \mathbf{v}_k = \Gamma_k, \quad (1)$$

$$\frac{\partial \alpha_k \rho_k \mathbf{v}_k}{\partial t} + \nabla \cdot \alpha_k \rho_k \mathbf{v}_k \mathbf{v}_k = -\alpha_k \nabla p + \nabla \cdot \alpha_k \boldsymbol{\tau}_k + \alpha_k \rho_k \mathbf{g} + \mathbf{M}_k + \mathbf{v}_{\text{int}} \Gamma_k, \quad (2)$$

where α , ρ , \mathbf{v} and p are the averaged volume fraction, density, velocity and pressure, respectively, the subscript k denotes a phase indicator, \mathbf{v}_{int} is the interfacial velocity, Γ_k is the phase change rate and \mathbf{M}_k is the interfacial momentum

transfer term. Essential term in the cavitation modeling is the vaporization rate, or the interfacial mass exchange Γ_k . For linear cavitation model it is governed by the Rayleigh equation for the single bubble dynamics:

$$r\ddot{r} + \frac{3}{2}\dot{r}^2 = \frac{\Delta p}{\rho_l}, \quad (3)$$

where r is the bubble radius and Δp is the effective pressure difference.

For a population of bubbles with a distribution function f , defined as the number of bubbles within the radius span of $(r, r + dr)$, the total mass transfer rate is given by:

$$\Gamma_v = \int_0^\infty f(r)4\pi r^2 \rho_b \dot{r} dr. \quad (4)$$

Approximate solution of Eq. (4) and further details can be found in [13].

1.2 1D Fluid Mechanics and 2D Multi-Body Dynamics

Modeling of the injector flow (except nozzle) in Hydsim is based on the one-dimensional theory of weakly-compressible fluid mechanics [14]. Pressure wave propagation in lines is calculated using variable fluid density and velocity of sound. Two-dimensional needle motion with 3 degrees-of-freedom (translation along x, y and z axes) and one-dimensional motion of other mechanical components (control valve body, amplifier pistons) is calculated by the classical theory of multi-body dynamics. Axial needle deformation due to varying pressure is considered by linear elasticity. For the leakage modeling in the clearance of the needle guide laminar flow theory is applied. Electric charge, mechanical strain and deformation of the piezoelectric stack actuator are calculated from the electro-mechanical lumped-parameter model described in [14].

2 Model of Common Rail Injector

Injector in question is a piezo-controlled common rail injector CRI3 from Bosch [15]. Basic features of the CRI3 injector are sharp injector rate, small pilot injection quantity (0.5 mm^3), reduced tolerances for low emission standards, multiple injections (up to 7 events per cycle), reduced static and dynamic forces (wear), fail-safe-principle, low noise and compact design. The injector is designed for the rail pressure up to 180 MPa (CRI3.1) and 200 MPa (CRI3.2), respectively. Schematic of the injector is shown in Fig. 1. The main assembly components of the injector are piezoelectric stack actuator, hydraulic amplifier (coupler), control

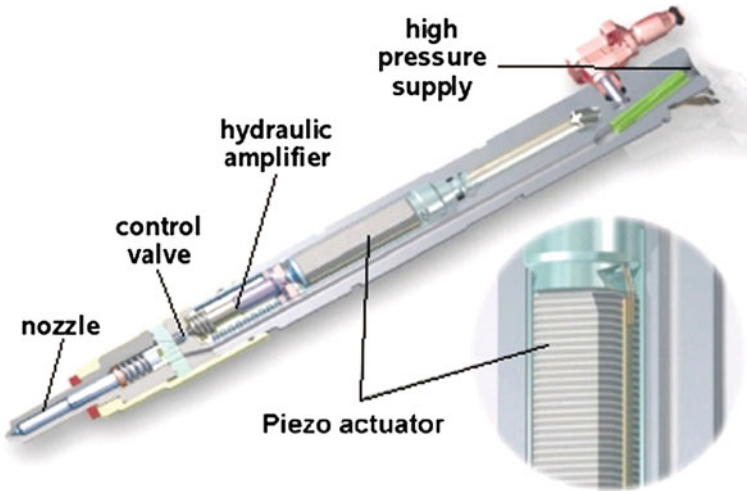


Fig. 1 Schematic of BOSCH CRI3 common rail injector

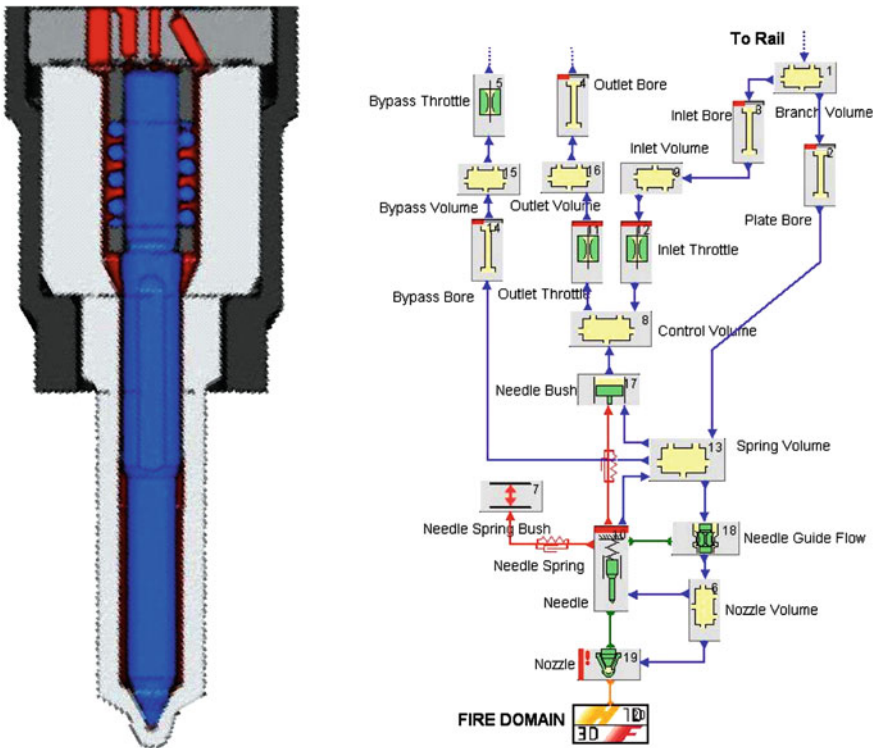


Fig. 2 Injector nozzle with needle and throttle plate (sketch and Hydsim model)

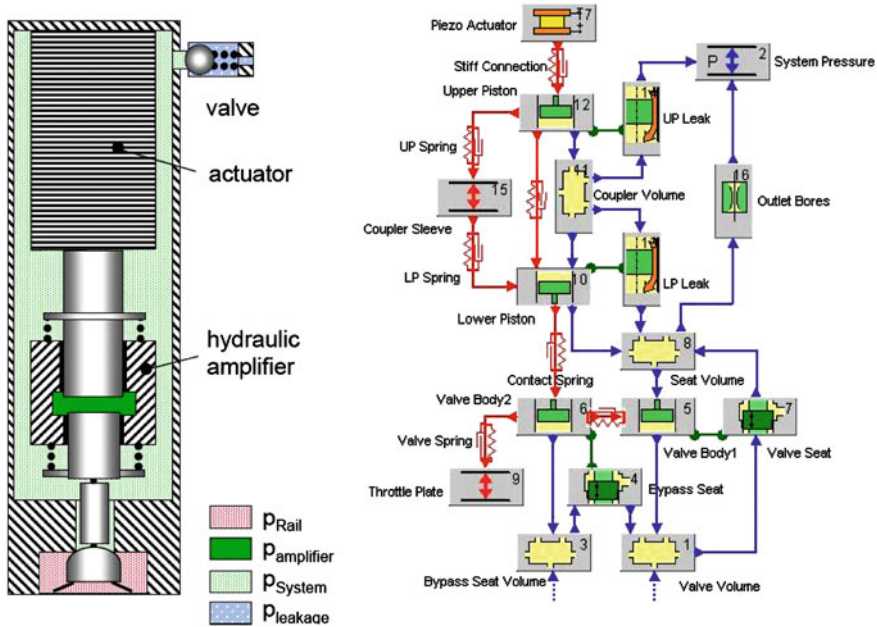


Fig. 3 Piezoelectric actuator and hydraulic amplifier (sketch and Hydsim model)

valve, throttle plate and nozzle. Schematic and Hydsim model of the nozzle (with Fire Link element) and throttle plate are shown in Fig. 2.

The piezoelectric stack actuator is schematically shown in Fig. 3. It consists of a dense pile of separately contacted layers (wafers) of electrically active ceramic material. The layers are assembled mechanically in series and connected electrically in parallel. When input voltage is applied to the stack actuator, electric field across the ceramic layers induces a mechanical strain, which results in an elongation of the stack. Detailed description of the piezoelectric actuator and its model can be found in [1].

3 Coupling Interface

Hydsim-Fire coupling interface is illustrated in Fig. 4: the left graph shows the centered needle (with 1 degree-of-freedom and one force component) while the right graph—eccentric needle (with 3 degrees-of-freedom and 3 force components).

As shown in Fig. 4, on each exchange step Fire transfers to Hydsim the following data:

- F_N —Force vector acting on needle tip
- q_{seat} —Flow rate through needle seat
- q_{holes} —Flow rate through nozzle holes
- p_{topV} —Boundary pressure below interface line

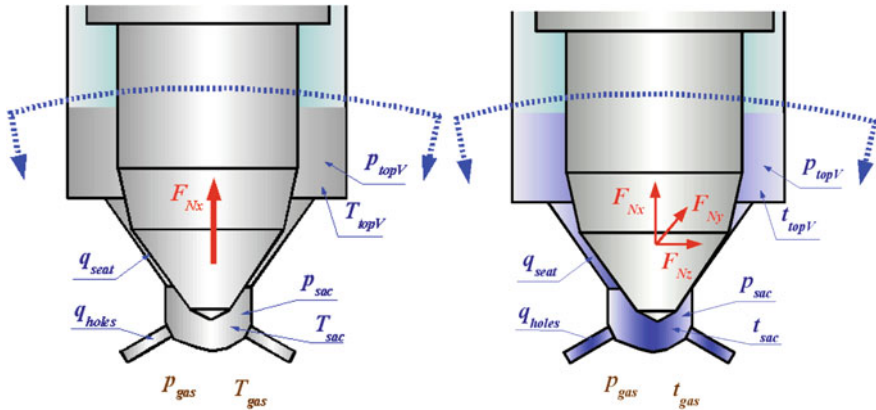


Fig. 4 CFD calculation domain with exchange variables (*left*—centered needle, *right*—eccentric needle)

- T_{topV} —Boundary temperature below interface line
- p_{sac} —Average pressure in sac volume
- T_{sac} —Average temperature in sac volume
- p_{gas} —Boundary pressure in spray chamber
- T_{gas} —Boundary temperature in spray chamber

At the end of the exchange time step Hydsim transfers to Fire the following data:

- X_d —Displacement vector of needle tip (3 components)
- p_{nozV} —Boundary pressure above interface line
- T_{nozV} —Boundary temperature above interface line

Our injector example considers two cases: centered needle model with 1 degree-of-freedom (longitudinal motion in z) and eccentric needle with 3 degrees-of-freedom (linear motion in x , y and z). The needle lift tolerance in axial (z) direction for co-simulation start is set to $2\ \mu\text{m}$. Axial needle motion is fully calculated from the system dynamics. To initiate radial needle motion in 3-DOF case, the initial condition along x axis is set to $-1\ \mu\text{m}$ (along y axis it is 0). With this starting condition, as long as the needle tip interferes with the conical seat contour, kinematic needle movement along the seat surface is imposed. Dynamic calculation of x and y motion starts when axial lift is high enough so that the needle tip gets out of contact with the seat. Note that radial needle motion is limited by the cylindrical gap between needle guide and nozzle body. In light duty common rail injectors this diametric gap is typically about $5\ \mu\text{m}$. In our model we allow the gap of $10\ \mu\text{m}$. If radial needle motion overcomes this gap (with $0.5\ \mu\text{m}$ tolerance), the injector wall reaction force is calculated and applied on the needle guide. At the current stage this calculation is done in a simplified way by introducing a stiff linear spring and damper at the contact (without consideration of the fluid film effects). Hydsim calculation step is 10^{-7} s, exchange step with Fire is 10^{-6} s. This

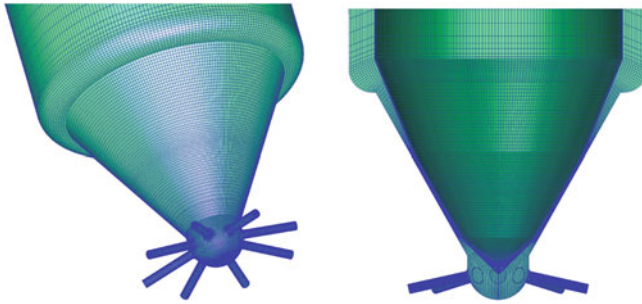


Fig. 5 CFD nozzle mesh (*left*–outside view, *right*–cross-section with needle)

step is applied only for the intervals where axial needle lift exceeds the tolerance (i.e. during injection).

4 Nozzle Mesh

Computational grid used in the CFD simulation is shown in Fig. 5. It consists of the hollow cylinder around the needle shaft, needle seat area with nozzle sac and eight cylindrical holes. For the case with 1-DOF needle, only one of the eight periodic 45° -segments is modeled (refer to [1]). For the case with 3-DOF needle, full 360° mesh is created as shown in Fig. 5. This mesh consists of 845280 hexahedral cells with 240 cell layers in the circumferential direction, so that one layer corresponds to 1.5° . Cell size in the narrowest needle seat gap is $0.3 \times 25 \mu\text{m}$. The outlet bore is meshed separately and connected to the sac volume by arbitrary-interfaces. The nozzle gap itself contains 50 cell rows in the radial direction (which is the main flow direction) and 11 rows in vertical direction. This mesh topology is chosen according to the AVL experience with nozzle flow simulation [13]. Needle movement is accomplished by the mesh-deformation at solver run-time. The mesh-deformation-function shifts the needle surface at each time step according to the needle displacement received from HydSim. After that, the position of the internal nodes is updated by the Laplace interpolation scheme. To prevent collapsing cells at zero or very small needle lift, a minimal gap size ($3 \mu\text{m}$ in the actual case) is maintained in the mesh.

5 Calculation Results

Calculation is carried out for the engine speed 2000 rpm and rail pressure 160 MPa. As our primary interest lies in the investigation of nozzle flow at small needle lifts, only the pilot injection is analyzed. This allows keeping the

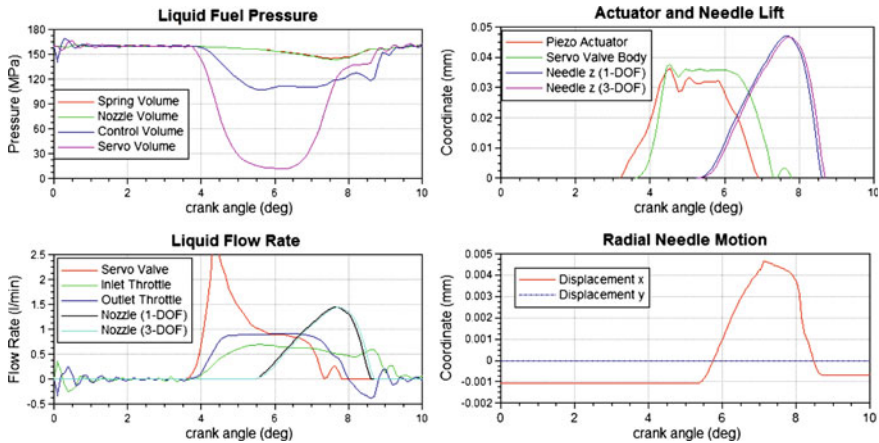


Fig. 6 1D results: pressure and flow rate in injector parts, needle motion for 1-DOF and 3-DOF cases

computational effort within a reasonable range. Two needle models with 1-DOF and 3-DOF needle motion are considered. Selected 1D calculation results are shown in Fig. 6. For convenience they are plotted in the crank angle domain. Maximum needle lift is about $50\ \mu\text{m}$ and injection quantity is $2.2\ \text{mm}^3$. Time delay between the actuation start (3.2°) and injection start (5.6°) is 2.4° or $200\ \mu\text{s}$. Note that at 5.6° the co-simulation between Hydsim and Fire begins. Axial needle lift and injection rate are nearly same for the 1-DOF and 3-DOF needle models. At opening 3-DOF needle moves from the initial shift ($-1\ \mu\text{m}$ in x) towards the center position along x axis, crosses the symmetry axis and reaches $4.5\ \mu\text{m}$ position on the opposite side. There it gets bounced back by the guide reaction forces and returns towards the center position.

Characteristic 3D calculation results are plotted in Figs. 7, 8, 9. Phase distribution is shown in Fig. 7. There blue color represents 100 % diesel liquid, red color—100 % diesel vapor. Needle reaches the prescribed tolerance of $2\ \mu\text{m}$ at Hydsim angle 5.6° (corresponds to zero time in Fire). On very opening, at needle lift of $3\ \mu\text{m}$ (Fire time $5\ \mu\text{s}$) light vaporization area is visible above the open side of the needle seat (due to eccentricity) which slowly vanishes within the next steps. From $10\ \mu\text{m}$ lift till full lift of $47\ \mu\text{m}$ cavitation does occur neither at seat nor in the holes. The needle seat starts cavitating again when the lift drops to $40\ \mu\text{m}$ (Fire time $190\ \mu\text{s}$). From the lift of about $20\ \mu\text{m}$ (Fire time $235\ \mu\text{s}$) till needle closing (Fire time $250\ \mu\text{s}$) cavitation ring at needle seat contracts gradually to the wider open area (due to radial shift) and spreads into the sac and holes. Note that different holes exhibit different cavitation patterns. In some holes cavitation area propagates till the outlet.

Figure 8 shows the pressure distribution in the nozzle. At opening one can clearly distinguish between the rail pressure ($160\ \text{MPa}$) above the needle seat and outlet pressure ($2\ \text{MPa}$) behind it. With the higher needle lift, the pressure in the

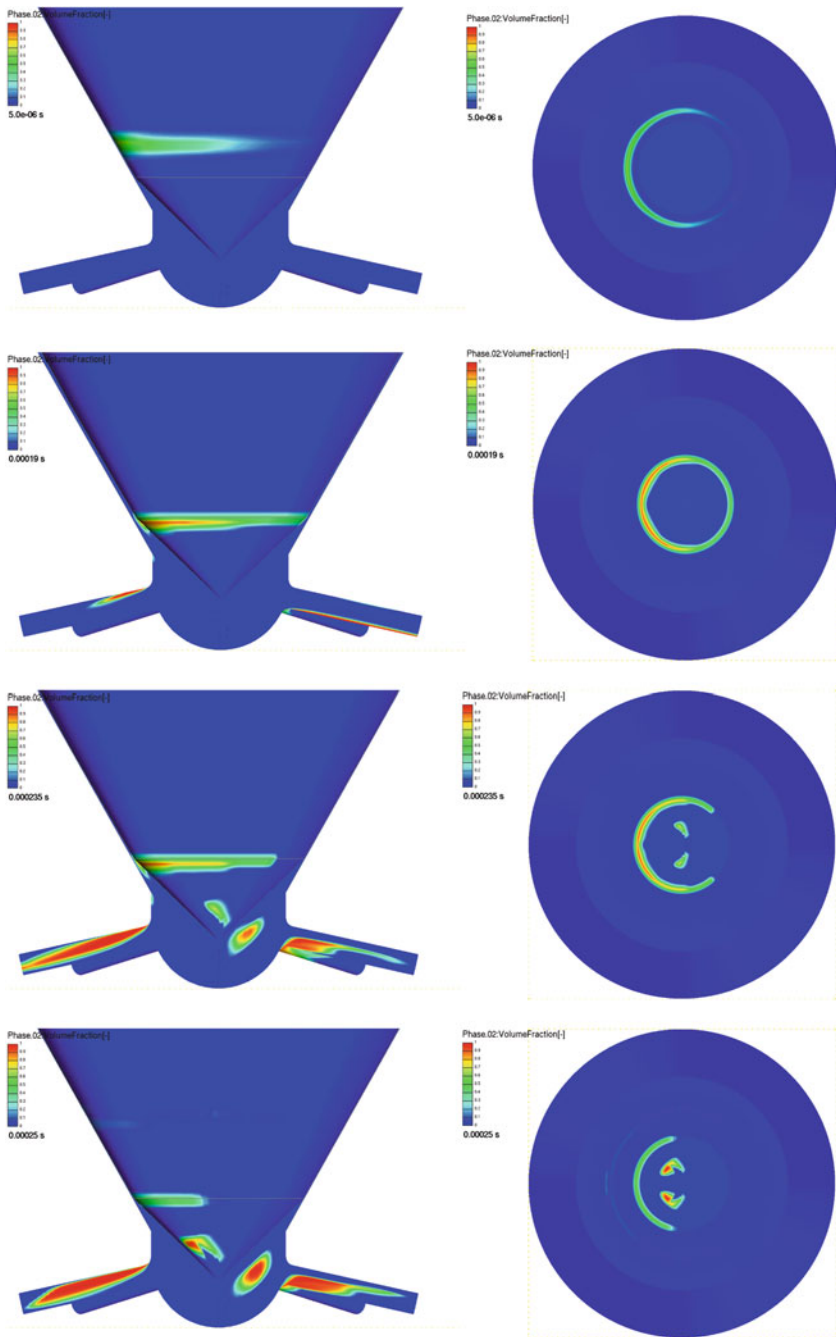


Fig. 7 Phase distribution for eccentric needle at time instants (from top): at 5 μ s, 190 μ s, 235 μ s and 250 μ s (*left graphs*—mid-plane nozzle cut, *right graphs*—bottom view on needle tip)

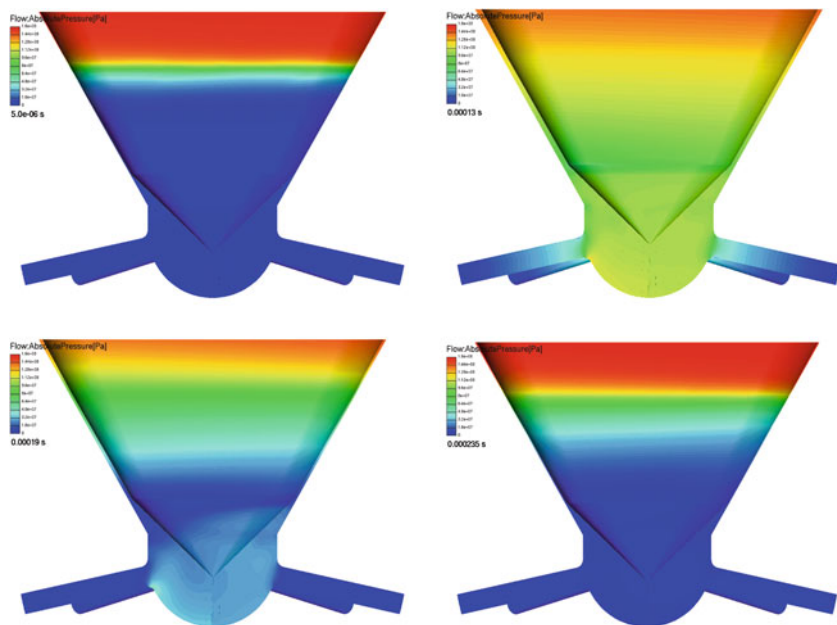


Fig. 8 Liquid pressure (*top: left*—at 5 μs , *right*—at 130 μs ; *bottom: left*—at 190 μs , *right*—at 235 μs)

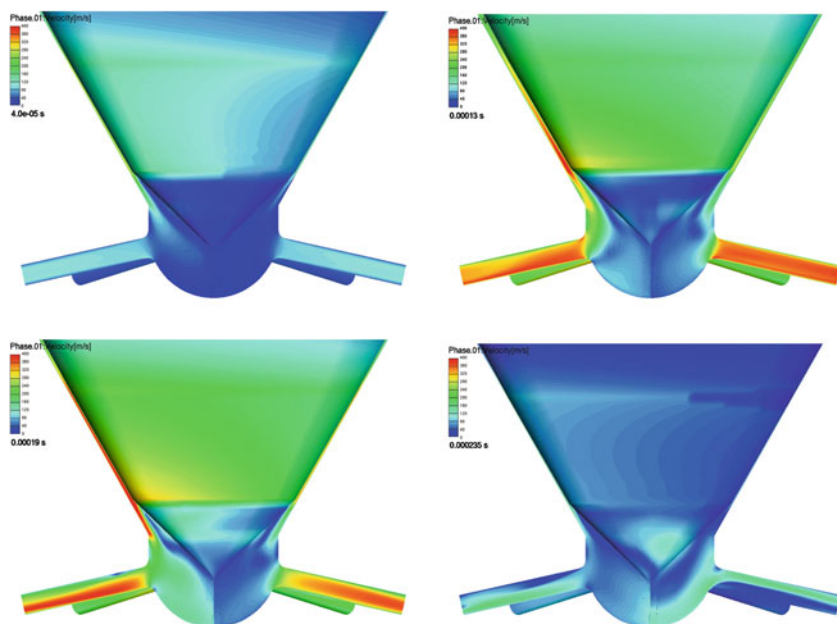


Fig. 9 Liquid velocity (*top: left*—at 40 μs , *right*—at 130 μs ; *bottom: left*—at 190 μs , *right*—at 235 μs)

nozzle sac gradually increases, and one can observe a continuous pressure drop across the seat. Due to the radial needle shift, the pressure distribution in the circumferential direction is not uniform, i.e. pressure around the seat stays higher at the narrower gap, thus inducing a radial force which is transferred to Hydsim and pushes the needle towards the central position. This effect can be observed not only at seat but also at needle guide if the latter gets close to the nozzle wall. Generally, at higher needle lifts, the radial needle motion is mainly limited by the gap width between the guide and nozzle wall. As stated earlier, the guide reaction force at its contact with the wall is calculated directly by Hydsim using a simplified way.

Figure 9 depicts the liquid velocity in the nozzle. Naturally, higher velocities occur in the wider open seat area, where needle eccentricity is the largest. Due to this effect the liquid velocities may get higher in the holes which are located closer to the wider open seat area. However, this strongly depends on the flow conditions in the nozzle sac. The highest velocity of about 400 m/s occurs at maximum needle lift of 47 μm at 7.6° (Fire time 130 μs).

6 Conclusion

Novel 1D/2D/3D injector and nozzle flow simulation technique is developed. Basically, this is a substantial extension of 1D/3D simulation method earlier published by the authors. The previous technique was limited to 1D (longitudinal) needle motion both from 1D injector modeling in Hydsim and 3D nozzle flow calculation in Fire. Now both software tools are extended in such a way that 2D motion of the needle with 3 DOFs (translation in x, y and z) can be simulated in Hydsim and respective mesh movement represented in Fire. Using this technique, a 1D/2D (longitudinal and transverse) motion of the needle can be coupled with the 3D nozzle flow and cavitation model as shown in the demonstration example. This allows modeling of a non-uniform pressure distribution and cavitating flow across the needle seat and nozzle holes.

References

1. Čaika V, Sampl P (2011) Nozzle flow and cavitation modeling with coupled 1D/3D AVL software tools. SAE Paper 2011-24-006, 10th international conference on engines for automobile, Capri, Naples, Italy, Sept 2011
2. Čaika V, Sampl P, Greif D (2011) Coupled 1D-3D simulation technique for diesel injector flow. In: Proceedings of JSAE 2011 annual congress, Yokohama, Japan, May 2011
3. Alajbegovic A, Grogger H, Phillip H (1999) Calculation of transient cavitation in nozzle using two-fluid method. In: Annual conference on liquid atomization and spray systems, Indianapolis, IN, USA, 1999, pp 209–213
4. Arcoumanis C et al (2000) Cavitation in real-size multi-hole diesel injector nozzles. SAE Trans J Engines, 2000-01-1249 109-3

5. Chen J, Heister D (1996) Modeling cavitating flows in diesel injectors. *Atomization Sprays* 6:709–726
6. Schmidt DP, Corradini ML (2001) The internal flow of diesel fuel injector nozzles. *Int J Engine Res* 2:1–22
7. Sou A, Kinugasa T (2010) Numerical simulation of developing cavitating flow in a nozzle of pressure atomizer. In: Thiesel conference on thermo- and fluid dynamic processes in diesel engines, Valencia, Spain, Sept 2010
8. Yuan W, Schnerr GH (2001) Cavitation in injection nozzles: effect of injection pressure fluctuations. In: Proceedings of the Fourth 4th international symposium on cavitation, Pasadena, CA, USA, 2001
9. Giannadakis E, Gavaises M, Arcoumanis C (2008) Modeling of cavitation in diesel injector nozzles. *Fluid Mech* 616:153–193
10. Wang DM, Greif D (2006) Progress in modeling injector cavitating flows with a multi-fluid method. In: ASME forum on cavitation and multiphase flow, FEDSM2006-98501, Miami, FL, USA, July 2006
11. Payri F et al (2009) A CFD study of the effect of needle movement on the cavitation pattern of diesel injectors. SAE paper 2009-24-0025. In: 9th interantional conference on engines for automobile, Capri, Naples, Italy, Sept 2009
12. Drew DA, Passman SL (1999) *Theory of multicomponent fluids*. Springer, New York
13. AVL Fire (2011) *Eulerian multiphase*. Graz, 2011
14. AVL Boost Hydsim (2011) *User's Guide*. Graz, 2011
15. Böcking F et al (2005) Passenger car common rail systems for future emissions standards. *MTZ* 7-8/2005, 66:552–557

Predicting the Effect of Fuel Path Controllable Parameters on the Performance of Combustion Controlled Diesel Engine

Zhijia Yang and Richard Stobart

Abstract *Research and/or Engineering Questions/Objective:* Diesel combustion process control is very important in optimizing diesel engine performance. There are few controllable parameters in engine fuel path which have effects on the combustion process and hence the engine performance. The objective of this study is to develop a control-oriented, low computational cost diesel combustion model and apply it in combustion process control system design. *Methodology:* The structure of a control-oriented low computational cost combustion model was developed based on sufficient knowledge and comparison of various fuel injection spray and combustion models in literature. The model parameters were identified from a Caterpillar C6.6 diesel engine installed in the Loughborough University laboratory. The model was further validated by the same engine test data both at steady operation points. The model was then used in predicting the effect of fuel path controllable parameters (start of injection and fuel rail pressure) on the engine performance output over all engine operation range. The engine performance output includes NO_x and soot emission out and IMEP value for each cycle. This model and the prediction result was finally used in designing a combustion process feedback control system. *Results:* This combustion model was validated to show that it has high accuracy both for engine steady operation point and transient. The simulation result shows the trade-off among NO_x and soot emission for varying start of injection and rail pressure. And this trade-off varies with engine speed and load. The engine test results indicate that the combustion process control system designed based on this combustion model and prediction results is able to improve the engine performance compared to look-up table fuel path control system.

F2012-A02-014

Z. Yang (✉) · R. Stobart
Loughborough, Leicestershire, UK
e-mail: z.yang2@lboro.ac.uk

Limitations of this study: The combustion model presented in this paper needs to be expanded to include air path and heat transfer dynamics. Model validation needs to cover VGT and EGR control input variation. *What does the paper offer that is new in the field in comparison to other works of the author:* Developing a control-oriented diesel combustion model; using the model in studying the engine performance space and the controllability of fuel path controllable parameters; and the synthesis of diesel combustion control system are all novel topics. *Conclusion:* A low computational cost combustion model for combustion process control purpose was developed and validated. The application of this model in control system design was implemented and was experimentally proved to be success in improving the engine performance both emission and fuel consumption. The IMEP feedback control either by main injection duration or by PDW is able to reduce combustion variations at steady state and has strong disturbance rejection performance to other fuel path inputs.

Keywords Diesel engine • Fuel path • Combustion model • NO_x emission • Soot emission

Appendix: Notation

COV	Coefficient of variation
DW	Dwell time
EGR	Exhaust gas recirculation
IMEP	Indicated mean effective pressure
NI	National instruments
NO _x	Nitrogen oxides
PDW	Post dwell time
PSR	Post split ratio
RP	Rail pressure
SOI	Start of injection
TDC	Top dead centre
VGT	Variable geometry turbocharger

1 Introduction

The sole purpose of combustion in a reciprocating piston engine is to shift the expansion process away from the compression process in order to generate a working cycle. So that the only reason for the use of fuel is to generate pressure in order to accomplish this task [1]. The way of the usage of fuel to generate pressure in either gasoline engine or diesel engine is via combustion. In diesel engine, the unavoidable by-products of combustion are mainly nitrogen oxides(NO_x) and particular matter (PM) emissions which are harmful to human health and need to be controlled to meet increasingly stringent government regulations [2]. There is intrinsic trade-off

phenomenon between engine mechanic work power output and emissions, trade-off between NO_x emission and soot emission for most of the engine control variables such as: start of injection (SOI), common rail fuel pressure (RP), exhaust gas recirculation (EGR) ratio and variable geometry turbocharger (VGT) vane open position etc. The fuel consumption and emission performance over all engine operation points under all possible air path and fuel path control variable ranges is extremely complicated because of high dimension and high nonlinearity characteristics. In order to control engine work with optimal or near optimal performance, correct knowledge and relative accurate model of engine combustion process is important. Otherwise, the engine aftertreatment system located in exhaust pipe need exhaust emission information to optimize its performance as well.

Immense research work has been carried out on control oriented combustion process and NO_x and PM emission formation model. For NO_x and PM emission model, from simple to complex, there are black box model, grey box model, zero-dimensional thermal dynamic model and three-dimensional CFD model [3]. For control system design, control-oriented model is required. As CFD model is too complicated and has long computation time, it does not fit for application in control system design and implementation. Black box model and grey box model are relatively simply but need long time to be trained and are not easy to be adjusted to cover all engine operation points [3, 4]. Recently, zero-dimensional thermal dynamic emission model has been intensely studied for control purpose [4–11]. It is a simplified physical phenomenal model. The model parameters are more easy to be identified while the computational cost is kept low enough to make it possible to be implemented online or embedded in engine control module.

A simplified combustion and zero-dimensional emission model was developed and validated in this paper. As only measured soot emission data which is also known as opacity is available in the test cell, soot model instead of total PM model was developed and validated. This model was later used in design a combustion process control based on fuel path inputs. The combustion control system shows that the engine performance both emission and fuel consumption are improved compared to engine look up table control. Tests of IMEP closed loop control based on main injection duration and post injection dwell time(PDW) shows it is a good way to directly feedback control engine combustion work output and reduce combustion variation.

2 Engine Model

The engine model developed in this paper is a cycle-by-cycle based zero-dimensional phenomenal model. It includes four sub model sections: injector model, air path model, combustion model and NO_x & soot emission model. This model is for simulation of conventional diesel engine which equipped with common rail, VGT and EGR system. The diagram of this model is depicted in Fig. 1. The controllable inputs to the diesel engine are categorized into two types:

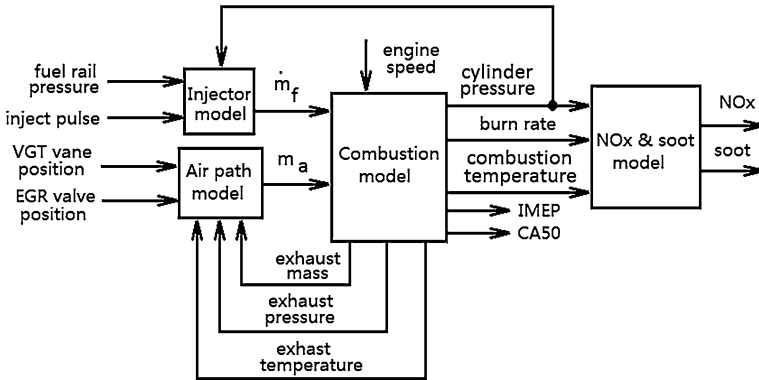


Fig. 1 Diagram of cycle-by-cycle based engine model

fuel path control variables and air path control variables. The fuel path control variables include: SOI, fuel rail pressure, injection pulse numbers, injection fuel ratio, injection dwell time etc. The air path control variables include: VGT vane position and EGR valve position. They are manipulated by engine control system to make engine to output power meanwhile satisfy emission and fuel consumption constraints. These emission and fuel consumption constraints should be within the feasible engine performance space. The model in Fig. 1 can give a whole picture of the engine feasible engine performance space and hence is useful in engine control system design either in control structure selection, or in setpoint determination. As this model also has dynamic information related to engine speed and cycle event, it could be used in feedback controller design. Except engine cycle event dynamics, there is also heat transfer thermal dynamics. But the later is neglected in this model for simplicity.

2.1 1-Injector Model

Injector model is used to calculate the injected fuel rate. There are two variables mainly affect the injected fuel rate: needle lift and pressure difference between common fuel rail pressure and cylinder pressure. The effect of pressure difference on needle lift shape is ignored. Hence, the needle lift shape is modelled as a one-order delay transfer function with a dead time. See Eq. (1)

$$\frac{NL}{Inj} = \frac{K_{NL}}{T_{NL}q s + 1} e^{-\tau_{NL}s} \quad (1)$$

where NL is needle lift, Inj is injection pulse, T_{NL} is injector needle lift response time, K_{NL} is a constant, τ_{NL} is injector needle lift response dead time. These model parameters are assumed to be the same for all engine operation points.

The pressure difference between common fuel rail pressure and cylinder pressure has effect on the injected fuel rate into the cylinder chamber. It is modelled as a linear Eq. (2)

$$\dot{m}_f = K_f(p_r - p_c)NL \quad (2)$$

where \dot{m}_f is injected fuel rate, K_f is a constant, p_r is common fuel rail pressure, p_c is cylinder pressure.

2.2 2-Air Path Model

The air path model is estimating the trapped air mass in cylinder chamber. The air path dynamics is neglected and the intake temperature is assumed to be constant. Then the intake pressure is modelled as a simple nonlinear correlation equation of VGT vane position and exhaust pressure. See Eq. (3)

$$p_i = K_a \alpha_{VGT} p_e + a_1 \quad (3)$$

where p_i is intake manifold pressure, α_{VGT} is VGT vane position in percentage, p_e is exhaust pressure, K_a and a_1 are constants. The EGR gas mass for a single cycle is estimated by a nonlinear correlation Eq. (4).

$$m_{EGR} = K_e \alpha_{EGR} m_e (p_e - p_i) \quad (4)$$

where m_{EGR} is EGR gas mass enters the cylinder chamber, α_{EGR} is EGR valve open position is in percentage, m_e is exhaust mass from a cylinder combustion exhaust. Then the intake air mass for one cycle is estimated in Eq. (5)

$$m_a = \frac{M_{air} p_i V_{BTDC}}{RT_i} - m_{EGR} \quad (5)$$

where m_a is trapped fresh air in cylinder chamber, M_{air} is air molecular weight, V_{BTDC} is cylinder chamber volume when piston is at BTDC, T_i is intake temperature.

2.3 3-Combustion Model

Combustion model is used to estimate the cylinder pressure, combustion temperature, heat release rate, IMEP and CA50. The outputs of combustion model are inputs to NOx & soot emission model. Ignore heat transfer and crevice mass loss, the heat release rate is modelled from the injected fuel mass rate in Eq. (6)

$$dQ = K_Q \dot{m}_f LHV \quad (6)$$

where dQ is heat release rate, K_Q is model constant, LHV is fuel low heat value. Then the cylinder pressure differential during combustion process is estimated by Eq. (7)

$$dp_c = (dQ - \frac{\gamma}{\gamma-1} p_c V_c) (\frac{\gamma-1}{V_c}) \quad (7)$$

where γ is isentropic constant, V_c is cylinder volume. The combustion temperature is computed by using Eq. (8)

$$T_c = \frac{M_{air} p_c V_c}{R m_a} \quad (8)$$

CA50 is the crank angle of the half heat release. IMEP is computed from cylinder pressure data by using Eq. (9)

$$IMEP = \int p dV_c \quad (9)$$

2.4 4-NOx Model

NOx model is NO model as 95 % of NOx formatted during the combustion process is NO. It uses Zeldovich mechanism in modelling NO formation rate. See Eq. (10)

$$d[NO]/dt = \sqrt{20.3 \exp\left(\frac{-21650}{T_c}\right) \cdot [O_2] \cdot [N_2]} \quad (10)$$

where, $[NO]$, $[O_2]$ and $[N_2]$ are concentration of N, O_2 and N_2 respectively. $[O_2]$ and $[N_2]$ are computed by using Eqs. (11) and (12).

$$[O_2] = \frac{0.21(n_a - n_{ba} - n_{O_2})}{V_c} \quad (11)$$

$$[N_2] = \frac{0.78n_a - n_{N_2}}{V_c} \quad (12)$$

where, n_a is the mole number of trapped air, n_{O_2} and n_{N_2} are mole number of consumed O_2 and N_2 . n_{ba} is the mole number of burned air which is computed by using Eqs. (13) and (14)

$$n_{bf} = \frac{Q}{LHV \cdot M_f} \quad (13)$$

$$n_{ba} = n_{bf} \cdot \frac{M_f \cdot AFR_{stoi}}{M_{air}} \quad (14)$$

where, n_{bf} is the mole number of burned fuel.

2.5 5-Soot Model

The soot model used in this paper is the same to that in [5]. Soot generation rate is a competition effect of soot formation rate and soot oxidation rate, see Eq. (15)

$$\frac{dm_s}{dt} = \frac{dm_{s,f}}{dt} - \frac{dm_{s,o}}{dt} \quad (15)$$

The soot formation rate and soot oxidation rate are calculated by using Eqs. (16) and (17) respectively

$$\frac{dm_{s,f}}{dt} = K_{s,f} \cdot n_f \cdot p_c^{0.5} e^{\frac{E_{s,f}}{RT_c}} \quad (16)$$

$$\frac{dm_{s,o}}{dt} = K_{s,o} \cdot m_s \cdot X_{O_2} \cdot p_c^{1.8} e^{\frac{E_{s,o}}{RT_c}} \quad (17)$$

where $K_{s,f}$ and $K_{s,o}$ are model constants, n_f is mole number of fuel, X_{O_2} is fraction of O_2 , $E_{s,f}$ and $E_{s,o}$ are activation energy of soot formation and soot oxidation respectively.

3 Engine Tests and Model Simulation Results

The engine used for model validation is CAT C6.6 heavy-duty off-highway engine. It is a 6 cylinder, 6.6 l engine equipped with a Caterpillar common rail fuel system, a high pressure EGR system and a variable geometry turbine (VGT). The type of cylinder pressure sensor is Kistler 6125B ThermoCOMP[®] Quartz Pressure Sensors. A Kistler 2854A Signal Conditioning Platform (SCP) with three 2-channel 5064B21 charge amplifiers provides the signal conditioning, including drift compensation. The NOx emission was measured by Drivven cRIO NOx sensor module. The engine control system was implemented in National Instrument(NI) Real Time(RT) control system with LabView program code. The air path and fuel path control inputs to the engine can be changed manually when engine is running at steady state operation point. All engine key variables like engine speed, engine torque, MAF, SOI, FRP and NOx emission from NOx sensor

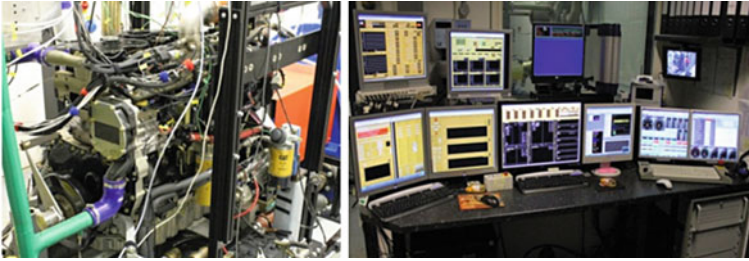
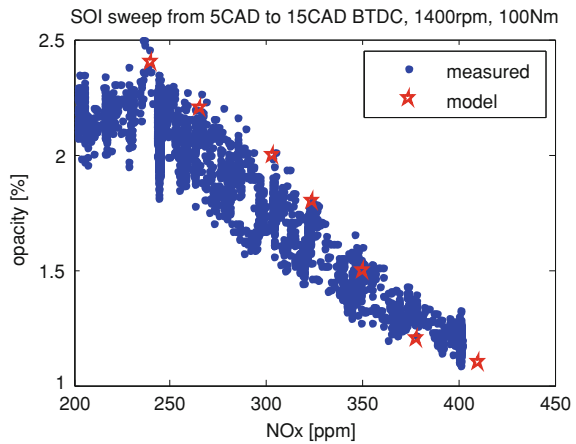


Fig. 2 Test engine and engine control desk

Fig. 3 NO_x and soot emission model estimation against measured value at engine speed 1400 rpm and 100 Nm output torque when SOI sweep



etc. are sampled at 30 Hz frequency and logged. The cylinder pressure data was sampled at one crank angle degree resolution and logged in a separate file. All engine tests were done on a test bed with a dyno system. For more information of this engine test system, see [12]. Figure 2 is the picture of the engine in cell and the engine control desk. The dynamometer used in the test bed is Schench Eddy Current dynamometer. The dynamometer control system is CP Cadet system.

Model parameters were identified by engine steady state test data by using MATLAB nonlinear solve function `fsolve`. EGR was not used in engine tests. Soot was validated to opacity measurement in [%]. NO_x was validated to measurement in [ppm]. Some of the model validation results are shown in Figs. 3,4,5 when two main fuel path inputs were swept separately while other control inputs were fixed. Based on the study of this model results of achievable the C6.6 engine performance, a combustion process controlled system was implemented with proper CA50 setpoint at different engine speed and torque. A transient test was done for comparing the emission and fuel consumption performance of combustion

Fig. 4 NOx and soot emission model estimation against measured value at engine speed 1200 rpm and 200 Nm output torque when SOI sweep

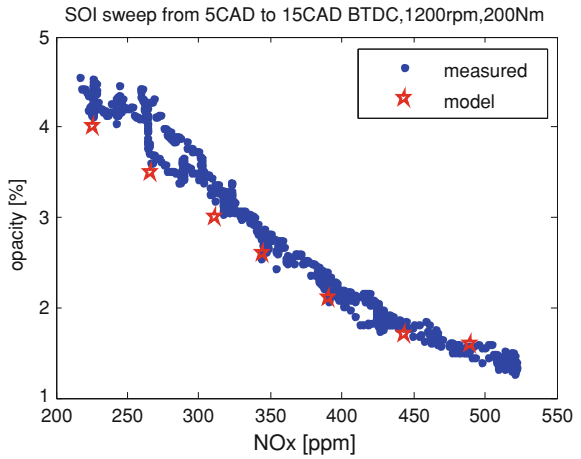


Fig. 5 NOx and soot emission model estimation against measured value at engine speed 1200 rpm and 200 Nm output torque when fuel rail pressure sweep

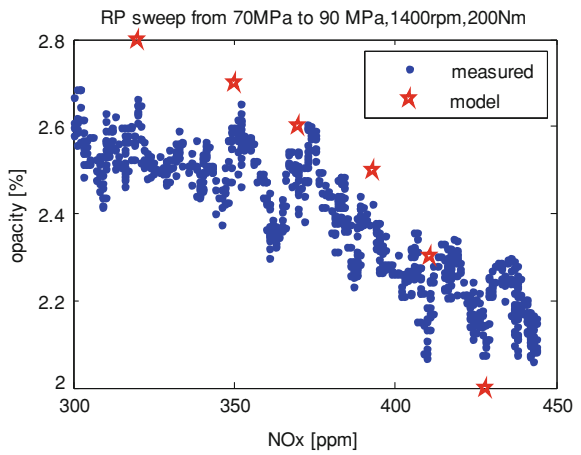


Fig. 6 Engine speed curve during the transient test

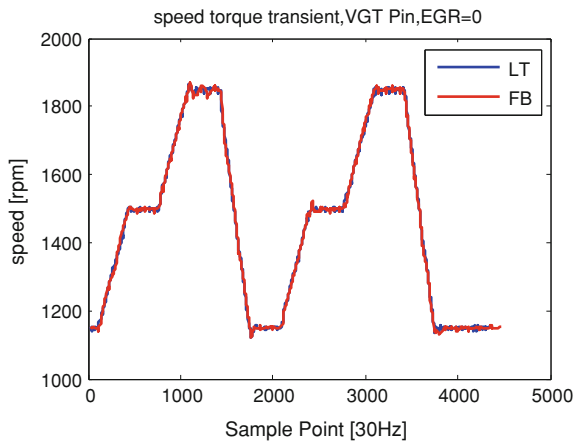


Fig. 7 Engine torque during the transient test

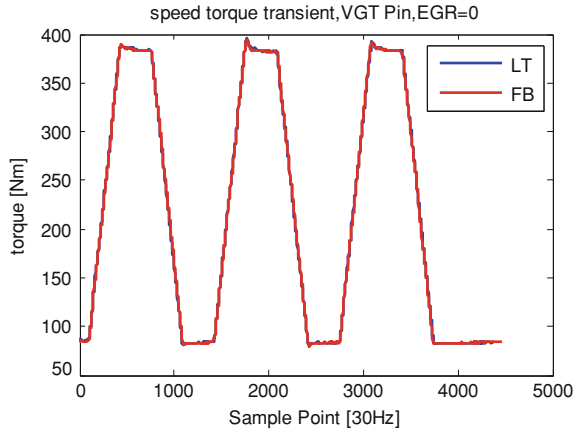


Fig. 8 Engine speed and torque scatter plot during the transient test

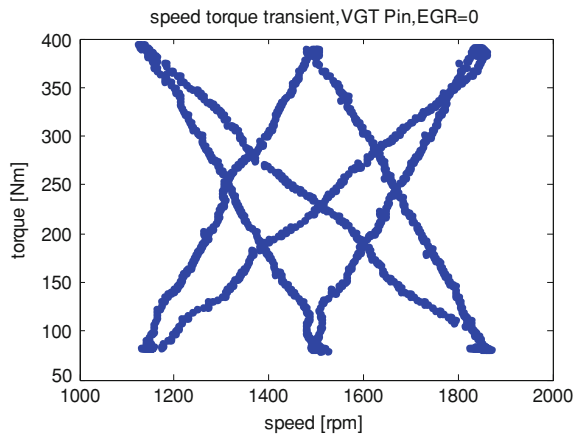


Fig. 9 NOx emission comparison between LT(SOI and rail pressure lookup table control) and FB(SOI and rail pressure feedback control)

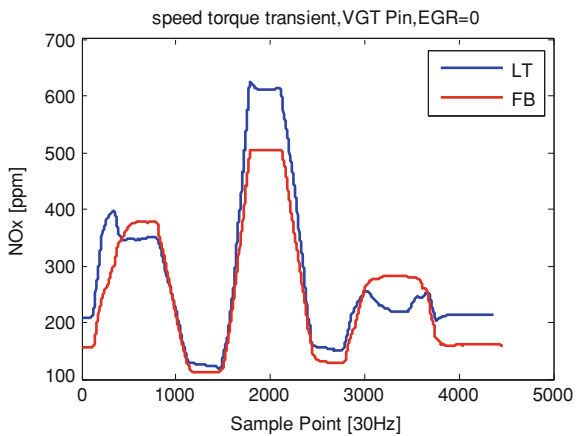


Fig. 10 Soot emission comparison between LT(SOI and rail pressure lookup table control) and FB(SOI and rail pressure feedback control)

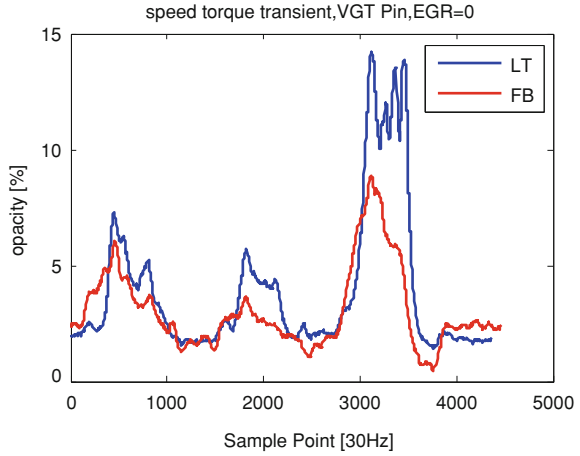
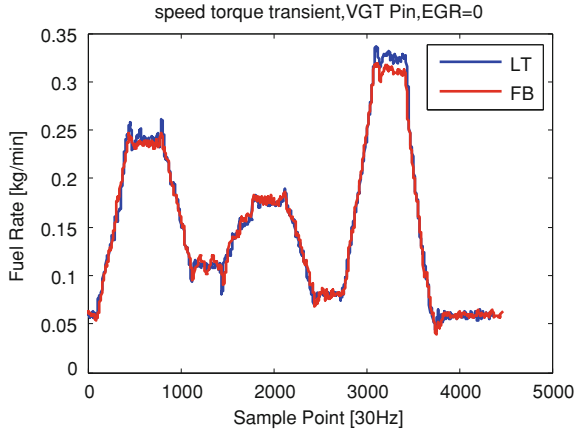


Fig. 11 Fuel consumption comparison between LT(SOI and rail pressure lookup table control) and FB(SOI and rail pressure feedback control)



feedback control and lookup table control. The results are shown in Figs. 6, 7, 8, 9, 10, 11. There are improvements both in NOx & soot emission and fuel consumption.

4 IMEP Feedback Control

IMEP is a measure of engine work output in terms of cylinder pressure. For 4 stroke diesel engine, its relationship to indicated torque is shown in Eq. (18)

$$T_i = \frac{IMEP \cdot 6V_c}{4\pi} \tag{18}$$

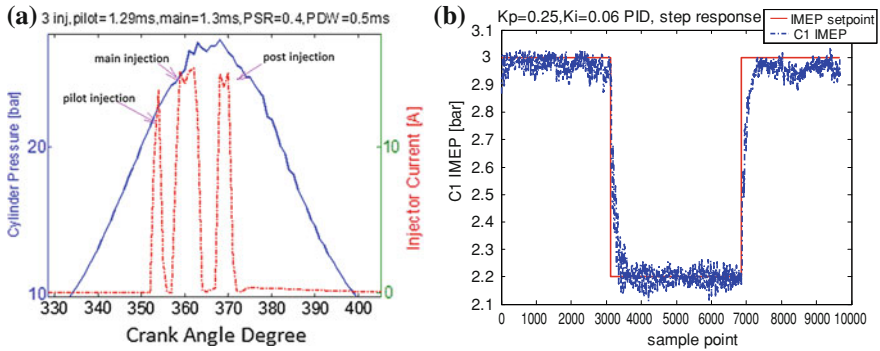


Fig. 12 **a** Cylinder 1 cylinder pressure and injection current for 3 injection mode; **b** Cylinder 1 IMEP step control response

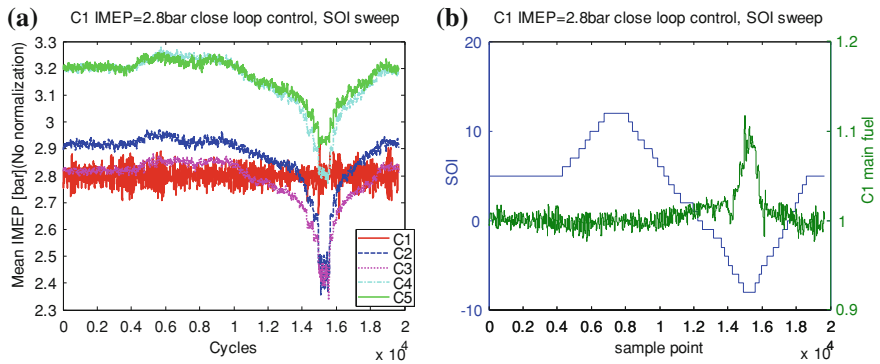


Fig. 13 Cylinder 1 IMEP feedback control test (SOI as disturbance). **a** 5 cylinder IMEP, only cylinder 1 IMEP is controlled; **b** SOI and main fuel injection duration

So if each cylinder’s IMEP is closed loop controlled, the engine work output is also controlled.

In this IMEP feedback control, the IMEP value was estimated from measured cylinder pressure data by using Eq. (9). The injection mode is three pulses, see Fig. 12a. Fuel input variable main injection duration or post injection dwell time (PDW) was used to control IMEP. Only cylinder one IMEP was closed loop controlled. The step response IMEP by main injection duration control is shown in Fig. 12b. As the cylinder six pressure sensor was broken, only five cylinders’ IMEP was plotted in Fig. 13a, b. Figure 13a shows that when SOI input was swept in the way shown in Fig. 13b, IMEP of cylinder one was maintained constant while other cylinders’ IMEP varied a lot with SOI changed. The main injection duration of cylinder one was plotted in Fig. 13b. The same phenomena was also

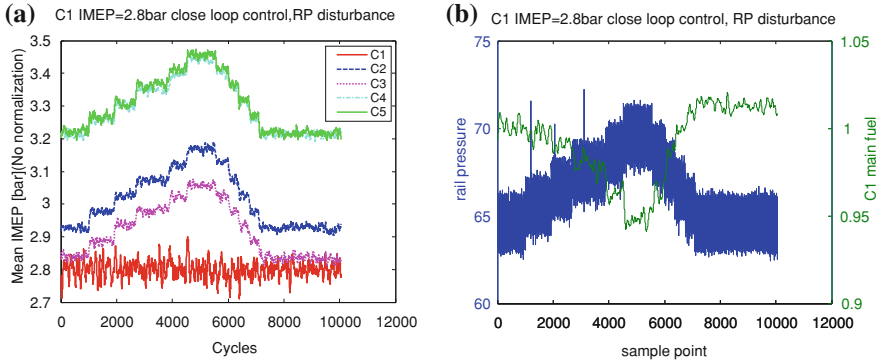


Fig. 14 Cylinder 1 IMEP feedback control test (rail pressure as disturbance). **a** 5 cylinder IMEP, only cylinder 1 IMEP is controlled; **b** rail pressure and main fuel injection duration

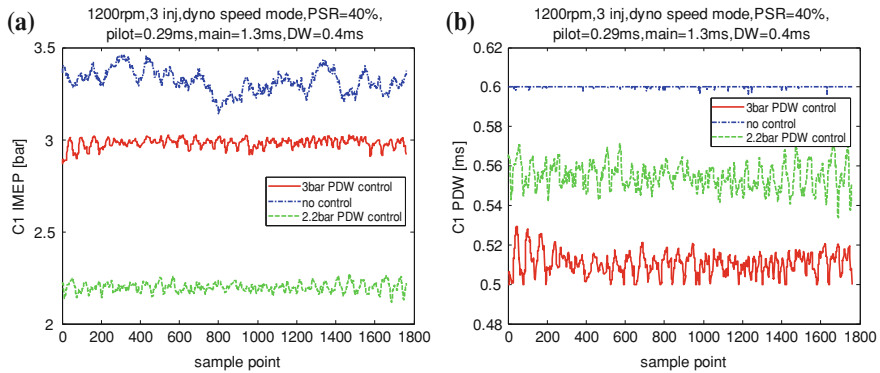


Fig. 15 Cylinder 1 IMEP COV comparison between with and without close loop control. **a** Cylinder 1 IMEP, with and without closed loop control; **b** PDW of with and without IMEP control

observed when fuel rail pressure was swept. See Fig. 14a, b. The IMEP closed loop control by PDW was shown in Fig. 15. It is obviously that the COV of IMEP was reduced by IMEP feedback control.

5 Conclusion

A low computational cost combustion model for combustion process control purpose was developed and validated. The application of this model in control system design was implemented and was experimentally proved to be success in

improving the engine performance both emission and fuel consumption. The IMEP feedback control either by main injection duration or by PDW is able to reduce combustion variations at steady state and has strong disturbance rejection performance to other fuel path inputs.

6 Future Work

The combustion model presented in this paper needs to be expanded to include air path and heat transfer dynamics. Model validation needs to cover VGT and EGR control input variation.

Acknowledgments The authors want to thank Edward Winward for all his support to the engine test and the preparation of this paper.

References

1. Oppenheim AK (2004) Combustion in piston engines. Springer, Berlin
2. Heywood JB (1988) Internal combustion engine fundamentals. McGraw_Hill, New York
3. Quérel C, Grondin O, Letellier C (2012) State of the art and analysis of control oriented NOx models. SAE paper 2012-01-0723
4. Alberer D, del Re L, Winkler S, Langthaler P (2005) Virtual sensor design of particulate and nitric oxide emission in a DI diesel engine. SAE paper 2005-24-063
5. Westlund A, Angstrom H, Lindstrom M (2010) Validation of a simplified model for combustion and emission formation in diesel engines based on correlations for spray penetration and dispersion. SAE paper 2010-01-1494
6. Oppenauer KS, Alberer D, de Re L (2010) Control oriented crank angle based analysis of soot dynamics during diesel combustion. SAE paper 2010-01-2015
7. Seykens XLJ, Baert RSG, Somers LMT, Willems FPT (2009) Experimental validation of extended NO and soot model for advanced HD diesel engine combustion. SAE paper 2009-01-0683
8. Catania A, Finssso R, Spessa ET, Catanese A, Landsmann G (2011) Combustion prediction by a low-throughput model in modern diesel engines. SAE paper 2011-01-1410
9. Schilling A, Amstutz A, Onder CH, Guzzella L (2006) A real-time model for the prediction of the NOx emission in DI diesel engines. In: Proceedings of the 2006 IEEE international conference on control applications, Munich, Germany, Oct 4–6 2006
10. Wilhelmsson C, Tuestal P, Johansson B, Widd A, Johansson R (2009) A physical two-zone NOx model intended for embedded implementation. SAE paper 2009-01-1509
11. Egnell R (2001) On zero-dimensional modelling of combustion and NOx formation in diesel engines. Doctoral thesis, Lund University
12. Winward E, Deng J, Stobart R (2010) Innovations in experimental techniques for the development of fuel path control in diesel engines. SAE paper 2010-01-1132

Influence of Biocellulose Derived Fuel Blends on Injection Properties

Sorin Sacareanu, Anghel Chiru, Alexandru Bogdan Muntean and Cornel Stan

Abstract Today, 88 % from the total amount of energy used worldwide is represented by fossil fuels (oil, natural gas and coal). Oil dependence required a diversification of fuels in the transport sector in general and road transport in order to stop global warming. Alternative fuels differ slightly in terms of such physical properties as: density, viscosity and bulk modulus, properties which influence the fuel injection parameters such as penetrability, Sauter Mean Diameter and vaporization rate. The European Union adopted Directive 2003/30/EC to enforce the use of biofuels and other alternative fuels. EU member states must achieve a target of 20 % of alternative fuels used in the transport sector. These lead to different combustion characteristics. The main objective of this paper is to determine the influence of alternative fuels produced by Fischer–Tropsch synthesis from the gasification of biomass used for compression ignited engines.

Keywords Biofuels · Diesel injection · Coupled 1D–3D simulations

1 Considerations Regarding the Tested Fuels

In order to evaluate the influence of biofuel characteristics on ICE performances, experimental research has been done in virtual and real environment. The tendency is to increase the concentration of synthetic fuels in the mixture leading to a 50 % after 2020.

F2012-A02-015

S. Sacareanu (✉) · A. Chiru · A. B. Muntean
Transilvania University of Brasov, Brasov, Romania
e-mail: sorin.sacareanu@unitbv.ro

C. Stan
University of Applied Science, Zwickau, Germany

In this study, mixtures of FT fuel and classic diesel have been used during numerical simulations. The concentrations were 20 % FT fuel and 80 % fossil diesel named FT20, and 50 % FT fuel and 50 % fossil diesel named FT50. These specific concentrations were chosen based on the European Commission Directive 2003/30/CE. Pure FT fuel combustion performances have been also studied.

ICE's energetic and ecologic parameters are in a direct dependence on fuels characteristics and on injection systems performances. Thus, it is necessary to optimize injection system's the parameters (penetrability, fuels spray atomization, pressure, injected volume) of the injection system considering the working regime and the fuel used. The optimization of the injection system requires experimental research as well as numerical simulations. In the last decade, the techniques of numerical simulations have evolved, presenting advantages such as possibilities of substantial time saving analysis, reduced number of materials, an increased number of parameters being studied, both design and functional, ease in designing a prototype stand. The properties of the fuels investigated in this work are presented in Table 1.

To be able to use the advantages of numerical simulations, the application must comply with certain criteria. Thus, it must perform the following functions:

- To be able to modeling the complex phenomena of the fuel injection;
- Consideration of most important parameters;
- Using a friendly interface;
- Optimum results for the desired parameters [4, 5].

In this study, LMS Image Lab AMESim application was used for the one-dimension simulation and AVL Fire for the 3D simulations. These applications meet the requirements previously mentioned.

2 Common-Rail Fueling System

At the moment, common-rail injection systems are the most common ones on the CI and SI engines market. The main characteristics of common-rail injection systems are: even fuel distribution on each cylinder, many injections per cycle due to injector electronic control, high injection pressure at low speed.

The virtual model of the common-rail injection system was done by "Forschung- und Transferenz Zentrum Zwickau (FTZ)" and was validated on the test-bed. The model was designed so it can be easily adapted to different requests coming from the analysis of the influence of fuels properties or from different working regimes. For the modeling part, the main components of the system were taken into consideration: the high pressure pump, the common-rail, the shape of the signal that controls the solenoid's valve, the injector, which is made of two parts (the solenoid with the discharge valve and the injection module with needle, needle spring and nozzle). The masses of the components and interaction with the fuel were also considered. The model illustrated in Fig. 1 represents a BOSCH CRI injection system with a

Table 1 Physical–chemical properties of tested fuels [3]

Property	Standard	Unit	EN590	B0	FT/B0 20/80	FT/B0 50/50	FT
Cetane number	EN ISO 5165		>51	52.1	62.7	65.8	76.7
Density at 15 °C	EN ISO 12185	kg/m ³	820–845	829	817	799	769.5
Viscosity at 40 °C	EN ISO 3104	mm ² /s	2.0–4.5	2.54	2.4	2.24	2.07
Inflammability point	EN ISO 2719	°C	>55	62	63	68	78
CFPP		°C		−12	−11	−10	−4
Lower calorific value	DIN 51900	MJ/kg		42.985	43.209	43.407	43.781
Elastic modulus		(bar)		15800	15200	14400	13000

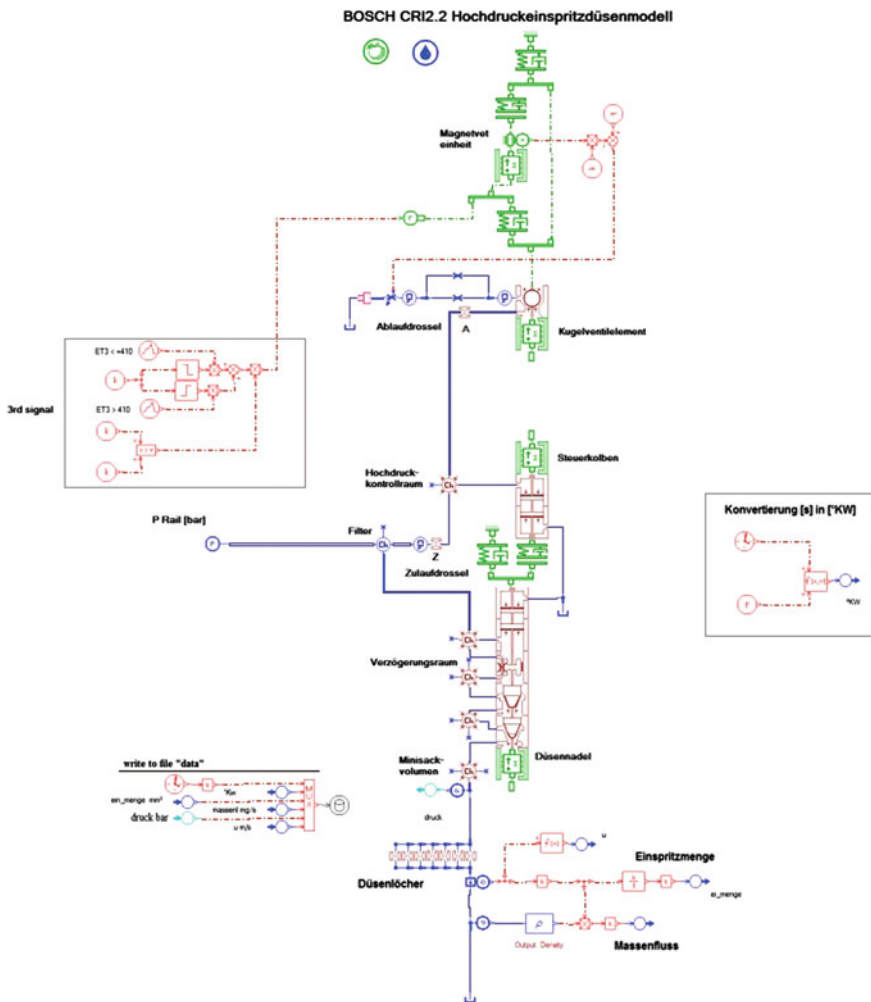


Fig. 1 AMESim model of the injection system [2]

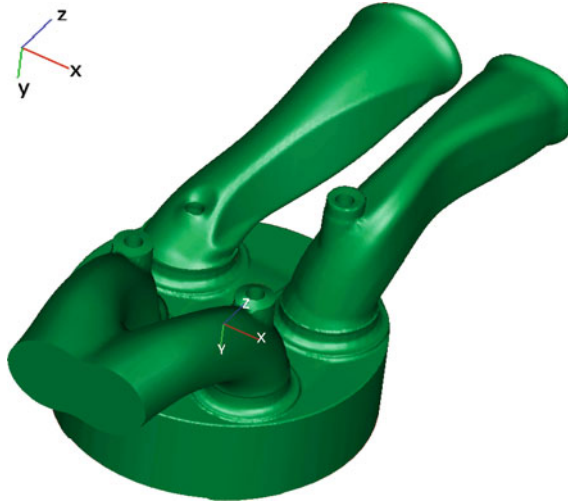


Fig. 2 CAD mode of the engine

Table 2 Characteristics of the simulated points

Engine speed (rpm)	2000	2000
M.E.P. (bar)	2	15
Rail Pressure (bar)	640	1150
Pilot injection	Da	Da

pressure of the common-rail ranging from 1000 to 1800 bar. The control of Injector's is done by a solenoid which determines the needle lift and the fuel injection through seven holes with a diameter of 200 μm . Besides the main injection, the system can provide two pilot injections.

The simulations have also considered the alternative fuels influences on the injection parameters such as the pressure in the injector's nozzle, injected fuel volume and mass flow, as well as the sprayed fuel speed. The simulations were done for two regimes as presented in Table 2 and the results were further used as input data for the 3D module.

The 3D model of the cylinder head channels (intake and exhaust) and combustion chamber, as illustrated in Fig. 2, were done in CATIA. Next, the parameters of the working fluids and the initial conditions were considered. The coefficients of fuel injection and combustion mathematical models request special attention.

3 Low Load Engine Simulation

The first regime investigated was at a speed of 2000 rpm and 2 bar MEP. In this case, the duration of the pilot injection was 0.41 ms (4.56 $^{\circ}\text{CAD}$, with 19.6 $^{\circ}\text{CAD}$

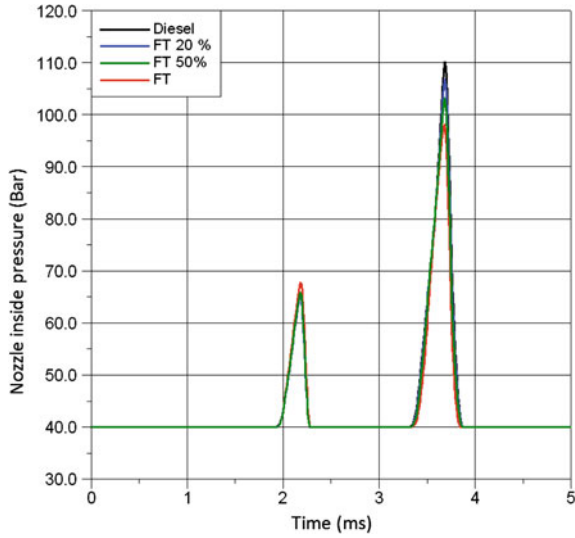


Fig. 3 Comparison of fuel pressure evolution

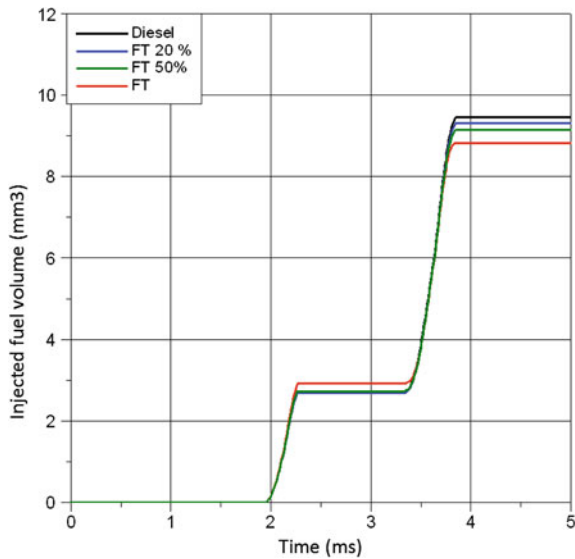


Fig. 4 Comparison of injected fuel volume

before TDC) and that of the main injection was 0.53 ms (6.72 °CAD, with 2 °CAD before TDC) [1].

The influence of fuel properties on pressure at the injector’s nozzle, the injected volume and mass flow, as well as on the fuel speed at the injector’s output is

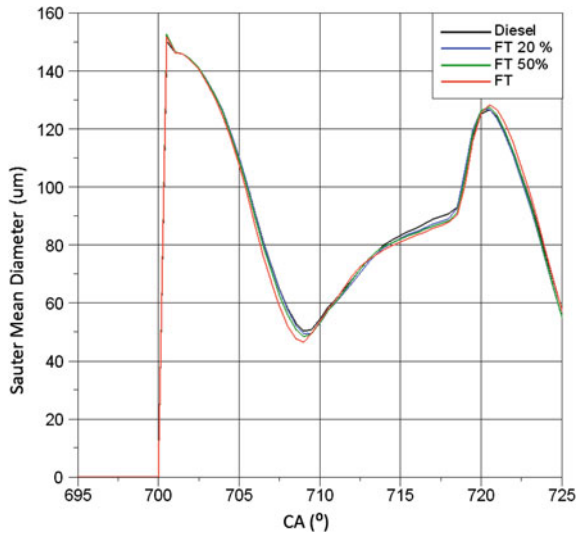


Fig. 5 Sauter Mean Diameter

presented in Figs. 3 and 4. It can be noticed that for the pilot injection, while increasing the FT fuel concentration in the mixture, the maximum pressure increased as well (with 4 % for pure FT fuel). At the same time, the main injection showed an opposite situation. The pressure in the injector's nozzle decreased with the increase of the FT fuel concentration up to the point where for pure FT the main injection pressure was with 11 % less than for reference diesel (98.3 bar for FT fuel compared to 110 bar for diesel fuel).

The evolution of the injected volume (Fig. 4) shows a perfect correlation with the pressure evolution discussed above. For pure FT fuel case the injected volume was 9 % higher than for diesel fuel due to a lower viscosity of the synthetic fuel. For the main injection case, the evolution of the injected volume showed that while increasing the FT concentration, the volume decreased due to a higher compressibility of the FT fuel (Table 1). For the FT fuel, the total volume injected was with 7 % lower compared with the diesel injected volume.

The evolution of Sauter Mean Diameter for the fuel drop was also analyzed in this study, as presented in Fig. 5. The analysis showed that the maximum values of the Sauter diameter were the same for all the fuels investigated. It can be noticed that the value of the average diameter of the drops at the end of the pilot injection for biofuels was lower than the value for the reference diesel used.

When analysing the impact of different fuel properties on spray tip penetration, we can see no major differences between them (Fig. 6).

By using fuel blends with high mass fraction of FT (20–50 %), the spray tip penetration will decrease with approximate 1 mm.

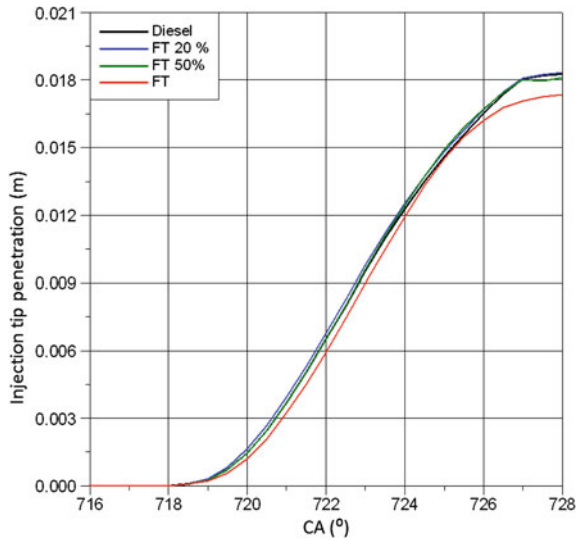


Fig. 6 Spray tip penetration for main injection

4 High Load Point Engine Simulation

Another topic which was studied is related to high load behavior of the injection system. The simulation point has the following characteristics: Mean Effective Pressure: 15 bar; Engine speed: 2000 rpm; Pilot Injection Time: 0.3 ms Pilot Injection Timing: 19.5° BTDC; Main Injection Time: 0.95 ms; Main Injection Timing: 10°.

The results of this simulation are presented in Fig. 7. By using synthetic fuels the peak in cylinder pressure will rise. Regarding the fuel injected volume, we can notice (Fig. 8) a slow increasing of this one. In previous cases, an increasing of FT mass fraction in fuel blend, leads to higher injected fuel volume.

On observing of pilot injection, the greatest differences were detected for 100 % FT, and the percentage volume was 4 % higher than pure diesel fuel.

The main injection case, also presents an increase of 6 % injected volume of pure FT in comparison with 100 % pure diesel.

Regarding SMD for pilot and main injection, presented in Fig. 9, we have found no significant differences. A very small decrease of SMD, was observed on the pilot injection. After the injector needle closes the nozzle holes, the SMD of the alternative fuels, presents a small decrease. This is due to the better atomization of the fuel.

If we exam the evolution of spray tip penetration, no major differences can be seen. However, the synthetic fuels have a slight increase of this parameter (Fig. 10).

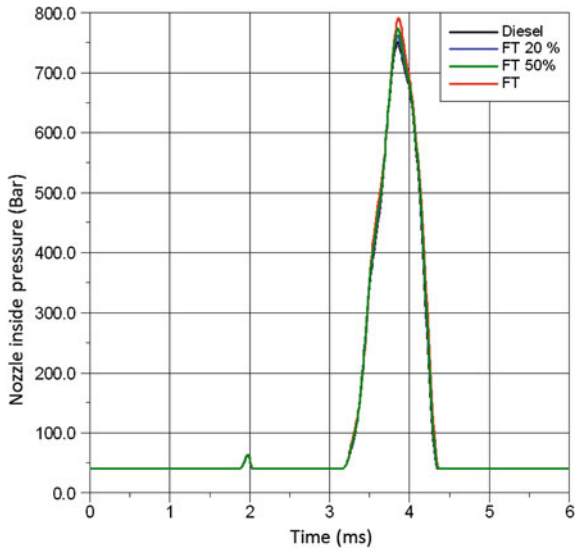


Fig. 7 Comparison of fuel pressure evolution

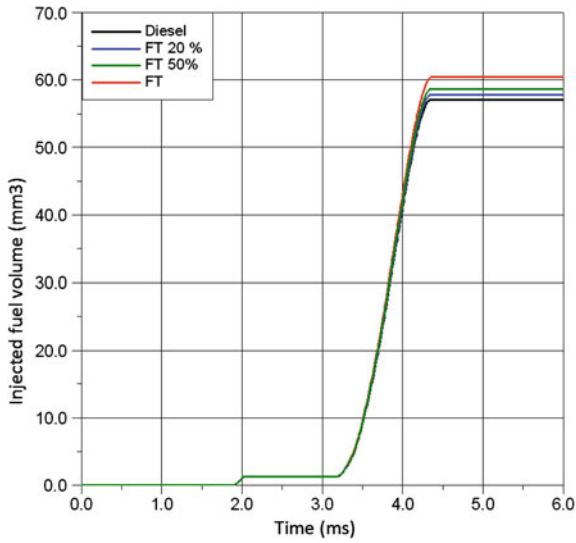


Fig. 8 Comparison of injected fuel volume

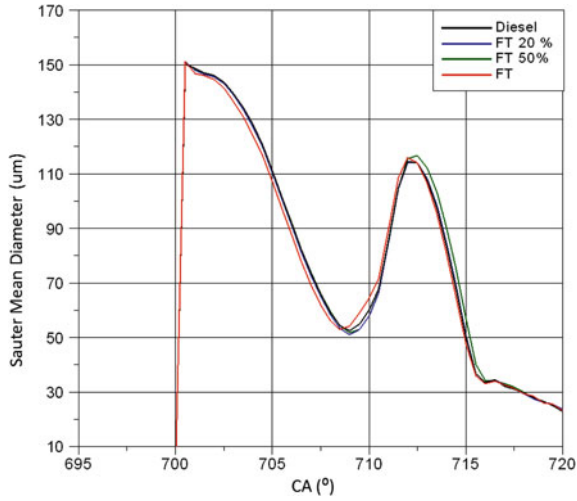


Fig. 9 Sauter Mean Diameter

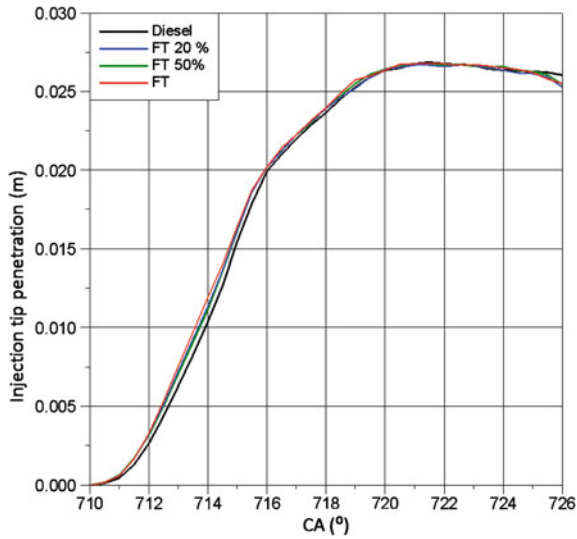


Fig. 10 Penetrability during main injection

5 Conclusions

The numerical analysis of sintetical fuels (FT) injection process regarding different sintetic fuels, leads to the following conclusions:

- The total volume of FT injected, was 7 % less than the reference fuel;
- In both cases: low engine loads, high engine loads, the injection process parameters (Injection pressures, SMD, Spray tip penetration) have not been influenced too much;
- The FT fuel blends, especially FT 20 and FT 50, are recommended in reciprocating engines without any disadvantages on fuel injection system.

The experience which was gained during the research stage in this study, correlated with engine development engineer's know-how, from Romania and Germany, allowed for the observation of the impact of mathematical coefficients on injection process performances. Those values can be used on new engine concepts.

This is the first time the sintetic fuel has been produced by FT technology. It has been tested and a simulation model of the injection process was built. All the information presented in this paper is very useful for engine development specialists.

Acknowledgments This paper is supported by the Sectoral Operational Programme Human Resources Development (SOP HRD), financed from the European Social Fund and by the Romania Government under the contract number POSDRU/88/1.5/S/59321 and POSDRU/6/1.5/S/6.

References

1. Săcăreanu S (2012) Cercetarea Influenței Regimurilor de Funcționare și a Caracteristicilor Carburanților Asupra Parametrilor Energetici și Ecologici ai Motoarelor cu Ardere Internă. Teză de Doctorat, Universitatea Transilvania, Brașov
2. Stan C (1999) Direkteinspritzsysteme für Otto- und Dieselmotoren. Springer, Berlin, ISBN 3-540-65287-6
3. Rauch R, Hofbauer H, Sacareanu S, Chiru A (2010) From gasification to synthetic fuels via Fischer-Tropsch Synthesis. Bulletin of Transilvania University of Brasov, vol 3(52). Series I—Engineering Sciences, ISSN 2065-2119, 2010
4. LMS AMESim user guide
5. AVL FIRE user guide

Research on the Effect of the Parameters of Common-Rail System on the Injection Rate

Guanjun Yu, Liguang Li, Jun Deng, Zhiqiang Zhang and Lin Yu

Abstract Based on the Bosch long tube method, an injection rate measurement system is set up. Then several parameters, such as drive voltage, injection timing and injection pressure, are changed independently to study their effects on injection rate. The result shows that: injection pressure and parameters of electrical control signal, such as drive voltage and injection pulse width, have significant effect on injection rate. There are suitable injection pressure and parameters which could optimize injection rate. An empirical formulas about the injection quantity and several parameters are established finally.

Keywords Injection rate · Bosch long tube method · Drive voltage · Injection pulse width · Injection pressure

1 Introduction

To meet more and more stringent emissions regulations [1], common-rail system, which was invented in 1990s, is applied on diesel engine as one of the key technologies owing to its great advantages on emission reduction and fuel economy. Common-rail system provides high injection pressure to injector, which can optimize the fuel atomization, accurate fuel–air mixing and form more homogeneous mixtures [2, 3]. Combining with electronic control technology, common-rail

F2012-A02-016

G. Yu (✉) · L. Li · J. Deng · Z. Zhang · L. Yu
Tongji University, Shanghai, China
e-mail: yuguanjun1986@126.com

system can provide accuracy control of the injection quantity, injection timing, injection rate [4], and multiple injection capabilities [5]. All of these help to improve combustion progress and reduce emission.

Mulemane et al. [6] employed a Bosch type injection-rate meter to measure needle lift, injection-rate/rate shape and injection pressure and concluded that the measured injection-rate is a strong function of injection pressure and hole diameter of the nozzle. Carlucci et al. [7] studied the injection rate of injectors equipped with standard and geometrically modified control valves based on Bosch method and observed a certain difference in the slope of the first part of the injection rate and suggested several geometrical modifications for the injectors. Qiao et al. [8] employed Bosch long tube method to study injection rate of a diesel engine and observed that pressure wave signal collected continues for a certain time after injector turns off, which seriously affects measuring accuracy. Li et al. [9] compared the injection rate obtained by Bosch method and rotating Cells method. The results suggested that Bosch method is reliable and convenient. They explained that this method has the highest accuracy when four reflected waves observed in the pressure wave signal collected. Tian et al. [10] studied injection pulse width and rail pressure on injection quantity, concluded that injection pulse width mainly influences injection rate and rail pressure mainly influence the length of the injection duration. Lu [11] also studied the effect of rail pressure and injection pulse width on injection rate, observed that injector responds more quickly at higher rail pressure and injector is not able to open regularly when the injection pulse width is shorter than a certain value.

This study investigates the effect of several controllable parameters, such as injection control signal, drive voltage, injection timing and injection pressure of common-rail system on the injection rate. Each of the controllable parameters is varied independently to study its influence on injection rate.

2 Experimental Setup

The injection rate measurement system based on Bosch long tube method [12, 13] is depicted in Fig. 1. This system consists of common-rail subsystem, injector control subsystem and signal acquisition subsystem. The common-rail subsystem mainly contains electric motor, high-pressure fuel pump, high-pressure fuel pipe, common-rail, pressure regulating valve and host computer. The injector control subsystem mainly contains embedded controller, booster circuit and injector. The signal acquisition subsystem mainly contains back-pressure valve, throttle valve, fuel pipe, piezoelectric pressure transducer, charge amplifier, data acquisition card and host computer. The parameters of injector are shown in Table 1.

Operating principle of this system is as follows. The common-rail subsystem provides high pressure fuels to the injector and the pressure in common rail is adjustable through pressure regulating valve and host computer. In injector control subsystem, embedded controller and booster circuit provide controllable signal to

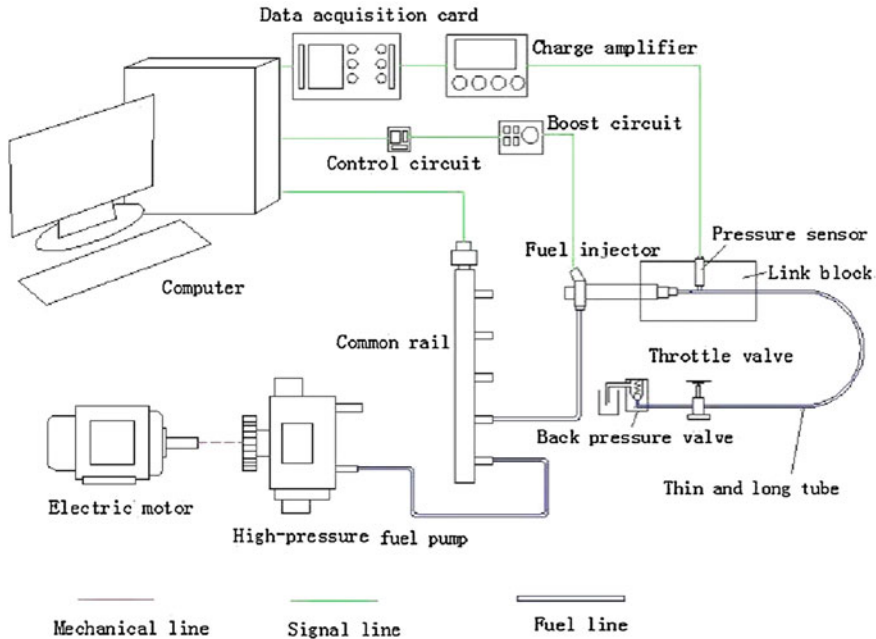


Fig. 1 Experimental setup of injection rate measurement system

Table 1 Parameters of injector

Number of nozzle	8
Nozzle hole cone angle (°)	150°
Diameter (mm)	0.12
Flow characteristic (ml/min at MPa)	750 at 10
Draw ratio	1:8
Resistance of solenoid valve (ohm)	0.9
Inductance of solenoid valve (μH)	294

injector which could achieve variable injection rate [14]. In signal collection subsystem, fuels are injected into a small chamber and the pressure in the chamber will change when injection happens. The pressure signal in the chamber is acquired. Then injection rate is calculated by integrating the pressure signal.

In the embedded controller, the PWM wave is chosen as the control signal [15, 16]. To open the injector as quickly as possible, a wider pulse (named as initial incentive time, IIT) is necessary at the beginning to produce heavy drive current (greater than 20 A). The wave shape of control signal and drive current is shown in Fig. 2. Because of mechanical and electronic control delay, the injector takes certain time to turn on or off after the drive current is produced or closed. The relationship of drive current and injector action is shown in Fig. 3.

Fig. 2 Shape of control signal and drive current

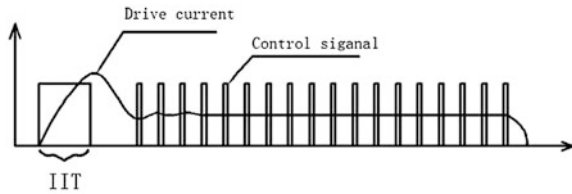


Fig. 3 Drive current and injector action

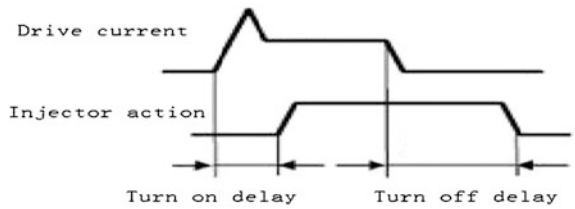
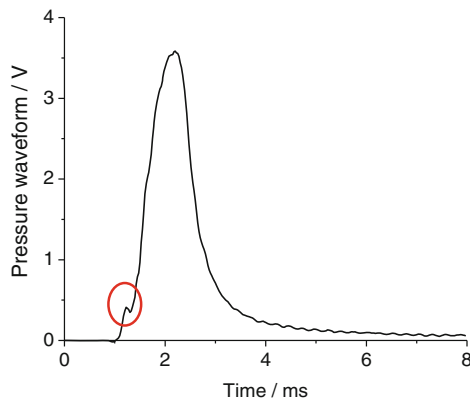


Fig. 4 Signal waveform with IIT less than 60 μ s



3 Results and Discussions

3.1 Effect of IIT on Injection Rate

Figures 4 and 5 separately show the signal waveform with IIT less and more than 60 μ s (The other conditions are that common rail pressure is 80 MPa, drive voltage is 90 V and the whole pulse of control signal is 500 μ s). A small wave crest is observed at the beginning in Fig. 4. It means the injector does not open regularly. The reason is that: when drive voltage is applied on the injector, drive current is produced in the solenoid valve in the injector and electromagnetic force is produced to pull the needle valve of the injector. As shown in Fig. 2, drive current increases linearly with the time-length of drive voltage. So if the IIT is too less, the drive current is lower than 20 A and the electromagnetic force is too small to open injector regularly. In order to open injector regularly, the IIT should be more than 60 μ s.

Fig. 5 Signal waveform with IIT more than 60 μ s

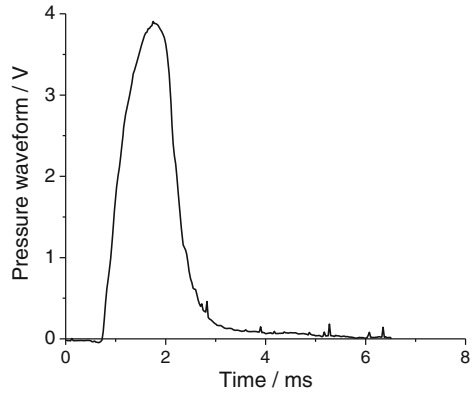
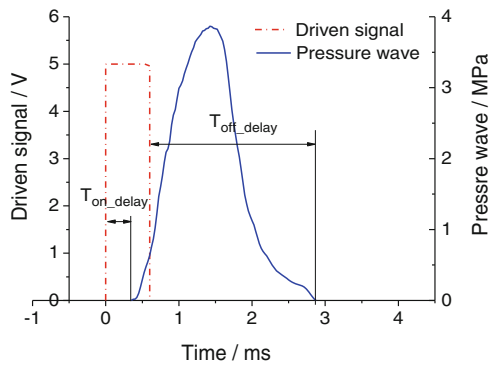


Fig. 6 Turn-on delay and turn-off delay



3.2 Effect of Drive Voltage on Injector Turn on Delay and Turn off Delay

Because of the signal propagation delay and the injector response delay, a delay time is observed between the control signal (PWM wave) and collected signal (pressure signal) in Fig. 6. The turn-on delay and turn-off delay is named as T_{on_delay} and T_{off_delay} for short.

The measuring results of T_{on_delay} and T_{off_delay} are shown in Fig. 7, in which the drive voltage is 70, 90 and 110 V. With the drive voltage increasing, the T_{on_delay} decreases and T_{off_delay} increases. The reason is as follows. Higher drive voltage produces heavier drive current, and heavier current takes less time to increase to threshold value (20 A) to open the injector. Meanwhile, the control circuit of the solenoid valve in the injector takes more time to release heavier current after the control signal is closed, which means the injector closes later. So the T_{off_delay} increases.

Fig. 7 Delay time under different drive voltage

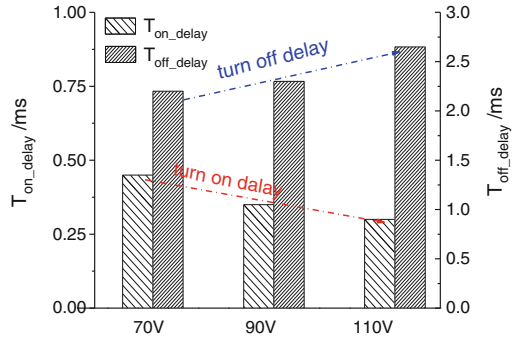
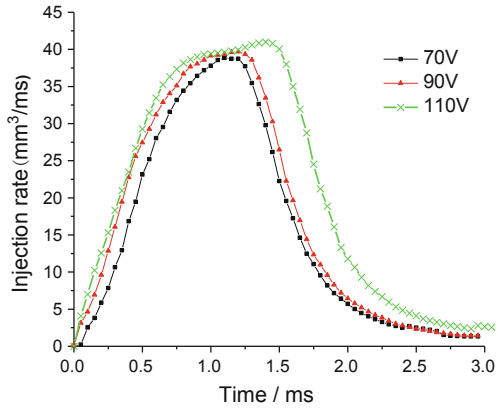


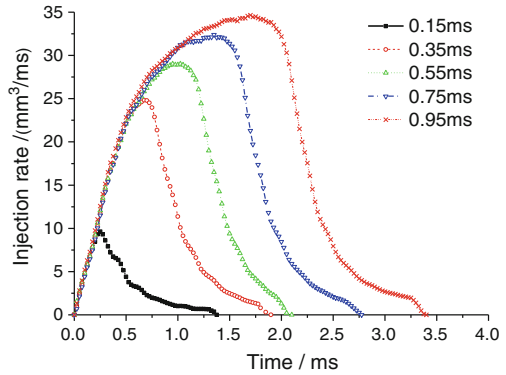
Fig. 8 Injection rate under different drive voltage



3.3 Effect of Drive Voltage on Injection Rate

Keeping rail pressure and injection pulse width constant, the effect of drive voltage on the injection rates is shown in Fig. 8. As shown in Fig. 8, the injection rate curve rises more rapidly and stays for longer time at the peak as the drive voltage increases, which means the injection quantity is larger. As shown in Sect. 3.2, higher drive voltage produces heavier drive current, and this leads to T_{on_delay} decreases and T_{off_delay} increases, which means the injector opens earlier and closes later. So injection rate curve rises more rapidly and falls more slowly under higher voltage. Meanwhile, little difference is observed at the peak of the injection rate curves in Fig. 8, because the peak value of injection rate is mainly determined by the structure parameters of the injector and the injection pressure when the injector is full open.

Fig. 9 Injection rate under different injection pulse width



3.4 Effect of Injection Pulse Width on Injection Rate

Figure 9 shows the effect of injection pulse width on injection rate. And the rail pressure is fixed as 100 MPa. The injection rate increases significantly with injection pulse width increasing. And the injection rate curve of narrow pulse width is irregular, such as 0.15 and 0.35 ms. The reason is that due to the structure limitation and injection characteristics, the injector is not able to open regularly when the injection width is too narrow. In other words, the structure and injection characteristics of the injector are primary for getting favorable injection rate. In Fig. 9, little difference is observed before the injection curves reach their peaks and the peak of the injection rate curve gets greater with the injection pulse width increasing. The reason is that the injector is partly open in these situations, and longer injection pulse width means that the needle valve of injector opens further.

3.5 Effect of Injection Pressure on Injection Rate

Figure 10 shows the effect of injection pressure on injection rate. And the same injection pulse width is fixed as 0.55 ms. With the injection pressure rising, fuels get greater kinetic energy and more fuel is injected from the injector, so the injection rate rises more rapidly. In Fig. 10, the peak of injection rate curve gets greater with the injection pressure rising. Because the injector control signal is the same, which means that the needle valve lift is the same at the peak, greater injection pressure makes that more fuel is injected and the peak is greater. In conclusion, injection quantity is greater with the injection pressure rising.

Fig. 10 Injection rate under different rail pressure

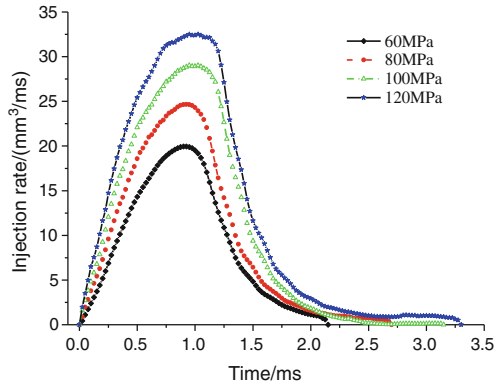


Fig. 11 Weighed and calculated injection quantity under different injection pressure and injection pulse width

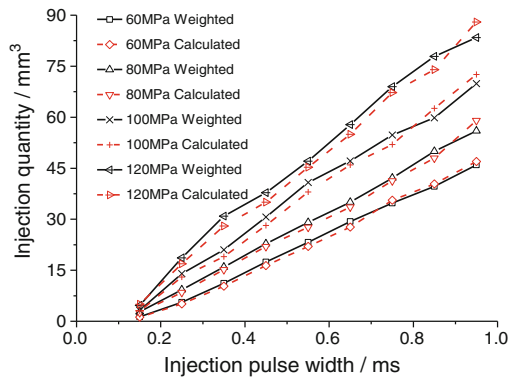


Table 2 Empirical formulas on injection quantity

Injection pressure (MPa)	Empirical formulas
60	$Q = 1.5904 * t^2 + 54.896 * t - 7.6267$
80	$Q = -7.735 * t^2 + 78.093 * t - 9.633$
100	$Q = -18.454 * t^2 + 101.26 * t - 10.498$
120	$Q = -14.5 * t^2 + 114.67 * t - 10.014$

Q = Injection quantity (mm³); t = Injection pulse width (ms)

3.6 Empirical Formulas on Injection Quantity

The comparison of weighed and calculated injection quantities is depicted in Fig. 11. The injection pulse width and rail pressure are varied from 0.15 to 0.95 ms, and 60 ~ 120 MPa, respectively. These are just a few of difference between the weighed and calculated injection quantities. So the test system and test results are credible.

In order to understand the relationship between the injection quantity and injection pressure and injection pulse width, empirical formals are established, which are listed in Table 2. These formals could be conducive to forecasting and controlling the injection quantity under the other injection pressure and injection pulse width.

4 Conclusions

This injection rate measurement system is able to acquire the injection rate under different operating condition. The effect of the parameters of common-rail system on the injection rate is studied in detail, which include injection control signal, drive voltage, injection timing and injection pressure. The conclusions are shown as below.

- (1) In order to effectively open the injector, the IIT of the drive signal must be longer than a certain value.
- (2) With the drive voltage rising, the turn-on delay of the injector reduces and the turn off delay increases, while injection rate and injection quantity increase slightly.
- (3) The injection pulse width should be longer than a certain value to ensure the injector working properly. With the injection pulse width rising, injection rate remains the same until the peak while the injection quantity increases significantly.
- (4) With the injection pressure rising, both the injection rate and injection quantity increase significantly.

Acknowledgments Partial support for the work from Geely Automotive Research Institute and the '111 plan' is gratefully acknowledged.

References

1. Wang W (2003) Three auto emission rule systems. *Des Manuf Diesel Engine* 4:4–8
2. Wen H, Lu J, Zou J (2010) Simulation analysis to injection rate of high-pressure common-rail injection system. *Small Intern Combust Engine Motorcycle* 39(6):4–7
3. Bianchi GM, Pelloni P, Filicori F (2000) Optimization of the solenoid valve behavior in common-rail injection systems. SAE paper, 2000-01-2042
4. Chen T, Guo L, Zhang X (2010) Research on DC-DC converter circuits for driving high speed solenoid valve in common rail injection system. *Small Intern Combust Engine Motorcycle* 39(3):71–74
5. Moone JD (2003) Drive circuit modeling and analysis of electronically-controlled fuel injectors for diesel engines. SAE paper, 2003-01-3361
6. Mulemane A, Han J-S, Lu P-H, Yoon S-J, Lai M-C (2004) Modeling dynamic behavior of diesel fuel injection systems. SAE paper, 2004-01-0536

7. Carlucci P, Giuffrida A, Ficarella A, Lanzafame R (2003) Investigation on realizing fuel rate shaping using a common rail injector. In: Proceedings of the 2003 spring technical conference of the ASME internal combustion engine division, vol 40, May 2003
8. Qiao X, Song Y (1995) Study on injection rate of diesel engine based on Bosch method. *Shandong Mach* 3:29–32
9. Li S, Li F (1981) Study on the measuring equipment for Bosch injection rate. *Chin Intern Combust Engine Eng* 2:9–15
10. Tian L, Song J, Qiao X, Zhen H; Li X (2004) Experimental study on injection process of electronically controlled common-rail diesel injection system. 26(5): 521–533
11. Lu J (2009) Simulating and experimental study of electronically controlled high-pressure common rail fuel injection system of diesel engine. Nanchang Univ, Nanchang
12. Li S, Li F (1981) Study on the measuring equipment for Bosch injection rate. *Chinese Intern Combust Engine Eng* 3:9–15
13. Li S (1981) Analysis of accuracy of wave form in Bosch injection rate. *Meas* 1:26–36
14. Pressman AI (1998) *Switching power supply design*, 2nd edn. McGraw-Hill, New York
15. Tian L, Song J, Qiao X (2004) Experimental study on injection process of electronically controlled common-rail diesel injection system. *Automot Eng* 26(5):521–533
16. Liu X, Wang Y, Chen Y (2011) Effects of solenoid valve drive current on fuel injection characteristics. *Trans Beijing Inst Technol* 31(5):514–518

The Influence of Diesel Nozzle Structure on Internal Flow Characteristics

Weidi Huang, Zhijun Wu, Ya Gao, Huifeng Gong, Zongjie Hu,
Liguang Li and Furu Zhuang

Abstract Based on X-ray CT scan technology in Shanghai Synchrotron Radiation Facility (SSRF), the inner structure of a side jet single-hole nozzle was obtained and its parameters around the inlet circle were measured. Further researches were carried out with the flow rate test bench about the influences of structure parameters symmetry on the internal flow characteristics and cavitation. Results showed that: the size deviation of inlet diameter, outlet diameter and nozzle length around the inlet circle are relatively small, while the inlet rounding radius is obviously distributed unevenly. Because of that, the cavitation had already showed up when the injection pressure was 40 MPa and the critical cavitation number equalled to 1.032, which should not take place according to the traditional theory. Thus, when relative studies are carried out, it is important for researches to take fully consideration of the size deviation of nozzle structure parameters, especially for the inlet rounding radius, to achieve more reliable conclusions.

Keywords X-ray CT scan · Structure parameters symmetry · Inlet rounding radius · Flow rate test · Cavitation

A2012-A02-017

W. Huang · Z. Wu (✉) · Y. Gao · H. Gong · Z. Hu · L. Li
School of Automotive Studies, Tongji University, Shanghai 200092, China
e-mail: zjwu@tongji.edu.cn

F. Zhuang
Wuxi Fuel Injection Equipment Research Institute, Wuxi 214063, China

1 Introduction

The injector nozzle is one of the most important parts in diesel engine. Nozzle geometry affects spray characteristics and therefore atomisation behaviour, which is decisive for engine performance and pollutant formation. A thorough understanding of the flow characteristics inside the nozzle is fundamental for predicting spray development. Cavitation, which had been proved strongly affect the flow characteristics of the nozzle exit and probably favours atomisation of the spray [1–3], is a very important phenomenon among nozzle inside flow characteristics. The main influence factors of cavitation can be divided into two groups, one is injection boundary conditions, such as injection pressure, back pressure, fuel properties; the other is nozzle inner structures, such as nozzle diameters, nozzle length, nozzle inlet rounding radius. However, during the previous researches about the effect of nozzle geometries on the nozzle internal flow and cavitation, the nozzle inner structure parameters normally were measured from a certain cross-section, which was normally selected randomly. If these results of measurements were adopted for further data analysis or simulation, it would probably cause mistakes. So the researches on the influences of nozzle parameter symmetry around the orifice circle are of great importance.

The methods to measure nozzle geometry can be mainly classified into three types: probe method, profile method, silicone molding model method [4–6]. Nevertheless, these methods normally have the problems of low accuracy, inconvenience or destructiveness. Moreover, some main parameters, like rounding radius at the inlet orifice, which proved to be one of the most important geometry parameters, are very hard to be measured through the above methods and therefore have been rarely researched yet. In recent years, X-ray CT scan technology is applied to measurements of the nozzle tip structure [7, 8]. Owing to the feature of high penetrating ability, the nozzle tip is scanned by high energy X-ray and three-dimension inner structure of nozzle tip can be obtained. And then all the nozzle structure parameters can be measured easily.

In this study, high energy X-ray Computerized Tomography (CT) scan was provided by Shanghai Synchrotron Radiation Facility (SSRF). Main parameters of the inner structure of a side jet single-hole nozzle including orifice inlet diameter, outlet diameter and inlet rounding radius were measured along the 360° orifice circumferential directions. Moreover, the injection rates of different nozzles were measured with a flow rate test bench to further understand the influence of nozzles inner structure symmetry around the orifice circle on the flow discharge coefficient and critical cavitation number.

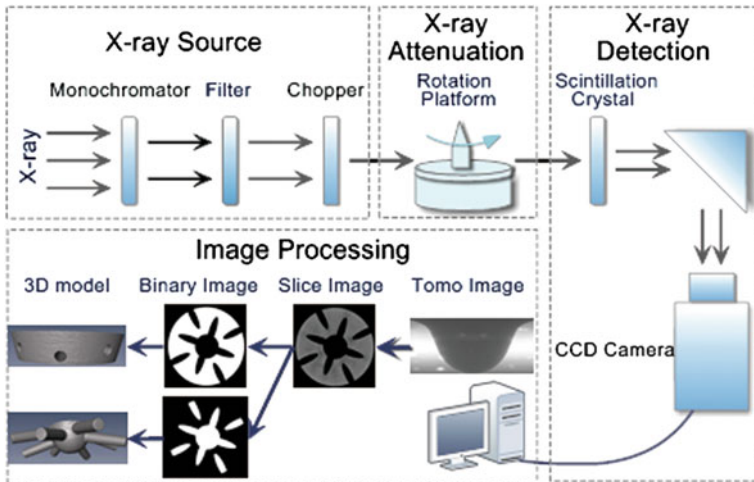


Fig. 1 Procedure of nozzle inner structure CT scan [10]

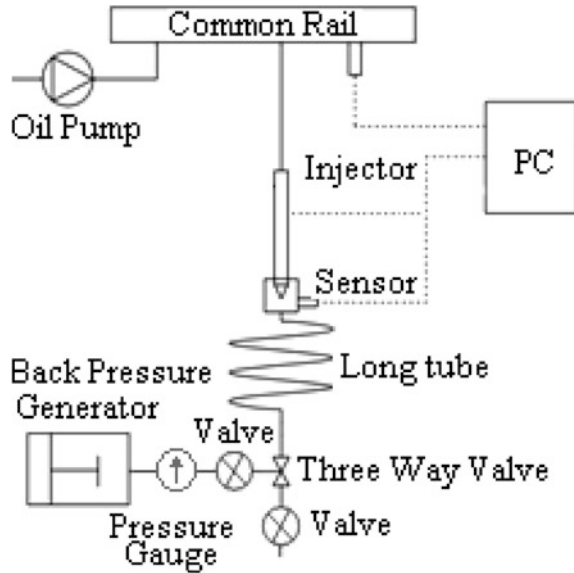
2 Experimental Setups and Conditions

2.1 High Energy X-ray Nozzle Geometries CT Scan

Comparing to the normal light source, high energy X-ray has excellent performance: high intensity and high stability. In this article, the internal structures of diesel nozzle tips were revealed on the X-ray Imaging and Biomedical Applications Beam Line (BL13W1) of the SSRF. The experiment setup is sketched in Fig. 1. By digital imaging processing the original slices were converted to binary slices and corresponding reversed slices to enhance the signal to noise ratio [8, 9].

The diesel nozzle is held on the specimen rotating platform. The synchrotron X-ray penetrates its tip and irradiates the scintillator to form absorption images in a charge-coupled device (CCD) camera. The pixel size of the CCD chip is $3.7 \times 3.7 \mu\text{m}$ and the chip is couple to the scintillator by an optical fiber. The X-ray photon energy of this beam line was tuned to 55 keV and the exposure time was set to 8 s. During the computed tomography (CT) scanning process, the specimen rotates 180° to obtain sufficient absorption images to generate slices. In accordance with the nozzle tip size and spatial resolution, a total of 540 absorption images were captured, and the slices were then reconstructed. The digital models created by reversed slices are used conventionally to reveal the detailed internal surfaces and structures of the orifices and to measure their geometrical dimensions directly, such as the orifice diameter and rounding radius at inlet orifice.

Fig. 2 Mass flow rate test bench



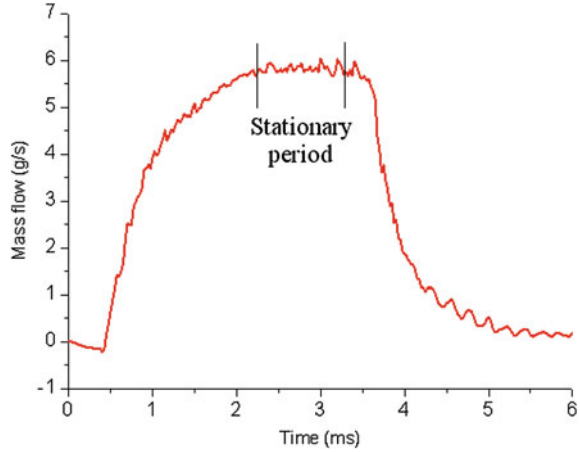
2.2 Flow Rate Test Bench

The flow characteristics test bench was set up to test the flow rate basing on the Bosch long tube method [11], which based on the one dimension pressure wave theory and calculate the injection rate and amount through the pressure changes in the long tube (see Fig. 2). The injection pressure was controlled by standard common rail system and can be fixed at different values (pressure deviation ± 0.1 MPa). The injector was mounted in a steel vessel filled with fuel, where the back pressure was controlled by a back pressure generator. The back pressure generator was a piston device, which use high pressure nitrogen as pressure source pushing piston to maintain a 0.1–8 MPa fuel back pressure output. The back pressure was measured with a pressure gauge (measurement accuracy ± 0.1 MPa) and the pressure wave inside the vessel was tested by a piezo pressure sensor (KISTLER 6123B).

2.3 Experiment Conditions

In order to extensively change the flow conditions in the injector orifice, tests are conducted at different injection pressure (P_i) of 30, 40, 50 and 60 MPa while back pressure (P_b) is varied every 0.5 MPa from 0.1 to 5 MPa. For the analysis required in this study, only the stationary value of the mass flow rate is measured (corresponding to the full needle lift conditions). For this reason, long injection pulse (3 ms) is employed in experiments in order to avoid the influence of the opening

Fig. 3 Mass flow rate for $P_i = 60$ MPa, $P_b = 5$ MPa



and closing of the needle, and mean value during the stationary period is obtained (see Fig. 3). Once the mass flow rate has been measured for each condition, the discharge coefficient can be obtained by combining the Bernoulli equation and the mass conservation equation:

$$C_d = \frac{\dot{m}}{A_o \sqrt{2\rho(P_i - P_b)}} \tag{1}$$

where \dot{m} is the mass flow rate, P_i is injection pressure and P_b the back pressure, ρ represents the liquid density, and A_o the geometric cross section of the orifice.

Because of the difficulties of taking direct information about flow characteristics inside a real nozzle, some indirect measurements to characterize cavitation were brought out. In this study, the cavitation number, which proposed by Nurick based on mass flow measurements [12], is adopted to characterize the cavitation. Nurick observed that mass flow obtained in stationary conditions increases as a linear function of the root of pressure drop until a point where it stabilizes due to the cavitation phenomena. At this point, “choked flow” occurs and cavitation number at this condition is called critical cavitation number.

$$\text{Cavitation Number } K = \frac{P_i - P_v}{P_i - P_b} \tag{2}$$

where P_v is the vapour pressure (5.0×10^{-3} MPa in this study). As it was previously explained, cavitation phenomenon in the orifice induces mass flow choking although injection-discharge pressure differential increases. For this reason, a decrease in C_d is expected when the flow reaches to this situation. For Cavitation conditions, C_d is described by the following expression:

$$C_d = C_c K^{1/2} \tag{3}$$

where C_c is the area contraction coefficient, which is related to nozzle geometry.

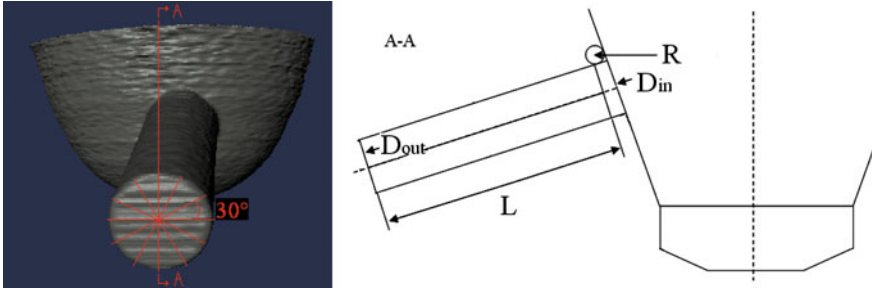


Fig. 4 Nozzle characteristic parameters of direct measuring

3 Experiment Results and Analysis

3.1 Nozzle Geometry Parameters Definition

In order to study the influence of nozzle internal structure symmetry on nozzle internal flow, four major parameters of nozzle are selected including orifice outlet diameter (D_{out}), inlet diameter (D_{in}), length (L) and inlet rounding radius (R), which the nozzle manufacturers are mainly concerned with in production. Definitions of parameter in measurement are presented in Fig. 4. It must be clarified that, in order to better reveal the influence of grinding techniques on orifice structure, the orifice inlet diameter is defined as the distance between the two midpoints of corresponding inlet rounding arcs, and the orifice length is defined as the distance between two midpoints of inlet and outlet diameter. In previous studies, the measuring methods are so limited that all the nozzle parameters are derived only from a certain cross-section, but in reality, there will be some fluctuation in the circumferential direction along the orifice. In this study, however, with the help of high precision 3D nozzle models created by X-ray tomography method, the parameters can be obtained from any circumferential direction along the orifice. As shown in Fig. 4, 12 measuring points are evenly distributed along the orifice circumference, and the interval is 30° . In that case, the nozzle orifice inlet diameter, outlet diameter, length and inlet rounding radius are acquired.

3.2 Results of Nozzle Geometry Structure Parameters Measurements

Measurements are taken according to the parameter definitions in 2.1, and the results are listed in Table 1. The measuring results state that, orifice inlet diameters, outlet diameters and lengths derived from each section are almost the same. Fluctuation is very small which represents good uniformity. Nevertheless, the inlet rounding radius presents large variations along circumferential direction. To scale

Table 1 Results of nozzle parameters measurements around the orifice inlet circle

Measure points	D _{in}	D _{out}	L	R	Measure points	D _{in}	D _{out}	L	R
0°	162.2	180.2	644.9	27.7	30°	158.0	179.3	639.0	32.7
60°	164.1	182.9	650.3	39.6	90°	156.8	171.3	649.4	31.5
120°	159.9	171.9	631.9	23.1	150°	159.8	185.5	644.8	18.6
180°	162.2	180.2	644.8	16.2	210°	158.0	179.3	639.0	24.3
240°	164.1	182.9	650.3	26.0	270°	156.8	171.3	649.4	31.4
300°	159.9	171.9	631.9	36.0	330°	159.8	185.5	644.8	23.7

the uniformity of parameters along the orifice circumference, mean deviation V_{AD} is adopted to reflect the disperse degree, that small value indicates better uniformity and vice versa. Computing formula is as follow:

$$V_{AD} = \frac{\frac{1}{n} \sum_{i=1}^n |X_i - \bar{X}|}{\bar{X}} \quad (4)$$

where X_i represents measured value, \bar{X} represents mean value.

According to Fig. 5, compared to the other parameters, the fluctuation level of inlet rounding radii along orifice circle is 10 times higher. The R data in Table 1 shows that this variation can reach to 200 % (from 16.2 to 39.6). In the measurement of nozzle, if there is only one radius taken from a particular section other than overall radii taken from various circle sections, large measurement error might exist, and therefore challenging the reliability of further experiment and analysis.

3.3 Results of Flow Rate Tests

In order to demonstrate the effect of the parameter deviation at the inlet circle on the flow characteristics and cavitations, the flow rate test bench is employed for the further studies and the cavitation number theory is adopted to analyze the cavitation phenomenon. This theory was proposed by Nurick [11] and had been widely used in the studies of cavitation.

About the relationship between the inlet rounding radius and nozzle internal flow, a very important empirical equation was brought up by Nurick [12] based on large amount of experiments:

$$R/D_{in} \geq 0.14 \quad (5)$$

No matter in what kind of flow conditions, cavitation would not happen inside the nozzle if relationship of R and D_{in} meets this equation. However, in his experiments, only the top jet single-hole nozzle was tested, that structure parameters distributed much more equally around the inlet circle. While in this study, the

Fig. 5 Compare of mean deviation of different nozzle structure parameters

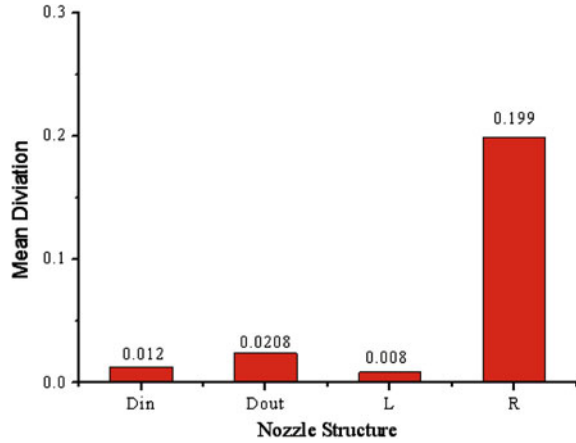
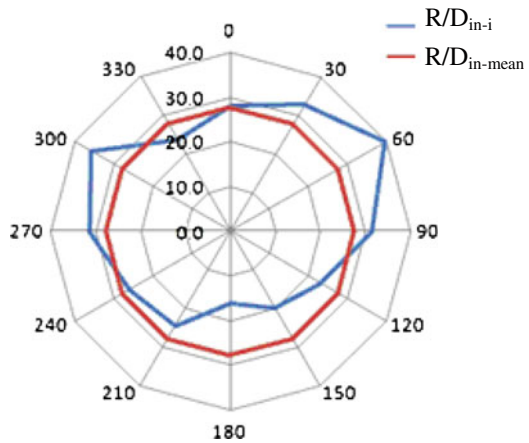


Fig. 6 Nozzle R/D distribution around orifice circle characteristics



structure parameters of the side jet nozzle, which widely used in practical engineering applications, is inevitably uneven along circumferential direction. As seen in Fig. 6, the mean R/D_{in} of the tested nozzle in this study equals to 0.155 and the mean deviation is up to 0.212. If the mean value of R/D_{in} is taken as the characteristic parameter, it would probably be concluded that no cavitation could be take place during the internal flow in this nozzle according to Nurick’s theory. However, as seen in Fig. 7, through the mass flow rate tests, it can be found out that the mass flow rate had already “choked up” and stabilized when the injection pressure is up to 40 MPa, which means that the cavitation inside the nozzle already appears. With the injection pressure increases, the cavitation tends to show up more easily, and when under injection pressure of 60 MPa, cavitation appears at almost every tested back pressure. The main reason for the difference between

Fig. 7 Mass flow rate to the root of pressure differential

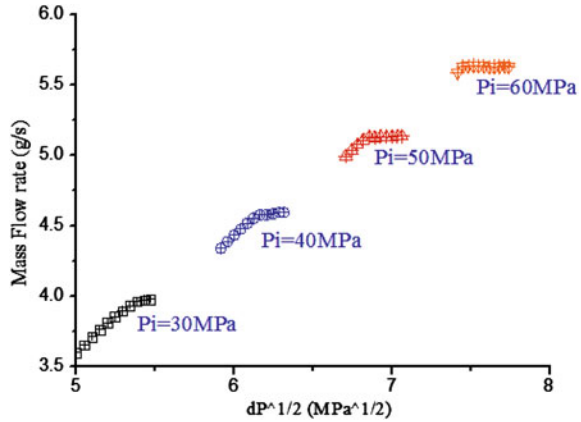
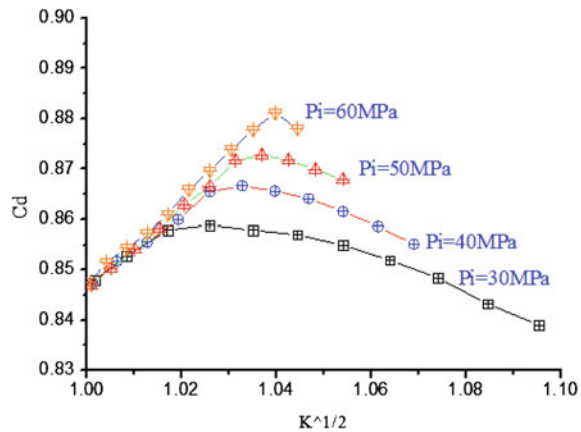


Fig. 8 Discharge coefficient to the root of cavitation number



experiments results and the theory is that R/D_{in} at some points around the inlet circle is quite low due to the uneven distribution, which would easily result to cavitation happening. So even if the mean value of R/D_{in} is larger than the critical number (0.14) predicted by the theory, the cavitation still appears inside the nozzle.

Furthermore, Eq. 3 was employed to find out the critical cavitation number, as seen in the Fig. 8. The root of critical cavitation number under injection pressure 40 MPa is 1.032, and then it increase linearly with injection pressure that, when injection pressure is 60 MPa, it goes up to 1.039. All above analysis demonstrates that the size deviation of structure parameters at inlet circle is of great importance to the relative studies of nozzle structure, or it may lead to big mistake if ignored.

4 Conclusion

In this study, the inner structure of a single-hole nozzle was obtained and structure parameters around the inlet orifice circle were measured. Then the influence of inner structure symmetry around the inlet orifice circle on the flow discharge coefficient and critical cavitation number was researched with the flow rate test bench. The results show that:

- (1) The size deviation of inlet diameter, outlet diameter and orifice length around the inlet circle of the tested nozzle are relatively small, and the mean deviation are lower than 0.02, while the mean deviation of the inlet rounding radius is ten times larger.
- (2) The mean value of R/D_{in} of the tested nozzle is 0.155. According to Nurick's theory, cavitation should not exist in the internal flow at any condition. However, in flow rate tests, cavitation has already showed up when injection pressure is up to 40 MPa, and becomes more intense when injection pressure increases. This is mainly due to the uneven distribution of inlet rounding radii (R) along orifice circle.
- (3) Taking fully consideration of the size deviation of nozzle structure parameters especially the inlet rounding radius in relative studies is of great importance to achieve reliable analysis and conclusion.

Acknowledgments This article is supported by the National Nature Foundation (51076118, 51006075), NCET-10-0605, the Fundamental Research Funds for the Central Universities (1700219089), and Shanghai Rising-Star Program (11QH1402500). Sincerely thanks for the great contributions of Xiao Tiqiao, Xie Honglan from SSRF and Wang Xiangben from Wuxi Fuel Injection Equipment Research Institute to this paper.

References

1. Payri F, Bermudez V, Payri R et al (2004) The influence of cavitation on the internal flow and the spray characteristics in the diesel injection nozzle. *Fuel* 83(4–5):419–431
2. Payri R, Salvador FJ, Gimeno J et al (2009) Study of cavitation phenomena based on a technique for visualizing bubbles in a liquid pressurized chamber. *Int J Heat Fluid Flow* 30(4):768–777
3. Som S, Ramirez AI, Longman DE et al (2011) Effect of nozzle orifice geometry on spray, combustion, and emission characteristics under diesel engine conditions. *Fuel* 90(3):1267–1276
4. Payri R, Salvador FJ, Gimeno J et al (2005) Determination of diesel sprays characteristics in real engine in-cylinder air density and pressure conditions. *J Mech Sci Technol* 19(11):2040–2052
5. Jung D, Wang W, Knafel A et al (2008) Experimental investigation of abrasive flow machining effects on injector nozzle geometries, engine performance, and emissions in a diesel engine. *Int J Automot Technol* 9(1):9–15

6. Macian V, Bermudez V, Payri R et al (2003) New technique for determination of internal geometry of a diesel nozzle with the use of silicone methodology. *Exp Tech* 27(2):39–43
7. Peiner E, Balke M, Doering L (2009) Form measurement inside fuel injector nozzle spray holes. *Microelectron Eng* 86(4–6):984–986
8. Wu Z, Li Z, Gao Y et al (2011) Measurement method for diesel nozzle internal geometry and size using high-energy synchrotron radiation X-ray. *J Jilin Univ (Eng Technol Edn)* 41(1):128–132
9. Wu Z, Li Z, Huang W et al (2012) Comparisons of nozzle orifice processing methods using synchrotron X-ray macro-tomography. *J Zhejiang Univ-Sci A* 13(3):182–188
10. Huang W, Wu Z, Li Z et al (2012) Diesel spray penetration model based on nozzle internal geometry. *Trans CSICE* 30(2):124–128
11. Matsuoka S, Yokota K, Kamimoto T (1969) The measurement of injection rate. *Proc Inst Mech Eng* 184(10):87–94
12. Nurick WH (1976) Orifice cavitation and its effect on spray mixing. *J Fluids Eng* 98(4):681–687

Analysis of Internal Flow Characteristics for GDI Injector

Bowen Zou, Shichun Yang, Kaiguo Li, Jingbo Li and Jungang Liu

Abstract *Research and/or Engineering Questions/Objective:* The performance of injector is very important to gasoline direct injection (GDI) engine control. The influence factors of internal flow characteristics for injector were researched. *Methodology:* The Euler multi-fluid model was built and used to analysis. Based on analysis of the internal flow with different mediums and different pressure difference, the flow characteristics of nozzle outlet orifice section were studied. *Results:* The discharge coefficient of nozzle was mainly influenced by the degree of cavitation. With the increase of cavitation level, the average velocity added and turbulence energy decreased on nozzle outlet orifice section. The cavitation level was depended on the bubble number density and pressure difference of inlet and outlet of injector. *Limitations of this study:* Spray characteristics of GDI injector should be investigated based on the results of this paper. *What does the paper offer that is new in the field in comparison to other works of the author:* Most previous analysis of occurrence position for cavitation phenomenon and influence parameters are from macroscopic perspective. This paper mainly analyzes microcosmic influence factors of the cavitation phenomenon within a GDI injector, and then the flow characteristics on orifices export section, which could provide experiential data for later spray simulation, and meanwhile important basis for simulation of the internal flow process. *Conclusion:* The cavitation level was mainly influenced by initial value of bubble number density, and increased with it added. Under the

F2012-A02-018

B. Zou (✉) · K. Li · J. Li · J. Liu
National NGV Engineering Research Center-China Automotive Engineering Research
Institute, Chongqing, China
e-mail: zbw469@126.com

S. Yang
School of Transportation Science and Engineering-Beihang University, Beijing, China

same condition, saturated vapour pressure of medium was higher, the influence of bubble number density was much greater. After the bubble number density was greater than $1e + 12$, the cavitation flow inside the injector tends to be stable. When pressure difference of inlet and outlet of injector was increased, cavitation intensified.

Keywords GDI injector · Euler multi-fluid model · Bubble number density · Flow characteristics · Cavitation

1 Introduction

Gasoline direct injection can improve fuel economy, and reduce pollutant emissions, especially under the part load conditions can reduce fuel consumption with the stratified charge lean-burn combustion (DISC), where the theoretical air—fuel ratio or slightly richer mixture is formed near the spark plug in the combustion chamber, and the rest is filled with pure air or combustion products diluted air [1–5]. The atomization quality of fuel is the main factor for the mixture formation in cylinder. Injector internal flow characteristics determine outlet conditions, affecting the atomization quality of fuel. For both stratified and homogeneous combustion, especially the cavitation phenomenon in nozzle internal flow has a promoting effect on fuel atomization.

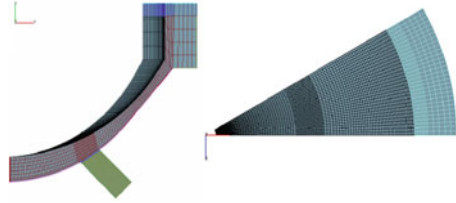
Gilles-Birth et al. completed the visualization experiment with the actual size for DISI porous injector, using unleaded gasoline. Cavitation is found, and divided into three categories: bubble, Oil film, and the string cavitation [6, 7].

Nouri et al. study the internal flow characteristics of an amplified six-hole GDI injectors for different flow rate, injection pressure and the needle valve lift, with water as the medium, by adjusting the Reynolds number and the number of holes to maintain the similarity of the internal flow of the enlarged injector with the actual injector. The cavitation phenomenon is found in the GDI injector, and the research of the cavitation formation and development process within the SAC chamber and injector is completed [8].

Aleiferis et al. performed an actual dimension visualization experiment for an GDI injector using different fuel, also confirmed the existence of cavitation under different temperature conditions [9, 10].

At present, the research on the internal flow of the GDI injector is mainly concerned with experimental method, flow phenomena, and nozzle structure etc.

The experiment is difficult to provide accurate orifice outlet to quantify the actual flow condition, therefore it is necessary to resort to numerical analysis. However, for most previous numerical simulations, analysis of occurrence position for cavitation phenomenon and influence parameters are from macroscopic perspective [11–15] and rarely from the microcosmic perspective for the influence of the flow characteristics on cavitation formation.

Fig. 1 Computational grid

This paper mainly analyzes microcosmic influence factors of the cavitation phenomenon within a GDI injector, and then the flow characteristics on orifices export section, which could provide quantitative data for later spray simulation, and meanwhile important basis for simulation of the internal flow process.

2 Modeling

2.1 Injector Geometry Model

The fuel injector model is the mini sac injector of the second generation GDI engine with 6 holes, and uniformly distributed holes at 45 degrees angle with the injector axis.

According to experimental model used by Nouri et al., it assumes that the injector orifice diameter is 4.1 mm, nozzle length 8.7 mm, ratio of length to diameter 2.12, and the maximum needle lift 2.02 mm [8]. The geometric model and corresponding refined grid is established depending on the experimental conditions for the 1/12 injector model because of symmetry, and the grid number is 86000, as shown in Fig. 1.

2.2 Numerical Model

The current internal flow simulation of GDI injector mainly has two kinds of methods, namely one dimensional flow calculation and two-phase flow simulation. Two-phase flow calculation could better reflect the orifice flow, and can provide instantaneous jet velocity, turbulent kinetic energy, flow coefficient and other parameters for primary breakup, and could improve the atomization process simulation. Therefore, this paper adopts the Eulerian multiphase model for analysis of the gas flow in the nozzle.

2.2.1 Conservation Equations

Eulerian multiphase flow method mainly adopts the phase interaction interface equation control, with each phase control equation solved independently. Due to the short injection duration, it is assumed that the field temperature for the inner flow maintain unchanged, and it is not necessary to solve the energy equation. Therefore, the two-phase mixing model is simplified as the mass and momentum conservation equations.

Equation of mass conservation:

$$\frac{\partial \alpha_k \rho_k}{\partial t} + \nabla \cdot \alpha_k \rho_k V_k = \sum_{l=1, l \neq k}^2 \Gamma_{kl}, \quad k = 1, 2 \quad (1)$$

where α_k is the volume fraction for phase k , $\sum_{k=1}^2 \alpha_k = 1$, V_k is velocity of phase k , Γ_{kl} stands for mass exchange between gas and liquid phase in the interface.

Equation of momentum conservation:

$$\begin{aligned} \frac{\partial \alpha_k \rho_k V_k}{\partial t} + \nabla \cdot \alpha_k \rho_k V_k V_k = & -\alpha_k \nabla p + \nabla \cdot \alpha_k (\tau_k + T'_k) + \alpha_k \rho_k f \\ & + \sum_{l=1, l \neq k}^2 M_{kl} + V_k \sum_{l=1, l \neq k}^2 \Gamma_{kl} \end{aligned} \quad (2)$$

where τ_k stands for viscous shearing stress, T'_k is the Reynolds stress, f stands for bodyforce, including gravity and inertia force, M_{kl} is the momentum exchange between gas and liquid phase, p stands for pressure, $p_k = p$ due to gas-liquid two phase at the same pressure field.

2.2.2 Cavitation Model

Cavitation exists within fuel injector for a gasoline direct injection engine injection process, through the establishment of cavitation model to solve the mass and momentum exchange between gas and liquid phase in the interface. Rayleigh-Plesset is used to calculate the time derivative of the bubble radius. When ignoring the surface tension of the liquid and liquid coefficient of dynamic viscosity effect, the mass exchange is simplified as:

$$\Gamma_l = \rho_g N''' 4\pi R^2 \sqrt{\frac{2}{3} \left(\frac{\Delta p}{\rho_l} - R\ddot{R} \right)} = -\Gamma_g \quad (3)$$

where N''' is number density of bubble, R stands for the bubble radius, subscript l is liquid phase, g is on behalf of gas phase. Effective pressure difference Δp mainly considers the influence of pressure perturbation on the bubble development:

$$\Delta p = p_v - \left(p - C_E \frac{2}{3} \rho_c k_c \right) \quad (4)$$

where C_E is Egler coefficient, depending on the local disturbance level.

According to the different method to solve the bubble radius, cavitation model is divided into linear which ignores inertia effect in the solving process and nonlinear cavitation model.

Interfacial momentum source includes bubble resistance and turbulent dissipation force in the cavitation formation:

$$M_l = C_D \frac{1}{8} \rho_l A_i''' |V_r| V_r + C_{TD} \rho_l k_l \nabla \alpha_g = -M_g \quad (5)$$

where C_D is the resistance coefficient for bubble, relating to the Reynolds number of the bubble. Turbulent motion plays a great role on vapor phase diffusion. For turbulent dissipation coefficient of the bubbly flow, C_{TD} generally takes 0.1 [16].

The standard $k - \varepsilon$ model is used for turbulence model in order to ensure the stability of the calculation.

3 Simulation Results

3.1 Simulation

In order to analyze the influence of internal flow characteristics on orifices export flow, respectively, gasoline and water is used as the medium for parameters calculation, with the inlet pressure of the injector being 0.33 0 MPa, the outlet pressure 0.113 MPa, cavitation number 2.00, valve lift 2.04 mm, and volume flow rate 1.14 l/s. When inlet pressure is 3.3 MPa, the flow characteristics of gasoline on orifices export section are researched (figure Gasoline_HP). Due to the short duration of the injection process, the temperature change is not considered. The comparative analysis related parameters on orifices export section is accomplished, including the turbulent kinetic energy Te , the average velocity v , gas volume fraction, and flow coefficient Cd .

3.2 Flow Characteristics on Orifices Export Section

Figures 2, 3, 4 shows the variation of the exit section parameters with the bubble number density. As can be seen from the figure, the variation of the cavitation extent with the initial number density of the bubble is the same. The cavitation extent increases with the bubble number density. However, for the same number density, the petrol cavitation is greater than water. The saturated vapor pressure of

Fig. 2 Turbulent energy variety on orifices export section with N'''

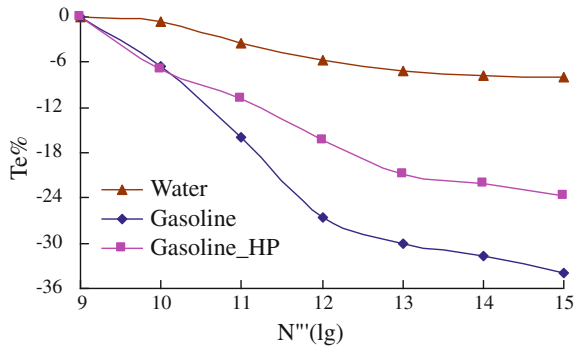


Fig. 3 Velocity variety on orifices export section with N'''

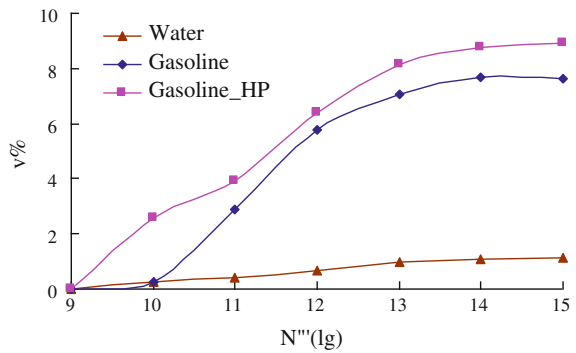
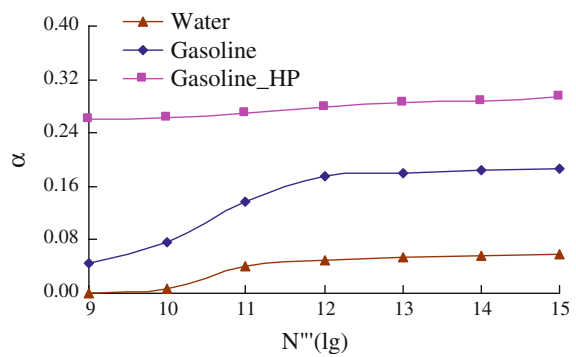


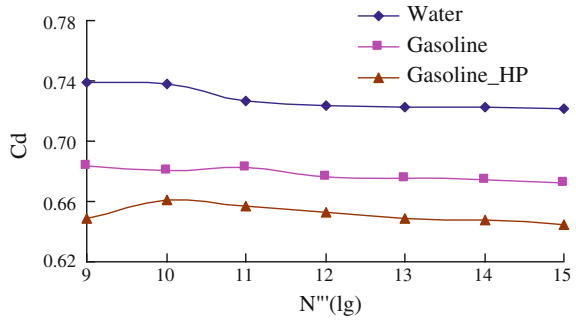
Fig. 4 Gas volume fraction variety on orifices export section with N'''



gasoline is greater than the water under the same conditions. Therefore, cavitation is more easily to occur for petrol at the same injection and ambient back pressure conditions.

When the bubble number density is less than $1e + 12$, the cavitation level aggravates with the number density, and the liquid average velocity is more affected by the gas disturbance on orifices export section. However, the liquid turbulent kinetic energy decreases, mainly due to the reduced liquid mass fraction.

Fig. 5 Discharge coefficient variety on orifices export section with N'''



As the bubble density increased, the cavitation level of gasoline on the section is smaller than water, while the average speed is increased more than water, due to the relatively small viscous for gasoline. In this process, the reduction of the turbulent kinetic energy for gasoline is greater than water, because the density of gasoline is less than water. When the bubble number density is greater than $1e + 12$, the change in gas volume fraction tends to a constant, indicating that the cavitation level within the injector tends to stabilize.

When the inlet pressure increases, the cavitation level is less affected by the bubble density, but more intensive. Cavitation generated more easily and being more stable due to the velocity increase with high inlet pressure. Along with the increase of the inlet pressure, the average velocity on orifices export section increased significantly. However, due to more stable flows, turbulent kinetic energy increases at a low level than that under a lower inlet pressure.

3.3 Discharge Coefficient Variety on Orifices Export Section

As can be seen from Fig. 5, for the same nozzle structure, the flow coefficient is more influenced by the cavitation level, and decreases with it for different fluid. For the same fluid, the flow coefficient change slightly with the bubble number density, under the same injection conditions. This is mainly because the bubble number density has certain effect on the cavitation level.

4 Conclusion

For GDI injector, outlet flow characteristics, determines the spray cone angle, penetration and the atomized particle size distribution, and thus affect the engine performance. In order to obtain more accurate flow characteristics, compared to traditional one-dimensional model, the accuracy of two-fluid model was improved, and the analysis of orifices flow influence parameters provided more detailed information. Conclusions are as follows:

1. The cavitation level is mainly influenced by initial value of bubble number density, and increased with it added. But the flow inside the injector tends to be stable after the bubble number density is greater than $1e + 12$.
2. Under the same conditions, the cavitation level of gasoline is greater than that of water, indicating that fluids with high saturated vapor pressure are more prone to produce cavitation, and the pressure difference between inlet and outlet of the injector was benefit to cavitation. With the increase of degree of cavitation, velocity of flow is increased and the turbulent kinetic energy decreased on orifices export section.
3. The nozzle flow coefficient is greatly affected by the degree of cavitation, and decreased with it.

References

1. Nouri JM, Hamid MA, Yan Y et al (2007) Spray characterization of a piezo pintle-type for gasoline direct injection engines. *J Phys: Conf Ser* 85:1–12
2. Wang X, Gao J, Jiang D et al (2005) Spray characteristics of high-pressure swirl injector fueled with methanol and ethanol. *Energy Fuels* 19:2394–2401
3. Li GW, Li F, Reitz RD (1999) Modeling fuel preparation and stratified combustion in a gasoline direct injection engine. SAE paper 1999-01-0175
4. Sandquist H, Lindgren R, Denbratt I (2000) Sources of hydrocarbon emissions from a direct injection stratified charge spark ignition engine. SAE Paper 2000-01-1906
5. Tomoda T, Sasaki S, Sawada D et al (1997) Development of direct injection gasoline engine-study of stratified mixture formation. SAE Paper 970539
6. Gilles-Birth I, Bernhardt S, Spicher U et al (2005) A study of the in-nozzle flow characteristics of valve-covered orifice nozzles for gasoline direct injection. SAE Paper 2005-01-3684
7. Gilles-Birth I, Rechs M, Spicher U, Bernhardt S (2006) Experimental investigation of the in-nozzle flow of valve covered orifice nozzles for gasoline direct injection. In: *Proceedings of the seventh international symposium on internal combustion diagnostics*, Baden–Baden, Germany, pp 59–78
8. Nouri JM, Mitroglou N, Yan Y et al (2007) Internal flow and cavitation in a multi-hole injector for gasoline direct-injection engines. SAE Technical Paper Series, 2007-01-1405
9. Serras-Pereira J, van Romunde Z, Aleiferis PG et al (2010) Cavitation, primary break-up and flash boiling of gasoline, iso-octane and n-pentane with a real-size optical direct-injection nozzle. *Fuel* 89:2592–2607
10. Aleiferis PG, Serras-Pereira J, Augoye A et al (2010) Effect of fuel temperature on in-nozzle cavitation and spray formation of liquid hydrocarbons and alcohols from a real-size optical injector for direct-injection spark-ignition engines. *Int J Heat Mass Transfer* 53:4588–4606
11. Wang X, Su W (2009) A numerical study of cavitating flows in high-pressure diesel injection nozzle holes using a two-fluid model. *Chin Sci Bull* 54(10):1655–1662
12. He Zhixia, Yuan Jianping, Li Detao et al (2005) Three dimensional numerical simulation of two phase turbulent flow in nozzle of diesel engines. *Chin Intern Combust Engine Eng* 26(6):18–21
13. Salvador FJ, Hoyas S, Novella R et al (2010) Numerical simulation and extended validation of two-phase compressible flow in diesel injector nozzles. *Proc IMechE* 225:545–563

14. Bergwerk W (1959) Flow pattern in diesel nozzle spray holes. Proc Inst Mech Eng 173(25):655–660
15. Isabell GB, Sören B, Ulrich S et al (2005) A study of the in-nozzle flow characteristic of valve covered orifice nozzles for gasoline direct injection. SAE Paper 2005-01-3684
16. Lopez de Bertodano M, Lahey RT Jr, Jones OC (1994) Turbulent bubbly two-phase flows in a triangular. Nucl Eng Des 146:43–52

Characteristics of Flash Boiling Fuel Sprays from Three Types of Injector for Spark Ignition Direct Injection (SIDI) Engines

Gaoming Zhang, Min Xu, Yuyin Zhang and David L. S. Hung

Abstract Spark ignition direct injection (SIDI) gasoline engines employ high fuel injection pressure to promote the liquid fuel atomization and vaporization in the combustion chamber. However, high fuel injection pressures normally lead the fuel spray over penetrating in engine cylinder, resulting in wall and/or piston wetting which cause high level of engine unburned hydrocarbon (UHC) and soot emissions. Recently, it has been found the fuel temperature could play important roles in spray atomization and vaporization processes. Especially, when the temperature of the fuel exceeds its local boiling point, the fuel is superheated and flash boiling occurs. Experiments of flash boiling sprays from a multi-hole DI injector show that the spray would undergo significant structural transformation under the superheated conditions. Both the atomization and vaporization are improved when the phenomenon of flash boiling occurs. Meanwhile, since various types of SIDI engine combustion systems utilize different fuel injector configurations to achieve desirable mixture formation and combustion, it is necessary to extend the existing knowledge of flash boiling spray from multi-hole injector to other types of injector, and characterize their flash boiling spray behaviour under the similar superheated conditions. In this paper, flash boiling sprays from three types of SIDI injectors, namely, multi-hole, swirl and outward opening injectors are investigated at a high pressure constant volume chamber. The primary focus is the spray from a multi-

F2012-A02-019

G. Zhang · M. Xu (✉) · Y. Zhang

National Engineering Laboratory for the Automotive Electronic Control Technology,
Shanghai Jiao Tong University, Shanghai, China

e-mail: zhgaom@gmail.com

D. L. S. Hung

University of Michigan - Shanghai Jiao Tong University Joint Institute, Shanghai Jiao Tong
University, Shanghai, China

hole injector as it is most widely used in modern SIDI engines. The temperature of the injector body can be regulated by placing the injector in a fixture which can be thermally controlled. Various laser diagnostics are applied to investigate the spray geometry, flow field, vaporization and droplet size distributions. The results show that the characteristics of flash boiling spray are mainly dominated by superheat degree, i.e., the difference between the fuel temperature and its boiling point, not as sensitive to the injection pressure as the non-flash boiling spray. The structures of flash boiling spray from all three types of injector differ from those of non-flash boiling spray significantly. However, the effects of injector configuration on the structure of flash boiling spray are insignificant, compared to the non-flash boiling sprays. This study reveals that using fuel temperature can be an effective parameter for controlling the spray structure, spray atomization and evaporation.

Keywords SIDI · Fuel spray · Flash boiling · Superheat · Injector type

1 Introduction

Spark ignition direction injection (SIDI) gasoline engine have become dominant in the recent automotive market, as SIDI engines have significantly improved fuel economy, faster transient response and lower cold start emissions, comparing to the traditional port fuel injection (PFI) gasoline engines [1, 2]. In SIDI engines, fuels are directly injected into the engine cylinder. After fast atomization and evaporation, the gaseous fuel mixes with fresh air to form combustible mixture. The mixture is then ignited by the spark plug. To improve the fuel atomization and vaporization, high injection pressure is a well-accepted way which the main injection system makers take. Currently the fuel injection pressure for SIDI engines is within 10–20 MPa and produce droplet sizing with Sauter mean diameter (SMD) in the range of 5–20 μm [3]. Although high injection pressure can improve the fuel atomization and vaporization, there are several disadvantages associated with it. First, high injection pressure normally causes long penetration of the spray. Under the limited space available in the engine cylinder, the over-penetrated spray could easily hit the piston surface and/or engine cylinder walls, resulting in dilution of the engine lubricant, abnormal combustion (pool fire), and high level of unburned hydrocarbon (UHC) and soot emissions [4, 5]. Besides, the droplet reduction effect of injection pressure is diminishing as the injection pressure increase to a high level. Thus, reduction of droplet size at high injection pressure is very limited and high-cost [6].

Recently, it was found that the fuel temperature could play a dominant role in the spray characteristics [7]. Experimental results from a multi-hole DI injector show that the spray characteristics are critically dependent on fuel temperature. Especially, when the fuel temperature exceeds the local boiling point, the fuel is superheated and the sprays experience flash boiling. Comparing to the non-flash boiling liquid spray, the flash boiling sprays show severe spray structure transformation [7], remarkable different fuel air mixing [8] and significantly

reduced droplet size [9]. All those observation indicates that different mechanisms governing the flash boiling spray atomization and vaporization process. Understanding those mechanisms and its implication to engine combustion will enable us make full use of its potential. Unfortunately, the current research and knowledge of flash boiling spray are far from that. Kim et al. [10] investigated the flash boiling liquid jets using ethanol. They concluded that the flash boiling spray had smaller droplet size, wider spray cone angle and shorter spray penetration than the non-flash boiling spray. Senda et al. [11] confirmed those characteristics and proposed to use flash boiling spray to achieve more homogeneous fuel–air mixture. Based on those experimental observations, Oza [12] did an analysis and proposed a simple model to describe the flash boiling phenomena. The widely accepted bubble formation and development mechanisms in the flash boiling were based on two-phase bubble dynamics that was proposed by Plesset [13]. Applying the flash boiling spray to real engine combustion system have been demonstrated recently and improvement on fuel economy and emission reduction have been reported [14]. From the literature survey we found most of flash boiling spray study was based on one aspect of spray atomization and vaporization. The totally different atomization and vaporization mechanisms of flash boiling spray formation makes those studies inadequate to provide a complete characterization of flash boiling spray, which is the objective of this study. The atomization, vaporization and mixing process of flash boiling sprays are systematically investigated with different types of injectors. The primary focus is the flash boiling sprays of multi-hole injector. Those results are anticipated to greatly increase the understanding of flash boiling sprays and provide a practical guidance for combustion system design.

2 Experiment Setup

Figure 1 shows the experimental setup for flash boiling spray characterization. A high pressure constant volume spray chamber is used for providing the ambient environment. The pressure inside the chamber can be regulated to above atmospheric (up to 2 MPa abs.) or below atmospheric vacuum (down to 20 kPa abs.) conditions using the high pressure nitrogen supply and the vacuum pump. Four quartz windows are mounted around the chamber walls to provide the optical access. The injectors are mounted at the top of the chamber with a high pressure fuel supply provided by a piston accumulator. To condition the fuel temperature, a water jacket is designed to surround the injector body. The water temperature is accurately controlled by an external heat exchanger. An Nd: YAG laser is used as the light source. Depending on the diagnostics objectives, the laser can be tuned to 532 or 266 nm. The laser beam is transformed to a thin light sheet by a set of lenses and guided into the chamber. The light sheet then illuminates one cross section of the spray. The resultant photons (either by scattering or fluorescence) are then collected by a CCD camera. The injector, laser and camera systems are synchronized by a programmable time unit (PTU).

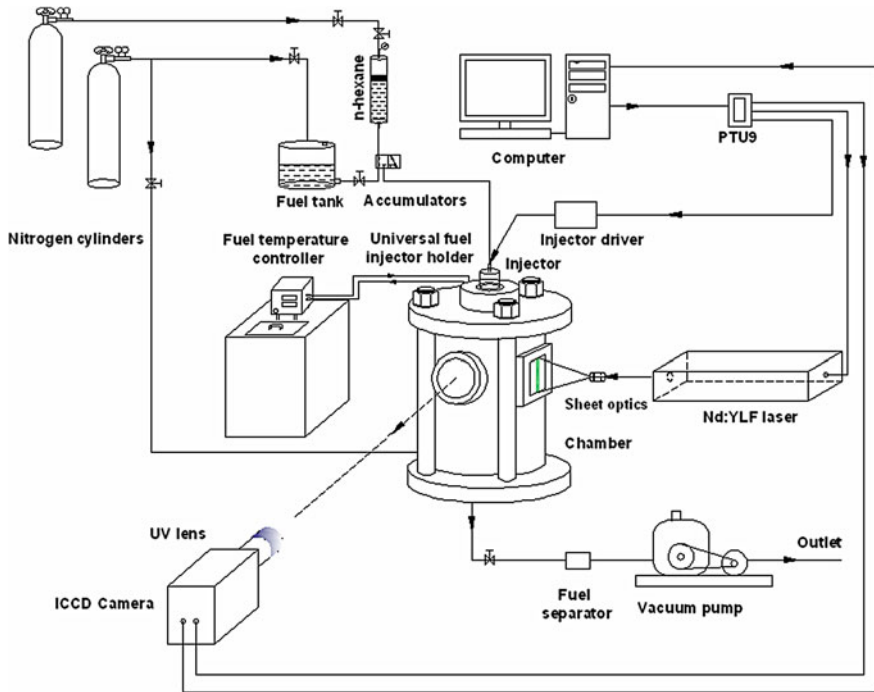


Fig. 1 Experimental setup for spray characterization

The injectors used in this study are one 8-hole injector, one swirl injector and one outward opening injector. The injected fuel is n-hexane. The laser diagnostics used are as following: planar Mie scattering for spray structure, particle image velocimetry (PIV) for the spray velocity fields, planar laser induced exciplex fluorescence (LIEF) for liquid/vapor phase imaging and laser sheet droplet sizing (LSD) for 2D droplet sizing.

3 Results and Discussions

3.1 Macroscopic Spray Structures

Figure 2 shows the spray laser sheet Mie scattering images from the multi-hole injector at various fuel temperature at ambient pressure of 40 kPa. The fuel superheat degree (SD) is defined as the difference between the fuel temperature and the local boiling point under the ambient conditions. The upper side image shows the spray structure in the cross section plan parallel with the injector axis. The lower side images are taken at the planes perpendicular to the injector axis 30 mm downstream the injector. All those images are taken at 0.8 ms after start of injection (ASOI).

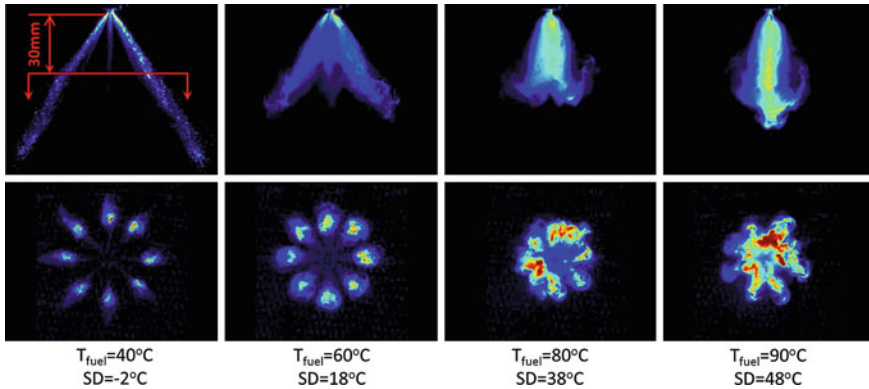


Fig. 2 Spray images of laser sheet Mie scattering at various fuel temperatures (injection pressure: 5 MPa, ambient pressure: 40 kPa, injection timing: 0.8 ms ASOI)

When the fuel is not superheated ($SD < 0$), the spray plume from each holes can be clearly identified in each direction. The spray pattern shows that all the plumes are uniformly distributed with the center of the injector tip. When SD is equal to or greater than $18^{\circ}C$ the spray plumes get wider. The axial spray images shows the widen plumes already start to interact with each other. This is the results of flash boiling which is induced by the superheat liquid. When high temperature liquid is suddenly released to an environment with pressure below its saturation pressure, the liquid becomes thermodynamically unstable. More obvious spray transformation can be found when the superheat degrees increases to 38 and $48^{\circ}C$. Under this superheat degree, the widen spray plume interacts so furiously that no individual spray plume from each nozzle can be identified. Spray plumes from different holes have been totally ‘collapse’ together to form a single solid spray. The spray images show that large amount of fuel concentrates in the centerline. When further heating the fuel to $90^{\circ}C$, the collapsing gets more serious.

The above macroscopic spray images indicate that the structure of flash boiling spray from multi-hole injectors is critically dependent on superheat degree. As the superheat degree increases, the originally widely separated plumes get wider. The interaction between different plumes causes the spray collapsing to form a solid spray. However, the mechanism governing the collapsing behavior needs to be further examined. From the dynamic stand point, the flow fields have close relationship with the spray structure. Knowledge of the flow field has significant value towards understanding the flash boiling spray mechanisms.

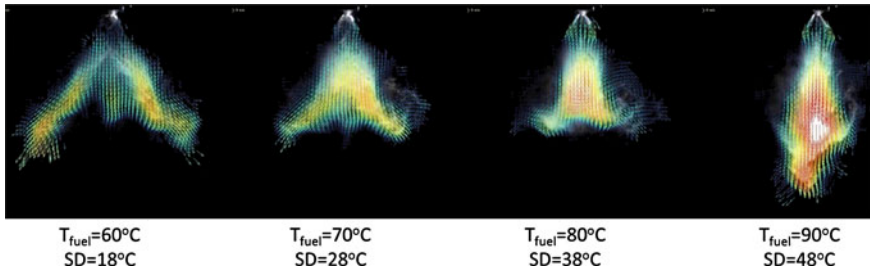


Fig. 3 Droplet velocity distributions in the plane of the axial direction [15]

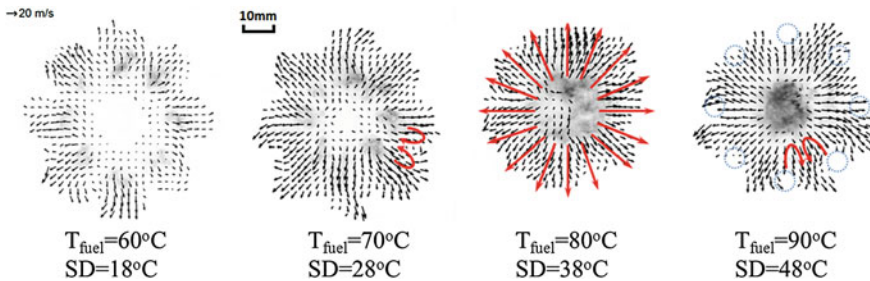


Fig. 4 Spray radial velocity distribution at various fuel temperature conditions [16, 17]

3.2 Spray Flow Fields

The 2D flow fields of the spray particles are obtained using planar particle image velocimetry (PIV). The flow fields at both directions are investigated. Figure 3 shows the results at axial direction.

At the superheat degree of 18 °C, the spray shows initial structural transformation. The largest velocities distribute at the tip region of the spray. The velocity towards the centerline is small. When increasing the superheat degree to 28 °C, the velocity towards the centerline increases significantly. That velocity takes large amount the spray particles to spray centerline. The velocity parallel with the injector axis is also largely maintained. Larger vortex structures are also presented at the front of the injector. At the superheat degree of 38 °C, the balance between those two velocities has been broken. The inwards velocity has caused the spray total collapsing towards the centerline. The spray particles have been greatly accelerated in the center of the collapsed spray. At the superheat degree of 48 °C, the trend is further reserved.

The velocity distribution at radial direction is shown in Fig. 4. The velocity at this direction clearly shows the velocity transformations and how the velocity affects the spray macroscopic structures. At low superheat degree, each spray plume has its individual identification. The interaction between different plumes is

negligible. When the superheat degree increases to 28 °C, the plume is widened which induces the interaction between adjacent plumes. A small velocity combination is formed. Those spray particles start to push each other to form a spray vortex. Spray particles are carried to the centerline and a compacted spray structure is formed, which is consistent with the previous observations. At the superheat degree of 38 °C, the adjacent plume interaction becomes so strong that a large amount of spray particles are pushed to the space between the plumes. Those velocity takes the spray particles outwards the spray. When the superheat degree finally increases to 48 °C, the velocity interaction dominates the spray pattern. The spray particles of the original plumes have been totally carried away by the velocity to form a new plume in the spray between the original located plumes.

From above analysis, we can conclude the spray macroscopic transformation is closely related with the velocity distribution. The velocity distribution under various superheat conditions directly induced different spray structures. Another important physical process affected by the velocity is the spray vaporization. As the flash boiling spray is a typical multiphase system, characterization of its vaporization process is important.

3.3 Liquid and Vapor Phase Distributions

The spray liquid and vapor phase distributions is characterized using laser induced exciplex fluorescence (LIEF) technique. LIEF technique is capable of separating the signal from different phases by adding two different fluorescing tracers. More discussion of LIEF technique can be found in [9].

Figure 5 shows the liquid and vapor phase distributions under different superheat degree. The initial spray transformation occurs within the first row images shown. At a superheat degree of 0 °C, individual spray liquid and vapor plumes are identified with a relatively low vapor intensity indicating limited vaporization. Comparing the first two images, superheat degree of 20 °C, the spray plumes become wider and more vaporization is observed at the higher fuel temperature condition. When closely examining the collapse of the spray, the distance between the plumes, little change is apparent for these conditions. The trend of wider spray plumes and increased vapor component continues where both the liquid and vapor phases of the spray begin to collapse.

More dramatic spray structural changes are observed at higher temperatures. At a superheat degree of 40 °C, both liquid and vapor components are observed throughout the image plane; illustrating the transfer of fuel toward the centerline of the injector axis. A nearly uniform liquid distribution is evident and the previously observed individual plumes collapse into a single plume. In particular, a narrow and highly concentrated vapor component is indicated, located centrally around the injector axis. Large vortices are also observed in both the liquid and vapor images, resulting in a narrowing of the spray-tip region. With increasing fuel

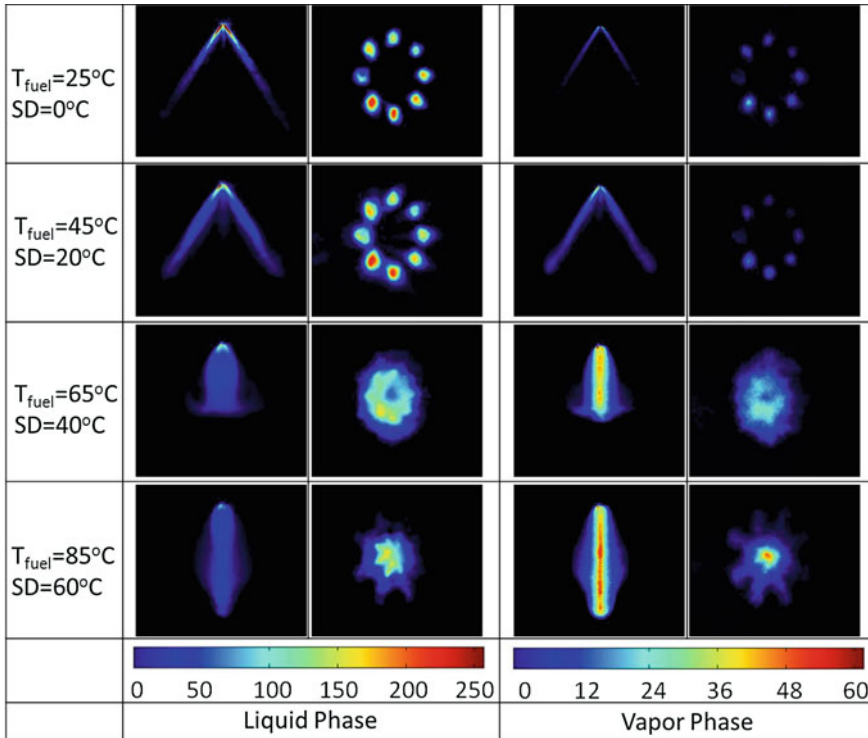


Fig. 5 Fluorescence intensity indicating spray liquid and vapor phase concentration distributions at different superheat conditions (injection pressure: 10 MPa, ambient pressure: 20 kPa, injection timing: 0.8 ms ASOI) [18]

temperature, the liquid phase continues to collapse toward the spray centerline and a vapor jet-like structure continues to narrow resulting in higher penetration. At a superheat degree of 60 °C, the spray is highly flashed and both the liquid and vapor components are focused toward the center of the injector.

The liquid and vapor distribution images show that different response of the two phases towards the superheat degrees. Although both liquid and phase collapsing as the superheat degree increases, the collapsing of liquid phase is more severe than the liquid phase. This behavior is probably because the smaller momentum the vapor phase makes it more sensitive to the velocity (pressure) changes as discussed in the last section. However, the different vapor distribution can be also attributes to the different vaporization mechanisms under superheat conditions. In the liquid region, the fuel vaporization is mainly governed by the surface vaporization and diffusion. Under superheat conditions, large vapor bubbles are generated inside the liquid spray. When the spray goes out of the injector, those bubbles can grow fast and explode. Comparing to the surface vaporization, this

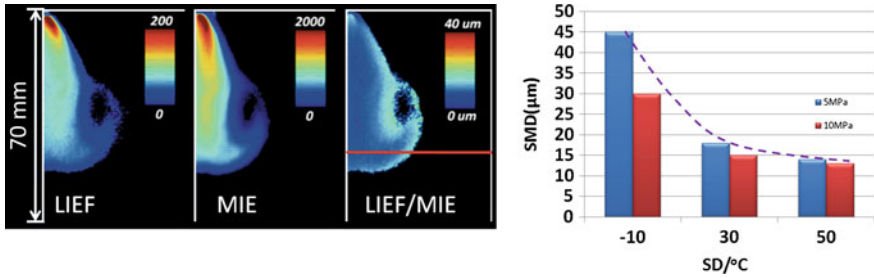


Fig. 6 Laser sheet droplet sizing technique and SMD results for flash boiling sprays

boiling vaporization is almost instant. The prompt atomization and vaporization can greatly enhance the fuel vaporization and thus affects the flow. So the vaporization and flow of flash boiling spray are also two closely coupled processes. They both decide the formation of flash boiling spray. The results of those two processes are anticipated to be faster vaporization and reduction of spray droplet diameters.

3.4 Droplet Diameter

The 2D droplet distribution at the axial plane is investigated using 2D laser sheet droplet (LSD) sizing technique [19]. The LSD technique is based on the LIEF technique of previous section and taking a spray Mie scattering image simultaneously. Figure 6 left shows the LSD principle. The right side images show the SMD 30 mm downstream the nozzle. As the injection pressure gets higher, the effects of injection pressure on droplet size diminishes. However, increasing the superheat degree can reduce the droplet size continuously. This result shows that superheat is the dominant factor to determine the atomization of flash boiling spray.

The above discussions focus on the sprays of multi-hole injector. From those results we found that flash boiling have the potential to form fuel–air mixture more quickly uniformly.

There are also other types of injectors used in today’s SIDI combustion systems. The spray characteristics of those injectors under superheat conditions have significant value for the combustion system design. The following section will discuss the flash boiling sprays from different injector types. Besides the multi-hole injector discussed above, we will focus on other two types of DI injectors used in SIDI engines, namely, high pressure swirl injector and outward opening injector.

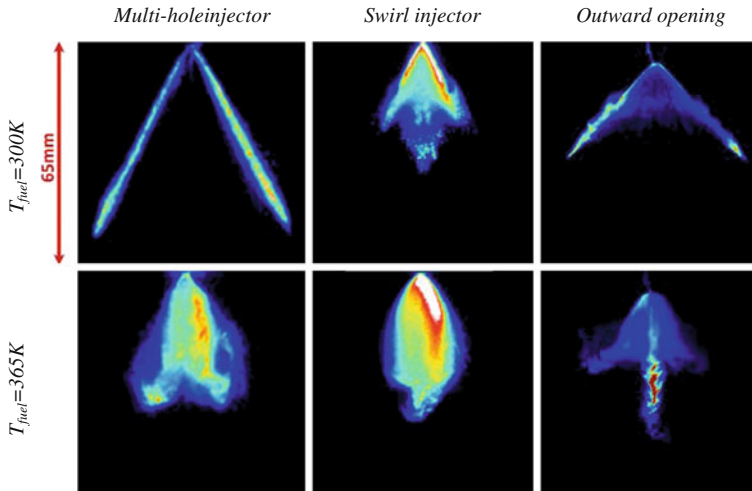


Fig. 7 Non-flash-boiling and flash boiling sprays from multi-hole injector, swirl injector and outward opening injector

3.5 Flash Boiling Spray of Different Types of Injector

Figure 7 shows the comparison between non-flash-boiling and flash boiling sprays from multi-hole injector, swirl injector and outward opening injector. Under non-flash boiling conditions, different spray structures are observed between each injector type. The mechanisms governing the spray atomization and vaporization are anticipated to be different. The multi-hole injector spray atomization is based on liquid jet breakup mechanisms, while the spray atomization from swirl and outward opening injector rely on liquid sheet breakup. Under superheat conditions, however, the similarity of spray structure from different types of injector is greatly improved. For all the three injector types, the spray collapsing behavior is observed, and a solid spray is formed in the spray center. Those similar spray structures indicating the flash boiling dominates the spray atomization and vaporization. The effects of injector configuration on spray formation have been greatly reduced. Based on these findings, we can participate that the previously observed spray structure changes for the multi-hole injector still exists for the swirl injector and the outward opening injector.

4 Conclusions

In this paper, the spray characteristics under superheat conditions from different types of injectors are investigated. The primary focus is the widely used multi-hole

injector. Various laser diagnostics are applied to understand the spray structure and spray formation mechanisms. The following conclusions can be drawn:

- (1) The flash boiling sprays of multi-hole injector have very different structures from the non-flash boiling sprays. The spray flow fields and prompt liquid vaporization are responsible for those differences.
- (2) The spray flow field and vaporization are two closely coupled processes which jointly affect the flash boiling spray formation. Quantitative measurements of those two parameters are critical to reveal the physical mechanisms governing the flash boiling atomization and vaporization.
- (3) The droplet size reduction effects of injection pressures degrade as the injection pressure gets higher. Increasing the superheat degree, however, can continuously reduce the droplet size. Controlling the superheat degree is a more effective way to achieve smaller droplet size.
- (4) The effects of injector configurations on spray formation are greatly reduced under flash boiling conditions. Similar mechanisms govern the spray atomization and vaporization for different injector configurations. Under superheat conditions, spray atomization and vaporization by flash boiling is dominant even when using different types of injectors.

Acknowledgments This research is supported by the National Natural Science Foundation of China (contract No. 51076093 and 51076090). The support from General Motor Company is greatly appreciated.

References

1. Zhao F, Lai MC, Harrington LD (1999) Automotive spark-ignition-direct-injection gasoline engines. *Prog Energy Combust Sci* 25(5):437–562
2. Drake MC, Haworth DC (2007) Advanced gasoline engine development using optical diagnostics and numerical modeling. *Proc Combust Inst* 31(1):99–124
3. Fansler TD, Drake MC et al (2009) Quantitative liquid and vapor distribution measurements in evaporating fuel sprays using laser-induced exciplex fluorescence. *Meas Sci Technol* 20(12):1–13
4. Serras-Pereira J, Aleiferis PG et al (2011) Imaging and heat flux measurements of wall impinging sprays of hydrocarbons and alcohols in a direct-injection spark-ignition engine. *Fuel* 91(1):264–297
5. Chin ST, Lee C, Fon F (2002) Numerical investigation of the effect of wall wetting on hydrocarbon emissions in engines. *Proc Combust Inst* 29(1):767–773
6. Lefebvre AH (1988) *Atomization and sprays*. Hemisphere Publishing Cooperation, New York
7. Zeng W, Xu M et al (2011) Atomization and vaporization for flash-boiling multi-hole sprays with alcohol fuels. *Fuel* 95(1):287–297
8. Zhang G, Xu M, Zhang Y et al (2011) Quantitative measurements of liquid and vapor distributions in flash boiling fuel sprays using planar laser induced exciplex technique. *SAE Paper* 2011-01-1879

9. Schmitz I, Leipertz A (2006) Comparison of the flash boiling influence on the spray structure of a high pressure swirl injector and of a multihole injector for GDI engines. In: ICLASS06-026, Kyoto, Japan
10. Kim YK, Iwai N et al (1980) Improvement of alcohol engine performance by flashing boiling injection. *JSAE Rev* 2:81–86
11. Senda J, Yamaguchi M et al (1994) Characteristics of spray injected from gasoline injector. *JSME Int J B* 37:931–936
12. Oza RD (1984) On the mechanism of flashing injection of initially sub-cooled fuels. *J Fluids Eng* 106:105–109
13. Plesset MS, Zwick SA (1954) The growth of vapor bubbles in superheated liquids. *J Appl Phys* 25:493–500
14. She J (2010) Experimental study on improvement of diesel combustion and emission using flash boiling injection. *SAE Papers*, 2010-01-0341
15. Zhang M, Xu M, Zhang Y et al (2010) High speed PIV evaluation of fuel sprays under superheated conditions. 14th ILASS-Asia, Jeju, Korea, pp 105–111
16. Zhang M, Xu M, Zhang Y et al (2011) Flow field evaluation of superheated fuel sprays using high-speed PIV. *SAE Technical Papers*, 2011-01-1880
17. Zhang M, Xu M, Zhang Y et al (2012) Flow field evaluation of superheated fuel sprays from a multi-hole injector using high-speed PIV. *SAE Papers*, 2012-01-0457
18. Zhang G, Xu M, Zhang Y (2010) Macroscopic characterization of flash boiling sprays using laser induced exciplex fluorescence technique from a multi-hole DI injector. In: 14th ILASS-Asia, Jeju, Korea, pp 112–118
19. Zeng W, Xu M, Zhang Y et al (2012) Laser sheet dropsizing of evaporating sprays using simultaneous LIEF/Mie technique. In: The 34th international symposium on combustion, Warsaw, Poland

Part III
Fuel and Lubricants

World's First 100 % LPG Long Haul Truck Conversion

Alberto Boretti and Charles Grummisch

Abstract Advanced Vehicle Technologies (AVT), a Ballarat Australia based company, has developed the World's first diesel to 100 % LPG conversion for heavy haul trucks. There is no diesel required or utilized on the trucks. The engine is converted with minimal changes into a spark ignition engine with equivalent power and torque of the diesel. The patented technology is now deployed in two Mercedes Actros trucks. The power output in engine dynamometer testing exceeds that of the diesel (in excess of 500hp horsepower and 2000 ft/lb torque). In on-road application the power curve is matched to the diesel specifications to avoid potential downstream power-train stress. Testing at the Department of Transport Energy & Infrastructure, Regency Park, SA have shown the Euro 3 truck converted to LPG is between Euro 4 and Euro 5 NOx levels, CO2 levels 10 % better than diesel on DT80 test and about even with diesel on CUEDC tests. The average fuel ratio of LPG tests versus diesel tests over 7 points from 80 to 180 kW is 1.67:1. The conversion is already operational in fleets. The conversion to LPG permits a better economy, a better environment and a better energy security. The truck conversion permits lower operating cost and significantly reduced fuel cost. The LPG has a lower fuel cost per unit energy. The savings are almost \$300 per 1000 km. These fuel costs are based on an average wholesale price including rebates over the past sixmonths of \$0.51/L LPG and \$1.46/L diesel. Longer

F2012-A03-008

A. Boretti (✉)
Missouri University of Science and technology, Missouri, USA
e-mail: a_boretti@yahoo.com

A. Boretti
University of Ballarat, Ballarat, Australia

C. Grummisch
Advanced Vehicle Technologies (AVT), Ballarat, Australia

maintenance intervals also permit lower cost and less downtime. The LPG has significant emissions reduction. The reduced carbon dioxide and particulate matter emissions are a result of the gaseous state and the better C/H ratio of the LPG. The CO₂-e advantage of the LPG engine is greater than the tailpipe 10 %. There is almost no particulate matter with LPG. The goal is to achieve Euro 5 (with the Euro 3 engine) in 1st half 2012 with no catalytic converter or urea filter. Finally, the LPG is locally produced and this reduces the dependence on the import of foreign oil. The current conversion kit is for a 3 pedal Euro 3 Actros, 26xx series. The company is working on a kit for the Euro 4 and 5 Actros engine, and also assessing other vendors' engines for conversion.

Keywords LPG · Diesel · Heavy duty truck · Fuel economy · Pollutant emissions · Energy security

1 LPG and Heavy Duty Truck Applications

As long as the price of crude oil increases and the threat of global warming and air pollution remain there will be a need for alternative fuels. Liquefied Petroleum Gas (LPG) has emerged as a perfect solution to these challenges: it is inexpensive, clean burning and relatively low in carbon content. Diesel engines have been the backbone of the transportation industry. Valued for their power, fuel economy and durability, diesel powered trucks are used worldwide. However, they are heavy emitters of particulate matter (PM) and oxides of nitrogen (NO_x). By converting diesel engines to run on LPG we can significantly reduce the problem of diesel pollution whilst also improving emissions of greenhouse gases (GHG). Such conversions are however not a simple matter of changing the fuel, many technical problems present particularly with engine optimisation and fuel injection control to ensure that engine performance is maintained and exhaust emissions minimised. It is the aim of this project to determine how this can be done.

Up until the early 1960s, railways dominated all but the shortest land-based freight task. Since then, vast improvements in road vehicle productivity and road infrastructure quality, the gradual removal of regulations restricting road freight carriage and the exponential growth in interstate trade has broadened the range of freight tasks for which road is better suited than rail. The Australian domestic freight task measured 521 billion tons kilometres in 2007, with 35 % carried by road [1]. The domestic freight task has doubled in size over the past 20 years, with an average growth of 3.5 % per annum. BITRE projections [1] suggest this trend will continue, although with slightly slower growth into the future, growing by approximately 3.0 % per annum until 2030. Over this period, road freight volumes are projected to more than double, with domestic demand for manufactured goods sustaining much of the growth, even if the global financial crisis dampens freight

growth in the near term. Energy transport accounts for the 14.5 % of the national carbon dioxide equivalent annual emissions [2].

Life-cycle emissions analysis of alternative fuels for heavy vehicles [3, 4] has shown the potential of gaseous fuels for heavy duty vehicles. There have been major advances in natural gas engines in recent years that mean that the present generation of natural gas vehicles have significantly lower emissions than the present generation of diesel vehicles. The emissions based on use in Original Equipment Manufacturer (OEM) vehicles are lower in all categories, GHG, important criteria pollutants, and air toxics. The lower particulate emissions and noise levels compared with diesel make it particularly attractive for urban areas. The major uncertainty relates to upstream and in-service leakage, on the other hand already sufficiently reduced in the present generation of OEM compressed or liquid natural gas (CGN or LNG) vehicles, and the lack of sufficient refuelling stations. The extra weight of CNG fuel tanks leads to slightly higher fuel consumption, or loss of payload in the case of buses, but this is less of a problem with LNG vehicles due to the higher energy density. Similarly, a dedicated LPG bus produces significantly lower emissions of important criteria pollutants, and lower embodied emissions of GHG. Toxic air pollutants from tailpipe emissions of LPG vehicles are much lower than those of diesel vehicles, but the greater upstream emissions of air toxics results in the embodied emissions of air toxics from LPG being much the same as those from diesel. The major disadvantage of LPG is the lack of market penetration of LPG dedicated heavy vehicles.

LPG is often incorrectly identified as propane. In fact, LPG is a mixture of petroleum and natural gases that exist in a liquid state at ambient temperatures when under moderate pressures (less than 1.5 MPa). The common interchanging of the two terms is explained by the fact that in the U.S. and Canada LPG consists primarily of propane. In many European countries, however, the propane content in LPG can be as low as 50 % or less. Composition of LPG (U.S. HD-5 standard) is Propane 85 % min by liquid volume, Propylene 5 % max by liquid volume, Butane and heavier HC 2.5 % max by liquid volume, Sulphur 120 ppm max by weight.

When compared with auto gas, HD-5 LPG emits more NO_x but less particulate matter. Emissions of hydrocarbons are similar. The main benefit of HD-5 compared with auto gas is that the compression ratio can be altered to suit this higher-octane fuel. Therefore, the lower particulate emissions and lower noise levels compared with diesel make it attractive for use in urban areas.

Improving the efficiency of internal combustion engines is the most promising and cost-effective approach to increasing vehicle fuel economy in the next 10–20 years [5]. Advanced combustion engines still have great potential for achieving dramatic energy efficiency improvements [5]. The primary hurdles that must be overcome to realize increased use of advanced combustion engines are the higher cost of these engines requiring expensive R&D when compared to conventional engines, and compliance with particularly stringent new emission regulations, with catalytic emission control technologies with other fuels much less mature than gasoline engine catalysts.

Australian standards ADR 80/03 requires compliance with EURO 5 standards for heavy duty trucks starting 1 January 2010 for new model vehicles and 1 January 2011 for all produced vehicles. Near future regulations will very likely follow EURO 6 standards. EURO 6 regulation proposal will introduce particularly stringent emission standards [6]. Procedure provisions will be defined for a whole suite of features, including test cycles, off cycle emissions, particulate number (PN), emissions at idling speed, smoke opacity, possibly introduction of NO₂ emission limit, correct functioning and regeneration of pollution control devices, crankcase emissions, On Board Diagnostic (OBD) systems and in-service performance of pollution control devices, durability, Portable Emission Measurement System (PEMS) to verify in-use emissions, CO₂ and fuel consumption, measurement of engine power, reference fuels, specific provisions to ensure correct operation of NO_x control measures. Particularly stringent emission limits will be set for CO, THC, NMHC, CH₄, NO_x, NO₂, NH₃, PM mass and PN number to be measured on different cycles, including various stationary and transient cycles. Implementation of these stringent emission standards is anticipated to cause a reduction in fuel efficiency due to the exhaust emission control devices needed to meet emissions regulations for both NO_x and PM without introduction of advanced combustion technologies to further improve combustion efficiency and reduce pollutant formation during combustion. Advanced combustion engine technologies are now focused on Internal Combustion Engines (ICEs) operating in advanced combustion regimes, including modes of low-temperature combustion (LTC), which increase efficiency beyond current advanced diesel engines and reduce engine-out emissions of NO_x and PM to near-zero levels. In addition to advanced combustion regimes, reduction of heat transfer, control of load by quantity of fuel injected and a wide range of waste heat recovery technologies may improve engine efficiency and reduce fuel consumption.

The most common alternative fuels in transport (to low sulphur diesel and petrol) are LPG, ethanol, CNG and LNG. The worldwide production and use of alternative fuels is growing rapidly in response to the GHG emission reduction and national fuel security. In Australia LPG is used in automotive applications in cars (almost all taxis) and special applications in close proximity to workers in confined or enclosed spaces such as fork lift trucks, concrete mixers and similar plant because of the inherent low emissions of the fuel related to its gas phase and small molecule size relative to conventional fuels. There have been few serious attempts to convert heavy duty diesel engines to LPG for the following reasons:

- Conversions have focused on CNG because its 130 octane number means only small or no change is needed from diesel engine combustion chamber shape;
- In many countries there is poor availability of both LPG and CNG outlets, and in many others where LPG is used for heating and cooking there is an excess of demand over supply;
- Engine manufacturers are reluctant to devote effort to developing engines for a niche or non-existent market.

Australia is unique in having an established LPG infrastructure with over 3,500 retail outlets for LPG distributed across the continent well in excess of those in the whole of North America, where they are largely confined to West and East Coast regions. Furthermore Australia produces about 30 % more LPG than it consumes and its availability will increase as more LNG plants come on stream as LPG is a liquid by-product from natural gas liquefaction. Inherently as a by-product LPG has only a minor energy production cost compared with gasoline and diesel where significant increase in production energy have occurred to meet the recently introduced Australian fuel quality standards reducing sulphur levels and meeting composition and test requirements with strict quality control. Moreover the GHG emissions associated with LPG production according to both GREET [7] and SIMA-PRO LCA analyses [8] are only about two-thirds of those of LS diesel and about 60 % of gasoline production. More important is that LPG has a 12 % reduction in CO₂ emission (because of its lower C/H ratio), and whilst not as low as NG (Methane), it requires negligible compression energy compared with NG gas compression (~7–11 % of gas energy) to CNG or liquefaction (~17 %) to LNG. The challenge for further use of LPG is to produce an engine that has equal or near equal thermal efficiency to diesel to thus obtain the benefits of fuel composition (12 %) and (8–20 %) less production and distribution energy.

Climate change, energy prices, energy security and public health are driving transport R&D on several fronts. It is well recognized that more energy-efficient and environmentally friendly transportation technologies especially based on gas fuelled ICEs would enable reduction of fuel consumption, CO₂ and pollutants emissions therefore improving energy security, environment, and economy. LPG is an Australia wide delivered alternative fuel, with future increased availability as a by-product of LNG production but with no uptake in the heavy duty engines market because of the lack of available dedicated engines or engine conversions. Although LPG inherently has reduced particulate and GHG emissions compared with diesel fuel because of its chemical composition and gas state, its low octane number if compared with CNG has prevented its application as a sole fuel for converted heavy duty diesel engines.

There is a lack of advanced internal combustion engines technologies specifically developed for LPG fuels, but covering this lack, advanced LPG engines have the potential to achieve thermal efficiencies exceeding 50 % both full load/part load while complying with EURO 6 emission standards without after treatment.

2 The AVT HDT LPG Experience

Advanced Vehicle Technologies (AVT), a Melbourne Australia based company, have developed the World's first diesel to 100 % LPG conversion for heavy haul trucks. There is no diesel required or utilized on the trucks; they are converted into a spark fired engine, with equivalent power and torque of the diesel, with minimal changes to the engine. The patented technology is now deployed in two Mercedes

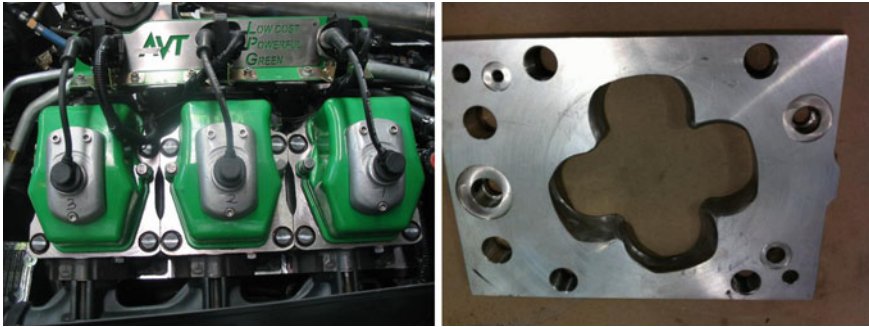


Fig. 1 The AVT technology—manifold mixture formation, throttle load control, turbulence plate to reduce the compression ratio and enhance combustion, spark ignition

Actros trucks. AVT has previously converted several other diesel engines, and have a proven track record of success.

The conversion is based on a patented “turbulence plate” technology, that reduces the compression ratio of the engine and enhances the combustion properties of the premixed LPG and air mixture that enters within the cylinder producing higher turbulence intensities and lower turbulence length scales, ultimately permitting higher burning rates through lower turbulence mixing times. Combustion is controlled by a spark discharge that ignites the premixed mixture. Load is controlled by throttling the intake.

A patented compression reduction fuel swirl plate reduces engine compression from 18:1 to less than 10:1 and allows the Mercedes engine to operate on spark ignition rather than compression ignition. The plate’s fuel swirl characteristics improve engine efficiency, resulting in better fuel consumption, more low-end torque and improved overall power. The cylinder head is also modified to accept spark plugs and an LPG induction system, with improved cooling performance. A new LPG electronic engine management system controls engine timing and fuel induction for maximum efficiency.

Figure 1 presents some figures that illustrate the AVT technology. Each engine cylinder has fitted a spark plug to replace the Diesel injector. The glow plug is also removed. The intake and exhaust are unaltered, as it is the bowl-in-piston. A turbulence plate masking the valve area is added with the purpose of increasing the turbulence intensity and reducing the turbulent length scale acting on the incoming intake flow and on the squish flows when the piston is approaching top dead centre. The main parameters of the converted engine are presented in Table 1. The mixture is created upstream of the combustion chamber introducing the LPG in the manifold. A throttle body controls the load by throttling the intake. The compression ratio in the highly turbocharged engine is reduced to 8.5:1.

The engine converted to LPG has been extensively tested in the AVT facility. The power output in dynamometer testing exceeds that of the Diesel (in excess of 370 kW power and 2,700 Nm torque). In on-road application the power curve is

Table 1 Basic data of the Actros engine (baseline)

Bore diameter (mm)	130.00
Stroke (mm)	150.00
Connecting rod length (mm)	150.00
Displacement per cylinder (l/cyl)	1.991
Displacement total (l)	11.946
Number of cylinders	6
Compression ratio	18.5
Bore/stroke ratio	0.867
Intake valve closure (degrees crank angle)	-115
Exhaust valve opening (degrees crank angle)	90
Intake valve opening (degrees crank angle)	320
Exhaust valve closure (degrees crank angle)	401

matched to the diesel specifications to avoid potential downstream power-train stress. The engine has a minimum brake specific fuel consumption BSFC of 0.19879 kg/kWh, which considering a LHV of 46.1 MJ/Kg corresponds to a maximum BRAKE EFFICIENCY of 39.18. The fuel considered is HD5 LPG and not auto gas. Figure 2 presents the measured engine performance curves—power, torque, compressor pressure ratio, brake specific fuel consumption, air and fuel flow rates, brake efficiency, intercooler pressure operating with an air-to-fuel ratio of 21.84 that correspond to an air-to-fuel equivalent ratio λ of 1.41. Spark advances were 14–16 degrees crank angle before top dead centre.

The operation of the engine has been extended and stable without major durability or performance degradation issues. The simple but extremely efficient and reliable engine conversion technology produces a spark ignited engine working with top efficiencies approaching 40 % and same full load power and torque curve of the Diesel.

Figure 3 presents the maps of a novel waste gated turbocharger to better deal with the spark ignition LPG operation delivering better torque outputs especially in the low rpm range. The novel turbocharger is part of the further refinement of the technology currently under study. These refinements more generally include: advanced turbocharging—to improve efficiency; exhaust gas recirculation—to improve efficiency and reduce emissions; advanced control—to operate knock free as close as possible to the maximum torque spark advance using the maximum boost allowed; advance mixture preparation—with a mixing of port and direct fuel injection to produce fully controlled homogeneous or stratified conditions within the cylinder; advanced ignition system—to permit load control throttle-less by quantity of fuel injected with jet ignition. Goal is to achieve Euro 6 emissions while improving both the full and part load fuel conversion efficiency with a simple after treatment system.

The vehicle with fitted the standard converted engine (performance map of Fig. 2) has been extensively tested on-road. The on-road testing has confirmed the conversion efficiency and reliability. The truck has been driven over short and long

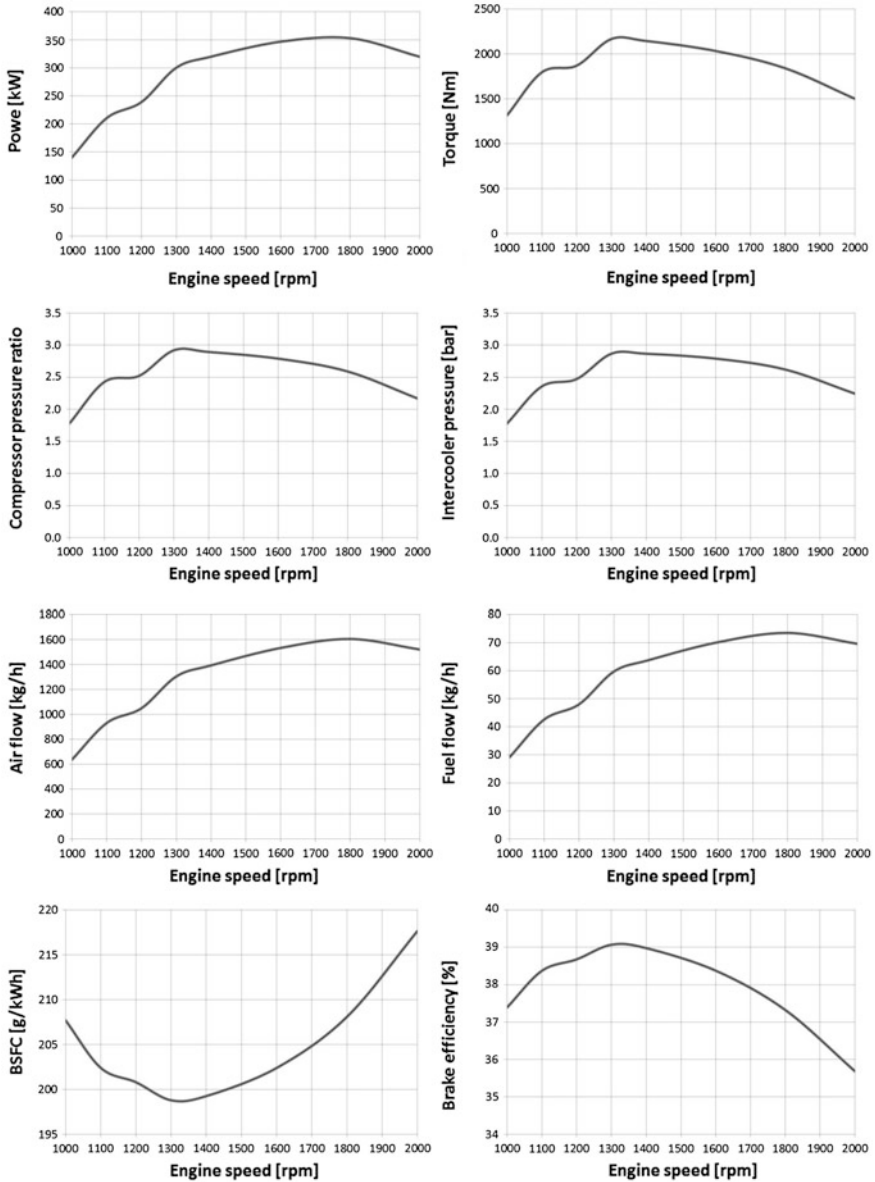


Fig. 2 Engine performance curves

distances within the Melbourne metropolitan areas, in Victoria and for interstate travel. Testing was also performed at the Department of Transport Energy & Infrastructure (DTEI), Regency Park, SA to independently assess performance and emissions.

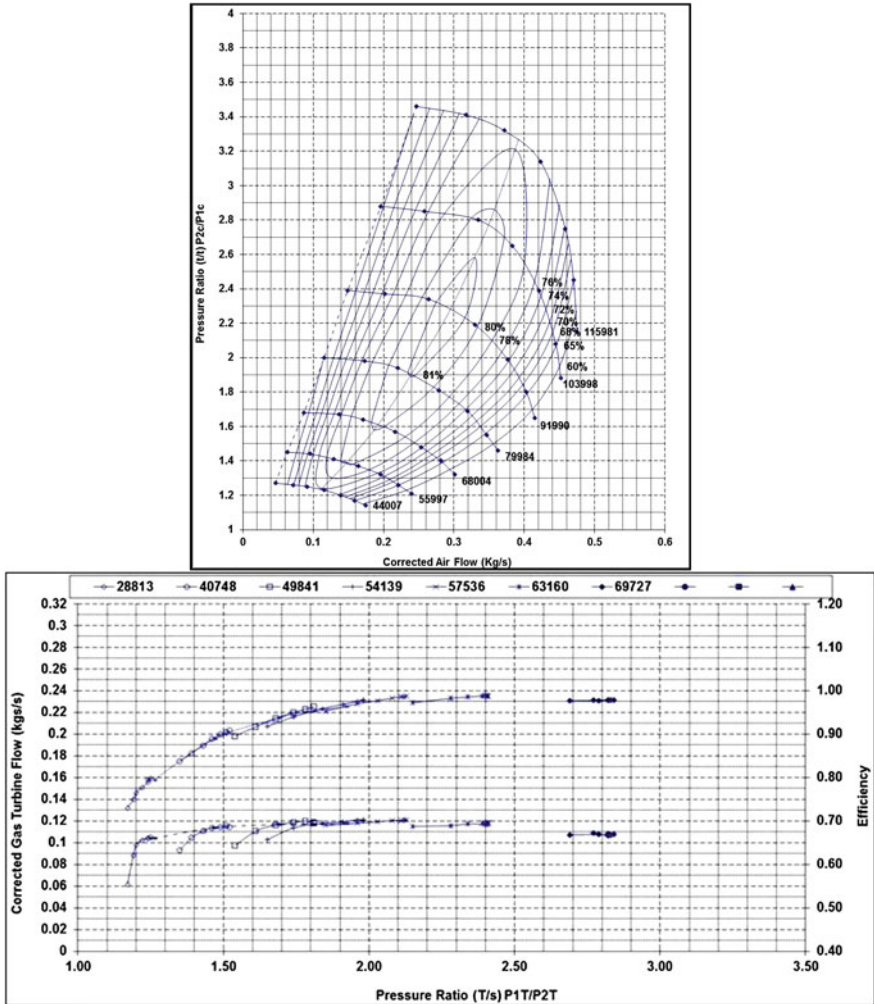


Fig. 3 New compressor and turbine maps

Vehicle tested is a Mercedes Benz Actros 2646, 12 litre V6, turbocharged and intercooled. Modifications are AVT phase II, LPG conversion kit. 4 × 250L usable LPG Manchester tanks have been installed. The DTEI Test conditions are vehicle loaded with flat bed trailer and 14 concrete blocks and weighed at 39.03 ton.

The South Australian Department for Transport, Energy and Infrastructure (DTEI) has an emissions test laboratory with a chassis dynamometer facility that can test light and heavy vehicles running on all fuel types including LPG. The facility is one of five labs certified to run the DT80 test in Australia. The laboratory is not, however, certified to perform ADR emissions tests (as the Euro III, Euro IV,

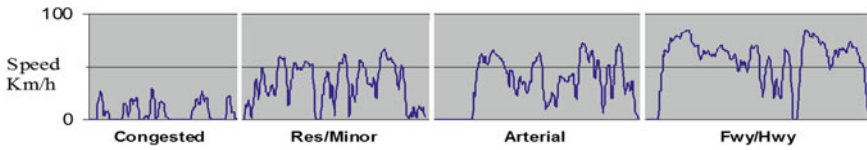


Fig. 4 CUEDC velocity schedule

and US EPA). The emissions equipment in the facility provides integrated results rather than bagged results, hence second by second fuel consumption and emissions data is available. Emissions measured are NO_x, CO, CO₂, CH₄, THC, PM₁₀, Opacity and fuel consumption, all emissions are reported as total grams, grams per kilometre, grams per ton kilometre and grams per kilowatt hour except for opacity that is measured as a percentage. All measurements are converted from ambient conditions, measured using a weather metre, to standard temperature and pressure STP.

The DTEI facility is set up for the in-service testing of vehicles, with the Composite Urban Emissions Drive Cycle (CUEDC) test being the most appropriate cycle to use in order to obtain in-service fuel consumption and emissions performance. CUEDC tests were developed as part of the Diesel NEPM Preparatory projects. They cover all diesel vehicle types including private passenger vehicles, light commercial vehicles, rigid trucks and articulated trucks and buses. Each CUEDC is split up into four road flow categories, representing driving on residential streets, in congested traffic conditions, on arterial roads and on free-ways, hence fuel consumption and emissions results are presented for each road type category as well as the overall results and the second by second emissions data. The CUEDC tests are hot start tests, but have also been performed as cold starts. Given that the amount of testing involved required more than one day testing the CUEDC test was also be performed as a cold start test. Development of the CUEDCs was commissioned by the Australian National Environment Protection Commission in 1998 as part of the Diesel National Environment Protection Measure. Data was collected in Sydney, Australia. CUEDCs were created with the intention to closely replicate actual Australian on-road urban driving. CUEDCs are used for chassis based dynamometer testing of both heavy and light vehicles. They are composed of four distinct drive cycle segments: congested, minor roads, arterial and highway. A set of the four CUEDC segments takes a total of about 30 min. There are six CUEDC cycles, one for each of the six ADR vehicle categories: MC, NA, NB, ME, NC, NCH. The particular cycle is depicted in the following Fig. 4.

In addition to these tests, DT80 short tests made by accelerations and decelerations were also performed. The DT80 test is presented in Fig. 5. The DT80 forms a part of the in-service diesel vehicle emission standard that has been proposed by the Commonwealth. The test involves accelerating the vehicle to 80 km/h at wide open throttle, three times. The emissions limits for the Actros when running on diesel according to the standard are 1.2 g/t km NO_x, 0.03 g/t km

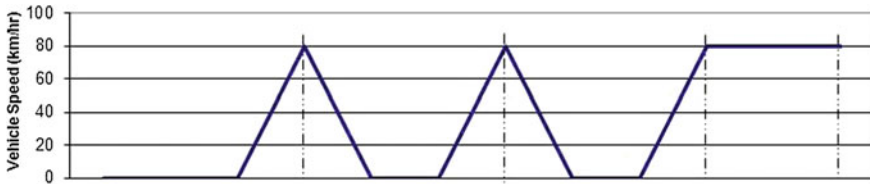


Fig. 5 DT80 velocity schedule

PM10 and less than 25 % average for opacity, there are no current in-service limits for LPG. This test will indicate the fuel consumption and emissions performance of the Actros at wide open throttle and be compared when running on diesel and LPG. The test will also ensure that when running on diesel the vehicle at least meets the DT80 in service emission standard.

The testing also includes steady state engine mapping i.e. determining the performance of the vehicle at full load, part loads while cruising at 100 km/h and idle. This testing will enable the project team to analyse the fuel consumption and emissions performance of the vehicle over its entire operating range.

Results of the tests are given as follows. Data for the drive Melbourne to Adelaide and return are also provided.

Testing at the Department of Transport Energy & Infrastructure, Regency Park, SA.

- 2 × DT80 tests (3974 & 3975), performed with truck failing on NOx by more than 20 %.
- 2 × CUEDC tests (3976 & 3977), performed and results printed and discussed.
- Adjustment made to fuel tables and two more DT80 tests (3978 & 3979), performed.
- NOx levels dropped to 40 % under the DT80 limit, a level considerably lower than Euro 3 diesel Actros.
- 2 × CUEDC tests (3983 & 3984), performed with results showing LPG truck somewhere between Euro 3 and Euro 4 NOx levels.
- CO₂ levels 10 % better than diesel on DT80 test and about even with diesel on CUEDC tests.
- Average fuel ratio against diesel over 7 points from 80 kW to 180 kW is 1.67:1.
- Fuel used for testing 434L for 361.4 k lm or 120L/100 klm. Diesel rate for testing 90L/100 klm. Ratio of 1.3:1.

Emission results	Segment	NOx	CO	CO2	CH4	THC	PM-LLSP	Opacity Av(%)	Opacity max(%)	FuelCon (L/100k)
g/km	1	30.338	30.015	4194.621	6.539	0.851	285.265	2.022	28.357	161.634
g/km.t	1	0.779	0.770	107.665	0.168	0.022	7.322			
g/kWh	1	14.713	14.556	2034.230	3.171	0.413	138.342			
g/km	2	16.441	14.030	2377.670	1.344	0.165	139.514	3.209	28.286	91.404

(continued)

(continued)

Emission results	Segment	NOx	CO	CO2	CH4	THC	PM-LLSP	Opacity Av(%)	Opacity max(%)	FuelCon (L/100k)
g/km.t	2	0.422	0.360	61.028	0.034	0.004	3.581			
g/kWh	2	6.418	5.477	928.233	0.525	0.065	54.466			
g/km	3	15.367	11.638	2188.193	1.505	0.186	123.157	2.766	27.966	84.048
g/km.t	3	0.394	0.299	56.165	0.039	0.005	3.161			
g/kWh	3	6.486	4.912	923.539	0.635	0.079	51.979			
g/km	4	13.096	2.809	1644.676	0.674	0.095	40.457	1.778	18.452	62.811
g/km.t	4	0.336	0.072	42.214	0.017	0.002	1.038			
g/kWh	4	6.143	1.318	771.427	0.316	0.045	18.976			

Emission results	NOx	CO	CO2	CH4	THC	PM-LLSP (mg/–)	Opacity Av(%)	Opacity max(%)	FuelCon (L/100k)
g/km	18.318	8.187	2580.050	1.581	0.262	128.801	2.432	32.265	98.773
g/km.t	0.470	0.210	66.223	0.041	0.007	3.306			
g/kWh	6.557	2.930	923.478	0.566	0.094	46.102			

DNEPM Limits	NOx (g/km.t)	PM (mg/km.t)	Average Opacity (%)
Limit	1.2	30.0	25.0
Result	PASS	PASS	PASS

Figures 6 and 7 present the emission test report for one of the CUEDC and one of the DT80 tests.

Figure 8 presents the NO₂, CH₄ and CO₂ emissions at different engine powers for the Diesel and the LPG trucks from these tests.

Figure 9 presents the fuel costs of Diesel and LPG. The fuel costs used are based on an average wholesale price including rebates over the past six months. They are \$0.51/L LPG and \$1.46/L diesel.

Figure 10 finally presents the litres/100 km of the diesel and the LPG operating at different conditions and the resulting \$/100 km

Data of the drive to Adelaide and return are also included as a reference to confirm the significant fuel economy benefits.

Drive to Adelaide.

- Total distance covered: 745.8 km.
- Total fuel used: 685 litres.
- Average fuel consumption: 91.84 l/100 km.
- Diesel consumption for the same trip and conditions: 52.3 l/100 km.
- Ratio of LPG to diesel fuel consumption in litres 1.76:1.

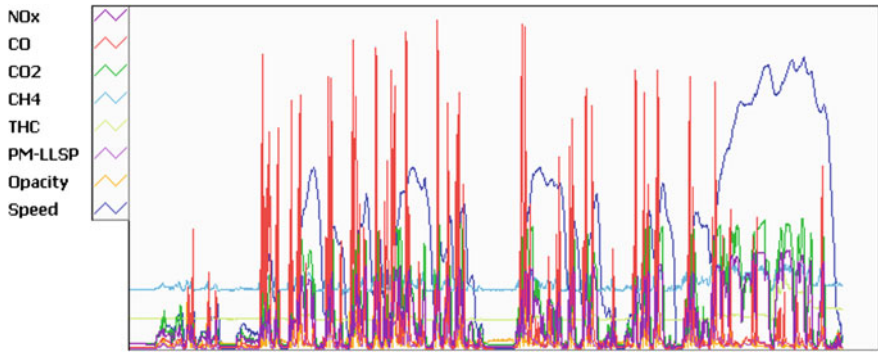


Fig. 6 Emission test report CUEDC

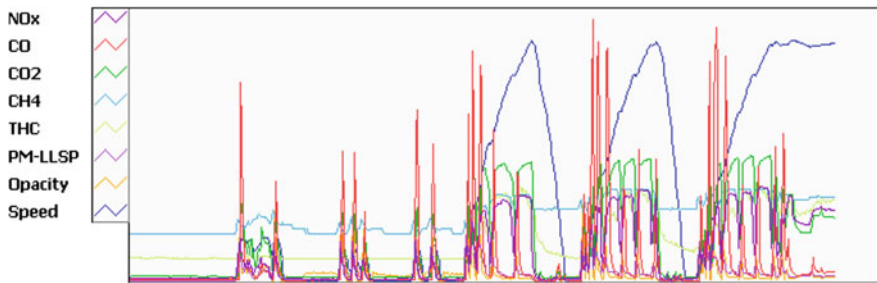


Fig. 7 Emission test report DT80

- Ratio of LPG to diesel fuel consumption by mass 1.1:1 (i.e. A 10 % efficiency advantage to the diesel as currently tested).
- Climb up through Pentland Hills saw minimum speed of 50 kph in 5 high @ 1900 RPM with 16 PSI boost.
- Diesel truck saw 50 kph min up the same section in Auto 7 low, 32 psi boost.
- Climb up Adelaide Hills, min speed 35 kph, 5 high @1900RPM.
- Diesel min speed: 40 kph, 6 high @1500 RPM, 32 psi boost.
- LPG truck cruised well with both speed limiter and cruise control operating flawlessly.

Return trip from Adelaide to AVT, Melbourne.

- Total distance covered including trip to Sergeants Transport in Ballarat, 737.3 klm.
- Fuel used on return trip 721.4 L.
- Average fuel consumption for the return trip 97.8 L/100 klm.
- Min speed up Adelaide hills 30kph @22psi boost, after coming to a complete stop on the hill and re-starting.

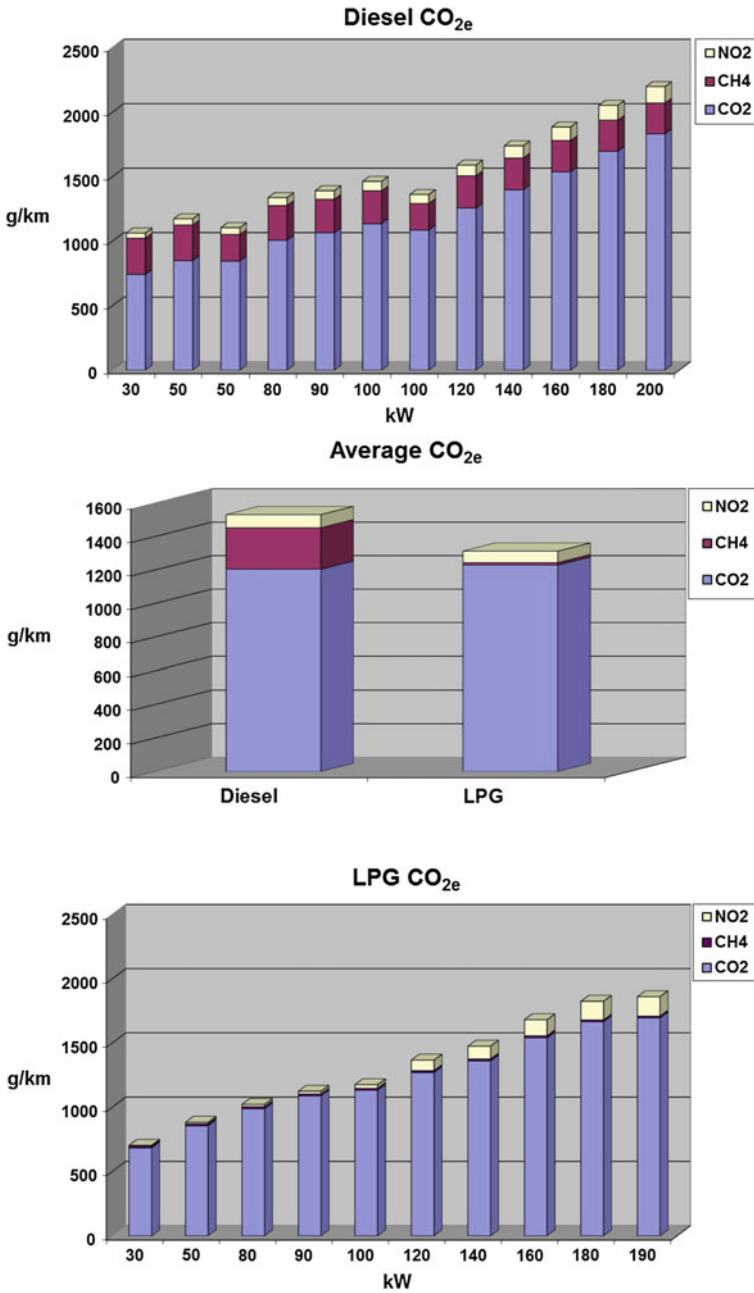


Fig. 8 NO₂ + CH₄ + CO₂ tailpipe emissions (as measured by SA DTEI on MB Actros 2646, averaged over 30–200 kW at the wheel)

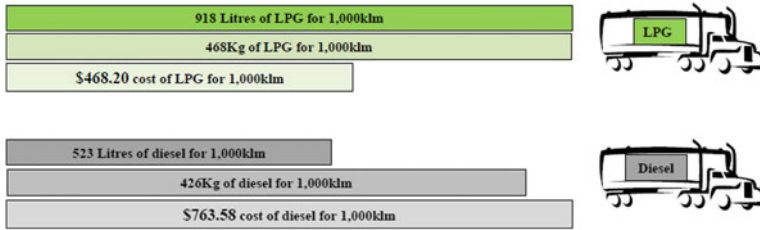


Fig. 9 Fuel costs of diesel and LPG converted vehicles

- Diesel speed for the same hill 40kph @32psi boost, without stopping and re-starting on hill.

Overall fuel usage.

- FE lpg Actros Total distance covered 1844.2 klm, fuel used 1840.4 L, Av 99.8 L/100 klm.
- 2646 Actros Total distance covered 1783.5 klm; fuel used 1050 L, Av 58.9 L/100 klm (with less distance covered in testing by 100 klm, so less weighting for higher consumption levels).
- Overall LPG to diesel ratio 1.69:1
- Oil usage for the entire trip 1.4 Litres.

The major advantages of the LPG are the reduced pollutant emissions with particular emphasis to the particulate, the improved energy security (reduced dependence on foreign imported oil), the reduced tailpipe and fuel life cycle carbon dioxide emissions, and finally the lower fuel cost. The fuel cost is a significant component of a truck operation. Therefore, the fuel economy may be the key motivation to convert a Diesel truck to LPG. The LPG converted vehicle permits a saving of almost 300 \$ every 1,000 km corresponding to a 40 % cut of the fuel bill.

3 Summary

The AVT technology permits significant fuel cost savings of almost \$300 per 1000 km. These savings permit a short time for pay-back the conversion costs.

The AVT technology permits significant emissions reduction of particulate, NOx, tailpipe NO₂, CH₄ and CO₂, fuel cycle CO_{2-e}. This makes the converted truck more environmentally friendly than the Diesel.

The AVT technology is simple and reliable and permits much longer maintenance intervals translating in lower cost and less downtime.

The current AVT conversion kit is for a 3 pedal Euro 3 Actros, 26xx series. The company is working on a kit for the Euro 4 and 5 Actros engine, and also assessing other vendors' engines for conversion.

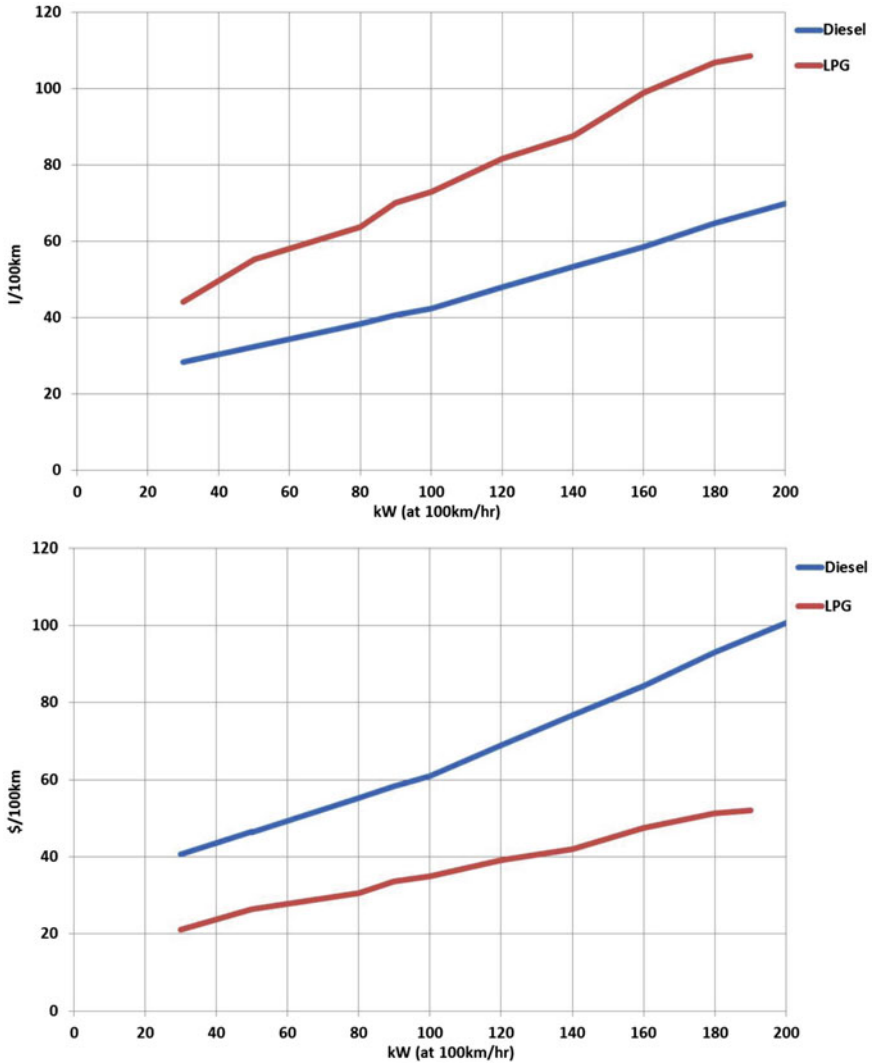


Fig. 10 Litres/100 km and \$/100 km comparison (as measured by SA DTEI on MB Actros 2646, based on wholesale prices less rebates Diesel \$1.44/l and LPG \$0.48/l)

The AVT technology has now been proven after 4 years and \$7million invested. Global patent is in place with many other barriers to entry including more patents possible.

The company is working on an enhanced kit/dedicated design for a LPG engine having better than Diesel fuel conversion efficiencies full and part load.

References

1. Australian Government Bureau of Infrastructure, Transport and Regional Economics (2009) Information sheet 34—road and rail freight: competitors or complements, DOTARS ID 08470, ISSN 1836-697X. www.bitre.gov.au/publications/23/Files/IS34_RoadRailFreight.pdf
2. Australian Government Department of Climate Change (2009) Australia's national greenhouse gas inventory: update quarterly estimates of Australia's national inventory: June quarter 2009. www.climatechange.gov.au/en/climate-change/~ /media/publications/greenhouse-acctg/national-greenhouse-accounts-june-2009.ashx
3. Australian Government, Department of the Environment, Water, Heritage and the Arts (2000) Life-cycle emissions analysis of alternative fuels for heavy vehicles—stage 1. www.environment.gov.au/settlements/transport/publications/pubs/lifecycle.pdf
4. Australian Government, Department of the Environment, Water, Heritage and the Arts (2000) Comparison of transport fuels final report (EV45A/2/F3C) to the Australian greenhouse office on the stage 2 study of life-cycle emissions analysis of alternative fuels for heavy vehicles. www.environment.gov.au/settlements/transport/comparison/pubs/comparison.pdf
5. US Department of energy, Energy efficiency and renewable energy, vehicle technology program (2009) FY 2009 progress report for advanced combustion engine research and development. www1.eere.energy.gov/vehiclesandfuels/pdfs/program/2009_adv_combustion_engine.pdf
6. www.delphi.com/pdf/emissions/Delphi-Heavy-Duty-Emissions-Brochure-2009.pdf
7. greet.es.anl.gov
8. simapro.rmit.edu.au/LCA/datadownloads.html

Analysis of Engine Oil Containing MoDTC on the Thermo-Oxidation Engine Oil Simulation Test (TEOST 33C)

Linchun Wang, Liping Wang and Guiyun Li

Abstract The Thermo-oxidation engine Oil Simulation Test (TEOST 33C), one request of the new ILSAC GF-5 specification for passenger car, has been developed as a simulation test to evaluate the “coking” of engine oil in turbocharger. Generally, molybdenum dithiocarbamate (MoDTC) is added into engine oil as an effective friction modifier to improve fuel economy. Zinc dialkyldithiophosphate (ZnDDP) has also been used as a multifunction additive in engine oils for more than 50 years. However, the results of this study showed that the coexistence of MoDTC and ZnDDP in engine oil could cause deposits accretion of the oil in the TEOST 33C. Pressurized Differential Scanning Calorimetry (PDSC) revealed that excess MoDTC led to the oxidative degradation of engine oil and there was no obvious relationship between oxidation stability and “coking” of engine oil. In addition, the elemental analysis of deposits demonstrated that deposits accretion was not caused by the increase ash of MoDTC. In summary, the MoDTC coexisted with ZnDDP might be acted as a “coking” catalyst under high temperature.

Keywords MoDTC · ZnDDP · TEOST 33C · PDSC · Deposits

1 Introduction

The vehicles and its accoutrements have taken many forms over the years in which the automobile has served civilization for both work and pleasure. In recent years, some advanced technological innovations have been developed and used to

F2012-A03-009

L. Wang (✉) · L. Wang · G. Li
PetroChina Lanzhou Lubricating Oil R&D Institute, Lanzhou 730060, China
e-mail: wangchunlin_rhy@petrochina.com.cn

improve fuel economy of vehicles, such as direct injection, variable valve and turbochargers. The turbocharged engine is more powerful and more efficient than the naturally aspirated engine. This is attributed to its excellent ability of forcing more intake air and proportionate fuel into the combustion chamber. Engine oil is pumped to lubricate the turbocharger bearing which is heated by over 650 °C exhaust stream and worked at high temperature. Thermal coking and oxidative degradation of engine oil in the turbocharger bearing area during hot shut-down may result in deposit build-up in the bearing area which can lead to the loss of engine performance and possible engine failure [1]. The Thermo-Oxidation Engine Oil Simulation Test (TEOST 33C) was developed as a lubricant test for the evaluation of turbocharger protection [2]. This test was demanded for International Lubricant Standardization and Approval Committee (ILSAC) GF-5 which required the mass of deposits in TEOST 33C under 30 mg [3].

As is well-known, energy conservation and emission reduction is one of the greatest focuses in today's world. For this reason, energy conserving engine oil has been developed to improve the fuel economy of passenger cars. There are two ways to improve the fuel economy of engine oil: lowering the viscosity of engine oil and adding friction modifiers into engine oil [4]. Molybdenum dithiocarbamate (MoDTC) is a very effective friction modifier to reduce engine friction and improve fuel economy. Many studies [5, 6] have shown that the friction-reducing activity of MoDTC is based on the exchange of functional groups with ZnDDP. On the other hand, MoDTC is reported to increase the deposits in TEOST 33C [7]. In this study, the influence of MoDTC and ZnDDP on the deposit of engine oil in Thermo-oxidation Engine Oil Simulation Test (TEOST 33c) was analyzed.

2 Summary of Test Method

2.1 *Thermo-Oxidation Engine Oil Simulation Test (TEOST 33C)*

TEOST 33C was based on ASTM D6335. A sample of the engine oil at a temperature of 100 °C that contains ferric naphthenate and is in contact with nitrous oxide and moist air is pumped at a set flow rate past a tared depositor rod. The rod is resistively heated through twelve, 9.5 min temperature cycles that go from 200 to 480 °C. When the twelve cycle program is complete, the depositor rod rinsed of oil residue and dried and the gross rod mass obtained. The sample is flushed from the system and filtered through a tared filter. The mass of deposits on the rod plus the mass of deposits on the filter is the total deposit mass. The test conditions are summarized in Table 1.

Table 1 Test condition for TEOST 33C

Program	Parameter
Sample volume, ml	116
Catalyst (Fe), ppm	100
Reactor temp, °C	100
Depositor rod temp, °C	200–480
Test cycle	12
Test duration, min	114
Pump rate, g/min	0.4
Wet air flow, ml/min	3.5
N ₂ O, ml/min	3.5

2.2 Pressurized Differential Scanning Calorimetry

PDSC was based on ASTM D6186. In this study, an oil sample of approximately 3.0 mg was employed. The oxidation of the oil was carried out in the presence of 50 ppm iron from an iron naphthenate oxidation catalyst. Testing was performed at 210 °C under 500 psig oxygen and an oxygen purge rate of 100 ml/min. Test results were reported as the oxidation induction time (OIT) resulting from an exothermic release of heat caused by oxidation of the thin-film of oil.

2.3 Elemental Analysis of Deposits

Elemental composition of the deposits was studied by X-ray Photoelectron Spectroscopy and CCHN-O analysis.

3 Experimental Details

3.1 Test Oils

Table 2 showed the properties of the oils used in this study. The lubricating oil-A was an API SM/GF-4 5w-30 oil containing ZnDDP (P % = 800 ppm), which was prepared by blending a baseline of API Group °C base oils, a SM/GF-4 additive package, a viscosity index modifier and a pour point depressant. Other test oils were fabricated by changing the content of ZnDDP and MoDTC. The test oils of oil-B to oil-E were prepared by adding equal ZnDDP (P % = 800 ppm) and different contents of MoDTC respectively; the test oils of oil-F to oil-J were fabricated by adding equal MoDTC (Mo % = 500 ppm) and different contents of ZnDDP, respectively.

Table 2 Test oil matrix

Oil code	P content (ppm)	Mo content (ppm)	TEOST 33C (mg)	PDSC (min)
Oil-A	800	0	42.5	17.7
Oil-B	800	200	43.9	18.5
Oil-C	800	330	46.3	21.8
Oil-D	800	500	47.4	19.7
Oil-E	800	700	58.4	18.2
Oil-F	0	500	22.8	–
Oil-G	200	500	33.8	–
Oil-H	400	500	34.9	–
Oil-I	600	500	46.0	–
Oil-J	800	500	47.4	–
Oil-K	800	0	19.0	18.4
Oil-L	800	200	26.6	19.0
Oil-M	800	330	40.2	22
Oil-N	800	500	52.0	18.4
Oil-O	800	700	62.0	18.1

The lubricating oil-K was an API SN/GF-5 5w-30 oil containing ZnDDP (P % = 800 ppm), which was prepared by blending a baseline of API Group °C base oils, a SN/GF-5 additive package, a viscosity index modifier and a pour point depressant. Other test oils from oil-L to oil-N were prepared by adding changing content of the MoDTC and equal ZnDDP (P % = 800 ppm).

4 Results and Discussion

4.1 Analysis of Deposit Formation Factors

The relationships of the MoDTC content and deposits in TEOST 33C have been showed in Fig. 1. The mass of deposits increased with the increasing MoDTC content. However, no linear relationship could be observed between the MoDTC content and deposits in TEOST 33C. Particularly, with more than 200 ppm of molybdenum content, the addition of MoDTC led to a significant increase in the deposit formation. Furthermore, Fig. 1 also indicated that the test oils with different additive package generated different mass of deposits in TEOST 33C. The oil prepared by blending SN/GF-5 additive package generated fewer deposits than the oil prepared by blending SM/GF-4 additive package at a low level of MoDTC content (0–300 ppm). This revealed that some components of additive package influenced deposits obviously.

Figure 2 displayed the relationship between the MoDTC content and OIT of PDSC at 210 °C. Originally, the OIT increased with the increasing addition of

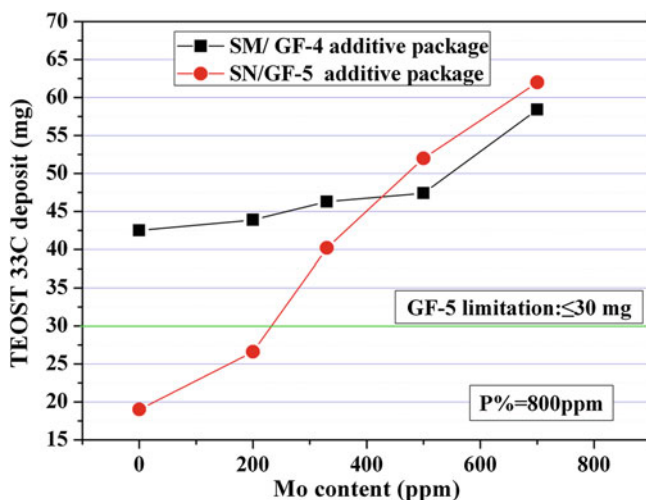


Fig. 1 Effect of MoDTC content on TEOST 33C

MoDTC. When the amount of Mo increased to 330 ppm, the sample oil showed the highest OIT. Then, the OIT reduced with increasing the addition of MoDTC. This phenomenon demonstrated that there was a maximize proportion of MoDTC to ZnDDP to improve oxidation stability of engine oil. Compared Fig. 1 with Fig. 2, there was no relationship between oxidation stability and “coking” of engine oil. Satoru Yoshida [7] used modified TEOST 33C with a temperature of 480 °C to evaluate the effects of test temperature. The results indicated that the high temperature test condition such as 480 °C promoted deposit accretion by engine oil containing MoDTC in the 33C.

As seen in Fig. 3, the engine oil containing one level MoDTC (Mo % = 500 ppm) and no ZnDDP generated fewer deposits, and the mass of deposits increased with increasing the addition of ZnDDP. It is suggested that few deposits (≤ 30 mg) were generated in a low content of ZnDDP and a high content of MoDTC. From Figs. 1 and 3, it can be seen that the concomitance of MoDTC and ZnDDP can accelerate deposit formation in TEOST 33C.

4.2 Elemental Analysis of Deposits

The deposits in the TEOST 33C were collected from the depositor rod. Fluorescent X-ray and CHN-O analysis were used to estimate the other elemental formation of deposits. Table 3 showed the elemental analysis results of new oils. Table 4 showed the elemental analysis deposits in the TEOST 33C. As shown in Table 2, more than 99 % elements of new oils consisted of C, H, N and O elements. The mass of other elements was attributed to the mass of additives in oils. In Table 3,

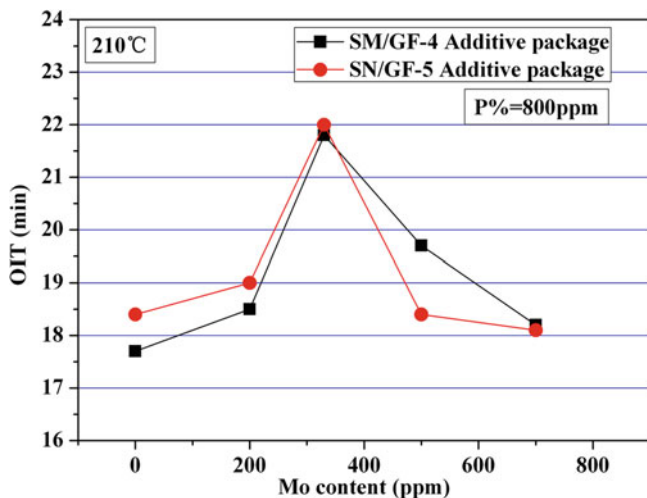


Fig. 2 Effect of MoDTC content on PDSC (210 °C)

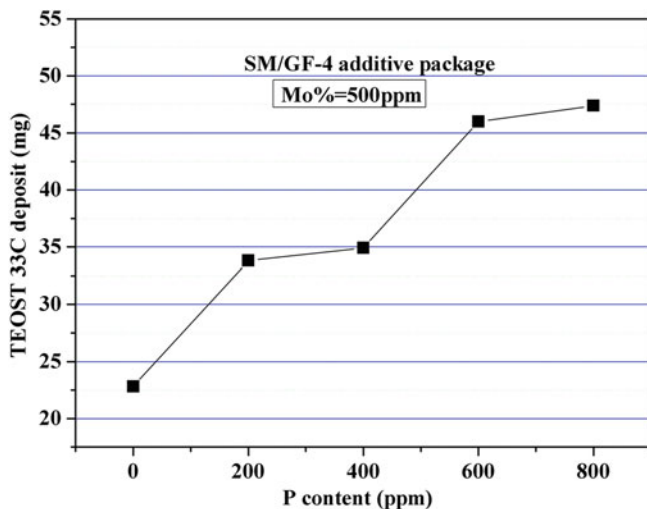


Fig. 3 Effect of ZDDP content on TEOST 33C

40–50 % of the deposit was comprised of C, H, N, and O elements. The high content of Ca in deposits indicated that Ca would be deposited more easily than other elements. It suggests that the detergent was easier than other additives to be adsorbed and deposited on the surface of depositor rod. Compared the mass of MoDTC in new oils with ash of molybdenum in deposits, the mass of molybdenum was not a significant source of deposits accretion.

Table 3 Elemental analysis of new oils

Oil code	CHNO (%)	S (%)	P (%)	Ca (%)	Zn (%)	Mo (%)
Oil-A	99.4	0.34	0.08	0.16	0.10	0.0
Oil-D	99.3	0.38	0.08	0.16	0.10	0.05
Oil-E	99.3	0.40	0.08	0.16	0.10	0.08
Oil-G	99.6	0.05	0.0	0.16	0.0	0.05

Table 4 Deposits in the TEOST 33C

Oil code	TEOST 33C (mg)	CHNO (%)	S (%)	P (%)	Ca (%)	Zn (%)	Mo (%)	Fe (%)
Oil-A	42.5	53.1	9.5	6.0	17.7	7.4	0.0	6.3
Oil-D	47.4	47.9	10.8	5.3	17.3	7.9	4.1	6.7
Oil-E	58.4	47.4	10.5	5.7	17.9	7.2	5.3	6.0
Oil-G	22.8	47.2	10.0	5.2	30.1	0.0	4.8	6.7

5 Conclusion

An investigation has been studied to evaluate the factors of engine oil containing MoDTC and ZnDDP on the TEOST 33C. Based on the experimental results of this study, the following conclusion could be drawn.

- (1) The MoDTC coexisted with ZnDDP could cause obvious deposits accretion of engine oil during TEOST 33C.
- (2) Test oils prepared by different additive packages and equal MoDTC generated different masses of deposits in TEOST 33C, but the trend of deposits accretion with the increase in addition of MoDTC was similar.
- (3) Oil with a low content of ZnDDP and a high content of MoDTC could generate few deposits.
- (4) There was a maximized proportion of MoDTC to ZnDDP to improve oxidation stability of engine oil.
- (5) There was no obvious relationship between oxidation stability and “coking” of engine oil.
- (6) 40–50 % of the deposits were consisted of C, H, N, and O.
- (7) The mass of molybdenum in new oil was not a significant source of deposits accretion in TEOST 33C.

Acknowledgements The authors would gratefully acknowledge the previous work of Satoru Yoshida and Yasushi Naitoh in research of TEOST 33C. Assistance from Wang aixiang and Xu jinbao is also acknowledged.

References

1. Keller J, Lowther H, Rogers T (1981) Lubricant performance in passenger car turbochargers. SAE Technical Paper 810016
2. Florkowski D, Selby T (1993) The development of a thermo-oxidation engine oil simulation test (TEOST). SAE Technical Paper 932837
3. ILSAC GF-5 (2009) Standard for passenger car engine oils
4. Tseregounis S, McMillan M, Olree R (1998) Engine oil effects on fuel economy in GM vehicles—separation of viscosity and friction modifier effects. SAE Technical Paper 982502
5. Korcek S et al (1998) Retention of fuel efficiency of engine oils. In: Proceedings of the 11th international colloquium, Esslingen
6. Arai K et al (1995) Lubricant technology to enhance the durability of low friction performance of gasoline engine oils. SAE Paper 952533
7. Yoshida S, Naitoh Y (2008) Analysis of deposit formation mechanism on TEOST 33C by engine oil containing MoDTC. SAE Paper 2008-01-2480

Effect of Ash-Less Antioxidants on Fuel Efficiency Retention of PCMO Containing MoDTC

Liping Wang, Linchun Wang, Guiyun Li and Xiaohong Xu

Abstract The anti-oxidation and fuel efficiency properties of both fresh and aged oils were evaluated using a modificatory Rotary Bomb Oxidation Test (RBOT) and Pressurized Differential Scanning Calorimetry (PDSC). The fuel efficiency properties of a set of engine oils were investigated before and after the aging process. Results of PDSC and SRV indicate that the type of antioxidants, their concentrations, and the ratio of phenol to amine have great effects on the anti-oxidation capability and fuel efficiency retention of the oils. The results show that the use of molybdenum dithiocarbamate (MoDTC) in combination with ash-less antioxidants can lead to pass the Sequence VIB test for fuel efficiency and durability as defined by the ILSAC GF-4 specification.

Keywords Fuel efficiency retention · Passenger car motor oil · Ash-less antioxidants · Molybdenum dithiocarbamate

1 Introduction

Fuel efficiency is one of the most important performance requirements for Passenger Car Motor Oil (PCMO) [1]. In order to increase the fuel efficiency and its retention of the engine oil, for example, the viscosity of the engine oil is lowered by decreasing the viscosity of the base oil or changing the viscosity index

F2012-A03-010

L. Wang (✉) · L. Wang · G. Li · X. Xu
PetroChina Lanzhou Lubricating Oil R&D Institute, Lanzhou 730060, China
e-mail: wanglipinglz_rhy@petrochina.com.cn

improver. However, friction coefficient cannot be reduced in the boundary lubricating condition where the viscosity does not contribute to mitigation of the friction [2, 3]. Consequently, a friction modifier (FM) has recently come to be added so as to reduce the wearing in the boundary lubricating area. With respect to the friction modifiers, it is known that organic molybdenum compound such as molybdenum dithiocarbamate and molybdenum dithiophosphate (MoDTP) are highly effective as described in some early papers [3, 4].

Since MoDTC contains no phosphorus, increase its addition amount does not cause decrease in the catalytic activity. MoDTC is used in combination with zinc dithiophosphate (ZnDTP) as an antioxidant, anti-wear and energy saving multi-function agent, however, ZnDTP contains phosphorus and gives adverse influence on the exhaust gas catalyst as mentioned above, its addition amount is limited so that good friction-mitigating effect cannot unfavorably be maintained for a long time [5, 6]. Further, it is proposed that ash-less antioxidants be used in combination with MoDTC, this combination does not afford adverse effect upon the exhaust gas catalyst. The MoDTC/ash-less antioxidants additive system is very effective on improving fuel efficiency, but the retention of fuel efficiency is gradually reduced during the aging process. Special attention should be given to fuel efficiency and its retention during the aging process [7, 8].

Thus, the objective of this study was to investigate the effect of MoDTC/ash-less antioxidants on the anti-oxidation and fuel efficiency retention capabilities using SRV and Rotary Bomb Oxidation Test (RBOT) tests, used in formulation of SM/GF-4 5 W-30 engine oils. The friction-reducing properties of a set of engine oils were investigated before and after the simulated aging process. Test results are then compared with those from the Sequence VIB results.

2 Experimental Procedure and Engine Oils

2.1 Test Methods

The following tests were conducted to evaluate the effects of antioxidant type, antioxidant concentration and antioxidant synergism on the fuel efficiency of Passenger Car Motor Oil (PCMO).

2.1.1 SRV

The friction coefficients of MoDTC/ash-less antioxidant additive system were investigated by an oscillating friction and wear apparatus, an Optimal SRV tester. Fig. 1 shows the schematic illustration of Optimal SRV friction and wear tester.

Fig. 1 Schematic view

2.1.2 RBOT

Engine oils were aged according to RBOT test procedure (ASTM D2272), which simulates a severe oxidation conditions. The samples were oxidized in the presence of water and a copper catalyst in a stainless steel pressure vessel under an initial pressure of 620 kPa.

2.1.3 PDSC

The Pressurized Differential Scanning Calorimetry (PDSC) test (ASTM D 6186) is a bench test designed to give an indication of the propensity of a formulated lubricant to oxidize. A small quantity of oil is weighed into a sample steel pan and placed in a test cell. The cell is heated to 210 °C and then pressurized with oxygen. It is held at a 210 °C and 3.5 MPa until an exothermic reaction occurs. The extrapolated onset time is measured and reported as the Oxidation Induction Time (OIT) for the lubricating oil.

2.2 Engine Oil Samples

The engine oil samples used in this study are defined in Table 2. All experiments were performed in an API SM quality SAE 5 W-30 PCMO. The base oil used was group III mineral oil of viscosity 31.0 mm²/s at 40 °C and 6.02 mm²/s at 100 °C. The concentrations of MoDTC and ZnDTP in the engine oil were adjusted at molybdenum concentration of 500 ppm and at phosphorus concentration of

Table 1 Lubricating oils used in the tests

Oil No	Classification	Characteristics	KV100° C, mm ² /s
Oil A	SAE 5 W-30	Mineral, group III	10.30
Oil B	SAE 5 W-30	Mineral, group III	10.32
Oil C	SAE 5 W-30	Mineral, group III	10.24
Oil D	SAE 5 W-30	Mineral, group III	10.34
Oil E	SAE 5 W-30	Mineral, group III	10.29

Table 2 PDSC-OIT@210 °C evaluation of engine oils

Oil No	Antioxidant types	Ratio of phenol to amine	Dosage/ %	PDSC-OIT/min
Oil A	Amines	/	a	12.2
Oil B	Phenols	/	a	14.6
Oil C	Amine/phenol	1:1	a	19.7
Oil D	Amine/phenol	1:1	2.0a	28.6
Oil E	Amine/phenol	2:3	2.0a	36.4

790 ppm by weight, respectively. Oil A, B, C, D and E contain the same amount of dispersants, detergents, viscosity index improver and other compounds, but differ in the relative amounts of ash-less antioxidant (Table 1).

3 Results and Discussion

3.1 Ant-oxidation Characteristics of Fresh Oils

Oxidative stability of engine oils were evaluated using PDSC, as illustrated in Table 2, very good anti-oxidancy can be achieved with engine oils that utilize the phenol-amine additive system. The OIT of OIL D and E are 2–3 degrees higher than the result of Oil A.

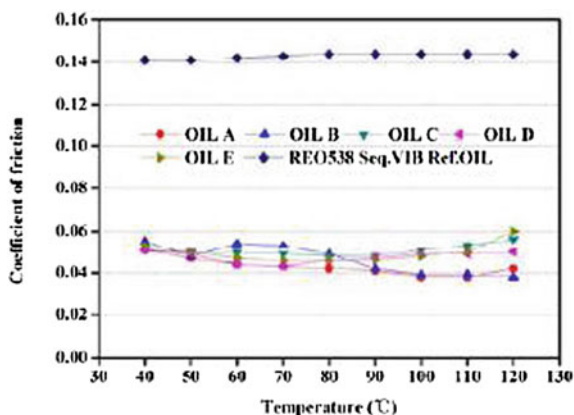
A combination of phenol and amine is more effective than phenol and amine alone in inhibiting oxidation in engine oils, since they work synergistically with each other in improving oxidation stability of engine oils.

3.2 Friction Characteristics of Fresh Oils

In the current study, we examine the friction coefficient of fresh and aged engine oils in controlled laboratory tests using a SRV test apparatus, cylinder-on-flat test rigs. The friction force is measured continuously. The test condition used for this test is given in Table 3.

Table 3 SRV test conditions

	Break in conditions	Actual test conditions
Load/N	50	400
Temperature/ °C	40	40–120
Amplitude/mm	1.5	1.5
Frequency/Hz	50	50
Test time/min	0.5	5.0

Fig. 2 Friction coefficients of fresh oils at different temperatures

The following test results were achieved on individual SRV machines according to the SRV HFRR test procedure.

The coefficients of friction (COF) did not change significantly by the used of phenol, amine and the combination of phenol/amine antioxidants as the tests progressed. The COF of all samples remained in the 0.04–0.06 range (Fig. 2).

Compared with the sequence VIB reference oil REO538, oil A–E containing MoDTC and ZnDTP can reduce the COF by approximately 0.08–0.10 from 40 to 120 °C. The frictional properties of oil A–E displayed as a trend the lowest COF, the synergistic action and formation of MoS₂ films by ZnDTP and MoDTC are attributed to the reduced friction properties.

It is clear that the friction coefficient of fresh oils containing the combination of phenol and amine began to increase with increasing the oil temperature when the temperature reached to 70 °C. On the contrary, the friction coefficient of fresh oils containing phenol and amine alone steadily decreased while the temperature reached to 70 °C.

These results suggest that the SRV test conditions may be unable to distinguish between different fresh engine oil samples containing different ash-less antioxidants.

Table 4 PDSC-OIT@210 °C evaluation of aged engine oils

No	PDSC-OIT/min		
	0 Hr Aged	8 Hr Aged	16 Hr Aged
Oil A	12.2	8.8	3.7
Oil B	14.6	9.3	5.8
Oil C	19.7	15.4	10.7
Oil D	28.6	21.5	13.5
Oil E	36.4	33.1	25.4

3.3 Engine Oil Ageing Test

Accelerated ageing test has been developed for the evaluation of engine oils using a standard RBOT apparatus according to ASTM D 2272 standard. Accelerated ageing tests were conducted on fresh oil samples during 8 and 16 h, respectively. The temperature of the bath was kept at 140 °C and the vessel is rotated at 100 rpm. This ageing method causes mainly anti-oxidant deterioration in the oil. After the tests, oxidative stability and friction properties of aged oils were evaluated using PDSC and SRV, respectively.

3.4 Ant-oxidation Characteristics of Aged Oils

Oxidative stability of aged oils were measured by PDSC, the results of this analysis are summarized in Table 4.

The present results showed that there is only a slight decrease in OIT for 8 h aging whereas the OIT values show a very sharp decrease for 16 h aging. Under the same conditions, the decrease in OIT is much more significant in Oil A–B as compared to Oil C–D. The results of Oil C and Oil D showed that the combination of phenol and amine is necessary for good anti-oxidancy, and the ratio of phenol to amine affected ant-oxidation characteristics more than dosage according to Oil D and Oil E.

3.5 Friction Characteristics of Aged Oils

Friction coefficients obtained with the different aged oils are presented in Fig. 3.

Figure 3a shows the friction-reducing properties of Oil A–E are partly lost after 8 h of oxidation. Friction coefficient increases suddenly from ultra-low value (0.04) to values above 0.10. It is known that the increase of friction coefficient can be attributed to the deterioration of ash-less anti-oxidants. And the friction-reducing property of Oil C is similar to that of Oil D, the result show that the dosage of phenol/amine antioxidant had little effect on the friction-reducing properties.

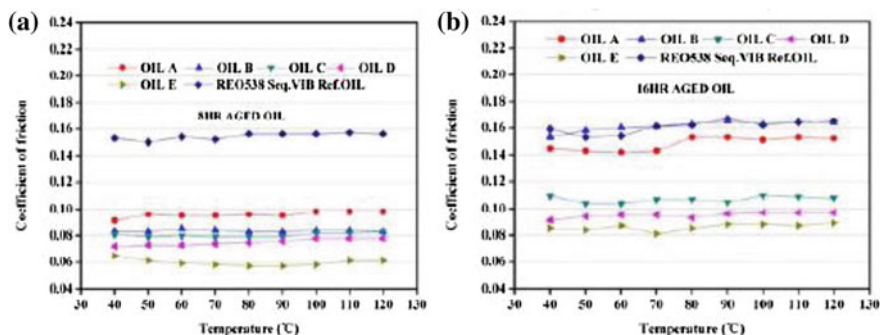


Fig. 3 COF of aged oils at different temperatures and aging hours (Left Fig. 3a; Right Fig. 3b)

Fig. 4 COF of aged oils of different aging hours

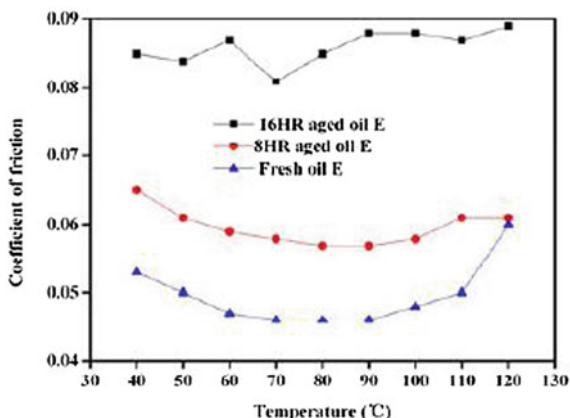


Figure 3b shows the friction-reducing properties of Oil B are completely equivalent to that of REO538 after 16 h of oxidation. The friction coefficient stays unchanged (of about 0.16) during the test process. Oil D and E exhibit a low friction coefficient of 0.08–0.10 and retain good friction-reducing behavior. But friction coefficients of the aged oils were higher than that of the fresh oils. The oils used for these investigations shows worse fuel efficiency retention due to aging time.

Figure 4 shows the change of friction coefficient of Oil E among fresh oil and aged oils of different aging hours. The increase of friction coefficient shows there has a tremendous impact on the fuel efficiency and it's retention of this oil. After 16 h of oxidation, the decrease of PDSC and the increase of COF indicate that the ash-less antioxidants have been deeply deteriorated.

Figures 3 and 4 show the superiority of the phenol-amine compounds in both friction reduction and friction reduction retention when compared to other fully formulated oils. Compositions with good anti-oxidation properties provide low coefficient of friction values, the lower coefficient of friction, the better the friction reducing property.

Table 5 Sequence VIB FEI2 engine test results

	Oil A	Oil B	Oil C	Oil D	Oil E	REO538 seq. VIB ref. oil
FEI 2, %	0.22	0.8	1.16	1.35	1.56	1.51

3.6 Fuel Efficiency Test Results-Seq. VIB

The impact of aging effects on engine oils' fuel efficiency retention can be observed respectively validated in Sequence VIB engine tests. Table 5 shows the Sequence VIB engine test results for oils A–E. The fuel economy improvement (FEI) results for stage2 are shown.

The FEI 2 results for Oils C, D and E were partially a result of these oils having lower aged friction coefficients than Oil A and B. Furthermore, Oil E had the lowest friction coefficient and passed the sequence VIB FEI2 limits. As a result, good correlation was observed between the friction coefficients after 16 h aging and FEI-2 results from the VIB test. Most interestingly, the results for Oils C, D and E show that oils containing phenol/amine and MoDTC have good fuel efficiency retention properties than Oils A and B that containing phenol and amine alone. The results illustrate the same synergism compared with that of the fresh oil.

4 Conclusions

Results of PDSC and SRV indicate that the type of antioxidants, their concentrations, and the ratio of phenolic to amine have great effects on the antioxidation capability and fuel efficiency retention of the oils.

The OIT and the frictional properties of both fresh and aged oils containing MoDTC were improved significantly with the addition of phenol and amine antioxidants.

The friction coefficients properties of the aged oil after RBOT tests were measured, and the results illustrate the same synergism compared with that of the fresh oil.

These results suggest that MoDTC in combination with phenolic and amine possess excellent antioxidative synergism and can extend the fuel efficiency retention. The results show that the use of MoDTC in combination with ash-less antioxidants can lead to pass the Sequence VIB test for fuel efficiency and durability as defined by the ILSAC GF-4 specification.

Acknowledgments The authors would like to thank the PetroChina Lubricant Company for supporting the fuel-economy engine oil research activities. This paper could not have been written without the support of the gasoline engine oil research working group. And the authors wish to thank Ms Lei Ailian and Wang Aixiang for their assistance with the SRV friction coefficient measurements and Mr Qiu Jianwei and Xu jinbao for performing RBOT engine oil aging tests.

References

1. Holmberga Kenneth, Anderssona Peter, Erdemirb Ali (2012) Global energy consumption due to friction in passenger cars. *Tribol Int* 47:221–234
2. Roshan Rupesh, Priest Martin, Neville Anne et al (2011) Friction modeling in boundary lubrication considering the effect of MoDTC and ZnDTP in engine oils. *Tribology Online* 6(7):301–310
3. Bovington CH (2010) Friction, wear and the role of additives in controlling them. *Chem Technol Lubr* 2:77–105
4. Skjoedt Martin, Butts Ryan, Assanis Dennis N et al (2008) Effects of oil properties on spark-ignition gasoline engine friction. *Tribol Int* 41(6):556–563
5. Yoshida S, Naitoh Y (2006) The effect of ash-less antioxidants type on friction reduction durability on engine oils containing MoDTC. SAE Technical Paper 2006-01-3415
6. Hu J, Hu Y, Qiu Z, Sun Y (2007) Evaluation on synergistic antioxidation of molybdenum dialkydithiocarbamate with arylamine antioxidant. SAE Technical Paper 2007-01-4135
7. Boffa A, Hirano S (2001) Oil impacts on sequence VIB fuel economy. SAE Technical Paper 2001-01-1903
8. Yamada Y, Ishimaru M, Yaguchi A, Inoue K et al (2000) Retention of friction reducing performance of MoDTC-containing fuel efficient gasoline engine oils during use. SAE Technical Paper 2000-01-2053

Semi-Empirical Correlations of Physical and Chemical Delay Period of Diesel-Gasoline Combustion

Wei Jet Thoo, Arman Kevric, Hoon Kiat Ng, Suyin Gan
and Paul Shayler

Abstract This study focuses on developing a semi-empirical ignition delay (ID) correlation which is able to predict the ID of various diesel-gasoline fuel blends under steady-state conditions. Prediction from chemical kinetic modelling is compared to experimental data to determine the influential parameters which control the change of ID with operating conditions. Physical and chemical processes are discriminated and the governing factors for both are identified. These governing factors or parameters are fitted into the Assanis' correlation, and parametric adjustment to the activation energy constant is performed to form the new chemical delay correlation. A physical delay correlation is developed from experimental findings. Finally, an empirical physical delay correlation and a theoretical chemical delay correlation are combined to form the new ID correlation. This correlation produces an average error of 4.9 % and a maximum error of 14 %. It is shown to perform better at high engine speed-load condition (at 2,000 rev/min and 8.5 bar BMEP), with an average error of only 2.6 % and a maximum error of 8.7 %. Physical and chemical processes are shown to be separate events under engine conditions such as steady-state, pre-ignition, fully warmed-up, and undiluted intake air.

F2012-A03-011

W. J. Thoo (✉) · H. K. Ng · S. Gan
Faculty of Engineering, The University of Nottingham Malaysia Campus,
Jalan Broga, 43500, Semenyih, Selangor, Malaysia
e-mail: weijet86@yahoo.co.uk

A. Kevric · P. Shayler
Engines Research Group, Department of Mechanical, Materials and Manufacturing
Engineering, The University of Nottingham, University Park, Nottingham, NG7 2RD, UK

Keywords Ignition delay correlation • Diesel-gasoline blends • Direct-injection compression ignition engine • Chemical kinetic mechanism • Physical and chemical processes

1 Introduction

Combustion of gasoline in a direct-injection compression ignition (DICI) engine has been reported to lower smoke and nitrous oxides (NO_x) emission as compared conventional combustion of fossil diesel. The main reason for this apparent benefit lies in the effect of the gasoline component in the fuel blend to significantly alter the ignition delay (ID) period. ID of DICI engine is known to govern the heat-release rate, which indirectly affects the NO_x and soot formation. ID period here typically involves physical processes such as atomisation of fuel droplets, air–fuel mixing and vaporisation of fuel droplets; chemical processes which comprised of the breakage of atomic bonds and release of heat energy. The delay period portions contributed by physical and chemical processes are henceforth known as physical delay and chemical delay. Development of the ID correlation which is able to predict IDs of gasoline combustion in DICI engine would aid to further understand how gasoline-diesel fuel mix can be optimise to control NO_x and soot emission.

In-cylinder conditions such as temperature and pressure vary drastically with crank angle, cold/warmed-up engine, transient/steady-state, and pre/post-ignition. These conditions have great influence over the ID period. Prakash et al. employed an ID correlation which was highly dependent on engine parameters to estimate the ignition delay in a dual fuel engine [1]. Variables considered were manifold pressure, mean piston speed, compression ratio, activation energy and cetane number. Building a correlation based on the engine parameters would be restrictive as it is not applicable to other engine make and type. Teng et al. studied the physical and chemical processes involved in a compression ignition (CI) engine fuelled with dimethyl ether [2]. Droplet diameter was demonstrated to an important factor in affecting the physical processes. A chemical delay correlation was then suggested with mixture temperature and pressure as the variables. The most popular ID correlation is the one developed by Assanis et al. [3]. It is the first ID correlation with fuel–air equivalence ratio (ER) as one of the variables. Most importantly, it claims to take account of both physical and chemical processes. Approach to estimate constants employed in correlations which are in Arrhenius form for different temperature range was also introduced [4]. Set against this background, the main aim for the reported work here is to formulate a semi-empirical correlation of the physical and chemical delays for gasoline-diesel combustion in a DICI engine.

Table 1 Specification of test engine

Engine specifications	
No. cylinders	4
Capacity	2.4 l
Bore	89.9 mm
Stroke	94.6 mm
Con rod length	149.8 mm
Compression ratio	18.4:1
Rated power	91.9 kW at 3800 rev/min
Maximum torque	285 Nm at 2,300 rev/min

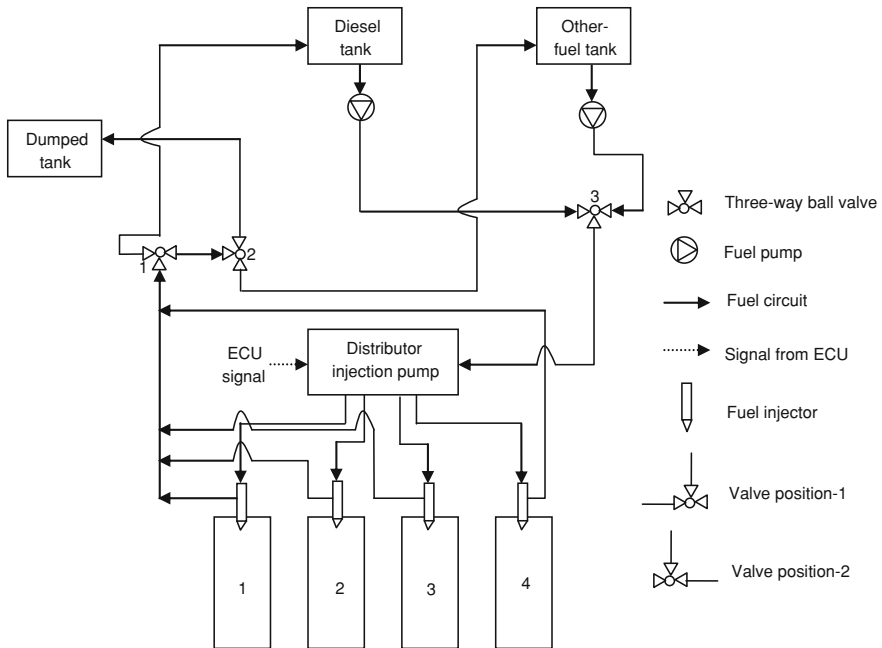


Fig. 1 A dual fuel tank fuel-injection system

2 Experimental Setup

2.1 Engine Setup

An experimental rig comprised of a 2.4 l DI turbocharged compression ignition engine with mechanical injection system is coupled with an electric motor/generator dynamometer and data acquisition instruments. The specification of the engine is shown in Table 1. The fuel injectors are triggered to open by the fuel pressure. For the current setup, the injectors open at 200 bar of fuel pressure.

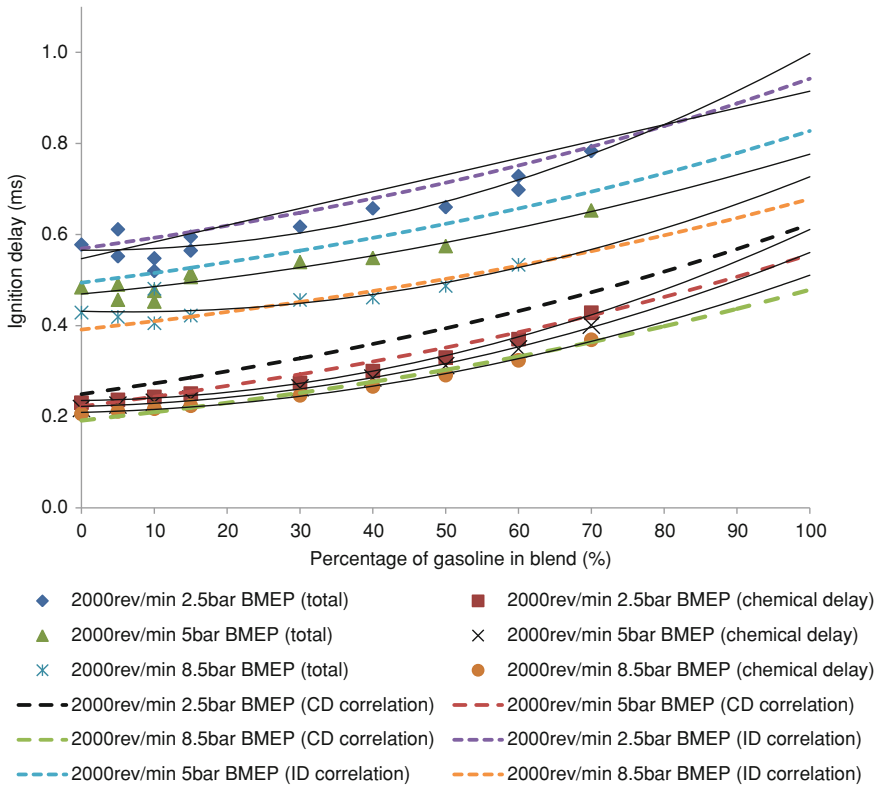


Fig. 2 Experimental IDs, predicted chemical delay by chemical kinetic modelling, and predicted chemical delay by correlation under three engine speed-load conditions

A dual fuel tank system is used to allow switching between diesel and gasoline-diesel blend to prevent fuel contamination as depicted in Fig. 1. The transition from diesel tank to other-fuel tank is done by the use of all three valves.

2.2 Test Fuel

All the diesel-gasoline fuel blends are prepared by simply mixing both types of fuels according to the desired volumetric compositions. The difference of density results in both the fuels to settle into two separate layers. Thus, the blends have to be well mixed before the start of the fuel injection system or engine rig. Lubricity additive, TOFA-S TK25, provided by Lubrizol is added to all fuel blends in a concentration of 300 ppm. This has been shown to be an effective concentration to overcome the lubricity problem [5] (Fig. 2).

2.3 Data Processing

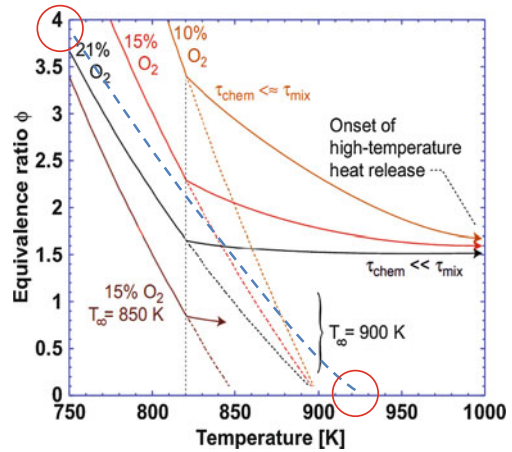
An optical shaft encoder is used to produce a trigger at top dead centre (TDC). This trigger is used in LabView to initiate the recording of data. The cylinder pressure and fuel line pressure are measured using two quartz pressure transducers. All tests are performed at fully warm, steady state conditions. Due to the limitation of crankshaft encoder resolution, pressure data is synchronised with time instead of crank angle. The time domain is converted to crank-angle domain with desired resolution by setting the right sampling frequency of the data-acquisition hardware. The sampling frequency is altered according to the engine speed to achieve a crank-angle resolution of 0.2° . A default injection strategy is employed throughout, where fuel is injected at -4° after top dead centre (ATDC). For engine testing, the start of combustion (SOC) is chosen as the point at which the net heat release rate first reaches 2 J/degree. The measured in-cylinder pressure data and fuel-line pressure data are exported into MATLAB for further analyses. Heat release analysis is performed using the method presented by Heywood [12]. The well-known equation used for the net heat release rate is shown below. The equation assumes that the cylinder contents are uniform in temperature and pressure at each instant in time during closed engine cycles (quasi static assumption). It also assumes that the contents of the cylinder can be modelled as an ideal gas.

$$\frac{dQ_n}{d\theta} = \frac{\gamma}{\gamma - 1} p \frac{dV}{d\theta} + \frac{1}{\gamma - 1} V \frac{dp}{d\theta} \quad (1)$$

3 Chemical Kinetic Modelling

The 0-D homogeneous batch reactor model in CHEMKIN is used for the modelling part of this reported work. Chemical kinetic mechanisms of n-heptane and iso-octane from Lawrence Livermore National Laboratory (LLNL) [7, 8], as well as toluene by Andrae [9] are combined as the surrogate fuel model for diesel-gasoline blends. Volumetric ratios 80/20 and 70/30 for n-heptane/toluene and iso-octane/toluene are used to represent diesel and gasoline, accordingly. The volumetric ratios for other mixtures are calculated based on these. N-heptane, iso-octane and toluene are used to represent n-alkanes, iso-alkanes and aromatics in diesel and gasoline as these are the most recognised and well-studied surrogates for these constituents. The relevance of these surrogate components have been verified through validation against literature shock tube and rapid compression machine (RCM) data for diesel and gasoline. The conditions tested are for initial pressures of 6–60 bar, initial temperatures of 650–1,350 K and mixture equivalence ratio of 1. For comparison purposes, mixture equivalence ratio is set at 4 and mixture temperature is set at 820 K as estimated from literature as depicted in Fig. 3 [6]. The variation of engine speed-load conditions would result in different

Fig. 3 The path of a fuel parcel in the equivalence ratio-temperature plane corresponding to an adiabatic mixing process followed by low-temperature heat release (adapted from [6])



sets of in-cylinder pressure traces. The mean pressures before the start of combustion and after the start of injection are employed. For 1,000 rev/min, mean pressure is 55 bar for all load conditions. For 2,000 rev/min, mean pressures are 68 bar, 76 bar, and 88 bar for engine loads of 2.5 bar, 5 bar, and 8.5 bar, respectively.

4 Experimental and Modelling Results

A series of engine tests with gasoline blended with diesel mixtures have been carried out. The variation of gasoline content in fuel blends display the effect of gasoline towards combustion in relative to the normal diesel combustion. ID period has been found to be increasing in a polynomial manner as gasoline in blends increases as shown in Fig. 2. Fuel-air equivalence ratio, temperature and pressure are shown to have significant effect on chemical delay prediction. Chemical delay periods predicted via chemical kinetic modelling show similar polynomial trends as the experimental ignition delay periods. It appears that the increase of ID with increasing gasoline component in the fuel blend is due to the increase of chemical delay. Physical delay is shown to be independent of the variation of diesel-gasoline blends as supported by Fig. 4. Figure 4 demonstrates that physical delay is constant throughout the fuel blends but varies with engine speed and load. Physical delays are accounted by extrapolating the linear premixed burn trend lines down to the zero premixed burn, when air-fuel mixture becomes combustible or heat release starts.

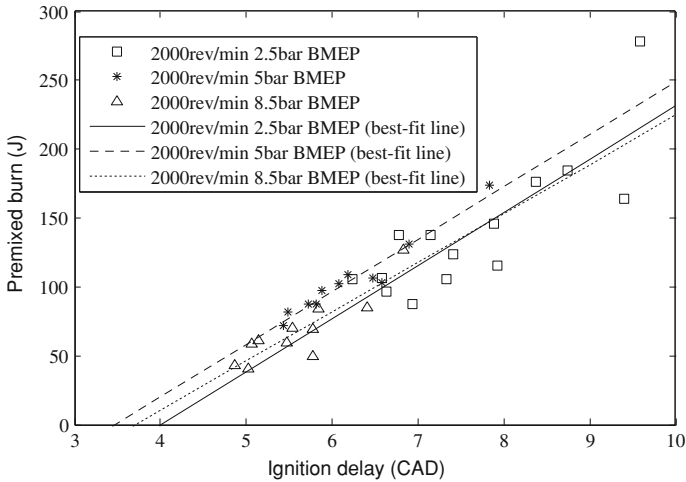


Fig. 4 Plot of premixed burn against ID (in crank angle degrees (CAD)) at test conditions for all gasoline-diesel fuel blends at 2000 rev/min

5 Ignition Delay Correlation

ID in DIC I engine has been found to be strongly affected by fuel–air equivalence ratio, temperature and in-cylinder pressure. These findings are consistent with other works emphasized on the development of ID correlations. The IDs measured from experiments are only valid at steady-state, fully warmed-up, pre-ignition, fixed start of injection (SOI) timing and undiluted intake air conditions. Therefore, the correlation shown in this study is valid for the same conditions only. Physical and chemical processes are perceived to occur simultaneously and the ignition delay correlation is shown in Eq. 2 [3]. However, both processes have been shown to occur separately, physical processes first followed by chemical processes. Chemical processes are dependent on fuel–air mixture equivalence ratio, fuel–air mixture temperature (T_m) and in-cylinder pressure (P_{cyl}). Theoretically, fuel injection pressure (P_{inj}), in-cylinder pressure, in-cylinder temperature (T_{cyl}), injector nozzle diameter (D_{noz}), and fuel droplet diameter (D_{drop}) are the main factors which affect the physical processes. Based on these factors, theoretical correlations for ID would be in the postulated form shown in Eqs. 3 and 4. A semi-empirical correlation which depends on both theoretical study and observation from experimental results would be in the form as expressed in Eq. 5. Despite that physical and chemical processes are treated as separate entities, physical processes are responsible for determining the fuel–air equivalence ratio and fuel–air mixture temperature suitable for the chemical processes to begin.

$$ID = 2.4\theta^{-0.2}P^{-1.02} \exp\left(\frac{2100}{T}\right) \tag{2}$$

Table 2 Comparison of predicted IDs between Assanis' correlation and experimental data

Conditions (Engine speed, BMEP)	Mean pressure (bar)	Mean temperature (K)	ER [3]	Experimental ID (ms)	Predicted ID (ms)	Error (%)
2,000 rev/min, 2.5 bar	68	967	0.116	0.578	0.437827115	24.23
2,000 rev/min, 5 bar	76	1,002	0.116	0.484	0.362316236	25.19
2,000 rev/min, 8.5 bar	88	1,055	0.116	0.429	0.280814641	34.49
1,000 rev/min, 2.5 bar	51.6	876	0.116	0.854	0.726999073	14.89
1,000 rev/min, 5 bar	53.8	848	0.116	0.705	0.754076025	7.01
1,000 rev/min, 7.5 bar	56.8	870	0.116	0.659	0.67016442	1.75

$$ID = \text{Physical delay } (P_{inj}, P_{cyl}, T_{cyl}, D_{noz}) + \text{Chemical delay } (ER, T_m, P_{cyl}) \quad (3)$$

$$ID = \text{Physical delay } (P_{cyl}, T_{cyl}, D_{drop}) + \text{Chemical delay } (ER, T_m, P_{cyl}) \quad (4)$$

$$ID = \text{Physical delay } (\text{Engine speed}, P_{cyl}) + \text{Chemical delay } (ER, T_m, P_{cyl}) \quad (5)$$

Table 2 shows the predicted ignition delay times with Assanis correlation in comparison with the experimental values. The maximum error in relation to the experimental ID values is 34.5 %. Despite this, it lacks of governing parameters for physical processes based on the variables considered in the correlation. Fig. 5 shows that the correlation is unable to capture the polynomial trend of fuel blends since a linear trend is presented instead. Arrhenius equation which is in the similar form as the Assanis' correlation is used by CHEMKIN to calculate the chemical kinetic mechanism of the modelling work. Fuel–air mixture equivalence ratio, temperature and in-cylinder pressure are found as the dictating factors which govern the prediction of chemical delay. Hence, mean temperature, mean pressure and the equivalence ratios in the Assanis' correlation are replaced by fuel–air temperature, ambient/in-cylinder pressure and averaged local fuel equivalence ratio, accordingly, to predict the chemical delay. Eq. 6 is the new correlation for the chemical delay. The activation energy constant for diesel has been revised to 1,900 and that for gasoline is set at 2,650. The new chemical delay correlation consists of two more variables which are the volumetric fraction of diesel (X_D) and gasoline (X_G). These additional variables would account for the variation of the fuel mix composition. The predicted chemical delay periods show good agreement with that predicted by CHEMKIN as illustrated in Fig. 2.

$$CD = 2.4ER^{-0.2}P_{cyl}^{-1.02}\exp\left(\frac{X_D1900 + X_G2650}{T_m}\right) \quad (6)$$

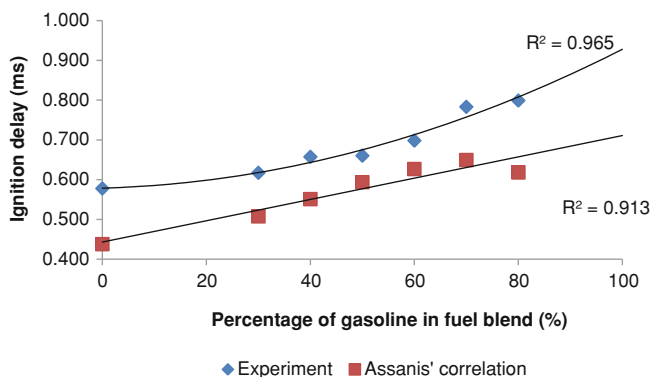


Fig. 5 Experimental and predicted IDs for various gasoline-diesel fuel blends

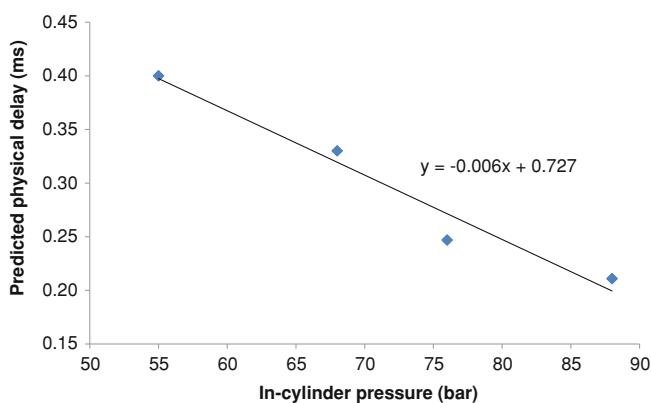


Fig. 6 Plot of predicted physical delay against in-cylinder pressure

As for physical delay correlation, a simplified equation is found using Fig. 6. Physical delay is simply estimated by translating the predicted chemical delays via CHEMKIN to assimilate the experimental IDs. The magnitude of translation, a constant value throughout the same engine speed-load condition, is taken as the predicted physical delay. When the predicted physical delays are plotted against the mean in-cylinder pressure during the period after SOI and before SOC, a linear trend line can be fitted across the data points. This eliminates the need of introducing engine speed as one of the factors in the physical delay correlation. Physical delay correlation is now expressed as Eq. 7. Hence, the ID correlation is the combination of both physical delay and chemical delay correlations as shown in Eq. 8. The validation of the final ID correlation is shown in Fig. 2. IDs predicted by the new ID correlation are comparable to the experimental data, with an average error of 4.9 % and a maximum error of 14 %. The correlation performs better at an engine speed of

2,000 rev/min and a brake mean effective pressure (BMEP) of 8.5 bar, with an average error of only 2.6 % and a maximum error of 8.7 %.

$$PD = -0.006P_{cyl} + 0.7276 \quad (7)$$

$$ID = -0.006P_{cyl} + 0.7276 + 2.4ER^{-0.2}P_{cyl}^{-1.02} \exp\left(\frac{X_D1900 + X_G2650}{T_m}\right) \quad (8)$$

6 Conclusion

Physical and chemical processes are separate events under engine conditions such as steady-state, pre-ignition, fully warmed-up, and undiluted intake air. In-cylinder pressure appears to be the most crucial factor which governs the physical delay. As for chemical delay, mixture temperature, equivalence ratio and in-cylinder pressure are the dictating factors. A semi-empirical correlation with an average error of 4.9 % and a maximum error of 14 % has been developed to represent the ID of diesel-gasoline fuel blends. The correlation appears to perform better at high engine speed-load condition (2,000 rev/min and 8.5 bar BMEP here), where the average error is 2.6 % and the maximum error is 8.7 %. The applicability of the correlation remains conservative, as it is only validated for this engine setup and operating conditions.

References

1. Prakash G, Ramesh A, Shaik A (1999) An approach for estimation of ignition delay in a dual fuel engine. SAE Technical Paper Series, 1999-01-0232
2. Teng H, McCandless J, Schneyer J (2003) Compression ignition delay (physical + chemical) of dimethyl ether- an alternative fuel for compression-ignition engines. SAE Technical Paper Series, 2003-01-0759
3. Assanis DN, Filipi ZS, Fiveland SB, Syrimis M (2003) A predictive ignition delay correlation under steady-state and transient operation of a direct injection diesel engine. Trans ASME 125:450–457
4. Hernandez JJ, Sanz-Argent J, Carot JM, Jabaloyes JM (2010) Ignition delay time correlations for a diesel fuel with application to engine combustion modelling. Int J Engine Res 11:199–206
5. Hildingsson L, Johansson B, Kalghatgi GT, Harrison AJ (2010) Some effects of fuel autoignition quality and volatility in premixed compression ignition engines. SAE Technical Paper Series, 4 2010-01-0607
6. Kook S, Bae C, Miles P, Choi D et al (2005) The influence of charge dilution and injection timing on low-temperature diesel combustion and emissions. SAE Technical Paper Series, 2005-01-3837
7. Curran HJ, Gaffuri P, Pitz WJ, Westbrook CK (1998) A comprehensive modelling study of n-heptane oxidation. Combust Flame 114:149–177
8. Mehl M, Curran HJ, Pitz WJ, Westbrook CK (2009) Chemical kinetic modelling of component mixtures relevant to gasoline. In: Proceedings of the European combustion meeting, Vienna, Austria, pp 14–17
9. Andrae JCG, Brinck T, Kalghatgi GT (2008) HCCI experiments with toluene reference fuels modelled by a semidetained chemical kinetic model. Combust Flame 155:696–712

The Energetic Potential of Engines Fueled with Biomass Derived Products

Anghel Chiru, Sorin Sacareanu, Ruxandra-Cristina Stanescu,
Cornel Stan and Peter Zima

Abstract The purpose of the one-dimensional numerical simulations done at FTZ (Forschung—und Transferenz Zentrum Zwickau) was to observe the influence of alternative fuels produced from wood biomass on engine energetic parameters like: pressure evolution in combustion chamber, rate of heat release, temperature distribution. The fuels used were represented by blends with 20, 50 and 100 % biomass biodiesel made by the Fischer–Tropsch synthesis. Based on the limitations of one-dimensional simulations, the study included 3D simulations (AVL FIRE) which have correctly estimated the complex phenomena related to diesel fuel injection and combustion.

Keywords Biodiesel · Fischer–Tropsch diesel · Compression ignited engine

F2012-A03-016

A. Chiru · R.-C. Stanescu
Transilvania University of Brasov, Brasov, Romania

S. Sacareanu (✉)
LMS Romania, Brasov, Romania
e-mail: sorin.sacareanu@unitbv.ro

CornelStan
University of Applied Science Zwickau, Zwickau, Germany

P. Zima
Hower Powertrain Gmbh, Oberboihingen, Germany

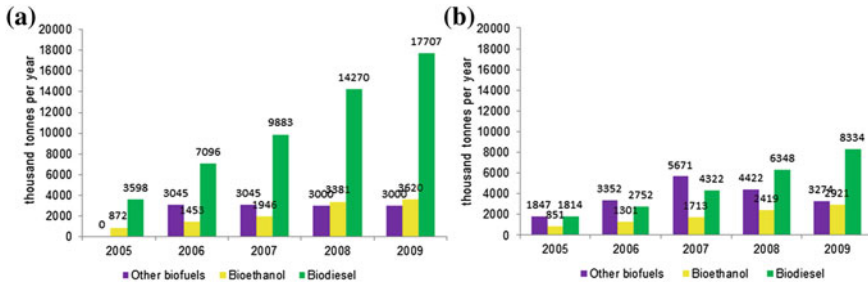


Fig. 1 Biofuels in the European Union: a production capacity and b production obtained [3, 4]

1 Aspects Regarding Alternative Fuels for Automobiles

The recent economic development has led to a significant increase in the demand of oil products. Thus, the market is seeking new solutions to produce and introduce oil products substitutes. From this perspective, biofuels represent a resource with a high potential for substituting fossil fuels in the transport sector.

Regulations were adopted have recently been adoptedrecently to support and extend the production and use of biofuels. Although initially they were considered a very profitable energy source, the targets set by the USA, European Union and other countries resulted in prices for biofuels feedstock comparable to oil prices and thus cutting of the estimated profits [1].

Biofuels have known limits therefore the European Commission has developed an action plan named Energy policy for Europe which imposes the use of maximum 10 % biofuels by 2020 for the transport sector in the European Union countries [2].

On a medium term, first generation biofuels have provided an unexpected resource, but the debates concerning the feedstock for these fuels shared with the food sector have determined the main producers to adopt a different approach. Also on a medium term, the biofuel production is estimated to increase from 1.8 billion barrels a day in 2010 to 2.7 billion barrels a day in 2015. On a long term it is estimated that second and third generation production technologies will become economically viable and this will result in a recovery in availability. In this context, the estimates show an increase in biofuel production to about 7.1 billion barrels a day in 2035 if the trend shown in Fig. 1 is maintained [3, 4].

In EU, Germany was the country with the highest biofuel production (37 %), followed by France (19 %). Romania recorded a total of 87 thousand tonnes in 2009, meaning a 0.59 % of total EU biofuel production [4]. The rapid increase in primary energy demand noticed in the last decades will continue, being a reflection of the population growth rate, economic activity, urbanization and industrial production.

2 Properties of the Synthetic Fuels Investigated

Using the experience acquired in the production of synthetic fuels, a method has been developed that allowed the production of a fuel from wood biomass by Fischer–Tropsch synthesis (FT). A gas mixture consisting of hydrogen and carbon monoxide is converted by FT synthesis in longer or shorter chains of hydrocarbons. Based on a mechanism of increasing the hydrocarbon chains, by means of catalyzers, the process allows the formation of certain chemical products (hydrocarbons) which can substitute classic fossil fuels. These hydrocarbons have been used to prepare several mixtures in combination with fossil diesel in different concentrations [5]. Properties of these mixtures are presented in Table 1.

In order to observe how the combustion performances and the compatibility with existent injection systems are influenced by the fuels used, the indicated effective parameters of an engine running at different loads and speed have been investigated on validated virtual models.

The characteristics of the engine used for tests are presented in Table 2. The functional behavior of the engine was studied when fueled with Euro5 diesel and also with a mixture of diesel fuel and 20 %, respectively 50 % FT fuel.

3 Simulation of the Combustion Process at Low Load

Simulations have been performed with AVL FIRE software, using the engine parameters shown in Table 2. This application has a specialized module for the evaluation of the combustion process in internal combustion engines. Pressure, speed and injection rate evolutions were obtained after one-dimensional numerical analysis. The working regime is characterized by a 2000 rpm speed and a mean effective pressure of 0.2 MPa. The total injected fuel per cycle was of 9 mm³, this being accomplished in two steps: pre-injection at 19.6 °CAD before TDC and main injection at 2 °CAD before TDC. The analysis of pressure, temperature and heat release rate evolution in the combustion chamber led to the following conclusions:

The increasing the concentration of FT fuel in the mixture led to an increase of cetane number from 52.1 to 76.7. The maximum pressure per cycle was recorded at 0.25 °CAD for 20 % FT, 0.45 °CAD for 50 % FT and 3 °CAD for 100 % FT before the maximum pressure obtained with diesel fuel. A comparison of the indicated pressure evolution is illustrated in Fig. 2;

By increasing the FT fuel in the mixture, the pressure rise gradient decreases by small amounts.

The following parameter investigated was the heat release rate, with its evolution shown in Fig. 3. The analysis of the heat release rate evolution, resulting from combustion, shows that the auto-ignition process is initiated with 6.4 °CAD

Table 1 Physical-chemical properties of tested fuels [6]

Property	Standard	Unit	EN590	B0	FT/B0 20/80	FT/B0 50/50	FT
Cetane number	EN ISO 5165		>51	52.1	62.7	65.8	76.7
Density at 15 °C	EN ISO 12185	kg/m ³	820–845	829	817	799	769.5
Viscosity at 40 °C	EN ISO 3104	mm ² /s	2.0–4.5	2.54	2.4	2.24	2.07
Inflamability point	EN ISO 2719	°C	>55	62	63	68	78
CFPP		°C		–12	–11	–10	–4
Lower calorific value	DIN 51900	MJ/kg		42.985	43.209	43.407	43.781
Elastic modulus		(bar)		15800	15200	14400	13000

Table 2 Engine characteristics

Number of cylinders	4 in line
Valves per cylinder	4
Induction capacity	1995 cc
Bore × stroke	84 × 90 mm
Maximum power	105 kW at 4000 rpm
Maximum torque	320 Nm at 1750 rpm
Compression ration	16:1
Injection system	Common-rail maximum injection pressure 1600 bar 7 holes solenoid injector
Pollution standard	Euro 5

before the one for the diesel fuel, i.e. at 3 °CAD after TDC. More over, the maximum heat release rate in case of FT fuel is 22 % lower than for diesel fuel. It decreases proportionally with the increase of diesel fuel concentration in the mixture, thus for the FT20 the differences are insignificant.

The analysis of the temperature in the combustion chamber, illustrated in Fig. 4, showed that the temperature decreases with the increase of the FT fuel in the mixture. Thus, the maximum temperature in the engine cycle decreases from 1195 K for diesel fuel to 1135 K for FT synthetic fuel.

For a better understanding of the combustion phenomena of the FT fuel, Fig. 5 [6] shows the analysis of the temperature distribution in the combustion chamber. The analysis was done for three sequences of the combustion process: at 6 °CAD, 6.5 °CAD and 10 °CAD after TDC respectively for each of the four fuels investigated. The analysis shows that the auto-ignition takes place earlier for the FT fuel. Due to a higher vaporizing characteristic in the case of the FT fuel, mixture homogeneity is also higher than for diesel fuel, as it can be noticed from the last series of images in Fig. 5. It can be notice that the uniformity of the temperature for the FT fuel in the combustion chamber is slightly higher than for diesel fuel.

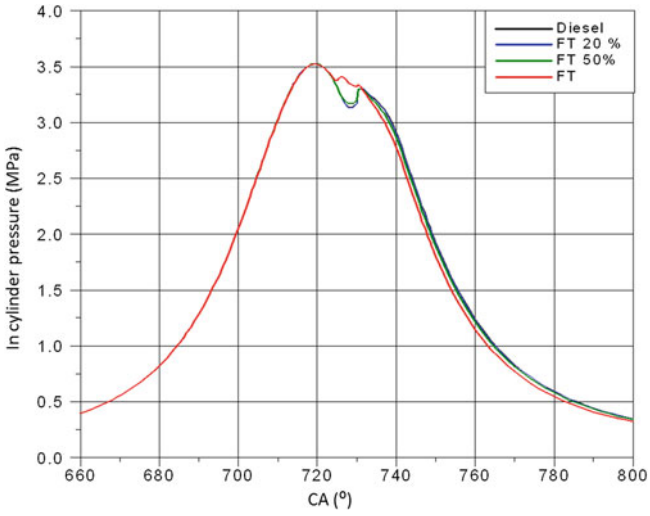


Fig. 2 Indicated pressure evolution, 2000 rpm, 0.2 MPa

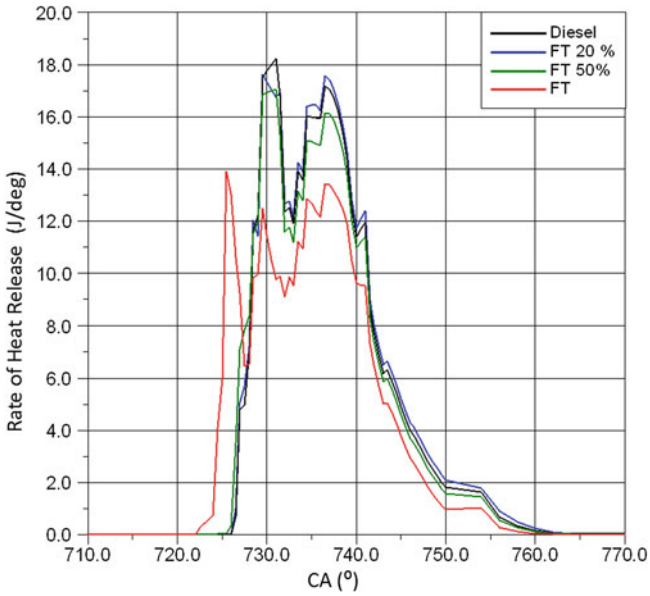


Fig. 3 Heat release rise evolution, 2000 rpm, 0.2 MPa

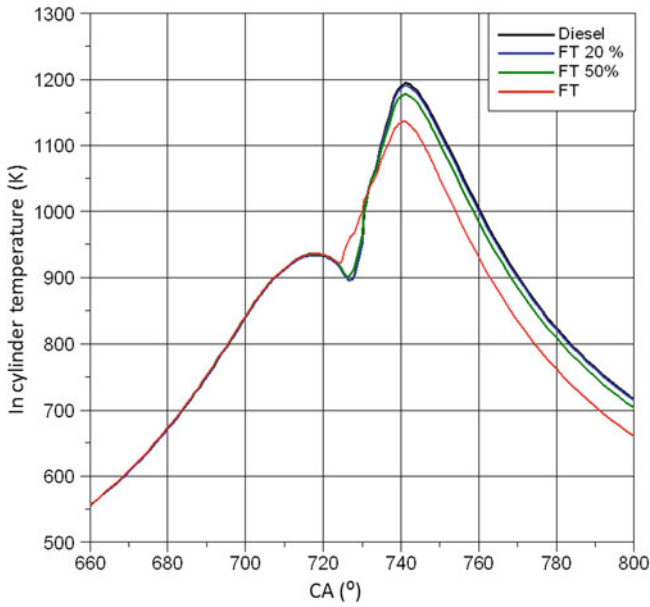


Fig. 4 Temperature evolution, 2000 rpm, 0.2 MPa

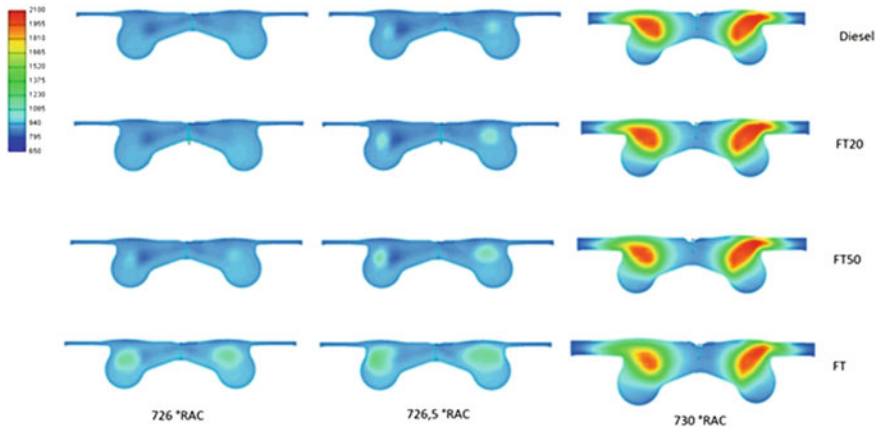


Fig. 5 Temperature distribution in the combustion chamber, 2000 rpm, 0.2 MPa

4 Simulation of the Combustion Process at High Load

In order to study the engine behavior at high load, the numerical simulation of the combustion process was done at a speed of 2000 rpm and 1.5 MPa load. Pre-injection was at 19.5 °CAD before TDC for 2.5 °CAD duration and the main

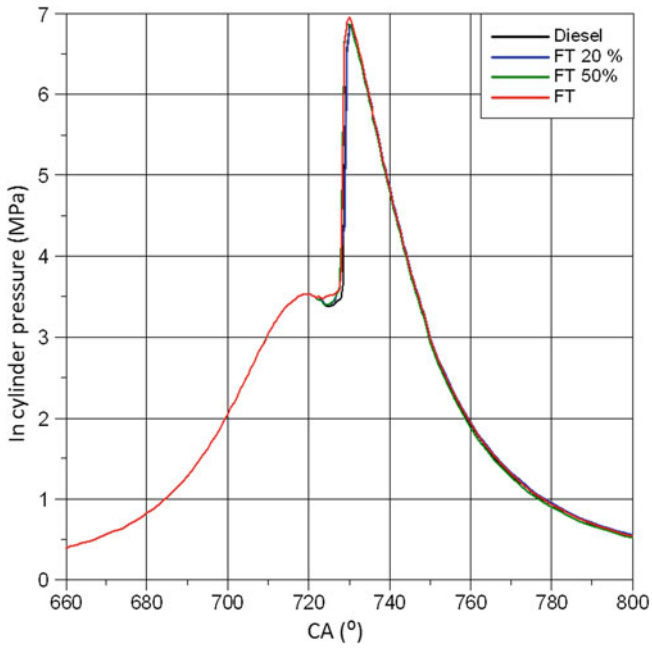


Fig. 6 Indicated pressure evolution, 2000 rpm, 1.5 Mpa

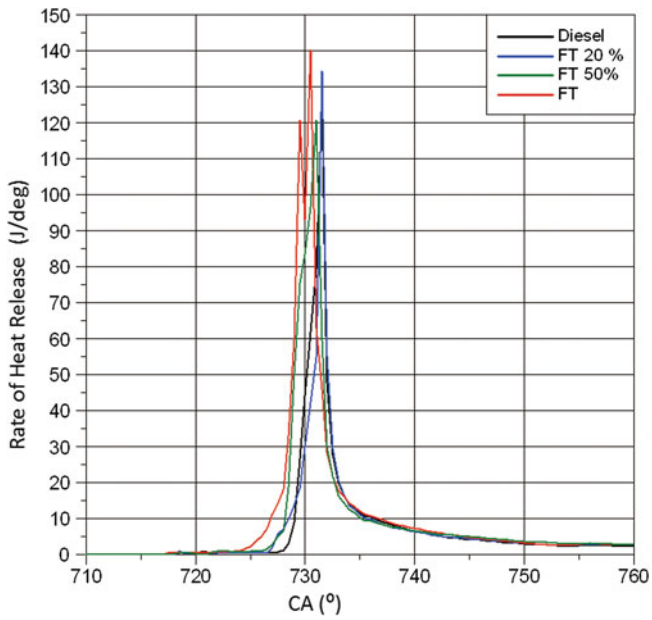


Fig. 7 Heat release rise evolution, 2000 rpm, 1.5 MPa

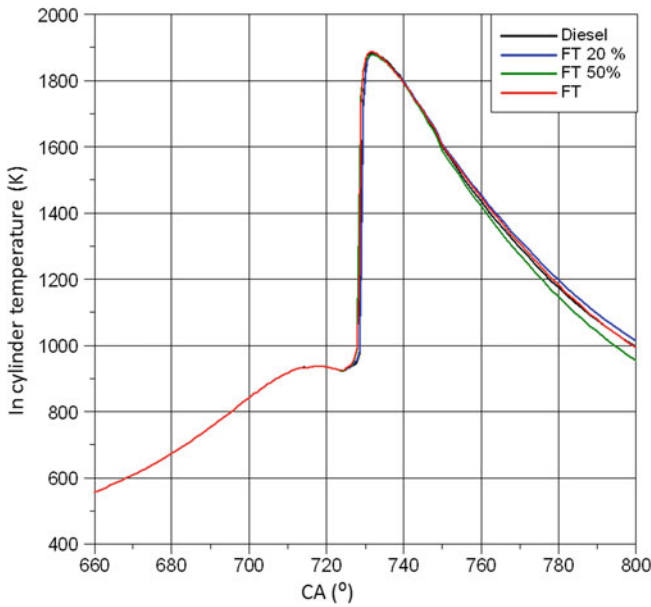


Fig. 8 Temperature evolution, 2000 rpm, 1.5 MPa

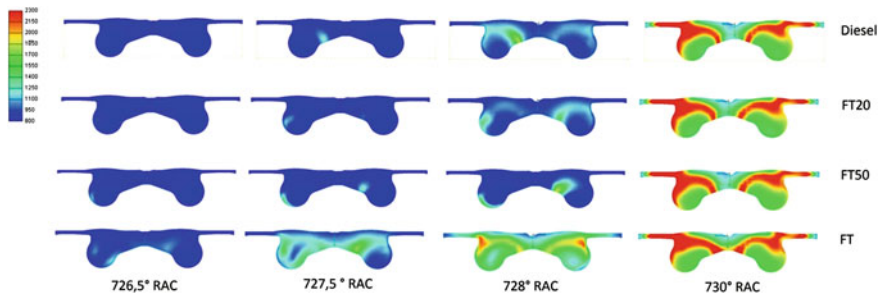


Fig. 9 Temperature distribution in the combustion chamber, 2000 rpm, 1.5 MPa

injection at 10 °CAD before TDC for 14.8 °CAD duration. Total injected fuel was of 60 mm³.

The parameters investigated in this case were the same as in the case of low load simulations. After analyzing these parameters, the following conclusions were drawn:

Pressure evolution in the combustion chamber follows the same trend, with no significant differences between the fuels used. The maximum pressure was approximately 1.3 % higher than for the diesel fuel, and delayed with about 1 °CAD. Figure 6 shows a comparison of pressure evolution in the combustion chamber for all the fuels tested.

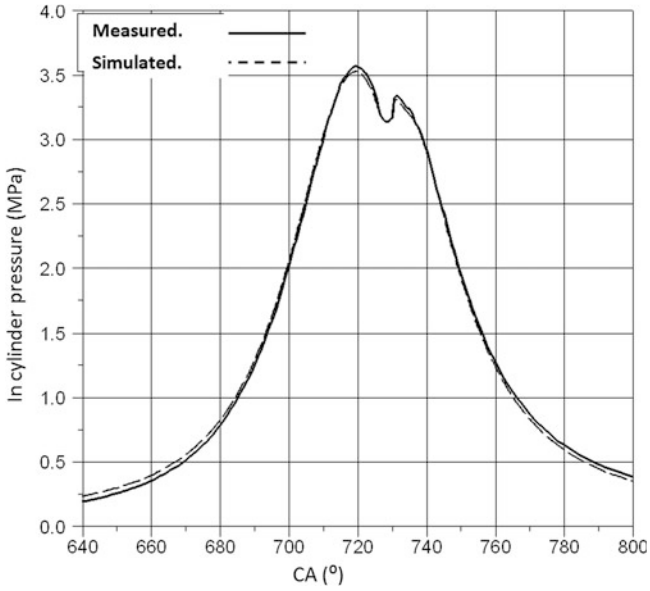


Fig. 10 Comparison of the pressure evolution for diesel fuel, 2000 rpm, 0.2 MPa

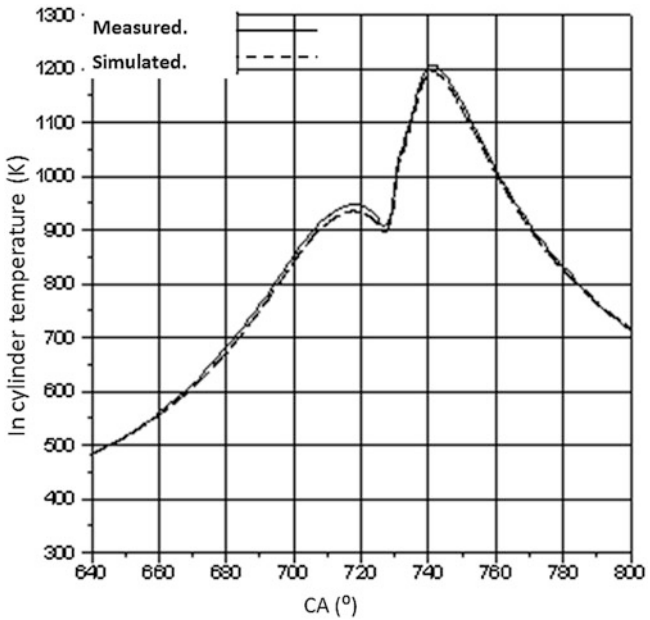


Fig. 11 Comparison of the temperature evolution for diesel fuel, 2000 rpm, 0.2 MPa

As shown in Fig. 7, the heat release characteristic is different than in the case of the engine running at low load. Therefore the maximum value of the heat release increases from 18 J/°CAD to approximately 140 J/°CAD, the oscillations are very much diminished, and the combustion duration is reduced with 10...12 °CAD. The tendency of reducing the auto-ignition delay as the synthetic fuel concentration increases is however kept. In the case of FT fuel, the auto-ignition delay is reduced with about 3 °CAD compared with diesel fuel. Also, the maximum heat release rate is 4 % higher for FT fuel compared with diesel. For the FT20 and FT50 fuels the differences were not significant.

The temperature of burnt and unburnt mixture from the combustion chamber, as illustrated in Fig. 8, presents the same evolution for all the fuels tested; the differences are under 1 %. For the FT, fuel the pressure rise gradient was recorded earlier with 2 °CAD compared to diesel fuel. The maximum temperature per cycle increases from 1195 to 1850 K compared to the low load regime.

By observing the temperature distribution in the cylinder, as shown in Fig. 9, the phases of the mixture during combustion can be determined. A smooth temperature distribution may be noticed for FT fuel compared with diesel.

5 Conclusions

At the end of this experimental and simulation work that represents the impact of fuel properties on combustion performances, we can conclude the following:

- The influences of the synthetic fuel concentration in the mixture on the evolution of the cylinder pressure, heat release rate and temperature are stronger for low load regimes;
- Heat release delay increases with the increase in the synthetic fuel concentration in the mixture;
- Auto-ignition delay decreases with the increase in the synthetic fuel concentration in the mixture;
- Temperature distribution in the combustion chamber is more uniform for FT fuel. This is due higher volatility over diesel and also due to the possibility of generating a homogeneous air-fuel mixture.

The numerical simulations have proven the compatibility of the investigated fuels with the injection systems in existing engines. Now, that the potential of these fuels was proved in virtual environment, it is required to confirm the results with experimental research.

The experimental research was focused on evaluation of the same parameters as in the case of numerical simulations. This allowed the correlation of the results obtained during simulations with the ones obtained during experimental research, thus validating the virtual model. Figures 10 and 11 show a comparison of in-cylinder pressure and temperature for diesel fuel at 0.2 MPa load. It can be

noticed that the differences between the values recorded from simulations and from the test-bed are very small. This is due to a precise CAD model of the engine, and also to the use of proper values for different parameters and coefficients of the mathematical model.

Acknowledgments This paper is supported by the Sectoral Operational Programme Human Resources Development (SOP HRD), financed from the European Social Fund and by the Romania Government under the contract number POSDRU/88/1.5/S/59321 and POSDRU/6/1.5/S/6.

References

1. Bechtold RL (2002) Alternative fuels—transportation fuels for today and tomorrow. SAE: SAE, 89, I.S.B.N.: 0-7680-0907-3
2. Brussels (ed) (2003) 2003/30/EC Directive of the European parliament and the council on the promotion of the use of biofuels or other renewable fuels for transport, pp L123/44–L123/45
3. S.O.o.t.E (2009) Communities energy transport and environment indicators; European Commission, Luxembourg
4. S.O.o.t.E (2011) Communities energy transport and environment indicators; European Commission, Luxembourg
5. Rauch R, Hofbauer H, Sacareanu S, Chiru A (2010) From gasification to synthetic fuels via Fischer–Tropsch synthesis. Bull Transilvania University Brasov Ser I Eng Sci 3(52):33. I.S.S.N pp 2065-2119
6. Sacareanu S (2012) Research of the working regimes and fuels characteristics on energetical and ecological parameters of internal combustion engines. Ph D thesis, Brasov, Romania
7. Stan C (1999) Direkteinspritzsysteme für Otto- und Dieselmotoren. Springer, Berlin. I.S.B.N.: 3-540-65287-6
8. AVL FIRE Users Guide
9. OPEC (2011) World oil outlook—2011. Organization of the Petroleum Exporting Countries, Vienna
10. Chiru A, Sacareanu S, Dica-Stanescu RC, Muntean AB (2011) Alternative fuel solution for internal combustion engines. The automobile and environment. Cambridge Scholars Publishing, Newcastle, pp 145–159

Fuel Formulation for Future Drive Train Developments

Máté Zöldy, András Holló, Zoltán Szerencsés,
Ferenc Kovács and Róbert Auer

Abstract Nowadays fuel quality standards provide clear instructions for both automotive industry and petroleum industry to produce vehicles and fuels for transportation. In midterm time horizon it will be changed. Fuel mix in the world but mainly in Europe will be much more inhomogeneous as it is know. Fuel development will focus more heterogeneously, different regions will have different energy pathways. Fuel producers have to be prepared for these times: it should be fuel development methodologies, that allow develop new fuel grades based on new recipes, components and additives for new uncommon engine and drive train solutions. In the process of continues fuel development more and more focus has to be done on the different market segments. This is a key factor of success in the fierce market competition of retailers in Europe. Segmentation could be based on utilization conditions, size or also fuel availability and prescriptions. Engines could be utilized at near optimal parameters if the fuel is specified for the conditions. MOL Group's recent goal was to set up new development methods that allow developing customer oriented fuels for special utilization segments. In our paper we give an overview about the heavy duty fleet testing as an important element to meet the customer expectations. A dual driven—technology push and market pull -development is presented. Carefully organized development process together with internal (refinery, supply chain, logistics, wholesale, retail) and external partners was carried out recently in MOL Group. Based on the already utilized application testing methodology and analytical background we developed a new method for fuel development for special market segments. In the paper we will present our results and work in the example of heavy duty market segment.

F2012-A03-017

M. Zöldy (✉) · A. Holló · Z. Szerencsés · F. Kovács · R. Auer
MOL DS Development, Budapest, Hungary
e-mail: mzoldy@mol.hu

We present the development goal establishment based on customer value creation, method to find and built up the new test environment and the born of the new product from the idea to the market introduction. We share our experiences in the example of an already fulfilled product development process. Method is developed and already tested on the current European market needs. It has to be proved with great differences, special engine/drive train and energy supply needs, e.g. fuel cell, pure butanol fuel etc. The presented dual driven development method and the example presented in this paper are uniquely summarizes the European fuel trends, market needs and give a successful answer to the challenges. Petroleum industry can remain the primer energy supplier of the mobility if it is able to diversify the fuel portfolio based on the customer's and vehicle producers' needs. The presented method and product are good examples how to create synergy between automotive developments and petroleum industry opportunities.

Keywords Diesel · Niche market · Heavy duty

1 Introduction

For transportation the main challenge is the reduction of its greenhouse gas (GHG) emission. One possible way from refinery point of view is the application of low carbon fuels, like biofuels. Recent studies in the meanwhile showed higher GHG emission for biofuels compared to conventional one, if we take into account the effect of indirect land use change (ILUC) [1]. However, the dependency of crude oil based fuels is especially significant in the aviation, freight, and marine industries where good alternatives to fossil jet and distillate fuels are hard to find and approve for daily use. From automotive industry point of view, the GHG reduction is only available through downsizing and hybridization in short term (till Y2025).

Crude oil dependency is also driving concerns about the future security of energy supplies while climate change concerns are driving energy efficiency improvements and the replacement of fossil fuels with renewable or alternative fuels. The degree to which fossil fuel replacement or decarbonisation should be taken place depends on many factors, such as vehicle compatibility, fuel efficiency and sustainability of alternative fuels on a well-to-wheels basis, the pace of development and investments in alternative fuels, the demand for alternative fuels from other sectors, cost of CCS technologies, the demand change (e.g. increased mobility, alternative fuel penetration in community transport) etc. By 2020 JEC [2] expects fossil fuel dominancy in European road transportation sector.

Thus, the total supply of non-renewable fuels is unlikely to keep pace with the growing global demand. Renewable and alternative energy and fuels will be required and work is already in progress to accelerate these developments. Due to regional differences in fuel infrastructure, imports, climate, water supply,

prevailing winds, available crop lands, and many other factors, the best alternative for one country or region may not necessarily be the best alternative for another. For this reason, a coherent and cost-effective transition from non-renewable to renewable energy and fuels will be a significant challenge [3].

The recent economic downturn will have had an impact on private technology investments but will be largely overcome by public intervention. Public–private partnerships and policy will contribute to the recovery of technology developments needed to meet the demanding objectives for GHG reductions and sustainable road transport. The need for trained engineers and scientists to create and implement these developments will have been recognized.

2 Fuel Markets in the Next Decades

Customer value proposition on specified markets with special products will be based on three pillars at the twenty first century. Although diesel and gasoline seems to be remaining the main products of refining industry in the next decades some other energy carriers and utilisation modes will have increasing role. Secondly product quality standards allow giving the same product for broad customer sectors. Thirdly twenty first century technology allows great variation in refinery and additive production.

Main fuel market premises could be summarized in the following bullet points:

By 2025, crude oil and natural gas will still be available in significant volumes and represent more than 80 % of the transportation energy demand. The primary sources for these products will continue to shift to politically unstable regions. Thus, most of the customers will utilise conventional diesel and gasoline fuelled vehicles [4].

EV options, driving by CO₂ emission reduction targets, will be growing in urban regions and in some densely populated corridors, for both passenger- as well as freight transport, with their share in new sold vehicles will not reach 15 % up to 2025. Most stakeholders assume [5–7] a realistic market share for new, electrically chargeable vehicles in the range of 2–10 % by 2025. For Europe, especially Mid- and Eastern Europe lower range of penetration because of the economic environment is expected [4]. EV vehicles will be a definitive niche market with high entry barriers. EU Climate Package will change fuel quality; higher biofuel blends (E10-15, B10-15 and E85, B100) will be on the market by 2025. Meanwhile alternative fuels, like LPG, CNG, DME, HVO and XTLs could also count as low carbon fuels [2020 passenger car—LPG: new sales: 2 % (0.4 million), sum in fleet: 2 % (5 million); CNG new sales: 4 % (0.8 million), sum in fleet: 2 % (5 million); XTL and HVO in diesel pool according to JEC Biofuels Programme Report [2]. High biofuel containing diesels in modified, developed engines will have local role in the high agriculture potential zones. Liquid gases will forge ahead in economical favourable environment and gas producing countries.

Road transportation will further increase in Europe. Long term freight transport could be handled as an independent markets segment based on its volume and its refuelling demand focuses on motorways. Fleet management systems, low operational cost and high availability are key factors of this sector [8].

Vehicle that utilised for daily trips only could be handled as a further special segment. The transportation need is systematic and recurrent, mainly between household, workplace and shopping- and service centres. Short distances are very usual, daily average is between 50 and 75 km. Expansion of new energy sources and drivetrain variations is expected in this segment.

3 Niche Market Fuel Development

3.1 *Determination of Market Specifications*

Fuel formulation for special market needs is presented in the example of heavy duty market segment. The users of the heavy duty vehicles contains different subgroups as long term freight transport, public passenger transport, agriculture, mine, industry etc. The common feature of this market, that the customers are very price sensitive, the yearly average procurement volume is large. Typical vehicle fuel consumption is between 25 and 50 L/100 km, and diesel engine volume is at least 5 L.

During the fuel development application test are fulfilled to earn application experiences. Engine and vehicle test are prescribed by CEC (Coordinating European Council) and ASTM (American Society for Testing and Materials). Application technology and testing driven development of diesel fuels mainly focuses on small and mid-size engines in engine bench development. DW10 and XUD9 tests are the most commonly used and CEC approved test that help to distinguish diesel fuels in automotive and refining industry. These tests give essential information about fuel behaviour in the fuel supply system, combustion chamber and after treatment system, but they cannot include the specialities of compression ignition engines that used mainly in freight transport and in coaches [9]. Clark et al. [10] presents results of their work about modelling heavy duty fuel economy on dynamometer test. Their results of the application of the black box neural network model and the commercial software model produced average percentage errors of the order of 10 and 4 %, respectively [12].

Table 1 shows the main parameters of the three most common utilised fuel development test for diesel. All of them is designed for passenger car (PC) size engines. These tests cannot be utilised for developing fuels for heavy duty (HD) engines. First the HD engines are much larger; the piston diameter for example could be 150 % of the PC engines. The friction surfaces are larger based on the size increase. It enables higher friction reduction with the precise formulation and

Table 1 Main parameters of the three most common utilised diesel development tests

Test code	Test type	Engine code	Test parameter	Engine volume
CEC F-098-08	Engine test	DW10	FAME content, power loss	2 L
CEC F-023-01	Engine test	XUD-9	Injector cleanliness	1.9 L
ASTM 5500	Vehicle test	Not specified	BMW test for fuel economy for passenger cars (PC)	n.a.

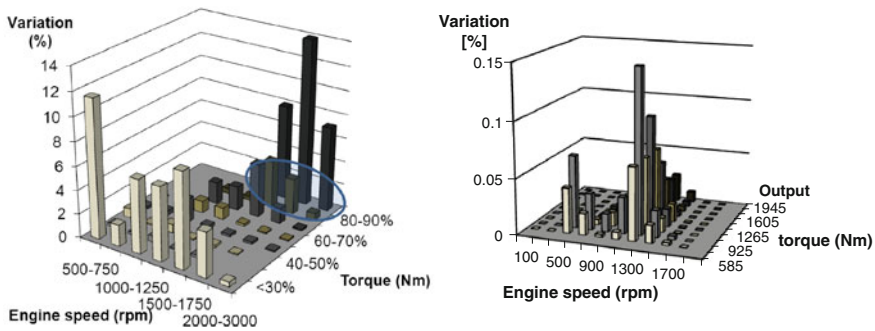


Fig. 1 Passenger car (*left*) and heavy duty (*right*) engine speed-torque variation [7]

additisation of the fuel. Secondly the HD engines mainly utilised in different conditions as it presented in Fig. 1.

Figure 1 shows that passenger car engines usually utilised in very various driving conditions. By contrast heavy duty engines typically utilised mainly in a good localisable torque and engine speed range. Armed with this knowledge the diesel components can be optimised for the quasi-stationer combustion. The case that there are engine bench tests for PC engines are available focused our attention to field tests, that could give more real life based result, but they need more organisation and energy to deliver the nearly same data accuracy.

3.2 Development of Fleet Test Method

Dual-driven product development is very effective tool to specify fuel sub market needs and develop special products. The dual driven process bases on two pillars: technology push and market pull. Possible sequence of executable actions is shown in Fig. 2.

A carefully organised fleet test with well-chosen test vehicles, test parameters and collaboration with additive supplier partners is a crucial element for get application technology information direct from the field. The main factors of test are test fleet selection and data acquisition–evaluation; refuelling facility and the product under development.

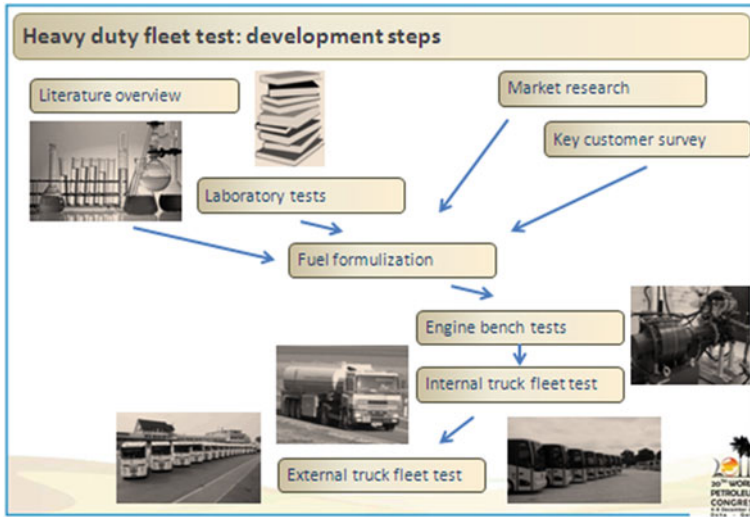


Fig. 2 Dual driven product development [8]

Test vehicle selection has to be done very accurately to have comparable results with different fuel recipes. Test vehicles should regularly carry on the same route with the nearly same load : unload ratio. Truck delivery helps also to have similar load conditions at the same route with different fuels. Test truck should have one refuelling point only, and it is prohibited for them to tank in other locations. If refuelling facility is electronically controlled then fuel amount could be also measured with refuelled volume. It can be a valuable control data. In the determination of the test truck number it has to be taken into account that it is beneficial to have the trucks at least duplicate (minimum two trucks with very similar technology) to exclude the uniqueness measurement errors. In the other hand it is advantageous to spread the tested vehicles technology level (i.e.: Euro class, engine type, etc.) as broad as possible.

Fleet test on heavy duty vehicles requires a special refuelling facility. The amount of the utilised fuel is high, the HD vehicles fuel consumptions could be five times above than PC. Thus a large fuel tank should be dedicated for the tests. The exact amount depends on the number of the test vehicles, on estimated average fuel consumption based on historical data, planned length of the test. This is very close connected to the wished mileage. Some developments on fuel quality have immediate effect; others need time to build up. If refuelling is electronically controlled and measured; and it is connected into an account network then it gives very useful data to control the fuel consumption of the test vehicles. In the test fulfilled in MOL DS Development we implement a 20,000 L tank on an open refuelling station connected into its account network. We calculated the volume of the tank (v_{tank} [liter]) based on the test vehicle number (n_{veh} [piece]), estimated average fuel consumption (FC_{avg} [L/100 km]), necessary mileage to control the expected changes (d) as presented in Eq. 1:

$$V_{\text{tank}} = n_{\text{veh}} \cdot d / 100 / FC_{\text{avg}}. \quad (1)$$

Test batch quality and quantity was frequently monitored not only in the fuel change period. We let only the test vehicles to be refueled. The internal fleet test was followed and external test, customers were involved to test the fuel with their vehicle fleet on their own running parameters.

The third main parameter, of course, was during the development the fuel, itself. It was the key factor that have to be reformulated and tested. In the first stages of the development batches on specification EN 590 were investigated, new recipes were developed, According to the customers' need. These fuels are utilizable without any special permission in vehicles that prescript to run on fuels that fulfills the requirements of EN 590. Later other fuels were tested with increased degree of freedom. From production point of view the tested fuels should be reproducible, blendable, additisable in low volume batches. They should be reproducible, representative with the technologies in MOL Group Refineries.

3.3 Fleet Test Data Acquisition End Evaluation

We ensured that in case of fleet testing a key factor is the test data acquisition. There are lot of parameters that could influence an investigated parameter. Vehicle acceleration, top torque, emission or fuel consumption could be effected by route, wind, temperature, driver, truck load, traffic situation, etc. [11]. In the other hand the goal is not to have a special fuel that could show its effect in a special vehicle or in special application environment. To able to check the expected changes fixing some some vehicle parameters are beneficial:

- different vehicle types (Euro classes, manual/automatic gear etc.), but at least two similar test vehicles,
- no consumption by loading/unloading,
- test trucks should have routes to fixed delivery places: they run over 80 % on the same route.

Test data acquisition accuracy based on the test duration and the type of data acquisition system. During our test we utilized parallel two data sources. In the case of fuel consumption for example we earn data from vehicle fleet management system, GPS, drivers log block and retail network refuelling data. It enabled cross-checks between the similar data types.

4 Test Results for Niche Market Development

To develop special fuel quality for the presented niche fuel market segment (heavy duty vehicles) fleet test is the special method were the customer expectations and fuel development results could be matched. During the fuel development process

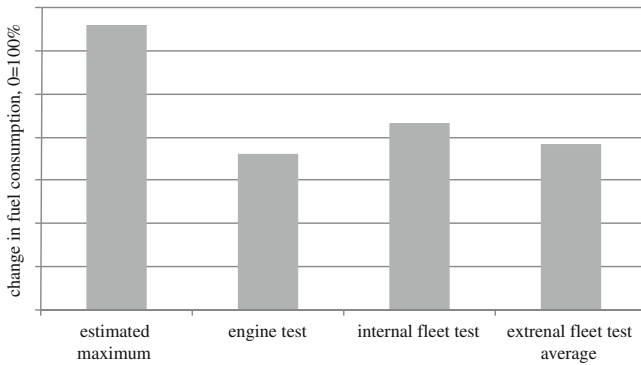


Fig. 3 Application test potential for develop fuels for special requirements

more than 15 different fuel recipes were tested with the presented fleet test method and the best rated (technically and economically) batch was selected for external partners. Some of our results are presented in Fig. 3, to ensure that development of special fuel qualities for market segments needs special development methods.

The bars in Fig. 3 present the theoretically estimated expectation based on the changes of C:H ratio, blending component characteristic, effect of special additives, etc. Second column shows the external fulfilled control engine bench test results with the developed fuel. Third column shows the results of internal fleet test result and last the results of external fleet tests are presented.

Results showed that based on the theoretical calculated maximum values the internal and external fleet test results are good tools to check the fuel improvement and modifying effects and create new fuels for satisfy special market needs.

5 Summary

In our paper the tendencies of the expected fuel quality changes were presented that are mostly based on the engine requirements. The estimated changes in the vehicle drivetrains, legal environment and vehicle utilisation behaviour can be followed only with specified energy carrier forms for the special market segments. Development of new fuels for niche markets/special segments need to widening the development facilities, methods to able to create new fuels for the special demands. In our paper as an example for a special market fuel and method development we presented heavy duty segment fuels and the developed fleet test method. Our results show that exact market requirements, fuel development with special investigation methods can result new fuel qualities that fulfil the special market needs and increases the customer satisfaction.

References

1. Searchinger T et al (2008) Supporting materials for use of U.S. croplands for biofuels increases greenhouse gases through emissions from land use change. Princeton University, pp 1–49. <http://www.princeton.edu/~tsearchi/writings/SupportingMaterials.pdf>
2. JEC Biofuels Programme: EU renewable energy targets in 2020: Analysis of scenarios for transport 2011
3. Ricardo: Concawe technical briefing 2011
4. Credit Suisse estimates
5. Shell Energy Scenarios to 2050 http://www-static.shell.com/static/aboutshell/downloads/aboutshell/signals_signposts.pdf
6. Conley J, Jarrett R, Nennelli A, Tóth-Nagy C, Clark N (2001) Emissions modeling of heavy-duty conventional and hybrid electric vehicles. SAE 2001-01-3675
7. Iván G, Ákos B, Ádám T (2011) Energetic analysis of plug-in electric vehicles. In: Heat engines and environmental protection: the role of renewables in energy generation. Balatonfüred, Magyarország, 2011.05.23-2011.05.25, pp 233–238 (ISBN:978-963-313-029-2)
8. Zöldy M, Holló A, Thernesz A (2011) Development of more efficient fuels for niche markets. In: 20th world petroleum congress, Doha, 2011.12.04-2011.12.08. Paper Block 3/Forum 3
9. Harrington W, Krupnick A (2012) Improving fuel economy in heavy-duty vehicles, resources for the future, March, Issue brief 12-01
10. Clark N, Thompson G, Delgado O (2009) Modeling heavy duty fuel economy based on cycle properties. West Virginia University, 24 Sept 2009
11. Miller T (2010) The road to improved heavy duty fuel economy, company directions in engine-efficiency and emissions research conference
12. Zöldy M, Török Á, Mészáros F, Zsombok I, Szoboszlai M (2009) A hazai közúti közlekedés várható jövője [Future of Hungarian transportation sector]. ERTRAC Hungary 1–34

MoS₂ Production Mechanism of MoDTC

Kazuhiro Umehara, Yukio Tatsumi
and Noriyoshi Tanaka

Abstract Automotive industries have strong interest in fuel economy. To enhance fuel economy, engine oils need to employ effective friction modifiers (FM). Molybdenum dithiocarbamate (MoDTC) is one of FM and superior in friction reduction performance to other FM especially in boundary lubrication regime. It is said that MoDTC produces MoS₂ layer on the rubbing surface to reduce friction, and ZDDP has a synergistic effect with MoDTC to produce MoS₂ layer effectively. In this paper, we analyzed the rubbing surfaces by several methods after rubbing with SRV tester to clarify the production mechanism of MoS₂ layer. Results by EPMA showed that the combination of MoDTC and ZDDP decreased molybdenum intensity and increased sulfur intensity on lubricating surface compared to MoDTC alone. Results by XPS showed that MoDTC produced both of MoS₂ and MoO₃ layers while the combination of MoDTC and ZDDP produced only MoS₂ layer selectively. Although ZDDP is an important sulfur supplier to MoDTC, at the same time ZDDP and MoDTC are under competing adsorption. We confirmed that a sulfur supplier to MoDTC played a very important role for producing MoS₂ layer.

Keywords Fuel economy · Friction modifier · MoDTC · MoS₂ layer · Sulfur supplier

F2012-A03-018

K. Umehara (✉) · Y. Tatsumi · N. Tanaka
Adeka Corporation, Tokyo, Japan
e-mail: k-umehara@adeka.co.jp

1 Introduction

Global warming is one of the most important issues for the environment, and reduction of CO₂ emissions is effective to solve this issue. So automotive industries have strong interest in fuel economy and are developing the new technology to improve the fuel consumption, for example hybrid engine system and downsizing of engine. In addition, fuel economy engine oil is also being developed. The main characteristic of fuel economy oil is as follows, one is to employ low viscosity and high VI base oil, and the other is friction modifier. MoDTC is superior in friction reduction performance to other FM especially in boundary lubrication regime. In Japan, MoDTC is widely used especially in gasoline engine oil [1, 2, 3]. It is said that MoDTC adsorbs onto the rubbing surface and produces MoS₂ layer. This MoS₂ layer reduces friction in the rubbing area [4, 5].

ZDDP has been used in engine oil as excellent anti-wear agent and anti-oxidant, and is well known to have a synergistic effect with MoDTC to produce MoS₂ layer [6]. However the production mechanism of MoS₂ layer is not defined completely. This paper shows the production mechanism of MoS₂ layer by both MoDTC alone and the combination of MoDTC and ZDDP by analysis of rubbing surfaces.

2 Experimental Method and Result

2.1 Test Samples

The chemical structures of MoDTC and ZDDP are shown in Fig. 1. This MoDTC consists of bi-nuclear molybdenum and dialkyl-dithiocarbamate with C8 alkyl chains. This ZDDP consist of mono-nuclear zinc and dialkyl-dithiophosphate with C8 alkyl chains.

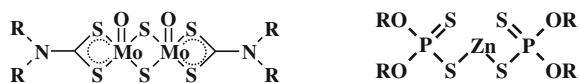
Table 1 shows each formulation of test oils. We formulated four samples. These samples employ different amounts of MoDTC and ZDDP with base oil which is mineral oil (Group-1, 4.1 mm²/s @100° C).

2.2 Friction Reduction Test

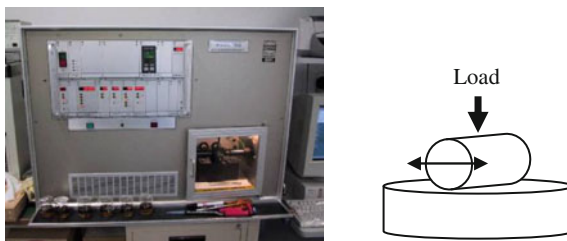
The friction reduction performance of MoDTC was investigated using SRV tester shown in Fig. 2.

This apparatus has a fixed disc, oscillating cylinder and a block heater. Test parameters are shown in Table 2.

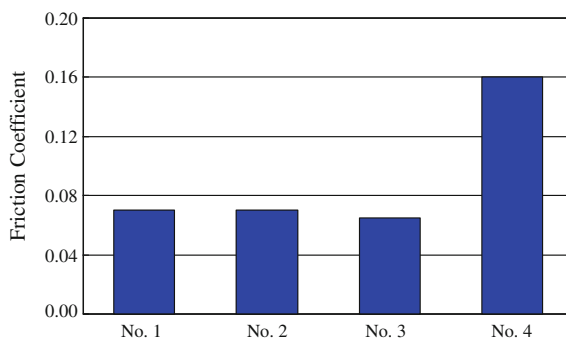
Friction coefficient of SRV test is shown in Fig. 3. The results of No. 1, No. 2 and No. 3 are low friction coefficient, on the other hand the result of No. 4 is high friction coefficient. These results show high concentration of MoDTC was not necessary in case of the combination with ZDDP.

Fig. 1 Structures of MoDTC and ZDDP**Table 1** Test oil formulation

Sample No	Additives
No. 1	MoDTC (Mo: 700 ppm) + ZDDP(P: 750 ppm)
No. 2	MoDTC (Mo: 700 ppm)
No. 3	MoDTC (Mo: 100 ppm) + ZDDP(P: 750 ppm)
No. 4	MoDTC (Mo: 100 ppm)

Fig. 2 Apparatus of SRV tester**Table 2** Test condition of SRV

Parameters	Conditions
Load	200 N
Contact pressure (Max)	0.21 GPa
Amplitude	1.0 mm
Frequency	50 Hz
Test temperature	80° C

Fig. 3 Friction coefficient result**Table 3** EPMA condition

Parameters	Conditions
Accelerating voltage	15 kV
Sample current	5×10^{-7}
Beam diameter	10 μm

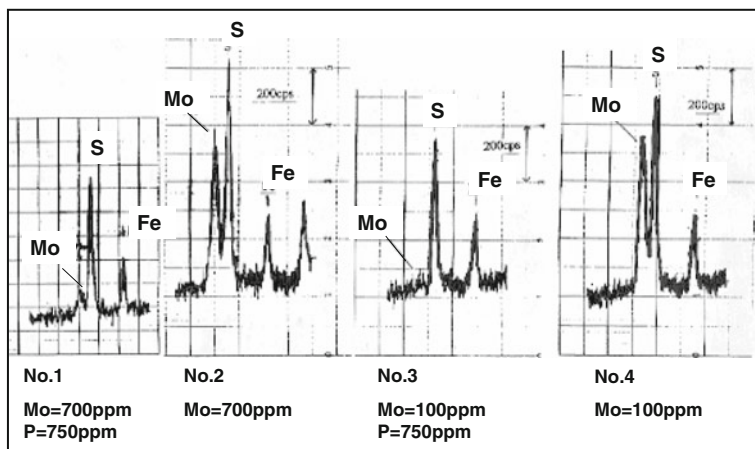


Fig. 4 EPMA spectrum of rubbing surface

Table 4 XPS condition

Parameters	Conditions
X-ray	MgKa
Ar ⁺ Sputtering	1.0 keV

2.3 Rubbing Surface Analysis

2.3.1 Electron Probe Micro Analyzer (EPMA)

Element distribution of rubbing surface was investigated by EPMA. Table 3 is test condition of EPMA.

Figure 4 shows EPMA spectrum of the rubbing surface. In No. 1 and No. 3, molybdenum intensity to sulfur is small compared with No. 2 and No. 4 respectively. This result shows ZDDP affects the molybdenum intensity of rubbing surface. It seems that ZDDP works as obstacle to MoDTC's adsorption on the rubbing surface.

2.3.2 X-ray Photoelectron Spectroscopy (XPS)

Chemical structure of rubbing surface was investigated by XPS. Table 4 is test condition.

Figure 5 shows XPS spectrum of MoS₂ and MoO₃. MoS₂ has strong peaks of 229 and 233 eV while MoO₃ has strong peaks of 233 and 236 eV.

Figure 6 shows XPS spectrum of the rubbing surface. No. 1's layer consists of MoS₂ while No. 2's layer consists of both MoS₂ and MoO₃. The same phenomenon was seen between No. 3 and No. 4.

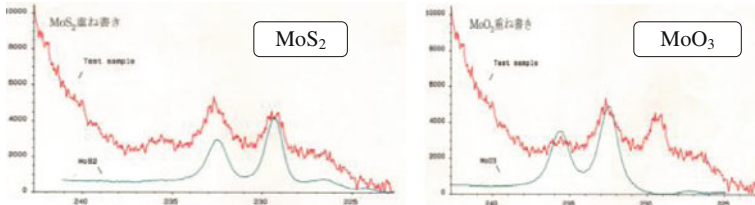


Fig. 5 XPS spectrum of MoS₂ and MoO₃

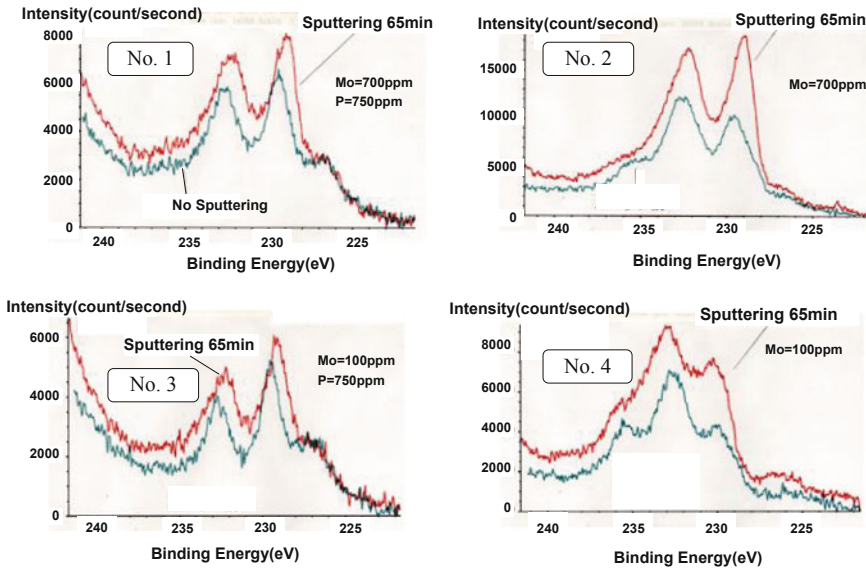


Fig. 6 XPS spectrum of test sample

Table 5 AES condition

Parameters	Conditions
Accelerating voltage	10 kV
Sample current	5×10^{-7} A
Beam diameter	<1 μ m

It seems that ZDDP disturbs MoDTC’s adsorption onto the rubbing surface, and at the same time works as a good sulfur supplier to produce MoS₂ layer on the lubricating surface.

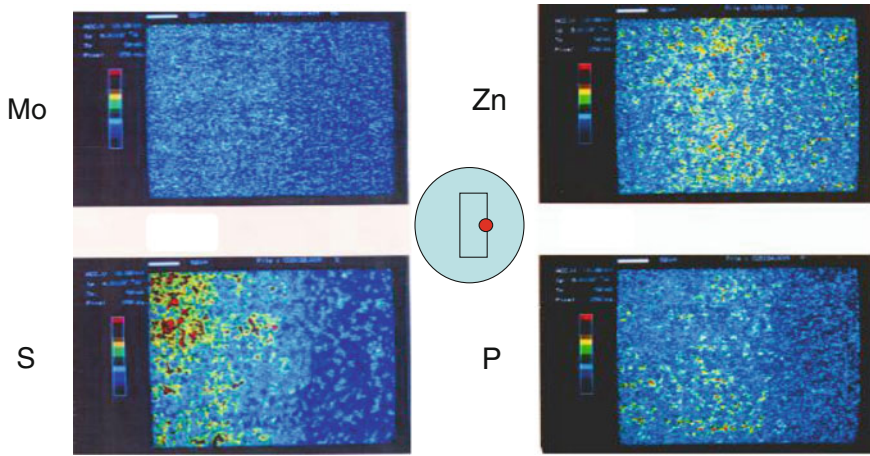
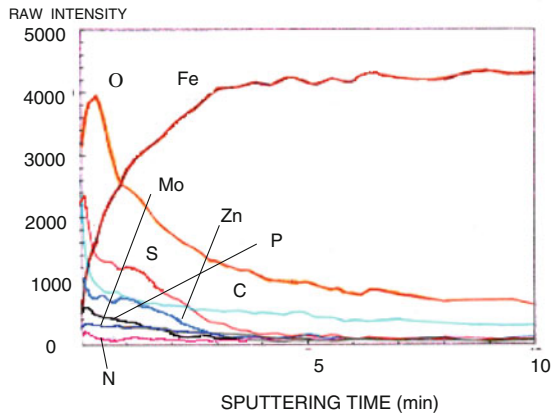


Fig. 7 XPS spectrum of sample No. 1

Fig. 8 Result of AES—sputtering



2.3.3 Auger Electron Spectroscopy (AES)

Element mapping of rubbing surface was investigated by AES. Table 5 shows AES test condition.

Figure 7 shows AES result of sample No. 1. Molybdenum and sulfur exist on the almost same area. This area is center of rubbing surface. On the other hand, zinc and phosphorus exist different area from Molybdenum and sulfur. This area is edge of rubbing surface. This result indicated that MoS₂ layer is produced on high sliding speed area and zinc and phosphorus complex layer is produced on slow sliding speed or zero speed area.

Figure 8 shows the result of AES when rubbing surface is sputtered. Sputtering rate is 40 angstrom per minute. The deeper from the surface, the weaker the

intensity of molybdenum and sulfur gradually. On the other hand, intensity of oxygen is strong. Lubricating film is formed on the oxidizing layer. Molybdenum contained layer was not thick.

3 Conclusion

The production mechanism of MoS₂ layer was investigated by several surface analyses. The conclusions obtained in this study are as follows,

- (1) MoDTC and ZDDP are under competing adsorption.
- (2) MoDTC produces MoO₃ and/or MoS₂ on the lubricating surface. When ZDDP exist with MoDTC, MoS₂ is produced selectively. Another role of ZDDP is a sulfur supplier to MoDTC.
- (3) Based on test results, one of the important point for developing more superior fuel economy engine oil is to find a good sulfur supplier which does not disturb MoDTC's adsorption onto the rubbing surface.

References

1. Akiyama K, Kawai H, Sugiyama S (1998) Development of fuel economy 5 W-20 gasoline engine oil. *Toyota Tech Rev* 47(2):18–22
2. Tanaka H, Nagashima T, Sato T, Kawauchi S, The effect of 0 W-20 low viscosity engine oil on fuel economy. SAE 1999-01-3468
3. Sagawa T, Ishikawa T, Nakamura K, Ueno T, Ando T, Ishikawa M, Development of 0 W-20 ILSAC GF-3 gasoline engine oil. SAE 2002-01-1636
4. Yamamoto Y, Gondo S (1989) Friction and wear characteristics of molybdenum dithiocarbamate and molybdenum dithiophosphate. *Tribol Trans* 32:251–257
5. Grossiord C, Varlot K, Martin J-M, Le Mogue Th, Esnouf C, Inoue K (1998) MoS₂ single sheet lubrication by molybdenum dithiocarbamate. *Tribol Int* 32(12):737–743
6. Muraki M, Wada H (1993) Frictional properties of organo molybdenum compounds in presence of ZnDTP under sliding condition (Part 1)—frictional properties of MoDTC and MoDTP. *J Jpn Soc Tribol* 38(10):919–926

Research on Cam & Tappet Friction Test Method for Anti-Wear Performance Evaluation of Engine Oil

Chensheng Zou, Shengjun Huang and Jun Yu

Abstract The objectives of the research project were to establish a test method to evaluate anti-wear performance of engine oil. Comparative research was done about the method and ACEA test method CEC L-38-94 to prove that the two methods have similar evaluation capacity for engine oil. A cam & tappet test rig was set up. The tests which refer to PV5106 were running at certain speed, temperature, pressure and time. Two reference oils of CEC L-38-94 with different wear protection behavior were tested to compare the results with TU3 test data. The same oil was tested two times for repeatability research. The cam and tappet wearing results showed a good repeatability. And the cam& tappet friction test method correlates with CEC L-38-94. This method has simple experimental condition, short running time and single operating condition. It's unable to completely simulate the actual working condition of engine. But the study certifies cam & tappet friction test method can be used to do wear evaluation. This method provides an effective technology for engine oil evaluation. It also provides convenient and efficient test data for engine oil research. It helps to save research cost and resources which conform to the concept of low carbon.

Keywords Cam tappet · Anti-wear · Tappet wear · Engine oil evaluation · Correlation

F2012-A03-020

C. Zou (✉) · S. Huang · J. Yu
PetroChina Dalian Lube Oil R&D Institute, Dalian, China
e-mail: zouchensheng_rhy@petrochina.com.cn

Fig. 1 Cam & tappet test rig

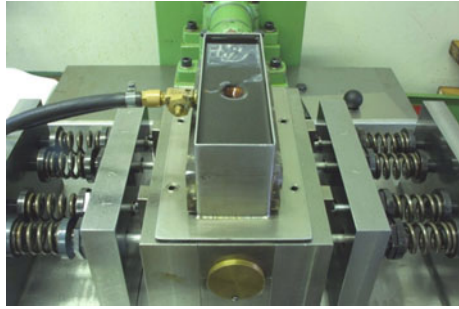
1 Introduction

The friction in automotive engines is mainly caused by three components: the engine bearings, the piston-ring assembly and the valve train [1]. Valve train friction losses account for 7.5–21 % of the total friction losses in internal combustion engines [2]. Compared with other engine parts, the valve train has not been studied abundantly, perhaps due to its complexity as it operates under a dynamic load, important and varying sliding speed, changing radius of curvature and poor lubrication [3, 4].

The chemical composition and physical structure of lubricant films strongly influence friction and wear in valve train [5]. In recent years, car engine keep the development of high-speed and high-power, which result in the increase of inertia force, spring force and sliding velocity of valve train. At the same time, the fuel economy concept leads to lighter viscosity. Optimal level of friction modifier or right balance of additives and base oil was considered more important. Accordingly, engine oils must be upgraded to keep pace.

The cam follower wear evaluation is considered as an important item of international advanced engine oil evaluation techniques. In ACEA lubricant evaluation method CEC L-51-98 (OM646) and CEC L-38-94 (PSA TU3 M/KDX), valve train is one of main performance indexes of test lubricant evaluation.

However engine test and road test cost too much. They are not enough for research on wear resistance of engine oil. This experimental research was based on close to practice cams and tappets under real lubrication condition in automotive engine, but simple work condition and short test cycle (Fig. 1). Advanced measurement technique was used to improve the test method.

Fig. 2 Friction test chamber

2 Test Equipments

2.1 Cam & Tappet Test Rig

Cam & tappet test rig models on the structure of vehicle valve. It is used operating a camshaft and tappets under real conditions but by means of an increased spring load. The tappets are distributed on both sides of the camshaft in same level. There's a spring in the lateral of each tappet (Fig. 2). Four nozzles are set above the cams to lubricate the test parts.

The following Fig. 3 shows the structure of the test rig. The camshaft is driven by an electric motor. The friction occurs on the contact surfaces of cams and tappets because of the spring force. Above the retaining device, the overflow container is located with the viewing windows and nozzles for the jet lubrication. Oil is supplied by a thermostat via a piping system with an oil filter into the overflow container [6]. In the sump below, there are a thermocouple and cooling pipe to control the oil temperature.

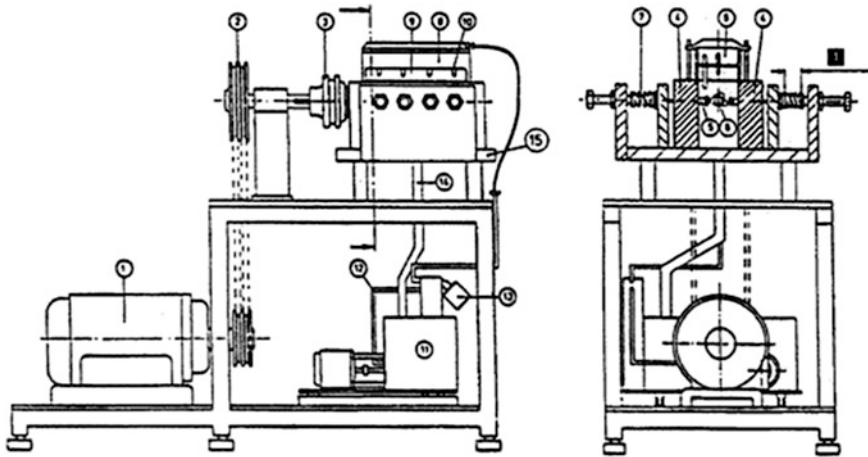
2.2 Test Rig Parameters

The power of the drive motor is 4 kW. Lubricant sump temperature can be controlled from 38 to 250 °C. And the maximum flow of lubricant is 20 L/min. Table 1 gives main parameters of the test rig.

2.3 Test Materials

The following Fig. 4 shows the picture of one set of test parts.

Camshafts and tappets produced by Marshall's Industrial were used throughout the project. Valve springs were supplied by IFT. Table 2 gives information about the test materials. Each set of test part (one camshaft and eight tappets) was used only once.



- 1- Drive motor;
- 2- Transmission;
- 3- Flexible coupling;
- 4- Retaining device;
- 5- Tappet;
- 6- Camshaft;
- 7- Valve spring;
- 8- Overflow container;
- 9- Viewing window;
- 10-Oil nozzle;
- 11-Thermostat;
- 12-Pipe supply;
- 13-Oil filter;
- 14-Pipe return;
- 15-Annular permanent

Fig. 3 Structure of test rig

Table 1 Cam & tappet test rig parameters

Components	Parameter (unit)	Value
Motor	Power (kW)	4
	Speed (rpm)	2,800
	Speed up (r/s)	140
Spring	Load (N)	0–1800
	Flow (L/min)	20
Thermostat	Thermal power (kW)	2
	Temperature (°C)	38–250

2.4 Measuring Equipments

The same positions of cam and tappet surface were measured before and after each test to calculate the wear values. The Accuracy of tappet and cam measuring instrument is both 1 μm.



Fig. 4 Test camshaft and tappets

Table 2 Test materials information

Components	Supplier	Type	Material	Order No.
Camshaft	Marshall's industrial	1	TL006:1997-06	E113109101FB1/05
Tappet	Marshall's industrial	1	TL005:1994-05	E113109101FB1/05
Valve spring A	IFT	Running-in		11-100-37A-5205A
Valve spring B	IFT	Main run		11-100-37A-5205B

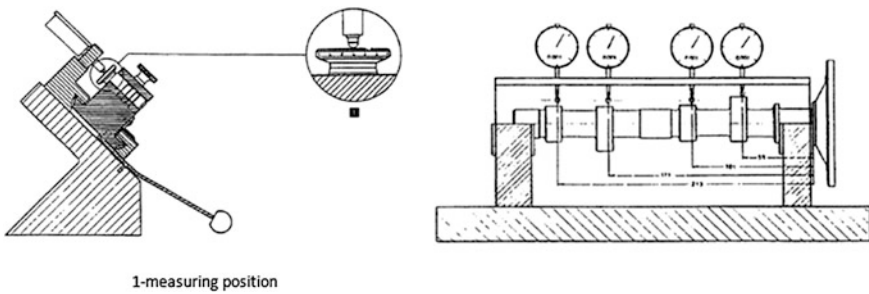


Fig. 5 Tappet (left) and camshaft (right) measuring instruments

2.4.1 Tappet Measuring Instrument

The following Fig. 5 shows the measuring positions of tappet surface.

2.4.2 Cam Measuring Instrument

Figure 5 shows the measurement principle of cam measuring instrument.

Table 3 Friction test condition

Phase	Time (h)	Speed (rpm)	Temperature (°C)	Spring load (N)
Running-in	1	2,000	90 ± 2	700
Main run	16	2,000	90 ± 2	1,700

3 Test Method

5 L lubricant oil was used for each test. Before it, all the spring loads and valve clearances should be adjusted. After 1 h running-in, spring A were replaced by spring B for 16 h main run. The loads and clearances should be adjusted again [6]. Table 3 gives the test conditions.

The test procedure refers to PV5106, which is a test method of Volkswagen. PV5106 is used to test the wear behavior of engine oils, especially in cam-tappet friction area. It's generally applicable for lubricants used in both gasoline and diesel engine with any pattern of cam follower.

4 Results and Analysis

4.1 Wear Evaluation

In PV5106, cam and tappet wear which were expressed in microns determines the anti-wear performance of engine oil. This study gives another parameter to do a supporting research on friction loss. It's "tappets weight loss".

Before test, the initial height of four cams and eight tappets were measured by the equipments shown in 2.4. Each tappet was weighed for better study. The same measurement was done after the test. The height loss and weight loss depend on the measurement results, those are,

$$w_C = \frac{\sum_{i=1}^4 \Delta H_i}{4} \quad (1)$$

$$w_T = \frac{\sum_{i=1}^8 \Delta h_i}{8} \quad (2)$$

$$G = \sum_{i=1}^8 \Delta G_i \quad (3)$$

where w_C is the mean of height loss of fore cams, expressed in μm , ΔH_i the height loss of cam I, μm , w_T the mean of height loss of eight tappets, μm , Δh_i the height loss

Table 4 Properties of test oils

Engine oil	SAE grade	KV @40 °C (cSt)	KV @100 °C (cSt)	Meet the standard requirements of
1#	15 W-40	106.5	14.19	
2#	5 W-40	82.73	14.16	ACEA A3/B4
3#	15 W-40	98.66	15.06	
4#	5 W-40	102	14.8	ACEA E7, API CI-4, SL
5#	15 W-40	121.3	16.36	

of the tappet i , μm , G the sum of weight loss of eight tappets, mg , ΔG_i the weight loss of the tappet i , mg . The height loss and weight loss values of different tests were analyzed and compared to define the anti-wear performance of engine oils.

4.2 Test Results

Table 4 gives some properties of five kinds of engine oil, which are numbered as 1#, 2#, 3#, 4# and 5#. 1# is the reference oil of the method while 2#, 3#, 4# and 5# are service oil. Properties of 2# and 4# are very good. 4# was purchased oversea. Comparatively, the properties of 3# and 5# which were blended during oil R&D may not be so good.

The five engine oils were used to run the friction test on the rig. The results of all tests were given in Table 5.

4.3 Repeatability

To verify the repeatability of the method, 2# and 5# engine oil were used to run repeat tests.

Figure 6 shows similar results of two tests of 2# oil, same as 5# oil. That indicates a good repeatability of this test method, which is effective for anti-wear performance evaluation.

4.4 Comparison

Figure 7 compares the Tappet height losses of all the five oils. It shows that, the results of 1#, 2# and 4# are much better than the other two oils. The tappet wear values of 2# and 4# are similar and better than the reference oil. These two oils show a good wear protection behavior. Test result of 3# and 5# is worse, and they need to update the additive formulation.

Table 5 Engine oil test results

Engine oil	Average cam wear (μm)	Average tappet wear (μm)	Tappets weight loss (mg)
1#	90	53.5	135
2# (First)	92.0	45.0	135.5
2# (Second)	81.8	49.4	129.5
3#	167.0	68.8	229.3
4#	95.8	45.0	91.8
5# (First)	94.8	78.6	281.9
5# (Second)	102.5	78.1	296.2

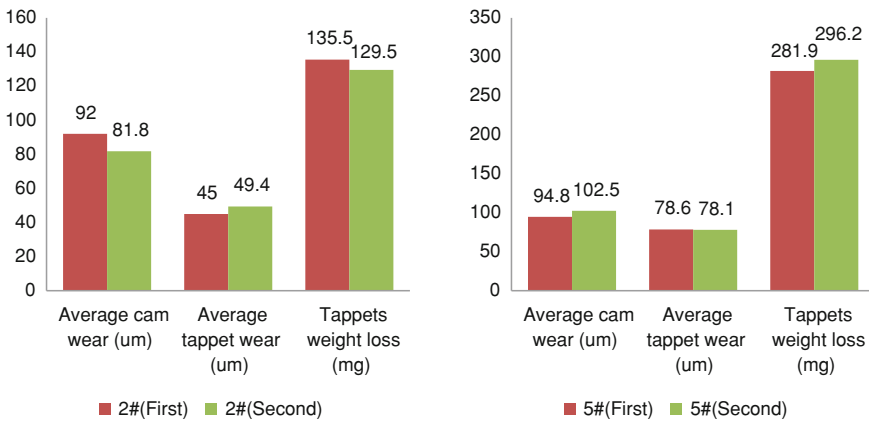


Fig. 6 Repeatability test result compare

The experimental research showed that average cam wear was not able to distinguish between good and bad anti-wear performance, as the numbers given in Table 4. But in addition, Fig. 8, which compares the tappet weight losses, shows a similar trend to tappet height losses.

4.5 Correlation

In valve train scuffing test method CEC L-38-94, the reference oils are RL194 and RL142 [7]. RL194 is the standard oil with better wear protection behavior, while RL142 is lower. The protocol to follow is given in Table 6.

To verify the effectiveness of this test method, TU3 (CEC L-38-94) reference oil RL142 and RL194 were used to run the cam & tappet test rig. Pictures were taken to describe the test parts after 16 h friction (Figs. 9 and 10). It seems that RL194 protect the cams and tappets better than RL142.

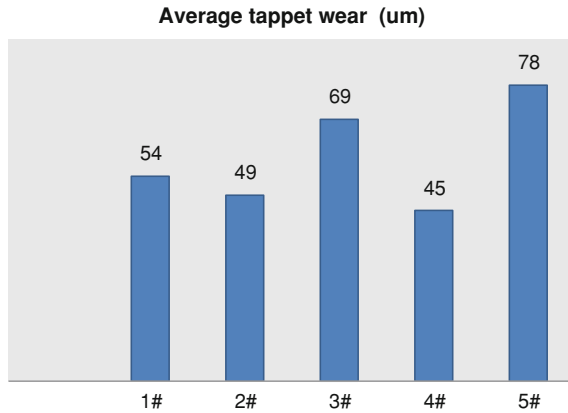


Fig. 7 Tappet wear values compare

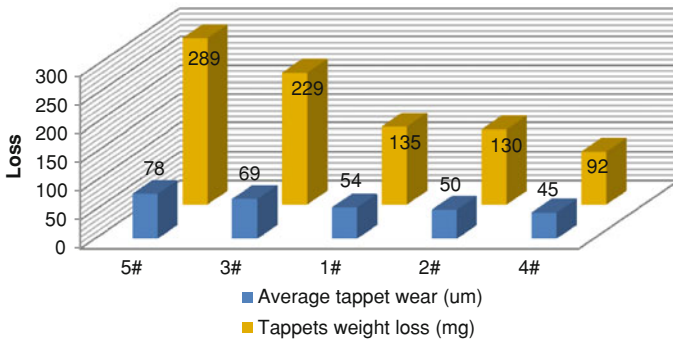


Fig. 8 Test results compare

Table 6 Cam wear values of CEC L-38-94 reference oil

Reference oil	RL142	RL194
Number of tests	14	19
Mean (μm)	9.09	3.48
Target (μm)	9.1	3.5

Surface profiler was used to compare the test parts of the two oils. Pt in Fig. 11 is the peak-valley difference of the whole tappet surface after test. It shows that tappets in RL142 were deeply worn.

Table 7 gives the specific results. It shows that RL194 shows a better performance in protecting the tappets while RL142 is worse. But cam wear results of the test are too closed to make a distinction of the two oils. 2# oil was used to run TU3 test method in Europe. The result data can be an addition for correlation research.



Fig. 9 Test tappets picture compare

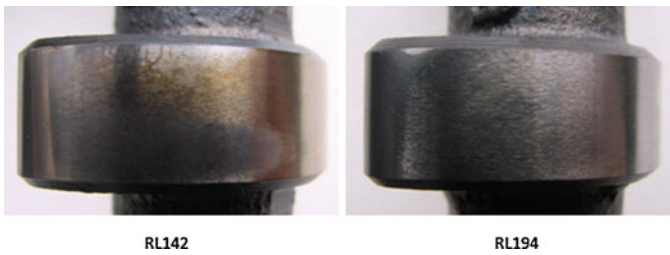


Fig. 10 Test cam picture compare

The statistics concept of correlation coefficient can be used to analyze the two test method quantitatively [8], it's

$$r_{XY} = \frac{\sum_{i=1}^n (X_i - \bar{X})(Y_i - \bar{Y})}{\sqrt{\sum_{i=1}^n (X_i - \bar{X})^2} \sqrt{\sum_{i=1}^n (Y_i - \bar{Y})^2}} \quad (4)$$

where X, Y were given in Table 7.

The more absolute value of correlation coefficient is closed to 1, the more the two sets of data correlate with each other. Otherwise, the more absolute value of correlation coefficient is closed to 0, the less the two sets of data correlate with

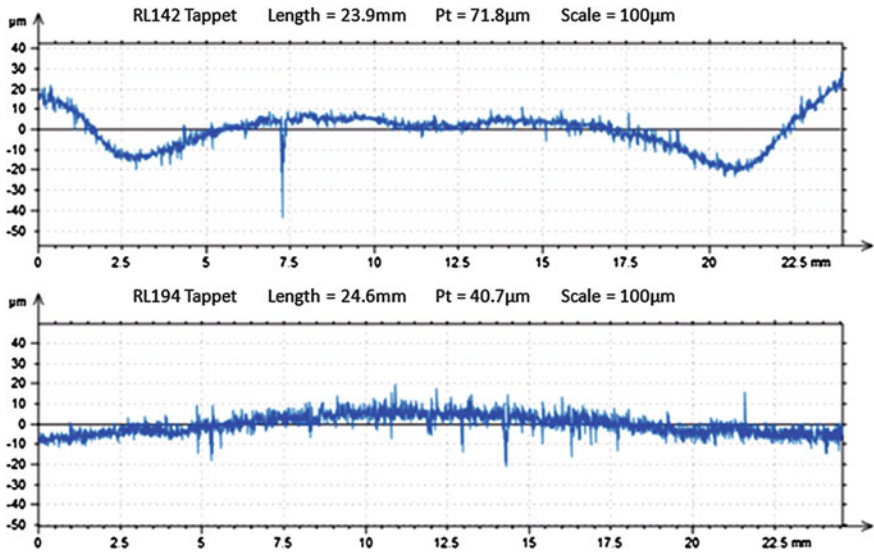


Fig. 11 Profile extractions of tappet surface of the two methods

Table 7 CEC RL142 and CEC RL194 test results

Reference oil	TU3 cam wear target(μm)-X	Average cam wear(μm)-Y'	Average tappet wear(μm)-Y''	Tappets weight loss(mg)-Y'''
RL142	9.1	93	94.5	307.2
RL194	3.5	94.5	77	249.6
2# (Average)	3.6	86.9	47.2	132.5

Table 8 The correlation coefficients

Item	Average cam wear	Average tappet wear	Tappets weight loss
Code	$r_{XY'}$	$r_{XY''}$	$r_{XY'''}$
Correlation coefficient	0.32	0.77	0.74

each other. Table 8 gives the correlation coefficients of three items- average cam wear, average tappet wear and tappets weight loss.

The correlation coefficient of average tappet wear is 0.77, which means the correlation between tappet wear of the method and cam wear of TU3 is close, and tappets weight loss support this conclusion. But the cam wear of the method doesn't show the same quality.

The research shows that, there's the same trend of the two test methods. In the aspect of average tappet wear and tappets weight loss, there is good correlation

between CEC L-38-94 and the test method we use in this article. But there is no correlation of the two methods in the way of cam wear measurement.

5 Summary

The investigations of cam & tappet friction test method shows that the repeatability of the test is good. The method is effective to evaluate the anti-wear performance of engine oil.

The comparison of the five engine oil test results shows that the method is available to be used as a filter to select the best oil from others in wear resistance. According to the test results, 2# and 4# which show a good wear protection behavior were recommended for using in vehicle engine.

The practice on weight measurement proved that weight loss is a good reference to support evaluation. Weight loss of tappets should be reported. In this research, cam wear can't be used to differentiate between better oils and worse ones. It may be just record in the report.

The research shows that the cam & tappet friction test method has the same effect as test method CEC L-38-94 to evaluate the anti-wear performance of engine oil. It can be used as an evaluation method for engine oil R&D.

The test procedure and oil working condition of this method could be further researched to meet requirements of original equipment manufacturers.

References

1. Anderson BS (1991) Company perspectives in vehicle tribology-volvo. In: 17th Leeds-Lyon symposium on tribology-vehicle tribology, Elsevier, pp 503–506
2. Messe S, Lubrecht AA (2000) Transient elasto hydrodynamic analysis of an overhead cam/tappet contact. Proc Inst Mech Eng Part J J Eng Tribol 214:415–425
3. Mufti RA (2004) Total and component friction in a motored and firing engine. PhD Thesis, School of Mechanical Engineering, University of Leeds, UK, p 276
4. Mufti RA, Jefferies A (2008) Novel method of measuring tappet rotation and the effect of lubricant rheology. Tribol Int 41:1039–1048
5. Willermet PA (1995) The composition of lubricant-derived surface layers formed in a lubricated cam/tappet contact II. Effects of adding overbased detergent and dispersant to a simple zdtf solution. Tribol Int 28:163–175
6. PV5106 (2006) Motorenöle Prüfung des Verschleißschutzverhaltens
7. CEC L-38-94 (2008) Part 11: referencing and precision statement
8. Yongsuo Liu (2004) Improvement of similarity measure: pearson product-moment correlation coefficient. J Chin Pharm Sci 13(3):180–186

An Experimental Study on Biodiesel Characteristics in a Common Rail Direct Injection Diesel Engine

Jae-Woong Kim, Hyung-Ik Kim, Yung-Jin Kim and Ki-Hyung Lee

Abstract Owing to increasing oil price caused by risk of oil depletion, many researchers have focused to develop various alternative energies. Biodiesel is one of those energies, which has been a hot-issue recently in automotive industries. Because biodiesel has similar characteristics as diesel, it is possible to use present gas stations, facilities and engine without any modification. It has also an advantage that the emission of biodiesel is lower than conventional diesel engine because it contains oxygen in the fuel. However biodiesel has some problems such as corrosiveness and high viscosity. Therefore, in this study, an experiment was conducted to use biodiesel fuel to solve these problems, and the characteristics of combustion and emission were evaluated according to the use of biodiesel blended with diesel fuel and it was compared with diesel fuel. As a result, we found that biodiesel has benefits of reduction in CO₂ and PM emissions compared to diesel fuel.

Keywords Biodiesel · Spray visualization · Common rail · Soybean · Canola

1 Introduction

Environmental pollution has been intensified by increasing CO₂ and harmful emissions which are generated from vehicles and industry facilities. In addition, risk of energy depletion has been raised rapidly caused by increasing energy

F2012-A03-021

J.-W. Kim (✉) · H.-I. Kim · Y.-J. Kim · K.-H. Lee
Department of Mechanical Engineering, Hanyang University, Seoul, Republic of Korea
e-mail: venator123@nate.com

demand of developing countries such as China and India. Up to now, most of the energies for transportation and production of electricity depend on fossil fuel. For these reasons, research on alternative energies is very important to save consumption of fossil fuel. Recently, biodiesel is spotlighting as one of the alternative energies. Since the characteristics of biodiesel are similar to diesel fuel and it is extracted through chemical process from the fat of animal or plant such as canola or soybean, the biodiesel has many merits to be used instead of fossil fuel. First, risk of the fuel depletion is very low because biodiesel is renewable to be produced continuously. Second, most of the harmful emission is exhausted in a lower level. Finally, greenhouse gas can be reduced by absorption of CO₂ in the Photosynthesis during the growth of the plant. For these reason, the use of biodiesel have been increased continuously [2].

In this study, we used canola and soybean to produce biodiesel. To analyze characteristic according to mixing ratio, we carried out the injection and engine tests. In the injection quantity test, we investigated the different characteristics between diesel fuel and biodiesel to consider the suitability for engine test. Then, we conducted engine performance experiment to analyze the combustion and emission characteristics.

2 Experimental Devices and Measurement

2.1 Biodiesel Production

We made two kinds of biodiesel fuel which were made of canola and soybean oil directly through the commercialized production machine in a laboratory by using the method of trans-esterification among the most popular four kinds of biodiesel production process. The method of trans-esterification is chemical reaction that acid and alkyl radical of ester is exchanged with reaction of acid, alcohol and another ester, as shown in Fig. 1 [3].

2.2 Experiment of Injection Quantity

An injection quantity measurement device is shown in Fig. 2. In order to measure the injection quantity according to injection pressure and duration, it was composed of a processing computer, a PCV controller, an injector driver, a high pressure pump and a low pressure pump. The same process was iterated 200 times according to the injection pressure and duration. Then, the total injection quantity was calculated and averaged. Test fuel and experimental condition are as shown in Table 1.

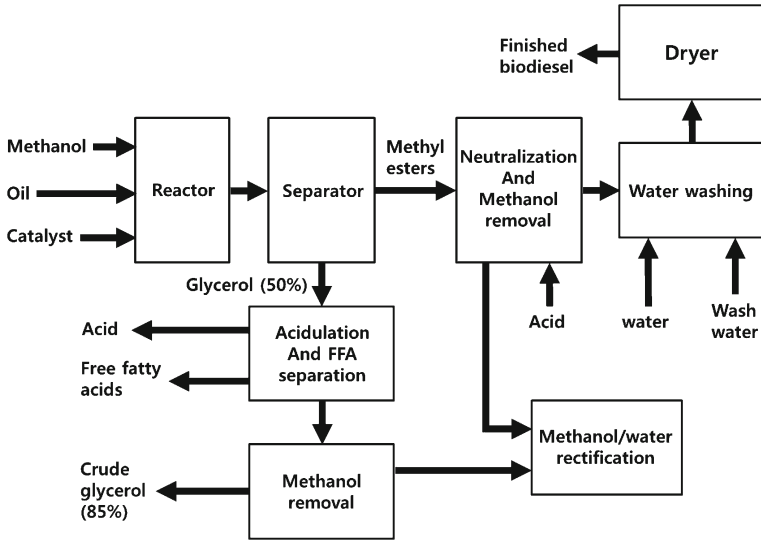


Fig. 1 Diagram of biodiesel of manufacturing process

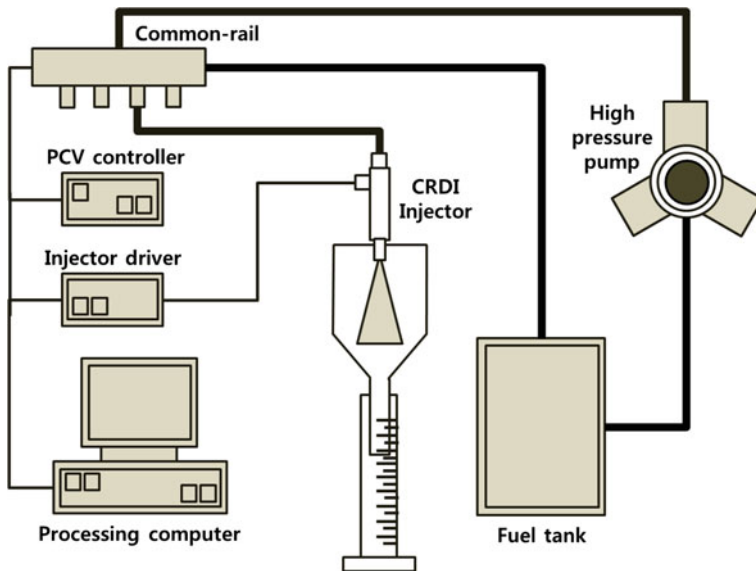
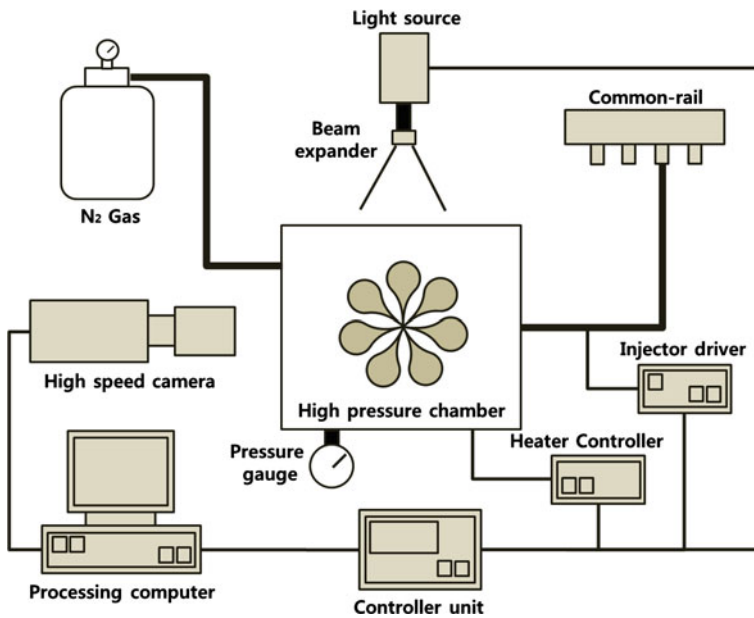


Fig. 2 Biodiesel making machine

Table 1 Experimental conditions of injection quantity test

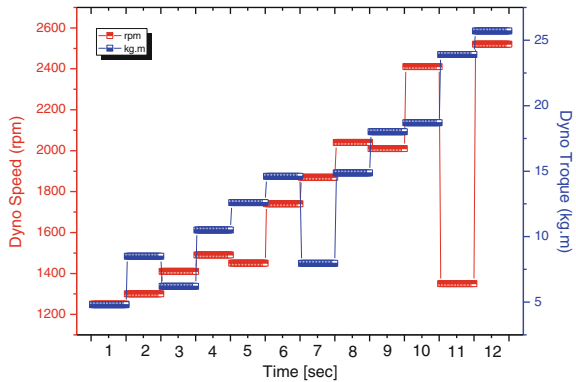
Contents	Condition
Used fuel	Diesel, BD5, 20, 35 % (Canola, Soybean)
Injection pressure (bar)	800, 1000, 1200
Injection duration (ms)	0.3–1.2

**Fig. 3** Schematic of spray visualization device

2.3 Spray Visualization

A spray visualization system was set for understanding characteristics of spray penetration and atomization. Experimental apparatus was designed to simulate conditions of pressure and temperature in a cylinder. And the pressure and temperature were controlled by using electric heater and nitrogen gas. The constant volume chamber was equipped with three large quartz windows. Light source was supplied through the quartz windows and a high speed camera set at the bottom side of the chamber [4]. The injection duration was used same data obtained from a previous experiment. Through this data, 20 mm^3 was chosen as the injection quantity Fig. 3.

Fig. 4 Engine test mode (12 point)



2.4 Engine Experiment

The engine experimental device to measure engine performance and emission characteristics with various types of biodiesel fuel was shown in Fig. 4. A 4 cylinder 4 valve common-rail direct injection engine and Meiden’s eddy current type dynamometer were used. Also, Smoke meter produced by AVL and Horiba MEXA-6900 emission analyzer were used to measure the emission gas. The engine test was carried out with the same fuels used for the earlier tests of injection quantity and spray visualization to compare the emission characteristics. Twelve test point as shown in this figure were selected from New European drive cycle (NEDC) driving mode. The engine rpm and torque were also controlled by using an ECU. In addition, the temperature of fuel, coolant, and oil were set at 30, 80, and 90 °C, respectively (Table 2) [5, 6].

3 Result

3.1 Biodiesel Production

In this study, soybean and canola(oil) biodiesels were produced using a commercialised machine. Then, we reproduced 5, 20, 35 % biodiesel under volumetric ratio of 100 % pure biodiesel. Figure 5 shows the samples of the pure biodiesel and Table 3 shows the properties of the biodiesels produced by the machine.

3.2 Comparison of Injection Quantity

When the injection pressure and duration increase, injection quantity increases linearly as shown in Fig. 6. In cases of 5, 20, 35 % mixing rates of soybean and canola, the results are a little different from 100 % diesel fuel but it is still acceptable

Table 2 Test engine specification

Description	Specification
Engine type	4 Stroke turbo-charged DI diesel engine
Number of cylinder	4
Bore × Stroke (mm)	83 × 92
Displacement volume (cc)	1991
Fuel injection system	Common rail (1600 bar)
Valve type	DOHC 4 valves per cylinder
Maximum power (ps/rpm)	146/4000
Maximum torque (kg m/rpm)	32/1800–2500

Fig. 5 Samples of pure biodiesel**Table 3** Properties of diesel and biodiesel

	Diesel	Soybean	Canola
Cetane number	40–55	54.64	55.52
Caloric value	42.06	39.11	40.45
Density	870	886.3	885.1
Kinematic viscosity	1.3–4.1	4.207	4.425
Flashing point	60–80	171	84
Oxygen	0	11	11
Sulfur content	0.05	0–0.0024	0–0.0024
	maximum	maximum	maximum

to use for the engine test. In addition, the injection quantity of canola has a little larger value than that of soybean. However, both fuels are possible to use in engine.

3.3 Comparison of Spray Behavior

Spray visualization was carried out for the different type of fuels with the same injection quantity of 20 mm³. Injection pressure and ambient pressure were also selected the same injection quantity condition. The fuels used for the spray visualization were diesel fuel and 5, 20, 35 % blended fuels (canola, soybean).

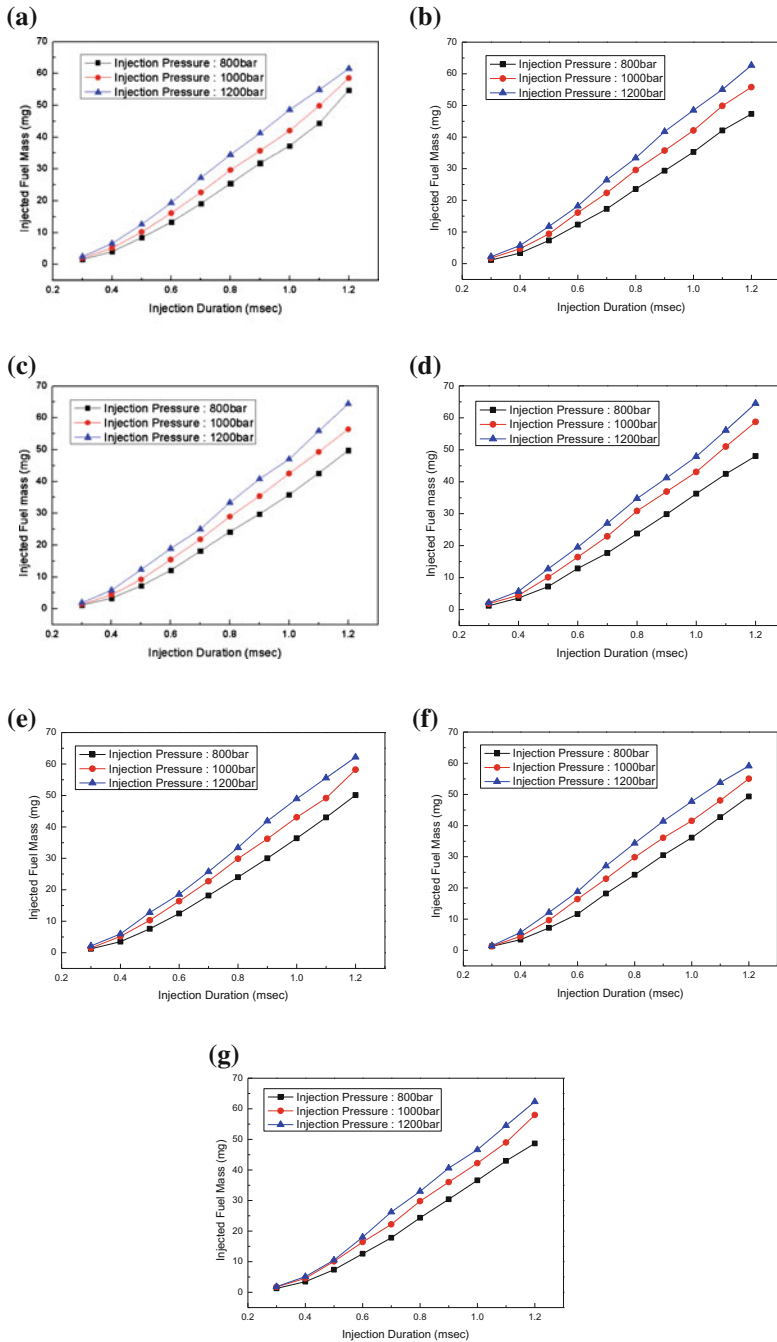


Fig. 6 Result of injection quantity according to various fuel. **a** Diesel, **b** Canola 5 %, **c** Canola 20 %, **d** Canola 35 %, **e** Soybean 5 %, **f** Soybean 20 %, **g** Soybean 35 %

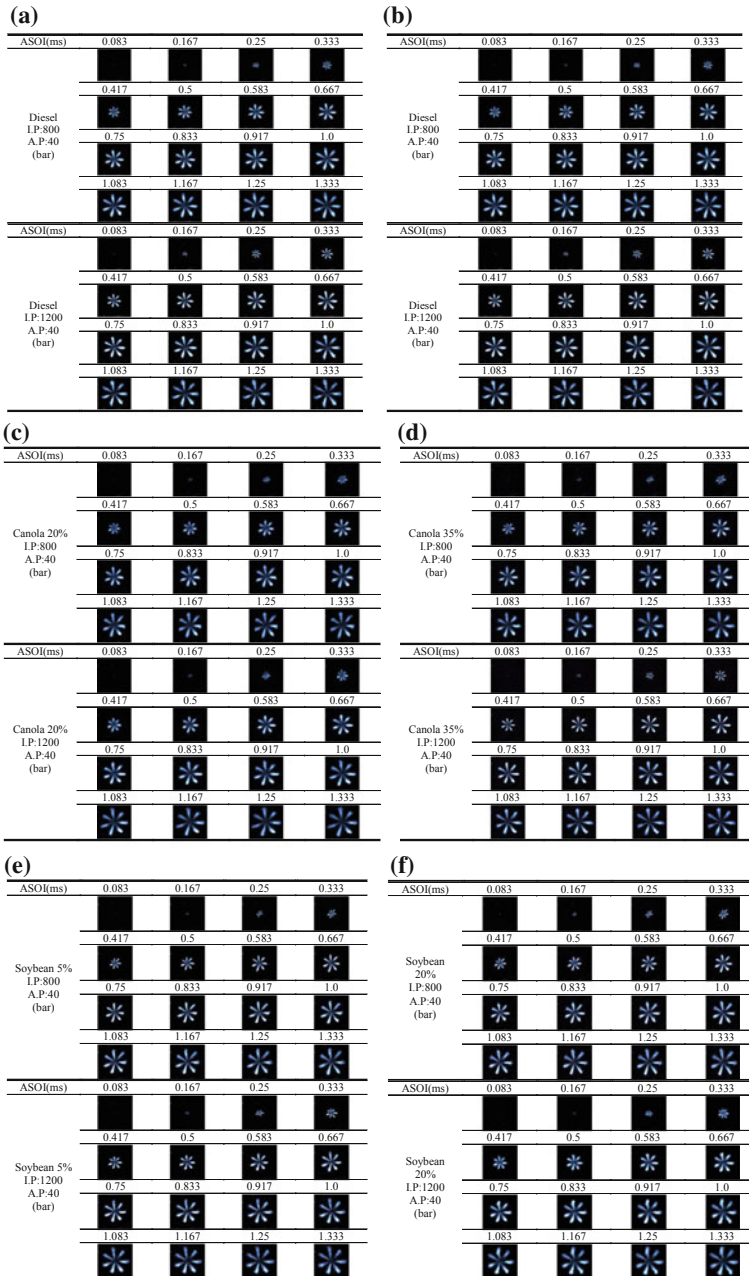


Fig. 7 Result of spray visualization according to injection and ambient pressure. **a** Diesel, **b** Canola 5 %, **c** Canola 20 %, **d** Canola 35 %, **e** Soybean 5 %, **f** Soybean 20 %, **g** Soybean 35 %

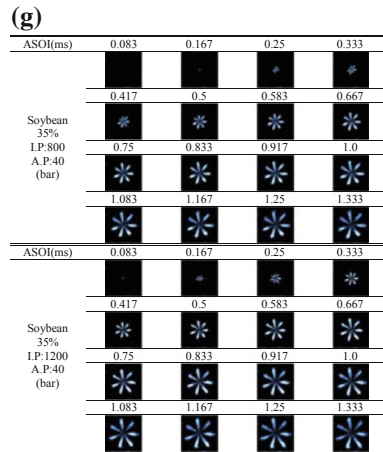


Fig. 7 continued

Injection pressure was changed from 800 to 1200 bar and the ambient pressure was set as 40 bar. Figure 7 shows the result of spray visualization. In this figure, I.P means injection pressure and A.P means ambient pressure. As shown in the Fig. 7, penetration was shorter when the injection pressure was lower and the ambient pressure was higher in all cases. On the other hand, the penetration lengths of two types of biodiesels blended fuels are shorter than diesel fuel in the same conditions. It is thought that two types of biodiesels have the higher viscosity. Especially, it was found that spray behavior diesel fuel is fairly different from the case of two 35 % biodiesel when condition was 1200 rpm and 40 bar.

Figure 8 shows the spray images according to the type of fuel at the same elapsed time after injection. This image result indicate that blended fuel have shorter penetration than that of diesel fuel. And when the mixing rate of blended fuel was higher, the penetration becomes shorter. In the case of injection characteristics, the injection delay is longer than diesel fuel and blended fuel was evaporated slowly than diesel fuel because blended fuel has a high kinematic viscosity as shown in Table 3.

3.4 Combustion and Emission Characteristics

3.4.1 Combustion Characteristics

The in-cylinder pressure and ROHR characteristics for the fuel types are compared in Figs. 9 and 10. From the result, we found that blended fuel has higher cylinder pressure and more advanced ROHR timing than that of diesel fuel. It is because that blended fuel has high cetane number and contains oxygen.

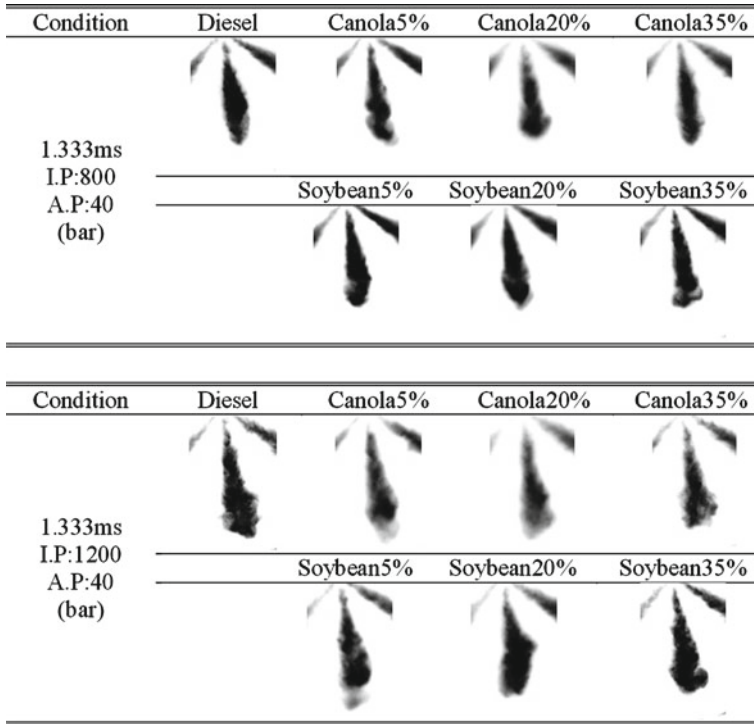


Fig. 8 Spray characteristics according to the fuel types

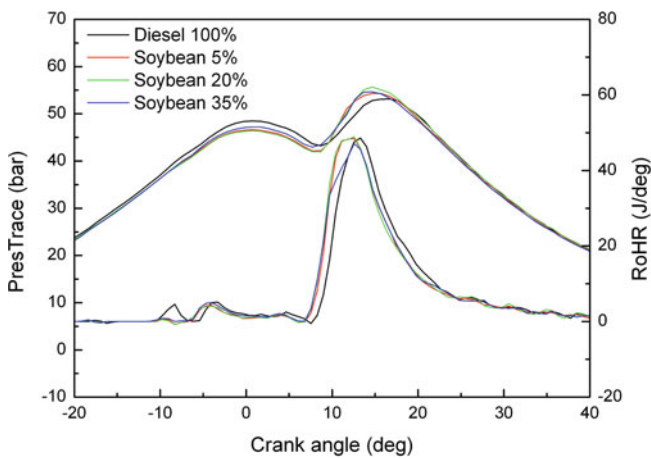


Fig. 9 PresTrace and ROHR characteristics of canola biodiesel

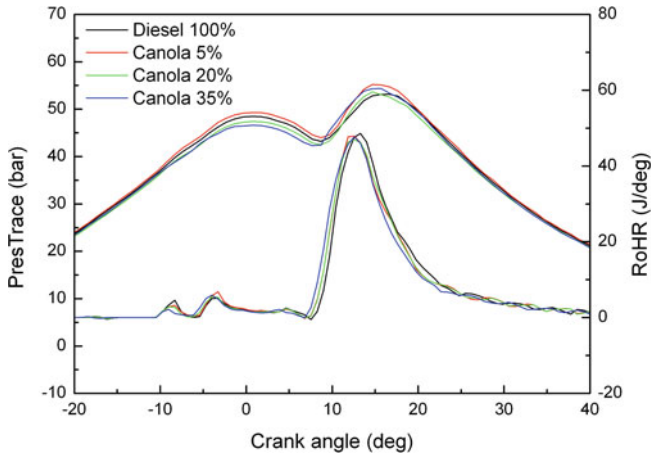


Fig. 10 Pressure trace and ROHR characteristics of soybean biodiesel

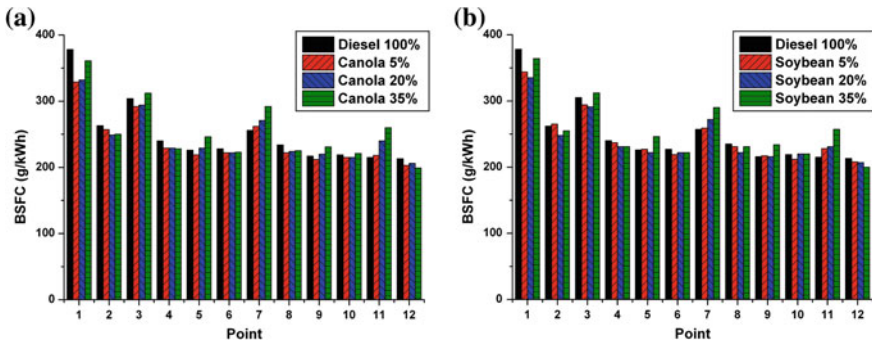


Fig. 11 BSFC according to mixing rate. a Canola, b Soybean

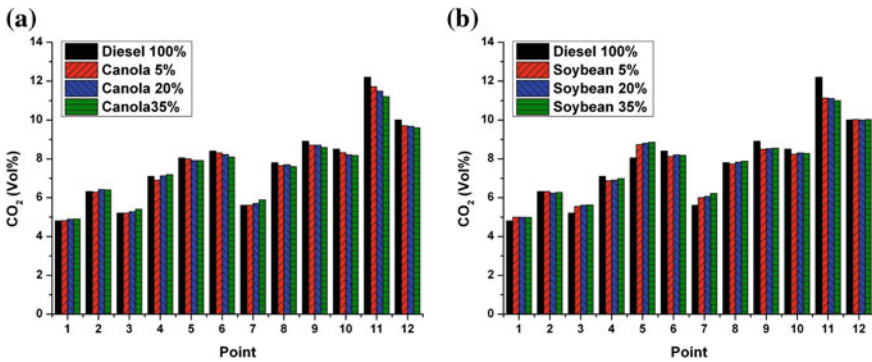


Fig. 12 CO₂ according to mixing rate. a Canola, b Soybean

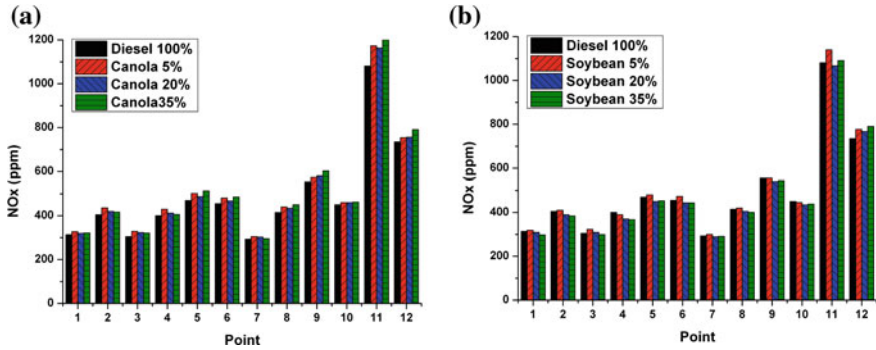


Fig. 13 NOx according to mixing rate. a Canola, b Soybean

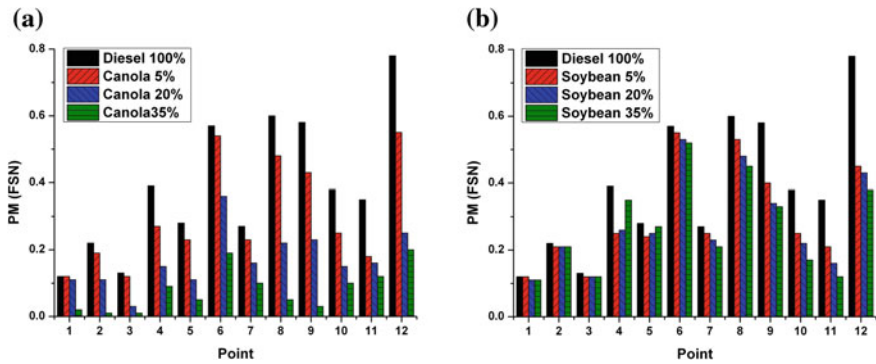


Fig. 14 PM according to mixing rate. a Canola, b Soybean

3.4.2 Emission Characteristics

BSFC according to the mixing rate is shown in Fig. 11. This result shows that the BSFC was increased slightly at few cases, because biodiesel has lower heating value than that of diesel fuel. This trend of biodiesels causes lower power than that of diesel fuel for the same injection quantity. Therefore, biodiesel must be injected more than diesel fuel for generating same power. Comparing canola and soybean biodiesel, there were no difference of BSFC.

CO₂ emission becomes lower according to increasing mixing rate in most cases, as shown in Fig. 12. It could be the reason why biodiesel has lower carbon content as shown in Table 3. From the comparison between canola and soybean biodiesel, we found that canola has a lower CO₂ level than soybean.

The NOx emission characteristics according to the biodiesel mixing rate were compared in most cases. The comparison results are shown in Fig. 13. NOx emission was increased significantly in low engine speed and high load conditions. It is expected that the combustion temperature of biodiesel increases NOx emission levels because biodiesel has oxygen content which promotes combustion.

From the compared results between canola and soybean biodiesels, canola has lower NO_x than those of soybean.

PM was significantly lower when the mixing rate of biodiesel increased, as shown in Fig. 14. It is thought that combustion is promoted with the oxygen content of biodiesel, and the carbon oxidation process is improved. From the comparison between canola and soybean biodiesel, it was found that canola produces lower PM than soybean.

4 Conclusions

- Injection quantity increased linearly when injection pressure and duration increased
- Characteristics of injection quantity of biodiesel was similar to diesel fuel
- Spray penetration was shorter at lower injection pressure and higher ambient pressure conditions. In addition, spray penetration of biodiesel was shorter than that of diesel fuel because of higher viscosity
- Biodiesel has longer injection delay and time needed to atomize because of higher kinematic viscosity
- Biodiesel has lower CO₂ emissions than diesel fuel because it has smaller diameter than diesel fuel. On the other hand, biodiesel has higher NO_x and lower PM emission level because it contained oxygen
- Canola biodiesel has better emission characteristics than soybean.

Acknowledgments This work was supported by the 2nd phase Brain Korea 21(BK21) program and the Industrial Strategic Technology Development Program (No. 10039673, Development of design technologies of core control algorithms and an ECU for clean diesel engines) funded by the Ministry of Knowledge Economy (MKE, Korea).

References

1. Lee Y. Status & prospect of biodiesel. *Autojournal* 32(4)
2. Stringer VL, Cheng WL (2009) Comparing the operation of an HSDI engine using multiple injection schemes with soybean biodiesel, diesel and their blends. SAE2009-01-0719
3. Yamane K, Kato T. Effect of refining process in biodiesel fuel production on fuel properties, diesel engine performance. JSAE 20030035, SAE2003-01-1930
4. Oh Y, Choi S. The study on atomization characteristics of biodiesel. KSAE10-B0097
5. Lee D, Roh H, Choi S and Lee C (2010) KSME: Combustion and emission characteristics of 4 cylinder common-rail di diesel engine with biodiesel blended fuel. Proceedings of KSME 2010 spring conference, pp 128–134
6. Hansen KF, Jensen G (1997) Chemical and biological characteristics of exhaust emissions from a DI diesel engine fuelled with rapeseed oil methyl ester (RME). SAE-971689

Engine Oil Antioxidant Selection for Delivering Superior Oxidation and Deposit Control Protection

Bo Liu and Vince Gatto

Abstract Engine oil formulators face a number of challenges when developing modern passenger car motor oils. In recent years greater performance demands have been placed on engine oils to deliver superior oxidation and deposit control protection. This has occurred concurrently with the mandated reductions of phosphorus driven by concerns to protect engine catalyst systems. This has forced the use of lower levels of zinc dialkyldithiophosphate (ZDDP) in modern engine oils. ZDDP is known to be one of the most cost effective antioxidants available. Reductions in its use must be compensated for by the use of other phosphorus-free antioxidants. A challenge exists for the engine oil formulators to identify the most cost effective alternatives to ZDDP while at the same time utilizing inexpensive and rapid, yet meaningful bench test techniques. This paper looks at the use of a bulk oil oxidation test (AlbOT), pressurized differential scanning calorimetry (PDSC), the Caterpillar Micro-Oxidation Test (CMOT) and the Thermo-Oxidation Engine Oil Simulation Test (TEOST-MHT) to evaluate and rank the robustness of passenger car engine oil performance for both oxidation protection and deposit control capabilities. These tests are utilized to screen a number of antioxidant systems in engine oils formulated with 500 ppm of phosphorus derived from ZDDP. The antioxidant components are selected from a series of commonly used and commercially available materials plus some developmental materials. These components include a molybdenum compound, alkylated diphenylamines, hindered phenolics, and new developmental and experimental multi-functional antioxidants. The performance of these fully

F2012-A03-023

B. Liu (✉)
Albemarle Chemicals, Nanjing, China
e-mail: bo.liu@albemarle.com

V. Gatto
Albemarle Corporation, Pasadena, USA

formulated engine oils are ranked in the selected bench tests in order to highlight the benefits of each antioxidant system under evaluation. Structure activity studies are carried out on a select group of tests in order to gain further insight as to how antioxidant chemical structure impacts oxidation and deposit control performance. The results point to significant performance benefits when multi-functional antioxidants are employed or when the optimum molecular weight antioxidant is selected.

Keywords Antioxidants · Engine oils · Oxidation · Deposit control · Bench test

1 Introduction

In recent years the types of basestocks available to formulate finished crankcase and industrial oils have changed. As greater demands are placed on finished oil oxidation performance, we have seen steady increase in the usage of hydrocracked, iso-dewaxed basestocks and polyalphaolefins in the finished oils. At the same time, the mandated reduction of phosphorus has been driven by concerns to protect engine catalyst systems. New product specifications result in those changes requiring lower finished oil volatility, longer oil drain intervals, and improved fuel economy. All these changes offer a number of challenges to the engine oil formulators in order to deliver superior oxidation and deposit control protection performance. As we are aware of, the passing limits for maximum deposits in the TEOST MHT[®] have dropped from 45 mg for GF-3 to 30 mg for GF-5. Zinc dialkyldithiophosphate (ZDDP) is known to be one of the most cost effective antioxidants available. The forced use of lower levels of ZDDP in modern engine oils must be compensated for by the use of other phosphorus-free antioxidants to achieve desirable deposit control performance.

Besides deposit formation, engine oils formulators must take into consideration of other aspects associated with lubricant oxidation, including viscosity change, and varnish formation etc. Oxidation tests are being utilized to optimize engine oil formulations for otherwise expensive engine sequence tests or field tests [1]. Our approach involves using a variety of bench tests to monitor different aspects of lubricant oxidation. This paper will present that a combination of tests can be used to help optimize engine oil formulations.

2 Modern Engine Oils Stabilization Needs

A schematic representation of what happens during the oxidation of modern engine oils is shown in Fig. 1. The various *R* groups represent different hydrocarbon chains of engine oils. The oxidation process produces hydroperoxides that are somewhat unstable at elevated temperatures. These hydroperoxides will cleave to form alkoxy radicals that can undergo one of two possible chemical transformations. They can

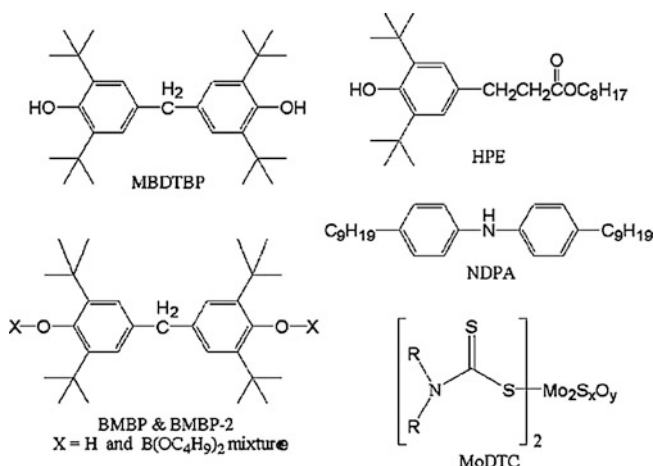


Fig. 2 Antioxidants used in this study

[12–15] involve a reservoir of oil samples passing a metal or glass surface heated at temperatures higher than 200 °C. They combine the traditional bulk oil oxidation test characteristics with thin-film oxidation conditions.

4 Bench Oxidation Studies of Mixed Antioxidant Systems in Low-P Engine Oils

A variety of mixed antioxidant systems are screened in the bench tests for identifying the most robust system to use in low phosphorous engine oils. Figure 2 shows the antioxidants chosen for this study. HPE and MBDTBP represent two different hindered phenolics commonly used in engine oils. MBDTBP possesses a high total phenolic content with the two hindered-phenolic groups. These phenolics are of low volatility and considered effective antioxidants for high temperature lubricant applications. Alkylated diphenylamine ADPA and molybdenum dithiocarbamate MoDTC are commercially available additives. A multi-functional antioxidant BMBP combines boron with the hindered phenolic functionality of MBDTBP. There are two versions. The material designated BMBP contains 22 wt. % MBDTBP and 1.8 wt. % boron, while the material designated BMBP-2 has 38 wt. % MBDTBP and 1.4 wt. % boron.

A model engine oil contained 4.80 wt. % succinimide dispersant, 1.80 wt. % overbased calcium detergent, 0.5 wt. % neutral calcium detergent, and 0.60 wt. % secondary zinc dialkyldithiophosphate, with the balance composed of Group II base oil. The Group II base oil had a kinematic viscosity @100 °C of 6.1 cSt and a viscosity index of 114. The various antioxidants mentioned above were added. The organomolybdenum compound MoDTC was added to deliver either 360 ppm

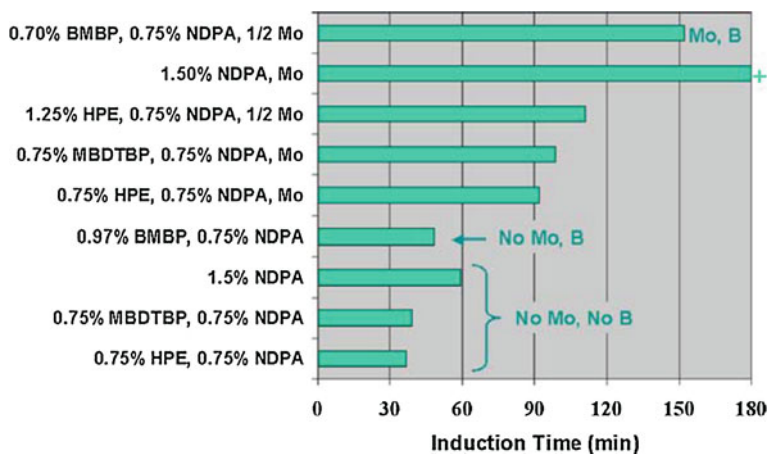


Fig. 3 Oxidation induction time of low-P engine oils by PDSC

(noted as Mo) or 180-ppm molybdenum ion (noted as $\frac{1}{2}$ Mo). All of the finished engine oil blends contained 500 ppm of phosphorus, 520 ppm of zinc, and 2400 ppm of calcium.

Oxidation bench test conditions are listed below:

4.1 Pressurized Differential Scanning Calorimetry

The general test operation is described in ASTM D 6186 [5]. An oil sample of approximately 3.0 mg was used in the presence of 50-ppm iron from an iron (III) naphthenate oxidation catalyst. Testing was performed at 180 °C under 500-psig oxygen and an oxygen purge rate of 100 mL/min. The oxidation induction time OIT results are shown in Fig. 3.

4.2 Albemarle Oxidation Test

This test is similar to ASTM D 2893 [16]. An engine oil sample of 300 mL was treated with 110 ppm iron from an iron (III) naphthenate oxidation catalyst. The sample is heated at 150 °C while dry oxygen is bubbled through the oil at a flow rate of 10 L/h. Aged oil samples are removed at every 24 h until the 168-h was reached or until a breakpoint caused by rapid viscosity increase. Kinematic viscosity of the aged oil samples was measured at 40 °C. The aged samples were also tested by FTIR for the formation of carbonyl oxidation products using the Peak Area Increase PAI method reported by Obiols [17]. The percentage increase in viscosity and PAI results are shown in Figs. 4 and 5.

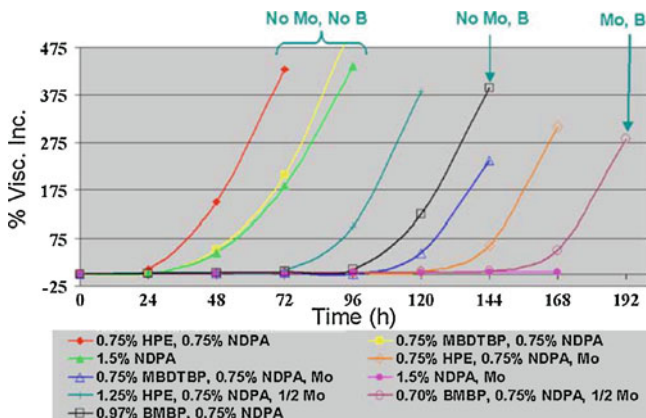


Fig. 4 Viscosity increase of low-P engine oils in the AlbOT

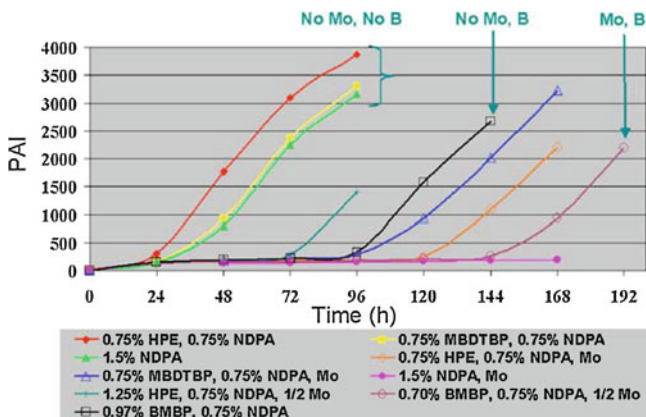


Fig. 5 Pai change of low-P engine oils in the AlbOT

4.3 Modified Caterpillar Micro-Oxidation Test

The procedure used in this study is a modified version of Caterpillar method [10]. An engine oil sample of approximately 20 L was accurately weighed and tested at 230 °C and an air flow of 20 mL/min. Sampling was performed at 10-min intervals. The time range for sampling depended upon the oxidative stability of the engine oil, varying from between 50 and 120 min for less stable oils to between 110 and 180 min for more stable oils. Weight percentage in deposits formed as a function of time, and the onset time to a rapid increase in deposit formation are shown in Figs. 6 and 7, respectively.

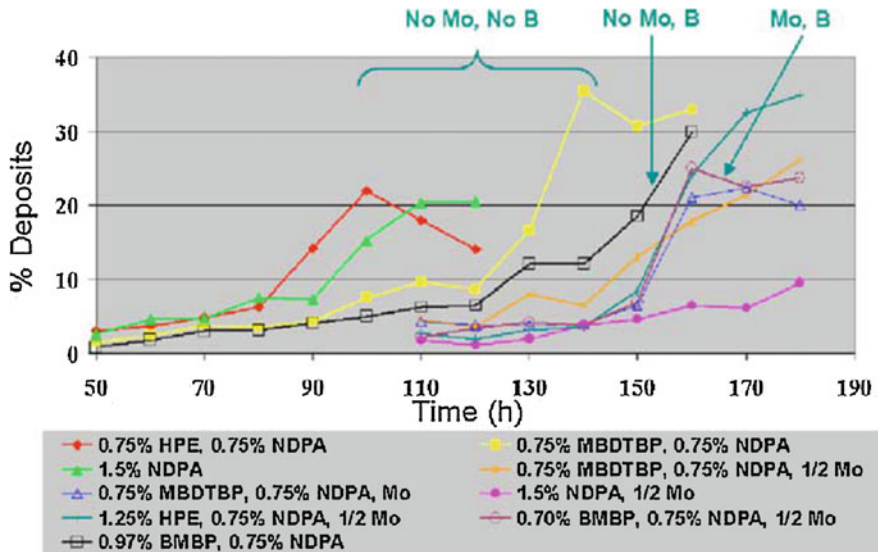


Fig. 6 Deposit formation of low-P engine oils in the CMOT

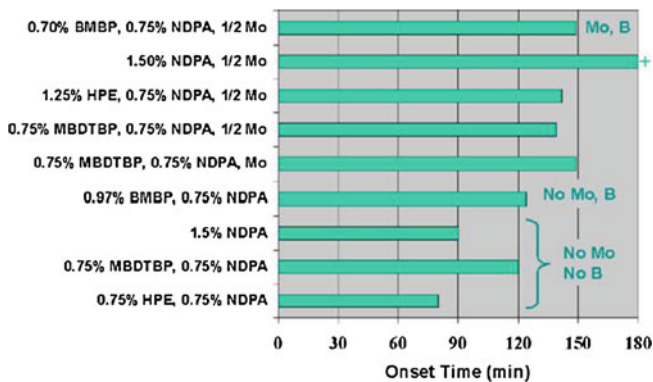


Fig. 7 Onset time of low-P engine oils in the CMOT

4.4 Thermo-Oxidation Engine Oil Simulation Test

The TEOST MHT-4[®] is designed to simulate high-temperature deposit formation in the piston ring belt area of modern engines per ASTM D 7097 [13]. Total rod deposits results are shown in Fig. 8.

Figure 3 shows PDSC OIT results for the low-P engine oils. The combination of ADPA and molybdenum has the strongest performance while the combination of HPE and ADPA is the weakest. Molybdenum appears to help extend OIT of the

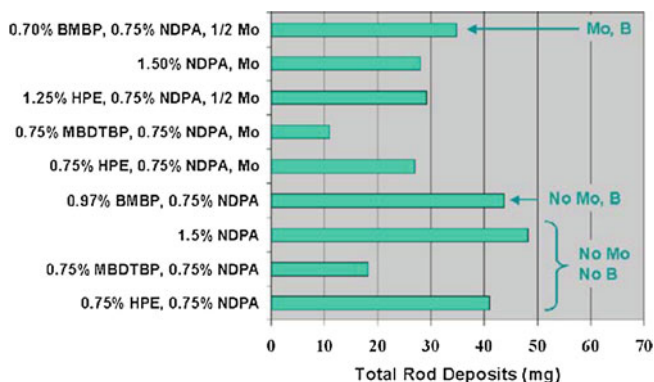


Fig. 8 Evaluation of low-P engine oils by TEOST MH

engine oils. Boron-containing systems tend to outperform similar boron-free systems, especially in the presence of molybdenum.

Figures 4 and 5 show the viscosity control performance and carbonyl compounds formation in AlbOT test. For the HPE/ADPA/molybdenum system, oxidation control is significantly improved with increasing molybdenum and decreasing HPE. Similar to the PDSC results, the best performing systems are either ADPA/molybdenum or MBDTBP/ADPA/molybdenum.

Figures 6 and 7 illustrate the control deposit formation and onset time to a rapid increase in deposit formation per CMOT test. The best performance comes from the ADPA/molybdenum combination with the onset time exceeding the 180-h test time. The next best is hindered phenolic/ADPA/molybdenum combinations. The molybdenum-free systems consisting of ADPA or HPE/ADPA have the poorest performance.

Figure 8 show the deposit formation control in the TEOST MHT[®] test. The antioxidant systems containing a combination of ADPA and MBDTBP perform well, with or without molybdenum. The NDPA/molybdenum system shows only modest performance in the TEOST[®]. The low deposit result for the MBDTBP/ADPA system relative to the all ADPA or mixed HPE/ADPA systems illustrates a very unique and powerful antioxidant synergism that exists in the presence or absence of molybdenum, consistent with what has been reported before [18].

Figure 9 shows TEOST results of engine oil samples containing BMBP-2 with a high level of MBDTBP. The treat level of BMBP-2 was varied from 0.70 to 1.40 wt. %. The exceptional TEOST deposit control is expected when treat level of BMBP-2 is high. Note these TEOST results are consistent with the MBDTBP/ADPA results in Fig. 8. It suggests the TEOST performance of BMBP and BMBP-2 can be attributed to the level of free MBDTBP present in the engine oil.

Table 1 summarizes the performance ranking of those antioxidant systems for each of the oxidation bench tests used in this study. It clearly shows that antioxidant system selection is very much dependent on the type of test being conducted. While ADPA/molybdenum appears to perform very well in the PDSC, AlbOT, and

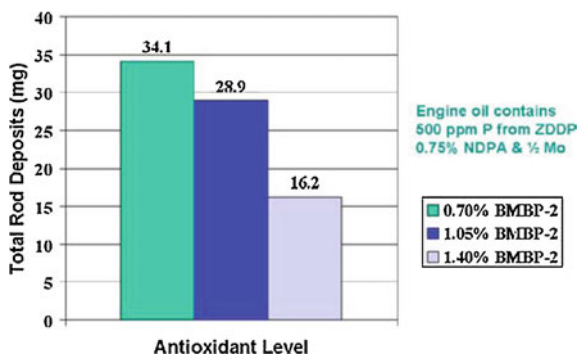


Fig. 9 Effect of BMBP-2 treat level on deposit formation in TEOST

Table 1 Antioxidant system ranking based on various bench tests

	Thin-film oxidation test	Bulk oil oxidation test
Chemical oxidation control	PDSC	AlbOT
	1 ADPA/Mo	1 ADPA/Mo
	2 BMBP/ADPA/Mo	2 BMBP/ADPA/Mo
Deposit or vanish control	CMOT	TEOST MHT
	1 ADPA/Mo	1 ADPA/MBDBP/Mo
	2 BMBP/ADPA/Mo or MBDTBP/ADPA/Mo	2 ADPA/MBDTBP

CMOT, the combination shows less effectiveness with regard to TEOST[®] deposit control. Alternatively, two MBDTBP/ADPA formulations that can reduce rod deposit below 25 mg, but they are less effective in the other tests. One promising candidate for further investigation is the mixed system consisting of BMBP-2/ADPA and molybdenum, especially if higher levels of BMBP-2 can be used.

5 Conclusions

This study reviewed a variety of bench tools available (PDSC, AlbOT, CMOT, and TEOST MHT[®]) for evaluating antioxidants’ performance in low-P engine oils. Those bench tests provide insights into the different aspects of the complex engine oil oxidation process. They can be categorized into bulk versus thin-film oxidation conditions, and chemical oxidation versus deposit formation parameters. Antioxidant system selection is very much dependent on the type of test being conducted. There are a number of observations worthy of further investigation. ADPA/molybdenum looks promising but requires the use of very high levels of

molybdenum in order to achieve reasonable TEOST[®] results. A new antioxidant system composed of BMBP-2/ADPA/molybdenum can achieve excellent deposit control results at high levels of BMBP-2. Finally, a traditional antioxidant combination of MBDTBP/ADPA is exceptionally effective in the TEOST[®], with or without molybdenum, but appears weak in some of the other tests. For engine oil formulators/designers, it is necessary to further optimize these antioxidant systems by taking into consideration the overall performance requirements of the engine oils, including the anti-wear and anti-friction properties of the boron and molybdenum containing additives.

References

1. Hutchings M, Chasan D, Burke R, Odorisio P, Rovani M, Wang W (1997) Heavy duty diesel deposit control...prevention as a cure. SAE paper No. 972954, pp 155–165
2. Gatto VJ, Grina MA (1999) Effects of base oil type, oxidation test conditions and phenolic antioxidant structure on the detection and magnitude of hindered phenolic/diphenylamine synergism. *Lubr Eng* 55(1):11–20
3. Migdal CA (2003) Antioxidants. In: Rudnick LR (ed) *Lubricant additives chemistry and applications*. Marcel Dekker, Inc., New York, pp 1–28
4. Gatto VJ, Bezjak YL (2006) The antioxidant properties of organomolybdenum compounds in engine oils. *Tribol Lubr Technol* 62(1):32–39
5. ASTM Standard D 6186-98 (1998) Standard test method for oxidation induction time of lubricating oils by pressure differential scanning calorimetry (PDSC). Annual book of ASTM standards, vol 05-03, ASTM International, West Conshohocken, PA
6. Hsu SM, Cummings AL, Clark DB (1982) Evaluation of automotive crankcase lubricants by differential scanning calorimetry. SAE paper No. 821252
7. Walker JA, Tsang W (1980) Characterization of lubricating oils by differential scanning calorimetry. SAE paper No. 801383
8. ASTM Standard D 4742-96 (1996) Standard test method for oxidation stability of gasoline automotive engine oils by thin-film oxygen uptake (TFOUT). Annual book of ASTM standards, vol 05.02, ASTM International, West Conshohocken, PA
9. Ku C-S, Hsu SM (1984) A thin-film oxygen uptake test for the evaluation of automotive crankcase lubricants. *Lubr Eng* 40(2):75–83
10. Zerla FN, Moore RA (1989) Evaluation of diesel engine lubricants by micro-oxidation. SAE paper No. 890239, pp 193–199
11. Gatto VJ, Elnagar HY, Moehle WE, Schneller ER (2007) Redesigning alkylated diphenylamine antioxidants for modern lubricants. *Lubr Sci* 19:25–40
12. ASTM Standard D 6335-036 (2003) Standard test method for determination of high temperature deposits by thermo-oxidation engine oil simulation test. Annual book of ASTM standards, vol 05-03, ASTM International, West Conshohocken, PA
13. ASTM Standard D 7097-05 (2005) Standard test method for determination of moderately high piston deposits by thermo-oxidation engine oil simulation test—TEOST MHT. Annual book of ASTM standards, vol 05.04, ASTM International, West Conshohocken, PA
14. Selby TW, Florkowski DW (1994) The development of a thermo-oxidation engine oil simulation test (TEOST). SAE 1993 Trans J Fuels Lubr 102(4):1870–1887
15. Selby TW, Florkowski DW (2000) The development of the TEOST MHT bench test of engine oil piston deposit tendency. In: *Proceedings of the 12th International college tribune, Technische Akademie Esslingen, Ostfildern, Germany, Supplement*, pp 55–62

16. ASTM Standard D 2893-03 (2003) Standard test method for oxidation characteristics of extreme-pressure lubrication oils. Annual book of ASTM standards, vol 05.01, ASTM International, West Conshohocken, PA
17. Obiols J (2003) Lubricant oxidation monitoring using FTIR analysis—application to the development of a laboratory bulk oxidation test and to in-service oil evaluation. JSAE technical paper No. 20030124, JSAE, Tokyo, Japan
18. Moehle WE, Cobb TW, Schneller ER, Gatto VJ (2007) Utilizing the TEOST MHT to evaluate fundamental oxidation processes in low phosphorus engine oils. Tribol Trans 50:96–103

Experimental Study of Influence of Gasoline Fuel with MMT on Aging Performance of Three-Way Catalyst

Shijin Shuai, Yinhui Wang, Junfeng Chen and Jianhua Xiao

Abstract The octane enhancing fuel additive Methylcyclopentadienyl Manganese Tricarbonyl (MMT) is widely used in China to meet market demand for octane in the unleaded gasoline pool, as the use of gasoline of the appropriate octane level is critical to obtaining optimal vehicle fuel economy. The impact of combustion products resulting from the use of MMT-containing gasoline on vehicle emissions control components has long been debated. In order to better understand this issue, a fundamental research program was undertaken to investigate the interactions of combustion products from MMT-containing gasoline with high cell density (600 cpsi) catalysts during severe catalyst operating conditions typical of those used to accelerate catalyst aging for the vehicle durability demonstration process. The paper reports on tests conducted to evaluate the influence of engine running condition, the absence or presence of MMT (at 18 mg Mn/l), and the impact of catalyst inlet temperatures on deposition phenomena occurring at the catalyst face that can lead to plugging. Additionally, a 1000 h test based upon the Type V durability procedure was conducted using MMT-containing gasoline (also at 18 mg Mn/l) to evaluate the impact of the additive under longer term exposure conditions more representative of those dynamic mode operation encountered during typical real-world vehicle operation. Results were consistent with the conclusion that catalyst backpressure was influenced primarily by the test cycle condition, as backpressure increase was only observed during continuous long term exposure of catalysts to MMT-containing fuel at the most severe catalyst inlet temperatures (820 °C) under steady-state operating conditions. Backpressure

F2012-A03-024

S. Shuai (✉) · Y. Wang · J. Chen · J. Xiao
State Key Laboratory of Automotive Safety and Energy, Tsinghua University,
Beijing, China
e-mail: wangyinhui@tsinghua.edu.cn

increase was not obviously observed under dynamic operating conditions regardless of the MMT concentration or temperature.

Keywords MMT · Three-way catalyst · Catalyst plugging · Driving cycle · Backpressure

1 Introduction

Methylcyclopentadienyl Manganese Tricarbonyl (MMT) is primarily used as a fuel additive to improve gasoline anti-knock properties by moderating the rate of combustion reactions that lead to detonation, which maintains the rate of combustion reactions to within the normal operating range. During combustion, MMT decomposes into manganese oxide particles that convert peroxides from the oxidation of n-alkanes into aldehydes and ketones. By inhibiting branch reactions in the flame front and interrupting the reaction chain, the ignition induction period is prolonged, the rate of energy release moderated and the anti-knock properties of the fuel improved [1, 2]. Vehicles designed to operate on higher octane gasoline (improved anti-knock properties) exhibit better fuel economy, higher performance and higher overall efficiency compared to vehicles designed to operate on lower octane gasoline. By contrast, vehicles operating on gasoline of an octane quality lower than the level they were designed to use will suffer from poorer reduced fuel economy and reduced performance.

In China, where the use of MMT-containing gasoline is prevalent, the primary specification upon which gasoline is sold is octane quality. The three grades available are 90 Research Octane Number (RON), 93 RON and 97 RON. The current China National Phase III gasoline specification allows the use of MMT at levels up to 16 mg Mn per liter. Use of MMT at this maximum level provides about 1.5 and 2.0 RON increase. MMT has been used extensively by gasoline refiners to meet the significant increase in octane demand experienced in the gasoline pool in China for over 10 years. During this time, the demand for gasoline octane has increased significantly through the combination of substantially higher gasoline consumption along with a shift in the dominant octane grade from 90 RON to 93 RON.

The effect of MMT on mobile vehicle emission control systems and components has been extensively researched and debated for over three decades [3–8]. Automobile manufacturers have expressed their concerns with MMT, stating that the use of MMT can impact the performance of vehicle exhaust emission control system performance, including plugging of high cell density three ways catalyst commonly used to achieve compliance with Euro IV and Euro V emissions standards [9–11]. The largest MMT manufacturer, Afton Chemical Corporation, has shown that MMT does not harm such catalysts or the environment, and, to the

contrary, provides a cost-effective way for refineries to save energy and reduce emissions. Much of the debate focuses on whether testing procedures and conditions for engine bench testing accurately reflect the impact of MMT on catalysts during real world use, as much of the information and data supporting claims of catalyst plugging are not representative of real-world driving conditions. For example, one automaker study showed that MMT can plug high cell density catalysts on a vehicle driven continuously at 130 km/h for more than 200 h, the equivalent of over 25,000 km of continuous mileage accumulation [9]. Conversely, Afton conducted a similar study did not observe such plugging when the test procedure incorporated dynamic mode elements. These dynamic mode elements represent real world vehicle operation, exposing the catalyst to temperature fluctuations and flow transients that avoid catalyst plugging occurrences.

This study was conducted to address the lack of in-depth investigation into purported catalyst plugging mechanisms by independent third parties. In this research, catalyst aging studies were used to investigate effects of the following variables on catalyst backpressure: (1) accelerated aging mode, (2) MMT content, and (3) catalyst inlet temperature. The mechanism of catalyst plugging is elucidated based upon these results.

2 Experimental

2.1 Engine Bench Setup

This study utilized a conventional engine bench setup, comprising a four cylinder engine, three-way catalyst(s), dynamometer, fuel delivery and meter system, along with additional instrumentation. The engine was a closed-loop, multi-point port fuel-injected, electronically controlled gasoline engine. Figure 1 shows the layout of the engine test bench used for accelerated catalyst aging and performance evaluation.

Catalysts used in this study were a high cell density 600 cpsi type supplied by Delphi. The space velocity for exhaust flow through the catalyst during aging and performance evaluation testing was at $40,000 \text{ h}^{-1}$. The dynamometer and control system (Hunan Xiang'yi Power Testing Instrument Co., Ltd.) included a CW160 electrical eddy current dynamometer, FC2010 engine measuring and control system, FC2110 throttle actuator and computer control unit. A CEB II emissions bench (AVL) was used to measure the concentrations of CO, THC and NO_x in the exhaust. In this study catalyst conversion efficiency performance is reported in terms of catalyst light off (50 % conversion) temperatures. A Dino-lite AM-413T digital microscope capable of magnification up to 200X was used to investigate the morphology of the front face and surface of aged catalysts. Table 1 shows other relevant engine parameters.

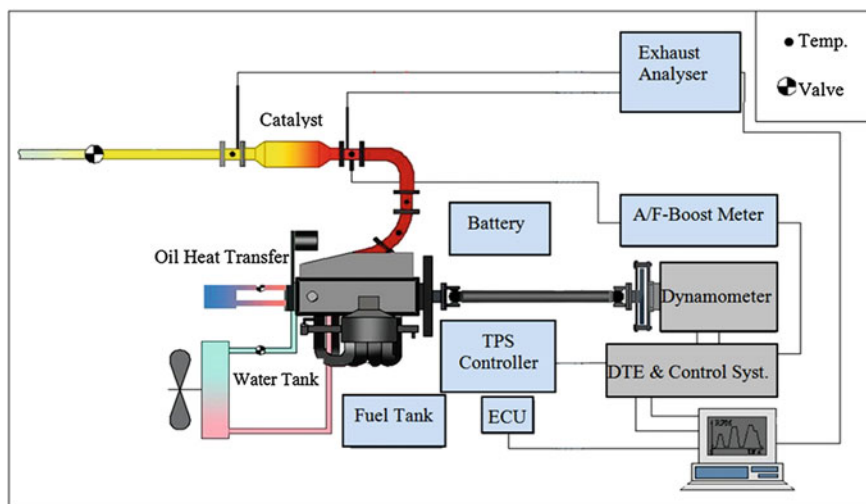


Fig. 1 Diagram of test bench for catalyst accelerated aging and performance evaluation

Table 1 Major test engine parameters

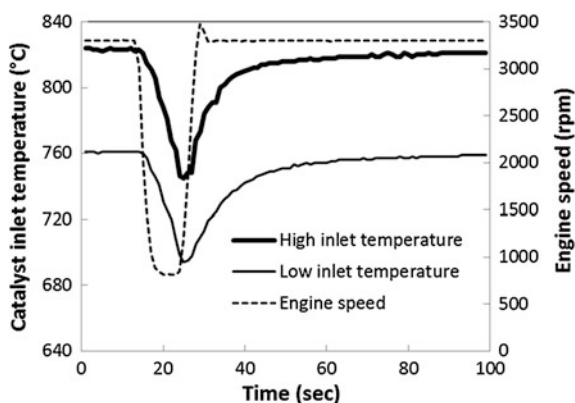
Number of cylinders	4
Bore/mm	91
Stroke/mm	86
Displacement/L	2.237
Compression ratio	8.8
Fuel delivery	Closed-loop electronic controlled MPI
Rated power/kW	76
Engine speed @ rated power/rpm	4,200–4,600
Maximum torque/N m	193
Engine speed at maximum torque/rpm	2,200–2,800

2.2 Experimental Approach

The impact of different test conditions during accelerated aging of three-way catalysts was examined in the context of three variables: (1) aging mode (i.e., engine operating cycle), (2) MMT content in the gasoline, and (3) catalyst inlet temperature. During these tests, otherwise identical three-way catalysts were aged on an engine bench and, at certain aging intervals, exhaust concentrations of NO_x, THC and CO were measured pre- and post-catalyst, along with exhaust backpressure. The effect of the three testing variables (i.e., aging mode, MMT content and temperature) on catalyst performance and backpressure was determined based upon these measurements. Table 2 summarizes the eight combinations of aging conditions tested.

Table 2 Catalyst accelerated aging test program

Number	Aging mode	MMT treat rate (mg Mn/L)	Catalyst inlet temperature (°C)	Aging time (h)
1	Fuel cut	0	760	200
2	Fuel cut	0	820	200
3	Steady-state	0	760	200
4	Steady-state	0	820	200
5	Fuel cut	18	760	200
6	Fuel cut	18	820	200
7	Steady-state	18	760	200
8	Steady-state	18	820	200

Fig. 2 Engine speed and catalyst inlet temperature profiles for the fuel cut cycle

This study examined two types of aging modes: (1) “steady-state,” referring to engine operation in a single continuous condition with air fuel ratio, catalyst inlet temperature, engine speed and other operating parameters remaining constant, and (2) “fuel cut,” referring to use of a repeating cycle consisting of a five-minute stoichiometric operating period (using conditions identical to steady-state mode) followed by five-second fuel cut. This fuel cut element simulated engine operation when a vehicle undergoes a closed throttle deceleration, which is frequently observed during normal driving behavior. Figure 2 shows the transient profile of engine speed and catalyst inlet temperature measured during fuel cut mode.

Two types of fuel were used for testing: (1) base fuel and (2) MMT-treated fuel. The base fuel contained no MMT and met Beijing Phase IV gasoline specifications. The MMT-treated fuel consisted of the same base fuel treated with MMT at 18 mg Mn/l. This treat rate was chosen as the 18 mg Mn/l level has been widely used in countries where catalyst-equipped vehicles operated in areas where MMT-containing gasoline use is common. Therefore, this treat rate comprehensively addressed the global MMT situation while also accounting for the current China

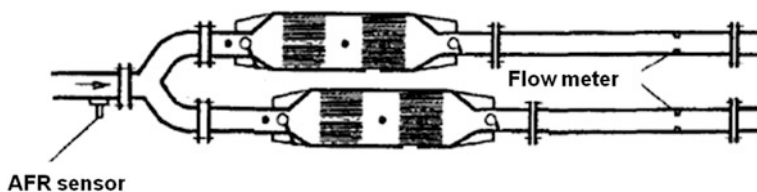


Fig. 3 Layout of exhaust pipes and catalysts

16 mg Mn/l National Phase III specification. Finally, two different catalyst inlet temperature conditions were chosen for testing. The higher and lower catalyst inlet temperatures of 820 and 760 °C, respectively, were achieved by dividing the exhaust flow and adjusting the length of each exhaust pipe ahead of each catalyst. An orifice flow meter was utilized to ensure that the exhaust flow was equally split into the two pipes. This layout is shown in Fig. 3. This exhaust and catalyst arrangement ensured that all test conditions, except for the catalyst inlet temperature, were identical for catalysts aged simultaneously. For testing with the fuel cut cycle, the inlet temperature refers to the temperature level used during the steady-state, stoichiometric part of that cycle.

3 Results and Discussion

3.1 Effect on Catalyst Back Pressure

With catalyst inlet temperature set at 820 °C using MMT-containing test fuel, catalyst backpressure increased by 130 %, reaching 2.3 times the initial back pressure after 200 h of aging. Under all other steady-state aging conditions, a less significant but still noticeable back pressure rise was observed after 200 h of aging (about a 40 % increase), regardless of catalyst inlet temperature or MMT concentration. Figure 4 summarizes results on the effect of aging time on backpressure using the steady-state mode.

After 200 h of aging on the fuel cut cycle, however, exhaust back pressure increased by less than 20 % under all testing conditions, regardless of temperature or MMT concentration. Figure 5 shows the effect of aging time on back pressure using the fuel cut aging mode, where very little back pressure increase was observed. By comparing Figs. 4 and 5, catalyst temperature, MMT concentration and accelerated aging mode are all shown to affect an increase in catalyst backpressure over time. When steady-state aging and MMT-containing fuel use were combined, backpressure increase was more dramatic at the higher catalyst inlet temperature than at the lower inlet temperature. The only condition where significantly higher backpressure was observed for MMT fuel was under constant high catalyst inlet temperature and steady-state mode. The rate of back pressure

Fig. 4 Effect of aging time on back pressure using steady state aging mode

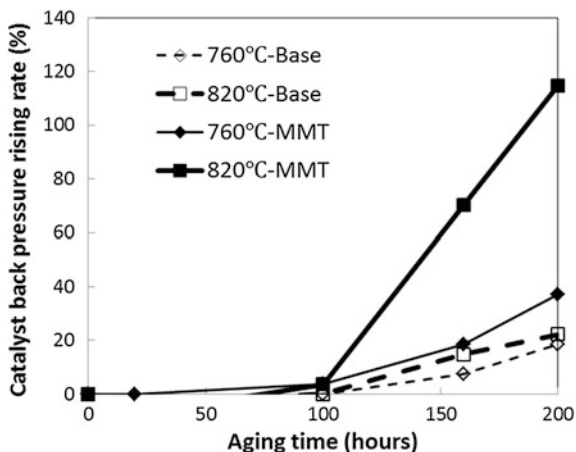
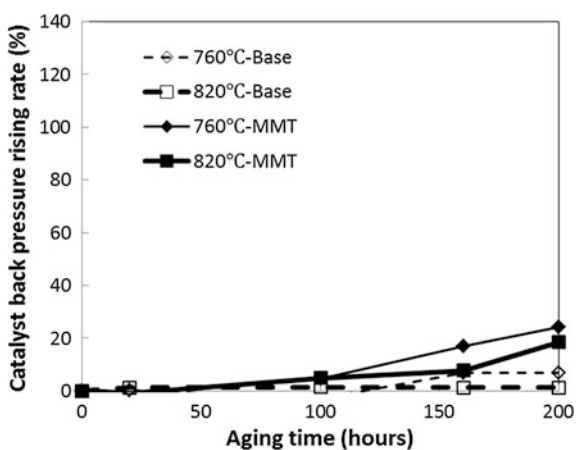


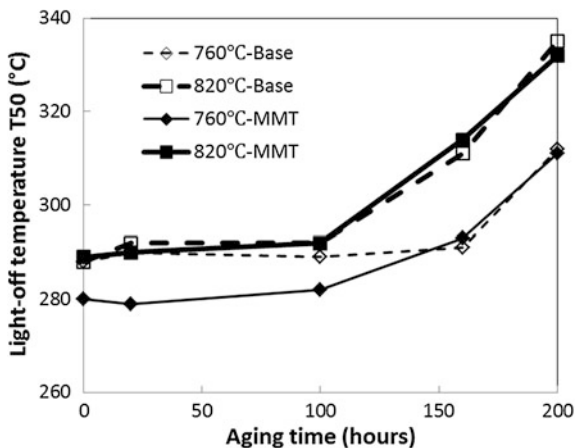
Fig. 5 Effect of aging time on back pressure using fuel cut aging mode



increase during fuel cut aging was much lower than during steady state aging, regardless of temperature or MMT content. Therefore, the only case that displayed significant backpressure rise was a testing condition that combined high temperature, MMT-containing fuel and steady state aging.

XRF/XRD analysis confirmed that manganese oxide deposits formed on the catalyst face when MMT-containing fuel was used. The presence of manganese oxide deposits did not indicate the occurrence of plugging or impact catalyst performance (either negatively or positively). Results from fuel cut aging suggest that interactions between MMT-related combustion products and catalyst surface are very weak, and that manganese oxide deposited on the catalyst is readily shed and removed from the catalyst surface during dynamic engine operation as a result of transients in exhaust flow rate and temperature.

Fig. 6 Effect of aging time on light-off temperature using steady state aging mode



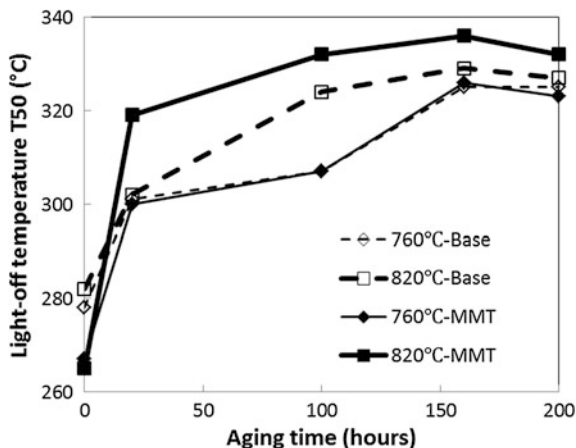
3.2 Effect on Catalyst Light-Off Temperature

Measured light-off temperatures for NO_x, HC and CO were found to be relative similar across the board and therefore are discussed collectively. After 100 h of aging in steady-state mode, light-off temperature started to increase. The rate of increase was higher for catalysts aged at the 820 °C inlet temperature compared to catalysts aged at the 760 °C inlet temperature. Light-off temperatures for catalysts aged at the same temperature were close to one another, regardless of the use of MMT-containing gasoline. Figure 6 shows the effect of aging time on light-off temperature during steady-state mode.

As with catalysts aged on the steady-state mode, light-off temperatures for catalysts aged on the fuel cut cycle rose significantly after 100 h of aging. Light-off temperatures were again higher for catalysts aged at the higher catalyst inlet temperature (820 °C). For catalysts aged at the 760 °C inlet temperature, light-off temperatures were similar for both base fuel and MMT fuel. At the higher inlet temperature of 820 °C, the catalyst aged on MMT fuel displayed slightly higher light-off temperatures after 200 h, although the difference was well within the expected range of normal testing and sample variability. Figure 7 shows the effect of aging time on light-off temperature for catalysts aged during fuel cut mode.

By comparing Figs. 6 and 7, light-off temperatures increased faster during the early stages of aging on the fuel cut cycle relative to steady-state aging under otherwise identical conditions. After 200 h of aging, light-off temperatures of fuel cut aged catalysts were slightly higher than those for steady state aged catalysts. The main factors impacting light-off temperatures were catalyst inlet temperature and aging mode, with no substantial correlation regarding the use of MMT. This was expected as higher catalyst inlet temperatures are known to lead to higher thermal load inside the catalyst and more rapid catalyst deterioration. Additionally, unburned fuel can enter into and oxidize inside the catalyst in fuel cut aging mode. Oxidation of unburned fuel inside the catalyst increases the thermal load on the

Fig. 7 Effect of aging time on light-off temperature using fuel cut aging mode



catalyst, accelerates catalyst deterioration and increases catalyst light-off temperature beyond that which would occur during a steady state cycle. The general trend in light-off temperature change during fuel cut aging was consistent with that occurring in real world use, with a rapid initial increase followed by a relatively stabilized level over the longer term. Therefore both backpressure and catalyst light off results from fuel cut mode aging were more consistent with real world experience than with results from steady state testing.




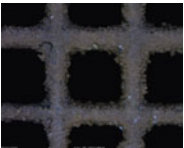



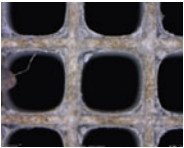
3.3 Effect on Catalyst Surface Morphology

Reddish-brown deposits were present on the front face of the catalyst surface after aging with MMT-containing fuel. The catalyst inlet face was gray-black after aging with base fuel use. Combining the results and analysis from previous sections, no substantial correlation between catalyst surface morphology and catalyst backpressure or light-off temperature performance was found. Table 3 shows the surface morphology of the front face of catalysts under different conditions as observed through a digital microscope.

3.4 Type V Durability Testing

Type V durability testing was performed in accordance with Phase IV emission standard in order to determine if the use of MMT can cause catalyst plugging in real world use. Normally, the Type V durability test is a whole vehicle test conducted on a track or dynamometer. In this study, however, the same engine that was used for steady-state and fuel cut cycle aging work was also used for Type V

Table 3 Inlet face morphology of 200-hour aged catalysts

	Steady state 760 °C	Fuel cut 760 °C	Steady state 820 °C	Fuel cut 820 °C
MMT				
Base				

durability testing. Only MMT fuel was used in the test, at a treat rate of 18 mg/l, for a testing duration of 1,000 h. Instead of using the dual catalyst and split piping arrangement shown in Fig. 3, a production catalyst and exhaust pipe system used from a gasoline vehicle equipped with this engine in an actual vehicle was used. A CEB-II emission bench (AVL) was used to measure concentrations of THC, CO and NO_x in the exhaust. Engine bench automation and control were accomplished with a FC2010 engine measuring and control system (Hunan Xiangyi Power Testing Instrument Co., Ltd.) and dynamometer. Detailed instructions for Type V durability cycle are as follows:

- The Type V durability test has 11 total operating cycles with a driving distance of 6 km for each cycle.
- The vehicle stops four times and engine idles for 15 s in each of the first nine cycles. The vehicle decelerates five times from cycle speed to 32 km/h in each cycle, and then accelerates gradually to the cycle maximum speed, using normal acceleration and deceleration rates. The maximum vehicle speeds for cycles one through nine range from 48 to 72 km/h.
- The vehicle drives at 89 km/h constant speed during the 10th cycle.
- The vehicle accelerates to the maximum speed of 113 km/h from the stop point at the beginning of the 11th cycle. Halfway through this cycle, the brakes are applied normally until the vehicle reaches a complete stop. The vehicle idles for 15 s and then accelerates to the maximum speed for a second time.

During the entire Type V test, very little backpressure increase was observed, with a total rise of less than 20 %. This performance confirmed that MMT-containing fuel will not cause catalyst plugging within the full vehicle useful life during normal use with a Mn content of 18 mg Mn/l. Recall that when MMT fuel was used under the condition of high temperature steady state aging, catalyst backpressure increased 130 % after 200 h of aging. Type V testing results confirmed the conclusion from fuel cut testing results that the interaction between the MMT-related combustion products and catalyst surface is very weak, and manganese oxide deposited on the catalyst surface is readily shed during dynamic

Fig. 8 Catalyst back pressure change during type V test

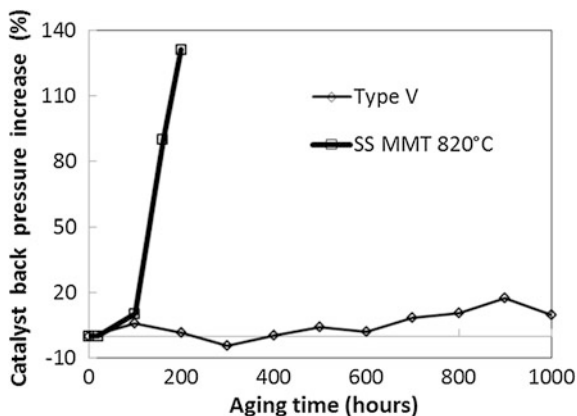
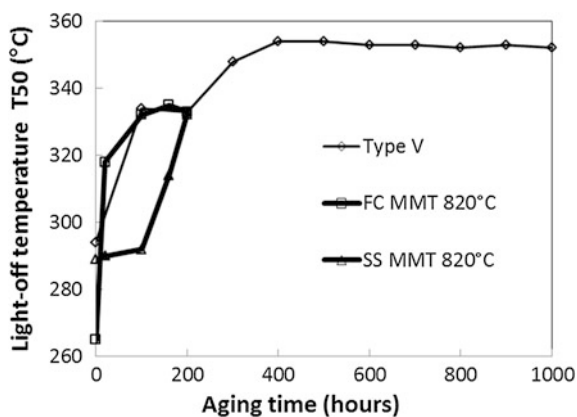


Fig. 9 Comparison of catalyst light-off performance during different aging cycles



engine operation. Transients in exhaust flow rate and temperature most likely lead to the removal of manganese oxide deposits during dynamic mode operation. Figure 8 shows the trend for catalyst backpressure during the Type V engine bench test.

During Type V aging, rapid deterioration was observed during the first 200 h, followed by very little deterioration after about 300 h. This trend in deterioration was similar to that observed during fuel cut cycle aging, and is consistent with that which would be expected to occur during real-world vehicle use. Combined with observations discussed on backpressure above, these results suggest that the relevant mechanisms present during Type V and fuel cut cycle aging are consistent with those typical of real-world vehicle operation, as both thermal aging characteristics and backpressure change are represented, and lead to the conclusion that the use of MMT-containing fuel does not negatively impact performance. Figure 9 summarizes catalyst light-off testing results for Type V, fuel cut cycle and steady-state cycle aging on MMT-containing fuel.

4 Conclusions

1. Significant catalyst backpressure increase is only observed during continuous steady-state operation with MMT-containing gasoline at catalyst inlet temperatures above 820 °C for an extended period of time (200 h). Noticeable but less significant backpressure increase is observed during continuous steady-state operation at both 760 and 820 °C in base fuel without MMT as well as at 760 °C with MMT. These results suggest that the steady-state test cycle does not accurately incorporate necessary aspects of real-world deposition phenomena, including those related to MMT combustion products.
2. The factors that affect the light-off temperature are primarily: (1) catalyst inlet temperature and (2) accelerated aging mode. The higher the catalyst inlet temperature, the faster the catalyst deteriorates. The fuel cut aging mode also accelerates the catalyst aging rate relative to the steady state aging condition. The general trend in catalyst light off performance as a function of aging time is more consistent with that expended during real world vehicle operation, characterized by a rapid initial deterioration followed by a long period of stable performance.
3. Reddish-brown deposits on the catalyst are observed when MMT-containing gasoline is used. When gasoline does not contain MMT, the catalyst surface is gray-black. There is no substantial correlation between catalyst surface morphology and its catalytic performance, or between catalyst performance and the presence of manganese oxide deposits on the catalyst face.

References

1. Gegen T, Ye Q et al (1999) The mechanism and industry application of several antiknock additives in unleaded gasoline. *Niaoning Chem Ind* 28(3):79
2. Callear AB, Norrish RGW (1959) Mechanism of antiknock. *Nature* 184(23):1794–1795
3. Yan Zhang, Ping Cui, Yan Ding et al (2006) The impact of MMT on the emission performance of light duty vehicle. *Environ Sci Res* 19(5):19–24
4. Faggan JE, Bailie JD, Desmond EA (1975) An evaluation of manganese as an antiknock in unleaded gasoline. SAE 750925
5. Benson JD (1977) Manganese fuel additive (MMT[®]) can cause vehicle problems. SAE 770655
6. Aradi AA, Roos JW (1994) The physical and chemical effect of manganese oxides on automobile catalytic converters. SAE 940747
7. Benson JD, Dana G (2002) The impact of MMT[®] gasoline additive on exhaust emissions and fuel economy of low emission vehicles (LEV). SAE 2002-01-2894
8. Schindler KP (2004) Impact of MMT on vehicle emission performance. Presented at Asian vehicle emission control conference (AVECC)
9. Shimuzu C, Ohtaka Y (2007) Parametric analysis of catalytic converter plugging caused by manganese-based gasoline additives. SAE 2007-01-1070

10. Roos JW, Cunningham LJ, Meffert MW (2007) The interaction of MMT[®] combustion products with the exhaust catalyst face. SAE 2007-01-1078
11. Meffert MW, Quinn TG, Guinther GH (2006) Evaluation of Factors affecting vehicle emission compliance using regional inspection and maintenance program data. SAE 2006-01-3406

Part IV
After Treatment and Emission Control

Study on Engine Performance Influenced by External Cooled EGR

Nan Jiang, Jifeng Liu, Xueen Zhang, Xiaojun Cheng, Yang Yang, Jianxian Chen, Gan Chen, Jianguang Zhou, Yongsheng Long and Jie Bai

Abstract The main purpose of Exhaust Gas Recirculation system (EGR) is to reduce nitrogen oxides of emissions and to improve the fuel economy when engine at part load. Simulation and a bench test have been done to study the effects on fuel efficiency and the potentiality of increasing the compression ratio of a 1.6 L naturally aspirated gasoline engine by the external cooled EGR technology. One dimensional performance simulation is used to predict the EGR ratio, by analysing engine power, economy and emissions of different amounts of exhaust gas. A bench test is used to calibrate the optimum EGR ratio at each engine operating condition and engine performance, and to analysis the impact on engine performance and operating parameters. The results show that: at the low to medium load conditions, application of the EGR technology only can reduce fuel consumption by up to 2 %, while by increasing the compression ratio and applying the EGR technology, fuel consumption can be reduced by up to 5 %, and reduce NO_x by more than 50 %. This study is based on the naturally aspirated gasoline engine. It is an advanced method to apply external cooled EGR technology on a naturally aspirated engine for reducing fuel consumption. Conclusion: The nitrogen oxides of emissions can be reduced and the fuel economy can be improved at part load by using the external cooled EGR technology for a naturally aspirated engine.

Keywords EGR · Fuel consumption · Emissions · Performance simulation · Bench test

F2012-A04-004

N. Jiang (✉) · J. Liu · X. Zhang · X. Cheng · Y. Yang ·
J. Chen · G. Chen · J. Zhou · Y. Long · J. Bai
Dongfeng Motor Corporation Technical Centre, Guangzhou, China
e-mail: jiangn@dfmc.com.cn

1 Background and Program

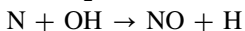
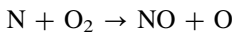
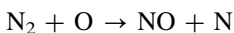
1.1 Background of EGR Technology

Exhaust Gas Recirculation system (EGR), puts part of the exhaust gas into the intake manifold to be re-engaged in the combustion process, which can effectively reduce the emissions of NO_x and fuel consumption. There are two ways to achieve it, one is the internal EGR, which uses the Variable Valve Timing (VVT) technology to retain some exhaust gas of the last cycle in the cylinder; the other is the external EGR, which puts part of the exhaust gas into the intake manifold by an external EGR pipe to be involved in combustion for the next engine work cycle [1]. At early stage, the main target of the external EGR technology is to reduce the emissions of NO_x. With the generation of the VVT technology, it was gradually replaced by the internal EGR technology. But now, with stricter requirements for fuel economy, the external EGR technology is used again. With the help of cooling technology, they can effectively achieve the goal of reducing fuel consumption. This paper shows the effect of the external EGR on reducing fuel consumption by test and simulation in a self-developed MPI engine.

1.2 The Principle of EGR in Energy Conservation and Emission Reduction

1.2.1 The Principle of EGR in Emission Reduction

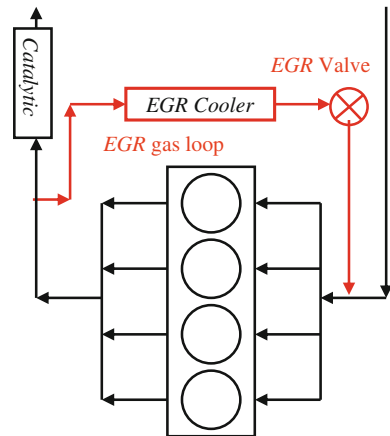
The EGR technology can reduce NO_x emissions effectively. The conditions of generating NO_x are high temperature and rich oxygen. The chemical reaction equations are as follows:



The mechanism of EGR technology to reduce NO_x emissions includes the following three points:

- (1) It reduces the oxygen concentration;
- (2) The exhaust gas contains large amounts of inert gas such as nitrogen, carbon dioxide, which increases the thermal capacity of the reactants and reduces the

Fig. 1 The diagrammatic illustration of an external cooled EGR system



maximum combustion temperature, when recycling into the combustion chamber,

- (3) Exhaust gas contains water vapor, carbon dioxide and other three-atom molecular gas, which have high heat capacity and can effectively reduce the maximum combustion temperature.

Note: as low temperature and incomplete combustion are the conditions for generating HC, CO and other exhaust gas, the EGR technology will increase the emissions of HC, CO to a certain extent [2, 3].

1.2.2 The Principle of EGR in Energy Conservation

The mechanism of EGR technology to reduce fuel consumption includes the following three points:

- (1) Reducing the different pressure between intake and exhaust can lower the pumping loss;
- (2) Cooled EGR can reduce the in-cylinder temperature, thereby to suppress knock, and to improve combustion;
- (3) It can improve the anti-knock property of an engine and therefore provide the possibility to appropriately increase the compression ratio of the engine [4–6].

1.3 Circuit Program of EGR System

There are two loop programs of EGR in the naturally aspirated engine, one get exhaust gas before the post-processor, and the other after the post-processor.

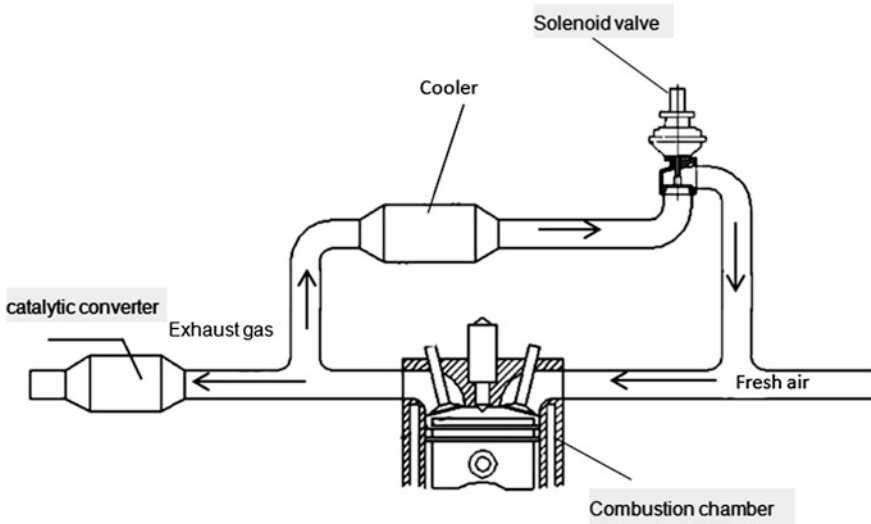


Fig. 2 The schematic of external cooled EGR system

The benefit of getting exhaust gas before the post-processor is more exhaust gas into the intake system because of the greater pressure; the exhaust gas is cleaner after the post-processor, which can less pollute the related parts. This paper focuses on a 1.6 L naturally aspirated engine to carry out the EGR technology using the program of getting exhaust gas before the post-processor Fig. 1.

1.4 The Composition of External Cooling EGR System

The test program of EGR system is shown in Fig. 2. Part of exhaust gas is taken before the post-processor and sent into the intake manifold through an EGR valve and a cooler, and then it participates in the in-cylinder combustion process. EGR valve controls the volume of exhaust gas by a real-time control unit. The EGR cooler adjusts the temperature of the exhaust gas to lower than 100 °C.

2 Simulation Analyses

2.1 Introduction of the Model

The 1-D simulation model built in GT-power is shown in Fig. 3. The intake system is on left, the exhaust system is on right, the valves and the cylinders are in middle.

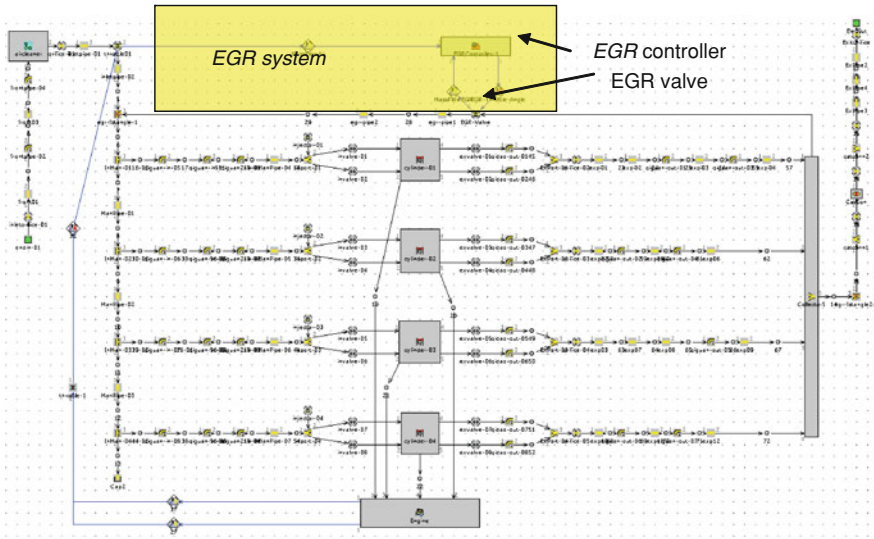


Fig. 3 The simulation model using EGR of an NA gasoline engine

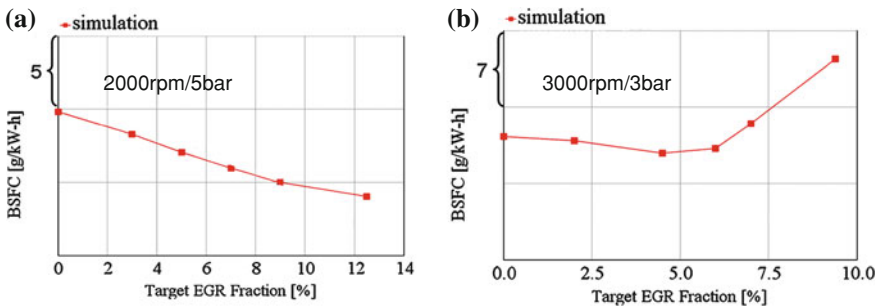


Fig. 4 Fuel consumption simulation analysis results a shows the results of 2000 rpm/5 bar, b of 3000 rpm/3 bar

The intake and exhaust manifolds are simplified from the 3-D geometry structure, the lift and curve style of the valves are the same as the real data. As the main work in this paper is focused on the influence of EGR to engine performance, there is no multi-program comparison on VVT, and the VVT of intake valve is using the data that optimal when the EGR was not applied.

A more precise combustion model called predicting SiTurb model is adopted, which can import the 3-D geometry of combustion chamber into the model (as shown in Fig. 3), to predict the combustion case more accurately. The main input parameter of this combustion model is the ignition time. As different EGR ratio can have different influence on combustion, we should adjust the ignition time

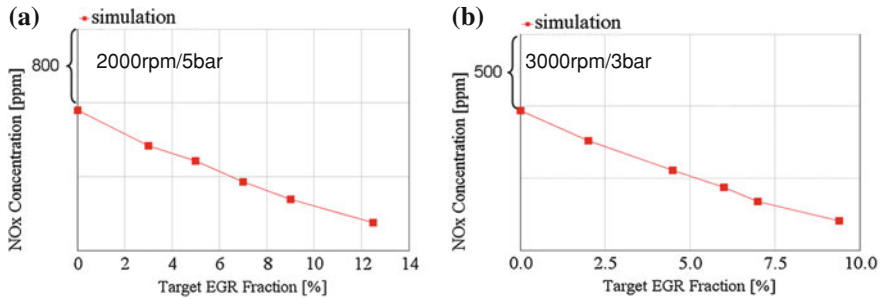


Fig. 5 NOx simulation analysis results **a** shows the results of 2000 rpm/5 bar, **b** of 3000 rpm/3 bar

according to different EGR ratio, and control the maximum pressure appearing during 12–15 °ATDC to get the minimum fuel consumption.

2.2 Simulation Results Analysis

The simulation results of fuel consumption on different cases is shown in Fig. 4, the x-axis represents the EGR ratio and the y-axis represent brake specific of fuel consumption.

It can be concluded that the trend of BSFC with the EGR ratio of change is different at different conditions. While at 2000 rpm/5 bar, the EGR ratio is 13 %, it has the best influence on reducing BSFC. While at 3000 rpm/3 bar, the EGR ratio is 4.5 %, it has some influence on reducing BSFC.

The simulation results of NOx emission at different condition is shown below, the x-axis represents the EGR ratio and the y-axis represents the NOx emission Fig. 5

It can be concluded that the trend of NOx with the EGR ratio of change is same at different conditions. The trend is as the EGR ratio increasing, the NOx emission reduces.

3 Experimental Studies

3.1 Bench Test System

The bench testing system for the EGR is shown in Fig. 6. The black arrows indicate the gas loop, the exhaust gas is led out before the catalytic, passing through the EGR cooler and EGR valve in order, then mixed with the intake system after the electronic throttle. The red arrows indicate the EGR cooling water loop, and then water is led out from the port of engine heater pipes and flow back

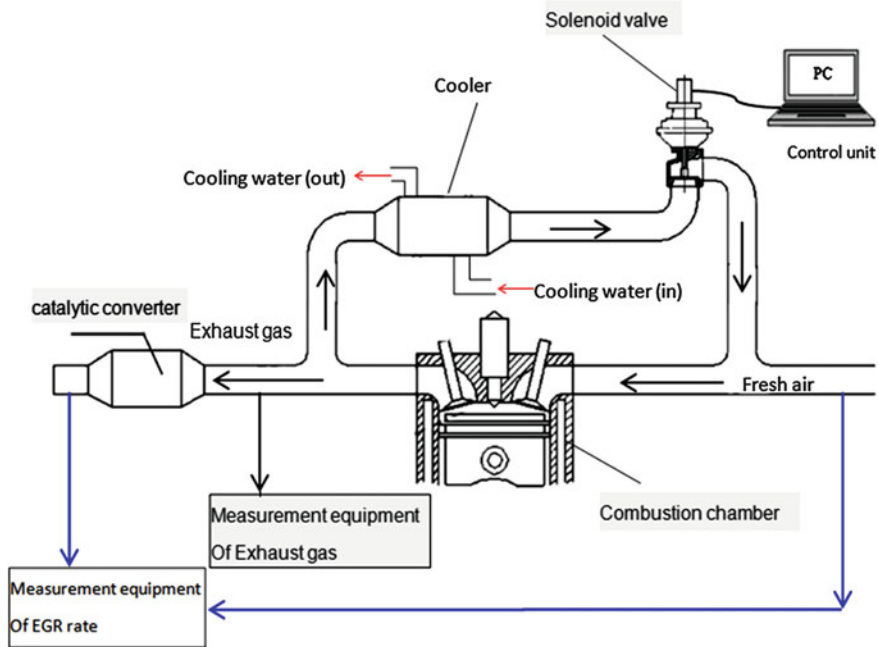


Fig. 6 EGR experiment diagram

to the engine through the EGR cooler. The blue arrows indicate the CO₂ measurement loop for calculation of the EGR ratio.

3.2 Bench Program and Working Conditions

The test is divided into four steps: (1) The original machine test; (2) Apply EGR test in original machine; (3) Compression ratio increased by 0.7 (high compression ratio) tests; (4) Apply EGR test in high compression ratio engine.

Five working conditions, which run a higher rate of NEDC cycle, are selected for each step as above. They are 1500 rpm/3.5 bar 2000 rpm/2 bar, 2000 rpm 5 bar, 3000 rpm/3 bar and 3000 rpm/11 bar which cover each load of low and medium speed, and their fuel consumption level can effectively represent comprehensive fuel consumption level.

Table 1 3000 rpm/3 bar the fuel consumption and emissions

Model	BSFC (%)	NOx (%)	HC (%)	CO (%)	Exhaust temperature (%)	EGR ratio (%)	Ignition advanced angle (°)
Oral engine +EGR	-0.8	-26.1	+7.5	-4.6	-20.5	6	+16
High compression	-2.9	+26.6	+29	+18	-5.2	0	0
High compression +EGR	-4.1	-51.8	+44.4	+13.1	-27.4	8.9	+12

3.3 Test Results Analysis

3.3.1 Comprehensive Analysis

In comprehensive comparison of the fuel consumption changes on the original engine, original engine applied with EGR, high compression engine and high compression engine applied with EGR. We can study changes of engine fuel consumption, emissions (NOx, HC, CO) changes, the exhaust gas temperature, ignition advance angle and other parameters.

The Table 1 shows that, at 3000 rpm/3 bar, fuel consumption was reduced by 0.8 % in application of EGR technology. In comprehensive application of EGR and high compression ratio technology, fuel consumption can be reduced by 4.1 %, meanwhile Nox decreased significantly, but HC and CO increased to some extent. After the application of EGR, the cylinder combustion is significantly improved, exhaust gas temperature has decreased greatly, and the ignition advance angle can be in advance a lot.

The test results are in good agreement with simulation predictions in Fig. 4. The fuel consumption reduces when EGR ratio is 4.5 % Fig. 7.

3.3.2 Detailed Analysis at 3000 rpm/3 bar

EGR technology affects the original engine in intake, combustion and other aspects, so the engine control parameters should be adjusted accordingly, such as the electronic throttle, ignition advance angle, VVT, the air–fuel ratio and other parameters. Different effects of the engine are caused by the different EGR rate. The main purpose of the experiment is to adjust the above parameters according to certain process to achieve optimal performance. The best performance means, on the premise of no compromise of performance, the engine can achieve the lowest specific fuel consumption and emissions performance within the acceptable range.

Select 3000 rpm/3 bar for detailed analysis.

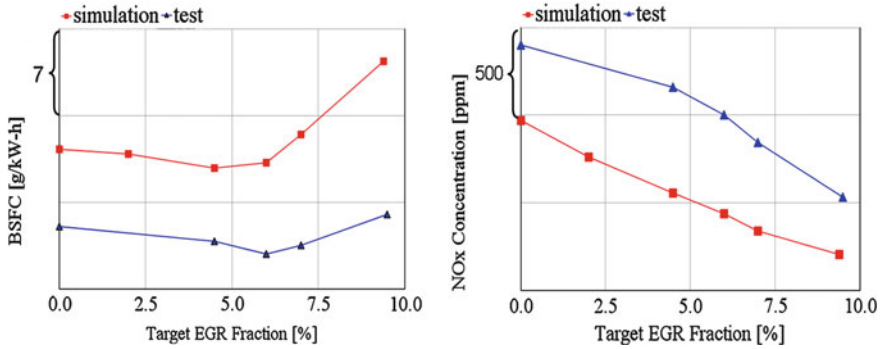


Fig. 7 Simulation and test results comparison chart

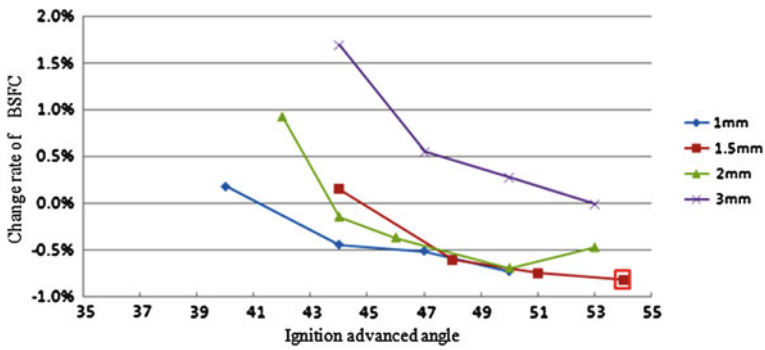


Fig. 8 Change rate of BSFC on original engine with EGR

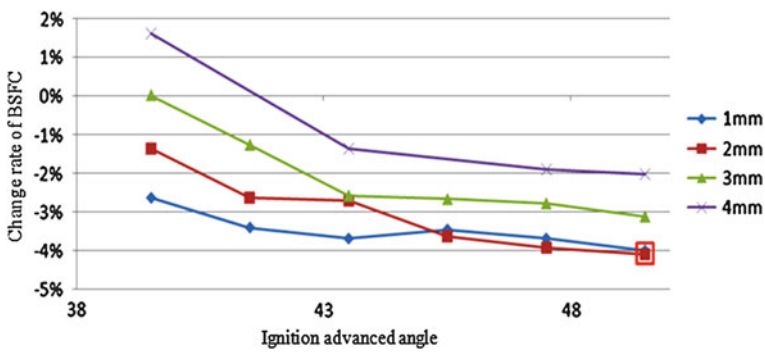


Fig. 9 Change rate of BSFC on high compression ratio engine with EGR

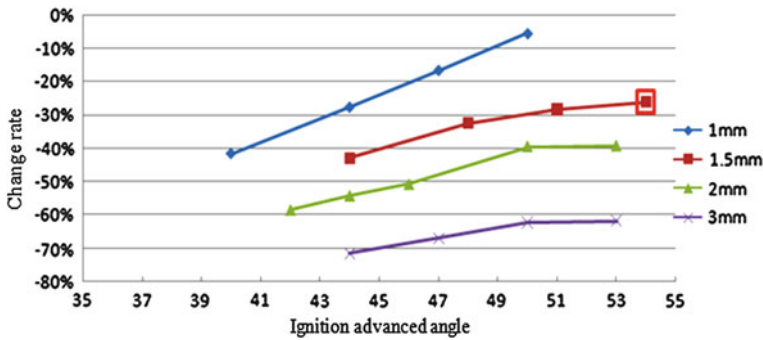


Fig. 10 Change rate of the emission of NOx on original engine with EGR

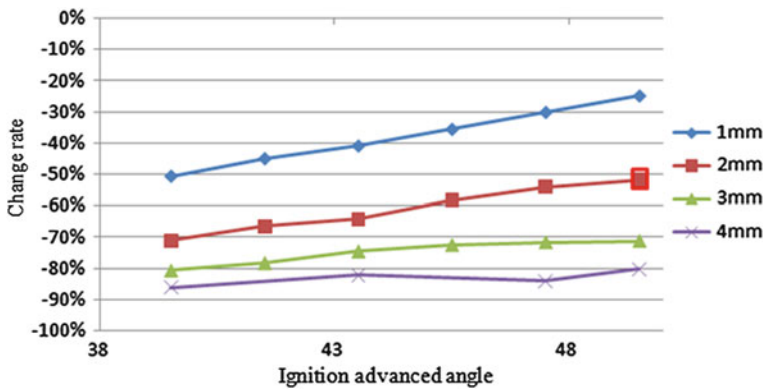


Fig. 11 Change rate of the emission of NOx on high compression ratio engine with EGR

In Figs. 8 and 9, the test results show the influence of different EGR valve opening lift, different ignition advance angle on fuel consumption. The x-axis represents the ignition advance angle, and the y-axis represents the oil consumption change rate in comparison to the original. Figure 8 shows change rate of BSFC original engine with EGR; Fig. 9 shows change rate of BSFC on a high compression ratio engine with EGR.

According to Figs. 8, 9 we can conclude that (1) the original engine applied with EGR, when the EGR valve opening lift is 1.5 mm (EGR rate is 6 %) and the ignition advance angle is approximately 54°, the optimal result is fuel consumption reduced by 0.8 %; (2) High compression ratio applied with EGR, when the opening of EGR valve lift is 2 mm (EGR rate is 8.9 %) and the ignition advance angle is approximately 52°, the optimal result is fuel consumption reduced by 4.1 %.

Figures 10 and 11 shows the test result influence of different ignition advance angle on NOx emission when EGR valve opens at different degree, in which the x-axis represents the ignition advance angle; the y-axis represents the NOx rate of change related to the original. Figure 10 shows change rate of NOx emission on the original engine applied EGR; Fig. 11 shows change rate of NOx emission on a high compression ratio applied with EGR.

According to Figs. 10 and 11, we can conclude that: (1) With the increasing of, ignition advance angle the capacity of reducing of NOx decreases; (2) With the increasing of opening lift of the EGR valve, the capacity of reducing NOx increases; (3) At the specific fuel consumption the best point (marked by red box), the NOx emissions of the original engine with EGR, high compression engine with EGR are reduced by approximately 26 and 51.8 % separately.

4 Conclusions

Through simulation and bench test, this paper studied the effect of fuel efficiency and the potentiality of improving the compression ratio of a 1.6 L naturally aspirated gasoline engine by the external cooled EGR technology. The conclusions are as follows:

- (1) The application of prediction combustion model in engine 1-D performance simulation can effectively predict the trend of the optimum EGR rate, NOx and other parameters.
- (2) The bench test results show that: in the low to medium load conditions, application of the EGR technology only can reduce fuel consumption by up to 2 %, while by increasing the compression ratio and applying the EGR technology, fuel consumption can be reduced by up to 5 %, and reduce NOx by more than 50 %.
- (3) The optimal EGR ratio calibration testing shows that: The optimal EGR ratio is adjusted by the electronic throttle, ignition advance angle, VVT angle, the air-fuel ratio, EGR valve opening degree and other parameters; With the ignition advance angle increases, the capacity of reducing NOx decreases; With the opening lift of the EGR valve increases, the capacity of reducing NOx increases correspondingly.

References

1. Zhang D (2005) GW2_8TDI Light vehicle diesel electronically controlled EGR system development. Journal of Jilin University, Jilin

2. Xiao K (2005) Exhaust gas recirculation system in turbocharged and intercooled diesel. Journal of Guangxi University, Guangxi
3. Six D, Van Herzele T et al. (2012) Development and testing of an EGR system for medium speed diesel engines. SAE2012-01-0680
4. Fujihara K, Nakamizo Y, Kojima M et al. (2009) Development of a NOx reduction system using exhaust valve controls in small engines for motorcycles. SAE 2009-32-0043, SETC 2009
5. Millo F, Mallamo F, Arnone-Lombardini L (2007) Analysis of different internal EGR solutions for small diesel engines. SAE2007-01-0128
6. Niemi SA, Paanu TPJ, Lauren MJ (2004) Effect of injection timing, EGR and EGR cooling on the exhaust particle number and size distribution of an off-road diesel engine. SAE 2004-01-1988

The Study on the Capacity of NO_x Storage-Reduction Catalyst for Lean-Burn Engine

Jianqiang Wang, Yuan Wang, Shuangxi Liu, Jidong Gao, Jie Ma and Meiqing Shen

Abstract Components in NO_x storage reduction (NSR) catalysts have been studied in order to identify their impact on NSR performance. In order to enhance the catalytic performance of the NSR catalyst, the hydrothermal stability and sulfur tolerance of the NSR catalyst were improved by developing new NSR formula. The results show that Pt/BaO/Ce_{0.7}Zr_{0.3}O₂ + Rh/Al₂O₃ catalyst has superior NSR activity, thermal stability and sulfur tolerance. The influence of space velocity, oxygen concentration and Lean-Rich period on the NSR activity was investigated.

Keywords Lean-burn engine · NO_x storage reduction · Thermal stability · Sulfur tolerance

1 Introduction

Lean-burn engines are attracting more and more attention than conventional gasoline engines due to their higher fuel efficiency and lower CO₂ emission. However, under lean-burn conditions, the toxic NO_x exhaust emissions cannot be efficiently reduced over the classical three-way catalysts in the presence of

F2012-A04-005

J. Wang (✉) · Y. Wang · S. Liu · J. Gao · J. Ma
China Automotive Technology and Research Center, Tianjin 300162, China
e-mail: wangjianqiang@catarc.ac.cn

M. Shen
School of Chemical Engineering and Technology, Tianjin University,
Tianjin 300072, China

excessive O_2 . Therefore, selective catalytic reduction (SCR) and NO_x storage-reduction (NSR) catalysts have been developed [1–3]. Because of their ability to achieve high NO_x conversions over a range of temperatures without the need for additional on-board reductant, and require less mounting space, NO_x Storage-Reduction (NSR) technology is regarded as the most practical technology for lean-burn gasoline and diesel vehicles. The development of advanced catalyst makes one of the major contributions to the improvement of NSR technology.

A typical NSR catalyst formulation contains NO_x storage components, noble metals and support oxides. The combined interactions of these three components efficiently remove NO_x from vehicle exhaust through the periodic operations of NO_x oxidation, NO_x sorption, NO_x release and NO_x reduction. Since the 1990s, NSR technology has been extensively studied, providing fundamental insights into the relevant reactions, mechanisms, kinetics, and roles of different catalytic components [4]. However, the role of every component in the NSR performance and the inter-component relationship are still not very clear. Meanwhile, the state-of-the-art NSR catalyst (Pt/BaO/ Al_2O_3) is weakly resistant to sulfur poisoning and thermal treatment. So it's necessary to develop the higher catalytic activity, thermal stability and sulphur tolerance NSR catalyst to meet the commercial requirements.

In this work, the influence of NO_x storage components, noble metals and support oxides on the catalytic activity was investigated. In this work, the influence of NO_x storage components, noble metals and support oxides on the catalytic activity was investigated. The influence of space velocity, oxygen concentration and Lean-Rich period on the NSR activity was investigated.

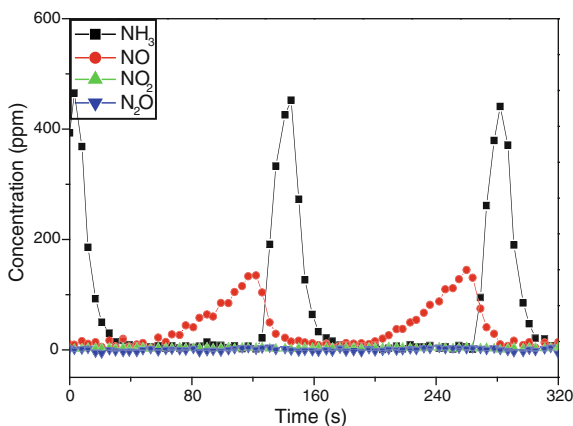
2 Experimental

Al_2O_3 supports (Shanghai Huaming Gona, designed as AC) are containing of 95.1 wt% Al_2O_3 and 4.9 wt% La_2O_3 . BaO/ Al_2O_3 was prepared as described by incipient-wetness impregnation of Al_2O_3 using $Ba(CH_3COO)_2$ solution. To clarify, the barium loading in all samples was denoted by the weight ratio of BaO to Al_2O_3 , i.e. BaO/ Al_2O_3 (w/w). After the impregnation, the sample was kept overnight at room temperature, and then the sample was dried at 120 °C for 12 h and then 500 °C for 3 h. For higher BaO loading (BaO/ $Al_2O_3 \geq 0.3$), successive impregnations were required. For Pt/BaO/ Al_2O_3 sample, Pt was loaded by incipient wetness impregnation, using $Pt(NO_3)_2$ solutions. Then the sample was placed at room temperature overnight, dried at 120 °C for 2 h, and calcined at 500 °C for 3 h subsequently.

For Pt–Rh/BaO/ Al_2O_3 sample, Pt and Rh was loaded by a certain ratio, using $Pt(NO_3)_2$ and $Rh(NO_3)_2$ solutions.

For Pt/BaO/ $Ce_{0.7}Zr_{0.3}O_2$ +Rh/ Al_2O_3 sample, BaO were loaded on $Ce_{0.7}Zr_{0.3}O_2$ support oxides by the incipient wetness impregnation. Pt and Rh were loaded respectively in BaO/ $Ce_{0.7}Zr_{0.3}O_2$ and Al_2O_3 supports by incipient wetness

Fig. 1 120 s (lean)–20 s (rich) NSR reaction profiles of NH₃, NO, NO₂, and N₂O



impregnation, and they were mixed in the weight ratio of 4:1 right before the catalytic tests.

The aging experiments were carried out in 5 % steam + air ($SV = 30000 \text{ h}^{-1}$) at 670 °C for 8 and 16 h, respectively.

The sulfur aging experiments were carried out in 8 % steam + 50 ppm SO₂ + air ($SV = 30000 \text{ h}^{-1}$) at 300 °C for 24 h.

The NSR activity was determined under multipoint isothermal conditions in the temperature range of 200–500 °C at an interval of 100 °C. The alternative pulses of lean (500 ppm NO + 7.5 % O₂ + 10 % CO₂ + 10 % H₂O) and rich (500 ppmNO + 7.5 % CO + 10 % CO₂ + 10 % H₂O) were injected under 120 s/20 s lean/rich cycles. The total flow rate is 1 L/min with the space velocity of 30000 h⁻¹. The outlet concentrations of NO, NO₂, NH₃, N₂O, CO, CO₂ and H₂O(g) were measured by NICOLET is10 FTIR equipped with a 2 m gas cell (As shown in Fig. 1). The NO_x conversion was calculated based on the following equations:

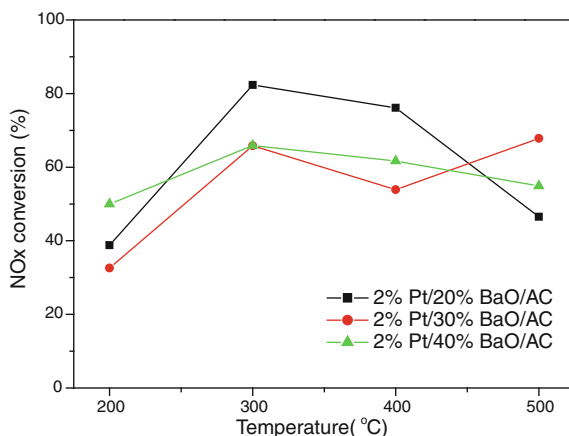
$$X_{\text{NO}_x} = \frac{\text{NO}_{\text{inlet}} - (\text{NO}_{\text{outlet}} + \text{NO}_{2\text{outlet}} + 2\text{N}_2\text{O}_{\text{outlet}})}{\text{NO}_{\text{inlet}}} \times 100 \%$$

3 Result and Discussion

3.1 Influence of Storage Component

As a storage component, generally alkali metals or alkaline earth metal compounds are common in use because of their high basicity. BaO is the most commonly studied NO_x trapping component among metal oxides, with a major contribution to the overall NO_x trapping capacity. Besides the NO_x storage step, BaO also plays some roles in the NO oxidation, NO_x release and NO_x reduction steps.

Fig. 2 Influence of storage component loading on NSR activity



Perusal of the literature shows the distribution and dispersion of Ba-containing species and consequently the influence on the reactivity can be distinctly influenced by the Ba-loading [3, 5, 6]. According to Lietti et al., the relative amount of Ba-containing phases (BaO , $\text{Ba}(\text{OH})_2$ and BaCO_3) was different with different Ba loading, which has various NO_x trap capacity [7]. The results show that 20 % Ba loading was the optimum (Fig. 2).

3.2 Influence of Noble Metal

The noble metals (NM) plays several key roles in the NO_x storage/reduction reaction steps, such as (I) NO oxidation under lean-burn conditions (II) NO_x storage under lean-burn conditions (III) NO_x reduction under rich-burn conditions, and (IV) sulfur tolerance and regenerability. Detailed investigations have showed that NSR activity is relating to the noble metal dispersion, which is decided by particle size, precursor and loading etc [8]. The present investigation was to investigate the correlation between Pt loading and NSR activity. The results show that the increase of Pt loading resulted in superior NSR activity. However the higher loading resulted in its relatively higher cost. So the optimum Pt loading was 2 %.

Generally, it has been reported that Pt shows higher NO oxidation activity than Rh and Pd, whereas Rh shows the highest NO_x reduction activity among Pt, Rh and Pd [5, 6, 9]. Therefore, it is very interesting to investigate Pt–Rh based bimetallic NSR catalysts to achieve a higher overall NO_x conversion. The bimetallic Pt/Rh samples were prepared with different Rh loading. The results show that the increase of Rh loading resulted in superior NSR activity, especially for low-temperature activity (Figs. 3 and 4).

Fig. 3 Influence of noble metals loading on NSR activity

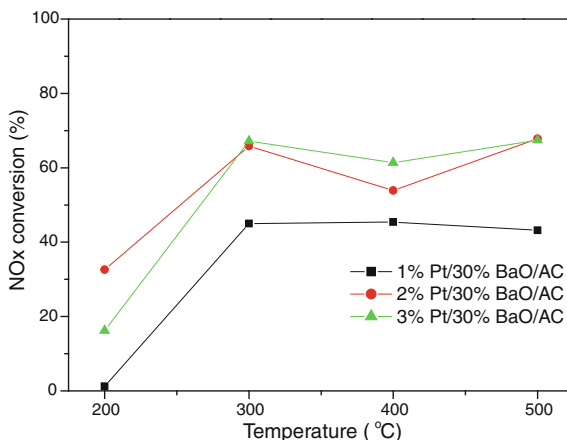
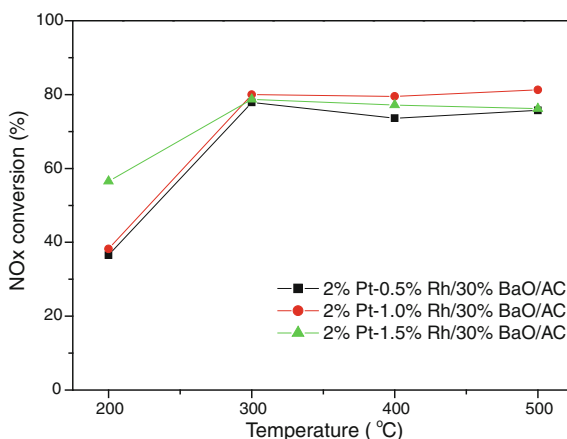


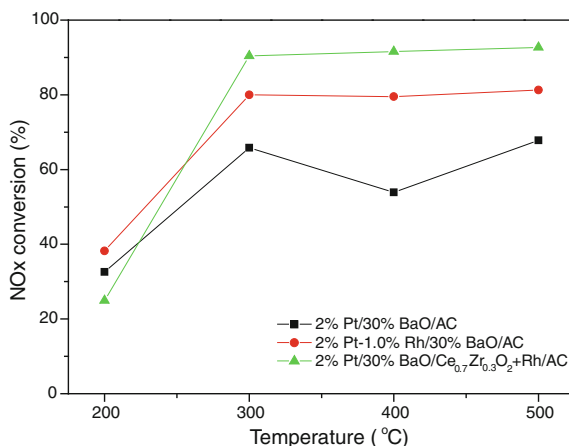
Fig. 4 Influence of noble metals on NSR activity



3.3 Influence of Support Oxides

The noble metals and the storage components are dispersed over a support; the support oxides is not only for dispersing NM and NOx storage components, but is of great importance for direct NOx trapping, N₂ selectivity modification, and sulfur tolerance improvement. Ceria-based materials have been shown to be beneficial for NSR catalysts [10]. Many current commercial samples have already incorporated ceria into NOx traps catalysts, although ceria-based materials are admitted to have several drawbacks. In comparison with pure CeO₂, ceria-zirconia (CZ) solid solutions are well known for their improved redox activities and thermal stability. Therefore, it is of interest to apply CZ as support for NSR catalysts. According to Strobel et al., Pt/Ba/Ce_xZr_{1-x}O₂ catalysts showed superior NSR performance, sulfur resistance and regeneration ability than Pt/Ba/Al₂O₃

Fig. 5 Influence of support oxides on NSR activity



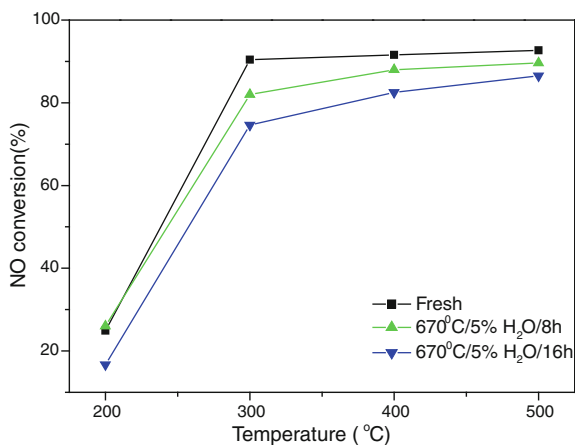
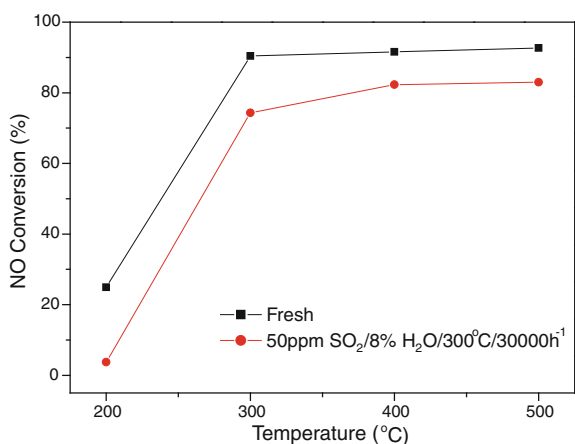
catalysts [11]. In the present work, Pt and Rh respectively supported on the Ba/CeO₂-ZrO₂ and Al₂O₃, which may improve the interaction between NM, storage component and support, resulted in the superior NSR activity. The results show that Pt/BaO/Ce_{0.7}Zr_{0.3}O₂ + Rh/AC catalyst has superior NSR activity (as shown in Fig. 5).

3.4 Hydrothermal Stability

Thermal degradation of NSR catalysts is primarily caused by high temperature desulfation treatment. Furthermore, during a rich-burn cycle, the oxidation of hydrocarbon, CO and H₂, generates heat at the catalyst surface and results in thermal degradation as well [3, 6]. Coarsening of the platinum particles and the loss of surface area of the NO_x storage materials are two of the factors that can contribute to the loss of NO_x storage capacity after thermal aging. The NSR performances of the hydrothermal aged catalysts are showed in Fig. 6. Aged catalysts exhibit different extents of NO_x storage capacity decline due to the consumption of BaCO₃ and the collapse of physical texture of support oxides at different levels. However, CZ solid solutions are well known for their improved redox activities and thermal stability [12]. Furthermore, Rhodium containing catalysts showed relatively little loss of activity upon hydrothermal aging [9, 13]. So best NSR performance and thermal stability was observed with bimetallic catalysts where the noble metals were separated.

3.5 Sulfur Tolerance

Sulfur typically present in the fuel and lubricant oils is oxidized to SO₂ during combustion. The SO₂ in the exhaust gas can adsorb on the catalyst and poison it. As concerns the noble metal, SO₂ can have negative as well as positive influence

Fig. 6 Influence of on NSR activity**Fig. 7** Influence of sulphur on NSR activity

on the catalyst's oxidation activity. In contrast to Pt, for Rh no loss of NO reduction activity was observed in the presence of SO₂. Furthermore Rh is a highly active NO reduction catalyst that enhances the regeneration of Ba-nitrates [9]. According to Corbos et al. [14], the Pt/Ba/Ce_xZr_{1-x}O₂ catalysts showed better sulfur resistance than Pt/Ba/Al₂O₃ catalysts. Meanwhile, the sulfates elimination under desulfation conditions was more efficient on Pt/Ba/Ce_xZr_{1-x}O₂ than on the Pt/Ba/Al₂O₃ catalyst. The Influence of sulfur on NSR activity is shown in Fig. 7. The results show that the Pt/BaO/Ce_{0.7}Zr_{0.3}O₂ + Rh/AC catalyst has superior sulfur tolerance.

Fig. 8 Influence of space velocity on NSR activity

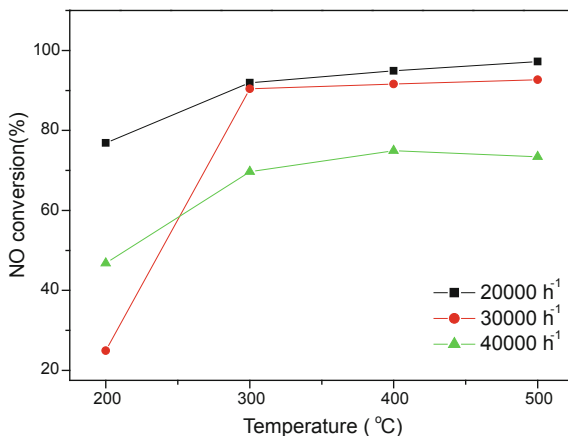
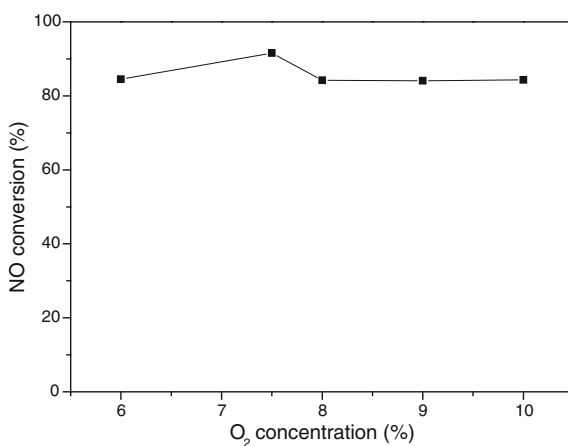


Fig. 9 Influence of O₂ concentration on NSR activity at 400 °C



3.6 Influence of Different Operating Conditions

The performance of an automotive catalytic converter is strongly influenced by the space velocity of the exhaust gases [15–18]. The catalyst conversion performance decreases with increasing space velocity and can be severely deteriorated when space velocity is increased beyond certain values. At higher space velocities, the exhaust gases passing through the catalyst may not have sufficient residence time for the catalytic reactions resulting in a reduced conversion performance. Low space velocities, on the other hand, yield excellent conversion performance, but may require low gaseous flow rates through the engine or the use of larger size catalysts. Figure 8 shows a comparison of the influence of different space velocities on the NSR performance. Obviously a higher space velocity (GHSV) reduces the conversion efficiency, because of short residence time.

Fig. 10 Influence of lean-rich time on NSR activity at 400 °C

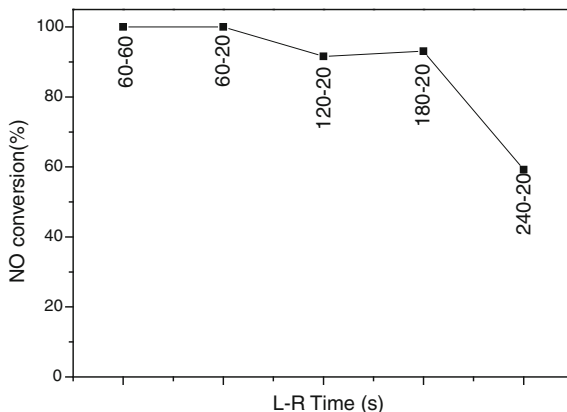


Figure 9 shows the influence of oxygen concentration in the lean phase on the NSR activity at 400 °C. These plots prove the zero-order kinetics with respect to oxygen for O₂ feed concentrations in the investigated range.

The lean pulse duration is varied keeping the rich phase duration constant at 20 s and the feed CO at 7.5 % and the temperature at 400 °C. It can be seen from Fig. 10 that NO conversion is a monotonically decreasing function of lean pulse duration. As we known, during the lean phase Pt sites are covered with oxygen. When the CO is injected it reacts with oxygen, enabling the subsequent adsorption and reduction of NO₂. If the lean pulse is too long in duration, not all of the NO₂ is reduced and the NO₂ conversion is incomplete. As the lean pulse duration is decreased, the additional CO consumes more oxygen, freeing up sites for NO₂ adsorption and reduction. This leads to an increase in NO₂ conversion.

4 Conclusion

The Pt/BaO/Ce_{0.7}Zr_{0.3}O₂ + Rh/AC catalyst shows superior NSR activity, thermal stability, sulfur tolerance and adaptability for different operating conditions.

References

1. Johnson TV (2010) Review of diesel emissions and control. SAE paper, 2010-01-0301
2. Johnson TV (2011) Diesel emissions in review. SAE paper, 2011-01-0304
3. Epling WS, Campbell LE, Yezerets A et al (2004) Overview of the fundamental reactions and degradation mechanisms of NO_x storage/reduction catalysts. Catal Rev Sci Eng 46(2):163–245
4. Miyoshi N, Katoh K, Tanaka T et al (1995) Development of new concept three-way catalyst for automotive lean-burn engines. SAE paper 950809

5. Roy S, Baiker A (2009) NO_x storage-reduction catalysis: from mechanism and materials properties to storage-reduction performance. *Chem Rev* 109:4054–4091
6. Liu G, Gao PX (2011) A review of NO_x storage/reduction catalysts: mechanism, materials and degradation studies. *Catal Sci Technol* 1:552–568
7. Lietti L, Forzatti P, Nova I, Tronconi E (2001) NO_x storage reduction over Pt-Ba/ γ -Al₂O₃ catalyst. *J Catal* 204:175–191
8. Abdulhamid H, Dawody J, Fridell E et al (2006) A combined transient in situ FTIR and flow reactor study of NO_x storage and reduction over M/BaCO₃/Al₂O₃ (M = Pt, Pd or Rh) catalysts. *J Catal* 244(2):169–182
9. Theis JR, Ura JA, McCabe RW (2007) The effects of platinum and rhodium on the functional properties of a lean NO_x trap. SAE paper, 2007-01-1055
10. Rohart E, Bellière-Baca V, Harlé V, Pitois C (2008) Ceria-based materials for DeNO_x catalysts very efficient at low temperature and with improved sulphur tolerance. SAE paper, 2008-01-0450
11. Strobel R, Krumeich F, Pratsinis SE, Baiker A (2006) Flame-derived Pt/Ba/Ce_xZr_{1-x}O₂: Influence of support on thermal deterioration and behavior as NO_x storage-reduction catalysts. *J Catal* 243:229–238
12. Lei C, Shen MQ, Yang M et al (2011) Modified textures and redox activities in Pt/Al₂O₃ + BaO/Ce_xZr_{1-x}O₂ model NSR catalysts. *Appl Catal B* 101(3–4):355–365
13. Büchel R, Pratsinisa SE, Baiker A (2012) Mono- and bimetallic Rh and Pt NSR-catalysts prepared by controlled deposition of noble metals on support or storage component. *Appl Catal B: Environ* 113–114:160–171
14. Corbos EC, Courtois X, Bion N, Marecot P, Duprez D (2008) Impact of the support oxide and Ba loading on the sulfur resistance and regeneration of Pt/Ba/support catalysts. *Appl Catal B: Environ* 80(1–2):62–71
15. Sharma M, Kabin K, Harold MP, Balakotaiah V (2005) Modeling of NO_x storage and reduction for diesel exhaust emission control. SAE paper, 2005-01-0972
16. Shamim T (2005) The effect of space velocity on the dynamic characteristics of an automotive catalytic converter. SAE paper, 2005-01-2160
17. Li YL, Roth S, Yassine M, Beutel T, Dettling J (2000) Study of factors influencing the performance of a NO_x trap in a light-duty diesel vehicle. SAE paper, 2000-01-2911
18. Xu LF, George G, Robert M et al (2008) The feasibility of an alumina-based lean NO_x trap (LNT) for diesel and HCCI applications. SAE paper, 2008-01-0451

New Techniques for Damage Assessment of Diesel Particulate Filters

Tim Hands and Qiang Li

Abstract The maximum soot load capacity for ceramic Diesel Particulate Filters (DPFs) is sometimes limited by a thermal crack failure mechanism associated with high temperature gradients which can occur during regeneration of highly loaded parts—particularly at low exhaust flow rates. The filter material and construction can be optimised for resistance to thermal cracking, however, the precise conditions which give rise to thermal failure of DPFs can be difficult to establish accurately and repeatably. For instance, thermal failure of DPFs may occur at the onset of the heating due to the exotherm of trapped soot, or during cooling (for instance at the fuel cut during deceleration or start of idle). The time of occurrence of thermal failure can help to establish the worst conditions for filters. Sectioning parts post-test is often conducted to establish the nature and location of any damage. However non-destructive testing allows for the possibility of progressive testing of single parts—allowing determination of the ‘Soot Mass Limit’. Post-test scanning techniques have been demonstrated (e.g. X-Ray/CT scanning). These allow non-destructive testing, but are generally expensive, and require the DPF to be removed from the can. This paper describes important considerations for application of two existing post-test evaluations as follows. (1) Radial and axial ultrasound ‘Time-of-flight’ measurement. (2) Internal imaging of the DPF with a small borescope. Also presented are two novel non-destructive techniques for assessing damage to DPFs as follows. (1) An *in situ* technique capable of measuring filter vibration events during DPF operation which may be associated with

F2012-A04-006

T. Hands
Cambustion Ltd, Cambridge, UK
e-mail: tim@cambustion.com

Q. Li (✉)
Cambustion China Office, Shanghai, China

thermal crack damage. A surface microphone coupled directly to the filter substrate through a hole in the can and intumescent matting measures brick vibration, while a background detector measures exhaust pipe and canning vibration events in order to discriminate metallic thermal expansion. Vibration and internal thermocouple data is presented from exothermic regenerations for several different filters loaded with soot on a commercial Diesel Particulate Generator with standard Diesel fuel and fuel treated with a catalytic additive. The extension of the technique to testing on a vehicle is demonstrated. (2) A relatively simple, post-test evaluation which involves reverse aspiration of DPF test parts with a cold Diesel soot aerosol generated with compressed air. The technique can locate DPF cells where the soot aerosol is not filtered though the substrate between the inlet and outlet channels. The deposition of soot on the substrate is shown to be an indicator of internal damage and, together with simple optical microscopy, can help to identify failure mechanisms. The paper presents examples of the above techniques to examine thermal damage to Silicon Carbide and Aluminium Titanate DPFs which have been subject to ‘worst case’ regenerations.

Keywords DPF · Crack · SML · DPG · Diesel

1 Introduction

The regeneration of heavily loaded Diesel Particulate Filters (DPF) parts can cause thermal damage to DPF substrates due to the high thermal gradients associated with the exothermic oxidation of the deposited soot.

The threshold of thermal damage depends on the physical properties of the DPF material used—including: thermal conductivity, heat capacity, material strength (fracture toughness K_{Ic}), Coefficient of Thermal Expansion (CTE), Young’s modulus (E), melting point/maximum application temperature. Further, the application of a catalytic coating to the DPF or addition of a fuel borne catalyst can significantly affect the threshold of exothermic reaction.

Most wall flow DPFs fall into two categories as follows:

- Monolith These have a single brick construction and are usually made from Cordierite.
- Segmented For vehicle applications, these are typically made from individual segments which are cemented together. They are usually made from Silicon Carbide.

The differences in the physical and thermal properties of these filter types leads to significant differences in thermal damage resistance (usually associated with loaded regeneration).

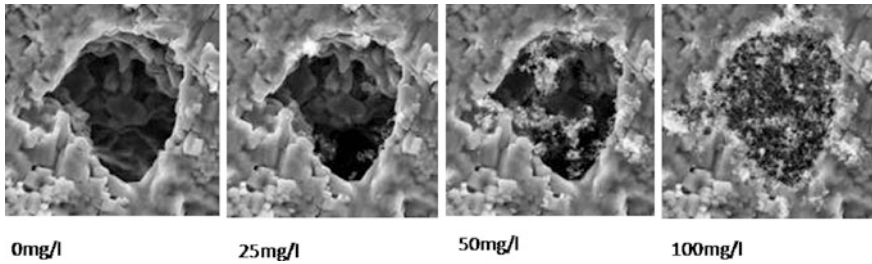


Fig. 1 TEM pictures of soot loading onto a DPF from clean (from [9])

1.1 Damage Assessment

An important part of Soot Mass Limit Testing is the method by which a part is determined to be damaged.

1.1.1 Filtration Performance

Concerning the degradation in the filtration performance of a part, the assessment of filtration should be made on a DPF part which is loaded from clean, since the filtration performance is a strong function of the soot loaded onto the part at small soot loads. Further, for small cracks, the accumulation of soot on the part can ‘bridge’ or plug the cracks and restore filtration performance. This behaviour of soot can be observed in Figs. 1 and 2.

Figure 2 shows the change in soot mass filtration efficiency following Soot Mass Limit tests of increasing severity with soot load measured with an AVL415S smoke meter.

Some workers have adopted the criterion for damage to a part to be a reduction in filtration efficiency of more than one percent at a total accumulated soot load of 0.5 g. By this criterion, the data in Fig. 2 indicates that the Soot Mass Limit for this part is between base load (6 g soot/l) and base load +15 % (6.9 g soot/l).

1.1.2 Mechanical Integrity

Although DPFs may leak due to missing end plugs or manufacturing faults, the cause of the degradation in filtration performance is generally due to internal cracks. Computerised Tomography using X rays can produce images of internal cracks (see Fig. 3).

However, this technique is relatively expensive and requires the DPF to be removed from its can. This paper describes alternative techniques to identify damaged parts.

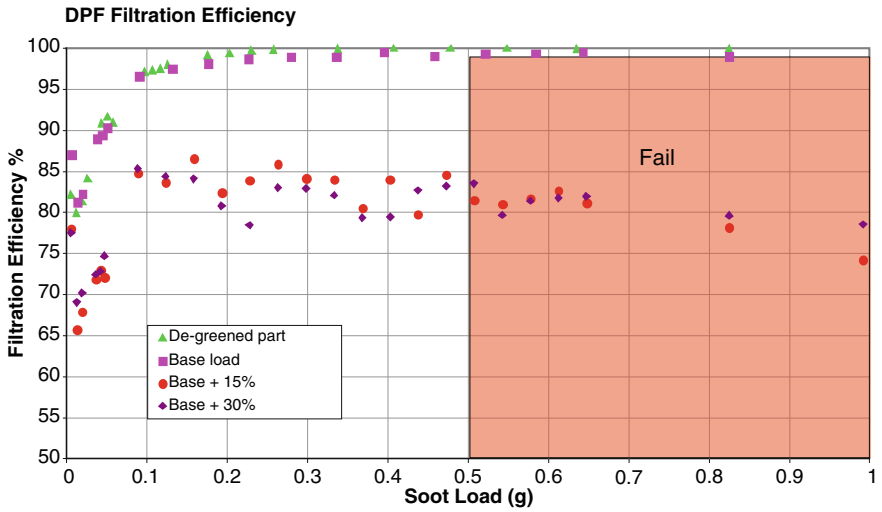
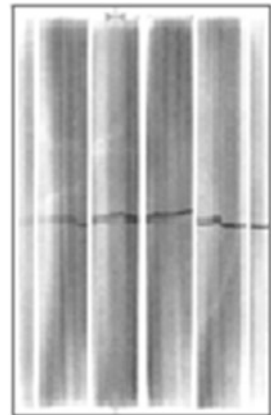


Fig. 2 Mass-based filtration efficiency of a DPF as a function of total soot load

Fig. 3 CT image of radial crack in SiC DPF from [1]



2 Instrumentation

2.1 Existing Post-Test Evaluation Techniques

This section discusses two techniques which can only be conducted post-test, when the sample is cooled and with reasonable access to the rear face of the DPF.

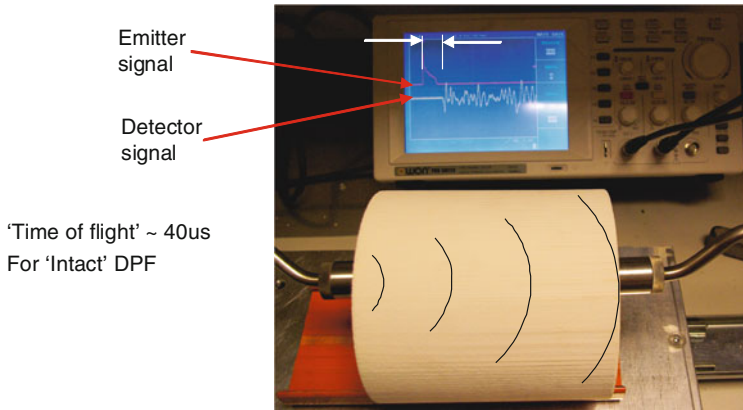


Fig. 4 Axial ultrasound measurement 'intact' DPF

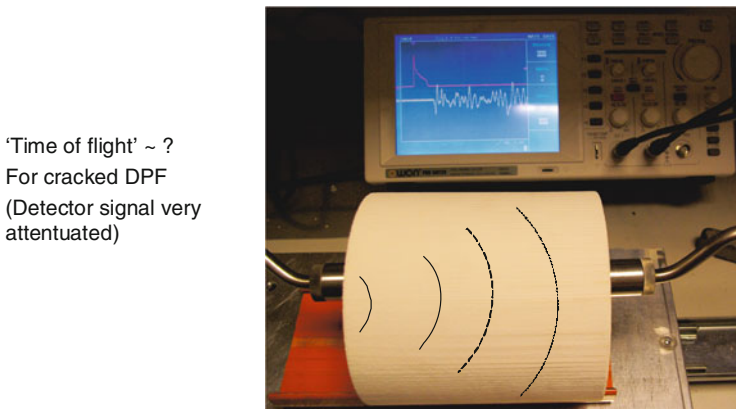


Fig. 5 Axial ultrasound measurement damaged DPF

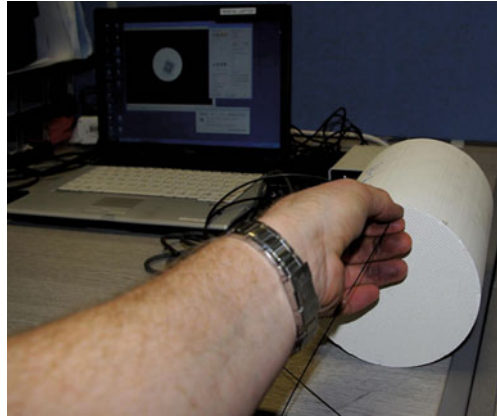
2.1.1 Ultrasound Time of Flight Measurement

The technique of non-destructive inspection of rigid materials via Acoustic Emission (AE) is well established [2]. Recently, it has been applied to alternative materials including asphalt [3] and ceramic monoliths [4, 5].

'Time of flight' measurements were made using a Pundit plus Model PC1006. The system uses a separate ultrasound emitter and detector and measures the transit time through the substrate. The experimental arrangement is shown in Figs. 4 and 5 for an 'intact' and damaged DPF respectively.

The figures above illustrate how a radial crack significantly attenuates and delays the detected signal. If the part is not canned (as shown in the figures), it is also possible to make radial measurements (across diameters of the DPF).

Fig. 6 Borescope inserted into exit cells of DPF



When making these measurements, the following considerations are important:

1. The coupling of the emitter and detector to the surface of the DPF has a strong effect on the detected signal. We have found that Blu-tack [6] with a thickness of ~ 2 mm gives good and repeatable acoustic coupling for the detector and emitter.
2. The compressive force by which the emitter and detector are coupled to the DPF also has a strong effect on the detected signal (a high compressive force can tend to close cracks which tends to reduce transit times and generally increase the energy in the transmitted signal). In order to obtain repeatable results, a mechanical arrangement which keeps this force constant is required.

2.1.2 Internal Borescope Inspection

Some workers have used a small diameter borescope (e.g. [7]) to inspect individual cells of a DPF. In order for the technique to work well, the part should be loaded with a small amount of soot. The optical fibre bundle (~ 0.5 mm diameter) is inserted down the exit cell of a DPF with suspected crack as shown in Fig. 6.

As the fibre is traversed along the length of the cell, where the cell walls are intact, there is no evidence of soot (see image 1 in Fig. 7). However, a cracked cell allows soot through from the inlet side of the DPF and a black line is observed (see image 2 in Fig. 7).

Note that this technique is most sensitive where there is good contrast between the DPF substrate and the soot (it is more difficult to locate cracks in SiC parts—which are generally dark grey).

Fig. 7 Images of intact channel (1) and damaged channel (2)

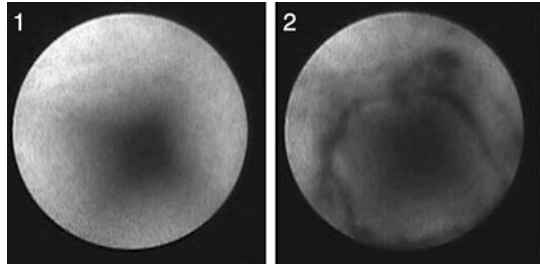


Fig. 8 Custom surface microphones with coupling rods



2.2 Novel evaluation techniques

2.2.1 In-situ: Custom Vibration Detectors

During ‘worst case’ regenerations of loaded DPFs on a burner-based DPF testing system (Cambustion DPG [8]) it was noted that damage to DPFs was associated with audible cracks. These were distinct from the metallic creaks associated with the rapid heating of the exhaust pipe and DPF can.

Custom surface microphones were developed where the microphone diaphragm is remote from the DPF substrate, but coupled to it via a rigid rod. These are shown in Fig. 8 and installed on a DPF test housing in Fig. 9.

The background sensor rod is coupled directly to the DPF can and responds primarily to vibration ‘events’ associated with the exhaust pipe and DPF can. The DPF crack sensor (2) in Fig. 9 is located in a stainless steel guide tube and the tip is resting directly onto the surface of the DPF (a small hole is cut in the intumescent matting to allow this). It responds primarily to vibration ‘events’ from the DPF itself.

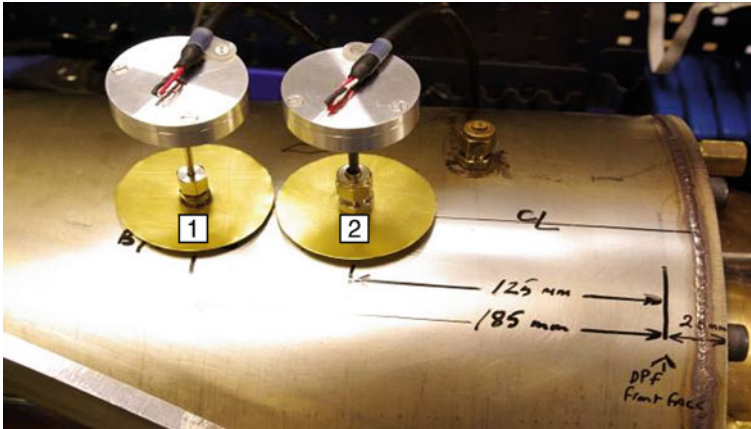


Fig. 9 Background (1) and DPF (2) crack sensors installed on DPF can

The raw vibration signals from these microphones are high-pass filtered in order to accentuate the events associated with cracks. The high-pass filtered signals are then monitored to produce a second by second output of DPF and background crack activity.

2.2.2 Post Test: Reverse Soot Aspiration

A damaged DPF part can provide a transit path for soot through a crack rather than through the wall of the filter. If a highly concentrated soot aerosol is blown through a DPF (from entry to exit), the portion of aerosol travelling through the walls of the DPF will be filtered and therefore no soot will arrive at the exit face. For a damaged part however, soot can travel from the entry face to the exit face without being filtered.

Some workers use a smoke aerosol and laser sheet on the entry face to observe this 'leakage'. An alternative novel technique conducted on a clean, cold DPF is illustrated below.

1. A sample of Diesel soot (typically several grams) is placed into a polythene bag which is sealed around the entry face of the DPF (upper picture).
2. Clean compressed air is blown backwards through the DPF (from exit to entry) creating a jet of air at the entry. This jet stirs the Diesel soot and creates a highly concentrated aerosol which then travels through the DPF (from entry to exit)—with a total flow rate similar to the compressed air jet.
3. As the air jet is moved over the surface of the suspect DPF, all cells of the DPF are exposed to highly concentrated Diesel aerosol (lower picture) (Figs 10, 11).

Where a part is damaged, the soot exiting the front face of the DPF via cracks leaves a black deposit. Figure 12 shows a part after reverse aspiration. Missing/

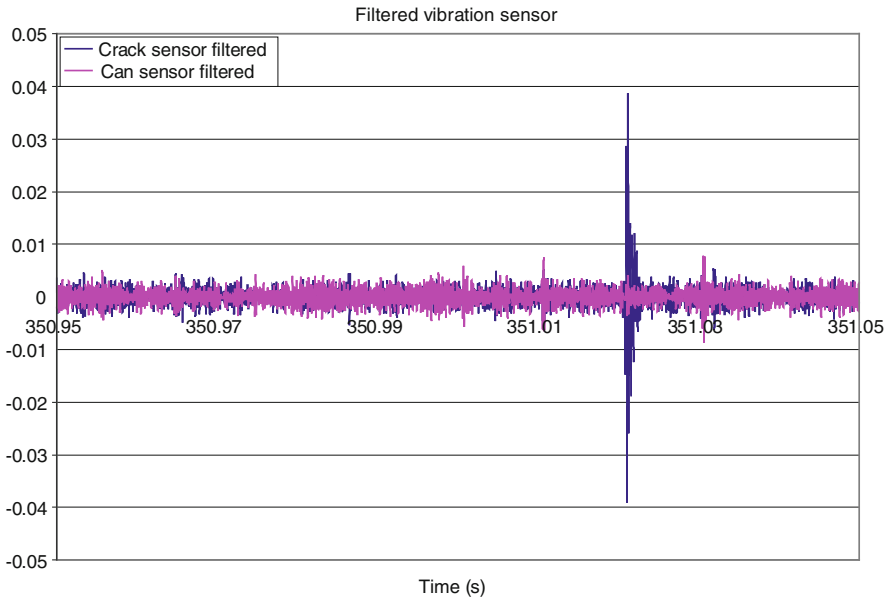


Fig. 10 DPF crack (blue) and can (pink) sensors filtered response to single brick crack



Fig. 11 Reverse aspiration of DPFs with soot aerosol

damaged plugs are evident at the bottom and top left of the image and a crack across the part is also evident.

Note that this technique is also most sensitive where there is good contrast between the DPF substrate and the soot (it is more difficult to locate cracks in SiC parts—which are generally dark grey).

Fig. 12 Crack and missing/damaged cell plugs



Table 1 DPF test program

Soot load (g/l)	SiC $5.66 \times 10''$	AT $5.66 \times 8''$
8	✓ (with Eolys fbc)	✓
12	✓ (with Eolys fbc)	✓ (with and without Eolys fbc)
15		✓

3 Test Program

Two Passenger car DPFs were tested as follows:

1. SiC uncoated $5.66'' \times 10''$.
2. Aluminium Titanate uncoated $5.66'' \times 8''$.

These parts were successively loaded to higher and higher soot loads and regenerated with a ‘worst case’ regeneration (heated to $\sim 700\text{C}$ inlet at 63 kg/hr, overall lean) whilst being continually monitored for cracks. The tests are summarised in Table 1.

The parts were instrumented with internal 0.5 mm thermocouples inserted from the rear face in order to resolve the temperature field during the regeneration (Table 3).

4 Results

4.1 SiC In Situ Crack Data

See Figs. 13–15.

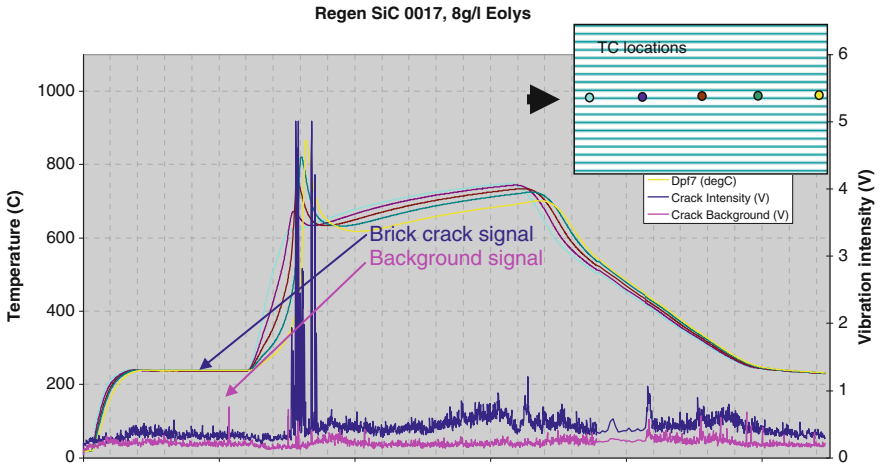


Fig. 13 SiC worst case regen, 8 g/l load with Eolys

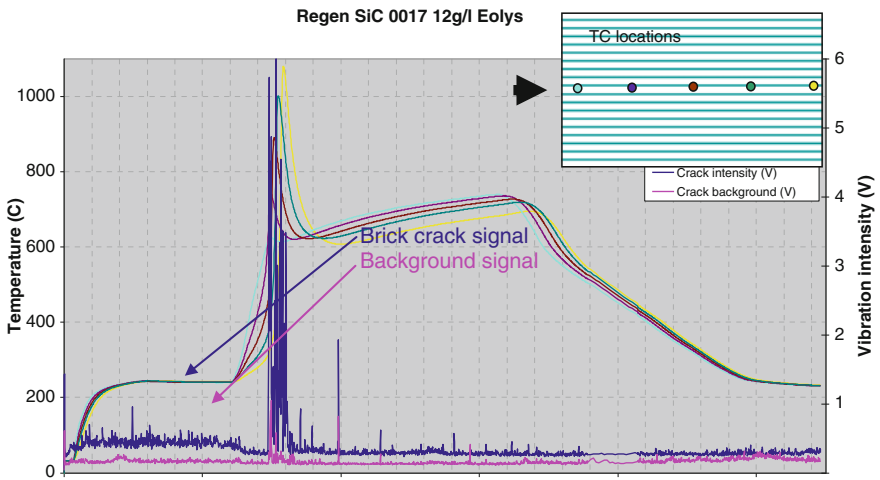


Fig. 14 SiC worst case regen, 12 g/l load with Eolys

Fig. 15 SiC DPF after 12 g/l worst case regeneration with Eolys



Table 2 Ultrasound transit times for AT DPF

Soot load before worst case regeneration	Average axial transit time over 16 segments (std deviation), us
Bare brick	43.8 (2.0)
8 g/l with fbc	42.0 (2.0)
12 g/l with fbc	62.1 (11.0)

4.2 *Sic Post Test Ultrasound Time of Flight Data*

See Table 2.

4.3 *At In Situ Crack Data*

See Figs. 16–18.

4.4 *At Post Test Ultrasound Time of Flight Data*

See Table 3.

5 Discussion

5.1 *SiC DPF*

Figures 13 and 14 show worst case regenerations following loads to 8 g/l and 12 g/l with Eolys fuel borne catalyst respectively. The axial thermocouples indicate the exotherms associated with the regenerations with the highest temperatures and temperature gradients occurring towards the rear of the DPF. The *in situ* crack sensors indicate significant ‘activity’ during the main exothermic phase of the regeneration (~800 s after the test start). Much of this activity is expected to be cracking of the cement between the 16 segments of the DPF. The ring cracks in Fig. 15 were only visible following the 12 g/l regeneration with the fuel borne catalyst.

During the tests described, the SiC part was instrumented with 25 internal thermocouples to resolve the internal temperature field. Figure 19, shows a false colour representation of this temperature field during the exotherm. The Thermocouple locations are indicated by the white dots on the upper picture, the right hand scale gives the temperature calibration for the thermocouples (in °C) and the base of the image consists of the 5 axial thermocouple and crack sensor outputs for the test. The

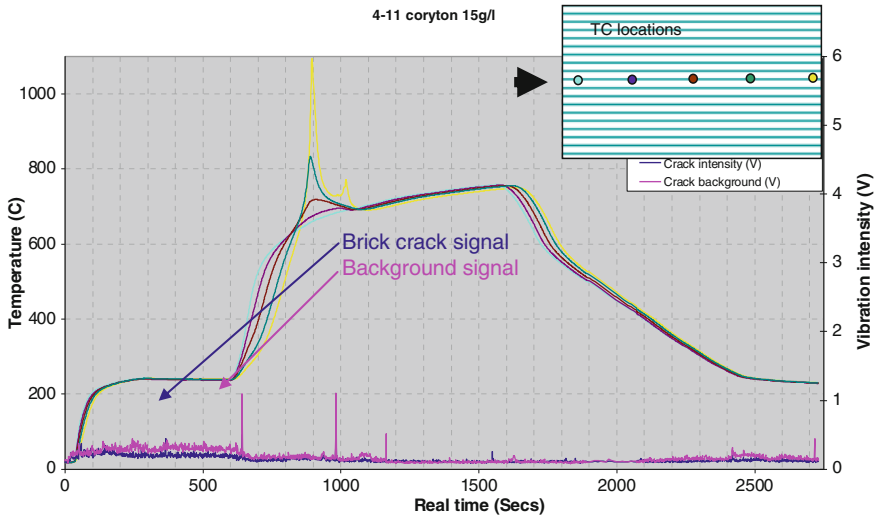


Fig. 16 AT worst case regen, 15 g/l load

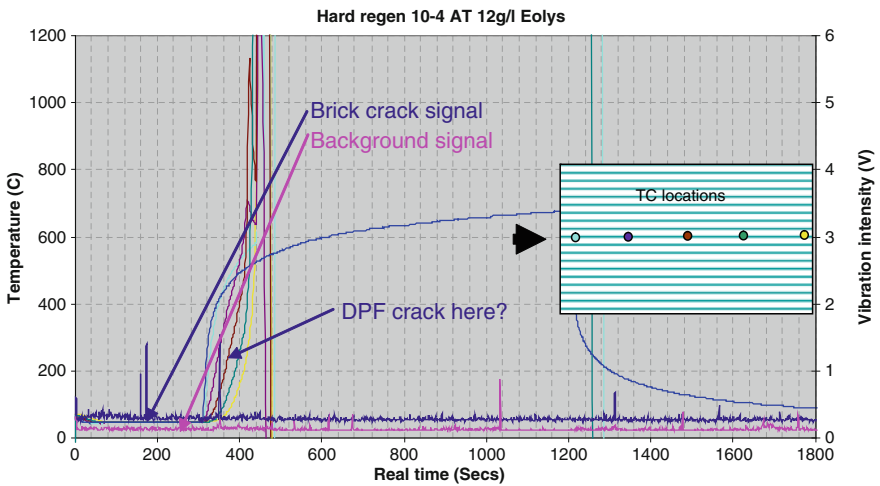


Fig. 17 AT after worst case regen, 12 g/l load with Eolys, from cold

black dot on this trace corresponds to the time at which the temperature field is calculated. Flow direction is indicated by the black arrow. The cement boundaries between the segments of the DPF are indicated by the dotted lines.

The data shows the maximum temperatures occurring towards the rear of the DPF. The temperature gradients ($^{\circ}\text{C}/\text{mm}$) are indicated by the spacing of the black lines which separate the colours. As expected for the segmented monolith, the highest temperature gradients occur across the cement boundaries on a radial axis.

Fig. 18 AT DPF following 12 g/l load with Eolys, from cold

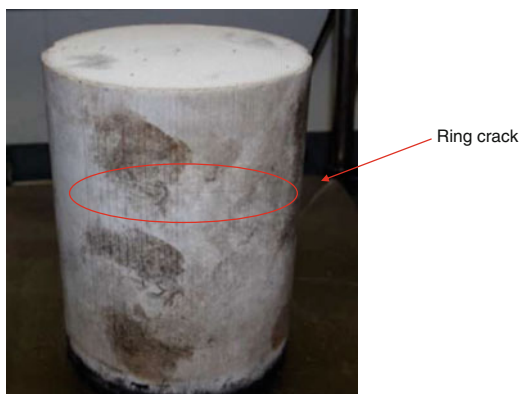


Table 3 Ultrasound transit times for SiC DPF

Soot load before worst case regeneration	Average axial transit time over 16 segments (std deviation), us
Bare brick	127.8 (3.2)
8 g/l	126.0 (2.6)
12 g/l	126.6 (2.8)
15 g/l	125.8 (2.6)
12 g/l from cold with fbc	284.4 (173)

The ultrasound time of flight data measured after each test shown in Table 2 indicates that the segments are intact at the 8 g/l fbc load, but that there is significant damage after the 12 g/l fbc load.

6 At DPF

Figure 16 shows a worst case regeneration for an AT part loaded to 15 g/l, but with no fuel borne catalyst. As above, the maximum temperatures and gradients occur towards the rear of the DPF, but the crack sensors do not indicate any activity. Following this test the ultrasound time-of light data indicates no damage to the part.

A test was conducted with a soot load of 12 g/l with the fuel borne catalyst the results are shown in Fig. 18. This regeneration was conducted from room temperature rather than 240 °C for the other tests, in order to increase the severity. The 0.5 mm Thermocouples were damaged during the regeneration (the thermal limit for these is around 1300 °C). The brick crack signal shows a single peak at around 350 s during the severe exotherm. Following the test the parts is clearly damaged indicated by the ring crack shown in Fig. 18. This is supported by the axial ultrasound time of flight measurements shown in Table 1 which indicate no damage up to the 15 g/l load, but damage after the 12 g/l load with fuel borne catalyst (Fig. 17).

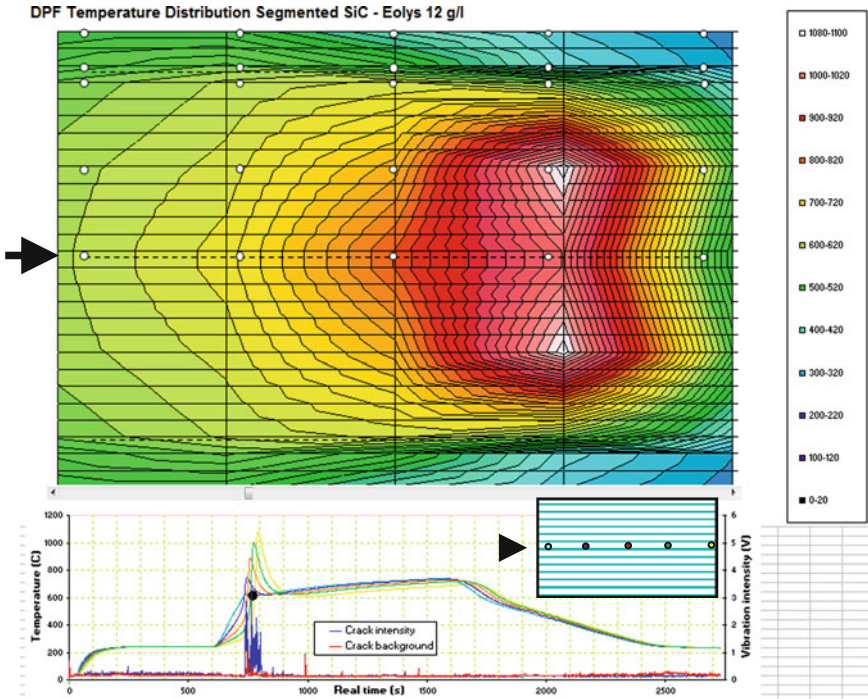


Fig. 19 SiC Internal temperature field during severe exotherm

7 Conclusions

Several techniques are described for evaluating the status of DPFs following worst case loaded regenerations.

A small borescope and a reverse aspiration with soot technique are demonstrated for post test evaluation of DPFs.

An ‘in situ’ crack detection technique indicates that a SiC part cracks significantly during the exothermic phase of the regeneration. For the SiC part, Ultrasound time-of flight measurements indicate that significant damage to the part only occurs after the 12 g/l, fuel born catalyst worst case regeneration. Cement cracks occur significantly at 8 g/l load. Concerning the AT DPF, the same technique indicated only a small response ahead of significant thermal damage to the part.

An ultrasound time of flight technique is demonstrated to be useful for assessing damage for both AT and SiC parts.

References

1. Kai R et al (2009) Thermal-mechanical durability of DOC and DPF after-treatment system for light heavy pickup truck application. SAE Paper 2009-01-2707
2. Evans AG et al (1974) Acoustic emission and crack propagation in polycrystalline alumina
3. Nesvijski E (2006) et al Spectral analysis of acoustic emission of cold cracking asphalt. NDT.net 11(10):171–177
4. Dase RN et al (2002) Evaluation of thermal shock resistance of cordierite honeycombs. Bull Mater Sci 25(2):127–132
5. <http://www.olympus-ims.com/en/applications/cracking-ceramic-diesel-particulate-filters/>
6. <http://www.blutack.com/>
7. <http://www.zibracorp.com/>
8. <http://www.cambustion.com/products/dpg>
9. Payne S (2011) Experimental studies of diesel particulate filtration. Ph.D Thesis Cambridge University Engineering Department, Cambridge, pp 170–173, August 2011

Dilution Air Refine System Used in Formaldehyde Measurement

Peipei Dai and Yunshan Ge

Abstract The intention of this paper is to demonstrate the advantages of the dilution air refine (DAR) system used in emission test for low emission vehicles, especially for formaldehyde emission test. Based on the DAR system, emissions from a passenger car fueled with methanol/gasoline blends (M15) were investigated. The car was tested over the New European Driving Cycle (NEDC). The typical legislated emissions were tested by a Horiba MEXA-7400LE motor exhaust gas analyzer. Formaldehyde was trapped on 2, 4-dinitrophenylhydrazine (DNPH)—coated silica cartridge and analyzed by high performance liquid chromatography (HPLC). Methylbenzene was sampled by Tenax TA and analyzed by thermal desorption-gas chromatography/mass spectrometer (TD-GC/MS). Results indicate that, compared to traditional CVS system, DAR can improve the measurement accuracy by decreasing and even eliminating the background concentration of dilution air, what's more, it can improve the measurement accuracy of formaldehyde emission effectively which makes DAR to be the preferred test system in measurement of unregulated emissions from light duty vehicles. And on this basis, pollutant emissions from the car fueled with methanol/gasoline blends were investigated. Results show that the car fueled with methanol/gasoline blends (M20/M30/M50) decreased the THC and CO by 39.68–46.98 % and 63.16–65.75 % respectively while increased the NO_x by 128.91–191.94 %. For unregulated pollutants, methanol/gasoline blends produce formaldehyde 12.06–77.59 % more than the baseline gasoline but the methylbenzene is 34.65–68.73 % less than that. The limitation of this study is that the measurements should be based on more vehicles to get much more exact data. This

F2012-A04-007

P. Dai (✉) · Y. Ge
National Lab of Auto Performance and Emission Test, Beijing Institute of Technology,
Beijing, China
e-mail: daipp1987@163.com

paper introduces the advantages of the dilution air refine system for the first time which are not mentioned in other papers before. The conclusion of this paper is that the DAR system can improve the measurement accuracy effectively especially for formaldehyde test and the methanol/gasoline blends produce less regulated pollutants and more formaldehyde. This problem can be solved by using additives and new three-way catalytic converters.

Keywords Dilution air refine · Measurement accuracy · Formaldehyde emission · Low emission vehicle · Methanol/gasoline blends

1 Introduction

With the growing concern of environment protection and the emission problems brought by using of alternative fuels, emission regulations become more stringent in worldwide. Low emission vehicles (LEV) put forward demand on the emissions' measurement accuracy. Except the typical legislated emissions such as hydrocarbons (HC), oxides of nitrogen (NO_x) and carbon monoxide (CO), the unregulated pollutants whose concentrations after the TWC are generally lower than 1 ppm [1–5] or even lower than the limit of detection have the same demand. The concentrations of exhaust pollutants diluted by CVS system are very close to or even lower than the background concentrations of dilution air, thus the test result corrected according to the background air can sometimes be negative which results in worse measurement accuracy and poor repeatability [6]. To improve the measurement accuracy of unregulated pollutants and the LEV's emission, the dilution air have to be further refined.

On the other hand, the below formula 1 shows that the measurement accuracy of pollutants is affected by concentrations of sample air bag, background concentrations of dilution air and the Dilution Factor (DF). Because the dilution ratio of CVS system is different in different working conditions, the DF (formula 2) is just an estimation, is affected by the background concentrations of THC, CO and NO_x in dilution air. Therefore, decreasing the background concentrations of dilution air is an important way to improve the measurement accuracy.

$$Mass = \rho \times \left(C_{sam.bag} - C_{amb.bag} \times \left(1 - \frac{1}{DF} \right) \right) \times V_{mix} \quad (1)$$

$$DF = \frac{13.4}{[CO_2]_{sam.bag} + [CO]_{sam.bag} + [THC]_{sam.bag}} \quad (2)$$

The traditional CVS system needs to be modified to solve this problem [7]. This paper introduces the feature of the dilution air refine system (DAR) and demonstrates its advantages by experiments on light-duty vehicles.

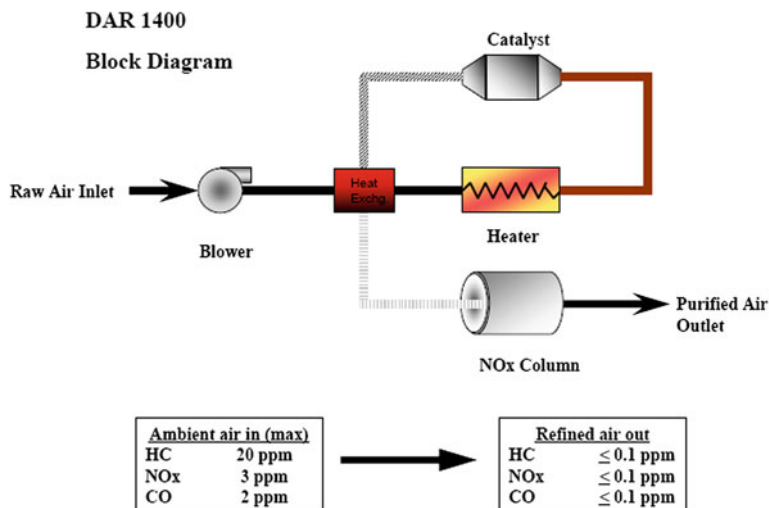


Fig. 1 Schematic diagram of the dilution air refine system

2 Introduction of the DAR System

This system is an air-purifying system designed to remove HC, CO and NO_x in the atmosphere. The schematic diagram of the dilution air refine system is illustrated in Fig. 1.

The air introduced into the purifying system by an inverter-controlled air blower is pre-heated with a gas-to-gas heat exchanger. Then it is heated to the set temperature with a sheath heater and introduced into a catalyst reactor. In the reactor, HC and CO are oxidized and decomposed with the catalyst. The purified air is cooled with an air-to-water heat exchanger, and then is purified passing through NO_x adsorption unit.

After the DAR system, the dilution air can be refined; the concentrations of the typical legislated emissions can be lower than 0.1 ppm.

3 Experimental Setup and Measurement

The experiments were performed using a passenger car that has displacement of 1.6 L and odometer of 17,591 km. Commercial 93 gasoline was used as the base fuel. Industrial grade methanol was mixed in fractions of 15 % by volume, and the fuel blends was thus named M15.

The car was tested on the chassis dynamometer. The cycle employed was the New European Driving Cycle (NEDC). In this test procedure, the car was conditioned at a temperature of 25 ± 2 °C over a time period of 16 h. The driving cycle simulates four ECE and one EUDC. The whole test lasts 1,180 s. The

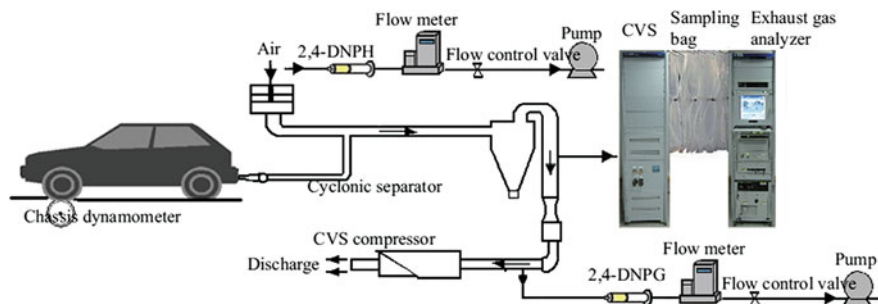


Fig. 2 Schematic diagram of the measurement for vehicle exhaust emissions

dilution system consists of traditional CVS system and the new CVS system equipped with DAR system which is named DAR-CVS system.

The schematic diagram of the measurement system for vehicle exhaust emissions is illustrated in Fig. 2. According to the test standard, the pollutants sampled in the airbags have to be analyzed by the Horiba MEXA-7400LE motor exhaust gas analyzer in 20 min after the test cycle.

In the test procedure, the exhaust emissions were diluted by CVS-7200S and CVS-7200S equipped with DAR-1400, respectively. Formaldehyde from the CVS-diluted (DAR-CVS-diluted) exhaust can be collected through a battery-operated air pump at a flow rate of 600 mL/min using a 2, 4-dinitrophenylhydrazine (DNPH)—coated silica cartridge [8]. Methylbenzene was sampled by Tenax TA and analyzed by thermal desorption-gas chromatography/mass spectrometer (TD-GC/MS) [9]. The following devices were used in the pretreatment to analyze the formaldehyde: a solid phase extractor, a 0.45 μm of Econofilter, high-performance liquid chromatography (HPLC), a 4.6×150 mm eclipse XDB C18 column, HPLC grade acetonitrile and the standard mixture contained by 14 components. The analysis conditions of HPLC are listed in Table 1.

Identification was made by matching retention time with those of commercial standard mixtures. The quantification was obtained by the five-point external standard method which is similar to methylbenzene.

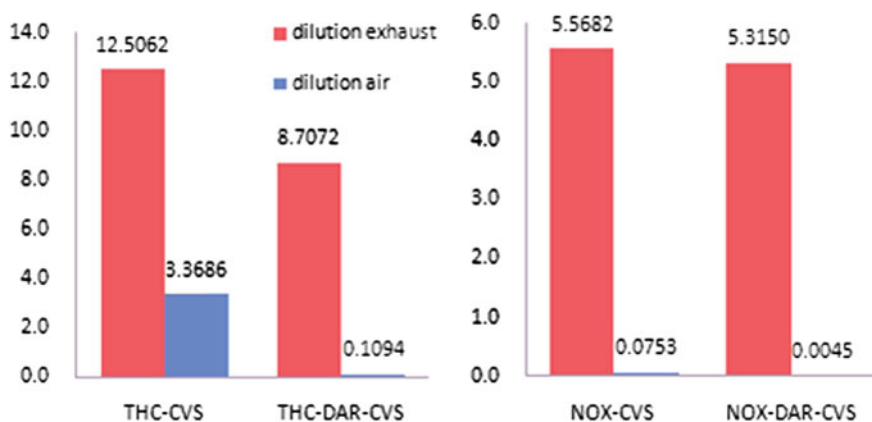
4 Results and Discussion

4.1 The Purification Efficiency of the DAR System

The concentrations of THC and NO_x in both dilution exhaust and dilution air are presented in Fig. 3. The background concentrations of THC and NO_x in dilution air were decreased by 96.71 and 93.96 % respectively. The proportions of dilution air in the dilution exhaust were reduced to 1.26 % and 0.08 % from 26.94 and

Table 1 Analysis conditions of HPLC

Items	Conditions	Items	Conditions
Flow rate	1.0 ml/min	Mobile phase	60 % acetonitrile/40 % water
Injection volume	25 μ l	Gradient	Constant gradient
Temperature	25 $^{\circ}$ C	Detection wavelength	360 nm

**Fig. 3** THC and NO_x emissions from CVS-diluted and DAR-CVS-diluted exhaust

1.35 % for THC and NO_x respectively. It is obvious that DAR system has a good purifying effect on THC and NO_x.

For that the formaldehyde emission is much less than the typical legislated pollutants, the influence of the formaldehyde's background concentration in dilution air on the measurement accuracy cannot be ignored. Fig. 4 presents the concentration of formaldehyde (FOR in Fig. 4) in both dilution exhaust and dilution air. The background concentration of formaldehyde was decreased by 61.97 %, and its proportion of dilution air in dilution exhaust was reduced to 3.6 % from the original 9.39 %, which demonstrates that the DAR system can refine the dilution air effectively. Figures 3 and 4 illustrate that DAR system can improve the measurement accuracy by decreasing or even eliminating the background concentration of the dilution air.

The emissions of the three typical legislated pollutants and formaldehyde are listed in Table 2. And also the Table 3 presents the measurement deviation.

The data indicates that compared with the traditional CVS system, the DAR system can make the test result of the three typical legislated pollutants more accurate with small fluctuation. At the same time, the measurement deviations of formaldehyde become smaller, the standard deviation and the RSD were decreased by 79.03 and 83.84 % respectively. So the DAR system can make the test results stable and lead to better experiment repeatability which is necessary in LEV's emission test especially in unregulated pollutants emission test like formaldehyde.

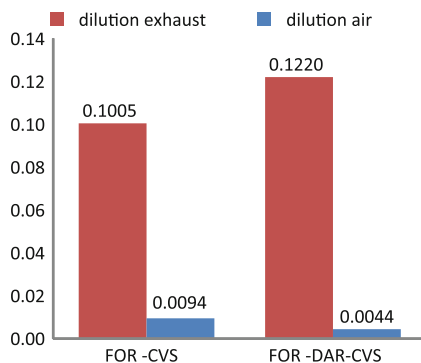


Fig. 4 Formaldehyde emissions from CVS-diluted and DAR-CVS-diluted exhaust

Table 2 Pollutant emissions from CVS-diluted and DAR-CVS-diluted exhaust

System	Test	THC (g/km)	CO (g/km)	NO _x (g/km)	Formaldehyde (mg/km)
Traditional CVS	1	0.075	0.503	0.158	1.4498
	2	0.086	0.620	0.133	1.3455
	3	0.073	0.527	0.124	1.4318
DAR-CVS	1	0.067	0.515	0.130	1.8217
	2	0.076	0.611	0.145	1.8320
	3	0.072	0.575	0.125	1.8087

4.2 Emissions from M20/M30/M50

In view of the DAR system can improve the measurement accuracy effectively, a series of experiments were set up on this basis to test the emissions of a passenger car fueled with methanol/gasoline blends. Industrial grade methanol was mixed in fractions of 20, 30, and 50 % by volume, thus the fuel blends were named M20, M30 and M50. Table 4 shows that the three typical legislated pollutants and two unregulated pollutants (formaldehyde and methylbenzene) emit from M20, M30 and M50 (these data are the relative emissions based on the pollutants from gasoline).

Compared with the baseline car fueled only with gasoline, THC and CO emissions from methanol/gasoline blends were decreased by 39.86–46.98 % and 63.16–65.75 %, respectively, while the NO_x emissions were increased by 128.91–191.94 %. This phenomenon is due to the fact that methanol contains only about 37.5 % carbon, while gasoline contains 85.8 % carbon. Moreover, methanol has a high oxygen content about 50 wt. %. So the methanol/gasoline blends contain more oxygen and less carbon than the base gasoline which enables the combustion reaction go to a more complete stage, thus reducing THC and CO emissions. The

Table 3 Measuring deviation from CVS system and DAR- CVS system

	THC	CO	NO _x	Formaldehyde
Standard deviation—traditional CVS (g/km)	0.0070	0.0618	0.0176	0.0558(mg/km)
RSD- CVS	8.97 %	11.24 %	12.73 %	3.96 %
Standard deviation-DAR- CVS(g/km)	0.0045	0.0485	0.0104	0.0117(mg/km)
RSD-DAR- CVS	6.29 %	8.55 %	7.81 %	0.64 %

Table 4 Emissions from DAR- CVS-diluted exhaust of vehicle fueled with gasoline/M20/M30/M50

Fuel	THC	CO	NO _x	Formaldehyde	Methylbenzene
Gasoline	1.0000	1.0000	1.0000	1.0000	1.0000
M20	0.6014	0.3425	2.3318	1.1206	0.5712
M30	0.5694	0.3684	2.2891	1.7289	0.6535
M50	0.5302	0.3488	2.9194	1.7759	0.3127

increase in NO_x is due to the more oxygen and the enhanced combustion temperature [10].

Formaldehyde emits from methanol/gasoline blends was increased by 12.06–77.59 % compared with that emits from gasoline, and with the increase of methanol content, the formaldehyde concentration also increased. This is because that methanol is free of hydrocarbons; however, the generation of formaldehyde from methanol is easier than from hydrocarbons. That is why the car fueled with methanol/gasoline blends emits less methylbenzene. Table 4 shows that the methylbenzene from methanol/gasoline blends was decreased by 34.65–68.73 %. Different from formaldehyde's situation, with the increase of methanol content, the methylbenzene concentration decreased instead.

5 Conclusions

Formaldehyde emission from the car fueled with methanol/gasoline blends is far less than the typical legislated pollutants, so the influence of the formaldehyde's background concentration in dilution air on the measurement accuracy cannot be ignored.

DAR system is able to improve the measurement accuracy effectively by decreasing the background concentrations of the dilution air which makes it necessary in LEV's emission test, especially in formaldehyde emission test.

Compared to the baseline car fueled only with gasoline, the THC and CO emissions from the car fueled with methanol/gasoline blends were decreased while the NO_x was increased. The formaldehyde emission from the methanol/gasoline blends was increased while the methylbenzene was decreased. With the increase of methanol content, the formaldehyde emission also increased while the methylbenzene emission decreased which is different from formaldehyde.

References

1. Kewei You, Heyue Zheng, Wulin Wang et al (2009) Study on Carbonyl Compounds Emissions from a Methanol Engine. *Chin Intern Combust Engine Eng* 30(6):5–9
2. Jianwei Tan, Yunshan Ge, Junfang Wang et al (2009) Investigation on emission characteristics of methanol vehicle's aldehyde and ketone pollutants. *Environ Sci* 30(8):2199–2203
3. Zhao Hong, Ge Yunshan, Hao Chunxiao et al (2010) Carbonyl compound emissions from passenger cars fueled with methanol/gasoline blends. *Sci Total Environ* 408:3607–3613
4. Zhao Hong, Ge Yunshan, Tan Jianwei et al (2011) Effects of different mixing ratios on emissions from passenger cars fueled with methanol/gasoline blends. *J Environ Sci* 11(23):1831–1838
5. Qiuwen You, Yunshan Ge, Kewei You et al (2009) Unregulated emissions from the gasoline vehicle. *Environ Sci* 30(2):335–341
6. Thiel, W Woegerbauer R and David Eason BMW Group. Measuring Near Zero Automotive Exhaust Emissions – Zero Is a Very Small Precise Number, SAE Technical Paper 2010-01-1301
7. Xu Libing Yu, Xiaoli Ge Yunshan (2004) Bag mini-diluter sampling system used in light-duty ULEV emission measurement. *Automot Eng* 26(6):652–654
8. USEPA (U. S. Environmental Protection Agency). Determination of formaldehyde in ambient air using adsorbent cartridge followed by high performance liquid Chromatography (HPLC). U. S. EPA Technical Assistance Document. EPA/625/R-96/010b (TO-11A)
9. USEPA (U.S. Environmental Protection Agency). Determination of volatile organic compounds in ambient air using active sampling onto sorbent tubes. U. S. EPA Technical Assistance Document. EPA/625/R-96/010b (TO-17)
10. Shenghua L, Cuty CER, Jiegang H (2007) Study of spark ignition engine fueled with methanol/gasoline fuel blends. *Appl Therm Eng* 27(11–12):1904–1910

A Study of SiC-Nanoparticles Porous Layer Formed on SiC-DPF Wall for Soot Oxidation

Keita Ishizaki, Shinichi Tanaka, Atsushi Kishimoto,
Masamichi Tanaka, Naoki Ohya and Nobuhiro Hidaka

Abstract The pore structure of DPF is known to have a significant effect on filtration efficiency, pressure drop, and soot oxidation. It is reported that the formation of a nanoparticle porous layer on the surface of the DPF inlet wall promotes soot oxidation [1–3]. However, the correlation between pore size in the nanoparticle layer and soot oxidation performance, the effect of the layer in actual use environments, and the oxidation mechanism involved have not yet been clarified. The research discussed in this paper therefore formed SiC nanoparticle porous layers of various pore sizes on the inlet wall surfaces of SiC-DPF (creating what will be termed “NPL-DPF” here) using the dip-coating method [4]. The NPL thickness was set at 20 μm to help enable uniform coating samples to be obtained. With regard to filter pressure drop without soot loading, results for a bare DPF and a Pt/ γ - Al_2O_3 -coated DPF (catalyzed DPF; Pt = 1 g/L) were virtually identical. For the NPL-DPF, pressure drop increased as pore size was reduced. By contrast, in the case of pressure drop following soot loading (3 g/L), despite the fact that results for pressure drop for the NPL-DPF were higher than those for the bare DPF, they were lower than those for the catalyzed DPF. It is possible to stop deep-bed filtration by forming a nanoparticle porous layer on the surface of the DPF inlet wall [1, 5]. With regard to soot oxidation performance, the T80 of an NPL-DPF (NPL pore size = 350 nm) was found to be 40 % lower than that of a bare DPF and identical to that of a catalyzed DPF. In addition, reducing the NPL pore size enhanced soot oxidation performance. X-ray photoelectron spectra (XPS), transmission electron microscopy (TEM), and

F2012-A04-008

K. Ishizaki · N. Ohya (✉)
Automobile R&D Center, Honda R&D Co., Ltd, Tochigi, Japan
e-mail: Keita_Ishizaki@n.t.rd.honda.co.jp

S. Tanaka · A. Kishimoto · M. Tanaka · N. Hidaka
New Technology Research Laboratory, Sumitomo Osaka Cement Co., Ltd, Chiba, Japan

hydrogen temperature-programmed desorption (H_2 -TPD) results indicated that the SiC nanoparticle surface was covered by a 5 nm SiO_2 oxide film. It was found that these oxidized SiC nanoparticles desorbed oxygen at around 450 °C. This desorbed oxygen promoted the oxidation of diesel soot. In addition, the filtration efficiency of the NPL-DPF without soot loading was 92 % against 78 % for the bare DPF.

Keywords Diesel vehicle · Particulate-emissions · Particulate filters · Soot-oxidation · Desorbed oxygen

1 Introduction

Diesel engines display a high level of thermal efficiency. Because of this, the engines have attracted attention as a means of reducing CO_2 emissions. However, diesel engines also present the issue of high levels of soot emissions. To respond to this issue, it is possible to efficiently remove soot using wall-flow DPF [6, 7]. If an excessive amount of soot is loaded in the DPF, however, the power and fuel efficiency of the engine may decline due to an increase in pressure loss. In an attempt to prevent this phenomenon, soot is removed through forced regeneration of the DPF by raising the exhaust gas temperature to around 600 °C. This procedure entails a fuel efficiency penalty, results in oil dilution [8], and increases thermal load, making it necessary to reduce the time taken for forced regeneration [6, 9–11]. Research is being conducted on various control methods and catalyst materials in order to reduce the frequency of forced regeneration. At present, platinum group metal (PGM) catalysts are the most widely used catalysts. PGM catalysts efficiently convert NO in exhaust gas into NO_2 , which promotes oxidation of diesel soot [7, 12, 13]. However, coating a DPF with a PGM catalyst reduces its soot mass limit (SML) [14], increasing the frequency of forced regeneration. The development of a DPF system that does not rely on PGM catalysts is also desirable from the perspectives of conserving resources and reducing costs. In a wall-flow DPF, gas diffusion in the soot cake layer promotes soot oxidation. Two samples of SiC DPF with soot loadings of 3 g/L were prepared, and plugs were cut from one of the samples on the DPF outlet side. Figure 1 shows the experimental apparatus and the results of an evaluation of soot oxidation for these two samples. The test conditions were identical to those shown in Fig. 5 below. The soot oxidation performance of the sample from which plugs had been cut on the outlet side, creating a flow-through honeycomb, declined due to the reduction of gas diffusion in the soot cake layer. This gas diffusion in the soot cake layer is strongly influenced by the pore structure of DPF.

The authors therefore conducted research with a focus on the pore structure of DPF, a vigorous area of research at present. It is possible to stop deep-bed filtration by covering the surface of the wall of the DPF inlet with an ultra-fine porous layer. The use of surface filtration in isolation increases the correlation of pressure drop with soot loading in comparison to a DPF with no porous layer [1, 5]. This would increase the accuracy of prediction of soot loading, and could be expected

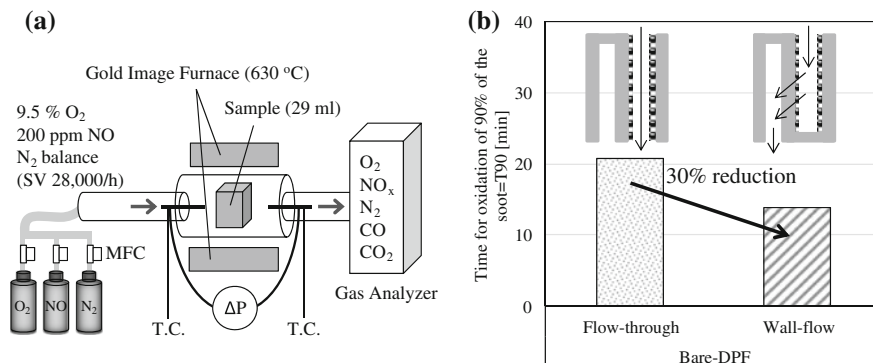


Fig. 1 **a** Experimental apparatus; **b** the results of an evaluation of soot oxidation for normal bare DPF (wall-flow) and the bare DPF from which plugs had been cut on the outlet side (flow-through) with soot loadings of 3 g/L

to reduce the frequency of regeneration. At the same time, filtration efficiency would be increased due to the lower permeability resulting from reduced DPF pore size [6, 15, 16]. In addition, it is reported that the formation of a SiC nanoparticle porous layer on the wall of the DPF inlet enhances soot oxidation performance [1–3]. It is indicated that this is a result of the desorption of adsorbed oxygen from the SiC nanoparticle surface, which has a high specific surface area [3, 17]. Given this, a DPF coated with a SiC nanoparticle layer could be considered the ideal filter structure. However, the effect of the diameter of the SiC particles on performance has not been studied sufficiently. The same is true of performance in actual use environments. In addition, it is also essential to further study the oxidation mechanism involved. This paper will first report on the effect of particle diameter in the SiC nanoparticle layer on filter pressure drop and soot oxidation activity. It will go on to discuss the results of analyses using XPS, TEM, H₂-TPD, and model gas tests. Conclusions will be presented at the end of the paper.

2 Effect of NPL Pore Size on Filter Pressure Drop

This section will discuss the effect of the pore size of a SiC nanoparticle layer on filter pressure drop. A SiC support (pore size/porosity/cpsi/size = 11 μm/42%/300 cpsi/34 mm × 34 mm × 25 mm = 29 ml) manufactured by IBIDEN Co., Ltd. was employed as the DPF support. The dip coating method was used to form the porous SiC layer [4]. The NPL pore size was adjusted to a range of 100 nm–4 μm by means of the diameter of the SiC nanoparticles forming the starting material. The manufactured NPL was pressureless-sintered at 1000 °C for 6 h in an Ar flow. The diameter of the pores of the sintered NPL was measured using the mercury infiltration method. The thickness of the NPL was fixed at 20 μm in order to achieve uniform NPL formation. A catalyzed DPF coated with Pt/γ-Al₂O₃ (Pt = 1 g/L; γ-

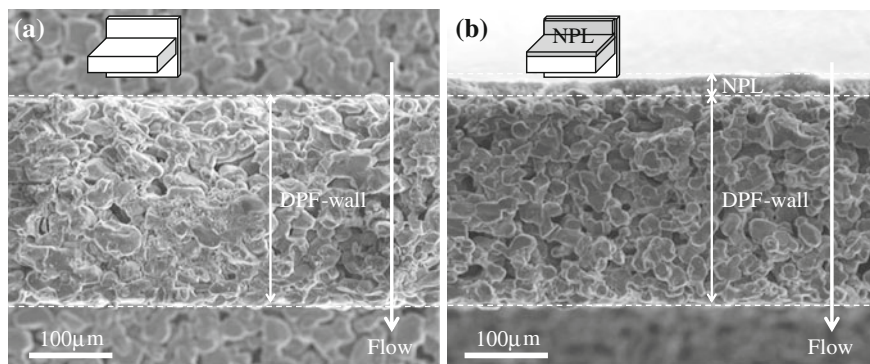


Fig. 2 The cross-sectional SEM images of **a** catalyzed DPF wall; and **b** NPL-DPF wall

$\text{Al}_2\text{O}_3 = 24 \text{ g/L}$) formed using the impregnation method [18] was prepared in order to provide samples for comparison. The coating is shown in Fig. 2.

Considering the thermal load in an exhaust system in which both a diesel oxidation catalyst (DOC) and a DPF were in a close-coupled position, all the evaluation samples were subjected to heat treatment at $700 \text{ }^\circ\text{C}$ for 30 h. The method used for soot loading was selected in order to achieve results similar to actual use conditions: Exhaust gas was diverted from downstream of the DOC (1.0 L) and directly introduced to the samples in a 2.2 L 4-cylinder turbocharged common-rail diesel engine in steady-state operation (1500 rpm; 70 N m) to load the filters with soot. Soot loading was set at 3 g/L. Under these conditions, the DOC was sufficiently activated, at a temperature of $350 \text{ }^\circ\text{C}$, and the state of the soot was close to that of dry soot. The filter pressure drop was measured with room-temperature air flowing at 100 L/min. A Horiba MEXA-7500D was employed for the measurements. Figure 3 shows the correlation between the NPL pore size and pressure drop before and after soot loading. As Fig. 3a shows, before soot loading, the bare DPF and the catalyzed DPF displayed an identical pressure drop. By contrast, for the NPL-DPF, pressure drop increased as the NPL pore size decreased. This is because permeability declines with reduced pore size [6, 15, 16]. As Fig. 3b shows, at a soot loading of 3 g/L, the pressure drop for the NPL-DPF was higher than the pressure drop for the bare DPF, but lower than that for the catalyzed DPF. This is because the NPL helps to prevent infiltration of soot into the walls of the DPF [1, 5]. When results for the bare DPF and the catalyzed DPF are compared, it can be conjectured that deep-bed filtration is occurring in both cases. However, despite the fact that the pressure drop for the two filters was identical before soot loading, results differed significantly following soot loading. In the case of the catalyzed DPF, the catalyst is unevenly supported inside the walls of the DPF (Fig. 2a). It can be considered that as a result of this, the gas flow in the walls of the DPF was non-uniform, and the amount of soot captured by deep-bed filtration increased. It is conjectured that pressure drop could be reduced if a method of achieving even catalyst support was available.

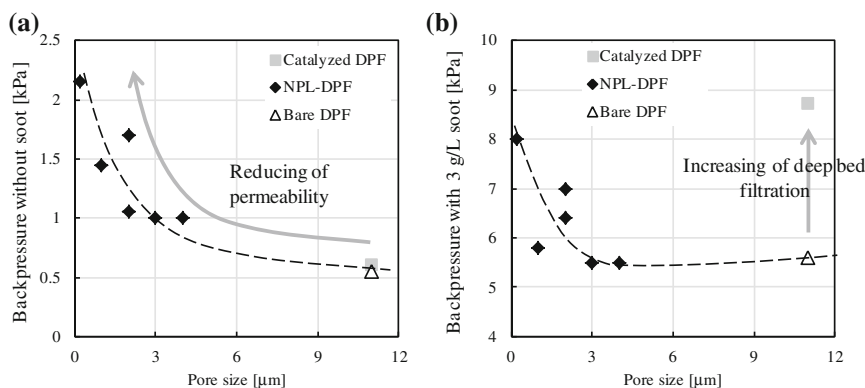


Fig. 3 The correlation between the NPL pore size and pressure drop with room-temperature air flowing at 100 L/min: **a** before soot loading; and **b** after 3 g/L soot loading

3 Effect of NPL Pore Size on Soot Oxidation Performance

This section will discuss the effect of the NPL pores on soot oxidation performance. Soot oxidation performance was evaluated using model gas tests. The temperature for the tests was set at 630 °C, with consideration of the actual operating environment (a nitrogen atmosphere was used until 630 °C, and temperature was increased at a rate of 40 °C/min). 9.5 % O₂, 200 ppm NO, N₂ balance, SV = 28000/h was selected as the model gas composition. A Horiba MEXA-7500D was employed for the measurements. The soot loading conditions were identical to those shown in Fig. 3b. Soot oxidation profiles were calculated from CO and CO₂ emissions.

Figure 4a shows the correlation between NPL pore size and soot oxidation performance (time for oxidation of 90 % of the soot = T90). There is a primary correlation between soot oxidation performance and pore size, with T90 becoming shorter as pore sizes are reduced. Figure 4b shows the correlation between T90 and CO selectivity. These results indicate that the amount of incomplete combustion was reduced by increasing soot oxidation performance. Figure 5a shows soot oxidation time, the elapsed time following addition of oxygen to the model gas, and the soot residual ratio. This result indicates that the time for oxidation of the soot (T90) for the NPL-DPF is 40 % lower than the time for the bare DPF, and almost identical with that for the catalyzed DPF. In addition, the soot oxidation profile for the NPL-DPF is almost identical to that for the catalyzed DPF. Figure 5b shows the soot residual ratio and normalized soot oxidation rate. The normalized soot oxidation rate is defined as the soot oxidation rate divided by the amount of residual soot, and is expressed in units of sec⁻¹. These graphs are based on the same measurement data. This result indicates that peaks occurred for the bare DPF and the catalyzed DPF following the addition of oxygen. The difference in pore structure is considered to be the reason that no peak was observed for the

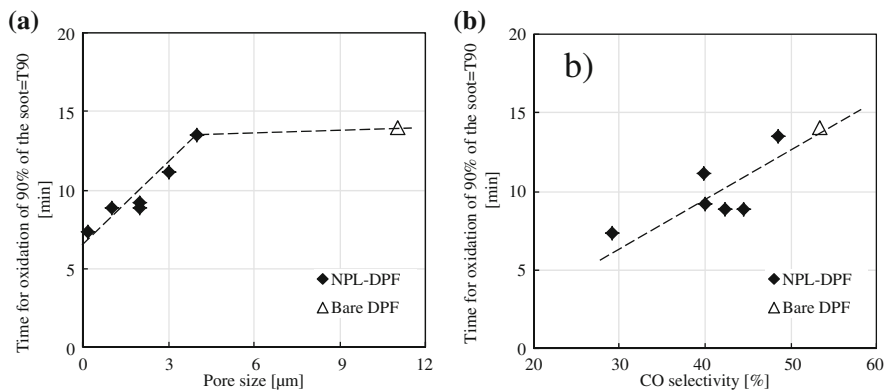


Fig. 4 a The correlation between NPL pore size and soot oxidation performance (T90); and b the correlation between T90 and CO selectivity. Soot loading was set at 3 g/L

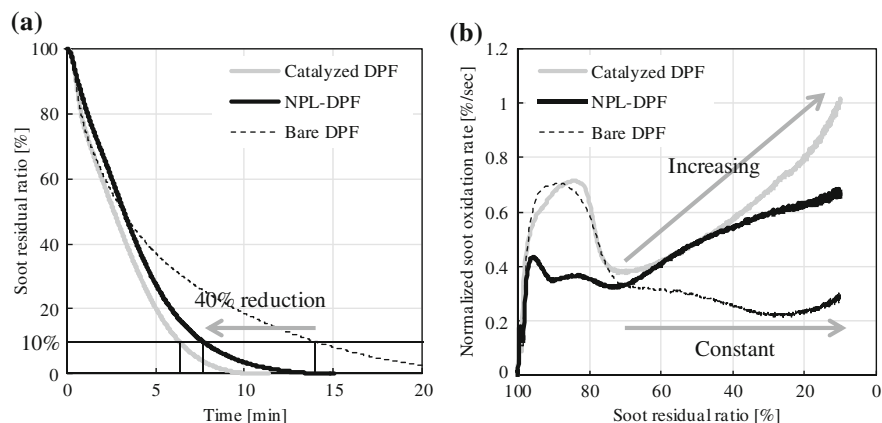


Fig. 5 Soot oxidation performance of NPL-DPF, bare-DPF and catalyzed DPF with soot loadings 3 g/L

NPL-DPF. Excepting the peak mentioned above, the normalized soot oxidation rate for the bare DPF was almost entirely constant. This result indicates that there is no difference in the oxidation characteristics of soot close to the surfaces of the DPF walls and soot that is not. This shows that the main mechanism is reaction with oxygen in the gas phase. It is also conjectured that gas diffusion in the soot cake layer is constant, irrespective of the amount of residual soot. By contrast, in the NPL-DPF and catalyzed DPF, the reduced amount of residual soot in the DPF resulted in an increased normalized soot oxidation rate. Given this, it is assumed that factors other than oxygen in the gas phase promote soot oxidation. It is also considered that the reaction proceeds from the vicinity of the boundary between the DPF and the soot.

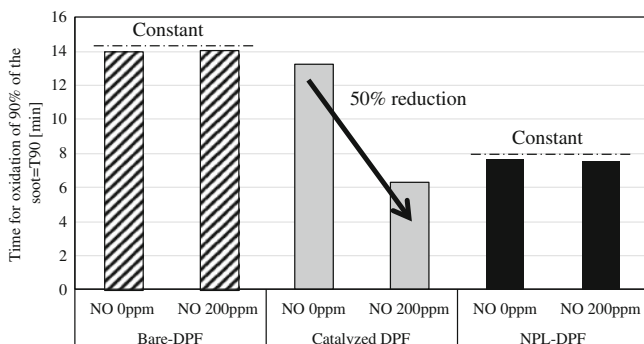


Fig. 6 T90 for the bare DPF, catalyzed DPF and NPL-DPF (NPL pore size = 350 nm) when the NO concentration in the model gas was varied (0 and 200 ppm). Soot loading was set at 3 g/L

Figure 6 shows T90 for the bare DPF, catalyzed DPF and NPL-DPF (NPL pore size = 350 nm) when the NO concentration in the model gas was varied (0 and 200 ppm). When there is no NO in the model gas, the soot oxidation performance of the catalyzed DPF declines, matching that of the bare DPF. This shows that in the catalyzed DPF, NO₂ promotes soot oxidation [7, 12, 13, 19]. By contrast, in the NPL-DPF, soot oxidation performance remains good whether or not NO is present, indicating the existence of factors other than NO₂ in this case.

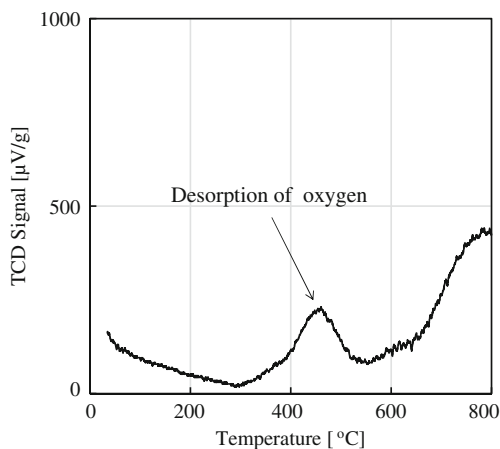
4 Analysis of Mechanism of Soot Oxidation in NPL

This section will discuss the mechanism of soot oxidation in NPL. The properties of the SiC nanoparticle surface in NPL were evaluated. SiC nanoparticles produced by Sumitomo Osaka Cement Co., Ltd., Tokyo were employed in the analysis. The chemical composition (mass ratio) was 98.90 % SiC, 0.90 % SiO₂, and 3.50 % C. The average particle size was 35 nm, and the specific surface area was 50.9 m²/g. The SiC nanoparticles were sintered and subjected to heat treatment under the same conditions as had been used for the NPL. TEM and XPS results showed that the nanoparticle surface was covered with a 5 nm-thick amorphous oxide layer composed of SiO₂ and SiO_xC_y.

H₂-TPD measurements of the SiC nanoparticles were conducted. The oxide layer covering the SiC nanoparticle surface was pretreated for 1 h at 800 °C in 5 % O₂/He in order to promote the adsorption of oxygen. Following this, the temperature of the layer was lowered to room temperature, and it was then heated to 800 °C at a rate of 10 °C/min in 5 % H₂/Ar. Hydrogen consumption was verified by TCD. Hydrogen consumption against temperature was taken as a measure of the amount of oxygen desorbed from the SiC nanoparticle surface.

Figure 7 shows the TPD curve for the nanoparticles. Two peaks occur at 450 and 800 °C on this curve. The peak at 450 °C represents the desorption of oxygen

Fig. 7 H₂-TPD curve for the SiC nanoparticles



from the surfaces of the nanoparticles. The fact that the oxygen adsorbed into the surfaces of the SiC nanoparticles was oxygen atoms produced by disaggregation of oxygen molecules was verified by subjecting the nanoparticles to a carbon oxide activity test using $^{18}\text{O}_2$. The results of these tests will be discussed in a separate report. By contrast, the peak at 800 $^{\circ}\text{C}$ was probably caused by the volatilization of SiO from the SiO_2 and SiO_xC_y oxide layer.

These results suggest that for the NPL-DPF, adsorbed oxygen in the SiC nanoparticle surface reacts with soot in addition to oxygen in the gas phase. It is thought that the increase in reaction paths resulting from this surface oxygen is the factor that promotes soot oxidation in the NPL-DPF. The amount of oxygen adsorbed into the nanoparticle surface increases exponentially with reduction in pore size. This result shows that the reduction of pore size promotes the oxidation of soot (Fig. 4a).

5 Results of Evaluation in Actual Engine

This section will discuss the results of evaluations conducted using an actual engine. Optimization of the dip-coating method made it possible to apply an NPL coating to a full-scale DPF, and performance evaluations were therefore able to be conducted on an engine test bench. A SiC support (pore size/porosity/cpsi/size = 11 $\mu\text{m}/42\%/300$ cpsi/ $\varnothing 5.66$ in \times 6 in = 2.47 L) manufactured by IBIDEN Co., Ltd. was employed as the DPF support. The NPL pore size was set at 350 nm in an attempt to balance low pressure drop and soot oxidation efficiency. The thickness of the NPL was fixed at 20 μm to make it possible to obtain uniform coating samples. A bare DPF and a catalyzed DPF (Pt = 1 g/L) with identical specifications to the previous evaluation were used to provide samples for comparison. All of the samples were subjected to heat treatment at 700 $^{\circ}\text{C}$ for 30 h. A 4-cylinder turbocharged common-rail diesel

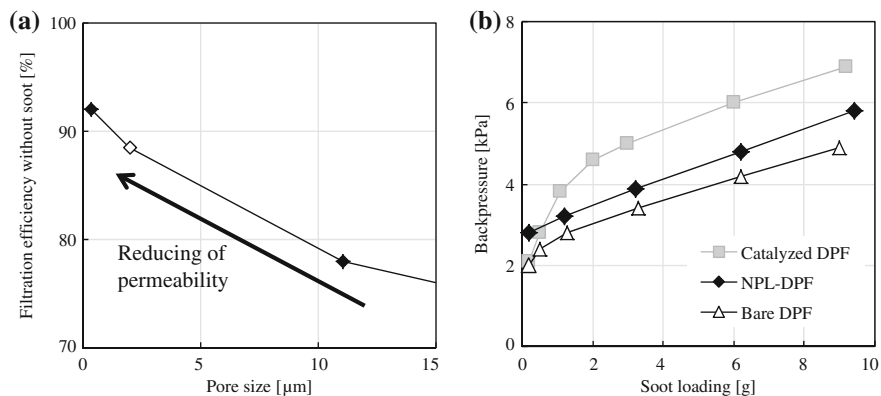
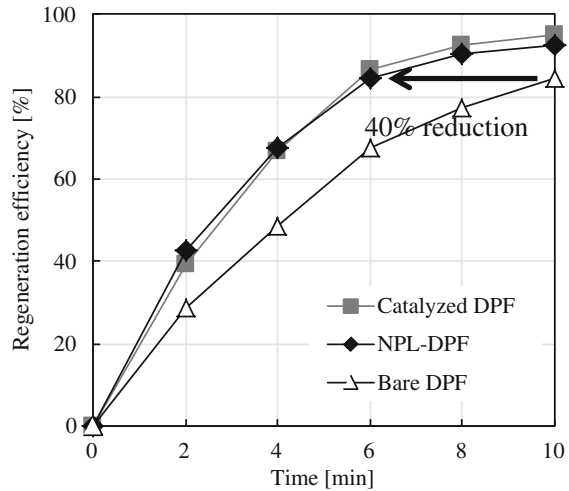


Fig. 8 a The correlation between pore size and filtration efficiency without soot loading; and b the correlation between soot loading and pressure drop

engine was employed in the evaluations, and the DOC (1.0 L) and DPF were used sequentially in close-coupled position. Measurements of filtration efficiency were conducted during steady-state operation at 1500 rpm and 30 N m. An AVL smoke meter was used for the measurements. The method used for measurement of pressure drop and soot oxidation performance is described below. With regard to soot loading, taking the actual use environment into consideration, a soot loading of 10 g (4 g/L) was used based on a repeated New European Driving Cycle (NEDC). For pressure drop, pressure drop values during cruise operation at 100 km/h in the Extra Urban Drive Cycle (EUDC) were plotted. For soot oxidation performance, the target temperature for forced regeneration during 2500 rpm 60 N m steady-state operation was 630 °C. After the temperature of the bottom edge of the DPF exceeded 550 °C, forced regeneration was suspended every 2 min, and soot oxidation efficiency was measured from weight measurements. Figure 8a shows the correlation between pore size and filtration efficiency. Reducing pore size increased filtration efficiency. The NPL-DPF (pore size: 350 nm) displayed a filtration efficiency of 92 %. Data for a pore size of 2 μm is reported in the literature [20]. Figure 8b shows the correlation between soot loading and pressure drop. Figures for soot loading are predicted figures based on actual measurements. For the NPL-DPF, the highest figure for pressure drop occurred without soot loading, and when soot loading exceeded approximately 1 g, figures for pressure drop became lower than figures for the catalyzed DPF. The NPL-DPF also displayed greater linearity in its pressure drop profile in relation to soot loading than the catalyzed DPF and the bare DPF. These are results of stopping deep-bed filtration, as discussed above.

Figure 9 shows the correlation between regeneration time and soot oxidation efficiency. The results show that T80 for a PGM-free full-sized NPL-DPF with a pore size of 350 nm was 40 % lower than that for a bare DPF and identical to that for a catalyzed DPF. The results discussed above demonstrate that an NPL-DPF displays good soot filtration efficiency, pressure drop characteristics, and soot

Fig. 9 The correlation between regeneration time and soot oxidation efficiency: soot loading was set at 10 g (4 g/L); and the target temperature for forced regeneration during 2500 rpm 60 N m steady-state operation was 630 °C



oxidation performance without using precious metals. A good correlation was also obtained between model gas test results and actual engine test results.

6 Conclusion

An NPL-DPF with a pore size of 350 nm realized a high level of soot oxidation performance and filtration efficiency, and a low pressure drop. The soot oxidation activity of this precious metal-free NPL-DPF is not only the product of increased uniform gas distribution, as in a soot cake layer, but also of the desorption of oxygen from oxidized SiC nanoparticles. The level of soot oxidation activity displayed by the filter is the same as that of a catalyzed DPF (Pt = 1 g/L).

Acknowledgments The authors would like to thank Professor Dr. Katsunori Hanamura of Tokyo Institute of Technology for his advice.

References

1. Mizutani T et al (2010) Performance verification of next generation diesel particulate filter. SAE Technical Paper, 2010-01-0531
2. Karin P et al (2010) Particulate matter trapping and oxidation on catalyst-membrane. SAE Int. J. Fuels Lubr 3(1):368–379
3. Nakamura K et al (2012) Soot oxidation characteristics of SiC nanoparticle membrane filters. SAE Technical Paper, 2012-01-0848
4. Kikuchi R et al (2001) Thick-film coating of hexaaluminate catalyst on ceramic substrates and its catalytic activity for high-temperature methane combustion. Appl Catal A Gen 218(1–2):101–111

5. Iwasaki S et al (2011) New design concept for diesel particulate filter. SAE Technical Paper, 2011-01-0603
6. van Setten BAAL (2001) Science and technology of catalytic diesel particulate filters. *Catal Rev* 43(4):489–564
7. Walker AP (2004) Controlling particulate emissions from diesel vehicles. *Top Catal* 28(1–4):165–170
8. Budde M et al (2011) Simulation and optical analysis of oil dilution in diesel regeneration operation. SAE Technical Paper, 2011-01-1844
9. Boger T et al (2008) Regeneration strategies for an enhanced thermal management of oxide diesel particulate filters. SAE Technical Paper, 2008-01-0328
10. John PA et al (1996) Catalysts for the oxidation of soot from diesel exhaust gases. I. An exploratory study. *Appl Catal B Environ* 8:57–78
11. Rocher L et al (2011) New generation fuel borne catalyst for reliable DPF operation in globally diverse fuels. SAE Technical Paper, 2011-01-0297
12. Hawker P et al (1997) Experience with a new particulate trap technology in Europe. SAE Technical Paper, 970182
13. Cooper BJ et al (1989) Role of NO in diesel particulate emission control. SAE Technical Paper, 890404
14. Kodama K et al (2008) Aftertreatment system for commercial diesel engine (2nd report). JSAE Technical Paper, 20085701, (in Japanese)
15. Karadimitra K et al (2004) Catalytic particle synthesis via aerosol spray pyrolysis and in situ deposition on porous filter materials. In: International conference for particle technology, 2004
16. Ido T et al (2005) Study on the filter structure of SiC-DPF with gas permeability for emission control. SAE Technical Paper, 2005-01-0578
17. Oki H et al (2010) Visualization of oxidation of soot nanoparticles trapped on a diesel particulate membrane filter. SAE Technical Paper, 2011-01-0602
18. Lee YW et al (2004) Improved performance of NO_x reduction by H₂ and CO over a Pd/Al₂O₃ catalyst at low temperatures under lean-burn conditions. *Catal Commun* 5:499–503
19. Setiabudi A et al (2002) The influence of NO_x on soot oxidation rate: molten salt versus platinum. *Appl Catal B Environ* 35:159–166
20. Furuta Y et al (2009) Study on next generation diesel particulate filter. SAE Technical Paper, 2009-01-0292

Enhancement of Regeneration Performance by a New Catalyzed DPF

Takeshi Matsumoto, Takeshi Mori, Satoshi Hirose
and Hiroto Takeuchi

Abstract The diesel particulate filters (DPF) used to remove particulate matter (PM) in exhaust gas from diesel engines need to have periodical active regeneration for burning PM accumulated in DPF. Since active regeneration is carried out at high exhaust temperatures of 600 °C or more, it involves issues of fuel economy and emissions. This report describes the effort to resolve these issues by taking steps to promote the oxidation of PM and reduce DPF regeneration time by catalyst coated DPF. Attention was focused on Silver (Ag) catalyst, which possesses a PM oxidation function, as a new catalyst. An analysis of the mechanism on the PM oxidation activity, an evaluation of its properties by various model gas testing, and results from evaluation of performance conducted using an engine bench are reported on. As the result of a search for catalyst material that promotes a PM oxidation reaction, it was found that Ag₂O was a highly active catalyst material. Furthermore, as the result of efforts to achieve greater stability in performance, Ag/Ce material was found to be a catalyst possessing both high performance and stability. The mechanism of Ag/Ce catalyst was analyzed by X-ray diffraction (XRD) and X-ray photoelectron spectroscopy (XPS). As a result, it was found that the supply of oxygen from complex oxides of Ce contributed to the formation of active species Ag₂O, which played a role in stabilizing performance. In order to presume the performance of Ag/Ce catalyst in practical use, regeneration tests under various different conditions by using a model gas test equipment was conducted. As a result of that, the Ag/Ce catalyst exhibited high PM oxidation performance compared to the conventional Pt catalyst under all the conditions that were conducted. It was also found in regeneration testing by using engine bench

F2012-A4-011

T. Matsumoto (✉) · T. Mori · S. Hirose · H. Takeuchi
Automobile R&D Center, Honda R&D Co., Ltd, Ichikai-machi, Haga-gun, Japan
e-mail: takeshi_matsumoto@n.t.rd.honda.co.jp

that Ag/Ce catalyst showed greater PM oxidation performance, as in model gas testing, by comparison with conventional technology. As the result of DPF regeneration simulation under NEDC mode conditions, a 43 % shortening effect on regeneration time relative to regeneration conditions when using conventional technology was confirmed. Furthermore, the oil-ash, heat and sulfur durability test were conducted by accelerated aging test. It was found that although Ag/Ce catalyst exhibited some reduction of performance due to ash accumulation, no reduction due to heat or sulfur was observed, showing that this catalyst possesses high durability.

Keywords Diesel emissions · Diesel aftertreatment · Catalyzed DPF · Silver (Ag) catalyst · PM oxidation

1 Introduction

Growth of the world economy has been accompanied by the consumption of large amounts of fossil fuels, and CO₂ emissions are growing rapidly. Since CO₂ is a causal factor in global warming, the reduction of CO₂ has become an urgent task. The automobile industry has focused on diesel engines with high thermal efficiency as one method for reducing CO₂ emissions. However, the fact that diesel engines exhaust large amounts of particulate matter (PM) has become an issue. At present, the diesel particulate filters (DPF) is a main method for trapping the PM in exhaust emissions and removing it [1–3]. The trapped PM leads to increase pressure loss, so that active regeneration needs to be conducted periodically to remove PM. In order to remove PM, the exhaust gas temperature needs to be raised to around 600 °C or higher, presenting serious issues of fuel consumption, emissions, and so on, during DPF regeneration. This report examines the catalyst coated DPF to promote PM oxidation and achieve the effect of reduced DPF regeneration time in order to resolve above mentioned issues. The focus was placed on Ag catalyst as a new material possessing a PM oxidation function. An analysis of the mechanism on the PM oxidation activity, an evaluation of its properties by various model gas testing and results from evaluation of performance conducted using an engine bench are reported in this paper.

2 Selection of PM Oxidation Catalyst

First, typical PM oxidation reaction types are shown in Table 1. PM oxidation is considered to consist mainly of three reactions. The first reaction is the spontaneous oxidation, where a direct reaction between PM and the oxygen in the exhaust gas results in oxidation under high temperature conditions around 600 °C or higher. The second is oxidation by gaseous NO₂, which is an oxidation type also used with

Table 1 PM oxidation reaction types

Reaction type	Reaction ($\text{CO}_x = \text{CO}_2 + \text{CO}$)	Comment
Spontaneous oxidation	$\text{PM} + \text{O}_2 \rightarrow \text{CO}_x + \text{H}_2\text{O}$	High temp > 600 °C
Oxidation by gaseous NO_2	$\text{PM} + \text{NO}_2 \rightarrow \text{CO}_x + \text{H}_2\text{O} + \text{NO}$	Lower temp due to high oxidation activity of NO_2
Catalytic oxidation	$\text{PM} + \text{O}^* \rightarrow \text{CO}_x + \text{H}_2\text{O}$	Oxidation by activated oxygen (O^*) on catalyst

existing mass-produced catalysts. In this reaction, the PM is oxidized by the NO_2 that is generated when the NO in exhaust gas is oxidized by Pt catalyst. Compared to O_2 , NO_2 has higher PM oxidizing activity, so that a reaction can proceed at a relatively low temperature [4]. The third is catalytic oxidation. In this type, PM is oxidized with oxygen species (O^*) activated by a catalyst [5]. Adsorbed oxygen on metallic catalyst or oxide catalyst or the lattice oxygen in metallic oxide is involved in the reaction. The present research focused on the third reaction type, catalytic oxidation, focusing on the oxidation of PM. First, the oxide catalyst that enables PM oxidation was selected. Catalytic oxidation of PM is characterized by being a reaction between solid catalyst and solid PM, so different materials compared to catalysts for gaseous emissions have to be taken into account [6]. For the present research, therefore, PM oxidation characteristics with oxides were investigated with the idea that surface oxygen or lattice oxygen included in an oxide would contribute to PM oxidation [7]. Figure 1 shows the PM oxidation performance of a variety of elements (oxides). With regard to PM oxidation performance, the PM oxidation peak temperatures where the calorific values measured by thermo gravimetry/differential thermal analysis (TG/DTA) and obtained from DTA characteristics reach high points were plotted as the PM oxidation performance. The test conditions were a rate of temperature increase of 20 °C/min; dry air at 200 ml/min; catalyst and PM were 9.5:0.5 mg; contact quality; tight contact (TC) (crushed and mixed by mortar and pestle for 2 min); PM species: diesel engine PM (including SOF of about 15 wt %); oxides preconditioned at 700 °C for 2 h; and unstable materials were used for testing without preconditioning. As shown in Fig. 1, PM can be oxidized at low temperatures by alkalines such as K_2O and BaO , as well as to some extent by oxides that melt and vaporize such as V_2O_5 , PbO , and RuO_2 . From all these elements, Ag_2O shows the lowest PM oxidation peak temperature. It was clear from various test results, however, that Ag_2O would decompose at about 400 °C and change into Ag metal, losing its better PM oxidation characteristics. A study was therefore carried out to stabilize the active species Ag_2O .

Figure 2 shows oxygen desorption temperature and PM oxidation temperature of the highly active Ag_2O , the stable oxides that do not decompose or vaporize (\diamond), and these oxides or mixed oxides with Ag coating (\bullet). The oxygen desorption temperature was defined as the oxygen desorption start temperature according to O_2 -TPD. The test conditions included preconditioning by heating at 40 °C/min up to 800 °C in atmosphere. After cooling in atmosphere, it was tested by heating in He gas (50 ml/min) at 10 °C/min to 800 °C.

Fig. 1 PM oxidation peak temperature of each element

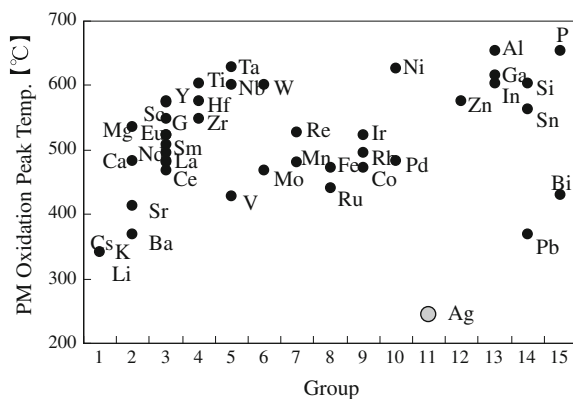
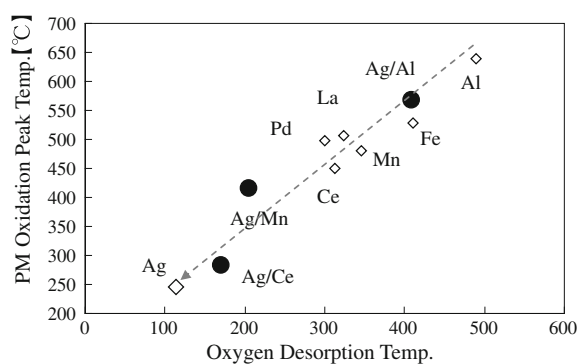


Fig. 2 Relationship between oxygen desorption temperature and PM oxidation temperature



The oxygen desorption start temperature indicates the easiness of oxygen to desorb, and a lower desorption start temperature indicates lower oxygen desorption energy. In other words, it can be considered highly active. It can be seen from Fig. 2 that Ag_2O has a lower oxygen desorption start temperature than the other oxides, indicating a very active PM oxidation reaction. Next, the results of examination of combinations of Ag with stable oxides and mixed oxides with the aim of stabilizing Ag_2O will be described. It is also the case with stable oxides that lower oxygen desorption start temperatures indicate that PM can be oxidized at lower temperatures. Combining Al_2O_3 , Mn complex and Ce complex oxides with Ag can make the desorption start temperatures lower than those of the original oxides and complex oxides. In other words, it is apparent that Ag coating can enhance the PM oxidation characteristics. However, since the oxygen desorption start temperature is higher than with Ag_2O alone, this can be taken as a step toward stabilization of Ag_2O . It was clear that the combination of Ag with Ce mixed oxides, which was capable of oxygen desorption at the lowest temperature, showed PM oxidation performance close to that of Ag_2O .

Figure 3 shows the repetition performance of Ag_2O and Ag/Ce catalysts when analyzing the PM oxidation peak temperatures by TG/DTA. As can be seen in

Fig. 3 Repetition performance of Ag₂O and Ag/Ce catalyst

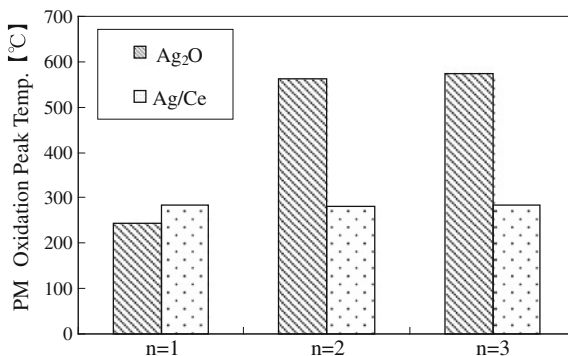
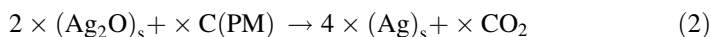
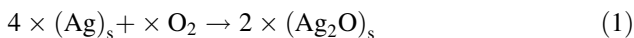


Fig. 3, Ag₂O showed higher oxidation performance in the first run. The results from the second run onwards show a substantial decrease in the PM oxidation performance. This is presumed to be because the Ag is metallized when the Ag₂O reacts with the PM or when it loses lattice oxygen due to decomposition from the heat, so that it is not re-oxidized. On the other hand, Ag/Ce catalyst maintains its performance, indicating that a combination of Ag and Ce can realize stable oxidation of PM. For the present research, Ag/Ce catalyst was selected as a PM oxidation catalyst that shows a high performance generally equal to Ag₂O, which is an active species, and that further keeps stable performance.

3 Mechanism of AG/CE Catalyst

Figure 4 shows the XRD pattern and Fig. 5 the XPS pattern of Ag/Ce catalyst. First, it is apparent from the XRD pattern that Ag is present in the form of metallic Ag. Additionally can be observed from the XPS results that it is present at the initial state (a) as Ag⁺, or in structure as a Ag₂O layer, several nm from the surface. With the reduction treatment of (b), it goes from this to a state in which the Ag₂O disappears to become Ag⁰, which is metallic Ag. It is apparent that with the oxidation treatment of (c), it returns again to Ag⁺. The following reaction formulas can be derived from the above results and from the results of Ag₂O reaction with PM (s indicates the surface layer).



That means, Ce mixed oxides coated by metallic Ag forms Ag₂O in the surface layer (1), the reaction of Ag₂O with PM reduces Ag₂O to Ag, and at the same time, the PM is oxidized (2). Then, the surface Ag is oxidized and Ag₂O is formed

Fig. 4 XRD pattern of Ag/Ce catalyst

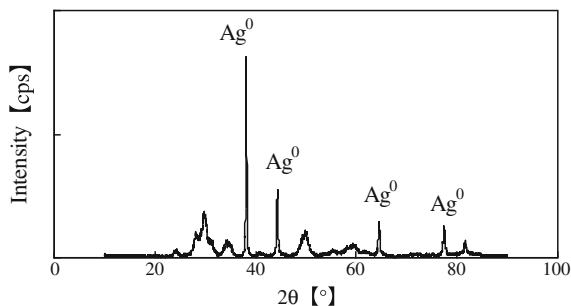
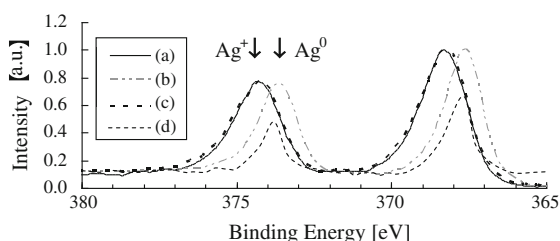


Fig. 5 XPS spectra of Ag/Ce catalyst (a) of initial state, (b) reduced by 5 % H_2/N_2 bal. and (c) oxidized by 20 % O_2/N_2 bal. and (d) comparison catalyst (Ag/ $\alpha\text{-Al}_2\text{O}_3$ initial state)



again. After this, reaction (1) and (2) is repeated (3). In other words, the catalytic reaction proceeds through the Ag oxidation–reduction cycle. On the one hand, based on the PM reaction results (Fig. 3) with Ag_2O alone, the Ag is not readily oxidized again, but taking into account that, with Ag/ $\alpha\text{-Al}_2\text{O}_3$, the Ag surface is in the state of a metallic state (Fig. 5), it appears likely that the supply of oxygen from Ce mixed oxides promotes the re-oxidation of the Ag catalyst, thus providing a stable catalytic function.

4 Results of Active Regeneration Test Using Model Gas

4.1 Active Regeneration Test

Ag/Ce catalysts having favorable PM oxidation characteristic were used to conduct active regeneration testing in a stream of gas simulating the engine exhaust during regeneration (Figs. 6, 7). The test used a DPF with catalyst coating and was carried out with a model gas testing apparatus. In the test procedure the DPF was loaded with PM in advance followed by an increase of the temperature to a specified level in a stream of N_2 gas. After that, NO and O_2 were introduced and the PM oxidation characteristics were evaluated. The test conditions are shown below.

Temperature: 580 °C (DPF internal temperature), O_2 concentration: 13 %
 NO concentration: 250 ppm, SV: 100,000/h, Catalyst size: 15 cc

Fig. 6 CO + CO₂ emissions profile during DPF regeneration

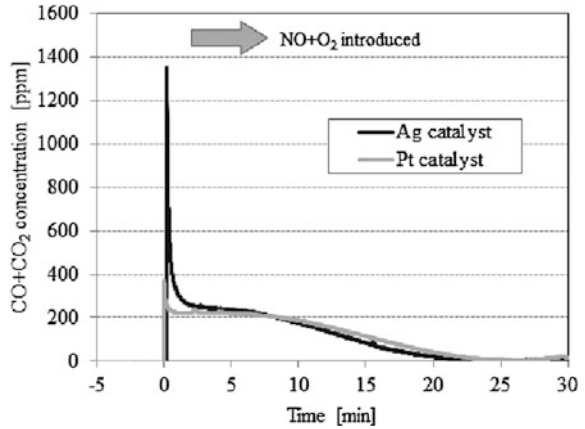
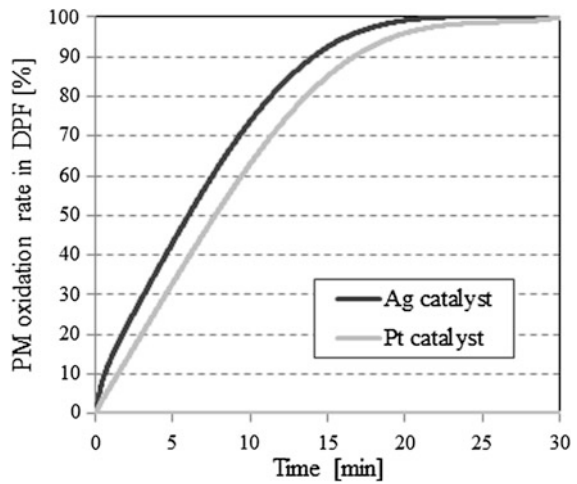


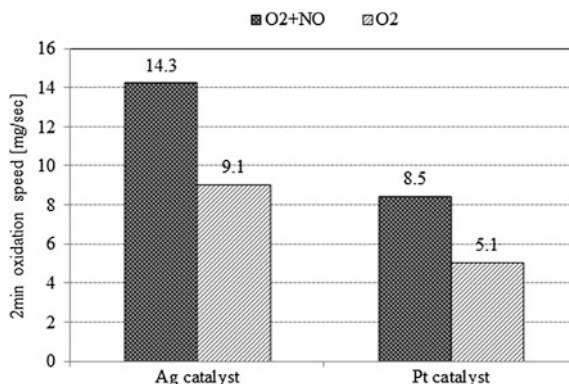
Fig. 7 Comparison of PM oxidation rates during DPF regeneration



PM species: Diesel engine PM, PM amount: 3 g/L, Catalyst system: DOC + DPF (2 BED)

Figure 6 shows the CO + CO₂ profile during PM oxidation with Ag catalyst and with Pt catalyst, which is a conventional technology. It can be confirmed that when NO and O₂ are introduced at 580 °C, CO + CO₂ formation starts due to the PM oxidation. With the Ag catalyst, in particular, CO and CO₂ reach a high level immediately after NO and O₂ are introduced. This indicates a catalytic reaction for PM oxidation. On the other hand, few minutes after regeneration start, the CO and CO₂ concentrations decreased, and the difference between the two catalysts is very small. This indicates an oxidation mostly without the catalyst and PM being in contact. Figure 7 shows the test results compared by PM oxidation rate. The Ag catalyst as compared with the Pt catalyst has an oxidation rate that is higher initially, and it is apparent that as a result, the time until all the PM has been burned is shortened.

Fig. 8 Influence of NO and O₂ gas on PM oxidation
580 °C, 13 %-O₂,
250 ppm-NO, engine PM



These results suggest that the Ag catalyst could promote the oxidation of PM even at such loose contact condition between catalyst and PM present in real DPF substrates. For the following tests, the average oxidation speed at the 2-min period after oxidation start, or the time (T₉₀) taken to reach 90 % of the oxidation rate, was used as an index of performance in model gas testing.

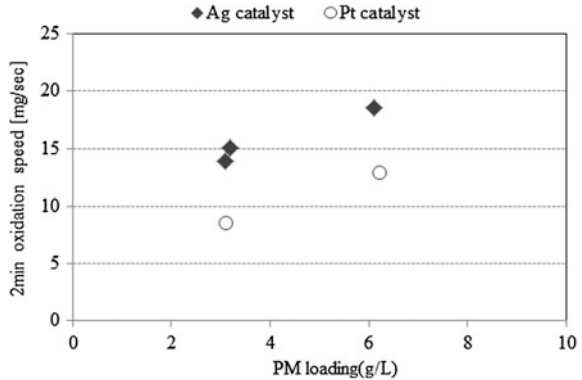
4.2 Influence of NO and O₂ Gas on PM Oxidation

Next, an examination was made of the influence of the gas introduced. For this test the performance was compared when O₂ and NO is introduced to the gas stream and if only O₂ is used (Fig. 8). Regardless of the catalyst used, the performance was lower when NO was not introduced than when NO was introduced. This suggests that an oxidation reaction resulting from the reaction between NO₂ and the PM was contributing. The performance of the Ag catalyst was better than that of the Pt catalyst, even comparing the Ag catalyst without NO and the Pt catalyst with NO. This suggested that the PM oxidation reaction was being promoted by active oxygen species from the catalyst. Given these results, PM oxidation promotion can be anticipated even under conditions of low NO concentration in engine exhaust gas, or even if a DPf is placed downstream from the NO_x aftertreatment device.

4.3 Influence of PM Accumulation Amount

The oxidation performance that occurs when the PM accumulation volume is changed was confirmed (Fig. 9). Testing was conducted with two levels of PM accumulation volume, 3 and 6 g/L. The results show that Ag catalysts obtained higher oxidation speeds than the Pt catalysts under both conditions. PM oxidation performance enhancement can be expected even in the final vehicle application, where the PM accumulation volume varies.

Fig. 9 Influence of PM accumulation amount 580 °C, 13 %-O₂, 250 ppm-NO, engine PM



4.4 Influence of O₂ Concentration and SV

As a next step the influence of SV and O₂ concentration was confirmed. Figure 10 shows the results obtained by comparing the oxidation speed at different SV and O₂-levels. As standard conditions an SV of 100,000/h and 13 % O₂ was selected. The other two tests were done either with lower SV or with lower O₂ concentration. The Ag catalyst showed higher performance than the Pt catalyst under conditions. This is thought to be due to the PM oxidation promotion effect of the Ag catalyst. The results of this model gas testing show that PM oxidation performance is substantially influenced not only by the catalyst but also by the O₂ concentration and SV value.

4.5 Influence of Regeneration Temperature

Next the influence of regeneration temperature was confirmed. Figure 11 shows the results of the regeneration testing conducted by setting fixed SV and O₂ concentration and changing the temperature (DPF inside temperatures of 530, 580 and 630 °C). It was observed that the Ag catalyst showed high PM oxidation performance relative to the Pt catalyst under all temperature conditions. When the regeneration temperature was reduced in 50 °C increments, the PM oxidation performance was substantially decreased and at 580 °C condition, the oxidation speed of the Ag catalyst is slightly lower compared to the Pt catalyst at 630 °C conditions (current condition).

Fig. 10 Influence of O₂ concentration and SV 580 °C, 250 ppm-NO, generator PM; PM loading 3 g/L

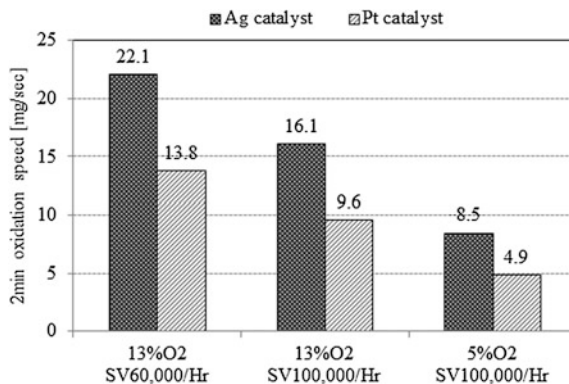
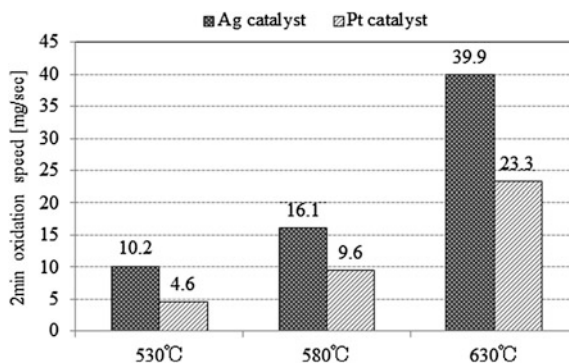


Fig. 11 Influence of DPF regeneration temperature 13 %-O₂, 250 ppm-NO, SV 100,000/h, generator PM, PM loading 3 g/L



4.6 Configuration of Regeneration Conditions

Given the above, the Ag catalyst was confirmed to be superior to the Pt catalyst under all conditions checked. It was clear, however, that this PM oxidation performance varied substantially with the environment of use, so that examination of methods of use that take those characteristics into account is needed. When regeneration temperature and regeneration time are taken as the parameters, the methods of using Ag catalyst could take the below directions (1) or (2).

	Regeneration temperature	Regeneration time
Condition (1)	Current conditions	Shorten
Condition (2)	Low temperature	Lengthen
Vary with PM amount, regeneration temperature		

Condition (1) describes the method of use under current regeneration temperature conditions, making use of the PM oxidation effect of the Ag catalyst to shorten the DPF regeneration time. Condition (2), on the other hand, is the method

of use that utilizes the PM low temperature oxidation effect of the Ag catalyst to lower the regeneration temperature below even the current level. In Condition (2), the thermal deterioration of the catalyst is suppressed by the lowered regeneration temperature. As a result, less precious metal is used, which can be anticipated to result in a substantial precious metal cost reduction. However, this lowers the oxidation speed by comparison with the current regeneration performance (630 °C, Pt catalyst) (Fig. 11), so that extension of the regeneration time is needed, raising concerns about possible negative impact on emissions and fuel consumption. Condition (1), on the other hand, is a method of use that has the regeneration temperature under current conditions and that aims to shorten the DPF regeneration time by raising the oxidation speed. This can be anticipated to have positive effects on catalyst thermal damage, emissions, and fuel consumption. Taking into account the results of various types of model gas tests using the Ag catalyst, the method of use under Condition (1) was adopted because it is expected to promote PM oxidation also with actual exhaust gases and to yield value for the vehicle.

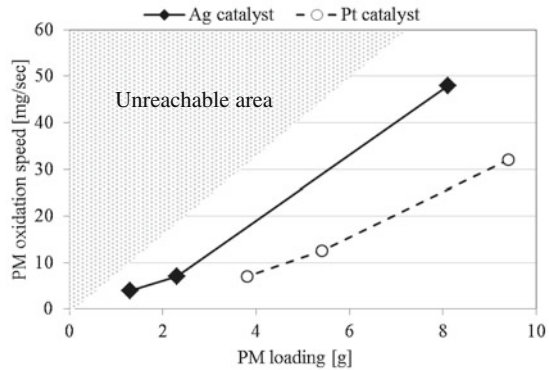
5 Results of Active Regeneration Testing on Engine Bench

The next step was to take the Ag catalyst that showed positive performance in the model gas testing and do active regeneration testing at the engine bench. The test conditions were set using the above mentioned Conditions (2) as a basis. The details are shown below. A 2.2-L DI/TC diesel engine was used to cause PM accumulation in a DPF under specified conditions. The exhaust gas temperature was then increased to raise the internal temperature of the DPF to approximately 620 °C to confirm the oxidation behavior of PM accumulated in the DPF.

Engine:	2.2- L DI/TC Diesel engine
Regeneration conditions:	Temperature 620 °C (DPF internal)
Operating conditions:	2500 rpm/15 Nm
PM accumulation amount:	8–10 g
Regeneration time:	2 min × 3 times
PM accumulation conditions:	ECE cycle repeated
Catalyst system:	DOC (1.0 L) + CSF (2.47 L)

Figure 12 shows the oxidation speed against the PM accumulation amount (remaining amount) during regeneration testing using Ag catalyst and Pt catalyst. The oxidation speed is calculated from the PM oxidation amount, which is derived from the DPF weight difference before and after 2-min regeneration testing, and from the regeneration time. As can be seen in Fig. 15 that the Ag catalyst shows higher PM oxidation speed than Pt catalyst at the engine bench testing just as it did in model gas testing. Comparison of the PM oxidation speed when the PM amount is 8 g shows that the oxidation speed with Ag catalyst is approximately 1.8 times that with Pt catalyst. Additionally it could be confirmed that only 40 % of the Pt

Fig. 12 DPF regeneration on the engine bench



catalyst had been oxidized, approximately 70 % of the Ag catalyst had been oxidized after 2-min regeneration. This suggests that initial oxidation is being promoted by the catalytic oxidation effect.

6 DPF Regeneration Simulation in NEDC

The results shown in Fig. 13 were used to conduct a simulation of DPF regeneration in the New European Driving Cycle (NEDC). The PM oxidation speed during DPF regeneration was derived by corrections for PM accumulation amount, temperature, O₂ concentration, and gas flow volume. Figure 13 shows the DPF regeneration simulation results. With the initial PM accumulation amount set to 7.4 g, DPF active regeneration control was applied under NEDC mode to raise the exhaust gas temperature. The PM oxidation speed at that time was used to calculate the time from the point when the DPF internal temperature reached 500 °C to the point in time when the PM was completely oxidized. The result for Pt catalyst was 524 s for complete oxidation, while for Ag catalyst it was only 299 s until oxidation was complete. The results show that the DPF regeneration time can be shortened by 43 % when Ag catalyst is used.

7 Durability Test Results

Confirmation of the durability was carried out by model gas testing of the influence of heat, sulfur, and ash, which are presumed to be factors in the deterioration of the catalyst [8].

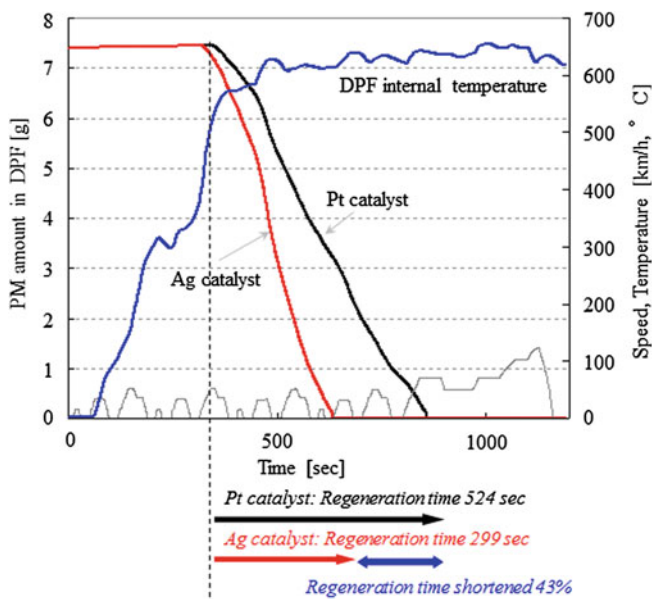


Fig. 13 Results of regeneration time simulation in NEDC

The conditions for each durability test are shown below.

- Heat-resistance test: 700 °C × 30 h with H₂O 6 %
- Sulfur-resistance test: Low temperature 250 °C × 20 min, 100 ppm-SO₂
High temperature 620 °C × 4 h, 100 ppm-SO₂
- Ash-resistance test: Calcium sulfate 44 g/L accumulated in DPF

As can be seen in Fig. 14, virtually no lowering of performance was seen from heat or sulfur. The performance is close to the performance of the Fresh sample. Additionally the performance is significantly improved compared to the Pt catalyst. On the other hand, the calcium sulfate used to simulate ash was accumulated in the DPF. After that, PM is accumulated and the oxidation testing takes place. The results confirm that oxidation time is increased by approximately 2 min compared to the Fresh catalyst. It is presumed that PM oxidation performance is reduced because the Ash inhibits the contact between the catalyst and the PM.

8 Influence of Ash Accumulation Amount

Due to concern that ash could reduce performance, the influence of ash accumulation amount on PM oxidation performance was confirmed (Fig. 15). With the Pt catalyst, PM oxidation performance was hardly changed at all even if ash is accumulated.

Fig. 14 Durability test results of Ag catalyst 600 °C, 13 %-O₂, 250 ppm-NO, Engine PM, PM loading 3 g/L

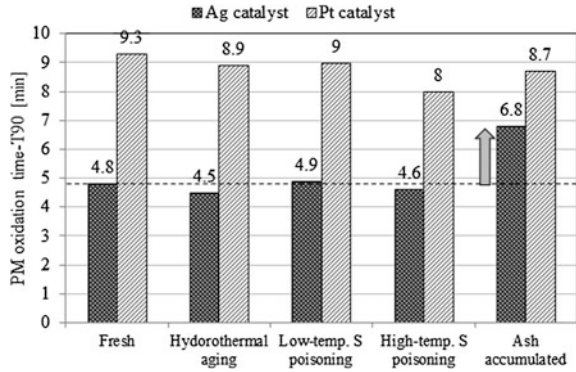
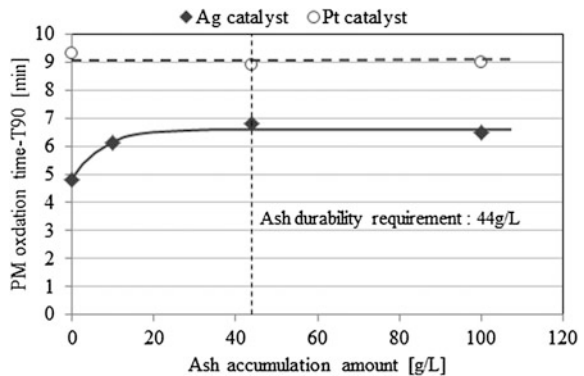


Fig. 15 Influence of ash accumulation volume



This is assumed to be because the oxidation progresses through the reaction between PM and NO₂, which is not influenced by contact condition between catalyst and PM.

With the Ag catalyst, on the other hand, ash accumulation initially causes a reduction in PM oxidation performance, but the results show that performance did not deteriorate further even when 44 g/L or more of ash was accumulated. These results suggest that ash causes the contact condition between the catalyst and the PM to deteriorate, and therefore is a factor that reduces PM oxidation performance. However, given that a part of the catalyst maintains its function even when the ash accumulation amount is equal to or greater than the equivalent of the guaranteed distance, the Ag catalyst is confirmed to be highly durable.

9 Conclusion

1. Different materials were investigated focused on PM oxidation reaction due to the catalyst. As a result, it was found that Ag/Ce material had very high performance and stability.

2. It became clear that, in the mechanism of the reaction between Ag/Ce catalyst and PM, the formation of active species Ag_2O was related to the supply of oxygen from Ce mixed oxides.
3. The results of regeneration testing by means of model gas showed that the Ag catalyst had higher PM oxidation performance than the conventional Pt catalyst. It was suggested that the Ag catalyst could promote the oxidation of PM even in the practical use with a loose contact condition between catalyst and PM in the DPF.
4. The Ag catalyst also showed high PM oxidation performance in engine bench testing, just as with the model gas, and it was confirmed to have a 43 % shortening of regeneration time in a DPF regeneration simulation in NEDC conditions.
5. Although some reduction in performance due to ash was found, no influences from heat and sulfur were observed, showing that the catalyst possesses high durability.

References

1. Salvat O et al (2000) Passenger car serial application of a particulate filter system on a common rail direct injection diesel engine. SAE Technical Paper 2000-01-0473
2. van Setten BAAL (2001) Science and technology of catalytic diesel particulate filters. Catal Rev 43(4):489–564
3. Walker AP (2004) Controlling particulate emissions from diesel vehicles. Top Catal 28(1–4):165–170
4. Jacquot F (2004) Soot oxidation by O_2 and/or NO_2 in the presence of catalysts under lean-burn and rich atmospheres. SAE Technical Paper 2004-01-1943
5. Bueno-Lopez A et al (2005) Active oxygen from CeO_2 and its role in catalysed soot oxidation. Catal Lett 99(3–4):203–205
6. Neef JPA et al (1997) Catalysts for the oxidation of soot from diesel exhaust gases II. Contact between soot and catalyst under practical conditions. Appl Catal B Environ 12:21–31
7. Machida Masato et al (2008) On the reasons for high activity of CeO_2 catalyst for soot oxidation. Chem Mater 20(13):4489–4494
8. Bodek K et al (2007) The effects of sulfated ash, phosphorus and sulfur on diesel aftertreatment systems—a review. SAE Technical Paper 2007-01-1922

Three Way Catalyst Modeling for HEV After Treatment System Design

Masayuki Tani, Masaaki Kubo and Shigemasa Shimojo

Abstract System simulation tools are effective in examining complex systems such as those of a hybrid electric vehicle (HEV). However, since most system issues originate in physical phenomena, it is necessary to reproduce the physical phenomena involved in order to resolve the issues. One problem that occurs especially in HEVs is that stopping and restarting the engine frequently can cause emission performance to deteriorate. To resolve this issue, the phenomena that occur in the catalyst must be reproduced accurately. Based on this reasoning, we have developed an exhaust system simulation tool that takes into account catalyst reactions and have experimentally used the tool in an effort to resolve the issue of HEV emission performance. This paper describes the newly developed simulation tool and the application results obtained.

Keywords System simulation · Hybrid electric vehicle · Three way catalyst · O₂ storage · NO_x reduction

1 Introduction

In order to execute the design of a powertrain system efficiently, it is necessary to consider the overall framework of the system configuration at the early stage of the development process. This involves examining the compatibility of the devices to

F2012-A04-012

M. Tani (✉) · M. Kubo · S. Shimojo
Nissan Motor Co., Ltd, Yokohama-shi, Japan
e-mail: masayuki_tani@mail.nissan.co.jp

be combined and the feasibility of the control logic. However, powertrain systems like HEV in recent years are composed of multiple devices and have a high degree of complexity. Experimental data and accumulated knowledge alone are not sufficient to study a proposed powertrain system thoroughly. Consequently, there are many times when the system performance cannot be fully elicited or it is necessary to rework a system during the development process. System simulation tools are regarded as being effective for resolving these problems.

A great deal of research has been done on simulation tools for use in studying energy management issues on HEVs, but there are few examples in the literature of studies concerning emission simulation techniques. Because of the priority placed on fuel economy, the engine of an HEV is repeatedly stopped and restarted, resulting in a lower catalyst temperature and a decline in catalyst conversion efficiency. These factors have more than a little impact on emission performance. In order to avoid such adverse effects, the potential trade-offs must be factored into the system design from the early stages of the development process. In the case of an HEV, there are more degrees of freedom for designing the system parameters, as typified by the motor assist mode. Accordingly, it is thought that operating modes may exist that would be advantageous for emission performance.

In this study, a system simulation tool was developed for examining the following characteristics of HEV operation that adversely affect emission performance. The new tool was then used in an effort to resolve the issue of HEV emission performance.

- Engine stop
- Engine restart

2 System Simulation Model and Results

2.1 Model Overview

Figure 1 shows the basic configuration of the engine system simulation model that was developed. In this study, the general-purpose 1D simulation code GT-SUITE of Gamma technologies was used as a system simulation tool. This simulation model consists of an engine model, a heat exchange model and a three-way catalyst (TWC) model. As the first step in the simulation flow, the engine operating point and coolant temperature are obtained from an energy management model and a thermal management model, respectively. Engine-out emissions (EOE), engine-out exhaust temperature (EOT) and exhaust gas flow rate are then calculated with a combustion model [1] [2]. Subsequently, a heat exchange takes place with the exhaust system, and tailpipe emissions (TPE) are calculated with the catalyst model.

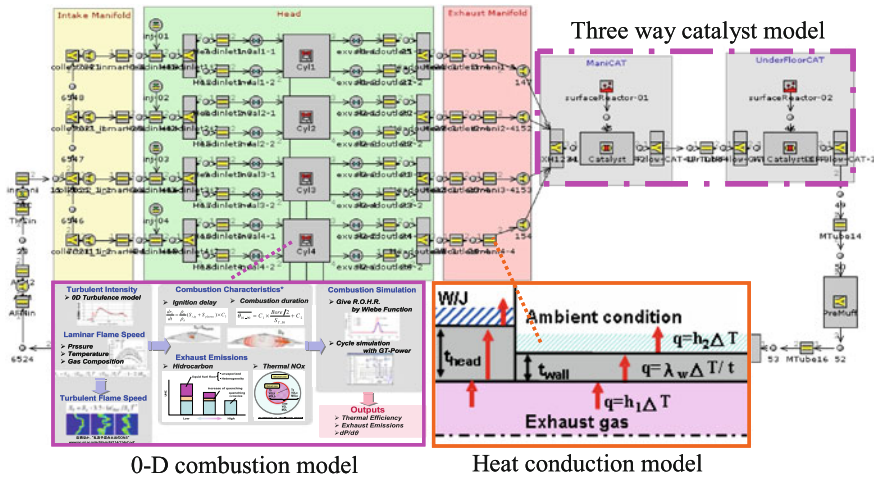


Fig. 1 Engine system simulation model of a L4 engine

2.2 Three-Way Catalyst Model

One of the major issues concerning HEV emission performance is the emission of nitrogen oxides (NOx) when the engine is restarted. This NOx emission is assumed to be influenced by oxygen (O₂) storage in the catalyst. Therefore, it is necessary to construct a model for reproducing the reactions taking place on the catalyst surface in order to predict the extent of that influence and implement suitable measures to deal with it. Several catalyst reaction models like that described in [3, 4] have been proposed which take into account surface reactions. However, because none of these models treats the mechanism causing the NOx emission at the time of engine restart, they would not be sufficient for the purpose of the present study. A general surface reaction model was used in this study as the basis for investigating a method of reproducing the NOx emission at the time of engine restart.

A small size catalyst was used in conducting a fundamental experiment for the purpose of analyzing the mechanism causing the NOx emission when the engine is restarted.

The experimental results are shown in Fig. 2. In this experiment, after saturating the catalyst with O₂, exhaust gas with a rich air fuel ratio (A/F) was passed through the catalyst and the tendency for NOx to be emitted was investigated. Under the conditions used in the experiment, the results in the figure show that NOx began to be emitted several seconds after the exhaust gas at the catalyst inlet turned A/F rich. While the O₂ storage function of the catalyst can compensate for an excess or deficient A/F in the inflowing exhaust gas, the experimental results suggest that the O₂ stored in the catalyst, rather than from NOx in the exhaust gas, was the preferential O₂ supply path. However, when oxygen stored in the catalyst was defined in the model as the preferential O₂ supply path, it gave rise to a contradiction in that NOx reduction became impossible even under a condition of λ = 1.

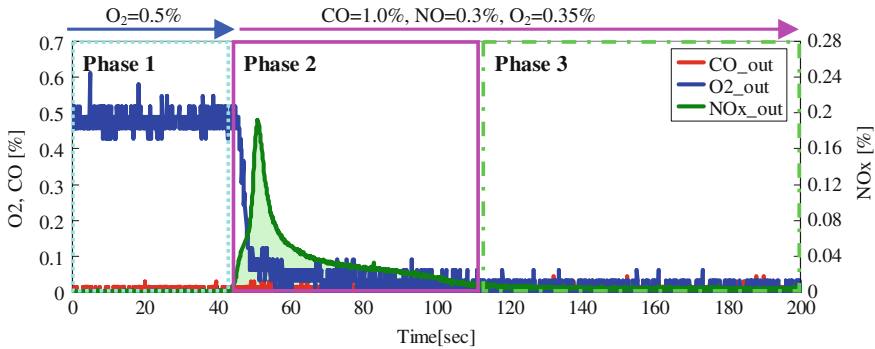
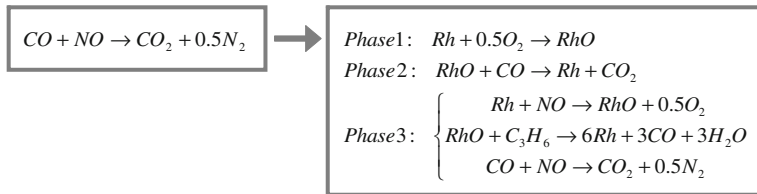


Fig. 2 Fundamental experiment of NOx reduction reaction

Table 1 NOx reduction reaction scheme



In an effort to overcome these issues, we defined a new NOx reduction scheme, consisting of the set of equations in Table 1, which assumes the NOx reduction reaction takes place via the medium of the precious metals as illustrated in Fig. 3. This new reduction scheme made it possible to reproduce both the NOx reduction reaction at $\lambda = 1$ and the NOx reduction reaction during O₂ storage. The comparison results for this reduction scheme are shown in Fig. 4. The results indicate that this newly adopted reaction mechanism made it possible to reproduce the NOx reduction reaction during O₂ storage. In addition, good results were also obtained in a simulation of prototype HEV conducted under the LA4 driving cycle when the TWC model was combined with the engine system model (Table 2; Fig. 5).

3 Application Example

3.1 Catalyst Temperature Reduction by Engine Stop

There was concern about a possible decline in the catalyst temperature in an HEV because of the frequent stopping of the engine. Therefore, a study was conducted to investigate the effect of stopping the engine on reducing the catalyst temperature

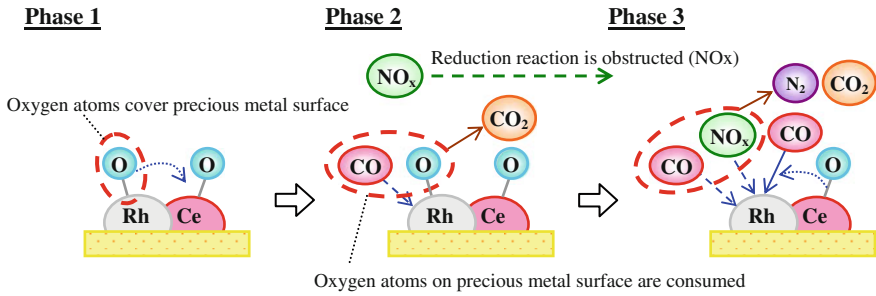


Fig. 3 NO_x reduction reaction mechanism

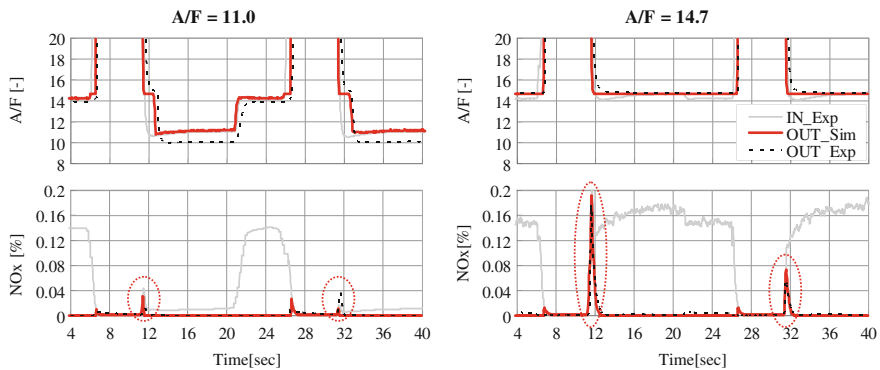


Fig. 4 NO_x reduction phenomena comparison. Experiment and simulation

Table 2 Specification of prototype HEV

Curb weight	Transmission	Displacement	Motor power	Battery capacity
2135 kg	7AT	3498cc	50 kW	1.4 kWh

in real-world driving. Figure 6 shows the exhaust system of the prototype HEV and the simulation model used in the study. From the left side, the figure shows the close-coupled catalyst and the underfloor catalyst. Models of the exhaust system and catalysts were created for use in conducting the simulation.

Figure 7 shows the results for the bed temperature of the underfloor catalyst during operation under the LA4 driving cycle. For the conventional engine, the bed temperature was kept high degree due to engine operating. However, for the HEV engine, stopping and restarting the engine repeatedly had the effect of reducing the catalyst bed temperature because the catalyst did not receive sufficient thermal energy from the exhaust gas during the short period of engine operation. These results indicate that, depending on the conditions for stopping and restarting the engine, the catalyst temperature may fall below the temperature for catalyst

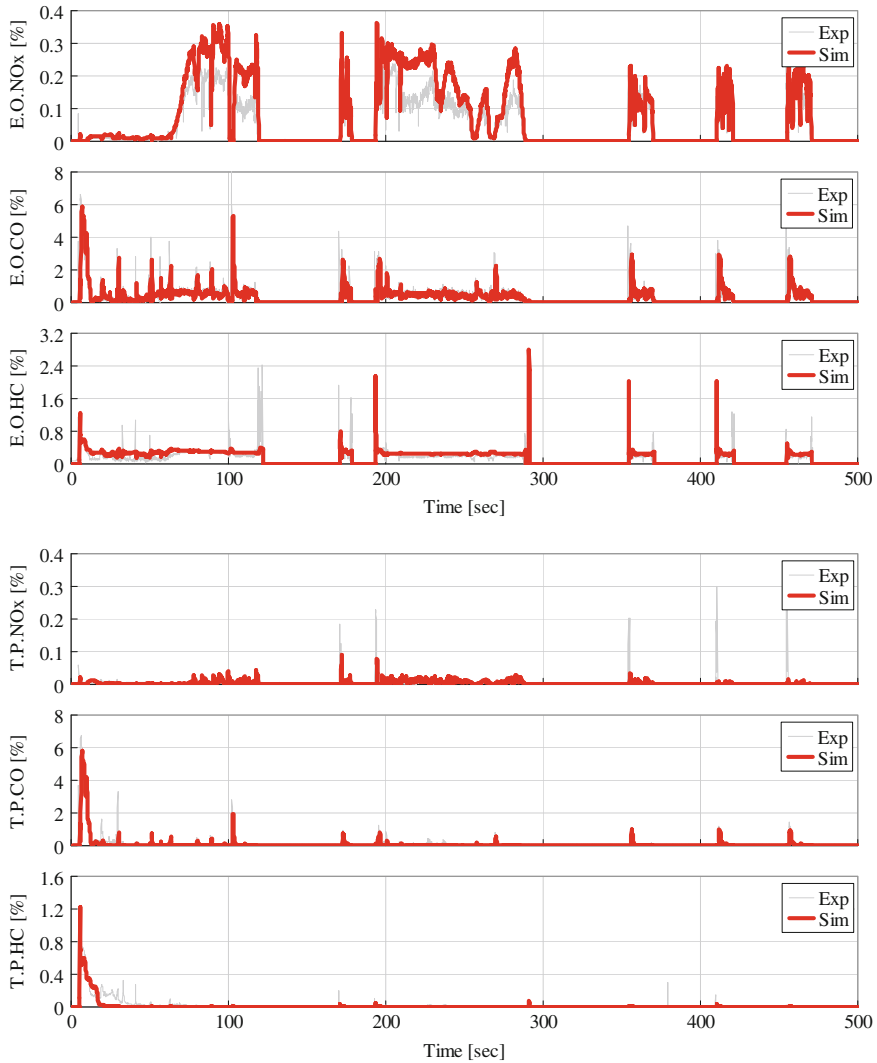


Fig. 5 Emission comparison on LA4 driving cycle. Experiment and simulation

activity after light-off, causing emission performance to deteriorate. In other words, in terms of energy management, it is also necessary to consider the effect on reducing the catalyst temperature when investigating the engine stopping time and the number of times the engine is stopped.

A study was then undertaken to investigate an improvement measure for preventing the catalyst temperature from falling below the catalyst operating temperature. The results of the investigation above showed that the underfloor catalyst

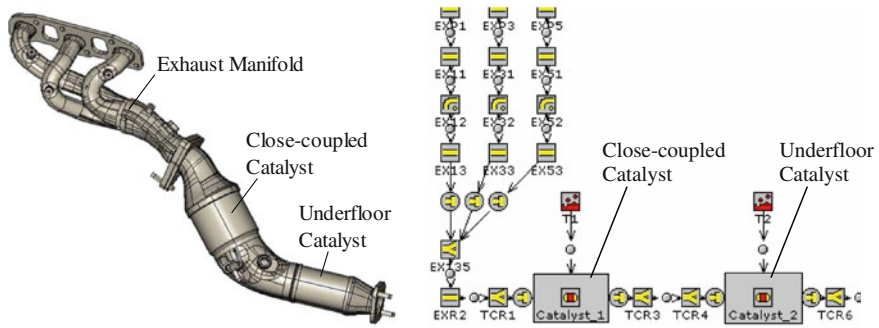


Fig. 6 Exhaust system of the prototype HEV and the simulation model

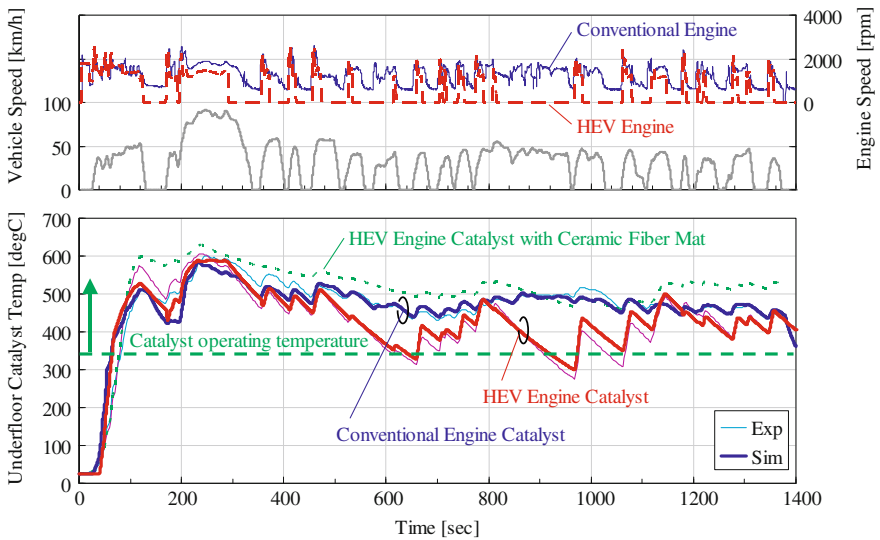
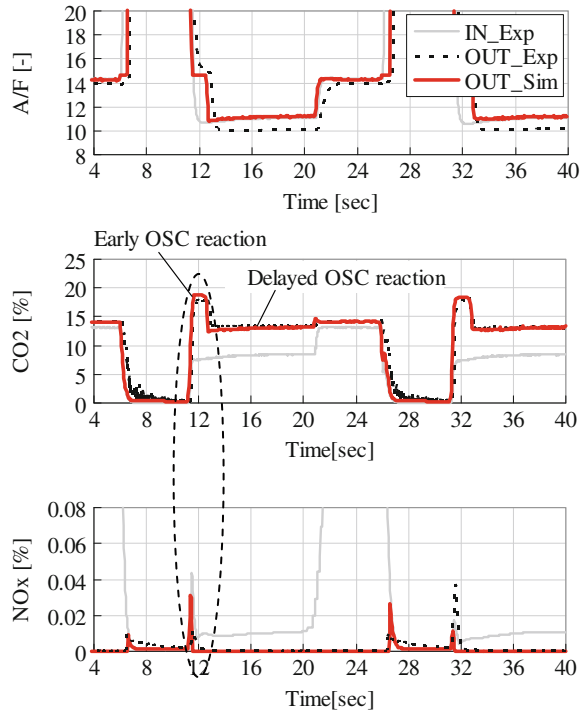


Fig. 7 Bed temperature of the underfloor catalyst on LA4 driving cycle

had not received sufficient heat at the time the engine was restarted, so a measure was examined for suppressing the drop in the catalyst temperature. The graph in Fig. 7 also shows the decline in the catalyst temperature for different heat radiations of the underfloor catalyst. The results indicate that the temperature decline can be mitigated by decreasing the heat radiation to the external of the catalyst. Under the conditions used in this study, the catalyst operating temperature was kept high degree by using the ceramic fiber mat as a catalyst mount.

Fig. 8 OSC reaction mechanism

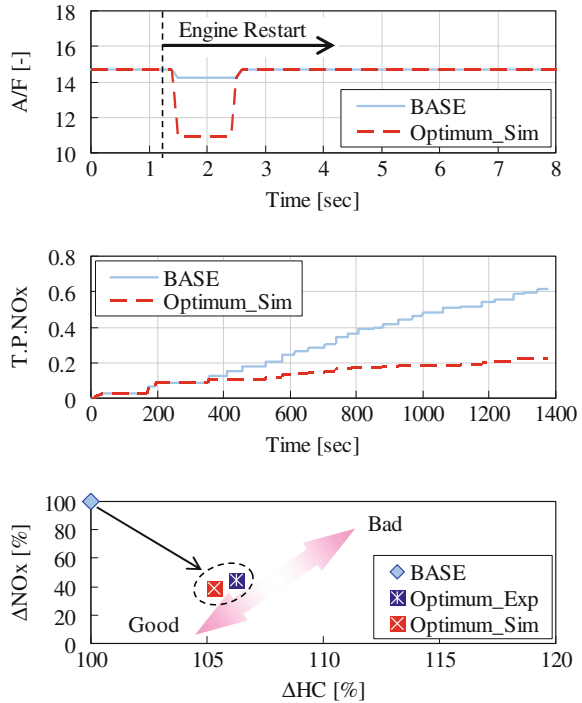


3.2 NO_x Emission at Engine Restart

The mechanism causing the NO_x emission at engine restart was analyzed both experimentally and by simulation. Figure 8 shows the results obtained in a study where the engine was repeatedly operated under rich and lean A/F conditions. The CO₂ emission level at the catalyst outlet was higher than at the inlet and the emission level tended to be divided into two stages. This implies the existence of two types of release reactions for the O₂ stored in the catalyst. It was observed that the end of the first-stage oxygen release reaction nearly coincided with the time when NO_x stopped being emitted. Therefore, it was inferred that the first-stage release reaction influenced NO_x reduction.

Based on this hypothesis, an attempt was made to reduce the NO_x emission level by changing the A/F profile at the time of engine restart. An A/F profile was defined that shortened as much as possible the duration of the first-stage oxygen release reaction. As a result, the NO_x emission level was reduced by approximately 60 % compared with the baseline level (Fig. 9).

Fig. 9 Examination of NOx reaction at HEV engine restart



4 Conclusion

A new simulation tool has been developed for modeling the exhaust system of HEVs in order to resolve the issue of their emission performance. It was assumed that a simulation tool which takes into account the actual physical phenomena occurring in the catalyst would be effective for this purpose. In order to demonstrate the validity of this simulation tool, it was used in a theoretical study to examine the characteristics of HEV operation that adversely affect emission performance. The following conclusions were drawn from the results obtained.

- A new NOx reduction scheme was devised for use in simulating the NOx emission that occurs when the engine of an HEV is restarted. This scheme assumes that the NOx reduction reaction takes place through the medium of the precious metals. It was verified that this scheme can reproduce the NOx reduction reaction both under a condition of $\lambda = 1$ and during O₂ storage.
- In an operating mode where the engine is repeatedly stopped and restarted, sufficient thermal energy is not supplied to the underfloor catalyst. It was found that the catalyst bed temperature might drop below the catalyst operating temperature depending on the engine operating conditions. It was confirmed in this study that using the ceramic fiber mat can keep the catalyst bed temperature high degree.

- It was observed that there are two main types of O₂ release reactions during O₂ storage, and it was found that the first-stage oxygen release reaction influences NO_x reduction. The results of this study showed that the application of an optimal A/F profile at the time of engine restart reduced the NO_x emission by approximately 60 % compared with the baseline level without causing any significant deterioration of the hydrocarbon level.

References

1. Watanabe K, Ito S, Tsurushima T (2010) A new quasi-dimensional combustion model applicable to direct injection gasoline engine. SAE 2010-01-0544
2. Cheng WK, Hamrin D, Heywood JB, Hochgreb S, Min K, Norris M (1993) An overview of hydrocarbon emissions mechanisms in spark-ignition engines. SAE932708
3. Tsinoglou DN, Koltsakis GC, Peyton Jones JC (2002) Oxygen storage modeling in three-Way catalytic converters. *Ind Eng Chem Res* 41:1152–1165
4. Katherine W, Hughes and Peter Florchinger (2002) Ultra Thinwall Light-off Performance – Varying Substrates, Catalysts, and Flow Rates; Models and Engine Testing [J]. SAE 2002-01-0352

Investigations of Ammonia Emissions from Euro 5 Passenger Cars Over a Legislative Driving Cycle

Piotr Bielaczyc, Andrzej Szczotka, Antoni Swiatek
and Joseph Woodburn

Abstract Vehicular ammonia emissions are currently unregulated, even though ammonia is harmful for a variety of reasons, and the gas is classed as toxic. Ammonia emissions represent a serious threat to air quality, particularly in urban settings; an ammonia emissions limit may be introduced in future legislation. Ammonia is not produced within the cylinder of an internal combustion engine in significant quantities. However, having reached its light-off temperature, a three-way catalyst can produce substantial quantities of ammonia through various reaction pathways. Production of ammonia is symptomatic of overly reducing conditions within the three-way catalyst (TWC), and its formation and emission depends on a wide range of factors. This study presents a brief literature review, and later reports on experimental data presenting ammonia emissions data from four Euro 5 passenger cars, using three different petrol fuels. All vehicles were tested on BOSMAL's chassis dynamometer over the New European Driving Cycle. For three of the vehicles, undiluted ammonia was quantified directly at tailpipe. The fourth vehicle was subjected to further investigations with the aid of Fourier Transform Infra-Red (FTIR) analysis of a range of compounds, including ammonia. Emission factors observed for the three vehicles are generally low in comparison to other studies, which may be a result of the favourable laboratory conditions, the relatively small, low-emission engines and the driving cycle employed. Second-by-second data obtained from a single vehicle operating on two fuels revealed small but significant differences in ammonia emissions, including the time of the initial ammonia surge. A range of metrics were examined to determine possible correlations between ammonia and

F2012-A04-014

P. Bielaczyc · A. Szczotka (✉) · A. Swiatek · J. Woodburn
BOSMAL Automotive Research and Development Institute Ltd,
Bielsko-Biala, Poland
e-mail: piotr.bielaczyc@bosmal.com.pl

other pollutants. No significant correlations were found; there was however some evidence of a trade-off between ammonia and NO_x . A brief analysis of NH_3 emissions in the context of RNC emissions revealed ammonia to make up roughly 40 % of the reactive nitrogen compounds (RNCs) released over the duration of the test cycle. Thus, the ammonia emissions observed are low but non-trivial and the issue of ammonia emissions and direct and indirect impacts on air quality is an important research direction. This paper reports on a continuation of an ongoing test programme conducted at BOSMAL focussing on unregulated emissions (including ammonia) from light-duty vehicles and the effects of increased proportions of ethanol in petrol on regulated and unregulated emissions.

Keywords Ammonia (NH_3) · Three-way catalyst (TWC) · Reactive nitrogen compounds (RNCs) · Light-duty vehicles · Unregulated emissions

1 Introduction

1.1 Ammonia as a Toxic Pollutant in the Exhaust Gas of SI Vehicles

In recent years, interest in the phenomenon of the emission of ammonia from vehicles has increased [1]. Ammonia (NH_3) has long been recognized as an automotive exhaust gas component [2] (the compound was first studied in the automotive context by Harkins and Nicksic in 1967 [3]). Ammonia is one of a group of lesser-known exhaust gases that has received relatively little attention in comparison to CO , NO_x and THC. Currently unregulated in the European and US markets, it belongs to a group of compounds which may feature in future regulations regarding exhaust emissions from light duty vehicles [1, 4].

In the atmosphere, NH_3 plays a significant role in the formation of secondary particulate matter (PM) [5]. Ammonia can participate in various reactions at ambient temperatures. The main products of these reactions are aerosols, the rate of formation of which is a strong function of the local atmospheric concentration of ammonia [4, 5]. Ammonia has a relatively short atmospheric residence time and a limited range [2, 4]. However, the secondary PM NH_3 produces can travel much further, and is widely recognized as being able to adversely affect human health, damage plants, corrode building materials and cause the acidification of rain and eutrophication of surface waters [4, 5]. Ammonia is a toxic pollutant, with a distinctive, disagreeable odour which is detectable by humans at relatively low concentrations.

A UNECE protocol [6] and an EU directive [7] set limits for total NH_3 emissions from EU member states, but set no specific quotas for the transport

Fig. 1 Schematic of a TWC's inputs and outputs of nitrogen atoms in various chemical forms [1]



sector. Active catalytic systems fitted to the latest Diesel-powered vehicles use urea to produce the ammonia required for selective catalytic reduction (SCR). The escape of ammonia from such a system is called ‘ammonia slip’ [4], and is undesirable because of the effects listed above. Euro 6 legislation (Regulation EC No. 595/2009 and Regulation EU No. 582/2011) will introduce a concentration-based limit of 10 ppm for heavy duty vehicles (with reference mass >2,610 kg) featuring selective catalytic reduction (SCR) systems, in recognition of the deleterious effects of NH_3 emissions. The Euro 6 SI proposal contains no mention whatsoever of ammonia. In the USA, the EPA’s National Emissions Inventory (NEI) identifies ammonia as a criteria pollutant and monitors NH_3 concentrations, but the gas has yet to be regulated in the automotive arena.

Ammonia is a natural atmospheric trace gas, but certain anthropogenic sources are significant. While various agricultural and municipal activities are major anthropogenic sources [4], vehicles equipped with three-way catalysts (TWCs) also contribute [1, 2, 4, 5, 8–18]. At multiple locations, ambient levels of ammonia have increased, even when taking into account increases in traffic volumes [1, 4]. Studies have found that even as emissions of regulated compounds have fallen, NH_3 emissions from road traffic appear to have risen [1, 4]. Despite the fact that emission of ammonia is normally associated with agricultural activities, areas with heavy/regular traffic have on occasion been found to show higher concentrations of NH_3 than rural areas with only light/occasional traffic [4, 13]. Field studies performed in tunnels and on large arterial roads may drastically underestimate rates of ammonia emission from SI vehicles, as the relatively static, low-acceleration driving observed is not conducive to ammonia formation [4, 14].

Ammonia is one of a number of simple nitrogen compounds emitted by SI vehicles equipped with TWCs. Ammonia and NO_x are reactive compounds featuring a nitrogen atom, earning them the name reactive nitrogen compounds (RNCs) [1, 4, 9]. The vast majority of the gas influx into the cylinder is relatively inert nitrogen (N_2). Most of the nitrogen in the intake air simply passes through the powertrain; some reacts to produce various RNCs, both in the cylinder during the combustion process and in the TWC during the aftertreatment process (Fig. 1). The relative proportions of these gases are not means fixed [8], and concentrations of these species can vary by orders of magnitude from second to second, depending on the engine operating point. Higher proportions of NH_3 at tailpipe indicate a general over reduction of NO_x . An increase in the efficiency of NO_x elimination may come at the expense of increased NH_3 emissions.

1.2 Formation of Ammonia in a Three-Way Catalyst

The formation of NH_3 within the cylinders and non-catalytic exhaust systems has long been known to be very limited [2, 3]. Post-catalyst (tailpipe) NH_3 levels are approximately two orders of magnitude greater than pre-catalyst (engine out) emissions, with little (if any) correlation between the two mass fluxes [3]. Thus, engine out emissions of NH_3 can effectively be negated. The detection of an NH_3 concentration above the atmospheric background level in automotive exhaust can be attributed to unintended side reactions occurring in the TWC. These side reactions include the steam reforming and water–gas shift reactions, both of which produce hydrogen, which can participate in further reactions to produce ammonia. There are multiple known and proposed NH_3 formation pathways, both relatively direct and indirect (involving many intermediates) and these processes remain under investigation. Precious metal type/loading, gas temperature, the relative fuel:air ratio (λ) and fuel sulphur content all influence the formation of NH_3 to varying degrees [3]. A range of NH_3 formation mechanisms have been suggested and are presented elsewhere [1, 4]. It is unlikely that any single reaction will be the only NH_3 formation route, and different reactions probably occur under different conditions, even for the same vehicle-TWC-fuel combination. Multiple reactions may even occur simultaneously, thereby boosting the production rate. However, a certain temperature normally has to be reached before the TWC can catalyze the reactions [9], analogous to an NH_3 production light-off temperature [1, 4].

In the literature, there is near-universal agreement that rich conditions favour NH_3 production [1, 4], although emission of NH_3 has been observed under certain lean conditions [1, 4]. However, one remote sensing study failed to find a significant correlation between λ and NH_3 emission [18], and previous work by the authors [1] found limited evidence of a correlation between λ and NH_3 emissions. Fuel-rich conditions mean the supply of reagents such as CO and HC is increased, and temperatures are higher. Lean operation also means hydrogen is not as chemically active [4]. Ideal conditions for the production of NH_3 appear to be fuel rich, oxygen-poor, with high engine out temperatures—the conditions encountered at higher loads, particularly during periods of aggressive acceleration. Ammonia formation has been reported to correlate somewhat with engine out CO and NO mass fluxes, although correlations are often relatively weak [4]. The correlation between λ and the NH_3 emission factor for a particular vehicle has been reported as potentially significant but relatively weak [4]. Investigations into the effects of fuel chemistry on NH_3 emission have primarily focused on fuel sulphur content. In laboratory experiments, the injection of sulphur dioxide into a TWC has been shown to inhibit ammonia formation under certain conditions [4, 16]. Despite concerns to the contrary, chassis dynamometer studies have revealed that for modern vehicles, low sulphur content fuel has a limited effect on ammonia emission [15], and may even reduce NH_3 emissions [4]. The aim of this paper is to obtain further information on emissions of NH_3 from Euro 5 vehicles operating on standard commercially available petrol, and to gain further insight into the NH_3 formation process with the aid of FTIR

Table 1 Key characteristics of the four test vehicles used in this study

Parameter	Vehicle 1	Vehicle 2	Vehicle 3	Vehicle 4
Vehicle type	Passenger car	Passenger car	Passenger car	Passenger car
Engine type	SI (MPI)	SI (MPI)	SI (MPI)	SI (MPI)
Approximate displacement (dm ³)	1.4	1.2	1.2	1.4
Emissions standard	Euro 5	Euro 5	Euro 5	Euro 5

spectroscopy using two different fuels, one of which contained 10 % v/v ethanol. Since interest is increasing in using greater proportions of ethanol in standard petrol fuel, research on the impact of increased fuel ethanol content on unregulated emissions (including ammonia) is a research priority.

2 Experimental Details

Two experiments were performed to obtain further information on ammonia emissions from Euro 5 passenger cars. In the first experiment, three vehicles (vehicles 1, 2 and 3) were tested, with tailpipe ammonia emissions quantified by a dedicated NH₃ analyser. In the second experiment, a single vehicle (vehicle 4) was tested, with analysis of ammonia and other compounds of interest in the raw exhaust gas performed at both at the pre cat and post cat sampling locations (in turn) by means of an FTIR analyser. Key characteristics of the test vehicles are presented in Table 1. Both tests were performed under laboratory conditions, as specified in EU legislation (24 °C, 45 % relative humidity) in BOSMAL's climate controlled Euro 5-6/SULEV compliant exhaust emissions laboratory (Fig. 2), described in detail elsewhere [19]. Both experiments were performed with the test vehicles mounted on a chassis dynamometer (Fig. 3); the well-known New European Driving Cycle (NEDC), the current European legislative cycle, was used as the test cycle. Regulated emissions were measured according to the EU legislative test procedure using a constant volume sampler and a set of exhaust emissions analysers (Fig. 4); these results are not presented here, but were analysed to ensure repeatability from test to test. Vehicles 1, 2 and 3 were each tested three times on a single fuel (see Table 2). Vehicle 4 was tested four times on each of the two test fuels (see Table 3)—twice with the FTIR analyser's sampling probe connected at the pre cat location, and twice with sampling taking place at the post cat location. Mean values of these repeat measurements were calculated and are presented in the Results section of this paper.

The NH₃ analyser used in the first experiment was an automotive NH₃/NO_x analyzer utilising a chemiluminescence detection method and featured heated sample tubing and measured NH₃ concentrations (0–1,000 ppm) at a frequency of 1 Hz. The FTIR analyser used in the second experiment featured a heated sampling line and pre-filter, and sampled the exhaust gas at a flow rate of 12.0 l/min. The FTIR technique was employed as it permits simultaneous analysis of a wide

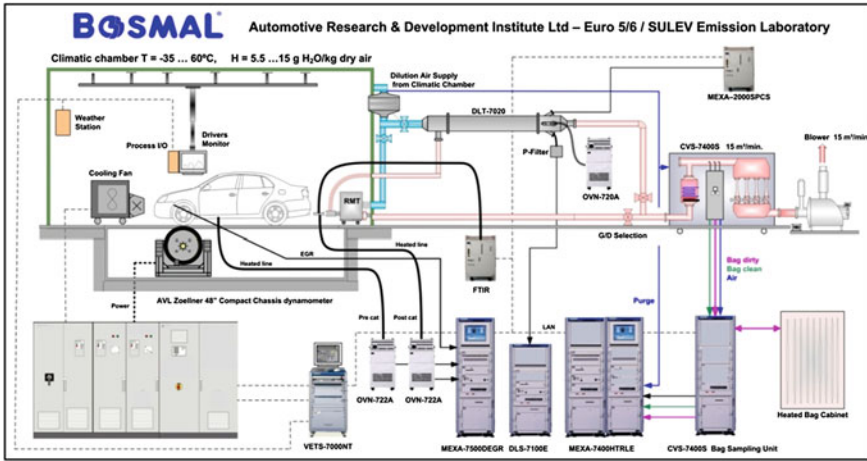


Fig. 2 Schematic overview of the exhaust emission laboratory, showing the chasis dynamometer, the climatic chamber, the various emissions measurements systems and the FTIR analyzer (NH_3/NO_x analyser not shown)

Fig. 3 Internal view of BOSMAL's climatic chamber, showing a vehicle mounted on the chasis dynamometer, together with the windspeed fan



range of chemical compounds present in the exhaust gas. The archiving of spectra at a frequency of 1 Hz permits post-processing to include analysis of additional chemical compounds.



Fig. 4 Exhaust emissions analysers for measurement of emissions of regulated compounds

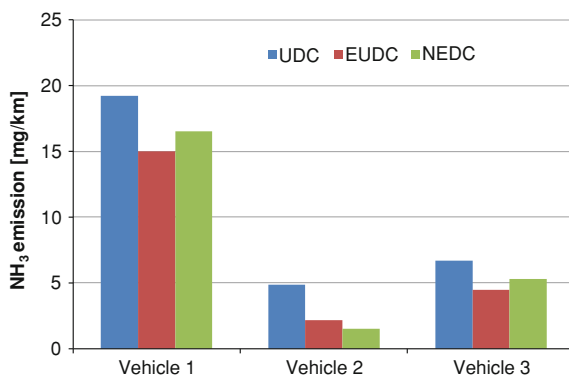
Table 2 Key properties of the petrol used in tests on vehicles 1, 2 and 3

Parameter	Value
Research Octane Number (–)	95.5
Density (kg/dm ³)	0.7535
Benzene content (% v/v)	<1.0
Aromatics (% v/v)	<35
Olefins (% v/v)	<18
Ethanol content (% v/v)	5
Sulfur content (mg/kg)	5.6

Table 3 Key properties of the two petrol fuels used in tests on vehicle 4

Parameter	Fuel A	Fuel B
Research Octane Number (–)	95.0	96.6
Density (kg/dm ³)	751.9	756.0
Benzene content (% v/v)	0.79	0.67
Aromatics (% v/v)	33.7	30.3
Olefins (% v/v)	0.9	10.5
Ethanol content (% v/v)	5.03	10.79
Sulfur content (mg/kg)	<3.0	8.4

Fig. 5 A comparison of ammonia emissions over the NEDC for three different vehicles



3 Results

3.1 Emissions of Ammonia from Three Euro 5 Vehicles

Ammonia was detected in the exhaust of all three test vehicles, albeit in low concentrations. Calculated NH_3 emissions per phase of the NEDC test cycle (UDC and EUDC) are shown in Fig. 5.

The ammonia emissions observed for the three vehicles were generally low—particularly for vehicles 2 and 3. Ammonia emission is known to vary with the driving cycle used for testing [14]. The NEDC is a relatively gentle cycle, with smooth, linear accelerations, and 37 % of the cycle is spent idling. As discussed in [11], harsh acceleration, particularly at high speed, can cause substantial NH_3 production. Such driving conditions are not a feature of the NEDC [1], which means lower NH_3 emissions are to be expected. Vehicle 1's higher mileage (and therefore greater catalyst ageing) may have been responsible for the greater emission of NH_3 observed. For each of the three test vehicles, emissions were noticeably higher during the first (cold start) phase of the cycle (the UDC), but emissions were of the same order of magnitude for the EUDC phase in all three cases.

3.2 Detailed Investigation of Ammonia Emissions from a Euro 5 Vehicle

Ammonia was detected in the exhaust of vehicle 4 at the post cat sampling location. At the pre cat sampling location, very low concentrations were detected, but for the most part these concentrations were close to the FTIR analyser's limit of detection. The second-by-second traces for both fuels (Figs. 6 and 7) were similar and showed a characteristic peak early on in the cycle (Fig. 8), followed by low fluctuating concentrations until the final, high speed part of the cycle, where concentrations were relatively high and sustained. When the FTIR analyser was

Fig. 6 Second-by-second ammonia emissions for vehicle 4 when operating on fuel 1, corrected for background concentrations

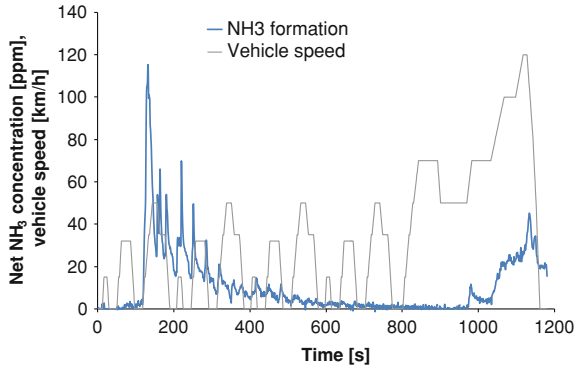


Fig. 7 Second-by-second ammonia emissions for vehicle 4 when operating on fuel 2, corrected for background concentrations

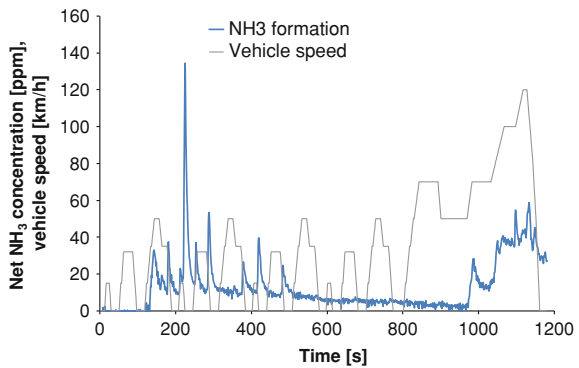
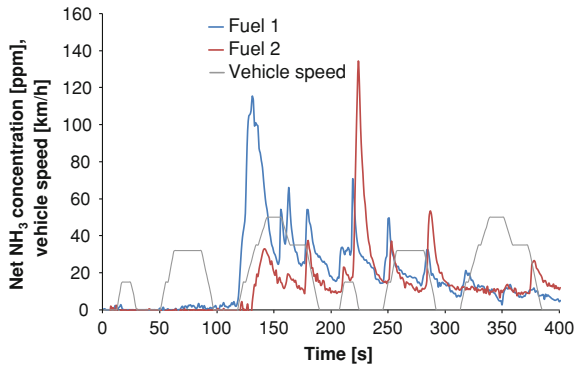


Fig. 8 Second-by-second ammonia emissions over the first 400 s of the UDC for vehicle 4 when operating on fuels 1 and 2, corrected for background concentrations



connected to the pre cat sampling location, very low concentrations of ammonia were detected in the exhaust gas (Fig. 9); post cat concentrations of NH_3 were up to almost two orders of magnitude higher than pre cat NH_3 concentrations and there was no correlation between these concentrations during the test cycle, for either fuel (Fig. 9). (This large difference in pre and post cat NH_3 concentrations, and the lack of correlation between pre and post cat NH_3 levels have been reported

Fig. 9 A scatterplot of pre and post cat NH_3 concentrations for vehicle 4 when operating on fuels 1 and 2

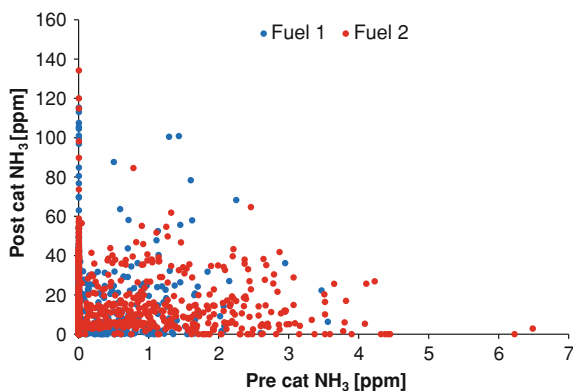
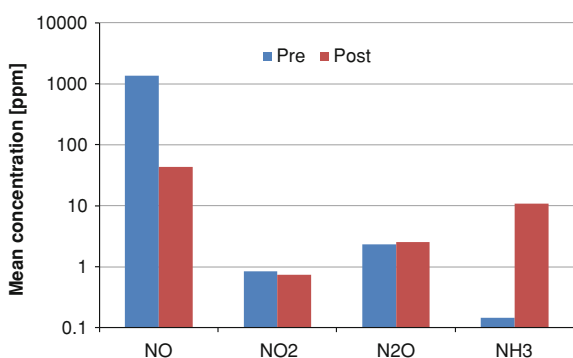


Fig. 10 Mean pre and post cat RNC species concentrations over the NEDC for vehicle 4 when operating on fuel 1 (note the \log_{10} scale)



previously [1, 4], and briefly discussed in [1]). The post cat NH_3 concentration was found not to correlate with vehicle speed or instantaneous acceleration. There was some indication that gear shifts coincided with small surges of NH_3 , but the magnitude of these surges varied greatly.

An examination of the mean concentrations of RNCs over the duration of the cycle for both fuels, at both the pre and post cat sampling locations revealed significant changes in the concentrations of NO and NH_3 , but insignificant changes in the concentrations of NO_2 and N_2O , as shown in Figs. 10 and 11. It would appear that the elimination of NO over the TWC came at the expense of the increase in the concentration of NH_3 . This trade-off hypothesis is supported by comparing the observed post cat concentrations of NH_3 and NO_x , which showed trade-off-like behaviour, as shown in Figs. 12 and 13 (i.e. when NH_3 concentrations were high, NO_x concentrations were low, and vice versa), testifying to the existence of two distinct regimes (oxidising or reducing conditions) within the TWC.

In addition to RNCs, concentrations of CO and THC were also measured when the FTIR analyser was connected to the pre cat sampling location. Using this data, pre cat concentrations of CO, NO, NO_2 , N_2O , NO_x , THC and CH_4 were plotted against post cat concentrations of NH_3 to check for correlations between

Fig. 11 Mean pre and post cat RNC species concentrations over the NEDC for vehicle 4 when operating on fuel 2 (note the log₁₀ scale)

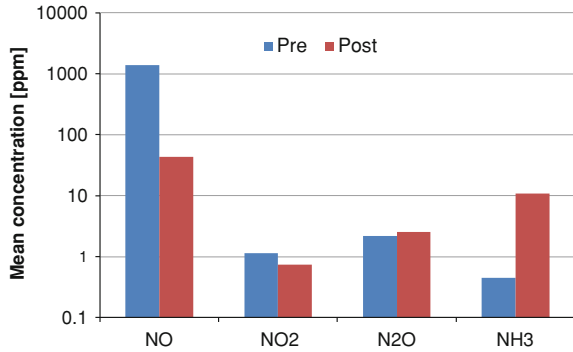
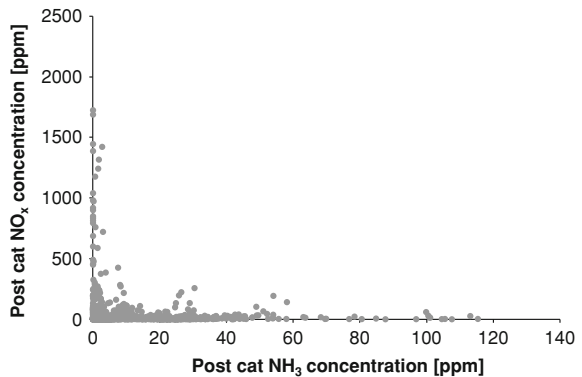


Fig. 12 A scatterplot of post cat NO_x concentrations against post cat NH₃ concentrations for fuel 1



concentrations of these pollutants Various weak correlations between pre cat gas concentrations and ammonia formation have been reported (briefly reviewed in [4]). In contrast to these previous discussions, data obtained from the experimental programme described in this paper failed to yield any meaningful correlations. However, the relationship between concentrations of the two pollutants did vary. In the case of methane (Fig. 14), NH₃ formation was high only where the pre cat methane concentration was high; whereas in the case of nitrogen monoxide (Fig. 15), NH₃ concentrations took a range of values, both near-zero and higher, for a wide range of NO concentrations and the maximum NH₃ concentration in fact appeared to decrease with pre cat NO_x concentration.

On the basis of the concentrations of NO, NO₂, N₂O and NH₃ (the reactive nitrogen compounds, RNCs), it is possible to calculate an RNC balance, specifically the proportion of RNCs in the exhaust gas which are in the form of NH₃. Such a calculation can be performed in the following way:

$$RNC \text{ as } NH_3 = \frac{[NH_3]}{\sum [NO], [NO_2], [N_2O], [NH_3]}$$

Fig. 13 A scatterplot of post cat NO_x concentrations against post cat NH₃ concentrations for fuel 2

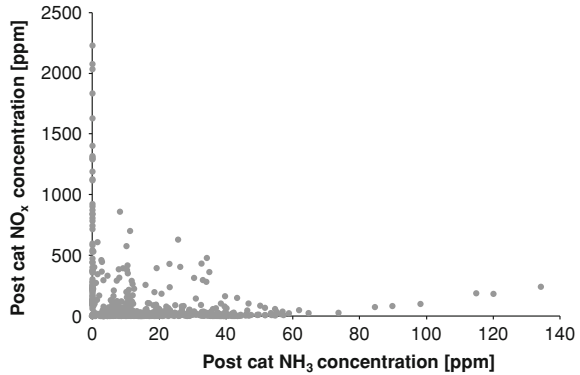


Fig. 14 A scatterplot of pre cat CH₄ concentrations against post cat NH₃ concentrations for fuels 1 and 2; the dashed line shows the upper boundary of NH₃ emissions increasing with increasing pre cat CH₄ concentration

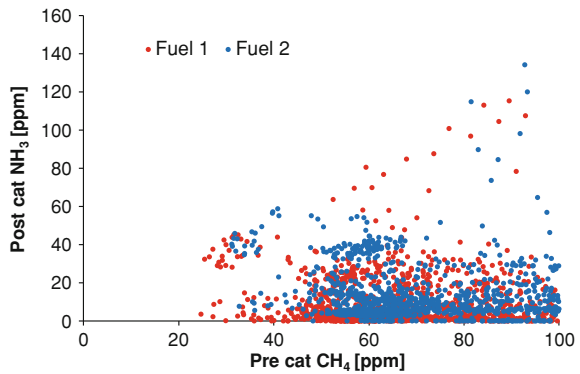
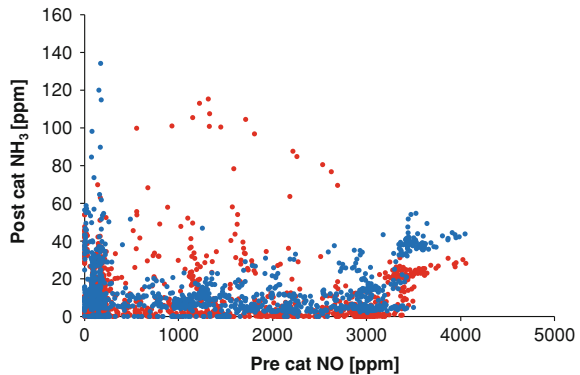
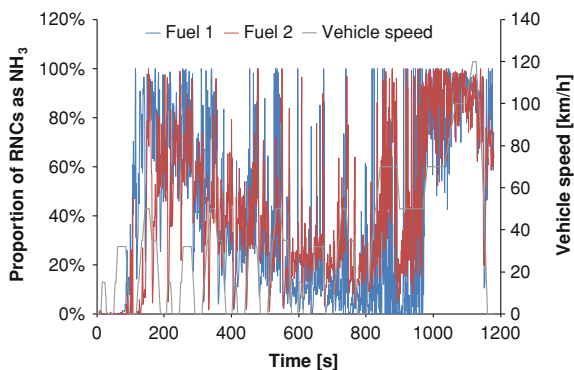


Fig. 15 A scatterplot of pre cat NO concentrations against post cat NH₃ concentrations for fuels 1 and 2; the dashed line shows the upper boundary of NH₃ emissions decreasing with increasing pre cat NO concentration



where $[X]$ is the instantaneous concentration of species X at any given time during the test cycle. Figure 16 shows the second by second RNC as NH₃ values for fuels 1 and 2. The proportion was very low ($<5.0\%$) for both fuels until around 90s, whereupon the NH₃ proportion started to take higher values. Indeed, a rapid surge was observed for both fuels, with occurred earlier for fuel 1 than for fuel 2

Fig. 16 The proportion of the measured concentrations of RNCs occurring as NH_3 as a function of time, for fuels 1 and 2



(probably due to the ethanol content of the fuel). This surge is indicative of TWC light-off; before light-off was achieved, NH_3 was not formed in significant quantities. Indeed, there are some indications that a critical temperature exists (variously reported as 320 °C [20] and around 300 °C [11], below which formation of NH_3 is extremely limited. Following this early surge, for the remainder of the cycle the proportion fluctuated rapidly and chaotically, ranging from close to 0–100 %. Over the duration of the NEDC, for fuels 1 and 2, 41.2 and 42.3 % (respectively) of the RNCs emitted were in the form of NH_3 (by concentration). Of the four RNCs measured, only two are regulated (NO and NO_2 , together as NO_x), and it is significant that unregulated NH_3 , made up around 40 % of the RNCs emitted. If control of RNCs is desired, this would require an emissions limit for NH_3 as well as for NO_x , since the proportion of RNCs emitted as NH_3 is non-trivial [9].

4 Conclusions

Emissions of ammonia from modern vehicles are generally low in comparison to emissions of other (regulated) compounds, but are quantifiable in a laboratory environment. Results presented here are low, but may represent a best case scenario. Accurate, repeatable measurement of ammonia is difficult to achieve [4]. The methodology for quantifying emissions of ammonia from automotive sources has yet to be perfected and research on test methodologies themselves is also a research priority. Repeating the same test procedure with vehicles featuring somewhat larger engines, over a more aggressive driving cycle and under less favourable conditions (lower ambient temperature, higher humidity, higher dynamometer loading coefficients) would likely lead to significantly higher emissions of NH_3 . The in-depth analysis of ammonia emission from vehicle 4 revealed emission of NH_3 to account for a substantial proportion of the RNC emissions, but failed to reveal any correlation between the pre cat exhaust gas composition and formation of ammonia. Similarly, no correlation between vehicle speed or acceleration was observed in this study. The proportion of RNCs

occurring as ammonia was of the order of 40 %—on the lower end of the 40–80 % range reported in [9] (although those authors' figures did not include the period before TWC light-off occurred), but somewhat might than the 22–27 % reported in a study which monitored RNC concentrations at roadside [21]. Catalyst design naturally focuses on the efficient elimination of regulated compounds, but greater consideration should perhaps be given to the influence of catalyst precious metals, fluid dynamics, thermal effects, etc. on the formation of unregulated species such as ammonia [1, 4]. As emissions limits for regulated compounds slowly approach the limits of detection, emissions of as-yet unregulated yet harmful compounds will increasingly come into focus as an air quality issue. Increasing concern over particulate matter concentrations, together with the pathways through which secondary PM can be formed, will ensure ammonia remains in an elevated position on the air quality agenda. In turn, this will surely cause increasing attention to be paid to ammonia emissions from vehicles.

References

1. Bielaczyc P, Szczotka A, Swiatek A, Woodburn J (2012) A Comparison of ammonia emission factors from light-duty vehicles operating on gasoline, liquefied petroleum gas (LPG) and compressed natural gas (CNG). *SAE Int J Fuels Lubr* 5(2):751–759. doi:[10.4271/2012-01-1095](https://doi.org/10.4271/2012-01-1095)
2. Whitehead J, Longley ID, Gallagher MW (2007) Seasonal and diurnal variation in atmospheric ammonia in an urban environment measured using a quantum cascade laser absorption spectrometer. *Water Air Soil Pollut* 183:317–329
3. Harkins J, Nicksic S (1967) Ammonia in auto exhaust. *Environ Sci Technol* 1(9):751–752
4. Bielaczyc P, Swiatek A, Woodburn J (2011) A technical discussion of the emission of ammonia from SI vehicles fitted with three-way catalysts. *Combustion Engines* (144):63–71
5. Erisman J, Schaap M (2004) The need for ammonia abatement with respect to secondary PM reductions in Europe. *Environ Pollut* 129:159–163
6. Protocol to the 1979 Convention on Long-Range Transboundary Air Pollution to abate Acidification, Eutrophication and Ground-level Ozone. United Nations Economic Commission for Europe, 1999. Available online: <http://www.unece.org>
7. Directive 2001/81/EC of the European Parliament and of the Council of 23 October 2001 on national emission ceilings for certain atmospheric pollutants. *Off J Eur Commun L* 309/22, 27.11.2001
8. Cape J, Tang YS, van Dijk N, Love L, Sutton MA, Palmer SC (2004) Concentrations of ammonia and nitrogen dioxide at roadside verges, and their contribution to nitrogen deposition. *Environ Pollut* 32(3):469–478
9. Heeb N, Saxer CJ, Forss A-M, Brühlmann S (2008) Trends of NO-, NO₂-, and NH₃-emissions from petrol-fuelled Euro-3- to Euro-4-passenger cars. *Atmos Environ* 42:2543–2554
10. Heeb N, Saxer CJ, Forss A-M, Brühlmann S (2006) Correlation of hydrogen, ammonia and nitrogen monoxide (nitric oxide) emissions of petrol-fueled Euro-3 passenger cars at transient driving. *Atmos Environ* 40:3750–3763
11. Heeb N, Forss A-M, Brühlmann S, Lüscherb R, Saxer CJ, Huga P (2006) Three-way catalyst-induced formation of ammonia—velocity- and acceleration-dependent emission factors. *Atmos Environ* 40:5986–5997

12. Perrino C, Catrambone M, Di Menno Di Bucchianico A, Allegrini I (2002) Gaseous ammonia in the urban area of Rome, Italy and its relationship with traffic emissions. *Atmos Environ* 36(34):5385–5394
13. Matsumoto R, Umezawa N, Karaushi M, Yonemochi S-I, Sakamoto K (2006) Comparison of ammonium deposition flux at roadside and at an agricultural area for long-term monitoring: emission NH_3 from vehicles. *Water Air Soil Pollut* 173:355–371
14. Durbin TD, Wilson RD, Norbeck JM, Wayne Miller J, Huai T, Rhee SH (2002) Estimates of the emission rates of ammonia from light-duty vehicles using standard chassis dynamometer test cycles. *Atmos Environ* 36(9):1475–1482
15. Durbin T, Pisanoa JT, Younglove T, Sauera CG, Rhee SH, Huai T, Wayne Miller J, MacKay GI, Hochhauser AM, Ingham MC, Gorse RA, Beard LK, DiCicco D, Thompson N, Stradling RJ, Rutherford JA, Uihlein J (2004) The effect of fuel sulfur on NH_3 and other emissions from 2000–2001 model year vehicles. *Atmos Environ* 38:2699–2708
16. Mejia-Centeno I, Martínez-Hernández A, Fuentes GA (2007) Effect of low-sulfur fuels upon NH_3 and N_2O emission during operation of commercial three-way catalytic converters. *Top Catal* 42–43
17. Huai T, Durbin T, Younglove T, Scora G, Barth M, Norbeck JM (2005) Vehicle specific power approach to estimating on-road NH_3 emissions from light-duty vehicles. *Environ Sci Technol* 39:9595–9600
18. Baum MM, Kiyomiya ES, Kumar S, Lappas AM, Kapinus VA, Lord HC (2001) Multicomponent remote sensing of vehicle exhaust by dispersive absorption spectroscopy. 2. Direct on-road ammonia measurements. *Environ Sci Technol* 35(18):3735–3741
19. Bielaczyc P, Szczotka A, Woodburn J (2011) Development of vehicle exhaust emission testing methods—BOSMAL's new emission testing laboratory. *Combustion Engines* 144:3–12
20. Mejía-Centeno I, Castillo S, Fuentes GA (2012) Enhanced emissions of NH_3 , N_2O and H_2 from a Pd-only TWC and supported Pd model catalysts: Light-off and sulfur level studies. *Appl Catal B* 119–120:234–240. doi:[10.1016/j.apcatb.2012.02.030](https://doi.org/10.1016/j.apcatb.2012.02.030)
21. Bishop GA, Peddle AM, Stedman DH, Zhan T (2010) On-road emission measurements of reactive nitrogen compounds from three California cities. *Environ Sci Technol* 44(9):3616–3620

A Study on Regulated and Unregulated Emissions from a Set of Five Gasoline and Ethanol Fueled Motorcycles

Renato Penteado, Luiz Carlos Daemme, Jürgen Krahl
and Fátima Zotin

Abstract The objective of this study was to investigate regulated and unregulated emissions from four motorcycles fueled with gasoline and one flex fuel motorcycle fueled with three different gasoline/ethanol blends. Regulated emissions (CO, HC, and NO_x) have been measured with 7000 series Horiba benches. Unregulated emissions (formaldehyde, acetaldehyde and ammonia) were measured with a SESAM series AVL Fourier Transform Infrared Analyzer (FTIR). Tests were conducted over a chassis dynamometer according to the 97/24/EC drive cycle. Pre and post catalytic (pre-cat and post-cat) converter data were collected. The results showed that catalytic converters designed to reduce regulated emissions from gasoline-powered motorcycles produce ammonia emissions as a by-product of catalytic conversion. The results regarding pre-cat and post-cat conversion aldehydes were analyzed and discussed. The main conclusion was that catalytic

F2012-A04-016

R. Penteado (✉) · L. C. Daemme
Institute of Technology for Development—LACTEC, Curitiba, Brazil
e-mail: renato@lactec.org.br, renato@pkconsult.com.br

L. C. Daemme
e-mail: luiz.carlos@lactec.org.br

R. Penteado
P&K Consulting, Curitiba, Brazil

J. Krahl
Coburg University of Applied Sciences and Arts, Coburg, Germany
e-mail: juergen.krahl@hs-coburg.de

F. Zotin
State University of Rio de Janeiro—UERJ, Rio de Janeiro, Brazil
e-mail: fzotin@uerj.br

conversion reduces aldehydes and regulated emissions on the tailpipe but increases ammonia emission levels significantly.

Keywords Emissions · Ammonia · Aldehydes · Motorcycle · Flex fuel

1 Introduction

Due to worldwide environmental constraints the control of vehicle emissions is becoming increasingly stringent. Regulated emissions limits have been reduced and the role of unregulated vehicle emissions is becoming more important. Aldehydes such as formaldehyde and acetaldehyde and ammonia have received special attention recently.

Regarding two-wheeled vehicles, the production and sales in the BRIC countries (Brazil, Russia, India, and China) have consistently increased in the last decade, mainly due to the economic growth. In China, the motorcycle industry produced and sold 26.69 and 26.59 million motorcycles, respectively, in 2010 [1]. In India, the two-wheeler production in 2010 was 11.79 million units [2]: total sales stood at 1.36 million units in the month of May 2012 compared to 1.22 million units in the same period last year registering a growth of 10.57 % [3]. In Brazil more than 2 million motorcycles were sold in 2011 including units equipped with a flex fuel engine, which can be fueled with gasoline, ethanol, or a gasoline/ethanol blend of any proportion. The regulated emissions limits in Brazil have been significantly reduced since 2009. Because of the introduction of new limits, motorcycles have been equipped with electronic injection systems and three-way catalytic converters for emissions abatement. However, these converters may also produce undesired reactions such as the formation of odoriferous hydrogen sulfide and ammonia [4].

To evaluate the performance of related catalytic converters, a number of tests were done in five different motorcycles. Regulated emissions such as CO, HC, and NO_x were measured. Unregulated emissions such as formaldehyde, acetaldehyde and ammonia were analyzed as well, due to their impact on the environment and on human health.

Regarding ammonia, some authors have referred to the importance of measuring this emission in the early 1990s [5]. In 2012, Penteadó and Daemme reported the emissions results from motorcycles fueled with gasoline. A direct correlation was observed between the increase in ammonia emissions and the exhaust gas temperature. The authors concluded that ammonia emissions are not negligible and suggested that further studies should be carried out covering other fuels such as ethanol [6].

This paper summarizes the emissions results from four motorcycles fueled with gasoline and presents results from a flex fuel motorcycle fueled with three ethanol/gasoline blends.

Table 1 Motorcycles specification

Motorcycle	Engine displacement (cm ³)	Emission regulation	Fuelling system type	Catalyst	Production year
BK1	300	Euro III	EFI	Yes	2010
BK2	125	Euro III	EFI	Yes	2009
BK3	125	Euro III	EFI	Yes	2010
BK4	125	Euro I	Carburetor	No	2003
BK5	150	Euro III	EFI	Yes	2011

2 Methodology

2.1 Test Procedure and Instrumentation

Tests were conducted over a chassis dynamometer according to the 97/24/EC drive cycle which is divided into six primary modules and one extra-urban cycle. Engines with up to 150 cm³ displacement were tested according to the 97/24/EC drive cycle and submitted only to the six primary modules. Engines with displacement above 150 cm³ were tested according to the 97/24/EC drive cycle and submitted to the six primary modules and one extra-urban cycle.

Regulated emissions (CO, HC, and NO_x) were measured with 7000 series Horiba benches. Unregulated emissions were measured with a SESAM series AVL Fourier Transform Infrared Spectroscopy (FTIR) analyzer. The catalytic converter efficiency was calculated by comparing the FTIR pre-cat and post-cat converter measurements. A minimum of three tests was performed for each analyzed situation.

2.2 Motorcycle Specifications

The technical data on the motorcycles are summarized in Table 1. It is important to point out that BK5 is a flex fuel engine motorcycle.

2.3 Fuel Specification

Four motorcycles were fueled with gasoline blended with 22 % anhydrous ethanol (E22) by volume, produced according to the Brazilian standard ABNT NBR 8689 [7]. One flex fuel motorcycle (BK5), was tested with different gasoline/ethanol blends: E22 (22 % ethanol and 78 % gasoline), E61 (50 % E22 and 50 % hydrous ethanol) and E100 (100 % hydrous ethanol).

Table 2 Regulated emissions (g/km)

Motorcycle	THC	SD	CO	SD	NO _x	SD	CO ₂	SD
BK 01	0.178	0.011	2.971	0.398	0.100	0.004	78.071	1.294
BK 02	0.241	0.012	0.893	0.078	0.085	0.007	51.291	1.710
BK 03	0.200	0.016	0.809	0.044	0.117	0.006	59.534	0.655
BK 04	0.899	0.036	11.698	0.300	0.103	0.001	36.289	0.616

3 Results

The results are presented in two blocks. The first block covers only gasoline fueled motorcycles (BK1 to BK4). The second block covers the gasoline/ethanol-fueled motorcycle (BK5).

3.1 Motorcycles BK1 to BK4 (Gasoline Fueled)

Table 2 presents the regulated emissions, obtained in tests according to 97/24/EC.

The unregulated emissions from motorcycles BK1 and BK2 can be seen in Fig. 1. Pre-cat and tailpipe measurements were performed and the influence of the catalyst on the emissions formation and reduction can be clearly observed.

Differently from the aldehydes, there was an important increase in the ammonia concentration after the catalytic converter, indicating that ammonia is generated at the catalyst. This phenomenon was identified by others authors who studied the emissions of vehicles equipped with TWC converters [8–11]. Ammonia emission was associated with a secondary pollutant of the de-NO_x process. Catalyst temperature and air-to-fuel ratio (λ) were found to be the more important parameters that affect the extent of NH₃ formation. According to Heeb et al. [12], NH₃ is formed in TWCs under reducing conditions ($\lambda < 1$), only after the catalyst light-off temperature is reached. NH₃ selectivities increase and become highest at moderate catalyst temperatures (below 300 °C), normally found in urban driving conditions. For motorcycles BK3 and BK4, measurements of unregulated emissions were taken only after the catalyst. The results are shown in Fig. 2.

3.2 Motorcycle BK5 (Gasoline/Ethanol Fueled)

Motorcycle 5 is Euro III category equipped with catalytic converter and a flex fuel engine fueled with E22; E61 and E100. To facilitate data analysis, the results are presented by type of fuel.

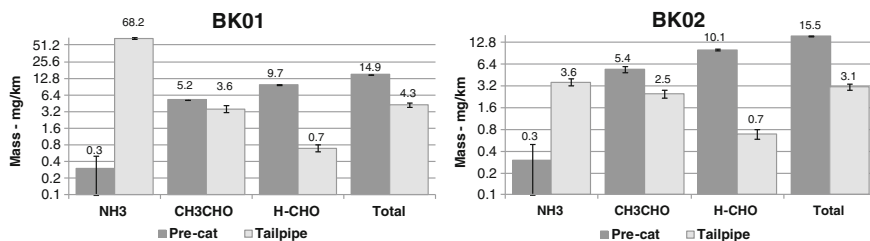


Fig. 1 Unregulated emissions from BK1 and BK2, pre-cat and post-cat

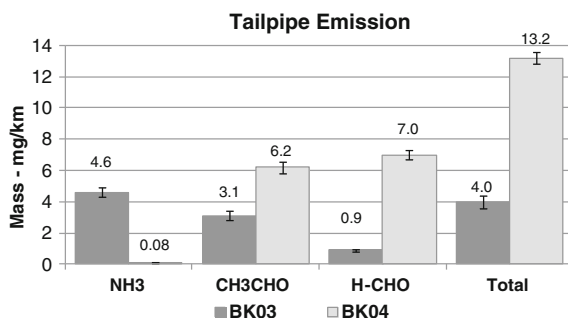


Fig. 2 Unregulated tailpipe emissions from BK3 and BK4

Table 3 Emissions with gasoline E22 (g/km)

	THC	CO	NOx	CO ₂
Average	0.191	1.056	0.066	50.629
SD	0.004	0.071	0.004	0.309

3.2.1 Fuel E22

Tables 3 and 4 present the regulated and unregulated emissions from E22.

Figure 3, which represents the emissions of acetaldehyde, shows that there is a difference between the emissions before and after the catalyst with the post-cat emissions being 71.5 % lower than the pre-cat values. Another important point to consider is the occurrence of increased post-catalyst emissions at some modes. This increase is expressed more significantly early in the cycle, around the first 109 s. This may be explained by two reasons. First, at the beginning of the cycle the engine is still cold and incomplete combustion may occur, especially with the increase of ethanol content in the fuel. This is most apparent when analyzing Fig. 5—and, especially, Fig. 5—5 which shows a sharp increase of acetaldehyde, mostly for pre-cat emissions. Second, in the starting phase the catalyst is cold and

Table 4 Unregulated emissions with gasoline E22 (mg/km)

BK5	Pre-cat emission			Tailpipe emission		
	Acetaldehyde	Formaldehyde	Total aldehydes	Acetaldehyde	Formaldehyde	Total aldehydes
Average	4.718	8.035	12.754	3.459	0.815	4.275
SD	0.055	0.083	0.103	0.166	0.058	0.157

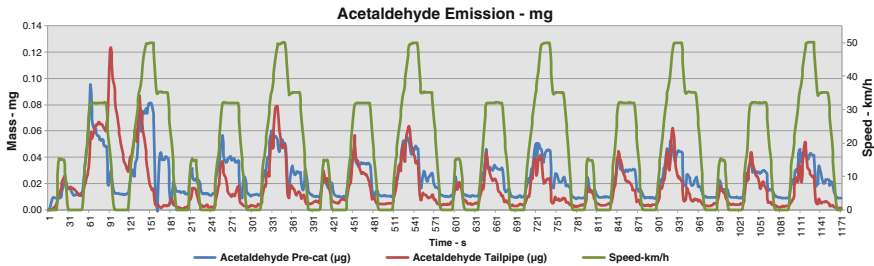


Fig. 3 Acetaldehyde emissions pre-cat and post-cat catalyst E22

unable to convert pollutants. In this case, it is important to note that the exhaust gas contains unconverted hydrocarbons and ethanol among other pollutants. According to the literature [13], the dehydrogenation of ethanol to acetaldehyde at CeO₂, a major component of automotive catalyst material, is favored in the presence of platinum or palladium, noble metals also traditionally used in these catalysts.

The emission of formaldehyde with a reduction of approximately 90 % after the catalyst was observed.

Figure 4 presents pre-cat and post-cat ammonia emissions. In both BK1 and BK2, the ammonia emissions improve after the catalytic conversion.

3.2.2 Fuel E61

Tables 5 and 6 present regulated and unregulated emissions from E61.

Figure 5—shows the acetaldehyde emission during the driving cycle with the post-cat emissions being approximately 65 % of pre-cat values. Similarly to E22, at the beginning of the test, the post-cat emissions are usually higher compared to the pre-cat measurements.

Figure 6 shows a reduction in post-cat formaldehyde emissions of approximately 86 % and Fig. 7 presents pre-cat and post-cat ammonia emissions.

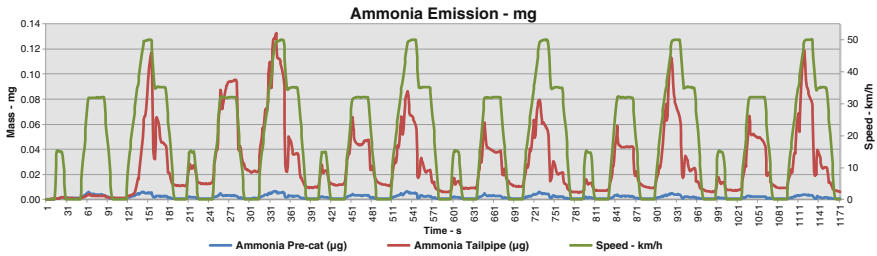


Fig. 4 Ammonia emissions pre-cat and post-cat catalyst E22

Table 5 Emissions with gasoline E61 (g/km)

	THC	CO	NOx	CO ₂
Average	0.130	0.693	0.095	49.711
SD	0.008	0.047	0.003	0.388

Table 6 Unregulated emissions with gasoline E61 (mg/km)

BK5	Pre-cat emission			Tailpipe emission		
	Acetaldehyde	Formaldehyde	Total aldehydes	Acetaldehyde	Formaldehyde	Total aldehydes
Average	9.509	8.846	18.355	6.197	1.122	7.319
SD	0.160	0.114	0.216	0.100	0.091	0.134

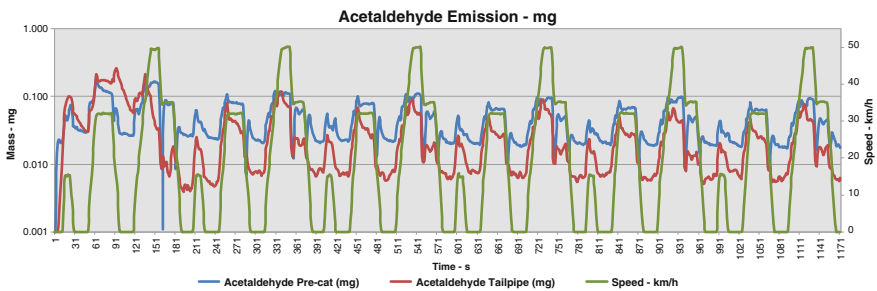


Fig. 5 Acetaldehyde emissions pre-cat and post-cat catalyst E61

3.2.3 Unregulated Emissions: E100 Fuel

Tables 7 and 8 present regulated and unregulated emissions from E100.

Figure 8 shows the E100 acetaldehyde emissions. In this case, the converter efficiency was approximately 63 %.

A formaldehyde conversion rate of approximately 78 % was measured; the test data are shown in Fig. 9. Formaldehyde emissions were observed to increase directly with the ethanol content, even at low temperatures. As pointed out earlier,

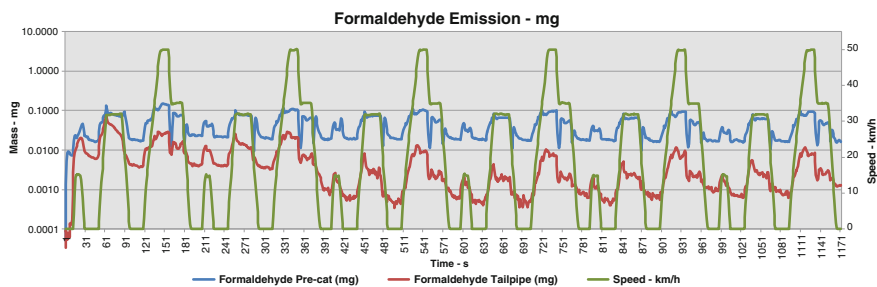


Fig. 6 Formaldehyde emissions pre-cat and post-cat E61

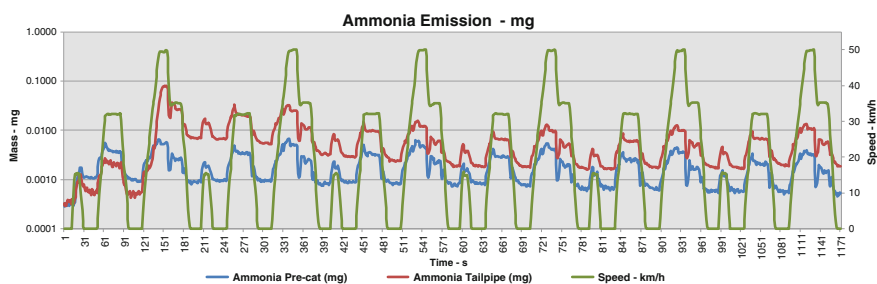


Fig. 7 Ammonia emissions pre-cat and post-cat E61

Table 7 Emissions with E100 (G/Km)

	THC	CO	NO _x	CO ₂
Average	0.252	1.048	0.070	48.818
SD	0.020	0.091	0.003	0.394

Table 8 Unregulated emissions with ethanol E100 (mg/km)

BK5	Pre-cat emission			Tailpipe emission		
	Acetaldehyde	Formaldehyde	Total aldehydes	Acetaldehyde	Formaldehyde	Total aldehydes
Average	49.826	19.532	69.358	31.472	4.345	35.817
SD	0.718	0.118	0.724	0.590	0.460	0.787

this may be because the catalyst is cold and presents low reactivity for oxidation reactions. As a consequence, the formaldehyde is not appropriately converted inside the catalyst.

Ammonia formation has been attributed to the reactions of NO with H₂ [14]. Hydrogen can be formed from hydrocarbons via steam reforming or from carbon monoxide (CO) and water (H₂O) via the water gas-shift reaction [15, 16]. The

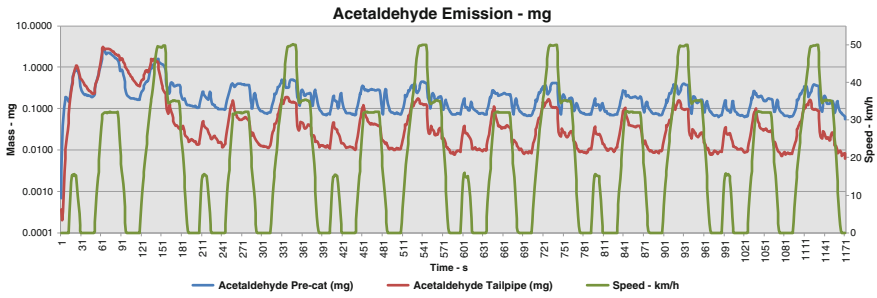


Fig. 8 Acetaldehyde emissions pre-cat and post-cat E100

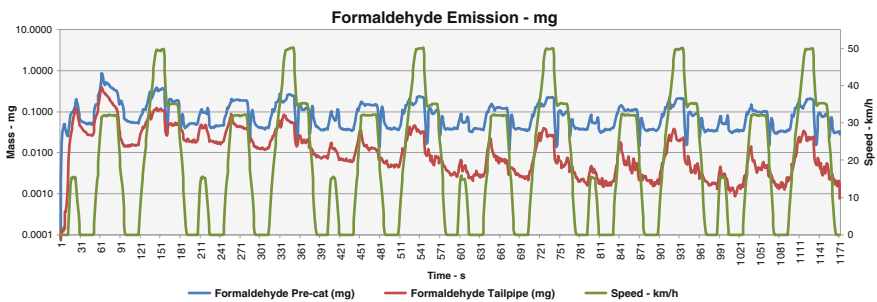


Fig. 9 Formaldehyde emissions pre-cat and post-cat E100

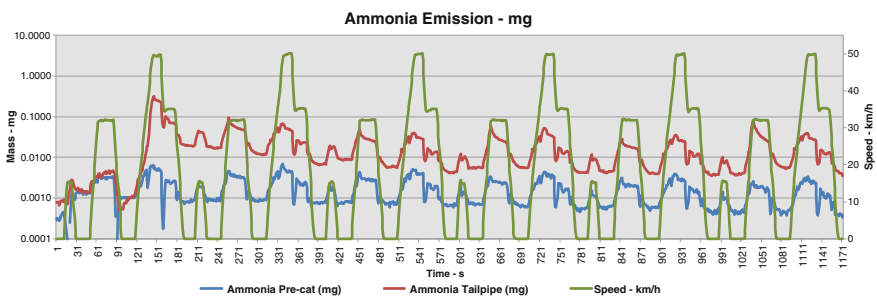


Fig. 10 Ammonia emissions pre-cat and post-cat E100

hydrogen produced by chemical reaction in the catalyst may react itself with NO or NO₂ (Fig. 10).

Le Phuc et al. [17], studying NO_x removal efficiency of Pt/Ba/Al model catalyst using cycling condition (lean/reach) with H₂ as reducing agent, identified that the NO_x reduction selectivity strongly depends on the hydrogen content which was introduced in the rich pulses. NH₃ is emitted when H₂ is present. Furthermore, the ammonia concentration increases with the amount of hydrogen.

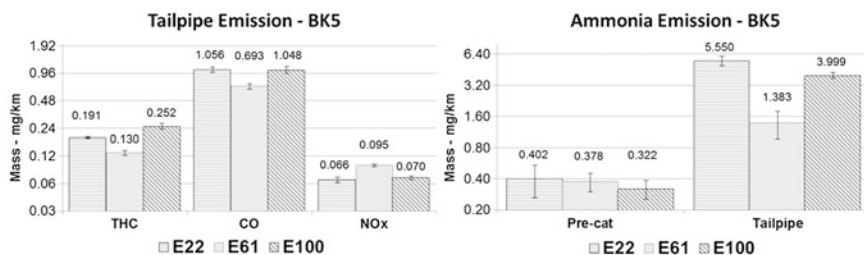


Fig 11 Regulated emissions (THC, CO and NOx) and unregulated emissions (Ammonia)

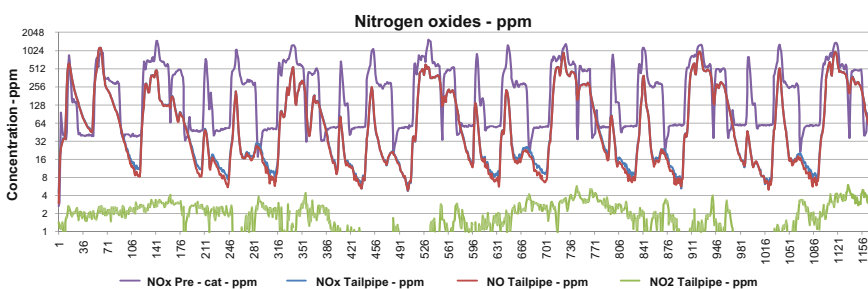


Fig. 12 NOx, NO and NO₂ pre-cat and tailpipe emissions for E61

Considering that ethanol can lead to hydrogen by partial oxidation or water–gas shift reaction [18], a comprehensive study needs to be done, including a thermodynamical analysis to assess the hydrogen impact of increasing ethanol content in the fuel that may induce higher ammonia emissions.

Regarding legislated emissions, Fig. 11 shows that small changes occur for CO and NOx emissions when E22 and E100 data are compared. However for the E61 blend, those differences are significant. This change may be due to a non-linear fuel behavior or due to the engine calibration, which is usually determined by the manufacturer. As well as in BK1 and BK2, an important increase in the ammonia concentration after the catalytic converter was observed.

As shown in Fig. 12, the tailpipe NOx emissions for E61 consist mainly of NO.

4 Conclusions

This study evaluated the regulated and unregulated emissions from five motorcycles and found that the effects of the operating conditions and the catalyst on these emissions are significant.

Regarding the aldehydes, acetaldehydes and formaldehydes had different behaviors inside the catalyst. Two aspects emerged from this analysis. First,

considering standard operation, it appears that the catalyst is effective in the conversion of formaldehyde (about 90 %) regardless of the type of fuel. However, for acetaldehyde, it appears that the increase in the ethanol content of the fuel is accompanied by a significant increase in emissions. This may be related to increased formation of acetaldehyde, probably via the dehydrogenation reaction of unconverted ethanol during the combustion process.

The second aspect concerns the beginning of the test cycle, when the catalyst is still cold. Under this condition, increased formation of aldehydes occurs. The combustion process can be compromised due to a high level of unconverted ethanol in the combustion chamber. Because of the low temperature, oxidation reactions are not favored, resulting in lower catalyst conversion. Furthermore, the dehydrogenation reaction of ethanol can take place at temperatures from 200 °C or at relatively low temperatures and seems to promote the formation of acetaldehyde under these conditions.

Regarding ammonia, motorcycles equipped with three-way catalytic converters presented a significant increase in emissions in the tailpipe exhaust gases. A direct correlation was observed between the increase in ammonia emissions and the exhaust gas temperature. At the moment, these effects cannot be explained on the basis of sound data. Future research may increase our understanding so as to optimize catalytic converters for high-ethanol fuels.

Nevertheless, the catalytic converters applied to all the tested motorcycles presented good efficiency regarding regulated emissions (THC, CO, and NO_x). The nonlinear results (CO and NO_x) obtained with E61 may be due to the engine calibration provided by the engine manufacturer.

Additional studies should be carried out covering different after-treatment exhaust gas devices and new motorcycle models. The authors suggest further research regarding the ammonia formation mechanism and emissions reduction catalytic converters.

Acknowledgments The authors acknowledge the Brazilian Ministry of Science and Technology (MCT), the Brazilian National Council for Scientific and Technological Development (CNPq), law number 8010/1990, Petrobras, and the staff of the Lactec Automotive Laboratory (LEME) for providing support for this work.

References

1. You A (2011) China's motorcycle industry recovers slowly in 2010. China automotive review. <http://www.chinaautoreview.com/pub/CARArticle.aspx>. Accessed 19 June 2012
2. SIAM—Society of Indian automobile manufacturers. Domestic sales trends. <http://www.siamindia.com/scripts/domestic-sales-trend.aspx>. Accessed 19 June 2012
3. Mahavir (2012) Indian motorcycles sales figures for May 2012, BikeAdvice. <http://bikeadvice.in/indian-bikes-sales-figures-2012/>. Accessed 19 June 2012
4. Zhang J (2008) Catalytic converter—Part I of automotive after-treatment system. In: Bowmannz (ed)

5. Faiz A, Weaver CS, Walsh MP (1996) Air pollution from motor vehicles. The World Bank, Washington. ISBN 0-8213-3444-1
6. Penteado R; Daemme LC (2012) An experimental investigation on regulated and unregulated emissions from four 4-stroke gasoline-powered motorcycle. SAE 12PFL-0392, Detroit
7. ASSOCIAÇÃO BRASILEIRA DE NORMAS TÉCNICAS-ABNT (2006) Light duty vehicles—testing fuels requirements. NBR standard 8689, Rev. 2006
8. Pierson WR, Brachaczek WW (1983) Emissions of ammonia and amines from vehicles on the road. *Environ Sci Technol* 17:757–760
9. Durbin TD, Wilson RD, Norbeck JM, Miller JW, Huai T, Rhee SH (2002) Estimates of the emission rates of ammonia from light-duty vehicles using standard chassis dynamometer test cycles. *Atmos Environ* 36:1475–1482
10. Huai T, Durbin TD, Miller JW, Pisano JT, Sauer CG, Rhee SH, Norbeck JM (2003) Investigation of NH₃ emissions from new technology vehicles as a function of vehicle operating conditions. *Environ Sci Technol* 37:4841–4847
11. Heeb NV, Forss A-M, Brühlmann S, Lüscher R, Saxer CJ, Hug P (2006) Three-way catalyst-induced formation of ammonia: velocity- and acceleration-dependent emission factors. *Atmos Environ* 40:5986–5997
12. Heeb NV, Saxer CJ, Forss AM, Brühlmann S (2008) Trends of NO-, NO₂-, and NH₃-emissions from gasoline-fueled Euro-3- to Euro-4-passenger cars. *Atmos Environ* 42:2543–2554
13. Silva AM (2006) Efeito da natureza do metal no mecanismo da reação de oxidação parcial do etanol em presença de catalisadores de Pt e Rh suportados em CeO₂. XX Simpósio Ibero-americano de Catálise
14. Livingston C, Rieger P, Winer A (2009) Ammonia emissions from a representative in-use fleet of light and medium-duty vehicles in the California south coast air basin. *Atmos Environ* 43:3326–3333
15. Barbier J, Duprez D (1994) Steam effects in three-way catalysis. *Appl Catal B* 4:105–140
16. Whittington BI, Jiang CJ, Trimm DL (1995) Vehicle exhaust catalysis: I. The relative importance of catalytic oxidation, steam reforming and water-gas shift reactions. *Catal Today* 26:41–45
17. Le Phuc N, Courtois X, Can F, Royer S, Marcot P, Duprez D (2011) *Appl Catal B: Environ* 102:353–361
18. Silva AM, Farias AMD, Costa LOO, Barandas SAPMG, Mattos LV, Fraga MA Noronha FB (2008) Partial oxidation and water gas shift reaction in an integrated system for hydrogen production from ethanol. *Appl Catal A Gen* 334:179–186

Strategies to Control Particulate Emissions of Gasoline Direct Injection Engines

Oliver Berkemeier, Klemens Grieser, Kay Hohenboeken, Evangelos Karvounis and K. Moritz Springer

Abstract In recent years gasoline engine powered vehicles have been improved significantly in many respects. Technical enablers like downsizing, turbocharging, direct fuel injection (DI), and variable valve timing [1, 2] have allowed for a simultaneous reduction of fuel consumption and improvement of vehicle performance. While still operating predominantly in homogeneous mode, modern downsized gasoline direct injection engines still present engineers with a number of technical challenges, of which many will require the highest level of inventiveness to overcome. Currently, great attention is paid to the further reduction of particulate emission. In this paper, potential approaches for controlling particulate emissions from direct injection gasoline engines are presented. The presentation includes methods for reducing combustion generated particulate emission as well as exhaust aftertreatment technology options. Special emphasis is given to the open technical issues accompanying each of the approaches, including the challenge of maintaining the already achieved performance and CO₂ reduction levels.

Keywords Direct injection · Particulate number · Calibration · EU6 · NEDC · GPF

Abbreviations

ATDC After Top Dead Centre
BMEP Break Mean Effective Pressure
BTDC Before Top Dead Centre
CA Crank Angle

F2012-A04-018

O. Berkemeier (✉) · K. Grieser · K. Hohenboeken · E. Karvounis · K. M. Springer
Ford Werke GmbH, Research and Advanced, Cologne, Germany
e-mail: oberkeme@ford.com

CAE	Computer Aided Engineering
CC	Close Coupled
DI	Direct Injection
EOI	End Of Injection
FRP	Fuel Rail Pressure
GDI	Gasoline Direct Injection
GPF	Gasoline Particulate Filter
GTDI	Gasoline Turbo Direct Injection
NEDC	New European Driving Cycle
OEM	Original Equipment Manufacturer
PFI	Port Fuel Injection
PCJ	Piston Cooling Jet
P&E	Performance & Emissions
PN	Particulate Number
PM	Particulate Mass
RPM	Rotations Per Minute
SOI	Start of Injection
TC	Turbo Charger
TWC	Three Way Catalyst
UB	Under Body

1 Introduction

Particulate emission by DI gasoline combustion engines is governed by a very complex system of interacting processes as illustrated by Fig. 1. The influencing factors are as multifaceted as e.g. engine thermal condition, injection and combustion process, oil introduction to the combustion chamber, etc. The control paths which are highlighted in the “cause and effect” diagram are the key elements addressed in this paper and will be categorised under two main subjects: combustion system optimization and after treatment measures.

2 Combustion System Optimization

Compared to Port-Fuel-Injection (PFI) concepts, there is a higher likelihood that conditions favouring soot particle formation may appear in a Direct-Injection (DI) combustion process. This is due to the shorter time available for air/fuel mixing and as well due to potential fuel impingement onto combustion chamber components. Consequently, special attention is required for injector positioning, spray targeting, fuel pressure level [3, 4] and injector flow capability.

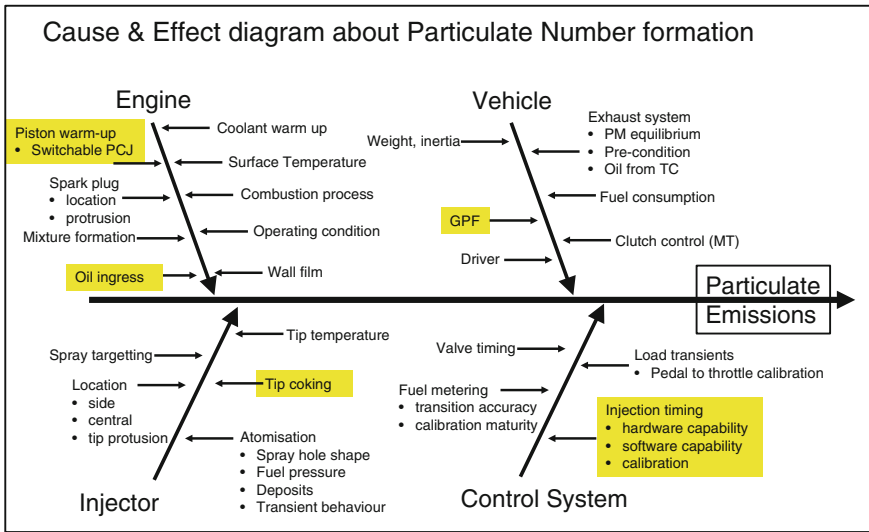


Fig. 1 Cause and effect diagram for particulate emissions

The interaction between the fuel spray and combustion chamber components is even more critical during engine warm-up when the respective surfaces are cold. Particularly in this phase, sophisticated injection strategies are required in order to facilitate improved engine warm up while minimizing spray-wall interaction. As the potential contribution of the engine warm-up phase to the overall particulate emission may be the most significant, development and application of such injection strategies is a key enabler of particulate emission reduction.

In order to illustrate the various effects discussed in this paper, diffusion flame visualization results will be utilized. They are obtained from a transparent engine in various operating conditions. Furthermore, vehicle emission test results from the NEDC cycle will be used to demonstrate the relative impact of the considered control parameters. The vehicle used for these tests was a Ford C-Max equipped with a 1.6l GTDI (Ecoboost) engine. Both, the transparent engine and the engine of the test vehicle were equipped with a centrally mounted DI system.

2.1 Component and Fuel Temperature

As already introduced above, the warm-up phase has the most significant influence on overall soot formation. This is mainly linked to the cold combustion chamber surfaces, on which fuel films may form if fuel spray impinges. This fuel film is not evaporating quickly enough to mix with the available air in time for being consumed by the propagating homogeneous premixed flame front. Instead, it burns later within a slow diffusion flame. Soot is usually formed in rich diffusion flames

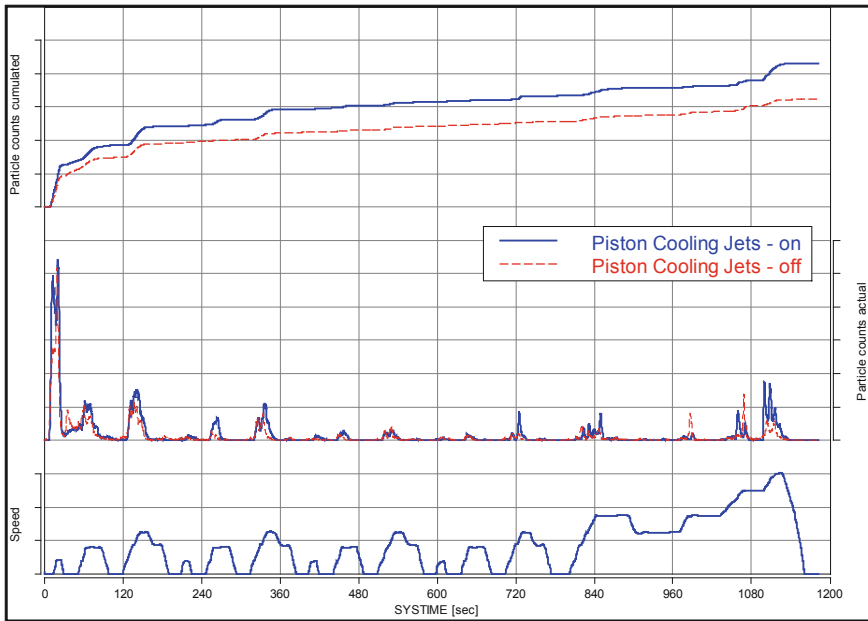


Fig. 2 NEDC particulate number emission with PCJ on/off

at high temperature ($\lambda > 0.6$, $1400 \text{ K} < T < 1900 \text{ K}$). The formation of soot can be visualised in combustion chambers by the observed incandescence attributed to glowing particles. Hence optical investigations of the combustion process are ideal tools to qualitatively assess soot formation inside a gasoline engine.

For a certain level of piston surface wetting, the amount of fuel that is not evaporated early enough to be consumed by the premixed flame is affected by both the temperature of the metal surface as well as the temperature of the fuel. Figure 2 reveals the influence of the piston surface temperature, as the latter is changed by means of switching Piston Cooling Jets (PCJ) on and off. When the PCJs are disabled, the piston warms-up faster, which in turn results in lower PN emissions.

Furthermore the fuel and coolant temperatures are important parameters that need to be controlled. Photographs from the transparent engine investigation (Fig. 3) depict the significant impact of fuel and coolant temperature on spray penetration and on spray shape. The upper pictures are taken at the End of Injection (EOI), while the lower ones are at around 100°CA ATDC when a diffusion flame is most visible. In this case, the engine was operating at a speed of 2840 rpm and a load of 3 bar Brake Mean Effective Pressure (BMEP). For warm conditions, the individual spray plumes are no longer clearly separated. They tend to join and form a wide fuel jet with a more widespread area of wall impingement. The transition to this spray structure with more apparent flush-boiling is also dependent on pressure conditions during injection as well as on injection timing.

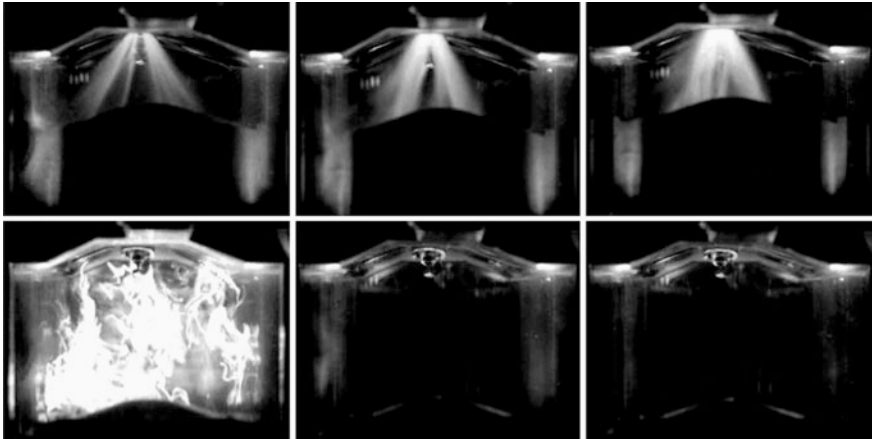


Fig. 3 Injection and combustion at three different temperatures (20, 60, 100 °C)

An additional conclusion can be drawn from the presented visualizations: a very thorough optimization process needs to be applied for the tuning of the DI combustion system, including spray targeting, covering a wide range of operating conditions. Rather simple geometrical representations of individual fuel sprays fail to capture such effects. Much more sophisticated CAE tools, modelling the complex interaction between the injected fuel and in-cylinder flow, and accounting for multiple physical processes, such as flash boiling for example, are required to predict the fuel spray development and subsequent mixture formation and combustion process.

2.2 Injection Strategy

In this section, calibration settings for minimised particulate formation are described for three phases: Engine Start, Catalyst Heating, and Warm Operation. In developing and optimizing these settings, besides minimizing generation of soot particles, all other typical combustion attributes such as the formation of gaseous emissions, combustion stability, fuel consumption, etc. need to be considered.

2.2.1 Engine Start

Figure 4 shows typical cold start ‘Start of Injection’ (SOI) settings within the capabilities of EU5 engine technology. Under such settings, during cold start, the injection is timed late in the compression stroke. As already described, this may lead to piston wetting and locally rich zones associated with particulate forming diffusion controlled combustion.

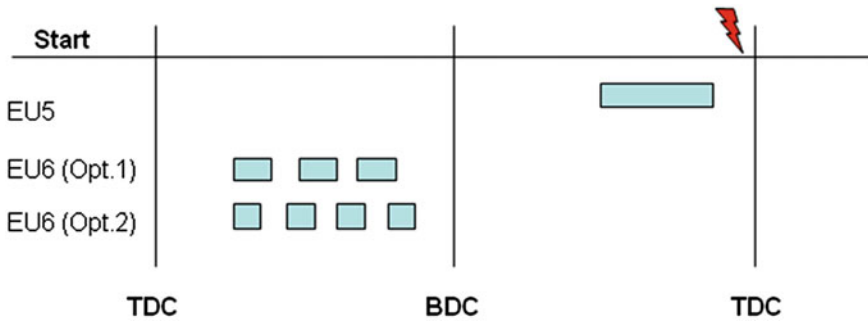


Fig. 4 Injection settings at engine start

Piston wetting must be minimized particularly during cold start. This can be realized by optimising the SOI settings and by splitting the injection into multiple (in this case three and four) events. In contrast to a single relatively long injection, multiple injections reduce the fuel spray penetration and hence minimize fuel impingement on surrounding walls. The selection of the optimum timing and split ratio depends on the injector technology capability and needs to be adapted to the particular engine operating point. It has also been found that such multiple injection strategies lose their effectiveness below a certain minimum injection pressure, potentially due to the spray momentum being reduced too drastically then, especially during the opening and closing phases of the injector nozzle [5].

2.2.2 Catalyst Heating

Catalyst heating mode is adopted in the beginning of the drive cycle and is normally completed within a short time. The exact duration of the catalyst heating mode depends largely on the ignition timing settings and the associated exhaust gas heat flux [6]. Usually the catalyst heating is already completed during the first driving “hill” of the NEDC profile. Figure 5 outlines catalyst heating strategies minimising particulate emission while observing all other important operation parameters, such as combustion stability, exhaust heat flux, HC emission, etc. The original injection strategy includes two main events, one early in the induction stroke, and one late during the compression stroke. The alternative strategy for minimizing wall wetting includes a double or triple injection during the induction stroke, followed by a small injection event during the compression stroke.

2.2.3 Warm-Up/Warm Operation

Under warm conditions it has been found beneficial to return to a single injection strategy because all components which may interact with the fuel spray are hot and hence the evaporation rate is higher. Alternatively, a split injection strategy can

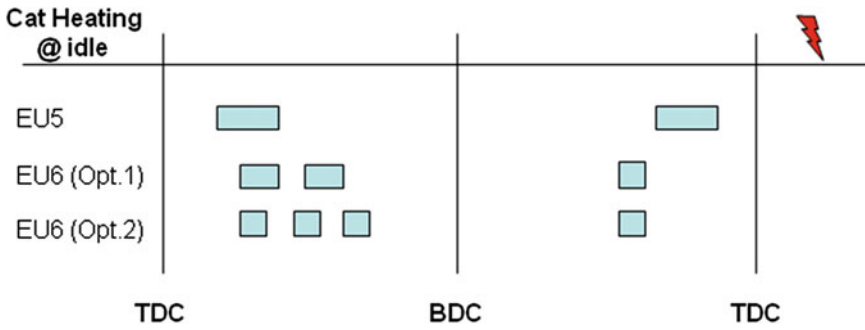


Fig. 5 Injection settings for catalyst heating mode at idle

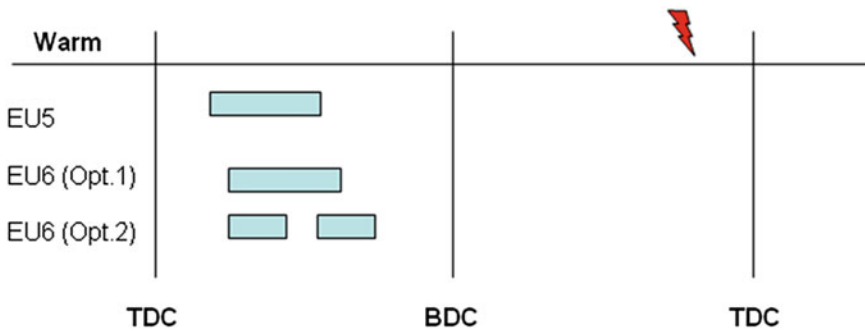


Fig. 6 Injection settings for warm conditions

also be beneficial, especially if fast acting injectors are utilized. Such an injection strategy is illustrated in Fig. 6.

The combined benefit of implementing injection strategies such as those presented in the previous paragraphs is demonstrated in Fig. 7 for a NEDC. The test result shows that a substantial contribution to the reduction of PN emissions can be achieved by adapting the injection calibration parameters.

The effect of adopting such injection strategies is also demonstrated in a single operating point by means of the visualization in Fig. 8. The operating conditions for the optical engine represent an extra urban speed/load point of the NEDC for given gear ratio and vehicle mass. The evolution of the injection, wall wetting, and subsequent diffusion combustion are compared for a single-injection and a triple-injection setting, during cold operation. One can clearly observe the diffusion flame for the simple injection settings on the left side, while the absence of such on the right side attests to the substantial reduction of particle formation by means of the triple injection. The upper pictures are taken at the end of the first injection whereas the lower pictures reflect the condition at 100 °CA ATDC. Both tests are performed at 20 °C fuel and coolant temperature.

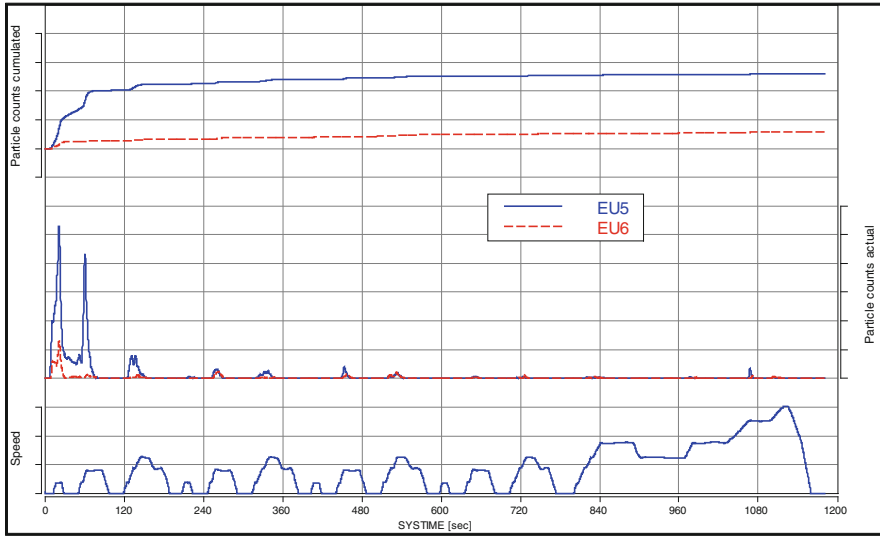


Fig. 7 Particulate number emission for EU5 versus preliminary EU6 calibration

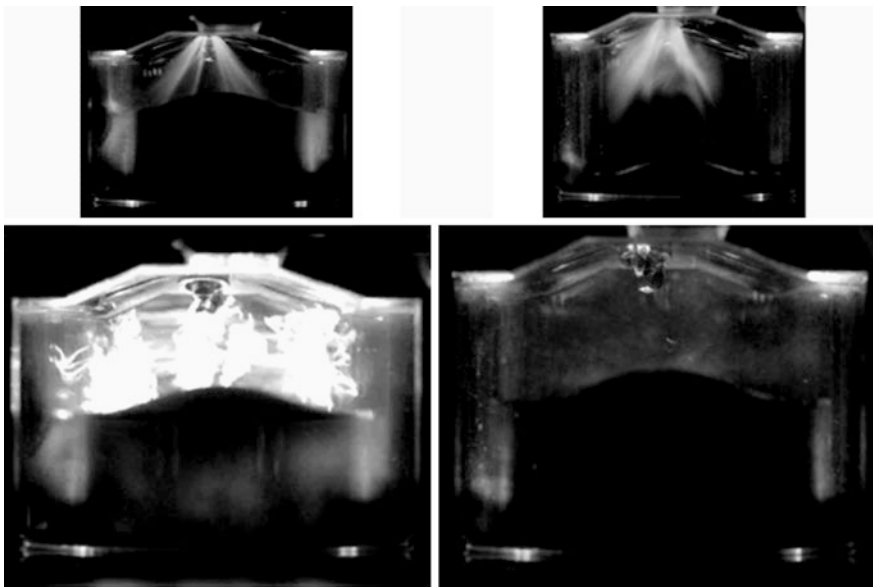


Fig. 8 Optical results EU5 versus preliminary EU6 calibration

It is, however, very important to note that the results presented in Figs. 7 and 8 are obtained with new injectors in clean condition. Effects like injector component aging and deposit formation at the injector tip change the picture substantially. This will be described more in detail in the next paragraph. Furthermore, adopting

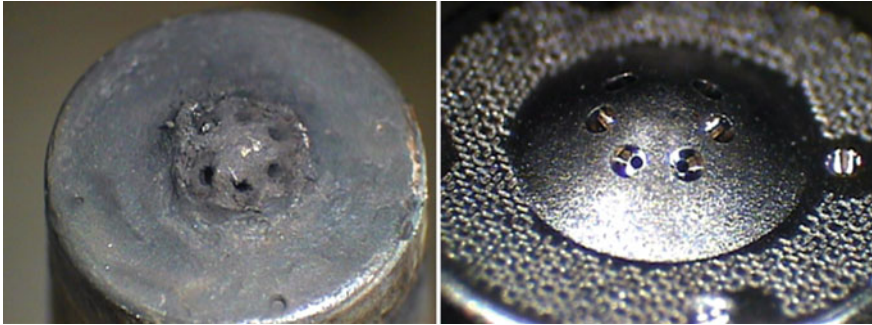


Fig. 9 Injector tips, coked and original condition

such injection strategies in a robust and reproducible manner requires a combination of injector and electronic control capabilities that support the accurate splitting of the injection process into multiple smaller events.

2.3 Injector Coking and Oil Ingress

Injector tip coking has been found to be one of the most influential factors governing the particulate generation by DI gasoline engines in the combustion chamber. The nature of the effect is illustrated in Fig. 9, where the heavy deposits at the tip of the injector on the left hand side are contrasted to the clean tip picture on the right side. The substantial impact that this kind of injector tip deposit has on particle emission is demonstrated in Fig. 10. It has been found that this increase of particulate emission can be attributed to both deterioration of spray characteristics (shape and penetration) as well as to a ‘sponge’ effect taking place at the injector tip. While the latter is not yet fully understood, transparent engine visualization lead to the hypothesis that some fuel is being absorbed by the porous deposit at the tip of the injector during injection, most likely during the injector opening and closing phases when the spray momentum is rather low. During the expansion stroke, the absorbed fuel evaporates after the main combustion has taken place and burns in a soot producing diffusion flame under rich conditions. Various transparent engine observations systematically reveal diffusion flame occurrence around the injector tip when in a coked condition.

Figure 10 illustrates the effect of yet another parameter that is difficult to control but has a significant influence on particle emissions: oil entering the combustion process or directly contaminating the exhaust manifold. This error state is one of the most critical factors to control over the lifetime of the vehicle. As an illustration of the relation between such an effect and particle emission, Fig. 10 includes the PN emission trace for an engine with a leaky turbocharger and clean injectors. Potential sources of oil can be manifold, such as leaky valve stem seals, piston rings, crankcase ventilation, etc. (test performed with clean injectors).

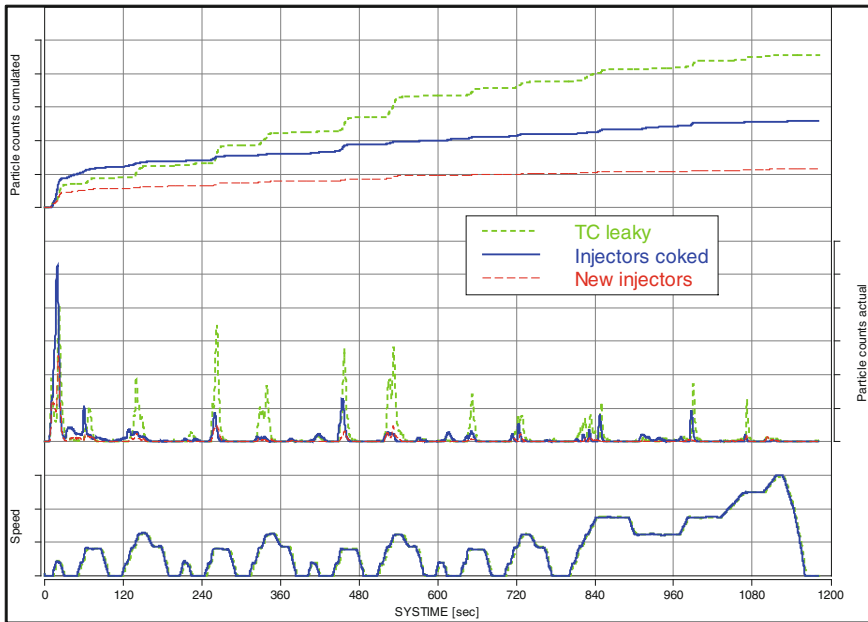


Fig. 10 Particulate number emission for coked injectors and leaky turbocharger

3 Aftertreatment Measures

Wall flow particle filters are well known from their application for diesel engines. The implementation of a similar technology for gasoline engines brings, however, a new set of technical challenges and technical maturity issues, which will be outlined in the following paragraphs.

Starting with the basic work cycle, the gas exchange process of a gasoline engine has a substantial impact on fuel consumption. A direct effect of the implementation of a wall flow particle filter in a gasoline engine exhaust system is the significant increase in backpressure, which in turn impacts the gas exchange work and the associated fuel consumption penalty. Therefore, any form of implementation of such technology for gasoline engines would need to be complemented by sufficient technology adaptation and optimization to ensure maintaining the fuel economy gains that have so hardly been obtained by gasoline engine technology in the recent years.

In terms of system development and integration, the same technical challenges that have already been the subject of long and extensive development phase for diesel engines have to be overcome for gasoline engine applications as well. Design integration in the existing vehicle platforms, as well as packaging and optimization of the system topology, will need to observe the complex trade-offs between the filtration function, the regeneration function, and the exhaust backpressure characteristics. Technology robustness against the different boundary

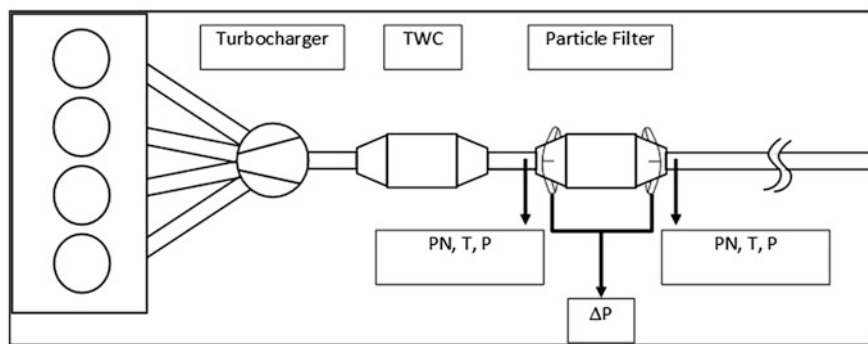


Fig. 11 Schematic test setup

conditions applying to gasoline engine exhaust systems, such as higher exhaust temperatures, different exhaust gas chemistry, etc., also needs to be developed. Last but not least, appropriate controls and diagnostic strategies, including sensors, need to be developed, implemented and field-tested.

In the following sections, some of the functional trade-offs and technical challenges will be illustrated by means of evaluating various alternatives as applied to a 1.6 L turbocharged direct-injection engine operated on a transient dynamometer. In these tests, alternative filter configurations have been attached to the exhaust system downstream of the Three Way Catalyst (TWC) but still in close coupled (CC) position. The filtration efficiency has been determined by sampling the exhaust gas up- and downstream of the particle filter with two condensation particle counters. Pressure, temperature, and gaseous emissions have also been measured in the same locations (Fig. 11).

3.1 Filtration Efficiency and Exhaust Back Pressure

Various configurations of wall-flow filters, with different substrate properties, i.e. filter material, porosity, mean pore size diameter, wall thickness and both bare and coated filters with different levels of washcoat were also considered. All filters have been de-greened and prepared for the test according to the same procedure and have been free of soot at the start of the test. The filtration efficiency of the filters has been assessed by means of simulated warm NEDC tests. Throughout the test series, the PN measurement was very repeatable and reliable. The pressure drop over each substrate has been measured while operating the engine at rated speed. At this speed, the engine load was increased in steps until rated power was reached.

A sample from the results obtained by means of such tests is shown in Fig. 12. The effects that substrate porosity, mean pore size, and wall thickness have on the trade-off between filtration efficiency and pressure drop (backpressure) is apparent

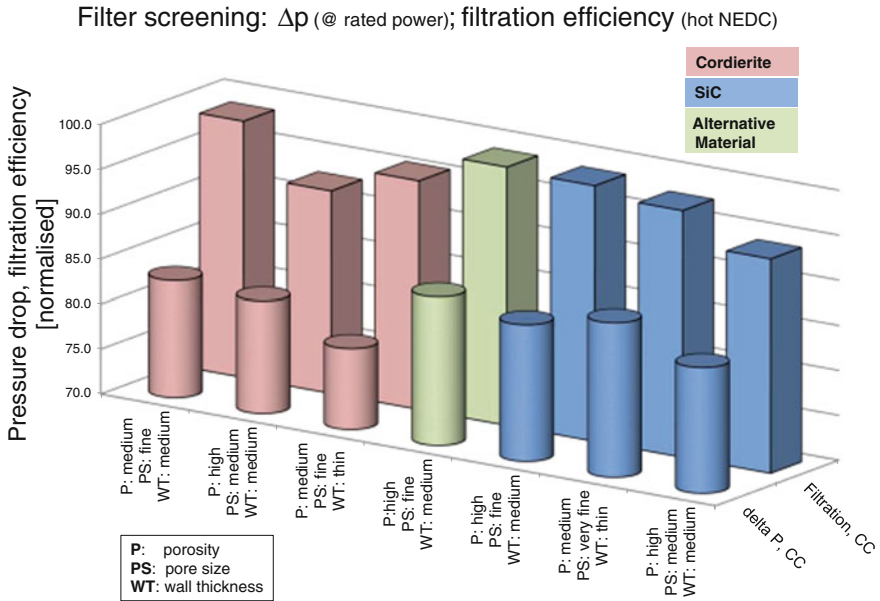


Fig. 12 Screening results, bare filter, 5.66'' × 6''

in these examples. Figure 13 illustrates the effects of coating on pressure drop. Balancing the act between any catalytic function requirements against backpressure and potential fuel consumption implications will be one of the key system optimization tasks in deploying wall-flow filter technology for gasoline engines. The geometrical optimization of the substrate configuration, e.g. length-over-diameter ratio in conjunction with packaging and exhaust architecture considerations, will also need to be carefully engineered, again with the implications on backpressure in mind.

3.2 GPF Regeneration

In order to ensure the lowest possible impact on fuel economy, the maximum potential for a passive regeneration of the particle filter during the widest range of vehicle driving conditions needs to be pursued. One of the key parameters affecting this capability is the location of the filter within the engine exhaust system, in particular the proximity to the engine exhaust manifold. The terms Close-Coupled (CC) and Under-Body (UB) are commonly used to refer to installations in which the filter is located close to, and respectively away from the engine exhaust manifold. Investigations indicate that conditions favouring passive regeneration occur during the EUCD phase of the NEDC cycle, where temperatures are sufficiently high and the required oxygen is available, especially during the deceleration phase with the

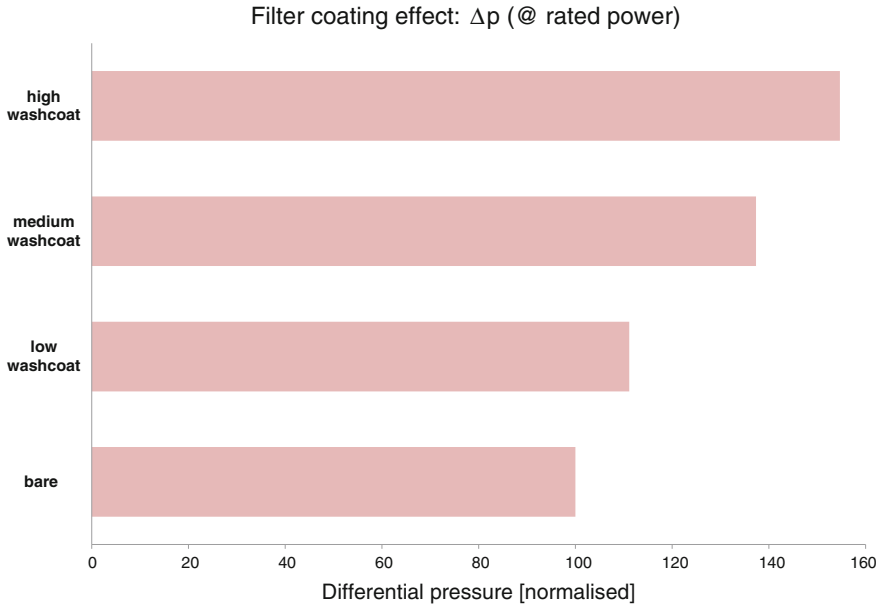


Fig. 13 Screening results with coated filter, 5.66'' × 6''

fuel shut off. In such conditions, a temperature of the order of 550 °C is reached upstream of the filter, when the latter is installed in a CC position, while the respective temperature is approximately 100 °C lower when the filter is located in the UB position. Systematic analysis of the burning characteristics of particulates typically found in gasoline exhaust has shown that a minimum temperature of around 500 °C is required to initiate combustion of the soot.

3.3 Maximum Filter Temperatures and Durability

Several tests have to be conducted in order to check the durability of a substrate for a specific vehicle application. The maximum filter temperature limit must not be exceeded to prevent the GPF from cracking and other forms of damage, such as melting, ash reaction, etc. The maximum temperature that can occur within the filter material is a function of the incoming exhaust gas temperature and the heat generated by the exothermic soot burning reaction, when regeneration takes place. The soot combustion generated heat is, in turn, governed by the amount of soot that has been accumulated in the filter, commonly referred to as Soot Loading. Under high exhaust temperature and high oxygen concentration, conditions under which regeneration will be normally initiated, there will be a smaller margin left for increasing the filter material temperature, until limits that are critical for the durability of the filter are reached. Consequently, appropriate monitoring

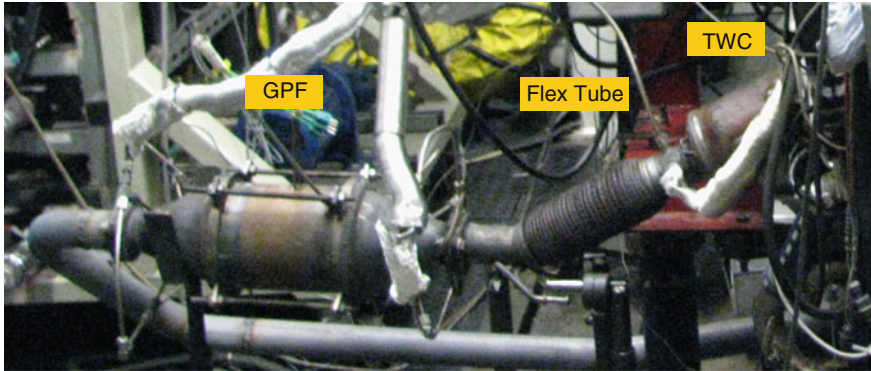


Fig. 14 Crack test exhaust system configuration

techniques for the level of soot loading, as well as countermeasures, in the event that the potential of overheating the filter is diagnosed, will be essential elements of any reliable implementation of the technology for customer use. Such a countermeasure would be, for example, the disabling of the fuel shut off during vehicle coast down.

As an illustration of the level of durability testing to which gasoline particulate filter technology will need to be subjected to, the thermal shock resistance test of a filter sample (cordierite substrate, medium porosity, medium wall thickness, fine pore size) is shown above. In this test sequence, the engine is warmed up to the operating point with the maximum exhaust system surface temperatures (Figs. 14, 15). As soon as all temperatures have reached steady-state levels, the engine is switched off and subsequently motored with open throttle, pumping ambient air. After a certain time interval, the engine is started again and brought to the same operating conditions of maximum exhaust system temperature, where it is kept until reaching steady-state, for a new motoring and firing cycle to follow, as shown in Fig. 15. While cycling between fired and motored operating conditions, extremely steep temperature gradients can be measured in the exhaust system components which creates extremely high stress levels, especially in the filter material. The alternating firing and motoring procedure is repeated for 1,200 cycles. By periodic acoustic discharge and speed of sound measurement techniques, monitoring of the filter for potential development of material failures throughout the process is facilitated.

3.4 Summary and Outlook

Vehicle emissions have been dramatically reduced over the last two decades, both in terms of gaseous pollutants, as well as the mass of particle emissions. In the continuous strive to minimize the environmental impact of vehicle exhaust gases,

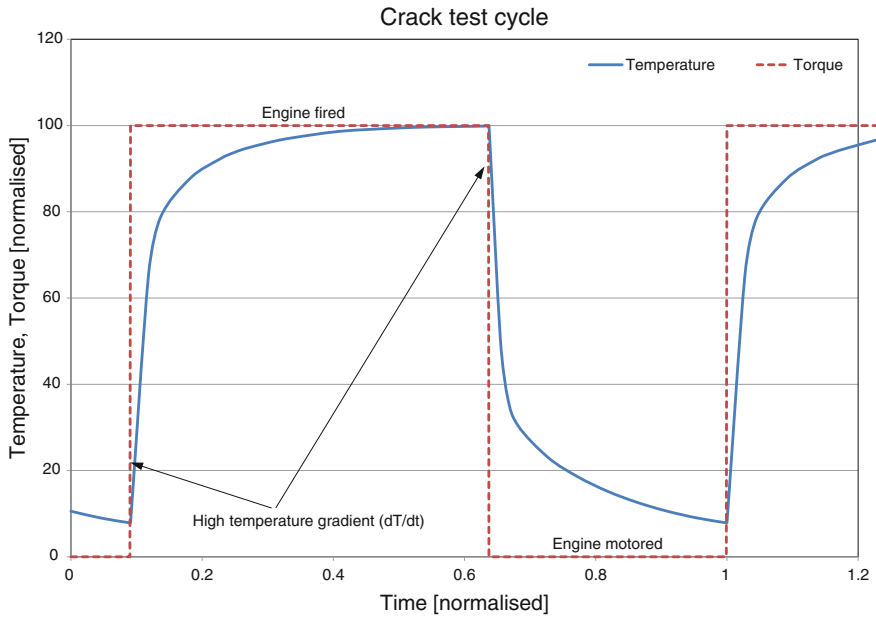


Fig. 15 Crack test cycle

one of next challenges is now the further reduction of particle number emission. For gasoline direct-injection powered vehicles, the campaign towards further reduction of particle number emission considers both measures to reduce generation of soot particles within the combustion chamber as well as technologies for filtering the generated particulate matter within the exhaust system.

In the direction of reducing particle emission at the source, the interaction of the fuel spray with combustion chamber boundaries, during cold operation, has been shown to hold some of the keys for success. Minimizing the potential for such an interaction by means of sophisticated injection strategies substantially reduces combustion generated soot. On the other hand, phenomena for which the physical understanding and the control measures are still being researched, such as e.g. injector tip coking and oil leakages to the air charge, present major risks for any such strategy to be robust. Understanding these phenomena and developing credible solutions for controlling them in a large-scale product implementation is the current undertaking with the highest priority within gasoline DI engine technology.

Particulate filters also present, at first glance, an attractive option for controlling particle emission. However, the inherent sensitivity of the gasoline working cycle to exhaust backpressure implies that robust technology and system solutions that overcome the effect of increasing backpressure, hence deteriorating fuel consumption and performance, need to be developed first. Besides of preventing such deterioration of attributes, potential solutions should also be engineered with minimum impact on total cost of ownership. Finding such solutions involves

working through challenging system interactions and functional trade-offs, such as filtration efficiency and backpressure, catalytic function and backpressure, etc. Whatever the technical solution to that challenge will be, it will also have to be subjected to a thorough vehicle integration, as well as a robustness and reliability development and a verification process before it can be deployed in a volume product.

References

1. Curtis E, Kunde O, McCarthy T, Philips P, Schamel A, Weber C, Wirth M (2010) EcoBoost : Downsized Gasoline DI Turbo Engines as the Backbone of Ford's CO₂ and Fuel Economy Product Strategy, FISITA, Budapest, 2010
2. Borrmann D, Friedfeld R, Pingen B, Stump L, Wirth M (2008) Gasoline Downsizing : challenges on the path to an attractive powertrain, engine & environment, Graz, 2008
3. Whitaker P, Kapus P, Ogris M, Hollerer P (2011) Measures to reduce particulate emissions from gasoline DI engines, SAE 2011-01-1219
4. Buri S, Dahnz C, Kubach H, Spicher U (2012) Reduction of soot emissions by increasing injection pressure up to 1000 bar in a DISI engine in stratified operation. Internationales symposium für Verbrennungsdiagnostik, Baden-Baden
5. Piock W, Hoffmann G, Berndorfer A, Salemi P, Fusshoeller B (2011) Strategies towards meeting future particulate matter emission requirements in homogeneous gasoline direct injection engines, SAE 2011-01-1212
6. Klauer N, Zülch C, Schwarz C, Schünemann E (2006) The new BMW turbocharged SULEV 2.0l Four Cylinder gasoline engine, MTZ m05-12-06

A New Environmental Friendly Zirconium–Titanic–Ceria–Tungsten Mixed Oxides for Durable NH₃-SCR deNO_x Catalysts

Jianqiang Wang, Jidong Gao, Jie Ma and Meiqing Shen

Abstract With increasing stringent automobile exhaust emission regulations for diesel vehicles advanced emission control systems may require SCR catalysts with substantially improved thermal durability. Zirconia–Titania–Ceria–Tungsten (ZrTiCeW) mixed oxides were evaluated in the selective catalytic reduction of nitrogen oxides (NO_x) by ammonia (NH₃-SCR). The hydrothermal aging and sulfur aging were performed under severe conditions. They were compared with a commercial V/W/Ti SCR catalyst treated in the same manner. ZrTiCeW exhibits the superior NO_x conversion performance and higher selectivity. The influence of space velocity, NO_x/NH₃ and NO/NO₂ on the NO_x conversion were investigated. The presence of NO₂ in the feed (NO₂/NO = 50/450) boosts the NO conversion in the low temperature range.

Keywords NH₃-SCR · Mixed oxides · Hydrothermal stability · Sulfur tolerance

1 Introduction

The abatement of nitrogen oxides from stationary and mobile sources has received much attention due to increasing environmental concerns and worldwide regulations. The most efficient and cost-effective technology to reduce NO_x emission

F2012-A04-022

J. Wang (✉) · J. Gao · J. Ma
China Automotive Technology and Research Center, Tianjin 300162, China
e-mail: wangjianqiang@catarc.ac.cn

M. Shen
School of Chemical Engineering and Technology, Tianjin University,
Tianjin 300072, China

under oxygen-rich is selective catalytic reduction (SCR) by ammonia [1, 2]. Well established NH_3 -SCR technique uses either $\text{V}_2\text{O}_5/\text{WO}_3\text{-TiO}_2$ or Zeolite based catalysts, NO_x being continuously reduced by NH_3 resulting in the selective formation of nitrogen and water. A major drawback of V_2O_5 based formulations is their poor thermal stability, in addition, V_2O_5 release poses serious environmental and toxicity problems [3]. Zeolite-based catalysts promoted by transition metal such as Fe and Cu represent an excellent solution to overcome the stability problems of V_2O_5 -based catalysts but may show disadvantages in stability after hydrothermal ageing and sulfur poisoning [4]. So it's necessary to develop the higher catalytic activity, hydrothermal stability and sulfur tolerance SCR catalyst to meet the commercial requirements.

Acidic zirconia materials and new mixed metal oxides have been recently proposed as alternative catalysts for the NH_3 -SCR process [5–8]. These systems may obey the need for higher activity at low temperature, better thermal durability and superior sulfur tolerance, particularly when the SCR function is combined with a diesel particulate filter. In present study, Zirconia–Titania–Ceria–Tungsten mixed oxides were prepared, and the SCR activities were investigated. The thermal stability, sulfur tolerance, Space velocity, NO_x/NH_3 and NO_2 -SCR were investigated.

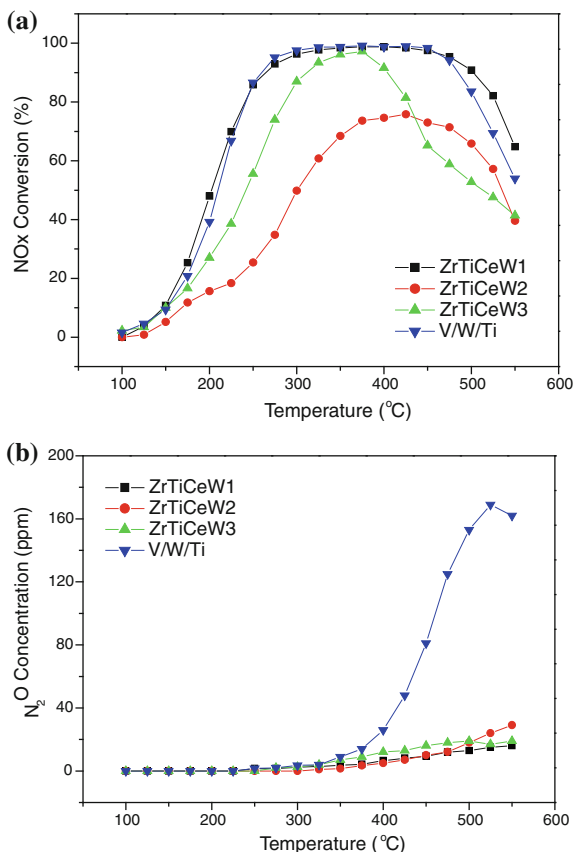
2 Experimental

Zirconia–Titania–Ceria–Tungsten (denoted as ZrTiCeW) powders were obtained by coprecipitation method. A solution was prepared by mixing with stirring ZrAC, TiCl_4 , $\text{Ce}(\text{NO}_3)_3 \cdot 6\text{H}_2\text{O}$ and $(\text{NH}_4)_{10}\text{W}_{12}\text{O}_{41} \cdot x\text{H}_2\text{O}$ with distilled water. This solution was gradually added into a stirred reactor containing ammonia solution. The pH of the medium was adjusted to ten by adding a solution of ammonia. After stirring for 30 min, the precipitate obtained was filtered and washed with distilled water. After being dried at 120 °C for 12 h, the precipitate was submitted to calcinations at 550 °C for 3 h.

For monolith catalysts, slurry was prepared by mixing 10 g of ZrTiCeW powder with 40 mL of deionized water and 2 ml alumina sol (containing 30 % Al_2O_3). The mixture was ball-milled for 12 h to obtain a slurry which comprised 90 % particles smaller than 10 μm and the resulting slurry was coated onto cordierite cores (15 mmD \times 18mmL) with a cell density of 400 cpsi (cells per square inch). The coated cores were dried at 120 °C for half an hour and calcined at 550 K for 3 h. The coating process was repeated once to obtain a target washcoat loading of 150 g/L.

The hydrothermal aging experiments were carried out in 5 % steam + air ($\text{SV} = 30000 \text{ h}^{-1}$) at 750 °C for 16 h and 900 °C for 2 h, respectively. The commercial V/W/Ti catalysts were subjected to the same ageing treatment as the ZrTiCeW catalysts.

Fig. 1 Effect of temperature over NO conversion over ZrTiCeW and commercial V/W/Ti catalysts **a** NO conversion. **b** N₂O formation



The sulfur aging experiments were carried out in 5 % steam + 600 ppm SO₂ + air (SV = 30000 h⁻¹) at 200 °C for 29 h.

The catalytic activity measurement was carried out in a tubular quartz reactor operated at atmospheric pressure. The gases were fed using a series of mass flow controllers. The total feed flow rate was 1580 mL/min, corresponding to a space velocity of 30,000 h⁻¹. The feed composition was 500 ppm NO, 500 ppm NH₃ and 5 % O₂ and with a balance of N₂. The reactor was heated in a tube furnace that controlled the temperature just upstream of the catalyst. Thermocouples were used to measure the temperature upstream and downstream of the catalyst sample. The concentrations of NO, NO₂, N₂O and NH₃ were measured by Thermofisher IS10 FTIR spectrometer equipped with a 2 m path length gas cell. The NO_x conversion was calculated based on the following equations:

$$X_{NOx} = \frac{NO_{inlet} - (NO_{outlet} + NO_{2outlet} + 2N_2O_{outlet})}{NO_{inlet}} \times 100\%$$

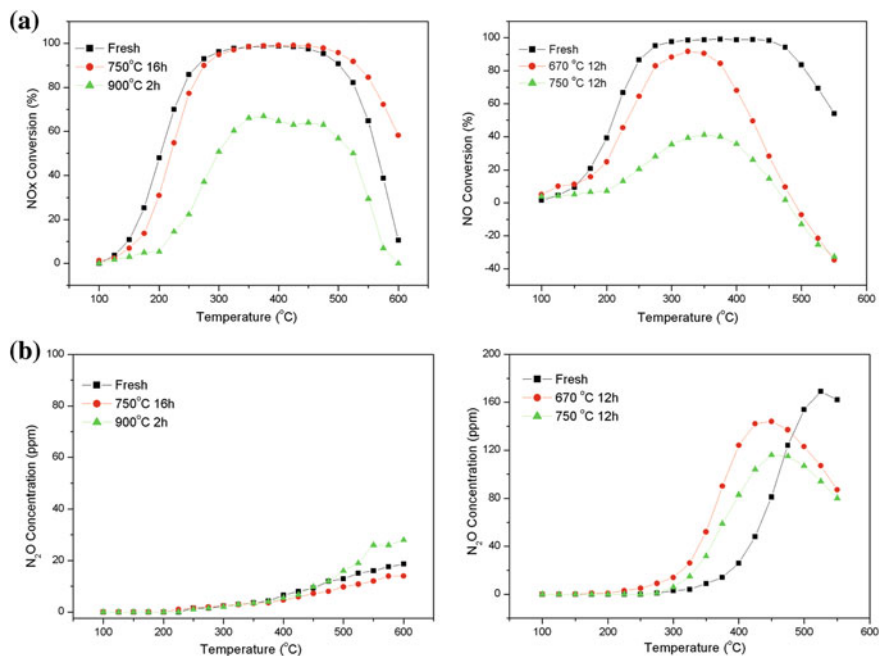


Fig. 2 Effect of temperature on NO conversion over fresh and aged ZrTiCeW1 and commercial V/W/Ti catalysts **a** NO conversion. **b** N₂O formation

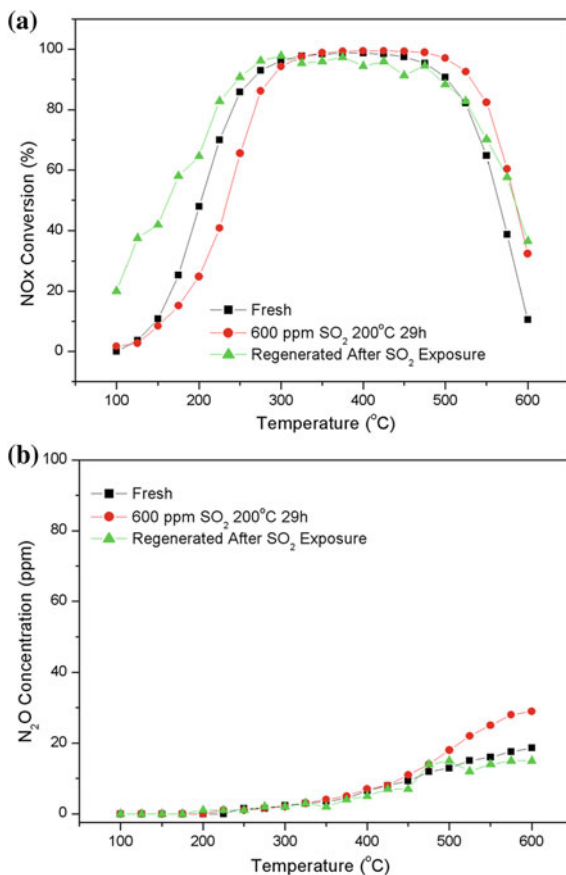
3 Result and Discussion

3.1 ZrTiCeW Catalysts

Figure 1a compares the NH₃-SCR performance of a commercial V/W/Ti catalyst and ZrTiCeW mixed oxides. The NO reduction activity profile of both ZrTiCeW and V/W/Ti catalysts resemble those observed in SCR reaction with a typical volcano-type shape. The activity increases with increasing reaction temperature up to ca. 300–450 °C where a maximum NO reduction activity is observed. At this point the activity starts to decrease due to ammonia oxidation reaction to NO, which is prevailing over its reaction to N₂. Noteworthy, ZrTiCeW1 and V/W/Ti catalyst exhibit similar activity below 475 °C, but show some divergence at higher temperatures. ZrTiCeW1 shows better performance than V/W/Ti catalyst.

Figure 1b shows the N₂O formation in the whole investigated temperature range. The formation of nitrous oxide may be taken as the primary indicator of decreasing selectivity of the SCR reaction and is usually observed at temperatures above 350 °C. It can be seen that the N₂O formation is much lower for ZrTiCeW catalysts than that for V/W/Ti catalyst. Thus secondary greenhouse emissions can be decreased for ZrTiCeW catalysts. So ZrTiCeW1 has been selected for further investigations.

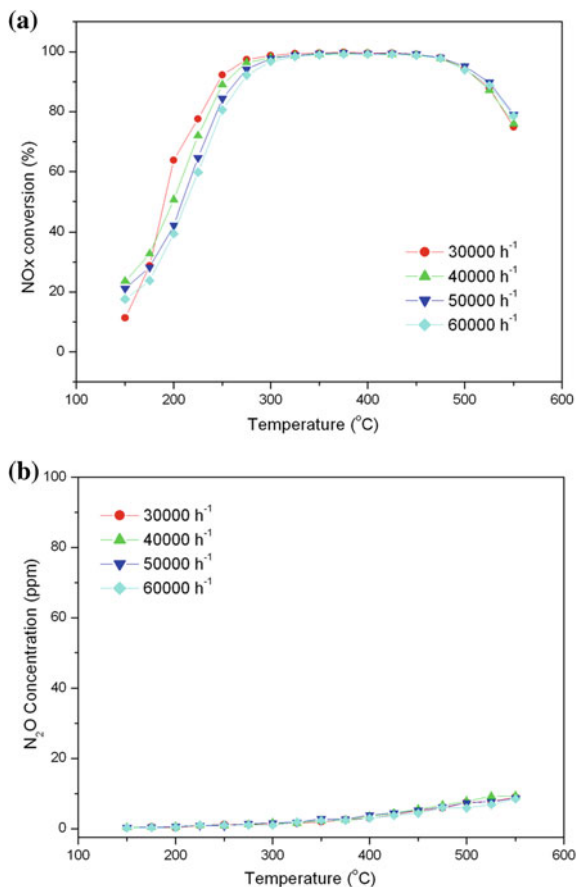
Fig. 3 NH₃-SCR performances for ZrTiCeW1 catalyst after exposure to equivalent of 15,000 miles with 2000 ppm fuel sulfur **a** NO conversion. **b** N₂O formation



3.2 Hydrothermal Stability

Figure 2 shows the NO conversion of ZrTiCeW1 and commercial V/W/Ti catalyst after different aging treatments. For the V/W/Ti catalyst, the NO_x conversion is surprisingly decreased in the whole investigated temperature range after hydrothermal aging at 670 °C/12 h. After hydrothermal aging at 750 °C/12 h, the NO_x conversion is decreased to below 40 %. For ZrTiCeW1 catalyst, the SCR performance remains high after hydrothermal aging at 750 °C/16 h. The NO_x conversion is only slightly decreased at low temperature ($T < 300$ °C) and increased at high temperature ($T > 450$ °C) compared to the fresh state. After aging at 900 °C/2 h, The SCR performance is also decreased but they still show 60 % conversion at 320–490 °C with very low N₂O concentrations.

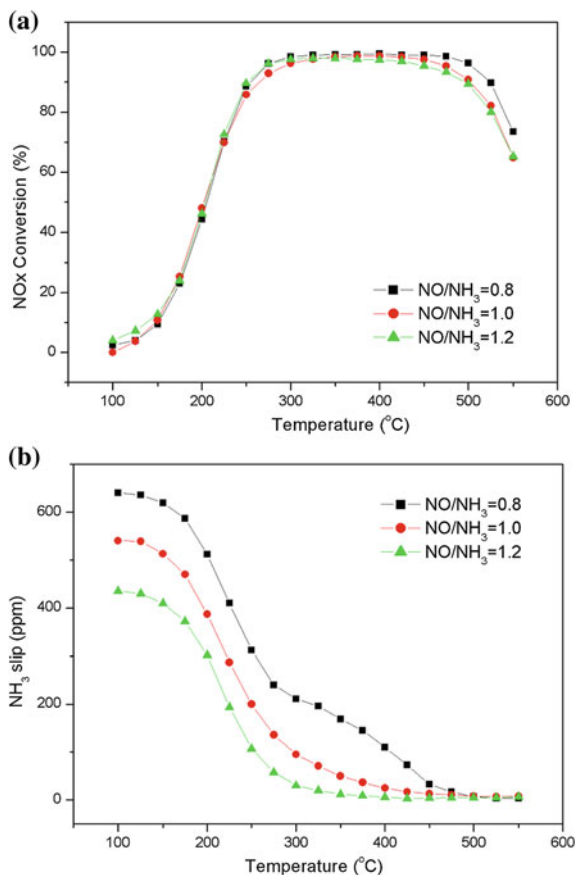
Fig. 4 NH_3 -SCR performance for different space velocities **a** NO conversion **b** N_2O formation



3.3 Sulfur Tolerance

As we known, V/W/Ti catalyst may be ideal to meet NOx emissions standards when high sulfur fuel is used. In china, the availability of low sulfur diesel fuel may not be guaranteed, so any NOx control system must be robust to high levels of fuel sulfur [9]. Poisoning with SO_2 was investigated at 200 $^{\circ}\text{C}$ by exposing the ZrTiCeW1 catalyst for 29 h to a gas mixture containing 600 ppm SO_2 (equivalent of 15,000 miles with 2000 ppm fuel sulfur) [10]. Figure 3 shows the performance of the ZrTiCeW1 catalyst before and after exposure to high sulfur levels. The low-temperature activity is vulnerable to high fuel sulfur levels. Anchoring of the sulfate species at the catalytic active sites led to a mild deactivation at temperatures below 300 $^{\circ}\text{C}$. Also, after regeneration at 600 $^{\circ}\text{C}$ the performance is in full

Fig. 5 Influence of NOx/
NH₃ ratio on the NH₃-SCR
performance **a** NO
conversion **b** N₂O slip



recovery. It should be noted that N₂O formation was not evidently increased after SO₂ exposure. Thus, ZrTiCeW1 catalyst does appear practical for markets where high fuel sulfur levels are expected.

3.4 Space Velocity

The performance of an automotive catalytic converter is strongly influenced by the space velocity of the exhaust gases [11]. The catalyst conversion performance decrease with increasing space velocity and can be severely deteriorated when space velocity is increased beyond certain values. Figure 4 shows the influence of various spaces on the NH₃-SCR performances for ZrTiCeW1 catalyst. It can be seen that the low temperature ($T < 300$ °C) activity is slightly reduced, while the high temperature activity keep almost unchanged.

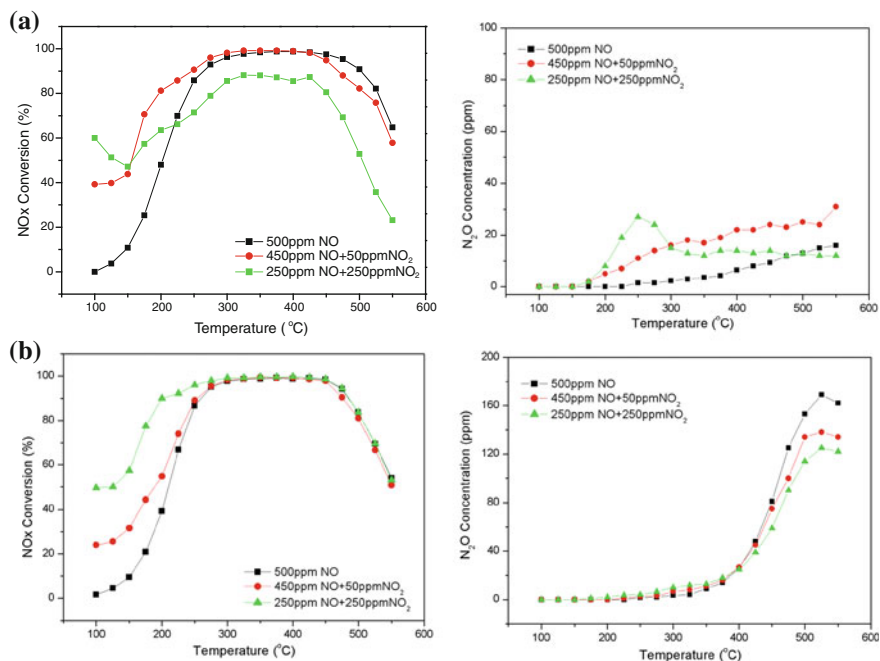


Fig. 6 Influence of NO₂/NO ratio on the NH₃-SCR performance **a** NO conversion **b** N₂O formation

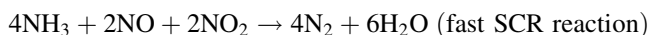
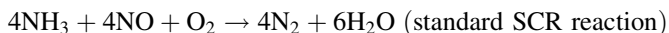
3.5 NO_x/NH₃

Generally, a 1:1 ratio of NH₃ molecules to molecules of NO + NO₂ is ideal for NO reduction. The additional NH₃ that is not used for NO_x reduction can be either to oxidize to N₂ and H₂O, to oxidize to NO_x over a catalyzed soot filter, or to pass out of the exhaust system as NH₃ [12].

Figure 5a shows the influence of NO_x/NH₃ ratio on the NH₃-SCR performance at a space velocity of 30000 h⁻¹. Figure 5b shows the NH₃ Slip out of the SCR catalyst sample for the test corresponding to Fig. 5a. It can be seen from Fig. 5 that for temperatures above 400 °C, over-injecting NH₃ can slightly lead to improved NO_x conversion efficiency. At the points below 400 °C, the level of NH₃ injected did not have any substantial impact on the NO_x conversion efficiency for the range of NO_x/NH₃ ratios tested. In conclusion, ZrTiCeW1 catalyst has better adaptability for different NO_x/NH₃ ratios.

3.6 Influence of the NO/NO₂ Ratio

The interest for the fast SCR reaction has considerably increased during the last years due to its higher DeNO_x potential at low temperatures:



The beneficial effect of the fast SCR reaction on the overall NO_x conversion has been reported by various authors [13–16]. Figure 6 shows the influence of NO₂/NO ratio on the NH₃-SCR performance for ZrTiCeW1 and V/W/Ti catalyst. Under the fast SCR regime, the V/W/Ti catalyst showed remarkable improvement for NO_x conversion in the low temperature (below 300 °C). For ZrTiCeW1 catalyst, the promotional effect of NO₂ is limited. The significant loss of conversion efficiency can be seen when NO₂ concentration is equal to 250 ppm.

4 Conclusion

In summary, the ZrTiCeW mixed oxides catalyst is promising materials for diesel aftertreatment to meet NO_x emissions targets for Euro IV, V or VI standard. In emerging markets where there is a risk of exposure to high sulfur fuel. Further, the hydrothermal stability is more critical as the use of catalytic diesel particulate filters becomes required by the newest regulations. The ZrTiCeW catalyst is the recommended materials.

References

1. Johnson TV (2011) Diesel emissions in review. SAE paper 2011-01-0304
2. Johnson TV (2012) Vehicular emissions in review. SAE paper 2012-01-0368
3. Chapman DM (2011) Behavior of titania-supported vanadia and tungsta SCR catalysts at high temperatures in reactant streams: Tungsten and vanadium oxide and hydroxide vapor pressure reduction by surficial stabilization. *Appl Catal A* 392:143–150
4. Cavataio G, Girard J, Patterson JE et al (2007) Laboratory testing of Urea-SCR formulations to meet tier 2 bin 5 emissions. SAE paper 2007-01-1575
5. Verdier S, Rohart E, Bradshaw H et al (2008) Acidic Zirconia materials for durable NH₃-SCR deNO_x catalysts. SAE paper 2008-01-1022
6. Verdier S, Crinière G, Larcher O (2007) Doped Zirconia with acidity and high thermal stability, for durable diesel catalysts. SAE paper 2007-01-0238
7. Rohart E, Krocher O, Casapu M et al (2011) Acidic Zirconia mixed oxides for NH₃-SCR catalysts for PC and HD applications. SAE paper 2011-01-1327
8. Marcotte N, Coq B, Savill-Jovitt C et al (2011) Multi-component zirconia titania mixed oxides: Catalytic materials with unprecedented performance in the selective catalytic reduction of NO_x with NH₃ after harsh hydrothermal ageing. *Appl Catal B* 105:373–376

9. Zhan R, Li ML, Shui L (2012) Updating China heavy-duty on-road diesel emission regulations. SAE paper 2012-01-0367
10. Girard JW, Montreuil C, Kim J et al (2008) Technical advantages of Vanadium SCR systems for diesel NO_x control in emerging markets. SAE paper 2008-01-1029
11. Shamim T (2005) The effect of space velocity on the dynamic characteristics of an automotive catalytic converter. SAE paper 2005-01-2160
12. Girard J, Snow R, Cavataio G, Lambert C (2007) The influence of ammonia to NO_x ratio on SCR performance. SAE paper 2007-01-1581
13. Madia G, Koebel M, Elsener M, Wokaun A (2002) The effect of an oxidation pre-catalyst on the NO_x reduction by ammonia SCR. *Ind Eng Chem Res* 41:3512–3517
14. Koebel M, Elsener M, Madia G (2001) Reaction pathways in the selective catalytic reduction process with NO and NO₂ at low temperatures. *Ind Eng Chem Res* 40:52–59
15. Koebel M, Madia G, Raimondi F, Wokaun A (2002) Enhanced reoxidation of vanadia by NO₂ in the fast SCR reaction. *J Catal* 209:159–165
16. Koebel M, Madia G, Elsener M (2002) Selective catalytic reduction of NO and NO₂ at low temperatures. *Catal Today* 73:239–247

Under Actuated Air Path Control of Diesel Engines for Low Emissions and High Efficiency

Chris Criens, Frank Willems and Maarten Steinbuch

Abstract This paper presents a new method for feedback control using the Exhaust Gas Recirculation (EGR) valve and Variable Geometry Turbine (VGT) of a diesel engine. The controller effectively counteracts disturbances in NO_x and PM emissions while maintaining the fuel efficiency. It is shown that by using a new combination of outputs, the controlled system has very good robustness properties. Using a mean-value engine model, which is extended with an emission model, the performance of the controlled system is examined in a simulation study with various applied disturbances; the feedback controller is shown to reduce the variation of emissions and pumping losses by 80–90 %. Compared to open loop control, the feedback controlled system has lower overall emissions by 14 % in NO_x , 19 % in PM and a simultaneous 0.7 % improvement of the brake specific fuel consumption is achieved.

Keywords Diesel engines · Air path · Emission control

1 Introduction

Diesel engines are the de facto standard means of propulsion for heavy duty trucks. They are popular for their excellent mileage and durability. By constant innovation, driven by legislation, diesel engines are also becoming much cleaner. In 2013

F2012-A04-024

C. Criens (✉) · F. Willems · M. Steinbuch
Eindhoven University of Technology, Eindhoven, The Netherlands
e-mail: c.h.a.criens@tue.nl

F. Willems
TNO Automotive, Helmond, The Netherlands

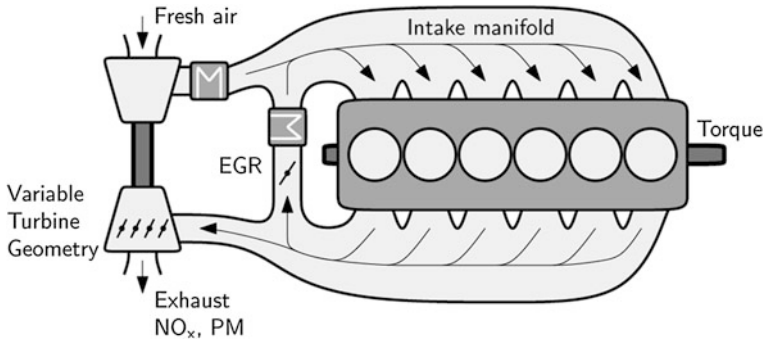


Fig. 1 A schematic representation of the diesel engine air path

the European Union will declare new emission standards, which dictate drastic cuts in exhaust emissions. The Nitrous Oxides (NO_x) emissions need to be reduced by 80 % compared to the current EURO V legislation; simultaneously the Particulate Matter (PM) emissions need to be halved. At the same time, fuel prices constitute a large part of the running cost of heavy duty commercial vehicles, which makes fuel efficiency also a top priority.

For diesel engines, legislation for NO_x and PM emissions is the most challenging. NO_x is formed during combustion, when high peak temperatures are reached. These temperatures cause the oxygen and nitrogen inside the combustion chamber to react and form NO_x . Lowering the peak combustion temperature will lower the NO_x formation rate. To lower the combustion temperature, diesel engines use an Exhaust Gas Recirculation (EGR) system. This EGR system recirculates cooled exhaust gas from the exhaust manifold into the intake manifold, where it mixes with fresh air. During combustion this exhaust gas acts as an inert gas, diluting the air–fuel mixture and increasing its thermal capacity. Figure 1 shows a schematic representation of a diesel engine equipped with an EGR system.

PM emissions consist mainly of soot which is formed during combustion in regions inside the combustion chamber where oxygen is scarce. Better availability of oxygen will reduce the amount of PM that is formed. In modern diesel engines, a Variable Geometry Turbine (VGT) is available. In such a turbine, the intake vane angle can be varied, which changes the flow properties of the turbine. By varying the intake vane angle, the pressure drop over the turbine changes, as well as its power output. Increasing the turbine power will result in a higher compressor speed and an increased intake air pressure. The flow of fresh air, and therefore oxygen, is increased accordingly. This way, the PM emissions are influenced.

EGR and VGT, combined with advanced fueling technology and exhaust gas aftertreatment systems such as Selective Catalytic Reduction (SCR) and Diesel Particulate Filters (DPF), should result in the low tailpipe emissions required for EURO VI. In this paper we will focus on engine control using EGR and VGT as actuators; these two actuators effectively control the air flow in a diesel engine.

The EGR-VGT control problem has been studied extensively in literature. An overview of control technologies up to 1998 can be found in [1]. Various control technologies have been applied to this control problem since then, of which we mention only a few here. In [2, 3] a robust μ -optimal approach is used. In [4] a switching strategy aimed at satisfying constraints and minimizing pumping losses is presented. In [5] a chapter is dedicated to the implementation of a Model Predictive Control (MPC) controller. In [6] a control approach for low emission diesel engines is presented. In [7] several different control schemes are compared and tested experimentally.

Often EGR-VGT control focuses on achieving the desired emissions by maintaining a certain fresh air flow and intake pressure. However, control of fresh air flow and intake pressure cannot take into account all uncertainties in the system behavior. Feedback control using direct engine-out emission measurements will further decrease the uncertainty in the engine out emissions. Along with the emissions, pumping losses, which are the torque losses due to pumping the air in and out of the cylinder, will become more significant as the emission requirements become stricter. The EGR and VGT are the main actuators that influence the pumping losses; therefore, it is important to take pumping losses into account during control design.

In [4] a control strategy was devised to minimize the pumping losses while maintaining the EGR dilution at a desired level and keeping the oxygen-fuel ratio above a minimum. And in [6] a control strategy aimed at minimizing emissions was presented.

In this paper we will present a control method that is able to provide feedback control using measurements of NO_x , PM and pumping losses. It expands on [6] by also taking into account pumping losses, resulting in a true MIMO controller, making full use of the available actuators. Compared to [4], significant changes are made such that the robustness properties are improved.

The paper is organized as follows. In the next section, the properties of the engine model used in this paper are explained. Using this model the main dynamic properties that are relevant for control design are investigated. A strategy for feedback control design is presented in the Sect. 4. This controller is tested in simulation and the results are presented in the Sect. 5. The paper ends with conclusions and directions for future research.

2 System Description

2.1 Hardware

For design and validation of the controller, a Simulink model of a six cylinder, 12 l, 360 kW heavy-duty diesel engine, equipped with a unit pump fuel injection system, is used. The model features a Variable Geometry Turbocharger (VGT) and a high pressure Exhaust Gas Recirculation (EGR) system. The model is able to predict the air flow in the engine as well as emissions and efficiency.

2.2 Engine Model

The engine model is a so called mean-value model. This means that the pulsating effects of the combustion cycles are averaged into continuous behavior. Also, the spatial variations are lumped into two discrete volumes.

For EGR-VGT control design, mean value type models are often used in literature, mainly because they are relatively accurate and simulate very fast.

The particular model is very similar to the one used in [2], but contains an additional emission model. It consists of a sixth order model to describe the air path [8]:

$$\begin{aligned}\dot{x} &= f(x, u, w) \\ y &= g(x, u, w)\end{aligned}$$

With states x , control inputs u , external inputs w and outputs y .

$$\begin{aligned}x &= [p_{im}, m_{air, fresh}, m_{inert}, p_{em}, T_{em}, \omega_t]^T \\ u &= [u_{VGT}, u_{EGR}]^T \\ w &= [\omega_e, W_f]^T \\ y &= [NO_x, PM, PL]^T\end{aligned}$$

The states x are respectively the intake manifold pressure, p_{im} , intake manifold fresh air mass, $m_{air, fresh}$, intake manifold inert air mass, m_{inert} , exhaust manifold pressure, p_{em} , exhaust manifold temperature, T_{em} , and turbocharger speed, ω_t . The inputs u are respectively the VGT vane angle in percent and EGR valve opening in percent. External disturbances w considered in this paper are respectively the engine speed, ω_e and fueling, W_f , in mg/inj. The outputs y used in this paper are respectively the NO_x and PM emissions in g/kWh and the pumping losses, PL , in Nm.

2.3 Emission Model

In addition to the engine air path model, an emission model is used. Based on the properties of the fresh air-exhaust mixture, engine speed and fueling, this model gives quantitative information on the NO_x and PM emissions.

The model consists of data maps that are filled with measured engine data. This makes modeling the physically and chemically difficult combustion dynamics redundant. A disadvantage of using a lot of measurement data in a model is the elaborate identification needed and the limited predictive qualities. The main advantage is that reliable results are obtained using relatively straightforward calculations. This makes this model very suitable for the intended goal of quantifying the effect the control actions have on the obtained emissions.

3 System Analysis

In this section some properties of the resulting system dynamics that are relevant for the control design are exemplified.

For both analysis and control design, it is important to keep in mind that the EGR-VGT control problem is inherently multi-input, multi-output (MIMO). Both the EGR and VGT are actuators that operate on the pressure difference between intake and exhaust manifold, which naturally couples their effects.

Opening the EGR valve will increase the flow of exhaust gas to the intake manifold. This reduces the flow of exhaust through the turbine and reduces the fresh air flow.

Changing the VGT vanes will change the pressure in the exhaust manifold and also changes the turbine speed. As a result, the boost pressure and fresh air flow will change as well. The difference between the intake manifold pressure and exhaust manifold pressure is the driving factor for EGR flow, hence this will change too. Both the EGR and VGT actuators have influences throughout the engine air path and therefore coupling is naturally present.

The controlled outputs of the engine are NO_x , PM and pumping losses. Where the pumping losses are used to quantify the main effect the air path has on the engine efficiency. This combination of outputs therefore reflects both the important emissions and the efficiency of the engine.

Including pumping losses as a third output has two main advantages for robustness. First, it improves the robustness in terms of performance. Second, it improves the robustness in terms of stability.

The reason for improved robustness of performance is that fuel efficiency is an important aspect of the engine performance. Pumping losses constitute the main influence of the air path on the fuel efficiency. A feedback controller that manages to keep the pumping losses close to the reference value will therefore improve the robustness in terms of performance.

The reason for improved stability when pumping losses are included is more complex. The effect can be calculated using the condition number, but has a physical interpretation as well. When only emissions are controlled, the system is naturally ill conditioned. We found that condition numbers after scaling of 20 and higher are common. This high condition number implies that the controlled system is likely to become unstable when uncertainties in the dynamic response are present. Including the pumping losses as a third output reduced the condition number for the operating point in this paper from 87 to 2.3; 87 is considered ill-conditioned and 2.3 well-conditioned. The allowed range of uncertain dynamics that will not cause instability is therefore increased significantly when pumping losses are included due to the improved conditioning. The physical interpretation for the ill conditioning of the NO_x -PM system is that a change of the inputs will result in a much larger change in the emissions when NO_x is traded for PM than when both NO_x and PM are lowered simultaneously. Therefore, the NO_x -PM

controlled system is conditioned. Because simultaneously lowering NO_x and PM using the EGR and VGT is combined with a significant increase of the pumping losses, including those as a third output improves the conditioning of the control problem.

3.1 Uncertain Dynamics

Apart from issues with the conditioning of the MIMO problem, diesel air path control is also made difficult due to the large amount of system uncertainty. Variations in external conditions such as ambient pressure, and internal conditions such as the engine speed or fuel input, result in a different response of the engine to changes in the system input. This difference in response could result in closed loop instability. Therefore the variation of the local dynamic response is investigated. This is done by identifying the behavior of the system at speeds and loads that vary from nominal.

Figure 2 shows that indeed the difference in response is significant. The design of the controller will have to be made such that it is stable, for all variations of the response that are encountered.

4 Control Design

The main result of this paper is the development of a feedback control strategy for emissions and efficiency. The controller design is a two-step process. Decoupling is combined with a diagonal control design. Figure 3 shows an overview of the control scheme.

4.1 Decoupling

For the two-input, three-output system, decoupling has a double purpose: it separates the output direction in which the EGR and VGT have no effect and it decouples the remaining two directions.

A Singular Value Decomposition (SVD) is used to achieve both the separation and the decoupling simultaneously. First, the system outputs are scaled to account for the relative importance and difference in units of the outputs. Input scaling is not needed, because both inputs are by default expressed in percent.

Scaling has a significant effect on the end result. It can be used to trade performance over the different outputs. The scaling values should reflect both the relative importance of the outputs and account for the difference in units. The controller in this paper uses the following scaling:

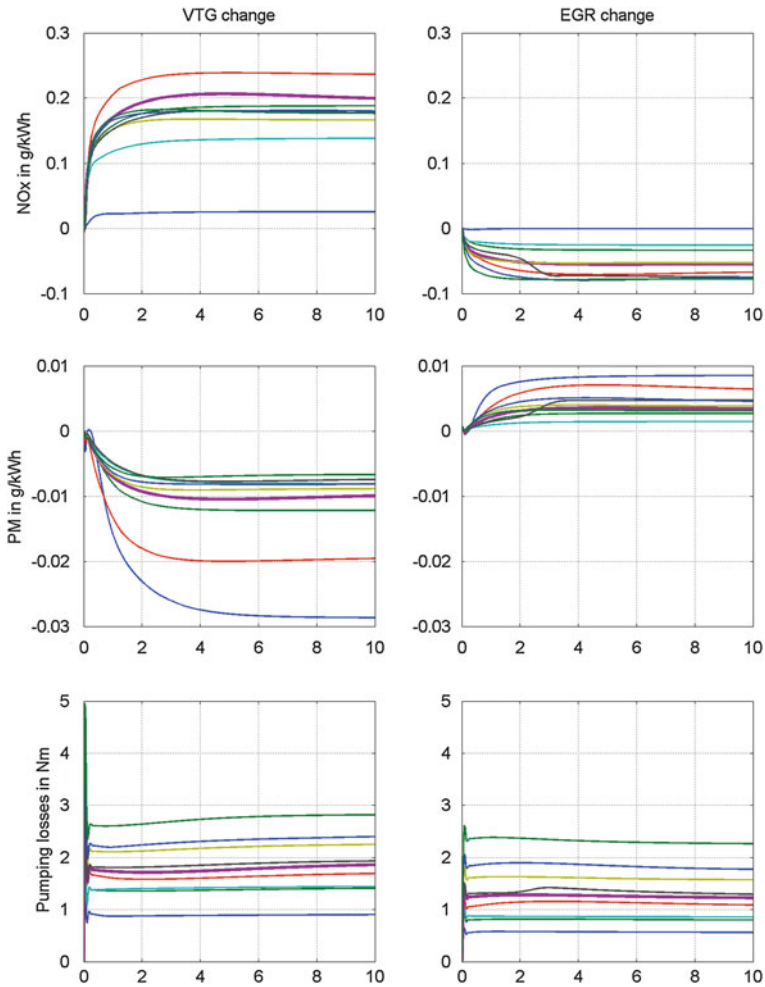


Fig. 2 The response of the nonlinear model under various conditions. The thicker *purple line* shows the nominal behavior. To create this figure, the nominal operating point was varied in the speed load region. The engine speed varied between 1213 and 1525 rpm. The fuel input varied between 80 mg/inj and 140 mg/inj

$$y_{\text{scaled}} = Sy = \begin{bmatrix} 1 & 0 & 0 \\ 0 & 5 & 0 \\ 0 & 0 & 0.05 \end{bmatrix} \begin{bmatrix} NO_x \\ PM \\ PL \end{bmatrix}$$

An essential part of the control strategy is the application of the singular value decomposition to separate the two controllable directions and find a decoupled input–output combination. The decoupling is based only on the steady state system gain, which simplifies both control design and implementation.

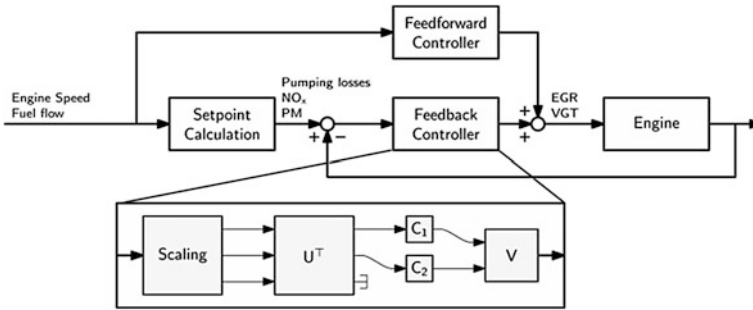


Fig. 3 A block scheme representation of the controller

Take $G_0 \in \mathbb{R}^{3 \times 2}$ the steady state gain matrix and $S \in \mathbb{R}^{3 \times 3}$ the scaling matrix. Then the singular value decomposition:

$$SG_0 = U\Sigma V^T$$

with diagonal Σ and orthonormal U and V can be used for decoupling.

The matrices U and V are orthonormal, therefore $U U^T = I$ and $V V^T = I$, with I an identity matrix of appropriate size. Pre- and post-multiplying $S G_0$ with respectively U^T and V results in the matrix $U^T S G_0 V = U^T U \Sigma V^T V = \Sigma$, which is known to be diagonal.

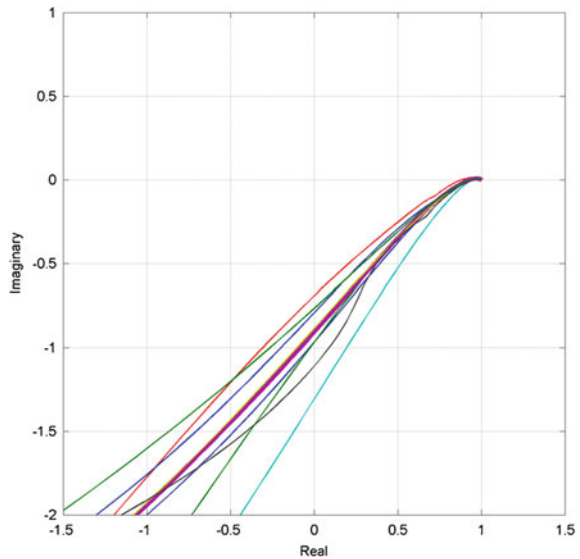
The implementation as shown in Fig. 3 decouples the system at steady state. Dynamically however the system is only approximately decoupled. These imperfections in decoupling are taken into account during the control design and stability analysis. Also, the variation in the engine response, which was identified in the Sect. 3.1, will result in imperfect decoupling which is taken into account during control design.

4.2 Control Design

The two feedback controllers C_1 and C_2 are designed using sequential loop-shaping techniques. The dynamics allow for a stable closed loop controlled system using PI control. A Notch filter is added to improve the closed loop behavior.

Using sequential loop-shaping, the MIMO behavior of the approximately decoupled system is accounted for. The generalized Nyquist criterion is used to check for stability of the MIMO system. Robust stability is included by performing the stability check for the set of systems identified in Fig. 2. This makes sure that the robustness of the closed loop system is sufficient. Figure 4 shows the Nyquist plots for the full set of systems.

Fig. 4 The Nyquist plot of the controlled system. It shows the real and complex part of $|C U^T S G V|$, with C , U , S , G and V respectively the transfer functions of the controller, output decoupling, scaling, plant and input decoupling



5 Results

To test the control system, two different simulations are performed with the closed loop system. The first is a step change of the references. This test shows the transient behavior of the controlled system. The second test is used to benchmark the performance of the controlled system when disturbances and uncertainties are present.

5.1 Step

To show the transient properties of the controlled system, step changes in the reference signal are applied. The results are shown in Fig. 5.

Clearly, tracking of the three reference signals is not perfect, even in steady state. The emissions of NO_x and particularly PM deviate from the reference values when a step change is requested. However, when looking at the middle-right plot, it is clear that the controller is able to achieve perfect tracking in the directions it has control authority (green and blue line). The error in these directions decreases to zero quickly, which means that within the capabilities of the system, the best possible tracking is achieved. The remaining error (red line) is outside of the control authority of the two actuators and is not feasible by the engine using the EGR valve and VGT as actuators.

The transient behavior in the two decoupled directions that are controlled is quick and without significant overshoot. A settling time of about one second is achieved.

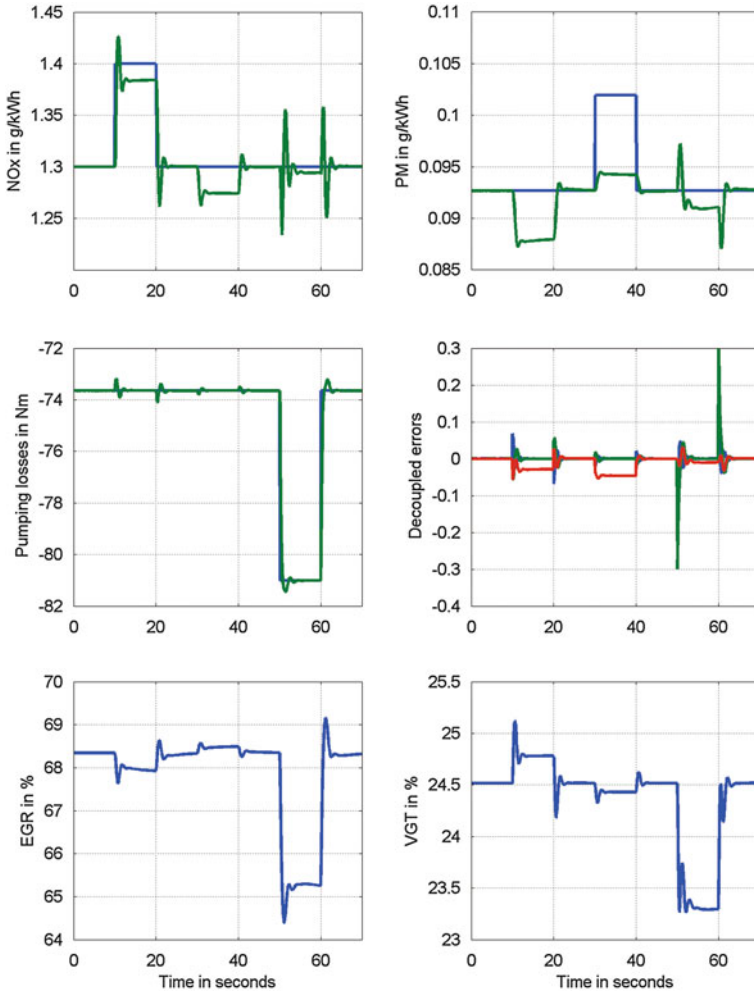


Fig. 5 The response of the controlled system to changes in the reference signals. The first three plots show the outputs (*green*) and their references (*blue*). The fourth plot shows the errors after being decoupled (i.e. in Fig. 3 after U^T), on two of these errors feedback is applied (*green* and *blue*), the *red* line is not actively controlled. The *bottom* two plots show the control actions

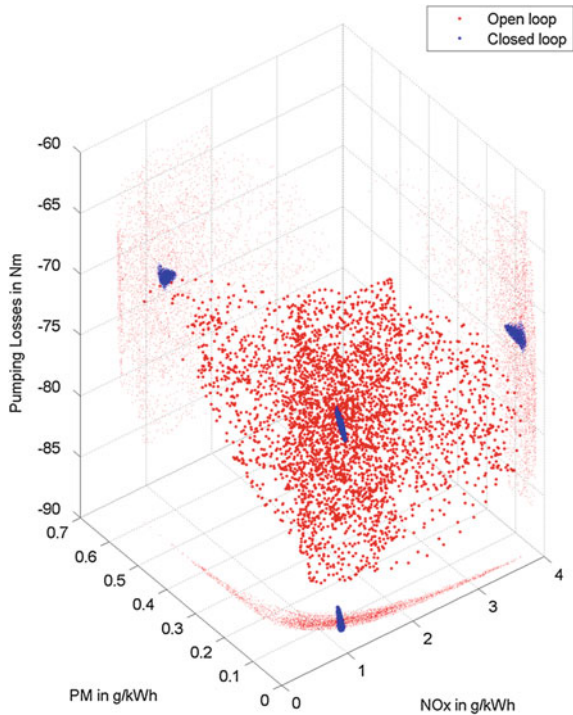
5.2 Disturbances

As a second test, the controlled system is evaluated for a combination of smoothly varying disturbances. Disturbances are applied in both the ambient conditions and the engine operating conditions. This simulates driving under various conditions using an engine that can deviate from nominal. All disturbances are applied as slowly varying sinusoidal disturbances with frequencies between 0.02 and 0.03 Hz. Because the frequencies of the disturbances are all chosen differently,

Table 1 Summary of the applied disturbances

	Nominal	Deviation
Ambient temperature (K)	300	15
Ambient pressure (Pa)	1.1×10^5	5×10^3
Engine speed (rpm)	1375	25
Engine torque (Nm)	775	25
Nominal VGT (%)	24.5	2
Nominal EGR (%)	68.3	2

Fig. 6 The results of two simulations with disturbances. In *red* an open loop controlled engine, in *blue* the engine with the feedback control system. In the middle, the *larger dots* show a 3 dimensional phase plot of a 3000 s simulation. To make the results easier to interpret, 2 dimensional projections are shown on the axes



over time, all combinations of disturbances are encountered. Table 1 summarizes the applied disturbances.

In Fig. 6 the results of a closed loop controlled engine are compared to an open loop controlled engine where the exact same disturbances are applied. The closed loop system is much better able to keep the emissions and pumping losses constant. Both the average values and the RMS deviations are calculated and shown in Table 2.

The direct goal of the closed loop controller in this case is to keep the difference between the reference outputs and the actual outputs as small as possible. This is reflected in the RMS error, which becomes respectively 12, 5 and 14 times smaller for NO_x, PM and pumping losses when feedback control is applied. This shows

Table 2 The results of the simulation with disturbances summarized

	Nominal	Closed loop		Open loop	
		Mean	RMS error	Mean	RMS error
NO _x in g/kWh	1.3	1.304	0.057	1.464	0.695
PM in g/kWh	0.0927	0.094	0.016	0.112	0.081
Pumping losses in Nm	-73.56	-73.56	0.361	-74.16	5.12
BSFC in g/kWh	216.58	216.58	-	218.18	-

that the controller is successful in counteracting disturbances, even though tracking of the underactuated control system cannot be perfect.

A second interesting result is that the closed loop controlled engine has about the same average performance as the nominal system, whereas the open loop controlled engine performs worse in terms of NO_x (14 %), PM (19 %) and fuel consumption (0.74 %) when disturbances are applied. The reason for the loss of performance of the open loop controlled system is that, particularly in the case of NO_x and PM emissions, the deviations in the direction of increasing NO_x and increasing PM are much larger than those in the direction of decreasing NO_x and PM. Using the suggested feedback control strategy, results in both a more economical and a more environmentally friendly engine.

6 Conclusions and Future Work

6.1 Conclusions

A new method for feedback control using the EGR valve and VGT is devised. Using only two actuators, closed loop feedback control of NO_x, PM and pumping losses is achieved. It is shown that the resulting controlled system is much more robust for uncertainties than a NO_x, PM controlled system. A simulation using multiple disturbances shows that the feedback controller decreases the effect of disturbances by a factor 5–14. The average emissions improved up to 19 % when compared to an open loop controlled system and a fuel efficiency gain of 0.7 % was realized.

6.2 Future Work

The performance of the controller was also tested on a real engine. Some modifications were needed to accommodate the difference in available sensors. We found that the experimental results are in agreement with both the theoretical and the simulation results presented here. These experimental results will be published soon.

References

1. Guzzella L, Amstutz A (1998) Control of diesel engines. *Control Syst* 18(5):53–71
2. Criens C, Willems F, Steinbuch M (2010) A systematic approach towards automated control design for heavy-duty EGR diesel engines. In: 10th international symposium on advanced vehicle control (AVEC)
3. Jung M, Glover K, Christen U (2005) Comparison of uncertainty parameterisations for h1 robust control of turbocharged diesel engines. *Control Eng Pract* 13(1):13–25
4. Wahlstrom J, Eriksson L, Nielsen L (2010) Egr-vgt control and tuning for pumping work minimization and emission control. *IEEE Trans Control Syst Technol* 18(4):993–1003
5. Stewart G, Borrelli F, Pekar J, Germann D, Pachner D, Kihás D (2010) Automotive model predictive control; models, methods and applications. *Toward a systematic design for turbocharged engine control*. Springer-Verlag, Berlin, pp 211–230
6. Stefanopoulou A, Kolmanovsky I, Freudenberg J (2000) Control of variable geometry turbocharged diesel engines for reduced emissions. *IEEE Trans Control Syst Technol* 8(4):733–745
7. van Nieuwstadt M, Kolmanovsky I, Moraal P, Stefanopoulou A, Jankovic M (2000) Egr-vgt control schemes: experimental comparison for a high-speed diesel engine. *IEEE Control Syst* 20(3):63–79
8. TNO (2005) Engine simulation tool DYNAMO. TNO Science and Industry

A Novel Alkali-Catalyzed Alpha-Alumina DPF with High Catalytic Activity and Durability

Keisuke Mizutani, Kensuke Takizawa, Hironobu Shimokawa,
Shuhei Oe and Naohisa Ohyama

Abstract A novel catalyzed diesel particulate filter (CDPF) consisting of an α -alumina DPF and an alkali-metal catalyst has been developed for the after-treatment of diesel soot. The α -alumina DPF (Al-DPF) was fabricated in a multi-segmented structure to relieve the thermal stress caused by the relatively high thermal expansion coefficient of α -alumina. The thermal and physical properties of the Al-DPF were analyzed and compared with those of the commercially available cordierite- and SiC-DPFs. The fundamental properties of the Al-DPF, including its particle filtration efficiency, pressure drop, and thermal durability were comparable to those of the conventional DPFs. Furthermore, the soot oxidation activity of the alkali-catalyzed Al-DPF (AC-Al-DPF) was evaluated using a 2.2 L diesel engine test bench. The soot oxidation rate of the AC-Al-DPF was 3-fold higher than that of a conventional Pt/Pd catalyzed SiC-DPF even after thermal aging at 800 °C for 50 h. Several accelerated durability tests were also conducted to clarify the negative effects of sulfur poisoning and ash accumulation on the catalytic activity of the AC-Al-DPF. The AC-Al-DPF demonstrated considerable stability against both sulfur poisoning and ash accumulation, which indicated that the alkali-catalyzed α -alumina DPF could be applied as an effective tool for the emission control of diesel soot.

Keywords Alkali-metal catalyst · Diesel particulate filter · Alumina-DPF · Soot oxidation · Diesel aftertreatment

F2012-A04-028

K. Mizutani · K. Takizawa (✉) · H. Shimokawa ·
ShuheiOe · N. Ohyama
Nippon Soken Inc, Nishio, Japan
e-mail: KEISUKE_MIZUTANI@soken1.denso.co.jp

1 Introduction

To improve the fuel efficiency of diesel engines, it is necessary to reduce the temperature and time required to burn off the soot captured by the diesel particulate filters (DPF). Many different types of catalysts have been studied for their potential application in soot combustion, and alkali metal catalysts have been reported to possess outstanding soot oxidation activity [1, 2]. Unfortunately, alkali metal catalysts are readily eluted in any moisture contained in the exhaust, and for this reason many attempts have been made to add water resistant properties to these catalysts [3–5].

The authors previously reported the development of an alkali metal-based catalyst with high soot oxidation activity, water resistance and thermal durability. This material was obtained by doping potassium carbonate onto a type of zeolite known as sodalite, with the resulting material being heated to induce a solid phase transformation [6]. The mechanism of water resistance exhibited by this catalyst has also been reported [7, 8]. In spite of these efforts, the soot oxidation activity of alkali metal catalysts invariably decreases with time and the DPF substrate is consequently damaged following periods of prolonged use because these catalysts can easily react with the DPF substrate materials such as cordierite (Cd) and silicon carbide (SiC) [9, 10]. Thus, a DPF substrate material that exhibits low levels of reactivity toward alkali metals is needed to allow for the practical application of alkali metal catalysts.

Alpha-alumina represents a possible solution to this problem because of its low reactivity with alkali metals and high thermal stability. In the current study, a multi-segmented α -alumina DPF (Al-DPF) has been fabricated and employed as a substrate for the newly developed alkali-metal catalyst. This paper describes the major characteristics of the Al-DPF and the soot oxidation activity of the alkali-catalyzed Al-DPF (AC-Al-DPF) under diesel engine exhaust, together with the results of a series of accelerated durability tests against sulfur poisoning and ash accumulation.

2 Experimental Setup

A schematic representation of the exhaust configuration used in the current study is shown in Fig. 1. A 2.2 L diesel engine equipped with a cooled exhaust gas recirculation was employed throughout the study for all of the necessary testing procedures. Each DPF test sample was installed downstream of a 0.8 L diesel oxidation catalyst (DOC) and the pressure drop was measured using a differential

Fig. 1 Engine and exhaust configuration

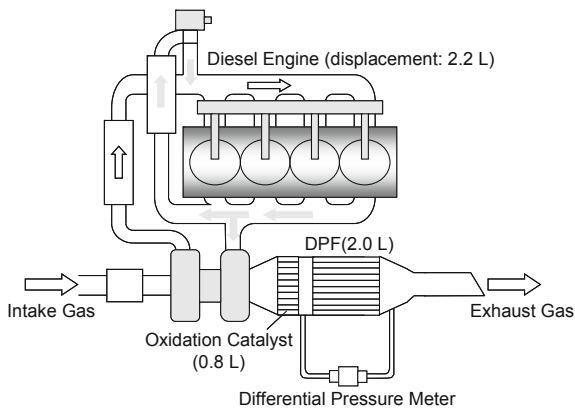
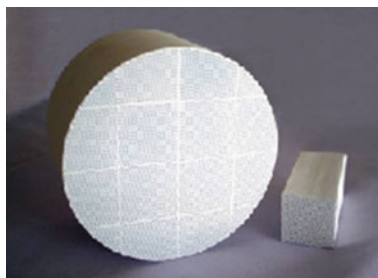


Table 1 Specifications of experimental equipment

Engine	
Engine type	Four cylinders direct injection (Common rail)
Displacement	2.2 L
Fuel	
Cetane index	53
FIA aromatics	19 vol%
Sulfur content	<10 ppm

Fig. 2 External appearance of the Al-DPF



pressure meter. Further detailed specifications of the experimental equipment are listed in Table 1.

Table 2 Thermal and physical properties of DPF substrates

	Cd-DPF	SiC-DPF	Al-DPF
<i>Structure</i>			
Diameter (mm)	160	160	160
Length (mm)	100	100	100
Form	Monolith	Segmented	Segmented
Segmented size (mm ²)	–	34*34	42*42
Cement layer (mm)	–	1	1
<i>Cell Design</i>			
Wall thickness (mil ^a)	12	10	12
Cell density (cps ^b)	300	300	300
<i>Pore design</i>			
Porosity (%)	49	42	54
Mean pore size (μm)	13	11	15
<i>Physical properties</i>			
Particle filtration efficiency (%)	>99.5	>99.5	>99.5
Compressive strength (MPa)	16.4	33.9	18.6
Young's modulus (GPa)	1.0	4.1	2.3
Poisson's ratio	0.31	0.17	0.24
<i>Thermal properties</i>			
CTE ^c [$\times 10^{-6}$ /°C (40–800 °C)]	0.4	4.6	7.9
Thermal conductivity [W/(m*K)]	1.0	36.2	5.6
Melting point (°C)	1460	2730	2050

^a milli inch length^b cells per square inch^c coefficient of thermal expansion

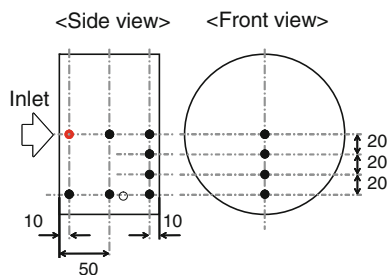
3 Performance Evaluation of Alpha-Alumina DPF Substrate

3.1 Thermal and Physical Properties of the Al-DPF

The Al-DPF substrate was fabricated with a multi-segmented structure, in a manner similar to that of the SiC-DPF substrate, to relieve the thermal stress caused by the high coefficient of thermal expansion (CTE) of α -alumina. The segment blocks were formed by extruding the raw materials, consisting mainly of α -alumina and inorganic binders, into a honeycomb structure and then heating them at 1650 °C for 10 h in the presence of oxygen. The calcined blocks were then bonded to fabricate an Al-DPF substrate of 2.0 L in volume (see Fig. 2).

Table 2 summarizes the thermal and physical properties of the Al-DPF and provides a comparison with the commercially available Cd- and SiC-DPFs. Filter designs were optimized to exhibit sufficient particle filtration efficiency and adequate mechanical strength. Thermal durability tests were concurrently conducted to evaluate the thermo-mechanical strength under soot combustion conditions because it was envisaged that the relatively low thermal conductivity and high CTE value might have a negative impact on the thermal shock resistance of the Al-DPF.

Fig. 3 Thermometric points inside the DPF substrates in the DTI test



3.2 Thermal Durability Test

The thermal durability of the Al-DPF substrate was evaluated in a drop-to-idle (DTI) test. For this particular test, a specified amount of diesel soot was loaded onto the DPF substrate and the temperature of the DPF substrate was then quickly raised by the exhaust port fuel injection. When the temperatures at the radial center and 10 mm in the axial direction from the inlet end of the DPF substrate reached 680 °C, the engine condition was dropped to idle. The DTI process led to a rapid temperature rise inside the DPF because of the sudden reduction in the convective heat removal and the uncontrolled combustion of the accumulated soot. The temperature rise inside the DPF substrate during subsequent uncontrolled regeneration was monitored at eight thermometric points, as shown in Fig. 3.

Figure 4 shows the relationship between the amount of diesel soot loaded on the various DPF substrates and the maximum temperature inside the DPFs during uncontrolled regeneration. For the Cd-DPF substrate, a maximum temperature of 1200 °C was reached when 8 g L⁻¹ of diesel soot was loaded. In contrast, the maximum temperature inside the Al-DPF substrate was 780 °C when the soot loading amount was increased to 13.5 g L⁻¹. The temperature behavior inside the Al-DPF was very similar to that displayed by the SiC-DPF. In addition, although the CTE of α -alumina was relatively high, no filter failures were observed throughout the testing process. This thermo-mechanical durability can be attributed to the adequate heat capacity of the Al-DPF and the thermal stress relief caused by the multi-segmented structure. These results suggested that the Al-DPF possessed the necessary level of thermal durability required for effective application in the aftertreatment system of diesel soot.

3.3 Pressure Drop Evaluation

System backpressure is a mandatory requirement for DPFs because it directly affects the engine power output and fuel economy. The pressure drop behavior of the Al-DPF in the absence of the catalyst was measured under steady-state exhaust gas flow and compared with the values from the commercially available Cd- and

Fig. 4 Maximum temperatures inside the DPF substrates at various diesel soot loadings

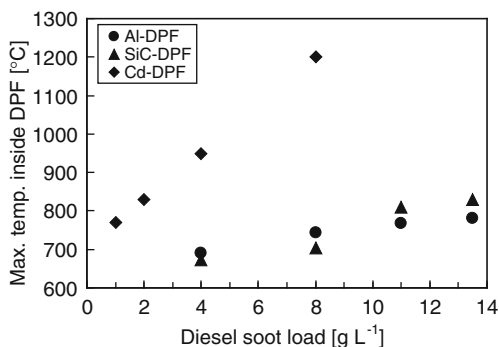
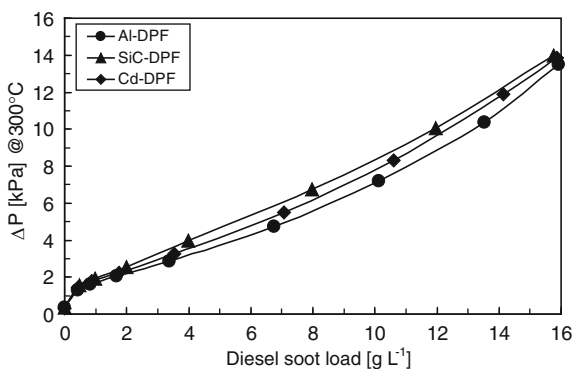


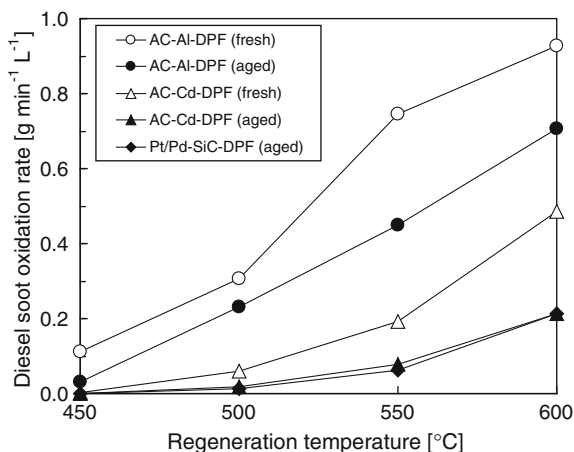
Fig. 5 Pressure drop behavior of the tested DPFs



SiC-DPFs of the same volume. The engine speed was fixed at 2000 rpm and the intake air mass was controlled throughout the testing period at 30 g s^{-1} . The differential pressure (ΔP) between the upper and lower stream of the filter was monitored until the cumulative amount of soot reached 16 g L^{-1} . The measured ΔP was then corrected to the value achieved at $300 \text{ }^\circ\text{C}$ to compensate for changes in the exhaust temperature.

As shown in Fig. 5, the pressure drop behavior of the Al-DPF was very similar to that of both the Cd- and SiC-DPFs indicating that the Al-DPF had no significant impact on the system backpressure and could be used as a feasible alternative to the conventional DPFs.

Fig. 6 Soot oxidation rate of the catalyzed-DPFs at fresh state (*open symbols*) and after thermal aging (*closed symbols*)



4 Soot Oxidation Activity of Alkali-Catalyzed Alpha-Alumina DPF

4.1 Soot Oxidation Activity Before and After Thermal Aging

An alkali-catalyzed Al-DPF (AC-Al-DPF) was prepared using a washcoat of approximately 40 g L^{-1} of the newly-developed alkali catalyst on the Al-DPF, followed by calcination in air at $650 \text{ }^\circ\text{C}$ for 3 h. To evaluate the effect of thermal aging, the AC-Al-DPF was subjected to heat treatment at $800 \text{ }^\circ\text{C}$ for 50 h. For the sake of comparison, alkali-catalyzed Cd-DPF (AC-Cd-DPF) and a commercially available SiC-DPF catalyzed with Pt/Pd (Pt/Pd-SiC-DPF, Pt/Pd loading; $0.6/0.3 \text{ g L}^{-1}$) were also subjected to the same treatments.

The diesel soot oxidation activity of each of these CDPFs was evaluated according to the following procedure. Initially, 8 g L^{-1} of diesel soot exhausted from a 2.2 L diesel engine was loaded onto the CDPFs. The CDPFs were then quickly heated by the exhaust port fuel injection to regeneration temperatures of 450, 500, 550 and $600 \text{ }^\circ\text{C}$. The duration of regeneration was 16 min for the regeneration temperatures of 450 and $500 \text{ }^\circ\text{C}$, and 7 min for temperatures of 550 and $600 \text{ }^\circ\text{C}$. The diesel soot oxidation rate per unit time and unit volume was calculated from the weight loss of the CDPFs during the regeneration process.

Figure 6 shows the relationship between regeneration temperature and the soot oxidation rate of each sample. Following thermal aging, Pt/Pd-SiC-DPF showed only negligible soot oxidation activity at $500 \text{ }^\circ\text{C}$, and an oxidation rate of only $0.21 \text{ g min}^{-1} \text{ L}^{-1}$ at $600 \text{ }^\circ\text{C}$.

For AC-Cd-DPF, although the soot oxidation rate of the fresh state was $0.49 \text{ g min}^{-1} \text{ L}^{-1}$ at $600 \text{ }^\circ\text{C}$, the value decreased to a level similar to that of Pt/Pd-

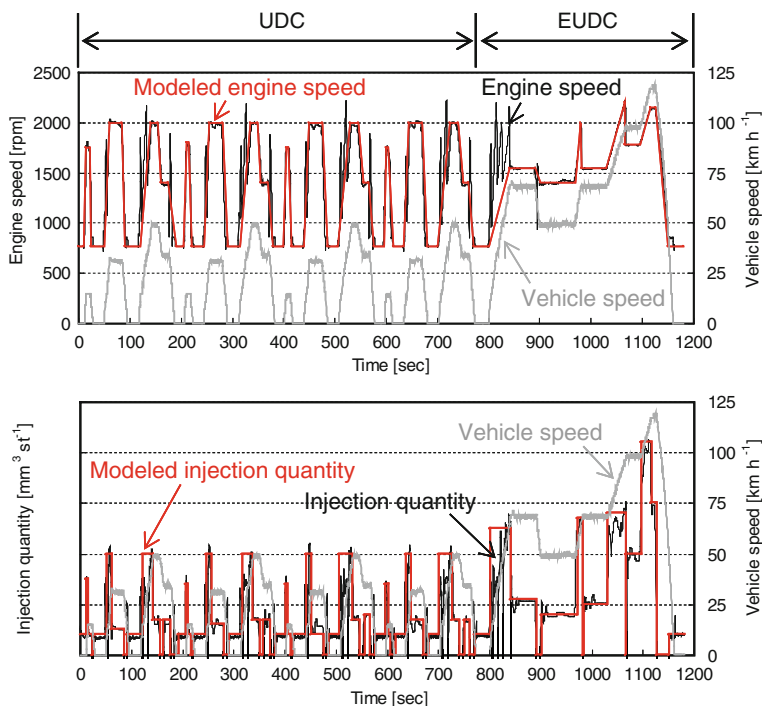


Fig. 7 Engine speed (*above*) and fuel injection quantity (*below*) in the NEDC

SiC-DPF following thermal aging. This result showed that the alkali catalyst coated on the Cd-DPF had been deactivated as a consequence of its reaction with cordierite.

In contrast, the AC-Al-DPF showed soot oxidation activity from 450 °C, with the oxidation rate reaching $0.93 \text{ g min}^{-1} \text{ L}^{-1}$ at 600 °C. Furthermore, the oxidation rate of the AC-Al-DPF at 600 °C was 3-fold greater than that of Pt/Pd-SiC-DPF even after thermal aging. The AC-Al-DPF exhibited higher soot oxidation activity than that of the Pt/Pd-SiC-DPF over the whole temperature range, and the oxidation rate of the AC-Al-DPF at 500 °C was almost equal to that of the Pt/Pd-SiC-DPF at 600 °C. The AC-Al-DPF therefore minimized the temperature and time required for the removal of accumulated soot.

4.2 Soot Combustion Test Results in Modeled NEDC Test Cycles

To investigate the soot oxidation performance and the temperature behavior of the AC-Al-DPF under actual regeneration conditions, a modeled New European Driving Cycle (NEDC) test was conducted on the engine test bench. The NEDC is composed of four segments of urban cycle (UDC) and an extra-urban cycle

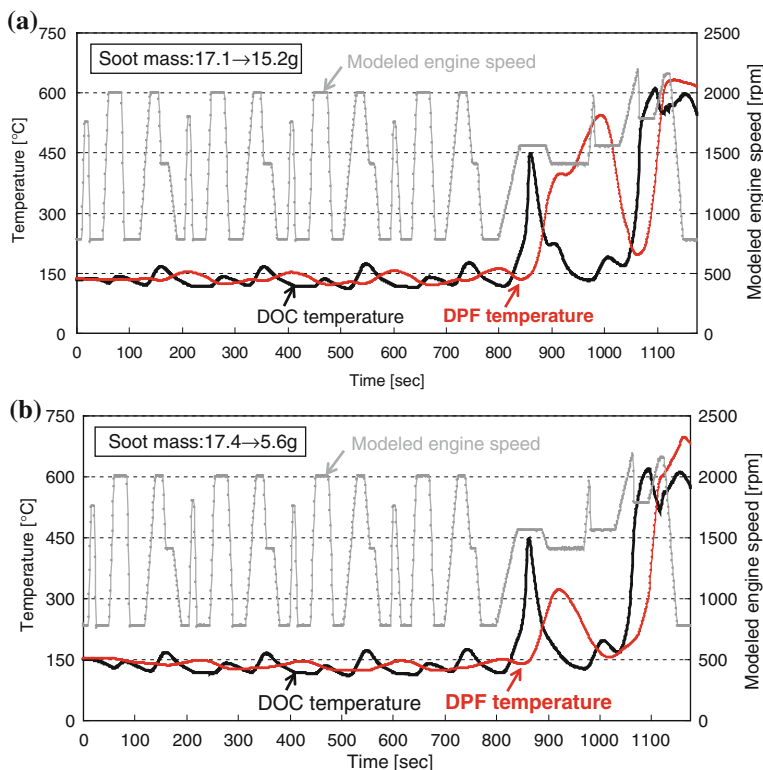


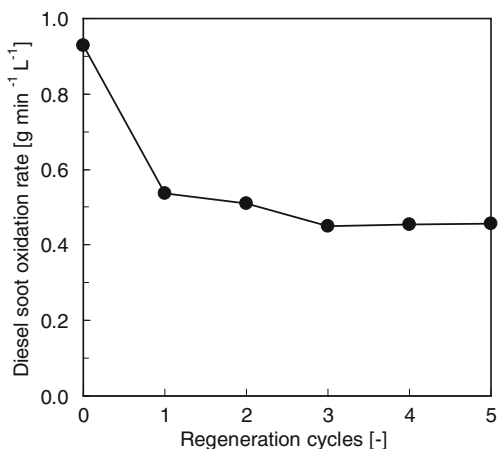
Fig. 8 Results of the modeled NEDC test; **a** Pt/Pd-Cd-DPF, **b** AC-Al-DPF

(EUDC) in the last segment. Engine speed and fuel injection quantity were controlled at the predetermined values, which were modeled based on preliminary vehicle test data from the NEDC model (see Fig. 7).

The AC-Al-DPF was subjected to thermal aging at 800 °C for 50 h and loaded with 8 g L⁻¹ of soot. The modeled NEDC test was conducted from a hot-start condition. When the temperature of the DOC reached 180 °C during the EUDC step, the DPF temperature was raised by the exhaust port fuel injection to regenerate the DPF. The mass of soot burned was measured by weighing the DPF before and after the test cycles and calculating the difference. The amount of soot exhausted during the testing period was also taken into account. As a reference, a Cd-DPF catalyzed with Pt/Pd (Pt/Pd-Cd-DPF) was also evaluated under the same conditions with a Pt/Pd loading of 0.6/0.3 g L⁻¹.

Figure 8 shows the DOC and DPF temperatures with engine speed and the variation in soot mass (inset left above) in the modeled NEDC test. For the Pt/Pd-Cd-DPF, although the DPF temperature increased quickly in the EUDC as a consequence of the relatively low thermal capacity of cordierite, the soot mass was reduced from 17.1 to 15.2 g during the course of the test and only a small amount

Fig. 9 Soot oxidation rate of the AC-Al-DPF after the accelerated sulfur poisoning test



of soot was removed. In contrast, the soot mass was reduced from 17.4 to 5.6 g in AC-Al-DPF following the test cycles. A drastic temperature rise caused by soot combustion was observed in the last EUDC step and the temperature inside the DPF reached approximately 700 °C. These results can be attributed to the difference in soot oxidation rates between the Pt/Pd catalyst and the alkali catalyst as described in the previous section.

5 Accelerated Durability Test Results

Sulfur poisoning and ash accumulation can exert a critical impact on the behavior of the CDPF system because sulfur can deactivate the active sites of the alkali catalyst and a deposited ash layer could prevent contact between the catalyst and the exhausted soot. Accelerated durability tests were therefore conducted to evaluate the effects of sulfur poisoning and ash accumulation.

5.1 Sulfur Poisoning

The effect of sulfur poisoning was evaluated using a cyclic regeneration test with high sulfur-content fuel. The high sulfur fuel was prepared by adding di-*tert*-butyl disulfide to diesel fuel as a sulfur source, and the sulfur content was adjusted to 200 ppm by mass. The test cycles included a variety of different acceleration and deceleration steps in which approximately 8 g L^{-1} of soot was accumulated, followed by a DPF regeneration step at 600 °C over a 7-min period. This test cycle was repeated five times.

The soot oxidation rate of the AC-Al-DPF after the each of the test cycles is shown in Fig. 9. It is clear from the figure that the soot oxidation activity of the AC-Al-DPF declined with each consecutive test cycle over the first three cycles and then reached a plateau for the remaining two cycles. Although this result indicated that the AC-Al-DPF could maintain a higher level of catalytic activity than that of the Pt/Pd-SiC-DPF shown in Fig. 6 following a highly-accelerated sulfur poisoning test, further investigation is required to clarify the long-term reliability of the material in a sulfur containing exhaust.

5.2 Ash Accumulation

Accelerated ash accumulation tests were conducted on the engine bench in a manner similar to the sulfur poisoning test, only high ash-content fuel was used instead. The high ash fuel was prepared by adding engine oil (CD 10W-30, 2 % v/v) to the diesel fuel. Upon completion of the ash accumulation through the cyclic regeneration, a test piece (30 mmD × 50 mmL) was cut out from the middle of the AC-Al-DPF and the thickness of the deposited ash layer was measured under an optical microscope. The soot oxidation rate of the test piece was evaluated according to the following procedure. Initially, 8 g L⁻¹ of soot was accumulated onto the test piece under diesel engine exhaust conditions, and the test piece was then inserted into the reaction furnace of a simulated gas generator (SIGU-2000, HORIBA, Japan) linked with a motor exhaust gas analyzer (MEXA-7000, HORIBA). The sample temperature was raised at a constant rate of 50 °C min⁻¹ in a N₂ flow. The gas was subsequently switched to 10 vol% O₂/N₂ mixture when the temperature reached 600 °C to regenerate the accumulated soot. The mass of combusted soot was calculated from the integrated amount of CO/CO₂ generation, and the soot oxidation rate was determined by the soot combustion amount per unit time during the 16-min regeneration process.

Figure 10 shows the soot oxidation rate measured on the test piece at a variety of different ash layer thicknesses. The microscopic images of accumulated ash are also shown in the same figure. When the thickness of the ash layer was less than 110 μm, no significant decrease in the soot oxidation activity was observed, whereas an obvious decline was observed when the thickness exceeded 140 μm. When the thickness of ash layer was greater than 180 μm, the soot oxidation rate tended to level out, likely because of the spontaneous combustion of soot without any catalysis. These results suggested that the alkali catalyst coated on the Al-DPF showed soot oxidation activity in the presence of an ash layer of up to 180 μm in thickness.

To elucidate the catalytic mechanism in the presence of an ash layer, quantitative analysis of the material was conducted using an electron probe micro analyzer (EPMA). Figure 11 shows the magnified view of a cell wall with an ash layer and the quantitative distribution of sodium (Na) as an active species. Measurement points (a), (b), (c) are points corresponding to distances of 5, 80, 150 μm from the

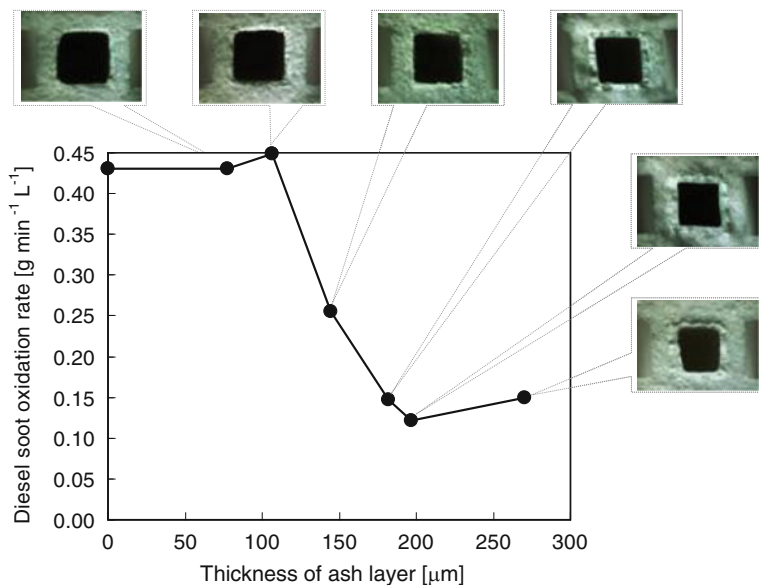


Fig. 10 Soot oxidation rate of the AC-Al-DPF after ash accumulation

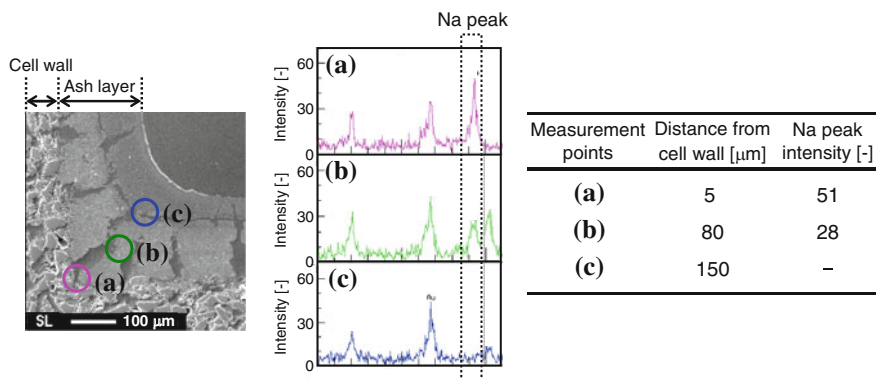


Fig. 11 Quantitative analysis of Na in the ash layer

cell wall, respectively. As can be seen from Fig. 11, Na was detected at points (a) and (b) in the ash layer, whereas it was not found at point (c), which indicated that the active species of the alkali catalyst could migrate into the ash layer over a certain distance. This result was in agreement with the oxidation performance study described above. Taken together, it is very likely that the occurrence of soot oxidation over the accumulated ash layer was caused by the migration of Na ion from the alkali catalyst into the ash layer.

6 Conclusions

A novel catalyzed diesel particulate filter (CDPF) consisting of an α -alumina DPF and an alkali-metal catalyst has been developed for the aftertreatment of diesel soot. The fundamental filter properties, soot oxidation activity, and thermal and chemical durability's of the material were evaluated. The main findings are as follows:

6.1 Filter Properties of the α -Alumina DPF

The α -alumina DPF (Al-DPF) was fabricated in a multi-segmented structure. The physical properties of the Al-DPF, including soot filtration efficiency, pressure drop, and thermo-mechanical strength were comparable to those of the conventional Cd- and SiC DPFs.

6.2 Soot Oxidation Activity of the Alkali-Catalyzed Al-DPF

The alkali-catalyzed Al-DPF (AC-Al-DPF) was prepared by coating approximately 40 g L^{-1} of the alkali catalyst onto the Al-DPF. The soot oxidation rate of the AC-Al-DPF was evaluated on an engine test bench using several different conditions. The AC-Al-DPF showed significantly higher oxidation activity than the conventional Pt/Pd catalyzed DPFs even after thermal aging at $800 \text{ }^\circ\text{C}$ for 50 h.

6.3 Stability Against Sulfur Poisoning and Ash Accumulation

Accelerated durability tests were conducted to investigate the effects of sulfur poisoning and ash accumulation on the performance of the AC-Al-DPF. The AC-Al-DPF maintained a moderate level of soot oxidation performance after several cycles of sulfur poisoning. In addition, the alkali catalyst coated on the Al-DPF showed soot oxidation activity even in the presence of an ash layer of up to $180 \text{ }\mu\text{m}$.

References

1. Mckee DW (1983) Fuel 62:170

2. An H, McGinn PJ (2006) *Appl Catal B* 62:46
3. Jimenez R, Garcia X, Cellier C, Ruiz P, Gordon AL (2006) *Appl Catal A* 297:125
4. An H, Su C, McGinn PJ (2009) *Catal Commun* 10:509
5. Zhang Z, Zhang Y, Wang Z, Gao X (2010) *J Catal* 271:12
6. Mizutani K, Ogura M (2007) Abstract of the 23rd annual meeting of Japan association of Zeolite, p 48
7. Kimura R, Elangovan SP, Ogura M, Ushiyama H, Okubo T (2011) *J Phys Chem C* 115:14892
8. Kimura R, Ogura M, Ushiyama H, Okubo T (2012) 109th Meeting of Catalysis Society of Japan, 2A04
9. Wu XX, Radvic LR (2005) *Carbon* 43:333
10. Iwachido K, Tanada H, Watanabe T, Yamada N, Nakayama O, Ando H, Hori M, Taniguchi S, Noda N, Abe F (2001) *SAE Paper* 2001-01-1298

A Super Clean Diesel Vehicle for us LEV III SULEV Category

First Report; A New Emission Strategy and Aftertreatment Management Control

Yuji Yasui, Hideki Matsunaga, Eiji Hashimoto, Naohiro Satoh,
Bart Schreurs, Hans Hardam, Masatoshi Yamada
and Toshiharu Takahashi

Abstract A Diesel vehicle has higher potential for CO₂ reduction than a gasoline vehicle. However, it was difficult for the diesel vehicle to become a global CO₂ reduction method, because the diesel vehicle cannot meet strict emission legislation such as LEV III legislation in US. Therefore, this research aims to reduce emissions of diesel vehicle to SULEV levels by using a Urea-selective-catalytic-reduction (Urea-SCR) system and unique engine and management controls. In order to achieve SULEV in FTP75 and US06 modes, both HC and NO_x should be reduced during the warming-up phase of the Urea-SCR system, and extremely high NO_x conversion efficiency after the warming-up phase is needed. The heat-up control using unique multiple injection and the early usage of exhaust gas recirculation (EGR) are applied to the warming-up phase. The dosing control using an NH₃ sensor is newly introduced to increase the NO_x conversion efficiency of the Urea-SCR system. When the air-fuel ratio combustion gas is kept at stoichiometric air-fuel ratio, a diesel oxidation catalyst (DOC) can indicate the same three-way conversion effect as a three-way catalyst (TWC) of a gasoline vehicle. The combination of the engine-out NO_x reduction by massive EGR, the three-way conversion effect of the DOC and the NO_x conversion effect of the Urea-SCR system is used during the warming-up phase in FTP75 and during acceleration phases in US06. This emission strategy was able to dramatically reduce NMHC

F2012-A04-030

Y. Yasui (✉) · H. Matsunaga · E. Hashimoto · N. Satoh
Honda R&D Co., Ltd Automobile R&D Center, Tochigi, Japan
e-mail: yuji_yasui@n.t.rd.honda.co.jp

B. Schreurs
Delphi Automotive PLC, Paris, France

H. Hardam · M. Yamada · T. Takahashi
Delphi Automotive Systems Japan, Ltd, Tokyo, Japan

and NO_x emissions in FTP75 and in US06, and achieved the reduction in the emissions below LEV III SULEV category's required levels.

Keywords Diesel • Emission • SCR • Air–fuel ratio • EGR

1 Introduction

The fuel consumption of an automobile has to be dramatically improved in order to avoid global warming and to resolve energy resource issues. Therefore, fuel consumption legislation for automobiles has been strengthened year by year.

As shown in Fig. 1, a diesel vehicle can indicate better fuel economy performance than a gasoline vehicle. As compared to the gasoline vehicle, the diesel vehicle can improve the fuel consumption by 20–30 %, and reduce CO_2 emission by 10–20 %. The diesel vehicle has significant potential to reduce CO_2 emission from automobiles [1].

HC, NO_x and CO emissions of the gasoline vehicle can be dramatically reduced by using a TWC because the air–fuel ratio of a gasoline engine can be easily kept at stoichiometric air–fuel ratio. On the other hand, a diesel engine is generally operated under lean air–fuel ratio condition. The TWC cannot reduce NO_x under lean air–fuel ratio condition. Therefore, it has been difficult for the diesel vehicle to achieve same emission performance as the gasoline vehicle. The diesel vehicle has not been one of global CO_2 reduction solutions because of the limitation of emission performance [2]. In other words, if the emission performance of the diesel vehicle can be dramatically improved, the diesel vehicle can become one of global CO_2 reduction solutions.

Consequently, this research aims to reduce the emissions of the diesel vehicle to LEV III SULEV category's required levels (hereafter, SULEV emission) in FTP75 mode and in US06 mode [3].

A Urea-SCR system [4, 5] is the mainstream of aftertreatment system for diesel vehicles in US, and can achieve the emissions of LEV II LEV and ULEV categories. Therefore, this research used a Urea-SCR system, and combined it with various unique control technologies in order to meet SULEV category.

Both NO_x and HC should be reduced before the activation of the Urea-SCR system in FTP75. Therefore, the heat-up control using multiple injections and the early usage of EGR are applied during the warming-up phase of the Urea-SCR.

The Urea-SCR system has to provide same NO_x conversion efficiency as the TWC of stoichiometric gasoline vehicle after the activation of the Urea-SCR system in FTP75. However, the Urea-SCR system cannot provide sufficient NO_x conversion efficiency when the temperature of a SCR catalyst cannot be kept at optimal temperature. In the meantime, this research investigates that the DOC indicates three-way conversion effect, if the air–fuel ratio of combustion gas is accurately kept at stoichiometric air–fuel ratio. Therefore, this research uses

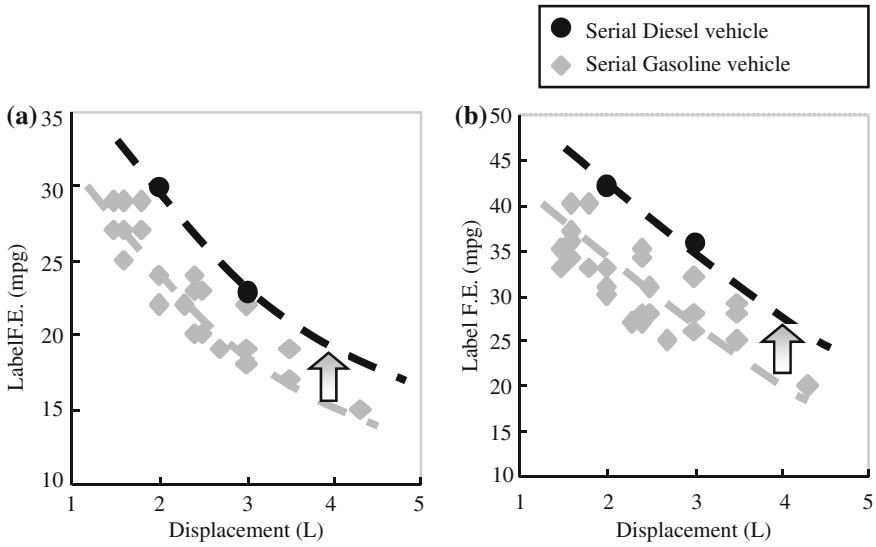


Fig. 1 Fuel economy comparison between gasoline vehicles and diesel vehicles in US market **a** City **b** Highway

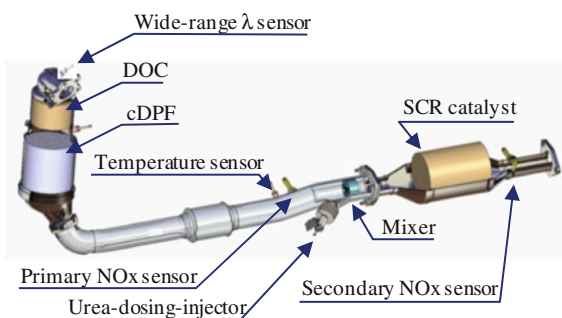
engine-out NO_x reduction by massive EGR and the three-way conversion effect of the DOC in order to assist the Urea-SCR system when the Urea-SCR system cannot provide sufficient NO_x conversion efficiency. In this research, this NO_x reduction mode is called “Triple NO_x Reduction”.

The NO_x conversion efficiency of the Urea-SCR system can be maximized by keeping the temperature of the SCR catalyst cannot be kept at optimal temperature and by maximizing the amount of stored NH_3 on the SCR catalyst. Consequently, the SCR catalyst is rapidly heated up and the temperature of the SCR catalyst is controlled at optimal temperature in this research. Furthermore, an NH_3 sensor is installed in the Urea-SCR system instead of a NO_x sensor. The Urea-dosing controller based on the output of the NH_3 sensor maximizes the amount of stored NH_3 while avoiding NH_3 slip downstream of the SCR catalyst.

The engine load becomes extremely high during acceleration phases in US06 mode. The Urea-SCR cannot keep same NO_x conversion efficiency as the TWC of the gasoline vehicle during the acceleration phases even if the amount of stored NH_3 on the SCR is maximized. This research uses Triple NO_x Reduction during acceleration phases in US06 mode also.

The issue of the emission strategy using only a general Urea-SCR system is mentioned in [Chap. 2](#), the new emission strategy to achieve SULEV emission (hereafter, SULEV emission strategy) in [Chap. 3](#). Aforementioned technologies for the SULEV emission strategy are explained in detail in [Chap. 4](#). The SULEV emission strategy was applied to a medium passenger equipped with a diesel engine (In-line 4, 2.2 L). The test results of the medium passenger are shown in [Chap. 5](#).

Fig. 2 The hardware configuration of the general Urea-SCR system



2 The Issue of the General Urea-SCR System

The general Urea-SCR system used in US market has the DOC, a catalyzed diesel particulate filter (cDPF) and the SCR catalyst as shown in Fig. 2. Two NO_x sensors are located upstream and downstream of the SCR catalyst, and a Urea-dosing-injector between the cDPF and the Urea-SCR catalyst. When the ratio between actual amount of stored NH_3 and the maximum amount of stored NH_3 of the SCR catalyst is defined as the NH_3 storage ratio, the Urea-dosing controller of the general Urea-SCR system keeps the NH_3 storage ratio at 30–60%. The NO_x conversion efficiency and the temperature of the SCR catalyst (hereafter, SCR temperature) in FTP75 and US06 modes are shown in Figs. 3 and 4.

As shown in Fig. 3, the activation speed of the SCR catalyst is very slow because there are a turbine system, the DOC and the cDPF upstream of the SCR catalyst. Accordingly, the general Urea-SCR system cannot provide sufficient NO_x conversion efficiency during warming-up phase. Furthermore, the NO_x conversion efficiency decreases in transient phases even if the SCR catalyst is activated.

In the meantime, the NO_x conversion efficiency in US06 mode also significantly reduces at transient phase as shown in Fig. 4 even if the SCR temperature is kept at the optimal temperature range.

The general Urea-SCR system has the potential to achieve ULEV 50 and ULEV 70 categories of LEV III. However, it is difficult for the general Urea-SCR system to meet SULEV category. It has the trade-off between HC and NO_x , because HC increases when the heat-up control is strengthened in order to hasten the activation timing of the SCR catalyst. On the other hand, NO_x conversion efficiency of the general Urea-SCR system might be improved by increasing the catalyst volume of the SCR catalyst and by increasing NO_2 generation on the cDPF. However, it is difficult to increase the catalyst volume of the SCR catalyst and the cDPF because of the limitation of space on a vehicle.

Consequently, “Breakthrough technology” is needed to achieve SULEV emission.

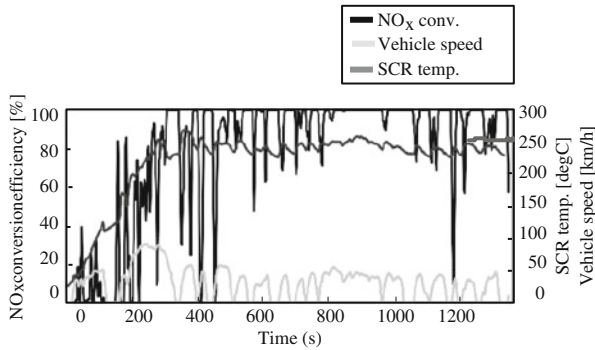
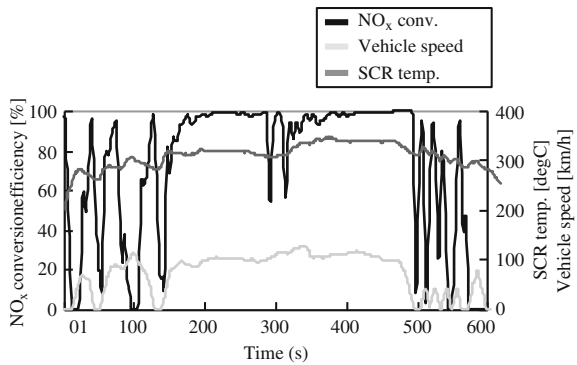


Fig. 3 The NOx conversion efficiency of the general Urea-SCR system in FTP75

Fig. 4 The NOx conversion efficiency of the general Urea-SCR system in US06



3 The New Emission Strategy for SULEV Emission

In order to achieve SULEV emission, both HC and NO_x are significantly reduced in FTP75 and NO_x during the acceleration phases in US06. Various technologies were researched in order to realise three requirements below in this research.

- A. Low-HC heat-up.
- B. To reduce NO_x upstream of the SCR catalyst (hereafter, SCR-in NO_x).
- C. To increase the NO_x conversion efficiency of the SCR catalyst.

The technologies to realise each requirement (hereafter, SULEV technologies) are as follows:

- For the requirement A
 - D-FIRE (Diesel - Fast Idle control for Rapid Engine heat-up)
- For the requirement B
 - High-EGR control
 - Stoichiometric air–fuel ratio control

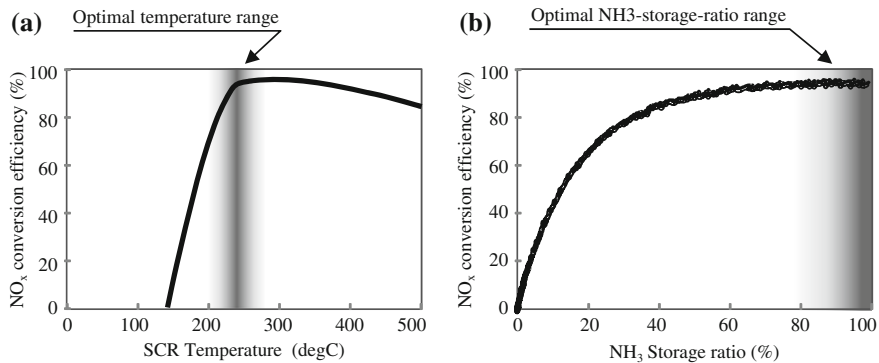


Fig. 5 The temperature and NH_3 -storage-ratio characteristics of the SCR catalyst **a** Temperature characteristic **b** NH_3 -storage-ratio characteristic

- For the requirement C

MID- NH_3 System

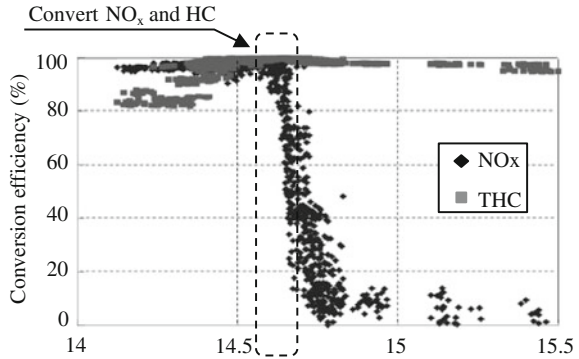
SCR temperature control

These technologies will be mentioned in detail in the explanation of the emission strategy for SULEV emission (hereafter, SULEV emission strategy) and in [Chap. 4](#).

This research focused on the characteristics shown in [Figs. 5](#) and [6](#) in order to determine the SULEV emission strategy. [Figure 5a](#) shows the NO_x conversion characteristic to the SCR temperature. The NO_x efficiency is maximized when the SCR temperature is kept at the range around 250 °C. Therefore, the SCR temperature control controls the SCR temperature at the optimal target range around 250 °C in this research. [Figure 5b](#) shows the NO_x conversion characteristic to the NH_3 storage ratio of the SCR catalyst. The higher the NH_3 storage ratio is, the higher the NO_x conversion efficiency of the SCR catalyst is. The general Urea-SCR system has not used up the potential of the SCR catalyst because it controls the NH_3 storage ratio at 30–60 %. In other words, the NO_x conversion efficiency of the SCR catalyst can be increased if the NH_3 storage ratio can be kept near 100 %. Consequently, this research uses the MID- NH_3 system mentioned later and maximizes the NH_3 storage ratio while suppressing NH_3 slip downstream of the SCR catalyst.

It is generally known that the TWC can indicate high three-way conversion efficiency under stoichiometric air–fuel ratio condition and the DOC high oxidation efficiency under lean air–fuel ratio condition. However, if the air–fuel ratio of combustion gas can be accurately kept at stoichiometric air–fuel ratio, the DOC can indicate three-way conversion effect as shown in [Fig. 6](#). This research uses the three-way conversion effect of the DOC in the SULEV emission strategy when the SCR catalyst cannot provide sufficient NO_x conversion efficiency.

Fig. 6 The NO_x and HC conversion characteristics of the DOC to the air–fuel ratio of combustion gas air–fuel ratio downstream of the DOC



The SULEV emission strategy for FTP75 is shown in Fig. 7. As aforementioned, if the heat-up control is strengthened to hasten the activation timing of the SCR catalyst, HC increases and SULEV emission cannot be achieved. Therefore, this research took the opposite strategy to the previous strategy using the general Urea-SCR system. The heat-up speed of the SCR catalyst was slowed down and D-FIRE is used as a heat-up control in order to suppress the increase in HC. Instead of slowing down the heat-up speed, EGR is used from the 1st hill of FTP75 mode in order to reduce engine-out NO_x. The SCR catalyst cannot provide sufficient NO_x conversion efficiency because the SCR temperature during the acceleration phase of 2nd hill cannot reach the optimal target range. This research improves NO_x conversion efficiency as much as possible by maximizing the NH₃ storage ratio. However, the NO_x reduction by both EGR and the SCR catalyst during the acceleration phase of the 2nd hill is not sufficient to achieve SULEV emission. Consequently, the stoichiometric air–fuel ratio control keeps the air–fuel ratio of combustion gas at stoichiometric air–fuel ratio, and achieves further reduction of NO_x by using the three-way conversion effect of the DOC. In other words, the combination of EGR, the DOC and the SCR catalyst reduces NO_x during the acceleration phase of the 2nd hill in the SULEV emission strategy. The concept to reduce NO_x by using EGR, the DOC is called “Triple NO_x Reduction”.

After the SCR temperature reached the optimal range, the SCR temperature control keeps the SCR temperature at the optimal target range and the dosing control for the MID-NH₃ system maximize the NH₃ storage ratio to maximize the NO_x conversion efficiency of the SCR catalyst. Moreover, when the ratio between total gas amount and re-circulated gas amount minus O₂ in a combustion chamber is defined as Inert-EGR, the High-EGR control maximizes Inert-EGR rate after the beginning of the 2nd hill. This research achieved same NO_x reduction as the TWC of the gasoline vehicle by using aforementioned emission strategy in FTP75 mode.

In the meantime, extremely high NO_x conversion efficiency is required during the acceleration phases in US06 mode. The Urea-SCR system cannot achieve the NO_x conversion efficiency to meet SULEV emissions in US06. Consequently, this research uses “Triple NO_x Reduction” during the acceleration phase of US06 mode as shown in Fig. 8.

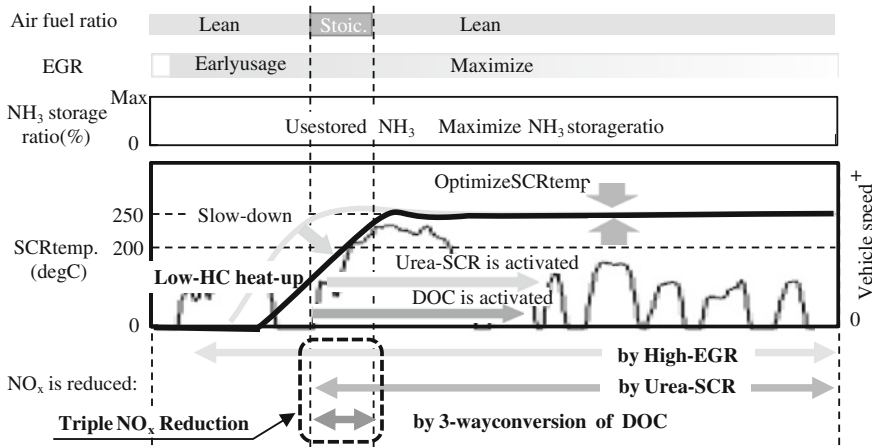


Fig. 7 The emission strategy to achieve SULEV emission in FTP75

4 The SULEV Technologies

4.1 D-Fire

The objective of D-FIRE is to heat up the DOC, the cDPF and the SCR catalyst while suppressing the increase in HC. A general heat-up control uses the injection pattern shown in Fig. 9a. This research focused on the exhaust-gas-temperature and emission characteristics shown in Fig. 10. When the number of fuel injection in a combustion cycle is increased, NO_x and HC decreases and the engine-out exhaust-gas-temperature increases. Therefore, D-FIRE conducts five fuel injections in a combustion cycle during fast idle condition and heat up the catalysts while suppressing the increase in HC.

4.2 Combustion Control for the High-EGR Control and the Stoichiometric Air-fuel Ratio Control

The stoichiometric air-fuel ratio control operates the engine at stoichiometric air-fuel ratio by increasing Inert-EGR, and not by increasing the injection amount of post injection. Therefore, both the High-EGR control and the stoichiometric air-fuel ratio control increase Inert-EGR rate more than that calibrated for the general Urea-SCR system, and have to stabilize combustion behaviour under transient conditions. When injection pattern and timing (hereafter, injection parameters) are determined on the basis of the target value of Inert-EGR rate and actual Inert-EGR rate causes the error against the target value because of the lag characteristic of a

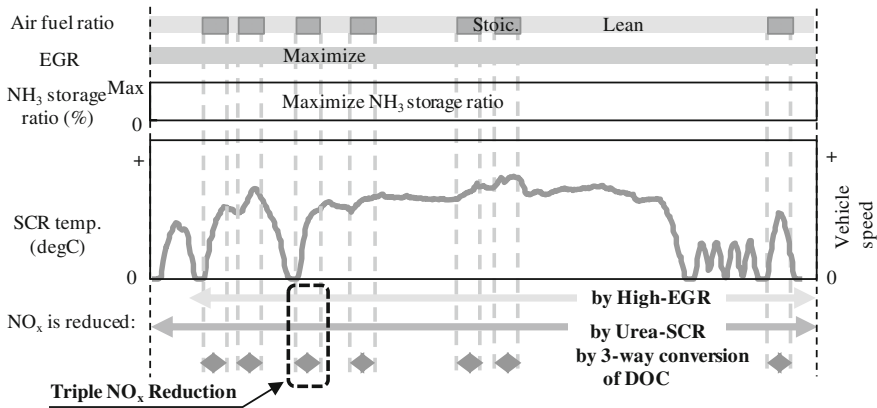
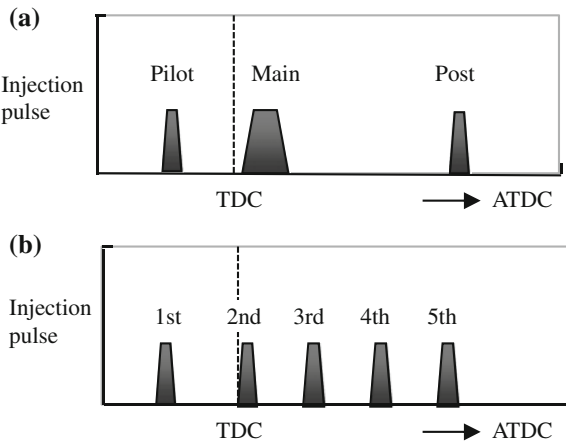


Fig. 8 The emission strategy to achieve SULEV emission in US06

Fig. 9 The injection patterns for the heat-up control



EGR system under transient condition, the combustion behaviour is worsened due to the miss-match of the injection parameters.

Consequently, this research uses the combustion control shown in Fig. 11. The combustion control estimates the estimation value of Inert-EGR rate on the basis of control parameters to the engine and acquired engine parameters, and determines the injection parameters on the basis of the estimation value of Inert-EGR rate, engine speed and driver’s demanded torque. It can stabilize the combustion behaviour under transient condition even if the High-EGR control and the stoichiometric air–fuel ratio control require high Inert-EGR.

Fig. 10 The exhaust-gas-temp. and emission characteristics to the number of fuel injection in a combustion cycle

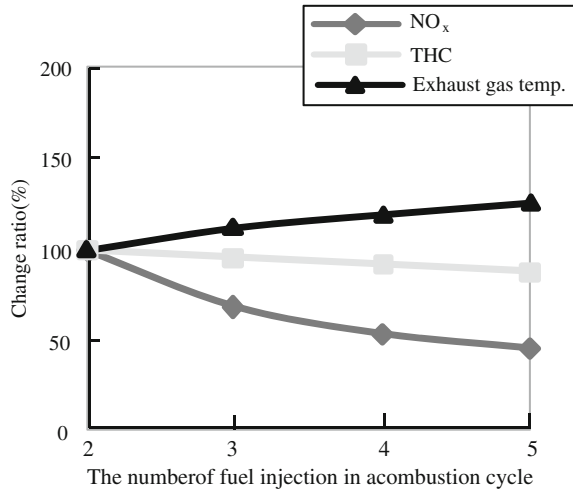
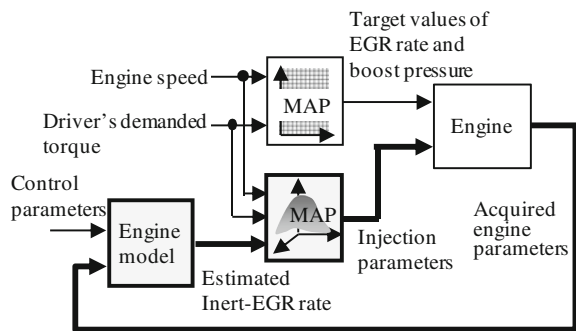


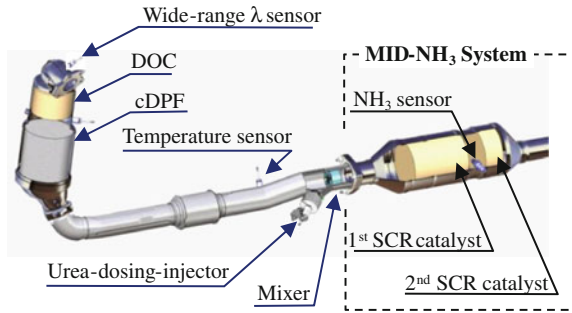
Fig. 11 The combustion control for the High-EGR control and the stoichiometric control



4.3 MID-NH₃ System

Figure 12 shows the hardware configuration of the SULEV aftertreatment system. The hardware configuration upstream of the SCR catalyst is same as the general Urea-SCR system. In the meantime, the hardware configuration around the SCR catalyst is modified as follows: The SCR catalyst is split into two bricks, and the NH₃ sensor is installed between the 1st and 2nd bricks instead of the NO_x sensors. The output of the NH₃ sensor means the concentration of NH₃ downstream of the 1st brick. The dosing controller determines Urea-dosing amount to keep the output of the NH₃ sensor at slight value. By doing this, the dosing controller can maximize and stabilize the NH₃ storage ratio on the 1st brick and achieve better NO_x conversion efficiency than the general Urea-SCR system. The 2nd brick traps NH₃ slip downstream of the 1st brick, and consumes this stored NH₃ to convert NO_x when NO_x slip downstream of the 1st brick occurs and Urea-dosing cannot be conducted Fig. 13.

Fig. 12 The hardware configuration of the SULEV aftertreatment system



5 Test Results

In order to confirm the NO_x reduction effect of the SULEV emission strategy, the two systems below were applied to the medium passenger car.

System1: Applied the SULEV technologies except of the stoichiometric air–fuel ratio control and maximized heat-up control.

System2: Applied all the SULEV technologies. (Applied SULEV emission strategy)

The system 1 does not use the stoichiometric control. In other words, it cannot use the concept of “Triple NO_x Reduction.” Therefore, the heat-up speed of the SCR catalyst was maximized in order to increase the NO_x conversion efficiency of the SCR catalyst as much as possible. Figure 14 is the comparison between the system 1 and the system 2 in CT phase of FTP75 mode. As shown in Fig. 14a, the system 1 was not able to reduce NO_x completely during acceleration phase of the 2nd hill. In the meantime, the system 2 conducted “Triple NO_x Reduction” during the acceleration phase of the 2nd hill as shown in Fig. 14b. The system 2 was able to reduce engine-out NO_x by using the High-EGR control as compared to the system 1. Furthermore, the three-way conversion effect of the DOC reduced SCR-in NO_x when the stoichiometric air–fuel ratio control kept the air–fuel ratio of combustion gas at stoichiometric air–fuel ratio. Finally, the MID-NH₃ system reduced the NO_x downstream of the SCR catalyst to approximately zero.

Consequently, it is confirmed that the concept of “Triple NO_x Reduction” was able to achieve significantly higher NO_x reduction than the system using only the Urea-SCR system.

The emission requirement for NO_x and NMOG is defined as the combined value of NO_x and NMOG in the SULEV 30 category of LEV III. Therefore, the target values for NO_x and NMHC for FTP75 were tentatively determined as 20 mg/mile and 10 mg/mile respectively. The combination value of NMOG and NO_x in US06 mode should be lower than 50 mg/mile to meet the SULEV category of LEV III. Here, the target values for NO_x and for NMHC in US06 were tentatively determined as 40 mg/mile and 10 mg/mile respectively.

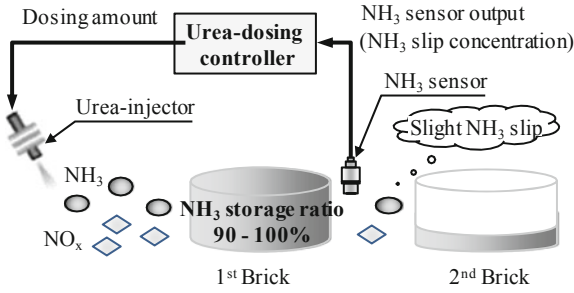


Fig. 13 The image of the dosing controller for the MID-NH3 system

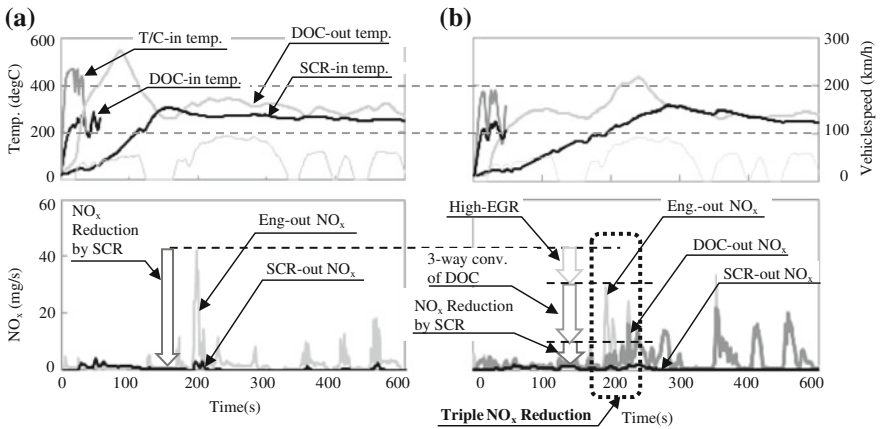


Fig. 14 The NOx reduction effect of SULEV emission strategy a System 1 (Only MID-NH3 system) b System 2 (SULEV Strategy)

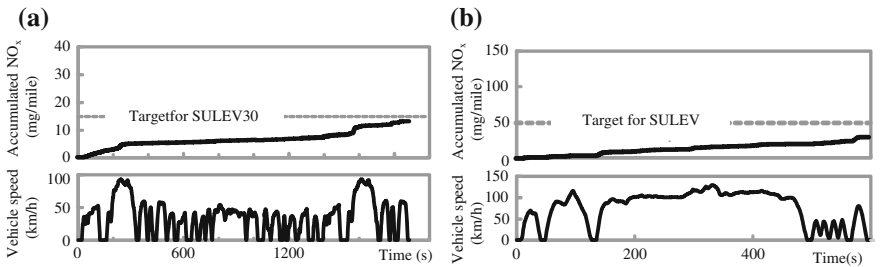


Fig. 15 The emission results of the SULEV emission strategy in FTP75 and US06 modes a FTP75 mode b US06 mode

Figure 15 shows the accumulated values of NO_x in FTP75 and in US06 when the SULEV emission strategy was applied. As shown in Fig. 5, the SULEV

strategy was able to make the accumulated values of NO_x lower than the target values. Furthermore, the accumulated value of NMHC in FTP75 mode was 8 mg/mile and that in US06 mode 5 mg/mile. The accumulated value of NMHC in FTP75 mode when the heat-up control was not used was 5 mg/mile. Therefore, it was confirmed that D-FIRE and the slowing-down of heat-up speed were succeeded in the suppression of the increase in HC.

Consequently, it was confirmed that the SULEV strategy was able to reduce NO_x and NMHC emissions to SUEV category's required levels.

6 Conclusion

In order to meet SULEV category of LEV-III, both NO_x and HC has to be dramatically reduced in FTP-75 mode, and extremely high NO_x reduction is needed in US06 mode. Therefore, this research proposed the concept of "Triple NO_x Reduction". In the concept, the engine-out NO_x reduction by the High-EGR control, the three-way conversion effect of the DOC by the stoichiometric air-fuel ratio control and the NO_x conversion efficiency of the Urea-SCR catalyst improved by MID- NH_3 system and the temperature management control were used. The Low-HC heat-up control using D-FIRE and "Triple NO_x Reduction" were used to FTP75 mode, and "Triple NO_x Reduction" was used during the acceleration phases of US06. As a result, this research achieved the reduction in NO_x and NMHC emissions below LEV III SULEV category's required levels under medium-passenger-car condition.

References

1. McMahon K et al (2008) American road: clean diesels for the real world. In: Diesel engine-efficiency and emissions research (DEER) conference
2. Onodera H et al (2008) Development of a diesel emission catalyst system for meeting US SULEV standards. SAE Paper No. 2008-01-0449
3. Matsunaga H, Yasui Y, Hardam H, Schreurs B et al (2012) A super clean diesel technology for US LEV-III SULEV. JSAE paper No.20125267
4. Paule M et al (2011) Challenges for the next generation of BlueTEC emission technology. SAE Paper No. 2011-01-0294
5. Shost M et al (2008) Monitoring, feedback and control of urea SCR dosing systems for NO_x reduction: utilizing an embedded model and ammonia sensing. SAE Paper No. 2008-01-1325

The Application of Nanometric Composite Materials in a Diesel Engine in the Aspect of Improvement of Deep Bed Filtration in a Diesel Particulate Filter

Jerzy Merkisz, Pawel Fuc, Piotr Lijewski and Andrzej Ziolkowski

Abstract The question of Diesel Particulate filter regeneration, despite many years of research, is still an existing problem. Currently, at the expense of the filter durability, the rate of variation of the thermodynamic parameters is increased in the exhaust systems in order to burn the particulate matter accumulated in the DPF filter. This is particularly the case for filters fitted in passenger vehicles operated in the urban cycle [1–3]. During the analysis the authors took into account the synergy of the aftertreatment components and the physical and chemical phenomena occurring in the integrated co-dependent aftertreatment systems in a diesel engine. The paper includes an analysis and results of tests performed under actual traffic conditions on vehicles fitted with modern aftertreatment systems [4–6]. In the performed tests stress was put on finding the possibility of improving of the DPF deep bed filtration through analysis of PM emission and size distribution. The considered area of investigations has been defined using nanometric composite materials based on highly porous supports of materials that are at the same time ionic conductors. For the research unique equipment has been used for tests under actual traffic conditions, which enabled a full analysis of the interactions of the gaseous emissions and particulate matter. An analysis of the PM size distribution and PM number has been performed during operation under actual traffic conditions.

Keywords Particulate matter · Diesel particulate filter · Research under real operating conditions

F2012-A04-031

J. Merkisz · P. Fuc (✉) · P. Lijewski · A. Ziolkowski
Poznan University of Technology, Poznan, Poland
e-mail: pawel.fuc@put.poznan.pl

1 Introduction

The most frequently used diesel particulate filter supports are cordierite supports, yet their durability and efficiency, particularly at longer periods of operation is limited. The basic problem is the increased flow resistance resulting from the clogging of the porous material, formation of ash in the interchangeably blanked cells of the support and material fracture resulting from various physical and chemical parameters of the filtering and/or blanking parts. Another limitation is the chemical processing in the aspect of formation of the active layer due to a lack of chemical activity of highly sintered cordierite (does not react with typical reducers and does not provide good conditions for low temperature catalyst application). In the case of SiC supports the problem is the low microporousness after the production process, which forces additional processing of chemical etching (hydrofluoric acid) or microsurface reduction with hydrogen to develop the surface. Classic SiC supports have low resistance to fracture resulting from the physical and chemical properties of the SiC-SiO₂ composite. Their advantages however are high thermal conductivity, high resistance to abrasion, resistance to breakability as well as resistance to chemical and gas induced corrosion. These advantages make the application of this SiC support in the atmosphere of exhaust gases purposeful from the point of view of its high efficiency in extended periods of operation. A significant elimination of the disadvantages of the classic SiC support forces the development of composite materials and parameters of the production process of the washcoat.

2 The Obtainment OF TiO₂-RuO₂-Composite Nanospheres Through the FSP Method

An example of a synthesis of the nanometric catalytic composite was the synthesis of the solid solution in TiO₂-RuO₂ system [7]. Isostructural oxides of TiO₂-RuO₂ of very good mixing properties in the nanospheres were obtained through the FSP method. The base products for the synthesis of the solid solution in TiO₂-RuO₂ system were isopropyl titanium alkoxide 97 % developed by Aldrich and ruthenium chloride 0.01 M RuCl₃ in the solution of ethanol.

The highest temperature range in which the sublayer of TiO₂ and the RuO₂ catalysts were in the flame zone was 860–900 °C in the H₂:O₂, ratio 1:1. The carrier gas in this case was argon with 4 % hydrogen.

In the FSP synthesis process nanometric bimodal spheres were obtained (two ranges of grain) of the powders, with the prevailing grain size of below 100 nm.

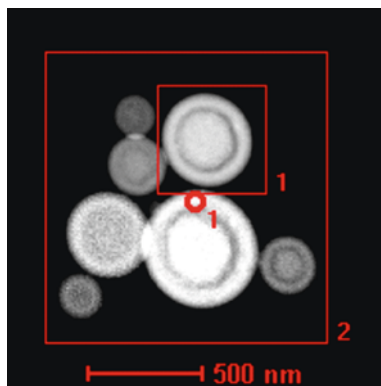


Fig. 1 HRTEM morphology of the $\text{TiO}_2\text{-RuO}_2$ colony [1]

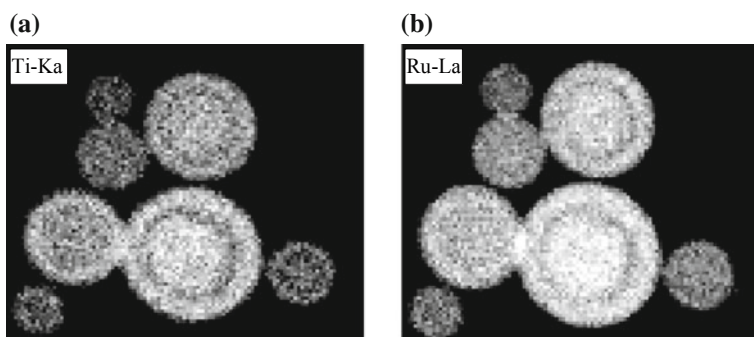


Fig. 2 HRTEM morphology of the $\text{TiO}_2\text{-RuO}_2$ colony showing the distribution of: **a** Ti-Ka; **b** Ru-La respectively [1]

Figure 1 presents the image of the colony of the $\text{RuO}_2\text{-TiO}_2$ nanospheres with a clearly shown nanospherical build. Figure 2 shows the distribution of Ti and Ru within the sphere.

Figure 3 presents the linear analysis of the distribution of atoms of Ti and Ru on the surface of the sphere of the diameter of 160 nm. In the solid solution of $\text{TiO}_2\text{-RuO}_2$ on the surface of the sphere, the crystals of RuO_2 are mixed 1:1 with the crystals of TiO_2 and form crystal structures of the solid solution in which titanium (on the atomic level) in the nano crystal structure blocks the thermal dissociation of ruthenium in the oxygen atmosphere. Figure 4 in the range of 5 nm presents the area of edge defects of the $\text{TiO}_2\text{-RuO}_2$ sphere obtained through the FSP method. The $\text{TiO}_2\text{-RuO}_2$ forming the external nanosphere layer allows good anchoring of the catalyst on the surface. Numerous edge defects occurring in the $\text{TiO}_2\text{-RuO}_2$ sphere suggest that the $\text{TiO}_2\text{-RuO}_2$ catalytic nanopowders obtained through FSP have an elevated proneness to form donors triggering the activation of oxygen.

Fig. 3 Linear analysis of the distribution of Ti and Ru on the surface of the sphere of the diameter of 160 nm

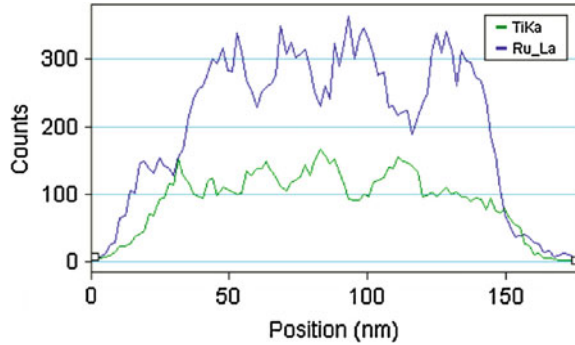
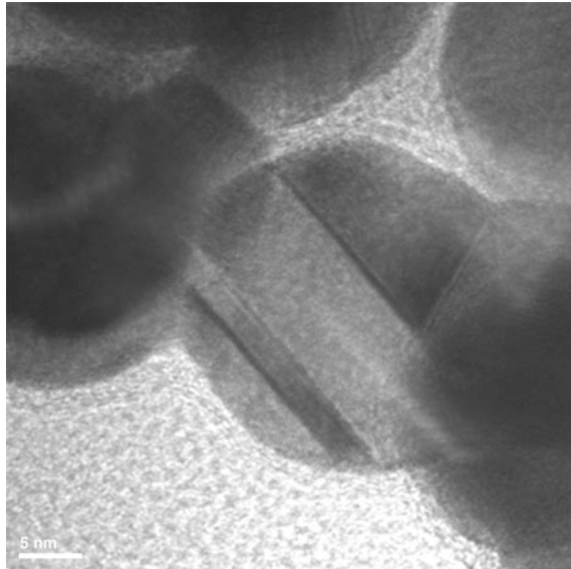


Fig. 4 HRTEM image of the edge defect of the $\text{TiO}_2\text{-RuO}_2$ sphere obtained through the FSP method



3 Experimental Research on the Catalytic Materials

Normative and short time simulations of the road conditions corresponding to selected driving cycles under different engine operating conditions (temperature, engine load, exhaust emissions) allow a simultaneous analysis of the exhaust components and particulate matter (PM). The values obtained from the latest technology measurements of the DOC catalyst and the DPF filter assembly (the structural part and the oxidation part) of own design and make can be compared to the values obtained in the measurements of the parameters of the OEM DPF filter. In the measurement system an oval DPF filter was used of the dimensions of $130 \times 150 \times 245$ mm manufactured by a French manufacturer. The filter was of the volume of 2.8 dm^3 . The tested catalytic system of the filter (the DOC part) was

Table 1 Basic parameters of the tested catalytic supports

Material/parameter	Cordierite	SiC	Al ₂ SiO ₅	Ti ₄ O ₇
Thermal expansion coefficient $\alpha \times 10^{-7}/C$	3–7	4–4.5	9	9
Melting point T_t (°C)	1460	2400	1600	1860
Thermal conductivity coefficient γ (W/m*K)	1	20	1	11.9–30
Thermal capacity (J/g*°C)	0.51	0.95	0.65	0.75
Resistance to thermal shocks T = 25–800 °C t = 1000 cycles	+	±	+	+
Specific mass (g/cm ³)	2.5	3.24	3.4	3.68
Young modulus E (GPa)	4.7	33.3	8.3	9.1
Porosity (%)	50–80	40–60	50–80	50–70
Size of pores (µm)	10–20	10–20	10–20	10–20
Average size of pores (µm)	–	10–12	15–18	14–17
Open porosity (mercury) (%)	–	49–51	45–65	40–60
Density of the channel cells (cells/mm ²)	200	0.35	0.465	80
Thickness of walls (mm)	0.15	0.25	0.33	0.29

of the volume of 0.7 dm³, while the filter itself was of the volume of 2.1 dm³. The filter channels were of the size of 100 cpsi.

For the test a catalyst was selected (as a substitute for commercial Pt catalyst)—of the nanosphere composition: TiO₂-0,1RuO₂-0,15 PdO₂. The catalyst was applied on seven SiC discs, surface modified with the Ti₄O₇ nanospheres of the size of 100 nm and the thickness of 20 nm. Such a design of the test system allowed a volume of 1.1 dm³. In the test a complex analysis of the possibilities of obtaining of composite, highly porous surface modified and fully modified sinters with such additives as: TiO₂, Al₂TiO₅, MgAl₄Si₅O₁₈. The assumptions were based on the results of complex investigations, some results of which have been shown in Table 1.

Nanotechnologically formed spheres (FSP method) such as Ti₄O₇ were used for the formation of sponge-like discs of the diameter of 100 mm, thickness 20 mm, porosity 80 % and pore size 80 ppi. Based on the nano intermetallic alloy technology and the production of self-supported highly porous DOC a series of catalytically active Pd–Ag, NiAl and Pd₃Ni sponge-like sinters were made.

4 Test Bed Investigations

Based on extensive data obtained in the urban and extra urban driving cycles verification test were performed on the engine test bed simulating the extra urban driving in order to answer the question of what the time is of the filter response to the engine parameters. The results obtained for the commercial filter and the tested material have been presented in Table 2.

Figure 5 present the characteristics of the obtained PM emissions: PM number and PM average size distribution for the engine speed $n = 2000$ rpm and the

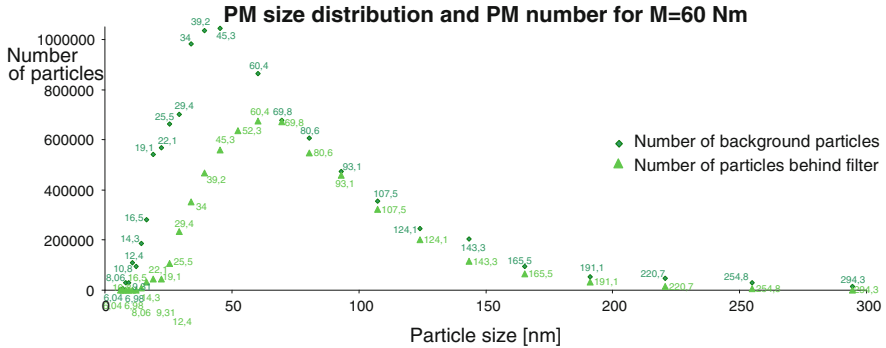


Fig. 5 PM size distribution and PM number at the engine load $M = 60$ Nm and engine speed $n = 2000$ rpm

engine load $M = 60$ Nm. The nature of the two curves shown in the first graph indicates a normal distribution. The first curve (dark green) shows the number of particles emitted for the engine operating conditions without a filter. For this curve we can see a maximum at the point 43.3 i.e. for the average PM sizes of 43.3 nm. The other curve (light green) shows the number of PM emitted for the engine operating conditions with a filter. For this curve we can see a maximum at the point of 60.4 i.e. for the average PM sizes of 60.4 nm. The shift of the curve showing the number of PM emitted for the system with a filter against the curve showing the operation without a filter is in line with the assumption that as the flow resistance grows, the number of collisions among the soot particles as well as between the soot particles and the walls increases, which leads to joining of the nanoparticles into aggregates.

5 Tests on the Commercial PM Filters in the City Traffic Under Actual Driving Conditions

The filter efficiency tests were carried out under actual traffic conditions in order to compare the urban and extra urban driving cycles for which DPF filter regeneration may be triggered. The tests were carried out in the urban cycle on the route lengths:

- (1) Vehicle A— $S = 11.96$ km; $V_a = 37$ km/h—technical specifications—Table 3.
- (2) Vehicle B— $S = 10.3$ km; $V_a = 19$ km/h—technical specifications—Table 4.

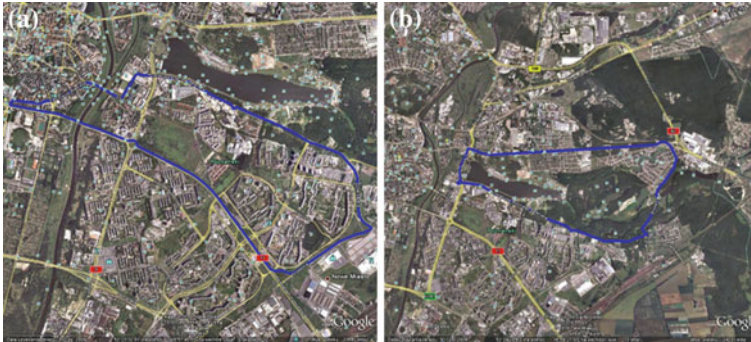
Figure 6 shows the routes that were used for the city traffic tests. The routes were chosen because of their length and characteristics. Because vehicles have to undergo homologation tests the routes were selected (their characteristics) so that the NEDC homologation conditions were reflected. This test as said earlier is

Table 3 Selected engine and vehicle parameters used for the tests of vehicle A

Displacement	Maximum power	Maximum torque
1896 cm ³	170 KM (125 KW) at 4000 rpm	350 Nm at 1800 rpm

Table 4 Selected engine and vehicle parameters used for the tests of vehicle B

Displacement	Maximum power	Maximum torque
1896 cm ³	115 KM (85 KW) at 4000 rpm	285 Nm at 1900 rpm

**Fig. 6** Route distances during urban traffic tests: **a** $S = 10.9$ km; **b** $S = 11.2$ km

composed of the urban and extra urban part. Each of these parts has different maximum driving speeds (52 and 120 km/h). That is why the routes (Fig. 6a, b) for the tests in the urban cycle under actual operating conditions were selected to simulate both parts of the NEDC test. In order to better picture the conditions of urban operation the selected routes were divided into two groups:

I urban driving—vehicle A—time span $t = 1181$ s— $t = 19.6$ min with average speed— $V_a = 37$ km/h—referred to as vehicle A (Fig. 6b),

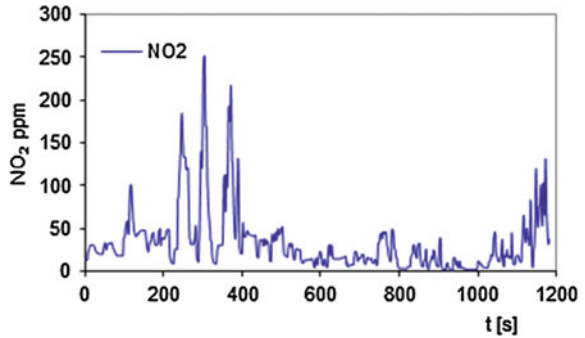
II urban driving—vehicle B—time span $t = 1181$ s = 19.6 min with average speed— $V_a = 19$ km/h—referred to as vehicle B (Fig. 6a).

Range I—vehicle A:

- minimum vehicle speed $V = 0$ km/h,
- maximum vehicle speed $V = 112$ km/h,
- minimum engine load $M = 0$ %,
- maximum engine load $M = 98$ %,
- driving time— $t = 19.6$ min.

The maximum concentration of NO_2 in the driving cycle for range I was 252.8 ppm—determined for the measuring time of 304 s and the minimum value of the NO_2 concentration in the driving cycle for this same range was 60 ppm determined for the measuring time of 918 s (Fig. 7).

Fig. 7 Dependence of the NO₂ concentration as a function of time for the tests under the conditions of actual operation for the urban cycle—vehicle A



When analyzing the first range the vehicle speed was within 0–112 km/h (for measurements made from $t = 21$ –785th second of the test). Lack of velocity occurred for 93 s, which constituted 8 % of the whole driving cycle. The minimum engine load $M = 0$ % (idle) occurred for the measurement made in time $t = 116$ s, which constituted 10 % of the whole driving cycle. The maximum engine load $M = 99$ % occurred for the measurement made in time $t = 748$ s.

Literature analysis and own research experience indicate that the soot deposited on the filter walls in the amount of 45 % of the total filter volume results in a deactivation of the EGR allowing an additional fuel injection in the exhaust stroke (post-injection). This process allows the exhaust gases in the exhaust system to reach the temperature of $T = 600$ °C, which is sufficient to trigger the soot afterburn. Such a state, however, is difficult to obtain under the conditions of start/stop driving, which is prevalent in the urban cycle. In such a case and in the case of vehicle driving with relatively low speeds the regeneration process is interrupted or does not initiate at all.

The graph of the particulate matter distribution (Fig. 8) shows that for the measurement range of vehicle A in the urban cycle the dominant particles are the ones of the size of 10,8 nm otherwise referred to as ultrafine— <1 μm .

Range II—vehicle B:

- minimum vehicle speed $V = 0$ km/h,
- maximum vehicle speed $V = 69$ km/h,
- minimum engine load $M = 0$ %,
- maximum engine load $M = 99$ %,
- driving time— $t = 19.6$ min.

The maximum concentration of NO₂ in the cycle (vehicle B) was 260 ppm—determined for the measuring time of $t = 733$ s and the minimum concentration of NO₂ in the driving cycle for this same range was 7 ppm determined for the measuring time $t = 835$ s (Fig. 9). The vehicle speed was recorded in the range of 0–66 km/h (for the measurements made in the 1st and 831th second respectively). Lack of velocity occurred for $t = 234$ s, which constituted 20 % of the whole driving cycle. The minimum engine load $M = 0$ %—(idle) occurred for $t = 11$ s, which constituted 1 % of the whole driving cycle. The maximum engine load

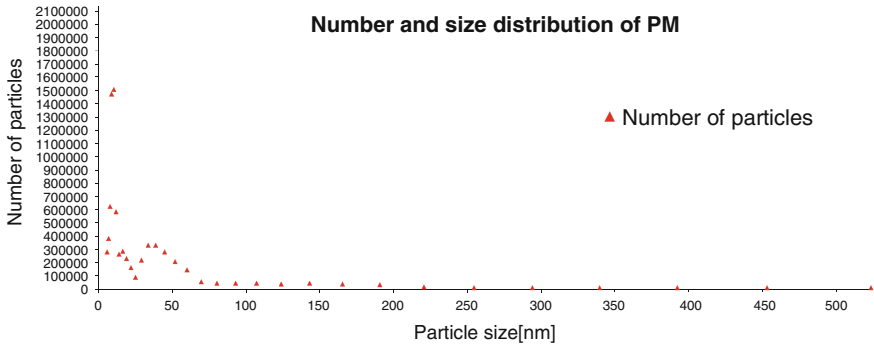


Fig. 8 Number and size distribution of PM under the conditions of actual operation for the urban cycle—vehicle A

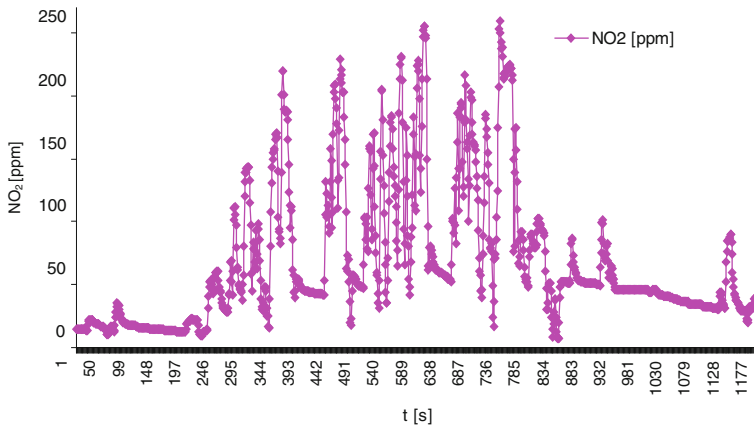


Fig. 9 The concentration of NO₂ under the conditions of actual city traffic operation marked as vehicle B

M = 99 % was observed for the measurement made in time t = 724 s. The whole route of the urban cycle for vehicle B was in the mixed mode. For the performed analysis it results that the vehicle speed of V > 60 km/h constituted 6 % of the whole urban driving cycle. In this cycle there was no road portion on which the vehicle would drive with the speed of V > 60 km/h for at least 10 min.

The concentration of NO₂ indicates that in t = 225–819 s there were numerous maximums. In the time span t = 594 s, the vehicle speed was higher than V > 40 km/h in time t = 45 s, which constitutes 8 % of the whole measurement road portion where the NO₂ maximums are visible. The NO₂ concentration maximums appeared many times in a single time span. The maximum NO₂ concentrations are for the measuring points: t = 603 s—NO₂ = 255 ppm and t = 733 s—NO₂ = 259 ppm. The analysis of speed V and load M has shown that the engine worked at idle seven times and there were 4 stops of the vehicle

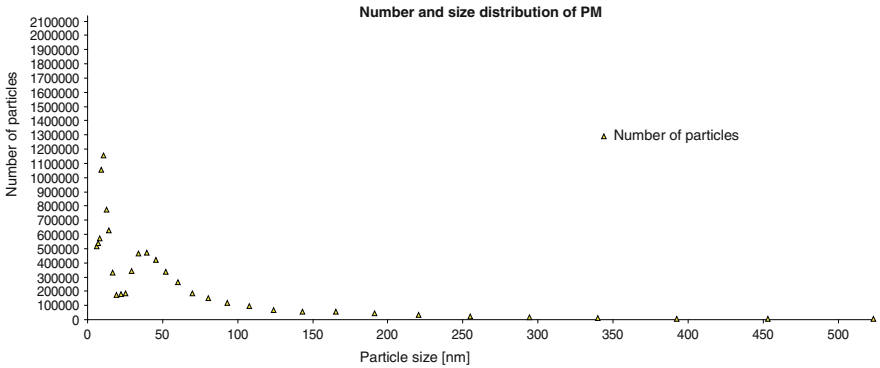


Fig. 10 PM number and size distribution under the conditions of actual city traffic operation marked as vehicle B

preceding the maximum NO₂ emissions. The total concentration of NO₂ in the whole measurement range $t = 1181$ s in the cycle of vehicle B was 80999.69 ppm NO₂ and was twice as high as the total concentration of NO₂ in the cycle of vehicle A—38805 ppm NO₂. The total time in which the vehicle operated at the speed of $V = 60$ km/h was 74 s. This time was insufficient to provide the thermal conditions for the regeneration process.

The graph of the distribution of the PM number (Fig. 10) shows that for the cycle of vehicle B (similarly to vehicle A) the dominant particles are the ones of the size of 10.8 nm otherwise referred to as ultrafine— $<1 \mu\text{m}$.

6 Conclusions

1. The research possibilities in nanoscale (TEM microscopy/HRTEM—high resolution TEM microscopy) allowed making assumptions for the production of materials based on nano structures (both single and multi component) of repeat composition, structure, size, physical and chemical properties.
2. The modification of many unwanted features was realized through melting in of the Ti₄O₇ nanospheres between the SiC grains and the covering SiO₂ enamel. This consisted in: an increased resistance of the material to fracture, an increase of the resistance to thermal shocks, a reduction of the thermal conductivity, an obtainment of better surface development, an increase of the microporosity of the sinter, an extension of the time of operation (even in the case of frequent regeneration cycles) and better activity.
3. The sponge-like sinters, obtained during the research from the Ti₄O₇ spheres and the Pd/Ag alloys showed high resistance to fracture and in the case of the sinters obtained from the Pd/Ag additional higher catalytic activity was

observed, which provides new potential for use of novel material of improved functional parameters by the automotive industry.

4. Statistical research carried out on the engine test bed as well as dynamic tests carried out based on the developed methodology of NEDC test simulation under actual operating conditions allowed a verification of the possibilities in the aspect of preliminary, comparative and criteria-based research.
5. The tests performed under actual operating conditions have shown the dynamics of the changes of the operating parameters and engine conditions and its influence on the functional parameters of the aftertreatment system i.e. catalytic converter (exhaust gases) and DPF filter (soot and ash).
6. The engines for the laboratory research and the vehicles for the on-road tests were carefully chosen. This allowed a verification of the parameters of the filtering devices under a variety of conditions and a development of the assumptions for the procedure of filter regeneration.

References

1. Czerwiński J, Comte P, Reutimann A, Mayer A (2011) Influence of (hydrous) ethanol blends on (particle) emissions of small 2- & 4-stroke scooters—Part 1. *Combustion Engines* 1/2011
2. Gao Y, Checkel MD (2007) Emission factors analysis for multiple vehicles using an on-board, in-use emissions measurement system. SAE Technical Paper Series 2007-01-1327
3. Zaigayew L, Shekhovtsov Y, Ignatov (2011) Research into particulate filter passive regeneration under operating conditions. *Combustion Engines* 4/2011
4. Merkisz J, Fuc P (2010) The exhaust emission from light duty vehicles in road test in urban traffic. International powertrains, fuels & lubricants meeting, Rio De Janeiro, Brazil. SAE Paper 2010-01-1558
5. Merkisz J, Lijewski P, Fuc P, Pielecha J (2010) Exhaust emission tests from agricultural machinery under real operating conditions. SAE 2010 commercial vehicle engineering congress, Chicago, USA. SAE Paper 2010-01-1949
6. Merkisz J, Fuc P, Lijewski P. (2011) The on-road operation of diesel particulate filter. *Combustion Engines* 3/2011
7. Fuć P (2008) Non Pt catalyst group in active part of new PM filter. SAE International Congress, 2008-01-1551, Shanghai 2008

Study on the PM_{2.5} and Ultra Fine PM Characteristics of Diesel Vehicle With DPF Under the Different Driving Conditions

Mengliang Li, Xiong Chen, Jiguang Wang and Yueyun Xu

Abstract Diesel particulate filter (DPF) can drastically reduce the mass of diesel PM (Particulate Matter) emission, as well as, it can significantly reduce the concentration of fine particulate, such as PM_{2.5}. In order to study the PM_{2.5} characteristics and the effect of driving conditions to the DPF filter efficiencies, the suitable filters were installed on the vehicles without any matching and calibration. Under NEDC, PM emission of upstream and downstream of DPF on five commercial diesel vehicles was tested by CVS, and the number concentration and mass concentration of PM was tested by ELPI. The results showed that DPF filter efficiencies can over 92 % for both PM₁₀ and PM_{2.5} under most operating conditions. However, under a fewer operating modes, such as a 200s period after cold start, and a 50s period before the end of NEDC which is a rapid slowdown period, the efficiencies of DPF filter is low. This paper reports a work on study for the PM_{2.5} and ultra fine PM characteristics of diesel vehicle with DPF under the different driving conditions, these impact factors for DPF filter efficiency with some conditions, by comparing both of number concentration and mass concentration on the PM size distribution before and after DPF. This paper reports the emission characteristics of PM_{2.5} and ultra-fine particles before and after DPF filter under different driving conditions. The results show that DPF filter can reduce PM emission significantly, but attention to the control of DPF filter is needed under the rapid slowdown condition.

F2012-A04-034

M. Li (✉) · X. Chen · Y. Xu
China Automotive Technology and Research Center, Tianjin, China
e-mail: chenxiong24@163.com

J. Wang
School of Automotive Engineering, Wuhan University of Technology, Wuhan, China

Keywords DPF · NEDC · PM2.5 · Number concentration · Mass concentration

1 Introduction

Ultra fine particulate PM_{2.5} in the air not only seriously harms human health, but also is considered to be main reason causing haze in many large cities. Therefore, many large cities such as Beijing have begun to monitor the PM_{2.5} concentration in the air. Meanwhile, as the Ambient Air Quality Standards revised in 2012, PM_{2.5} even more was included in evaluation index of routine air quality. As a major source of elemental carbon component of PM_{2.5} in the air, emissions from diesel vehicles have become an increasing concern.

DPF can drastically reduce the PM emission, and effectively reduce PM_{2.5} emissions from diesel vehicles. Many studies have been done for the evaluation of DPF performance test methods by research institutions at home and abroad. Test of DPF filtering performance is completed in the engine test bench, by running a period of stable load conditions and then calculating the filtering efficiency of DPF, initially the efficiency reaching more than 85 % [1]. Many emission tests for before and after installing DPF under NEDC driving conditions are done. However, the results of weighing PM show that the filtration efficiency of DPF exists large difference comparing with engine test bench, and the filtrating effect is worse than stable loading conditions. In this paper, light-duty diesel vehicles equipped with DPF are studied, by testing the diesel vehicles emission state and size distribution of the PM concentration before and after installing DPF under NEDC. By comparing the size distribution of PM_{2.5} number concentration and mass concentration before and after installing DPF under different driving conditions, the diesel vehicle emission characteristic of PM_{2.5} under specific driving conditions is studied.

2 Test Vehicle

The test selects a light-diesel vehicle meeting State IV standard, the specific parameters shown in Table 1. The authors transform the vehicle exhaust system, installing the oxidation catalytic converter (DOC) and particulate filter (DPF). The DPF adopts wall-flow ceramic honeycomb filter, relying on burner injection to complete active regeneration.

3 Test Program and Equipment

According to requirements of light-duty diesel vehicle I-type test, the vehicle runs on a laboratory drum and tests under NEDC driving condition [2]. Collect PM from emission by using constant volume dilution system (CVS), then get PM

Table 1 Test vehicle

Project	Parameter
Total mass	3,300 kg
Curb mass	2,140 kg
Rated power	85 kW
Displacement	2.4 L
Mileage	4,560 km

emission factor (mg/km) by weighing and calculating. Measure the exhaust flow and per-second transient concentration of all PM size from upstream and downstream of DPF by portable emission measurement system (PEMS). Exhaust emission from before and after installing DPF is tested by using I-type test, and records transient PM concentration respectively.

The main part of test is done on chassis dynamometer and PEMS. PM comprehensive emission level before and after installing DPF under NEDC is compared by chassis dynamometer. The PM number concentration and mass concentration of upstream and downstream of DPF are compared by PEMS, moreover, are compared the particulate transient concentration and emission under different driving conditions. On-board Portable Emission Measurement System (PEMS) assembles OBS-2200 using for measuring gaseous pollutants emission and Electrical Low Pressure Impactor (ELPI) using for measuring PM emission concentration. ELPI can measure real-time PM number concentration and mass concentration of 12 aerodynamic diameter segment, recording PM size range of 0.007–10 μm [3]. ELPI records all PM emission conditions from Engine ignition to the end of NEDC cycle, processing the ELPI data by mean value method, then get the mean number concentration and mean mass concentration of PM for each test. Besides, the exhaust flows measured by pitot tube flow meter of OBS-2200 are brought into measurement and calculation of ELPI, then can calculate the total PM emission of the entire test, moreover can calculate the PM emission of any driving modes in the cycle according to requirements.

4 Analysis of Test Result

4.1 Analysis of Emission Results

The I-type test emission results shown in Table 2 are measured by full-flow dilution system before and after installing DPF. From the results, there is little difference and fine consistency between two tests after installing DPF. Several test results are far below the limits of State IV, and achieve fine effects. In the process of test, the data read by DPF controller shows that DPF does not regenerate. The reason maybe that the fuel does not inject into by for combustion from engine ignition to the end of test, leading to the result that exhaust temperature is not heated to the required regeneration temperature.

Table 2 Emission result

Y/N installing DPF	Emission factor				
	HC g/km	CO g/km	NO _x g/km	HC + NO _x g/km	PM mg/km
N	0.05	0.05	0.38	0.43	41.7
Y	0.014	0.013	0.37	0.39	19.07
Y	0.01	0.01	0.38	0.39	19.94
Limits of State IV	————	0.74	0.39	0.46	60
Limits of State V	————	0.5	0.18	0.23	5

From the test results before and after transforming exhaust system, we can see that HC and CO emission are reduced by more than 70 %. The reason is that it oxidizes much unburned HC and CO exhausted from original engine after installing DOC, however NO_x emission changes little and almost is not affected. From difference of PM emission results, mainly concerning the changes before and after installing DPF, we can find that PM emission are reduced about 50 % after installing DPF and filtration efficiency of the PM is obviously lower than environmental protection industry standard HJ451-2008 (Technical requirement for environmental protection product After-treatment devices for diesel vehicle exhaust) which requires filtration efficiency of wall-flow DPF than 85 % [4].

By CVS, the PM emission factor got by calculation of Quality Law is the mean (mg/km) value of the total PM emission with the total mileage in the entire test cycle. The filtration efficiency of DPF on PM got by calculating the PM emission factor before and after installing DPF only reflects the comprehensive level of DPF under the entire NEDC driving cycles, does not reflect the filtration effect of DPF under different driving modes. In order to get the actual level of PM filtration efficiency under each driving modes, PM transient concentration before and after installing DPF should be analyzed [5].

4.2 PM Emission Concentration under NEDC

Through analyzing the mean instantaneous PM concentration under the entire test cycle, authors find that the filtration efficiency of DPF on PM can achieve more than 90 % under most driving conditions. Figure 1 is the filtration efficiency of DPF on PM_{2.5}. The low filtration efficiency of DPF may be caused by some tiny operating conditions, so need analyze the instantaneous concentration before and after DPF under NEDC cycle.

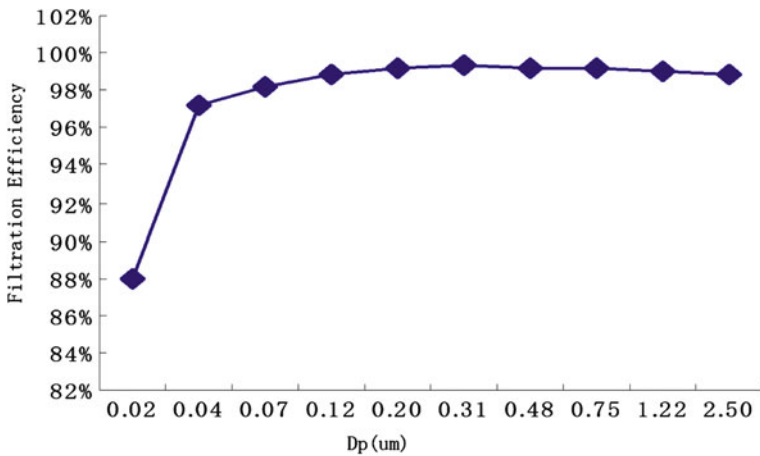


Fig. 1 Filtration efficiency of DPF on PM_{2.5} number concentration

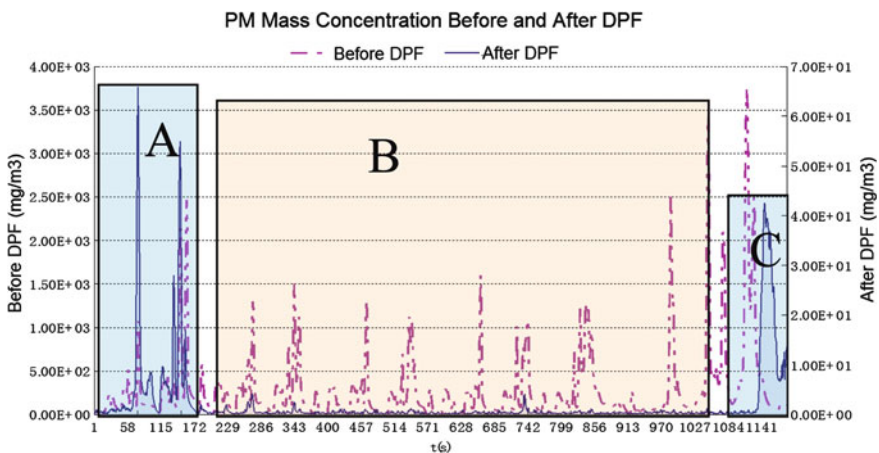


Fig. 2 PM mass concentration contrast before and after DPF

4.2.1 PM Concentration Distribution before and after DPF under NEDC

I-type test adopts NEDC driving cycle, which consists of a 780 s urban driving cycle consisting of four repeated ECE-15 driving cycles and a 400 s extra-urban driving cycle.

I-type test is adopted by the vehicle installing active regeneration DPF. Then test the PM mass concentration before and after DPF in real-time by ELPI. PM mass concentration curve are shown in Fig. 2. From the concentration curve, the PM concentration difference between before and after DPF is obvious, and most of PM can be filtered by DPF. The PM concentration closes to zero after filtering

Table 3 PM mass concentration contrast at A B C stage

Sampling location	Mean value(mg/m ³)			Max value(mg/m ³)		
	A	B	C	A	B	C
After DPF	15.85	0.46	20.45	65.86	4.20	42.56
Before DPF	269.51	309.97	207.09	2465.82	3759.59	664.27
Reduction efficiency (%)	94.120	99.853	90.123	97.329	99.888	93.593

especially in the 2nd, 3rd, 4th cycle unit of urban driving cycle and 350s before extra-urban driving cycle (before the slowdown stage).

However, the PM mass concentration after DPF is very high in 200s period after cold start and 50s period before the end of NEDC (the slowdown stage of extra-urban driving cycle), such as A and C stage showing in Fig. 2. Meanwhile, PM mass concentration before DPF in A and C stage resembles with the other stage, which demonstrates that high PM emission mainly exist in A and C stage.

The max and mean PM mass concentration of A, B, C stage is shown in Table 3, the data can quantify the differences of the DPF filtering effect on PM in these three stages. By contrasting the PM mass concentration before and after DPF in A, B, C stage, filtration efficiency of the B stage the max and mean concentration cut down by DPF reaches 99 %, and A, C stage filtration efficiency are lower than B stage. The max and mean PM mass concentration of B stage almost reaches zero after DPF. The A, C stage max and mean PM mass concentration are lower than B stage before DPF. However, the A, C stage max and mean PM mass concentration are higher than B stage after DPF. So the A, C stage become the main PM emission sources. Compare A stage of cold start, the reduction of C stage PM mass concentration is weaker.

4.2.2 Calculation and Analysis of Modal Mass under Part of NEDC Driving Condition

For comparing the differences of PM emission before and after DPF, the NEDC driving condition is divided into a 200s high PM emission period after cold start (A), low PM emission period in cycle (B) and a 50s high PM emission period before the end of NEDC (C). The A, B, C stage PM emission is shown in Fig. 3. It is easy to find that A, C stage account for less than 30 % of the entire cycle, but the PM emission account for 70 %. It indicates that the A, C stage filtration efficiency of DPF on PM is lower, further actual PM emission is higher than the expected emission.

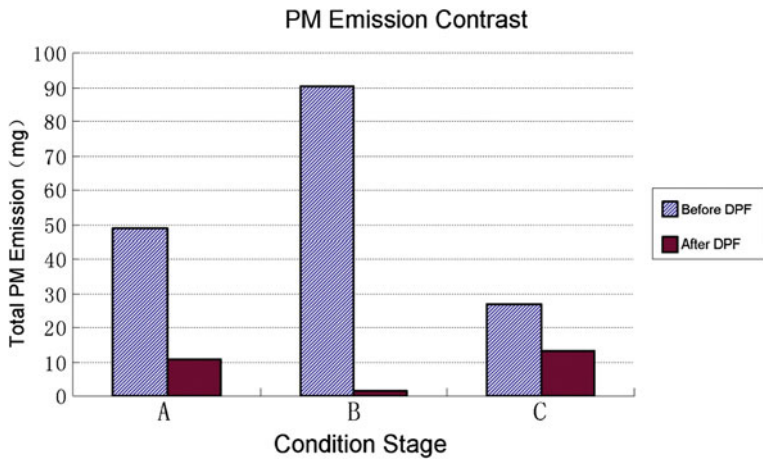


Fig. 3 PM Emission contract among A B C stage

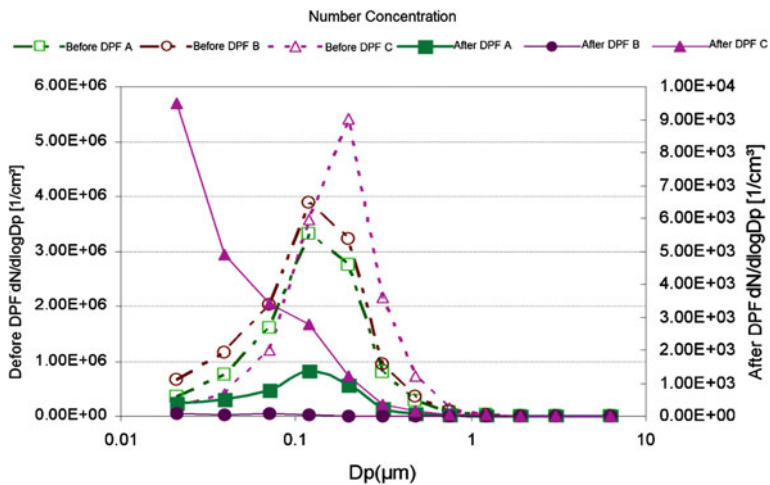


Fig. 4 PM number concentration in the size distribution

4.2.3 Distribution Characteristics of PM Mass Concentration and Number Concentration in Particle Size at A B C Stage

The above analysis shows that filtration efficiency of DPF on PM at the three stages. A large number of PMs are exhausted at the stage A and C. The following paper will analyze the size of PM which has not been well controlled. Both of number concentration and mass concentration on the PM size distribution before and after DPF are shown in Figs. 4 and 5.

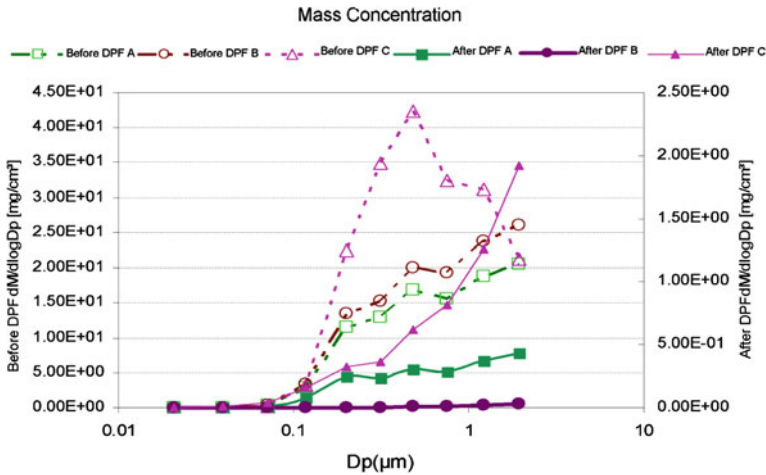


Fig. 5 PM mass concentration in the size distribution

Figure 4 shows the PM number concentration. The number concentration of particulate matter exhausted from engine is mainly concentrated in 0.04–0.75 μm particle size segment at the three stages. The PM number concentration is almost reduced to zero by DPF at the stage B. The number concentration of stage A and B has the similar species distribution, having the same peak at the PM size of 0.12 μm. Relative to stage A and B, the distribution curve of number concentration at stage C has a little offset to the larger particle size, and there is a bigger peak.

The number concentration on the PM size distribution shows large differences among the three stages after DPF. The peak of number concentration is reduced dramatically at stage B. The curve of stage C has a great change and the number of ultrafine particles gets larger. Stage A is the start condition. In this stage, the filtration efficiency to the PM in any size is very high, but is much lower than stage B, which is the reason for the high PM emission peak at the stage A in the Fig. 1. The PM number concentration in each particle size is slashed at the normal urban driving conditions cycle (stage B). At the stage C, the distribution curve gets into an open distributed to the small particle size, and the number concentration of the total size is larger than the value at stage A. This phenomenon is not caused by the DPF regeneration, because that during this cycle there was no the reproduction signal was monitored, the exhaust gas temperature has not reached the regeneration temperature. The stage C is a 50s period before the end of NEDC which is a rapid slowdown period.

PM_{2.5} number concentration exhausted from engine is mainly concentrated in PM size larger than 0.2 μm from Fig. 5. After filtration, the PM_{2.5} number concentration of stage C is almost zero. According to above analysis, PM_{2.5} size distributed in 0.04–0.75 μm can be fully filtered. Thus the filtering effect of DPF on PM_{2.5} is fine in normal driving.

Before DPF, mass concentration of PM_{2.5} distributed about in 0.5 μm is larger at stage C, however, mass concentration of PM_{2.5} is reduced with the size increasing. PM number concentration at stage C is less than stage A and B for PM size less than 1 μm . The mass concentration trend of all PM size at stage A and B is same, which the mass concentration increases with the size increasing. But the mass concentration of all PM size at stage A is less than stage B.

After DPF, at stage B, the mass concentration of all PM size is almost zero, so the filtration efficiency of DPF on PM is almost 100 % at this stage. However, at stage A, PM in all size still has a certain mass concentration after filtering; the filtration efficiency of DPF on PM becomes worse. At stage C, compared with stage B, PM in all size still has a certain mass concentration after filtering, especially mass concentration of larger PM (more than 0.3 μm) increases sharply with size increasing. As Fig. 4, mass concentration of PM in stage C is largest after DPF. The reason maybe that in slowdown period of extra-urban driving cycle, exhaust airflow has a short term reverse negative pressure on part of PM (especially ultra fine PM) adsorbed in filter body wall, causing part of PM falling off from filter body wall. Then the falling PMs strike through the wall with exhaust airflow and cannot be absorbed by filter, finally causes high PM emissions.

After analyzing mass concentration and number concentration before and after DPF at three stages of NEDC, the filtration efficiency in the initial stage of the cycle cold start and the high-speed slowdown stage in the end of the cycle is low, causing the actual reductions of DPF on PM lower than expected value before and after DPF.

5 Conclusion

The study demonstrates that filtration efficiency of DPF on PM exhausted from diesel vehicles changes a lot under the driving conditions, in other words, reductions of DPF on PM changes with the different driving conditions. In normal driving, PM_{2.5} exhausted from engine can be filtered thoroughly by DPF. After analyzing PM number concentration and mass concentration, it is easy to find that filtration efficiency of DPF can reaches more than 92 % under NEDC driving condition, so the filtering effect is ideal. However, filtering effect is worse in a 200s period after cold start and a 50s deceleration period of extra-urban driving cycle, so more than 70 % PM is exhausted in those periods, causing the total filtration efficiency of DPF only reaches 52 % under NEDC driving condition. The reason maybe that in deceleration period of extra-urban driving cycle, exhaust airflow have a short term reverse negative pressure on part of PM (especially ultra fine PM) adsorbed in filter body wall, causing part of PM falling off from filter body wall. Then the falling PM crashes through the wall with exhaust airflow and cannot be absorbed by filter, finally causes high PM emission.

References

1. Li M, Jing X, Zhang Y (2007) PM emission of diesel vehicle with DPF under lug- down mode. *Automot Eng* 29(8):660–663
2. GB 18352.3-2005 (2005) Limits and measurement methods for emissions from light-duty vehicles (III,IV)
3. Xu Y, Li M, Fang M (2010) A study on the PM emission characteristics of light diesel vehicle equipped with DPF. *Automot Eng* 32(12):1030–1037
4. HJ451-2008 (2008) Technical requirement for environmental protection produce after-treatment for diesel vehicle exhaust
5. Hu Y, Li M, Li J (2010) An experimental study on the performance of exhaust after treatment devices in diesel vehicle. *Automot Eng* 32(5):451–454

The Model Based Control Strategy for an Advanced UREA-SCR System

Zhi Liu, Hongrong Wang and Yongfu Wang

Abstract Currently the advanced UREA-SCR system is one of the most popular technology to meet the strict emission standards as Euro IV or above. In order to reach high NO_x conversion and low NH₃ slip, the urea dosing rate needs to be calculated and controlled precisely. This paper describes an advanced UREA-SCR system based on model based control strategy and advanced diaphragm urea dosing pump. The strategy can be seen as a virtual closed-loop control method for the dosing rate calculation, and it was integrated with the advanced diaphragm urea dosing pump for the tailpipe urea dosing. A SCR chemical reaction model was developed to describe the concentration of different species inside the SCR catalyst. Three different reactions were taken as the foundation of the model, including fast reaction, normal reaction and slow reaction. To simplify the process of calculation, the catalyst model was divided to three cells. In each cell, the NH₃ storage ability was estimated and the results were taken as the feedback signals for the controller. A virtual closed-loop control method was developed to calculate the dosing rate. The model was tuned under different engine running conditions, the exhaust gas temperature was controlled between 250 and 400 °C and the NH₃/NO_x molar ratio was controlled between 0.8 and 1.1. An advanced-diaphragm urea dosing pump was developed to finish the urea dosing activity. The results of transient engine running experiment show that the NO_x conversion efficiency can reach 85 % while keeping the average NH₃ slip under 15 ppm, the peak average NH₃ slip under 30 ppm. And the dosing rate error can be controlled less than 3 %.

Keywords Diesel engine · UREA-SCR · Model based control · NO_x · SCR

F2012-A04-036

Z. Liu (✉) · H. Wang · Y. Wang
China Automotive Engineering Research Institute, Chongqing, China
e-mail: jackeyliu@caeri.com.cn

1 Introduction

As one of the main technology method to meet the Euro IV or more strict emission regulation, SCR technology has been widely used all over the world. Compared with another main technology-EGR, SCR has the advantage of simple structure, obvious effect to reduce NO_x emission and has low fuel consumption. To control the dosing rate of UREA, the system needs to take the balance of NO_x conversion efficiency and ammonia slip into account. That means if the system has a smaller UREA dosing rate than requested, the NO_x conversion efficiency will be affected, and the ammonia slip will be reduced. And if the system has a larger UREA dosing rate than requested, though the NO_x conversion efficiency can reach a higher level, the ammonia slip will exceed the standard. When the engine runs in a steady state, it is easy to adjust the dosing rate to balance the NO_x conversion efficiency and ammonia slip. But when the engine runs in transient state, it is hard to reach the balance.

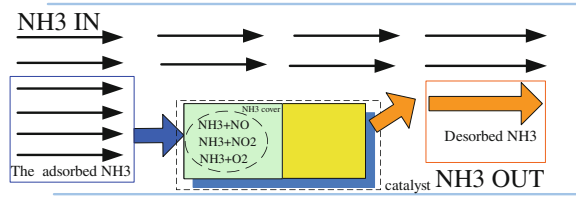
To control the ammonia slip, some catalyst companies are carrying out the research of clean-up catalyst. This kind of catalyst consists with reduction part and oxidation part. The reduction acts as a reduction catalyst to reduce the NO_x, and the oxidation part acts as a oxidation catalyst to reduce the extra ammonia. Compared with other SCR catalyst, the clean-up catalyst may leads to larger UREA dosing rate and the cost will increase. And the OBD will have requirement on the diagnostic of the catalyst, which makes the SCR system more complex.

To consider the balance between the NO_x conversion efficiency and ammonia slip, this article develops a SCR reaction model to estimate the chemical reaction and ammonia storage inside the catalyst. And the control strategy makes use of the ammonia storage as feedback to adjust the requested dosing rate. Unlike the black-box control strategy, the model based control strategy understands the chemical process inside the catalyst, thus it can predict what is going to happen of NO_x conversion. The ammonia storage factor is estimated as a virtual sensor. To realize the high quality control, an advanced-diaphragm urea dosing pump was also developed to finish the urea dosing activity.

2 SCR Chemical Reaction Model

Inside the SCR catalyst, there are several different types of chemical reactions, including reduction reaction, oxidation reaction and ammonia adsorption and desorption.

Fig. 1 Change of ammonia



2.1 Ammonia Concentration Model

After the ammonia goes into the catalyst, there are two types of change inside catalyst.

The one is adsorption and desorption. From the upstream to the downstream of the catalyst, the ammonia is adsorbed to the surface of the catalyst. At the same time, the ammonia is released from the surface of the catalyst, this is called desorption. The adsorption and desorption are shown in Fig. 1.

The other one is chemical reaction. On the surface of SCR catalyst, because of the adsorbed ammonia, the activation energy decreases a lot. As a result, the ammonia reacts with NOx, and the NOx is converted to N₂ and H₂O.

According to the Law of conservation of mass, we can get the equation to describe the change of the ammonia mass [1].

$$\frac{\partial}{\partial t} [gas] = -v \frac{\partial [gas]}{\partial x} - r_{[gas]} \tag{1}$$

From the equation, we can know that the change of ammonia concentration consists of two parts, including the mass diffusion and the chemical reaction.

2.1.1 Adsorption and Desorption

We can describe the adsorption and desorption process with the equation as:

$$r_{[NH_3]} = r_{[a]} - r_{[d]} \tag{2}$$

The $r_{[a]}$ is the rate of ammonia adsorption, the $r_{[d]}$ is the rate of ammonia desorption. And the $r_{[a]}$ minus $r_{[d]}$ is the change of concentration of ammonia by the effect of adsorption and desorption.

The $r_{[a]}$ can be calculated as [1]:

$$r_{ads} = k_{ads} [NH_3] (1 - \theta) \tag{3}$$

The $r_{[d]}$ can be calculated as [1]:

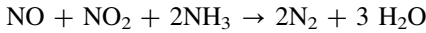
$$r_{des} = k_{des} e^{\frac{-E_{des}(1-\theta)}{RT}} \theta \tag{4}$$

The k_{ads} is the reaction constant of the adsorption reaction. And the k_{des} is the reaction constant of the desorption reaction. θ is the ammonia coverage rate of the catalyst surface .

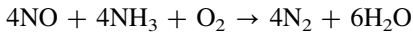
2.1.2 Chemical Reaction

There are three types of NOx reduction reactions listed as follows:

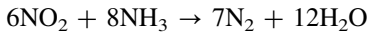
Fast reaction:



Normal reaction:



Slow reaction:



We can describe the reduction reaction rate as:

$$r_{\text{NO}_x} = k_{\text{NO}_x} e^{-\frac{E_{\text{NO}_x}}{RT}} [\text{NO}_x] \theta \quad (5)$$

The k_{NO_x} represents the reduction reaction constant, the E_{NO_x} represents the reaction activation energy, the $[\text{NO}_x]$ represents the concentration of the NOx and θ is the ammonia coverage rate of the catalyst surface.

From the Eq. (1)–(5), we can know that four parts contribute to the change of the ammonia surface coverage, the ammonia adsorption rate, the ammonia desorption rate, the NOx reduction reaction rate and the ammonia oxidation rate.

With the four different reaction equations, we can build the model of the reactions inside the catalyst and to describe the ammonia surface coverage.

3 Reaction Model Calibration

Once we get the model of the chemical reaction rate inside the catalyst, we need to calibrate the parameters of the calibration. The parameters are listed as follows [2]:

k_{ads}	reaction constant of the adsorption reaction
k_{des}	reaction constant of the desorption reaction
E_{des}	reaction activation energy of the desorption
α	surface coverage dependence for desorption
E_{NO_x}	reaction activation energy
k_{NO_x}	NOx reduction reaction constant

And the input of the model includes NOx concentration, ammonia concentration, the flow mass of exhaust gas and the temperature in the upstream of catalyst.

To simplify the calculation process of the reaction inside the catalyst, the catalyst is divided into three cells, we assume that inside each cell, the concentration of NOx and ammonia, the temperature are the same in every point. As

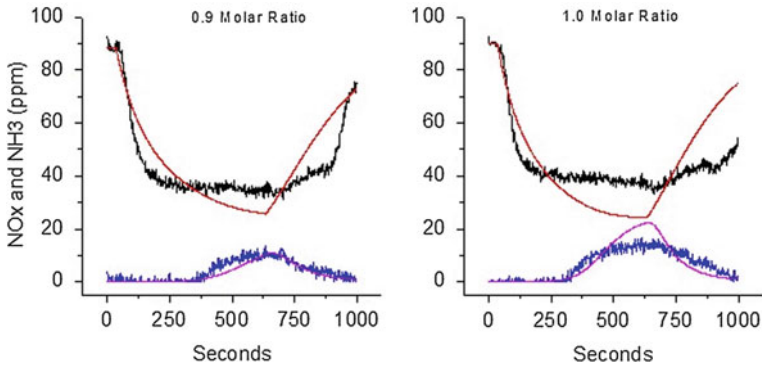


Fig. 2 225 °C, tuning result

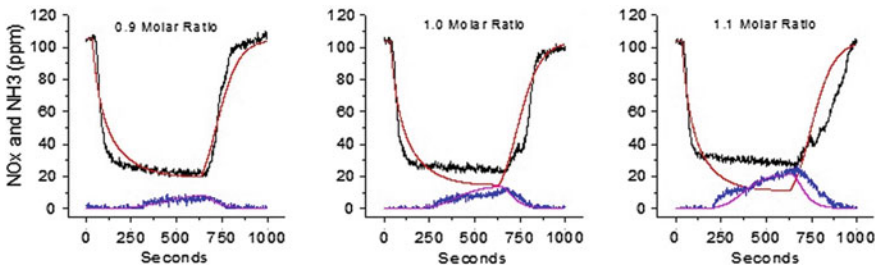


Fig. 3 250 °C, tuning result

showed in the picture, we build the three ammonia coverage virtual sensor to estimate the ammonia coverage.

To calibrate the six parameters, different calibration experiments are designed. The ammonia NO_x ratio varies from 0.9 to 1.1, and the temperature in the upstream of the catalyst varies from 225 to 400 °C. The compare between the testing result and the model calculation are showed as follows (Figs. 2, 3, 4 and 5).

- Testing condition: 225 °C, molar ratio from 0.9 to 1.0.
- Testing condition: 250 °C, molar ratio from 0.9 to 1.1.
- Testing condition: 350 °C, molar ratio from 0.9 to 1.1.
- Testing condition: 400 °C, molar ratio from 0.8 to 0.9.

After we got the data, we make use of the Mathwork toolbox to fit the model, and get the best result.

4 Model Based Control

The model based control strategy makes use of the model to estimate the NO_x conversion efficiency and the catalyst surface coverage [3].

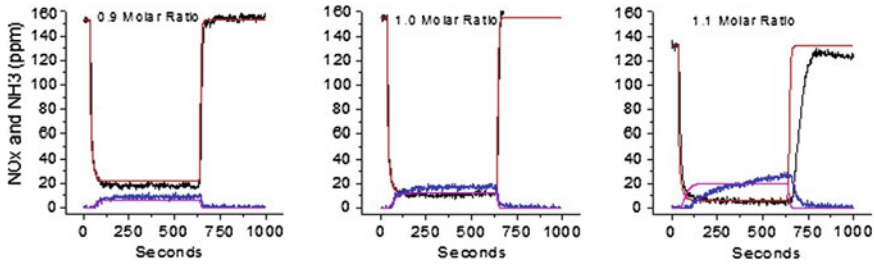


Fig. 4 350 °C, tuning result

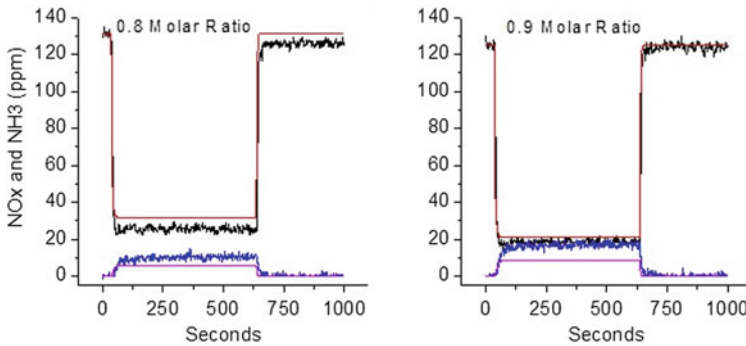


Fig. 5 400 °C, tuning result

The strategy includes two parts: the UREA dosing calculation and the NOx conversion efficiency calculation. The UREA dosing calculation make use of the engine exhaust mass, NOx exhaust concentration and the temperature in the upstream of the catalyst as the input, to calculate the requested UREA dosing rate. The NOx conversion efficiency calculation makes use of the model to calculate NOx conversion efficiency.

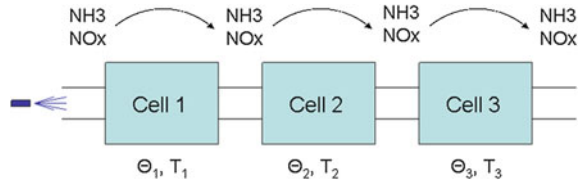
4.1 Urea Dosing Calculation

The UREA dosing calculation includes two different modular.

4.1.1 Thermal Model

The goal of the thermal model is to predict the temperature inside the SCR catalyst and the Diesel Particulate Filter. The exhaust flow mass and temperature will be used as the input values.

Fig. 6 Three cells



4.1.2 PID Controller

The UREA dosing rate is controlled by a PID controller. The catalyst is divided into three parts. We assume that inside every cell, the condition is exactly the same in every point (Fig. 6).

The theta from cell3 is used as feedback. The goal of the controller is to keep the model calculated theta within the requested level. The controller is a typical PID controller, includes open controller, proportional controller, integration controller and derivation controller.

5 UREA Dosing System

An advanced UREA dosing pump was developed to carry out the activity of UREA dosing. The pump includes two modules, the pump and the control system.

5.1 Pump

The pump inhales the UREA from the UREA container, and by the use of motor, the UREA is imported into the pump at the pressure about 2–3 bar. The UREA dosing pump receives the command from dosing rate calculation module, and doses the requested amount of UREA into the exhaust pipe. The dosing pump has the air assistant system to help the UREA hydrolyze to ammonia. The flow pressure is built by the drive of diaphragm pump which is driven by the motor. The dosing pump can carry out the dosing rate accurately, and when the environment temperature under 5 °C, the heater can start to heat up the dosing pump.

5.2 Control System

The control system can control the work of the pump. It includes MCU module, the DC/DC module, the signal process module, the actuator drive module and the CAN-BUS communication module. Those modules are integrated together and installed with the pump.

Fig. 7 Test platform

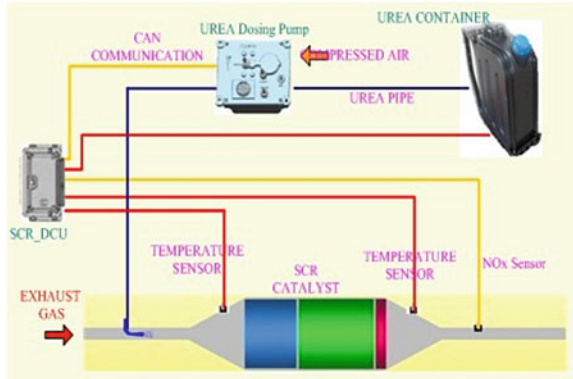
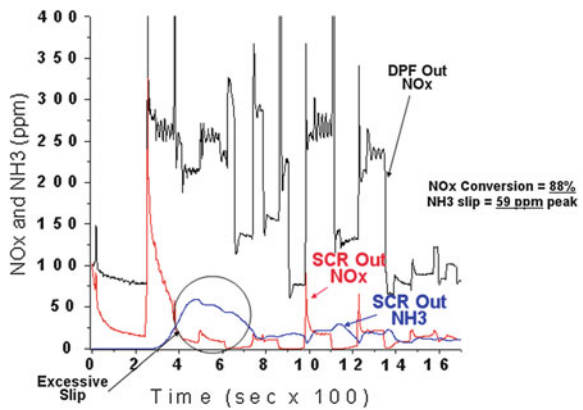


Fig. 8 ESC test result



6 Experiment

Several different types of experiments are carried out to verify the performance of the control strategy.

6.1 Test Platform Configuration

The test platform consists of SCR catalyst, temperature sensor, UREA Dosing Pump and DCU. The configuration is shown in Fig. 7.

As shown in the Fig. 7, the UREA Dosing Pump and SCR_DCUs are developed by CAERI. We integrate every part into the SCR system. The selected engine's volume is 12.8 L, and the max power is 480 Hp.

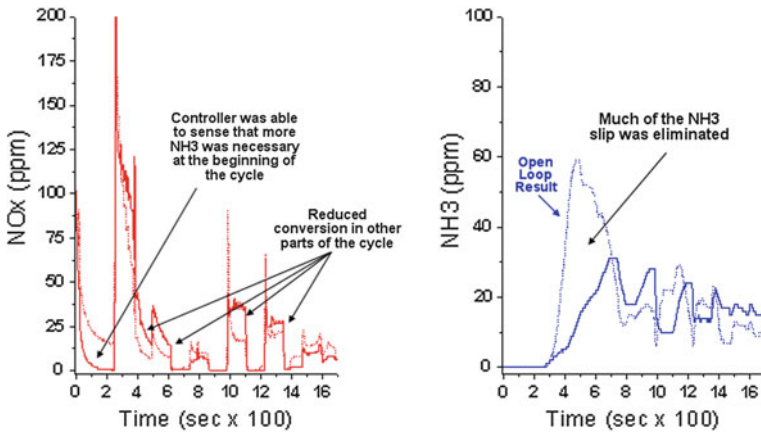


Fig. 9 ESC test result

6.2 Test

Because the UREA system are almost used in the heavy duty truck, so the ESC cycle is selected to run steady state condition, and the FTP cycle is selected to carry out the experiments [4].

6.2.1 ESC Result

The open loop control strategy and closed-loop strategy are both verified in the ESC result and parts of the results are shown in the following figures (Fig. 8).

From the ESC condition open-loop experiment, we can see that the NOx conversion is closed to 90 %, but the NH₃ slip seems too high (Fig. 9).

From the ESC condition closed-loop control, we can see that the NH₃ slip decreases a lot because of the feedback of the coverage of the ammonia on the surface of catalyst.

6.2.2 FTP Tests

The FTP tests are consists of four parts, the NYNF, LANF, LAFY, NYNF. The results of the FTP cycle are shown as follows (Fig. 10).

We can see that compared with the open-loop control strategy, the closed-loop control strategy can decrease the ammonia slip while keeping the NOx conversion efficiency seems as the same as open-loop control, that means the efficiency is closed to 90 %.

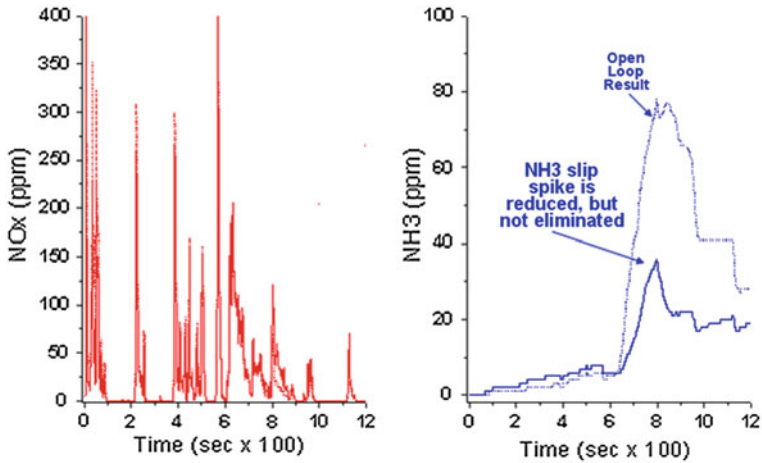


Fig. 10 FTP test result

7 Conclusion

An advanced SCR system was introduced in this paper, including model based control strategy and advanced urea dosing pump. The experiments showed that this advanced system can have a high NH_3 conversion efficiency (closed to 90 %) while keeping a low NH_3 slip. The max NH_3 slip is about 30 ppm and the average NH_3 slip is less than 10 ppm. And the dosing rate error can be controlled in a very low level.

References

1. Lietti L, Nova I (1997) Dynamics of the SCR-DeNOx reaction by the transient response method. *Reactor Kinetics Catal* 43(10):2559–2570
2. Wang DY, Yao S, Shost M (2008) Ammonia sensor for closed-loop SCR control. *SAE Technical Paper Series*, 2008-01-0919
3. Wilams F, Cloudt R, van den Eijnden E (2007) Is closed-loop SCR control required to meet future emission targets? *SAE Technical Paper Series*, 2007-01-1574
4. Chadwell CJ (2011) SCR model and control. South West Research Institute, October 2011

The NO_x Conversion Efficiency Depending on the Deviation of SCR System Components and Amount of Soot Loading in c-DPF

Hyoung Sik Kim, Jong Ik Jeon, Chang Eun Choi and Won Kun Kim

Abstract In this study, the parameters of SCR system which have an effect on NO_x conversion efficiency have been investigated. The NO_x sensor located in front of SCR catalyst and the urea injector dosing urea solutions to the SCR catalyst play important roles in NO_x conversion efficiency of SCR system. First, NO_x conversion efficiency has been decreased when NO_x sensor reads engine out NO_x emissions lower than the actual engine out NO_x emissions, because it brings about the lack of urea injection quantity. Second, the NO_x conversion efficiency has been also decreased when urea injector doses less amount of urea solution than the system required. Finally, Applying the aged catalyst system (DOC, c-DPF, SCR) and the soot loading amount in c-DPF also have effects on the change of NO_x conversion efficiency.

Keywords SCR · NO_x sensor · Urea dosing injector · NO₂/NO_x ratio · CRT

1 Introduction

Diesel vehicle should meet the most stringent emission legislation to launch US market. SCR is the one of the promising NO_x purification method, which has the benefit in fuel consumption and the stability in durability. In this reason, some of

F2012-A04-041

H. S. Kim (✉) · J. I. Jeon · C. E. Choi · W. K. Kim
Hyundai-Kia Motors, Seoul, Korea
e-mail: min771478@hyundai.com

Table 1 SCR reaction rate

	Reactants	Product	NO ₂ /NO _x ratio (%)	Reaction rate
Fast SCR	2NH ₃ + NO + NO ₂	2N ₂ + 3H ₂ O	50	↑↑↑
Standard SCR	4NO + 4NH ₃ + O ₂	4N ₂ + 6H ₂ O	0	↑↑
Slow SCR	6NO ₂ + 8NH ₃	7N ₂ + 12H ₂ O	100	↑

car makers have already developed/is developing diesel vehicles with SCR system. In this study, the result and discussion regarding the key factors which effects on tailpipe NO_x will be presented. Test has done with Tier2 Bin5 vehicle application which is equipped with V6 3.0L engine and exhaust after-treatment system (DOC/c-DPF/Urea SCR System). The test has performed with FTP-75 driving cycle. This study shows the test result and analysis of the difference of NO_x conversion efficiency. The main four parameters which cause the difference of the NO_x conversion efficiency are as below,

- 1 The NO_x sensor which has minimum characteristic
- 2 The urea injector which has minimum characteristic
- 3 The 120 K aged catalyst system (DOC/c-DPF/SCR)
- 4 The soot loaded c-DPF

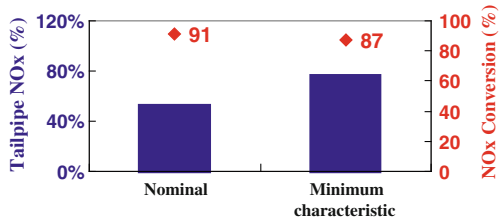
Topics 1 and 2 which cause the difference of NO_x conversion efficiency are closely related with the urea dosing quantity. And topics 3 and 4 which cause the difference of NO_x conversion efficiency are closely related with NO₂/NO_x ratio. The NO₂ content of exhaust gas makes the difference of reaction rate when NO_x emissions react with the NH₃ at the SCR catalyst.

The NO_x (Nitrogen Oxides) emissions are composed of NO (Nitric Oxide) and NO₂ (Nitrogen Dioxide). The NO_x which reacted with NH₃ resolves N₂ and H₂O as shown in Table 1 and the reaction is largely divided into three kinds [1, 2].

2 The Change of NO_x Conversion Efficiency by SCR System Component

The injection quantity of urea is determined by engine-out NO_x which is read from the upstream NO_x sensor. The difference of urea quantity which is caused by tolerance of the NO_x sensor can have an effect on the change of NO_x conversion efficiency. Also, the deviation of urea quantity from the tolerance of urea injector itself can influence on the NO_x conversion efficiency. In this paper, the NO_x sensor and the urea injector which have minimum characteristic are used to investigate the effectiveness on NO_x conversion efficiency and tailpipe NO_x emissions.

Fig. 1 Test results with the minimum characteristic NOx sensor (The tailpipe NOx (%) is normalized with 50 K Tier2 Bin5 emission standard)



2.1 The Difference of NOx Conversion Efficiency Depending on the NOx Sensor

The NOx conversion efficiency and tailpipe NOx emissions which have been tested with the minimum characteristic NOx sensor are shown in Fig. 1. The base test is carried out with nominal NOx sensor. When the minimum characteristic NOx sensor has been applied, the test result shows 4 % decrease of NOx conversion efficiency and the tailpipe NOx has been increased 46 % at the same test condition but NOx sensor.

The reason of decrease of NOx conversion efficiency is that NOx sensor read lower than actual engine-out NOx emissions. Therefore, NOx can not be purified due to the lack of reacting NH₃. As shown in Table 2, NOx sensor read 12 % lower so that urea injection quantity becomes 11 % lower. Therefore if the NOx has ±10 % tolerance specification, the tailpipe NOx increase is excessive. So it is necessary to strengthen the NOx sensor Spec within ±5 % [3].

Figure 2 shows under-reading of NOx amount which is emitted from the engine in comparison to the nominal NOx sensor. Therefore, the tailpipe NOx is higher as much as 0.1 mg/sec at FTP-75 phase2 driving cycle and the tailpipe NOx is much worse when the vehicle has higher space velocity such as acceleration condition.

2.2 The Difference of NOx Conversion Efficiency Depending on the Urea Injector

The urea injector plays an important role in dosing the urea to the SCR catalyst. Because of the deviation on the urea injector, the NOx conversion efficiency and the tailpipe NOx has been changed, as shown in Fig. 3. The NOx conversion efficiency has been decreased 2 % and the tailpipe NOx has been increased 27 % when the minimum characteristic urea injector has been applied. Because the urea injector doses the less amount of urea not so much as the DCU has been instructed. Even though the NOx sensor reads same NOx amount, the tailpipe NOx is higher than test which has been carried out with nominal urea injector, as shown in Fig. 4.

Table 2 The NOx & Urea quantity depend on NOx sensor (DCU value)

	NOx quantity (g)	Urea quantity (g)	Remark
Nominal	2.25	3.68	Exchange of the NOx sensor
Minimum characteristic	1.98	3.27	
Difference	12 %↓	11 %↓	Phase2 and 3

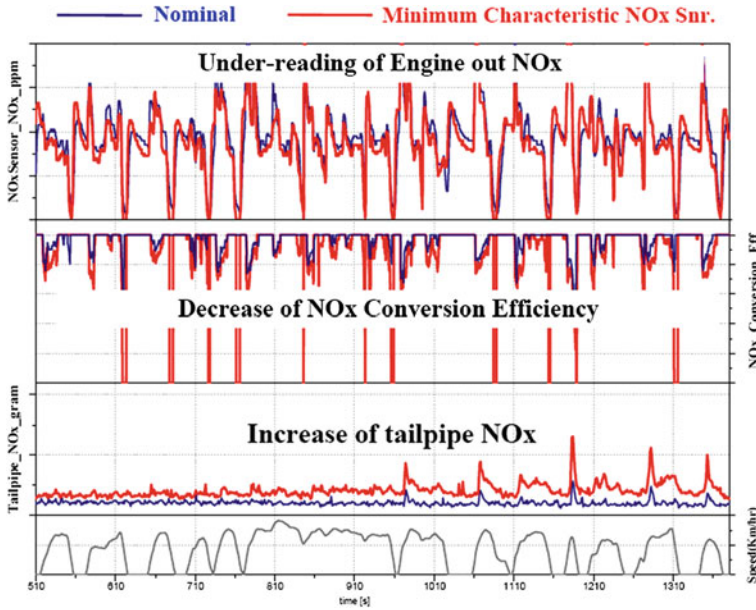
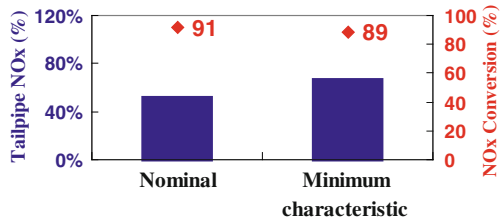


Fig. 2 The NOx emissions and NOx conversion efficiency depend on NOx sensor at FTP-75 phase2 driving cycle

Fig. 3 Test result with the minimum characteristic urea injector



2.3 The difference of NOx Conversion Efficiency Depending on NOx Sensor and Urea Injector

When the NOx sensor and the urea injector which have the minimum characteristic have been applied at same time, the NOx conversion efficiency has been changed

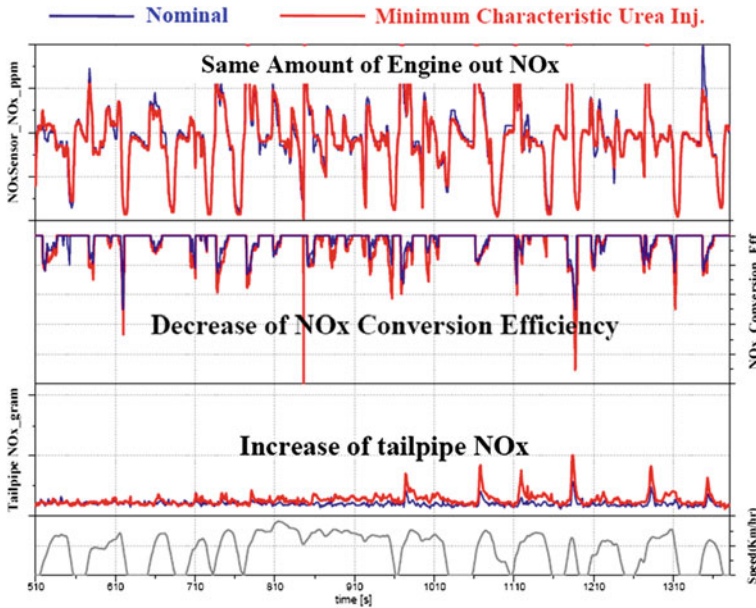
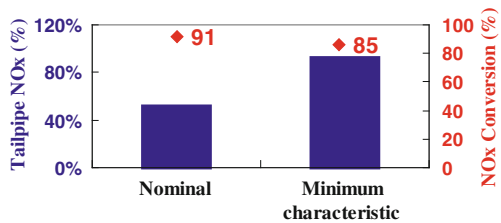


Fig. 4 NOx emissions and NOx conversion efficiency depend on urea injector at FTP-75 phase2 driving cycle

Fig. 5 Test result with the minimum characteristic NOx sensor and urea injector



to 85 % which is 6 % less than the test which has been carried out with the nominal NOx sensor and urea injector. And the tailpipe NOx has been sharply increased 77 % as shown in Fig. 5. And the Table 3 represents the change of DCU recognition value.

The reason why the tailpipe NOx has been increased is listed below.

Firstly, the less NOx amount is read from the NOx sensor, the less urea quantity is injected. Therefore the NOx conversion efficiency becomes worse as shown in Fig. 6. Secondly, since applying the urea injector which has a minimum quantity characteristic, the actual urea injection quantity is less than the DCU has been instructed. The 6 % decrease of NOx conversion efficiency is from the NOx sensor and the urea injector respectively. The 4 % is caused by the minimum characteristic NOx sensor and the 2 % is from the minimum characteristic urea injector with single parameter.

Table 3 The NOx & Urea quantity depend on NOx sensor & urea injector (DCU value)

	NOx quantity (g)	Urea quantity (g)	Remark
Nominal	2.25	3.68	Exchange of
Minimum characteristic	2.05	3.43	the NOx sensor and urea injector
Difference	9 %↓	7 %↓	Phase2 and 3

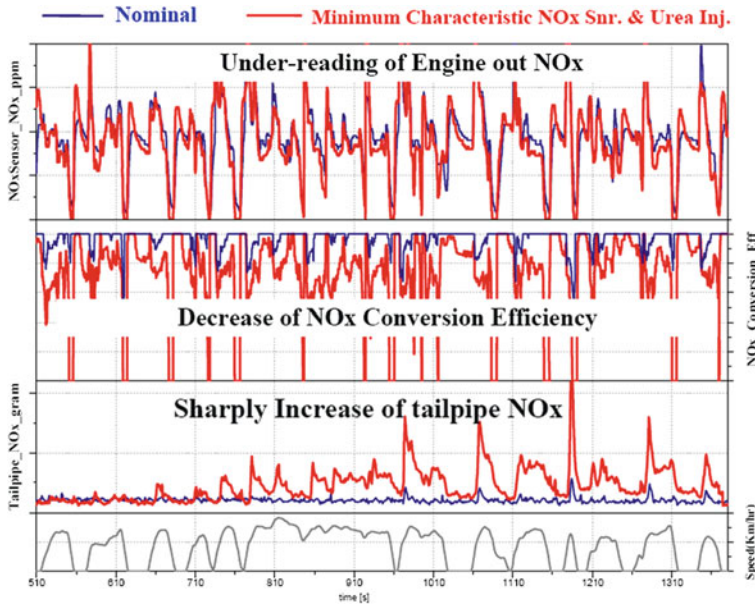


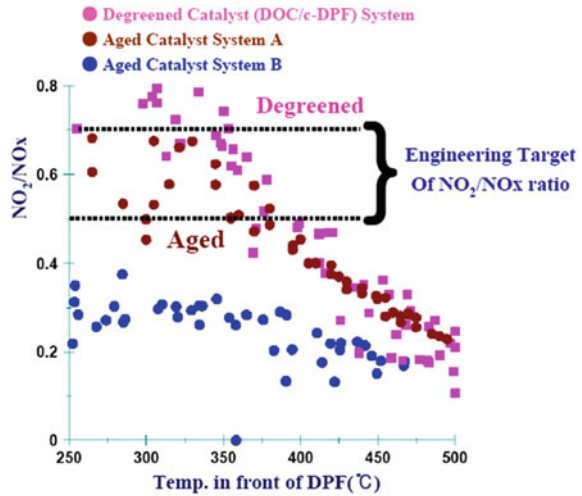
Fig. 6 NOx emissions and NOx conversion efficiency depend on NOx sensor & urea injector at FTP-75 phase2 driving cycle

3 The change of NO_x Conversion Efficiency by NO₂/NO_x Ratio

The NOx conversion efficiency strongly depends on the NO₂ content in the NOx emissions which is measured from the front of SCR catalyst, because NO₂/NOx ratio is closely related with the SCR reaction rate, as shown in Table 1

We ascertain that the thermal deactivation of DOC (Diesel Oxidation Catalyst) and c-DPF (coated Diesel Particulate Filter) which causes the change of NOx conversion because the NO₂/NOx ratio reduced gradually through the entire vehicle useful life. And, the NOx conversion efficiency is also affected by the soot loading at the c-DPF. As the NO₂ has been used for soot oxidation, the NO₂/NOx ratio has been changed.

Fig. 7 The change of NO₂ ratio by the exhaust gas temperature, degreened and aged, measured at engine test bench



3.1 The Change of NOx Conversion Efficiency by Aged Catalyst System (DOC, c-DPF, SCR)

To achieve the maximum NOx conversion efficiency with the aged catalyst system, which is as much as the degreened catalyst, at least 50 % of NO₂/NOx ratio condition is necessary. As mentioned at Table 1, the SCR reaction rate is maximized when the NO₂/NOx is 50 %.

As shown in Fig. 7, it shows the production of NO₂ measured from the engine test bench at the steady state. The NO₂ ratio is decreased rapidly up to 30 % with catalyst system B. Typically Fe-Zeolite SCR catalyst with aged DOC/c-DPF catalyst system requires at least 50 % of NO₂/NOx ratio to obtain the equivalent NOx conversion efficiency with degreened DOC/c-DPF catalyst system. Therefore the engineering target of NO₂/NOx ratio has been defined lower than 70 % for degreened DOC/c-DPF catalyst system and higher than 50 % for Aged DOC/c-DPF catalyst system [2, 4].

Considering the full useful life of vehicle and the space velocity of the catalysts, the 70 % of NO₂ ratio is reasonable with the degreened DOC/c-DPF catalyst system. The DOC/c-DPF catalyst system (system A) shows the level of NO₂ formation is within the engineering target. The test has been carried out with aged DOC/c-DPF catalyst system (System A) which is equivalent to 120 K mile. The test result is described below.

As shown Figs. 8 and 9, the total NOx conversion efficiency has been reduced 4 % and the tailpipe NOx has been increased 64 %. Remarkably, 9 % reduction of NOx conversion efficiency has been observed in the phase3, as shown in Fig. 13.

Fig. 8 Test result with the aged catalyst system (DOC, c-DPF, and SCR) (The tailpipe NOx (%) is normalized with 50 K (degreened) and 120 K (aged) Tier2 Bin5 emission standard respectively)

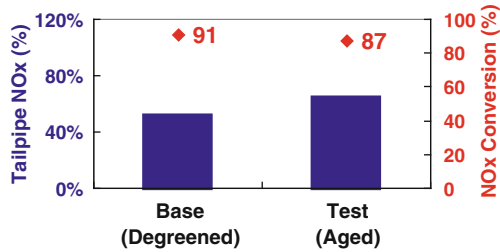
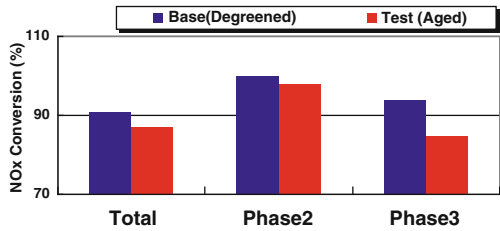


Fig. 9 The difference of NOx conversion efficiency with the aged catalyst system (DOC, c-DPF, SCR) at phase2 and phase3



After the hot soaking period at FTP-75 driving cycle, the c-DPF has been exposed to the relatively cold state on phase3 driving cycle compare to phase2 driving cycle. The average temperature of c-DPF is around 230 °C. Therefore the performance of NO₂ generation is reduced.

As shown Fig. 10, the difference of NOx conversion efficiency of the Fe-Zeolite SCR catalyst (Umicore co.) which used in this test has been caused by the change of NO₂/NOx ratio between degreened catalyst system and aged catalyst system. Thus, the 50 % of NO₂/NOx ratio is required to achieve the maximum NOx conversion efficiency with aged catalyst system at the relatively low temperature range, such as phase3 driving cycle [4].

In addition, if the SCR catalyst has a thermal degradation, the storage capacity of NH₃ in the SCR catalyst is reduced, as shown in Fig. 11. In the case of degreened Fe-Zeolite SCR catalyst, Fe exists at the state of ions on the Zeolite surface. On the contrary, Fe exists as a metallic oxide at the aged SCR catalyst; therefore the storage capacity is reduced.

In this study, the calibration of DCU has been carried out for the purpose of minimizing the NH₃ slip with the aged catalyst system (DOC, c-DPF, SCR) considering the reduction of the storage capacity. The test result shows 0 ppm of NH₃ slip on average at overall FTP-75 driving cycle when the degreened catalyst system (DOC, c-DPF, SCR) has been applied. On the other hand, the NH₃ slip has been occurred within 7 ppm on average with the aged catalyst system (DOC, c-DPF, SCR).

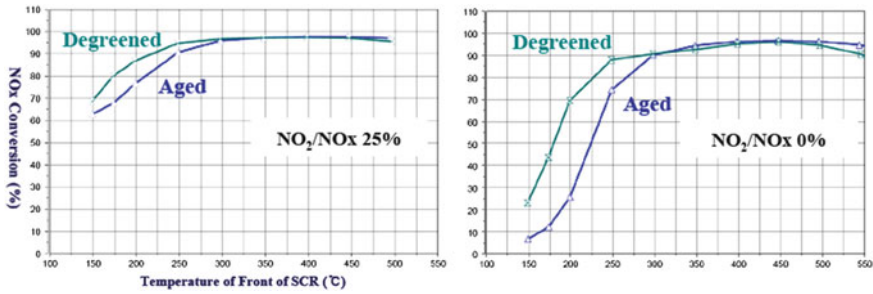
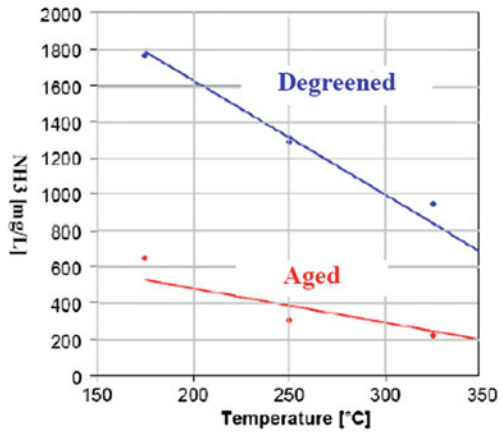


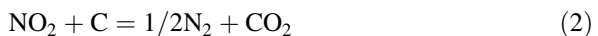
Fig. 10 NOx conversion efficiency depending on NO₂/NOx ratio, space velocity (SV) 30 k h⁻¹ measured at Umicore gas bench

Fig. 11 NH₃ storage capacity of SCR catalyst as function of temperature, measured at Umicore gas bench, degreened and aged



3.2 The Change of NOx Conversion Efficiency by Soot Loading Amount on the c-DPF

According to reaction Eq. (1), (2) if the soot deposits on the inside of c-DPF, the NO₂ is converted to NO by soot oxidation. It brings about the NO₂/NOx ratio decrease. Therefore it has a negative effect to the NOx conversion efficiency at the aspect of SCR catalyst.



Generally, above reaction takes place actively at 250–300 °C temperature range in front of c-DPF.

As shown in Fig. 12, the change of NOx conversion efficiency has been confirmed with soot loaded c-DPF. And the hydrothermally aged catalyst system for the DOC/c-DPF and degreened catalyst for the SCR have been applied.

Fig. 12 The change of NOx conversion efficiency with soot loading amount on the c-DPF

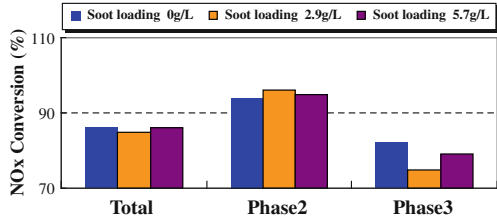
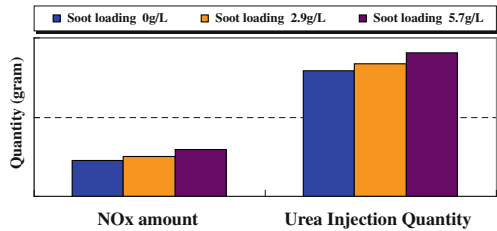


Fig. 13 The change of the NOx amount and the urea injection quantity according to soot loading amount on the c-DPF



The difference of NOx conversion efficiency at FTP-75 phase2 driving cycle is within 1 %. On the other hand, the difference of NOx conversion efficiency is 7 % at phase3 driving cycle, because the phase3 driving cycle is exposed to the relatively cold state compare to phase2 driving cycle. When the exhaust gas passes through the c-DPF, the oxidation of NO has more effect than reduction of NO₂ according to the CRT (Continuously Regenerating Technology) effect at phase2 driving cycle which has around 260 °C c-DPF average temperature. On the contrary, opposite tendency has shown at phase3 driving cycle which has around 230 °C c-DPF average temperature [5].

The NOx sensor itself can read the 100 % of NO but recognizes approximately 80 % of NO₂. When the CRT effect has been occurred, it would have an effect on the wrong recognition of the engine out NOx amount. The NOx sensor would be recognized more NOx amount than actual engine out NOx amount, because NOx sensor has 80 % cross-sensibility to NO₂. Therefore it makes the urea injection to be increased.

As shown in Fig. 13, when the c-DPF has 5.7 g/L of soot loading amount, the NOx sensor has been recognized the NOx amount around 6.9 % higher than the actual engine out NOx. It also leads to around 7.1 % increase of the urea injection quantity.

As the NO₂ ratio has been decreased physically by CRT effect with soot loaded c-DPF, it has a negative effect on NOx Conversion efficiency. However it also has an effect on increasing the injection quantity of urea. So, the overall NOx conversion efficiency has no significant change on FTP-75 driving cycle according to the soot loaded amount on the c-DPF.

4 Conclusion

In this study, the difference of NO_x conversion efficiency has been identified with hardware variation and the parameters which make NO₂/NO_x ratio change. And the following results are obtained.

- (1) The variation of NO_x sensor and the urea injector would make the difference of NO_x conversion raise up to 6 %. And it has been identified that the NO_x sensor is more sensitive than the urea injector about the change of NO_x conversion efficiency. Therefore, the NO_x sensor should be tightened the flow management at relatively less recognition field such as under the 50 ppm of engine out NO_x emissions.
- (2) The reduction of NO_x conversion efficiency is 4 % when the aged catalyst system (DOC/c-DPF/SCR) has been applied. Therefore the 50 % of NO₂/NO_x ratio is necessary to achieve the maximum NO_x conversion efficiency with the aged catalyst system.
- (3) The overall NO_x conversion efficiency has no significant change on FTP75 driving cycle according to the soot loaded amount on the c-DPF.
- (4) In Conclusion, supposing that the NO_x sensor have to be with ± 5 % Spec, the engineering target of the tailpipe NO_x emissions should be around 50 % to the Tier2 Bin5 50 K emission standard and at least, over 90 % of NO_x conversion efficiency is necessary for LDV (Light Duty Vehicle) application considering any tolerance of SCR system.

References

1. Lambert C Hammerle R, McGill R, Khair M, Sharp C (2004) Technical advantages of urea SCR for light-duty and heavy-duty diesel vehicle applications. SAE2004-01-1292
2. Bremm S, Kurze S, Pfeifer M (2008) Bluetec emission control system for the US tier 2 Bin 5 legislation. SAE 2008-01-1184
3. Choi C-E, Kim C-G, Kim K-Y, Han T-S (2008) SCR monitoring for USA Tier2 and Europe Euro6 OBD. JSAE. 372-20085242
4. Kamasamudram K, Currier NW, Szailer T, Yezerets A (2010) Why Cu- and Fe-zeolite SCR catalysts behave differently at low temperatures, SAE. 2010-01-1182
5. Joo K, Jo J-H, Kim CD, Lee J-h, Kim H-j (2008) The study of NO_x reduction using urea-SCR system with CPF and DOC for light duty vehicle; the diesel NO_x reduction system. SAE. 2008-01-1183

Detailed Investigation of Filtration and Regeneration Processes in a Diesel Particulate Filter System

Seungmok Choi and Kyeong Lee

Abstract This experimental work focuses on examining the detailed filtration and regeneration processes of diesel particulate filter (DPF) system under reaction with various gas emissions. To visualize these processes, we fabricated a unique thermal reactor visualized through a quartz plate, in which a 2-inch diameter \times 6-inch long cordierite filter was placed. The cylindrical filter was bisected to examine internal microstructures. Other major components consist of a series of 6 kW electric heater units and a microscopic imaging system. This bench-scale DPF system is connected to the engine exhaust pipe, from where engine-out exhaust emissions were bypassed to the DPF system at a constant flow rate. The filtration and regeneration processes were then visualized to examine soot loading and oxidation phenomena on the channel surfaces, along with measurements of pressure drops across the filter. The mass of soot loading was accurately measured at the DPF inlet by a tapered element oscillating microbalance (TEOM). As a result, three consecutive filtration stages were identified from the pressure drop data and soot loading video images: (1) deep-bed filtration in which the pressure drop significantly increased, (2) transitional filtration, and (3) soot cake formation in which the pressure drop gradually increased to the end of filtration. The mass of soot loading was also measured at each stage. In the DPF regeneration experiment followed by the completion of soot loading, three different regeneration stages were identified, where the degree of pressure drop tended to be different each other. For regeneration, both raw exhaust emissions and NO₂-added exhaust

F2012-A04-045

S. Choi · K. Lee (✉)

Transportation Technology R&D Center, Argonne National Laboratory, 9700 South Cass Avenue, Argonne, Illinois, 60439, U. S. A

e-mail: klee@anl.gov

emissions were used as reactants for soot. The regeneration with NO₂-added emissions was performed at two different DPF inlet temperatures, 400 and 500 °C. The results showed that the NO₂-added exhaust emissions significantly enhanced regeneration by reducing the total regeneration time, while overall regeneration behaviours turn out to be similar between the two different reactant mixtures, both cases showing three different regeneration stages and a similar pressure drop trend.

Keywords Diesel particulate filter • Filtration • Regeneration • Particulate emissions • Soot cake

1 Introduction

Regulations for particulate matter (PM) emissions have been very stringent over the world for recent years. For examples, the current Euro-5 PM emission standards for light duty vehicles require a ten times lower limit than did the Euro-3 ones: 0.005 g/km for the Euro-5. Moreover, the number of particulates, which are larger than 23 nm in diameters, will be regulated in a limit of 6.0×10^{11} particles/km [1], which many diesel manufactures are struggling to meet. In this sense, diesel particulate filter (DPF) systems have been known to be a most efficient tool that can control the tail-pipe PM emissions. Indeed, the increasingly strict emissions standards have urged engine manufactures to develop advanced DPF systems. To meet upcoming emissions standards, however, they still need to improve the performance of existing DPF systems, such as attaining high regeneration efficiency, reducing the back pressure caused by soot and ash build-up, improving material durability, or developing a smart control system. In particular, an effective thermal management system is necessary to prevent the failure of DPF system that is occurred by the oxidation of excess soot deposit, called thermal runaway, during the regeneration process.

DPFs are generally made of ceramic materials, such as cordierite or silicon carbide, and have a wall-flow type configuration in a honeycomb structure [2]. While engine exhaust emissions pass through DPF filter walls, the particulates are trapped both in micro pores (the deposition of soot particles inside filter walls, called “deep-bed” filtration) and on filter channel surfaces (a formation of bulk soot, called “soot cake” on the incoming flow channels) [3, 4]. The soot loaded in the filter increases the back pressure in the exhaust system, eventually leading to the low fuel economy [5]. Therefore, the soot cake needs to be removed by regeneration either periodically or continuously. Major soot oxidation typically starts at the exhaust gas temperature of about 550 °C, but the DPF inlet temperature of raw diesel exhaust emissions is hard to reach this temperature at normal engine operating conditions. Therefore, two typical regeneration methodologies have been developed: active regeneration that operates in control of engine parameters or some external heating hardware, such as electric heater, burner, or

microwave, and passive regeneration that reduces the oxidation temperature (or lower the soot activation energy). There are several passive regeneration technologies: for examples, utilizing catalytic reactions on catalyst-coated filter materials, using NO_2 gases converted from engine-out NO emissions by a diesel oxidation catalyst (DOC), or using fuel-borne catalyst in diesel fuel [4].

Examining the thermo-physical properties of diesel particulates underlying the filtration and regeneration processes is quite important for DPF related studies. Fundamental research on PM emissions, such as characterization of particulate morphology, nano-structures, and detailed thermo-physical properties [6–8] has been extensively conducted. Based on these fundamental studies, Chiatti et al. performed DPF research in consideration of soot morphology [9]. And there have also been numerous DPF studies by computational modeling and experimental approach [10–12].

There have been very few studies on visualization of filtration and regeneration processes. Hanamura and co-workers visualized the regeneration process on a filter channel at a macro scale [13] and continued to work on micro-scale examinations for particulate trapping and soot oxidation in a filter membrane [14, 15]. In the literature, direct comparison between results from visualization and pressure drop across the filter sample was unavailable. Daido and Takagi [16] visualized filtration and regeneration processes for both cordierite and SiC filters at micro-scales, and analyzed correlations between the micro-images and pressure drop data. They successfully examined regeneration process at several different regeneration steps. In these studies, they analyzed filtration processes in a transition period from the deep-bed filtration to soot cake formation and relations between the amount of soot in the deep-bed filtration and the degree of regeneration. However, no information was available for the total mass of soot loading. NO_2 effects on soot oxidation were not examined in regeneration either.

In our study, filtration and regeneration processes were visualized on a 2-inch diameter 6-inch long cordierite filter by using a series of stereo-microscope and image acquisition system. Pressure drops across the filter membrane were also measured to correlate the visual observations with characteristics of filtration/regeneration processes. The regeneration characteristics were examined for both raw exhaust emissions and 1,000 ppm NO_2 -added exhaust emissions at different DPF inlet temperatures, where the effects of NO_2 and O_2 were evaluated. The DPF inlet temperature of exhaust emissions was control by a series of electric heater units. All these measurements were performed at a constant flow rate of exhaust emissions bypassed to the bench-scale DPF to simulate flow conditions in practical DPF systems.

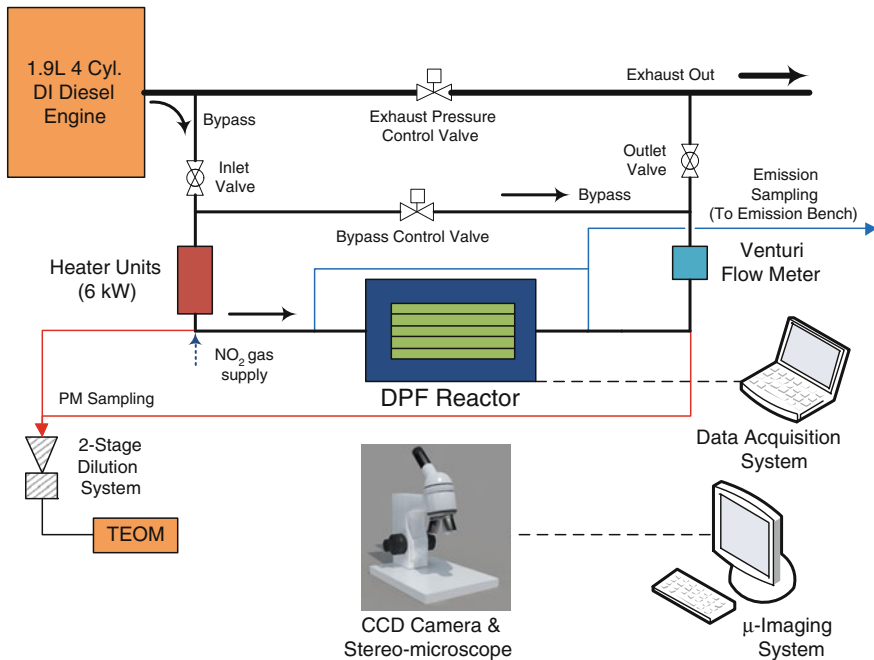


Fig. 1 Schematic of a bench-scale DPF test system

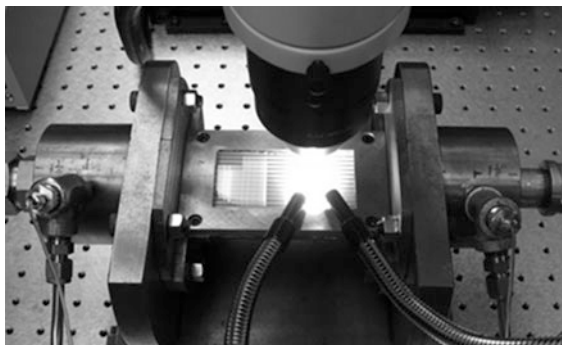
2 Experimental Setup and Conditions

2.1 Experimental Setup

A unique bench-scale DPF test system, equipped with an optically accessible DPF reactor and a micro-imaging system, has been built to conduct DPF filtration and regeneration tests. Figure 1 shows a schematic of the entire experimental setup. A 1.9 L 4-cylinder turbocharged direct injection diesel engine was used to carry out DPF experiments in real engine exhaust emission conditions. Exhaust emissions were bypassed from the main exhaust pipe of the engine to the DPF test system. During the entire filtration and regeneration experiments, the flow rate of emissions passing through the DPF maintained constant by means of an automatic control valve, communicating with a venturi flow meter via a controller. Electric heater units, which delivered a total power of 6 kW, were connected to the upstream of DPF reactor to raise the exhaust temperature for DPF regeneration. 1,000 ppm NO_2 gases were added to the downstream of the heater units to investigate the effect of NO_2 on soot oxidation process.

A bisected 2-inch diameter 6-inch long cordierite filter was placed in the DPF reactor, which was visualized through a 3-1/2 inch by 1-3/4 inch quartz window. Soot deposition and oxidation on the surfaces of incoming flow channels were

Fig. 2 A DPF reactor with a quartz visualization window and a stereo-microscope



visualized by the micro-imaging system, which consists of a stereo-microscope, a high resolution digital CCD camera, and image acquisition software. The high magnification real-time video images were recorded to a high capacity computer. Figure 2 shows the DPF reactor setup with a quartz window and a stereo-microscope, and the specifications of filter used in this research are listed in Table 1.

Temperatures at the inlet and outlet of DPF and pressure drops across the DPF were measured during both filtration and regeneration processes. The mass concentrations of particulate emissions crossing the DPF were also measured both upstream and downstream the DPF by a TEOM instrumented with a 2-stage particulate sampling/dilution system. And the total mass of soot loaded in the DPF was calculated by integrating the instantaneous soot mass concentrations measured above with respect to the constant emissions flow rate. In addition, the concentrations of gaseous emissions, such as NO_x , HC, CO, and O_2 , were measured by an emissions bench both upstream and downstream the DPF reactor.

2.2 Experimental Conditions

The light-duty diesel engine operated at a constant speed-load, 2,000 rpm-4.7 bar BMEP, so that the exhaust gas compositions (see Table 2) were maintained constant throughout the tests. Table 3 shows test conditions for the filtration and regeneration. During the filtration, the soot mass concentration in the constant exhaust emissions flow (12.46 kg/h) was measured to be 15.8 mg/m^3 , which is equivalent to that of a standard DPF ($\Phi 5.66 \text{ inch} \times \text{L6 inch}$) used in a practical system at the specific engine operating speed-load condition. Accordingly, the total soot mass per filter volume of 1.8–2.1 g/L was evaluated to be loaded in the DPF after the completion of a filtration. For DPF regenerations, three sets of oxidizing conditions were given: an O_2 -only regeneration case and two NO_2 -added regeneration cases at two different gas temperature conditions, as indicated in Table 3. For the O_2 -only regeneration, the exhaust emissions were heated up to

Table 1 DPF specifications

Substrate	Cordierite
Size	$\Phi 2'' \times L 6''$ half-cut
Cell density [cps]	200
Wall thickness [in]	0.012
Porosity [%]	48
Mean pore size [micron]	13

Table 2 Exhaust gas composition at the DPF inlet

THC [ppmC3]	24
CO [ppm]	140
NO _x /NO [ppm]	400/360
CO ₂ [vol %]	9.85
O ₂ [vol %]	9.8

over 500 °C at the DPF inlet. In the case of NO₂-added regenerations, a 10 vol % NO₂ gas in N₂ was supplied to the exhaust emissions so that the NO₂ concentration became 1,000 ppm at the DPF inlet. Indeed, the 1,000 ppm NO₂ concentration could be higher than those at typical diesel operating conditions, where a majority of NO_x emissions (>90 %) consists of NO. However, we considered the cases that our diesel engine produces high NO_x levels, such as high load or no EGR operating conditions that employ a diesel oxidation catalyst (DOC) system. DOCs are known to convert NO to NO₂, which enable us to examine NO₂ effects on DPF regeneration. With 1,000 ppm NO₂ added to the exhaust emissions, regeneration experiments were conducted at two different DPF inlet gas temperatures, 400 and 500 °C. The mass flow rate of the exhaust gas passing through the DPF was also fixed to 12.46 kg/hr for all regeneration cases.

3 Result and Discussion

3.1 Filtration Process

During the filtration, measured pressure drops and soot loading mass were synchronized with the soot loading images to be able to correlate with actual soot loading conditions. The graph in Figure 3 shows pressure drops by soot loading, which were normalized by the volume flow rate of incoming exhaust emissions. The flow rate was measured in each filtration range. The soot loading images corresponding to specific filtration condition (marked on the pressure drop trace) are displayed in the lower part of Fig. 3.

As also discussed in other studies [4], three distinct filtration stages were clearly identified during the filtration experiment in this work; deep-bed filtration, transition filtration, and soot cake formation. When the exhaust emissions pass through

Table 3 Filtration and regeneration test conditions

Filtration	Soot conc. [mg/m^3 @ std.]	15.8
	Total soot mass loaded [g/L]	1.8–2.1
	DPF inlet temp. [$^{\circ}\text{C}$]	150–200
	Mass flow rate [kg/h]	12.46
	Avg. Space Velocity [h^{-1}]	88,683
O_2 -regeneration	O_2 conc. [vol %]	9.8
	DPF inlet temp. [$^{\circ}\text{C}$]	500–540
	Mass flow rate [kg/h]	12.46
	Space Velocity [h^{-1}]	142,510
NO_2 -added Regeneration	NO_2 conc. [ppm]	1,000
	DPF inlet temp. [$^{\circ}\text{C}$]	400/500
	Mass flow rate [kg/h]	12.46
	Space Velocity [h^{-1}]	121,767/142,510

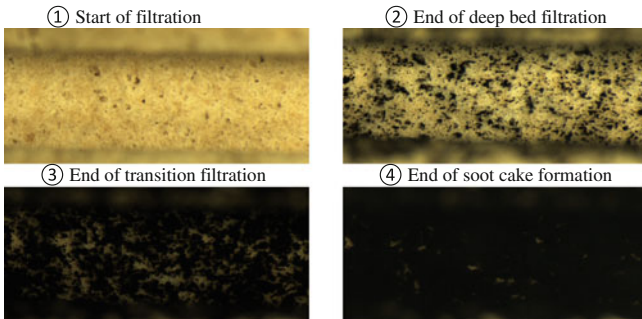
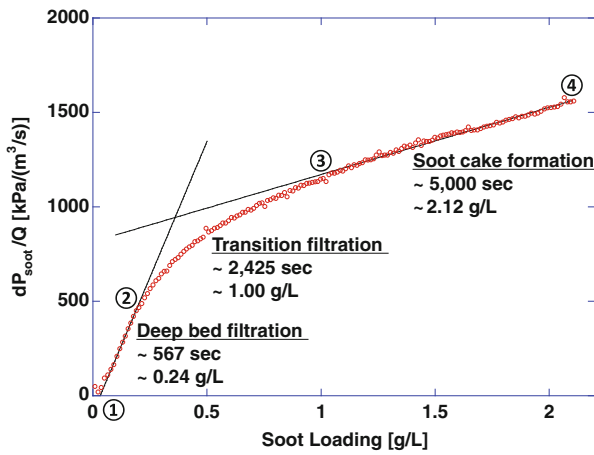


Fig. 3 Pressure drop trace during filtration process and visualization images at different filtration stages

the clean filter (①), soot particles in the exhaust emissions are first deposited in the filter walls, filling the effective pores initially open. During this deep-bed filtration, the pressure drop dramatically increases in linear tendency with respect to the soot loading mass, resulting in a large number of black spots remaining on the effective pores in filter walls at the end of this stage, due to the soot filtration. However, the amount of soot loading in this period is fairly small (0.24 g/l), compared to those in other filtration periods. The image ② shows this loaded soot at the end of deep-bed filtration stage, where almost all the effective pores appear to be clogged. A transitional period in filtration takes place after completion of the deep-bed filtration but before start of soot cake formation. In this period, the pressure drop linearity shown in the deep-bed filtration period is transformed to a parabolic curve, where the pressure drop increases at lower rates. This period maintains a nearly same order of time period as the initial deep-bed filtration period. The image ③ shows the soot deposition at the end of transitional filtration period. With further filtration, the filter wall surfaces are fully covered by soot to form soot cake, in which the pressure drop increase gradually in a linear fashion. A total of 2.12 g/l soot was loaded for 5,000 s of the entire filtration. The soot loading image at the end of entire filtration processes is displayed in the image ④. The information for time and soot loading mass measured in this experimental work can be used to validate data from simulation or modelling studies, while the soot loading images will also be useful to help researchers understand the DPF filtration process.

3.2 Regeneration Process

The soot oxidation phenomena during regeneration were observed in detail in association with the measured pressure drops synchronized with soot oxidation images. The graph in Fig. 4 shows the pressure drop trace plotted with respect to regeneration time. The corresponding soot oxidation images are also displayed at each regeneration stage in the figure, with the same numbering on the pressure drop curve.

Three distinct regeneration stages were identified, each of which involves a linear pressure drop period. In the first regeneration stage (①→②), the pressure drop decreased at a moderate rate, while no noticeable change was observed in terms of soot cake configuration. Daido et al. [16] referred to this stage as “Before PM Oxidation”, because no noticeable pressure drop change was identified in his research. In our study, however, the moderate decrease of pressure drop observed in the first stage must be caused by soot oxidation. The image ② shows that the filter channel surface still appears to be fully covered with soot cake until the first regeneration stage overs. This signifies that a majority of the effective pores maintain closed by soot in the pores and soot cake on the channel surface, while soot oxidation, as indicated by the reduction in pressure drop, still occurs in the

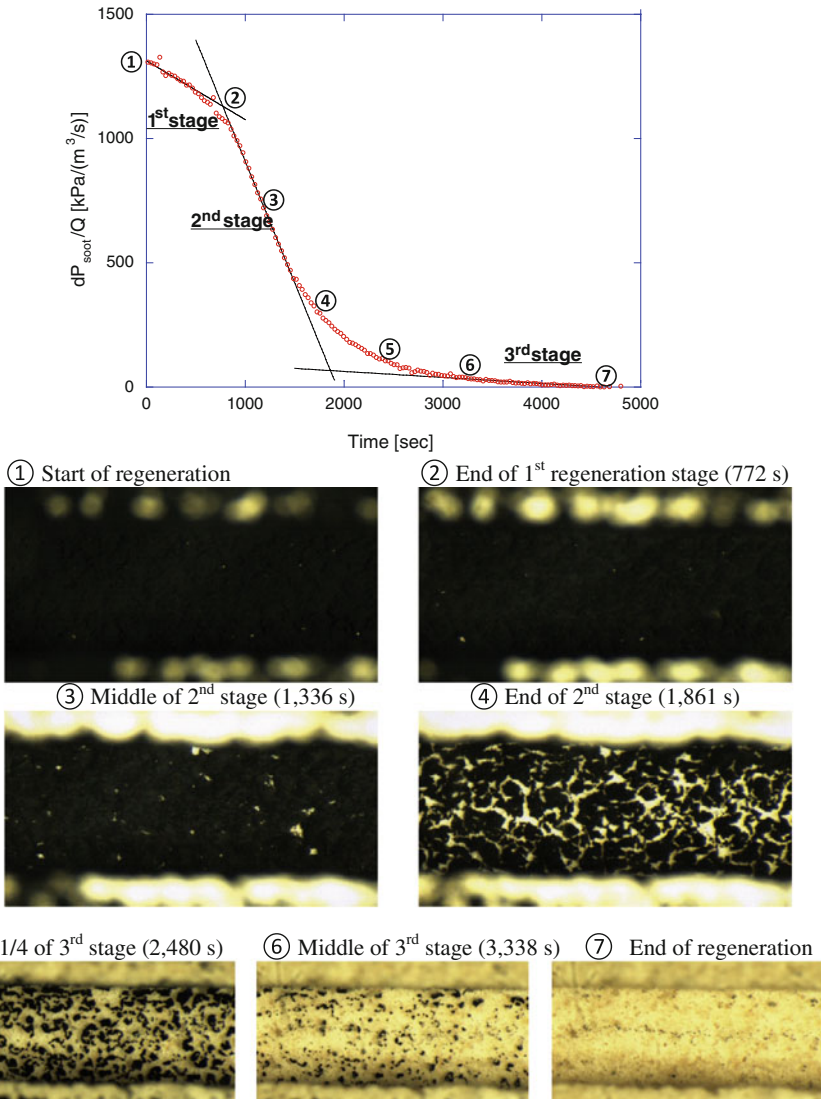


Fig. 4 Pressure drop trace during regeneration and visualization images at different regeneration stages (1,000 ppm NO₂-added; DPF inlet temperature of 400 °C)

pores with a loss of soot cake thickness. Therefore, permeability in the walls should increase, resulting in a moderate decrease of pressure drop.

Further soot oxidation finally starts to open the pores in the second stage (see the image ③), which indicates some removal of soot both in the pores and on the channel surface. In this period, the pressure drop decreases significantly because the wall permeability should have increased at a high level. While this second

regeneration stage continues to proceed to the end, the pores further open and lead to a dramatic linear decrease of pressure drop (② → ③ → ④). The number of open pores, initially shown on the soot cake (image ③), dramatically increased at the end of this second stage, as shown in the image ④. In the transition from the second to third stage, a majority of pores looked open and soot cake oxidation proceeded to quite a bit high level (image ⑤). In the final third stage, only some portion of soot cake seems to remain on the channel (image ⑤) and the remaining soot cake further oxidizes to the completion of regeneration (image ⑥), returning to the near initial condition of clean filter (image ⑦). It is interesting to note that the pressure drop decreases quite gradually with time (⑤ → ⑥ → ⑦ in the graph), although a majority of soot cake deposited on the channel surface oxidizes in this period.

3.3 Effects of Various Gaseous-Emissions Conditions on Regeneration

Regeneration tests were conducted under three different exhaust gas conditions: 9.8 vol % O₂ (existing in the exhaust emissions) at 500 °C, and 1,000 ppm NO₂-added at two different temperatures, 400 and 500 °C. NO₂ gases are known to be an oxidant more reactive than O₂ for soot, which can reduce the oxidation temperature by the lowered activation energy and finally promote soot oxidation in a passive way of DPF regeneration. The graph shown in Fig. 5 exhibits pressure drop traces for the three different regeneration conditions. All the three regeneration experiments showed three distinct regeneration stages as shown above, regardless the emissions conditions. To find the correlations of these 3-stage regenerations between the different exhaust compositions, we compared visualization images at three different regeneration stages for raw exhaust emissions (9.8 vol % O₂ at 500°C) (①-②-③) and 1,000 ppm NO₂-added emissions (at 400 °C) (①'-②'-③'). The numberings ①-②-③ and ①'-②'-③' stand for the status at several seconds after the start of 2nd stage (① and ①'), at the end of the second linear pressure drop stage (② and ②'), and before the end of third stage, respectively. Corresponding soot oxidation images are also displayed in the Fig. 5

Results show that the soot images are quite similar between the two corresponding inlet conditions at the same regeneration stages (①-①', ②-②', and ③-③'). These qualitative observations indicate that the actual soot oxidation characteristics can be well correlated at each regeneration stage identified by the pressure drop, regardless inlet gas conditions. A noticeable result is that the degree of oxidation rate appears to be quite a bit higher with NO₂-added emissions than does with 9.8 vol % O₂ emissions, indicated by the higher gradient of pressure drops, distinctive particularly in the stage 2. This behavior is verified by the quantifications of oxidation times as below.

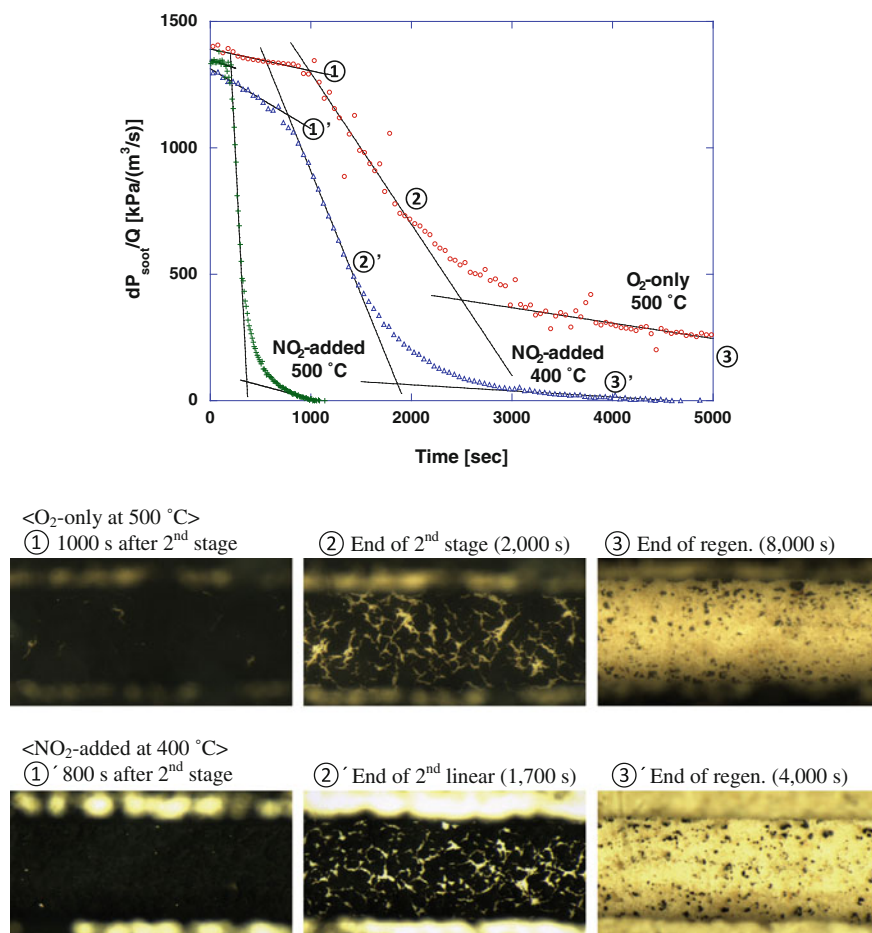


Fig. 5 Pressure drop traces during regeneration process under three different inlet gas conditions and visualization images for regeneration with 9.8 vol % O₂ emissions at 500 °C and 1,000 ppm NO₂-added emissions at 400 °C

Table 4 lists the total regeneration time and the time duration in each regeneration stage, calculated based on the recorded video images. With 9.8 vol % O₂ emissions at 500 °C, the entire regeneration took almost two and half hours (9,042 s) to complete the oxidation of about 2 g/L soot deposit. However, the 1,000 ppm NO₂-added emissions accelerated the regeneration at a much higher rate (regeneration time of 1,072 s), which simply indicates an about nine (9) times higher oxidation rate. Even at the lower temperature condition of 400 °C, the NO₂-added emissions enhanced regeneration at an almost two (2) times higher rate than did O₂-only emissions at 500 °C.

Table 4 Regeneration times (seconds) calculated for each inlet gas condition

	9.8 vol % O ₂ @ 500 °C	NO ₂ -added @ 400 °C	NO ₂ -added @ 500 °C
1st stage	982	772	206
2nd stage	1,518	1,089	157
3rd stage	6,541	2,751	709
Total	9,042	4,612	1,072

4 Conclusions

The filtration and regeneration processes of bare cordierite filters were investigated in detail by means of microscopic visualization, along with the measurement of pressure drops across the DPF. The regeneration was performed under three different gas conditions, including the presence of NO₂ at two temperatures of 400 and 500 °C as well as the raw exhaust emissions. The results showed detailed soot loading and oxidation behaviors in relation with filter pressure drop characteristics.

1. Three consecutive filtration stages were clearly identified: deep-bed filtration, transition filtration, and soot cake formation. Each stage illustrated the filtration process in sequence, such that the deep-bed filtration created a high degree of linear gradient in the pressure drop and the gradual increase of pressure drop indicated the soot cake formation on the filter channels, while a transitional period exists between the two filtration periods.
2. Three distinct regeneration stages were identified, each of which showed a linear fitting line for the pressure drop curve. In the first stage, soot oxidation occurred in deep pores as well as on the wall surface. In the visual observation, the effective pores were still clogged by soot but the pressure drop across the filter gradually decreased in a linear fashion, indicating a potential increase of soot permeability in the wall. The second stage was revealed to have a highest rate of pressure drop, attributed to the continuous opening of effective pores identified on the soot cake surfaces. Finally, the remaining soot cake was completely cleaned up in the third regeneration stage, while the pressure drop decreased gradually to the end.
3. The regeneration experiments with three different inlet gas conditions (O₂-only and NO₂-added emissions) illuminated that corresponding soot oxidation behaviors were quite similar, as indicated by a similar 3-stage pressure drop trace, regardless of inlet gas condition. These behaviors were also proved by the microscopic visualization images.
4. NO₂ significantly promoted soot oxidation in regeneration. The 1,000 ppm NO₂ addition to the exhaust emissions completely oxidized the loaded soot at a nine (9) times higher rate than did raw exhaust emissions at 500 °C.

Acknowledgments This work is supported by the Advanced Engine Combustion Program operated by the U. S. Department of Energy.

References

1. DieselNet Website: <http://www.dieselnet.com/standards/eu/ld.php>
2. Khair M (2003) A review of diesel particulate filter technologies. SAE technical paper 2003-01-2303
3. Konstandopoulos AG, Papaioannou E (2008) Update on the science and technology of diesel particulate filters. *KONA Powder Part J* 26:36–65
4. Zhang Z, Yang SL, Johnson JH (2002) Modeling and numerical simulation of diesel particulate trap performance during loading and regeneration. SAE technical paper 2002-01-1019
5. Tandon P, Heibel A, Whitmore J, Kekre N, Chithapragada K (2010) Measurement and prediction of filtration efficiency evolution of soot loaded diesel particulate filters. *Chem Eng Sci* 65:4751–4760
6. Lee KO, Zhu J, Ciatti SA, Yozgatligil A, Choi MY (2003) Sizes, graphitic structures and fractal geometry of light-duty diesel engine particulates. SAE technical paper 2003-01-3169
7. Lee KO, Zhu J (2004) Evolution in size and morphology of diesel particulates along the exhaust system. SAE technical paper 2004-01-1981
8. Lee KO, Zhu J (2005) Effects of exhaust system components on particulate morphology in a light-duty diesel engine. SAE technical paper 2005-01-0184
9. Chiatti G, Chiavola O, Falcucci G (2009) Soot morphology effects on DPF performance. In: Presented at SAE World Congress. 2009-01-1279
10. Konstandopoulos AG, Kostoglou M, Skaperdas E, Papaioannou E, Zarvalis D, Kladopoulou E (2000) Fundamental studies of diesel particulate filters: transient loading, regeneration and aging. SAE technical paper 2000-01-1016
11. Konstandopoulos AG, Kostoglou M, Vlachos N, Kladopoulou E (2005) Progress in diesel particulate filter simulation. SAE technical paper 2005-01-0946
12. Haralampous O, Koltsakis G, Samaras Z, Vogt C et al (2004) Reaction and diffusion phenomena in catalyzed diesel particulate filters. SAE technical paper 2004-01-0696
13. Hanamura K, Suzuki T, Tanaka T, Miyairi Y (2003) Visualization of combustion phenomena in regeneration of diesel particulate filter. SAE technical paper 2003-01-0836
14. Tsuruta T, Hanamura K (2007) Visualization study of PM trapping and reaction phenomena in micro-structural pores through cross section of DPF wall. SAE technical paper 2007-01-0917
15. Karin P, Cui L, Rubio P, Tsuruta T, Hanamura K (2009) Microscopic visualization of PM trapping and regeneration in micro-structural pores of a DPF wall. 2009-01-1476
16. Daido S, Takagi N (2009) Visualization of the PM deposition and oxidation behavior inside the DPF wall. 2009-01-1473